Lawrence Berkeley National Laboratory
LBL Publications

Title

Selected Works of L. Jackson Laslett Volume III

Permalink

https://escholarship.org/uc/item/9z62s87k

Author

Lawrence Berkeley National Laboratory

Publication Date

1987-09-01

Copyright Information

This work is made available under the terms of a Creative Commons Attribution License, available at https://creativecommons.org/licenses/by/4.0/

eScholarship.org Powered by the California Digital Library
University of California

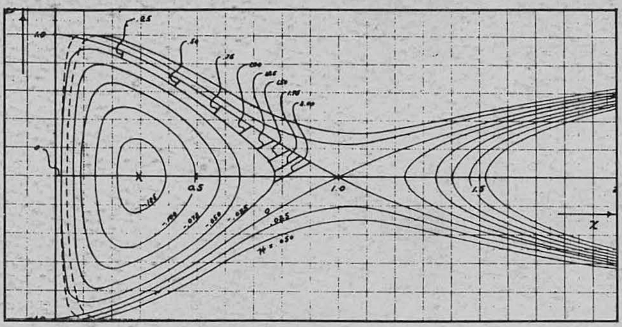

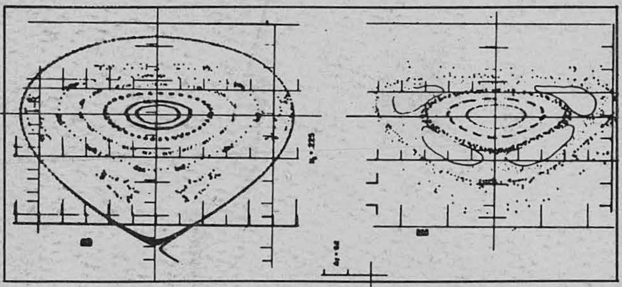

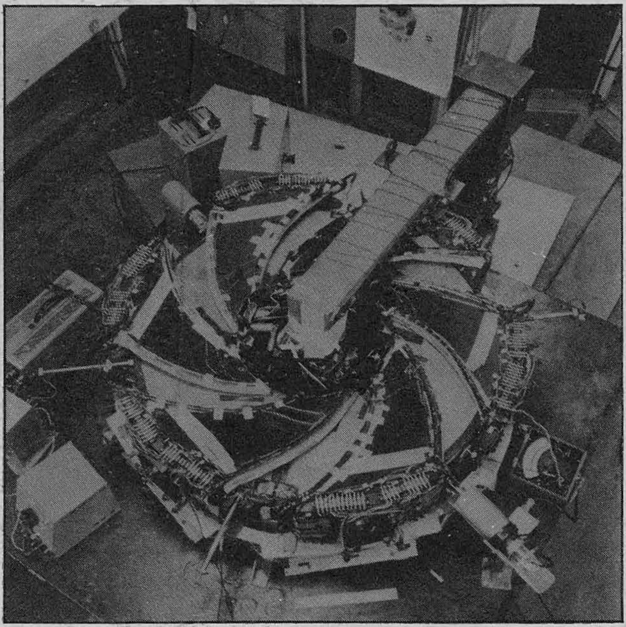

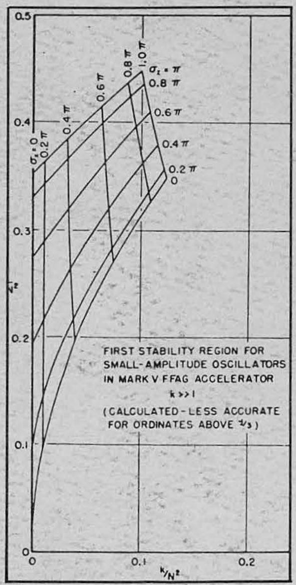

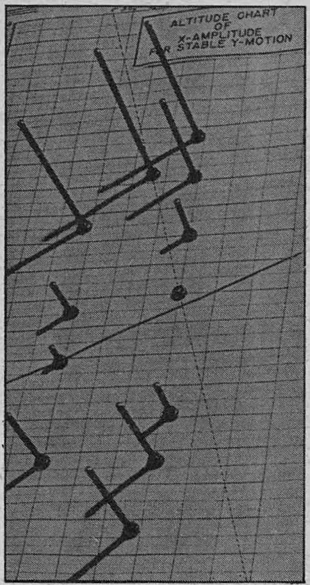

PUB-616
Volume III
September 1987

RECEIVED
LAWRENCE
BERKELEY LABORATORY

OCT 6 1987

LIBRARY AND
DOCUMENTS SECTION

Selected Works of L. Jackson Laslett

Lawrence Berkeley Laboratory
University of California
Berkeley, California 94720

Prepared for the U.S. Department of Energy
under Contract DE-AC03-76SF00098

PUB-616 v.3 c.1

DISCLAIMER

This document was prepared as an account of work sponsored by the United States Government. While this document is believed to contain correct information, neither the United States Government nor any agency thereof, nor the Regents of the University of California, nor any of their employees, makes any warranty, express or implied, or assumes any legal responsibility for the accuracy, completeness, or usefulness of any information, apparatus, product, or process disclosed, or represents that its use would not infringe privately owned rights. Reference herein to any specific commercial product, process, or service by its trade name, trademark, manufacturer, or otherwise, does not necessarily constitute or imply its endorsement, recommendation, or favoring by the United States Government or any agency thereof, or the Regents of the University of California. The views and opinions of authors expressed herein do not necessarily state or reflect those of the United States Government or any agency thereof or the Regents of the University of California.

PUB-616
Volume III
September 1987

Selected Works of L. Jackson Laslett

Lawrence Berkeley Laboratory
University of California
Berkeley, California 94720

Prepared for the U.S. Department of Energy under Contract DE-AC03-76SF00098

Table of Contents

Volume I

Volume II

Section 1: Single Particle Dynamics in Fixed Field Alternating Gradient Accelerators

Formal Publications

MURA Notes and Other Documents

Section 2: Magnets and Magnetic Fields

Section 3: Electromagnetism - Image Forces in Presence of Boundaries, etc

Volume III

Section 4: Coherent Collective Instabilities

Section 5. Impedances

Section 6. Beam Transport for Heavy Ion Fusion

Section 7. Nonlinear Dynamics, Stochasticity, Stochastic Diffusion and All That

Section 8. Other Research Fields

3

Electromagnetism – Image Forces in Presence of Boundaries, etc.

(Continued from volume II)

IMAGE FIELD OF A STRAIGHT BEAM OF ELLIPTICAL CROSS-SECTION*

-- Sequel --

L. Jackson Laslett

19 January 1970

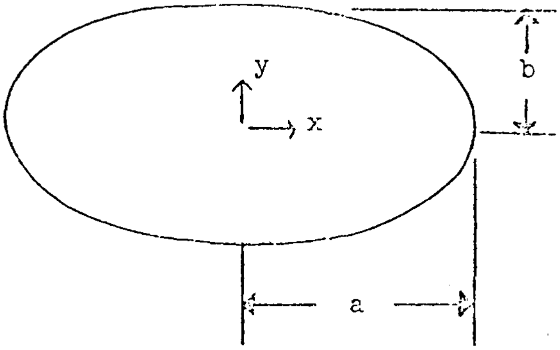

1. The electrostatic image-field coefficient for an extended straight beam, of constant density throughout and of elliptical cross-section, has been discussed in ERAN-49. In that report an infinite plane conducting boundary surface was taken to be at y = - h with respect to the centre of the beam, and the image fields were examined along an axis that passes through the centre of the beam and is parallel to the conducting sheet.

The non-linearity of E_x _vs._ x was found to be not so pronounced but that one might, in the interest of convenience, employ simply the coefficient ϵ_1 evaluated at the _centre_ of the beam. In this spirit we note here that one can easily evaluate, in closed form, this quantity

$$\epsilon_1 \equiv \frac{h^2}{4\lambda} \frac{\partial E_x^{(Im)}}{\partial x}$$

$$= \frac{h^2}{4\lambda} \left(- \frac{\partial E_y^{(Im)}}{\partial y} \right)$$ at the centre of the beam,

namely at y = + 2h if the origin is now shifted to the centre of the elliptical image-charge distribution (λ e.s.u. per cm). For this purpose we refer to the formula

$$E_y = 4\pi\rho \frac{ab}{a^2 - b^2} \left[\sqrt{y^2 + a^2 - b^2} - y \right]$$ (contd)

---

* Work supported by the U.S. Atomic Energy Commission.

$$= \frac{4\lambda}{a^2 - b^2} \left[\sqrt{y^2 + a^2 - b^2} - y \right]$$

given (for $x = 0$, $y \geq b$) on p. 5 of ERAN-44*.

By differentiation we now find

$$- \frac{\partial E_y}{\partial y} = \frac{4\lambda}{a^2 - b^2} \left[1 - \frac{y}{\sqrt{y^2 + a^2 - b^2}} \right]$$

and

$$- \frac{\partial E_y{}^{(Im)}}{\partial y} \Bigg]_{\substack{\text{Beam}\\ \text{Centre}}} = \frac{4\lambda}{a^2 - b^2} \left[1 - \frac{2h}{\sqrt{4h^2 + a^2 - b^2}} \right] .$$

Hence, based on the field gradients at the centre of the beam,

$$\begin{aligned} \epsilon_1 &= \frac{h^2}{4\lambda} \left(- \frac{\partial E_y{}^{(Im)}}{\partial y} \right) \\ &= \frac{h^2}{a^2 - b^2} \left[1 - \frac{2h}{\sqrt{4h^2 + a^2 - b^2}} \right] \\ &= \frac{h^2}{F^2} \left[1 - \left(1 + \frac{F^2}{4h^2}\right)^{-\frac{1}{2}} \right] , \end{aligned}$$

where we have written

$$F = \sqrt{a^2 - b^2} .$$

In the form of a series development,

$$\begin{aligned} \epsilon_1 &= \frac{1}{8} \sum_{m=0}^{\infty} (-1)^m \frac{(2m+1)!}{2^{4m}\, m!\,(m+1)!} \left(\frac{F^2}{h^2} \right)^m \\ &= \frac{1}{8} \left[1 - \frac{3}{16} \frac{F^2}{h^2} + \frac{5}{128} \frac{F^2}{h^4} - \cdots \right] . \end{aligned}$$

Thus, for $h \gg F$, ϵ_1 tends toward the value $\epsilon_1 \cong \frac{1}{8}$.

---

* *Cf*. Eqn. (32) of L. C. Teng, ANLAD-59 (1953).

Numerical values of ϵ_1 are listed below, for a few values of h, when computed in this manner for beams with a = 1.0 and b = 0.4 or 0.5.

ϵ_1 AT THE CENTRE OF AN ELLIPTICAL BEAM

$\left.\begin{array}{l} a = 1.0 \\ b = 0.4 \end{array}\right\} F^2 = 0.84$ $\qquad$ $\left.\begin{array}{l} a = 1.0 \\ b = 0.5 \end{array}\right\} F^2 = 0.75$

h	ϵ_1	h	ϵ_1
2.0	0.120284	2.0	0.120770
1.5	0.116879	1.5	0.117693
1.0	0.108225	1.0	0.109783
0.75	0.098223	0.75	0.100481
0.50	0.078211	0.50	0.081357
0.40	0.065220	——	——

2. The work discussed up to this point has been for a conducting surface that is parallel to the <u>major</u> axis of the elliptical charge distribution, and hence is appropriate for application near "spill out" when the greater of the semi-axes (here denoted by "a") is in the z-direction. For generality, in the interests of completeness, one may wish to obtain results that are derived in the spirit of paragraph 1 above but that consider the image surface to be parallel to the <u>minor</u> axis (b) of the beam. One may presume that the result for ϵ_1 will be an analytic function of the beam parameters, a and b, but the following explicit derivation may be appropriate as a check.

Accordingly, we now take the x and y semi-axes to be a and b respectively, with a > b as before, and locate a similar image distribution of opposite sign (+λ e.s.u. per cm) a distance 2h to the <u>left</u> of the beam. We then need to evaluate the derivative $-\dfrac{\partial E_x^{(Im)}}{\partial x}$ of the image field at a point x = 2h,

```
> T
   01/17/73   13.27.38

L
    1.                DIMENSION H(6)
    2.                H(1)  =  2.0
    3.                H(2)  =  1.5
    4.                H(3)  =  1.0
    5.                H(4)  =  0.75
    6.                H(5)  =  0.50
    7.                H(6)  =  0.40
    8.        10      READ, A, B
    9.                PRINT07, A, B
   10.                IF (B .GT. A) GO TO 10
   11.                FS = A*A - B*B
   12.                F = SQRT(FS)
   13.                PRINT13, F
   14.                M = 6
   15.                IF (B .GT. H(6)) GO TO 40
   16.        20      DO 30 I=1,M
   17.                R = FS/(H(I)*H(I))
   18.                EPS = (1 - 1/SQRT(1 + R/4))/R
   19.                PRINT10, H(I), EPS
   20.        30      CONTINUE
   21.                GO TO 10
   22.        40      M = M - 1
   23.                GO TO 20
OK

↑XEQ
 BEGIN XEQ

 ENTER... A, B,
1.0,0.4

  A= 1.000  B= 0.400
  F= 0.916515139
  H(1)= 2.000000  EPS= 0.120284
  H(2)= 1.500000  EPS= 0.116879
  H(3)= 1.000000  EPS= 0.108225
  H(4)= 0.750000  EPS= 0.098223
  H(5)= 0.500000  EPS= 0.078211
  H(6)= 0.400000  EPS= 0.065220

 ENTER... A, B,
1.0,0.5

  A= 1.000  B= 0.500
  F= 0.866025404
  H(1)= 2.000000  EPS= 0.120770
  H(2)= 1.500000  EPS= 0.117693
  H(3)= 1.000000  EPS= 0.109783
  H(4)= 0.750000  EPS= 0.100481
  H(5)= 0.500000  EPS= 0.081357
```

y = 0 with respect to the centre of this image-charge distribution. Again we write

$$F = \sqrt{a^2 - b^2}$$

and employ the results of ERAN-44.

Along the positive x-axis (y = 0) we have $u = \frac{\pi}{2}$, so

$$x = F \operatorname{Cosh} v.$$

Also (ERAN-44, p.4), since then cos 2u = -1, the exterior potential of the image is

$$\Phi = -\lambda(2v + \epsilon^{-2v})$$

at points along the x-axis, and

$$\begin{aligned} E_x &= 2\lambda(1 - e^{-2v})\frac{dv}{dx} \\ &= \frac{2\lambda}{F}\,\frac{1 - e^{-2v}}{\operatorname{Sinh} v} \\ &= \frac{4\lambda}{F}\,\epsilon^{-v} , \end{aligned}$$

$$\begin{aligned} \frac{\partial E_x}{\partial x} &= -\,\frac{4\lambda}{F}\,e^{-v}\,\frac{dv}{dx} \\ &= -\,\frac{4\lambda}{F^2}\,\frac{e^{-v}}{\operatorname{Sinh} v} \\ &= -\,\frac{8\lambda}{F^2}\,\frac{1}{e^{2v} - 1} . \end{aligned}$$

Solving the equation 2h = F Cosh v for the value of the curvilinear coördinate v at the centre of the beam, we find

$$e^{\pm v} = \frac{2h}{F}\left[1 \pm \sqrt{1 - (\tfrac{F}{2h})^2}\,\right]$$

and

$$e^{\pm 2v} = 2(\tfrac{2h}{F})^2\left[1 \pm \sqrt{1 - (\tfrac{F}{2h})^2}\,\right] - 1.$$

Accordingly,

$$\left.\frac{\partial E_x^{(Im)}}{\partial x}\right|_{\substack{\text{Beam}\\ \text{Centre}}} = -\,\frac{\lambda}{h^2}\cdot\frac{1}{1 + \sqrt{1 - (\frac{F}{2h})^2} - (\frac{F}{2h})^2} \qquad \text{(contd)}$$

$$= -\frac{4\lambda}{F^2}\left\{\left[1-\left(\frac{F}{2h}\right)^2\right]^{-\frac{1}{2}} - 1\right\}.$$

Hence, finally,

$$\epsilon_1 \equiv \frac{h^2}{4\lambda}\left[-\frac{\partial E_x^{(Im)}}{\partial x}\right]$$

$$= \frac{h^2}{F^2}\left[\left(1-\frac{F^2}{4h^2}\right)^{-\frac{1}{2}} - 1\right]$$

$$\doteq \frac{1}{8}\left[1 + \frac{3}{16}\frac{F^2}{h^2} + \frac{5}{128}\frac{F^4}{h^4} + \cdots\right],$$

with

$$F = \sqrt{a^2 - b^2} .$$

SUMMARY

To adapt these results to the customary notation, in which "b" refers to the axial semi-axis and "a" refers to the radial semi-axis, write

$$F = \sqrt{|a^2 - b^2|} .$$

then, at the centre of the beam, we obtain

If $a > b$:

$$\epsilon_1 = \frac{h^2}{F^2}\left[\left(1-\frac{F^2}{4h^2}\right)^{-\frac{1}{2}} - 1\right]$$

$$\doteq \frac{1}{8}\left[1 + \frac{3}{16}\frac{F^2}{h^2} + \frac{5}{128}\frac{F^4}{h^4} + \cdots\right];$$

If $a < b$:

$$\epsilon_1 = \frac{h^2}{F^2}\left[1 - \left(1+\frac{F^2}{4h^2}\right)^{-\frac{1}{2}}\right]$$

$$\doteq \frac{1}{8}\left[1 - \frac{3}{16}\frac{F^2}{h^2} + \frac{5}{128}\frac{F^4}{h^4} - \cdots\right].$$

In either case, then, we may write the electrostatic image coefficient at the centre of the elliptical beam as

$$\epsilon_1 = \frac{h^2}{a^2 - b^2}\left[\left(1 - \frac{a^2 - b^2}{4h^2}\right)^{-\frac{1}{2}} - 1\right],$$

where

a = radial semi-axis

and

b = axial semi-axis,

while h denotes the radial clearance from the centre of the beam to the conducting boundary (assumed to be essentially plane).

Numerical values of ϵ_1 (denoted EPS1) are presented on the following sheets,* for various values of b and h in units of the radial semi-axis "a" $(a = 1,\ h \geq a)$.

It is noted that for $a > b$, the values of ϵ_1 will exceed $\frac{1}{8}$ since, physically, a portion of the image-charge distribution is relatively close to the centre of the beam. For $a = b$, $\epsilon_1 = \frac{1}{8} = 0.125$ under the present assumptions of a straight beam and a plane boundary.

---

* It will be recalled that the notation of the previous computational results, presented on p.4 of this report (ERAN-49-bis), interchanges the significance of the semi-axes a, b. Thus those earlier runs correspond, in the present notation, to b equal to 2.5 or 2.0, respectively, with h decreasing from 5.0 to 1.0 or from 4.0 to 1.0 in the two cases shown.

```
> T
  01/19/78   13.41.04

↑XEQ
 BEGIN XEQ

  A= 1.000000   B= 0.100000   H= 1.000000   EPS1= 0.154324
  A= 1.000000   B= 0.100000   H= 1.200000   EPS1= 0.143332
  A= 1.000000   B= 0.100000   H= 1.400000   EPS1= 0.138239
  A= 1.000000   B= 0.100000   H= 1.600000   EPS1= 0.134862
  A= 1.000000   B= 0.100000   H= 1.800000   EPS1= 0.132650
  A= 1.000000   B= 0.100000   H= 2.000000   EPS1= 0.131117
  A= 1.000000   B= 0.100000   H= 2.200000   EPS1= 0.130066
  A= 1.000000   B= 0.100000   H= 2.400000   EPS1= 0.129173
  A= 1.000000   B= 0.100000   H= 2.600000   EPS1= 0.128541
  A= 1.000000   B= 0.100000   H= 2.800000   EPS1= 0.128040
  A= 1.000000   B= 0.100000   H= 3.000000   EPS1= 0.127639
  A= 1.000000   B= 0.100000   H= 3.200000   EPS1= 0.127313
  A= 1.000000   B= 0.100000   H= 3.400000   EPS1= 0.127044
  A= 1.000000   B= 0.100000   H= 3.600000   EPS1= 0.126819
  A= 1.000000   B= 0.100000   H= 3.800000   EPS1= 0.126630
  A= 1.000000   B= 0.100000   H= 4.000000   EPS1= 0.126469
  A= 1.000000   B= 0.100000   H= 4.200000   EPS1= 0.126331
  A= 1.000000   B= 0.100000   H= 4.400000   EPS1= 0.126211
  A= 1.000000   B= 0.100000   H= 4.600000   EPS1= 0.126107
  A= 1.000000   B= 0.100000   H= 4.800000   EPS1= 0.126016
 PAUSING
↑GO, 10
  A= 1.000000   B= 0.100000   H= 5.000000   EPS1= 0.125936

  A= 1.000000   B= 0.200000   H= 1.000000   EPS1= 0.153207
  A= 1.000000   B= 0.200000   H= 1.200000   EPS1= 0.143165
  A= 1.000000   B= 0.200000   H= 1.400000   EPS1= 0.137792
  A= 1.000000   B= 0.200000   H= 1.600000   EPS1= 0.134537
  A= 1.000000   B= 0.200000   H= 1.800000   EPS1= 0.132433
  A= 1.000000   B= 0.200000   H= 2.000000   EPS1= 0.130922
  A= 1.000000   B= 0.200000   H= 2.200000   EPS1= 0.129855
  A= 1.000000   B= 0.200000   H= 2.400000   EPS1= 0.129047
  A= 1.000000   B= 0.200000   H= 2.600000   EPS1= 0.128430
  A= 1.000000   B= 0.200000   H= 2.800000   EPS1= 0.127945
  A= 1.000000   B= 0.200000   H= 3.000000   EPS1= 0.127557
  A= 1.000000   B= 0.200000   H= 3.200000   EPS1= 0.127241
  A= 1.000000   B= 0.200000   H= 3.400000   EPS1= 0.126981
  A= 1.000000   B= 0.200000   H= 3.600000   EPS1= 0.126763
  A= 1.000000   B= 0.200000   H= 3.800000   EPS1= 0.126580
  A= 1.000000   B= 0.200000   H= 4.000000   EPS1= 0.126424
  A= 1.000000   B= 0.200000   H= 4.200000   EPS1= 0.126290
  A= 1.000000   B= 0.200000   H= 4.400000   EPS1= 0.126174
  A= 1.000000   B= 0.200000   H= 4.600000   EPS1= 0.126073
  A= 1.000000   B= 0.200000   H= 4.800000   EPS1= 0.125985
  A= 1.000000   B= 0.200000   H= 5.000000   EPS1= 0.125907

  A= 1.0000^00  B= 0.300000   H=
                                1.000000   EPS1= 0.151335
  A= 1.000000   B= 0.300000   H= 1.200000   EPS1= 0.142673
  A= 1.000000   B= 0.300000   H= 1.400000   EPS1= 0.137154
  A= 1.000000   B= 0.300000   H= 1.600000   EPS1= 0.134005
  A= 1.000000   B= 0.300000   H= 1.800000   EPS1= 0.131993
```

```
A=  1.000000   B=  0.300000   H=  2.000000   EPS1=  0.130596
A=  1.000000   B=  0.300000   H=  2.200000   EPS1=  0.129537
A=  1.000000   B=  0.300000   H=  2.400000   EPS1=  0.128589
A=  1.000000   B=  0.300000   H=  2.600000   EPS1=  0.128044
A=  1.000000   B=  0.300000   H=  2.800000   EPS1=  0.127750
A=  1.000000   B=  0.300000   H=  3.000000   EPS1=  0.127481
A=  1.000000   B=  0.300000   H=  3.200000   EPS1=  0.127122
A=  1.000000   B=  0.300000   H=  3.400000   EPS1=  0.126874
A=  1.000000   B=  0.300000   H=  3.600000   EPS1=  0.126676
A=  1.000000   B=  0.300000   H=  3.800000   EPS1=  0.126497
A=  1.000000   B=  0.300000   H=  4.000000   EPS1=  0.126349
A=  1.000000   B=  0.300000   H=  4.200000   EPS1=  0.126222
A=  1.000000   B=  0.300000   H=  4.400000   EPS1=  0.126113
A=  1.000000   B=  0.300000   H=  4.600000   EPS1=  0.126017
A=  1.000000   B=  0.300000   H=  4.800000   EPS1=  0.125933
A=  1.000000   B=  0.300000   H=  5.000000   EPS1=  0.125860


A=  1.000000   B=  0.400000   H=  1.000000   EPS1=  0.143914
A=  1.000000   B=  0.400000   H=  1.200000   EPS1=  0.140576
A=  1.000000   B=  0.400000   H=  1.400000   EPS1=  0.136635
A=  1.000000   B=  0.400000   H=  1.600000   EPS1=  0.133257
A=  1.000000   B=  0.400000   H=  1.800000   EPS1=  0.131424
A=  1.000000   B=  0.400000   H=  2.000000   EPS1=  0.130146
A=  1.000000   B=  0.400000   H=  2.200000   EPS1=  0.129221
A=  1.000000   B=  0.400000   H=  2.400000   EPS1=  0.128525
A=  1.000000   B=  0.400000   H=  2.600000   EPS1=  0.127996
A=  1.000000   B=  0.400000   H=  2.800000   EPS1=  0.127569
A=  1.000000   B=  0.400000   H=  3.000000   EPS1=  0.127231
A=  1.000000   B=  0.400000   H=  3.200000   EPS1=  0.126956
A=  1.000000   B=  0.400000   H=  3.400000   EPS1=  0.126729
A=  1.000000   B=  0.400000   H=  3.600000   EPS1=  0.126540
A=  1.000000   B=  0.400000   H=  3.800000   EPS1=  0.126380
A=  1.000000   B=  0.400000   H=  4.000000   EPS1=  0.126244
A=  1.000000   B=  0.400000   H=  4.200000   EPS1=  0.126127
A=  1.000000   B=  0.400000   H=  4.400000   EPS1=  0.126026
A=  1.000000   B=  0.400000   H=  4.600000   EPS1=  0.125938
A=  1.000000   B=  0.400000   H=  4.800000   EPS1=  0.125861
A=  1.000000   B=  0.400000   H=  5.000000   EPS1=  0.125793


A=  1.000000   B=  0.500000   H=  1.000000   EPS1=  0.145367
A=  1.000000   B=  0.500000   H=  1.200000   EPS1=  0.138703
A=  1.000000   B=  0.500000   H=  1.400000   EPS1=  0.134749
A=  1.000000   B=  0.500000   H=  1.600000   EPS1=  0.132314
A=  1.000000   B=  0.500000   H=  1.800000   EPS1=  0.130701
A=  1.000000   B=  0.500000   H=  2.000000   EPS1=  0.129574
A=  1.000000   B=  0.500000   H=  2.200000   EPS1=  0.128753
A=  1.000000   B=  0.500000   H=  2.400000   EPS1=  0.128137
A=  1.000000   B=  0.500000   H=  2.600000   EPS1=  0.127662
A=  1.000000   B=  0.500000   H=  2.800000   EPS1=  0.127283
A=  1.000000   B=  0.500000   H=  3.000000   EPS1=  0.126985
A=  1.000000   B=  0.500000   H=  3.200000   EPS1=  0.126743
A=  1.000000   B=  0.500000   H=  3.400000   EPS1=  0.126541
A=  1.000000   B=  0.500000   H=  3.600000   EPS1=  0.126373
A=  1.000000   B=  0.500000   H=  3.800000   EPS1=  0.126231
A=  1.000000   B=  0.500000   H=  4.000000   EPS1=  0.126109
A=  1.000000   B=  0.500000   H=  4.200000   EPS1=  0.126005
```

```
A=  1.000000   B=  0.500000   H=  4.400000   EPS1=  0.125915
A=  1.000000   B=  0.500000   H=  4.600000   EPS1=  0.125837
A=  1.000000   B=  0.500000   H=  4.800000   EPS1=  0.125783
A=  1.000000   B=  0.500000   H=  5.000000   EPS1=  0.125732


A=  1.000000   B=  0.600000   H=  1.000000   EPS1=  0.142327
A=  1.000000   B=  0.600000   H=  1.200000   EPS1=  0.136455
A=  1.000000   B=  0.600000   H=  1.400000   EPS1=  0.133214
A=  1.000000   B=  0.600000   H=  1.600000   EPS1=  0.131132
A=  1.000000   B=  0.600000   H=  1.800000   EPS1=  0.129829
A=  1.000000   B=  0.600000   H=  2.000000   EPS1=  0.128850
A=  1.000000   B=  0.600000   H=  2.200000   EPS1=  0.128137
A=  1.000000   B=  0.600000   H=  2.400000   EPS1=  0.127666
A=  1.000000   B=  0.600000   H=  2.600000   EPS1=  0.127264
A=  1.000000   B=  0.600000   H=  2.800000   EPS1=  0.126946
A=  1.000000   B=  0.600000   H=  3.000000   EPS1=  0.126628
A=  1.000000   B=  0.600000   H=  3.200000   EPS1=  0.126434
A=  1.000000   B=  0.600000   H=  3.400000   EPS1=  0.126313
A=  1.000000   B=  0.600000   H=  3.600000   EPS1=  0.126169
A=  1.000000   B=  0.600000   H=  3.800000   EPS1=  0.126043
A=  1.000000   B=  0.600000   H=  4.000000   EPS1=  0.125945
A=  1.000000   B=  0.600000   H=  4.200000   EPS1=  0.125857
A=  1.000000   B=  0.600000   H=  4.400000   EPS1=  0.125780
A=  1.000000   B=  0.600000   H=  4.600000   EPS1=  0.125713
A=  1.000000   B=  0.600000   H=  4.800000   EPS1=  0.125655
A=  1.000000   B=  0.600000   H=  5.000000   EPS1=  0.125603

A=  1.000000   B=  0.700000   H=  1.000000   EPS1=  0.138333
A=  1.000000   B=  0.700000   H=  1.200000   EPS1=  0.133965
A=  1.000000   B=  0.700000   H=  1.400000   EPS1=  0.131449
A=  1.000000   B=  0.700000   H=  1.600000   EPS1=  0.129872
A=  1.000000   B=  0.700000   H=  1.800000   EPS1=  0.128815
A=  1.000000   B=  0.700000   H=  2.000000   EPS1=  0.128070
A=  1.000000   B=  0.700000   H=  2.200000   EPS1=  0.127525
A=  1.000000   B=  0.700000   H=  2.400000   EPS1=  0.127114
A=  1.000000   B=  0.700000   H=  2.600000   EPS1=  0.126796
A=  1.000000   B=  0.700000   H=  2.800000   EPS1=  0.126546
A=  1.000000   B=  0.700000   H=  3.000000   EPS1=  0.126344
A=  1.000000   B=  0.700000   H=  3.200000   EPS1=  0.126180
A=  1.000000   B=  0.700000   H=  3.400000   EPS1=  0.126044
A=  1.000000   B=  0.700000   H=  3.600000   EPS1=  0.125930
A=  1.000000   B=  0.700000   H=  3.800000   EPS1=  0.125834
A=  1.000000   B=  0.700000   H=  4.000000   EPS1=  0.125752
A=  1.000000   B=  0.700000   H=  4.200000   EPS1=  0.125682
A=  1.000000   B=  0.700000   H=  4.400000   EPS1=  0.125621
A=  1.000000   B=  0.700000   H=  4.600000   EPS1=  0.125568
A=  1.000000   B=  0.700000   H=  4.800000   EPS1=  0.125521
A=  1.000000   B=  0.700000   H=  5.000000   EPS1=  0.125480

A=  1.000000   B=  0.800000   H=  1.000000   EPS1=  0.134125
A=  1.000000   B=  0.800000   H=  1.200000   EPS1=  0.131132
A=  1.000000   B=  0.800000   H=  1.400000   EPS1=  0.129476
A=  1.000000   B=  0.800000   H=  1.600000   EPS1=  0.128396
A=  1.000000   B=  0.800000   H=  1.800000   EPS1=  0.127666
A=  1.000000   B=  0.800000   H=  2.000000   EPS1=  0.127150
A=  1.000000   B=  0.800000   H=  2.200000   EPS1=  0.126771
A=  1.000000   B=  0.800000   H=  2.400000   EPS1=  0.126484
```

```
A= 1.000000   B= 0.800000   H= 2.600000   EPS1= 0.126262
A= 1.000000   B= 0.800000   H= 2.800000   EPS1= 0.126037
A= 1.000000   B= 0.800000   H= 3.000000   EPS1= 0.125945
A= 1.000000   B= 0.800000   H= 3.200000   EPS1= 0.125830
A= 1.000000   B= 0.800000   H= 3.400000   EPS1= 0.125735
A= 1.000000   B= 0.800000   H= 3.600000   EPS1= 0.125655
A= 1.000000   B= 0.800000   H= 3.800000   EPS1= 0.125587
A= 1.000000   B= 0.800000   H= 4.000000   EPS1= 0.125530
A= 1.000000   B= 0.800000   H= 4.200000   EPS1= 0.125480
A= 1.000000   B= 0.800000   H= 4.400000   EPS1= 0.125436
A= 1.000000   B= 0.800000   H= 4.600000   EPS1= 0.1254[illegible]
A= 1.000000   B= 0.800000   H= 4.800000   EPS1= 0.125367
A= 1.000000   B= 0.800000   H= 5.000000   EPS1= 0.125339


A= 1.000000   B= 0.900000   H= 1.000000   EPS1= 0.129637

A= 1.000000   B= 0.900000   H= 1.200000   EPS1= 0.128130
A= 1.000000   B= 0.900000   H= 1.400000   EPS1= 0.127319
A= 1.000000   B= 0.900000   H= 1.600000   EPS1= 0.126767
A= 1.000000   B= 0.900000   H= 1.800000   EPS1= 0.126371
A= 1.000000   B= 0.900000   H= 2.000000   EPS1= 0.126124
A= 1.000000   B= 0.900000   H= 2.200000   EPS1= 0.125923
A= 1.000000   B= 0.900000   H= 2.400000   EPS1= 0.125773
A= 1.000000   B= 0.900000   H= 2.600000   EPS1= 0.125663
A= 1.000000   B= 0.900000   H= 2.800000   EPS1= 0.125571
A= 1.000000   B= 0.900000   H= 3.000000   EPS1= 0.125497
A= 1.000000   B= 0.900000   H= 3.200000   EPS1= 0.125437
A= 1.000000   B= 0.900000   H= 3.400000   EPS1= 0.125387
A= 1.000000   B= 0.900000   H= 3.600000   EPS1= 0.125345
A= 1.000000   B= 0.900000   H= 3.800000   EPS1= 0.125309
A= 1.000000   B= 0.900000   H= 4.000000   EPS1= 0.125279
A= 1.000000   B= 0.900000   H= 4.200000   EPS1= 0.125253
A= 1.000000   B= 0.900000   H= 4.400000   EPS1= 0.125233
A= 1.000000   B= 0.900000   H= 4.600000   EPS1= 0.125211
A= 1.000000   B= 0.900000   H= 4.800000   EPS1= 0.125194
A= 1.000000   B= 0.900000   H= 5.000000   EPS1= 0.125173



A= 1.000000   B= 1.100000   H= 1.000000   EPS1= 0.120234
A= 1.000000   B= 1.100000   H= 1.200000   EPS1= 0.121653
A= 1.000000   B= 1.100000   H= 1.400000   EPS1= 0.122544
A= 1.000000   B= 1.100000   H= 1.600000   EPS1= 0.123110
A= 1.000000   B= 1.100000   H= 1.800000   EPS1= 0.123501
A= 1.000000   B= 1.100000   H= 2.000000   EPS1= 0.123783
A= 1.000000   B= 1.100000   H= 2.200000   EPS1= 0.123992
A= 1.000000   B= 1.100000   H= 2.400000   EPS1= 0.124152
A= 1.000000   B= 1.100000   H= 2.600000   EPS1= 0.124277
A= 1.000000   B= 1.100000   H= 2.800000   EPS1= 0.124376


A= 1.000000   B= 1.100000   H= 3.000000   EPS1= 0.124456
A= 1.000000   B= 1.100000   H= 3.200000   EPS1= 0.124521
A= 1.000000   B= 1.100000   H= 3.400000   EPS1= 0.124576
A= 1.000000   B= 1.100000   H= 3.600000   EPS1= 0.124622
```

```
  A= 1.000000   B= 1.100000   H= 3.800000   EPS1= 0.124660
  A= 1.000000   B= 1.100000   H= 4.000000   EPS1= 0.124693
  A= 1.000000   B= 1.100000   H= 4.200000   EPS1= 0.124722
  A= 1.000000   B= 1.100000   H= 4.400000   EPS1= 0.124746
  A= 1.000000   B= 1.100000   H= 4.600000   EPS1= 0.124766
  A= 1.000000   B= 1.100000   H= 4.800000   EPS1= 0.124787
  A= 1.000000   B= 1.100000   H= 5.000000   EPS1= 0.124803
  A= 1.000000   B= 1.200000   H= 1.000000   EPS1= 0.115550
  A= 1.000000   B= 1.200000   H= 1.200000   EPS1= 0.118266
  A= 1.000000   B= 1.200000   H= 1.400000   EPS1= 0.119973
  A= 1.000000   B= 1.200000   H= 1.600000   EPS1= 0.121111
  A= 1.000000   B= 1.200000   H= 1.800000   EPS1= 0.121965
  A= 1.000000   B= 1.200000   H= 2.000000   EPS1= 0.122436
  A= 1.000000   B= 1.200000   H= 2.200000   EPS1= 0.122909
  A= 1.000000   B= 1.200000   H= 2.400000   EPS1= 0.123238
  A= 1.000000   B= 1.200000   H= 2.600000   EPS1= 0.123495
  A= 1.000000   B= 1.200000   H= 2.800000   EPS1= 0.123709
  A= 1.000000   B= 1.200000   H= 3.000000   EPS1= 0.123866
  A= 1.000000   B= 1.200000   H= 3.200000   EPS1= 0.124002
  A= 1.000000   B= 1.200000   H= 3.400000   EPS1= 0.124115
  A= 1.000000   B= 1.200000   H= 3.600000   EPS1= 0.124210
  A= 1.000000   B= 1.200000   H= 3.800000   EPS1= 0.124298
  A= 1.000000   B= 1.200000   H= 4.000000   EPS1= 0.124359
  A= 1.000000   B= 1.200000   H= 4.200000   EPS1= 0.124418
  A= 1.000000   B= 1.200000   H= 4.400000   EPS1= 0.124470
  A= 1.000000   B= 1.200000   H= 4.600000   EPS1= 0.124515
  A= 1.000000   B= 1.200000   H= 4.800000   EPS1= 0.124554
 PAUSING
↑GO, 10
  A= 1.000000   B= 1.200000   H= 5.000000   EPS1= 0.124589



  A= 1.000000   B= 1.400000   H= 1.000000   EPS1= 0.106822
  A= 1.000000   B= 1.400000   H= 1.200000   EPS1= 0.111279
  A= 1.000000   B= 1.400000   H= 1.400000   EPS1= 0.114579
  A= 1.000000   B= 1.400000   H= 1.600000   EPS1= 0.116846
  A= 1.000000   B= 1.400000   H= 1.800000   EPS1= 0.118453
  A= 1.000000   B= 1.400000   H= 2.000000   EPS1= 0.119642
  A= 1.000000   B= 1.400000   H= 2.200000   EPS1= 0.120535
  A= 1.000000   B= 1.400000   H= 2.400000   EPS1= 0.121225
  A= 1.000000   B= 1.400000   H= 2.600000   EPS1= 0.121767
  A= 1.000000   B= 1.400000   H= 2.800000   EPS1= 0.122201
  A= 1.000000   B= 1.400000   H= 3.000000   EPS1= 0.122554
  A= 1.000000   B= 1.400000   H= 3.200000   EPS1= 0.122845
  A= 1.000000   B= 1.400000   H= 3.400000   EPS1= 0.123087
  A= 1.000000   B= 1.400000   H= 3.600000   EPS1= 0.123290
  A= 1.000000   B= 1.400000   H= 3.800000   EPS1= 0.123463
  A= 1.000000   B= 1.400000   H= 4.000000   EPS1= 0.123611
  A= 1.000000   B= 1.400000   H= 4.200000   EPS1= 0.123739
  A= 1.000000   B= 1.400000   H= 4.400000   EPS1= 0.123850
  A= 1.000000   B= 1.400000   H= 4.600000   EPS1= 0.123947
  A= 1.000000   B= 1.400000   H= 4.800000   EPS1= 0.124032
  A= 1.000000   B= 1.400000   H= 5.000000   EPS1= 0.124107
```

```
A= 1.000000   B= 1.600000   H= 1.000000   EPS1= 0.097315
A= 1.000000   B= 1.600000   H= 1.200000   EPS1= 0.104247
A= 1.000000   B= 1.600000   H= 1.400000   EPS1= 0.108982
A= 1.000000   B= 1.600000   H= 1.600000   EPS1= 0.112313
A= 1.000000   B= 1.600000   H= 1.800000   EPS1= 0.114743
A= 1.000000   B= 1.600000   H= 2.000000   EPS1= 0.116544
A= 1.000000   B= 1.600000   H= 2.200000   EPS1= 0.117983
A= 1.000000   B= 1.600000   H= 2.400000   EPS1= 0.118990
A= 1.000000   B= 1.600000   H= 2.600000   EPS1= 0.119839
A= 1.000000   B= 1.600000   H= 2.800000   EPS1= 0.120582
A= 1.000000   B= 1.600000   H= 3.000000   EPS1= 0.121079
A= 1.000000   B= 1.600000   H= 3.200000   EPS1= 0.121539
A= 1.000000   B= 1.600000   H= 3.400000   EPS1= 0.121924
A= 1.000000   B= 1.600000   H= 3.600000   EPS1= 0.122248
A= 1.000000   B= 1.600000   H= 3.800000   EPS1= 0.122524
```

```
A= 1.000000   B= 1.600000   H= 4.000000   EPS1= 0.1227[illegible]
A= 1.000000   B= 1.600000   H= 4.200000   EPS1= 0.122976
A= 1.000000   B= 1.600000   H= 4.400000   EPS1= 0.1231[illegible]3
A= 1.000000   B= 1.600000   H= 4.600000   EPS1= 0.1233[illegible]
A= 1.000000   B= 1.600000   H= 4.800000   EPS1= 0.123435
A= 1.000000   B= 1.600000   H= 5.000000   EPS1= 0.123556


A= 1.000000   B= 1.800000   H= 1.000000   EPS1= 0.0898[illegible]
A= 1.000000   B= 1.800000   H= 1.200000   EPS1= 0.097375
A= 1.000000   B= 1.800000   H= 1.400000   EPS1= 0.103383
A= 1.000000   B= 1.800000   H= 1.600000   EPS1= 0.107632
A= 1.000000   B= 1.800000   H= 1.800000   EPS1= 0.110625
A= 1.000000   B= 1.800000   H= 2.000000   EPS1= 0.113240
A= 1.000000   B= 1.800000   H= 2.200000   EPS1= 0.115133
A= 1.000000   B= 1.800000   H= 2.400000   EPS1= 0.116566
A= 1.000000   B= 1.800000   H= 2.600000   EPS1= 0.117734
A= 1.000000   B= 1.800000   H= 2.800000   EPS1= 0.118679
A= 1.000000   B= 1.800000   H= 3.000000   EPS1= 0.119454
A= 1.000000   B= 1.800000   H= 3.200000   EPS1= 0.120096
A= 1.000000   B= 1.800000   H= 3.400000   EPS1= 0.120634
A= 1.000000   B= 1.800000   H= 3.600000   EPS1= 0.121093
A= 1.000000   B= 1.800000   H= 3.800000   EPS1= 0.121473
A= 1.000000   B= 1.800000   H= 4.000000   EPS1= 0.121818
A= 1.000000   B= 1.800000   H= 4.200000   EPS1= 0.122103
A= 1.000000   B= 1.800000   H= 4.400000   EPS1= 0.122352
A= 1.000000   B= 1.800000   H= 4.600000   EPS1= 0.122572
A= 1.000000   B= 1.800000   H= 4.800000   EPS1= 0.122767
A= 1.000000   B= 1.800000   H= 5.000000   EPS1= 0.122933


A= 1.000000   B= 2.000000   H= 1.000000   EPS1= 0.081357
A= 1.000000   B= 2.000000   H= 1.200000   EPS1= 0.090775
A= 1.000000   B= 2.000000   H= 1.400000   EPS1= 0.097713
A= 1.000000   B= 2.000000   H= 1.600000   EPS1= 0.102375
A= 1.000000   B= 2.000000   H= 1.800000   EPS1= 0.106763
A= 1.000000   B= 2.000000   H= 2.000000   EPS1= 0.109733
A= 1.000000   B= 2.000000   H= 2.200000   EPS1= 0.112125
A= 1.000000   B= 2.000000   H= 2.400000   EPS1= 0.113932
A= 1.000000   B= 2.000000   H= 2.600000   EPS1= 0.115476
A= 1.000000   B= 2.000000   H= 2.800000   EPS1= 0.116691
A= 1.000000   B= 2.000000   H= 3.000000   EPS1= 0.117693
A= 1.000000   B= 2.000000   H= 3.200000   EPS1= 0.118527
A= 1.000000   B= 2.000000   H= 3.400000   EPS1= 0.119229
A= 1.000000   B= 2.000000   H= 3.600000   EPS1= 0.119824
A= 1.000000   B= 2.000000   H= 3.800000   EPS1= 0.120332
A= 1.000000   B= 2.000000   H= 4.000000   EPS1= 0.120775
A= 1.000000   B= 2.000000   H= 4.200000   EPS1= 0.121155
A= 1.000000   B= 2.000000   H= 4.400000   EPS1= 0.121432
A= 1.000000   B= 2.000000   H= 4.600000   EPS1= 0.121772
A= 1.000000   B= 2.000000   H= 4.800000   EPS1= 0.122029
A= 1.000000   B= 2.000000   H= 5.000000   EPS1= 0.122256


A= 1.000000   B= 2.200000   H= 1.000000   EPS1= 0.074465
A= 1.000000   B= 2.200000   H= 1.200000   EPS1= 0.084526
A= 1.000000   B= 2.200000   H= 1.400000   EPS1= 0.09[illegible]83[illegible]
A= 1.000000   B= 2.200000   H= 1.600000   EPS1= 0.098131
```

```
A= 1.000000   B= 2.200000   H= 1.800000   EPS1= 0.103676
A= 1.000000   B= 2.200000   H= 2.000000   EPS1= 0.106282
A= 1.000000   B= 2.200000   H= 2.200000   EPS1= 0.109386
A= 1.000000   B= 2.200000   H= 2.400000   EPS1= 0.111271
A= 1.000000   B= 2.200000   H= 2.600000   EPS1= 0.113046
A= 1.000000   B= 2.200000   H= 2.800000   EPS1= 0.114577
A= 1.000000   B= 2.200000   H= 3.000000   EPS1= 0.115813
A= 1.000000   B= 2.200000   H= 3.200000   EPS1= 0.116846
A= 1.000000   B= 2.200000   H= 3.400000   EPS1= 0.117717
A= 1.000000   B= 2.200000   H= 3.600000   EPS1= 0.118453
A= 1.000000   B= 2.200000   H= 3.800000   EPS1= 0.119094
A= 1.000000   B= 2.200000   H= 4.000000   EPS1= 0.119640
A= 1.000000   B= 2.200000   H= 4.200000   EPS1= 0.120112
A= 1.000000   B= 2.200000   H= 4.400000   EPS1= 0.120535
A= 1.000000   B= 2.200000   H= 4.600000   EPS1= 0.120901
A= 1.000000   B= 2.200000   H= 4.800000   EPS1= 0.121225
A= 1.000000   B= 2.200000   H= 5.000000   EPS1= 0.121511

A= 1.000000   B= 2.400000   H= 1.000000   EPS1= 0.065122
A= 1.000000   B= 2.400000   H= 1.200000   EPS1= 0.075670
A= 1.000000   B= 2.400000   H= 1.400000   EPS1= 0.086260
A= 1.000000   B= 2.400000   H= 1.600000   EPS1= 0.093453
A= 1.000000   B= 2.400000   H= 1.800000   EPS1= 0.098557
A= 1.000000   B= 2.400000   H= 2.000000   EPS1= 0.102653
A= 1.000000   B= 2.400000   H= 2.200000   EPS1= 0.105340
A= 1.000000   B= 2.400000   H= 2.400000   EPS1= 0.108453
A= 1.000000   B= 2.400000   H= 2.600000   EPS1= 0.110596
A= 1.000000   B= 2.400000   H= 2.800000   EPS1= 0.112362
A= 1.000000   B= 2.400000   H= 3.000000   EPS1= 0.113829
A= 1.000000   B= 2.400000   H= 3.200000   EPS1= 0.115063
A= 1.000000   B= 2.400000   H= 3.400000   EPS1= 0.116109
A= 1.000000   B= 2.400000   H= 3.600000   EPS1= 0.117082
A= 1.000000   B= 2.400000   H= 3.800000   EPS1= 0.117769
A= 1.000000   B= 2.400000   H= 4.000000   EPS1= 0.118433
A= 1.000000   B= 2.400000   H= 4.200000   EPS1= 0.119011
A= 1.000000   B= 2.400000   H= 4.400000   EPS1= 0.119515
A= 1.000000   B= 2.400000   H= 4.600000   EPS1= 0.119963
A= 1.000000   B= 2.400000   H= 4.800000   EPS1= 0.120357
A= 1.000000   B= 2.400000   H= 5.000000   EPS1= 0.120707


A= 1.000000   B= 2.600000   H= 1.000000   EPS1= 0.063468
A= 1.000000   B= 2.600000   H= 1.200000   EPS1= 0.073223
A= 1.000000   B= 2.600000   H= 1.400000   EPS1= 0.081926
A= 1.000000   B= 2.600000   H= 1.600000   EPS1= 0.088339
A= 1.000000   B= 2.600000   H= 1.800000   EPS1= 0.094478
A= 1.000000   B= 2.600000   H= 2.000000   EPS1= 0.098963
A= 1.000000   B= 2.600000   H= 2.200000   EPS1= 0.102602
A= 1.000000   B= 2.600000   H= 2.400000   EPS1= 0.105573
A= 1.000000   B= 2.600000   H= 2.600000   EPS1= 0.108020
A= 1.000000   B= 2.600000   H= 2.800000   EPS1= 0.110053
A= 1.000000   B= 2.600000   H= 3.000000   EPS1= 0.111755
A= 1.000000   B= 2.600000   H= 3.200000   EPS1= 0.113193
A= 1.000000   B= 2.600000   H= 3.400000   EPS1= 0.114415
A= 1.000000   B= 2.600000   H= 3.600000   EPS1= 0.115463
A= 1.000000   B= 2.600000   H= 3.800000   EPS1= 0.116366
```

```
    A= 1.000000   B= 2.600000   H= 4.000000   EPS1= 0.117140
    A= 1.000000   B= 2.600000   H= 4.200000   EPS1= 0.117533
  PAUSING
 ↑GO,13

    A= 1.000000   B= 2.600000   H= 4.400000   EPS1= 0.118433
    A= 1.000000   B= 2.600000   H= 4.600000   EPS1= 0.118962
    A= 1.000000   B= 2.600000   H= 4.800000   EPS1= 0.119430
    A= 1.000000   B= 2.600000   H= 5.000000   EPS1= 0.119847
    A= 1.000000   B= 2.800000   H= 1.000000   EPS1= 0.057339
    A= 1.000000   B= 2.800000   H= 1.200000   EPS1= 0.065135
    A= 1.000000   B= 2.800000   H= 1.400000   EPS1= 0.077141
    A= 1.000000   B= 2.800000   H= 1.600000   EPS1= 0.084475
    A= 1.000000   B= 2.800000   H= 1.800000   EPS1= 0.090455
    A= 1.000000   B= 2.800000   H= 2.000000   EPS1= 0.095367
    A= 1.000000   B= 2.800000   H= 2.200000   EPS1= 0.099337
    A= 1.000000   B= 2.800000   H= 2.400000   EPS1= 0.102641
    A= 1.000000   B= 2.800000   H= 2.600000   EPS1= 0.105332
    A= 1.000000   B= 2.800000   H= 2.800000   EPS1= 0.107675
    A= 1.000000   B= 2.800000   H= 3.000000   EPS1= 0.109637
    A= 1.000000   B= 2.800000   H= 3.200000   EPS1= 0.111246
    A= 1.000000   B= 2.800000   H= 3.400000   EPS1= 0.112646
    A= 1.000000   B= 2.800000   H= 3.600000   EPS1= 0.113850
    A= 1.000000   B= 2.800000   H= 3.800000   EPS1= 0.114391
    A= 1.000000   B= 2.800000   H= 4.000000   EPS1= 0.115727
    A= 1.000000   B= 2.800000   H= 4.200000   EPS1= 0.116539
    A= 1.000000   B= 2.800000   H= 4.400000   EPS1= 0.117235
    A= 1.000000   B= 2.800000   H= 4.600000   EPS1= 0.117709
    A= 1.000000   B= 2.800000   H= 4.800000   EPS1= 0.118446
    A= 1.000000   B= 2.800000   H= 5.000000   EPS1= 0.118932


    A= 1.000000   B= 3.000000   H= 1.000000   EPS1= 0.052331
    A= 1.000000   B= 3.000000   H= 1.200000   EPS1= 0.063541
    A= 1.000000   B= 3.000000   H= 1.400000   EPS1= 0.072636
    A= 1.000000   B= 3.000000   H= 1.600000   EPS1= 0.080834
    A= 1.000000   B= 3.000000   H= 1.800000   EPS1= 0.086535
    A= 1.000000   B= 3.000000   H= 2.000000   EPS1= 0.091752
    A= 1.000000   B= 3.000000   H= 2.200000   EPS1= 0.096079
    A= 1.000000   B= 3.000000   H= 2.400000   EPS1= 0.099634
    A= 1.000000   B= 3.000000   H= 2.600000   EPS1= 0.102792
    A= 1.000000   B= 3.000000   H= 2.800000   EPS1= 0.105845
    A= 1.000000   B= 3.000000   H= 3.000000   EPS1= 0.107399
    A= 1.000000   B= 3.000000   H= 3.200000   EPS1= 0.109236
    A= 1.000000   B= 3.000000   H= 3.400000   EPS1= 0.110312
    A= 1.000000   B= 3.000000   H= 3.600000   EPS1= 0.112172
    A= 1.000000   B= 3.000000   H= 3.800000   EPS1= 0.113352
    A= 1.000000   B= 3.000000   H= 4.000000   EPS1= 0.114332
    A= 1.000000   B= 3.000000   H= 4.200000   EPS1= 0.115235
    A= 1.000000   B= 3.000000   H= 4.400000   EPS1= 0.116030
    A= 1.000000   B= 3.000000   H= 4.600000   EPS1= 0.116784
    A= 1.000000   B= 3.000000   H= 4.800000   EPS1= 0.117409
    A= 1.000000   B= 3.000000   H= 5.000000   EPS1= 0.117967


  END XEQ.
```

CURRENT IMAGES INDUCED IN AN INFINITE PLANE CONDUCTING SHEET OF THICKNESS s AND VOLUME RESISTIVITY ρ_V. *

L. Jackson Laslett

Lawrence Radiation Laboratory
University of California
Berkeley, California

31 March, 1970

I. Notation

We consider a 2-dimensional "current dipole", $P(t)$ abamp·cm, formed of currents in the $\pm z$ direction and situated at $y = -h$. Parallel to this current dipole is placed an infinite conducting sheet, of thickness s, that fills the region $0 < y < s$. The specific volume resistivity of the sheet is denoted ρ_V abohm.cm; we shall also employ the (d.c.) "surface resistance" $\rho_S = \rho_V/s = 2\pi\nu$, so that $\rho_V = 2\pi\nu s$.

We shall, most particularly, examine the case in which $P(t)$ is a step function, of magnitude P_0, that is turned on at $t = 0$ $[P'(t) = P_0 \cdot \delta(t)]$. Results for other functions $P(t)$ in principle can readily be synthesized from the solution for the step-function case.

As is customary, displacement currents are neglected and the currents induced in the conducting sheet have a density (abamp/cm^2) given by $-\frac{1}{\rho_v}\frac{\partial\vec{A}}{\partial t}$ in terms of the total vector potential. $\vec{A}$.

II. Basic Analysis

The 2-dimensional current dipole is taken to have, if isolated, a vector potential (z-component)[1]

$$A^{(0)} = 2P_o \frac{y+h}{x^2+(y+h)^2}$$

$$= 2P_o \int_0^\infty e^{-k(y+h)} \cos kx \, dk,$$

for $t \geqslant 0$ in the step-function case. We then take the total vector potential to be given by

$$A_z = A^{(0)} + A^{(I)},$$

where $A^{(I)}$ denotes the contribution that induced eddy currents make to the total vector potential $A_z\hat{e}_z$. The condition $\nabla \times \vec{B} = 4\pi\vec{J}$ or $\nabla \times [\nabla \times \vec{A}] = 4\pi\vec{J}$ then requires that $A^{(I)}$ be "harmonic" $(\nabla^2 A_z = 0)$ for $y < 0$ and $y > s$, while

$$\frac{\partial^2 A^{(I)}}{\partial x^2} + \frac{\partial^2 A^{(I)}}{\partial y^2} - \frac{4\pi}{\rho_v}\frac{\partial A^{(I)}}{\partial t} = \frac{8\pi}{\rho_v} P'(t) \frac{y+h}{x^2+(y+h)^2} \quad \text{for} \quad 0 < y < s.$$

We also require continuity of $A^{(I)}$ at the surfaces $y = 0, s$ and of $\partial A^{(I)}/\partial y$ at $y = s$. Moreover, once a volume distribution of current has been established in the sheet $(t > 0)$, we require continuity of $\partial A^{(I)}/\partial y$ at the interface $y = 0$.

III. Fourier and Laplace Transformations, in x and t Respectively

We write

$$A^{(I)} = \begin{cases} \displaystyle\int_0^\infty F_+(t;k)e^{-k(y-s)} \cos kx \, dk & \text{For } y > s \\ \displaystyle\int_0^\infty F(y,t;k) \cos kx \, dk & \text{For } 0 < y < s \\ \displaystyle\int_0^\infty F_-(t;k)e^{ky} \cos kx \, dk & \text{For } y < 0. \end{cases}$$

Such a solution clearly is harmonic in the regions $y < 0$ and $y > s$, while the function $F(y,t;k)$ must satisfy the differential equation

$$\frac{\partial^2 F}{\partial y^2} - k^2 F + \left[\frac{2}{\nu s}\frac{\partial F}{\partial t}\right] = \frac{4}{\nu s} P'(t) e^{-k(y+h)}.$$

The continuity conditions at the upper interface require that $\partial F/\partial y = -kF$ at $y = s$. At the lower interface we similarly require that $\partial F/\partial y = +kF$, at $y = 0$, after a volume distribution of currents has been established in the sheet. At the instant the current dipole has been turned on $(t = 0)$, however, a surface current

$$j(x) = -\frac{1}{\pi} P_o \int_0^\infty k e^{-kh} \cos kx \, dk = \frac{P_o}{\pi} \frac{x^2 - h^2}{(x^2+h^2)^2},$$

with a vector potential

$$A^{(I)}_{t=0} = -2P_o \int_0^\infty e^{-k(|y|+h)} \cos kx \, dk,$$

will arise to prevent immediate penetration of magnetic field into the sheet; at this moment there will be a discontinuity of slope such that $\frac{\partial F}{\partial y} = k(F + 4P_o e^{-kh})$ at $y = 0$, $t = 0$. More explicitly, we can say that at this initial instant

$$F(y, t = +0; k) = -2P_o e^{-k(y+h)}$$

throughout the sheet.

A Laplace transformation of the partial differential equation for $F(y,t;k)$ can be conveniently written for all subsequent times by thinking of the impulse P' as having disappeared, but introducing

$F(t = 0) = -2P_o e^{-k(y+h)}$. We thus obtain the ordinary differential equation for $\overline{F}(y)$:[2]

$$\frac{d^2\overline{F}}{dy^2} - (k^2 + \frac{2p}{\nu s})\overline{F} = \frac{4}{\nu s} P_o e^{-k(y+h)} .$$

This differential equation is to be solved subject to the boundary conditions $d\overline{F}/dy = \mp k\overline{F}$ at $y = s, 0$ (respectively). We find

$$\overline{F} = \frac{2P_o}{p} \left[2k \frac{(K+k)e^{K(s-y)} + (K-k)e^{-K(s-y)}}{(K+k)^2 e^{Ks} - (K-k)^2 e^{-Ks}} - e^{-ky} \right] e^{-kh} ,$$

where

$$K \equiv \sqrt{\frac{2p}{\nu s} + k^2} .$$

The corresponding Laplace transforms of F_+ and F_- are

$$\overline{F}_+ = \frac{2P_o}{p} \left[\frac{4Kk}{(K+k)^2 e^{Ks} - (K-k)^2 e^{-Ks}} - e^{-ks} \right] e^{-kh}$$

and

$$\overline{F}_- = \frac{2P_o}{p} \left[2k \frac{(K+k)e^{Ks} + (K-k)e^{-Ks}}{(K+k)^2 e^{Ks} - (K-k)^2 e^{-Ks}} - 1 \right] e^{-kh} ,$$

by continuity. The last of these expressions is of greatest interest for describing directly the eddy-current fields in the neighborhood of the dipole source.

IV. Examination of the Solution for t Small

The correctness of the results can be checked, if desired, and some insight gained into their implications, if one examines these results for p large and thereby obtains the behavior at very early times. For p large, we have, to lowest order, $K \cong \sqrt{\frac{2p}{\nu s}}$. Then

$$\bar{F} \doteq \frac{2P_o}{p}\left[2k\sqrt{\frac{\nu s}{2p}}\; e^{-\sqrt{\frac{2p}{\nu s}}\,y} - e^{-ky}\right] e^{-kh}$$

$$= -\,2P_o\left[\frac{1}{p}\,e^{-ky} - \sqrt{2\nu s}\;\frac{k}{p^{3/2}}\; e^{-\sqrt{\frac{2p}{\nu s}}\,y}\right] e^{-kh}$$

$$\frac{d\bar{F}}{dy} \doteq 2P_o k\left[\frac{1}{p}\,e^{-ky} - \frac{2}{p}\,e^{-\sqrt{\frac{2p}{\nu s}}\,y}\right] e^{-kh}$$

Note: One expects that with p very large the 2nd term retained within the square bracket for $d\bar{F}/dy$ will be negligible unless y is exactly zero, but will combine with the 1st term to give $d\bar{F}/dy = -\,2P_o\,\frac{k}{p}\,e^{-kh}$ when $y = 0$. (This behavior already reflects the discontinuity of $\partial A/\partial y$ at $y = 0$.)

Also

$$\bar{F}_{-} \doteq -\,2P_o\left[\frac{1}{p} - \sqrt{2\nu s}\;\frac{k}{p^{3/2}}\right] e^{-kh} \;.$$

From this last approximation we find the inverse Laplace transforms[3]

$$F_{-} \cong -\,2P_o\left[1 - 2k\,\sqrt{\frac{2\nu s t}{\pi}}\right] e^{-kh} \;,$$

when t is small, for the function that pertains to the image potential $A^{(I)}$ at points below the sheet $(y < 0)$.

Accordingly, we expect that, when $y < 0$ and t is small,

$$A^{(I)} \doteq - 2P_o \left[\int_0^\infty e^{-k(h-y)} \cos kx \, dk - 2 \sqrt{\frac{2\nu st}{\pi}} \int_0^\infty k e^{-k(h-y)} \cos kx \, dk \right]$$

$$= - 2P_o \left\{ \frac{h-y}{x^2 + (h-y)^2} + 2 \sqrt{\frac{2\nu st}{\pi}} \; \frac{x^2 - (h-y)^2}{[x^2 + (h-y)^2]^2} \right\} .$$

It may be noted that, to first order in $\sqrt{\nu st}$, this result can be written

$$A^{(I)} \doteq - 2P_o \frac{H - y}{x^2 + (H-y)^2} ,$$

where

$$H = h + 2 \sqrt{\frac{2\nu st}{\pi}}$$

- - thus, in this approximation, the image that initially is situated at $y = h$ recedes to $y = H = h + 2 \sqrt{2\nu st/\pi}$ at subsequent early times $(t < \frac{s}{2\nu} = \frac{\pi s}{\rho_s} = \frac{\pi s^2}{\rho_v})$.

V. Examination of the Solution for t Large

The implications when t is large of the solutions presented in Sect. III can be examined by treating p as small.[4] In this limit one may write

$$K - k \cong \frac{p}{k\nu s} - \frac{1}{2k}\left(\frac{p}{k\nu s}\right)^2 \quad \text{and} \quad (K-k)^2 \cong \left(\frac{p}{k\nu s}\right)^2 .$$

By a somewhat tedious Taylor-series development of $\overline{F}_-$ through terms of order $(K-k)^2$ we then find, for $s \to 0$,

$$\overline{F}_- \cong - \frac{2P_o}{k\nu}\left[1 - \frac{p}{k\nu}\right] e^{-kh}$$

$$\cong - 2\,\frac{P_o}{k\nu + p}\, e^{-kh}.$$

By taking the inverse Laplace transform of this last form, we then obtain

$$F_- \cong - 2P_o\, e^{-k(h+\nu t)}$$

and

$$A^{(I)} = - 2P_o \int_0^\infty e^{-k(h+\nu t)} \cos kx\, dk$$

$$= - 2P_o\, \frac{h + \nu t - y}{x^2 + (h+\nu t-y)^2}$$

$$= - 2P_o\, \frac{H - y}{x^2 + (H-y)^2} \qquad (\text{for } y < 0),$$

where now

$$H = h + \nu t.$$

Accordingly, in this large-t approximation $(s \ll \nu t)$, the image that is situated above the sheet (in order to describe the effect of eddy currents as felt below the sheet) recedes from its initial position $y = h$ with a constant speed v $(= \rho_s/2\pi)$. This is the well-known result of Maxwell, for the case of a thin infinite sheet, to which reference was made in ERAN-37.

VI. References and Notes

[*] Work supported by the U.S. Atomic Energy Commission. For previous work, see LRL Reports ERAN 37 - 39 (July, 1969).

[1] The Fourier integral form follows from B.O. Peirce, "A Short Table of Integrals", #506, p. 64.

[2] The Laplace transform of $F(t)$ will be denoted $\bar{F}(p) \equiv \int_0^\infty e^{-pt} F(t)dt$. The Laplace transform of a time derivative is then given by

$$\overline{\frac{\partial F}{\partial t}} \equiv \int_0^\infty e^{-pt} \frac{\partial F}{\partial t}\, dt = Fe^{-pt} \Big|_0^\infty + p \int_0^\infty e^{-pt} F(t)dt$$

$$= - F(0) + p\bar{F}.$$

[Cf. J.C. Jaeger, "An Introduction to the Laplace Transformation", (Methuen, London; Wiley, New York).]

[3] The connection between the behavior of a function for t small and the asymptotic character of its Laplace transform (p large) is discussed by G. Doetsch, "Theorie und Anwendung der Laplace-Transformation" (Dover, New York, 1943), Part III, Chapt. 13, Sect. 1.1 (p. 243 ff).

[4] Cf. G. Doetsch (op. cit., ref. 3), esp. Part III, Chapt. 13, Sect. 2 (p. 247).

MAGNETIC IMAGE FIELDS FROM THE PARALLEL TRANSVERSE MOTION OF A LINE CURRENT WITHIN A THIN-WALLED CIRCULAR CYLINDER OF NON-VANISHING SURFACE RESISTIVITY*

L. Jackson Laslett

Lawrence Radiation Laboratory
University of California
Berkeley, California

16 February 1970

I. Statement of the Problem

A steady line current $I\hat{e}_z$ e.m.u. moves its location along a radial trajectory $r = h(t)$, $\theta = 0$ within a thin-wall conducting circular cylinder of radius R and surface resistivity ρ e.m.u. (abohms) per square. It is desired to find the vector potential or magnetic-field components of the "image currents" induced in the cylinder -- most particularly the azimuthal field component $B_\theta^{(I)}$ of the image currents evaluated at the location $r = h(t)$, $\theta = 0$ of the line current I.

II. Solution

The solution to the problem posed in Sect. I should be obtainable from the results of ERAN-39 (31 July 1969). In that report it was shown that, for a step-function two-dimensional dipole P_o at $r = h$, $\theta = 0$ that is turned on at t_o, we have (for $t_o < t$) the following z-directed vector potential of the image currents:

$$A^{(I)} = -\frac{2}{h} P_o \sum_{n=1}^{\infty} \left\{ \begin{matrix} \left(\frac{hr}{R^2}\right)^n \\ \text{or} \\ \left(\frac{h}{r}\right)^n \end{matrix} \right\} (\cos n\theta)\, e^{-n \frac{v}{R}(t - t_o)} \quad \text{for} \left\{ \begin{matrix} r \le R \\ \\ r \ge R \end{matrix} \right.$$

$$= P_o \cdot F\,(h, r, \theta, t - t_o),$$

where F can be written in closed form as (contd)

---

*Work supported by the U.S. Atomic Energy Commission.

$$F = -2\cdot\left\{\begin{array}{l} \dfrac{r}{R^2}\,\dfrac{\cos\theta - \dfrac{hr}{R^2}\,E\,(t,t_o)}{1-2\,\dfrac{hr}{R^2}\,(\cos\theta)\;E(t,t_o) + [(\dfrac{hr}{R^2})\;E(t,t_o)]^2} \\ \\ \dfrac{1}{r}\,\dfrac{\cos\theta - \dfrac{h}{r}\,E\,(t,t_o)}{1-2\,\dfrac{h}{r}\,(\cos\theta)\;E(t,t_o) + [(\dfrac{h}{r})\;E(t,t_o)]^2} \end{array}\right\}\cdot E(t,t_o)\ \text{for}\left\{\begin{array}{l} r \leq R \\ \\ r \geq R\ , \end{array}\right.$$

with $E(t,t_o) \equiv e^{-\frac{v}{R}(t-t_o)}$ and $v \equiv \frac{\rho}{2\pi}$ [with ρ expressed in abohms (e.m.u.) per square].

If now -- to return to the problem that was posed -- a constant current I (e.m.u.) moves in radius at the constant azimuth angle $\theta = 0$ with $h = h(t)$, one expects that the vector potential of the image field in this case will be:

$$A^{(I)} = I\int_{-\infty}^{t}\frac{dh(t')}{dt'}\,F\Big(h(t'),\ r,\ \theta,\ t-t'\Big)\,dt'$$

and the total vector potential will be this $A^{(I)}$ supplemented by the direct vector potential $\mathbf{A}^{(0)}$ of the current itself at its instantaneous position $\mathbf{h}(t)$. Explicitly this latter is (with an arbitrary zero):

$$\begin{aligned} A^{(0)} &= -\,I\,\ell n\,\frac{|\vec{r}-\vec{h}|}{R^2} \\ &= -\,I\,\ell n\,\frac{h^2 - 2rh\,\cos\theta + r^2}{R^2} \\ &= 2\,I\left\{\left[\sum_{n=1}^{\infty}\frac{1}{n}\,(\frac{h}{r})^n\cos n\theta\right] - \ell n\,\frac{r}{R}\right\}, \end{aligned}$$

this last (series) form applying only for $\mathbf{r} > \mathbf{h}$.

III. Check of the Proposed Solution

To test the results suggested in Sect. II, we note that the "induced currents" in the wall at $r = R$ have a surface density (e.m.u. of current per centimeter of circumferential distance)

$$J = \frac{1}{4\pi}\left[B_\theta\Big|_{R^+} - B_\theta\Big|_{R^-}\right] = \frac{1}{4\pi}\left[\frac{\partial A}{\partial r}\Big|_{R^-} - \frac{\partial A}{\partial r}\Big|_{R^+}\right] = \frac{1}{4\pi}\left[\frac{\partial A^{(I)}}{\partial r}\Big|_{R^-} - \frac{\partial A^{(I)}}{\partial r}\Big|_{R^+}\right].$$

However this same current density must also be given by

$$J = \frac{\mathcal{E}}{\rho} = -\frac{1}{\rho}\frac{\partial A}{\partial t}\Big|_R = -\left[\frac{1}{\rho}\left(\frac{\partial A^{(0)}}{\partial t} + \frac{\partial A^{(I)}}{\partial t}\right)\right]\Bigg|_R .$$

Hence we require:

$$\frac{\partial A^{(I)}}{\partial r}\Big|_{R^-} - \frac{\partial A^{(I)}}{\partial r}\Big|_{R^+} + \frac{2}{v}\frac{\partial A^{(I)}}{\partial t}\Big|_R = -\frac{2}{v}\frac{\partial A^{(0)}}{\partial t}\Big|_R .$$

As a check of whether this requirement is in fact satisfied by the solutions proposed, we may apply the series forms and write the condition

$$I\int_{-\infty}^{t}\frac{dh(t')}{dt}\left[\frac{\partial}{\partial r}F_{r<R}\big(h(t'),r,\theta,t-t'\big) - \frac{\partial}{\partial r}F_{r>R}\big(h(t'),r,\theta,t-t'\big)\right]_R dt' +$$

$$+\frac{2}{v}I\left[\frac{dh(t)}{dt}F\big(h(t),R,\theta,0\big) + \int_{-\infty}^{t}\frac{dh(t')}{dt'}\frac{\partial F}{\partial t}\Big|_R dt'\right] \overset{?}{=} -\frac{2}{v}\frac{\partial A^{(0)}}{\partial t}\Big|_R$$

as

$$-\frac{4I}{R^2}\sum_{n=1}^{\infty} n\left[\int_{-\infty}^{t}\frac{dh(t')}{dt'}\left(\frac{h}{R}\right)^{n-1} e^{-n\frac{v}{R}(t-t')}dt'\right]\cos n\theta - \frac{4I}{vR}\frac{dh(t)}{dt}\sum_{n=1}^{\infty}\left(\frac{h}{R}\right)^{n-1}\cos n\theta \; +$$

$$+\frac{4I}{R^2}\sum_{n=1}^{\infty} n\left[\int_{-\infty}^{t}\frac{dh(t')}{dt'}\left(\frac{h}{r}\right)^{n-1} e^{-n\frac{v}{R}(t-t')}dt'\right]\cos n\theta$$

$$\overset{?}{=} -\frac{4I}{vR}\frac{dh(t)}{dt}\sum_{n=1}^{\infty}\left(\frac{h}{R}\right)^{n-1}\cos n\theta .$$

This relation is seen indeed to be identically satisfied. In addition to satisfying this boundary condition at $r = R$, the forms proposed for the vector potential are continuous and $A^{(0)}$ has the proper singularity at $r = h$. The solutions elsewhere are harmonic ($\nabla^2 A = 0$), as required, and fall off reasonably as $r \to \infty$. The vector potential could be supplemented, if desired, by the vector potential of a constant and uniform (t-independent and θ independent) surface current at the radius R, to represent a uniformly distributed return D.C. current ($-I$) in the cylinder, but this would contribute <u>no field</u> to any point in the <u>interior</u>.

If we accept the vector potential expressed in the proposed series forms as correct, it is readily verified that the closed-form expressions are equivalent and hence may also be adopted as solutions to the problem that was posed.

IV. The Image Field at the Location of the Given Current

At $r = h$, $\theta = 0$ we have the image field $\vec{B}^{(I)} = B_\theta^{(I)} \hat{e}_\theta$, with $B_\theta^{(I)}$ given by $-\left.\frac{\partial A^{(I)}}{\partial r}\right|_{h,0}$.

Hence we may write

$$B_\theta^{(I)} = -I \int_{-\infty}^{t} \frac{dh(t')}{dt'} \frac{\partial}{\partial r} F\Big(h(t'), r, 0, t-t'\Big)\Big|_{r=h} dt' ,$$

where (using the forms for $r < R$)

$$\frac{\partial}{\partial r} F\Big(h(t'), r, 0, t-t'\Big)\Big|_{r=h} = -\frac{2}{R^2} \sum_{n=1}^{\infty} n \left[\frac{h(t)h(t')}{R^2}\right]^{n-1} e^{-n \frac{v}{R}(t-t')}$$

$$= -\frac{2}{R^2} \frac{E(t,t')}{\left[1 - \frac{h(t)h(t')}{R^2} E(t,t')\right]^2} ,$$

with $E(t,t') = e^{-\frac{v}{R}(t-t')}$.

V. Illustrative Examples

A. Exponential Movement of the Current

As an illustration, it is interesting and informative to consider the case in which the current moves outward exponentially from a very small radius value at a very early time. We accordingly take

$$h(t) = h_o e^{\frac{t-t_1}{\tau}} \qquad \text{and} \qquad \frac{dh(t)}{dt} = \frac{h_o}{\tau} e^{\frac{t-t_1}{\tau}} .$$

Then the result given in Sect. IV becomes, employing the closed-form expression for $\frac{\partial}{\partial r} F\Big(h(t'),r,0,t-t'\Big)\Big|_{r=h}$,

$$B_\theta^{(I)} = \frac{2}{R^2} I \int_{-\infty}^{t} \frac{h_o}{\tau} e^{\frac{t'-t_1}{\tau}} \frac{e^{-\frac{v}{R}(t-t')}}{\left[1 - \frac{h_o^2}{R^2} e^{\frac{t-t_1}{\tau}} e^{\frac{t'-t_1}{\tau}} e^{-\frac{v}{R}(t-t')}\right]^2} dt'$$

$$= \frac{2Ih_o}{\tau R^2} e^{-(\frac{t_1}{\tau} + \frac{vt}{R})} \int_{-\infty}^{t} \frac{e^{(\frac{1}{\tau} + \frac{v}{R})t'}}{\left[1 - \frac{h_o^2}{R^2} e^{\frac{t-2t_1}{\tau} - \frac{vt}{R}} e^{(\frac{1}{\tau} + \frac{v}{R})t'}\right]^2} dt'$$

and, by writing $t' = t - \zeta$,

$$B_\theta^{(I)} = \frac{2Ih_o}{\tau R^2} e^{\frac{t-t_1}{\tau}} \int_{0}^{\infty} \frac{e^{-(\frac{1}{\tau} + \frac{v}{R})\zeta}}{\left[1 - \left(\frac{h_o}{R} e^{\frac{t-t_1}{\tau}}\right)^2 e^{-(\frac{1}{\tau} + \frac{v}{R})\zeta}\right]^2} d\zeta$$

$$= - \frac{2\ I}{h_o\ e^{\frac{t-t_1}{\tau}}} \ \frac{1}{1 + \frac{v\tau}{R}} \ \frac{1}{1 - \left(\frac{h_o}{R} e^{\frac{t-t_1}{\tau}}\right)^2 e^{-(\frac{1}{\tau} + \frac{v}{R})\zeta}} \Bigg|_0^\infty$$

$$= \frac{2\ I}{h_o\ e^{\frac{t-t_1}{\tau}}} \ \frac{1}{1 + \frac{v\tau}{R}} \left[\frac{1}{1 - \left(\frac{h_o\ e^{\frac{t-t_1}{\tau}}}{R}\right)^2} - 1\right]$$

(contd)

(contd)

$$= \frac{2I}{1+\frac{v\tau}{R}} \frac{h_o e^{-\frac{t-t_1}{\tau}}}{R^2 - \left(h_o e^{-\frac{t-t_1}{\tau}}\right)^2} = \frac{2I}{1+\frac{v\tau}{R}} \frac{h}{R^2 - h^2} \; .$$

If one has a very good conductor serving as the image cylinder, so that ρ and hence v are small, or if the location of the current is changing rapidly, so that τ is small, our result indicates that in this limit ($v\tau \ll R$) we shall have

$$B_\theta^{(I)} \cong 2I \frac{h}{R^2 - h^2} \; .$$

This result is that expected under circumstances such that the cylinder can be regarded as a surface into which virtually no flux will penetrate -- in this limiting situation the image field is that of a line current $-I$ situated at $r = \frac{R^2}{h}$, or a distance $\frac{R^2}{h} - h$ away from the current I at $r = h$, and the consequent value of $B_\theta^{(I)}$ is $\frac{2I}{R^2/h - h} = 2I \frac{h}{R^2 - h^2}$ in agreement with the result found above. In the more general case ($v\tau$ not necessarily small in comparison to R), the image field at the location of the line current I is reduced by the factor $\frac{1}{1+\frac{v\tau}{R}}$ in this example.

B. Sinusoidal Oscillation of the Current

A similar evaluation of $B_\theta^{\prime(I)}$ may be attempted for a line current whose position oscillates with simple-harmonic motion (sinusoidally) about the central axis of the image cylinder. In this case we take

$$h(t) = A \sin \omega t \quad \text{and} \quad \frac{dh(t)}{dt} = A\omega \cos \omega t .$$

We now find the necessary integrals to be more elaborate, so we here confine our attention to the terms in the result that are first-order in the amplitude A (the terms of next-higher order are of order A^3). The result obtained then is

(contd)

$$B_\theta^{(I)} \cong 2I \frac{A}{R^2} \frac{\omega}{\omega^2+(\frac{v}{R})^2} [\omega \sin \omega t + \frac{v}{R} \cos \omega t]$$

$$= 2I \frac{A}{R^2} \frac{\omega}{\sqrt{\omega^2+(\frac{v}{R})^2}} \sin (\omega t + \phi),$$

where

$$\tan \phi = \frac{v/R}{\omega} = \frac{\rho}{2\pi \omega R} .$$

For $\omega \gg \frac{v}{R}$ this result approaches $2I \frac{A}{R^2} \sin \omega t = \frac{2Ih}{R^2}$, as obtained in subsection A above for rapid motion of the current if we now employ the approximation that h is small.

There is also present, however, the out-of-phase component of the image magnetic field, namely

$$\frac{2I}{R^2} \frac{v/R}{\omega^2+(\frac{v}{R})^2} A\omega \cos \omega t = \frac{2I}{R^2} \frac{v/R}{\omega^2+(\frac{v}{R})^2} \frac{dh}{dt} .$$

This possibly-small out-of-phase component leads to an inward force from the residual image magnetic field when dh/dt is positive (and vice-versa) for this parallel-displacement mode.

It may be mentioned that retention of only the initial terms of the series developments presented in this report -- as, in effect, has been done in this last example -- confines attention to image fields of low multipole order (cf. ERAN-38 and ERAN-39).

ADDENDUM

(23 February 1970)

The Image Field of a Suddenly Established Current

1. The solution to the image-field problem that arises when a current I is suddenly created at a radius h_o should be obtainable from the dipole-step-function solution given on p. 4 and p. 7 of ERAN-39, namely from

$$A_{P_o}^{(I)} = -\frac{2}{h} P_o \sum_{n=1}^{\infty} \left\{ \begin{matrix} (\frac{hr}{R^2})^n \\ \text{or} \\ (\frac{h}{R}) \end{matrix} \right\} (\cos n\theta)\, \epsilon^{-n\frac{v}{R}(t - t_o)}$$

$$= -2P_o \left\{ \begin{matrix} \dfrac{r}{R^2} \dfrac{\cos\theta - \frac{hr}{R^2} E(t,t_o)}{1 - 2\frac{hr}{R^2} E(t,t_o)\cos\theta + [(\frac{hr}{R^2})E(t,t_o)]^2} \\ \text{or} \\ \dfrac{1}{r} \dfrac{\cos\theta - \frac{h}{r} E(t,t_o)}{1 - 2\frac{h}{r} E(t,t_o)\cos\theta + [(\frac{h}{r}) E(t,t_o)]^2} \end{matrix} \right\} \cdot E(t,t_o)$$

for $r \lessgtr R$ and with $E(t,t_o) = \epsilon^{-\frac{v}{R}(t-t_o)}$. It is only necessary simply to form

$$A_{Curr}^{(I)} = \frac{I}{P_o} \int_o^{h_o} A_{P_o}^{(I)}\, dh.$$

We then augment this result with the direct vector potential of

(i) an isolated doublet, formed by a current +I at $r = h_o$ and -I at the axis:

$$A_P^{(0)} = 2I \left\{ \begin{matrix} \sum_{n=1}^{\infty} \frac{1}{n}(\frac{r}{h_o})^n \cos n\theta - \ln\frac{h_o}{r} & r < h_o \\ \text{or} & \\ \sum_{n=1}^{\infty} \frac{1}{n}(\frac{h_o}{r})^n \cos n\theta & r > h_o \end{matrix} \right.$$

(contd)

$$= - I \,\ell n\left[1 - 2\,\frac{h_o}{r}\cos\theta + \left(\frac{h_o}{r}\right)^2\right],$$ and

(ii) a current +I on the axis and a return current -I uniformly distributed over a cylindrical surface situated (to be definite) at $r = R$:

$$A^{(0)}_{I\text{ on axis}} + A^{(0)}_{-I\text{ at }R} = \begin{cases} 2I\,\ell n\,\frac{R}{r} & r_i < r < R \\ 0 & r > R. \end{cases}$$

Accordingly, employing the series expansions, we have

$$A^{(I)} = -2I\sum_{n=1}^{\infty}\left[\int_0^{h_o} h^{n-1}dh\right]\left\{\begin{matrix} \left(\frac{r}{R^2}\right)^n \\ \text{or} \\ \left(\frac{1}{r}\right)^n \end{matrix}\right\}(\cos n\theta)e^{-n\frac{v}{R}(t-t_o)} \qquad (r \lessgtr R)$$

$$= -2I\sum_{n=1}^{\infty}\frac{1}{n}\left\{\begin{matrix} \left(\frac{h_o r}{R^2}\right)^n \\ \text{or} \\ \left(\frac{h_o}{r}\right)^n \end{matrix}\right\}(\cos n\theta)e^{-n\frac{v}{R}(t-t_o)} \qquad (r \lessgtr R),$$

or the closed-form expressions (that can be obtained directly by integration

$$A^{(I)} = I\begin{cases} \ell n\{1 - 2\frac{h_o r}{R^2}\,E(t,t_o)\cos\theta + [(\frac{h_o r}{R^2})E(t,t_o)]^2\} & (r < R) \\ \text{or} & \\ \ell n\{1 - 2\,\frac{h_o}{r}\,E(t,t_o)\cos\theta + [(\frac{h_o}{r})E(t,t_o)]^2\} & (r > R). \end{cases}$$

These forms, if used in conjunction with the $A^{(0)}$ given above, give the total potential $A = A^{(0)} + A^{(I)}$:

(contd)

$$A = \begin{cases} 2I \; \{ \sum\limits_{n=1}^{\infty} \frac{1}{n} [(\frac{r}{h_o})^n - (\frac{h_o r}{R^2})^n e^{-n \frac{v}{R}(t-t_o)}] \cos n\theta + \ell n \frac{R}{h_o} \} & r < h_o < R \\ \quad \text{or} & \\ 2I \; \{ \sum\limits_{n=1}^{\infty} \frac{1}{n} [(\frac{h_o}{r})^n - (\frac{h_o r}{R^2})^n e^{-n \frac{v}{R}(t-t_o)}] \cos n\theta + \ell n \frac{R}{r} \} & h_o < r < R \\ \quad \text{or} & \\ 2I \sum\limits_{n=1}^{\infty} \frac{1}{n} (\frac{h_o}{r})^n [1 - e^{-n \frac{v}{R}(t-t_o)}] \cos n\theta & h_o < R < r \end{cases}$$

$$= \begin{cases} I \; \ell n \left\{ \dfrac{1 - 2 \frac{h_o r}{R^2} E(t,t_o) \cos\theta + [(\frac{h_o r}{R^2}) E(t,t_o)]^2}{1 - 2 \frac{h_o}{r} \cos\theta + (\frac{h_o}{r})^2} (\frac{R}{r})^2 \right\} & r_i < r < R \\ \quad \text{or} & \\ I \; \ell n \left\{ \dfrac{1 - 2 \frac{h_o}{r} E(t,t_o) \cos\theta + [(\frac{h_o}{r}) E(t,t_o)]^2}{1 - 2 \frac{h_o}{r} \cos\theta + (\frac{h_o}{r})^2} \right\} & r > R. \end{cases}$$

It will be noted that these forms for the total vector potential A vanish at and outside the boundary $r = R$ when $t = t_o$ and that correspondingly $B_r = \frac{1}{r} \frac{\partial A}{\partial \theta}$ likewise vanishes for $r \geq R$, $t = t_o$ -- *i.e.*, there is no initial flux penetration of the boundary. To continue a check of the expressions proposed, we first form

$$J \Big|_{r=R} = \frac{1}{4\pi} [(B_\theta)_{R^+} - (B_\theta)_{R^-}] = \frac{1}{4\pi} [\frac{\partial A}{\partial r}\Big|_{R^-} - \frac{\partial A}{\partial r}\Big|_{R^+}]$$

$$= - \frac{I}{2\pi R} [1 + 2 \sum_{n=1}^{\infty} (\frac{h_o}{R})^n (\cos n\theta) \, e^{-n \frac{v}{R}(t-t_o)}]$$

$$= - \frac{I}{2\pi R} \left\{ 1 + 2 \frac{h_o}{R} \frac{\cos\theta - \frac{h_o}{R} E(t,t_o)}{1 - 2 \frac{h_o}{R} E(t,t_o) \cos\theta + [(\frac{h_o}{R}) E(t,t_o)]^2} E(t,t_o) \right\} .$$

We then also form

$$\frac{1}{\rho}(-\dot{A})_{r=R} = \frac{1}{2\pi v}(-\dot{A})_{r=R}$$

$$= -\frac{I}{\pi R}\sum_{n=1}^{\infty}\left(\frac{h_o}{R}\right)(\cos n\theta)\; e^{-n\frac{v}{R}(t-t_o)}$$

$$= -\frac{I}{\pi}\frac{h_o}{R^2}\;\frac{\cos\theta - \frac{h_o}{R}E(t,t_o)}{1-2\frac{h_o}{R}E(t,t_o)\cos\theta + [(\frac{h_o}{R})\,E(t,t_o)]^2}\;E(t,t_o).$$

We thus see, from these expressions, that the current density in the cylinder is correctly related to the <u>induced</u> <u>electric</u> <u>field</u> $\mathcal{E} = -\dot{A}$ through the surface resistivity ρ, <u>save</u> <u>for</u> the D.C. term $-\frac{I}{2\pi R}$ in J. This uniform (θ-independent) return current of course must be sustained in this model by other means -- *e.g.*, by electrostatic fields.

As for the B_θ field, the total B_θ field near h_o is given by

$$A = \begin{cases} 2I\left\{\sum_{n=1}^{\infty}\left[\frac{h_o^n}{r^{n+1}} + \frac{h_o^n r^{n-1}}{R^{2n}}\, e^{-n\frac{v}{R}(t-t_o)}\right]\cos n\theta + \frac{1}{r}\right\} & r > h_o \\ \text{or} & \\ 2I\left\{\sum_{n=1}^{\infty}\left[-\frac{r^{n-1}}{h_o^n} + \frac{h_o^n r^{n-1}}{R^{2n}}\, e^{-n\frac{v}{R}(t-t_o)}\right]\cos n\theta\right\} & r < h_o \end{cases}$$

$$= 2I\left[\frac{r - h_o\cos\theta}{r^2 - 2h_o r\cos\theta + h_o^2} + h_o\,\frac{\cos\theta - \frac{h_o r}{R^2}E(t,t_o)}{R^2 - 2h_o rE(t,t_o)\cos\theta + [\frac{h_o r}{R}E(t,t_o)]^2}\,E(t,t_o)\right].$$

Of the terms shown, those that do not involve the time-dependent exponential factors $e^{-\frac{v}{R}(t-t_o)}$ or $E(t,t_o)$ represent just the B_θ field of an isolated wire that is situated at $r = h_o$, $\theta = 0$ and carries a current $+I$. The force on this wire thus may be calculated by employing solely the remaining field -- that we might term the "image field" and denote by $B_\theta^{(I)}$.

Thus, in summary, we have at the location of the current the image field

$$B_\theta^{(I)} = - \left.\frac{\partial A^{(I)}}{\partial r}\right|_{r=h_o}$$

$$= \frac{2I}{h_o} \sum_{n=1}^{\infty} \left(\frac{h_o}{R}\right)^{2n} \epsilon^{-n \frac{v}{R}(t-t_o)}$$

$$= \frac{2Ih_o}{R^2} \frac{1 - \left(\frac{h_o}{R}\right)^2 E(t,t_o)}{1 - 2\left(\frac{h_o}{R}\right)^2 E(t,t_o) + \left[\left(\frac{h_o}{R}\right)^2 E(t,t_o)\right]^2} E(t,t_o)$$

$$= \frac{2Ih_o}{R^2} \frac{E(t,t_o)}{1 - \left(\frac{h_o}{R}\right)^2 E(t,t_o)} .$$

This last form is immediately interpretable, as are the image-field components $B_r^{(I)}$, $B_\theta^{(I)}$ at any point within the cylinder, as the field that would arise from an image current $-I$ at a radial location $\tilde{H}$ that is the "image" $\tilde{H} = R^2/\tilde{h}_o$ of a point that recedes towards the axis as $\tilde{h}_o = h_o \cdot E(t,t_o)$; *i.e.*, $\tilde{H} = \frac{R^2}{h_o} \epsilon^{+\frac{v}{R}(t-t_o)}$.

2. The solution to the image-field problem that arises when a current I is suddenly created at a radius h_o also should be obtainable immediately from the results in the body of the present report. In this instance we would set $h(t)$ equal to h_o times a unit step function (S) of $t-t_o$ for evaluating the image fields by use of the formula

$$A^{(I)} = I \int_{-\infty}^{t} \frac{dh(t')}{dt} F\left(h(t'),r,\theta,t-t'\right) dt'$$

for the vector potential of these fields. With the argument $h(t')$ in F a step function and $\frac{dh(t')}{dt'} = h_o\ \delta(t'-t_o)$, we now may write

(contd)

$$A^{(I)} = I \int_{t_o-\epsilon}^{t_o+\epsilon} \frac{dh(t')}{dt'} F\Big(h(t'),r,\theta,t-t_o\Big)\, dt'$$

$$= I \int_{o}^{h_o} F(h,r,\theta,t-t_o)\, dh$$

$$= I\, h_o \langle F \rangle_{\text{h-average}}$$

Now from the body of this report we have

$$F_{r\leq R} = -2\,\frac{r}{R^2}\,\frac{\cos\theta - \frac{hr}{R^2}E(t,t_o)}{1-2\,\frac{hr}{R^2}(\cos\theta)\,E(t,t_o) + [(\frac{hr}{R^2})\,E(t,t_o)]^2}\,E(t,t_o),$$

so

$$h_o\Big\langle F_{r\leq R}\Big\rangle = -2\,\frac{r}{R^2}\int_o^{h_o}\frac{[\cos\theta - \frac{hr}{R^2}E(t,t_o)]E(t,t_o)}{1-2\,\frac{hr}{R^2}(\cos\theta)\,E(t,t_o) + [(\frac{hr}{R^2})\,E(t,t_o)]^2}\,dh$$

$$= \ell n\left\{1 - 2\,\frac{h_or}{R^2}\,(\cos\theta)\,E(t,t_o) + [(\frac{h_or}{R^2})\,E(t,t_o)]^2\right\}$$

and

$$A^{(I)}_{r\leq R} = I\,\ell n\left\{1 - 2\,\frac{h_or}{R^2}\,(\cos\theta)\,E(t,t_o) + [(\frac{h_or}{R^2})E(t,t_o)]^2\right\}.$$

From the image potential just written, we find the following θ-component of field:

$$-\frac{\partial A^{(I)}}{\partial r} = \frac{2\,I\,h_o}{R^2}\,\frac{\cos\theta - \frac{h_or}{R^2}E(t,t_o)}{1-2\,\frac{h_or}{R^2}(\cos\theta)\,E(t,t_o) + [(\frac{h_or}{R^2})E(t,t_o)]^2}\,E(t,t_o),$$

and when evaluated at $r = h_o$, $\theta = 0$ gives

(contd)

$$B_\theta^{(I)} = \frac{2\,I\,h_o}{R^2}\,\frac{E(t,t_o)}{1 - (\frac{h_o}{R})^2\;E(t,t_o)}\;,$$

as found in Section 1 of this Addendum.

The writer is indebted to Dr. Lloyd Smith of this Laboratory for penetrating comments concerning questions that arose with respect to the treatment undertaken in Section 1 of the Addendum.

THE IMAGE-FIELD POTENTIAL
OF A UNIFORMLY-CHARGED ELLIPSE
SITUATED BETWEEN A SET OF
CONDUCTING HYPERBOLIC SURFACES

CONTENTS

THE IMAGE-FIELD POTENTIAL OF A UNIFORMLY-CHARGED ELLIPSE SITUATED BETWEEN A SET OF CONDUCTING HYPERBOLIC SURFACES

L. J. Laslett

I. INTRODUCTION

In considering the significance, for the transport of intense charged-particle beams, of image fields arising from charges induced in nearby conducting surfaces, attention has previously been given to boundary surfaces that are circular or that have a fundamental rotational symmetry period of 180 degrees -- so that terms of the form $r^2 \ {\sin \atop \cos} (2\theta)$ can readily arise in the image-field potential and linear contributions to the image-field components can readily be present. Results for some such cases have been presented elsewhere by the present writer.(1,2)

As non-linear aspects of such image fields may become important, there may be utility in extending work of this nature to treat the case of significantly extended beams, such as has been done for an elliptical beam (of constant charge density) co-axially situated within a circularly-cylindrical conducting wall (Appendix C). It also may be of interest to examine image fields that are present for slightly displaced extended distributions, in order to examine the possible "coherent" effects that act on the beam as a whole.

A situation of particular interest -- and that has motivated the work described in the present Note -- is that in which the boundary surfaces have the shape of (four) hyperbolic sections $[x^2-y^2 = \pm\ c^2]$, such as would be provided by the electrodes of an electrostatic quadrupole-focussing system (and that, in this application, of course could not be shielded from the beam). We accordingly have undertaken to treat the 2D electrostatic problem of an elliptical beam (with semi axes a and b, oriented in the x and y directions, respectively) situated inside conducting cylindrical boundaries of hyperbolic cross-section $x^2-y^2 = \pm c^2$. The analysis will cover the case in which the elliptical beam may be displaced, by distances δ_x, δ_y along the x and y axes, so that its center lies at the point δ_x, δ_y. [These conditions, that still are somewhat special -- namely the orientation of the elliptical beam boundary with respect to the four hyperbolic electrodes -- are adopted in the interests of simplicity, but are believed to refer to situations of greatest practical interest.] With respect to the charge distribution within the elliptical beam boundary, we furthermore assume the charge density to be constant across the beam cross-section, although it may be difficult to reconcile this assumption with a stationary distribution for a beam significantly affected by the image fields whose characteristics we seek.

In the work that follows the linear charge density of the beam will be taken to be $\lambda=1$ esu/cm and results will be stated in e.s.u. for that linear density.(3) With respect to dimensional (geometric) scaling, we anticipate that fields will be of the form

$$\vec{E} = \frac{1}{c}\, \vec{f}\left(\frac{a}{c}, \frac{b}{c}, \frac{\delta_x}{c}, \frac{\delta_y}{c}; \frac{x}{c}, \frac{y}{c}\right).$$

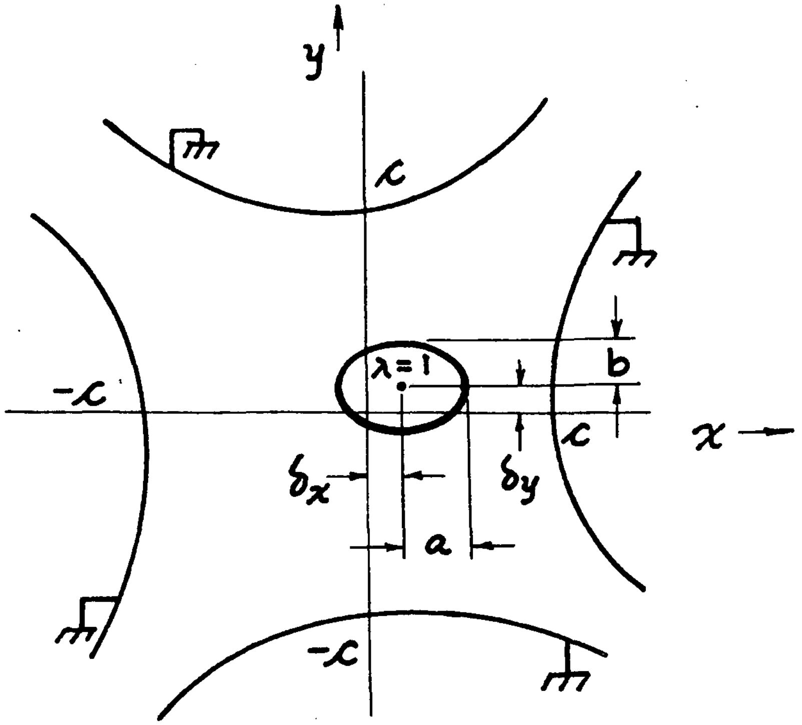

II. THE TRANSFORMATIONS

The conformal transformations that we have found suitable for solution of the present problem are described in some detail in Appendix A. The "Green's Function" from which one can construct the fields of the elliptical beam (even if displaced, as shown) by (numerical) integration is that of a line charge λ situated at a point whose location we shall denote at this stage by (a, b). It has proven convenient to regard the solution of this problem to be formed as the sum of four problems (see Appendix A).

For each Case, the appropriate transformation or transformations lead to new coordinate values for the source points (and correspondingly for field points) that may be denoted by primes (corresponding to whichever new plane is being considered). Such transformations have been programmed as a Sub-routine, for subsequent use. The results of such programmed transformations can be checked by observations of conformality between traces made in each of two different planes, by checking the correctness of the Cauchy-Riemann conditions, or (equivalently) by examining the values of ∇^2 Re(z') & ∇^2 Im (z'), or etc.

III. THE POTENTIAL FUNCTIONS

Following the appropriate transformations, the potential functions for each of the cases may be evaluated (in terms of coordinates for their respective final planes) and the results, when summed, provide the desired total potential for the Green's-Function problem posed above. By subtraction of the "direct" potential (i.e., for the isolated source), the associated "image-field" potential also is obtained.

Such results, as obtainable at this stage, of course can be subjected to some checks of correctness -- thus:

(i) The total potential should approach zero as the field-point approaches the hyperbolic boundary surfaces.

(ii) The image-field potential should appear to be such that its gradient is divergence-free in the interior, while the total potential should exhibit an incipient singularity ($V \cong -2\lambda \ln |\vec{\Delta r}|$) in the immediate vicinity of a line source; and

(iii) A pair of sources close to the x-axis and close to the pole tip at (c,o) likewise should exhibit in that neighborhood potential or field characteristics close to those which would be expected for an image charge (-2λ) situated behind the pole tip by approximately the same distance as these charges are in front of this pole tip.

With such checks performed, to the extent deemed desirable, the corresponding results for the full (possibly displaced) ellipse are evaluated by integration over the area of the elliptical beam. Initially, for simplicity, this integration was performed computationally by a Monte-Carlo integration, but this procedure was soon replaced by a more economical (and, in practice, more precise) procedure employing a double Gaussian integration (using our LBL source routine, GB (developed by Gene Golub), and normally employing n=32 in our work).

Again such final results can be subjected to certain checks (some similar to those mentioned for the Green's function), of which we mention the following:

(i) The total potential should approach zero as the field point approaches the hyperbolic boundary surfaces;

(ii) For a small ellipse displaced so as to be situated close to the pole tip at (c, o) of one of the boundary hyperbolae, the potential or field quantities in that neighborhood should exhibit characteristics close to those expected for a similar image charge, of opposite charge, a similar distance behind the pole tip;

(iii) For a centered beam of very small dimensions, the image-field potential should approach that expected (save for an arbitrary constant) from an independent analytic examination of the specific case of a centered line charge;(4) and

(iv) The "direct" field, or its associated potential function ($V^{(T)} - V^{(I)}$) should have the character expected for a uniformly charged ellipse -- say, most particularly, within the beam itself.(5)

With this description of our analysis and of the types of tests to which our computational work has been subjected, we turn now to certain results that have thereby been obtained.

IV. RESULTS

In operating the Program GBIMG or its succesor GB4MG it is convenient to make one or more of three types of scan, once the relevant dimensional parameters are specified (namely, c, the semi-axes a & b, and δ_x, δ_y):

(i) A scan along the x-axis,

(ii) A scan along the y-axis, &/or

(iii) A scan around a circle in the z-plane (centered on the origin, and with the radius typically taken to be R = 0.9c). In any such scan the image potential at a succession of field points is printed (in e.s.u., for λ=1.0 statcoulomb/cm) and (in the most modern version of the Program) also the total potential. In the scan with respect to angle (#iii), a "standard" scan may be chosen, in which the angles of the field points are the thirty-six values

5 Deg., 15. Deg., 25. Deg., . . . 355. Deg. in Program GB4MG. If this option is elected, one then may ask the program to print the Fourier coefficients of the image-field potential, developed in the form

$$V^{(I)} = c_0 + \sum_{k=1}^{17} c_k \left(\frac{r}{c}\right)^k \cos k\theta + \sum_{k=1}^{18} s_k \left(\frac{r}{c}\right)^k \sin k\theta$$

-- in which some of the higher-order coefficients may be expected to have somewhat lesser accuracy than those of lower order. In this case the Program also evaluates and prints the inferred field strength at the centroid of the ellipse (point δ_x, δ_y), as computed from the negative gradient of this trigonometric development evaluated at the point δ_x, δ_y. Also (optionally) the average image-field components, $\langle E_x^{(I)} \rangle_{Av.}$ and $\langle E_y^{(I)} \rangle_{Av.}$, are obtainable by means of a double Gaussian integration of $E_x^{(I)}$ and $E_y^{(I)}$ over the area of the ellipse.

A. The Centered Beam

The characteristics of the image fields of a centered beam perhaps are best described in terms of the Fourier coefficients of the image-field potential

$$V^{(I)} = c_0 + \sum_{k=1}^{17} c_k \left(\frac{r}{c}\right)^k \cos k\theta ,$$

of which only coefficients c_k with k even will be non-zero in this case. Accompanying Tables present such results (only for c_k with $k \leq 12$)

(i) For a/b=3/2 (and, in one case, for $a/b=\frac{1}{3/2}$),

(ii) For a/b close to unity (actually 16/15), and

(iii) For a/b=2.

Clearly the change of the value of the ratio a/b to its reciprocal will result only in a reversal of sign of the coefficients c_2, c_6 and c_{10} (and so forth, if the tabulation were continued), while the remaining coefficients would remain unaffected.

The striking feature of all these results (in contrast to that frequently found for other image configurations) is the pronounced presence of fourth-order coefficients (c_4, c_8, c_{12}), attributable to the variation of the boundary (with its four-fold symmetry). These fourth-order coefficients in fact do not vary greatly with the size (or shape) of the beam, and for beams of moderate dimensions approach values(4) characteristic of a line charge at the origin

$$[\ c_4 \to -\frac{\pi^2}{48} \doteq -0.205617,\ c_8 \to -\frac{7\pi^4}{23040} \doteq -0.029595^{-}].$$

$c = 1.0 \quad \delta = 0.$

Cases with $a/b = 3/2$ (or $\frac{1}{3/2}$)

	$a = 0.15$	0.30	0.45	0.60	0.75	$\begin{bmatrix}0.50\end{bmatrix}$	0.80	0.90
	$b = 0.10$	0.20	0.30	0.40	0.50	$\begin{bmatrix}0.75\end{bmatrix}$	0.533333 ...	0.60
c_0	+0.2415605	+0.2415002	+0.2412389	+0.2405338	+0.2390389	+0.2390389	+0.2382890	+0.2362921
c_2	-0.0025702	-0.0102822	-0.0231469	-0.0412083	-0.0645817	+0.0645817	-0.0735908	-0.0935155
c_4	-0.205620	-0.205672	-0.205898	-0.206511	-0.207825	-0.207825	-0.208492	-0.210291
c_6	-0.000423	-0.001692	-0.003817	-0.006831	-0.010829	+0.010829	-0.012411	-0.016018
c_8	-0.02960	-0.02962	-0.02972	-0.02998	-0.03057	-0.03057	-0.03087	-0.031705
c_{10}	-0.0001	-0.0004	-0.0009	-0.0016	-0.0026	+0.0026	-0.00303	-0.00400
c_{12}	-0.0051	-0.0051	-0.0052	-0.0053	-0.0055	-0.0055	-0.0056	-0.0059

$\lambda = 1.$ (e.s.u.)

$c = 1.0 \quad \delta = 0.$

ALMOST - CIRCULAR BEAMS

	a = 0.16 b = 0.15	0.32 0.30	0.48 0.45	0.64 0.60	0.80 0.75			
c_0	+0.2415642	+0.2415605	+0.2415445	+0.2415012	+0.2414101			
c_2	-0.0006374	-0.0025497	-0.0057369	-0.0101999	-0.0159404^-			
c_4	-0.205617	-0.205620	-0.205634	-0.205671	-0.205750			
c_6	-0.000105^-	-0.000419^+	-0.000944	-0.001679^-	-0.002626			
c_8	-0.02959_4	-0.029595	-0.029601	-0.029617	-0.029650^+			
c_{10}	-0.0000_2	-0.00010	-0.00022	-0.00039	-0.00062			
c_{12}	-0.0051	-0.0051	-0.0051	-0.0051	-0.0051^+			

$\lambda = 1.$ (e.s.u.)

$c = 1.0 \qquad \delta = 0.$

CASES WITH a/b = 2.

	a = 0.2 b = 0.1	0.4 0.2	0.6 0.3	0.8 0.4				
c_0	+0.2415414	+0.2411940	+0.2396821	+0.2355548				
c_2	-0.0061688	-0.0246923	-0.0557264	-0.0998993				
c_4	-0.205637	-0.205937	-0.207257	-0.210965				
c_6	-0.001015	-0.004073	-0.009298	-0.017211				
c_8	-0.029602	-0.029733	-0.030315	-0.032025				
c_{10}	-0.00024	-0.00096	-0.00223	-0.00434				
c_{12}	-0.0051	-0.0052	-0.0054	-0.0060				

The remaining significant Fourier coefficients in the image-field potential (i.e., c_2, c_6, & c_{10}), for any fixed value of a/b, evidently scale fairly closely in direct proportion to the square of the transverse linear dimensions of the beam relative to c (see following Tables) -- e.g., $\overset{\sim}{\propto}$ $\left(\frac{ab}{c^2}\right)$ -- and of course become small as the centered beam approaches circularity.

a/b = 2

$\frac{a}{c}$	$\frac{b}{c}$	$\frac{c_2}{ab/c^2}$	$\frac{c_6}{ab/c^2}$	$\frac{c_{10}}{ab/c^2}$
0.8	0.4	-0.31218_5	-0.05378	-0.0135_6
0.6	0.3	-0.30959	-0.05166	-0.0124
0.4	0.2	-0.3086_5	-0.05091	-0.012
0.2	0.1	-0.3084_4	-0.0507_5	-0.012

a/b = 1.5

$\frac{a}{c}$	$\frac{b}{c}$	$\frac{c_2}{ab/c^2}$	$\frac{c_6}{ab/c^2}$	$\frac{c_{10}}{ab/c^2}$
0.90	0.60	-0.17318	-0.0297	-0.0074
0.80	0.53333...	-0.17248	-0.0291	-0.0071
0.75	0.50	-0.17222	-0.0289	-0.0069
0.60	0.40	-0.17170	-0.0285^{-}	-0.0067
0.45	0.30	-0.17146	-0.0283	-0.0067
0.30	0.20	-0.17137	-0.0282	-0.0067
0.15	0.10	-0.17135	-0.0282	-0.0067

a/b = 16/15

$\frac{a}{c}$	$\frac{b}{c}$	$\frac{c_2}{ab/c^2}$	$\frac{c_6}{ab/c^2}$	$\frac{c_{10}}{ab/c^2}$
0.80	0.75	-0.02657	-0.004377^{-}	-0.0010
0.64	0.60	-0.02656	-0.004372	-0.0010
0.48	0.45	-0.02656	-0.00437_0	-0.0010
0.32	0.30	-0.02656	-0.00436_{5-}	-0.0010
0.16	0.15	-0.02656	-0.0043_7	-0.001

For a and b interchanged, the signs of these coefficients reverse.

To extend this discussion we may now inquire how the coefficients c_2, c_6, and c_{10} scale with respect to the ratio a/b. A cursory examination of the data already presented suggests that the quantities $\frac{c_2}{(ab/c^2)}$, etc. may scale approximately in direct proportion to ln (a/b) -- a behavior that would lead to these coefficients vanishing when a=b and reversing in sign when a/b is replaced by its inverse. To examine this issue in some greater detail we have performed computations for a sequence of cases in which the product ab has the constant value 0.2520 c^2, while various values are assumed by the ratio a/b. The Fourier coefficients found for these cases are presented in tabular form below, followed by a tabular summary of the quantities $\frac{c_2}{(ab/c^2)}$, $\frac{c_6}{(ab/c^2)}$, and $\frac{c_{10}}{(ab/c^2)}$. These latter quantities, plotted against ln (a/b), yield the graphs shown on the Figures that follow and suggest a very close to linear dependence upon ln (a/b) in each case -- at least for the interval $0.625 = \frac{5}{8} \leq \frac{a}{b} \leq \frac{8}{5} = 1.6$, approximately.

We accordingly might suggest that, for approximate **practical** work, one may represent these coefficients of the image-field potential of a centered ellipse by the handy formulas

$$c_2 = -0.426759 \left(\frac{ab}{c^2}\right) \ln\left(\frac{a}{b}\right)$$

$$= -0.98265 \left(\frac{ab}{c^2}\right) \log_{10}\left(\frac{a}{b}\right),$$

$$c_6 = -0.07097 \left(\frac{ab}{c^2}\right) \ln\left(\frac{a}{b}\right)$$

$$= -0.16342 \left(\frac{ab}{c^2}\right) \log_{10}\left(\frac{a}{b}\right),$$

$$c_{10} = -0.01695 \left(\frac{ab}{c^2}\right) \ln\left(\frac{a}{b}\right)$$

$$= -0.03902 \left(\frac{ab}{c^2}\right) \log_{10}\left(\frac{a}{b}\right)$$

-- or, more simply,

$$c_2 = -0.98 \left(\frac{ab}{c^2}\right) \log_{10} \left(\frac{a}{b}\right),$$

$$c_6 = -0.16 \left(\frac{ab}{c^2}\right) \log_{10} \left(\frac{a}{b}\right), \text{ and}$$

$$c_{10} = -0.039 \left(\frac{ab}{c^2}\right) \log_{10} \left(\frac{a}{b}\right).$$

$c = 1.0 \qquad \delta = 0.$

CASES WITH $a \cdot b = 0.2430 \times c^2$, cont'd

	a = 0.504	0.5	0.45	0.40	0.35	0.30	0.84	
	b = 0.50	0.504	0.56	0.63	0.72	0.84	0.30	
c_0	0.2415641	0.2415641	0.2412470	0.2401169	0.2374956	0.2315825	0.2315825^{+}	
c_2	-0.0008258^{-}	0.0008258^{-}	0.0228585	0.0488521	0.0820725	0.1291658	-0.1291658^{-}	
c_4	-0.2056170	-0.2056170	-0.2058913	-0.2068757	-0.2092024	-0.2146843	-0.2146843	
c_6	-0.0001358	0.0001358	0.0037690	0.0081242	0.0139265^{+}	0.0229729	-0.0229729	
c_8	-0.0295939	-0.0295939	-0.0297130	-0.0301456	-0.0311983^{-}	-0.0338541	-0.0338541	
c_{10}	-0.0000319	0.0000319	0.0008883	0.0019399	0.0034303	0.0060938	-0.0060938	
c_{12}	-0.0051216^{+}	-0.0051216^{+}	-0.0051636	-0.0053182	-0.0057093	-0.0067893	-0.0067893	

$c = 1.0 \qquad \delta = 0.$

CASES WITH $a \cdot b = 0.02520 \times c^2$

	$a = 0.28$ $b = 0.90$	0.90 0.28	0.80 0.315	0.75 0.336	0.70 0.36	0.60 0.42		
c_0	0.2273171^+	0.2273172	0.2339056	0.2363015^-	0.23819843^-	0.2406963^-		
c_2	0.1548658	-0.1548658	-0.1129270^-	-0.0934314	-0.0746071	-0.0378169		
c_4	-0.2188537	-0.2188537^-	-0.2124908	-0.2102829	-0.2085726	-0.2063697		
c_6	0.0285348	-0.0285347	-0.0197118	-0.0160024	-0.0125911	-0.0062614		
c_8	-0.0360484	-0.0360483^+	-0.0327610	-0.0317019	-0.0309090^+	-0.0299223		
c_{10}	0.0080129	-0.0080129	-0.0050753	-0.0039992	-0.0030753	-0.0014851		
c_{12}	-0.0077804	-0.0077804	-0.0063288	-0.0059039	-0.0055998	-0.0052380^-		

$\delta = 0.$

CASES WITH $a \cdot b = 0.2520 \times c^2$

a, b ln (a/b)		0.50, 0.504 -0.007968	0.45, 0.56 -0.218689	0.40, 0.63 -0.454255	0.35, 0.72 -0.721318	0.30, 0.84 -1.029619_4
$\frac{c_2}{(\frac{ab}{c^2})}$		0.003277	0.090708	0.193857_5	0.325684_5	0.512563^-
$\frac{c_6}{(\frac{ab}{c^2})}$		0.000539	0.014956	0.032239	0.055264	0.091162
$\frac{c_{10}}{(\frac{ab}{c^2})}$		0.000126_6	0.003525	0.007698	0.013612	0.024182

a, b ln (a/b)		0.90, 0.28 1.167605	0.80, 0.315 0.932039	0.75, 0.336 0.802962	0.70, 0.36 0.664976	0.60, 0.42 0.356675
$\frac{c_2}{(\frac{ab}{c^2})}$		-0.614547	-0.448123	-0.370759_5	-0.296060	-0.150067
$\frac{c_6}{(\frac{ab}{c^2})}$		-0.113233	-0.078221_4	-0.063501_6	-0.049965^-	-0.024847
$\frac{c_{10}}{(\frac{ab}{c^2})}$		-0.031797	-0.020140	-0.015870	-0.012203_6	-0.005893

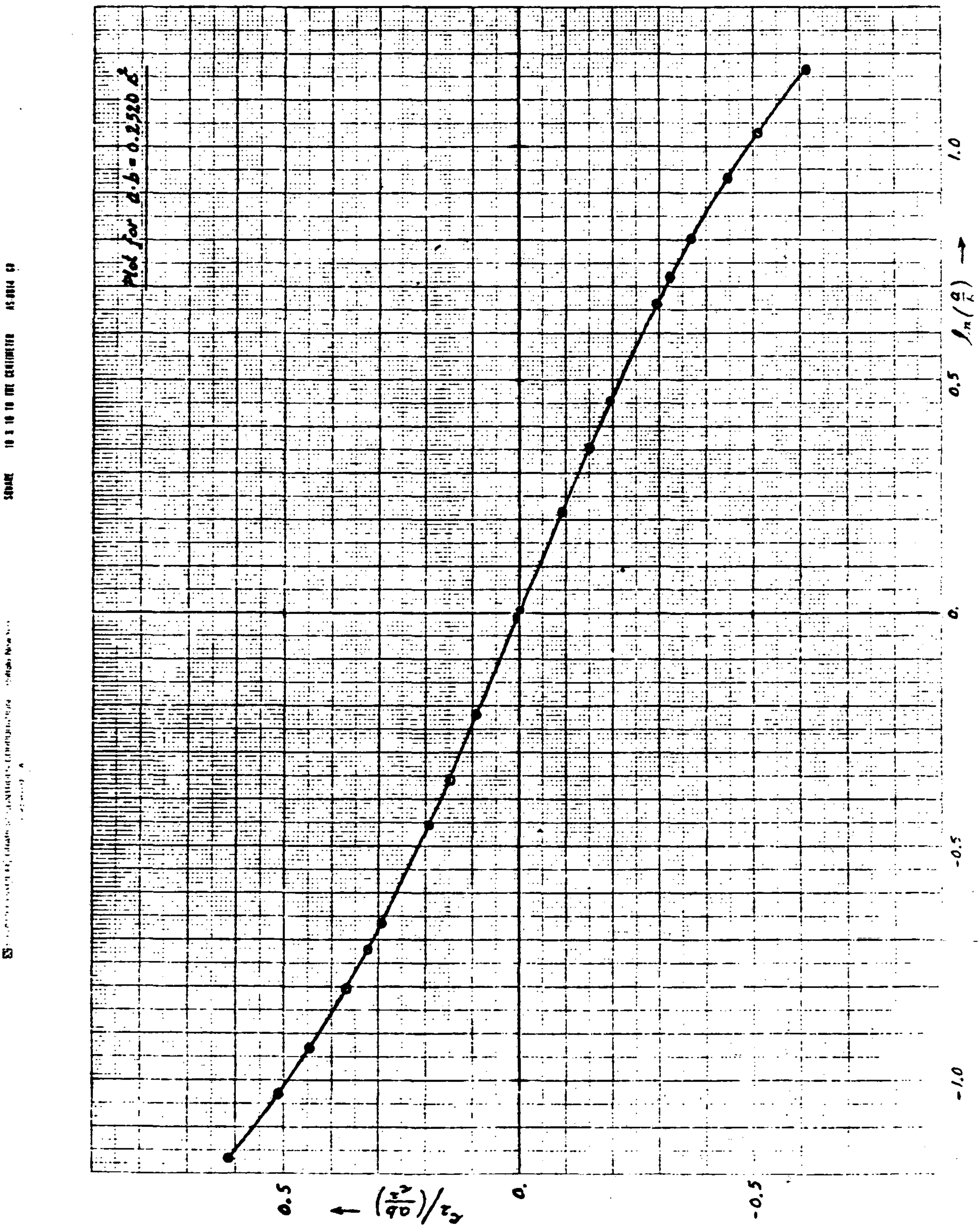
Plot for a·b = 0.2520 c²
$\ln(a/b)$ →
$r_2/(ab/r_2)$ →
-1.0
-0.5
0.
0.5
1.0
0.5
0.
-0.5
SQUARE 10 X 10 TO THE CENTIMETER

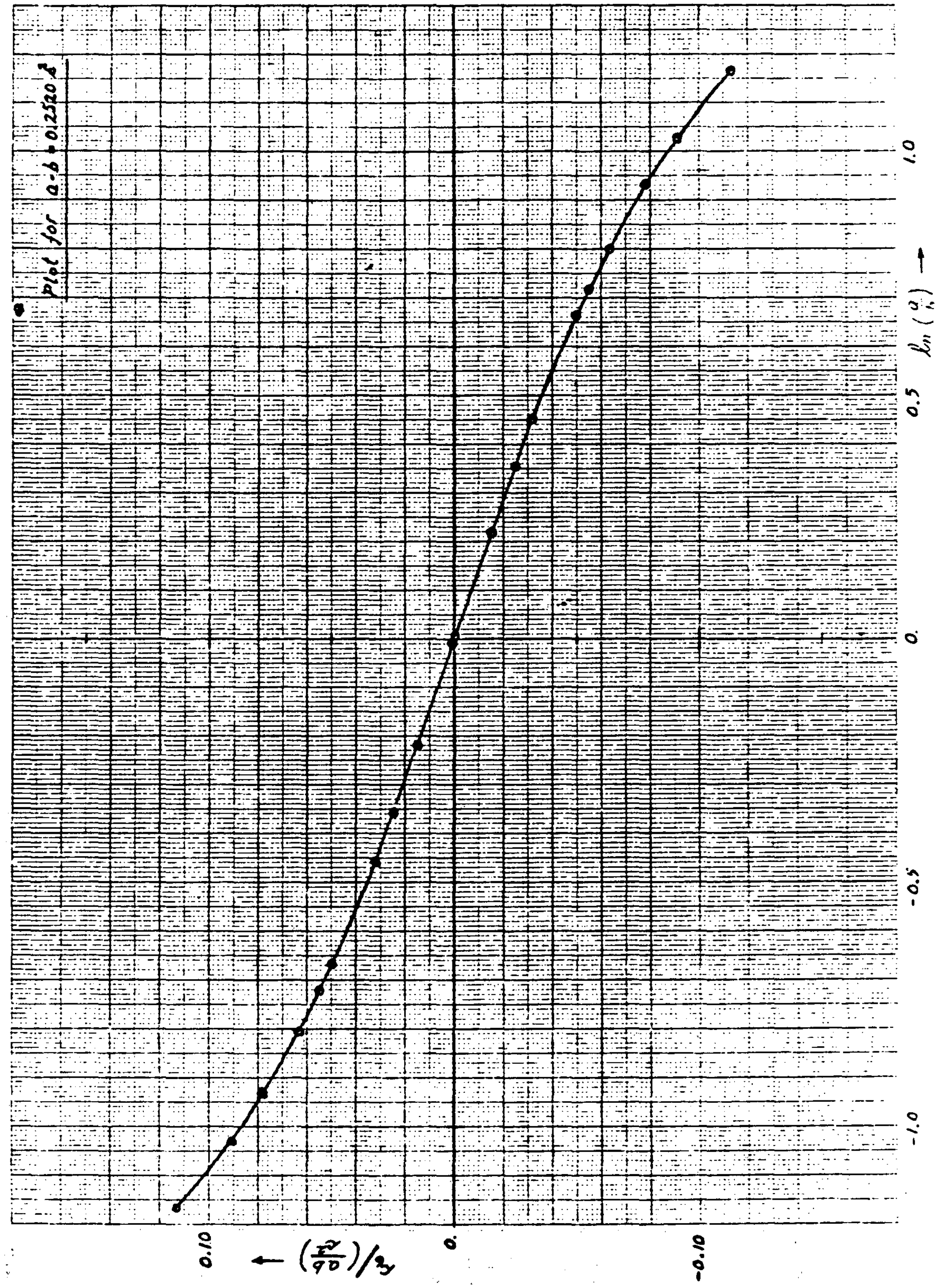
Plot for a-b = 0.2520 Å
1.0
0.5
0
-0.5
-1.0
$f_{11}(\frac{a}{r_1})$ →
0.10
0.
-0.10
← $(\frac{F^2}{qD})/3$

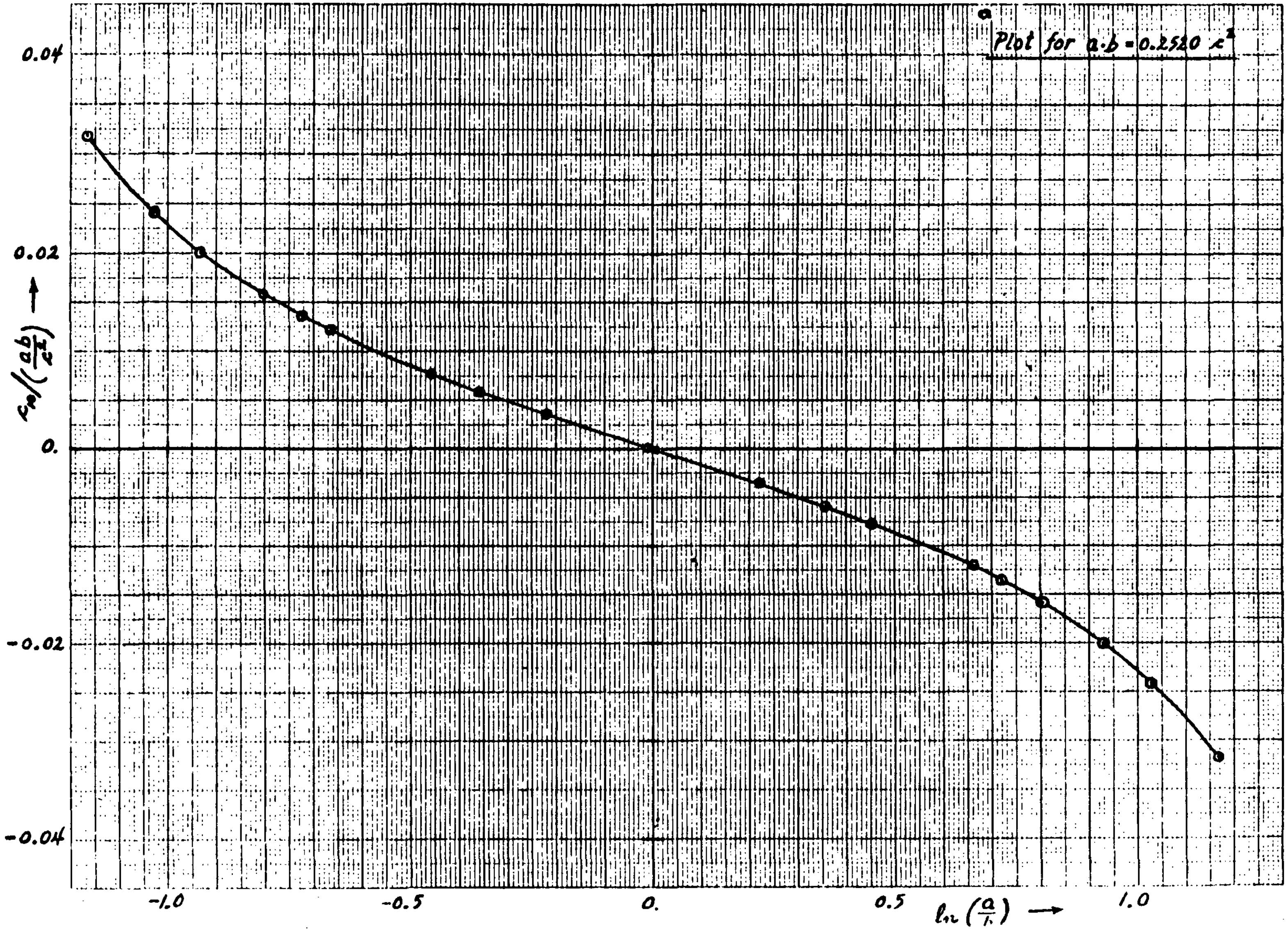
Plot for a·b = 0.2520 c²
$c_m/(\frac{ab}{c^2})$ →
0.04
0.02
0.
-0.02
-0.04
-1.0
-0.5
0.
0.5
1.0
$\ln(\frac{a}{r})$ →

With respect to the fourth-order coefficients c_4, c_8, . . . for such a centered ellipse, on the other hand, these might be taken simply as having values identical to those for a central line charge (as a lowest-order approximation) -- namely

$c_4 \cong -0.2056$,

$c_8 \cong -0.0296$, and

$c_{12} \cong -0.0051$

B. The Displaced Beam

In the case that the elliptical beam is displaced, as a whole, we have concentrated our attention on the effect that a displacement has on the development of the following quantities:

(i) the Fourier coefficients c_k and s_k in the image-field potential.

(ii) the components of the image field evaluated at the centroid of the displaced ellipse, obtained from the Fourier coefficients as

$$E_x^{(I)}(\delta_x,\delta_y) = -\frac{1}{c} \Sigma\, k\left(\frac{r}{c}\right)^{k-1} [c_k \cos (k-1)\,\theta + s_k \sin (k-1)\,\theta]$$

$$E_y^{(I)}(\delta_x,\delta_y) = -\frac{1}{c} \Sigma\, k\left(\frac{r}{c}\right)^{k-1} [s_k \cos (k-1)\,\theta - c_k \sin (k-1)\,\theta],$$

where (in this application) r, θ are the polar co-ordinates of the centroid and summations extend from $k=1$ through $k=17$ or 18 for terms proportional to c_k or s_k, respectively.

(iii) the average image-field components, $\left\langle E_x^{(I)} \right\rangle_{av.}$, and $\left\langle E_y^{(I)} \right\rangle_{av.}$, obtained by integrations, over the area of the ellipse, of expressions similar to those written immediately above.

1. For Displacements Exclusively in the x Direction

Before describing and discussing results obtained when non-zero displacements are present in both the x and y directions, we first present some results (obtained with the simpler program GBIMG) for cases in which the displacement is only in the x direction ($\delta_x = \delta$, $\delta_y = 0$). One finds that the three quantities $-c_1/c$, $E_x^{(I)}(\delta,0)$, and $\left\langle E_x^{(I)} \right\rangle_{av.}$ are all comparable and are odd functions of δ. For a circular beam ($a/b = 1$), moreover, these quantities are independent of beam size, and the values of $E_x^{(I)}(\delta, 0)$ and $\left\langle E_x^{(I)} \right\rangle_{av.}$ are identical--as is to be expected, since the external direct field of a circular beam is independent of its radius. For this circular beam, however, the quantities $E_x^{(I)}(\delta, 0)$ and $\left\langle E_x^{(I)} \right\rangle_{av.}$, while remaining equal to one another for a circular beam, exhibit noticeable non-linearity as a function of δ/c.

Values of the quantities c_1, and $E_x^{(I)}$ (δ, o), and $\langle E_x^{(I)} \rangle_{av.}$ for the image fields have been computed and tabulated for several combinations of values for the parameters a/b, ab/c^2, and δ/c. We recognize that the quantity c_1 should be a function simply of these dimensionless ratios, while the remaining two (field-like) quantities similarly should be $\frac{1}{c}$ times functions of these same ratios -- and all are for $\lambda = 1$ (e.s.u.). The attached tabulations of this nature (for c=1) accordingly should be of some utility in themselves for application to specific cases. In addition, however, it appears that -- for cases in which a/b does not differ greatly from unity, and the ratios ab/c^2 and δ/c are each reasonably small -- one may write the approximate handy formulas

$$c_1 \cong -1.6 \left[1.0 + 0.21 \left(\frac{ab}{c^2}\right) \ln \left(\frac{a}{b}\right)\right] \frac{\delta}{c}$$

$$= -1.6 \left[1.0 + 0.48 \left(\frac{ab}{c^2}\right) \log_{10} \left(\frac{a}{b}\right)\right] \frac{\delta}{c} ,$$

$$E_x^{(I)} (\delta, 0) \cong 1.6 \left[1.0 + 0.73 \left(\frac{ab}{c^2}\right) \ln \left(\frac{a}{b}\right)\right] \frac{\delta}{c^2}$$

$$= 1.6 \left[1.0 + 1.68 \left(\frac{ab}{c^2}\right) \log_{10} \left(\frac{a}{b}\right)\right] \frac{\delta}{c^2},$$

$$\langle E_x^{(I)} \rangle_{av.} \cong 1.6 \left[1.0 + 1.71 \left(\frac{ab}{c^2}\right) \ln \left(\frac{a}{b}\right)\right] \frac{\delta}{c^2}$$

$$= 1.6 \left[1.0 + 3.94 \left(\frac{ab}{c^2}\right) \log_{10} \left(\frac{a}{b}\right)\right] \frac{\delta}{c^2}.$$

The extent to which these formulas provide values differing somewhat from the more exact values obtained from runs with Program GBIMG--when δ/c differs significantly from zero, a/b differs significantly from unity, and ab/c^2 is significant--is illustrated by the following tabulation of results for cases that might be regarded as typical of situations of interest. Agreement is found amongst all these cases substantially within 10 percent, and chiefly with an error appreciably less than this amount.

<u>c = 10.</u>			c_1		$E_x^{(I)}$ (δ, 0)		$\langle E_x^{(I)} \rangle_{av.}$	
a.	b.	δ	COMPUTER	FORMULA	COMPUTER	FORMULA	COMPUTER	FORMULA
4.	3.	1.	-0.1584	-0.1612	0.01645	0.01640	0.01702	0.01695
3.	4.	1.	-0.1562	-0.1588	0.01564	0.01560	0.01510	0.01505
4.	3.	2.	-0.3183	-0.3223	0.03499	0.03281	0.03620	0.03389
3.	4.	2.	-0.3136	-0.3177	0.03326	0.03119	0.03213	0.03011
3.	2.	1.	-0.1581	-0.1608	0.01633	0.01628	0.01673	0.01667
2.	3.	1.	-0.1565	-0.1592	0.01575	0.01572	0.01537	0.01533
3.	2.	2.	-0.3176	-0.3216	0.03473	0.03257	0.03559	0.03333
2.	3.	2.	-0.3142	-0.3184	0.03350	0.03143	0.03269	0.03067
6.	4.	1.	-0.1609	-0.1632	0.01724	0.01714	0.01897	0.01866
4.	6.	1.	-0.1545	-0.1568	0.01426	0.01486	0.01345	0.01334
6.	4.	2.	-0.3236	-0.3265	0.03669	0.03427	0.04046	0.03733
4.	6.	2.	-0.3099	-0.3135	0.03145	0.02973	0.02868	0.02667
7.5	5.0	1.	-0.1633	-0.1651	0.01796	0.01778	0.02086	0.02016
5.0	7.5	1.	-0.1533	-0.1549	0.01433	0.01423	0.01208_5	0.01184
6.	3.	1.	-0.1623	-0.1642	0.01768	0.01746	0.02012	0.01942
3.	6.	1.	-0.1537	-0.1558	0.01455	0.01454	0.01260	0.01258
6.	3.	2.	-0.3267	-0.3283	0.03765	0.03491	0.04302	0.03883
3.	6.	2.	-0.3081	-0.3117	0.03097	0.02909	0.02691	0.02517

2. For Possible Displacements in both the x and y Directions

The displacement of the beam center, from the origin, is now represented by δ_x, δ_y. The lack of generality thus consists only in restricting the results to be cited here to cases in which (for simplicity) the principal axes of the elliptical beam are taken to be parallel to the x, y co-ordinate axes.

Values of $\left\langle E_x^{(I)} \right\rangle_{\text{av.}}$ and $\left\langle E_y^{(I)} \right\rangle_{\text{av.}}$ have been computed (Program GB4MG, stored in Library JACKSON), for various values of δ_x, δ_y, for several combinations of values of a and b. If all dimensions of the problem (c; a, b; δ_x, δ_y) are scaled by a common factor, we expect the fields to vary in proportion to $\frac{1}{c}$; also an interchange of b with a and of δ_y with δ_x will be expected to lead to an interchange of $E_y^{(I)}$ with $E_x^{(I)}$. The image-field potential and the components of the image field itself moreover may be expected to be respectively even or odd functions of δ_x and of δ_y. Finally, if b=a (circular beam), the average field values $\left\langle E_x^{(I)} \right\rangle_{\text{av.}}$ and $\left\langle E_y^{(I)} \right\rangle_{\text{av.}}$ should be independent of the common value of a,b.

Results for the cases that have been run (esp., with c=1. and a/b equal to 1.25, 1.35, or 1.50) can be seen in tabular form. We have attempted to describe these results for $\left\langle E_x^{(I)} \right\rangle_{\text{av.}}$ and $\left\langle E_y^{(I)} \right\rangle_{\text{av.}}$ as derivable (approximately) as the gradient (with respect to δ_x, δ_y) of a function - POT (denoted POTM in a Least-Squares fitting routine FITD2 of Library JACKSON)

$$\left\langle E_x^{(I)} \right\rangle_{\text{av.}} = \frac{\partial}{\partial \delta_x} (\text{-POT}), \qquad \left\langle E_y^{(I)} \right\rangle_{\text{av.}} = \frac{\partial}{\partial \delta_y} (\text{-POT}),$$

where

$$\begin{aligned} \text{-POT} = {} & A_1 \left(\frac{\delta_x}{c}\right)^2 + A_4 \left(\frac{\delta_y}{c}\right)^2 \\ & + A_2 \left(\frac{\delta_x}{c}\right)^4 + A_7 \left(\frac{\delta_x}{c}\right)^4 + A_5 \left(\frac{\delta_x}{c}\right)^2 \left(\frac{\delta_y}{c}\right)^2 . \end{aligned}$$

[It was not judged desirable, in this effort to represent -POT, to go beyond terms of 4 th order. Greatest utility may be expected to accrue for situations in which $|\delta_x/c|$ and $|\delta_y/c|$ each are less than (or do not exceed) 0.15].

We thus attempt the representation of our results in the form

$$\left\langle E_x^{(I)} \right\rangle_{av.} = \frac{1}{c} [2 A_1 (\frac{\delta_x}{c}) + 4 A_2 (\frac{\delta_x}{c})^3 + 2 A_5 (\frac{\delta_x}{c})(\frac{\delta_y}{c})^2]$$

$$\left\langle E_y^{(I)} \right\rangle_{av.} = \frac{1}{c} [2 A_4 (\frac{\delta_y}{c}) + 4 A_7 (\frac{\delta_y}{c})^3 + 2 A_5 (\frac{\delta_x}{c})^2 (\frac{\delta_y}{c})].$$

For convenience in possible future dynamical computations, finally, we have attempted to represent the coefficients A_1, A_2, A_4, A_5, and A_7 by simple <u>approximate</u> functions of the parameters ab/c^2 and a/b (or $\log_{10} (\frac{a}{b})$) as follows:

$$A_1 \cong 0.785 + 3 \frac{ab}{c^2} \log_{10} \frac{a}{b}, \qquad A_2 \cong 0.834 + 3 \frac{ab}{c^2} \log_{10} \frac{a}{b},$$

$$A_4 \cong 0.785 - 3 \frac{ab}{c^2} \log_{10} \frac{a}{b}, \qquad A_7 \cong 0.834 - 3 \frac{ab}{c^2} \log_{10} \frac{a}{b},$$

$$A_5 \cong -[2.48_{64} + (6.5 \frac{ab}{c^2} \log_{10} \frac{a}{b})^2].$$

Thus for $c = 10.$ cm, $a = 4.32$ cm, $b = 3.20$ cm

$(ab/c^2 = 0.13824$ and $a/b = 1.35)$

and with $\delta_x = 1.$ cm, $\delta_y = 0.5$ cm $(\delta_x/c = 0.1, \delta_y/c = 0.05)$, we would compute from the "handy formula" for $\left\langle E_x^{(I)} \right\rangle$ the result $\left\langle E_x^{(I)} \right\rangle_{av.} = \frac{1}{10.} [1.701126 \times 0.1] = \frac{0.1701126}{10.} = 0.01701126$ (for $\left\langle E_x^{(I)} \right\rangle_{av.}$ expressed in statvolts/cm when $\lambda = 1.0$ statcoulomb/cm), while if all physical (spatial) dimensions had been one-tenth as great $(c = 1.0)$ we would obtain an image field ten times greater--namely 0.1701126 for $\left\langle E_x^{(I)} \right\rangle_{av.}$

For this latter case (c being unity) the program GB4MG prints

$\left\langle E_x^{(I)} \right\rangle_{av.} = 0:1709450$

The adequacy of the handy (approximate) formulas just proposed may be indicated by the following table, in which for c=1 and $\delta_x/c = \delta_y/c = 0.15$ we list first the values of $\left\langle E_x^{(I)} \right\rangle_{av.}$ and $\left\langle E_y^{(I)} \right\rangle_{av.}$ from GB4MG computations and then (on the line that follows) the same quantities as estimated by the handy formulas.

c = 1.0

Average Image Field At $\delta_x/c = 0.15$, $\delta_y/c = 0.15$

a/c	b/c	$c \left\langle E_x^{(I)} \right\rangle$	$c \left\langle E_y^{(I)} \right\rangle$
0.338 821 487	0.295 140 668	0.2359 0.2356	0.2243 0.2243
0.40	0.32	0.2423 0.2416	0.2182 0.2183^{-}
0.55	0.44	0.2536 0.2519	0.2079 0.2078^{-}
0.65	0.52	0.2634 0.2605	0.1994^{-} 0.1989
0.432	0.32	0.2481 0.2468	0.2128 0.2129
0.54	0.40	0.2587 0.2562	0.2034 0.2033^{-}
0.675	0.50	0.2761^{-} 0.2708	0.1889^{+} 0.1881^{-}
0.45	0.30	0.2544 0.2522	0.2072 0.2075^{-}
0.60	0.40	0.2747 0.2692	0.1900 0.1897
0.75	0.50	0.3033 0.2908	0.1684 0.1666
a = b		0.2301 0.2300	0.2301 0.2300

N = 32, UNLESS OTHERWISE INDICATED

$\left\langle E_x^{(I)} \right\rangle_{av.}$ & $\left\langle E_y^{(I)} \right\rangle_{av.}$

c = 1.0

a_m = 0.338821487 b_m = 0.295140668 R = 0.96

δ_y ↓ \ δ_x →	0.	0.05	0.10	0.15
0.	▨	0.08082663 0.	0.1641968 0.	0.2527371 0.
0.05	0. 0.07710680	0.08020871 0.07648903	0.1629574 0.7463233	0.2508683* 0.07152556
0.10	0. 0.1566461	0.07835341 0.1554090	0.1592368 0.1516912	0.2452597 0.1454724
0.15	0. 0.2411192	☒	0.1530260 0.2336685	0.2359025 0.2243233

δ_x = .15, δ_y = .075

0.2485318
0.1080434

δ_x = .075, δ_y = .075

0.1199442
0.1143313

δ_y = .15, δ_x = .075

0.1136670
0.2369308

	From 13 Cases		From 16 Cases
A_1 =	0.8039980	or	0.8040216
A_4 =	0.7669757	or	0.7669926
A_2 =	0.8532866	or	0.8528030
A_7 =	0.8170315	or	0.8166176
A_5 =	-2.488301	or	-2.487639

by FITD2

GB4MG

c = 1.0

$a_m = 0.40$, $b_m = 0.32$

$\left\langle E_x^{(I)} \right\rangle_{av.}$ & $\left\langle E_y^{(I)} \right\rangle_{av.}$

R = 0.96

δ_y \ δ_x	0.	0.05	0.10	0.15	0.20
0.		.08288833 0.	.1683879 0.	.2592025 0.	
0.05	0. .07514553	.08226903 .07452655	.1671447 .07266513	.2573251 .06954687	
0.10	0. .1526708	.08041053 .1514322	.1634146 .1477079	.2516940 .1414711	
0.15	0. .2350174	.07731037 .2331569	.1571944 .2275646	.2423092 .2182049	
0.20					
0.25					

$$\left\langle E_x^{(I)} \right\rangle_{av.}$$

$$\left\langle E_y^{(I)} \right\rangle_{av.}$$

c = 1.0

$a_m = 0.55$, $b_m = 0.44$

R = 0.96

δ_y \ δ_x	0.	0.05	0.10	0.15	0.20
0.		.08652265 0.	.1757875 0.	.2706475 0.	
0.05	0. .07184918	.08589880 .07122595	.1745332 .06934983	.2687484 .06620037	
0.10	0. .1459979	.08402831 .1447524	.1707732 .1410037	.2630572 .1347130	
0.15	0. .2247973	.08091364 .2229306	.1645144 .2173142	.2535896 .2078948	
0.20					
0.25					

$\left\langle E_x^{(I)} \right\rangle_{av.}$

$\left\langle E_y^{(I)} \right\rangle_{av.}$

c = 1.0

$a_m = 0.65$, $b_m = 0.52$

R = 0.96

δ_y \ δ_x	0.	0.05	0.10	0.15	0.20
0.		.08969047 0.	.1822497 0.	.2806762 0.	
0.05	0. .06913150	.08906060 .06850251	.1809816 .06660731	.2787515 .06341977	
0.10	0. .1405044	.08717344 .1392487	.1771828 .1354660	.2729878 .1291064	
0.15	0. .2164037	.08403561 .2145254	.1708688 .2088685	.2634142 .1993639	
0.20					
0.25					

$c = 1.0$ & $\left\langle E_x^{(I)} \right\rangle_{av.}$ & $\left\langle E_y^{(I)} \right\rangle_{av.}$

$a_m = 0.432$, $b_m = 0.32$ R = 0.96

$\delta_y \downarrow$ \ $\delta_x \rightarrow$	0.	0.05	0.10	0.15	0.20
0.	▨	.08475825 0.	.1721933 0.	.2650833 0.	
0.05	0. .07342470	.08413693 .07280386	.1709450 .07093586	.2631958 .06780326	
0.10	0. .1491860	.08227325 .1479444	.1672015 .1442096	.2575369 .1379485	
0.15	0. .2296766	.07916730 .2278140	.1609649 .2222123	.2481148 .2128272	
0.20					
0.25					

$c = 10.$

$a_m = 4.32$ $b_m = 3.20$

(R = 9.6)

$\longrightarrow$ $\delta_x = 1.0$, $\delta_y = 0.5$: $\boxed{.01709450}$ $\boxed{.007093586}$

NOTE: If all spatial dimensions scaled simiarly, field components change in inverse proportion.

NOTE: $E_x(\delta)$, $\langle E_x \rangle$ & $E_y(\delta)$, $\langle E_y \rangle$ are close to $-c_{1/c}$ & $-s_{1/c}$, respectively, and (with $a_m = b_m$) $\langle E_x \rangle = E_x(\delta)$, $\langle E_y \rangle = E_y(\delta)$

(R=0.96)

$a_m = b_m \rightarrow$ $c = 1.00$, $a_m = 0.372$ $b_m = 0.372$

δ_x	δ_y	c_1 s_1	$E_x(\delta)$ $E_y(\delta)$	$\langle E_x \rangle$ $\langle E_y \rangle$
0.1	0.	-.1572868 0.	.1603891 0.	.1603891 0.
0.1	0.05	-.1571291 -.07825915	.1591516 .07647937	.1591516 .07647937
0.1	0.1	-.1566619 -.1566619	.1554348 .1554348	.1554348 .1554348
0.	0.1	0. -.1572868	0. .1603891	0. .1603891

$$\left\langle E_x^{(I)} \right\rangle_{av.}$$

&

$$\left\langle E_y^{(I)} \right\rangle_{av.}$$

$c = 1.0$

$a_m = 0.54,\ b_m = 0.40$ $\qquad$ $R = 0.96$

$\delta_x \rightarrow$ $\delta_y \downarrow$	0.	0.05	0.10	0.15	0.20
0.	▨	.08817417 0.	.1791550 0.	.2758696 0.	
0.05	0. .07041504	.08754741 .06978904	.1778940 .06790368	.2739579 .06473560	
0.10	0. .1430981	.08566892 .1418477	.1741152 .1380827	.2682312 .1317586	
0.15	0. .2203643	.08254335 .2184923	.1678300 .2128569	.2587121 .2033969	
0.20					
0.25					

$\left\langle E_x^{(I)} \right\rangle_{av.}$

$\& \left\langle E_x^{(I)} \right\rangle_{av.}$

c = 1.0

$a_m = 0.675,\ b_m = 0.50$

R = 0.96

δ_y \ δ_x	0.	0.05	0.10	0.15	0.20
0.		.09377064 0.	.1905914 0.	.2936711 0.	
0.05	0. .06582642	.09313038 .06518739	.1892999 .06325952	.2917046 .06000871	
0.10	0. .1338328	.09121380 .1325588	.1854346 .1287162	.2858210 .1222394	.3958613 .1130065
0.15	0. .2062345	.08803280 .2043330	.1790220 .1985995	.2760666 .1889424	
0.20			.1701007 .2752079		
0.25					

$$\left\langle E_x^{(I)} \right\rangle_{av.}$$

&

$$\left\langle E_y^{(I)} \right\rangle_{av.}$$

$c = 1.0$

$a_m = .45,\ b_m = .30$

$R = 0.96$

δ_y ↓ / δ_x →	0.	0.05	0.10	0.15	0.20
0.	▨	.08678270 0.	.1763175 0.	.2714689 0.	.3753420 0.
0.05	0. .07162080	.08615843 .07099716	.1750623 .06911969	.2695679 .06596748	.3727701 .06150147
0.10	0. .1455360	.08428678 .1442898	.1712995 .1405387	.2638715* .1342431	.3650664 .1253285
0.15	0. .2240908	.08117057 .2222234	.1650369 .2166043	.2543963 .2071791	.3522637 .1938453
0.20	0. .3097377	.07681203 .3072494	.1562823 .2997649	.2411627 .2872213	.3344059 .2694986
0.25	0. .4051049				
0.30	0. .5130844				

$\delta_x = 0.10$

$\delta_y = 0.15$

.1342431
.2638715

* Reciprocally, for $\left.\begin{array}{l} a_m = 0.30 \\ b_m = 0.45 \end{array}\right\}$.

$$\left\langle E_x^{(I)} \right\rangle_{av.}$$

&

$$\left\langle E_y^{(I)} \right\rangle_{av.}$$

c = 1.0

$a_m = 0.6$, $b_m = 0.4$

R = 0.96

δ_y \ δ_x	0.	0.05	0.10	0.15	0.20	0.25
0.		.09333310 0.	.1896959 0.	.2922732 0.	.4045882 0.	.5307490 0.
0.05	0. .06617088	.09269409 .06553306	.1884071 .06360912	.2903116 .06036584	.4019141 .05574169	
0.10	0. .1345276	.09078108 .1332559	.1845499 .1294206	.2844423 .1229578	.3939168 .1137490	
0.15	0. .2072924	.08760540 .2053938	.1781492 .1996698	.2747096 .1900313	.3806684 .1763119	
0.20	0. .2867639	.08318344 .2842471	.1692421 .2766630	.2611798 .2639044	.3622791 .2457711	
0.25	0. .3753668					
0.30	0. .4757151					

$$\left\langle E_x^{(I)} \right\rangle_{av.} \quad \& \quad \left\langle E_y^{(I)} \right\rangle_{av.}$$

c = 1.0

$a_m = .75$, $b_m = .50$ R = 0.96

δ_y \ δ_x	0.	0.05	0.10	0.15	0.20
0.		.1025356 0.	.2085882 0.	.3219207 0.	.4468460 0.
0.05	0. .05938263	.1018637 .05871287	.2072271 .05668636	.3198324 .05324866	.4439670 .04829958
0.10	0. .1208547	.09985625 .1195230	.2031605 .1154947	.3135949* .1086637	.4353669 .0988322
0.15	0. .1865265	.09653645 .1845480	.1964388 .1785652	.3032916 .1684281	.4211692 .1538542
0.20	0. .2585535	.09194053 .2559484	.1871404 .2480758	.2890574 .2347535	.4015916 .2156390
0.25	0. .3391666				

* Reciprocally, for $\left.\begin{array}{l} a_m = 0.50 \\ b_m = 0.75 \end{array}\right\}$ $\delta_y = 0.15$, $\delta_x = 0.10$:

$$\boxed{\begin{array}{c} .1086632 \\ .3135957 \end{array}}$$

$$\left\langle E_x^{(I)} \right\rangle_{av.}$$

$$\left\langle E_y^{(I)} \right\rangle_{av.}$$

$c = 1.0$

$a_m = 0.6$, $b_m = 0.6$

$R = 0.96$

δ_y \ δ_x	0.	0.05	0.10	0.15	0.20	0.25
0.		.07895164 0.	.1603891 0.	.2468736 0.	.3411269 0.	.4461357 0.
0.05	0. .07895164	.07833419 .07833419	.1591516 .07647938	.2450101 .07337896	.3386261 .06901632	
0.10	0. .1603891	.07647938 .1591516	.1554348 .1554348	.2394145 .1492241	.3311199 .1404894	
0.15	0. .2468736	.07337896 .2450101	.1492241 .2394145	.2300697 .2300697	.3185942 .2169382	
0.20	0. .3411269	.06901632 .3386261	.1404894 .3311199	.2169382 .3185942	.3010138 .3010137	
0.25	0. .4461357					

use average

Values below diagonal
recorded by symmetry.

$\langle E_x^{(I)} \rangle_{av.}$

& $\langle E_y^{(I)} \rangle_{av.}$

c = 1.0

$a_m = 0.36$, $b_m = 0.36$ R = 0.96

δ_x / δ_y	0.	0.05	0.10	0.15	0.20	0.25
0.	▨	.07895164 0.	.1603891 0.	.2468736 0.	.3411269 0.	.4461357 0.
0.05	0. .07895164	.07833419 .07833419	.1591516 .07647937			
0.10	0. .1603891	.07647937 .1591516	.1554348 .1554348			
0.15	0. .2468736					
0.20	0. .3411269					
0.25	0. .4461357					

Values below diagonal
recorded by symmetry

Values for

$a_m = b_m$

are identical to those
for other $a_m = b_m$ (e.g., $a_m = b_m = 0.60$).

C. Illustrations

To illustrate these image effects--*e.g.*, in relation to the "direct" field of the beam--we have considered the particular case of a $\lambda=1$ beam with $a=7.5$, $b=5.0$ and $f=\sqrt{a^2 - b^2} = \sqrt{31.25} \cong 5.590$. Such a beam may be typical of one traversing an A-G focusing structure as adopted for an induction linear accelerator for a heavy-ion driver in a HIF research program. Curves are presented graphing E_x *vs.* x at $y = 0$ and E_y *vs.* y for $x = 0$ when such an ellipse is situated centrally between four hyperbolic grounded conductors characterized by $x^2 - y^2 = \pm c^2$ with $c = 10$.

For comparison we also present similar curves for two alternative boundary surfaces:

a concentric circular boundary (R=10.), or

an elliptical boundary that fits snugly (and hence confocally) around the beam.

One should recognize that in the case in which hyperbolic boundaries are present, the distinctive feature of the image fields is perhaps not their magnitudes but rather the pronounced content of third-order terms (arising from the term $c_4 \; r^4 \; \cos 4\theta$ in the image-field potential). Accordingly, for $a>b$, this can result in the image-field contribution to $E_y^{(I)}|_{x=0}$ remaining quite small for all $|x| \leq b$. Thus, in the present example, by the time that the contribution of c_2 to $E_y^{(I)}|_{x=0}$ has become somewhat significant (say at $y \tilde{=} 4$ in this example) the contribution of c_4 may virtually cancel the c_2 contribution:

	$y = 3.75$	$y = 4.00$
Contribution from c_2	-0.00484	-0.00517
Contribution from c_4	+0.00438	+0.00532

with, at these radii, terms of higher order individually contributing amounts less than 10^{-4} in magnitude.

GRAPH PAPER GRAPHIC CONTROLS CORPORATION Buffalo, New York Printed in U.S.A. SQUARE 10 X 10 TO THE HALF INCH 45 0813 G1

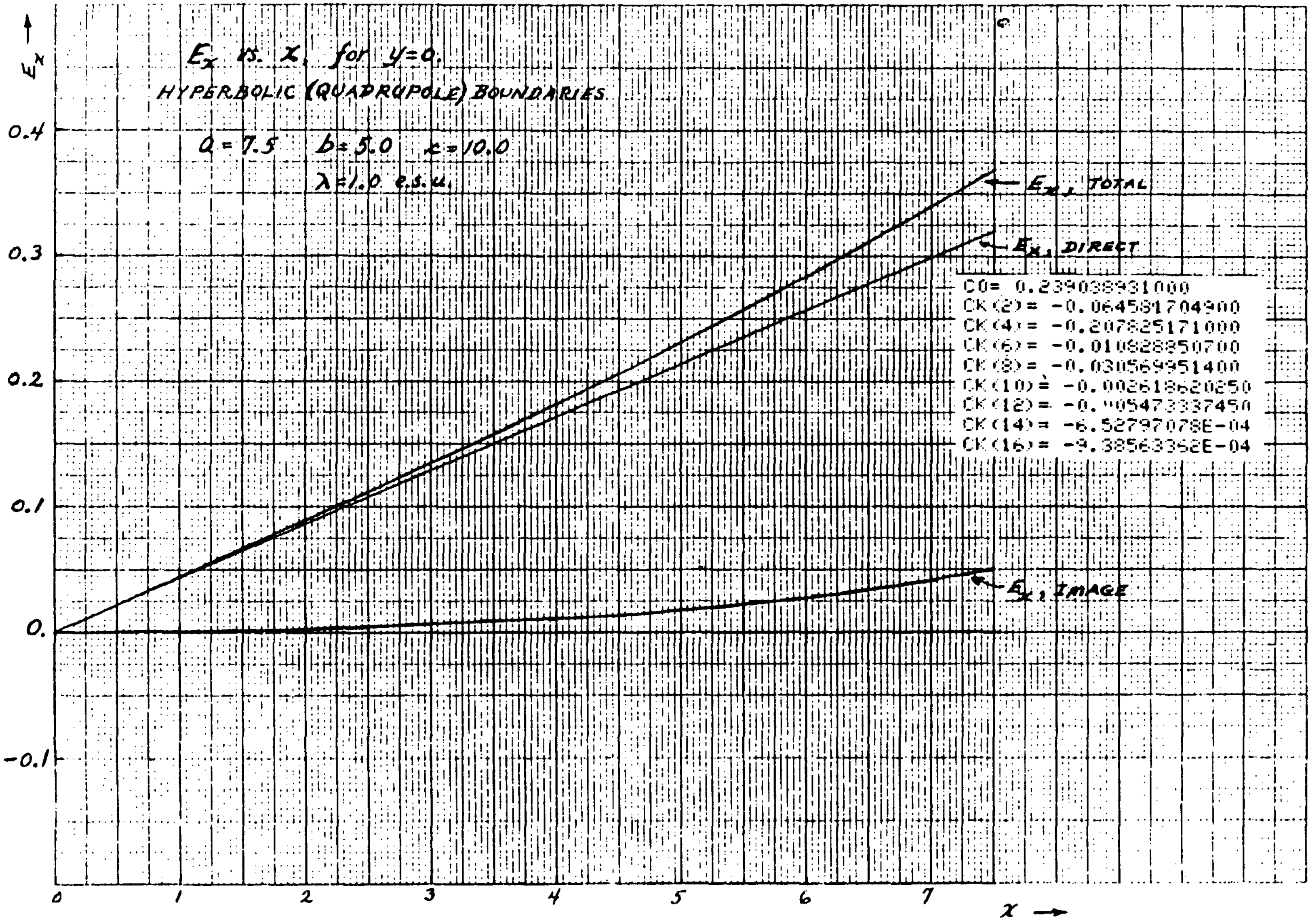

```
C0=  0.239038931000
CK(2)=  -0.064581704900
CK(4)=  -0.207825171000
CK(6)=  -0.010828850700
CK(8)=  -0.030569951400
CK(10)=  -0.002618620250
CK(12)=  -0.005473337450
CK(14)=  -6.52797078E-04
CK(16)=  -9.38563362E-04
```

GRAPH PAPER GRAPHIC CONTROLS CORPORATION
Buffalo, New York Printed in U.S.A.
SQUARE 10 X 10 TO THE HALF INCH AS-0813-61

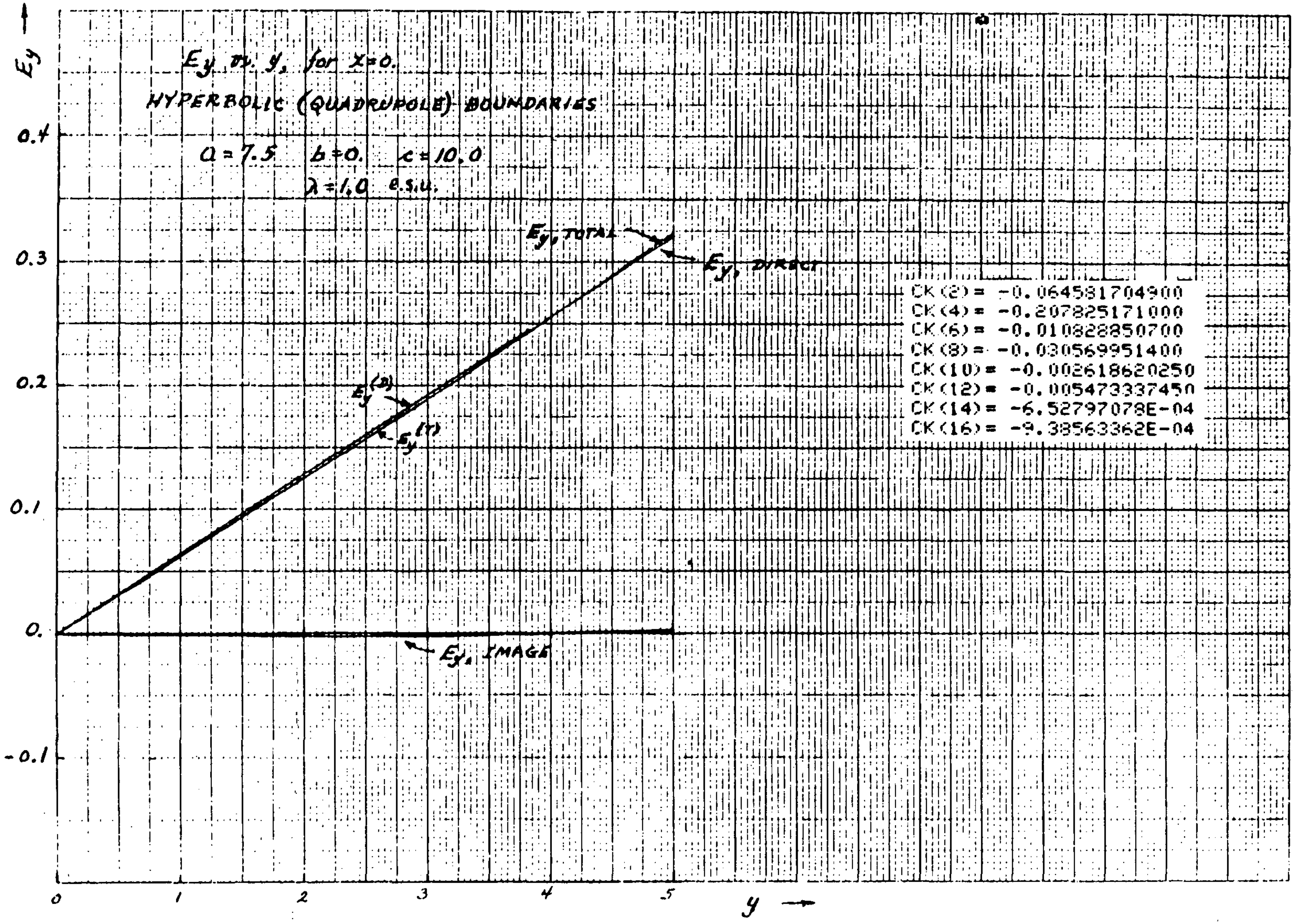

```
CK(2)= -0.064581704900
CK(4)= -0.207825171000
CK(6)= -0.010828850700
CK(8)= -0.030569951400
CK(10)= -0.002618620250
CK(12)= -0.005473337450
CK(14)= -6.52797078E-04
CK(16)= -9.38563362E-04
```

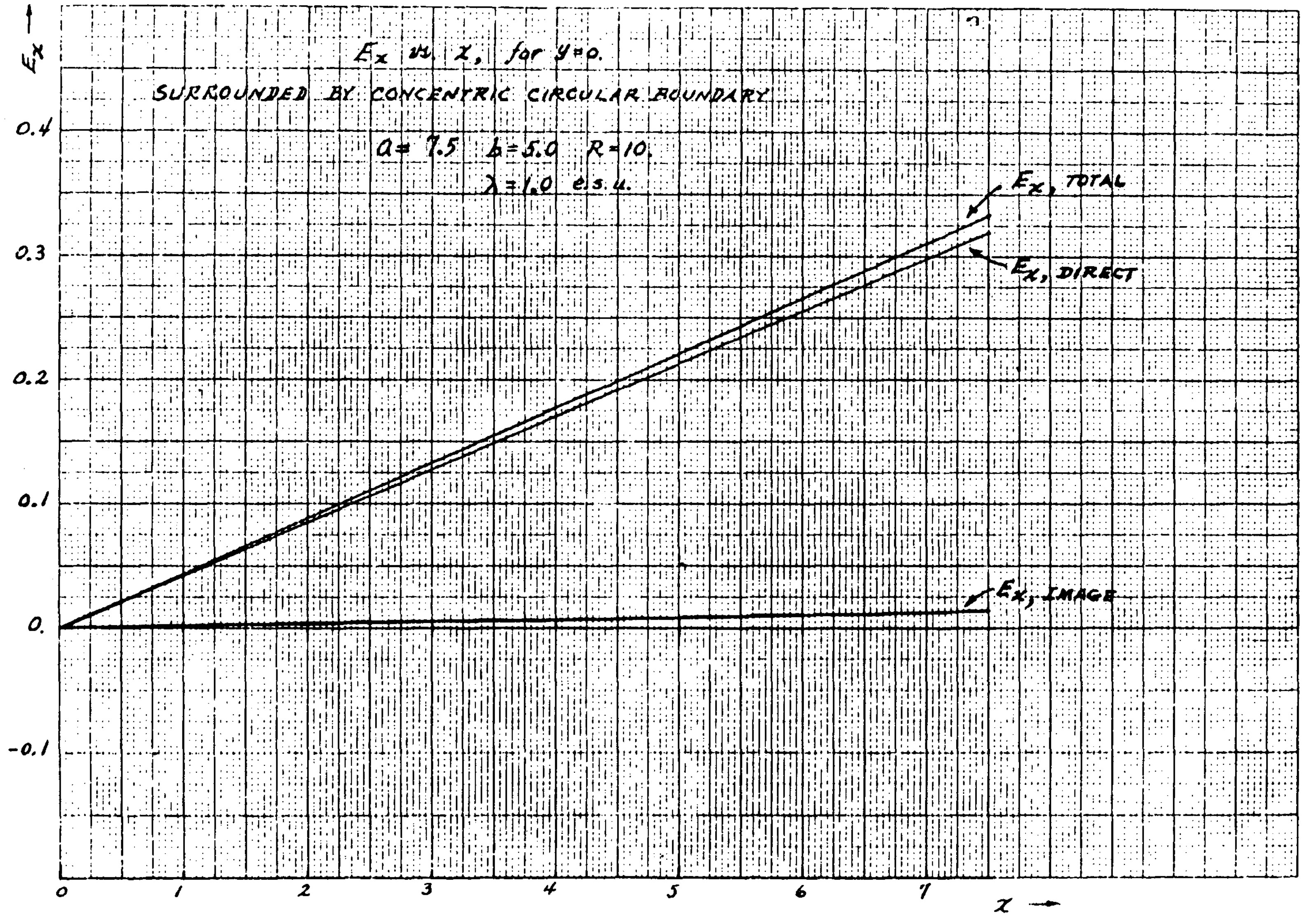
E_x vs x, for $y=0$.
SURROUNDED BY CONCENTRIC CIRCULAR BOUNDARY
$a=7.5$ $b=5.0$ $R=10$.
$\lambda=1.0$ e.s.u.
E_x, TOTAL
E_x, DIRECT
E_x, IMAGE
E_x
0.4
0.3
0.2
0.1
0.
-0.1
0
1
2
3
4
5
6
7
x

GRAPH PAPER GRAPHIC CONTROLS CORPORATION Buffalo, New York Printed in U.S.A.

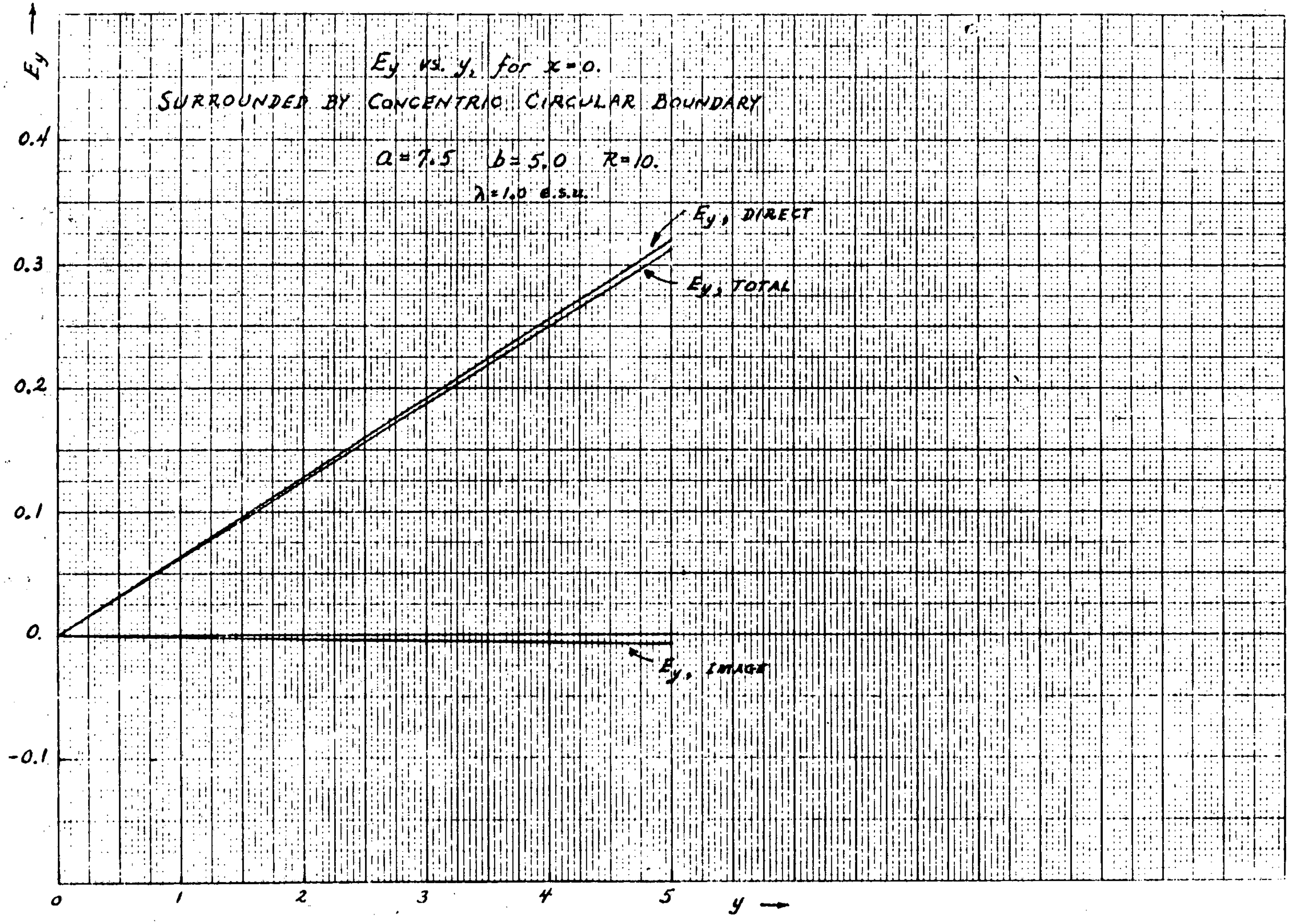

E_y vs. y, for $x = 0$.

SURROUNDED BY CONCENTRIC CIRCULAR BOUNDARY

$a = 7.5$ $b = 5.0$ $R = 10.$

$\lambda = 1.0$ e.s.u.

GRAPHIC CONTROLS CORPORATION SQUARE 10 X 10 TO THE HALF INCH
Buffalo, New York Printed in U.S.A.

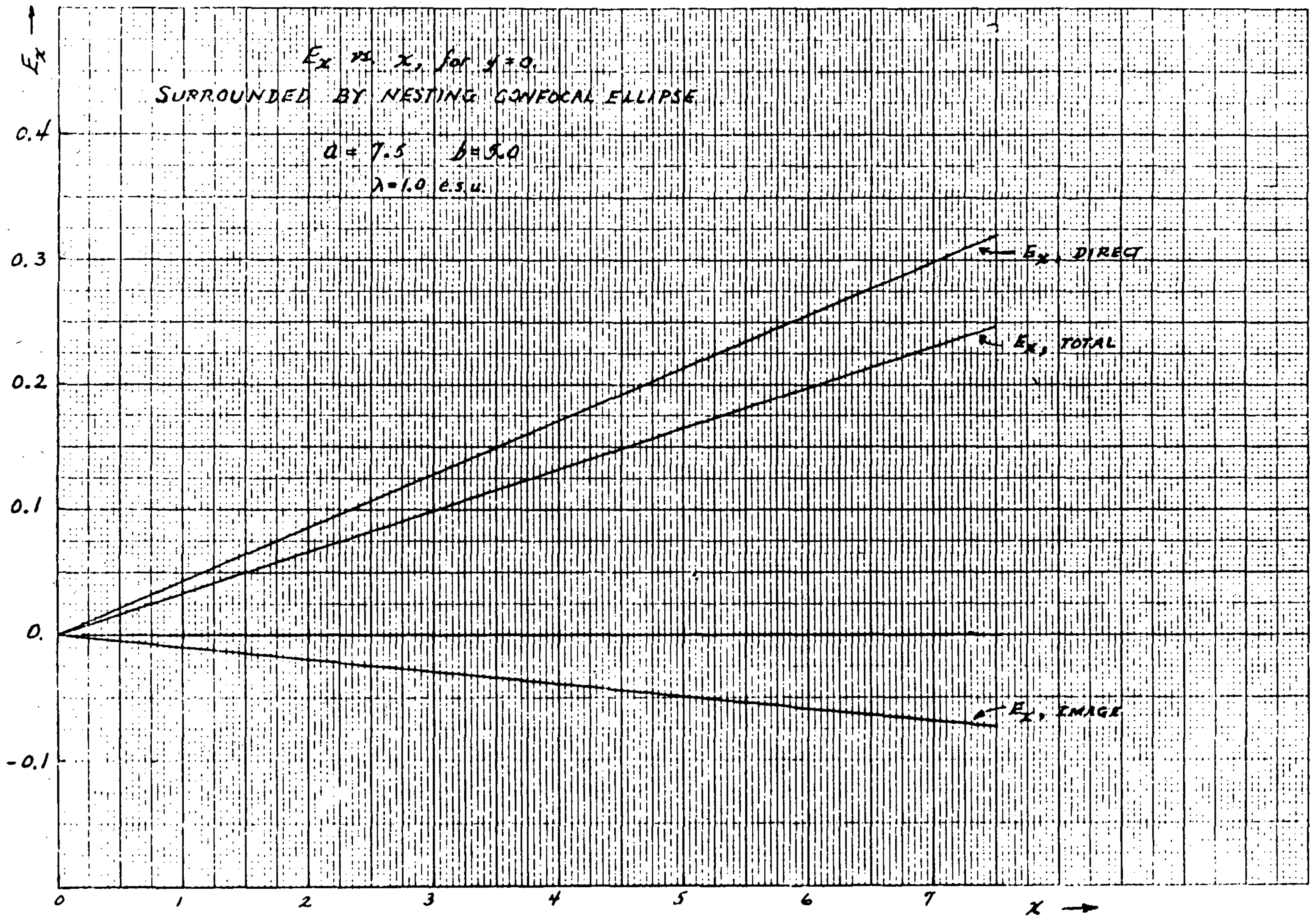

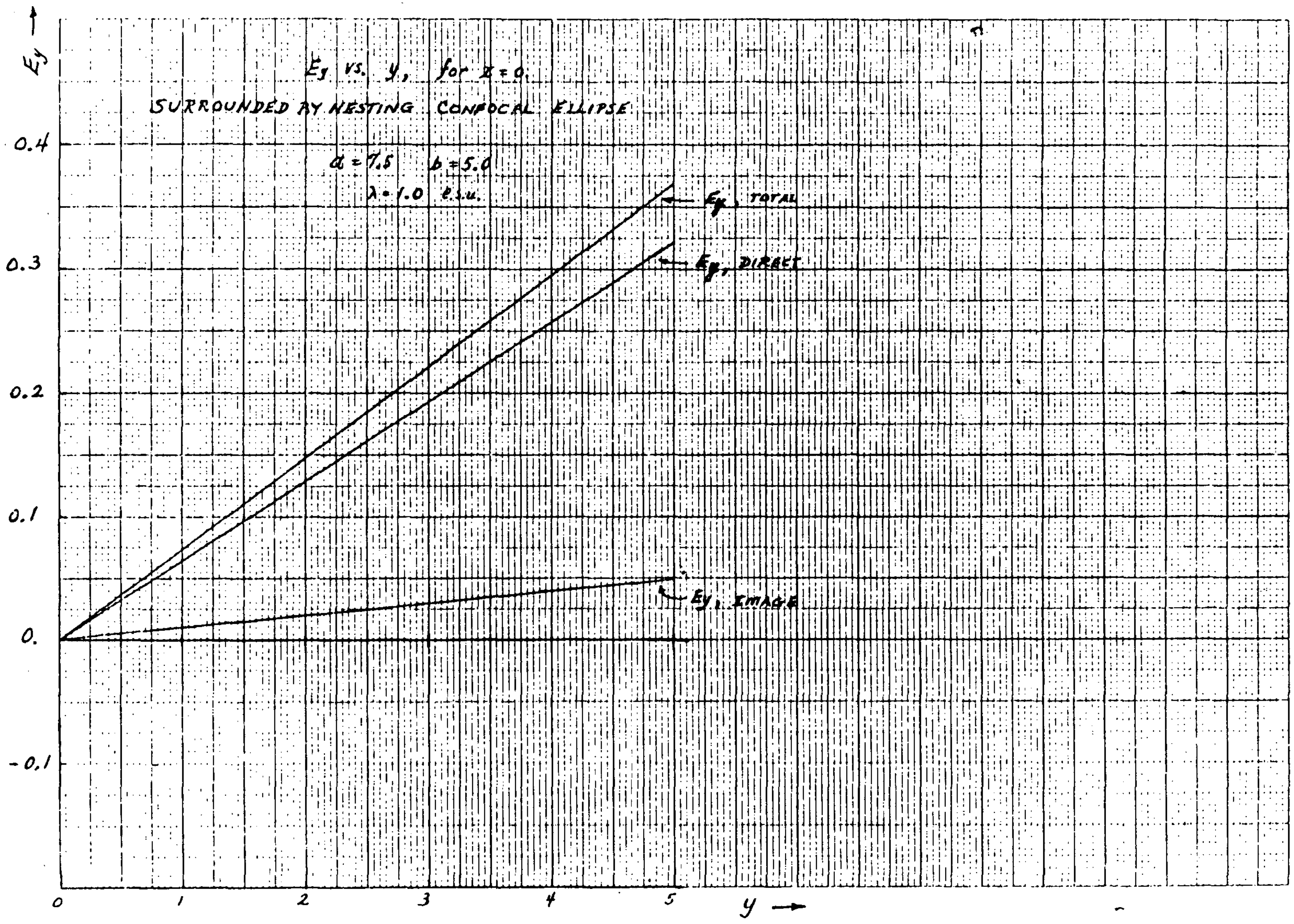
E_y vs. y, for $x = 0$.
SURROUNDED BY NESTING CONFOCAL ELLIPSE
$a = 7.5$ $b = 5.0$
$\lambda = 1.0$ e.s.u.
E_y, TOTAL
E_y, DIRECT
E_y, IMAGE
E_y
0.4
0.3
0.2
0.1
0.
-0.1
0
1
2
3
4
5
y

[We recall that the coefficient c_2 in the image-field formula is present as a result of the eccentricity of the ellipse, while a significant value of c_4 will occur even when a/b=1 (as a result of the 4-fold character of the boundary structure presented by the hyperbolic surfaces.)]

A circular boundary concentrically surrounding as elliptical beam also gives rise to non-linear image fields, but such effects appear to be less dramatic--and indeed in the example treated here the image fields are seen to be rather weak. The image fields resulting from the confocal elliptical boundary (that in our example snugly surrounds the beam) appear to be reasonably pronounced in magnitude, while being linear. It may be pointed out that, as Regenstreif has already noted (CERN Report CERN/PS/DL 77-37)* the image field due to the presence of the surrounding circular chamber _reduces_ the field arising from the isolated beam in the direction parallel to the _major_ axis and _increases_ the isolated-beam field in the direction parallel to the _minor_ axis.

Returning to the case of the elliptical beam centered within the four hyperbolic boundaries, one will recognize that the cancellation we have seen to occur between the c_2 and c_4 - terms in forming $E_y^{(I)}|_{x=0}$ is associated with a corresponding very flat plot of image-field potential _vs_. y at x=0. Finally, with respect to the displacement of such a beam, by an amount δ along the x axis, we present here a curve of relevant fields that then arise [$E_x(\delta, 0)$ and $\langle E_x \rangle_{av.}$] and that exhibit some non-linear character as a function of δ.

---

* Final reference cited in our Appendix C.

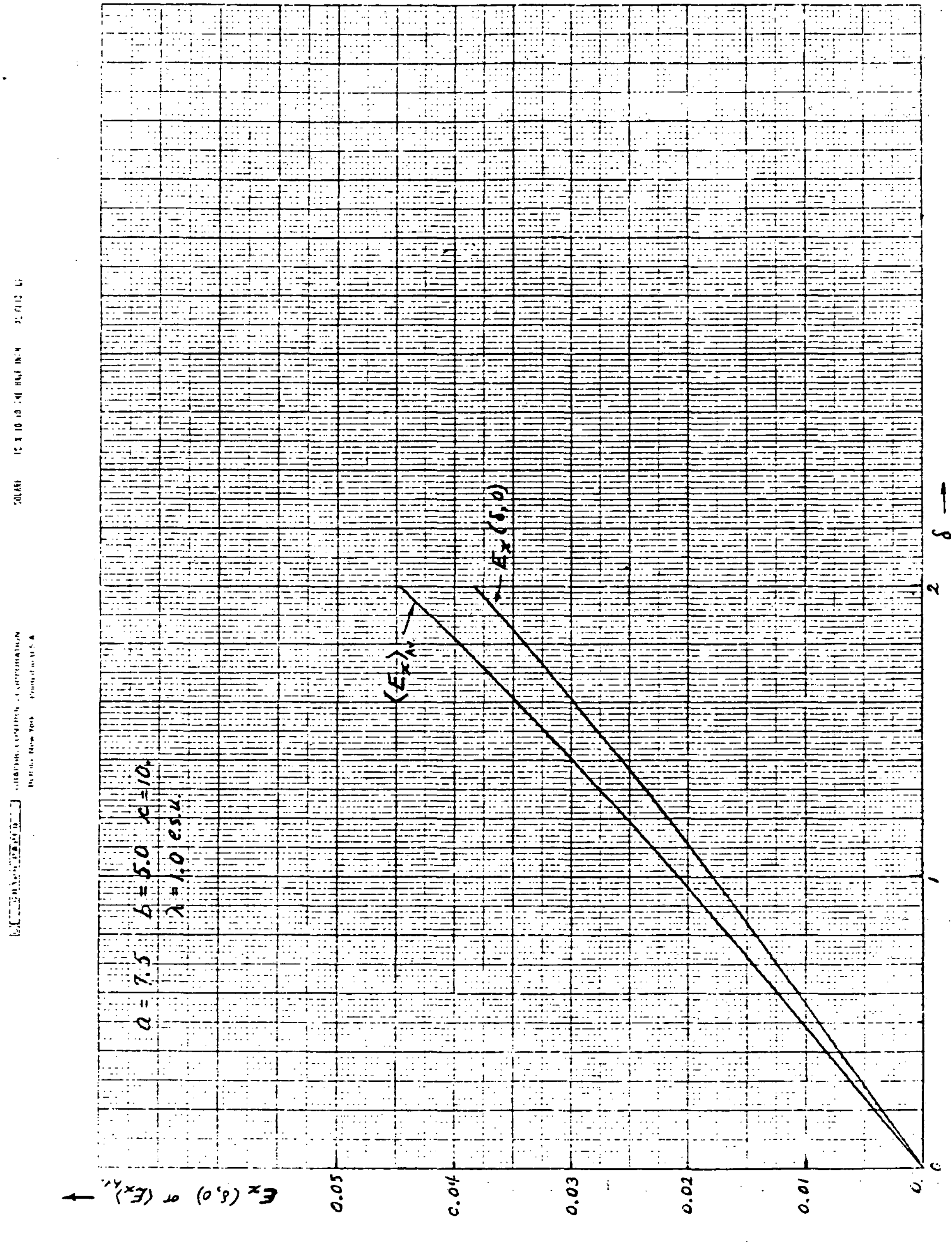
$a = 7.5$ $b = 5.0$ $\kappa = 10$,
$\lambda = 1.0$ e.s.u.
$\langle E_x \rangle_{\lambda}$
$E_x(\delta, 0)$
0.05
0.04
0.03
0.02
0.01
0.
0
1
2
δ →
$E_x(\delta, 0)$ or $\langle E_x \rangle_{\lambda}$, →

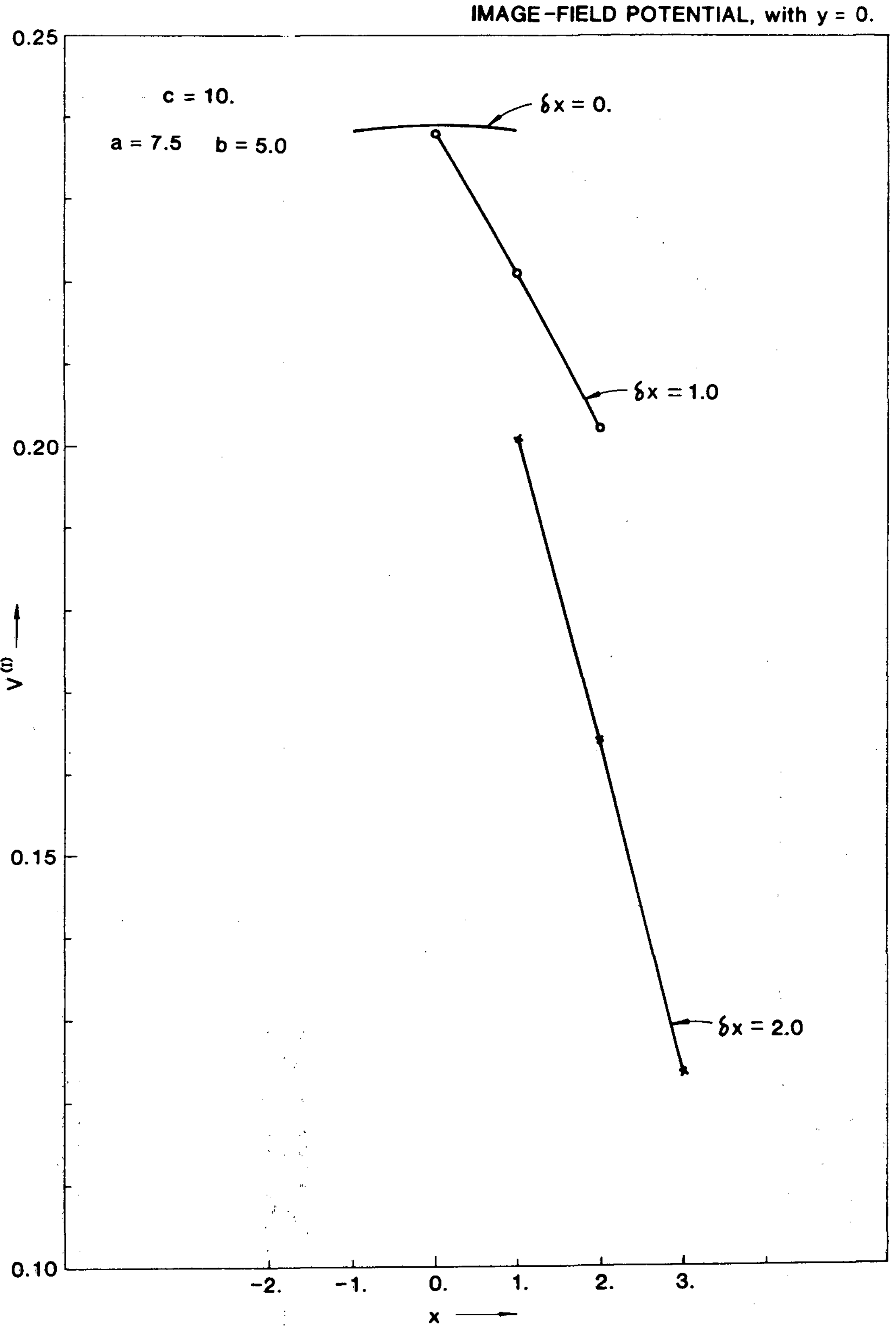

XBL 807-10721

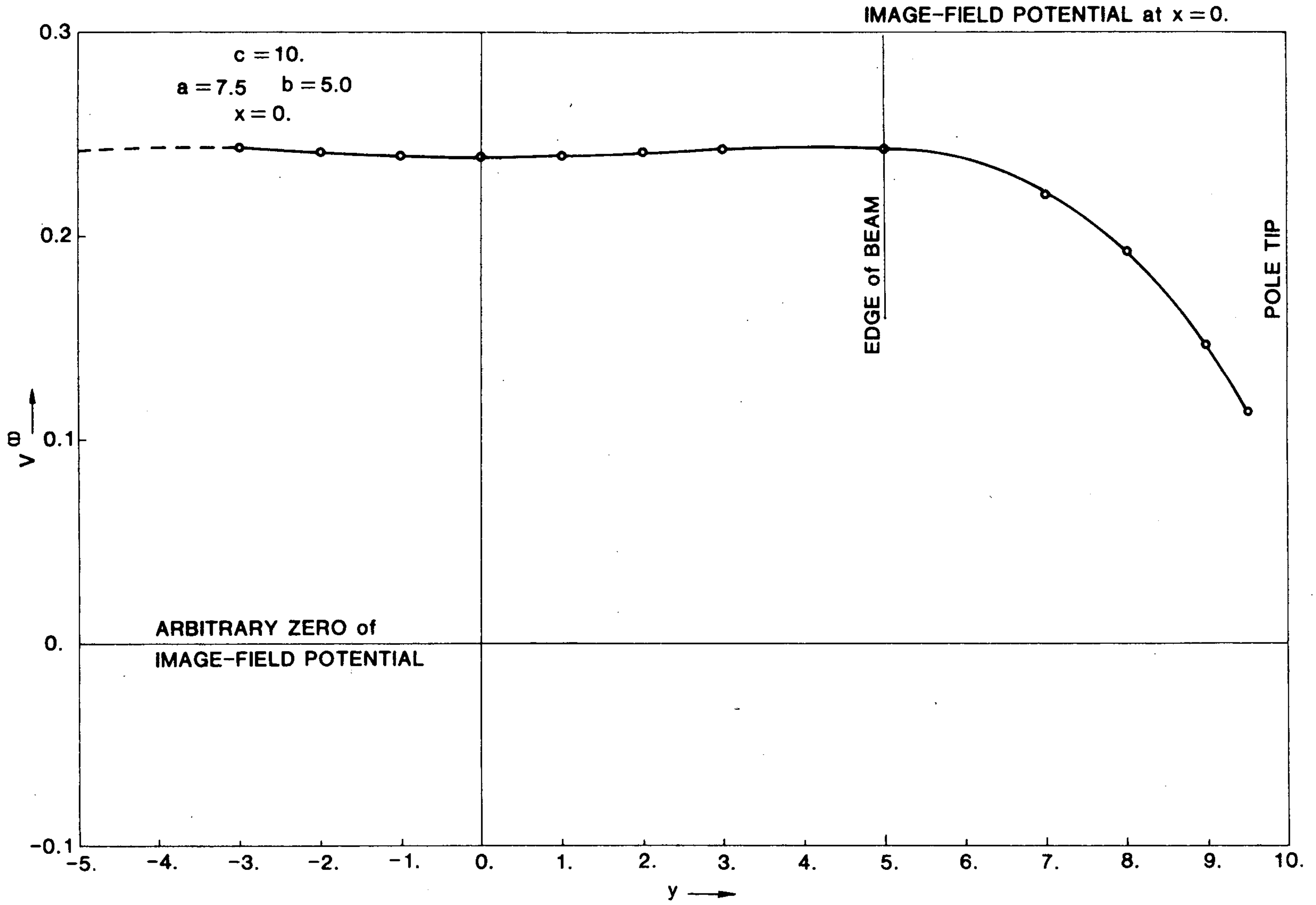

XBL 808-10720

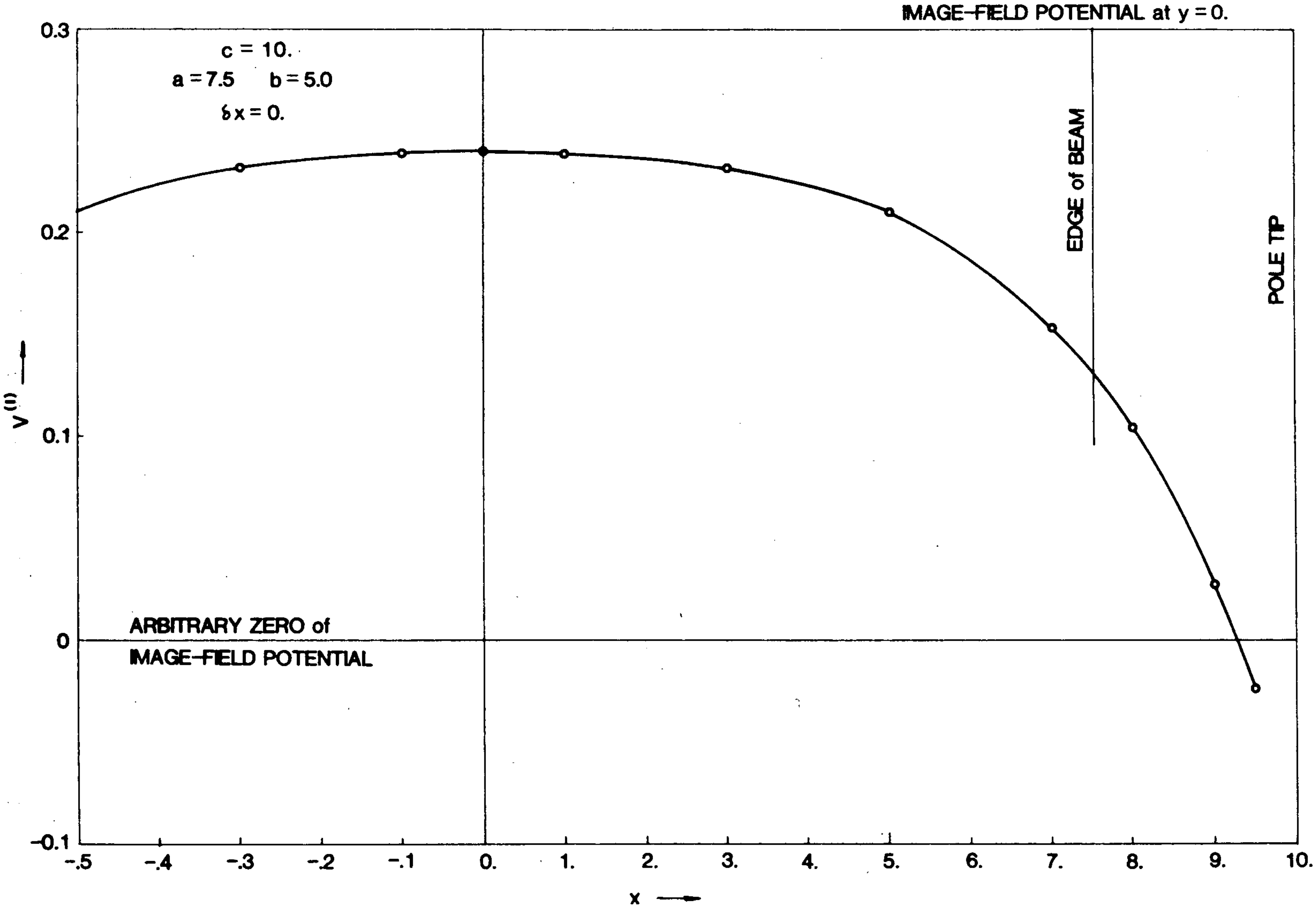

XBL 807-10719

V. SUMMARY

The problem considered was an evaluation of the 2D image field* that arises from an elliptical charge distribution situated within four hyperbolic surfaces $x^2 - y^2 = \pm c^2$. The principal axes of the ellipse (semi-axes a & b) are taken to be parallel to the x and y axes of the co-ordinate system, but the semi-axis in the x direction (a) need not necessarily be greater than that in the y direction (b). The charge density throughout the ellipse is regarded as constant, with an overall linear density $\lambda = +1$ esu/cm and with results expressed in un-rationalized cgs electrostatic units. The elliptical charge distribution may be either centrally located between the four hyperbolic surfaces, or displaced from the center by a distances δ_x, δ_y along the x and y axes. [Note: The effect of a displacement exclusively along the y-axis is readily inferrable from results obtained for an x-axis displacement with the ratio a/b inverted.]

Aided by some preliminary reformulation of this problem through the use of some conformal transformations discussed in Appendices, the problem just posed has been solved computationally (Program GBIMG or GB4MG) to provide the image-field potential (as well as the approximate total--image + direct--potential) at any field point (x, y) situated within the circle r=c, and numerical finite-differences evaluations of -grad V would provide one means of obtaining the corresponding electric fields. Alternatively, however, a loop scan to evaluate potential values at a sequence of points equally spaced around a circle provides values that the program then (optionally) has been designed to analysize into a truncated trigonometric series for

---

* The term "image" here refers to the surface distribution of charge induced on the surrounding conductors.

the image-field potential in the form

$$V^{(I)} = c_o + \sum_{k=1}^{17} c_k \left(\frac{r}{c}\right)^k \cos k\theta + \sum_{k=1}^{18} s_k \left(\frac{r}{c}\right)^k \sin k\theta$$

--from which image fields can be obtained by evaluating the negative gradient of this expression. The same coefficients as are generated for this trigonometric development then also (optionally) can be employed to evaluate both the image field at the <u>centroid</u> of the beam (at δ_x, δ_y) and the <u>average</u> field (obtained by Gaussian integration over the area of the possibly displaced beam)-- as may be of interest in connection with the dynamical movement of the beam as-a-whole.

Results obtained in many runs (with different values for the various relevant parameters) have been recorded in a number of Tables and several graphs have been drawn to illustrate such results. A most distinctive property of the image field for this configuration is the pronounced contribution of a $c_4 \left(\frac{r}{c}\right)^4 \cos 4\theta$ term in the associated image-field potential function ($r<c$) and the consequent third-order non-linearily in the components of the image field itself. Thus for a centrally-located circular beam (independent of the size of $a(=b)$ relative to c) one finds the image-field potential to be in excellent agreement with

$$V^{(I)} = \text{const.} - \lambda \left[\frac{\pi^2}{48} \left(\frac{r}{c}\right)^4 \cos 4\theta + \frac{7\pi^4}{23040} \left(\frac{r}{c}\right)^8 \cos 8\theta + \ldots\right],$$

as predicted for this case by Lloyd Smith.$^{(4)}$ [Note eccentricity of the ellipse can give rise to coefficients c_2 <u>etc.</u>, and a displacement to coefficients c_1, s_1 <u>etc.</u>, but coefficients c_4 <u>etc.</u> can always be expected as a consequence of the 4-fold character of the boundary surfaces.]

The results obtained for image fields (or for total--direct plus image--fields) that would act on individual particles of the beam in the present configuration have been compared (or contrasted) with the corresponding fields that would arise from a few other boundary configurations that have been examined in the past. As stated previously, the distinctive feature of the configuration examined here appears to be the pronounced non-linearity--say of $E_x^{(I)}|_{y=0}$ vs. x (as is particularly noticeable for a>b, when c_2 and c_4 terms add in forming E_x rather than effect some considerable cancellation).

It will be recognized that the results presented here lack significance to some extent in that the assumed constant density of charge throughout an elliptical beam may not represent a truly stationary distribution of charge in view of the special dynamical effects that may arise from non-linear image forces acting on the particles of the beam. We are not at this time in a position to comment further concerning the dynamical consequences of the non-linear forces whose existance has been emphasized here (perhaps also, in some applications, with a distinctive AG or non-AG character) and certainly not concerning the extent to which the assumed constant density distribution will differ significantly from one that has a stationary character. It may, however, be of interest to suggest that, as G. Lambertson has kindly commented, the non-linearities introduced by the 4-fold character of the hyperbolic boundary structure considered here might be reduced or suppressed by use of a more circular structure (perhaps composed of many isolated electrodes) onto which appropriate potentials could be individually applied to create, when desired, a suitable (e.g., quadrupole) applied electric field.

Finally, for possible practical use (or for approximate dynamical computations) we have undertaken to provide some approximate handy formulas to describe in broad terms the salient results of the present work--thus (with λ=1 statcoulomb/cm):

For a Centered Beam:

$$c_2 \cong -0.98 \left(\frac{ab}{c^2}\right) \log_{10} \left(\frac{a}{b}\right)$$

$$c_4 \cong -0.2056$$

$$c_6 \cong -0.16 \left(\frac{ab}{c^2}\right) \log_{10} \left(\frac{a}{b}\right)$$

$$c_8 \cong -0.0296$$

$$c_{10} \cong -0.039 \left(\frac{ab}{c^2}\right) \log_{10} \left(\frac{a}{b}\right)$$

$$c_{12} \cong -0.0051,$$

where $\log_{10}$ denotes the logarithm to the base 10. Similarly

For a Beam Displaced only in the x Direction:

$$c_1 \cong -1.6 \left[1.0 + 0.48 \left(\frac{ab}{c^2}\right) \log_{10} \left(\frac{a}{b}\right)\right] \frac{\delta_x}{c}$$

$$E_x^{(I)} (\delta_x, 0) \cong 1.6 \left[1.0 + 1.68 \left(\frac{ab}{c^2}\right) \log_{10} \left(\frac{a}{b}\right)\right] \frac{\delta_x}{c^2},$$

$$\left\langle E_x^{(I)} \right\rangle_{av.} \cong 1.6 \left[1.0 + 3.94 \left(\frac{ab}{c^2}\right) \log_{10} \left(\frac{a}{b}\right)\right] \frac{\delta_x}{c^2},$$

where we may be overlooking, however, non-linear dependencies on δ_x that could be significant for sufficiently great values of δ_x/c.* Also, more generally,

For a Beam Displaced by δ_x, δ_y:

$$\left\langle E_x^{(I)} \right\rangle_{av.} \cong \frac{1}{c} \left[2 A_1 \left(\frac{\delta_x}{c}\right) + 4 A_2 \left(\frac{\delta_x}{c}\right)^3 + 2 A_5 \left(\frac{\delta_x}{c}\right) \left(\frac{\delta_y}{c}\right)^2\right]$$

$$\left\langle E_y^{(I)} \right\rangle_{av.} \cong \frac{1}{c} \left[2 A_4 \left(\frac{\delta_y}{c}\right) + 4 A_7 \left(\frac{\delta_x}{c}\right)^3 + 2 A_5 \left(\frac{\delta_x}{c}\right)^2 \left(\frac{\delta_y}{c}\right)\right]$$

---

* See, however, alternative (more extended) approximate expressions proposed immediately below for $\left\langle E_x^{(I)} \right\rangle_{av.}$ and $\left\langle E_y^{(I)} \right\rangle_{av.}$ for cases in which both δ_x and δ_y may be non-zero.

where

$$A_1 \cong 0.785 + 3\,\frac{ab}{c^2}\,\log_{10}\frac{a}{b}, \qquad A_2 \cong 0.834 + 3\,\frac{ab}{c^2}\,\log_{10}\frac{a}{b},$$

$$A_4 \cong 0.785 - 3\,\frac{ab}{c^2}\,\log_{10}\frac{a}{b}, \qquad A_7 \cong 0.834 - 3\,\frac{ab}{c^2}\,\log_{10}\frac{a}{b},$$

$$A_5 \cong -[2.48_{64} + (6.5\,\frac{ab}{c^2}\,\log_{10}\frac{a}{b})^2\,].$$

VI ACKNOWLEDGEMENTS

It is a pleasure to acknowledge, with thanks, the continued interest and assistance in this work by Dr. Lloyd Smith, whose initial comments concerning the possible importance of image-field effects with hyperbolic boundary surfaces stimulated the investigation whose results are reported here. The writer also expresses his thanks to Swapan Chattopadhyay for several helpful discussions during the initial stages of the effort. The work has received essential support from within the HIF program of the U. S. Department of Energy, which support also is gratefully acknowledged.

VII. REFERENCES AND NOTES

1. L. J. Laslett, "On Intensity Limitations Imposed by Transverse Space-Change Effects in Circular Particle Acceleration," in Proc. 1963 Summer Study on Storage Rings, Accelerators and Experimentation at Super-High Energies (J. W. Bittner, ED.), pp. 324 - 367 (BNL 7534, Brookhaven National Lab., Upton, Long Island N.Y.; 1963).
2. L. Jackson Laslett, "Electrostatic and Magnetostatic Image-Field Coefficients", Proc. VII Internat. Conf. High Energy Accelerators (Yerevan-Tsahkadzor, 1969), v. II, pp. 362 - 375 (Acad. Sci. Armenian SSR, Yerevan; 1970).
3. If one wishes to interpert the results presented in this note in terms of MKS-C (SI) units, one may regard the results as applying to a charge density of 1 coulomb/meter, employ meters as distance units throughout, and divide reported values of potential (or field-strength) by $4\pi\varepsilon_0$ to obtain results in volts (or volts/meter).

$$\left[\frac{1}{4\pi\varepsilon_0} = \frac{\mu_0}{4\pi}\ c^2 = 10^{-7}\ c^2 \cong 8.987_{554} \times 10^9\ ;\ \ 4\pi\varepsilon_0 \cong 1.1126_5 \times 10^{-10}\right]$$

4. Lloyd Smith (private communication) has kindly provided, as a result of analytic evaluation of the image-field potential of a unit line charge centrally situated between the hyperbolic electrodes ($x^2 - y^2 = \pm\ c^2$), the expression

$$V^{(I)} = \text{Const.} -\lambda \left[\frac{1}{4}\left(\sum_{n=0} \frac{(-1)^n}{(n+1)^2}\right) \left(\frac{r}{c}\right)^4 \cos 4\theta + \frac{1}{32}\left(\sum_{n=0} \frac{(-1)^n}{(n+1)^4}\right) \left(\frac{r}{c}\right)^8 \cos 8\theta + \ldots\right.$$

$$= \text{Const.} -\lambda \left[\frac{\pi^2}{48} \left(\frac{r}{c}\right)^4 \cos 4\theta + \frac{7\pi^4}{23040} \left(\frac{r}{c}\right)^8 \cos 8\theta + \ .\ .\ .\ \right],$$

so that (for example)

$$E_{x \text{ or } y}^{(I)}\Bigg|_{\substack{y=0 \\ \text{or } x=0}} = \frac{\lambda}{c}\left[\frac{\pi^2}{12}\left(\frac{x \text{ or } y}{c}\right)^3 + \frac{7\pi^4}{2880}\left(\frac{x \text{ or } y}{c}\right)^7 + \ldots\right]$$

$$\cong \frac{\lambda}{c}\left[0.822467\left(\frac{x \text{ or } y}{c}\right)^3 + 0.23676^{-}\left(\frac{x \text{ or } y}{c}\right)^7 + \ldots\right]$$

Our computational program for a small, almost circular, beam (with $\lambda=1$), centered at the origin ($a = 0.11\ c$, $b = 0.10\ c$, and $\delta_x = \delta_y = 0$) gives results for which the 4θ and 8θ terms in $V^{(I)}$ imply

$$E^{(I)}_{x \text{ or } y}\Bigg|_{\substack{y=0\\ \text{or } x=0}} \left[\doteq \frac{1}{c}\ \left[\ 0.82247^{-}\ \left(\frac{x \text{ or } y}{c}\right)^3 + 0.23675\ \left(\frac{x \text{ or } y}{c}\right)^7 + \ldots \right]\right.$$

(in agreement with Dr. Smith's results for the limiting case of a centered beam), while harmonic contributions to $V^{(I)}$ other than those of the type $4n\theta$ have been seen to tend to zero as the (centered) beam becomes small in its physical dimensions. This illustrates a case in which the 4-fold symmetry of the boundary introduces dominant non-linear terms into the image fields that act on individual particles of the beam.

5. Within an elliptical beam (with $\lambda=1$), of constant charge density throughout its cross-section, one expects the "direct" self field to be (6) the linear field noted below:

   Along the x axis:

   $$E_x = 4\,\frac{x}{a(a+b)} \qquad \text{(e.s.u.)},$$

   Along the y axis:

   $$E_y = 4\,\frac{y}{b(a+b)} \qquad \text{(e.s.u.)}.$$

6. L. C. Teng, "Transverse Space-Change Effects", ANLAD-59 (Argonne National Laboratory, Argonne, Ill.; February 1, 1963). See also early papers cited in Ref. 1.

APPENDIX A

THE TRANSFORMATION

The starting configuration to be analyzed, and that in a sense serves as a Green's Function, is that sketched below--in which a unit line charge (λ=1 e.s.u.) is situated at a, b within grounded hyperbolic cylinders $x^2 - y^2 = \pm c^2$.

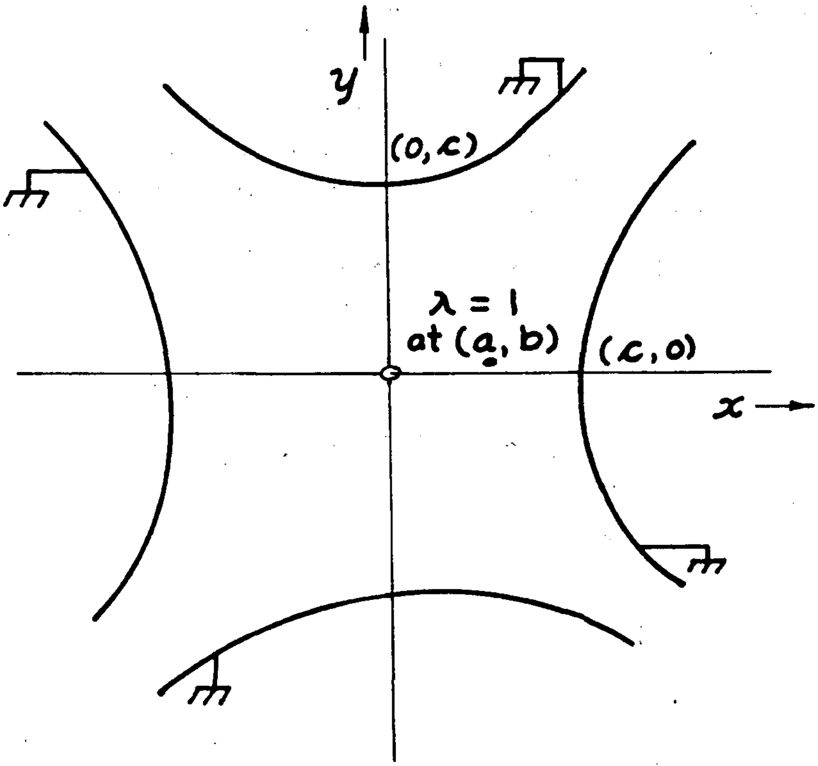

The solution to this problem will permit, by subsequent integration (in practice, numerical integration), the evaluation of the electrostatic potential function for a charged beam situated within this set of hyperbolic conducting surfaces.

The electrostatic problem just posed can be taken to have the solution provided by one-fourth of the sum of the solutions to the four problems presented by the four sketches that follow:

CASE IA

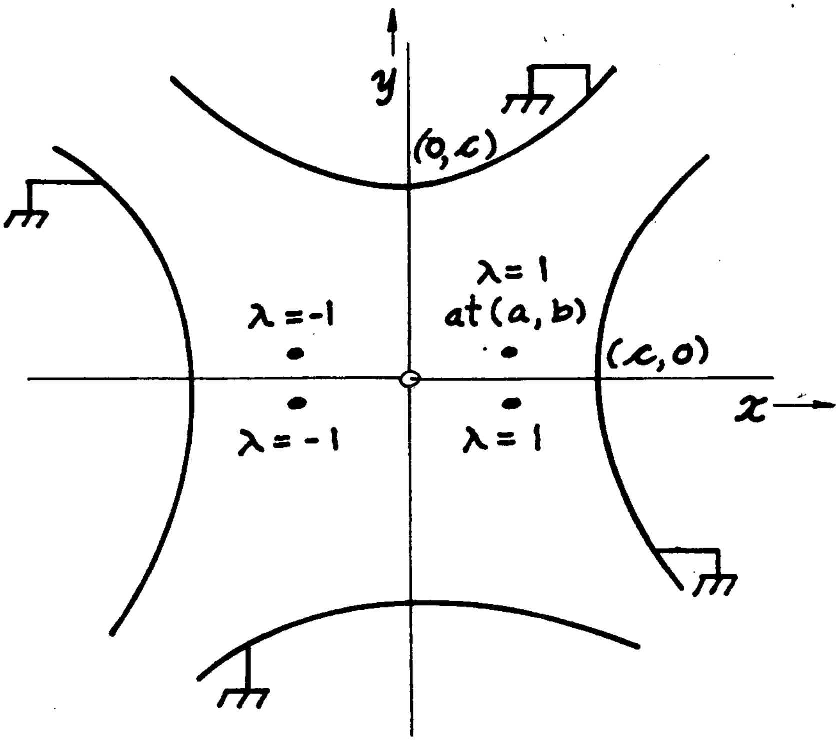

CASE IB

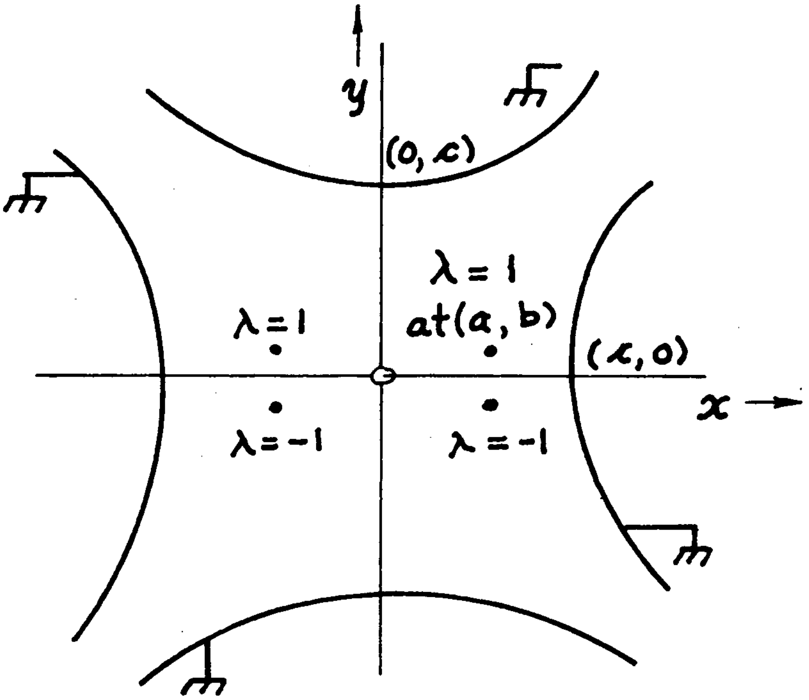

CASE II

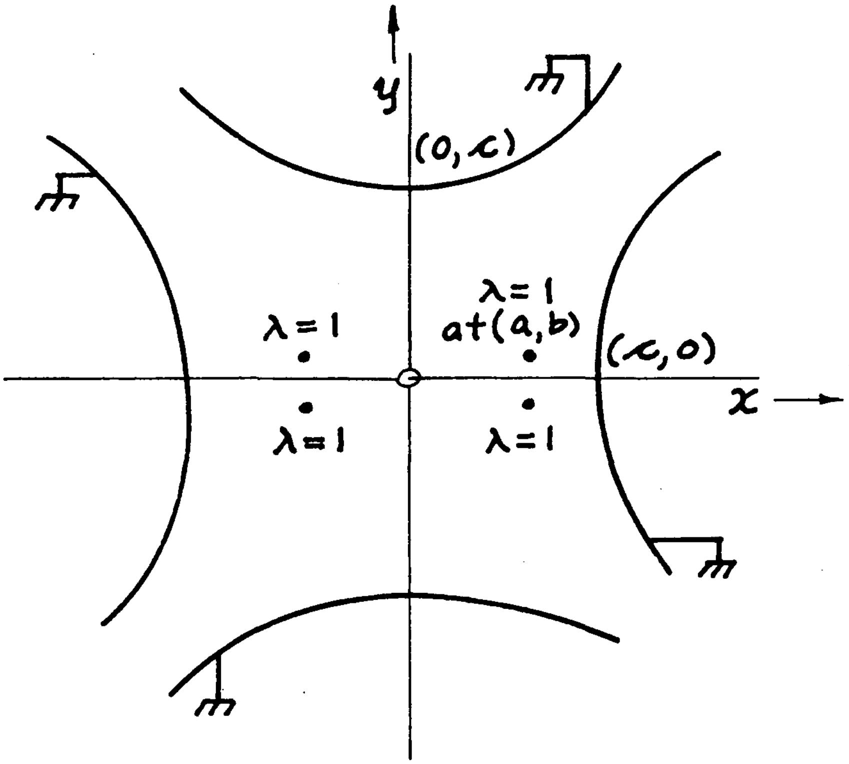

CASE III

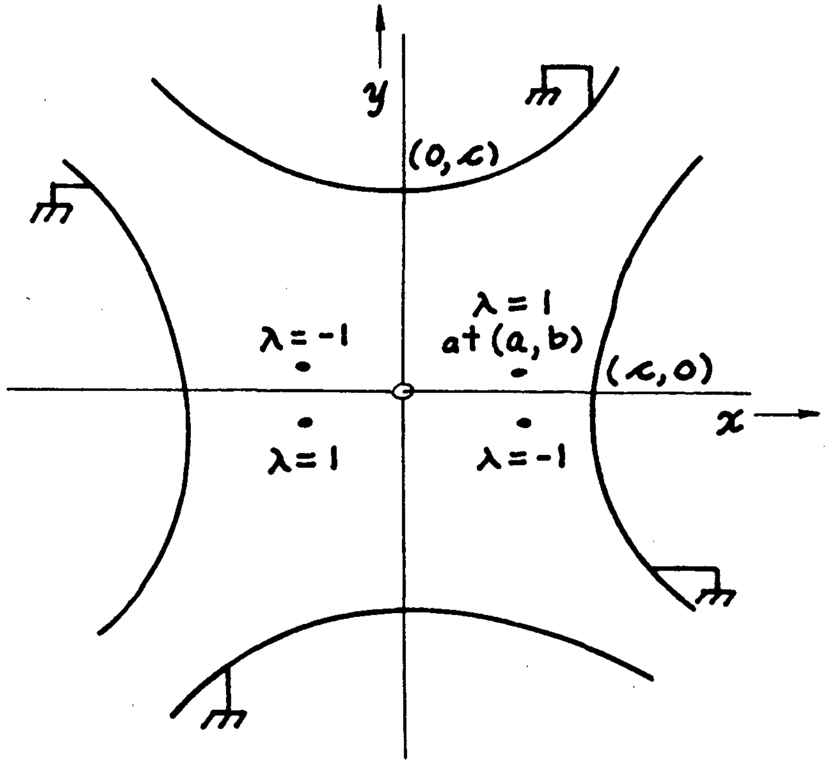

In these several cases the x and y axes become either equipotential surfaces (V=0) or stream lines, as follows:

CASE	x-axis	y-axis
IA	Stream Line	V=0.
IB	V=0.	Stream Line
II	Stream Line	Stream Line
III	V=0.	V=0.

We accordingly may analysize each of these individual cases by first applying a conformal transformation (or transformations) applicable directly in each case to the first quadrant.* We note, moreover, that Case IB becomes identical, with respect to the potential function, to Case IA if the source co-ordinates a, b are interchanged and if the field-point co-ordinates x, y also are interchanged.

We now continue by first examining Case II, for which both co-ordinate axes constitute stream lines.

---

*Solutions obtained for situations in which both the source point and the field point lie in the first quadrant can subsequently be so re-interpreted to account for situations in which one or both of these points may lie in any other quadrant.

CASE II.

We first apply the transformation $z' = (z/c)^2$; i.e.,

$$\left. \begin{aligned} x' &= (x^2 - y^2) / c^2 \\ y' &= 2\,x\,y / c^2 \end{aligned} \right\}$$

to obtain in the z′ plane the situation sketched immediately below, in which the full line segment $-1 < x' < 1$, $y' = 0$ constitutes a stream line:

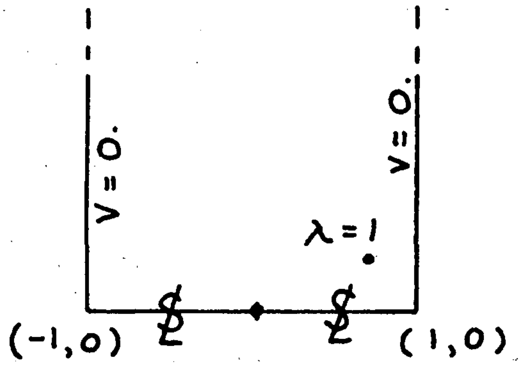

Equivalent to this situation, of course, is the extension shown below,

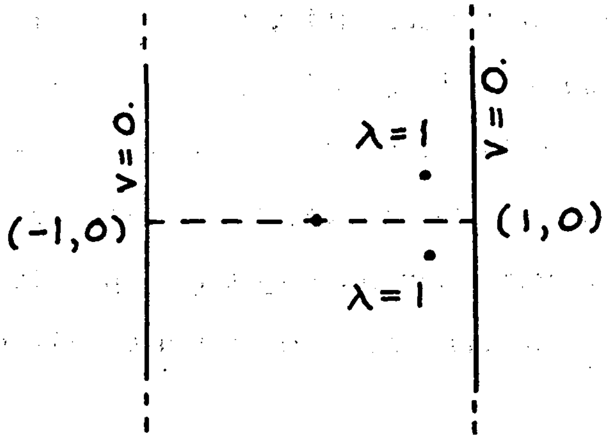

in which (through inclusion of the second line charge, below the dashed line) the dashed line automatically constitutes a stream line.

The problem of a single unit line charge situated between a pair of parallel conducting plates is a familiar one (Appendix B), so, with reference to the preceding sketch, we may apply the result of that case (by superposition of results for unit line charges at a', b' and at a' , $-b'$, with a field point at x', y') to obtain

$$V_{II} = - \left[\ln \frac{\operatorname{Cosh} \frac{\pi}{2} (y' - b') - \cos \frac{\pi}{2} (x' - a')}{\operatorname{Cosh} \frac{\pi}{2} (y' - b') + \cos \frac{\pi}{2} (x' + a')} + \ln \frac{\operatorname{Cosh} \frac{\pi}{2} (y' + b') - \cos \frac{\pi}{2} (x' - a')}{\operatorname{Cosh} \frac{\pi}{2} (y' + b') + \cos \frac{\pi}{2} (x' + a')} \right] ,$$

where $x' = (x^2 - y^2) /c^2$ $\qquad a' = (a^2 - b^2) /c^2$

$y' = 2\, x\, y / c^2$ $\qquad b' = 2\, a\, b / c^2$.

Although this result for Case II has been derived for source and field points in Quadrant I of the original z plane, it is evident from the symmetry of the original sketch describing this case that a reversal of sign of any one or more of the quantities a, b, x, or y would affect neither the magnitude nor sign of the potential function V_{II} for this Case II. We accordingly, for this evaluation, may perform the transformation from unprimed to single-primed variables by use of $|a|$, $|b|$, $|x|$, and $|y|$ -- and then evaluate V_{II} through use of the formula presented (in terms of primed variables) above.

CASE III:

The situation designated as Case III may be treated by again introducing the transformation $z' = (z/c)^2$ for transformation of the first quadrant of the z plane. In this case, however, the full line segment $-1 < x' < 1$, $y' = 0$ is to be regarded as characterized by V=0. -- as indicated below:

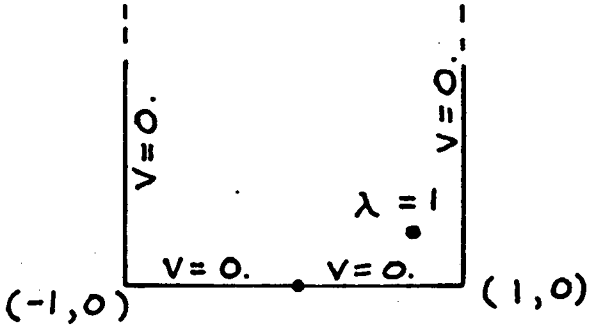

or, equivalently,

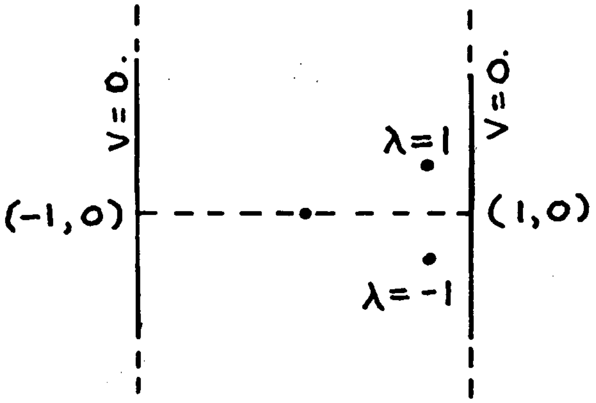

where, in this latest diagram, the introduction of the line charge λ = -1 below the dashed line automatically results in this dashed line assuming the potential value V=0.

Accordingly, for this Case III, we again may make the transformation from unprimed to single-primed variables (taking the former with positive values, as if they were in the first quadrant of the z plane) and then make use of the known results for a line charge between parallel conducting plates. In this instance, however, we note the assignment of the <u>negative</u> value $\lambda = -1$ to the line charge at a', $-b'$ and write

$$V_{III} = - \left[\ln \frac{\operatorname{Cosh} \frac{\pi}{2} (y' - b') - \cos \frac{\pi}{2} (x' - a')}{\operatorname{Cosh} \frac{\pi}{2} (y' - b') + \cos \frac{\pi}{2} (x' + a')} - \ln \frac{\operatorname{Cosh} \frac{\pi}{2} (y' + b') - \cos \frac{\pi}{2} (x' - a')}{\operatorname{Cosh} \frac{\pi}{2} (y' + b') + \cos \frac{\pi}{2} (x' + a')} \right] .$$

With V_{III} evaluated through use of primed variables derived from $|a|$, $|b|$, $|x|$, and $|y|$, inspection of the original z-plane sketch for Case III indicates that each change of sign of a, b, x, or y should imply a sign reversal of V_{III}. With V_{III} orginally evaluated as indicated above, we then append the instruction that IF $a \cdot x \cdot b \cdot y < 0$, then a sign reversal of V_{III} is to be imposed.

CASE IA.

For Case IA we once again may transform from $|a|$, $|b|$, $|x|$, $|y|$ to the single-primed variables in the manner indicated previously--now resulting in the boundary-value problem sketched below:

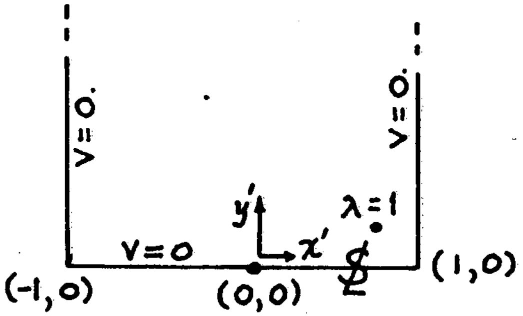

z′ plane

in which the left-hand portion of the x′ axis (-1<x′<0) is to be at zero potential, while the right-hand portion (0<x′<1) constitutes a stream line.

A sequence of two additional transformations now serves, first, to straighten out the 90° corners, and then, second, to bend upward again the portions of the boundary that are at zero potential. Thus, following the transformation to the single-prime variables, we perform the Schwartz-Christoffel transformation

$$z'' = \sin \frac{\pi}{2} z' \qquad \text{(i)}$$

i.e., $$\left.\begin{aligned} x'' &= \sin \frac{\pi}{2} x' \ \text{Cosh} \frac{\pi}{2} y' \\ y'' &= \cos \frac{\pi}{2} x' \ \text{Sinh} \frac{\pi}{2} y' \end{aligned}\right\} ,$$

followed by an inversely somewhat similar Schwartz-Christoffel transformation

$$z''' = \frac{2}{\pi} \sin^{-1} (2z'' - 1)$$

$$\left[\text{or, equivalently,} \quad z'' = \frac{1 + \sin \frac{\pi}{2} z'''}{2}\right] . \qquad \text{(ii)}$$

The results of these additional transformations, (i) & (ii), then are as sketched below:

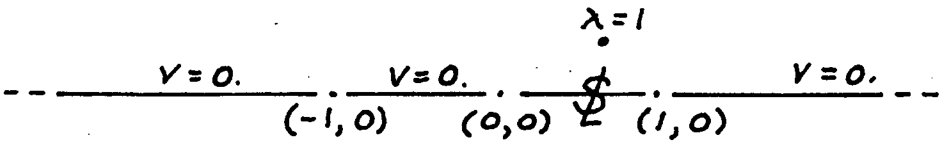

z'' plane

and

z''' plane

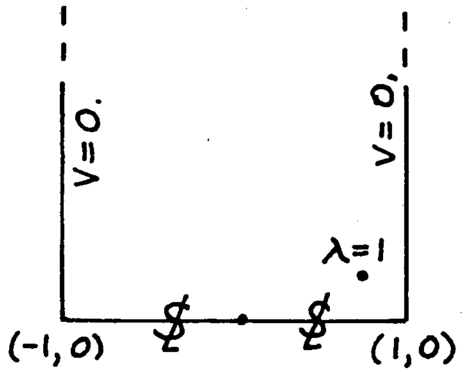

The resulting problem, as presented in the z''' plane, is thus seen to be identical to that presented in the z´ plane of Case II. For the present Case IA, then, we accordingly write

$$V_{IA} = - \left[\ln \frac{\operatorname{Cosh} \frac{\pi}{2} (y''' - b''') - \cos \frac{\pi}{2} (x''' - a''')}{\operatorname{Cosh} \frac{\pi}{2} (y''' - b''') + \cos \frac{\pi}{2} (x''' + a''')} \right.$$

$$\left. + \ln \frac{\operatorname{Cosh} \frac{\pi}{2} (y''' + b''') - \cos \frac{\pi}{2} (x''' - a''')}{\operatorname{Cosh} \frac{\pi}{2} (y''' + b''') + \cos \frac{\pi}{2} (x''' + y''')} \right] .$$

For z-plane values such that $a \cdot x < 0$ the result so computed for V_{IA} should be reversed in sign.

Case IB.

As was noted earlier, the problem posed by Case IB becomes identical to that of Case IA if we interchange the x-plane values of a with b and of x with y. For Case IB, then, we accordingly first obtain new values for the single-prime variables

$$x' = (|y|^2 - |x|^2) / c^2 \qquad a' = (|b|^2 - |a|^2) / c^2$$

$$y' = 2\ |xy|\ / c^2 \qquad b' = 2\ |ab|\ / c^2$$

and then, with these single-prime variables, proceed through the same succeeding transformations as before to obtain new values of the corresponding triple-prime variables. With these new triple-prime variables, one next evaluates V_{IB} through substitution into the formula given previously for V_{IA} and then reverses the sign of the result if the original z-plane coordinates are such that $b \cdot y < 0$.

SUMMARY

The total potential of the single unit line charge in the problem originally posed ($\lambda = 1.$ e.s.u., at a, b) then is given by

$$V^{(T)} = \frac{1}{4}\ (V_{IA} + V_{IB} + V_{II} + V_{III}).$$

The associated image-field potential is then obtained by subtracting the "direct" potential--specifically by forming*

$$V^{(I)} = V^{(T)} + \ln \frac{(x - a)^2 + (y - b)^2}{c^2} \ .$$

---

*$V^{(I)}$ as so formed clearly has been assigned an arbitrary additive constant to its value. The subtraction procedure, as defined, also clearly will be inoperative if the field-point and source point coincide.

APPENDIX B

POTENTIAL OF A LINE CHARGE PARALLEL TO, AND BETWEEN, TWO PARALLEL GROUNDED CONDUCTING PLATES

For parallel conducting planes at $y = \pm h$ and a line charge λ (c.g.s. e.s.u.) at $x = x_1$, $y = y_1$, the transformation $z' = \exp \frac{\pi\,(z + i\,h)}{2h}$ carries the conducting planes to the x' axis of the z' plane. The points $z = \pm\, i\, h$ ($x = 0$, $y = \pm\, h$) lie at $z' = \mp\, 1$. The source point goes to z'-plane coordinates $-e^{\pi x_1/2h} \sin \frac{\pi y_1}{2h}$, $e^{\pi x_1/2h} \cos \frac{\pi y_1}{2h}$, its image then becomes $-e^{\pi x_1/2h} \sin \frac{\pi y_1}{2h}$, $-e^{\pi x_1/2h} \cos \frac{\pi y_1}{2h}$, and the field point becomes $-e^{\pi x/2h} \sin \frac{\pi y}{2h}$, $e^{\pi x/2h} \cos \frac{\pi y}{2h}$ in this z' plane.

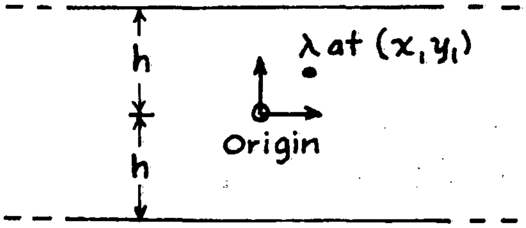

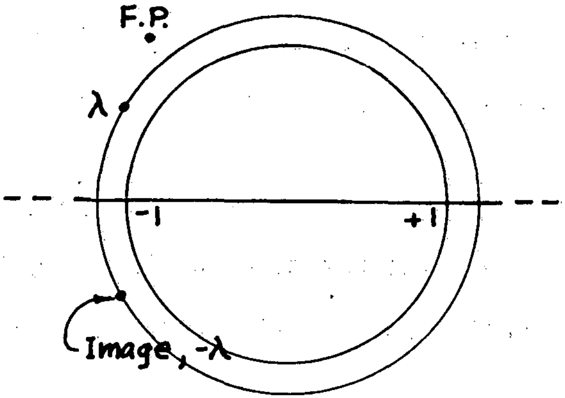

The potential function then becomes

$$V = -\lambda \ln \left[\frac{\left(e^{\pi x/2h} \sin \frac{\pi y}{2h} - e^{\pi x_1/2h} \sin \frac{\pi y_1}{2h}\right)^2 + \left(e^{\pi x/2h} \cos \frac{\pi y}{2h} - e^{\pi x_1/2h} \cos \frac{\pi y_1}{2h}\right)^2}{\left(e^{\pi x/2h} \sin \frac{\pi y}{2h} - e^{\pi x_1/2h} \sin \frac{\pi y_1}{2h}\right)^2 + \left(e^{\pi x/2h} \cos \frac{\pi y}{2h} + e^{\pi x_1/2h} \cos \frac{\pi y_1}{2h}\right)^2} \right]$$

---

* The transformation employed in this Appendix was introduced in Appendix. B, 1 (pp. 352-353) of L. J. Laslett, "On Intensity Limitations Imposed by Transverse Space - Charge Effects in Circular Particle Accelerators," in Proc. 1963 Summer Study on Storage Rings, Accelerators and Experimentation at super-High Energies (J. W. Bittner, Ed.), pp. 324-367 (BNL 7534, Brookhaven National Lab., Upton, Long Island, N.Y.; (1963).

and after some algebraic manipulation is found to be expressible as

$$V = -\lambda \ln \left[\frac{\mathrm{Cosh}\, \frac{\pi (x - x_1)}{2h} - \cos \frac{\pi (y - y_1)}{2h}}{\mathrm{Cosh}\, \frac{\pi (x - x_1)}{2h} + \cos \frac{\pi (y + y_1)}{2h}} \right] .$$

With a re-orientation of the diagram, to become

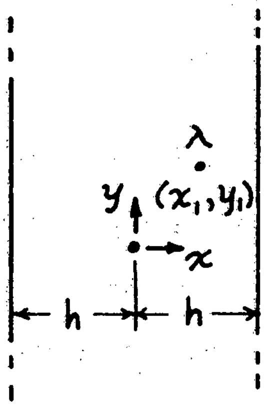

the result may be written

$$V = -\lambda \ln \left[\frac{\mathrm{Cosh}\, \frac{\pi}{2h} (y - y_1) - \cos \frac{\pi}{2h} (x - x_1)}{\mathrm{Cosh}\, \frac{\pi}{2h} (y - y_1) - \cos \frac{\pi}{2h} (x + x_1)} \right] .$$

It is this last form of which we have made use in Appendix A of the present work, with allowances of differences in notation and with recognition of the fact that (in these applications) more than one line charge may need be considered present.

APPENDIX C

IMAGE FIELDS FROM AN ELLIPTICAL BEAM SURROUNDED BY A CONFOCAL ELLIPTICAL CYLINDER OR BY A COAXIAL CIRCULAR CYLINDER

For comparison with some of the results presented in the body of the present report, we summarize here results for cases in which a uniform elliptical beam is surrounded either (1) by a confocal elliptical cylinder or (2) by a coaxial circular cylinder.

1. Surrounding Confocal Elliptical Cylinder*

We consider here a uniform elliptical beam with semi-axes a and b (focal length $f = \sqrt{a^2 - b^2}$) surrounded by a confocal elliptical conducting cylinder. In this case it is found that the image fields are strictly linear. The result has been briefly included in some of our early transport computations, but appeared to be of little consequence in that work.

The electrostatic potential problem in this case may be analyzed in terms of elliptical co-ordinates generated by the transformation

$$z = x + i\,y = f \operatorname{Cosh}(u + i\,v),$$

namely

$$\left.\begin{array}{l} x = f \operatorname{Cosh} u \cos v \\ y = f \operatorname{Sinh} u \sin v \end{array}\right\} .$$

---

*E. Regenstreif, CERN / PS / DL 76-4 (C.E.R.N., Geneva, Switzerland; June 1976). L. Jackson Laslett (Lawrence Berkeley Laboratory), unpublished.

The major and minor semi-axes of the beam boundary then are

$a = f \text{ Cosh } u_E$ and $b = f \text{ Sinh } u_E$,

where u_E refers to the edge of the beam. From the well known* expression for the "direct" field of such a beam (when isolated),

$$E_x^{(D)} = 4\lambda \frac{x}{a\,(a+b)} \quad \text{and} \quad E_y^{(D)} = 4\lambda \frac{y}{b\,(a+b)} \quad \text{(e.s.u.)}$$

within the beam, we may write the associated direct potential function as

$$V^{(D)} = -\,2\lambda \left[\frac{x^2}{a\,(a+b)} + \frac{y^2}{b\,(a+b)} \right] + \text{const.}$$

$$= -\,2\lambda \frac{f^2}{a+b} \left[\frac{1}{a} \text{Cosh}^2 u \cos^2 v + \frac{1}{b} \text{Sinh}^2 u \sin^2 v \right] + \text{const.}$$

$$= -\,\lambda \frac{f}{a+b} \left[\frac{\text{Cosh } 2u + 1}{2 \text{ Cosh } u_E} (1 + \cos 2v) + \frac{\text{Cosh } 2u - 1}{2 \text{ Sinh } u_E} (1 - \cos v) \right] + \text{const.}$$

within the beam ($u \leq u_E$), and correspondingly

$$\frac{\partial V^{(D)}}{\partial u} = -\,\lambda \frac{f}{a+b} \left[\frac{\text{Sinh } 2u}{\text{Cosh } u_E} (1 + \cos 2v) + \frac{\text{Sinh } 2u}{\text{Sinh } u_E} (1 - \cos 2v) \right]$$

at the boundary. This direct internal potential and normal derivative may be matched to a harmonic external direct potential function

$$V^{(D)} = -\,\lambda \frac{f}{a+b} \left[e^{u_E - 2u} \cos 2v + 2\, e^{u_E} \cdot u \right] + \text{const.}$$

for $u \geq u_E$.

---

* L. C. Teng, "Transverse Space-Charge Effects", ANLAD-59 (Argonne National Laboratory, Argonne, Ill.; February 1, 1963).

The image field required to make the surrounding elliptical conductor ($u = u_w$) an equipotential then must be characterized by the supplementary potential function

$$V^{(I)} = + \lambda \frac{f}{a+b} \left[\frac{e^{u_E - 2u_w}}{\text{Cosh } 2u_w} \text{ Cosh } 2u \cos 2v \right] + \text{const.},$$

$$= \lambda \frac{f}{a+b} \frac{e^{u_E - 2u_w}}{\text{Cosh } 2u_w} \left[2 \frac{x^2 - y^2}{f^2} + 1 \right] + \text{const.},$$

or simply by

$$V^{(I)} = \frac{2\lambda}{a+b} \frac{e^{u_E - 2u_w}}{f \text{ Cosh } 2u_w} \cdot (x^2 - y^2) \qquad [u \leq u_w].$$

It is noted that this potential implies exclusively linear image fields in this case.

In the special case that the elliptical tube fits snugly around the beam ($u_w \to u_E$), $V^{(I)}$ becomes

$$V^{(I)} = 2\lambda \frac{a-b}{a+b} \frac{x^2-y^2}{a^2+b^2}$$

(since $e^{-u_E} = \text{Cosh } u_E - \text{Sinh } u_E = \frac{a-b}{f}$ and

$\text{Cosh } 2 u_E = \text{Cosh}^2 u_E - \text{Sinh}^2 u_E = \frac{a^2+b^2}{f^2} = \frac{a^2+b^2}{a^2-b^2}$).

In this case, then, the image fields become

$$E_x^{(I)} = -4\lambda \frac{a-b}{a+b} \frac{x}{a^2+b^2} \text{ and } E_y^{(I)} = + 4\lambda \frac{a-b}{a+b} \frac{y}{a^2+b^2} \qquad (u_w = u_E).$$

To obtain, finally the total space-charge field for this special case, we add

$$E_x^{(D)} = 4\lambda \frac{x}{a(a+b)} \quad \text{or} \quad E_y^{(D)} = 4\lambda \frac{y}{b(a+b)}$$

to obtain

$$E_x = 4\lambda \frac{b}{a} \frac{x}{a^2+b^2} \quad \text{and} \quad E_y = 4\lambda \frac{a}{b} \frac{y}{a^2+b^2} \qquad (u \leq u_E = u_w)$$

with $\nabla \cdot \vec{E} = \frac{4\lambda}{ab} = 4\pi \frac{\lambda}{\pi ab} = 4\pi\rho$ (as required). It was these components of space-charge field that were employed in some brief tests of beam transport and that led to the conclusion that image fields introduced no pronounced effects in such a configuration as that just discussed.

2. Surrounding Coaxial Circular Cylinder*

With the elliptical beam again characterized by semi-axes a, b and with the focal length $f = \sqrt{a^2 - b^2}$, the surrounding conducting surface is now taken to be a co-axial circular cylinder of radius R. In this case the image-field potential at a point r, θ can be written conveniently in the multipole form

$$V^{(I)} = 2\lambda \ln \left[2 \left(\frac{R}{f}\right)^2 \right] - \lambda \sum_{n=1} c_n \left(\frac{f}{R}\right)^{2n} \left(\frac{r}{R}\right)^{2n} \cos 2n\theta,$$

where $$c_n = \frac{(2n-1)!}{2^{2n-1}\, n!\, (n+1)!} .$$

Thus the image field at points along the x-axis can be written

$$E_x^{(I)} \Big|_{y=0} = - \frac{\partial V^{(I)}}{\partial r} \Big|_{\theta=0}$$

$$= \lambda \sum_{n=1} 2\, n\, c_n \frac{f^{2n}\, r^{2n-1}}{R^{4n}} = \lambda \sum_{n=1} 2\, n\, c_n \frac{f^{2n}\, x^{2n-1}}{R^{4n}} \quad \text{(e.s.u.)},$$

where the c_n are as before. The form just shown exhibits most explicity the occurrence of fields of various harmonic orders. The closed form presented by Regenstreif gives this same result as

---

* E. Regenstreif CERN/PS/DL 77-37 (C.E.R.N., Geneva, Switzerland; October 1977). L. Jackson Laslett (Lawrence Berkeley Laboratory), unpublished.

$$E_x^{(I)} \Big|_{y=0} = 4\lambda \frac{R^4}{f^2 x^3} \left[1 - \sqrt{1- (\frac{fx}{R^2})^2} - \frac{1}{2} (\frac{fx}{R^2})^2 \right]$$

in our units.

The corresponding forms for the image field along the y axis are

$$E_y^{(I)} \Big|_{x=0} = \lambda \sum_{n=1} (-1)^n \, 2n \, c_n \frac{f^{2n} y^{2n-1}}{R^{4n}}$$

$$= - 4\lambda \frac{R^4}{f^2 y^3} \left[1 - \sqrt{1+ (\frac{fy}{R^2})^2} + \frac{1}{2} (\frac{fy}{R^2})^2 \right] .$$

```
  HIV0311
0                        XXXX  XXXX   XXX  XXXX  X   X
                         X   X X   X X   X X   X  X X
                         XXXX  XXXX  X   X X   X   X
                         X   X X  X  XXXXX X   X   X
                         XXXX  X   X X   X XXXX    X
0               4541 01 . . .DECK . 03 APR 80 . 12.55 . 4541 01
                .                                             .
 XXXXXXXXXXXX   .                                             .
       X        .                                             .
       X        .                                             .
       X        .                                             .
 XXXXXXXXXXXX   .                                             .
                .                                             .
                .                                             .
 X          X   .                                             .
 XXXXXXXXXXXX   .                                             .
 X          X   .                                             .
                .                                             .
                .                                             .
       XXXXXX   .                                             .    XXXX XXXXX
    XXX         .                                             .   X    X     X
 XXX            .                                             .   X    X     X
    XXX         .                                             .   X    X     X
       XXXXXX   .                                             .   XXXXXXXXXXXX
                .                                             .
 XXXXXXXXXXXX   .                                             .   XXXXXXXXXXXX
 X          X   .                                             .   X          X
 X          X   .                                             .   X          X
 X          X   .                                             .   X          X
 XXXXXXXXXXXX   .                                             .   XXXXXXXXXXXX
                .                                             .
 XXXXXXXXXXXX   .                                             .   XXXXXX
 X     X    X   .                                             .         XXX
 X     X    X   .                                             .            XXX
 X     X    X   .                                             .         XXX
  XXXXX XXXX    .                                             .   XXXXXX
                .                                             .
                .                                             .
                .                                             .   X          X
                .                                             .   XXXXXXXXXXXX
                .                                             .   X          X
                .                                             .
                .                                             .
                .                                             .   XXXXXXXXXXXX
                .                                             .        X
                .                                             .        X
                .                                             .        X
                .                                             .   XXXXXXXXXXXX
                .                                             .
                4541 01 .THURSDAY . 03 APR 80 . 12.55 . 4541 01
                   XXXXX X     XXXXX XXXXX XXXX        XXXXX
                   X     X     X   X X   X X   X       X
                   XXX   X     X   X X   X XXXX        XXXX
                   X     X     X   X X   X X  X            X
                   X     XXXXX XXXXX XXXXX X   X        XXX
```

```
G34MG,12,4000,52000,456004,LASLETT
*6600,NOTAPES,PSS
FLOOR(3)
LIBCOPY(LASLETT,LIB/RBP,FATTY)
LIBCOPY(SOURCE,FIL/FBR,GB)
COPY(INPUT,1RM,LIB,1RM,FIL,1F,DECK/PBR)
RETURN,LGO.
RUN76(SCR,NL15000,I=DECK)
TTY.
LGO(TAPETTY,TAPETTY)
EXIT.
DMP.
DMP(16200)
TEXT,TAPETTY,(XEQ ERROR).
EXIT.
TEXT,TAPETTY,(COMP. ERROR).
FIN.
SESAME.
      PROGRAM G34MG(INPUT,OUTPUT)
      COMMON / COFOU / C, DX, DY, RADIUS, VBEG, VEND,
     $ KASES, STEP, VISAV(36)
      COMMON / GOLUB / N, AM, BM, UG(128), WG(128)
      DIMENSION BG(128), XG(128), CG(128), ENDPTS(2)
      DIMENSION IRAY(7)
      DATA KASTOD, PI /
     $ 171737517002305024055B, 17216220773250420551B /
      DATA POT, TOP /
     $ 17206220773250420551B, 17175057460333447104B /
      DATA KIND, KPTS / 1, 0 /
      NMAX = 128             $  NSAVE = 0
      ROD = PI/180.          $  DOR = 180./PI
*
      CALL OPNTTY
*
      PRINT 9000  $  CALL DATE(L)  $  PRINT 9003, L
*
C >>> DIAGNOSTIC PRINT OF POT (=PI/2) ^ TOP (=2/PI)
*     PRINT 9004, POT, POT, TOP, TOP  $  PRINT 9000
*
10    PRINT 9010  $  CALL DATA(C,1)   $  C = ABS(C)
12    IF  (C .LE. 0.)  GO TO 10  $  PRINT 9011, C
14    PRINT 9000  $  PRINT 9112  $  CALL DATA(AM,1,BM,1)
      AM = ABS(AM)                 $  BM = ABS(BM)
15    PRINT 9111  $  CALL DATA(DX,1,DY,1)
      IF ((AM+ABS(DX)) .GE. C) GO TO 14
      IF ((BM+ABS(DY)) .GE. C) GO TO 14
      PRINT 9000  $  PRINT 9011, C
      PRINT 9000  $  PRINT 9115, AM, BM, DX, DY
      PRINT 9021  $  READ 9001, Q
      IF (Q .EQ. 1HN) GO TO 800
      RAM = 1./AM $  RBM = 1./BM
*
18    LOOP = 0    $  LINE = 1
      PRINT 9160  $  READ 9001, Q
      IF (Q .EQ. 1HX) GO TO  20
      IF (Q .EQ. 1HY) GO TO  30
      IF (Q .EQ. 1HD) GO TO  40  $  GO TO 100
20    PRINT 9161  $  CALL DATA(VBEG,1,VEND,1,KASES,1)
      PRINT 9164  $  CALL DATA(Y,1)
      LOOP = 1    $  GO TO 104
30    PRINT 9162  $  CALL DATA(VBEG,1,VEND,1,KASES,1)
      PRINT 9165  $  CALL DATA(X,1)
```

```
      LOOP = 2      $  GO TO 104
40    KEEP = 0      $ KASES = 36 $ VEND = 355. $ VBEG = 5.
      PRINT 9170   $  READ 9001, Q
      IF (Q .NE. 1HY) GO TO 41
      PRINT 9167   $  READ 9001, Q
      IF (Q .EQ. 1HN) LINE = 0
      KEEP = 1      $   GO TO 42
41    PRINT 9163   $  CALL DATA(VBEG,1,VEND,1,KASES,1)
42    PRINT 9166   $  CALL DATA(RADIUS,1)
      LOOP = 3      $  GO TO 104
*
100   PRINT 9000   $  PRINT 9022  $  CALL DATA(X,1,Y,1)
      IF (((X*X-Y*Y)**2) .LT. (C**4)) GO TO 102
      PRINT 9011, C  $  GO TO 100
102   CALL TRANS(X,Y,X1,Y1,X2,Y2,X3,Y3,C,MALO)
      IF (MALO .EQ. 1)  GO TO 100
      CALL TRANS(X,Y,XP1,YP1,XP2,YP2,XP3,YP3,C,MALO)
      IF (MALO .EQ. 1)  GO TO 100
      PRINT 9000   $  PRINT 9025, X, Y, C
*     PRINT 9026, X1, Y1
*     PRINT 9027, X2, Y2
*     PRINT 9028, X3, Y3
      PRINT 9000   $  PRINT 9120  $  READ 9001, Q
      PRINT 9000   $  IF (Q .NE. 1HY) GO TO 800
*
104   PRINT 9000   $  PRINT 9125  $  CALL DATA(N,1)
      IF (IABS(N) .GT. NMAX) GO TO 104
      LOOK = 0      $  PRINT 9130  $  READ 9001, Q
      IF (Q .EQ. 1HY) LOOK = 1   $  PRINT 9000
      N = MAX0(MIN0(IABS(N),NMAX),1)
      IF (N .EQ. NSAVE) GO TO 108  $  NSAVE = N
      CALL GAUSSQ(KIND,N,ALPHA,BETA,
     $KPTS,ENDPTS,BG,XG,CG)
      IF (KIND .GT. 4) GO TO 108
      IF (KPTS .NE. 0) GO TO 108
      L = N/2  $  IF (L .EQ. 0) GO TO 108
      IF ((L+L-N) .NE. 0) XG(L+1) = 0.
      DO 106 M=1,L  $  K = N-M+1
      XG(K) = 0.5*(XG(K) - XG(M))   $  XG(M) = -XG(K)
      CG(K) = CG(M) = 0.5*(CG(K) + CG(M))
106   CONTINUE
*
108   IF (LOOK .EQ. 1) PRINT 9000
      DO 110 M=1,N  $  UG(M) = XG(M)  $  WG(M) = CG(M)
      IF (LOOK .EQ. 1) PRINT 9135, M, XG(M), M, CG(M)
110   CONTINUE
*
115   IF (LOOP .EQ. 0) GO TO 200
      KASES = MAX0(IABS(KASES),2)
      IF((LOOP.EQ.3).AND.(KEEP.EQ.1)) KASES=MAX0(KASES,4)
      STEP = (VEND-VBEG)/(KASES-1.)
*
      DO 240 KS=1,KASES           $  MALO = 0
      GO TO (121,122,123) LOOP
121   X = VBEG + (KS-1.)*STEP  $  GO TO 130
122   Y = VBEG + (KS-1.)*STEP  $  GO TO 130
123   ARG = RDD*(VBEG + (KS-1.)*STEP)
      X = RADIUS*COS(ARG)  $  Y = RADIUS*SIN(ARG)
*     GO TO 130
130   IF (((X*X-Y*Y)**2) .LT. (C**4)) GO TO 132
      MALO = 1        $  PRINT 9191  $  GO TO 235
132   CALL TRANS(X,Y,X1,Y1,X2,Y2,X3,Y3,C,MALO)
```

```
      IF (MALO .EQ. 0) GO TO 133
      PRINT 9190     $  GO TO 235
133   CALL TRANS(Y,X,XP1,YP1,XP2,YP2,XP3,YP3,C,MALO)
      IF (MALO .EQ. 0) GO TO 200
      PRINT 9190     $  GO TO 235
*
200   IF (LINE .EQ. 1) PRINT 9000
                        SUMS = 0. $ SUMVTS = 0.
      DO 220 J=1,N   $  SUMT = 0. $ SUMVTT = 0.
      WS = CG(J)   $  S = XG(J)
      DO 210 I=1,N
      WT = CG(I)   $  T = XG(I)   $  ARG = PI*(T+1.)
      A = 0.5*AM*(S+1.)*COS(ARG) + DX
      B = 0.5*BM*(S+1.)*SIN(ARG) + DY
      IF (A .NE. X)  GO TO 202  $  IF (B .NE. Y) GO TO 202
      PRINT 9180
      IF (LOOP .NE. 0) GO TO 235  $  GO TO 250
202   CALL TRANS(A,B,A1,B1,A2,B2,A3,B3,C,MALO)
      IF (MALO .EQ. 0) GO TO 203  $  PRINT 9190
      IF (LOOP .NE. 0) GO TO 235  $  GO TO 250
203   CALL TRANS(B,A,AP1,BP1,AP2,BP2,AP3,BP3,C,MALO)
      IF (MALO .EQ. 0) GO TO 204  $  PRINT 9190
      IF (LOOP .NE. 0) GO TO 235  $  GO TO 250
204   CALL GET4V(A,B,X,Y,A1,B1,X1,Y1,A3,B3,X3,Y3,
     $AP3,BP3,XP3,YP3,C,VTOT,VIMG,MALO)
         SUMT = SUMT + WT*VIMG
      SUMVTT = SUMVTT + WT*VTOT
210   CONTINUE
         SUMS = SUMS + WS*(S+1.)*SUMT
      SUMVTS = SUMVTS + WS*(S+1.)*SUMVTT
220   CONTINUE     $  VIMG = 0.25*SUMS
                      VTOT = 0.25*SUMVTS
      IF (LINE .EQ. 0) GO TO 225
*     PRINT 9151, X, Y, C, N, VIMG
      PRINT 9152, X, Y, C, N, VIMG, VTOT
225   IF (LOOP .NE. 3) GO TO 235
      IF (KEEP .NE. 1) GO TO 235
      VISAV(KS) = VIMG
*
235   CONTINUE     $  IF (MALO .NE. 0) KEEP = 0
      IF (LOOP .EQ. 0) GO TO 250
240   CONTINUE
*
      IF (LOOP .NE. 3) GO TO 250
      IF (KEEP .NE. 1) GO TO 250
      PRINT 9171  $  READ 9001, Q
      IF (Q .EQ. 1HY) CALL FOUVI
*
250   PRINT 9000  $  PRINT 9140     $  READ 9001, Q
      IF (Q .EQ. 1HY) GO TO 104
*     GO TO 775
*
775   PRINT 9000  $  CALL STATUS(IRAY)
      CUSR = 0.001*FLOAT(IRAY(3))  $  PRINT 9700, CUSR
800   PRINT 9019  $  READ 9001, Q
      IF (Q .EQ. 1HT) GO TO 990
820   PRINT 9030  $  READ 9001, Q
      IF (Q .EQ. 1HC) GO TO  10
      IF (Q .EQ. 1HS) GO TO  12
      IF (Q .NE. 1HF) GO TO 800
      PRINT 9000  $  PRINT 9115, AM, BM, DX, DY
      PRINT 9000  $   GO TO  19
```

```
*
980   PRINT 9000  $  CALL STATUS(IRAY)
      CUSR = 0.001*FLOAT(IRAY(3))  $  PRINT 9700, CUSR
*
990   PRINT 9900
*
9000  FORMAT(* *)
9001  FORMAT(A1)
9002  FORMAT(O20)
9003  FORMAT(* *,29X,A10,///)
9004  FORMAT(* BOT =*F17.14,*,  *,O20,* (OCTAL)*,/,
     $* TOP =*F17.14,*,  *,O20,* (OCTAL)*,/)
9010  FORMAT(* TYPE C*)
9011  FORMAT(*   C =*F15.10)
9012  FORMAT(* *,/,* TYPE A ∧ B*)
9015  FORMAT(*   A =*F15.10,*   B =*F15.10,
     $*   C =*F15.10)
*9016 FORMAT(*  A1 =*F15.10,*  B1 =*F15.10)
*9017 FORMAT(*  A2 =*F15.10,*  B2 =*F15.10)
*9018 FORMAT(*  A3 =*F15.10,*  B3 =*F15.10,/)
9019  FORMAT(* MORE OR TERMINATE? -- M OR T*)
9020  FORMAT(* REVISE C? -- Y OR N*)
9021  FORMAT(* CONTINUE WITH THESE SOURCE LOCATIONS?*,
     $* -- Y OR N*)
9022  FORMAT(* ENTER FIELD-POINT CO-ORDINATES, X ∧ Y*)
9025  FORMAT(*   X =*F15.10,*   Y =*F15.10,
     $*   C =*F15.10)
9026  FORMAT(*  X1 =*F15.10,*  Y1 =*F15.10)
9027  FORMAT(*  X2 =*F15.10,*  Y2 =*F15.10)
9028  FORMAT(*  X3 =*F15.10,*  Y3 =*F15.10,/)
9029  FORMAT(* *,/,
     $* POTENTIALS FOR LAMBDA = 1.0  (E.S.U.)*,/,
     $*  VTOT =*F16.10,/,*  VIMG =*F16.10,/)
9030  FORMAT(* NEW FIELD-POINT, SOURCE POINTS, OR C?*,
     $* -- F, S, OR C*)
9111  FORMAT(* TYPE DELTAX ∧ DELTAY*)
9112  FORMAT(* TYPE SEMIA ∧ SEMIB*)
9115  FORMAT(* SEMI-AXES*,1H*,/,
     $*  AM =*F15.10,*  BM =*F15.10,/,
     $*  DX =*F15.10,*  DY =*F15.10,/)
9120  FORMAT(* PERFORM GAUSSIAN INTEGRATION?*,
     $* -- Y OR N*)
9125  FORMAT(* TYPE N  (LE 128 -- EG, 32)*)
9130  FORMAT(* PRINT NODES ∧ WEIGHTS? -- Y OR N*)
9135  FORMAT(*  XG(*I3,*) =*E22.14,*  CG(*I3,
     $*) =*E22.14)
9140  FORMAT(* REPEAT WITH NEW N? -- Y OR N*)
9150  FORMAT(* *,I3,* ORDER,   IMAGE*,
     $* POTENTIAL =*F16.10,*  (E.S.U.)*,/)
9151  FORMAT(* X =*F14.10,*  Y =*F14.10,*  C =*F14.10,/,
     $* *,I6,* ORDER,*,F23.10,
     $* IMAGE POTENTIAL (E.S.U.)*,/)
9152  FORMAT(* X =*F14.10,*  Y =*F14.10,*  C =*F14.10,/,
     $* *,I6,* ORDER,*,F23.10,
     $* IMAGE POTENTIAL (E.S.U.)*,/,
     $* *,13X,F23.10,* TOTAL POTENTIAL*,/)
9160  FORMAT(* LOOP FIELD-POINT X, Y, DEG, OR NOT?*,
     $* -- X, Y, D, OR N*)
9161  FORMAT(* TYPE FIRST, FINAL, AND KASES FOR X*)
9162  FORMAT(* TYPE FIRST, FINAL, AND KASES FOR Y*)
9163  FORMAT(* TYPE FIRST, FINAL, AND KASES FOR DEGREES*)
9164  FORMAT(* TYPE Y*)
```

```
9165  FORMAT(* TYPE X*)
9166  FORMAT(* TYPE RADIUS*)
9167  FORMAT(* PRINT POTENTIALS FROM SCAN? -- Y OR N*)
9170  FORMAT(* USE STANDARD DEGREE VALUES? -- Y OR N*)
9171  FORMAT(* COMPUTE AND TABULATE FOURIER*,
     $* COEFFICIENTS? -- Y OR N*)
9180  FORMAT(* *,/,* SOURCE ∧ FIELD POINTS COINCIDE*,
     $4H ***,/)
9181  FORMAT(* *,/,* SOURCE ∧ BOUNDARY POINTS*,
     $* COINCIDE*,4H ***,/)
9190  FORMAT(* *,/,* NEGATIVE ARGUMENT*,
     $* OF SQUARE ROOT*,4H ***,/)
9700  FORMAT(* *,F11.3,* CU'S REMAIN*,/)
9300  FORMAT(* *,25X,18H*** END OF RUN ***,/)
*
      STOP
      END
      SUBROUTINE TRANS(U0,V0,U1,V1,U2,V2,U3,V3,C,MALO)
      DATA POT, TOP /
     $ 17206220773250420551B, 17175057460333447104B /
       RCS = 1./(C*C)
      MALO = 0
      IF (U0 .EQ. 0.) GO TO 40
      IF (V0 .EQ. 0.) GO TO 50
      U1 = RCS*(U0*U0 - V0*V0)
      V1 = 2.*RCS*ABS(U0*V0)
      EV = EXP(POT*V1)   $  REV = 1./EV   $  ARGU = POT*U1
      U2 = 0.5*SIN(ARGU)*(EV+REV)
      V2 = 0.5*COS(ARGU)*(EV-REV)
      AL = 2.*U2 - 1.    $  ALS = AL*AL   $    BES = 4.*V2*V2
       S = 1. + 2.*(BES-ALS) + (BES+ALS)**2
      IF (S .GE. 0.) GO TO 05
      MALO = 1
      RETURN
05     SS = SQRT(S)
      ARS = 0.5*(1. + ALS + BES - SS)
        H = 0.5*(SS - 1. + ALS + BES)
      IF ((ARS .GE. 0.) .AND. (H .GE. 0.)) GO TO 07
      MALO = 1
      RETURN
07    SH = SQRT(H)
      U3 = TOP*ASIN(SQRT(ARS))
      IF (AL .GE. 0.) GO TO 10   $  U3 = -U3
10    V3 = TOP*ALOG(SQRT(H+1.) + SH)
      RETURN
40    V2 = V1 = 0.        $  U3 = -1.
      U1 = -(V0*V0)*RCS
      U2 = SIN(POT*U1)
      ARG = 1. - 2.*U2   $  ARGSM = ARG*ARG - 1.
      IF (ARGSM .GE. 0.) GO TO 45
      MALO = 1
      RETURN
45    V3 = TOP*ALOG(ARG + SQRT(ARGSM))
      RETURN
50    U1 = (U0*U0)*RCS   $  V3 = V2 = V1 = 0.
      U2 = SIN(POT*U1)
      U3 = TOP*ASIN(2.*U2 - 1.)
      RETURN
      END
      SUBROUTINE GET4V(A,B,X,Y,A1,B1,X1,Y1,A3,B3,X3,Y3,
     $AP3,BP3,XP3,YP3,C,VTOT,VIMG,MALO)
       DATA POT / 17206220773250420551B /
```

```
      E = EXP(POT*(BP3-YP3))    $  BHM3 = 0.5*(E + 1./E)
      E = EXP(POT*(BP3+YP3))    $  BHP3 = 0.5*(E + 1./E)
      E = EXP(POT*(B3-Y3))      $  CHM3 = 0.5*(E + 1./E)
      E = EXP(POT*(B3+Y3))      $  CHP3 = 0.5*(E + 1./E)
      E = EXP(POT*(B1-Y1))      $  CHM1 = 0.5*(E + 1./E)
      E = EXP(POT*(B1+Y1))      $  CHP1 = 0.5*(E + 1./E)
      BCM3 = COS(POT*(AP3-XP3))
      BCP3 = COS(POT*(AP3+XP3))
      CCM3 = COS(POT*(A3-X3))
      CCP3 = COS(POT*(A3+X3))
      CCM1 = COS(POT*(A1-X1))
      CCP1 = COS(POT*(A1+X1))
      E3O = (BHM3-BCM3)/(BHM3+BCP3)
      E3I = (BHP3-BCM3)/(BHP3+BCP3)
      F3O = (CHM3-CCM3)/(CHM3+CCP3)
      F3I = (CHP3-CCM3)/(CHP3+CCP3)
      F1O = (CHM1-CCM1)/(CHM1+CCP1)
      F1I = (CHP1-CCM1)/(CHP1+CCP1)
      P1B = E3O*E3I
      P1A = F3O*F3I
       P2 = F1O*F1I
       P3 = F3O/F3I
      IF   (A*X .LT. 0.)   P1A = 1./P1A
      IF   (B*Y .LT. 0.)   P1B = 1./P1B
      IF (A*X*B*Y .LT. 0.)  P3 = 1./P3
      VTOT = -0.25*ALOG(P1A*P1B*P2*P3)
      PRO = ((A-X)**2 + (B-Y)**2)/(C**2)
      VIMG = VTOT + ALOG(PRO)
*
      RETURN
      END
      SUBROUTINE FOUVI
C >>> FOURIER ANALYSIS OF IMAGE-FIELD POTENTIAL.
      COMMON / COFOU / C, DX, DY, RADIUS, VBEG, VEND,
     $ KASES, STEP, VISAV(36)
      COMMON / GOLUE / N, AM, BM, UG(128), WG(128)
      DIMENSION CK(18), SK(18)
      DATA PI, POT /
     $ 17216220773250420551B, 17206220773250420551B /
      ROD = PI/180.   $  NKASES = 36
      IF (KASES .GT. NKASES) RETURN
      IF (KASES .LE. 4)      RETURN
      KH = KASES/2  $  KM = KH - 1  $  RKASES = 1./KASES
      PRINT 902  $  CK(18)=CK0=SK18=0.  $  FS=F=1.
*
C >>> OBTAIN FOURIER COEFFICIENTS OF IMAGE POTENTIAL
      DO 100 LS=1,KASES
      CK0 = CK0 + VISAV(LS)
      SK18 = SK18 + FS*VISAV(LS)  $  FS = -FS
100   CONTINUE
      CK0 = RKASES*CK0  $  SK(18) = RKASES*SK18
      PRINT 903, CK0
      IF (RADIUS .EQ. 0.) RETURN
      RADFAC = RADIUS/C  $   RRADFAC = C/RADIUS
      DO 250 KS=1,KM      $   F = RRADFAC*F
      SUMSI = SUMCO = 0.
      DO 200 LS=1,KASES
      ARG = ROD*(VBEG + (LS-1.)*STEP)
      SUMCO = SUMCO + VISAV(LS)*COS(KS*ARG)
      SUMSI = SUMSI + VISAV(LS)*SIN(KS*ARG)
200   CONTINUE
      CK(KS) = 2.*F*RKASES*SUMCO
```

```
      SK(KS) = 2.*F*RKASES*SUMSI
      PRINT 904, KS, CK(KS), KS, SK(KS)
250   CONTINUE   $   SK(KH) = RPADFAC*F*SK(KH)
      PRINT 907, KH, SK(KH)
*
      DOC = (SQRT(DX**2 + DY**2))/C  $  TH = 0.
      IF ((DX.NE.0.).OR.(DY.NE.0.)) TH = ATAN2(DY,DX)
      EYDEL = EXDEL = 0.      $  F = 1.
      DO 280 L=1,KH
      COLM = COS((L-1.)*TH)   $  SILM = SIN((L-1.)*TH)
      EXDEL = EXDEL + L*F*(CK(L)*COLM + SK(L)*SILM)
      EYDEL = EYDEL + L*F*(SK(L)*COLM - CK(L)*SILM)
      IF (L .EQ. KH) GO TO 260
      F = F*DOC
260   CONTINUE
280   CONTINUE
      EXDEL = -EXDEL/C  $  EYDEL = -EYDEL/C
      PRINT 910, EXDEL, EYDEL
*
      PRINT 900  $  PRINT 905   $  READ 901, Q
      IF (Q .EQ. 1HN) GO TO 400          $  PRINT 906
C >>> OBTAIN (OPTIONALLY) CHECK SUMS
      DO 350 LS=1,KASES        $  F = 1.
      ARG = RDD*(VBEG + (LS-1.)*STEP)  $  SUM = CK0
      DO 300 KS=1,KH           $  F = RADFAC*F
      SUM = SUM+F*(CK(KS)*COS(KS*ARG)+SK(KS)*SIN(KS*ARG))
300   CONTINUE
      PRINT 908, LS, VISAV(LS), SUM
350   CONTINUE   $  PRINT 900   $  PRINT 900
*
400   PRINT 920  $  READ 901, Q $ IF (Q .EQ. 1HN) RETURN
C >>> INTEGRATE FIELD OVER (DISPLACED) ELLIPSE
      SUMSY = SUMSX = 0.
      DO 450 J=1,N  $  SUMTY = SUMTX = 0.
      WS = WG(J)  $  S = UG(J)
      DO 440 I=1,N
      WT = WG(I)  $  T = UG(I)  $  ARG = PI*(T+1.)
      A = 0.5*AM*(S+1.)*COS(ARG) + DX
      B = 0.5*BM*(S+1.)*SIN(ARG) + DY
      ROC = (SQRT(A*A + B*B))/C $  ANG = ATAN2(B,A)
      EY = EX = 0.  $  F = 1.
      DO 430 L=1,KH
      COLM = COS((L-1.)*ANG)  $  SILM = SIN((L-1.)*ANG)
      EX = EX + L*F*(CK(L)*COLM + SK(L)*SILM)
      EY = EY + L*F*(SK(L)*COLM - CK(L)*SILM)
      IF (L .EQ. KH) GO TO 420
      F = F*ROC
420   CONTINUE
430   CONTINUE
      SUMTX = SUMTX + WT*EX
      SUMTY = SUMTY + WT*EY
440   CONTINUE
      SUMSX = SUMSX + WS*(S+1.)*SUMTX
      SUMSY = SUMSY + WS*(S+1.)*SUMTY
450   CONTINUE
      EXAVG = -0.25*SUMSX/C
      EYAVG = -0.25*SUMSY/C
      PRINT 921, EXAVG, EYAVG
      RETURN
*
900   FORMAT(* *)
901   FORMAT(A1)
```

```
902   FORMAT(* *,//,* VIMG = CK(0)+SUM((RADIUS/C)*,
     $5H**L)*,*((CK(L)*,7H*COS(L*,*TH)+SK(L)*,
     $11H*SIN(L*TH)),//)
903   FORMAT(*     FOURIER COEFFICIENTS*,//,
     $*  CK( 0) =*E16.8)
904   FORMAT(*  CK(*I2,*) =*E16.8,*  SK(*I2,*) =*E16.8)
905   FORMAT(* TABULATE CHECK SUMS? -- Y OR N*)
906   FORMAT(* *,//,*  ORIGINAL COMPUTED VALUES*,
     $7X,* FOURIER SUM*,/)
907   FORMAT(* *,25X,*  SK(*I2,*) =*E16.8,/)
908   FORMAT(*  VI(*I2,*) =*E16.8,
     $*  SUM =*E16.8)
910   FORMAT(* *,/,* COHERENT FIELD AT DX,DY IS EX =*,
     $E14.6,*,    EY =*E14.6,/)
920   FORMAT(* INTEGRATE FOR AVG. FLD.*,
     $* (OR COHERENT FORCE PER UNIT LAMBDA)?*,
     $* -- Y OR N*)
921   FORMAT(* *,/,* AVG IMAGE FIELD ON BEAM , EXAV =*,
     $E14.6,*, EYAV =*F14.6,/)
*
      END
```

```
222222222.222222222.222222222.222222222.222222222.222222222.222222222.222222222.
222222222.222222222.222222222.222222222.222222222.222222222.222222222.222222222.
222222222.222222222.222222222.222222222.222222222.222222222.222222222.222222222.
```

```
222222222.222222222.222222222.222222222.222222222.222222222.222222222.222222222.
222222222.222222222.222222222.222222222.222222222.222222222.222222222.222222222.
222222222.222222222.222222222.222222222.222222222.222222222.222222222.222222222.
222222222.222222222.222222222.222222222.222222222.222222222.222222222.222222222.
        1        2        3        4        5        6        7        8

 HIV0511                                                                       2

 **BKY72J*C 03 APR 80 12.54.08.

 $  0.25;     10 PAGES:    521 PRINT LINES:  PRINTER  12, E0
 B I L L B O A R D     WRITEUPS SUBSET BKYNEWS WAS LAST CHANGED MAR 31
                       HANDBOOK SUBSET CHANGES WAS LAST CHANGED MAR 03


APR 2              NO SQUARE PEGS
YOU HAVE AN UNPARALLELED OPPORTUNITY TO HEAR THE PEGS,
BKY'S A CAPELLA MUSIC MASTERS, AT A GALA ALL FOOL'S DAY CONCERT AT 3 00 PM
ON FRI APRIL 4 IN THE 50B TRAINING ROOM (50B/2265), WHEN THE PEGS WILL
SING ALL NEW MATERIAL, SOME OF IT TRANSCRIBED ESPECIALLY FOR THE
OCCASION. A GOOD TIME WILL BE HAD BY ALL.

APR 2              6000S CACHE UP
THE 6000S GSS CACHE IS NOW READY FOR USE.  SEE THE WRITEUPS SUBSET GSS
FOR INFORMATION.  WRITEUPS SUBSET GSS WILL BE UPDATED ON MONDAY, 7 APRIL,
TO INCLUDE EXAMPLES OF USING THE CACHE CONTROL CARDS (FETCHGS, ENTERGS,
AND ERASEGS).

MAR 31             SOURCE LIBRARY HIT LIST
AS ANNOUNCED IN THE MARCH, 1980, NEWSLETTER, MANY ROUTINES
FROM THE SOURCE LIBRARY WILL BE REMOVED FROM THE PSS TOMORROW,
APRIL 1, AND PLACED ON GSS TAPE 13214. SEE WRITEUPS SUBSET ANTIQUE
AND/OR THE CONSULTANTS FOR DETAILS.

MAR 06             CHANGES FOR VAX USERS OF THE ZETA PLOTTER
ON TUESDAY, MARCH 11, THE GRAFPAC DRIVERS FOR THE ZETA PLOTTER ON VAX
COMPUTERS LBLG AND LBLH WILL BE SIGNIFICANTLY MODIFIED.  ZETA TAPES CREATED
ON LBLG OR LBLH ON OR AFTER THIS DATE MUST BE READ ON BKY WITH THE ARGUMENT
M=BKYVAX ON THE CODE9 CONTROL CARD --
                   CODE9,NF=0,M=BKYVAX,...
PLEASE DIRECT ANY QUESTIONS TO DEBBIE CAHN, X5849.

FEB 25             NEW FTN4 COMPILER AVAILABLE FOR TESTING.
A NEW FTN4 COMPILER (FTN4.8, LEVEL 508), CONTAINING MANY FTN4 BUG FIXES,
WILL BE PUT ON THE 7600 SYSTEM ONLY ON TUESDAY MARCH 4.  WE ENCOURAGE
YOU TO TEST IT IN THE MEANTIME, ESPECIALLY IF YOUR PROGRAMS HAVE CAUSED
THE CURRENT FTN4 TO ABORT.  THE TEST VERSION IS AVAILABLE ON PSS AS FOLLOWS -
                   FETCHPS,FTN4,FTN4,FTN4.
                   FBSIZE,FTN4=0.
PLEASE REPORT BUGS TO THE CONSULTANTS, X5981, OR RICHARD FRIEDMAN, X5279.


   TO CALL A CONSULTANT DIAL X5981, (415) 486-5981 OR 451-5981 (FTS)
```

```
  HIVO311
0                        XXXX  XXXX   XXX  XXXX  X   X
                         X   X X   X X   X X   X  X X
                         XXXX  XXXX  X   X X   X   X
                         X   X X  X  XXXXX X   X   X
                         XXXX  X   X X   X XXXX    X
0               4541 01 . . .DECK . 03 APR 80 . 12.53 . 4541 01
                .                                             .
 XXXXXXXXXXXX   .                                             .
       X        .                                             .
       X        .                                             .
       X        .                                             .
 XXXXXXXXXXXX   .                                             .
                .                                             .
                .                                             .
 X          X   .                                             .
 XXXXXXXXXXXX   .                                             .
 X          X   .                                             .
                .                                             .
                .                                             .
       XXXXXX   .                                             .    XXXX XXXXX
    XXX         .                                             .   X    X     X
 XXX            .                                             .   X    X     X
    XXX         .                                             .   X    X     X
       XXXXXX   .                                             .   XXXXXXXXXXXX
                .                                             .
 XXXXXXXXXXXX   .                                             .   XXXXXXXXXXXX
 X          X   .                                             .   X          X
 X          X   .                                             .   X          X
 X          X   .                                             .   X          X
 XXXXXXXXXXXX   .                                             .   XXXXXXXXXXXX
                .                                             .
 XXXXXXXXXXXX   .                                             .   XXXXXX
 X     X    X   .                                             .         XXX
 X     X    X   .                                             .            XXX
 X     X    X   .                                             .         XXX
  XXXXX XXXX    .                                             .   XXXXXX
                .                                             .
                .                                             .
                .                                             .   X          X
                .                                             .   XXXXXXXXXXXX
                .                                             .   X          X
                .                                             .
                .                                             .
                .                                             .   XXXXXXXXXXXX
                .                                             .        X
                .                                             .        X
                .                                             .        X
                .                                             .   XXXXXXXXXXXX
                .                                             .
                4541 01 .THURSDAY . 03 APR 80 . 12.53 . 4541 01
0                  XXXXX X     XXXXX XXXXX XXXX        XXXXX
                   X     X     X   X X   X X   X       X
                   XXX   X     X   X X   X XXXX        XXXX
                   X     X     X   X X   X X  X            X
                   X     XXXXX XXXXX XXXXX X   X        XXX
```

```
FITD2,12,4000,51000.456004,LASLETT
*6600,NOTAPES,PSS
FLOOR(3)
LIBCOPY(LASLETT,LIB/RBR,FATTY)
COPY(INPUT,1RM,LIB,1R,DECK/RBR)
RETURN,LGO.
RUN76(SCR,NL15000,I=DECK)
TTY.
LGO(TAPETTY,TAPETTY)
EXIT.
DMP.
DMP(13600)
TEXT,TAPETTY,(XEQ ERROR).
EXIT.
TEXT,TAPETTY,(COMP. ERROR).
FIN.
SESAME.
      PROGRAM FITD2(INPUT,OUTPUT)
      DIMENSION DX(30), DY(30), EX(30), EY(30)
      DIMENSION U(5), V(5)
      DIMENSION A(5), E(5,6), SCR(5,4)
      DIMENSION IRAY(7)
*
      CALL OPNTTY
*
      PRINT 9000  $  CALL DATE(L)  $  PRINT 9003, L
*
10    PRINT 9000
      PRINT 9010  $  CALL DATA(AM,1,BM,1,C,1)
      PRINT 9011, AM, BM, C
11    PRINT 9000  $  PRINT 9020  $  CALL DATA(KASES,1)
      IF ((KASES.LT.5) .OR. (KASES.GT.30)) GO TO 11
      PRINT 9021, KASES
*
      DO 12 K=1,KASES
      PRINT 9022, K, K  $  CALL DATA(V1,1,V2,1)
      DX(K) = V1  $  DY(K) = V2
      PRINT 9023, K, K  $  CALL DATA(V1,1,V2,1)
      EX(K) = V1  $  EY(K) = V2
12    CONTINUE     $  PRINT 9000
13    PRINT 9000  $  KM = 0
      DO 14 K=1,KASES
      PRINT 9025, K, DY(K), DY(K), EX(K), EY(K)
14    CONTINUE     $  PRINT 9000
15    PRINT 9030  $  CALL DATA(K,1)
      IF (K .EQ. 0)  GO TO 18
      IF ((K.LT.1).OR.(K.GT.KASES)) GO TO 15  $  KM = 1
      PRINT 9022, K, K  $  CALL DATA(V1,1,V2,1)
      DX(K) = V1  $  DY(K) = V2
      PRINT 9023, K, K  $  CALL DATA(V1,1,V2,1)
      EX(K) = V1  $  EY(K) = V2  $  GO TO 15
18    IF (KM .NE. 0)  GO TO 13
      PRINT 9000  $  PRINT 9032  $  READ 9001, Q
      IF (Q .EQ. 1HN) GO TO 10   $  PRINT 9000
      LOOK = 1     $  PRINT 9033  $  READ 9001, Q
      IF (Q .EQ. 1HN) LOOK = 0
*
      DO 40 N=1,5  $  E(N,6) = A(N) = 0.
      DO 30 M=1,5  $  E(N,M)  = 0.
30    CONTINUE
40    CONTINUE
*
```

```
      DO 100 K=1,KASES
      DXS = DX(K)*DX(K)            $  DYS = DY(K)*DY(K)
      U(1) = 2.*DX(K)              $  V(1) = 0.
      U(2) = 4.*DX(K)*DXS          $  V(2) = 0.
      U(3) = 0.                    $  V(3) = 2.*DY(K)
      U(4) = 2.*DX(K)*DYS          $  V(4) = 2.*DY(K)*DYS
      U(5) = 0.                    $  V(5) = 4.*DY(K)*DYS
      DO 60 N=1,5
      E(N,6) =  A(N)  = A(N) + U(N)*EX(K) + V(N)*FY(K)
      DO 50 M=N,5
      E(M,N) = E(N,M) = E(N,M) + U(N)*U(M) + V(N)*V(M)
50    CONTINUE
60    CONTINUE
      IF (K .LT. KASES) GO TO 80
      IF (LOOK .EQ. 0)  GO TO 80
      DO 65 N=1,5  $  PRINT 9035, N, A(N)
65    CONTINUE     $  PRINT 9000
      DO 75 N=1,5
      DO 70 M=N,5  $  PRINT 9038, N, M, E(N,M)
70    CONTINUE
75    CONTINUE     $  PRINT 9000
80    CONTINUE
100   CONTINUE
*
      CALL MATINV(E,5,1,DET,5,SCR)
*
      PRINT 9000  $  PRINT 9040, DET  $  PRINT 9000
*
      IF (DET .EQ. 0.) GO TO 980       $  PRINT 9000
      PRINT 9011, AM, BM, C
*
      DO 210 L=1,5  $  IND = L
      IF (L .EQ. 3) IND = 4
      IF (L .EQ. 4) IND = 5
      IF (L .EQ. 5) IND = 7
      PRINT 9045, IND, E(L,6)
210   CONTINUE     $  PRINT 9000
      IF (AM .NE. BM) GO TO 250
      E(3,6) = E(1,6) = 0.5*(E(1,6) + E(3,6))
      E(5,6) = E(2,6) = 0.5*(E(2,6) + E(5,6))
      DO 220 L=1,5  $  IND = L
      IF (L .EQ. 3) IND = 4
      IF (L .EQ. 4) IND = 5
      IF (L .EQ. 5) IND = 7
      PRINT 9045, IND, E(L,6)
220   CONTINUE     $  PRINT 9000
*
250   PRINT 9000
      DO 290 K=1,KASES
      DXS = DX(K)**2  $  DYS = DY(K)**2
      POTM = E(1,6)*DXS + E(2,6)*DXS*DYS
     $ + E(3,6)*DYS + E(4,6)*DXS*DYS + E(5,6)*DYS*DYS
      FLDX = 2.*(E(4,6)*DYS+2.*E(2,6)*DXS+E(1,6))*DY(K)
      FLDY = 2.*(E(4,6)*DXS+2.*E(5,6)*DYS+E(3,6))*DY(K)
      PRINT 9050,DX(K),DY(K),EX(K),EY(K),K,FLDX,FLDY,POTM
290   CONTINUE     $  PRINT 9000
*
970   PRINT 9000  $  CALL STATUS(IRAY)
      CUSR = 0.001*FLOAT(IRAY(3))   $  PRINT 9700, CUSR
980   PRINT 9002  $  PRINT 9500  $  READ 9001, Q
      IF (Q .NE. 1HT) GO TO 10
      PRINT 9000  $  CALL DATE(L)  $  PRINT 9003, L
```

```
990    PRINT 9900
*
9000  FORMAT(* *)
9001  FORMAT(A1)
9002  FORMAT(* *,/,* *,17(4H****),/)
9003  FORMAT(* *,29X,A10,//)
9010  FORMAT(* *,/,* TYPE (FOR RECORD) A, B, ∧ C*)
9011  FORMAT(* *,/,*    A =*F15.10,
     $*    B =*F15.10,*    C =*F15.10,/)
9015  FORMAT(*  I(*I1,*) =*I2,*    J(*I1,*) =*I2)
9020  FORMAT(* TYPE KASES  (GE 5,  LE 30)*)
9021  FORMAT(* *,60X,I2,* KASES*)
9022  FORMAT(* TYPE DX(*I2,*) ∧ DY(*I2,*)*)
9023  FORMAT(* TYPE EX(*I2,*) ∧ EY(*I2,*)*)
9025  FORMAT(* K =*I3,*    DX =*F7.4,*  DY =*F7.4,
     $*    EX =*F11.8,*  EY =*F11.8)
9030  FORMAT(* TO CORRECT, TYPE K INDEX -- OTHERWISE 0*)
9032  FORMAT(* PROCEED WITH THESE DATA? -- Y OR N*)
9033  FORMAT(* PRINT VECTOR ∧ MATRIX ELEMENTS?*,
     $* -- Y OR N*)
9035  FORMAT(*        RHS(*I1,*) =*E18.10)
9038  FORMAT(*        E(*I1,*,*I1,*) =*E18.10)
9040  FORMAT(* DETERMINANT =*E18.10)
9045  FORMAT(* *,9X,*A*I1,* =*E14.6)
9050  FORMAT(* DX =*F8.4,*        DY =*F8.4,/,
     $* EX =*F12.8,*  EY =*F12.8,5X,*K =*I3,
     $12X,*INPUT DATA*,/,
     $* FX =*F12.8,*  FY =*F12.8,
     $*   -POT =*F13.8,*    FROM FIT*,/)
9500  FORMAT(* MORE OR TERMINATE? -- M OR T*)
9700  FORMAT(* *,F11.3,* CJ'S REMAIN*,/)
9980  FORMAT(* *,25X,18H*** END OF RUN ***,/)
*
      STOP
      END
      SUBROUTINE MATINV(V,N,M,DET,IDIM,SCR)
      DIMENSION V(IDIM,1),SCR(IDIM,1)
      CALL MATIN (V,N,V(1,N+1),M,DET,IDIM,SCR,SCR(1,3),SCR(1,4))
*
      RETURN
      END
      SUBROUTINE MATIN (A,N,B,M,DETERM,IDIM,INDEX,IPIVOT,PIVOT)
C     MATRIX INVERSION WITH ACCOMPANYING SOLUTION OF LINEAR EQUATIONS
      DIMENSION A(IDIM,1),B(IDIM,1),INDEX(IDIM,1),IPIVOT(1),PIVOT(1)
      EQUIVALENCE (IROW,JROW), (ICOLUM,JCOLUM), (AMAX, T, SWAP)
C     INITIALIZATION
      DETERM=1.0
      DO 20 J=1,N
   20 IPIVOT(J)=0
      DO 550 I=1,N
C     SEARCH FOR PIVOT ELEMENT
      AMAX=0.0
      DO 105 J=1,N
      IF (IPIVOT(J) .EQ. 1) GO TO 105
      DO 100 K=1,N
      IF (IPIVOT(K)-1) 80, 100, 740
   80 IF (ABS(AMAX) .GE. ABS(A(J,K))) GO TO 100
      IROW=J
      ICOLUM=K
      AMAX=A(J,K)
  100 CONTINUE
  105 CONTINUE
```

```
      IF (AMAX .EQ. 0.0) GO TO 800
      IPIVOT(ICOLUM)=IPIVOT(ICOLUM)+1
C     INTERCHANGE ROWS TO PUT PIVOT ELEMENT ON DIAGONAL
      IF (IROW .EQ. ICOLUM) GO TO 260
      DETERM=-DETERM
      DO 200 L=1,N
      SWAP=A(IROW,L)
      A(IROW,L)=A(ICOLUM,L)
  200 A(ICOLUM,L)=SWAP
      IF (M .LE. 0) GO TO 260
      DO 250 L=1,M
      SWAP=B(IROW,L)
      B(IROW,L)=B(ICOLUM,L)
  250 B(ICOLUM,L)=SWAP
  260 INDEX(I,1)=IROW
      INDEX(I,2)=ICOLUM
      PIVOT(I)=A(ICOLUM,ICOLUM)
      DETERM=DETERM*PIVOT(I)
C     DIVIDE PIVOT ROW BY PIVOT ELEMENT
      A(ICOLUM,ICOLUM)=1.0
      DO 350 L=1,N
  350 A(ICOLUM,L)=A(ICOLUM,L)/PIVOT(I)
      IF (M .LE. 0) GO TO 380
      DO 370 L=1,M
  370 B(ICOLUM,L)=B(ICOLUM,L)/PIVOT(I)
C     REDUCE NON-PIVOT ROWS
  380 DO 550 L1=1,N
      IF (L1 .EQ. ICOLUM) GO TO 550
      T=A(L1,ICOLUM)
      A(L1,ICOLUM)=0.0
      DO 450 L=1,N
  450 A(L1,L)=A(L1,L)-A(ICOLUM,L)*T
      IF (M .LE. 0) GO TO 550
      DO 500 L=1,M
  500 B(L1,L)=B(L1,L)-B(ICOLUM,L)*T
  550 CONTINUE
C     INTERCHANGE COLUMNS
      DO 710 I=1,N
      L=N+1-I
      IF (INDEX(L,1) .EQ. INDEX(L,2)) GO TO 710
      JROW=INDEX(L,1)
      JCOLUM=INDEX(L,2)
      DO 705 K=1,N
      SWAP=A(K,JROW)
      A(K,JROW)=A(K,JCOLUM)
      A(K,JCOLUM)=SWAP
  705 CONTINUE
  710 CONTINUE
  740 RETURN
  800 DETERM = 0.

      RETURN
      END
```

```
333333333.333333333.333333333.333333333.333333333.333333333.333333333.333333333.
333333333.333333333.333333333.333333333.333333333.333333333.333333333.333333333.
333333333.333333333.333333333.333333333.333333333.333333333.333333333.333333333.
```

```
333333333.333333333.333333333.333333333.333333333.333333333.333333333.333333333.
333333333.333333333.333333333.333333333.333333333.333333333.333333333.333333333.
333333333.333333333.333333333.333333333.333333333.333333333.333333333.333333333.
333333333.333333333.333333333.333333333.333333333.333333333.333333333.333333333.
        1         2         3         4         5         6         7         8

 HIV0311                                                                       3

 **BKY72J*C 03 APR 80 12.55.36.

$  0.24;       6 PAGES;     305 PRINT LINES;  PRINTER  12, EQ
B I L L B O A R D     WRITEUPS SUBSET BKYNEWS WAS LAST CHANGED MAR 31
                      HANDBOOK SUBSET CHANGES WAS LAST CHANGED MAR 03


APR 2               NO SQUARE PEGS
YOU HAVE AN UNPARALLELED OPPORTUNITY TO HEAR THE PEGS,
BKY'S A CAPELLA MUSIC MASTERS, AT A GALA ALL FOOL'S DAY CONCERT AT 3:00 PM
ON FRI APRIL 4 IN THE 50B TRAINING ROOM (50B/2265), WHEN THE PEGS WILL
SING ALL NEW MATERIAL, SOME OF IT TRANSCRIBED ESPECIALLY FOR THE
OCCASION. A GOOD TIME WILL BE HAD BY ALL.

APR 2               6000S CACHE UP
THE 6000S GSS CACHE IS NOW READY FOR USE.  SEE THE WRITEUPS SUBSET GSS
FOR INFORMATION.  WRITEUPS SUBSET GSS WILL BE UPDATED ON MONDAY, 7 APRIL,
TO INCLUDE EXAMPLES OF USING THE CACHE CONTROL CARDS (FETCHGS, ENTERGS,
AND ERASEGS).

MAR 31              SOURCE LIBRARY HIT LIST
AS ANNOUNCED IN THE MARCH, 1980, NEWSLETTER, MANY ROUTINES
FROM THE SOURCE LIBRARY WILL BE REMOVED FROM THE PSS TOMORROW,
APRIL 1, AND PLACED ON GSS TAPE 13214. SEE WRITEUPS SUBSET ANTIQUE
AND/OR THE CONSULTANTS FOR DETAILS.

MAR 06              CHANGES FOR VAX USERS OF THE ZETA PLOTTER
ON TUESDAY, MARCH 11, THE GRAFPAC DRIVERS FOR THE ZETA PLOTTER ON VAX
COMPUTERS LBLG AND LBLH WILL BE SIGNIFICANTLY MODIFIED.  ZETA TAPES CREATED
ON LBLG OR LBLH ON OR AFTER THIS DATE MUST BE READ ON BKY WITH THE ARGUMENT
M=BKYVAX ON THE CODE9 CONTROL CARD --
                    CODE9,NF=0,M=BKYVAX,...
PLEASE DIRECT ANY QUESTIONS TO DEBBIE CAHN, X5849.

FEB 25              NEW FTN4 COMPILER AVAILABLE FOR TESTING.
A NEW FTN4 COMPILER (FTN4.8, LEVEL 508), CONTAINING MANY FTN4 BUG FIXES,
WILL BE PUT ON THE 7600 SYSTEM ONLY ON TUESDAY MARCH 4.  WE ENCOURAGE
YOU TO TEST IT IN THE MEANTIME, ESPECIALLY IF YOUR PROGRAMS HAVE CAUSED
THE CURRENT FTN4 TO ABORT.  THE TEST VERSION IS AVAILABLE ON PSS AS FOLLOWS -
                    FETCHPS,FTN4,FTN4,FTN4.
                    FBSIZE,FTN4=0.
PLEASE REPORT BUGS TO THE CONSULTANTS, X5981, OR RICHARD FRIEDMAN, X5279.


    TO CALL A CONSULTANT DIAL X5981, (415) 486-5981 OR 451-5981 (FTS)
```

Addendum to HI-FAN-117

"The Image-Field Potential of a Uniformly Charged Ellipse Situated Between A Set of Conducting Hyperbolic Surfaces"

L. Jackson Laslett

March 1985

In an earlier report [HI-FAN-117 (LBID-244), July 1980] we analyzed the image-field potential that arises from the image charges induced, by a (possibly displaced) elliptical beam, in a set of 2-D quadrupole electrodes

$$x^2-y^2 = \pm c^2.$$

The beam was taken to be of uniform charge density (λ=1, in electrostatic units) and the semi-axes were denoted "a" and "b" (for the x and y directions, respectively).

Computational options (e.g., in version GB4MG, as stored in library Jackson) included the analysis of this image-field potential into Fourier components or multipole coefficients in terms of r,θ variables taken with respect to the origin. Dr. Lloyd Smith has recently expressed an interest, however, in certain similar multipole coefficients, for the image-field potential, computed with respect to an r,θ origin situated at the center of the displaced beam. Such coefficients (as well as correct values for image fields at the beam center) can be readily obtained by only minor modifications to Program GB4MG -- viz:

> Values of x and y evaluated on line 121 should be augmented respectively by DX and DY; the DO-LOOP index KH on line 382 should be replaced by 1 (unity); and the quantities DX and DY should be deleted from the expressions on the respective lines 411 and 412.

Such results for c_1,s_1,c_3, and s_3 moment coefficients are summarized on the attached Table for a circular beam displaced (i) along the x-axis or (ii) at 45° to the x-axis.

c = 10.0 a = 3.0 b = 3.0

λ = 1.0

Displ.		Fourier Coefficients for Image-Field Potential About Center of Displaced Beam				Image Field Components at Center of Displaced Beam	
δx	δy	c_1	s_1	c_3	s_3	E_x	E_y
0.5	0.	-0.07895	0.	-0.05165	0.	0.007895	0.
1.0	0.	-0.16039	0.	-0.10480	0.	0.016039	0.
2.0	0.	-0.34113	0.	-0.22305	0.	0.034113	0.
3.0	0.	-0.56529	0.	-0.37657	0.	0.056529	0.
4.0	0.	-0.86288	0.	-0.61024	0.	0.086288	0.
5.0	0.	-1.27931	0.	-1.02932	0.	0.127931	0.
0.5	0.5	-0.07833	-0.07833	-0.05173	+0.05173	0.007833	0.007833
1.0	1.0	-0.15543	-0.15543	-0.10537	+0.10537	0.015543	0.015543
2.0	2.0	-0.30101	-0.30101	-0.22542	+0.22542	0.030101	0.030101
3.0	3.0	-0.42706	-0.42706	-0.37133	+0.37133	0.042706	0.042706
4.0	4.0	-0.52477	-0.52477	-0.54644	+0.54644	0.052477	0.052477
5.0	5.0	-0.58777	-0.58777	-0.74303	+0.74303	0.058777	0.058777

4

Coherent Collective Instabilities

Charge	Distance from Field Point
Original λ_1	$y_1 - y$ above
$-\lambda_1$	$2h - y_1 - y$ above
$-\lambda_1$	$2h + y_1 + y$ below
$+\lambda_1$	$4h - y_1 + y$ below
$+\lambda_1$	$4h + y_1 - y$ above
$-\lambda_1$	$6h - y_1 - y$ above
$-\lambda_1$	$6h + y_1 + y$ below
...	...

The upward-directed electric field due to the images alone then is:

$$E_{\text{image}} = 2\lambda_1 \left[\frac{1}{2h-y_1-y} - \frac{1}{2h+y_1+y} + \frac{1}{4h-y_1+y} - \frac{1}{4h+y_1-y} + \frac{1}{6h-y_1-y} - \frac{1}{6h+y_1+y} + \ldots\right] \quad \text{(B.4a)}$$

$$= 4\lambda_1 \left[\frac{y_1 + y}{4h^2 - (y_1 + y)^2} + \frac{y_1 - y}{16h^2 - (y_1 - y)^2} + \frac{y_1 + y}{36h^2 - (y_1 + y)^2} + \ldots\right] \quad \text{(B.4b)}$$

$$\doteq \frac{\lambda_1}{h^2} \Big\{[(y_1 + y) + (1/9)(y_1 + y) + (1/25)(y_1 + y) + \ldots\ ]$$

$$+ [(1/4)(y_1 - y) + (1/16)(y_1 - y) + \ldots\ ]\Big\} \quad \text{(B.4c)}$$

$$= \frac{\lambda_1}{h^2}\left[(y_1+y)(1^{-2} + 3^{-2} + 5^{-2} + \ldots) + (1/4)(y_1-y)(1^{-2} + 2^{-2} + 3^{-2} + \ldots)\right] \quad \text{(B.4d)}$$

$$= \frac{\lambda_1}{h^2}\left[(y_1 + y)\frac{\pi^2}{8} + (y_1 - y)\frac{\pi^2}{24}\right] \quad \text{(B.4e)}$$

$$= \frac{\pi^2\lambda_1}{12h^2}(y + 2y_1) , \quad \text{(B.4f)}$$

in agreement with Eq. (B.3).

Reprinted from THE REVIEW OF SCIENTIFIC INSTRUMENTS, Vol. 32, No. 3, 267-276, March, 1961
Printed in U. S. A.

Coherent Electromagnetic Effects in High Current Particle Accelerators: II. Electromagnetic Fields and Resistive Losses*

V. KELVIN NEIL AND DAVID L. JUDD
Lawrence Radiation Laboratory, University of California, Berkeley, California

AND

L. JACKSON LASLETT†
Ames Laboratory, Iowa State University, Ames, Iowa, and Midwestern Universities Research Association, Madison, Wisconsin

(Received October 13, 1960)

Coherent electromagnetic fields arising from an azimuthally modulated beam are considered. The beam is completely enclosed in a toroidal vacuum tank of rectangular cross section and highly conducting walls. Expressions are given for the image currents arising from low harmonics of the beam circulation frequency. These expressions are then used to evaluate resistive losses in the walls of the chamber. Expressions are given for fields arising from harmonics of the revolution frequency high enough that the beam may be in resonance with a characteristic mode of the vacuum chamber. The results are generalized to provide a description of the electric field in the neighborhood of a resonance. Numerical examples of resistive losses are given, indicating that these effects will not be serious for circulating currents of the order of 1 amp. Some properties of high-order Bessel functions, required for a description of the resonant chamber modes and the energy lost in their excitation, are developed in an appendix.

I. INTRODUCTION

In most particle accelerators currently in use, the total number of particles is not sufficiently large to produce coherent effects that warrant special consideration. As the number of particles and thus the circulating current in the machine is increased, some of these accompanying phenomena may become troublesome.

In this paper we investigate the electromagnetic fields arising from the current and charge distributions of a beam of particles in an accelerator vacuum tank.[1] In general, such a beam of high velocity particles will have an azimuthal variation in density which will give rise to large coherent electromagnetic fields. It is noted that these fields contain "resonant" and "nonresonant" parts, the former arising from a resonant excitation of the cavity modes at a multiple of the particle circulation frequency.[2] These resonant fields are of particular interest because of the forces they exert on coasting beams, which may produce instabilities.[3] This problem will be treated in Part III of the series, where use will be made of the results presented here.

The electromagnetic fields associated with the particles provide a mechanism for loss of energy from the beam. These losses are of two types. The first is the resistive loss arising from image currents in the walls of the vacuum chamber and is largely due to the low harmonics of the beam circulation frequency. This loss may be calculated to a good approximation by neglecting the curvature of the vacuum tank. The second loss is due to wall currents specifically associated with resonant modes which may be excited by a high harmonic of the orbital frequency. Expressions are given for the power dissipated by each of these effects, and numerical examples are given which indicate that such losses are negligible in many practical instances.

Sections II, III, and IV are devoted to determining the nonresonant fields, resonant fields, and fields near resonance, respectively. Section V contains numerical examples of energy loss, while the Appendixes are devoted to a discussion of the properties of the resonant modes.

II. NONRESONANT FIELDS

For the lower-order harmonics, the wall currents are substantially divergence-free image currents (i.e., uninfluenced appreciably by time dependent induced charges), distributed in such a manner that the normal component of the magnetic field vanishes at the boundaries. Since the field configuration will be substantially that found in a straight pipe of rectangular cross section and transverse dimensions small in comparison to a wavelength, the distribution of image currents can be found readily by methods analogous to those employed in corresponding two-dimensional electrostatic problems.[1] Therefore, we employ a coordinate system $(x, y, z \equiv R\theta)$ in which the toroid is straightened.

The current distribution

$$I = \sum_n I_n \cos n(\theta - \omega_0 t), \tag{2.1}$$

---

* This work was done under the auspices of the U. S. Atomic Energy Commission.

† Now in London with the Office of Naval Research.

[1] The treatment given in this paper is somewhat intuitive (and consequently simple) in its approach, and therefore not as rigorous as might be desired. A more extensive, rigorous treatment may be found in V. Kelvin Neil, "A study of some coherent electromagnetic effects in high-current particle accelerators," (thesis) Lawrence Radiation Laboratory Report UCRL-9124 (April 26, 1960).

[2] The possible existence of resonance is discussed in the Appendixes; see also reference 3.

[3] C. E. Nielsen, A. M. Sessler, and K. R. Symon, *Proceedings of the International Conference on High-Energy Accelerators and Instrumentation* (CERN, Geneva, Switzerland, 1959), pp. 239-252, especially p. 246.

Reprinted by permission of the American Institute of Physics.

centrally located within a metallic chamber enclosing the region

$$-w/2 \leqslant x \leqslant w/2, \quad -h/2 \leqslant y \leqslant h/2,$$

gives rise to an image current distribution as follows: On the top and bottom we have

$$I_{\text{surf}} = \frac{1}{w} \sum_n I_n \left[\sum_m \operatorname{sech}(2m+1)\frac{\pi}{2}\frac{h}{w} \times \cos(2m+1)\pi\frac{x}{w} \right] \cos n(\theta - \omega_0 t); \tag{2.2a}$$

and on the sides,

$$I_{\text{surf}} = \frac{1}{h} \sum_n I_n \left[\sum_m \operatorname{sech}(2m+1)\frac{\pi}{2}\frac{w}{h} \times \cos(2m+1)\pi\frac{y}{h} \right] \cos n(\theta - \omega_0 t), \tag{2.2b}$$

directed azimuthally. For $h \ll w$, the expression for the surface current in the top and bottom boundaries may be simplified by writing it in the approximate form[4,5]

$$I_{\text{surf}} \cong \frac{1}{w} \sum_n I_n \left[\int_0^\infty \operatorname{sech}(\pi h/w)t \cos(2\pi x/w)t dt \right] \times \cos n(\theta - \omega_0 t) \tag{2.3}$$
$$= \frac{1}{2h} \sum_n I_n \operatorname{sech}\frac{\pi x}{h} \cos n(\theta - \omega_0 t).$$

The nonresonant contribution to the resistive loss is immediately obtained from Eqs. (2.2a and b) in terms of the surface resistances appropriate to the frequencies of the individual harmonics,[6] as

$$P = \pi \mathcal{R}_1 \left[\frac{R}{w} \sum_m \operatorname{sech}^2(2m+1)\frac{\pi}{2}\frac{h}{w} + \frac{R}{h} \sum_m \operatorname{sech}^2(2m+1)\frac{\pi}{2}\frac{w}{h} \right] \left[\sum_n n^{\frac{1}{2}} I_n^2 \right], \tag{2.4}$$

in which R denotes the radius of the accelerator. If $h \ll w$, the first of the two sums over m distinctly dominates, and one may write

$$P \cong \pi \mathcal{R}_1 \frac{R}{w} \left[\int_0^\infty \operatorname{sech}^2(\pi h/w) t dt \right] \cdot \sum_n n^{\frac{1}{2}} I_n^2$$
$$= \mathcal{R}_1 \frac{R}{h} \sum_n n^{\frac{1}{2}} I_n^2. \tag{2.5}$$

Equation (2.5) could have been obtained directly from the approximate expression, Eq. (2.3), which in this limit was given for the surface-current density in the upper and lower surfaces.

If desired the expressions just derived for the resistive loss may alternatively be expressed in terms of the Fourier coefficients of the linear charge density or of the number of particles per radian at the orbit radius R_B. Thus we may write

$$\lambda = \sum_n \lambda_n \cos n(\theta - \omega_0 t) \text{ charge per unit length} \tag{2.6a}$$

and

$$N = \sum_n N_n \cos n(\theta - \omega_0 t) \text{ particles per radian,} \tag{2.6b}$$

by use of the relations

$$I_n = \omega_0 R_B \lambda_n \tag{2.7a}$$

and

$$\lambda_n = e N_n / R_B. \tag{2.7b}$$

The electromotive force per turn associated with the resistive loss, furthermore, is given by

$$V = (2\pi/e\omega_0)(P/N_t), \tag{2.8}$$

where N_t denotes the total number of particles in the beam. Thus the nonresonant resistive loss alternatively may be expressed conveniently in the forms

$$V = 2\pi^2 e \omega_0 \mathcal{R}_1 \left[\frac{R}{w} \sum_m \operatorname{sech}^2(2m+1)\frac{\pi}{2}\frac{h}{w} + \frac{R}{h} \sum_m \operatorname{sech}^2(2m+1)\frac{\pi}{2}\frac{w}{h} \right] \left[\sum_n n^{\frac{1}{2}} \frac{N_n^2}{N_t} \right], \tag{2.9}$$

or for $h \ll w$,

$$V \cong 2\pi e \omega_0 \mathcal{R}_1 \frac{R}{h} \sum_n n^{\frac{1}{2}} \frac{N_n^2}{N_t}. \tag{2.10}$$

---

[4] W. Gröbner and N. Hofreiter, *Integraltafel* (Springer-Verlag, Vienna, 1950), Part II, Sec. 335, Eq. (11a), p. 136.

[5] The result for the case $w/h \to \infty$ may also be obtained directly by reference to a corresponding electrostatic problem treated by William R. Smythe in his *Static and Dynamic Electricity* (McGraw-Hill Book Company, Inc., New York, 1950), 2nd ed. Sec. 4.20, p. 85, for a line charge centrally located between a pair of parallel conducting plates. From Smythe's result, the current density in the boundary surfaces becomes

$$I_{\text{surf}} = -\frac{1}{\pi} \sum_n I_n \left\{ \frac{d}{dx} \left[\tan^{-1}\left(\tanh\frac{\pi x}{2h} \right) \right] \right\} \cos n(\theta - \omega_0 t)$$
$$= -\frac{1}{2h} \sum_n I_n \operatorname{sech}\frac{\pi x}{h} \cos n(\theta - \omega_0 t),$$

as found in our Eq. (2.3). This result also follows from the analysis by W. K. H. Panofsky and M. Phillips in their *Classical Electricity and Magnetism* (Addison Wesley Publishing Company, Inc., Reading, Massachusetts, 1955), Chap. 3, Sec. 6, p. 45 ff.

[6] The surface resistance is defined as the resistivity ρ divided by the skin depth δ. It may be written $\mathcal{R} = n^{\frac{1}{2}} \mathcal{R}_1$, where the surface resistance for the fundamental frequency is in mks units,

$$\mathcal{R}_1 = \rho/\delta_1 = (\mu_0 \omega_0 \rho / 2)^{\frac{1}{2}} = \mu_0 \omega_0 \delta_1 / 2.$$

Correspondingly, the skin depth for the fundamental frequency is

$$\delta_1 = (2\rho/\mu_0 \omega_0)^{\frac{1}{2}}.$$

III. FIELDS ASSOCIATED WITH A RESONANT MODE

It is well known that in a straight wave guide, all electromagnetic modes have phase velocities greater than the velocity of light c. As shown in Appendix I, at any radius within a toroidal cavity it is possible to find modes that have, at that radius, azimuthal phase velocities less than c. Such modes have eigenfrequencies that are very high harmonics of the beam circulation frequency. It is therefore possible for an azimuthally modulated beam of relativistic particles to excite one or more electromagnetic modes of the chamber.[2] The fields of such high-order modes may be large. The concomitant resistive losses then warrant separate evaluation, despite the relatively low magnitudes of the Fourier components responsible for the excitation of these modes. The curvature of the chamber is essential for the excitation of the resonant modes, and these high-order solutions may well show a radial dependence that differs materially from that of a simple circular function. It is expedient, therefore, to use cylindrical polar coordinates (r,θ,z) and to consider the fields expressed in terms of solutions (Z) of Bessel's equation, with the imposition of boundary conditions at $r=a$, b appropriate to the type of mode under consideration.

Rather than commencing with a general solution for the electromagnetic fields excited by the beam and then extracting a particular resonant term, it is convenient to employ from the start only the field components that are associated with the resonant mode of interest. Power will be supplied to such a mode by the work that the beam current performs against the longitudinal electric field E_θ. Excitation will be strongest if E_θ is precisely out of phase with the beam current. In the steady state, this power may be equated to the resistive losses in the chamber walls. Both the level of the electromagnetic excitation and the power loss are thereby determined in terms of the appropriate Fourier component of the beam current. In what follows, we employ this procedure to obtain expressions for the power loss associated with a resonant TE mode and, independently, for the loss arising from a resonant TM mode. In each case the results are expressed in terms of the loss factor Q of the chamber for the particular mode under consideration.

We assume that the beam has a negligible cross-sectional area and is located at $r=R_B$, $z=0$. For a resonant mode of angular frequency ω_r, the power is given by

$$P=\int_{\text{circumference}} I(-E_\theta)ds=2\pi R_B\langle -E_\theta I\rangle_{\text{av}}. \qquad (3.1)$$

The loss factor is defined by

$$Q=\omega_r\frac{[\text{stored energy}]}{P}, \qquad (3.2)$$

so that the power may be written as[7]

$$P=\frac{(2\pi R_B)^2\langle -E_\theta I\rangle_{\text{av}}{}^2}{\omega_r[\text{stored energy}]}Q. \qquad (3.3)$$

For a resonant TE mode within a chamber of inner and outer radii a and b, one may employ a field configuration of the form (mks units):

$$B_\theta=-Ank\frac{Z}{r}\sin kz\cos n(\theta-\omega_0 t) \qquad (3.4a)$$

$$B_r=-Ak\frac{dZ}{dr}\sin kz\sin n(\theta-\omega_0 t) \qquad (3.4b)$$

$$B_z=Aq^2Z\cos kz\sin n(\theta-\omega_0 t) \qquad (3.4c)$$

$$E_\theta=-A\omega_r\frac{dZ}{dr}\cos kz\cos n(\theta-\omega_0 t) \qquad (3.4d)$$

$$E_r=-An\omega_r\frac{Z}{r}\cos kz\sin n(\theta-\omega_0 t) \qquad (3.4e)$$

$$E_z=0. \qquad (3.4f)$$

Here Z represents a solution of Bessel's equation, $d/dr[r(dZ/dr)]+[q^2r-(n^2/r)]Z=0$, subject to the Neumann boundary conditions $[dZ/dr]_a=[dZ/dr]_b=0$; $q^2+k^2=\omega_r^2/c^2$; k is an odd multiple of π/h; $\omega_r=n\omega_0$; and the phase intentionally has been chosen so that $-E_\theta$ is in phase with the current $I_n\cos n(\theta-\omega_0 t)$.

With these fields, then, we have

$$\langle -E_\theta I\rangle_{\text{av}}=\frac{I_n}{2}A\omega_r\left[\frac{dZ}{dr}\right]_B, \qquad (3.5)$$

the subscript B denoting that the derivative is to be evaluated at $r=R_B$. The stored energy is

$$\frac{\epsilon_0}{2}\int\int\int E^2dv+\frac{1}{2\mu_0}\int\int\int B^2dv$$
$$=\frac{\pi A^2h}{2\mu_0}q^2\left(\frac{\omega_r}{c}\right)^2\int_a^b rZ^2dr. \qquad (3.6)$$

Accordingly, we have

$$\begin{aligned}P_{\text{TE}}&=2\pi\mu_0c^2I_n{}^2\frac{R_B{}^2}{\omega_rq^2h}\frac{[dZ/dr]_B{}^2}{\int_a^brZ^2dr}Q_{\text{TE}}\\&=2\pi\mathfrak{z}I_n{}^2\frac{R_B{}^2}{(\omega_r/c)q^2h}\frac{[dZ/dr]_B{}^2}{\int_a^brZ^2dr}Q_{\text{TE}},\end{aligned} \qquad (3.7)$$

where $\mathfrak{z}$ denotes $(\mu_0/\epsilon_0)^{\frac{1}{2}}=\mu_0c=120\pi=377$ ohms. In cases for which the annular width of the chamber is small in

---

[7] It will be noted that the convenience of this form lies in the fact that it may be used to evaluate P in terms of I (or its Fourier component I_n) and Q *without any special normalization* of the fields which describe the resonant mode of interest.

comparison to the diameter ($w \ll 2R$), this last result may be written conveniently in the approximate form

$$P_{\mathrm{TE}} \cong 16\pi \mathfrak{z} I_n{}^2 \frac{R}{(\omega_r/c)q^2w^3h} \frac{[dZ/du]_B{}^2}{\int_{-1}{}^1 Z^2du} Q_{\mathrm{TE}}, \qquad (3.8)$$

where the dimensionless variable u is such that

$$r \equiv \tfrac{1}{2}(b+a)+(w/2)u, \qquad (3.9)$$

with

$$w \equiv b-a.$$

The loss factor Q_{TE} may also be evaluated[8] in the conventional way from these fields and expressed in terms of the relevant properties of the characteristic solution Z:

$$Q_{\mathrm{TE}} = \frac{\mathfrak{z}}{4\mathfrak{R}} \frac{(\omega_r/c)^3h}{k^2} \left\{ 1+\frac{h}{4q^2}\left[\frac{n^2}{b}\left(1+\frac{b}{a}\frac{[Z(a)]^2}{[Z(b)]^2} \right) \right.\right.$$
$$\left.\left. +\frac{q^4b}{k^2}\left(1+\frac{a}{b}\frac{[Z(a)]^2}{[Z(b)]^2} \right) \right] \frac{[Z(b)]^2}{\int_a{}^b rZ^2dr} \right\}^{-1}. \qquad (3.10)$$

Again some simplification results for $w \ll 2R$, for which we have

$$Q_{\mathrm{TE}} \cong \frac{\mathfrak{z}}{4\mathfrak{R}} \frac{(\omega_r/c)^3h}{k^2} \left\{ 1+\frac{h}{2q^2w}\left(\frac{n^2}{R^2}+\frac{q^4}{k^2} \right) \right.$$
$$\left. \times\left(1+\frac{[Z(-1)]^2}{[Z(1)]^2} \right) \frac{[Z(1)]^2}{\int_{-1}{}^1 Z^2du} \right\}^{-1}, \qquad (3.11)$$

where the arguments of Z are now understood to represent values of the dimensionless variable u.

Under potentially resonant conditions, the required properties of the characteristic function Z can depend in a fairly sensitive way on the parameters of the structure and are best determined by computation. Typical values (cf. reference 8, Table IX) in a resonant situation are

$$\frac{[Z(-1)]^2}{[Z(1)]^2} \cong 0.85, \quad \frac{[Z(1)]^2}{\int_{-1}{}^1 Z^2du} \cong 0.52,$$

and, for a beam centrally located within the aperture (at $u=0$),

$$\frac{[dZ/du]_B{}^2}{\int_{-1}{}^1 Z^2du} \cong 0.42.$$

For a resonant TM mode, similarly, one may employ a field configuration of the form (mks units):

$$B_\theta = -A\frac{\omega_r}{c^2}\frac{dZ}{dr} \sin kz \cos n(\theta-\omega_0 t) \qquad (3.12a)$$

$$B_r = -A\frac{n\omega_r}{c^2}\frac{Z}{r} \sin kz \sin n(\theta-\omega_0 t) \qquad (3.12b)$$

$$B_z = 0 \qquad (3.12c)$$

$$E_\theta = -Ank\frac{Z}{r} \cos kz \cos n(\theta-\omega_0 t) \qquad (3.12d)$$

$$E_r = -Ak\frac{dZ}{dr} \cos kz \sin n(\theta-\omega_0 t) \qquad (3.12e)$$

$$E_z = -Aq^2Z \sin kz \sin n(\theta-\omega_0 t), \qquad (3.12f)$$

in which the solution Z of Bessel's equation now must conform to the Dirichlet boundary conditions

$$Z(a) = Z(b) = 0. \qquad (3.13)$$

With these fields we have

$$\langle -E_\theta I \rangle_{\mathrm{av}} = \frac{I_n}{2} Ank\left[\frac{Z}{R}\right]_B, \qquad (3.14)$$

and the stored energy is

$$\frac{\epsilon_0}{2}\int\int\int E^2dv+\frac{1}{2\mu_0}\int\int\int B^2dv$$
$$= \frac{\pi A^2hq^2}{2\mu_0c^2}\left(\frac{\omega_r}{c}\right)^2 \int_a^b rZ^2dr. \qquad (3.15)$$

Accordingly, we may write

$$P_{\mathrm{TM}} = 2\pi\mathfrak{z}I_n{}^2 \frac{n^2k^2}{(\omega_r/c)^3q^2h} \frac{Z_B{}^2}{\int_a{}^b rZ^2dr} Q_{\mathrm{TM}}, \qquad (3.16)$$

and for $w \ll 2R$,

$$P_{\mathrm{TM}} \cong 4\pi\mathfrak{z}I_n{}^2 \frac{n^2k^2}{(\omega_r/c)^3q^2Rwh} \frac{Z_B{}^2}{\int_{-1}{}^1 Z^2du} Q_{\mathrm{TM}}. \qquad (3.17)$$

Finally, the loss factor Q_{TM} may be evaluated[8] for this mode, with the result

$$Q_{\mathrm{TM}} = \frac{\mathfrak{z}}{4\mathfrak{R}}\frac{\omega_r}{c}h \left\{ 1+\frac{bh}{4q^2}\left[1+\frac{a}{b}\frac{(dZ/dr)_a{}^2}{(dZ/dr)_b{}^2} \right] \right.$$
$$\left. \times\frac{(dZ/dr)_b{}^2}{\int_a{}^b rZ^2dr} \right\}^{-1}, \qquad (3.18)$$

which, for $w \ll 2R$, may be written

$$Q_{\mathrm{TM}} \cong \frac{\mathfrak{z}}{4\mathfrak{R}}\frac{\omega_r}{c}h \left\{ 1+\frac{2h}{q^2w^3}\left[1+\frac{(dZ/du)_{-1}{}^2}{(dZ/du)_1{}^2} \right] \right.$$
$$\left. \times\frac{(dZ/du)_1{}^2}{\int_{-1}{}^1 Z^2du} \right\}^{-1}. \qquad (3.19)$$

The required properties of the characteristic function Z are again best determined by computation. Illustrative values (reference 8, Table VIII) are

---

[8] L. Jackson Laslett and William Lewish, Ames Laboratory Report IS-189, Iowa State University, Ames, Iowa, 1960 (unpublished work).

$$\frac{(dZ/du)_{-1}{}^2}{(dZ/du)_1{}^2}\cong 0.04, \quad \frac{(dZ/du)_1{}^2}{\int_{-1}^1 Z^2du}\cong 8.4,$$

and, for a centrally located beam,

$$\frac{Z_B{}^2}{\int_{-1}^1 Z^2du}\cong 0.79.$$

Because q is of the order of n/b (or n/R, for $w\ll 2R$), and $n^2(w/2R)^3$ is normally of the order of unity under resonant circumstances, it may be seen that the second term in the denominator of Q_{TM} will be very much smaller than unity. In contrast, the second term in the denominator of Q_{TE} could play a strong or even dominating role. This situation may be regarded as arising in the following way. In the TE mode, the B_z field component is (for n sufficiently large to attain resonance) by far the largest of the three components of $\mathbf{B}$. The associated current, which is in the side walls only, consequently dominates. For a TM mode, on the other hand, component B_z vanishes and there is no such dominance as occurs in the TE mode. For the TM resonance, the factor $\int_{-1}^1 Z^2du$ enters in estimating energy stored and the resistive loss in the upper and lower surfaces. It thus effectively cancels, in the evaluation of Q_{TM}. With the TE fields, the energy involves this integral and the loss is determined by the quantities $[Z(-1)]^2$ and $[Z(1)]^2$ which serve to specify the current density I_θ associated with B_z at $r=a, b$.

It is appropriate, therefore, to simplify Eqs. (3.11) and (3.19), which were applicable only for $w\ll 2R$, as

$$Q_{\mathrm{TE}}\cong\frac{\mathfrak{z}}{16\mathfrak{R}}\frac{(\omega_r/c)^3w^4}{R\eta^3n^2}\frac{\int_{-1}^1 Z^2du}{[Z(-1)]^2+[Z(1)]^2}, \tag{3.20}$$

and

$$Q_{\mathrm{TM}}\cong\frac{\mathfrak{z}}{4\mathfrak{R}}\frac{\omega_r}{c}h. \tag{3.21}$$

Here η denotes $w/2R$ and the product η^3n^2 is a convenient quantity to employ in estimating the location of the resonances that may be excited in a chamber of small transverse dimensions. Finally, if Eqs. (3.20) and (3.21) are combined, respectively, with Eqs. (3.8) and (3.17), the following resistive losses result:

$$P_{\mathrm{TE}}=\pi\frac{\mathfrak{z}^2}{\mathfrak{R}}I_n{}^2\frac{(\omega_0R/c)^2}{\eta^3n^2}\frac{w}{h}\frac{[dZ/du]_B{}^2}{[Z(-1)]^2+[Z(1)]^2}, \tag{3.22}$$

$$P_{\mathrm{TM}}=(2m+1)^2\left(\frac{\pi}{2}\right)^3\frac{\mathfrak{z}^2}{\mathfrak{R}}I_n{}^2\frac{(w/h)^2}{(\omega_0R/c)^2\eta^3n^2}\frac{Z_B{}^2}{\int_{-1}^1 Z^2du}. \tag{3.23}$$

IV. FIELDS NEAR RESONANCE

The stability of an intense beam will be influenced by the self-generated electric fields which are enhanced by proximity to resonance. For the purposes of Part III of this series, we extend the results of Sec. II to obtain required expressions for the longitudinal electric field. Under resonant conditions, the longitudinal electric field of a TE mode is of the form of Eq. (3.4d) in which coefficient A is expressible through use of Eqs. (3.1) and (3.5) as

$$A=\frac{P}{\pi I_nR_B\omega_r[dZ/dr]_B}. \tag{4.1}$$

By use of Eqs. (3.7) and (4.1), the longitudinal electric field at resonance is found to be

$$E_\theta=-2\mathfrak{z}I_n\frac{Q_{\mathrm{TE}}R_B}{(\omega_r/c)q^2h}\frac{[dZ/dr]_B{}^2}{\int_a^b rZ^2dr}\cos(n\theta-\omega_rt). \tag{4.2}$$

Equation (4.2) may be generalized for frequencies near the resonant frequency by replacing

$$Q_{\mathrm{TE}}\cos(n\theta-\omega_rt)$$

by

$$\omega^2\frac{(\omega_r{}^2/Q_{\mathrm{TE}})\cos(n\theta-\omega t)+(\omega_r{}^2-\omega^2)\sin(n\theta-\omega t)}{(\omega_r{}^2-\omega^2)^2+(\omega_r{}^2/Q_{\mathrm{TE}})^2},$$

wherein we have not distinguished between ω and ω_r, except in the arguments of the circular functions and in the resonant term $(\omega_r{}^2-\omega^2)$. With this substitution, Eq. (4.2) may be written

$$E_\theta=\mathfrak{z}I_n\frac{R_B}{(\omega_r/c)q^2h}\frac{[dZ/dr]_B{}^2}{\int_a^b rZ^2dr}\times\left[\frac{i\omega^2e^{i(n\theta-\omega t)}}{(\omega_r{}^2-\omega^2)-i(\omega_r{}^2/Q_{\mathrm{TE}})}-\frac{i\omega^2e^{-i(n\theta-\omega t)}}{(\omega_r{}^2-\omega^2)+i(\omega_r{}^2/Q_{\mathrm{TE}})}\right] \tag{4.3}$$

and gives the field generated by a current $I_n\cos(n\theta-\omega t)$, or by $\frac{1}{2}I_n[e^{i(n\theta-\omega t)}+e^{-i(n\theta-\omega t)}]$. For the perturbation analysis of Part III, it is convenient to employ specifically the complex field associated with a perturbation of the number of particles per radian, expressed in the form of a complex number. A perturbation

$$\delta N=N_ne^{i(n\theta-\omega t)},$$

or an associated perturbed current

$$\delta I=e\omega_0N_ne^{i(n\theta-\omega t)},$$

should thus, from Eq. (4.3), have associated with it the longitudinal field

$$E_\theta=2i\mathfrak{z}eN_n\frac{cR_B}{nq^2h}\frac{[dZ/dr]_B{}^2}{\int_a^b rZ^2dr}\omega^2\times\frac{e^{i(n\theta-\omega t)}}{(\omega_r{}^2-\omega^2)-i(\omega_r{}^2/Q_{\mathrm{TE}})}. \tag{4.4}$$

When $w\ll 2R$, $q\approx n/R$ and Eq. (4.4) may be written in the somewhat simpler approximate form

$$E_\theta \cong 16 i \mathfrak{Z} e N_n \frac{cR^2}{n^3 w^3 h} \frac{[dZ/du]_B{}^2}{\int_{-1}{}^1 Z^2 du} \omega^2 \times \frac{e^{i(n\theta-\omega t)}}{(\omega_r{}^2-\omega^2)-i(\omega_r{}^2/Q_{\mathrm{TE}})}. \quad (4.5)$$

To proceed in a similar way to evaluate the longitudinal electric field of a TM mode near resonance, we have

$$A = P/\pi I_n n k Z_B \quad (4.6)$$

from Eqs. (3.1) and (3.14). By use of Eqs. (3.16) and (4.6), the resonance longitudinal electric field, Eq. (3.12d) is

$$E_\theta = -2\mathfrak{Z} I_n \frac{Q_{\mathrm{TM}} n^2 k^2}{(\omega_r/c)^3 q^2 R_B h} \frac{Z_B{}^2}{\int_a{}^b r Z^2 dr} \cos(n\theta-\omega_r t). \quad (4.7)$$

For frequencies near the resonant frequency, Eq. (4.7) is generalized in the same manner as employed in connection with the TE resonance to read

$$E_\theta = \mathfrak{Z} I_n \frac{n^2 k^2}{(\omega_r/c)^3 q^2 R_B h} \frac{Z_B{}^2}{\int_a{}^b r Z^2 dr} \times \left[\frac{i\omega^2 e^{i(n\theta-\omega t)}}{(\omega_r{}^2-\omega^2)-i(\omega_r{}^2/Q_{\mathrm{TM}})} - \frac{i\omega^2 e^{-i(n\theta-\omega t)}}{(\omega_r{}^2-\omega^2)+i(\omega_r{}^2/Q_{\mathrm{TM}})} \right]. \quad (4.8)$$

For a perturbation $\delta N = N_n e^{i(n\theta-\omega t)}$, Eq. (4.8) gives the associated field

$$E_\theta = 2 i \mathfrak{Z} e N_n \frac{k^2 c}{n(\omega_0/c)^2 q^2 R_B h} \frac{Z_B{}^2}{\int_a{}^b r Z^2 dr} \omega^2 \times \frac{e^{i(n\theta-\omega t)}}{(\omega_r{}^2-\omega^2)-i(\omega_r{}^2/Q_{\mathrm{TM}})}; \quad (4.9)$$

for $w \ll 2R$, with $q \approx n/R$ and $k = (2m+1)\pi/h$, we have

$$E_\theta \cong 4(2m+1)^2 \pi^2 i \mathfrak{Z} e N_n \frac{cR^2}{n^3 (\omega_0 R/c)^2 w h^3} \frac{Z_B{}^2}{\int_{-1}{}^1 Z^2 du} \omega^2 \times \frac{e^{i(n\theta-\omega t)}}{(\omega_r{}^2-\omega^2)-i(\omega_r{}^2/Q_{\mathrm{TM}})}. \quad (4.10)$$

V. NUMERICAL EXAMPLES

TABLE I. Parameters of three accelerators and the nonresonant energy loss per particle per turn. The circulating current assumed in the calculation is I_C, and $f_0 = \omega_0/2\pi$ is the particle circulation frequency. The parameters α and $\langle\theta^2\rangle_{\mathrm{av}}$ characterize the extent of particles in rf phase.

Machine	$\mathfrak{R}_1$ (ohms)	R/h	I_c (amp)	f_0 (cps)	α	$\langle\theta^2\rangle_{\mathrm{av}}$	δE (ev)
Bevatron	3.14×10^{-3}	50	4	2.5×10^6	1		3.56
CERN	1.37×10^{-3}	10^3	1	4.8×10^5	0.1		24.6
Stanford	$10 \quad \times10^{-3}$	36	1	2.5×10^7		0.014	21.8

We have calculated the nonresonant power loss using the parameters of the Berkeley Bevatron, a typical strong focusing machine such as the CERN proton synchrotron, and the Stanford electron storage rings. Results are given in Table I. For a proton machine in which the radio-frequency operates on a harmonic m, ($m=1$ for the bevatron, $m=20$ for AGS) we take the azimuthal distribution of particles to be

$$N(\theta) = \frac{2N}{\pi m \alpha}[1-(\theta/\alpha)^2]^{\frac12},$$

in which N is the total number of particles. This distribution leads to Fourier coefficients of the current given by

$$I_n = \frac{2e\omega_0 N}{\pi n \alpha} J_1(n\alpha) = \frac{4 I_C}{n\alpha} J_1(n\alpha),$$

for n an integral multiple of m. Other Fourier coefficients are zero. The total circulating current is I_C. The azimuthal distribution of particles in the Stanford storage rings will be taken as Gaussian. We thus have

$$N(\theta) = (2\pi\langle\theta^2\rangle_{\mathrm{av}})^{-\frac12} \exp[-\tfrac12\theta^2/\langle\theta^2\rangle_{\mathrm{av}}],$$

from which it follows that

$$I_n = I_C \exp[-n^2\langle\theta^2\rangle_{\mathrm{av}}/2].$$

The resistivity ρ of the conducting walls is taken somewhat arbitrarily to be 10^{-4} ohm-cm for all numerical examples. If the true resistivity ρ_t of the walls is known, the results in Table I should be altered by a factor $10^2\rho_t{}^{\frac12}$, with ρ_t in ohm-centimeters.

We have calculated the resonant power loss for the bevatron only, using Eq. (3.22). Inserting values $R_B = 50$ ft, $b = 52$ ft, $h = 1$ ft, and $\gamma = 6$ into Eq. (A-18), we find that resonance can occur for $n \approx 650$. The ratio w/h is 4 for this machine, and the resonant energy loss δE is of the order of 0.1 ev. For the strong focusing machine, we insert $R_B = 100$ m, $b = 100.15$ m, $h = 0.1$ m, and $\gamma = 25$ into Eq. (A-18), and find that resonance is possible at values of $n \sim 8\times10^5$. This is sufficiently high that the resonant energy loss is negligible.

For the electron storage rings, we use $R_B = 142$ cm, $b = 150$ cm, $h = 5$ cm, and $\gamma = 10^3$. Resonance is found to be possible with the 275th harmonic, but the 275th Fourier component of the Gaussian distribution is so small that resonant power losses do not warrant consideration.

APPENDIX I

Azimuthal Phase Velocities and Possible Resonance

The eigenfrequencies ω_l of the cavity modes which can be excited by the beam are given by $(\omega_l/c)^2 = q^2 + (p\pi/h)^2$

with q the characteristic value of Bessel's equation and p an odd integer. The angular phase velocity is simply ω_l/n, and the azimuthal phase velocity v_θ is $\omega_l r/n$. We thus have

$$(v_\theta/c)^2=(qr/n)^2+(p\pi r/nh)^2.$$

Obviously the second term may be made negligibly small by choosing $p=1$ and $n\gg\pi r/h$. For $p>1$, this term may still be made small, but only for much larger values of n. With this term negligibly small, we may have $v_\theta<c$ at any radius r within the vacuum tank for which $qr/n<1$. It is then possible for a relativistic beam of particles to be circulating with a velocity coinciding with the phase velocity of the mode. This is the resonant condition referred to in this work. We now show that for sufficiently large n it is possible to satisfy $qr/n<1$ at any radius within a toroidal cavity.

For TE modes the appropriate solution of Bessel's equation is

$$Z_n(r)=Y_n'(qa)J_n(qr)-J_n'(aq)Y_n(qr),$$

with the values of q determined by the boundary condition $Z_n'(b)=0$. In Fig. 1 we have plotted qualitatively the function $J_n'(x)/Y_n'(x)$ vs x for large values of n. The maximum of the curve occurs at $x=n$, and the half-width is of the order of $n^{\frac{1}{3}}$. The lowest characteristic value q_0 may be found approximately by selecting $q_0a<n$ and $n<q_0b<j'_{n1}$ such that

$$J_n'(q_0a)/Y_n'(q_0a)=J_n'(q_0b)/Y_n'(q_0b).$$

The first zero of J_n' is designated by j_{n1}', and occurs approximately at $x=n+0.81n^{\frac{1}{3}}$ for large n. The ratio b/a is fixed and determines how far down the curve we must place our values. Thus in Fig. 1, the portion of the vacuum tank for which $q_0r/n<1$ holds is represented by the region of the abscissa between q_0a and n.

For fixed b/a, the portion of the vacuum tank for which $q_0r/n<1$ does not hold diminishes to zero as n approaches infinity. This can be seen by noting that q_0 is of the order of n/b and thus $q_0b-q_0a\sim n(1-a/b)$. For any b/a, it is possible to choose a value of n such that this quantity is very much greater than the half-width of the curve, which is of order $n^{\frac{1}{3}}$. We must then place q_0b very close to its maximum value j_{n1}', while q_0a is located far to the left of n. The portion of the vacuum vessel represented by the region of the abscissa between n and j_{n1}' therefore becomes negligibly small, as n increases without limit, compared to the portion between q_0a and n. In the latter portion, $q_0r/n<1$ holds. More accurate values of q_0 will be found in Appendix II.

For TM modes, the appropriate solution of Bessel's equation is

$$Z_n(r)=Y_n(qa)J_n(qr)-J_n(qa)Y_n(qr),$$

with the values of q determined by the boundary condition $Z_n(b)=0$. The lowest characteristic value may be found approximately by a graphical technique analogous to that used above. In Fig. 2 we have plotted qualitatively the function $J_n(x)/Y_n(x)$ vs x. For large n, the first zero j_{n1} of J_n, occurs approximately at $n+1.86n^{\frac{1}{3}}$, while y_{n2}, the second zero of Y_n, occurs approximately at $n+2.54n^{\frac{1}{3}}$. Hence for large n the first characteristic value for TM modes always has the limits $n+1.86n^{\frac{1}{3}}<qb<n+2.54n^{\frac{1}{3}}$. Again, more quantitative evaluation will be found in Appendix II. We merely wish to point out here that, for this first TM solution, the condition $qr/n<1$ holds for some portion of the vacuum-tank aperture.

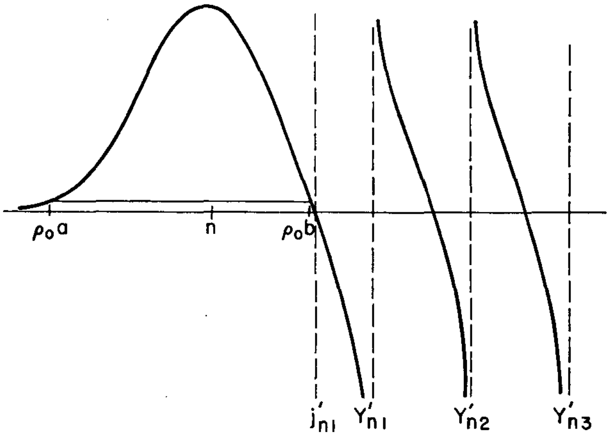

FIG. 1. Qualitative graph of $J_n'(x)/Y_n'(x)$ for large n. The radial aperture of the vacuum tank is represented by the region of the abscissa between q_0a and q_0b. The ith zero of J_n' is j_{ni}', and the ith zero of Y_n' is y_{ni}'.

APPENDIX II

High-Order Solutions of Bessel's Equation for a Narrow Annulus

A. Introduction

The lowest characteristic values q, and the associated characteristic functions $Z(r)$, of interest here are those which arise from Bessel's equation when n is large and when $(b-a)/(b+a)\ll 1$. As shown in Appendix I, the lowest characteristic values will be in the neighborhood of n/b. To find whether a resonant electromagnetic mode will be excited by a modulated beam moving within the vacuum chamber, however, the characteristic values must be determined with some accuracy, because of the strong cancellation involved in computing the quantity $k=[(n\omega_0/c)^2-q^2]^{\frac{1}{2}}$. This quantity assumes values which are odd multiples of π/h in resonant modes. It is accordingly appropriate to examine directly[8] the characteristic solutions of Bessel's equation, subject to our particular boundary conditions, without reference to the customary Bessel and Neumann functions J_n and Y_n.

B. Analysis

It is convenient to introduce the quantity

$$\eta \equiv (b-a)/(b+a) = w/2R_0$$

and, because of the strong cancellation mentioned above, to define

$$\delta \equiv \eta^2[(qR_0)^2 - n^2] \tag{A.1a}$$

and

$$u \equiv 2(r-R_0)/w. \tag{A.1b}$$

In terms of these quantities, we have $r = R_0(1+\eta u)$, with $-1 \leqslant u \leqslant 1$, and Bessel's equation assumes the form

$$\frac{d}{du}\left[(1+\eta u)\frac{dZ}{du}\right] + \left[\delta(1+\eta u) + \frac{(2+\eta u)}{(1+\eta u)}\eta^3 n^2 u\right] Z = 0. \tag{A.2}$$

For $\eta \ll 1$, the characteristic values δ and the characteristic functions for this equation may be obtained[8] by a perturbation method provided n is not too large. In this way we find for the first Neumann solution (TE mode)

$$\delta \cong \frac{1}{3}\eta^4 n^2 - \frac{8}{15}\eta^6 n^4, \tag{A.3a}$$

$$Z \propto 1 + \eta^3 n^2 [u - (u^3/3)]. \tag{A.3b}$$

For the first Dirichlet solution (TM mode)

$$\delta \cong \left(\frac{\pi}{2}\right)^2 - \frac{\eta^2}{4} + \left(1 - \frac{6}{\pi^2}\right)(n^2 - \tfrac{1}{4})\eta^4, \tag{A.4a}$$

$$Z \propto \left\{ \cos\frac{\pi}{2}u + \frac{1}{\pi}(n^2 - \tfrac{1}{4})\eta^3 \right.$$
$$\left. \times \left[(1-u^2)\sin\frac{\pi}{2}u - \frac{2}{\pi}u\cos\frac{\pi}{2}u\right]\right\}(1+\eta u)^{-\frac{1}{2}}; \tag{A.4b}$$

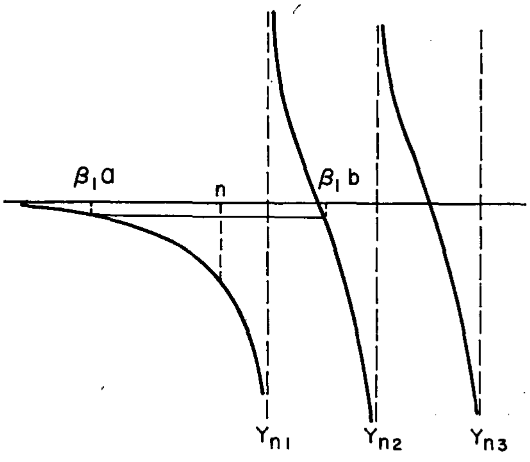

FIG. 2. Qualitative graph of $J_n(x)/Y_n(x)$ for large n. The radial aperture of the vacuum tank is represented by the region of the abscissa between qa and qb. The ith zero of J_n is j_{ni} and the ith zero of Y_n is y_{ni}.

and for the second Neumann solution (TE mode)

$$\delta \cong \left(\frac{\pi}{2}\right)^2 + \tfrac{3}{4}\eta^2 + \left(1 + \frac{10}{\pi^2}\right)\eta^4 n^2, \tag{A.5a}$$

$$Z \propto \sin\frac{\pi}{2}u - \tfrac{1}{2}\eta\left(u\sin\frac{\pi}{2}u + \frac{2}{\pi}\cos\frac{\pi}{2}u\right)$$
$$-\frac{1}{\pi}\eta^3 n^2\left[\left(1 + \frac{4}{\pi^2} - u^2\right)\cos\frac{\pi}{2}u + \frac{2}{\pi}u\sin\frac{\pi}{2}u\right]. \tag{A.5b}$$

The region of applicability of the foregoing expressions is that for which $\eta^3 n^2 \ll 1$. Of greater significance for our present purposes, however, are the results for the case $\eta^3 n^2 > 1$, which we discuss below.

Since our interest here is confined to the case $\eta \ll 1$, it is convenient to approximate the differential equation for Z by

$$\frac{d^2 Z}{du^2} + [\delta + 2\eta^3 n^2 u] Z = 0. \tag{A.6}$$

Solutions of this approximate equation may then be written explicitly in terms of Bessel functions of order $\frac{1}{3}$. Specifically, we take

$$Z \propto \xi^{\frac{1}{2}}\left[J_{\frac{1}{3}}\left(\frac{\xi^{\frac{3}{2}}}{3\eta^3 n^2}\right) + J_{-\frac{1}{3}}\left(\frac{\xi^{\frac{3}{2}}}{3\eta^3 n^2}\right)\right], \tag{A.7}$$

where ξ denotes $\delta + 2\eta^3 n^2 u$. The particular ratio of the coefficients of $J_{\frac{1}{3}}$ and $J_{-\frac{1}{3}}$ is selected to ensure a decreasing exponential solution to the left of the "classical turning point," $u_c = -\delta/2\eta^3 n^2$. When $\eta^3 n^2$ is fairly large in comparison to unity, such a solution will drop sufficiently rapidly in that region to satisfy the boundary condition required at $u = -1$ (i.e., at $r = a$).

Asymptotic forms for the characteristic values of δ may then be found immediately by application of the desired boundary conditions at $u = 1$, with the aid of published tables.[9] The following estimates of δ, applicable in cases in which $\eta^3 n^2$ is at least somewhat larger than unity, are obtained. For the first Neumann solution (TE mode)

$$\delta \cong -2\eta^3 n^2 + 1.61724\eta^2 n^{\frac{4}{3}}, \tag{A.8}$$

for the first Dirichlet solution (TM mode)

$$\delta \cong -2\eta^3 n^2 + 3.71151\eta^2 n^{\frac{4}{3}}, \tag{A.9}$$

for the second Neumann solution (TE mode)

$$\delta \cong -2\eta^3 n^2 + 5.15619\eta^2 n^{\frac{4}{3}}. \tag{A.10}$$

The nature of the characteristic functions can be seen conveniently from a graph (Fig. 3) of

---

[9] National Bureau of Standards Computation Laboratory, *Tables of Bessel Functions of Fractional Order* (Columbia University Press, New York, 1948–49), Vols. I and II.

$$Z \propto v^{\frac{1}{2}}[J_{\frac{1}{3}}(v^{\frac{3}{2}})+J_{-\frac{1}{3}}(v^{\frac{3}{2}})] \quad \text{vs} \quad v, \tag{A.11}$$

with v defined by the relation

$$v \equiv \frac{\delta+2\eta^3n^2u}{3^{\frac{2}{3}}\eta^2n^{\frac{4}{3}}}. \tag{A.12}$$

The various characteristic solutions of interest are then depicted by this curve, with the $u=1$ boundary appropriately located at the maximum, zero, or minimum of the function plotted. When η^3n^2 is large, the solutions are highly localized near $u=1$. Their values exceed $(1/e)Z_{\max}$ only in an interval Δu of width $1.35\eta^{-1}n^{-\frac{2}{3}}$, $2.39\eta^{-1}n^{-\frac{2}{3}}$, or $3.12\eta^{-1}n^{-\frac{2}{3}}$, respectively, for the three characteristic solutions discussed here. This property, and others useful in the application of the characteristic solutions, depend only upon the value of η^3n^2 and may be estimated from the graph or evaluated computationally.[8]

C. *The Possibility of Resonance*

The possibility that an azimuthally modulated beam may excite a resonant electromagnetic mode of a toroidal vacuum chamber may be examined by reference to the equation

$$k=[(n\omega_0/c)^2-q^2]^{\frac{1}{2}}, \tag{A.13}$$

where $k=(2m+1)\pi/h$. In terms of the average radius of the chamber, R_0 and the radius of the particle orbit R_B, this relation may be written

$$(qR_0)^2=n(\beta R_0/R_B)^2-(2m+1)^2(\pi R_0/h)^2 \tag{A.14a}$$

or

$$\delta=\eta^2n^2[(\beta R_0/R_B)^2-1]-[(m+\tfrac{1}{2})\pi w/h]^2. \tag{A.14b}$$

For a relativistic beam moving close to the center of the aperture, $\beta R_0/R_B$ will be close to unity. The ratio w/h is normally greater than unity. For resonance to occur, therefore, δ must be somewhat negative and hence, η^3n^2 would be roughly of order unity for the lower-order resonant modes. Somewhat lower values of n could give rise to resonant excitation if $R_B<R_0$, while β materially less than unity will require larger values of n. There is, in fact, a limiting value for the particle energy below which resonance will not occur, even with $R_B=a$, as can be seen from the following argument. If we have

$$R_B=R_0-w/2, \tag{A.15}$$

we can write

$$\delta=\eta^2n^2[\beta^2/(1-\eta)^2-1]-[(m+\tfrac{1}{2})\pi w/h]^2, \tag{A.16}$$

and resonance certainly cannot occur in any mode if we have

$$\eta^2n^2[\beta^2/(1-\eta)^2-1]<-2\eta^3n^2,$$

i.e., for

$$\beta^2/(1-\eta)^2-1+2\eta<0,$$

$$\beta^2<(1-2\eta)(1-\eta)^2,$$

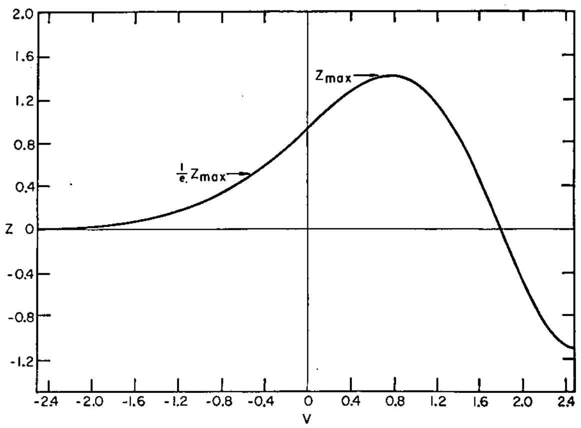

FIG. 3. Graph of the universal radial function $Z(v)$, as defined by Eqs. (A.11) and (A.12).

or

$$\gamma^2<\frac{1}{1-(1-2\eta)(1-\eta)^2}\cong\frac{1}{4\eta}. \tag{A.17}$$

For $R_B=R_0$, however, significant resonances may arise for values of n sufficiently great that η^3n^2 is in the range 4 to 30. A convenient general expression is obtained from Eq. (A.14b) by neglecting terms proportional to $(\eta^3n^2)^{\frac{2}{3}}$ which appear in Eqs. (A.8) through (A.10). The first resonance then is seen to occur for harmonic numbers such that

$$\eta^2n^2\left[\left(\frac{\beta b/R_B}{1+\eta}\right)^2-1\right]=-2\eta^3n^2+\left(\frac{\pi w}{2h}\right)^2,$$

$$n=(\pi R_B/h)[1-1/\gamma^2-(1-2\eta)(1+\eta)^2(R_B/b)^2]^{-\frac{1}{2}} \tag{A.18}$$

$$\cong(\pi R_B/h)[1-1/\gamma^2-(R_B/b)^2]^{-\frac{1}{2}}. \tag{A.18a}$$

D. *Salient Properties of the Characteristic Solution*

With $\eta^3n^2>1$, the characteristic solutions differ considerably from simple circular functions. This fact affects the coupling between the beam and the electromagnetic fields and modifies the numerical values of the loss factor Q. For purposes of this paper it may suffice to state that computational results[8] indicate

$$[dZ/du]_0^2/\{[Z(-1)]^2+[Z(1)]^2\}$$

does not appreciably exceed 0.40 for the first Neumann solution (for $\eta^3n^2\sim3$). For the second Neumann solution, this quantity assumes the value $\pi^2/8$ for η^3n^2 small, vanishes for $\eta^3n^2\sim6$, attains a maximum value of approximately 4.0 for $\eta^3n^2\sim20$, and decreases thereafter. The quantity $[dZ/du]_0^2/\int_{-1}^{1}Z^2du$ for the first Neumann solution has a maximum value of approximately 0.71 at $\eta^3n^2\sim4$, drops to 0.41 at $\eta^3n^2\sim10$, and becomes less than 0.13 for $\eta^3n^2\gtrsim20$. For the second Neumann solution it is

$\pi^2/4$ for $\eta^3 n^2$ small, vanishes for $\eta^3 n^2 \sim 6$, attains a maximum value of approximately 4.5 for $\eta^3 n^2 \sim 20$, and decreases thereafter. Finally, for the first Dirichlet solution, the quantity $[Z(0)]^2/\int_{-1}^{1} Z^2 du$ drops steadily from a value unity for $\eta^3 n^2$ small, to 0.79 for $\eta^3 n^2 \sim 4$, 0.37 at $\eta^3 n^2 \sim 10$, and 0.10 at $\eta^3 n^2 \sim 20$.

Reprinted from THE REVIEW OF SCIENTIFIC INSTRUMENTS, Vol. 32, No. 3, 276–279, March, 1961
Printed in U. S. A.

Reprinted by permission of the American Institute of Physics.

Coherent Electromagnetic Effects in High Current Particle Accelerators: III. Electromagnetic Coupling Instabilities in a Coasting Beam*

L. JACKSON LASLETT†
Ames Laboratory, Iowa State University, Ames, Iowa, and Midwestern Universities Research Association, Madison, Wisconsin

AND

V. KELVIN NEIL AND ANDREW M. SESSLER‡
Lawrence Radiation Laboratory, University of California, Berkeley, California

(Received October 13, 1960)

The electromagnetic interaction of an intense relativistic coasting beam with itself, including the effect of a nonperfectly conducting vacuum tank, or a quiescent rf cavity, is investigated theoretically. It is shown that the resonances that may occur between harmonics of the particle circulation frequencies and the electromagnetic modes of the cavities can lead to a longitudinal instability of the beam. A criterion for stability of the beam against such longitudinal bunching is obtained as a restriction on the shunt impedance of the rf cavity, or the Q of the vacuum tank. This criterion contains the energy spread and intensity of the coasting beam, as well as the parameters of the accelerator. Numerical examples are given which indicate that, in general, the resonances with the vacuum tank will not cause instabilities, while those with an rf cavity can be prevented from causing instabilities by choosing the shunt impedance at a sufficiently low but still convenient value.

I. INTRODUCTION

IN the second article (Part II) of this series[1] it was shown that a resonance can occur between a beam of particles in an accelerator and the characteristic electromagnetic modes of the vacuum tank. It is possible that this resonance could lead to instabilities in an intense relativistic coasting beam. This problem is distinguished from the longitudinal instabilities investigated previously by a number of authors[2,3] because resonance can occur only with modes characterized by short wavelengths in the azimuthal direction. Thus we shall be dealing with perturbation frequencies that are very high harmonics of the particle circulation frequency.

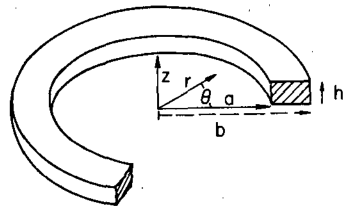

FIG. 1. Cutaway view of toroidal cavity.

We shall again take a toroid with rectangular cross section as a model of the vacuum tank (Fig. 1), neglecting all windows, discontinuities, and straight sections. The conductivity of the walls is sufficiently high to allow the vanishing of the tangential electric field to be used as a boundary condition in the solution of Maxwell's equations. Therefore, we can use the results in Part II of this series.

The stability of the coasting beam may also be affected by the presence of an rf cavity through which the beam must pass. If the cavity has an eigenfrequency near a harmonic of the beam circulation frequency, a resonance condition exists between the beam and the cavity. Such a resonance generally occurs for a much lower harmonic than the resonance with the modes of the vacuum tank. For purposes of this calculation we assume that the cavity is not driven externally.

Transverse particle motion will be neglected throughout this work, except insofar as it contributes to the cross-sectional area of the beam. The density of particles in the unperturbed beam is taken as being uniform azimuthally. In Sec. II we assume an infinitesimal perturbation that preserves the cross-sectional dimensions of the beam.

---

* This work was done under the auspices of the U. S. Atomic Energy Commission.

† Now in London with the Office of Naval Research.

‡ Permanent address: Ohio State University, Columbus, Ohio.

[1] V. K. Neil, D. L. Judd, and L. J. Laslett, Rev. Sci. Instr. 32, 267 (1961).

[2] A. A. Kolomensky and A. N. Lebedev, *Proceedings of the CERN Symposium on High Energy Accelerators, Geneva 1959* (CERN, Geneva, 1959), p. 115.

[3] C. E. Nielsen, A. M. Sessler, and K. R. Symon, *Proceedings of the CERN Symposium on High Energy Accelerators, Geneva, 1959* (CERN, Geneva, 1959), p. 239.

It is then possible to solve the linearized one-dimensional Vlasov equation to obtain a dispersion relation that gives the allowed values of the perturbation frequency. This dispersion relation contains the azimuthal electric field generated by the perturbation, and in Sec. III convenient expressions are cited for this component of the electric field, using results from Part II of this series.

Section IV is devoted to a discussion of the dispersion relation. A criterion for stability is derived that places an upper limit on the quality factor Q of the resonant mode of the vacuum tank. If the beam is near a resonance with the rf cavity, this criterion can be expressed as an upper limit on the input impedance of the cavity. These criteria contain the total number of particles in the machine as well as the energy spread of the coasting beam. Numerical estimates using the parameters of two quite different accelerators are given in Sec. V and indicate that instabilities arising from excitation of vacuum tank modes will not, in general, be a serious problem. Instabilities induced by an rf cavity, on the other hand, may place significant upper limits on the input impedance of rf cavities used in beam stacking schemes.

II. DISPERSION RELATION

It will be convenient in what follows to introduce the action variable W, which is defined by

$$W=\int_{E_0}^{E}\frac{dE}{f(E)}. \tag{2.1}$$

Here E is the energy of the particle and f the instantaneous circulation frequency of the particle. The variable W is canonically conjugate to the angle variable ϕ describing the particle's position in azimuth. In the absence of an applied radio-frequency voltage, the equations of motion are given by

$$\dot{W}=2\pi eRE_\phi$$

and (2.2)

$$\dot{\phi}=2\pi f.$$

The effective azimuthal electric field is designated by E_ϕ.

We may denote the distribution function for particles in synchrotron phase space by $\Psi(W,\phi,t)$, and it can then be shown[3] that Ψ satisfies the one-dimensional Vlasov equation,

$$\frac{\partial\Psi}{\partial t}+\dot{\phi}\frac{\partial\Psi}{\partial\phi}+2\pi e\langle RE_\phi\rangle\frac{\partial\Psi}{\partial W}=0, \tag{2.3}$$

in the well-justified approximation of ignoring collisions between particles. In Eq. (2.3), $\langle RE_\phi\rangle$ involves the longitudinal electric field averaged over the beam cross section. For the investigation described here, we may safely replace this average by the orbit radius times the electric field at the center of the beam.

Since the unperturbed coasting beam is assumed to be uniform in azimuth, the unperturbed distribution of particles in $W-\phi$ space may be described by a function $\psi_0(W)$. We shall consider an infinitesimal perturbation such that the total distribution function $\Psi(\phi,W,t)$ may be written as

$$\Psi(\phi,W,t)=\psi_0(W)+\psi_1(n,W,\omega)e^{i(n\phi-\omega t)}. \tag{2.4}$$

Note that the perturbation does not affect the transverse distribution of particles. Linearizing Eq. (2.3) leads to

$$\psi_1(n,W,\omega)=-2\pi ie\langle RE_\phi\rangle\frac{\partial\psi_0/\partial W}{(\omega-n\dot{\phi})}. \tag{2.5}$$

The electric field in Eq. (2.5) arises from the charge and current densities of the perturbation only. The particle density associated with the perturbation is

$$\delta N=N_ne^{i(n\phi-\omega t)}, \tag{2.6}$$

where

$$N_n=\int\psi_1(n,W,\omega)dW, \tag{2.7}$$

and the associated azimuthal electric field at the beam center may be written as

$$\langle RE_\phi\rangle=\epsilon N_ne^{i(n\phi-\omega t)}. \tag{2.8}$$

The quantity ϵ thus defined will be investigated in the next section. If we insert Eq. (2.8) into Eq. (2.5) and use Eq. (2.7), the condition for a solution to the Vlasov equation becomes

$$1=-2\pi ie\epsilon\int\frac{d\psi_0}{dW}\frac{dW}{(\omega-n\dot{\phi})}. \tag{2.9}$$

The particular dependence of ψ_0 upon W is not important as long as $d\psi_0/dW$ has no discontinuities. A completely realistic distribution function would necessarily vanish for values of W corresponding to particles moving faster than the velocity of light. For convenience, however, we shall take a Lorentz (resonance) line shape for ψ_0 and set

$$\psi_0(W)=\frac{N(\Delta W)}{2\pi^2[(W-W_0)^2+(\Delta W)^2]}. \tag{2.10}$$

This function falls off as W^{-2} for large values of W, and this behavior should not appreciably affect the results of the calculation. In Eq. (2.10), N is the total number of particles circulating in the machine. The distribution is centered about the value $W=W_0$ and has a characteristic width ΔW. The integral in Eq. (2.9) may be evaluated by integration along the W axis, if we assume that ω has a small positive imaginary part,[3] and we use the relation

$$\dot{\phi}(W)=\dot{\phi}(W_0)+2\pi f\left(\frac{df}{dE}\right)(W-W_0).$$

One obtains

$$\int \frac{d\psi_0}{dW}\frac{dW}{(\omega-n\dot{\phi})}=-\frac{nkN}{2\pi}\frac{1}{(\omega-n\omega_0+i\tau)^2}, \tag{2.11}$$

in which $k=2\pi f df/dE$, ω_0 is the central frequency of the beam [equal to $\dot{\phi}(W_0)$], and $\tau=n|k|\Delta W$ is $n/2$ times the characteristic frequency spread of the distribution.

Having evaluated this integral, we have reduced Eq. (2.9) to the form

$$1=iekNn\epsilon(\omega-n\omega_0+i\tau)^{-2}. \tag{2.12}$$

The next section is devoted to a discussion of the quantity ϵ.

III. AZIMUTHAL ELECTRIC FIELD

For resonances with the accelerator tank we may use directly the result of Part II Eqs. (4.4), (4.5), (4.9), and (4.10) to obtain

$$\epsilon=B_t\frac{i\omega^2}{(\omega_r^2-\omega^2)-i(\omega_r^2/Q_{\mathrm{TE}})}, \tag{3.1}$$

with

$$B_t=\frac{2ecR^2\mathfrak{z}[dZ/dr]_B{}^2}{nq^2h\int_a^b rZ^2dr} \tag{3.2}$$

for a resonance in the first possible mode. The notation is is that of Part II of this series.

Although the contribution to the azimuthal electric field from the resonant mode is the major contribution, other contributions also arise from current and charge distributions that vary as $\exp(in\phi)$. These additional contributions may be attributed to the excitation of modes characterized by the same value of n, but having more than one wavelength in the r and z directions. A more general treatment of this problem, including the excitation of nonresonant modes, shows that the nonresonant contributions to the electric field have little effect on the results of the dispersion analysis. We shall therefore use the expression for ϵ of Eq. (3.1) in the dispersion relation.

For resonance with an rf cavity, we may proceed from Eq. (2.9) of Part I of this series,[4] and write the effective azimuthal electric field as

$$E_\phi=-\frac{e\omega_r Z_c N_n e^{i(n\phi-\omega t)}}{2\pi Rn} \tag{3.3}$$

which is a valid expression if the perturbation frequency is exactly equal to the resonant frequency of the cavity. If the cavity is being driven slightly off resonance, we may write

$$\langle rE_\phi\rangle=\frac{ie\omega_r\omega^2(Z_c/Q_c)N_n e^{i(n\phi-\omega t)}}{2\pi n(\omega_r^2-\omega^2-i\omega_r^2/Q_c)}.$$

It follows immediately that

$$\epsilon=B_c\frac{i\omega^2}{\omega_r^2-\omega^2-i\omega_r^2/Q_c} \tag{3.4}$$

with

$$B_c=eZ_c\omega_r/2\pi nQ_c. \tag{3.5}$$

IV. CRITERION FOR STABILITY

Either for resonance with a tank mode or resonance with the rf cavity, we may write the dispersion relation, Eq. (2.12), in the form

$$-1=ekNnB\omega^2\left[\omega_r^2-\omega^2-\frac{i\omega_r^2}{Q}\right]^{-1}(\omega-n\omega_0+i\tau)^{-2}, \tag{4.1}$$

with B given by Eqs. (3.2) or (3.5). One can see that the fourth-order equation, Eq. (4.1), has various roots corresponding to possible instabilities. One root is always stable $(\omega\sim-\omega_r)$, two correspond to the longitudinal instability of a coasting beam treated previously, and the root in which $\omega\sim\omega_r$ corresponds to the possible instability associated with the electromagnetic mode with eigenfrequency ω_r. Setting $\omega=\omega_r+\nu$, we solve for ν by linearizing the dispersion relation in ν. The imaginary part of ν is then obtained as a function of $\omega_r-n\omega_0$. The criterion for stability is $\mathrm{Im}\nu<0$, and since the $\mathrm{Im}\nu$ is largest for $\omega_r-n\omega_0\approx\pm\tau$, we make this substitution to obtain

$$\nu=\frac{A\omega_r\pm 2\omega_r\tau^2/Q}{2\left(-\frac{\omega_r}{Q}\tau-A\right)\pm i\left(2\tau+\frac{\omega_r}{Q}\right)\tau}, \tag{4.2}$$

where $A=ekNnB$. The plus or minus signs refer to the choice of $\omega_r-n\omega_0=\pm\tau$.

Observing that $Q\gg1$, we have as a criterion for stability

$$\left[-A\omega_r\mp\frac{2\omega_r}{Q}\tau^2\right]\left[\left(\frac{\tau\omega_r}{Q}+A\right)\pm\left(2\tau+\frac{\omega_r}{Q}\right)\tau i\right]<0 \tag{4.3}$$

or

$$\pm\left(-A\pm\frac{2\tau^2}{Q}\right)<0. \tag{4.4}$$

By appropriate choice of the sign, depending upon whether k is positive or negative (corresponding to the beam's being below or above the transition energy), we obtain as the most stringent requirement for stability[5]:

---

[4] V. K. Neil and A. M. Sessler, Rev. Sci. Instr. **32**, 256 (1961).

[5] If n is sufficiently large that resonances occur with higher-order electromagnetic modes, the coupling factors which enter in the coefficient B_t of Eq. (3.2), and which appear in expressions for evaluation of Q_{TE}, may be modified materially. From the WKB form of the function $Z(r)$, however, estimates of the relevant factors can be obtained which suggest that the factor n^4 in Eqs. (4.6) and (4.7) will increase rapidly enough to ensure that no more stringent limitations on particle number or wall conductivity will result from

$$Q<2\tau^2/e|k|NnB. \tag{4.5}$$

We now may use the definitions of k and τ which, after substitution of B for the case of a tank resonance yields

$$Q_t<\frac{1}{2}\frac{n^4\left|\dfrac{df}{dE}\right|(\Delta E)^2h}{Nf(m_0c^2)r_0R^4}\left[\frac{\displaystyle\int_a^b rZ^2dr}{(dZ/dr)_B{}^2}\right], \tag{4.6}$$

where r_0, the classical electron radius, is 2.8×10^{-13} cm. For $w\ll R$ this may be written as

$$Q_t<\frac{1}{16}\frac{n^4\left|\dfrac{df}{dE}\right|(\Delta E)^2hw^3}{Nf(m_0c^2)r_0R^3}\left[\frac{\displaystyle\int_{-1}^1 Z^2dx}{(dZ/dx)_B{}^2}\right]. \tag{4.7}$$

A few illustrative values for the last bracket can be found in Part II, while tables of values are in reference 8 of Part II of this series.

For resonance with an rf cavity, we obtain as the condition of stability from Eq. (4.5) that the shunt impedance Z_c must satisfy

$$Z_c<\frac{nc\mathfrak{z}\left|\dfrac{df}{dE}\right|(\Delta E)^2}{(m_0c^2)r_0Nf^2}. \tag{4.8}$$

The quantity $\mathfrak{z}$ is the impedance of free space, which is equal to 377 ohms in mks units, and $4\pi/c$ in cgs units.

V. NUMERICAL EXAMPLES

A. rf Cavity Resonance

As an example of a resonance with an rf cavity, we take the MURA 40-Mev electron model[6]:

$$f(df/dE)=1.1\times10^{12}\ \text{Mev}^{-1}\ \text{sec}^{-2},$$
$$f=25\times10^6\ \text{sec}^{-1},$$
$$n=1,$$
$$\Delta E=3\ \text{Mev},$$
$$N=1.5\times10^{13}.$$

The shunt impedance Z_c must be less than 3200 ohms, to prevent a longitudinal instability. This limit is sufficiently high to ensure no difficulty.

As a second example, we might consider a hypothetical proton storage ring for 15-Bev particles. As reasonable parameters, we take

$$df/dE=0.70\ \text{Mev}^{-1}\ \text{sec}^{-1},$$
$$f=10^6\ \text{sec}^{-1},$$
$$n=10,$$
$$\Delta E=300\ \text{Mev},$$
$$N=10^{14}.$$

In this case the shunt impedance of an rf "maintaining cavity" must be less than 5.1×10^5 ohms, which would preclude the use of a very high Q cavity such as otherwise might have been used in such a device. For example, the cavities at the Cambridge electron accelerator have shunt impedances of 10^7 ohms.[7]

B. Tank Resonances

As a first example, we consider the MURA electron model in which the vacuum tank has a height of 5 cm, an inner radius of 122 cm, and an outer radius of 224 cm. The 38-Mev beam will be stacked at a radius of 203 cm. From Eq. (A-18) of Part II, the estimated n value for the first resonance is approximately 200, but the coupling factor

$$\int_{-1}^1 Z^2dx\bigg/\left(\frac{dZ}{dx}\right)_B^2$$

is so small that the restriction on Q_t is satisfied by a vacuum tank made of even the best conducting material imaginable.

As a second example, we consider a full scale FFAG accelerator for which the following parameters might be typical:

$a=7\times10^3$ cm, $\quad f=10^6\ \text{sec}^{-1}$,
$b=7300$ cm, $\quad df/dE=0.70\ \text{Mev}^{-1}\ \text{sec}^{-1}$,
$R_B=7275$ cm, $\quad E=15$ Bev, $\Delta E=300$ Mev,
$h=15$ cm, $\quad N=10^{14}$.

The first resonance is at $n=30\,000$, and once again there need be no concern about a longitudinal instability for any physically realizable cavity.

---

the presence of such higher-order modes. With high-order resonances present, of course, more than one resonance can occur within a sufficiently small frequency interval that the coupling with the beam is enhanced, and a somewhat stronger limitation can result. But if n were high enough so that many resonances would fall within the range where interaction with the beam occurs, variation of phase amongst the several modes excited by the beam would appear to suppress the reactive feature of the coupling which permits instabilities to develop.

[6] The MURA Staff, *Proceedings of the CERN Symposium on High Energy Accelerators, Geneva, 1959* (CERN, Geneva, 1959), p. 71.

[7] M. S. Livingston, *Proceedings of the CERN Symposium on High Energy Accelerators, Geneva, 1959* (CERN, Geneva, 1959), p. 335.

Reprinted from THE REVIEW OF SCIENTIFIC INSTRUMENTS, Vol. 36, No. 4, 436–448, April 1965
Printed in U. S. A.

Reprinted by permission of the American Institute of Physics.

Transverse Resistive Instabilities of Intense Coasting Beams in Particle Accelerators*

L. JACKSON LASLETT, V. KELVIN NEIL, AND ANDREW M. SESSLER
Lawrence Radiation Laboratory, University of California, Berkeley and Livermore, California

(Received 7 December 1964)

The transverse electromagnetic interaction of an intense azimuthally uniform beam of particles with itself, including the effect of a resistive vacuum tank, is investigated theoretically. It is shown that a beam of particles all having velocity v is unstable against the development of transverse waves having a phase velocity close to $(1-\nu/n)v$, where ν is the number of transverse free betatron oscillations occurring in one revolution and n is a positive integer greater than ν. The growth rate for the instability is proportional to $N/\sigma^{\frac{1}{2}}$, where N is the number of particles in the beam and σ is the conductivity of the surface material of the vacuum tank. Stabilizing mechanisms are examined by means of the Vlasov equation and it is shown that a spread in the quantity $(n-\nu)v$, evaluated for particles in the unperturbed beam, will prevent the instability. A criterion for the spread required is shown, in the limit of walls of high conductivity, to depend upon the beam intensity and energy as well as upon certain geometrical properties of the accelerator, but not upon the conductivity. Numerical examples covering a range of particle accelerators are presented, and suggest that the theory is in agreement with the coherent beam behavior recently observed in a number of accelerators.

I. INTRODUCTION

AMPLIFICATION of longitudinal density fluctuations in an electron beam by the resistance in the surrounding walls has been predicted theoretically and demonstrated experimentally.[1,2] The companion paper[3] to this article treats the occurrence of this phenomenon in particle accelerators. Recently a number of particle accelerators have exhibited an instability that consists of a coherent vertical oscillation of the particle beam.[4–6] The purpose of our work is to develop a theory of the transverse instability that is conceptually related to the theory of the resistive wall amplifier. Our detailed investigation was suggested by the earlier work of de Packh,[7] and is more general than any of the above analyses in that details of the particle dynamics are incorporated, although not in a strictly self-consistent manner. This sophistication is vital in obtaining a threshold for the instability. The analysis follows that of the companion paper on longitudinal resistive instabilities[3] but is complicated by the more involved electromagnetic fields associated with the transverse motion.

A beam of particles with angular-circulation frequency ω_0 executing coherent vertical oscillations generates travel-

---

[*] Research supported by the U. S. Atomic Energy Commission.

[1] C. K. Birdsall, G. R. Brewer, and A. V. Haeff, Proc. IRE 41, 865 (1953).

[2] J. R. Pierce, Bell System Tech. J. **30**, 626 (1951).

[3] V. K. Neil and A. M. Sessler, Rev. Sci. Instr. **36**, 429 (1965).

[4] C. P. Curtis *et al.*, "Beam Experiments with the MURA 50 MeV FFAG Accelerator," *Proceedings of the International Conference on High Energy Accelerators, Dubna, 1963* (Atomizdat, Moscow, 1964), p. 620.

[5] F. E. Mills and G. K. O'Neil, "Vertical Instabilities in Electron Storage Rings," *Proceedings of the Brookhaven Summer Study on Storage Rings, Accelerators and Experimentation at Super-High Energies* (BNL-7534, 1963), pp. 368, 375 (Brookhaven National Laboratory, Upton, New York, 1963).

[6] M. Q. Barton, J. G. Cottingham, and A. Tranis, Rev. Sci. Instr. **35**, 624 (1964).

[7] D. de Packh, Naval Research Laboratory, Washington, D. C., private communication to MURA, 2 May 1963.

ing waves with angular frequency $\omega=(n\pm\nu)\omega_0$, where n is an integer and ν is the number of betatron wavelengths per revolution. In the absence of resistivity in the surrounding walls these oscillations are stable. The associated electromagnetic force on the beam is 90° out of phase with the vertical velocity of the beam, and merely shifts the betatron oscillation frequency. If this shift is sufficient to change the betatron wavelength to a value corresponding to an accelerator resonance, the beam becomes unstable. Generally a change in ν of about 0.25 is sufficient. This mechanism has been examined in detail in a recent publication.[8] The resulting space-charge limit is ample in most machines.

In the presence of resistive walls, the fields associated with the wave having $\omega=(n-\nu)\omega_0$ exert a force on the beam that has a component in phase with the coherent vertical velocity. This is the "slow wave," or "negative-energy" wave. It has a phase velocity less than the directed velocity of the particles, and may lead to an exponentially growing transverse oscillation of the beam. Ultimately the energy required for the transverse motion comes from the longitudinal motion of the particles. The electromagnetic force on the beam arising from the wave with $\omega=(n+\nu)\omega_0$ has a component 180° out of phase with the coherent vertical velocity. This is the "fast wave," or "positive-energy wave." It has a phase velocity greater than the directed velocity of the particles and leads to exponentially damped vertical oscillations.

The crucial role of a dissipative mechanism in the occurrence of an instability has been encountered in the so-called "hose instability" of a stream of particles passing through a plasma.[9] In this instance it is collisions between plasma particles that render the beam unstable against transverse oscillations, and such a phenomenon could occur in particle-accelerator beams. Our treatment assumes that the beam is in vacuum so that the walls must supply the dissipative mechanism. The presence of background plasma could well have an effect upon the instability considered here.

The analysis is given for a beam with uniform density in the azimuthal direction, as is the physical situation in Ref. 4. Most experimental observations have been made with beams that are bunched by an externally driven rf cavity. It is not clear whether bunching is unimportant, but the methods invoked here are not powerful enough to treat an azimuthally varying density in the unperturbed beam. The perturbation considered is a small vertical displacement of the beam. The displacement has the form $\exp[i(n\theta-\omega t)]$, where θ is the azimuthal angle around the machine. In Sec. II approximate expressions for the electromagnetic fields associated with the displacement are calculated for vacuum tanks of circular cross section and rectangular cross section. In the latter geometry, the conductivity of the side walls is assumed to be infinite. Finite conductivity is considered present only in the top and bottom surfaces. In Sec. III these fields are combined with the Vlasov equation so that a dispersion relation for the allowed values of the frequency ω can be derived.

Section IV is devoted to a discussion of the dispersion relation. It is shown that for a beam of particles all having the same values of ν and ω_0, finite conductivity always leads to an instability. The characteristic growth time is given by Eq. (5.2); it is a function of the geometry and beam energy and is directly proportional to $\sigma^{\frac{1}{2}}/N$, where σ is the conductivity of the wall material and N is the total number of particles in the beam. The instability is suppressed if the particles have a sufficient spread in their values of ν and/or ω_0. Both of these quantities are functions of particle energy and of the betatron oscillation amplitude. A criterion derived for stability shows that the requisite spread is directly proportional to N. The required spread is independent of σ in the limit of highly conducting walls. In Sec. V we summarize the results of the calculation in a form convenient for application to a large number of existing and contemplated accelerators, and also present some numerical examples.

II. ELECTROMAGNETIC FIELDS

As mentioned in Sec. I the treatment presented here is not strictly self consistent. We use a simple model of the beam as a source for the fields. When the dispersion relation is discussed in Sec. IV, various equilibrium distributions of particles are considered. These do not in general give rise to the same charge and current distributions used in this section. The implications of this are discussed in greater detail below. As the major curvature of the vacuum tank has little influence on the results of this calculation, we solve Maxwell's equations in a straight waveguide.

A. Rectangular Cross Section

The geometry we consider first is that illustrated in Fig. 1. The current and charge densities in the unperturbed beam are taken as uniform in the direction of motion (y direction). The center of the beam is located at $z=0$ and the particle density is uniform in the region $-(\tau/2)<z<(\tau/2)$. The position and shape of the beam in the x direction is arbitrary at this stage. The equilibrium

---

[8] L. Jackson Laslett, "On Intensity Limitations Imposed by Transverse Space-Charge Effects in Circular Particle Accelerators," *Proceedings of the Brookhaven Summer Study on Storage Rings, Accelerators and Experimentation at Super-High Energies* (BNL-7534, 1963) p. 324 (Brookhaven National Laboratory, Upton, New York, 1963).

[9] H. Chang, "The Hose Instability of a Finite, Pinched, Relativistic, Electron Beam Penetrating an Infinite, Field-Free Temperature Plasma," Stanford Research Institute Technical Report 201 (Stanford Research Institute, Menlo Park, California, 1963) (unpublished).

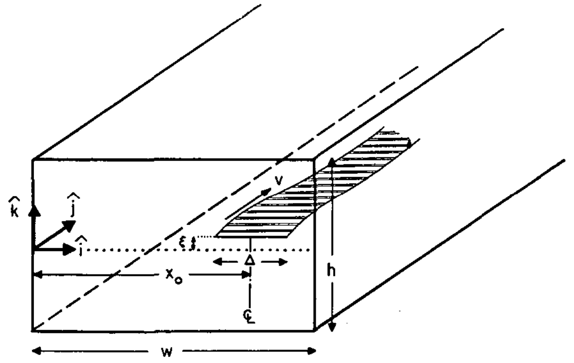

FIG. 1. The geometry of the beam and vacuum tank for the model with rectangular cross section.

charge density ρ and current density j_y are thus

$$\rho=\begin{cases}\lambda G(x)/\tau, & |z|<\tau/2\\ 0, & |z|>\tau/2,\end{cases} \qquad (2.1\text{a})$$

$$j_y=v\rho,$$

with λ the charge per unit length. The function $G(x)$ is normalized so that

$$\int_0^w G(x)dx=1.$$

All particles move in the y direction with speed v. For purposes of this section it is assumed that the perturbation consists of a rigid displacement of the entire beam. Every particle in the beam at position y and time t is displaced a distance Δz given by

$$\Delta z=\xi e^{i(ky-\omega t)}, \qquad (2.2)$$

where ξ is a constant and $\xi\ll\tau$. The perturbation gives rise to no azimuthal bunching. The electric and magnetic fields arising from the perturbation have the following sources

$$\rho_1=\rho_t-\rho,\quad j_{y1}=j_{yt}-j_y,\quad j_{z1}=j_{zt}, \qquad (2.3)$$

where a subscript t indicates the total quantity and a subscript 1 a perturbed quantity. Equilibrium quantities carry no subscript. It is apparent from the preceding equations that

$$\rho_1=(\lambda/\tau)\xi G(x)[\delta(z-\tau/2)-\delta(z+\tau/2)]e^{i(ky-\omega t)}, \qquad (2.4\text{a})$$

$$j_{1y}=\rho_1 v, \qquad (2.4\text{b})$$

$$j_{1z}=\begin{cases}i(kv-\omega)(\lambda/\tau)\xi G(x)e^{i(ky-\omega t)}, & |z|<\tau/2\\ 0, & |z|>\tau/2.\end{cases} \qquad (2.4\text{c})$$

Since the instability is characterized by frequencies and wave numbers such that $(\omega/kv)^2\ll1$, we treat ω/kv as negligible and solve the following quasistatic equations for the perturbed fields:

$$\nabla\cdot\mathbf{E}_1=4\pi\rho_1,\quad \nabla\times\mathbf{E}_1=0, \qquad (2.5)$$
$$\nabla\cdot\mathbf{B}_1=0,\quad \nabla\times\mathbf{B}_1=4\pi\mathbf{j}/c.$$

Gaussian units are used throughout this work. Only the contribution to $\mathbf{E}_1$ from the finite conductivity [Eq. (2.11) below] has nonzero curl. Solutions to the complete Maxwell's equations also have been obtained, and the resulting vertical force per unit charge is presented below [Eq. (2.17b)]. Some of the numerical examples in Sec. V utilize this complete expression. We first present field expressions that satisfy the boundary conditions appropriate to walls of infinite conductivity. Expressions for the fields must satisfy Eq. (2.5) and the condition that the normal component of $\mathbf{B}_1$ and the tangential component of $\mathbf{E}_1$ vanish at the walls of the pipe ($z=\pm h/2$, $x=0$, and $x=w$). The fields must satisfy the appropriate discontinuity conditions at $z=\pm\tau/2$. We expand the function $G(x)$ in a Fourier series

$$G(x)=(2/w)\sum_s g_s\sin\eta x, \qquad (2.6)$$

with $\eta=s\pi/w$ and s an integer. The dimensionless quantities g_s are given by

$$g_s=\int_0^w G(x)\sin\eta x dx. \qquad (2.7)$$

The subscript s on η has been suppressed for brevity throughout the rest of this report.

It may be verified that Eqs. (2.5) as well as the boundary conditions are satisfied by the following expressions: In the regions $|z|>\tau/2$ we have

$$\mathbf{E}_1=\sum_s A_s\{\sinh\ell(z\mp h/2)[\eta\cos\eta x\hat{\imath}+ik\sin\eta x\hat{\jmath}]$$
$$+\ell\cosh\ell(z\mp h/2)\sin\eta x\hat{k}\}, \qquad (2.8\text{a})$$

and

$$\mathbf{B}_1=\sum_s B_s\{\cosh\ell(z\mp h/2)[\eta\sin\eta x\hat{\imath}-ik\cos\eta x\hat{\jmath}]$$
$$-\ell\sinh\ell(z\mp h/2)\cos\eta x\hat{k}\}, \qquad (2.8\text{b})$$

where $\hat{\imath}$, $\hat{\jmath}$, and $\hat{k}$ are unit vectors along the coordinate axes, and $\ell^2=k^2+\eta^2$. The upper signs apply for $z>\tau/2$ and the lower signs for $z<-\tau/2$. In the region $|z|<\tau/2$ we have

$$\mathbf{E}_1=\sum_s C_s\{\sinh\ell z\,[\eta\cos\eta x\hat{\imath}+ik\sin\eta x\hat{\jmath}]$$
$$+\ell\cosh\ell z\sin\eta x\hat{k}\}, \qquad (2.9\text{a})$$

$$\mathbf{B}_1=\sum_s D_s\{\cosh\ell z\,[\eta\sin\eta x\hat{\imath}-ik\cos\eta x\hat{\jmath}]$$
$$-\ell\sinh\ell z\cos\eta x\hat{k}\}$$
$$+\frac{8\pi i(kv-\omega)}{w\tau}\lambda\xi\sum_s\frac{g_s}{\ell^2c}[ik\sin\eta x\hat{\imath}-\eta\cos\eta x\hat{\jmath}]. \qquad (2.9\text{b})$$

The factor $\exp[i(ky-\omega t)]$ is understood to be appended to each of the above expressions. In accordance with an earlier remark, we neglect ω/kv compared to unity in what follows. The coefficients A_s, B_s, C_s, and D_s are to be determined from the jump conditions at $z=\pm\tau/2$.

With finite conductivity in the top and bottom surfaces, $\mathbf{E}_1$ and $\mathbf{B}_1$ must satisfy the conditions

$$E_{1x}=(1-i)\mathcal{R}B_{1y},\quad E_{1y}=-(1-i)\mathcal{R}B_{1x} \tag{2.10a}$$

on the top surface $(z=h/2)$, and

$$E_{1x}=-(1-i)\mathcal{R}B_{1y},\quad E_{1y}=(1-i)\mathcal{R}B_{1x} \tag{2.10b}$$

on the bottom surface $(z=-h/2)$, where $\mathcal{R}=(\omega/8\pi\sigma)^{\frac{1}{2}}$ and σ is the conductivity of the wall material in sec^{-1}. Satisfaction of these conditions can be accomplished by adding small corrections $\mathbf{E}_1'$ and $\mathbf{B}_1'$ to the fields in the regions $|z|>\tau/2$. We may express $\mathbf{E}_1'$ as

$$\mathbf{E}_1'=\mp(1-i)\mathcal{R}e^{i(ky-\omega t)}\sum_s B_s\cosh\ell(z\mp h/2)\times[ik\cos\eta x\hat{\imath}+\eta\sin\eta x\hat{\jmath}], \tag{2.11}$$

which is valid for $|z|>\tau/2$. This contribution to the electric field has no component in the z direction and thus cannot contribute to the vertical force on the beam other than through its effect on the coefficients A_s and C_s. The effect is small compared to the contribution from $\mathbf{B}_1'$, and we shall in fact use only Eqs. (2.8a) to (2.9a) to determine A_s and C_s. The field given by Eq. (2.11) serves merely to determine $\mathbf{B}_1'$ in the regions $|z|>\tau/2$. From the equation

$$\nabla\times\mathbf{E}_1'=-(1/c)(\partial\mathbf{B}_1'/\partial t) \tag{2.12}$$

we derive

$$\mathbf{B}_1'=\mp e^{i(ky-\omega t)}\sum_s B_sZ_s\{\sinh\ell(z\mp h/2)\times[\eta\sin\eta x\hat{\imath}-ik\cos\eta x\hat{\jmath}]-\ell\cosh\ell(z\mp h/2)\cos\eta x\hat{k}\}, \tag{2.13}$$

where $Z_s=(1+i)\mathcal{R}c\ell/\omega$. Note that B_{1x}' and B_{1y}' are zero at $z=\pm h/2$, so that Eqs. (2.10) remain satisfied.

Equation (2.9b) is sufficiently general to represent the entire magnetic field (including the contribution from finite conductivity) in the region $\tau/2>|z|$ provided the coefficients D_s are properly chosen. Using Eqs. (2.8a) and (2.9a) for the electric field together with Eqs. (2.4a) and (2.6) for the surface-charge density at $z=\tau/2$, we obtain

$$A_s=(8\pi\lambda/\tau)\xi g_s\sinh(\ell\tau/2)/w\ell\sinh(\ell h/2), \tag{2.14a}$$

$$C_s=(8\pi\lambda/\tau)\xi g_s\sinh[\ell(\tau-h)/2]/w\ell\sinh(\ell h/2). \tag{2.14b}$$

Analogously, using Eqs. (2.8b), (2.9b), and (2.13) for the magnetic field, we obtain

$$B_s=\frac{8\pi\eta\beta\lambda\xi g_s\sinh(\ell\tau/2)}{\tau\ell^2w[\sinh(\ell h/2)+Z_s\cosh(\ell h/2)]}, \tag{2.15a}$$

$$D_s=\frac{8\pi\eta\beta\lambda\xi g_s\{\sinh[\ell(\tau-h)/2]-Z_s\cosh[\ell(\tau-h)/2]\}}{\tau\ell^2w[\sinh(\ell h/2)+Z_s\cosh(\ell h/2)]}. \tag{2.15b}$$

Since the boundary conditions [Eqs. (2.10a) and (2.10b)] are valid only to first order in $\mathcal{R}$, we keep Z_s to first order in D_s, which leaves

$$D_s=\frac{8\pi\eta\beta\lambda\xi g_s}{\ell^2w\tau\sinh(\ell h/2)}\left\{\sinh[\ell(\tau-h)/2]-Z_s\frac{\sinh(\ell\tau/2)}{\sinh(\ell h/2)}\right\}. \tag{2.16}$$

In the next section we employ a vertical force per unit charge $\langle E_{1z}-\beta B_x\rangle$ found by averaging the quantity $E_{1z}-\beta B_{1x}$ over the width of the beam. This average is obtained by multiplying by $G(x)$ and integrating over x. The result of this operation is to replace the factor $g_s\sin\eta x$ by g_s^2 in the expressions for E_{1z} and B_{1x}. Furthermore, we consider the products $\ell\tau$ and ℓz to first order only in these expressions. Using Eqs. (2.9), (2.14b), and (2.16) with the definition of Z_s, and making some simplifications, we obtain

$$\langle E_{1z}-\beta B_{1x}\rangle=\frac{4\pi\lambda\xi}{\tau w}\sum_s g_s^2\left\{\ell\tau\left[\gamma^{-2}+\left(\frac{k\beta}{\ell}\right)^2\right]\coth\left(\frac{\ell h}{2}\right)-2\gamma^{-2}+(1+i)\left(\frac{c\tau}{\omega}\right)\mathcal{R}\left[\eta\beta\operatorname{csch}\left(\frac{\ell h}{2}\right)\right]^2\right\}, \tag{2.17a}$$

where $\gamma^{-2}=1-\beta^2$. Note that the factor $\exp[i(ky-\omega t)]$ is not included. Treating ℓh to all orders while keeping only first-order terms in $\ell\tau$ and ℓz is valid if $\tau\ll h$. In the examples given in Sec. V, it turns out that it is also a good approximation to treat ℓh to first order only; thus the restriction $\tau\ll h$ is really not imposed.

If the complete Maxwell's equations are solved with the same sources and boundary conditions as above, the following expression for $\langle E_{1z}-\beta B_{ix}\rangle$ results:

$$\langle E_{1z}-\beta B_{1x}\rangle=\frac{4\pi\lambda\xi}{\tau w}\sum_s g_s^2\left\{\left[\frac{\mu}{\gamma^2}+\frac{k^2}{\mu}(\beta_w-\beta)^2\right]\tau\coth\left(\frac{\mu h}{2}\right)-\frac{2}{\gamma^2}+(1+i)\frac{c\tau\mathcal{R}}{\omega\mu^2}\left[\mu^4\beta^2+\mu^2k^2(\beta_w^2-\beta^2)+\left(\frac{k\omega}{c}\right)^2(\beta_w-\beta)^2\right]\operatorname{csch}^2(\mu h/2)\right\}, \tag{2.17b}$$

with $\mu^2=\ell^2-(\omega/c)^2$ and $\beta_w=\omega/kc$. We have kept $\mu\tau$ to first order only. Equation (2.17a) results if we set $\beta_w=0$ in Eqs. (2.17b).

B. Circular Cross Section

The second geometry we consider is that of Fig. 2, in which both the beam and the wave guide have circular cross sections. If, as above, we consider a beam with uniform density rigidly displaced in the z direction, it is possible to derive simple expressions for the perturbed

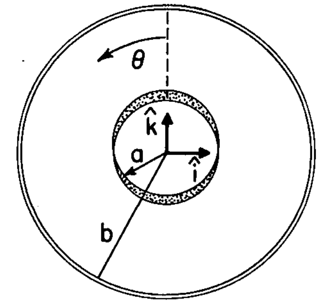

FIG. 2. The geometry of the beam and vacuum tank for the model with circular cross section.

fields. These expressions are valid provided second-order terms in kb are negligible compared to unity; this is true if the wavelength of the perturbation is very much larger than the radius of the pipe. Except for the contribution from finite wall conductivity, the following treatment does not include components of $\mathbf{E}_1$ and $\mathbf{B}_1$ along the pipe (y components). These are indeed first order in kr, but since they do not enter into the transverse force on the beam, we shall not concern ourselves with them.

In cylindrical coordinates (r,θ,y) we have the following sources for the fields:

$$\rho_1=\rho_0\xi\cos\theta\,\delta(r-a)e^{i(ky-\omega t)}, \tag{2.18a}$$

$$j_{1y}=\rho_1 v, \tag{2.18b}$$

with ρ_0 the charge density in the unperturbed beam. It is not necessary to include j_{1z} as a source in order to obtain the transverse force within the limits of this approximation. We can in fact consider $k=0$ except in the exponential factor, since no first-order terms in k occur. Inside the beam we have uniform E_{1z} and B_{1x} as the only field components needed to satisfy Eqs. (2.5). In cylindrical coordinates these components become

$$\mathbf{E}_1=E_{1z}(\cos\theta\hat{r}-\sin\theta\hat{\theta})e^{i(ky-\omega t)}, \tag{2.19a}$$

$$\mathbf{B}_1=B_{1x}(\sin\theta\hat{r}+\cos\theta\hat{\theta})e^{i(ky-\omega t)}, \tag{2.19b}$$

with $\hat{r}$ and $\hat{\theta}$ unit vectors. In the region $a<r<b$ we have

$$\mathbf{E}_1=\mathcal{E}\{[(b/r)^2+1]\cos\theta\hat{r} \\ +[(b/r)^2-1]\sin\theta\hat{\theta}\}e^{i(ky-\omega t)}, \tag{2.20a}$$

$$\mathbf{B}_1=\mathcal{B}\{[(b/r)^2-1]\sin\theta\hat{r} \\ -[(b/r)^2+1]\cos\theta\hat{\theta}\}e^{i(ky-\omega t)}. \tag{2.20b}$$

The procedure we employ now deviates from that used with rectangular geometry. We first evaluate the coefficients in Eqs. (2.19) and (2.20), then add contributions $\mathbf{E}_1'$ and $\mathbf{B}_1'$ arising from finite wall conductivity. The usual conditions at $r=a$ yield

$$E_{1z}=-2\pi\rho_0\xi[1-(a/b)^2],\quad \mathcal{E}=2\pi\rho_0\xi(a/b)^2, \tag{2.21a}$$

$$B_{1x}=\beta E_{1z},\qquad \mathcal{B}=-\beta\mathcal{E}. \tag{2.21b}$$

Whereas in the pipe of rectangular cross section it was possible to satisfy the conditions Eqs. (2.10a) and (2.10b) exactly, it is now possible to satisfy the condition

$$E_{1y}'=-(1-i)\mathcal{R}B_{1\theta} \tag{2.22}$$

only to first order in $\mathcal{R}$. We add a contribution E_{1y}' that satisfies Eq. (2.22), with Eqs. (2.20b) and (2.21b) inserted for $B_{1\theta}$. In the limit $k\to 0$, the expression for E_{1y}' is simply

$$E_{1y}'=-4\pi\beta\rho_0\xi(a/b)^2(1-i)\mathcal{R}(r/b)\cos\theta e^{i(ky-\omega t)}, \tag{2.23}$$

which is valid for all values of r. We determine $\mathbf{B}_1'$ from Eqs. (2.12) and (2.23),

$$\mathbf{B}_1'=-4\pi\beta\rho_0\xi(a/b)^2(1+i)(c\mathcal{R}/\omega b) \\ \times(\sin\theta\hat{r}+\cos\theta\hat{\theta})e^{i(ky-\omega t)}. \tag{2.24}$$

Note that $\mathbf{B}_1'$ is not equal to zero at $r=b$, and that is why Eq. (2.22) is satisfied to first order only. This expression is valid for all values of r.

The vertical force per unit charge $E_{1z}-\beta B_{1x}$ must now include the contributions from Eqs. (2.19) and (2.24). We again use brackets for consistent notation, although in this geometry they do not imply any averaging process. The factor $\exp[i(ky-\omega t)]$ is again omitted, and we have

$$\langle E_{1z}-\beta B_{1x}\rangle=-2\pi\rho_0\xi\{\gamma^{-2}[1-(a/b)^2] \\ -2(\beta a/b)^2(1+i)(c\mathcal{R}/\omega b)\}. \tag{2.25}$$

III. DERIVATION OF THE DISPERSION RELATION

In order to study the dynamics of particles in an accelerator, we employ the Vlasov equation in cylindrical coordinates r, θ, z, instead of rectangular coordinates x, y, z. Here θ should not be confused with the notation of Sec. II.B and Fig. 2. We make the substitution $ky\to n\theta$, $y\to R\theta$ in the formulas for the vertical force, where R is the radius at which the beam circulates. The particle-distribution function ψ is a function of z, P_z, θ, and W, where $W=2\pi(P_\theta-P_0)$ is 2π times the deviation in canonical angular momentum from the average value for particles in the beam. The equation satisfied by the total distribution ψ_t is

$$\frac{\partial\psi_t}{\partial t}+\dot{\theta}\frac{\partial\psi_t}{\partial\theta}+\langle\dot{W}\rangle\frac{\partial\psi_t}{\partial W}+\dot{z}\frac{\partial\psi_t}{\partial z}+\langle\dot{P}_z\rangle\frac{\partial\psi_t}{\partial P_z}=0, \tag{3.1}$$

where, as in the previous section, brackets indicate an average over the width of the beam when applicable.

In the equilibrium configuration, W is a constant of the motion. We shall take the amplitude a of axial betatron oscillations as the second constant of the motion, and choose the equilibrium distribution function ψ of the form

$$\psi=Nh(a)f(W)/(2\pi)^2R, \tag{3.2}$$

where N is the total number of particles in the beam. The functions h and f are normalized so that

$$\int h(a)ada=1,\quad \int f(W)dW=1, \tag{3.3}$$

Under the influence of the perturbation, we have

$$\psi_t=\psi(W,a)+\psi_1(W,a)e^{i(n\theta-\omega t)}, \tag{3.4a}$$

$$\langle\dot{P}_{zt}\rangle=\langle\dot{P}_z\rangle+e\langle E_{1z}-\beta B_{1x}\rangle e^{i(n\theta-\omega t)}, \tag{3.4b}$$

$$\langle\dot{W}_t\rangle=\langle\dot{W}_1\rangle, \tag{3.4c}$$

where the appropriate expression, Eq. (2.17) or Eq. (2.25), is to be used for $\langle E_{1z}-\beta B_{1x}\rangle$. We are not considering azimuthal density variations, in which case $\langle\dot{W}_1\rangle$ is negligible. Inserting Eqs. (3.4) into Eq. (3.1) and linearizing leads to

$$i(n\dot{\theta}-\omega)\psi_1+\dot{z}\frac{\partial\psi_1}{\partial z}+\langle\dot{P}_z\rangle\frac{\partial\psi_1}{\partial P_z}=-e\langle E_{1z}-\beta B_{1x}\rangle\frac{\partial\psi}{\partial P_z}. \tag{3.5}$$

We now assume that $\dot{P}_z$ is linear in z so that the equations of motion for a particle in the unperturbed beam are

$$\ddot{z}+\nu_z^2\Omega^2 z=0, \tag{3.6a}$$

$$\dot{\theta}\equiv\Omega=\omega_0+k_0W, \tag{3.6b}$$

where ν_z is the axial betatron wavenumber, ω_0 is the average particle circulation frequency, and k_0 is a characteristic parameter of the accelerator. Equation (3.6a) is only approximate because ν_z (as well as Ω) is actually a function of a and the motion is not simple harmonic. This fact is very important, and in the next section is shown to be the major stabilizing mechanism. However, for the purpose of solving Eq. (3.5), it is sufficient to write the solutions to Eqs. (3.6) as

$$z=a\sin\phi, \tag{3.7a}$$

$$P_z=m\nu_z a\cos\phi, \tag{3.7b}$$

$$\theta=\Omega t, \tag{3.7c}$$

in which $\phi=\nu_z\Omega t$, and m is the average relativistic transverse mass of particles in the beam.

With the above approximations it is easy to show that Eq. (3.5) may be written

$$i(n\Omega-\omega)\psi_1+\nu_z\Omega(\partial\psi_1/\partial\phi)=-e\langle E_{1z}-\beta B_{1x}\rangle(\partial\psi/\partial P_z). \tag{3.8}$$

Furthermore, neglecting the dependence of ν_z on a, we have

$$\frac{\partial\psi}{\partial P_z}=\frac{\partial\psi}{\partial a}\frac{\partial a}{\partial P_z}=\frac{\cos\phi}{m\nu_z\Omega}\frac{\partial\psi}{\partial a}. \tag{3.9}$$

This approximation omits terms in ψ_1 that are first order in the quantity $(a^2/\nu_z)(\partial\nu_z/\partial a^2)$. These small terms have little influence on the results. With Eq. (3.9) used in Eq. (3.8), we have a first-order equation in one variable. After some simplification, the solution may be written as

$$\psi_1=\frac{-ie\langle E_{1z}-\beta B_{1x}\rangle}{m\nu_z\Omega}\frac{\partial\psi}{\partial a}\left[\frac{(\omega-n\Omega)\cos\phi+i\nu_z\Omega\sin\phi}{(\omega-n\Omega)^2-\nu_z^2\Omega^2}\right]. \tag{3.10}$$

From our perturbed distribution function ψ_1 we now compute a dipole moment per unit length $P(\theta,t)=pe^{i(n\theta-\omega t)}$, where

$$p=e\int z\psi_1 a\,da\,d\phi\,dW. \tag{3.11}$$

Inserting Eqs. (3.10) and (3.7a) and performing the ϕ integration, we have

$$p=(\pi e^2/m)\langle E_{1z}-\beta B_{1x}\rangle\int(\partial\psi/\partial a)a^2\,da\,dW. \tag{3.12}$$

We come now to the basic approximation in our treatment. In general the distribution functions ψ and ψ_1 will not lead to current and charge distributions consistent with those assumed in Sec. II. Therefore the expressions for $\langle E_{1z}-\beta B_{1x}\rangle$ are not strictly applicable. In particular, the perturbed force may have z dependence other than the weak function $\cosh\ell z$, which we have approximated to unity. A general self-consistent analytic treatment of an arbitrary ψ seems impossible. However, investigation has shown that physically reasonable axial distributions of particles in the unperturbed beam lead to a vertical force that is quite well approximated by the treatment in Sec. II, so long as the conditions $\ell\tau\ll 1$ or $ka\ll 1$ are satisfied. To complete the quasi-self-consistent treatment here, we equate the dipole moment per unit length p with the quantity $\lambda\xi$ in Eq. (2.17) and with $\pi\rho_0a^2\xi$ in Eq. (2.25).

Inserting ψ from Eq. (3.2) and $\langle E_{1z}-\beta B_{1x}\rangle$ from Eq. (2.17) into Eq. (3.13), we derive the dispersion relation

$$1=\frac{e^2NI}{mwR}\sum_s g_s^2\left\{\left[\gamma^{-2}+\left(\frac{k\beta}{\ell}\right)^2\right]\ell\coth\left(\frac{\ell h}{2}\right)\right.$$
$$\left.-\left(\frac{2}{\gamma^2\tau}\right)+(1+i)\left(\frac{c\mathcal{R}}{\omega}\right)\left[\eta\beta\operatorname{csch}\left(\frac{\ell h}{2}\right)\right]^2\right\}, \tag{3.13}$$

where

$$I=\int\frac{h'(a)f(W)a^2\,da\,dW}{[(\omega-n\Omega)^2-\nu_z^2\Omega^2]}. \tag{3.14}$$

If Eq. (2.25) for $\langle E_{1z}-\beta B_{1x}\rangle$ is employed, we obtain

$$1=-\frac{e^2NI}{2\pi mRa^2}\left\{\gamma^{-2}\left[1-\left(\frac{a}{b}\right)^2\right]-2(1+i)\left(\frac{c\mathcal{R}}{\omega b}\right)\left(\frac{\beta a}{b}\right)^2\right\}. \tag{3.15}$$

It is convenient to introduce the quantities U_r and V_r by the definitions

$$U_r=\frac{e^2N}{\nu_z\omega_0\gamma m_0wR}\sum_s g_s^2\left\{\left[\gamma^{-2}+\left(\frac{k\beta}{\ell}\right)^2\right]\ell\coth\left(\frac{\ell h}{2}\right)-\left(\frac{2}{\gamma^2\tau}\right)\right\}, \tag{3.16a}$$

$$V_r=\frac{e^2N\mathcal{R}\beta}{\nu_z\gamma m_0w\omega}\sum_s g_s^2\eta^2\operatorname{csch}^2\left(\frac{\ell h}{2}\right). \tag{3.16b}$$

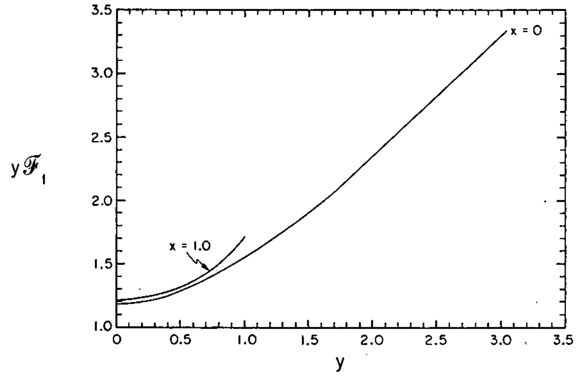

FIG. 3. The function $\mathcal{F}_1(h/w,\Delta/h)$, which is defined in Eq. (3.23a) and expresses the long-wavelength part of the real frequency shift arising from image effects. It can be seen that $\mathcal{F}_1$ is almost independent of its first argument. For large y, $\mathcal{F}_1(0,y)\rightarrow 1$; the deviation from unity being only 5% at $y=4.0$. For small y, $y\mathcal{F}_1$ approaches a constant of order-of-magnitude unity.

Alternatively, for the pipe of circular cross section we introduce U_c and V_c by the definitions

$$U_c=-e^2N[1-(a/b)^2]/2\pi\nu_z\omega_0\gamma^3m_0Ra^2, \quad (3.17a)$$

$$V_c=e^2N\beta\mathcal{R}/\pi\nu_z\gamma m_0\omega b^3. \quad (3.17b)$$

In Eqs. (3.16) and (3.17) we have replaced m by γm_0, where m_0 is the rest mass of the particle. In terms of these equations, the dispersion relation becomes

$$1=\nu_z\omega_0[U+(1+i)V]I. \quad (3.18)$$

If U_r and V_r are inserted into Eq. (3.18), it is identical to Eq. (3.13). Alternatively, if U_c and V_c are inserted, Eq. (3.18) is identical to Eq. (3.15).

If we employ the more general expression, Eq. (2.17b) for $\langle E_{1z}-\beta B_{1x}\rangle$ in the pipe of rectangular cross section, still another set of definitions for U and V results. We call these U_g and V_g. They are defined by

$$U_g=(e^2N/\nu_z\omega_0\gamma m_0wR)[\mathrm{Re}-(2/\gamma^2\tau)\sum_s g_s^2], \quad (3.19a)$$

$$V_g=(e^2N\mathcal{R}/\nu_z\omega_0\gamma m_0wR)\,\mathrm{Im}, \quad (3.19b)$$

where

$$\mathrm{Re}=\sum_s g_s^2\left\{\left[\frac{\mu}{\gamma^2}+\frac{k^2}{\mu}(\beta_w-\beta)^2\right]\coth\left(\frac{\mu h}{2}\right)\right\}, \quad (3.20a)$$

$$\mathrm{Im}=\left(\frac{c}{\omega}\right)\sum_s\left(\frac{g_s}{\mu}\right)^2[\mu^4\beta^2+\mu^2k^2(\beta_w^2-\beta^2)$$
$$+(k\omega/c)^2(\beta_w-\beta)^2]\,\mathrm{csch}^2(\mu h/2). \quad (3.20b)$$

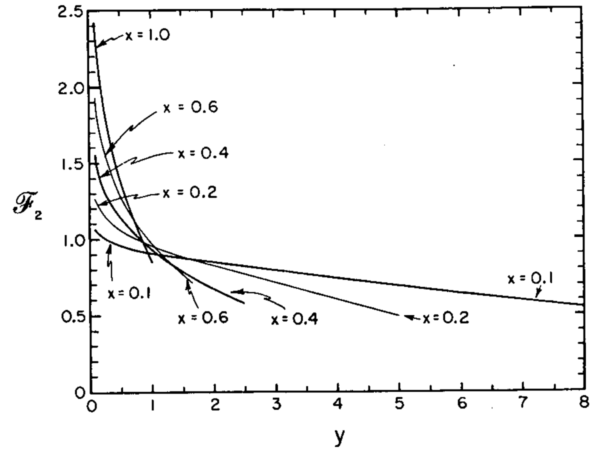

FIG. 4. The function $\mathcal{F}_2(h/w,\Delta/h)$, which is defined in Eq. (3.23a) and expresses the dominant contribution in the relativistic limit to the part of the real frequency shift arising from image effects. For most applications $x=h/w$ is small, and then $\mathcal{F}_2(x,y)$ is approximately equal to $\mathcal{F}_2(0,0)=1$ and decreases linearly with increasing second argument.

These general expressions may prove useful in some applications. We have evaluated them for a particular choice of $G(x)$ that has two parameters, namely a beam of width Δ with center located at x_0, as indicated in Fig. 1.

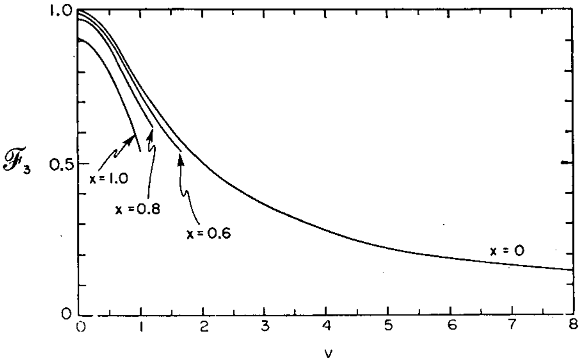

FIG. 5. The function $\mathcal{F}_3(h/w,\Delta/h)$, which is defined in Eq. (3.23b) and expresses the imaginary part of the frequency shift. The function is relatively independent of its first argument, especially as in most applications $h/w<0.5$. $\mathcal{F}_3(0,0)$ is unity, and this affords an order-of-magnitude estimate unless y is greater than unity—which usually is not the case.

The functional form taken was

$$G(x)=\begin{cases}(\pi/2\Delta)\cos[\pi(x-x_0)/\Delta], & |x-x_0|<\Delta/2\\ 0, & |x-x_0|\geqslant\Delta/2\end{cases} \quad (3.21)$$

and a 7094 FORTRAN Program was developed to evaluate the quantities Re and Im.[10]

In most applications $k\ll 1/w$ and $1/h$; and in this limit the formulas for Re and Im can be considerably simplified. Simple neglect of the k^2 terms in Eq. (3.20) would be valid, however, only in the nonrelativistic limit because the dominant k-independent term in Re varies as $1/\gamma^2$. In order to obtain formulas valid at all energies in the small k limit, we retain the k^2 correction to the $1/\gamma^2$ term in Re, but neglect k^2 in all other occurrences. Thus $\mu\approx\eta$, and Eq.

---

[10] IBM 7094 FORTRAN program MESS, Computer Center, Lawrence Radiation Laboratory, University of California, Berkeley, 1963 (unpublished).

(3.20) yields

$$\mathrm{Re}\approx\frac{1}{\gamma^2}\sum_s g_s^2\eta\coth\frac{\eta h}{2}+k^2(\beta_w-\beta)^2\sum_s g_s^2\frac{1}{\eta}\coth\frac{\eta h}{2},\tag{3.22a}$$

$$\mathrm{Im}\approx(c\beta^2/\omega)\sum_s g_s^2\eta^2\operatorname{csch}^2\eta h/2.\tag{3.22b}$$

Note that Eq. (3.22a) is *not* a valid expansion of Eq. (3.20) through terms in k^2.

For the beam configuration of Eq. (3.21), with $x_0=w/2$, and in the limit of $n\ll R/w$ and R/h, Re and Im depend upon the geometrical parameters in a simple way. Thus we may define functions $\mathcal{F}_i$ by

$$\mathrm{Re}=\frac{\pi^2 w}{8h\Delta\gamma^2}\mathcal{F}_1\left(\frac{h}{w},\ \frac{\Delta}{h}\right)+\frac{k^2(\beta_w-\beta)^2w^2}{4h}\mathcal{F}_2\left(\frac{h}{w},\ \frac{\Delta}{h}\right),\tag{3.23a}$$

$$\mathrm{Im}=(2\pi c\beta^2 w/3\omega h^3)\mathcal{F}_3(h/w,\Delta/h).\tag{3.23b}$$

There is no τ dependence in the $\mathcal{F}_i$ functions, graphs of which are presented in Figs. 3, 4, and 5. In the figure captions we summarize some of the properties of the $\mathcal{F}_i$ functions and suggest various approximations that can be employed to obtain convenient analytic formulas for Re and Im, and hence for all of the results of this paper. Numerical comparisons of Eq. (3.23) and Eq. (3.20) are presented for four very different examples in Table I, where the agreement is seen to be excellent.

From the definition of g_s [Eqs. (2.1a), (2.6), and (2.7)], it follows that

$$\sum_s g_s^2=\frac{w}{2}\int_0^w G^2(x)dx,\tag{3.24}$$

which for the distribution of Eq. (3.21) yields

$$\sum_s g_s^2=\frac{\pi^2 w}{16\Delta}.\tag{3.25}$$

Combining Eqs. (3.19), (3.23), and (3.25), we have

$$U_g=\frac{\pi^2e^2N}{8\nu_z\omega_0\gamma^3m_0hR\Delta}\left[\mathcal{F}_1\left(\frac{h}{w},\frac{\Delta}{h}\right)-\frac{h}{\tau}+\frac{2\gamma^2k^2(\beta_w-\beta)^2w\Delta}{\pi^2}\mathcal{F}_2\left(\frac{h}{w},\frac{\Delta}{h}\right)\right],\tag{3.26a}$$

$$V_g=(2\pi e^2N\beta\mathcal{R}/3\nu_z\gamma m_0h^3\omega)\mathcal{F}_3(h/w,\ \Delta/h).\tag{3.26b}$$

IV. ANALYSIS OF THE DISPERSION RELATION

In order to illustrate the characteristics of the instability, we first consider a beam with no spread in canonical angular momentum and take $f(W)=\delta(W)$. We further neglect the dependence of ν_z and Ω on a. The integral I defined by

TABLE I. A comparison between the exact computational results [Eqs. (3.20) and (3.21)] and the approximation valid for $n\ll R/h$ and R/w [Eq. (3.23)] for three different accelerators. In all cases Im is given very well by the approximate formulas. For the Bevatron and proton-storage rings, $\mathcal{F}_2$ is negligible; for the electron-storage rings, $\mathcal{F}_1$ and $\mathcal{F}_2$ give comparable contributions. In the MURA accelerator $n=3$ and $R/w=2$; so the criterion for the validity of the approximation is not satisfied, yet the approximate formula gives Re within a factor of three of the correct value and gives Im almost exactly.

Accelerator	n	R (cm)	h (cm)	w (cm)	x_0 (cm)	Δ (cm)	$\omega_0\times10^{-7}$ (sec^{-1})	ν_z	β	γ	$\mathcal{F}_1$	$\mathcal{F}_2$	$\mathcal{F}_3$	$\frac{\pi^2w}{8h\Delta\gamma^2}\mathcal{F}_1$ (cm^{-1})	$\frac{k^2(\beta_w-\beta)^2w^2}{4h}\mathcal{F}_2$ (cm^{-1})	Approximation of Eq. (3.23) Re (cm^{-1})	Approximation of Eq. (3.23) Im (cm^{-1})	Exact evaluation Re (cm^{-1})	Exact evaluation Im (cm^{-1})
Bevatron at injection energy	1	1.8×10^3	30.5	122	61	76	0.31	0.85	0.186	1.02	1.13	0.72	0.41	0.0666	6.78×10^{-7}	0.0666	8.29	0.0701	8.53
13 BeV proton storage rings	17	1.3×10^4	7.0	15	7.5	4.9	0.23	8.75	0.998	14.3	1.97	1.06	0.85	0.0052	3.86×10^{-6}	0.0052	123	0.00525	123.1
Stanford 500 MeV electron-storage rings	1	160	3.8	12.7	6.35	0.3	18.8	0.88	1.0	1000	15.2	1.4	1.0	2.09×10^{-4}	4.49×10^{-4}	6.58×10^{-4}	646	6.77×10^{-4}	637
MURA 40 MeV electron accelerator at stacking energy	3	200	5	100	90	5	15.8	2.8	1.00	70	1.55	0.91	0.76	0.0156	0.0887	0.1043	1270	0.0342	1255

Eq. (3.15) becomes simply

$$I=-2/[(\omega-n\omega_0)^2-\nu_z^2\omega_0^2], \tag{4.1}$$

[since $\int h'(a)a^2da=-2$], and from Eq. (3.18) we have

$$(\omega-n\omega_0)^2=\nu_z^2\omega_0^2-2\nu_z\omega_0(U+V+iV). \tag{4.2}$$

This is a cubic equation in ω in view of the factor $1/\omega$ in V. However if $V\lesssim U$ and $U\ll\nu_z\omega_0$ (as is generally true), two roots of Eq. (4.2) are given approximately by

$$\omega=(n\pm\nu_z)\omega_0\mp(U+V+iV), \tag{4.3}$$

with $\omega=(n\pm\nu_z)\,\omega_0$ inserted in V. The upper signs represent a "fast wave" that is damped. For $n>\nu_z$, the lower signs represent a "slow wave" that grows exponentially with an e-folding time τ_0 given by

$$\tau_0=V^{-1}. \tag{4.4}$$

For $n<\nu_z$, the lower signs represent a wave that has phase velocity in the negative θ direction. This wave is also damped because V is negative.

We are therefore interested in values of ω near $(n-\nu_z)\omega_0$. The integrand in Eq. (3.14) may be separated by partial fractions, which yields

$$[(\omega-n\Omega)^2-\nu_z^2\Omega^2]^{-1}=(2\nu_z\Omega)^{-1}\{[\omega-(n+\nu_z)\Omega]^{-1} -[\omega-(n-\nu_z)\Omega]^{-1}\}. \tag{4.5}$$

The singularity of the first term on the right-hand side is of no interest, and dropping the term will have negligible effect on the results. Further, we replace $(2\nu_z\Omega)^{-1}$ by $(2\nu_z\omega_0)^{-1}$ in Eq. (4.5). The dispersion relation then becomes

$$2=-(U+V+iV)\int\frac{h'(a)a^2da\,f(W)dW}{[\omega-(n-\nu_z)\Omega]}. \tag{4.6}$$

The only mechanism effective in stabilizing the beam against vertical oscillations is a spread in the quantity S defined by

$$S\equiv(n-\nu_z)\Omega. \tag{4.7}$$

In general both ν_z and Ω are functions of a and W. We may write

$$\Omega=\omega_0+(\partial\Omega/\partial W)W+(\partial\Omega/\partial a^2)a^2, \tag{4.8a}$$

$$\nu_z=\nu+(\partial\nu_z/\partial W)W+(\partial\nu_z/\partial a^2)a^2. \tag{4.8b}$$

The quantity $\partial\Omega/\partial W$ is equal to k_0, where k_0 was defined by Eq. (3.6b). The dependence of Ω on a^2 is quite weak, so we will neglect the a^2 term in Eq. (4.8a). The quantities U and V defined in the previous section are not independent of ω, but it is a good approximation to replace ω by $(n-\nu)\omega_0$ in these expressions. Further, whenever ν_z occurs in U and V we shall replace it with ν, thus neglecting the dependence of U and V on a and W. For purposes of the dispersion analysis, U and V are simply constants.

We now introduce some short-hand notation for use in what follows. Let $y=a^2$ and let S_w and S_y be given by

$$S_w\equiv\partial S/\partial W=(n-\nu)k_0-\omega_0(\partial\nu_z/\partial W), \tag{4.9a}$$

$$S_y\equiv\partial S/\partial y=-\omega_0(\partial\nu_z/\partial y). \tag{4.9b}$$

Since we are searching for a solution to Eq. (4.6) in the region $\omega\approx(n-\nu)\omega_0$, we define a quantity δ by

$$\delta=\omega-(n-\nu)\omega_0. \tag{4.10}$$

Using this notation and noting that $a^2(dh/da)da=y(dh/dy)dy$, we may rewrite Eq. (4.6) as

$$-\frac{2(U+V-iV)}{[(U+V)^2+V^2]}=\int\frac{(dh/dy)ydy\,f(W)dW}{[\delta-S_wW-S_yy]}. \tag{4.11}$$

A spread in both W and y can be treated only with great difficulty, so we consider the effect of each separately. First let S_y be zero, and consider a spread in W. There is some question as to the validity of this, since the dynamics of the $W-\theta$ motion were disregarded in the previous section when we neglected the $\dot{W}_1$ in the Vlasov equation. It seems proper, however, to consider the stabilizing effect of a spread in W, since the axial betatron frequency of a particle does depend on its canonical angular momentum. The choice of $f(W)$ is fraught with pitfalls, as discussed in the companion paper.[3] In particular, we must choose $f(W)$ such that $f'(W)\rightarrow0$ as $f(W)\rightarrow0$ for some maximum value W_m in order that the stability criterion be valid in the limit $V\rightarrow0$. However, a Gaussian distribution gives a fairly realistic stability criterion. We choose

$$f(W)=(1/\pi^{\frac12}q)e^{-W^2/q^2}, \tag{4.12}$$

and Eq. (4.11) becomes

$$\frac{S_wq(U+V-iV)}{[(U+V)^2+V^2]}=\mp\frac{1}{\pi^{\frac12}}\int_{-\infty}^{\infty}\frac{e^{-x^2}dx}{x-x_1}\equiv\mp\mathfrak{z}(x_1), \tag{4.13}$$

in which $x_1=\delta/q|S_w|$. The minus sign on the right applies if $S_w>0$ and the plus sign for $S_w<0$. The stability criterion is independent of the signs of S_w and $U+V$. Equation (4.13) is in general useful for specific numerical examples and should be used in conjunction with tables of the function $\mathfrak{z}(x_1)$.[11] We are interested in solutions for real x_1 (real δ). The ratio $V/(U+V)$ determines x_1, and the value of q required for stability is then found from either the real or imaginary parts of the equation.

As an example, consider the equation when $|U|\ll V$. The real and imaginary parts of the left-hand side are both approximately equal to $S_wq/2V$. The value of x_1 satisfying $\mathrm{Re}\,\mathfrak{z}(x_1)=\mathrm{Im}\,\mathfrak{z}(x_1)$ is $x_1=0.7$. We have $\mathrm{Re}\,\mathfrak{z}(0.7)=1.03$, and thus $S_wq\gtrsim2.06V$ is the stability criterion. The frequency shift δ is equal to $1.44V$ at the stability limit.

---

[11] B. D. Fried and S. D. Conte, *The Plasma Dispersion Function* (Academic Press Inc., New York, 1961).

An example of general interest is that for which $|U| \gg V$. We must choose x_1 such that $|\mathrm{Re}\,\mathfrak{z}(x_1)| \gg \mathrm{Im}\,\mathfrak{z}(x_1)$, which is satisfied for large x_1 where the asymptotic expansion is valid. This expansion is

$$\mathfrak{z}(x_1) = i\pi^{\frac{1}{2}} \exp(-x_1^2) - 1/x, \tag{4.14}$$

and from the real part of Eq. (4.13) we have $x_1 \approx U/q|S_w|$, or $\delta = U$. The frequency shift is the same as if no damping were present. The criterion for stability may be found by solving the transcendental equation

$$x_1 e^{-x_1^2} = V/\pi^{\frac{1}{2}} U \tag{4.15}$$

for x_1 and thus the value of q necessary for stability. However, we note that the dispersion relation cannot be satisfied if the frequency shift δ lies outside the range of S in the beam. Any realistic $f(W)$ will extend over a finite range, $-W_m < W < W_m$. Provided the condition $|U| \gg V$ holds, a necessary criterion for stability is $|S_w| W_m > |U|$, or

$$|(n-\nu)k_0 - \omega_0(\partial\nu/\partial W)| W_m > |U|. \tag{4.16}$$

We now consider stabilization by means of the nonlinearities in the accelerator as characterized by S_y. We set $S_w = 0$ in Eq. (4.11) [or $f(W) = \delta(W)$], which then becomes

$$\frac{2S_y(U+V-iV)}{[(U\pm V)^2+V^2]} = \int_0^\infty \frac{(dh/dy)y\,dy}{y-y_1}, \tag{4.17}$$

with $y_1 = \delta/S_y$. As S_y may be either positive or negative, care must be taken in evaluating the imaginary part of the integral. We note that for real y_1, solutions exist only for $y_1 > 0$, and therefore δ has the sign of S_y. For $S_y > 0$, $\mathrm{Im}\delta > 0$ corresponds to $\mathrm{Im}y_1 > 0$. Thus in the limit $\mathrm{Im}\delta \rightarrow 0$ (the stability limit), the pole in the complex y plane approaches the real axis from above. The opposite is true if $S_y < 0$. With this in mind we write Eq. (4.17) in a form valid for real y_1,

$$\frac{2S_y(U+V-iV)}{[(U+V)^2+V^2]} = \mathcal{P}\int_0^\infty \frac{(dh/dy)y\,dy}{y-y_1} \pm i\pi y_1\left(\frac{dh}{dy}\right)_{y=y_1}, \tag{4.18}$$

where $\mathcal{P}$ indicates the principal value. The plus sign is used if $S_y > 0$, the minus sign if $S_y < 0$. Equation (4.18) will be satisfied only for those values of y_1 for which $h'(y_1) < 0$. In addition, $U+V$ may be positive or negative. This fact caused no concern in the previous example where the sign of $S_w(U+V)$ merely determined the sign of δ. Here the sign of $S_y(U+V)$ has a more important role, as we shall see below.

In order that the theory be valid in the limit $|U| \gg V$, the function $h(y)$ must have the property that $h' \rightarrow 0$ as $h \rightarrow 0$ for some maximum value $y = y_m$. It is not necessary that h' be zero at any other value of y, but the condition $yh'(y) \rightarrow 0$ as $y \rightarrow 0$ is necessary. It seems reasonable that any realistic distribution of betatron amplitudes will have these properties. As a useful example we choose

$$h(y) = (6/y_m)(1-y/y_m)^2, \tag{4.19}$$

a monotonically decreasing function of y. We shall examine this form in detail, and then merely state the results obtained from other distributions. Differentiating Eq. (4.19) with respect to y and inserting the result in Eq. (4.18) yields

$$\rho(1-\rho) = |S_y| y_m V/6\pi[(U+V)^2+V^2], \tag{4.20}$$

with $\rho \equiv y_1/y_m$. The principal-value integral is easily evaluated, and from the real terms in Eq. (4.18) we have

$$\tfrac{1}{2} - \rho + \rho(1-\rho)\ln\left(\frac{1-\rho}{\rho}\right) = -\frac{S_y y_m(U+V)}{6[(U+V)^2+V^2]}. \tag{4.21}$$

Dividing Eq. (4.21) by Eq. (4.20), we have

$$\frac{1}{2\rho(1-\rho)} - \frac{1}{(1-\rho)} + \ln\left(\frac{1-\rho}{\rho}\right) = -S_y\pi(U+V)/V|S_y|, \tag{4.22}$$

from which the appropriate value of ρ may be obtained.

Consider first the conditions $S_y(U+V) > 0$ and $|U| \gg V$. The right-hand side of Eq. (4.22) is a large negative number and therefore ρ must be very nearly unity. We neglect the logarithm, set $\rho(1-\rho)$ equal to $1-\rho$ in Eqs. (4.20) and (4.22), and obtain

$$|S_y| y_m \gtrsim 3U, \tag{4.23}$$

a stability criterion independent of V. The frequency shift δ, which is equal to $S_y y_1$, is very nearly equal to $S_y y_m$. If $S_y(U+V) < 0$ and $|U| \gg V$, the right-hand side of Eq. (4.22) is a large positive number, and therefore ρ must be very small compared to unity. The first term on the left-hand side of Eq. (4.22) dominates. We set $\rho(1-\rho) = \rho$ in both Eqs. (4.20) and (4.22) to again obtain $|S_y| y_m \gtrsim 3U$ for the stability criterion. But notice that $\delta = S_y y_m \rho$ is now very much less (in absolute value) than $S_y y_m$. Thus in the limit $|U| \gg V$ the sign of $S_y(U+V)$ does not affect the stability criterion, but it does determine the magnitude of the frequency shift. Numerical analysis of Eq. (4.22) shows that the above stability criterion is quite a good approximation for $|U| > 5V$.

We next consider the limit $|U| \ll V$. If $S_y > 0$, the right-hand side of Eq. (4.22) is approximately equal to $-\pi$ and a value of $\rho \approx 0.8$ results. If $S_y > 0$, the right-hand side of Eq. (4.22) is $\approx +\pi$ and a value of $\rho \approx 0.2$ results. But in either case, the left-hand side of Eq. (4.20) is approximately equal to 0.16, and the criterion for stability becomes

$$|S_y| y_m \gtrsim 2\pi V, \tag{4.24}$$

independently of the sign of S_y. In the event that $U+V\ll V$, the right-hand side of Eq. (4.22) is very small and the equation is satisfied by $\rho=0.5$. From Eq. (4.20) we obtain the criterion

$$|S_y|y_m \geqslant 3\pi V/2. \qquad (4.25)$$

The numerical factors in Eqs. (4.23), (4.24), and (4.25) result from the particular form of $h(y)$ chosen. With the one exception discussed below, the qualitative dependence of the stability criterion upon U and V is not sensitive to the form of $h(y)$. The exception is a distribution $h(y)$ that is constant out to some value $y=Y$, then falls to zero at $y=Y+\Delta$, where $\Delta\ll Y$. This distribution closely resembles that experimentally determined for the stacked beam in the MURA electron accelerator.[4] Analysis of such a distribution reveals that only the quantity Δ enters the criterion for stability. In the investigation, only the limit $U\gg V$ was considered, and the resulting stability criterion is

$$|S_y|\Delta \geqslant U. \qquad (4.26)$$

The spread in betatron amplitudes characterized by Y is not instrumental in suppressing the instability.

Although the spread in S from a distribution in W and from a distribution in a have been treated separately, it seems reasonable that the two contributions would occur additively in the stability criterion. One attempt was made to consider a distribution in both variables, and results of the involved analysis did indeed exhibit the additive property. We therefore state that, in the limit $|U|\gg V$, the stability criterion is to a good approximation

$$\Delta S > |U|, \qquad (4.27)$$

where ΔS is the total spread in S, including the contributions from distributions in W and a. In the limit $V\gg|U|$, the criterion may be written

$$\Delta S > V, \qquad (4.28)$$

and in this limit our theory is completely self consistent. The model used in Sec. II to calculate the vertical force on the beam gives only an approximate expression for U. In contrast, the electromagnetic force characterized by V arises from charges and currents in the surrounding walls. If the transverse dimensions of the beam are much smaller than the dimensions of the vacuum tank, this latter force is independent of the model chosen.

V. RESULTS AND EXAMPLES

The first result of Sec. IV is that the characteristic growth time of the instability, for a beam with no spread in ν_z or ω_0, is given by Eq. (4.4), namely,

$$\tau_0 = 1/V, \qquad (5.1)$$

where V is defined by Eqs. (3.17b), (3.19b), and (3.20b) or (3.26b), and $\omega\approx(n-\nu_z)\omega_0$. For circular geometry,

$$\tau_0 = \pi\nu_z(n-\nu_z)\gamma b^3/r_0 N R \mathcal{R} c, \qquad (5.2)$$

where $r_0=e^2/m_0c^2$ is the classical electron (or proton) radius. In rectangular geometry, and when $n\ll R/w$ and R/h, we have

$$\tau_0 = 3\nu_z(n-\nu_z)\gamma h^3/2\pi r_0 N R \mathcal{R} c \mathfrak{F}_3(h/w,\Delta/h), \qquad (5.3)$$

which is in close agreement with Eq. (5.2) when $h\ll w$ and $\Delta\ll h$ so that $\mathfrak{F}_3\rightarrow 1$, and h is replaced by $2b$. The most general expression is that given by Eqs. (3.19b) and (3.20b), but Eq. (5.3) with Fig. 5 should suffice for most applications.

The second result of Sec. IV [Eqs. (4.27) and (4.28)] is that the spread in the quantity $S\equiv(n-\nu_z)\Omega$ necessary to stabilize the coherent motion is approximately $|U|+V$, where U is defined by Eqs. (3.17a), (3.19a), and (3.20a) or (3.26a). If the particles are not extremely relativistic, $|U|\gg V$, and for circular geometry the criterion for stability becomes

$$\Delta S > N r_0 c[1-(a/b)^2]/2\pi\nu_z\beta\gamma^3 a^2. \qquad (5.4)$$

For rectangular geometry with $n\ll R/w$ and R/h, we have the criterion $\Delta S>|U_g|+V_g$, where

$$U_g = \frac{\pi^2 r_0 N c}{8\nu_z\beta\gamma h\Delta}\left[\frac{1}{\gamma^2}\mathfrak{F}_1\left(\frac{h}{w},\frac{\Delta}{h}\right) - \frac{h}{\gamma^2\tau} + \frac{2\nu_z{}^2\beta^2 w\Delta}{\pi^2R^2}\mathfrak{F}_2\left(\frac{h}{w},\frac{\Delta}{h}\right)\right], \qquad (5.5a)$$

$$V_g = 2[\pi r_0 N c \mathcal{R} R/3\nu_z(n-\nu_z)\gamma h^3]\mathfrak{F}_3(h/w,\,\Delta/h). \qquad (5.5b)$$

In the nonrelativistic case, $V_g\ll U_g$ and the term $\mathfrak{F}_2$ is negligible. For a beam that is thin vertically, $\tau\ll h$ and $\mathfrak{F}_1$ can also be neglected and Eq. (5.5a) affords a convenient analytic expression which is valid in a different regime (ribbon beam) than that of Eq. (5.4) (circular beam). The most general expression is that given by Eqs. (3.19); Eq. (5.5) with Figs. 3, 4, and 5 suffices for most considerations.

The application of the theory to actual accelerators is severely restricted by the assumption that the unperturbed beam is azimuthally uniform. The MURA accelerator[4] is

TABLE II. Computational results for the MURA accelerator. The sensitivity to parameters can be judged by the fact that changing h to 3 cm makes Re≈0.060. This is the dominant term in U_g, so a corresponding change would occur in the threshold criterion.

N	$\mathcal{R}\times10^5$	Re (cm^{-1})	Im (cm^{-1})	$(U_g/N)\times10^9$ (sec^{-1})	$(V_g/N\times10^9)$ (sec^{-1})
3	0.346	0.034	1255	12	1.85
4	0.846	0.033	208	12	0.75
5	1.15	0.032	113	11	0.56
6	1.38	0.031	77	11	0.46

a case where this assumption is acceptable, as would be proton-storage rings in which no rf is employed.

A. Azimuthally Uniform Beams

1. *MURA 40 MeV Electron Accelerator*

We take as parameters of the accelerator[4,12]:

$R=200$ cm
$h=5$ cm
$w=100$ cm
$x_0=90$ cm
$\Delta=5$ cm

$\tau=1$ cm
$\gamma=70$
$\omega_0=1.58\times10^8$ sec^{-1}
$\nu_z=2.8$
$\sigma=10^{17}$ sec^{-1},

and employ Eq. (3.20) to obtain the results presented in Table II. To estimate the nature of the instability we need to evaluate ΔS, which we write in the form

$$\Delta S=\left[(n-\nu_z)\frac{\partial\Omega}{\partial E}-\frac{\partial\nu_z}{\partial E}\Omega\right]\Delta E+\left[(n-\nu_z)\frac{\partial\Omega}{\partial a^2}-\frac{\partial\nu_z}{\partial a^2}\Omega\right]\Delta a^2. \quad (5.6)$$

$$\Delta S\equiv\Delta S_E+\Delta S_{a^2}.$$

The various coefficients are,

$\partial\Omega/\partial a^2\approx0$;

$\partial\nu_z/\partial E=-3.0\times10^{-3}$ MeV^{-1}, a measured quantity;

$\partial\Omega/\partial E=-0.34\times10^6$ sec^{-1} MeV^{-1}, theoretically derived;

$\partial\nu_z/\partial a^2=1.0\times10^{-2}$ cm^{-2}, theoretically derived from nonlinear orbit studies.

The energy spread in the beam ΔE, is observed to be 2.0 MeV; the *full* amplitude spread corresponds to $\Delta a^2=1.0$ cm^2, but if the distribution is flat except for a small region [as is discussed after Eq. (4.25)], then that small region would have a greatly reduced effective Δa^2. From the parameters given and from Table II we derive the results in Table III. The observed instability would be damped for all n values if $\Delta a^2\approx1.0$ cm^2, but for the smaller value of Δa^2 the observed threshold for $n=4$ and $N=2\times10^{12}$ can be explained by the theory. The reduced value of ΔS_E at $n=4$ comes from a sensitive cancellation—an observation first made by Swenson.[12] If, for example, $\partial\nu_z/\partial E=-2.6\times10^{-3}$ MeV^{-1}, then the threshold would agree exactly with observation. The observation[4] of instability only for $n>2$ is in good agreement with the general theory, and τ_0 agrees semiquantitatively with the observed growth rates.

TABLE III. Comparison between ΔS and $|U|+V$ for the MURA accelerator.

		$\Delta a^2=1$ cm^2	$\Delta a^2=0.01$ cm^2	$N=2\times10^{12}$	
n	$S_E\times10^{-6}$ (sec^{-1})	$\Delta S_{a^2}\times10^6$ (sec^{-1})	$\Delta S_{a^2}\times10^{-6}$ (sec^{-1})	$(\lvert U\rvert+V)\times10^{-6}$ (sec^{-1})	τ_0 (msec)
3	0.81	−1.58	−0.016	0.028	0.27
4	0.13			0.025	0.67
5	−0.54			0.024	0.90
6	−1.22			0.023	1.1

2. *Proton-Storage Rings*

The instabilities one might expect in a storage ring have been studied by Hereward as part of the design study of the CERN intersecting storage rings. We recommend his paper[13] for a detailed application of the theory. Here we shall simply give an example having parameters that are typical of relativistic proton-storage rings. We take

$R=130$ m
$h=7$ cm
$w=15$ cm
$x_0=7.5$ cm
$\Delta=5$ cm
$\tau=1$ cm

$\gamma=25$
$\omega_0=2.3\times10^6$ sec^{-1}
$\nu_z=8.75$
$\sigma=10^{16}$ sec^{-1} (stainless steel)
$\mathcal{R}=0.87\times10^{-5}$,

from which, for $n=17$, we obtain by means of Eq. (3.23) and Figs. 3, 4, and 5 the values Re$=0.0016$ cm^{-1} and Im$=120$ cm^{-1}. The growth time for $N=2\times10^{14}$ photons—which is the CERN design goal—is 3.6 msec, so the instability must be damped if the storage rings are to operate successfully. Hereward considers the various contributions to ΔS that either occur in the ring design or can be explicitly built into the design. One possibility for stabilization is through nonlinearities, i.e., amplitude dependence of ν_z. From the above numbers ($N=2\times10^{14}$) we deduce that $U_g=1050$ sec^{-1} and $V_g=290$ sec^{-1}. To stabilize this with nonlinearities we would need

$$|\Delta S_{a^2}|\approx\left|-\left(\frac{\partial\nu_z}{\partial a^2}\right)\Omega\Delta a^2\right|\approx1340\text{ sec}^{-1}, \quad (5.7)$$

or a spread in tune within the beam of

$$\Delta\nu\equiv(\partial\nu_z/\partial a^2)\Delta a^2\approx5.8\times10^{-4}. \quad (5.8)$$

This is a relatively modest value, and presumably could be designed into the storage rings. Of course, all values of $n>\nu_z$ must be considered to obtain the most stringent requirement on $\Delta\nu$.

B. Azimuthally Bunched Beams

Clearly the theory must be extended before it can be rigorously applied to accelerators with longitudinally bunched beams. On the other hand, the theory of this

---

[12] D. A. Swenson, "On the Threshold for the Coherent Vertical Instability," MURA TN-421, 2 July, 1963 (unpublished).

[13] H. Hereward, "Dissipative Transverse Instabilities in the Storage Rings," CERN AR/Int. SG 64-8, 16 April, 1964 (unpublished).

report can be used to gain insight into the expected result of such an analysis. We proceed in this *ad hoc* manner, modifying the theory in three elementary regards:

(i) The local charge density in the bunch is employed in all formulas so that if L is the length of a bunch and there are h bunches, then whenever $(N/2\pi R)$ appears it is to be replaced by N/Lh. This changes formulas by the ratio $Lh/2\pi R$, which is simply the bunching factor B of Ref. 8.

(ii) If the beam is under the influence of rf, then particles will sweep through a range of energies during a synchrotron oscillation. If the growth time of the instability is less than a synchrotron period, then the analysis of this paper should apply, but if the instability growth time is long compared to the synchrotron period, then the evaluation of ΔS must be modified. In particular, the term ΔS_E will average to zero if $\partial\Omega/\partial E$ and $\partial\nu_z/\partial E$ are independent of E (as they are, to first approximation). Thus the effective stabilizing mechanisms are greatly restricted, namely to intrinsic nonlinearities ΔS_{a^2}, external octupole fields (not sextapoles), and nonlinear terms in the dependence of Ω upon E.

(iii) Clearly n is no longer a good mode number in the case of a bunched beam and we expect different n values to be coupled.

Phenomena for bunched beams, that are evidently the analog of the instability treated in this report have been observed in the Stanford electron rings,[5] the Cosmotron,[6] the Cornell electron synchotron,[14] the Argonne zero-gradient synchrotron,[15] and (possibly) in the Bevatron.[16] Detailed analysis for some of these accelerators either appears in the literature or will be published in the future. We restrict ourselves here to one example, namely a crude evaluation for the Cosmotron, where the phenomenon has been studied in most detail and in fact has been suppressed by a feedback technique.[6] Stabilization by means of an external octupole has been extremely effective both at Cornell where it allowed a hundred-fold increase in intensity,[14] and at Stanford where it allowed an eighty-fold increase in intensity.[17] Both machines are now limited by injection capabilities.

As parameters for the phenomenon observed at the Cosmotron we take

$$\begin{array}{ll}
R=950\text{ cm} & \beta=0.5\\
w=65\text{ cm} & \nu_z=0.875\\
h=16\text{ cm} & f_0=1.5\times10^6\text{ sec}^{-1}\\
\tau=2\text{ cm} & \mathcal{R}\approx1\times10^{-5}\\
\Delta=10.6\text{ cm} & B=0.25,
\end{array}$$

where some parameters—such as $\mathcal{R}$—are only rough estimates. Employing the formulas for circular geometry with $n=1$ and taking $a=1$ cm and $b=8$ cm, we find that $N\tau_0=1.2\times10^9$ sec, and $\Delta S/N=4.1\times10^{-6}$ sec^{-1}. The observations are that $N=5\times10^{11}$ protons is close to threshold, with a growth time of the order of 10 msec. The value of τ_0 at this intensity is 2.4 msec—in remarkably good agreement with the observations. The threshold is experimentally observed to be a strong function of operating conditions, being lowest under those conditions where $\partial\nu_z/\partial E$ is not zero but where $\partial^2\nu_z/\partial E^2$ is small.[6] Under these conditions, if we ascribe the threshold to a $\partial\nu_z/\partial a^2$ term, then the threshold corresponds to a tune spread across the beam $\Delta\nu=a^2(\partial\nu_z/\partial a^2)\approx0.22$. This is comparable with the amount needed to shift ν_z to the integral resonance at $\nu_z=1.0$, and might well be representative of the beam quality in the accelerator. Finally, we note that the mode mixing expected for bunched beams has been observed.[6] It is possible to excite the instability by an applied rf with frequency $\omega=(1+\nu_z)\omega_0$. This is in marked contrast with the experience of MURA,[4] where the beam is azimuthally uniform and only the $(n-\nu_z)\omega_0$ components, for $n>\nu_z$, are unstable.

ACKNOWLEDGMENTS

The authors wish to thank Ed Rowe, Dr. Fred Mills, and Dr. Don A. Swenson of MURA; also Dr. Lloyd Smith and Dr. Warren Heckrotte of the Lawrence Radiation Laboratory for many informative, helpful, and encouraging conversations. The authors are also grateful for the intensive review of this work by Dr. Ernest Courant of the Brookhaven National Laboratory, and, in particular, for his pointing out a fundamental error in the original manuscript. They are indebted to Mrs. Barbara Steinberg of the Lawrence Radiation Laboratory for assistance with the numerical computations.

---

[14] D. F. Edwards and R. R. Wilson, Department of Physics, Cornell University (private communication, 1964).

[15] F. E. Mills, MURA, Stoughton, Wisconsin (private communication, 1963).

[16] T. Elioff, Lawrence Radiation Laboratory (private communication, 1963).

[17] B. Gittleman, Department of Physics, Stanford University, (private communication, 1963).

ON INTENSITY LIMITATIONS IMPOSED BY TRANSVERSE SPACE-CHARGE EFFECTS IN CIRCULAR PARTICLE ACCELERATORS

L. J. Laslett
Lawrence Radiation Laboratory

Contents

ON INTENSITY LIMITATIONS IMPOSED BY TRANSVERSE SPACE-CHARGE EFFECTS IN CIRCULAR PARTICLE ACCELERATORS

L. J. Laslett
Lawrence Radiation Laboratory

I. Introduction

The influence of space-charge forces on the frequency of betatron oscillations has been recognized for many years as one mechanism which will impose a limit on the number of particles that can be accommodated within a circular accelerator. The implications of the space-charge forces which act on an individual particle have been discussed in several early papers[1-3] and in a recent report by Teng.[4] Attention has also been directed by a number of workers, in particular by members of the Midwestern Universities Research Association staff, to the importance of image forces in this phenomenon.[5]

The intensity limit which arises because of the transverse space-charge effect has provided a powerful argument for the use of high-energy injection, since, because of the almost complete cancellation of the electric and magnetic forces when the effect of image fields may be neglected, the number

---

[1] D.W. Kerst, Phys. Rev. 60, 47 (1941).

[2] J.P. Blewett, Phys. Rev. 69, 87 (1946).

[3] D.L. Judd, "A Study of the Injection Process in Betatrons and Synchrotrons", California Institute of Technology thesis (Pasadena, 1950).

[4] L.C. Teng, "Transverse Space-Charge Effects", Argonne National Laboratory Report ANLAD-59 (Argonne, Illinois; February 1, 1963). The papers presented on August 26 by Drs. Lloyd Smith and P. Lapostolle at the 1963 International Accelerator Conference at Dubna are of interest for obtaining self-consistent solutions to the transverse space-charge behavior of a particle beam.

[5] See, for example, J. van Bladel, "Image Forces in the Third MURA Model", Midwestern Universities Research Association Report MURA-466 (Madison, Wisconsin; June 12, 1959).

of particles which can be accepted is proportional to $\beta^2\gamma^3$. As we shall see, however, image forces can distort this energy dependence when the ratio of the aperture to the transverse beam dimensions becomes comparable to or less than γ, and the limit to the number of particles will become proportional to γ at high energies. In seeking the attainment of high intensity by means of high-energy injection, therefore, one must employ a sufficiently large aperture to insure that image effects are suppressed or inject at an energy considerably higher than would be required if image effects were negligible. In practice, a careful optimization of the design would be appropriate in order to achieve the best balance between aperture and injection energy for achievement of the desired intensity.

In addition to the space-charge forces which act on an individual particle in the beam, a second phenomenon, involving the transverse movement of the beam as a whole, may be of importance. This latter effect, which of course arises in its entirety from image forces, could lead to an instability for coherent transverse motion of an intense beam. Because, as will be indicated in greater detail below, the forces which could lead to single-particle or to coherent instability are not identical, it may prove to be quite complicated to provide compensating fields which will suppress both of these phenomena.

In the sections which follow we shall give a general discussion of the transverse space-charge phenomena, as they may affect axial stability in a circular accelerator; present some field coefficients that represent the image effects in certain particular geometrical configurations that are analyzed in the Appendices; and finally give some illustrative numerical examples. The influence of space-charge neutralization is ignored in the present report, in the supposition that the time required for complete neutralization of the beam normally is long compared to the duration of the injection process. The work reported here has benefited from discussions which the writer has enjoyed with staff of the Brookhaven National Laboratory, the Lawrence Radiation Laboratory, the Midwestern Universities Research Association, and the Stanford Linear Accelerator Center.

II. Transverse Space-Charge Effects -- Axial Stability Limit

A. Single-Particle Stability

1. The Assumed Fields

The electric and magnetic fields which arise from the collective action of a uniform isolated beam of elliptical cross section have been evaluated by Teng.[4] In Gaussian units, the field strengths at a distance y above the center of a beam with semi-major (radial) and semi-minor (axial) axes denoted respectively by a and b are

$$\vec{E}_{\text{unbunched}} = 4\lambda \frac{y}{b(a+b)} \hat{j} \tag{1a}$$

$$\vec{H}_{\text{unbunched}} = -4\lambda\beta \frac{y}{b(a+b)} \hat{i}\,, \qquad (y < b) \tag{1b}$$

for the transverse distribution of density assumed by Teng, where the linear charge density (λ) is related to the number of particles in the beam (N) and to the orbit radius (R) by

$$\lambda = \frac{Ne}{2\pi R}\,. \tag{2}$$

The fields represented by Equations (1a) and (1b) will be modified by the presence of nearby conducting or ferromagnetic material through the supplementary effect of so-called image fields. In addition, for a given total number of particles, the peak fields, experienced by some of the particles in the beam, will be enhanced - and the maximum attainable intensity correspondingly reduced - if the beam is bunched azimuthally by action of the rf acceleration system or if significant fine structure is otherwise present in the density distribution.

The beam distribution accordingly will be characterized by a "bunching factor", B ($B \leq 1$) representing the ratio of the average to the maximum linear charge or particle density. The relevant fields for an isolated beam accordingly will be taken as

$$\vec{E} = \vec{E}_{\text{unbunched}} \times (1/B) \; ; \tag{3a}$$

and

$$\vec{H} = \vec{H}_{\text{unbunched}} \times (1/B) \; , \tag{3b}$$

of which

$$\vec{H}_{dc} = \vec{H}_{\text{unbunched}} \tag{3b'}$$

$$\vec{H}_{ac} = \vec{H}_{\text{unbunched}} \times (1/B - 1) \; . \tag{3b''}$$

To each of these fields [(3a), (3b'), and (3b")] must be appended appropriate correction factors to account for the supplemental image fields.

The electrostatic field, $\vec{E}$, will be modified by the presence of a vacuum chamber with conducting walls through the addition of terms which insure that the chamber surface (most simply taken as formed by parallel conducting planes, a distance 2h apart) be an equipotential. Likewise, the dc component of the magnetic field, $\vec{H}_{dc}$, will be modified so as to insure that, if possible, this field is directed perpendicular to the surfaces of ferromagnetic magnet poles (most simply taken as formed by parallel pole surfaces, a distance 2g apart). The ac magnetic fields of the beam will be influenced by skin-effect currents induced in the conducting walls of the vacuum chamber, so as to result in a net ac field which is tangential to this boundary, and the correction factor required in this case may be expected to be identical to that applicable to the electrostatic field. For a beam of reasonably small transverse dimensions, these various correction fields may be considered as evaluated adequately without regard for the cross-sectional size of the beam, and, for small displacements of the test particle, will give rise to forces proportional to the displacement y.

The fields to be employed in analysis of single-particle stability accordingly will be written

$$\vec{E} = \frac{4\lambda}{B}\left[1 + \epsilon_1 \frac{b(a+b)}{h^2}\right] \frac{y}{b(a+b)}\,\hat{\jmath} =$$

$$= \frac{2}{\pi}\,\frac{1}{B}\,\frac{Ne}{R}\left[1 + \epsilon_1 \frac{b(a+b)}{h^2}\right] \frac{y}{b(a+b)}\,\hat{\jmath}\,, \tag{4a}$$

$$\vec{H}_{dc} = -4\lambda\beta\left[1 - \epsilon_2 \frac{b(a+b)}{g^2}\right] \frac{y}{b(a+b)}\,\hat{\imath} =$$

$$= -\frac{2}{\pi}\,\beta\,\frac{Ne}{R}\left[1 - \epsilon_2 \frac{b(a+b)}{g^2}\right] \frac{y}{b(a+b)}\,\hat{\imath}\,, \tag{4b'}$$

and

$$\vec{H}_{ac} = -4\lambda\beta\left(\frac{1}{B} - 1\right)\left[1 + \epsilon_1 \frac{b(a+b)}{h^2}\right] \frac{y}{b(a+b)}\,\hat{\imath} =$$

$$= -\frac{2}{\pi}\left(\frac{1}{B} - 1\right)\beta\,\frac{Ne}{R}\left[1 + \epsilon_1 \frac{b(a+b)}{h^2}\right] \frac{y}{b(a+b)}\,\hat{\imath}\,, \tag{4b''}$$

where ϵ_1 and ϵ_2 are numerical factors for which expressions applicable to specific geometrical configurations of practical interest are given below (sub-section 3) and where the lengths h and g respectively serve to characterize conveniently the semi-apertures of the vacuum chamber and magnet gap.

Because the effect of bunching has been explicitly taken into account in writing Equations (4a-b"), the quantity λ should be taken here as representing the average linear charge density, as given by Eq. (2). It may be remarked that in some configurations of possible practical interest the dc component of the beam also gives rise to an axial magnetic field component which effectively is independent of position; such a field component is not considered to affect directly the frequency of axial betatron oscillations, however, and is not included in Eq. (4b') or in the equation of motion which follows.

2. The Equation of Motion

The linear equation for the steady-state axial betatron oscillation of a test particle in the presence of a beam of N identical particles may be written in the smooth approximation as

$$\frac{d^2y}{d\theta^2} + (n + K_E + K_M + K_S)\, y = 0 \,, \tag{5}$$

where n is the effective field index of the applied magnetic field and in which

$$K_E = -\frac{2}{\pi}\frac{1}{B}\frac{N r_p R}{\beta^2 \gamma\, b(a+b)}\left[1 + \epsilon_1 \frac{b(a+b)}{h^2}\right] \tag{6a}$$

$$K_M = \frac{2}{\pi}\frac{N r_p R}{\gamma\, b(a+b)}\left[1 - \epsilon_2 \frac{b(a+b)}{g^2}\right] \tag{6b}$$

$$K_S = \frac{2}{\pi}\left(\frac{1}{B} - 1\right)\frac{N r_p R}{\gamma\, b(a+b)}\left[1 + \epsilon_1 \frac{b(a+b)}{h^2}\right] , \tag{6c}$$

by use of Equations (4a), (4b'), and (4b"). The coefficients K_E, K_M, and

K_S represent respectively the electrostatic effect of the bunched beam, the effect of the magnetostatic dc component of the beam, and the magnetic effect of the ac component of the beam as modified by the skin-effect currents induced in the chamber surface. The quantity r_p denotes the "classical radius" $(\frac{e^2}{M_o c^2})$ for the particle, and may be taken as 1.536×10^{-16} cm for a proton (rest mass equivalent to 938 Mev).

The shift of betatron frequency which results from the space-charge terms included in Eq. (5) is given by

$$\Delta(\nu_y^2) = K_E + K_M + K_S \tag{7}$$

and leads to the space-charge limit

$$N = B\frac{\pi}{2}\frac{b(a+b)}{r_p R}\frac{\nu_{y_o}^2 - \nu_y^2}{1 + \frac{b(a+b)}{h^2}\left[\epsilon_1(1 + B\beta^2\gamma^2) + \epsilon_2 B\beta^2\gamma^2(h^2/g^2)\right]}\beta^2\gamma^3 \tag{8a}$$

$$= B\frac{\pi}{2}\frac{h^2}{r_p R}\frac{\nu_{y_o}^2 - \nu_y^2}{\epsilon_1\left(B + \frac{1}{\beta^2\gamma^2}\right) + \epsilon_2 B\frac{h^2}{g^2} + \frac{h^2}{b(a+b)}\frac{1}{\beta^2\gamma^2}}\gamma \tag{8b}$$

$$= \frac{\pi}{2}\frac{h^2}{r_p R}\frac{\nu_{y_o}^2 - \nu_y^2}{\epsilon_1\left[1 + \frac{1}{B(\gamma^2 - 1)}\right] + \epsilon_2\frac{h^2}{g^2} + \frac{1}{B(\gamma^2 - 1)}\frac{h^2}{b(a+b)}}\gamma\,, \tag{8c}$$

in which ν_y refers to the frequency (oscillations per revolution) of the nearest axial betatron oscillation resonance, below the low-intensity value, to which the oscillation may be shifted. The form of the Eq. (8a) is most suitable for indicating the correction factor,

$$F = \left\{1 + \frac{b(a + b)}{h^2}\left[\epsilon_1(1 + B\beta^2\gamma^2) + \epsilon_2 B\beta^2\gamma^2(h^2/g^2)\right]\right\}^{-1} , \qquad (9)$$

that must be applied to the usual formula for the space-charge limit of an isolated beam, but the form of Eq. (8c) may be more convenient for computation (when $h^2/ab < B\gamma^2$) and indicates more clearly the following characteristics of the transverse space-charge limit at high energy:

(i) The space-charge limited intensity becomes substantially proportional to γ;

(ii) The aperture dimensions become more important, and the beam dimensions correspondingly less so, in determining the space-charge limit; and

(iii) The bunching factor (B) becomes relatively less important [due to the almost complete elimination of 1/B from the sum of the coefficients K_E and K_S, given respectively by Equations (6a) and (6c), when β^2 is near unity and by virtue of the identity of the image-force coefficients (ϵ_1) that appear in these equations].

3. The Image-Force Coefficients

The image-force coefficients, ϵ_1 and ϵ_2, which have been introduced in Equations (6a-c), can be evaluated directly by the use of image charges or currents in certain simple two-dimensional configurations, and in other two-dimensional cases use may be made of conformal transformations to obtain an equivalent problem for which the solution by image techniques or other means is readily apparent.

a. The electrostatic image coefficient, ϵ_1

(1) Plane-parallel conducting surfaces

The simplest configuration for the electrostatic problem - and hence also for the equivalent problem concerning the ac magnetic field, in which the boundary conditions are satisfied by virtue of skin-effect currents induced in the conducting surfaces - is evidently that of two infinite parallel conducting planes, at elevations h above and below a line charge λ_1. The supplemental electric field at a point situated a distance y directly above the line charge can be obtained immediately by summing the effects produced by an infinite series of images, of alternating sign, or by use of a simple conformal transformation (Appendix B). The additional electric field at this point is vertically directed, of amount

$$E_{image} = \frac{\pi^2\lambda_1}{12h^2} y , \qquad (10)$$

and hence is in the same direction as the field $2\lambda_1/y$ which arises directly from a localized line charge. The coefficient ϵ_1, which was introduced in Eq. (4a), is thus seen to be

$$\epsilon_1 = \frac{\pi^2}{48} \qquad (11)$$

for the boundary surfaces considered here.

(2) Elliptical boundary

It has been pointed out by Dr. John P. Blewett[6] that use of a conducting vacuum chamber with a circular cross section would provide the advantage

---

[6] J.P. Blewett, private conversation (July, 1963).

of suppressing the coefficient ϵ_1 which otherwise is of major importance in determining the intensity limit which results from the requirement of single-particle stability. Since use of a chamber with a strictly circular cross section may prove inconvenient because of other practical design considerations, it is of interest to obtain the image-force coefficient for a chamber of elliptical cross section. Unfortunately, as will be seen, any substantial departure of the cross section from circularity results in the coefficient ϵ_1 assuming a value that is comparable to the value $\pi^2/48$ for the plane-parallel case. As will be noted in Section B, moreover, the image forces that arise from a coherent transverse displacement of the beam as a whole clearly will not vanish for a chamber of circular cross section.

The rather lengthy analysis of the image effects for an elliptical boundary, of semi-axes w (radially) and h (axially), has been outlined in Appendix D and leads to results expressible in terms of the complete elliptic integral K(k) of the first kind and modulus k. The modulus k is to be selected so that

$$\frac{K'}{K} = \frac{2}{\pi} \tanh^{-1} \frac{h}{w} , \qquad (12)$$

where K' denotes $K(k') = K(\sqrt{1 - k^2})$. In terms of this notation, the supplemental electric field at a distance y above a line charge at the center of the ellipse is

$$E_{\text{image}} = \frac{2\lambda_1}{3(w^2 - h^2)} \left[\frac{2(2 - k^2)K^2}{\pi^2} - 1\right] y , \qquad (13)$$

and the image-force coefficient accordingly is

$$\epsilon_1 = \frac{1}{6[(w/h)^2 - 1]} \left[\frac{2(2 - k^2)K^2}{\pi^2} - 1\right] . \qquad (14)$$

This result includes, as limiting cases, the results for the case of parallel planes and for a circular cylinder; approximate values of the coefffficient ϵ_1 for certain special cases of the axis ratio are listed in Table I below (see also Fig. 1).

TABLE I

Values of the electrostatic image coefficient ϵ_1
for a cylinder of elliptical cross section

w/h	k^2	ϵ_1
1	0	0
5/4	0.838	0.090
4/3	0.904	0.107
3/2	0.965_5	0.134
2/1	0.998	0.172
∞	1	$\frac{\pi^2}{48} \doteq 0.20562$

b. The magnetostatic image coefficient, ϵ_2

(1) Plane-parallel magnet poles

For extended plane ferromagnetic poles, the magnetostatic image coefficient ϵ_2 can be obtained immediately by summing the effects produced by an infinite set of current images of identical sign, or by use of a simple conformal transformation (Appendix C). The additional magnetic field at a point y directly above a line current I_1 is parallel to the pole surface and is oppositely directed to the field $2I_1/y$ (e.m.u.) which arises from the line current alone. The strength of the supplemental

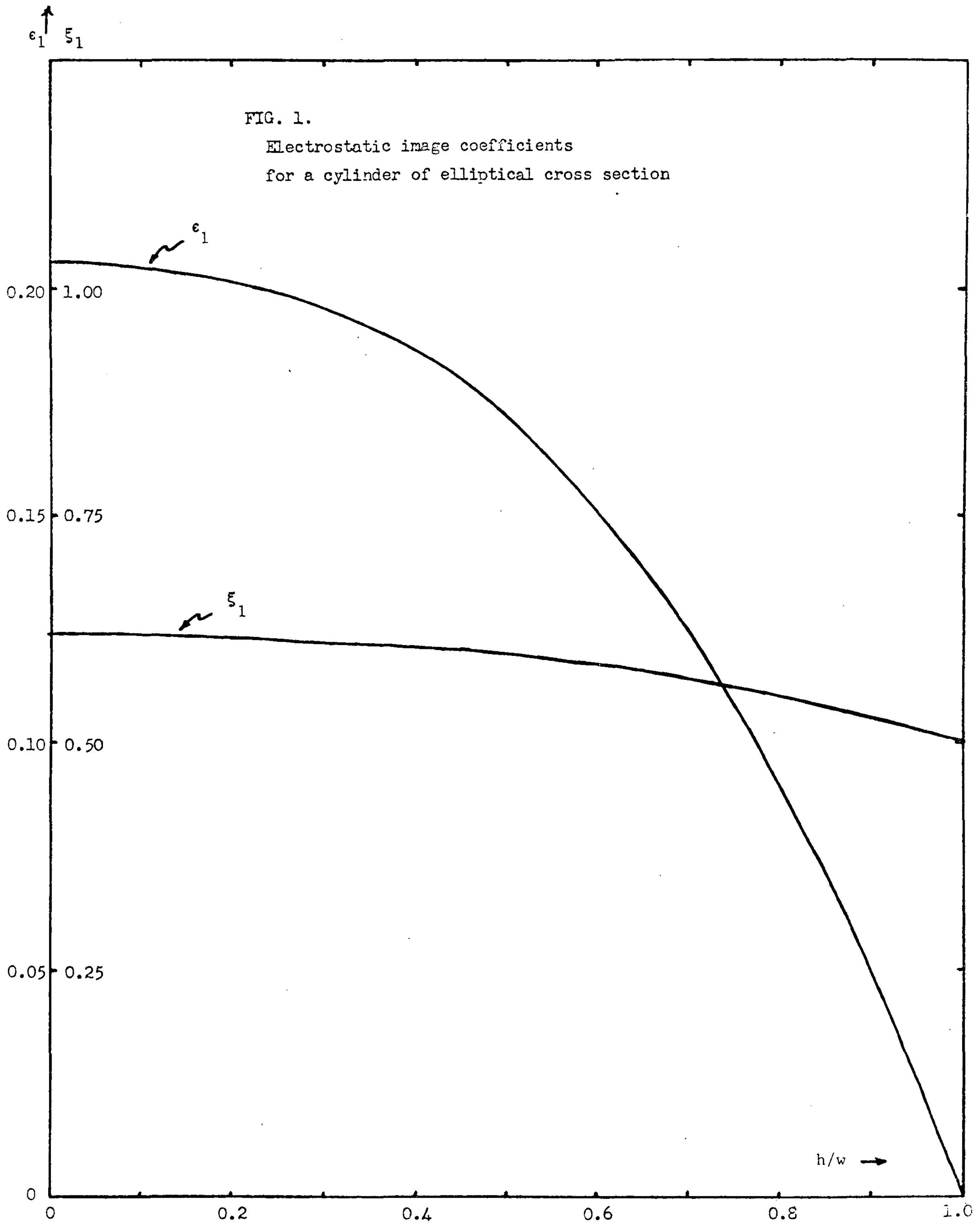

FIG. 1.
Electrostatic image coefficients
for a cylinder of elliptical cross section

field is

$$H_{\text{image}} = \frac{\pi^2 I_1}{6\,g^2}\,y\ . \tag{15}$$

The image-force coefficient ϵ_2, which was first introduced in Eq. (4b'), accordingly becomes

$$\epsilon_2 = \frac{\pi^2}{24} \tag{16}$$

for the boundary surfaces considered here.

(2) Wedge-shaped magnet gap

Since in practice the magnet poles are commonly designed to provide a magnetic field whose strength in the median plane is characterized by a substantial gradient (field index, $n \equiv -\frac{R}{H}\frac{dH}{dr}$), it is of interest to investigate whether the value of ϵ_2 is markedly modified in such circumstances. The detailed equations for the magnetic field generated by the beam may be different in form for various geometrical arrangements of the ferromagnetic material, and, in special cases, application of the usual boundary condition $H_t = 0$ may be incompatible with the necessary condition $\oint \vec{H}\cdot\vec{d\ell} = 4\pi\,\Sigma I$. In particular, it is found that, in addition to the expected radial component of field above and below the beam, an axial field component which effectively is independent of position may arise if the presence of the magnet yoke or some other feature of the geometrical configuration produces a lack of symmetry with respect to a vertical plane through the beam.*

---

*The presence of a substantially constant magnetic field component, typically given approximately by $\frac{\pi I_1}{g}\hat{j}$, may be noted in the work of van Bladel (op. cit.,[5] Sect. III), wherein an image-field component of $\pi\hat{j}$ gauss is shown in the neighborhood of a 50-amp beam (I_1 = 5 e.m.u.) when g = 5 cm. In this same report van Bladel investigates, evidently successfully, means of compensating the total image field in the median plane.

A rather simple magnet configuration for the production of a non-uniform field is that represented by a wedge-shaped gap, of half-angle α, with the beam current situated a distance X from the vertex of the wedge. The distance X may be identified with the reciprocal of the relative field gradient,

$$X = -\frac{H}{dh/dr} = \frac{R}{n}\,, \tag{17a}$$

and α may be related to the half-gap at the beam location by the equation

$$\alpha = \tan^{-1}\frac{g}{X} = \tan^{-1}\frac{g}{R/n}\,. \tag{17b}$$

By an analysis outlined in Appendix E, one finds an image field given by

$$\vec{H}_{\text{image}} = \frac{I_1}{X}\left\{\left(\frac{\pi}{\alpha} - 1\right)\left(\frac{\pi}{\alpha} - 5\right)\frac{y}{6X}\,\hat{i} + \left(\frac{\pi}{\alpha} - 1\right)\left[1 + \left(\frac{\pi}{\alpha} - 5\right)\frac{x}{6X}\right]\hat{j}\right\} \tag{18a}$$

$$\doteq I_1\left\{\pi^2\left[1 - \frac{6}{\pi}\left(\frac{g}{R/n}\right) + \left(\frac{2}{3} + \frac{5}{\pi^2}\right)\left(\frac{g}{R/n}\right)^2\right]\frac{y\hat{i} + x\hat{j}}{6g^2}\right.$$

$$\left. + \pi\left[1 - \frac{1}{\pi}\left(\frac{g}{R/n}\right) + \frac{1}{3}\left(\frac{g}{R/n}\right)^2\right]\frac{1}{g}\,\hat{j}\right\}\,.^{*} \tag{18b}$$

Since the image coefficient ϵ_2 serves to characterize the horizontal component of the image field at points directly above the beam, we obtain

$$\epsilon_2 = \left(\frac{\pi}{\alpha} - 1\right)\left(\frac{\pi}{\alpha} - 5\right)\frac{g^2}{24X^2} \tag{19a}$$

$$\doteq \frac{\pi^2}{24}\left[1 - \frac{6}{\pi}\left(\frac{g}{R/n}\right) + \left(\frac{2}{3} + \frac{5}{\pi^2}\right)\left(\frac{g}{R/n}\right)^2\right]\,. \tag{19b}$$

Typically $g \ll R/n$ $(\alpha \ll 1)$ and the coefficient ϵ_2 then becomes substantially $\pi^2/24$, in agreement with the result obtained in sub-section (1) for plane-parallel magnet poles.

---

[*] The presence of a constant field component approximately given by $\frac{\pi I_1}{g}\,\hat{j}$ for $g \ll R/n$, of which mention was made in the footnote on p. 337, is evident from Eq. (18b).

(3) Other pole configurations

Other idealized two-dimensional pole configurations also are susceptible to analysis. The results would be of interest in permitting a comparison to be made between the image fields which arise in such cases and those present in the wedge-shaped gap that was considered in the preceding sub-section. In order that the gradient will be substantially constant over a limited region in the neighborhood of the beam, it might be considered desirable to locate the beam at a point of inflection for the median-plane magnetic field that is produced by the application of a magnetomotive force between the poles. Poles formed by two parallel circular cylinders of ferromagnetic material afford the advantage of permitting one to select independently both the semi-aperture (g) and the relative gradient (n/R), while locating the beam at a point of inflection for the median-plane field.[7] Such a pole system suffers, however, from the omission of a yoke structure to connect the two cylinders, as would be desirable in any practical application of this arrangement, and detailed analysis of the image fields for this case appears to require, moreover, a formidable amount of algebraic work.

Another pole configuration of possible interest for checking the results found for the wedge-shaped gap is that in which the pole surfaces are described by the hyperbolic cylinders $y^2 - x^2 = s^2$ (asymptotes at $\pm 45^\circ$) and by the vertical plane $x = 0$. For determining the image fields for the general case in which a line current is located at the point (X,y), it would be convenient to average the results for the following two cases: (i) line

---

[7] The magnetic field produced by a specified magnetomotance applied between the cylinders may be evaluated in a manner similar to that appropriate for an analogous electrostatic problem discussed by Smythe: W.R. Smythe, "Static and Dynamic Electricity" (McGraw-Hill Book Company, Inc., New York, 1950) 2nd Ed., Sect. 4.17, pp. 80-82.

currents I_1 at (X,y) and at $(X,-y)$; and (ii) a line current I_1 at (X,y) and $-I_1$ at $(X,-y)$. Analysis of this problem again involves considerable algebraic effort, but for the simplified case in which the beam and field point are located in the median plane, at $X + \delta_1$ and $X + \delta$ respectively, the image field can be shown to be

$$\vec{H}_{\text{image}} = \frac{I_1}{X}\left[\frac{s^2 + 3X^2}{s^2 + X^2} - \frac{1}{2}\left(\frac{s^2 - X^2}{s^2 + X^2}\right)^2 \frac{\delta}{X} - \frac{1}{2}\,\frac{s^4 + 2X^2s^2 + 5X^4}{(s^2 + X^2)^2}\,\frac{\delta_1}{X}\right]\hat{j}\,, \qquad (20a)$$

for δ and δ_1 small. Application of the condition $\nabla x\vec{H} = 0$ permits generalization of Eq. (20a) to include the case in which the field point is located a small distance, y, from the x-axis:

$$\vec{H}_{\text{image}} = \frac{I_1}{X}\left[\frac{s^2 + 3X^2}{s^2 + X^2}\,\hat{j} - \frac{1}{2}\,\frac{s^4 + 2X^2s^2 + 5X^4}{(s^2 + X^2)^2}\,\frac{\delta_1}{X}\,\hat{j} - \frac{1}{2}\left(\frac{s^2 - X^2}{s^2 + X^2}\right)^2 \frac{y\hat{i} + \delta\hat{j}}{X}\right], \qquad (20b)$$

for $y_1 = 0$. In limiting cases, Eq. (20b) may be simplified to

$$\vec{H}_{\text{image}} \doteq \frac{I_1}{X}\left[\hat{j} - \frac{y\hat{i} + (\delta + \delta_1)\hat{j}}{2X}\right], \qquad \text{for } s \gg X\,; \qquad (20b')$$

$$\vec{H}_{\text{image}} \doteq \frac{I_1}{X}\left[3\hat{j} - \frac{y\hat{i} + (\delta + 5\delta_1)\hat{j}}{2X}\right], \qquad \text{for } s \ll X\,. \qquad (20b'')$$

The results expressed by Equations (20b') and (20b") are consistent with those given for a wedge-shaped gap by Eq. (E.4a) of Appendix E, if in these respective cases we set the half-angle α equal to $\pi/2$ or $\pi/4$, and if we identify x with δ, x_1 with δ_1, and set y_1 equal to zero. The image-force coefficient, ϵ_2, accordingly assumes the value $-\frac{g^2}{8X^2}$ in these limiting cases, as follows from Eq. (19a) with the substitution of $\pi/2$ or $\pi/4$ for α; in cases of practical importance, however, α would be taken as small ($g \ll R/n$) and interest would be directed to the dominant term of Eq. (19b).

B. Stability with Respect to a Collective Transverse Displacement

1. The Assumed Fields

In examining the stability of the beam with respect to a transverse displacement of the beam as a whole, it again is appropriate to consider separately the electrostatic field, the dc component of the magnetic field, and the ac magnetic field which occur in the presence of conducting or ferromagnetic boundaries. We now require these components of the image fields at a point x,y which coincides with the location of a displaced beam ($x_1 = x$, $y_1 = y$). We shall characterize these image fields by coefficients, ξ_1 and ξ_2, which, for consistency with the notation of Section A, are defined as follows in terms of the axial component of electric field from a line charge λ_1 and the radial component of magnetic field from a dc current I_1:

$$E_y = 4\,\lambda_1\,\xi_1\,\frac{y}{h^2}\,, \tag{21a}$$

$$H_x = 4\,I_1\,\xi_2\,\frac{y}{g^2}\,. \tag{21b}$$

2. The Equation of Motion

In a manner analogous to the procedure followed in Section A2, especially Equations (5) and (6a-c), we write the differential equation for axial betatron oscillation of the beam centroid as

$$\frac{d^2y}{d\theta^2} + (n + K_E' + K_M' + K_S')\,y = 0 \tag{22}$$

where

$$K_E' = -\frac{2}{\pi}\,\frac{1}{B}\,\frac{N\,r_p\,R}{\beta^2\gamma\,h^2}\,\xi_1 \tag{23a}$$

$$K'_M = -\frac{2}{\pi}\,\frac{N\,r_p\,R}{\gamma\,g^2}\,\xi_2 \qquad (23b)$$

$$K'_S = \frac{2}{\pi}\left(\frac{1}{B} - 1\right)\frac{N\,r_p\,R}{\gamma\,h^2}\,\xi_1\,. \qquad (23c)$$

By again identifying $\Delta(\nu_y^2)$ with $K'_E + K'_M + K'_S$, one obtains the space-charge limit imposed by the requirement of axial stability for coherent transverse motion:

$$N = \frac{\pi}{2}\,\frac{h^2}{r_p\,R}\;\frac{\nu_{y_o}^{\;2} - \nu_y^{\;2}}{\xi_1\left[1 + \dfrac{1}{B(\gamma^2 - 1)}\right] + \xi_2(h^2/g^2)}\;\gamma\,.^{*} \qquad (24)$$

The result expressed by Eq. (24) is clearly of the same form as Eq. (8c) when the self-field term $\dfrac{1}{B(\gamma^2 - 1)}\cdot\dfrac{h^2}{b(a + b)}$ is omitted from the denominator; as will be pointed out in the following sub-section, the numerical coefficients ξ_1 and ξ_2 will differ, however, from the coefficients ϵ_1 and ϵ_2 that are employed in Eq. (8c). Nevertheless, to the extent that the coefficients ξ_1, ξ_2 and ϵ_1, ϵ_2 are of a similar order of magnitude, the coherent and incoherent space-charge limits that are respectively expressed by Equations (24) and (8c) will be comparable when γ is large ($B\gamma^2 \gg h^2/ab$).

---

*If the beam location (y_1) is flopping on successive revolutions rapidly (in comparison to the leakage time for ac fields of such frequencies through the metallic chamber wall), the y_1-term in the so-called dc component of the magnetic field will be alternating also and would be subject to the boundary conditions imposed by the presence of the vacuum chamber. In this case we may replace g^2 by h^2 and ξ_2 by $-\xi_1$ in Eq. (24), with the result

$$N = \frac{\pi}{2}\,\frac{h^2}{r_p\,R}\,\frac{B}{\xi_1}\,(\nu_{y_o}^{\;2} - \nu_y^{\;2})\,\gamma\,(\gamma^2 - 1) \qquad (24')$$

$$= \frac{\pi}{2}\,\frac{h^2}{r_p\,R}\,\frac{B}{\xi_1}\,(\nu_{y_o}^{\;2} - \nu_y^{\;2})\,\beta^2\gamma^3 \qquad (24'')$$

and note a consequent pronounced enhancement of the space-charge limit for stability of collective transverse motion. We are indebted to Dr. K.R. Symon for helpful discussion of this point.

3. The Image-Force Coefficients

a. The electrostatic image coefficient, ξ_1

(1) Plane-parallel conducting surfaces

The supplemental image field for a line charge λ_1 situated in a gap of height 2h between infinite parallel conducting planes can be derived directly by summing the contributions from an infinite series of images or by use of a simple conformal transformation. From the results of work described in Appendix B, the supplemental electric field is

$$E_y = \frac{\pi^2 \lambda_1}{12\, h^2}(y + 2y_1) \qquad (25a)$$

for a line charge (λ_1) displaced a distance y_1 from the median plane and the field point located directly above the charge at a distance y from the median plane. To obtain the image field at the center of the displaced beam, we set $y_1 = y$ and find

$$E_y = \frac{\pi^2 \lambda_1}{4\, h^2}\, y , \qquad (25b')$$

so that [see Eq. (21a)]

$$\xi_1 = \frac{\pi^2}{16} . \qquad (25b'')$$

It is noted that the value of ξ_1 given by Eq. (25b") is three times the value of ϵ_1 given by Eq. (11) for the identical boundary configuration.

(2) Elliptical boundary

Similarly, with the notation introduced in sub-section A3a(2), the results of Appendix D lead to the following expression for the electric image field arising from small vertical displacements from the center of an elliptical conducting cylinder:

$$E_y = \frac{\lambda_1}{3(w^2 - h^2)} \left\{ 2 \left[\frac{2(2 - k^2)K^2}{\pi^2} - 1\right] y + \left[\frac{4(1 + k^2)K^2}{\pi^2} - 1\right] y_1 \right\} . \qquad (26a)$$

Again setting $y_1 = y$, this becomes

$$E_y = \frac{\lambda_1}{w^2 - h^2}\left[\frac{4K^2}{\pi^2} - 1\right] y \qquad \text{(26b')}$$

and

$$\xi_1 = \frac{1}{(w/h)^2 - 1}\left[\frac{K^2}{\pi^2} - \frac{1}{4}\right] . \qquad \text{(26b'')}$$

The result (26b') includes as a limiting case the image field which arises from the displacement of a line charge within a circular cylinder ($E_{image} = \frac{2\lambda_1}{h^2/y - y} \cong \frac{2\lambda_1}{h^2} y$, $\xi_1 = \frac{1}{2}$), and also that for infinite parallel conducting planes ($\xi_1 = \frac{\pi^2}{16}$, as obtained previously). Approximate values of the coefficient ξ_1 for certain special cases of the axis ratio are listed in Table II below:

TABLE II

Values of the electrostatic image coefficient ξ_1 for a cylinder of elliptical cross section

w/h	k^2	ξ_1
1	0	0.5
5/4	0.838	0.553
4/3	0.904	0.559
3/2	0.965_5	0.575
2/1	0.998	0.599
∞	1	$\frac{\pi^2}{16} \doteq 0.61685$

A remarkably small variation of ξ_1 is evident from the values given in Table II and from the graph shown in Fig. 1.

b. The magnetostatic image coefficient, ξ_2

(1) Plane-parallel magnet poles

The supplemental image field for a current I_1 situated in a gap of height 2g between infinite plane-parallel ferromagnetic slabs can be derived immediately by summing the contributions from an infinite set of images or by use of a simple conformal transformation. From the results of work described in Appendix C, the supplemental magnetic field is

$$H_x = \frac{\pi^2 I_1}{12\, g^2} (2y + y_1) \tag{27a}$$

for a current (I_1) displaced a distance y_1 from the median plane and the field point located directly over this current at a height y above the median plane. To obtain the image field at the center of the displaced beam, we set $y_1 = y$ and find

$$H_x = \frac{\pi^2 I_1}{4\, g^2}\, y\,, \tag{27b'}$$

so that [see Eq. (21b)]

$$\xi_2 = \frac{\pi^2}{16}\,. \tag{27b''}$$

It is noted that the value of ξ_2 given by Eq. (27b") is three-halves the value of ϵ_2 given by Eq. (16) for the identical pole configuration.

(2) Wedge-shaped magnet gap

With the same notation as employed in sub-section A3b(2), the results of Appendix E lead to the following expression for the image field arising from small vertical displacements from the central plane of a wedge-shaped magnet gap:

$$\vec{H}_{image} = \frac{I_1}{X}\left\{(\frac{\pi}{\alpha} - 1)(\frac{\pi}{\alpha} - 5)\frac{y}{6X}\,\hat{i} + \left[(\frac{\pi}{\alpha})^2 + 2\right]\frac{y_1}{12\,X}\,\hat{i}\right.$$

$$\left. + (\frac{\pi}{\alpha} - 1)\,\hat{j} + (\frac{\pi}{\alpha} - 1)(\frac{\pi}{\alpha} - 5)\frac{x}{6X}\,\hat{j} - \left[(\frac{\pi}{\alpha})^2 - 1\right]\frac{x_1}{6X}\,\hat{j}\right\} \quad (28a)$$

$$\doteq I_1\left\{\frac{\pi^2}{6}\left[1 - \frac{6}{\pi}(\frac{g}{R/n}) + (\frac{2}{3} + \frac{5}{\pi^2})(\frac{g}{R/n})^2\right]\frac{y}{g^2}\,\hat{i}\right.$$

$$+ \frac{\pi^2}{12}\left[1 + 2(\frac{1}{3} + \frac{1}{\pi^2})(\frac{g}{R/n})^2\right]\frac{y_1}{g^2}\,\hat{i}$$

$$+ \pi\left[1 - \frac{1}{\pi}(\frac{g}{R/n}) + \frac{1}{3}(\frac{g}{R/n})^2\right]\frac{1}{g}\,\hat{j}$$

$$+ \frac{\pi^2}{6}\left[1 - \frac{6}{\pi}(\frac{g}{R/n}) + (\frac{2}{3} + \frac{5}{\pi^2})(\frac{g}{R/n})^2\right]\frac{x}{g^2}\,\hat{j}$$

$$- \frac{\pi^2}{6}\left[1 + (\frac{2}{3} - \frac{1}{\pi^2})(\frac{g}{R/n})^2\right]\frac{x_1}{g^2}\,\hat{j}\,, \quad (28b)$$

where the coordinates of the current and field point are respectively $(X + x_1,\ y_1)$ and $(X + x,\ y)$ with respect to the vertex of the wedge, X is identified as R/n, and $\alpha = \tan^{-1} g/X = \tan^{-1}\frac{g}{R/n}$ [Equations (17a-b)].

The terms of interest for determination of ξ_2 are those which involve y and y_1 ; with y_1 set equal to y, we obtain

$$H_x = \frac{I_1}{4X^2}\left[(\frac{\pi}{\alpha})^2 - 4(\frac{\pi}{\alpha}) + 4\right]y \quad (29a)$$

$$\doteq \frac{\pi^2 I_1}{4\,g^2}\left[1 - \frac{4}{\pi}(\frac{g}{R/n}) + 2(\frac{1}{3} + \frac{2}{\pi^2})(\frac{g}{R/n})^2\right]y \quad (29b)$$

and

$$\xi_2 = \frac{1}{16}\left[(\frac{\pi}{\alpha})^2 - 4(\frac{\pi}{\alpha}) + 4\right](\frac{g}{X})^2 \quad (30a)$$

$$\doteq \frac{\pi^2}{16}\left[1 - \frac{4}{\pi}\left(\frac{g}{R/n}\right) + 2\left(\frac{1}{3} + \frac{2}{\pi^2}\right)\left(\frac{g}{R/n}\right)^2\right] . \qquad (30b)$$

The dominant term in Eq. (30b) is seen to be in agreement with the value $\xi_2 = \pi^2/16$ that is given by Eq. (27b") for plane-parallel poles $(\frac{n}{R} \to 0)$.

III. Examples

To illustrate the relative importance of energy and aperture in determining the transverse space-charge limit, numerical examples are presented in Table III for a proton synchrotron of 120 meters radius (as might be representative of an AGS designed for a final energy in the neighborhood of 30 or 35 Bev). The bunching factor, which plays an important role only at the lower energies, is taken somewhat arbitrarily as 3/8. The frequency of betatron oscillations is considered to be shifted by action of the space-charge forces from 8.75 oscillations per revolution to the half-integral resonant value of 8.50. Beam dimensions such that $b(a + b) = 5.25\ \mathrm{cm}^2$ are assumed, although these dimensions influence the results strongly only when the energy is low or the gap relatively large. The space-charge limits as determined by single-particle stability were computed by use of Eq. (8c) and the limits for the stability of coherent axial oscillation were evaluated by Eq. (24).* In all cases, plane-parallel magnet poles were assumed, so that $\epsilon_2 = \pi^2/24$ and $\xi_2 = \pi^2/16$.

---

*Since the space-charge limits given in Table I for stability of coherent beam displacement have been computed by use of Eq. (24), they may be considered as more representative of limits imposed by proximity to an integral resonance, for reasons indicated in the footnote to Eq. (24). In addition, considerations which have been carried out by the CERN group in regard to a multi-hundred Gev accelerator suggest that the bunching factor (B) necessarily will differ from unity by a greater amount than is the case in the example considered here.

TABLE III

Illustrative values of transverse space-charge limits, for protons[a]

$B = 3/8$, $a = 2$ cm, $b = 1.5$ cm, $R = 12{,}000$ cm, $\nu_{y_o}^2 - \nu_y^2 = (8.75)^2 - (8.50)^2 = 4.3125$

[The limiting number of particles is given by the values in the Table times 10^{14}.]

	Plane-Parallel Chamber			3:2 Chamber Aperture			Circular Chamber Aperture		
h = g:	3 cm	6 cm	10 cm	3 cm	6 cm	10 cm	3 cm	6 cm	10 cm
w:	∞	∞	∞	4.5 cm	9 cm	15 cm	3 cm	6 cm	10 cm
	Space-Charge Limit for Individual-Particle Stability								
ϵ_1:	$\pi^2/48 = 0.20562$			0.134			0		
ϵ_2:	$\pi^2/24 = 0.41123$			0.41123			0.41123		
K.E.$_{\text{inj.}}$									
50 Mev	0.00735	0.00807	0.00824	0.00764	0.00815	0.00827	0.00826	0.00832	0.00833
200 Mev	0.0350	0.0396	0.0408	0.0365	0.0401	0.0409	0.0397	0.0410	0.0412
1 Bev	0.313	0.429	0.465	0.333	0.437	0.469	0.378	0.455	0.476
5 Bev	2.80	7.62	12.05	3.12	8.19	12.54	3.96	9.53	13.60
10 Bev	5.89	20.4	43.0	6.63	22.6	46.4	8.67	28.2	54.4
	Space-Charge Limit for Stability of Coherent Beam Displacement								
ξ_1:	$\pi^2/16 = 0.61685$			0.575			0.5		
ξ_2:	$\pi^2/16 = 0.61685$			0.61685			0.61685		
K.E.$_{\text{inj.}}$									
50 Mev	0.0214	0.0857	0.238	0.0229	0.0917	0.255	0.0262	0.105	0.291
200 Mev	0.0850	0.340	0.945	0.0904	0.361	1.00	0.102	0.407	1.13
1 Bev	0.393	1.57	4.37	0.411	1.65	4.57	0.448	1.79	4.98
5 Bev	1.64	6.57	18.2	1.70	6.80	18.9	1.82	7.28	20.2
10 Bev	3.10	12.4	34.4	3.21	12.8	35.6	3.42	13.7	38.0

---

[a] $r_p = 1.536 \times 10^{-16}$ cm, for protons of rest mass equivalent to 938 Mev.
For the injection energies cited, we take γ respectively as 1.053, 1.213, 2.066, 6.330, and 11.66.

Several characteristic features of the space-charge phenomenon are apparent from the entries in Table III:

(i) At low energy, or for large apertures, the more stringent limitation is imposed by the requirement of single-particle stability, since the direct action of the beam fields on the particle is then dominant. At higher energies, when the image fields are of greater significance, the requirement for collective stability becomes the more important, since the image-field coefficients are greater for this case.

(ii) The number of particles is effectively proportional to $\beta^2\gamma^3$ only at the lower energies, but this dependence is followed over a somewhat more extended range of energy if the aperture is large. (Note, for example, that the ratio of $\beta^2\gamma^3$ for 200 Mev and 50 Mev kinetic energy is 4.96.) At high energies, the acceptable number of particles is substantially proportional to γ.

(iii) Similarly, the size of the aperture is of major importance at high energies, where the number of particles may vary directly as h^2. The <u>shape</u> of the vacuum-chamber aperture, however, does not appear from the examples considered ($h = g$) to be of great importance.

APPENDIX A

APPLICATION OF CONFORMAL TRANSFORMATIONS

In two-dimensional electrostatic problems, the method of conformal transformations employs a potential function that is the real or imaginary part of an analytic function ($W = U + iV$) of the complex position vector ($z = x + iy$). By virtue of the Cauchy-Riemann conditions, the potential (U or V) satisfies the two-dimensional Laplace equation, and the magnitude of the electric field strength is given by

$$E = \left| \frac{dW}{dz} \right| \quad . \tag{A.1}$$

If, for an isolated line charge of strength λ (e.s.u. per cm), we take $W = -2\lambda \log z$ (where z denotes the position of the field point with respect to the line charge), the potential function is*

$$\text{Potential} = U = -2\lambda \log |z| \quad , \tag{A.2a}$$

$$\vec{E} = - \text{grad } U = 2\lambda \frac{\hat{r}}{r} \quad , \text{ and} \tag{A.2b'}$$

$$|E| = \frac{2\lambda}{r} = \left| \frac{dW}{dz} \right| . \tag{A.2b''}$$

With steady line currents in a two-dimensional problem, the Cartesian magnetic-field components and the vector potential (A, with $\vec{A} = A\hat{k}$) similarly satisfy the two-dimensional Laplace equation. Again a complex analytic function (W) may be employed, with $\vec{H} = \text{curl } \vec{A} = \hat{k} \times (-\text{grad } A)$ and A expressed by U or V. For an isolated line current of strength I (e.m.u.), we may take $W = 2\,I \log z$, with

---

*We employ natural logarithms in this analysis.

$$A = U = -2\,I \log|z| \quad , \tag{A.3a}$$

$$\vec{H} = \hat{k} \times (-\mathrm{grad}\ U) = 2\,I\,\frac{\hat{k} \times \hat{r}}{r}, \text{ and} \tag{A.3b'}$$

$$|H| = \frac{2I}{r} = \left|\frac{dW}{dz}\right| \text{ oersted.} \tag{A.3b''}$$

The usual boundary condition to be satisfied at the surface of ferromagnetic material of high permeability is $H_t = 0$, or $\partial A/\partial n = 0$ and the orthogonal function remains constant along the boundary. This requirement must be abandoned, however, if its application would violate the basic equation $\oint \vec{H}\cdot\vec{d\ell} = 4\pi\,\Sigma I$, as would be the case for a current-carrying conductor threading a tube of ferromagnetic material. The magnetic-field lines can be visualized as a system orthogonal to the flow lines in a current-flow or heat-flow problem in which, with similar geometry, the line current becomes a source and the ferromagnetic material assumes the property of very high resistance to the flow of current or heat. The magnetic-field lines are curves which then become, in this analogy, the electric or thermal equipotentials.

In the case of alternating currents, the phenomenon of skin effect will prevent the ac magnetic field from penetrating into neighboring conductors, and the magnetic field must be tangential at the surface of these conductors. The magnetic-field lines of a two-dimensional problem involving alternating currents directed exclusively in the z-direction thus constitute a system orthogonal to that given by the electric-field lines of the geometrically similar electrostatic problem, and the magnitude of the magnetic field will be just I/λ times the value of $\left|\frac{dW}{dz}\right|$ for the corresponding electrostatic case.

In all cases, determination of the complex function W may be aided by use of intermediate conformal transformations in which the strength of the sources remains unchanged. Electrostatic field lines which go to infinity may, however, be interpreted as associated with a sink represented by a negative charge, and this charge will have to be included whenever the point at infinity is transformed to within the finite region of the next complex plane; an analogous situation in a magnetostatic problem would involve transforming a return current at infinity so that this current would fall in the finite region of the complex plane.

APPENDIX B

IMAGES IN INFINITE PARALLEL CONDUCTING PLANES

1. Application of Conformal Transformation

The transformation

$$z' = \exp \pi(z + ih)/2h \tag{B.1}$$

is useful for transforming the boundaries of interest to the real axis of the z'-plane and carries the region between the plates into the upper half of this new complex plane.

z	z'
$\infty + ih$	$-\infty$
ih	-1
$-\infty$	0
$-ih$	$+1$
$\infty - ih$	$+\infty$

With the line charge λ_1 located at $z = iy_1$ and the field point at $z = iy$, the electrostatic potential may be written directly by use of a single image $(-\lambda_1)$ in the z_1-plane:

$$U = -2\lambda_1 \log \left| \frac{\exp i\pi(y+h)/2h - \exp i\pi(y_1+h)/2h}{\exp i\pi(y+h)/2h - \exp -i\pi(y_1+h)/2h} \right| \tag{B.2a}$$

$$= -2\lambda_1 \log \left| \frac{\sin \pi y/2h - \sin \pi y_1/2h}{1 + \cos \pi(y+y_1)/2h} \right| \tag{B.2b}$$

$$\doteq -2\lambda_1 \log \left\{ \frac{\pi}{4} \frac{|y - y_1|}{h} \left[1 + \frac{\pi^2}{48} \frac{y^2 + 4y\,y_1 + y_1^2}{h^2} \right] \right\} \tag{B.2c}$$

$$\doteq -2\lambda_1 \log \left(\frac{\pi}{4} \frac{|y - y_1|}{h} \right) - \frac{\pi^2 \lambda_1}{24\,h^2} (y^2 + 4yy_1 + y_1^2) \,. \tag{B.2d}$$

The image-field, as derived from the image-dependent term in Eq. (B.2d), then is

$$\vec{E}_{\text{image}} = \frac{\pi^2 \lambda_1}{12h^2} (y + 2y_1)\, \hat{j} \,, \qquad \text{for } x = x_1 \,. \tag{B.3}$$

This result is employed in the body of the present report in writing Equations (10) and (25a).

2. Direct Summation of Image Fields

The result expressed by Eq. (B.3) can be derived directly by summing the field contributions of an infinite series of images of alternating sign. The following system of images applies:

Charge	Distance from Field Point
Original λ_1	$y_1 - y$ above
$-\lambda_1$	$2h - y_1 - y$ above
$-\lambda_1$	$2h + y_1 + y$ below
$+\lambda_1$	$4h - y_1 + y$ below
$+\lambda_1$	$4h + y_1 - y$ above
$-\lambda_1$	$6h - y_1 - y$ above
$-\lambda_1$	$6h + y_1 + y$ below
...	...

The upward-directed electric field due to the images alone then is:

$$E_{image} = 2\lambda_1 \left[\frac{1}{2h-y_1-y} - \frac{1}{2h+y_1+y} + \frac{1}{4h-y_1+y} - \frac{1}{4h+y_1-y} + \frac{1}{6h-y_1-y} - \frac{1}{6h+y_1+y} + \ldots\right] \quad \text{(B.4a)}$$

$$= 4\lambda_1 \left[\frac{y_1 + y}{4h^2 - (y_1 + y)^2} + \frac{y_1 - y}{16h^2 - (y_1 - y)^2} + \frac{y_1 + y}{36h^2 - (y_1 + y)^2} + \ldots\right] \quad \text{(B.4b)}$$

$$\doteq \frac{\lambda_1}{h^2} \Big\{[(y_1 + y) + (1/9)(y_1 + y) + (1/25)(y_1 + y) + \ldots]$$
$$+ [(1/4)(y_1 - y) + (1/16)(y_1 - y) + \ldots]\Big\} \quad \text{(B.4c)}$$

$$= \frac{\lambda_1}{h^2} \left[(y_1+y)(1^{-2}+ 3^{-2}+ 5^{-2}+ \ldots) + (1/4)(y_1-y)(1^{-2}+ 2^{-2}+ 3^{-2} + \ldots)\right] \quad \text{(B.4d)}$$

$$= \frac{\lambda_1}{h^2} \left[(y_1 + y)\frac{\pi^2}{8} + (y_1 - y)\frac{\pi^2}{24}\right] \quad \text{(B.4e)}$$

$$= \frac{\pi^2\lambda_1}{12h^2} (y + 2y_1) , \quad \text{(B.4f)}$$

in agreement with Eq. (B.3).

APPENDIX C

IMAGES IN INFINITE PLANE-PARALLEL FERROMAGNETIC POLES

1. Application of Conformal Transformation

The field which arises from the images of a line current (I_1) in infinite plane-parallel ferromagnetic poles can be computed readily by aid of the transformation (B.1) that was introduced in Appendix B. The single image ($-\lambda_1$), which was employed in the z'-plane for the purpose of the electrostatic computation, now becomes replaced by a positive line current ($+I_1$). In addition, however, a line current $-I_1/2$ at $x = -\infty$ in the z-plane is transformed to $z' = 0$. This current, together with its image (of like sign) in the x'-axis, constitute a current ($-I_1$) whose contribution to the potential must be included. [The significance of the line current $-I_1/2$ at $x = -\infty$ may be appreciated most clearly by visualizing the analogous problem of conduction current or heat flow, in which half the flow lines emerging from the given source I_1 pass to the left to terminate on a "sink" (of source strength $-I_1/2$) at $x = -\infty$.]

With the line current I_1 located at $z = iy_1$ and the field point at $z = iy$, and with a pole separation of 2g, the potential function becomes in this case:

$$A = U = -2\, I_1 \log \left| \frac{\left[\exp i\pi(y+g)/2g - \exp i\pi(y_1+g)/2g\right] \times \left[\exp i\pi(y+g)/2g - \exp -i\pi(y_1+g)/2g\right]}{\exp i\pi(y+g)/2g} \right| \tag{C.1a}$$

$$= -2\, I_1 \log \left[2 \left|\sin \pi y/2g - \sin \pi y_1/2g\right|\right] \tag{C.1b}$$

$$\doteq -2\, I_1 \log \left\{\frac{\pi|y - y_1|}{g}\left[1 - \frac{\pi^2}{24}\,\frac{y^2 + yy_1 + y_1^2}{g^2}\right]\right\} \tag{C.1c}$$

$$\doteq -2\, I_1 \log \left(\pi\frac{|y - y_1|}{g}\right) + \frac{\pi^2\, I_1}{12\, g^2}\,(y^2 + yy_1 + y_1^2)\ . \tag{C.1d}$$

The image field, as obtained by evaluation of $\hat{k} \times (-\text{grad } U)$ for the image-dependent terms in Eq. (C.1d), is in the x-direction and of the amount

$$H_{\text{image}} = \frac{\pi^2 I_1}{12\, g^2} (2y + y_1) , \qquad \text{for} \quad x = x_1. \tag{C.2}$$

This result is employed in the body of the report in writing Equations (15) and (27a).

2. Direct Summation of Image Fields

As in the electrostatic problem for infinite plane-parallel conducting plates, the magnetostatic problem to which Eq. (C.2) applies also can be solved directly by summing the field contributions of an infinite series of images. The locations of the required image currents are the same as for the line charges considered in Sect. 2 of Appendix B, but in the present case the sign of each image is that of the original current ($+I_1$).

The horizontal magnetic field of the images ($\vec{H} = H_x \hat{\imath}$) is

$$H_{\text{image}} = 2I_1 \left[\frac{1}{2g-y_1-y} - \frac{1}{2g+y_1+y} - \frac{1}{4g-y_1+y} + \frac{1}{4g+y_1-y} + \frac{1}{6g-y_1-y} - \frac{1}{6g+y_1+y} + \ldots\right] \tag{C.3a}$$

$$= 4I_1 \left[\frac{y_1 + y}{4g^2 - (y_1 + y)^2} - \frac{y_1 - y}{16g^2 - (y_1 - y)^2} + \frac{y_1 + y}{36g^2 - (y_1 + y)^2} + \ldots\right] \tag{C.3b}$$

$$\doteq \frac{I_1}{g^2} \Big\{[(y_1 + y) + (1/9)(y_1 + y) + (1/25)(y_1 + y) + \ldots]$$
$$- [(1/4)(y_1 - y) + (1/16)(y_1 - y) + \ldots]\Big\} \tag{C.3c}$$

$$= \frac{I_1}{g^2} \left[(y_1 + y)(1^{-2} + 3^{-2} + 5^{-2} + \ldots) - (1/4)(y_1 - y)(1^{-2} + 2^{-2} + 3^{-2} + \ldots)\right] \tag{C.3d}$$

$$= \frac{I_1}{g^2} \left[(y_1 + y)\frac{\pi^2}{8} - (y_1 - y)\frac{\pi^2}{24}\right] \tag{C.3e}$$

$$= \frac{\pi^2 I_1}{12g^2} (2y + y_1) , \qquad \text{in agreement with Eq. (C.2).} \tag{C.3f}$$

APPENDIX D

ELECTROSTATIC IMAGES IN AN ELLIPTICAL CONDUCTING CYLINDER

We are concerned here with the image fields which arise from an elliptical conducting cylinder, of which the upper portion extends from the point A ($x = w$) through B ($y = h$) to A_1 ($x = -w$). The center is at the origin (0,0), and the foci F, F_1 are at $x = \pm\sqrt{w^2 - h^2}$. Sufficient generality will be obtained for the work of this report by locating the line charge (λ_1) and the field point (F.P.) on the y-axis, at $z = iy_1$ and $z = iy$, respectively.

In order that specific boundary conditions may be applied along the line AA_1, despite the asymmetry introduced when $y_1 \neq 0$, it is convenient to consider the potential in the z-plane as the average of the potentials which would result in the following two cases:

Case I: The entire boundary, $OFABA_1F_1O$, of the region contained within the upper half of the ellipse is at constant (zero) potential.

Case II: The elliptical boundary is at constant (zero) potential, but the horizontal axis, AA_1 is a stream line.

These two cases would respectively arise if identical charges (λ_1) were located at $z = \pm iy_1$, or if charges of equal magnitude and opposite sign ($\pm\lambda_1$) were located at these two symmetrical points. In either case, the portions of the y-axis from λ_1 to B and to 0 are stream lines.

The transformation

$$z' = m \sin^{-1} \frac{z}{\sqrt{w^2 - h^2}} \tag{D.1}$$

will transform the region within the upper half of the ellipse to that within a rectangle in the z'-plane. A second transformation,

$$z'' = q \,\mathrm{sn}\left(\frac{2K}{\pi} \frac{z'}{m}, k\right) \tag{D.2a}$$

$$= q \,\mathrm{sn}\left(\frac{2K}{\pi} \sin^{-1} \frac{z}{\sqrt{w^2 - h^2}}, k\right), \tag{D.2a'}$$

in turn will transform this region to that above the x"-axis of the z"-plane. The boundary point B lies at $x'' = \pm \infty$, the points A and A_1 at $\pm p$, and the points F and F_1 at $\pm q$. In Equations (D.2a,a'), K denotes the complete elliptic integral of the second kind,

$$k \equiv q/p \,, \tag{D.2b}$$

and k is selected so that

$$\frac{K'}{K} = \frac{2}{\pi} \tanh^{-1} \frac{h}{w} \,. ^{*} \tag{D.2c}$$

---

*K' denotes K(k'), where $k' \equiv \sqrt{1 - k^2}$. [For numerical values and helpful relations concerning elliptic functions and integrals, see, for example, E. Jahnke and F. Emde, "Tables of Functions (Funktionentafeln)" (Dover Publications, New York, 1945), Chapters V and VI.]

Point	z	z'	z"
0	0	0	0
λ_1	iy_1	$im\ \sinh^{-1}\frac{y_1}{\sqrt{w^2 - h^2}}$	iy_1''
F.P.	iy	$im\ \sinh^{-1}\frac{y}{\sqrt{w^2 - h^2}}$	iy''
B	ih	$im\ \tanh^{-1}\frac{h}{w}$	$\pm\infty$
A, A_1	$\pm w$	$m\ (\pm\frac{\pi}{2} + i\ \tanh^{-1}\frac{h}{w})$	$\pm p$
F, F_1	$\pm\sqrt{w^2 - h^2}$	$\pm m\ \frac{\pi}{2}$	$\pm q$

The location of the field point in the z"-plane is given by

$$z'' = iy'' = q\ \mathrm{sn}(\frac{2iK}{\pi}\ \sinh^{-1}\frac{y}{\sqrt{w^2 - h^2}}\ ,\ k) \tag{D.3a}$$

$$= iq\ \mathrm{tn}(\frac{2K}{\pi}\ \sinh^{-1}\frac{y}{\sqrt{w^2 - h^2}}\ ,\ k'), \tag{D.3b}$$

and a similar equation relates the coordinates y_1'' and y_1 of the line charge. In Case I, for which the entire boundary, BA_1OAB is at zero potential, the required potential function can be written immediately in terms of the coordinates in the z"-plane:

$$U_I = -\ 2\lambda_1\ \log\left|\frac{y'' - y_1''}{y'' + y_1''}\right|\ . \tag{D.4}$$

For Case II, in which the line segment A_1F_1OFA is a stream line while the remainder of the x"-axis is at zero potential, additional transformations are required. A possible systematic procedure employs the following:

(i) the transformation

$$z''' = t\sqrt{(z''/y_1'')^2 + 1}\ , \tag{D.5}$$

to bring the charge λ_1 to the origin of the z'''-plane [with the result that the stream line from $z'' = iy_1''$ to the origin of the z''-plane becomes a portion $(-t \le x''' \le t)$ of that segment (AA_1, between the points $x''' = \pm t\sqrt{(p/y_1'')^2 + 1}$) of the x'''-axis which constitutes a stream line]; an image charge, λ_1, should also be imagined as located at the origin, an infinitesimal distance below the x'''-axis, in order that the strength of the original source λ_1 be confined, as it should, to the upper half of the z'''-plane;

(ii) the transformation

$$z^{iv} = \frac{2u}{\pi}\sin^{-1}\frac{z'''/t}{\sqrt{(p/y_1'')^2 + 1}} \tag{D.6a}$$

$$= \frac{2u}{\pi}\sin^{-1}\sqrt{\frac{z''^2 + y_1''^2}{p^2 + y_1''^2}}\ , \tag{D.6b}$$

to fold upward by 90° the zero-potential portions of the x'''-axis; and

(iii) the transformation, analogous to that employed in Sect. 1 of Appendix B,

$$z^v = v\exp\left[i\,\frac{\pi}{2}\,(1 - \frac{z^{iv}}{u})\right]\ , \tag{D.7}$$

to bring the vertical equipotentials that extend between $\pm i\infty$ at $x^{iv} = \pm u$ into coincidence with the entire x^v-axis. By Eq. (D.7), the z^v-coordinates of the line charge (strength $2\lambda_1$) and of the field point above it become respectively $z_1^v = iy_1^v = iv$ and $z^v = iy^v = iv\exp\frac{\pi}{2}\frac{y^{iv}}{u}$.

For Case II, therefore, the potential function may be written

$$U_{II} = -4\lambda_1 \log \left| \frac{y^{v} - v}{y^{v} + v} \right| \tag{D.8a}$$

$$= 4\lambda_1 \log \operatorname{ctnh} \frac{\pi}{4} \frac{y^{iv}}{u} \tag{D.8b}$$

$$= 4\lambda_1 \log \operatorname{ctnh} \left(\frac{1}{2} \sinh^{-1} \sqrt{\frac{y''^2 - y_1''^2}{p^2 + y_1''^2}} \right) \tag{D.8c}$$

$$= 4\lambda_1 \log \frac{\sqrt{p^2 + y''^2} + \sqrt{p^2 + y_1''^2}}{\sqrt{y''^2 - y_1''^2}} . \tag{D.8d}$$

By averaging the potentials U_I and U_{II}, given by Equations (D.4) and (D.8d), we obtain the result

$$U = \lambda_1 \log \left[\frac{y'' + y_1''}{y'' - y_1''} \left(\frac{\sqrt{p^2 + y''^2} + \sqrt{p^2 + y''^2}}{\sqrt{y''^2 - y_1''^2}} \right)^2 \right] , \tag{D.9a}$$

which may be expressed in terms of the coordinates y and y_1 in the original z-plane as

$$U = 2\lambda_1 \log \frac{\sqrt{k^2 \operatorname{tn}^2 (\frac{2K}{\pi} \sinh^{-1} \frac{y}{\sqrt{w^2 - h^2}}, k') + 1} + \sqrt{k^2 \operatorname{tn}^2 (\frac{2K}{\pi} \sinh^{-1} \frac{y_1}{\sqrt{w^2 - h^2}}, k') + 1}}{k \left[\operatorname{tn}(\frac{2K}{\pi} \sinh^{-1} \frac{y}{\sqrt{w^2 - h^2}}, k') - \operatorname{tn}(\frac{2K}{\pi} \sinh^{-1} \frac{y_1}{\sqrt{w^2 - h^2}}, k') \right]} \tag{D.9b}$$

To be published in the Proceedings of the
III All-Union National Conference on
Particle Accelerators, Moscow,
Oct. 2 - 4, 1972

LBL-1072

Transverse Two-Stream Instability in the Presence of Strong Species-Species and Image Forces

L.J. Laslett, D. Möhl, and A.M. Sessler

TRANSVERSE TWO-STREAM INSTABILITY IN THE PRESENCE OF STRONG SPECIES-SPECIES AND IMAGE FORCES

L.J. Laslett and A.M. Sessler*

Lawrence Berkeley Laboratory
University of California
Berkeley, California 94720

and

D. Möhl

CERN
Geneva 23, Switzerland

ABSTRACT

The theory of coherent transverse oscillations of two particle species is extended to include strong species-species and image forces. It is shown that in general the species-species force can considerably alter the instability threshold. Conversely, it is shown that the limit on the performance of an electron ring accelerator imposed by the requirement of stable ion electron oscillations, is not significantly improved by the inclusion of images.

---

* Work supported by the U.S. Atomic Energy Commission.

The potential expressed by Eq. (D.9b) may be expanded,* noting that $k' \equiv \sqrt{1 - k^2}$, to give the result

$$U \doteq -2\lambda_1 \left\{ \log\left(\frac{kK}{\pi} \frac{y-y_1}{\sqrt{w^2-h^2}} \right) + \frac{1}{6(w^2-h^2)} \left[\left(\frac{2(2-k^2)K^2}{\pi^2} - 1\right) y^2 + \left(\frac{4(1+k^2)K^2}{\pi^2} - 1\right) y y_1 + \left(\frac{2(2-k^2)K^2}{\pi^2} - 1\right) y_1{}^2 \right] \right\} , \tag{D.9c}$$

and the vertical image field becomes

$$E_{\text{image}} = \frac{\lambda_1}{3(w^2-h^2)} \left\{ 2\left[\frac{2(2-k^2)K^2}{\pi^2} - 1 \right] y + \left[\frac{4(1+k^2)K^2}{\pi^2} - 1 \right] y_1 \right\} , \tag{D.10}$$

as has been employed in writing Equations (13) and (26a) in the body of the report.

The results expressed by Eq. (D.10) may be checked for two limiting cases – that of parallel planes ($w \to \infty$), and that of a circular cylinder ($w \to h$). In the first of these,

$$k \doteq 1, \qquad K' \doteq \frac{\pi}{2}, \qquad \text{and} \quad K \cong \frac{\pi^2}{4} \frac{w}{h},$$

---

*$$\text{sn}(u,k) \doteq u - \frac{k^2+1}{6} u^3 + \frac{k^4 + 14\,k^2 + 1}{120} u^5 ,$$

as may be obtained by expanding the elliptic integral

$$u = \int_0^{\text{sn}\,u} \frac{dt}{\sqrt{1 - t^2}\,\sqrt{1 - k^2 t^2}} .$$

Then

$$\text{cn}(u,k) \doteq 1 - \frac{1}{2} u^2 + \frac{4k^2 + 1}{24} u^4$$

and

$$\text{tn}(u,k) \doteq u - \frac{k^2 - 2}{6} u^3 + \frac{k^4 - 16\,k^2 + 16}{120} u^5 .$$

In expanding factors of the form $y'' - y_1''$, terms through third order must be retained, in order that terms of second order will remain in the expansion after $y - y_1$ has been factored out.

in order that $\frac{K'}{K}$ equal $\frac{2}{\pi}\tanh^{-1}\frac{h}{w} \doteq \frac{2}{\pi}\frac{h}{w}$. Then

$$\underset{w \to \infty}{E_{\text{image}}} \to \frac{\lambda_1}{3w^2}\left\{\frac{\pi^2}{4}\frac{w^2}{h^2}\,y + \frac{\pi^2}{2}\frac{w^2}{h^2}\,y_1\right\} = \frac{\pi^2\lambda_1}{12\,h^2}(y + 2y_1)\ ,$$

in agreement with Eq. (B.3) or (B.4f) of Appendix B.

In the second limiting case,

$$k^2 \cong 8(w - h)/h, \qquad K' \cong \log\sqrt{\frac{2h}{w-h}}\ , \qquad \text{and} \quad K^2 \cong \frac{\pi^2}{4}\left(1 + \frac{k^2}{2}\right).$$

Then

$$\underset{w \to h}{E_{\text{image}}} \to \frac{\lambda_1}{6h(w - h)}\left\{2\left[\left(1 - \frac{k^2}{2}\right)\left(1 + \frac{k^2}{2}\right) - 1\right] y + \left[(1 + k^2)\left(1 + \frac{k^2}{2}\right) - 1\right] y_1\right\}$$

$$= \frac{\lambda_1 k^2}{4h(w - h)}\,y_1 = \frac{2\lambda_1}{h^2}\,y_1\ ,$$

as is directly obtainable from calculation of the image field which results from an image charge situated a distance h^2/y_1 from the center of a circular cylinder of radius h [see the discussion in the text following Eq. (26b")].

APPENDIX E

MAGNETIC IMAGES FOR A WEDGE-SHAPED GAP

We consider here a wedge-shaped gap, of half-angle α, between ferromagnetic poles. The reference point, which serves as the origin of the z-plane, is situated on the median plane of the gap a distance X from the vertex. The current (I_1) and field point will be located with respect to this reference point by coordinates, (x_1, y_1) or (x, y), which themselves are small in comparison to the half-gap

$$g = X \tan \alpha \, . \tag{E.1a}$$

Since the magnetostatic potential which would be generated by a pair of magnet poles in this configuration is proportional to the angular coordinate taken about the vertex as a center,[8] the distance X would equal $- \left.\frac{H}{dH/dr}\right|_X$ and we may set

$$X = \frac{R}{n} \, , \tag{E.1b}$$

where n is the so-called "field index" which measures the relative gradient of the magnetic field. With this simple pole configuration, however, the field gradient may not be as constant as would be desirable in practice, but the arrangement described may serve as a useful model for the investigation of image forces resulting from the presence of a line current in the magnet gap.

The transformation

$$z' = ia' \left(\frac{z}{X} + 1\right)^{\pi/2\alpha} \tag{E.2}$$

will transform the region between the ferromagnetic boundaries into the upper half of the z'-plane, with the vertex of the wedge (z = -X) transformed to z' = 0 and the reference point to z' = iy' = ia'. The potential function then may be written

---

8. See, for example, Sir James Jeans, "The Mathematical Theory of Electricity and Magnetism" (Cambridge University Press, Cambridge, 1948), Sect. 318.

$$A = U = -2I_1 \log \left| \left[(x' + iy') - (x_1' + iy_1') \right] \left[(x' + iy') - (x_1' - iy_1') \right] \right| \tag{E.3a}$$

$$= -2I_1 \log \left\{ a'^2 \left| \left[\left(1 + \frac{x+iy}{X}\right)^{\pi/2\alpha} - \left(1 + \frac{x_1+iy_1}{X}\right)^{\pi/2\alpha} \right] \times \left[\left(1 + \frac{x+iy}{X}\right)^{\pi/2\alpha} + \left(1 + \frac{x_1-iy_1}{X}\right)^{\pi/2\alpha} \right] \right| \right\} \tag{E.3b}$$

$$\doteq -2I_1 \log \left(\frac{\pi a'^2}{\alpha} \frac{\sqrt{(x-x_1)^2 + (y-y_1)^2}}{X} \right) - I_1 \left\{ \left(\frac{\pi}{\alpha} - 1\right)\frac{x+x_1}{X} + \left(\frac{\pi}{\alpha} - 1\right)\left(\frac{\pi}{\alpha} - 5\right)\frac{x^2+x_1^2 - y^2-y_1^2}{12\,X^2} - \left[\left(\frac{\pi}{\alpha}\right)^2 - 1 \right] \frac{x\,x_1}{6\,X^2} - \left[\left(\frac{\pi}{\alpha}\right)^2 + 2 \right] \frac{y\,y_1}{12X^2} \right\} . \tag{E.3c}$$

By forming $\hat{k} \times (-\text{grad } U)$, one obtains the supplementary image field

$$\vec{H}_{\text{image}} = \frac{I_1}{X} \left\{ \left(\frac{\pi}{\alpha} - 1\right)\left(\frac{\pi}{\alpha} - 5\right)\frac{y}{6X}\,\hat{i} + \left[\left(\frac{\pi}{\alpha}\right)^2 + 2 \right]\frac{y_1}{12\,X}\,\hat{i} + \left(\frac{\pi}{\alpha} - 1\right)\hat{j} + \left(\frac{\pi}{\alpha} - 1\right)\left(\frac{\pi}{\alpha} - 5\right)\frac{x}{6X}\,\hat{j} - \left[\left(\frac{\pi}{\alpha}\right)^2 - 1 \right]\frac{x_1}{6X}\,\hat{j} \right\} \tag{E.4a}$$

$$\doteq I_1 \left\{ \frac{\pi^2}{6} \left[1 - \frac{6}{\pi}\left(\frac{g}{R/n}\right) + \left(\frac{2}{3} + \frac{5}{\pi^2}\right)\left(\frac{g}{R/n}\right)^2 \right] \frac{y}{g^2}\,\hat{i} + \frac{\pi^2}{12} \left[1 + 2\left(\frac{1}{3} + \frac{1}{\pi^2}\right)\left(\frac{g}{R/n}\right)^2 \right] \frac{y_1}{g^2}\,\hat{i} + \pi \left[1 - \frac{1}{\pi}\left(\frac{g}{R/n}\right) + \frac{1}{3}\left(\frac{g}{R/n}\right)^2 \right] \frac{1}{g}\,\hat{j} + \frac{\pi^2}{6} \left[1 - \frac{6}{\pi}\left(\frac{g}{R/n}\right) + \left(\frac{2}{3} + \frac{5}{\pi^2}\right)\left(\frac{g}{R/n}\right)^2 \right] \frac{x}{g^2}\,\hat{j} - \frac{\pi^2}{6} \left[1 + \left(\frac{2}{3} - \frac{1}{\pi^2}\right)\left(\frac{g}{R/n}\right)^2 \right] \frac{x_1}{g^2}\,\hat{j} \right\} , \tag{E.4b}$$

where in going from Eq. (E.4a) to (E.4b) we have made use of Equations (E.1a) and (E.1b) to identify X with R/n and α with $\tan^{-1} \frac{g}{R/n}$, and have considered g small in comparison to R/n.

Equation (E.4a) may be checked in two limiting cases, of which the first is that for which $\alpha \to 0$ and $X \to \infty$ so that $\alpha X \to g$. Physically this corresponds to the magnet surfaces becoming the faces of plane-parallel poles, with a yoke situated at a great distance to the left. In this case the image field becomes

$$\vec{H}_{(i)} = I_1 \left\{ \left[\frac{\pi}{g} + \frac{\pi^2}{6} \frac{x - x_1}{g^2}\right] \hat{j} + \frac{\pi^2}{12} \frac{2y + y_1}{g^2} \hat{i} \right\} .$$

In this result the horizontal field component agrees with Equations (C.2) and (C.3f) of Appendix C, the term $\frac{\pi^2 I_1}{6\ g^2}(x - x_1)\ \hat{j}$ is consistent with the condition $\nabla \times \vec{H} = 0$, and the component $\frac{\pi I_1}{g} \hat{j}$ is the field expected from an infinite set of current images in the yoke (images separated vertically by 2g and situated a large distance to the left).

In the limiting case that $\alpha \to \frac{\pi}{2}$, the distance X represents the distance by which the reference point is located to the right of the face of an infinite plane slab of ferromagnetic material. The field given by Eq. (E.4a),

$$\vec{H}_{(ii)} = I_1 \left[\left(\frac{1}{X} - \frac{x + x_1}{2\ X^2}\right) \hat{j} - \frac{y - y_1}{2\ X^2} \hat{i} \right] ,$$

is just the field to be expected at a point $X+x$ to the right of the slab by virtue of an image current (I_1) situated a distance $X+x_1$ to the left of the slab when the difference in elevation is $y-y_1$:

$$\vec{H}_{(ii)} = 2I_1 \left[\frac{2X + x + x_1}{(2X + x + x_1)^2 + (y - y_1)^2} \hat{j} - \frac{y - y_1}{(2X + x + x_1)^2 + (y - y_1)^2} \hat{i} \right]$$

$$\doteq I_1 \left[\frac{1}{X} \left(1 - \frac{x + x_1}{2X}\right) \hat{j} - \frac{y - y_1}{2\,X^2} \hat{i} \right],$$

as was obtained from Eq. (E.4a) for the case $\alpha \to \frac{\pi}{2}$.

QUADRATIVE FORCES THAT DRIVE COHERENT RADIAL MOTION OF A BEAM IN THE NEIGHBORHOOD OF THIN, IMPERFECTLY-CONDUCTING SIDE PLATES *

Glen R. Lambertson and L. Jackson Laslett

Lawrence Radiation Laboratory
University of California
Berkeley, California

July 8, 1971

I. INTRODUCTION

A coherent transverse instability of the electron ring has been observed in some recent experiments with the LRL "Compressor IV" device. This instability evidently involves a radial collective motion, as is indicated by probe measurements and by the detection of strong electromagnetic signals with the characteristic frequency $(1 - \nu_r) \cdot f_o$.† The radial instability has been observed at times for which the radius of the ring beam is considerably less than the radius of the inflector structure or of similar devices that are situated near the outer boundary of the vacuum chamber -- it is of interest, therefore, to investigate the extent to which radially-directed forces in quadrature with the radial displacement could arise from the presence of imperfectly-conducting layers (~ 10 to 50 ohms per square) on the side walls of the chamber.

In this report we present, in Sect. II, a simple analysis of the radial quadrature forces that could act on the particles of a precessing ring beam to drive the instability in question when poorly-conducting side plates are situated near-by. The analysis takes no account of the presence

---

* Work supported by the U.S. Atomic Energy Commission.

† f_o denotes the cyclotron frequency, and $\nu_r f_o$ is the frequency of coherent radial betatron oscillations.

of dielectric walls (that themselves may be lossy) and, for simplicity, considers first the case of a "straightened-out" beam that oscillates transversely about an otherwise linear trajectory. An Appendix provides a correction factor that should be applied to the magnetic component of the force (the magnetic component typically being dominant) to allow for the circular nature of the true equilibrium orbit. The dynamical implications of these forces are discussed in Section III, and a numerical example is given in Sect. IV.

It will be recognized that a complete dynamical analysis of the collective motion requires, in addition, an evaluation of in-phase perturbation forces that may arise from a small coherent transverse oscillation of the beam and also must consider the Landau damping that can be introduced by virtue of a spread in the energy or oscillation-amplitude of the particles in the beam. The in-phase forces frequently may arise, however, from "self-fields" that are independent of the surroundings and the Landau-damping coefficients of course are determined by the character of the externally-applied magnetic field, so neither of these effects are treated in the present report. It will be recalled, however, that evaluation of the quadrature forces will lead directly to an estimate of growth rate for the instability when (as may be the case in the recent Compressor IV experiments) the Landau damping is insufficient to suppress the instability.

II. ANALYSIS, FOR A STRAIGHTENED-OUT BEAM

A. Magnetic Forces

With a thin surface layer of resistive material, the thickness Δ is sufficiently small, in relation to the characteristic skin-depth parameter δ (e.g., by a factor of several thousand), that the magnetic field arising from an oscillating beam may be assumed to penetrate the layer virtually unimpeded. The associated flux changes then permit the computation of induced currents and of the asociated fields that then can react on the beam.

We now consider a ring beam, of radius "a", that is oscillating transversely with an amplitude A. In a straightened-out geometry, this beam may be regarded as providing a current I whose position is described by

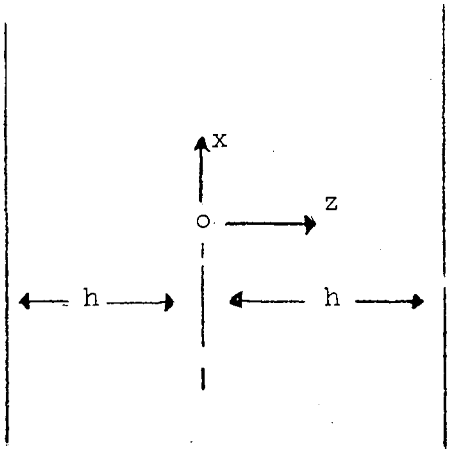

$$x_b = A \cos \left(\frac{y}{a} - \omega t\right),$$

where, in the lowest mode,

$$\omega = (1 - \nu_r) \left(\frac{\beta c}{a}\right)$$

$$= (1 - \nu_r)\, \omega_o .$$

With x, y, z denoting the coordinates of an observation point, the vector potential for the magnetic field of this beam may be written as $\vec{A} = A_y\, \hat{e}_y$, with (in the long-wavelength limit)

$$A_y = \frac{\mu_o I}{2\pi} \ell n \frac{1}{r} = -\frac{\mu_o I}{4\pi} \ell n\, r^2$$

$$= -\frac{\mu_o I}{4\pi} \ell n \left[(x - x_b)^2 + (z - z_b)^2\right]$$

and

$$A_y = -\frac{\mu_o I}{4\pi} \ell n \left[(x - x_b)^2 + h^2\right]$$

at the location of the side walls.

Then

$$\dot{A}_y\Big|_{z=\pm h} = \frac{\mu_o I}{2\pi} \frac{x - x_b}{(x - x_b)^2 + h^2} \dot{x}_b$$

$$= \frac{\mu_o I}{2\pi} \omega A \frac{x - x_b}{(x - x_b)^2 + h^2} \sin\left(\frac{y}{a} - \omega t\right),$$

and the induced current per unit width in each of the thin side plates is

$$J_y = -\frac{1}{R_s} \dot{A}_y$$

$$= -\frac{\mu_o \omega I}{2\pi R_s} A \frac{x - x_b}{(x - x_b)^2 + h^2} \sin\left(\frac{y}{a} - \omega t\right),$$

where R_s is the (d.c.) surface resistance (ohms per square) of the side plates. Such a current distribution over the two side plates will lead to a magnetic field component at the beam that, in terms of

$$X = x - x_b,$$

is given by

$$B_{z_I}\Big|_{z=0} = 2 \int_{-\infty}^{\infty} \frac{\mu_o X}{(X^2 + h^2)^2} J_y \, dX$$

$$= -\frac{\mu_o^2 \omega I}{2\pi^2 R_s} A \left[\int_{-\infty}^{\infty} \frac{X^2}{(X^2 + h^2)^2} dX \right] \sin\left(\frac{y}{a} - \omega t\right)$$

$$= -\frac{\mu_o^2 \omega I}{4\pi h R_s} A \sin\left(\frac{y}{a} - \omega t\right) = -\frac{\mu_o^2 I}{4\pi h R_s} \dot{x}_b ,$$

or

$$B_{z_I}\Big|_{z=0} = \frac{\mu_o^2 \omega I}{4\pi h R_s}\, ix$$

if we adopt a complex notation ($e^{-i\omega t}$) for this field component and for the displacement (x) at the point on the beam where this field is evaluated. [These same results for a straightened-out beam are also obtained if the conducting plates are not located to the side but are above and below the beam (Appendix A), or if, alternatively, the beam is situated within a circular tube (Appendix B).]

A result similar to that just written is obtained if one takes into account the circular character of the orbit (see Appendix C), and requires only the inclusion of a dimensionless correction factor $f(\frac{h}{a})$ that typically might have a value in the neighborhood of 0.5 and that approaches unity as $\frac{h}{a}$ tends toward zero.* These results moreover may be expressed conveniently in terms of the "impedance of space", $Z_o = \sqrt{\mu_o/\epsilon_o} = 377$ ohms, and the wavelength $\lambda = c/f = 2\pi\ c/\omega$ [$= \frac{2\pi a}{\beta(1 - \nu_r)}$ for the lowest mode]. We thus write

$$B_{z_I}\Big|_{z=0} = -\frac{\mu_o^2 I}{4\pi h R_s} f(\frac{h}{a})\, \dot{x}_b = i\,\frac{\mu_o^2 \omega I}{4\pi h R_s} f(\frac{h}{a})\, x$$

$$= -\frac{\mu_o Z_o I}{4\pi c h R_s} f(\frac{h}{a})\, \dot{x}_b = i\,\frac{\mu_o \omega Z_o I}{4\pi c h R_s} f(\frac{h}{a})\, x = i\,\frac{\mu_o Z_o I}{2h\lambda R_s} f(\frac{h}{a})\, x.$$

---

* Values of the function $f(\frac{h}{a})$, as obtained by numerical integration, are tabulated vs. h/a at the end of Appendix C.

B. Electric Forces

An effect of comparable, although usually of lesser importance arises from the currents associated with the movement of electrostatic images induced in the side walls by the ring charge. For the purposes of the analysis that follows, the electrostatic images are considered to be identical to those induced in perfectly conducting walls, but, by virtue of the surface resistance, the currents associated with the movement of these charges develop a tangential electric field that extends from the surface of the plates into the interior region where the beam is situated. For sufficiently resistive walls, the tangential fields can impede movement of the image charges and reduce the electric forces.

With a straightened-out geometry, the electrostatic problem of a charged ring in the presence of side walls at potential zero leads to the scalar potential function

$$\Phi = \frac{\lambda}{\pi\epsilon_o} \sum_{k=0}^{\infty} \frac{1}{2k+1} \cos \frac{(2k+1)\pi}{2h} z \; e^{-\frac{(2k+1)\pi}{2h}|X|}$$

where λ denotes the charge per unit length and (as before) $X = x - x_b = x - A \cos (\frac{y}{a} - \omega t)$. The induced charge density accordingly is*

$$\sigma = \pm \epsilon_o \left. \frac{\partial\Phi}{\partial z} \right|_{z=\pm h}$$

$$= - \frac{\lambda}{2h} \sum_{k=0}^{\infty} (-1)^k \, e^{-\frac{(2k+1)\pi}{2h}|X|}$$

---

* As a check of the result given for the induced charge density σ, one may note that the total charge induced per unit width on one plate is correctly given, by use of the above formula, as

$$- \frac{\lambda}{4h} \int_{-\infty}^{\infty} \frac{dX}{\operatorname{Cosh} \frac{\pi X}{2h}} = - \frac{\lambda}{\pi} \int_{0}^{\infty} \operatorname{Sech} u \, du = - \frac{\lambda}{2} .$$

$$= - \frac{\lambda}{4h} \frac{1}{\mathrm{Cosh}\,\frac{\pi X}{2h}} .$$

Now $\dot{\sigma} = - \left(\frac{\partial\sigma}{\partial X}\right) \dot{x}_b$, since $X = x - x_b$, and the "equation of continuity" (conservation of charge) states that $\nabla \cdot \vec{J} + \dot{\sigma} = 0$, or $\frac{\partial J_x}{\partial x} = - \dot{\sigma}$, where J_x is the surface-current density associated with $\dot{\sigma}$. We thus are led to the expected result

$$J_x = \sigma \cdot \dot{x}_b = - \frac{\lambda}{4h} \frac{1}{\mathrm{Cosh}\,\frac{\pi X}{2h}} \dot{x}_b .$$

The surface resistance then requires a tangential electric field, at the surfaces $z = \pm h$, of the amount

$$E_{x_I}\Big|_{z=\pm h} = \frac{R_s}{s} J_x$$

$$= - \frac{\lambda R_s}{4h} \frac{1}{\mathrm{Cosh}\,\frac{\pi X}{2h}} \dot{x}_b$$

and, for later use, this may be developed as a Fourier integral

$$E_{x_I}\Big|_{z=\pm h} = - \frac{\lambda R_s}{2\pi} \left[\int_0^\infty \frac{\cos kX}{\mathrm{Cosh}\,kh} dk \right] \dot{x}_b .$$

Because $E_{x,I}$ is a Cartesian component of an electrostatic field, it is a harmonic function in the region $-h < z < h$ and in the present instance is an <u>even</u> function of z. Accordingly $E_{x,I}$ may be written as

$$E_{x_I} = - \frac{\lambda R_s}{2\pi} \left[\int_0^\infty \frac{\text{Cosh } kz \cos kX}{\text{Cosh}^2 \, kh} \, dk \right] \dot{x}_b$$

for $- h < z < h$, and at the location of the ring becomes

$$E_{x_I} \Big|_{\substack{X \to 0 \\ z = 0}} = - \frac{\lambda R_s}{2\pi} \left[\int_0^\infty \frac{dk}{\text{Cosh}^2 \, kh} \right] \dot{x}_b$$

$$= - \frac{\lambda R_s}{2\pi h} \dot{x}_b = - \frac{\lambda}{2\pi \epsilon_o hc} \frac{R_s}{Z_o} \dot{x}_b .$$

For comparison with the results obtained in Sect. IIA for the quadrature magnetic field of a straightened-out beam, we may note here the ratio of the electric to the magnetic forces suggested by this analysis:

$$\frac{F_E}{F_M} = \frac{E_{x,I}}{\beta \, B_{z,I}} = \frac{\frac{\lambda}{2\pi h} R_s}{\beta c \, \frac{\mu_c^2 I}{4\pi h R_s}} = \frac{2}{\mu_c^2} \frac{\lambda}{\beta c I} R_s^2$$

$$= \frac{2}{\mu_o^2 \beta^2 c^2} R_s^2 = 2 \left(\frac{R_s}{\beta Z_o} \right)^2 .$$

Normally this ratio will be considerably less than unity -- thus with $\beta = 0.98$ and $R_s = 50$ ohms per square, the ratio becomes

$$\frac{F_E}{F_M} = 2 \left(\frac{50}{0.98 \text{ x } 377} \right)^2 = 0.0366 = \frac{1}{27.3} ,$$

and only for a surface resistance at least as high as 266 ohms per square does this ratio become as large as unity.

The foregoing analysis for these walls will apply under conditions where the magnetic field penetrates the wall but electric images are free to develop. We believe the applicable region is defined by

$$R_s \gtrsim 10^3 \sqrt{\frac{\omega\mu\mu_o}{2\sigma}} \quad \text{and} \quad R_s \lesssim \frac{\mu_o c}{2} \frac{c}{\omega h} .$$

III. DYNAMICAL CONSEQUENCES

It has been shown in Sect. IIA that a magnetic field of magnitude $\frac{\mu_o \omega Z_o |I|}{4\pi c h R_s} A \, f\left(\frac{h}{a}\right)$ exists at the beam and has such a phase that it lags by 90^o the displacement of the beam current. Thus the radial outward force arising from this field attains its maximum value at any point when the displacement is zero but the charged particles (considered for the moment as having a charge $+q$) are moving outward with a radial velocity component $v_r = \nu_r \omega_o A$. There accordingly is a mechanism for energy to be added to the transverse mode of particle movement -- specifically at a rate

$$P = \frac{d}{dt}\left(\frac{\gamma m_o \nu_r^2 \omega_o^2 A^2}{2}\right) = \gamma m_o \nu_r^2 \omega_o^2 A \frac{dA}{dt} = \left\langle F_r v_r \right\rangle_{\text{time avg.}}$$

---

[*] In more specific detail, the motion of N particles undergoing a "slow wave" collective oscillation may be described by the equations

$$\phi_n = \frac{2\pi n}{N} + \omega_o t,$$

$$x_n = A \cos\left(\nu_r \omega_o t + \frac{2\pi M}{N} n + \alpha\right) = A \cos\left[M\phi_n - (M - \nu_r)\omega_o t + \alpha\right], \text{ and}$$

$$\dot{x}_n = -\nu_r \omega_o A \sin\left(\nu_r \omega_o t + \frac{2\pi M}{N} n + \alpha\right) = -\nu_r \omega_o A \sin\left[M\phi_n - (M - \nu_r)\omega_o t + \alpha\right] .$$

Since the displacement of the beam is then described by

$$x_b = A \cos\left[M\phi - (M - \nu_r)\,\omega_o t + \alpha\right],$$

Accordingly, by use of the magnetic field previously evaluated, and introducing a factor $\frac{1}{2}$ to obtain the time average, we obtain

$$\frac{1}{A}\,\frac{dA}{dt} = \frac{\mu_o}{8\pi}\,\frac{\omega Z_o\, q\, \beta\, I}{\gamma m_o \nu_r \omega_o\, h\, R_s}\; f\left(\frac{h}{a}\right)$$

$$= \frac{\mu_o}{16\pi^2}\,\beta\,\frac{n\, q^2\, \omega\, Z_o}{\gamma\, m_o \nu_r\, h\, R_s}\; f\left(\frac{h}{a}\right)$$

$$= \frac{n\, r_e\, \beta\, \omega\, Z_o}{4\pi\, \gamma\, \nu_r\, h\, R_s}\; f\left(\frac{h}{a}\right),$$

where n represents the total number of particles and r_e is the classical particle radius $\left(= \frac{q^2}{4\pi\, \epsilon_o\, m_o c^2}\right)$. Thus, from the magnetic field alone, we expect an exponential growth of amplitude (in the absence of Landau damping suppression) characterized by the lapse rate

$$\frac{1}{\tau_M} = \frac{N\, r_e\, \beta\, \omega\, Z_o}{4\pi\, \gamma\, \nu_r\, h\, R_s}\; f\left(\frac{h}{a}\right),$$

with $\omega = (1 - \nu_r)\, \omega_o$ for the lowest mode of collective radial oscillation.

The electric force has been seen (Sect. IIB) to be less than the magnetic force, in the ratio

---

with an angular speed of precession given by $\frac{\omega}{M} = \frac{M - \nu_r}{M}\, \omega_o$, a lagging outwardly-directed force thus is of the form

$$F_r = F_{max.} \cos[M\phi - (M - \nu_r)\, \omega_o t + \frac{\pi}{2} + \alpha]$$

$$= -F_{max.} \sin[M\phi - (M - \nu_r)\, \omega_o t + \alpha]$$

and attains its maxima in phase with the radial velocity components $\dot{x}_n$ of the particles.

$\frac{F_E}{F_M} = 2\left(\frac{R_s}{\beta\, Z_o}\right)^2$ if the factor $f(\frac{h}{a})$ -- whose analogue was not evaluated for the electric field -- is ignored. We therefore estimate the corresponding electric field contribution to the lapse rate as

$$\frac{1}{\tau_E} = \frac{N\, r_e\, \omega\, R_s}{2\pi\, \beta\, \gamma\, \nu_r\, h\, Z_o}$$

and take the total lapse rate to be

$$\frac{1}{\tau} = \frac{1}{\tau_M} + \frac{1}{\tau_E}$$

with the greater contribution normally arising from the term $\frac{1}{\tau_M}$.

IV. NUMERICAL EXAMPLE

As a numerical example, suppose

$\gamma = 5,\qquad \beta = 0.98,\qquad r_e = 2.82 \times 10^{-13}\text{cm},\qquad \nu_r = \frac{3}{4}$,

$R_s = 50$ ohms per square, $\omega = 4.4 \times 10^{-8}\ \text{sec}^{-1}$

(as would correspond to $\Delta = 2 \times 10^{-6}$cm and $\delta = 6 \times 10^{-3}$cm, if $\rho = 1.0 \times 10^{-4}$ ohm·cm),

$h = 3.5$ cm, and $f\,(\frac{h}{a}) = 0.56$.

Then the magnetic contribution to the lapse rate is characterized by the e-folding time

$$\tau_M = \frac{4\pi\, \gamma\, \nu_r\, h\, R_s}{N\, r_e\, \beta\, \omega\, Z_o\, f\,(\frac{h}{a})}$$

$$= 4\pi \frac{5 \times \frac{3}{4} \times 3.5 \times 50}{N \times 0.98 \times 2.82 \times 10^{-13} \times 4.4 \times 10^{-8} \times 377 \times 0.56}$$

$$= \frac{3.2 \times 10^{5}}{N} \text{ sec.}$$

Thus, for $N = 10^{11}$, 10^{12}, or 10^{13} particles, one respectively obtains, from the magnetic field alone, a growth time

$$\tau_M = 3.2\ \mu\text{sec}, \quad 320\ \text{ns}, \quad \text{or} \quad 32\ \text{ns}$$

in the absence of any suppression of the instability through the mechanism of Landau damping. One normally would expect the growth rate of the instability to be increased, and the characteristic growth time to be correspondingly decreased, by a few percent due to the concurrent effect of the quadrature electric field.

APPENDIX A

The Quadrature Magnetic Field From A Straightened-Out Beam Oscillating Vertically Between Thin Top and Bottom Imperfectly-Conducting Plates

As Dr. Sessler has reminded us, previous workers have investigated -- again for a straightened-out geometry -- a problem similar to that considered in Sect. IIA of the present report but in which the resistive wall completely enclosed the beam current I. Thus it may be of some interest here first to inquire whether the presence of resistive strips solely above and below the beam ($x = \pm h$) would lead to a quadrature component of magnetic field, $B_I\Big|_{z=0}$, similar to that cited in the body of this report. [In Appendix B a similar investigation is made for a transversely oscillating beam centrally located within a thin-walled resistive tube of circular cross-section.]

Proceeding as before, we have

$$\dot{A}_y\Big|_{x=\pm h} = \pm \frac{\mu_o I}{2\pi} \quad \frac{h}{h^2 + z^2} \quad \dot{x}_b$$

$$= \pm \frac{\mu_o I}{2\pi} \omega A \frac{h}{h^2 + z^2} \quad \sin\left(\frac{y}{a} - \omega t\right)$$

and

$$J_y = \mp \frac{\mu_o I}{2\pi R_s} \omega A \frac{h}{h^2 + z^2} \quad \sin\left(\frac{y}{a} - \omega t\right).$$

Then, at the location of the beam, we have

$$B_{z_I}\Big|_{\text{near beam}} = \int_{-\infty}^{\infty} \frac{\mu_o h}{2\pi(h^2 + z^2)} \left[J_y\Big|_{x=h} - J_y\Big|_{x=-h} \right] dz$$

$$= - \frac{\mu_o^2 \omega I}{2\pi^2 R_s} A \left[\int_{-\infty}^{\infty} \frac{h^2}{(h^2 + z^2)^2} dz \right] \sin \left(\frac{y}{a} - \omega t\right)$$

$$= - \frac{\mu_o^2 \omega I}{4\pi h R_s} A \sin \left(\frac{y}{a} - \omega t\right),$$

a result that is precisely identical to that found in the body of this report (Sect. IIA) for a straightened-out beam oscillating transversely between imperfectly-conducting side plates.

APPENDIX B

The Quadrature Magnetic Field From A Straightened-Out Beam Oscillating Transversely within a Thin-Walled Resistive Tube of Circular Cross-Section

The analysis of Appendix A, for a straight beam oscillating vertically between top and bottom plates, led to the same quadrature magnetic-field component (B_{z_I}) as was obtained in the body of this report for the case in which the conducting plates were at the side. We now sketch a similar analysis for a straight beam centrally located within a thin walled circular tube and oscillating transversely in the x direction.

In the same spirit as in the preceding work we accordingly write

$$\dot{A}_y\Big|_{\Theta\ \text{wall}} = \frac{\mu_o I}{2\pi}\left[\frac{x - x_b}{(x - x_b)^2 + (z - z_b)^2}\right]\Bigg|_{\substack{x_b \to 0 \\ z_b \to 0}} \cdot \dot{x}_b$$

$$= \frac{\mu_o I}{2\pi h} \sin\theta\, \dot{x}_b ,$$

with θ measured from the positive z axis toward the positive x axis[*] and (in analogy to the notation for the previous planar situations) h denotes the radius of the circular tube.

---

[*] i.e., $z = h\cos\theta$ and $y = h\sin\theta$ at the wall, so that a positive rotation of θ would advance a right-handed screw in the direction of the positive y axis. Similarly r will denote here the plane-polar radial coordinate in the transverse x, z plane.

Then

$$J_y = -\frac{\mu_o I}{2\pi h R_s} \omega A \sin\theta \sin\left(\frac{y}{a} - \omega t\right).$$

The local transverse variation of the magnetic field associated with J_y may be described in terms of a (harmonic) vector potential

$$A_{y_I} = -\frac{\mu_o^2 \omega I}{4\pi R_s} A \begin{Bmatrix} \frac{h}{r} \\ \\ \frac{r}{h} \end{Bmatrix} \sin\theta \sin\left(\frac{y}{a} - \omega t\right) \qquad \begin{matrix} h \leqslant r \\ \\ r \leqslant h \end{matrix}$$

and leads to a uniform (z-directed) field

$$B_{z_I} = -\frac{\mu_o^2 \omega I}{4\pi h R_s} A \sin\left(\frac{y}{a} - \omega t\right)$$

in the interior $(r < h)$ -- as is characteristic of a first-harmonic surface-current distribution on the surface of a circular cylinder. Again this result is seen to be identical to the result obtained earlier for side plates (Sect. IIA) and for top and bottom plates (Appendix A).

APPENDIX C

The Quadrature Magnetic Field of a Ring Current Oscillating Transversely Between Thin, Imperfectly-Conducting Side Plates

In Sect. IIA of this report the quadrature magnetic image field was evaluated for a straightened-out beam. We here revise that analysis to take into account the curved (circular) character of the reference orbit. The vector potential $\vec{A} = A_\phi \hat{e}_\phi$, that describes the magnetic field for an isolated d.c. beam of current $I\hat{e}_\phi$ circulating about the z axis, may be written

$$A_\phi = \frac{\mu_o}{2} I a \int_o^\infty J_1 (ka) J_1 (kr) e^{-k|z|} dk,$$

where "a" denotes the radius of the ring current.* If the beam has its center displaced from the origin of the coordinate system to a point with polar coordinates A, ϕ_b, this same result may be written

$$A_\phi = \frac{\mu_o}{2} I a \int_o^\infty J_1 (ka) J_1 (k [r - A \cos (\phi - \phi_b)] e^{-k|z|} dk$$

for A small.

---

[*] As a check, one may note that the B_z field on the axis is given by

$$B_z\Big|_{r=0} = \underset{r\to 0}{L} \left[\frac{1}{r} \frac{\partial}{\partial r} (rA_\phi)\right] = \frac{\mu_o}{2} \int_o^\infty k J_1 (ka) e^{-k|z|} dk$$

$$= \frac{\mu_o}{2} I \frac{a^2}{(a^2 + z^2)^{3/2}}$$

by use of the formula cited, in agreement with the well known result [MKS units] for the field on the axis of a circular current loop.

If the beam is precessing, additional current components in principle may be present, but the expression just written still may represent a major part of the vector potential -- with A denoting the radius of the circle described by the orbit center as a result of the precession and ϕ_b advancing at the angular rate of precession (ω). Under these circumstances, the time derivative of the vector-potential component A_ϕ is given by

$$\dot{A}_\phi = - \frac{\mu_o \, \omega \, I \, a \, A}{2} \int_o^\infty k \, J_1(ka) \, J_1'(k[r - A \cos (\phi - \phi_b)] \sin (\phi - \phi_b) \, e^{-k|z|} dk,$$

where the prime on the second J_1 function denotes differentiation of this function with respect to its argument. The induced surface-current density (per unit width) then is

$$J_\phi = - \frac{1}{R_s} \dot{A}_\phi \Big|_{z=\pm h}$$

$$= \frac{\mu_o \, \omega \, I \, a \, A}{2 \, R_s} \int_o^\infty k \, J_1(ka) \, J_1'(k[r - A \cos (\phi - \phi b)])\sin (\phi - \phi_b) e^{-kh} d$$

$$= \frac{\mu_o \, \omega \, I \, a}{2 \, R_s} \int_o^\infty k e^{-kh} \, J_1(ka) \, J_1'(kr_1) \sin \phi_1 \, dk,$$

where we have introduced r_1, ϕ_1 as the polar coordinates of the observation point relative to the precessing beam center.

Such a current distribution will give rist to a supplemental magnetic field that can be derived from a vector potential

$$A_{\phi_{1_I}} = \begin{cases} \displaystyle\int_0^\infty C(k)e^{-kh}(e^{kz} + e^{-kz})\, J_1'(kr_1) \sin \phi_1 \, dk & |z| \leqslant h \\ \displaystyle\int_0^\infty C(k)\,(e^{kh} + e^{-kh})\, e^{-k|z|} J_1'(kr_1) \sin \phi_1 \, dk & h \leqslant |z| \end{cases}$$

(an even function of z), where the coefficient $C(k)$ is determined by the requirement $H_{r_1, I}\Big|_{z=h^+} - H_{r_1, I}\Big|_{z=h^-} = J_\phi$ to be

$$C(k) = \frac{\mu_o^2 \,\omega\, I\, a\, A}{4\, R_s}\, e^{-kh}\, J_1(ka).$$

Thus, in the region $|z| < h$, the supplemental magnetic field may be obtained from the vector potential

$$A_{\phi_{1I}} = \frac{\mu_o^2\, \omega\, I\, a\, A}{2\, R_s} \int_0^\infty e^{-2kh} \operatorname{Cosh} kz\, J_1(ka)\, J_1'(kr_1) \sin \phi_1 \, dk$$

Accordingly, by evaluating $\frac{1}{r_1} \frac{\partial}{\partial r_1}(r_1 A_{\phi_1, I})$ at $r_1 = a$, $z = 0$ we obtain

$$B_{z_I} = \frac{\mu_o^2\, \omega\, I}{2\, R_s}\, A \left[\int_0^\infty e^{-2kh} \left(\frac{1}{ka} - ka\right) [J_1(ka)]^2 \, dk \right] \sin(\phi - \phi_b)$$

We denote the integral shown in the square brackets by $-\frac{1}{2\pi h} f(\frac{h}{a})$ with the expectation that $f(\frac{h}{a}) \sim 1$ for $h \ll a$ [see below]. In terms of this notation

$$B_{z_I} = -\frac{\mu_o^2\,\omega\, I}{4\pi\, h\, R_s}\; A\, f(\tfrac{h}{a})\, \sin(\phi - \phi_b).$$

The radial coordinate of the beam at a particular point (as distinguished from the coordinate of a particular particle in the beam) departs from the reference value "a" by the amount $A \cos(\phi - \phi_b)$, for $A \ll a$, where ϕ_b advances at the angular rate ω. The quantity $\omega A \sin(\phi - \phi_b)$ accordingly is analogous to the transverse velocity $\dot{x}_b$ of the line current for which the magnetic field was evaluated in Sect. IIA. Thus by re-writing the expression given immediately above as

$$B_{z_I} = -\frac{\mu_o^2\, I}{4\pi\, h\, R_s}\; f(\tfrac{h}{a})\, \dot{x}_b,$$

the results previously obtained for this magnetic field component are seen to be applicable if adjusted by inclusion of the correction factor

$$f(\tfrac{h}{a}) = -\,2\pi h \int_0^\infty e^{-2kh} \left(\frac{1}{ka} - ka\right) [J_1(ka)]^2\, dk$$

$$= 2\pi \int_0^\infty e^{-2v} \left(\frac{v}{h/a} - \frac{h/a}{v}\right) \left[J_1\left(\frac{v}{h/a}\right)\right]^2 dv.$$

The correction factor $f(\frac{h}{a})$ has been evaluated numerically* for several values of its argument, with the results tabulated below and $f(\frac{h}{a})$ becoming

---

* Teletype program ROMBESl, used in conjunction with BESTABl that contains coeffcients for evaluating the Bessel function J_1, and the remote-submittable program BESSl. The integration variable x in these programs is taken to be given by $v = \frac{x}{1-x}$, so that $dv = \frac{dx}{(1-x)^2}$ and the range of integration is $0 \leqslant x \leqslant 1$. The required values of J_1 are obtained by means of "polynominal approximations" attributed to E.E. Allen and quoted as equations 9.4.4 and 9.4.6 by F.W.J. Oliver in M. Abramowitz and I.A. Stegun (Eds.), "Handbook of Mathematical Functions", Chap. 9, pp. 369-370.

close to unity for $\frac{h}{a}$ small (as expected).

$\frac{h}{a}$	$f(\frac{h}{a})$
0.010	0.9698
0.020	0.9414
0.025	0.9277
0.030	0.91429
0.040	0.88838
0.05	0.863479
0.10	0.751155
0.15	0.654167
0.20	0.568507
0.25	0.491871
0.30	0.422817
0.35	0.360392
0.40	0.303924
0.45	0.252901
0.50	0.206901

To be published in the Proceedings of the
III All-Union National Conference on
Particle Accelerators, Moscow,
Oct. 2 - 4, 1972

LBL-1072

Transverse Two-Stream Instability in the Presence of Strong Species-Species and Image Forces

L.J. Laslett, D. Möhl, and A.M. Sessler

TRANSVERSE TWO-STREAM INSTABILITY IN THE PRESENCE OF STRONG SPECIES-SPECIES AND IMAGE FORCES

L.J. Laslett and A.M. Sessler*

Lawrence Berkeley Laboratory
University of California
Berkeley, California 94720

and

D. Möhl

CERN
Geneva 23, Switzerland

ABSTRACT

The theory of coherent transverse oscillations of two particle species is extended to include strong species-species and image forces. It is shown that in general the species-species force can considerably alter the instability threshold. Conversely, it is shown that the limit on the performance of an electron ring accelerator imposed by the requirement of stable ion electron oscillations, is not significantly improved by the inclusion of images.

---

* Work supported by the U.S. Atomic Energy Commission.

1. INTRODUCTION

The transverse coupling instability of relativistic stabilized beams has long been a subject of intensive study (e.g. ref. 1-5). Recently, it has been emphasized,$^{5)}$ that this two-stream instability can impose a severe limit to the acceleration rate attainable in an electron ring accelerator (ERA).

A similar type of instability can also occur in synchrotrons or storage rings when particles of the opposite charge are trapped in the main beam.$^{6),7),8)}$

In the present note we extend the theory to include -- in an approximate way -- the influence of space-charge forces acting between particles of the same beam ("species-species forces"), as well as image forces due to the presence of walls. For simplicity, and because they are the most unstable modes, we shall concentrate on dipole oscillations.

We find that species-species forces and images can considerably -- and in many cases adversely -- affect the instability threshold. In fact, to explain the instability in the Bevatron it seems vital to include electron - electron forces in the theory.

In an electron ring accelerator acceleration column, where axial focussing is provided only by ion-electron forces and electron images, we hoped that the inclusion of images would relax the ion-electron instability threshold. We shall show this is not the case.

2. OUTLINE OF THE SOLUTION

We start with the equation of motion for a test particle of each species. We include three types of forces, a "single particle force", a "coherent force" and a "coupling force". The single particle force is proportional to the displacement of the test particle, the coherent force is proportional to the displacement of the entire same beam of particles similar to the test particle, and the coupling force is proportional to the displacement of the other beam. Each of these force coefficients is modified by images and/or species-species forces.

We assume harmonic oscillation of the beam centers and average the single particle response over all beam particles. The averaging process takes frequency spread into account. The eigenvalues and eigenvectors, of the coupled system which describes the motion of the two beam centers, determine the mode frequency (and hence thresholds and growth rates) and the relative amplitudes of the two beams.

3. EQUATIONS OF MOTION

To be specific, and clearly without loss of generality, we take the beam species to be electrons (the replacements for proton beams is made in Section 7). We normalize all frequencies to the average electron revolution frequency (Ω_o) and denote the beam (electron) frequencies by lower case q's and the stationary species (proton) frequencies by capital Q's. The equations of motion of the two test particles are

$$\frac{1}{\Omega_o{}^2}\left(\frac{\partial}{\partial t} + \Omega\,\frac{\partial}{\partial\theta}\right)^2 x + q^2\,x + q_u^2\,\bar{x} - q_c^2\,\bar{y} = 0,$$

$$\frac{1}{\Omega_o{}^2}\,\frac{\partial^2 y}{\partial t^2} + Q^2 y + Q_u^2\,\bar{y} - Q_c^2\,\bar{x} = 0, \tag{1}$$

where x and y are the transverse coordinates (in the same direction) of the test electron and test ion.

The quantities q^2, Q^2, q_u^2, etc. will be discussed in more detail in the examples given below. We remark, here, that in the absence of species-species forces and of images:

$$q^2 = q_c^2 + q_o^2\,\frac{\Omega^2}{\Omega_o^2} \quad (= Q_e^2 = Q_1^2 + \lambda^2),$$

$$q_u^2 = 0,$$

$$(q_c^2 = Q_1^2), \tag{2}$$

$$Q^2 = Q_c^2 = \frac{m\gamma}{M}\;f\;q_c^2\;(= Q_i^2)\;,$$

$$Q_u^2 = 0,$$

where we give in parentheses the notation of Koshkarev and Zenkevitch[5]. The external focussing is characterized by q_o^2, $\frac{m\gamma}{M}$ is the (relativistic) mass ratio between electrons and ions, and $f = \frac{N_i}{N_e}$ the fractional ion loading. The quantities q_c and Q_c are -- in this approximation -- the electron and ion bounce frequencies in the potential well of the other beam. The quantities q_u^2 and Q_u^2 are in general closely related to the coefficient (U + V + iV) of Ref. 9) which determines single beam stability (resistive wall effect, etc.). For the electrons we have, e.g.,

$$q_u^2 \approx -2q\Omega_o^{-1}(U + V + iV). \tag{3}$$

4. SOLUTION

We solve (1) by assuming that the beam centers oscillate harmonically in time and space:

$$\begin{aligned}\bar{x} &= \bar{\xi} \exp[i(n\theta - \nu\Omega_o t)],\\ \bar{y} &= \bar{\zeta} \exp[i(n\theta - \nu\Omega_o t)],\end{aligned} \tag{4}$$

and regarding the $\bar{x}$- and $\bar{y}$- terms in (1) as driving forces. In finding the response of the test particle we, as is usual in Landau damping calculations, ignore transients and take $\mathrm{Im}(\nu) \geq +0$ -- hence concentrating on the unstable range.

In the case where nonlinearity in the oscillation direction is negligible the single particle response ξ and ζ is simply the steady state solution of a driven harmonic oscillator. In the case of important nonlinearity in the oscillation we use the results of Ref. 10) to obtain approximate expressions for ξ and ζ valid for small amplitude and small nonlinearity.

We introduce normalized distribution functions $f(p)$, $g(a^2)$, $h(b^2)$ for the electrons, and $F(p)$, $G(a^2)$, $H(b^2)$ for the ions, that describe the momentum distribution, and the distribution of the incoherent betatron amplitudes of the particles, with b referring to the direction of the oscillation. We assume that the distributions are uncorrelated so that the beam center is determined by:

$$\bar{\xi} = \int \xi\, f(p) g(a^2) h(b^2)\, dp\,da^2 db^2, \tag{5}$$

$$\bar{\zeta} = \int \zeta\, F(p)G(a^2)H(b^2)\; dp\,da^2\,db^2. \tag{5}$$

Thus we obtain:

$$\begin{aligned} \bar{\xi}\,(1 + i_u) - \bar{\zeta}\, i_c &= 0, \\ \bar{\zeta}\,(1 + I_u) - \bar{\xi}\, I_c &= 0, \end{aligned} \tag{6}$$

where

$$\begin{aligned} i_u &= \int q_u^2\, \frac{f(p)[-b^2h'(b^2)]g(a^2)}{q^2 - (\nu - n\frac{\Omega}{\Omega_o})^2}\; dp\,da^2\,db^2, \\ i_c &= \int q_c^2\, \frac{f(p)\,[-b^2h'(b^2)]g(a^2)}{q^2 - (\nu - n\frac{\Omega}{\Omega_o})^2}\; dp\,da^2\,db^2\,, \end{aligned} \tag{7}$$

and I_u and I_c are similar dispersion integrals for the ions (with $\Omega = 0$).

5. APPROXIMATIONS

We know that the values of dispersion integrals, such as (7), are primarily determined by the width of the distribution functions.9),11) Hence we approximate (7) by neglecting the variation of the q^2-coefficients in the numerator and keeping only the first-order variation of the coefficients in the denominator. Furthermore, we circumvent questions of self-consistency and assume that the coefficients and the distribution functions can be independently selected. Thus, we write the characteristic equation, associated with (6), in the form

$$(\Delta q^2 + q_u^2)(\Delta Q^2 + Q_u^2) - q_c^2 Q_c^2 = 0 \tag{8}$$

where:

$$\begin{aligned} 1/\Delta q^2 &= \int \frac{f(p)g(a^2)[-b^2h'(b^2)]}{q^2 - (\nu - n)^2}\; dp\,da^2\,db^2\,, \\ 1/\Delta Q^2 &= \int \frac{F(p)G(a^2)[-b^2H'(b^2)]}{Q^2 - \nu^2}\; dp\,da^2\,db^2. \end{aligned} \tag{9}$$

The combined effect of three spreads can be treated only with difficulty. Double dispersion integrals have in fact been treated in Ref. 11). The result is that the spread effective for damping is not the sum of the spreads, but rather the Landau damping is mainly determined by the larger of the two spreads. Hence we shall consider only the effect of a single spread; namely the largest.

Finally, one may make a further approximation which we call the "slow wave approximation"; namely we expand the denominators of (9) in partial fractions and keep the term which is largest when $\nu \approx (n-q)$, and when $\nu \approx Q$. In this approximation -- and by expanding $q \cong q_o + s(\partial q/\partial s)_o$, etc. -- (8) takes the form

$$\left(\Delta q - \frac{q_u^2}{2q_o}\right)\left(\Delta Q + \frac{Q_u^2}{2Q_o}\right) + \frac{q_c^2 Q_c^2}{4q_o Q_o} = 0 \tag{10}$$

with

$$\Delta q = \left[\int \frac{f(s)ds}{(n-q_o) - \nu + \Delta_e' s}\right]^{-1} ,$$

$$\Delta Q = \left[\int \frac{F(s)ds}{Q_o - \nu + \Delta_i' s}\right]^{-1} , \tag{11}$$

and

$$\Delta_e' = \left[\frac{\partial}{\partial s}\left(n\,\frac{\Omega(s)}{\Omega_o} - q(s)\right)\right] .$$

$$\Delta_i' = \left(\frac{\partial Q}{\partial s}\right)_o . \tag{12}$$

The quantity s is one of the spreading parameters p, a^2 or b^2, and

$$f(s)\;ds = \begin{cases} f(p)dp & \text{or} \\ g(a^2)da^2 & \text{or} \\ -b^2\,\dfrac{dh(b^2)}{db^2}\,db^2 & \text{[see ref. 8],} \end{cases} \tag{13}$$

$$\int f(s)ds = 1.$$

Alternatively, we employ the term "improved slow wave approximation" for the approximation in which we retain (8) but approximate the factors that arise from the fast-wave terms by the ν-value (n-q) and Q.

6. STABILITY CONDITIONS

A. Analytic Results

Stability conditions can be obtained from (8) or (10), by finding the boundary (on which ν is real) of the unstable zone (in which the imaginary part of ν is positive). To this end, the integrals of (9), or (11), need to be evaluated; and in Table I we summarize results, for the essential component of (9) and (11), resulting from two different choices of distribution functions. The Lorentzian distribution is studied, despite its unphysically long tails, because the analysis is simple and because it can be employed to establish an interesting general result (see Sect. 8). For accurate results, a truncated distribution is required.

In the case of δ-functions for f(s) and F(s) (no frequency spreads) the eigenfrequencies are determined from

$$[(\nu-n)^2 - q^2 - q_u^2][\nu^2 - Q^2 - Q_u^2] - q_c^2 Q_c^2 = 0. \tag{14}$$

For a Lorentzian line, $[f(s) \propto (4s^2 + \Delta_e^2)^{-1},\ F(s) \propto (4s^2 + \Delta_i^2)^{-1}]$, with equal slow wave and fast wave frequency spread and with Δ_e and Δ_i the full widths at half maximum, equation (14) is valid with $\nu \to \nu + i\,\Delta_e/2$ in the first factor and $\nu \to \nu + i\,\Delta_i/2$ in the second factor. If, in addition, $\Delta_e \approx \Delta_i = \Delta$, the condition for stability is

$$\Delta \geqslant 2(1/\tau_0), \tag{15}$$

where τ_0^{-1} is the growth rate in the absence of dispersion.

In the neighborhood of a resonance we may use the improved slow-wave approximation. In the absence of frequency spread, (14) yields

$$\nu = \tilde{Q} + d \pm i \sqrt{\frac{q_c^2 Q_c^2}{4\tilde{Q}\tilde{q}} - d^2} \quad , \tag{16}$$

where

$$\begin{aligned} d &= \tfrac{1}{2}(n - \tilde{q} - \tilde{Q}), \\ \tilde{Q}^2 &= Q^2 + Q_u^2 \ , \end{aligned} \tag{17}$$

$$\tilde{q}^2 = q^2 + q_u^2 , \tag{17}$$

and resonance occurs when $d \approx 0$. For the Lorentzian line, and in improved slow wave approximation,

$$\nu = \tilde{Q} + d - i \left(\frac{\Delta_e+\Delta_i}{4}\right) \pm i \sqrt{\frac{q_c^2 Q_c^2}{4\tilde{q}\tilde{Q}} - \left[d - i \left(\frac{\Delta_e-\Delta_i}{4}\right)\right]^2} , \tag{18}$$

with Δ_p and Δ_e the full widths at half maximum in the frequencies Q and $\left|n \frac{\Omega}{\Omega_o} - q\right|$. Stability of the solution (18) requires spreads such that

$$\Delta_e \Delta_i \geqslant \frac{q_c^2 Q_c^2}{\tilde{q}\tilde{Q}} \left[1 + \left(\frac{4d}{\Delta_e+\Delta_i}\right)^2\right]^{-1} . \tag{19}$$

To suppress an instability that occurs within a narrow resonant frequency band (where d will be close to zero), (19) provides the convenient sufficient condition

$$\Delta_e \Delta_i \geqslant \frac{q_c^2 Q_c^2}{\tilde{q}\tilde{Q}} \tag{20}$$

For values of q_o etc. that are considered to be essentially known (e.g., from Table II). It is of interest to note, from (19) or (20), that both Δ_e and Δ_i must be non-zero to suppress the instability.5)

Finally we turn to the case of the semi-circular distribution (see Table I). For this distribution the damping is very different for the fast and the slow waves and hence it is not reasonable to assume $\Delta_+ = \Delta_-$. Rather, we employ the slow wave approximation and completely disregard the non-resonant fast wave to obtain:

$$\begin{aligned} \nu = Q + \frac{Q_u^2}{Q} + d_1 - \frac{i}{2} (\bar{\Delta}_e + \bar{\Delta}_i) \\ \pm i \sqrt{\frac{q_c^2 Q_c^2}{qQ} - \left[d_1 - \frac{i}{2} (\bar{\Delta}_e - \bar{\Delta}_i)\right]^2} , \end{aligned} \tag{21}$$

with

$$d_1 = \frac{1}{2}\left[\left(n-q - \frac{q_u^2}{q}\right) - \left(Q + \frac{Q_u^2}{Q}\right)\right], \tag{22}$$

$$\bar{\Delta}_e = \sqrt{\Delta_e^2 - (n-q-\nu)^2} \; ,$$

$$\bar{\Delta}_i = \sqrt{\Delta_i^2 - (Q-\nu)^2} \; . \qquad (22)$$

After considerable algebraic manipulation it can be seen that stability requires:

$$\bar{\Delta}_e\bar{\Delta}_i \geq \frac{q_c^2Q_c^2}{qQ}\left[1 + \left(\frac{2d_1}{\bar{\Delta}_e+\bar{\Delta}_i}\right)^2\right]^{-1} \qquad (23)$$

Again within a narrow band of instability, associated with the resonance $d_1 \cong 0$ (where $n - q - \nu \cong q_u^2/q$ and $|Q-\nu| \cong Q_u^2/Q$), we may write

$$\bar{\Delta}_e\bar{\Delta}_i \geqslant \frac{q_c^2Q_c^2}{qQ}$$

or

$$\left[\Delta_e^2 - \left(\frac{q_u^2}{q}\right)^2\right]^{1/2}\left[\Delta_i^2 - \left(\frac{Q_u^2}{Q}\right)^2\right]^{1/2} \geqslant \frac{q_c^2Q_c^2}{qQ} \qquad (24)$$

as a sufficient condition for suppression of the instability. The second of the forms (24) clearly implies that we must require

$$\Delta_e > \left|\frac{q_u^2}{q}\right|$$

and

$$\Delta_i > \left|\frac{Q_u^2}{Q}\right| . \qquad (25)$$

The condition (23) is similar to the condition (19) found for the Lorentzian distribution -- or (24) is similar to (20) -- but with the width parameters modified to correct for the anomolous results arising from the extensive tails of the Lorentz distribution [e.g., in the manner suggested by (29) of Sect. 6B below]. It is evident that for wave frequencies removed from the central beam frequency there is reduced Landau damping. With the abruptly terminated semi-circular distributions that led to (23) et seq., this limitation is explicitly indicated by the conditions (25). Again we note that both $\bar{\Delta}_e$ and $\bar{\Delta}_i$ must be non-zero to insure stability.

B. Numerical Formulation

For numerical work we proceed directly from (8) and (9) and again employ Lorentzian distributions in s, with $\delta_{\pm}$ denoting full widths at half maximum in the quantities $\left| n \frac{\Omega}{\Omega_o} \pm q \right|$ for the fast and slow waves of the electron component and $\Delta_{\pm}$ correspondingly for the ions. If we then let

$$x_{\mp} = \nu - (n \mp q_o), \qquad X_{\mp} = \nu \pm Q_o \;, \tag{26}$$

and write

$$\begin{aligned} g_{\mp} &= x_{\mp} + i\,\delta_{\mp}, \qquad G_{\mp} = X_{\mp} + i\Delta_{\mp} \;, \\ h &= g_{+} - g_{-} - 2q_o, \quad H = G_{+} - G_{-} - 2Q_o, \end{aligned} \tag{27}$$

we then find

$$\begin{aligned} \left[q_o(x_{-} + g_{-})(x_{+} + g_{+}) + hq_u^2 \right] \left[Q_o(X_{-} + G_{-})(X_{+} + G_{+}) + HQ_u^2 \right] & \\ - hHq_c^2 Q_c^2 = 0. & \end{aligned} \tag{28}$$

The imaginary parts of the expressions written above for $g_{\mp}$, $G_{\mp}$ are seen to imply a damping that is independent of the distance by which the actual frequency is displaced from the peak of the distribution. This results from the unphysically extensive tails of the Lorentz distributions that were assumed for evaluation of Δq^2 and ΔQ^2. For this reason we have elected to replace, in the numerical work, these expressions by

$$\begin{aligned} g_{\mp} &= x_{\mp} + i \, \frac{\delta_{\mp}^2}{\left| x_{\mp} \right|^2 + \delta_{\mp}^2} \left| \delta_{\mp} \right| \;, \\ G_{\mp} &= X_{\mp} + i \, \frac{\Delta_{\mp}^2}{\left| X_{\mp} \right|^2 + \Delta_{\mp}^2} \left| \Delta_{\mp} \right| \end{aligned} \tag{29}$$

in the expectation that a more realistic type of distribution will be described in this way. With this replacement we obtain an equation for which roots have been sought computationally.[12)]

From computational tests that employed parameters similar to those introduced in the example of the following Section, it was found (i) that the values of the fast-wave dispersion parameters δ_+, Δ_- for the two species had little effect on the stability threshold (although it may be necessary that they be, for example, some 3% of the respective slow-wave quantities δ_-, Δ_+), and (ii) that (19) [or (20)] can be safely taken as a stability criterion to be applied to the slow-wave dispersion parameters after modification in the manner indicated by (29). It was confirmed, moreover, that, as expected,[5)] stabilization could not be obtained by introducing dispersion into just one of the two species.

7. PROTON SYNCHROTRONS AND STORAGE RING

We assume that electrons created by scattering with the background gas remain trapped in the circulation beam. Further, we assume the electrons to be uniformly distributed around the circumference, and we neglect the influence of the background gas ions. We take the proton and electron minor radii as equal.

The proton and electron frequencies relevant to this case are given in Table II. In many situations of interest one can use, to a good approximation, simplified relations obtained by taking $q \approx \nu_{z_o}$ and neglecting images.

In this approximation the stability conditions (24) and (25) are conveniently expressed in terms of the "space charge q-shift", q_1, so that one requires

$$\bar{\Delta}_e \bar{\Delta}_p > f \frac{q_1^{3}}{\nu_{z_o}} \sqrt{\frac{M\gamma}{m}} \ ,$$

$$\Delta_e > f\, q_1 \sqrt{\frac{M\gamma}{m}} \ , \qquad (30)$$

$$\Delta_p > \frac{q_1^{2}}{\gamma^{2} \nu_{z_o}} \ ,$$

where

$$q_1^{2} = (2/\pi)\, \frac{N_p r_p R}{\gamma b(a+b)} \ . \qquad (31)$$

Let us, as an example, discuss the case of the Bevatron, where an instability of the debunched beam at 6 GeV has been observed, and has been cured by the provision of clearing fields.[7)]

For typical operating conditions at 6 GeV we find $q_1{}^2 = 4 \times 10^{-3}$ and $\nu_{z_0} \approx 0.9$. (More details may be found in Ref. 13.) Hence, for stability we require

$$\sqrt{\Delta_p^2 - (1.2 \times 10^{-4})^2}\ \sqrt{\Delta_e^2 - (6.3f)^2} \geqslant 2.5 \times 10^{-2} f. \qquad (32)$$

If we assume the relatively large spreads $\Delta_e = 1.5$, $\Delta_p = 0.04$, we find a threshold neutralization $f = 0.24$. Neglecting electron-electron forces, the threshold f would be a tolerable $f > 1$. Hence, in the case of the Bevatron, species-species forces appear to play a dominant role in the determination of the threshold. This situation is generally the case in a proton ring if the proton frequency spread is large and/or γ is small.

8. AXIAL STABILITY IN THE ERA

In the acceleration column of an ERA, or of any similar system in which translational invariance of the configuration can be legitimately assumed, it follows from equation (1) that

$$q^2 + q_u{}^2 - q_c{}^2 = 0,$$
$$Q^2 + Q_u{}^2 - Q_c{}^2 = 0. \qquad (33)$$

From (17), we may write

$$\tilde{q}^2 = q_c{}^2,$$
$$\tilde{Q}^2 = Q_c{}^2. \qquad (34)$$

As we shall see below, the invariance conditions imply that images hardly effect the axial stability conditions in an ERA.

Frequency parameters for an ERA have been derived in Ref. (14). They are presented in Table III. These formulas can be simplified by assuming

$$1 \gg f \gg \frac{1}{\gamma^2}$$

$$\frac{R^2}{b(a+b)} \gg P/8,\ \frac{\epsilon_e}{(S_e-1)^2}\,, \tag{35}$$

in which case image contributions only appear in $q_u^{\ 2}$ and q_o^2.

For the Lorentzian distribution, equation (14) is valid with the replacement discussed just following equation (14). In view of (33), this equation is independent of images. Thresholds are as has been discussed in the literature,$^{5)}$ and above threshold we have the stability condition (20), which takes the <u>image-independent form</u>:

$$\Delta_e\Delta_i \geqslant q_c Q_c\,. \tag{36}$$

We note that the condition (36) will normally not be satisfied except for working points with very small values of q_c and/or Q_c. Such working points, however, are unattractive because both q_c and Q_c are "figures of merit" of an ERA device -- since $Q_c^{\ 2}$ is a measure of the holding power of the ring and $q_c^{\ 2}$ determines the fractional ion loading.

For the semi-circular distribution, or the modified Lorentz distribution, the thresholds and damping conditions depend slightly upon the image terms. We have undertaken numerical studies in order to ascertain the effect, on the instability, of images and dispersion. We concentrate on the $n = 1$ (dipole) instability and we refer to Table III and postulate parameters such that $\gamma = 40$, $C_1 \equiv 4(\frac{\mu}{N_e})\,\frac{R^2}{b(a+b)} = 5.0 \times 10^{-13}$,

$C_2 \equiv 4(\frac{\mu}{N_e})\,\frac{P}{8} = \frac{1}{60.} \times 10^{-13}$, and $C_3 \equiv 4(\frac{\mu}{N_e})\,\frac{\epsilon_e}{(S_e-1)^2} = 0.05 \times 10^{-13}$.

(Such coefficients might result, approximately, from $R = 3.5$ cm, $a = 0.30/\sqrt{2}$ cm, $b = 0.15/\sqrt{2}$ cm, and $|S_e-1| = 0.625/3.5$). Then, with $M/m = 1836$, we write

$$q_u^{\ 2} = (C_1/1600 + C_2 - \mathcal{K}C_3)\cdot N_e$$

$$q_c^{\ 2} = (C_1 + C_2 - \mathcal{K}C_3)\cdot N_i$$

$$q^2 = q_c^{\ 2} - q_u^{\ 2}$$

$$Q_u^2 = (40/1836)q_c^2$$

$$Q_c^2 = (40/1836)(C_1 + C_2 - \varkappa C_3)\cdot N_e$$

and

$$Q^2 = Q_c^2 - Q_u^2 ,$$

where $\varkappa$ is a "flag" that, if set equal to unity, introduces the effect of a strong electrostatic focussing. The dispersion may be controlled by means of a parameter η such that $\delta_- = \delta_+ = \eta q$ and $\Delta_- = \Delta_+ = \eta Q$.

With these substitutions introduced into (28), as modified by (29), one may solve for the roots computationally, along a trajectory on which (for example) $f = N_i/N_e$ is held constant, and so examine the variation of the threshold vs. the damping coefficient η. With the ratio $N_i:N_e$ equal to one and one-half percent, and with images absent ($\varkappa = 0$), one finds in this way virtually no change of the threshold until $\eta > 0.4$, and even with η as large as unity the particle abundances are permitted to increase by only 43 percent. Under similar circumstances dispersion is found to be somewhat more effective when image focussing is present ($\varkappa = 1$), but the gains are trivial until $\eta > 0.4$ and η should exceed 0.93 to achieve a doubling of the permissible particle numbers.

In examining an alternative trajectory on which the ratio $N_i:N_e$ is taken to be one-half of one percent, it appears desirable to have image focussing present ($\varkappa = 1$) since the ion focussing can be expected to be weak. Under these conditions the effect of the dispersion coefficient η has been found to be somewhat greater than was the case for the trajectory mentioned earlier, although the effect remains small until η exceeds 1/2. Somewhat more striking effects do develop at the larger values of η -- thus, with $N_i/N_e = 0.005$, dispersion characterized by $\eta = 0.88$ permits a doubling of the particle numbers and, at $\eta = 1$ and $N_e = 5 \times 10^{13}$, stability is obtained for $N_i \leqslant 4.67 \times 10^{11}$, i.e. for $f \leqslant 0.0093$ (cf. the Figure on p. 5 of ERAN-177,[12] which suggests the ability of strong dispersion to open up a narrow stable corridor through a region of small N_i).

In summary, the numerical studies have shown that with physically achievable damping terms the stability threshold is only slightly changed from that which obtains in the absence of damping; a result in accord with (36) and with the conclusions of Zenkevich and Koshkarev.[5] We conclude that neither Landau damping nor image effects and species-species forces are capable of any considerable extension of the stable working range in an ERA-column.

REFERENCES

1. G.I. Budker, "Relativistic Stabilized Electron Beams", Proc. of the Second International Conf. on High Energy Accelerators, CERN 1959, p. 58 (1959).
2. B.V. Chirikov, Atomic Energy 19, p. 239 (1965).
3. T.K. Fowler, "Notes on the Interaction of Electron Ring with Ions", The Symposium on Electron Ring Accelerators, Lawrence Radiation Laboratory Report UCRL-18103, p. 457 (1968).
4. F.E. Mills, "Mutual Oscillations of Ions and Electrons in the ERA", The Symposium on Electron Ring Accelerators, Lawrence Radiation Laboratory Report, UCRL-18103, p. 448 (1968).
5. P.R. Zenkevich, D.G. Koshkarev, "Coupling Resonances of the Transverse Oscillations of Two Circular Beams", Institute of Theoretical and Experimental Physics (Moscow) Report 1060, (1970); Particle Accelerators 3, 1 (1972).
6. V.I. Balbekov, A.A. Kolamenskii, Soviet Phys.-Techn. Phys. 12, 1487 (1968).
7. H. Grunder, G. Lambertson, "Transverse Beam Instabilities at the Bevatron", The Proceedings of the 8th International Conf. on High Energy Accelerators, CERN 1971, p. 308 (1971).
8. H.G. Hereward, "Coherent Instability due to Electrons in a Coasting Proton Beam", CERN-Report 71-15 (1971).
9. L.J. Laslett, V.K. Neil, A.M. Sessler, Rev. Sci. Instrum. 36, 436 (1965).
10. H.G. Hereward, "Landau Damping by Nonlinearity", CERN-Report MPS-DL 69-11 (1969).
11. K. Hubner, V.G. Vaccaro, "Dispersion Relations and Stability of Coasting Particle Beams", CERN-Report ISR-TH 70-44 (1970).
12. L.J. Laslett, "Numerical Work Relating to Stability of Electron-Ion Collective Motion", LBL Internal Report ERAN-181 (Jan. 1972); L.J. Laslett, "A Numerical Illustration of the Effect of Dispersion on the Electron-Ion-Instability", LBL Internal Report ERAN-177 (Dec. 1971); L.J. Laslett, "Numerical Evaluation of Roots of a Dispersion Equation Considered Relevant to the CERN ISR", LBL Internal Report ERAN-175 (Nov. 1971). We are indebted to V. Brady for assistance in the development and use of the computational programs employed in the numerical work.

13. D. Möhl, A.M. Sessler, "Proton-Electron Coupling Instability in the CPS and the Bevatron, Lawrence Berkeley Laboratory Int. Report ERAN-186 (March, 1972).

14. I.N. Ivanov et al.,"Motion of Particles in the Adgezator", JINR Report P9-4132 (1968); L.J. Laslett, "On the Focussing Effects Arising from the Self Fields of a Toroidal Beam", LBL Internal Report ERAN-30 (April, 1969).

Table I - The Dispersion Integral I

a.) Definitions

$$I = \int \frac{f(s)ds}{q^2-(\nu-n\frac{\Omega}{\Omega_o})^2} \cong \frac{1}{2q}\left[\int \frac{f(s)ds}{\nu-n\frac{\Omega}{\Omega_o}+q} - \int \frac{f(s)ds}{\nu-n\frac{\Omega}{\Omega_o}-q}\right]$$

$$q = q_o + \frac{\partial q}{\partial s} s$$

$$\Omega = \Omega_o + \frac{\partial \Omega}{\partial s} s$$

$$\Delta_\pm = s_{1/2} \left| \frac{\partial q}{\partial s} \pm \frac{1}{\Omega_o} \frac{\partial \Omega}{\partial s} \right|$$

$s_{1/2}$ is the half width of $f(s)$ (full width at half maximum or half width at bottom).

b.) Lorentzian Distribution

$$f(s) = \frac{2}{\pi} \frac{s_{1/2}}{(s_{1/2}^2 + 4s^2)}$$

$$I = \frac{1}{2q_o}\left[\frac{1}{\nu-(n-q_o)+\frac{i\Delta_-}{2}} - \frac{1}{\nu-(n+q_o)+\frac{i\Delta_+}{2}}\right]$$

If $\Delta_+ = \Delta_-$: $I = \dfrac{1}{q^2-(\nu+\frac{i\Delta}{2}-n)^2}$

c.) Semi-circle Distribution

$$f(s) = \begin{cases} \frac{2}{\pi s_{1/2}^2}\sqrt{s_{1/2}^2 - s^2} & |s| \leq s_{1/2} \\ 0 & |s| \geq s_{1/2} \end{cases}$$

Table I (cont.)

$$I = \frac{1}{q_o}\left[\frac{1}{\nu-(n-q_o) + i\bar{\Delta}_-} - \frac{1}{\nu-(n+q_o) + i\bar{\Delta}_+}\right]$$

$$\bar{\Delta}_+ = \sqrt{\Delta_+^2 - [\nu-(n+q_o)]^2}$$

$$\bar{\Delta}_- = \sqrt{\Delta_-^2 - [\nu-(n-q_o)]^2}$$

Table II - Frequencies of Vertical Oscillation of a Coasting Proton Beam Partially Neutralized by Electrons*

1. Proton frequencies:†

$$q^2 = \nu_{z_o}^2 + 4\mu \left[\frac{1}{b(a+b)} \left(f - \frac{1}{\gamma^2} \right) + \frac{\epsilon_1}{h^2} (f-1) - \frac{\epsilon_2 \beta^2}{g^2} \right] R^2$$

$$q_u^2 = \frac{4\mu}{\gamma^2} \left[\frac{1}{b(a+b)} + \frac{\epsilon_1 - \xi_1}{h^2} \right] R^2$$

$$q_c^2 = 4\mu f \left[\frac{1}{b(a+b)} + \frac{\epsilon_1 - \xi_1}{h^2} \right] R^2 = q_u^2 f \gamma^2$$

2. Electron frequencies ($\beta_e = 0$):

$$Q^2 = 4\mu \frac{M\gamma}{m} \left[\frac{1}{b(a+b)} (1-f) + \frac{\epsilon_1}{h^2} (1-f) \right] R^2$$

$$Q_u^2 = 4\mu \frac{M\gamma}{m} f \left[\frac{1}{b(a+b)} + \frac{\epsilon_1 - \xi_1}{h^2} \right] R^2 = q_c^2 \frac{M\gamma}{m}$$

$$Q_c^2 = 4\mu \frac{M\gamma}{m} \left[\frac{1}{b(a+b)} + \frac{\epsilon_1 - \xi_1}{h^2} \right] R^2 = Q_u^2 / f$$

where:

$$\mu = \frac{N_p r_p}{2\pi R \gamma} \qquad f = \frac{N_e}{N_p} ,$$

---

* Curvature effects are ignored, and the beam is assigned to be centered in the vacuum chamber.

† In writing the proton frequencies, we have set $\beta = 1$, save in the last (magnetostatic) term of the equation for q_o^2.

$\epsilon_1, \epsilon_2, \xi_1$: Image coefficients

h: Half height of vacuum chamber

g: Half height of magnet gap

r_p: Classical proton radius

Table III - Electron and Ion Frequencies for Axial Motion in an ERA-Column * ††

1. Electron frequencies:†

$$q_o^2 = 4\mu \left[\frac{R^2}{b(a+b)} \left(f - \frac{1}{\gamma^2}\right) - \frac{P}{8} + \frac{\epsilon_e(1-f)}{(S_e-1)^2} - \beta^2 \frac{\epsilon_m}{(S_m-1)^2} \right]$$

$$q_u^2 = 4\mu \left[\frac{R^2}{b(a+b)\gamma^2} + \frac{P}{8} - \frac{\epsilon_e}{(S_e-1)^2} + \beta^2 \frac{\epsilon_m}{(S_m-1)^2} \right]$$

$$q_c^2 = 4\mu f \left[\frac{R^2}{b(a+b)} - \frac{\epsilon_e}{(S_e-1)^2} \right]$$

2. Ion frequencies:

$$Q^2 = 4\mu \left(\frac{m\gamma}{M}\right)(1-f) \left[\frac{R^2}{b(a+b)} - \frac{\epsilon_2}{(S_e-1)^2} \right]$$

$$Q_u^2 = q_c^2 \frac{m\gamma}{M}$$

$$Q_c^2 = q_c^2 \frac{m\gamma}{Mf} ,$$

where:

$$\mu = \frac{N_e r_e}{2\pi R\gamma} , \quad f = \frac{N_i}{N_e} .$$

* Uniform external guide field assumed.

† $\beta_e \approx 0$

$P = 2 \ln[16R/(a+b)]$

S_e = Radius of Electric image cylinder/R

S_m = Radius of magnetic image cylinder/R

$\epsilon_e \approx \epsilon_m \approx 0.125$ image coefficients

r_e: Classical electron radius

†† We are indebted to Prof. M. Reiser for a recent communication concerning his analysis of toroidal field gradients [Max-Planck-Institute for Plasma Physics Report IPP 0/14 (Munich-Garching, July 1972)] that called to our attention the appropriate form of certain terms indicated in Table III.

SOME REMARKS CONCERNING THE COLLECTIVE TRANSVERSE OSCILLATION OF A D.C. BEAM IN THE PRESENCE OF RESISTIVE WALLS*

L. Jackson Laslett

Lawrence Berkeley Laboratory
University of California
Berkeley, California

May, 1973

SOME REMARKS CONCERNING THE COLLECTIVE TRANSVERSE OSCILLATION OF A D.C. BEAM IN THE PRESENCE OF RESISTIVE WALLS*

L. Jackson Laslett

May 25, 1973

The "coherent force" to be applied in the case of an unbunched beam oscillating transversely with a displacement y within a highly conducting chamber is normally taken to be expressible as [1]

$$F = 4\lambda e\ [\ \xi_1 - \beta^2(\xi_1 - \epsilon_1)]\ \frac{y}{h^2}$$

$$= \frac{2}{\pi}\ \frac{Nr_c}{Rh^2}\ (m_oc^2)\ [\xi_1 - \beta^2(\xi_1 - \epsilon_1)]\ y$$

if D.C. magnetic image forces are negligible, where the first term within the square bracket arises from electric image terms and the second from current images. The portion of the formula that involves $\xi_1 - \epsilon_1$ is regarded as arising from the vertical movement (within a conventional synchrotron chamber) of the longitudinal D.C. beam current, which results in A.C. magnetic image fields (subject to boundary conditions appropriate to A.C. fields). These A.C. magnetic fields are considered to be derivable,[1] for a beam at $y = y_1$, from the image field computed at y_1 (through use of A.C. boundary conditions) for the beam at y_1 (contribution proportional to ξ_1) minus the field similarly computed at y for an undisplaced beam (contribution proportional to ϵ_1). For a pair of plane-parallel conducting surfaces at ±h, $\epsilon_1 = \pi^2/48$ and $\xi_1 = \pi^2/16$; [2] for a circularly cylindrical conducting tube of radius h surrounding a beam on its axis, $\epsilon_1 = 0$ and $\xi_1 = \frac{1}{2}$. [2]

The terms shown in the expression for F thus represent the effect of

(i) a defocusing electric image field (e.s.u.)

$$E = 4\lambda\ \xi_1 \frac{y}{h^2} \qquad \text{and}$$

(ii) a focusing magnetic field (e.m.u.)

$$H = 4I\ (\xi_1 - \epsilon_1)\ \frac{y}{h^2}\ .$$

---

* Work supported by the U.S. Atomic Energy Commission.

In certain cases of interest in which the chamber walls have appreciable resistance, the magnetic image fields given by the expression written immediately above will arise immediately from a step-displacement y but subsequently will decay (due to attenuation and possible redistribution of the image currents) in a manner conveniently characterized by the characteristic Maxwell velocity [3] v ($v = R_s/2\pi$ for surface resistance in e.m.u., or $v = 2R_s/\mu_o$ in the MKSA system)[4] and a characteristic dimension h of the structure. Thus, in particular, for an infinitesimal displacement of the beam from the axis of a thin circular cylinder of radius h, the decay is characterized by the simple factor $\exp[-v\cdot(t - t_o)/h]$. For currents suddenly established (or displaced) between two thin plane-parallel side plates, the time dependence may be more elaborate, but the important initial decay again appears [5] to be reasonably well represented by the exponential factor just mentioned, with h now denoting the half-gap.

To obtain the time variation of the magnetic contribution F_M to the force F when the displacement y is an arbitrary (small) specified function of time, it therefore may be appropriate as well as convenient to write this contribution as arising from an image field

$$H = \frac{4I}{h^2}(\xi_1 - \epsilon_1)\int_{-\infty}^{t}\dot{y}(\tau)\exp[-v\cdot(t - \tau)/h]\,d\tau$$

and

$$F_M = -\frac{2}{\pi}\frac{Nr_c}{Rh^2}(m_oc^2)\,\beta^2\,(\xi_1 - \epsilon_1)\int_{-\infty}^{t}\dot{y}(\tau)\exp[-v\cdot(t - \tau)/h]\,d\tau \quad .$$

For an <u>oscillatory</u> (SHM) variation of y, represented by the factor $\exp(j\omega t)$, these expressions become

$$H = \frac{4I}{h^2}(\xi_1 - \epsilon_1)\frac{\omega^2 + j\omega\frac{v}{h}}{\omega^2 + (v/h)^2}\,y$$

$$= \frac{4I}{h^2}(\xi_1 - \epsilon_1)\left[\frac{\omega^2}{\omega^2 + (v/h)^2}\,y + \frac{v/h}{\omega^2 + (v/h)^2}\,\dot{y}\right] ,$$

$$F_M = -\frac{2}{\pi}\frac{Nr_c}{Rh^2}(m_oc^2)\,\beta^2\,(\xi_1 - \epsilon_1)\frac{\omega^2 + j\omega\, v/h}{\omega^2 + (v/h)^2}\,y \; , \quad \text{and}$$

$$F = \frac{2}{\pi}\frac{Nr_c}{Rh^2}(m_oc^2)\left[\xi_1 - \beta^2(\xi_1 - \epsilon_1)\frac{\omega^2 + j\omega\, v/h}{\omega^2 + (v/h)^2}\right]y \quad .$$

The frequency dependence implied by the complex expression just given for H, if applied to a thin circular cylinder of radius h and surface resistance R_s, can be compared (and confirmed) by reference to earlier reports[6] that were specifically concerned with this particular geometrical configuration (setting, for this purpose, $\epsilon_1 = 0$ and $\xi_1 = 1/2$ in the above).

The imaginary part of F, as given by the last expression above, can be converted to the quantity V, frequently employed in dispersion analyses of collective motion, by multiplication of $\text{Im}(-F/y)$ by the factor

$$\frac{1}{2\nu(\beta c/R)} \; \frac{1}{\gamma m_o}$$

to obtain

$$V = \frac{N r_c \beta c}{\pi \nu \gamma h^2} (\xi_1 - \epsilon_1) \frac{\omega(v/h)}{\omega^2 + (v/h)^2} ,$$

with $v = R_s/2\pi$ (e.m.u.). The analysis of magnetic-field behavior that has led to the magnetic contributions contained in all of the foregoing formulas is believed to be basically correct for $R_s \ll Z_o$ and a wall thickness $\lesssim \delta$ [where Z_o denotes the "impedance of space" ($120\,\pi$ ohms) and δ is the "skin-depth" characteristic of the wall material]. The result cited here for V has been checked[5] by comparison with results obtained computationally [for a beam situated on the axis of a circular stainless-steel cylinder of variable thickness and setting $\omega = (1 - \nu)\omega_o$] from a program[7] based on general methods developed at CERN by Zotter.[8] Excellent agreement was found for the range of thicknesses limited by the conditions $R_s < 0.12\, Z_o$ and wall thickness $< \delta/1.7$, and the physical principles employed in the preceding discussion thus should be applicable throughout an extensive range of values for R_s that will comfortably include those of interest in the ERA program. [For approximate work the range of applicability might be taken to extend between the limits $R_s < Z_o/2$ and wall thickness $< 1.7\,\delta$.]

From the form of the of the expression given for V, it is apparent that this quantity will be inversely proportional to R_s when the wall resistance is high, but should be directly proportional to R_s for walls of rather low surface resistance -- *i.e.*, for R_s less than the value

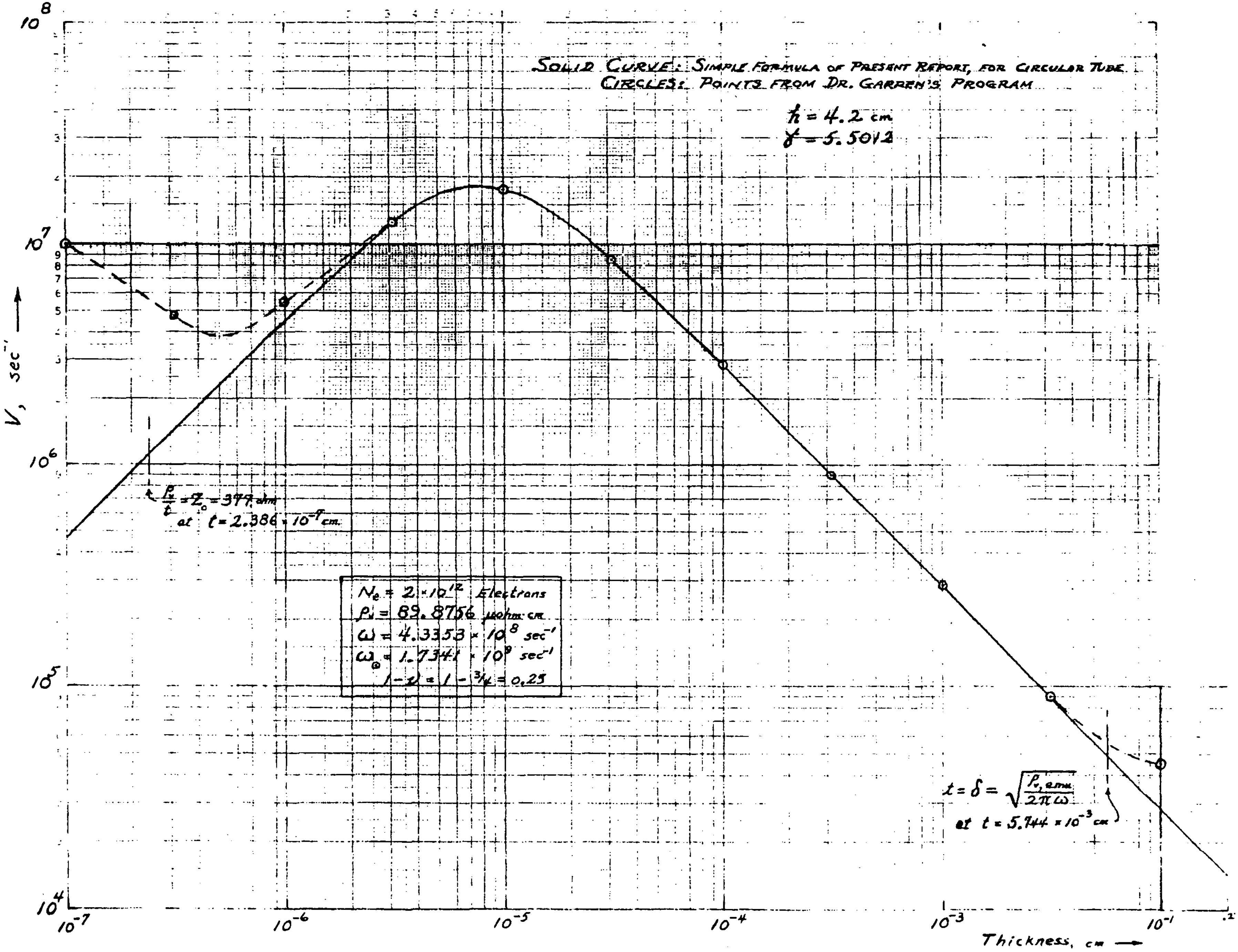
SOLID CURVE: SIMPLE FORMULA OF PRESENT REPORT, FOR CIRCULAR TUBE
CIRCLES: POINTS FROM DR. GARREN'S PROGRAM
$h = 4.2$ cm
$\gamma = 5.5012$
$N_e = 2 \times 10^{12}$ Electrons
$\rho_v = 89.8756$ μohm·cm
$\omega = 4.3353 \times 10^{8}$ sec^{-1}
$\omega_{\odot} = 1.7341 \times 10^{9}$ sec^{-1}
$1 - \nu = 1 - 3/4 = 0.25$
$\frac{\rho_v}{t} = Z_0 = 377$ ohm
at $t = 2.386 \times 10^{-9}$ cm.
$t = \delta = \sqrt{\frac{\rho_{v,\,emu}}{2\pi\omega}}$
at $t = 5.744 \times 10^{-3}$ cm
V, sec^{-1}
10^{8}
10^{7}
10^{6}
10^{5}
10^{4}
10^{-7}
10^{-6}
10^{-5}
10^{-4}
10^{-3}
10^{-1}
.2
Thickness, cm

$\mu_o h\omega/2 = \mu_o h(M - \nu)\omega_o/2$ (MKSA units) at which the value of V is a maximum.

An early analysis [9] was made specifically for the magnetic effect of image currents induced magnetically by a beam oscillating radially between thin plane resistive side walls at $z = \pm h$. The analysis considered the surface resistance R_s to be large (but $\ll Z_o$). A "curvature factor" f was introduced into the result, but shall be considered in the following discussion to be unity -- as would be the case for an orbit radius that is large in comparison to the half-gap h. The growth rate that was deduced in this work as arising from the image currents induced in the side walls (with Landau damping ignored) was found to be the same when the conducting plates are taken to be situated above and below a straightened-out beam [10] and also when such a beam is situated near the axis of a thin circularly-cylindrical resistive tube. [11] The result for this growth rate, if identified with V, reads (after an adaptation of notation that includes replacement of R_s by $\mu_o v/2$ and Z_o by $\mu_o c$)

$$V = \frac{1}{\tau_M} = \frac{N r_e \beta\omega c}{2\pi\nu\gamma h v} \quad ,$$

with v again denoting the Maxwell velocity. The law governing the decay of induced image-current effects is exactly known in simple terms as $\exp[-v\cdot(t - t_o)/h]$ only for the cylindrical geometry, and the formula just given for V [9-11] will be seen to agree exactly in the limit $v/h \gg \omega$ with the formula given previously for V with $\epsilon_1 = 0$ and $\xi_1 = 1/2$ (as is appropriate for the cylindrical geometry). The result obtained in Ref. 9, in which $V \propto 1/R_s$, thus is seen to be applicable for <u>large</u> values of R_s (but for R_s not as great as Z_o), and presumably retains its validity until v becomes comparable to or less than ωh -- *i.e.*, until R_s becomes comparable to or less than $(\mu_o/2)\omega h$ (MKSA units). More generally (until the resistance is so low that the skin depth becomes comparable to the wall thickness), it might be reasonable to apply the factor

$$\frac{(v/h)^2}{\omega^2 + (v/h)^2}$$

to the results of Ref. 9.

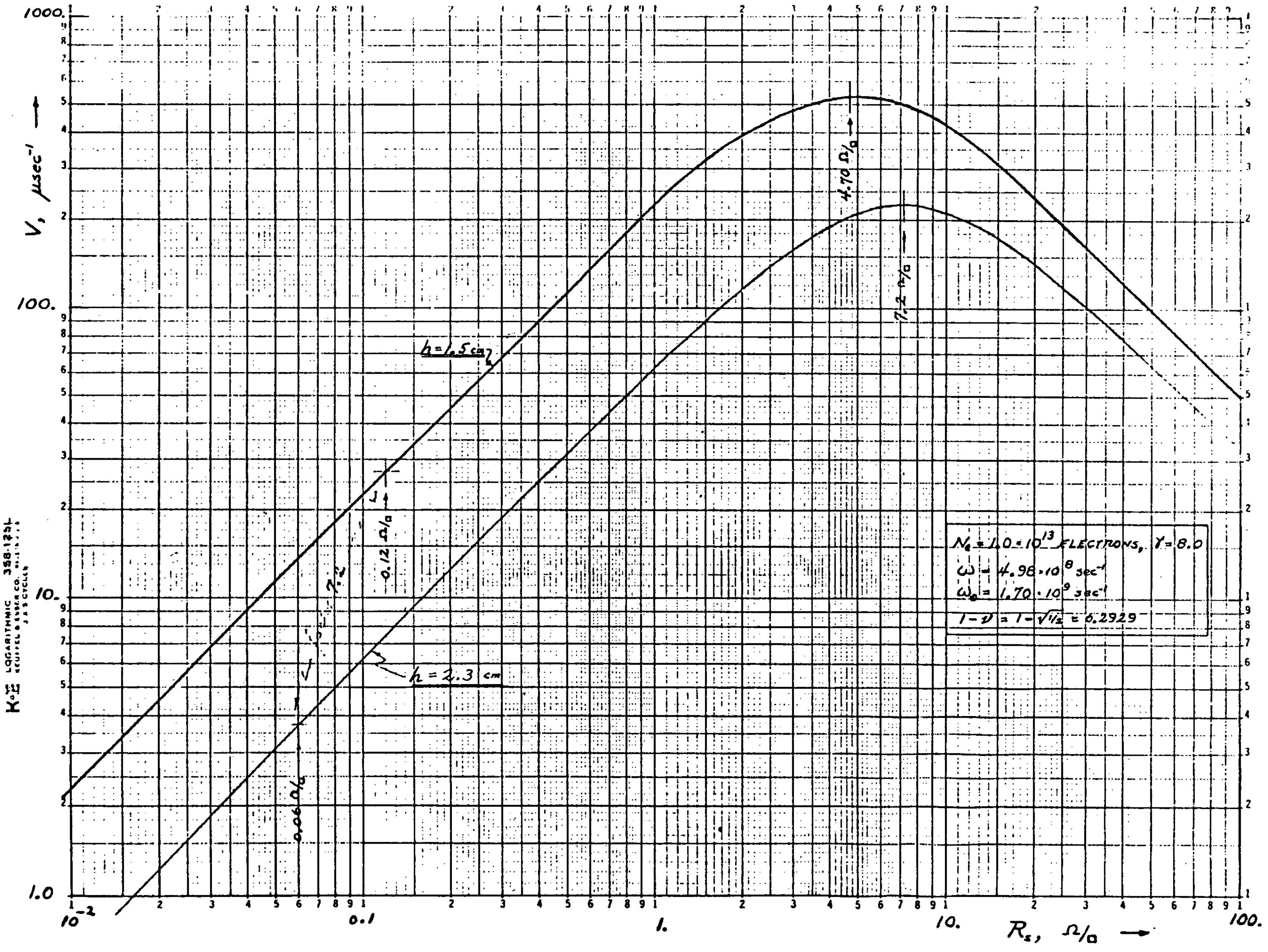
$N_e = 1.0 \cdot 10^{13}$ ELECTRONS, $\gamma = 8.0$
$\omega = 4.98 \cdot 10^{8}\ sec^{-1}$
$\omega_0 = 1.70 \cdot 10^{9}\ sec^{-1}$
$1 - \nu = 1 - \sqrt{1/2} = 0.2929$
$h = 1.5\ cm$
$h = 2.3\ cm$
$4.70\ \Omega/\square$
$7.2\ \Omega/\square$
$0.12\ \Omega/\square$
$0.06\ \Omega/\square$
7.2
$V,\ \mu sec^{-1}$
1000.
100.
10.
1.0
10^{-2}
0.1
1.
10.
100.
$R_s,\ \Omega/\square$
K&E LOGARITHMIC 358-125L
KEUFFEL & ESSER CO.
3 X 5 CYCLES

References and Notes:

1. L. Jackson Laslett and L. Resegotti, Proc. VI Internat. Conf. High Energy Accelerators (CEAL-2000, Cambridge Electron Accelerator, Cambridge, Massachusetts; 1967), p. 150 ff.

2. L. Jackson Laslett, Proc. 1963 Summer Study on Storage Rings, Accelerators and Experimentation at Super-High Energies (BNL 7534, Brookhaven Nat'l Laboratory, Upton, Long Island, New York; 1963), p. 324 ff.

3. James Clerk Maxwell, "A Treatise on Electricity and Magnetism," Ed. 3, V. II, Part IV, Ch. XII, Sect. 658-659 (1891; Dover Publications, New York; 1954).

4. The characteristic velocity v may be simply evaluated in cm/ns by use of $v = R_s/2\pi$ with R_s expressed in "ohms per square."

5. L. Jackson Laslett, "Current Understanding of ERA" -- Invited Paper presented at the 1973 U.S. Nat'l Particle Accelerator Conference (San Francisco, California; 5-7 March 1973).

6. L. Jackson Laslett, ERAN-61 (16 February 1970) and Addendum (23 February 1970) -- and earlier reports cited therein (e.g., ERAN-38 and ERAN-39). In the formulas of ERAN-61, R denotes the cylinder radius, while the quantity h_o or $h(t)$ represents the location of the current and should be taken to be small for a beam on or near the axis of the cylinder.

7. A. Garren, ERAN-123 (1971).

8. B. Zotter, CERN 65-15 Rev. (CERN, Geneva, Switzerland; 1969).

9. Glen R. Lambertson and L. Jackson Laslett, ERAN-157 (1971).

10. Ref. 9, Appendix A.

11. Ref. 9, Appendix B.

Particle Accelerators
1983 Vol. 13 pp. 145–178
0031-2460/83/1303/0145$06.50/0

© Gordon and Breach, Science Publishers, Inc.
Printed in the United States of America

Reprinted by permission of Gordon & Breach.

STABILITY OF THE KAPCHINSKIJ-VLADIMIRSKIJ (K-V) DISTRIBUTION IN LONG PERIODIC TRANSPORT SYSTEMS[†]

I. HOFMANN,[‡] L. J. LASLETT, L. SMITH, AND I. HABER[§]

Lawrence Berkeley Laboratory, University of California, Berkeley, California 94720 U.S.A.

(Received October 13, 1982)

Transport of intense beams of heavy ions over long distances may be restricted by space-charge induced transverse instabilities. The stability of the microcanonical, or K-V, distribution is analyzed with the help of the Vlasov equation, and reduced to a study of the characteristics of solutions for a set of ordinary differential equations with periodic coefficients. Numerical solutions for various periodic solenoid and quadrupole focusing channels are derived and provide information concerning stable regions of propagation in terms of betatron tune depression. The results are compared with computer simulation examples of beams in solenoid and quadrupole focusing channels to check linear growth rates and establish nonlinear saturation levels of instabilities. Conclusions are drawn for the design of a quadrupole lattice providing stable transport.

I. INTRODUCTION

The possibility of using high-energy heavy ions as the igniting mechanism for inertially confined fusion has necessitated a consideration of transporting currents in the kilo-ampere range for distances of the order of kilometers without significant degradation of beam emittance. In addition to the usual problems of field and alignment tolerances, there arises the question of the stability of beam propagation in a vacuum against fluctuation in self-forces arising from initial deviations from the desired distribution of the beam in the four-dimensional transverse phase space.

The most powerful analytic technique for investigating this problem is a linearization of the Vlasov equation about a known stationary solution, coupled with the appropriate equations for the perturbed electromagnetic fields. If the external focusing force is constant, an infinite variety of stationary solutions can readily be generated, since any function of the Hamiltonian is a solution of the Vlasov equation and the corresponding self electrostatic potential can be obtained by integrating Poisson's equation.[1] It furthermore is possible to show[2] that a large class of such stationary solutions is stable against arbitrary fluctuations.

For the more realistic situation of a focusing channel consisting of quadrupoles or discrete solenoids, however, the Hamiltonian function is not a constant of the motion and hence cannot be used directly to provide a stationary solution of the Vlasov equation. To our knowledge, the microcanonical distribution investigated by

---

[†] This work was supported by the Assistant Secretary for Defense Programs, Office of Inertial Fusion, Laser Fusion Division, U.S. Department of Energy, under Contract No. DE-AC03-76SF00098.

[‡] Max-Planck-Institut für Plasmaphysik, 8046 Garching, West Germany.

[§] Naval Research Laboratory, Washington, D.C.

Kapchinskij and Vladimirskij[3] (K-V), for which individual-particle restoring forces are linear functions of the displacement, is the only distribution for which a stationary (i.e., periodic) solution can be constructed. Because of its singular character, it is probably more susceptible to instability than real beams and so we have performed the present investigation concerning its stability characteristics in the hope that the results may serve as a conservative guide to identifying regions in parameter space that might be dangerous.

We proceed by presenting in Sect. II the general framework of the linearized Vlasov analysis. This is followed in Sect. III by application to periodic solenoid and to quadrupole focusing systems. Specific results are given (Sect. IV) for several perturbation modes in such systems (with the governing equations becoming increasingly complex for modes of high order) and suggest the particular importance of a "third-order" mode. In Sect. V, we compare the linear growth of the third-order mode found in both the analytic theory and in computer simulation. Simulation will also be used to establish the practical significance of the remaining instabilities. The implications of these results are discussed in Sect. VI.

We observe that intensity is frequently related to the ratio ν/ν_0 for beams in a continuous solenoid and to σ/σ_0 in a periodic channel. Here ν denotes the betatron oscillation "frequency" (with time replaced by distance), and σ the phase advance of betatron oscillations per focusing period; ν_0, σ_0 are the corresponding values for zero intensity.

II. GENERAL FORMULATION OF THE LINEARIZED VLASOV ANALYSIS

We use the distance s along the transport channel as the independent variable and write the total Hamiltonian function as

$$H = \frac{1}{2}(p_x^2 + p_y^2) + \frac{1}{2}[\kappa_x(s)x^2 + \kappa_y(s)y^2] + V(x, y; s), \tag{1}$$

where

$$\kappa_x = K_x - \frac{Q}{a(a+b)}, \quad \kappa_y = K_y - \frac{Q}{b(a+b)},$$

$K_{x,y}$ represent the external force constants [$\pm B'(s)/[B\rho]$ for quadrupoles, and $(\frac{1}{2}B/[B\rho])^2$ for solenoids in the Larmor frame],

$$Q = \frac{4Nq^2 r_p}{A\beta^2\gamma^3},$$

qe is the ion charge, A is the ion mass/proton mass, N is the number of ions per unit length, r_p is the classical proton radius, $e^2/(4\pi\epsilon_0 M_{p,0}c^2)$ (MKSA units), $a(s)$ and $b(s)$ are respectively the x and y half widths of the matched (periodic) beam envelope [as determined by the K-V envelope equations—Ref. 3, Eqs. (46) and (47)], and

$$V = \frac{q}{A}\frac{4\pi\epsilon_0 r_p/e}{\beta^2\gamma^3} \times \text{electrostatic potential function due to perturbations.}$$

The first two terms in Eq. (1) represent the unperturbed Hamiltonian, which is not a constant of the motion for *s*-dependent focusing, and the terms proportional to *Q* describe the effect of transverse components of the space-charge force for a K-V distribution.

We now make use of the Courant-Snyder[4] functions $\beta(s)$ and $\alpha(s)$ for the unperturbed orbits, for which (with dots denoting d/ds)

$$\alpha_{x,y} = -\frac{1}{2}\dot{\beta}_{x,y}, \frac{1}{2}\ddot{\beta}_{x,y} - \frac{1}{4}\dot{\beta}^2_{x,y}/\beta_{x,y} - 1/\beta_{x,y} = -\beta_{x,y}\kappa_{x,y},$$

and[3,4]

$$\beta_x(s) = a^2(s)/\epsilon,\ \beta_y(s) = b^2(s)/\epsilon,$$

where $\pi\epsilon$ represents the emittance (assumed to be identical in the two transverse planes). The form of the governing Hamiltonian function can thereby be simplified through introduction of a transformation defined by the generating function

$$F = \frac{x}{\beta_x^{1/2}}\left[\bar{p}_x - \frac{\alpha_x}{2}\frac{x}{\beta_x^{1/2}}\right] + \frac{y}{\beta_y^{1/2}}\left[\bar{p}_y - \frac{\alpha_y}{2}\frac{y}{\beta_y^{1/2}}\right], \tag{2}$$

followed by a scaling transformation $\tilde{x} = \bar{x}/\epsilon^{1/2}$, $\tilde{p}_x = \bar{p}_x/\epsilon^{1/2}$, etc., so that

$$\tilde{x} = x/(\beta_x\epsilon)^{1/2},\ \tilde{p}_x = (\beta_x/\epsilon)^{1/2}\,[p_x + (\alpha_x/\beta_x)x], \tag{3}$$

and similarly for $\tilde{y}$, $\tilde{p}_y$. The new Hamiltonian function then becomes

$$\tilde{H} = \frac{1}{2\beta_x}(\tilde{p}_x^{\,2} + \tilde{x}^2) + \frac{1}{2\beta_y}(\tilde{p}_y^{\,2} + \tilde{y}^2) + \frac{1}{\epsilon}V. \tag{4}$$

In the remainder of this work we shall omit, for brevity, the tilde that distinguishes these new (dimensionless) phase-space variables. In terms of these variables the unperturbed orbits can now be written as pseudo-harmonic oscillations

$$\left.\begin{aligned} x(s') &= x(s)\cos[\psi_x(s') - \psi_x(s)] + p_x(s)\sin[\psi_x(s') - \psi_x(s)],\\ p_x(s') &= p_x(s)\cos[\psi_x(s') - \psi_x(s)] - x(s)\sin[\psi_x(s') - \psi_x(s)],\end{aligned}\right\} \tag{5}$$

with $\psi_x(s) = \int^s dz/\beta_x(z)$, and similarly for $y(s')$ and $p_y(s')$.

From Eqs. (5) it is evident that $x^2 + p_x^{\,2}$ and $y^2 + p_y^{\,2}$ are individually constants of the unperturbed motion. The unperturbed K-V distribution function, moreover, may now be written as

$$f_0 = \frac{N}{\pi^2}\,\delta(x^2 + p_x^{\,2} + y^2 + p_y^{\,2} - 1), \tag{6}$$

with δ denoting the Dirac delta function.

With the introduction of a perturbing distribution function f_1, the linearized Vlasov equation provides the total derivative along the unperturbed trajectories in phase space,

$$\begin{aligned}\frac{Df_1}{Ds} &\equiv \left\{\frac{\partial}{\partial s} + \frac{1}{\beta_x}\left[p_x\frac{\partial}{\partial x} - x\frac{\partial}{\partial p_x}\right] + \frac{1}{\beta_y}\left[p_y\frac{\partial}{\partial y} - y\frac{\partial}{\partial p_y}\right]\right\}f_1 \\ &= \frac{2N}{\pi^2\epsilon}\left[p_x\frac{\partial V}{\partial x} + p_y\frac{\partial V}{\partial y}\right]\cdot\delta'(x^2 + p_x{}^2 + y + p_y{}^2 - 1),\end{aligned} \tag{7}$$

wherein δ' denotes the derivative of the delta function with respect to its argument. Eq. (7) can be solved by integrating over the unperturbed trajectories. Introducing $\psi'_{x,y} \equiv \psi_{x,y}(s')$ as ancillary variables, Eq. (7) thus leads to

$$f_1 = \frac{2N}{\pi^2\epsilon}\left[\int^s ds'\left(\frac{\partial}{\partial\psi_x'} + \frac{\partial}{\partial\psi_y'}\right)V(x', y'; s')\right]\delta'(x^2 + p_x{}^2 + y^2 + p_y{}^2 - 1), \tag{8}$$

and (when we neglect the longitudinal field component) Poisson's equation becomes, in terms of our scaled variables and the associated distribution function,

$$\begin{aligned}\nabla^2 V &\equiv \frac{1}{a^2}\frac{\partial^2 V}{\partial x^2} + \frac{1}{b^2}\frac{\partial^2 V}{\partial y^2} \\ &= -\frac{Q}{\pi\epsilon ab}\int_0^s ds'\left(\frac{\partial}{\partial\psi_x'} + \frac{\partial}{\partial\psi_y'}\right) \\ &\quad\times \int_0^\infty d(p^2)\delta'(p^2 - (1 - x^2 - y^2))\int_0^{2\pi} d\theta V(x', y'; s'),\end{aligned} \tag{9}$$

subject to the boundary condition that the external fields vanish at infinity.[5] By noting that

$$\int_0^\infty dz\, g(z)\delta'(z - z_0) = -\left.\frac{dg}{dz}\right|_{z=z_0} - g(0)\,\delta(z_0), \tag{10}$$

we see that Poisson's equation, as expressed by Eq. (9), leads to (i)

$$\begin{aligned}&\frac{1}{a^2}\frac{\partial^2 V}{\partial x^2} + \frac{1}{b^2}\frac{\partial^2 V}{\partial y^2} \\ &\quad= \frac{Q}{\pi\epsilon ab}\int^s ds'\left(\frac{\partial}{\partial\psi_x'} + \frac{\partial}{\partial\psi_y'}\right)\left.\left[\frac{d}{d(p^2)}\int_0^{2\pi} d\theta V(x', y'; s')\right]\right|_{p^2 = 1 - x^2 - y^2}\end{aligned} \tag{11}$$

in the interior of the beam, and (ii) to a relation that reflects the presence of an effective surface charge (that describes the effect of an infinitesimal perturbation of the beam boundary)

$$\begin{aligned}&\frac{1}{a^2}\frac{\partial^2 V}{\partial x^2} + \frac{1}{b^2}\frac{\partial^2 V}{\partial y^2} \\ &\quad= \frac{2Q}{\epsilon ab}\left.\left[\int^s ds'\left(\frac{\partial}{\partial\psi_x'} + \frac{\partial}{\partial\psi_y'}\right)V(x', y'; s')\right]\right|_{p=0}\delta(1 - x^2 - y^2).\end{aligned} \tag{12}$$

By introducing elliptic coordinates (ξ, ζ) defined (in terms of our scaled coordinates, for $a > b$) by

$$x = (h/a) \operatorname{Cosh} \xi \cos \zeta \text{ and } y = (h/b) \operatorname{Sinh} \xi \sin \zeta \tag{13}$$

(where $h^2 = a^2 - b^2$, and with $\operatorname{Cosh} \xi = a/h$, $\operatorname{Sinh} \xi = b/h$ at the boundary $x^2 + y^2 = 1$), Eq. (12) may be written as

$$\frac{\partial^2 V}{\partial \xi^2} + \frac{\partial^2 V}{\partial \zeta^2} = \frac{2Qh^2}{\epsilon ab} (\operatorname{Cosh}^2 \xi - \cos^2 \zeta) \times \left[\int^s ds' \left(\frac{\partial}{\partial \psi_x'} + \frac{\partial}{\partial \psi_y'} \right) V(x', y'; s') \right]_{p=0} \delta(1 - x^2 - y^2). \tag{14}$$

The discontinuity of the electric field at the beam boundary accordingly becomes

$$\Delta \frac{\partial V}{\partial \xi} = \frac{Q}{\epsilon} \int^s ds' \left(\frac{\partial}{\partial \psi_x'} + \frac{\partial}{\partial \psi_y'} \right) V(\cos \zeta \cos(\psi_x' - \psi_x), \sin \zeta \cos(\psi_y' - \psi_y); s'). \tag{15}$$

A consistent solution is obtained if we can find a function $V(x, y; s)$ that satisfies Eqs. (11) and (15), where $\Delta(\partial V/\partial \xi)$ is such as to match the solution interior to the beam to a harmonic ($\partial^2 V/\partial \xi^2 + \partial^2 V/\partial \zeta^2 = 0$) outwardly decreasing solution external to the beam.

III. APPLICATION TO SOLENOID AND QUADRUPOLE FOCUSING

Finding a closed expression for the solutions of Eqs. (11) and (15) appears hopeless, but a brief inspection of these equations shows that they can be satisfied by potential functions that are finite polynominals in x and y interior to the beam and finite sums of $e^{-n\xi} e^{\pm in\zeta}$ exterior to the beam. Finite polynominals emerge as a result of our choice of a K-V distribution for the stationary beam. The derivative of the delta function in Eq. (7) suggests that the perturbations describe distortions of the hyper-ellipsoid in four-dimensional phase space (*cf.* final sentence in Sect. III of Ref. 6).

(*a*) *Solenoid focusing*

In the simplest case of continuous s-independent focusing, with $K_x = K_y = K$, $\beta_x = \beta_y = \beta$ and both K and β independent of s, then $\psi_x = \psi_y = s/\beta$ and solutions are of the form $V \propto e^{i\omega s} G(x, y)$. Gluckstern[6] has concluded that in this case $G(x, y)$ can be expressed by means of hypergeometric functions

$$G = \left(\frac{r}{a}\right)^m \begin{pmatrix} \cos m\phi \\ \sin m\phi \end{pmatrix} {}_2F_1\left(-j, m + j, m + 1; \frac{r^2}{a^2}\right) \tag{16}$$

in terms of unscaled polar coordinates, where a is the radius of the unperturbed beam and

$$j = 0, 1, 2, \ldots, \quad m = 0, 1, 2 \ldots, \text{excluding } j = m = 0.$$

The "order" of the mode (highest power of r appearing in the function G) is $2j + m$. Gluckstern has also indicated[7] the manner in which this solution may be employed to obtain an algebraic equation whose roots must all be real to insure stability of the matched K-V beam. Stability limits for the modes described here can be conveniently described in terms of the factor ν/ν_0 by which space-charge forces may be permitted to depress the individual-particle oscillation frequency within the matched beam (Table I). It is clear that intensities limited to values such that $\nu/\nu_0 > 0.3985$ are those for which the $m = 0$ modes may be expected to be stable, and the results presented in Table I suggest that this restriction may also be sufficient to insure stability of the higher-order modes for an uninterrupted solenoid transport system.

When the focusing strength of the solenoid is not constant but is periodically s-dependent, the matched beam radius (a) becomes a (periodic) function of s. The function $a(s)$ may be sought computationally in such cases, and the entire investigation of beam stability conducted in a manner analogous to that adopted for quadrupole-focusing systems.

(*b*) *Quadrupole focusing*

For the case of alternating-gradient quadrupole focusing $[K_y(s) = -K_x(s)]$, we have not found a general closed form for the potential analogous to that indicated by Eq. (16). The analysis of Sect. II leads, however, to a procedure that can be followed to determine the stability characteristics of individual perturbation modes. As will be shown, moreover, the eigenvalues that characterize the stability or instability of a mode can be determined by reference solely to terms of the highest power in x and y and of highest harmonic order in ζ in Eqs. (11) and (15).

(i) Example:

To illustrate this procedure we first consider a simple example that will be seen to correspond to a coherent oscillation of the beam as-a-whole. In this example the internal potential is assumed to be, in terms of the scaled coordinate x, $V_i = A(s)x$.

It is seen that Eq. (11) is trivially satisfied by this potential function, since $\nabla^2 V = 0$ and

$$\frac{d}{d(p^2)} \int_0^{2\pi} d\theta\, x' = \frac{d}{d(p^2)} \int_0^{2\pi} d\theta\, [x \cos(\psi_x' - \psi_x) + p \cos\theta \sin(\psi_x' - \psi_x)] = 0.$$

To treat the boundary Eq. (15), we employ the elliptic coordinates introduced earlier, writing V_i as $V_i = A(s)\,(\operatorname{Cosh}\xi/\operatorname{Cosh}\xi_0) \cos\zeta$ and taking the exterior potential to be $V_0 = A(s)e^{-(\xi-\xi_0)}\cos\zeta$, where ξ_0 is such that $\operatorname{Cosh}\xi_0 = a/h$. By employing these forms, $\Delta\,(\partial V/\partial\xi) = -A(s)(1 + b/a)\cos\zeta$ and Eq. (15) leads to the integral equation

$$\frac{a+b}{a} A(s) = \frac{Q}{\epsilon} \int^{s} ds'\, A(s') \sin(\psi_x' - \psi_x). \tag{17}$$

Then by differentiating twice the integral ($I(s)$) that appears in Eq. (17), one finds that it satisfies the differential equation

$$\begin{aligned}\frac{d^2 I}{d\psi_x{}^2} &= -[I + \beta_x A(s)] \\ &= -\left[1 + \frac{Q}{\epsilon}\frac{\beta_x a}{a+b}\right] I \\ &= -\left[1 + \frac{\beta_x{}^2 Q}{a(a+b)}\right] I.\end{aligned} \tag{18}$$

With the quantities a, b, β_x, and ψ_x determinable (e.g., numerically) as periodic functions of s, numerical integrations of Eq. (18) through one period of the transport channel will provide the elements of the matrix that advances the vector I, dI/ds through this interval. The eigenvalues of this matrix provide the frequency of the perturbation mode, and none may have an absolute value exceeding unity if this mode is to be stable.

We note that, by use of the previously cited relation connecting the Courant-Synder parameter β_x (and its derivatives) to the force constant κ_x, the differential Eq. (18) for I in this case may be transformed to

$$\frac{d^2}{ds^2}(\sqrt{\beta_x}\, I) + K_x(\sqrt{\beta_x}\, I) = 0 \tag{19}$$

—which will be recognized as of the form expected for a simple coherent oscillation. Similarly, adoption of a potential function whose dependence on the scaled coordinates is of the form $V_i = A(s)\, x^2 + B(s) y^2$ will lead to a pair of coupled second order equations equivalent to those customarily taken to represent a linear perturbation of the envelope equations.

(ii) General Treatment:

More generally, we assume a potential function of the form

$$V_n = \sum_{m=0}^{n} A_m(s)\, x^{n-m} y^m + \sum_{m=0}^{n-2} A_m{}^{(1)}(s)\, x^{n-m-2} y^m + \ldots \tag{20}$$

in the interior. For a given order n, "even" and "odd" modes conveniently may be treated separately on the basis of whether the index m in Eq. (20) is restricted to even or to odd integer values.

For the stability analysis, Eq. (11) provides a set of coupled algebraic equations that relate the functions $A_m(s)$ to integrals of the form

$$I_{j;k,l} = \int^s ds'\, A_j(s') \sin[k(\psi'_x - \psi_x) + l(\psi'_y - \psi_y)] \tag{21}$$

while Eq. (15) provides a second set of such equations, and these equations taken together can be solved (at any s for which $a(s)$, $b(s)$ are known) to express each individual A_j in terms of the integrals defined by Eq. (21). From Eq. (21), moreover, one finds that

$$C_{k,l}(s)\frac{d}{ds}\left[C_{k,l}(s)\frac{dI_{j;k,l}}{ds}\right] + I_{j;k,l} = -C_{k,l}(s)\,A_j, \tag{22a}$$

where

$$C_{k,l} \equiv [k/\beta_x + l/\beta_y]^{-1}. \tag{22b}$$

With the A_j obtainable (as just mentioned) in terms of the $I_{j';k,l}$, Eqs. (22a) constitute a set of coupled second order differential equations for the latter quantities, and numerical integrations through one period of the structure will provide the elements of the matrix that advances such quantities (and their first derivatives) through one period of the transport channel.

(iii) Computational Procedures:

Computational programs have been devised to perform the computations outlined above, for various modes of order up through $n = 6$. Computations of this nature for quite large values of n may not be of practical importance. In a realistic beam with a natural spread of individual particle wavelengths (as may result from a nonlinear space-charge force), it is very unlikely that fine-grained transverse density variations (large n) persist through several periods. Computational results of Sect. IIIa pertaining to focusing in a continuous (s independent) solenoid-focusing system indicate, moreover, that the most stringent stability conditions are those imposed by modes of order less than 6 or 8.

To summarize the procedure followed in examining the stability of any particular perturbation mode, one first specifies the type of periodic lattice one wishes to employ[9] and a value of beam intensity (e.g., Q—or the parameter Q'—cited in Ref. 8). By a convergent iterative procedure one then determines initial conditions (for a, b, and their first derivatives) that lead to periodic (matched) solutions of the envelope equations, and, with this solution obtained, the individual-particle tune σ is also obtainable (i.e., from solutions of the equations of motion for individual particles, or as $\sigma_x = \epsilon \int_0^{2L} ds/a^2$ etc). With this information available, the computations are then repeated to include (for various initial values of the $I_{j;k,l}$ and their first derivatives) integration of the differential equations for the integrals $I_{j;k,l}$. [Note that integration of these equations requires repeated evaluations of the relations that express the quantities A_j in terms of the $I_{j';k,l}$—as can be done by use of a matrix-inversion/simultaneous-equation-solver routine.] Such integrations yield the elements of the matrix that advances these integrals (and their first derivatives) through one period of the structure, and the eigenvalues λ (and eigenvectors, if desired) of such a matrix are then determined. The occurrence of any eigenvalue of magnitude greater than unity then is indicative of instability for the perturbation mode under consideration, and the magnitude of such an eigenvalue denotes the factor, per period, by which such a perturbation ultimately (in the linear regime) will be expected to grow.

IV. COMPUTATIONAL RESULTS

Based on the analysis of Sect. III, we have examined computationally the behavior of several types of modes—both for a periodically interrupted solenoid system (Fig. 1a) and for a periodic alternating-gradient quadrupole (FODO) transport channel (Fig. 1b), although with greater emphasis on the quadrupole systems.[10] It is convenient and efficient, in all such cases, to employ "scaled variables." Useful parameters for describing a particular situation are the phase advances σ_0 and σ (of individual-particle transverse oscillations per period of the structure, respectively for a zero intensity beam and for a beam of intensity characterized by the parameter Q'[8]), and (for a given lattice) the "tune depression" factor σ/σ_0 will serve as a useful index of beam intensity.

In addition to the magnitudes of the eigenvalues that characterize the behavior of a perturbation mode, their phase angles, Φ [defined, with an ambiguity of 360°, as $\tan^{-1}$ $(\mathrm{Im}\,\lambda/\mathrm{Re}\,\lambda)$ and evaluated so that $-180° < \Phi \leq 180°$] also are of interest. Thus, with eigenvalues occurring as complex-conjugate and as reciprocal pairs, the development of an instability indicated by an eigenvalue moving away from the unit circle in the complex plane can occur either (i) when eigenvalues become real, or (ii) when at least

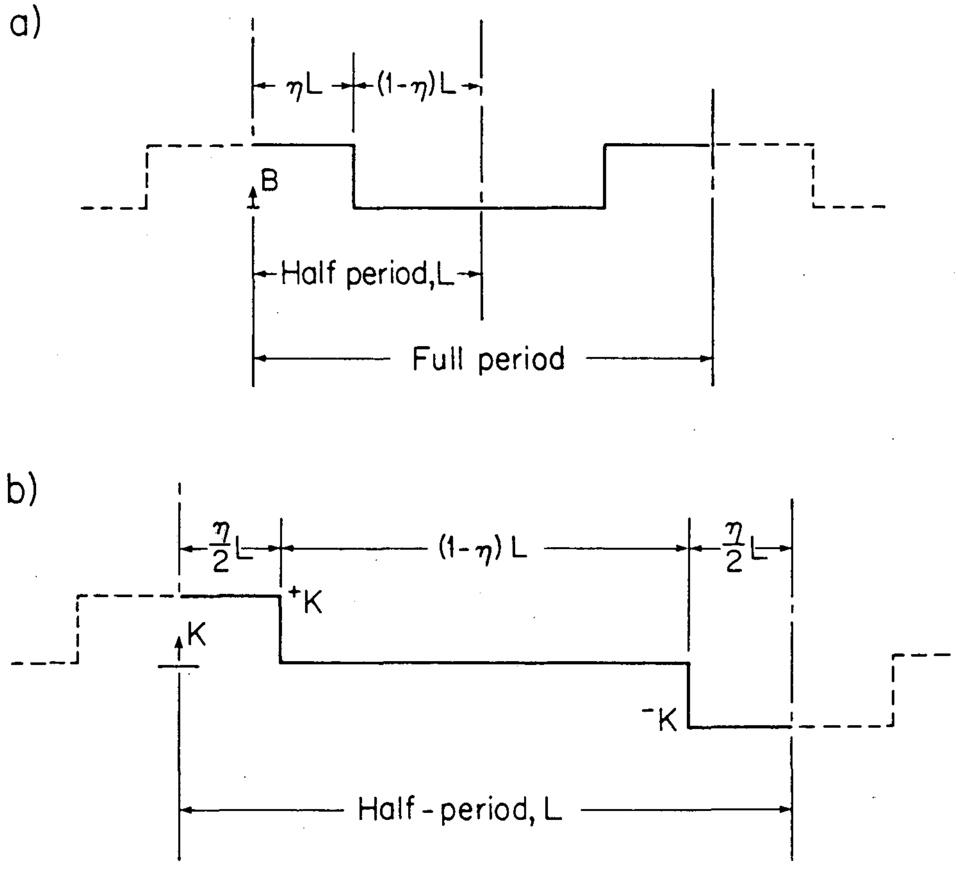

FIGURE 1. Assumed periodic transport lattice, (a) with interrupted solenoid elements and (b) with quadrupole lenses. η denotes the fraction of the lattice occupied by lens elements.

two pairs are present, as a result of a confluence having occurred at the threshold of instability. In the first of these cases (and if $\Phi \neq 0$), the mode frequency becomes locked to the period of the lattice ("inhomogenous" or "structure" resonance).

Results are best presented as regions of instability on a plot of σ vs. Q', since it has been found that the locations of these regions and the associated growth rates within them depend primarily on σ/σ_0 and are remarkably insensitive to changes of the lattice structure—particularly for instabilities that arise as a result of a confluence of eigenvalues.

(a) *Interrupted-solenoid focusing*

The solenoid modes we have studied can be classified in terms of indices corresponding to those introduced by Gluckstern.[6] We present specific results for symmetric interrupted solenoid systems with an occupancy factor of 1/2 ($\eta = 1/2$ in Fig. 1a).

(i) Envelope Modes:

$$j = 1, m = 0, \text{ with } V \propto r^2 \text{ and } \delta a_y = \delta a_x;$$
$$j = 0, m = 2, \text{ with } V \propto r^2 \sin 2\phi \text{ and } \delta a_y = -\delta a_x.$$

At zero intensity the true phases of the eigenvalues for these modes are $|\Phi| = 2\sigma_0$ and the phase will decrease as the intensity is increased. Accordingly, if $\sigma_0 > 90°$, there thus is the opportunity, with either type of mode, for an instability to develop at an intensity such that $|\Phi|$ becomes 180° (an example of a structure resonance). This behavior is illustrated by the curves of $|\Phi|$ vs. Q' on Fig. 2 for the case in which $\sigma_0 = 120°$, and by

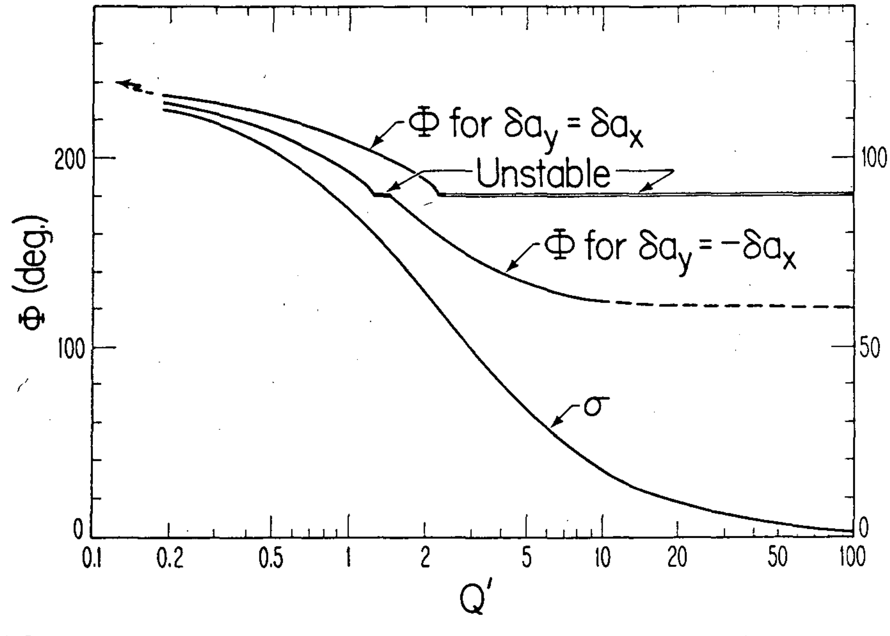

FIGURE 2. Behavior of envelope modes for an interrupted-solenoid system for which $\eta = 1/2$ and $\sigma_0 = 120°$, with regions of instability indicated by heavy lines on plots of Φ vs. Q'.

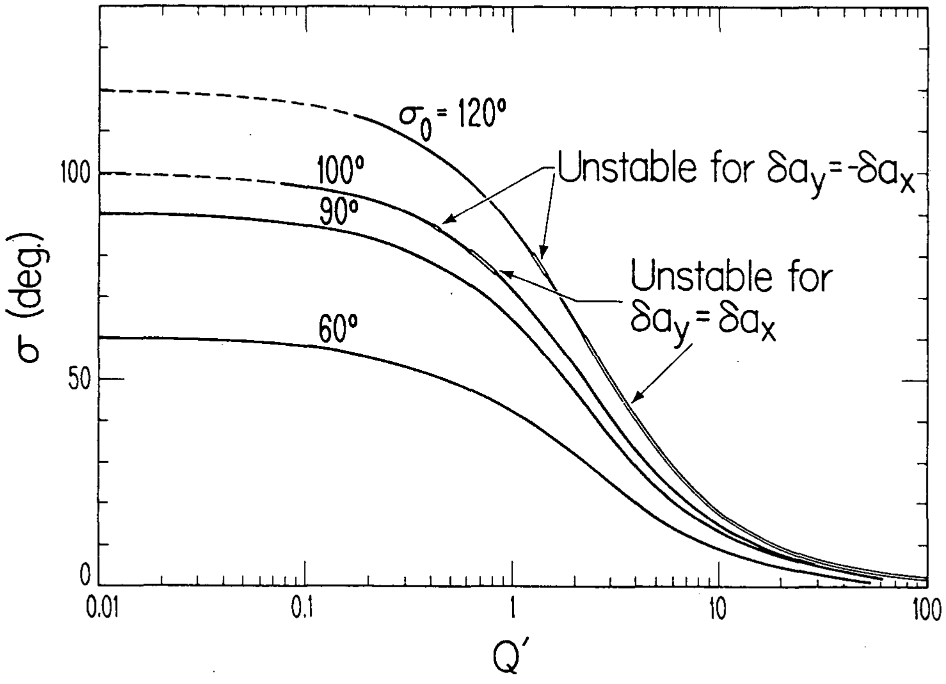

FIGURE 3. Behavior of envelope modes for interrupted-solenoid systems for which $\eta = 1/2$ and $\sigma_0 = 120°, 100°, 90°$, and 60°.

the regions of instability shown on the curves of σ vs. Q' in Fig. 3. From Fig. 3 it is seen that, as expected, the envelope instabilities occur only for $\sigma_0 > 90°$. The instability region for the $\delta a_y = \delta a_x$ mode becomes quite extensive, moreover, when σ_0 is as large as 120°.

(ii) "Fourth Order" and "Sixth Order" Modes:

$j = 2, m = 0$, with $V \propto r^4$ + terms of lower order;
$j = 3, m = 0$, with $V \propto r^6 + \ldots$.

As illustrated by Figs. 4 and 5, each of these modes exhibits minor patches of instability—which may not warrant concern. More significant are the extended regions of instability that are seen to develop for values of σ/σ_0 close to the values of ν/ν_0 shown in Table I for modes of 4th or 6th order respectively (and $m = 0$).

(iii) $R^4 \cos 2\phi$ and $R^4 \cos 4\phi$ Modes:

$j = 1, m = 2$, with $V \propto r^4 \cos 2\phi$ + terms of lower order;
$j = 0, m = 4$; with $V \propto r^4 \cos 4\phi$.

Examination of stability of these modes (choosing $\sigma_0 = 120°, 90°$, and 60°) indicates the occurrence only of short patches of instability—as are expected to become possible (for $\sigma_0 > 45°$) when eigenvalues with initial phase angles of $4\sigma_0$ (or $2\sigma_0$) cross the real axis as the intensity is increased, but that have been seen also to arise as a result of a

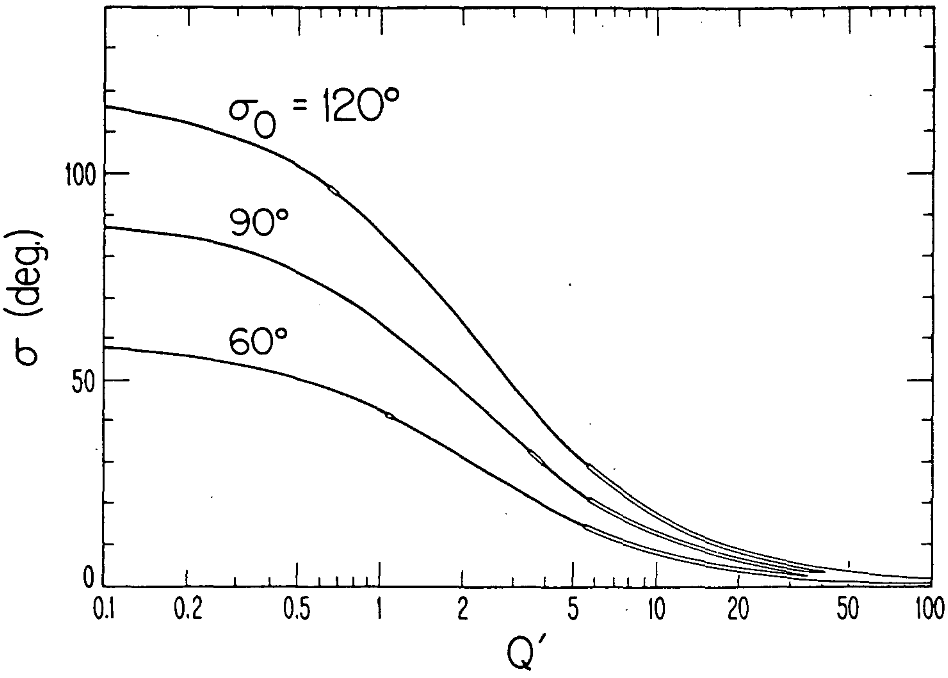

FIGURE 4. Behavior of fourth-order mode ($j = 2$, $m = 0$) for interrupted-solenoid systems for which $\eta = 1/2$ and $\sigma_0 = 120°, 90°$, and 60°.

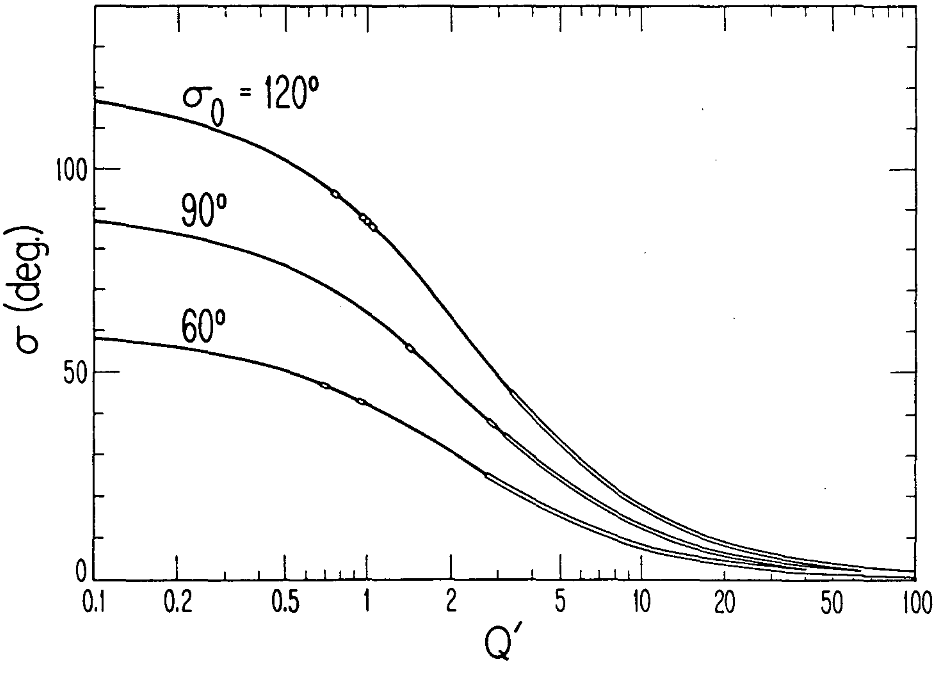

FIGURE 5. Behavior of sixth-order mode ($j = 3$ $m = 0$) for interrupted-solenoid systems for which $\eta = 1/2$ and $\sigma_0 = 120°, 90°$, and 60°.

TABLE I

Threshold Values of v/v_0

a) For Modes of Even Order				b) For Modes of Odd Order			
Order, $2j + m$ \ m	0	2	4	Order, $2j + m$ \ m	1	3	5
2	Stable	Stable	----	1	Stable	----	----
4	0.2425	Stable	Stable	3	Stable	Stable	----
6	0.3859	0.1741	Stable	5	Stable	Stable	Stable
8	0.3985	0.2582	0.1384	7	0.2874	0.2184	Stable
10	0.3972	0.2314^-	0.1396	9	0.3235	0.3124	0.2038
12	0.3921	0.1885	0.2940	11	0.3373^-	0.3246^+	0.2608
14	0.3861	0.1971^+	0.3205^-	13	0.3425	0.3148	0.2248
16	0.3798	0.1898^-	0.3263	15	0.3439^-	0.2968	0.2072
18	0.3728^-	0.2062^-		17	0.3432	0.2757	
20	0.3680	0.2305		19	0.3415		

confluence. No extensive regions of instability are found, however, and one notes that no instability of these modes is expected in a continuous solenoid (see Table I).

(*b*) *FODO quadrupole focusing*

We have investigated the behaviour of several modes, for different values of the occupancy factor η, in the symmetrical lattice of Fig. 1b. It is noticeable that for quadrupole focusing the instabilities of a given order become more numerous than those found for the $m = 0$ solenoid modes. This occurs because, for example, the solenoid modes ($j = 3$, $m = 0$), ($j = 2$, $m = 2$), ($j = 1$, $m = 4$), and ($j = 0$, $m = 6$) are all contained in the sixth order quadrupole case, but extended regions of instability appear in close analogy to the solenoid case. It appears, however, that the onset of regions of pronounced instability can be associated either with a definite value of eigenvector phase Φ (as in the case of the envelope instability) or with a value of σ/σ_0 that depends only slightly on the occupancy factor (η) of the lattice and on the value of σ_0, so that specific results will be cited here chiefly for $\eta = 1/2$ (Fig. 1b). We first present results for modes of even order.

(i) Envelope ("Second-Order Even") Mode:

As was found to be the case for the envelope modes in an interrupted solenoid transport system (Sect. IV, a, i), we find that envelope instabilities in a FODO focusing structure occur only if $\sigma_0 > 90°$. This behavior is illustrated in Fig. 6 for $\eta = 1/2$, wherefrom it is evident that very extensive regions of instability for this mode develop when σ_0 is substantially greater than 90°.

(ii) Second-Order Odd Mode:

The second-order odd mode will not lead to instabilities in a symmetrical FODO structure if (as is customary) $\sigma_0 < 180°$.

(iii) Fourth-Order Even Mode:

Computations pertaining to the fourth-order even mode (requiring evaluation of the eigenvalues of a 14×14 matrix) indicate the appearance of a substantial number of

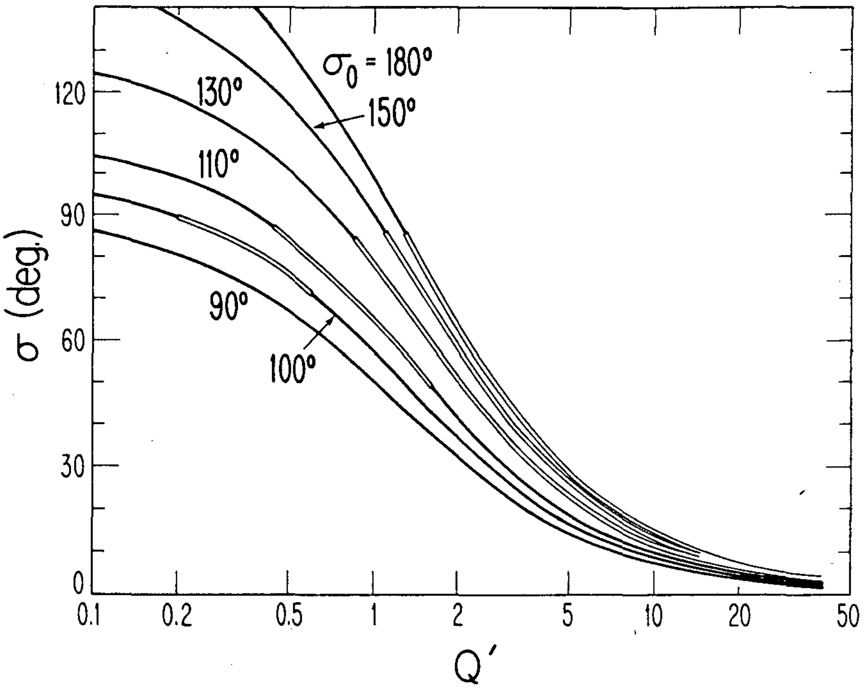

FIGURE 6. Behavior of envelope mode for quadrupole systems with $\eta = 1/2$ and $\sigma_0 = 180°, 150°, 130°, 110°, 100°$, and 90°.

regions of instability that are of somewhat limited extent (Fig. 7). [In Fig. 7, or in similar graphs, regions of very restricted instability may not always be fully depicted.] For $\sigma_0 < 90°$ [as appears desirable in order to avoid potential envelope instabilities (Sub-sect i)], however, the most substantial instability is that which on Fig. 7 is shown to occur for $Q' \gtrsim 3$. The particular unstable fourth-order mode just mentioned is one in which the eigenvalue λ has assumed a real (positive) value.

This significant extended instability of a fourth-order even mode provides an opportunity to illustrate that the threshold for such a mode is given almost uniquely by σ/σ_0 (Table II) and that such a threshold value of σ/σ_0 is surprisingly close to a corresponding threshold value of ν/ν_0 for a continuous solenoid (namely, in this instance, to the value 0.2425 shown in Table I for the mode $j = 2, m = 0$, for which the associated phase advance also is zero).

(iv) Sixth-Order Even Mode:

As with the fourth-order even mode, the sixth-order even mode exhibits a substantial number of patches of instability and ultimately develops an extended instability when the tune depression is sufficiently great (Fig. 8). As was found for the fourth-order even instability, the onset of this extended instability is given almost uniquely by σ/σ_0. The threshold value of σ/σ_0 for this mode again is close to a threshold value of ν/ν_0 for a continuous solenoid—specifically to the value 0.3859 shown in Table I for $j = 3$,

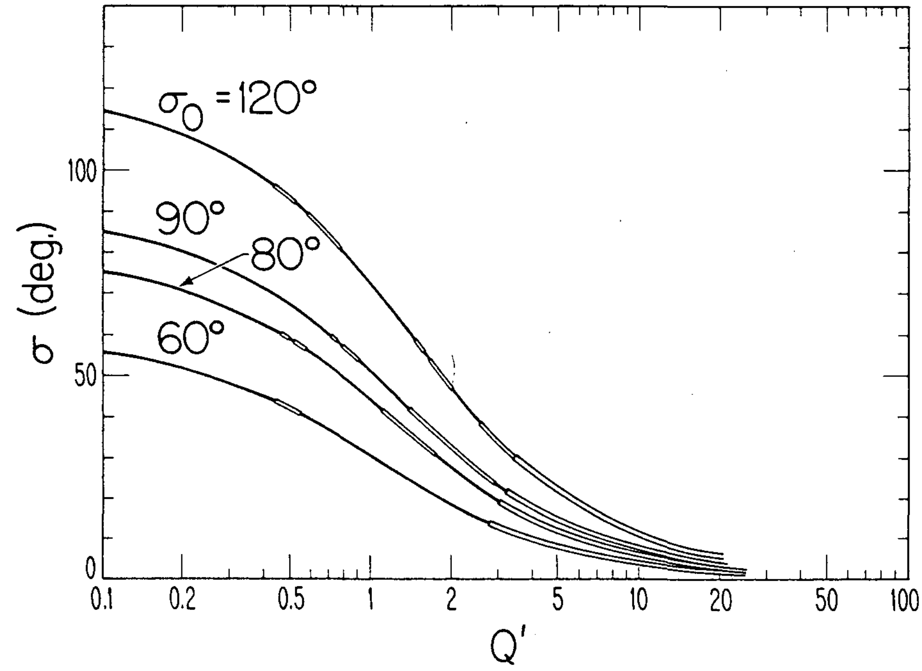

FIGURE 7. Behavior of fourth-order even mode for quadrupole systems with $\eta = 1/2$ and $\sigma_0 = 120°$, 90°, 80°, and 60°.

TABLE II
Instability Thresholds for Extended 4th Order Even Mode

Occupancy Factor	For $\sigma_0 = 60°$			For $\sigma_0 = 90°$		
η	Q'	σ(deg.)	σ/σ_0	Q'	σ(deg.)	σ/σ
1	3.055	14.58	0.2430	3.713	22.03	0.2448
1/2	2.572	14.58	0.2430	3.130	22.03	0.2448
1/4	1.925	14.58	0.2430	2.347	22.02	0.2447
1/6	1.598	14.58	0.2430	1.950	22.02	0.2447

$m = 0$. [It is of interest to note that the maximum threshold value of v/v_0 shown in Table I for $m = 0$ modes is not markedly greater than the value cited here, namely the value 0.3985 for $j = 4$, vs. 0.3859 for $j = 3$.]

(v) Third-Order Modes:

The third-order mode shows regions of pronounced instability, that appear to account for simulation results presented in the following Section (Sect. V). Because the quadrupole lenses were taken to be very short in the simulation work, we present our results for cases in which $\eta = 1/6$ or $\eta = 1/10$.

The instabilities are shown in Fig. 9 for a FODO lattice with $\sigma_0 = 90°$ and $\eta = 1/10$. The small region of instability shown on Fig. 9 as originating at $\sigma \simeq 57.3°$ and

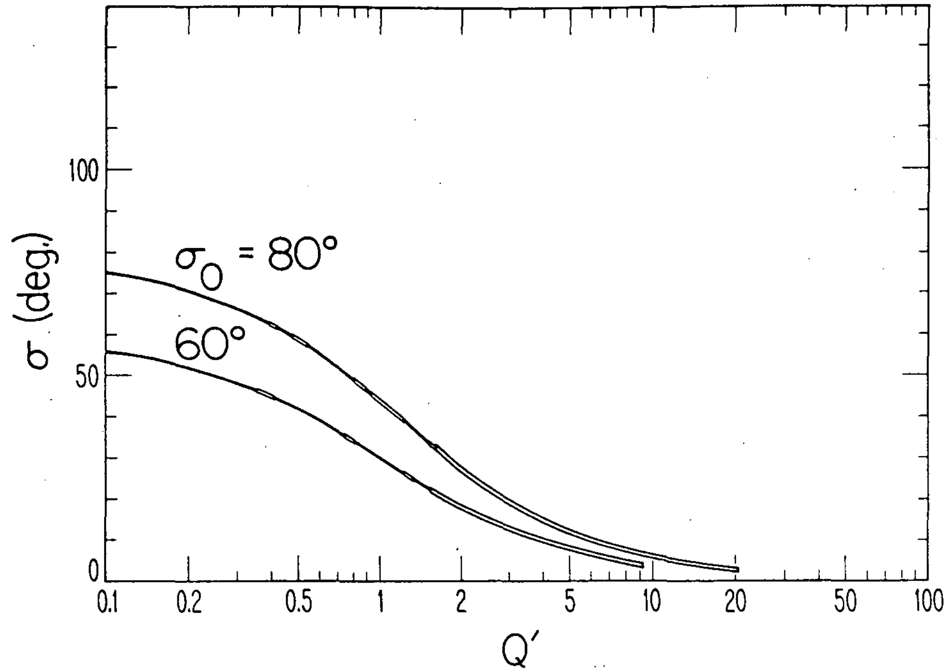

FIGURE 8. Behavior of sixth-order even mode for quadrupole systems with $\eta = 1/2$ and $\sigma_0 = 80°$ and $60°$.

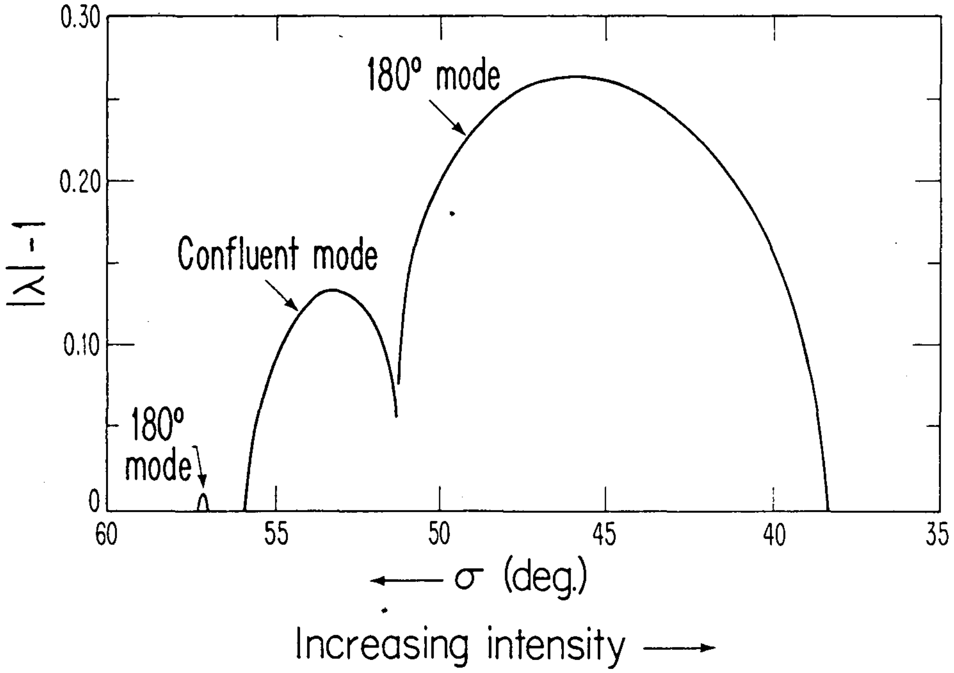

FIGURE 9. Behavior of third-order mode for a quadrupole system with $\eta = 1/10$ and $\sigma_0 = 90°$.

the major instability centered near $\sigma = 45°$ are attributable to eigenvalue phases having been depressed from $\Phi_0 = 3\sigma_0 = 270°$ to become 180°, thus indicating a structure resonance, while the instability that originates for $\sigma \simeq 56°$ arises from a confluence of eigenvalues. With $|\lambda|$ seen to become as large as approximately 1.27, it is of interest to examine the possibility of avoiding such a strong instability. The "180-degree" modes may be avoided by use of a lattice for which $\sigma_0 \leq 60°$, and it appears also that no confluent third-order mode then will occur (Fig. 10). We remark in passing that in an interrupted-solenoid focusing system we also have found[11] (Fig. 11) unstable 180-degree modes similar to those shown in Fig. 9 for the FODO quadrupole transport system.

(vi) Fifth-Order Mode:

Our computations pertaining to the fifth-order mode did not indicate any substantial instabilities that would account for the simulation results. We find that a quadrupole lattice with $\sigma_0 = 60°$ exhibits only moderate patches of instability for the fifth-order mode until the tune has been markedly depressed to $\sigma \simeq 10°$ (Fig. 12).

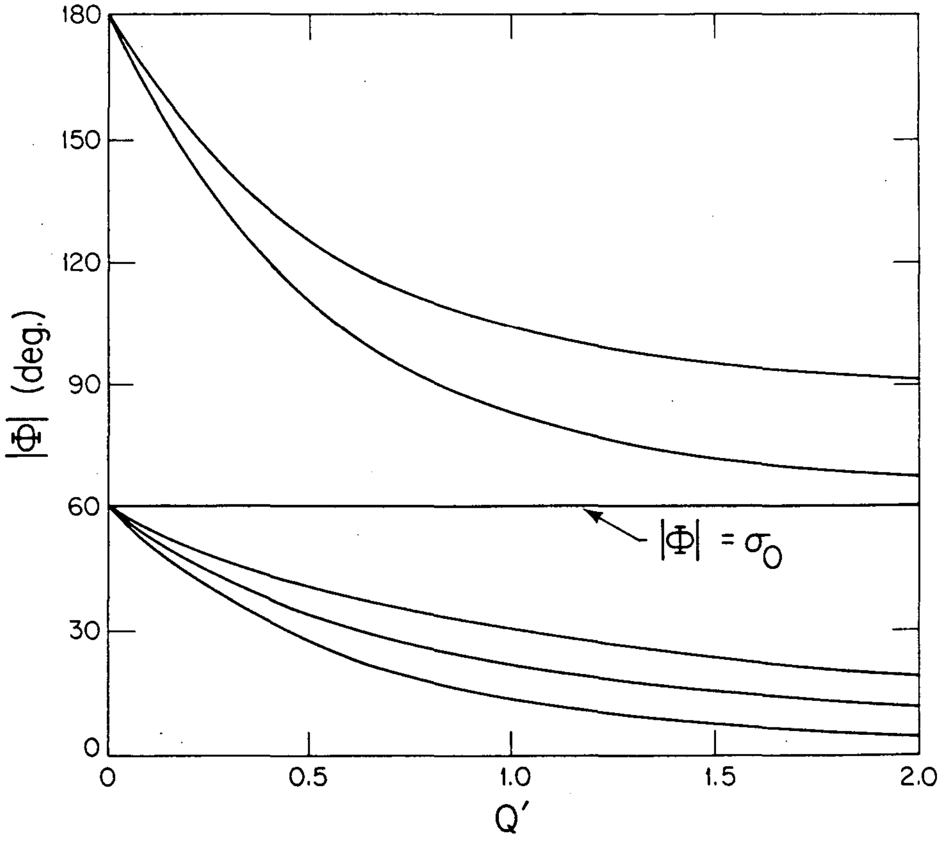

FIGURE 10. Depression of eigenvalue phase, $|\Phi|$, for third-order modes of a quadrupole system with $\eta = 1/6$, and $\sigma_0 = 60°$.

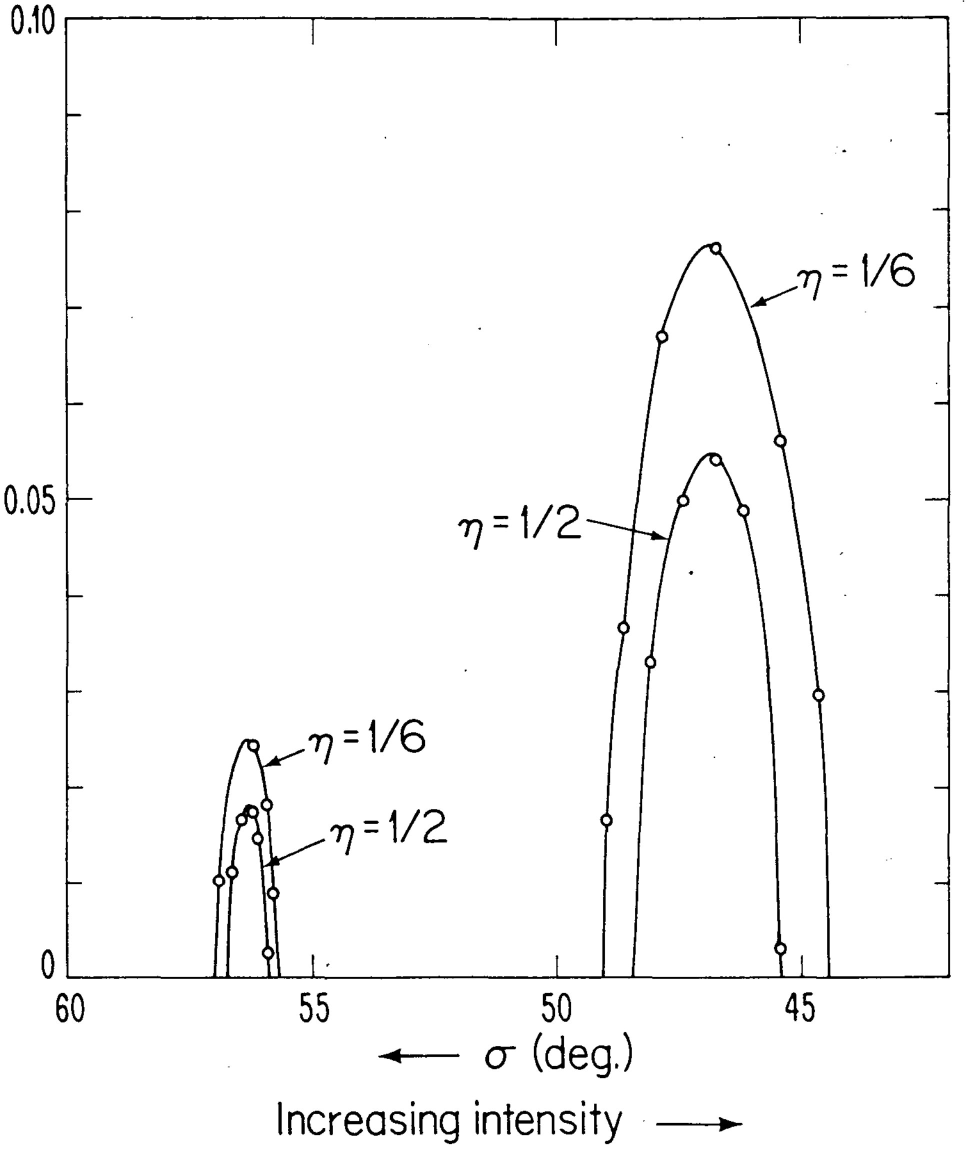

FIGURE 11. Behavior of third-order mode for interrupted-solenoid systems for which $\eta = 1/2$ or $\eta = 1/6$ and $\sigma_0 = 90°$.

V. COMPARISON WITH SIMULATION RESULTS

Computer simulation provides a possibility of testing the results obtained from analytic theory (and vice versa). The simulation programs used here are based on the particle-in-cell method; they employ typically of the order of 10^4 simulation particles and solve Poisson's equation with a fast Poisson solver. Results obtained from different

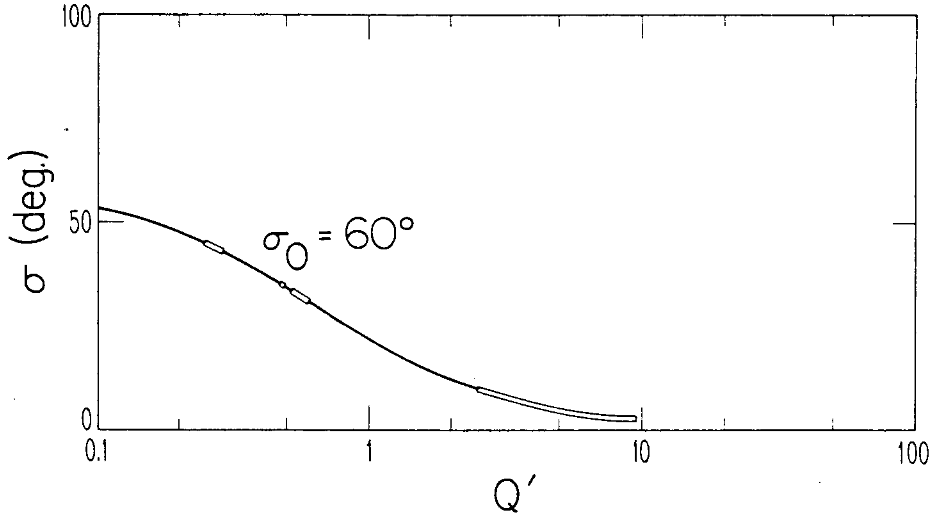

FIGURE 12. Behavior of fifth-order even mode for a quadrupole system with $\eta = 1/6$ and $\sigma_0 = 60°$.

simulation programs developed independently[12–18] have been found to yield essentially the same conclusions (apart from variations due to different statistical sets for the initial distribution).

Simulation not only allows the study of the initial growth of an instability within the validity of the linearized theory [section V (a)]; it also provides information on the nonlinear saturation of an instability and its effect on beam quality (for instance the r.m.s. emittance). In section V (b) it will be seen that large linear growth rates do not necessarily induce deterioration of beam quality.

(*a*) *Growth of third-order mode within the linearized theory*

The theoretical results obtained for the third-order even mode strongly suggested that this mode could account for the strong instability observed in simulation computations[15] (see also following section) with a K-V beam whose tune is depressed from $\sigma_0 = 90°$ to $\sigma \simeq 45°$. The expected strong instability is characterized by an eigenvalue that is real, but negative—a feature indicated by the simulation results, wherein distortions of projected phase-space distributions (and their boundaries) were observed to oscillate with respect to the origin with a period twice that of the structure, while the centroid of the distribution remained essentially undisturbed. A quantitative check of the correspondence between theory and the simulation work accordingly was undertaken in order to establish the validity of each of these approaches. We compared both the relative magnitudes of various moments of the distribution (e.g., $\langle xp_x{}^2\rangle_{av.}$, etc.) and the shape of the evolving distortion of projections of the distribution (e.g., for a projection onto the p_y, y plane). Such comparisons were undertaken both at "full-period" points (i.e., at the centers of F-quadrupole lenses) and at "half-period" points (centers of D lenses).

In making such a comparison it will be realized that the growing perturbation will be characterized by an arbitrary initial amplitude and phase, so that "x-like" (even) moments ($\langle x^3\rangle_{av.}$, $\langle xy^2\rangle_{av.}$, etc.) may be intercompared at full-period points but separately from "y-like" (odd) moments ($\langle y^3\rangle_{av.}$, $\langle x^2y\rangle_{av.}$, etc.). The growing magnitudes of x-like moments at half-period points in a symmetrical FODO lattice may be compared, however, with the growth of y-like moments at full-period points. All such moments, of course, should grow in magnitude in proportion to $|\lambda|^P$, where P denotes the number of periods traversed by the beam, and should alternate in sign once per period. Simulation data appropriate for evaluation will be restricted to an interval wherein the perturbation has grown sufficiently to dominate statistical noise, but has not become significantly influenced by the onset of (nonlinear) saturation. In practice, certain moments are more pronounced than others and the most pronounced moments accordingly are the most suitable for statistically significant intercomparison.

The theoretical description of a developing instability requires retention of terms beyond the leading term in the expression for the perturbation potential. Since the coefficients that determine the moments depend significantly on the value assigned to σ within the zone of instability, the trajectories of the individual simulation particles were examined to establish a value of $\sigma \simeq 45.7°$ (with an associated theoretical eigenvalue $\lambda \simeq -1.27$, for $\eta = 1/6$). The theoretical values of the coefficients required for the present comparison were then evaluated for these conditions.

(i) Comparison of moments

The growth and satisfactory intercomparison of x-like moments at full-period points is illustrated by Figs. 13–15, where we have used a value of $\lambda = -1.26$. Curves (a) are based on individual fits of the moments $\langle x^3\rangle_{av.}$, etc., to curves of the form $Y = S\lambda^{P-18}$, while curves (b) are drawn with the values of S for the respective moments constrained to be in the theoretically expected ratio. Figures 16–18 similarly indicate the behavior of three y-like moments at full-period points. Analogous plots (not shown) have indicated similar performance for moments evaluated at half-period points, and the values of the respective y-like or x-like moments moreover were found to be correctly related to the values of the corresponding x-like or y-like moments at the full-period points.

(ii) Comparison of boundary curves

We investigated the form of significantly distorted boundary curves for a two-dimensional projection of the simulation results arising from a perturbed four-dimensional phase-space distribution. Such simulation results are influenced by statistical fluctuations and may be sensitive to the development of nonlinearities in the dynamics. Comparisons with theory are most effectively made for the (p_x, x) or (p_y, y) projections and we have considered these both at full-period points and at half-period points, since fitting the boundary to the expected theoretical forms for such projections requires adjustment of only *one* coefficient, namely that giving the initial value of the perturbation. Empirically, the values of this coefficient found from such fits appear to be somewhat better characterized by a growth factor $\lambda \simeq -1.22$ than by $\lambda = -1.26$ (possibly because of an incipient nonlinearity), but the values inferred from data that pertain to periods near $P = 11$ have been found to agree within a few percent with those expected from examination of the moments. A fit to the (p_y, y) projection of the simulation results is shown in Fig. 19 for $P = 16$. Other projections (i.e., y vs. x and p_y vs. p_x) have also shown agreement between the computation and simulation results.

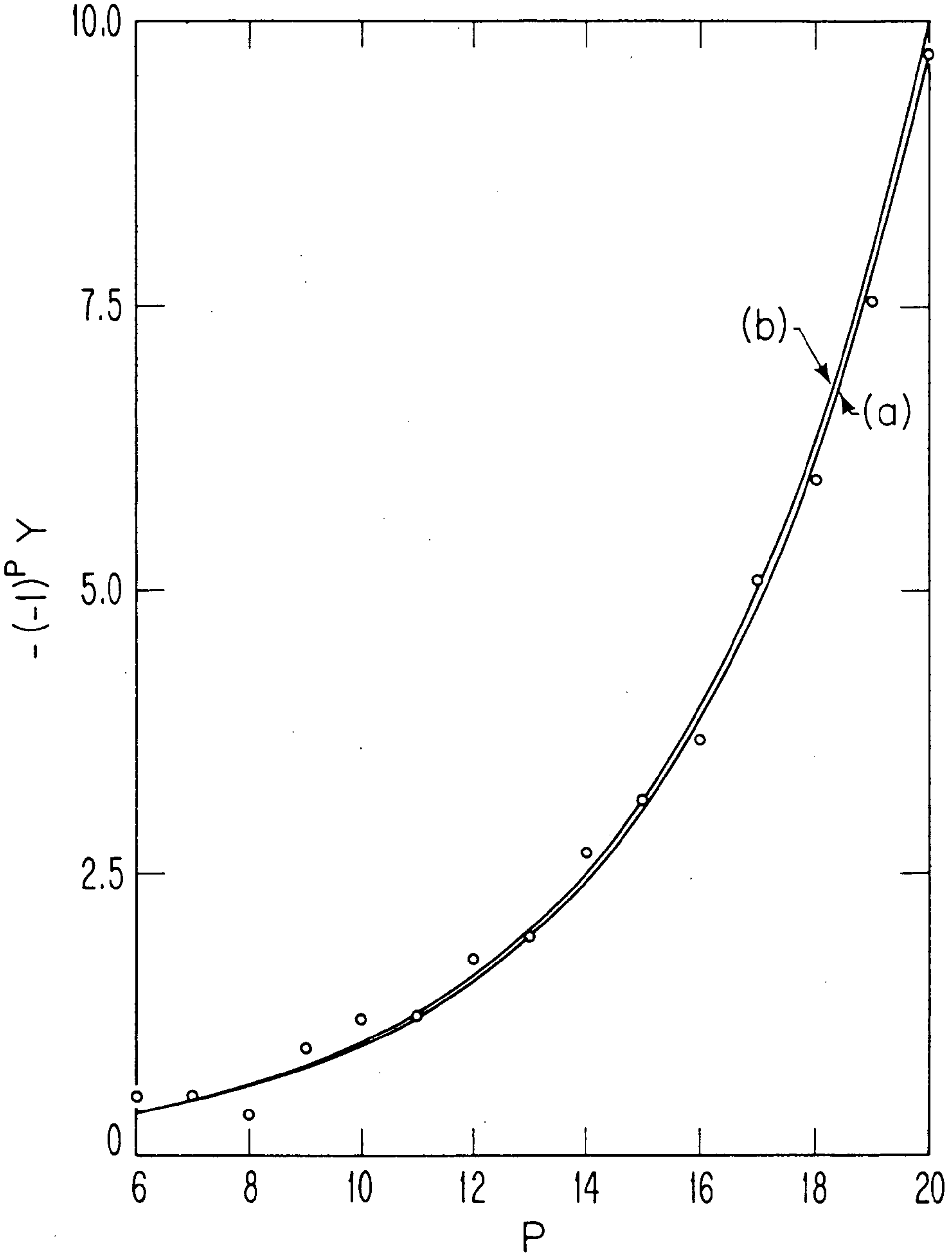

FIGURE 13. Growth of the moment $Y = \langle xp_x^2\rangle_{av.}$ at integer period numbers, from simulation computations. Curve (a) is based on a fit of this individual moment to the form $Y = S\lambda^{P-18}$, while the curve (b) is such that the values of S for this and other moments of the same type are constrained to be in the theoretically expected ratio.

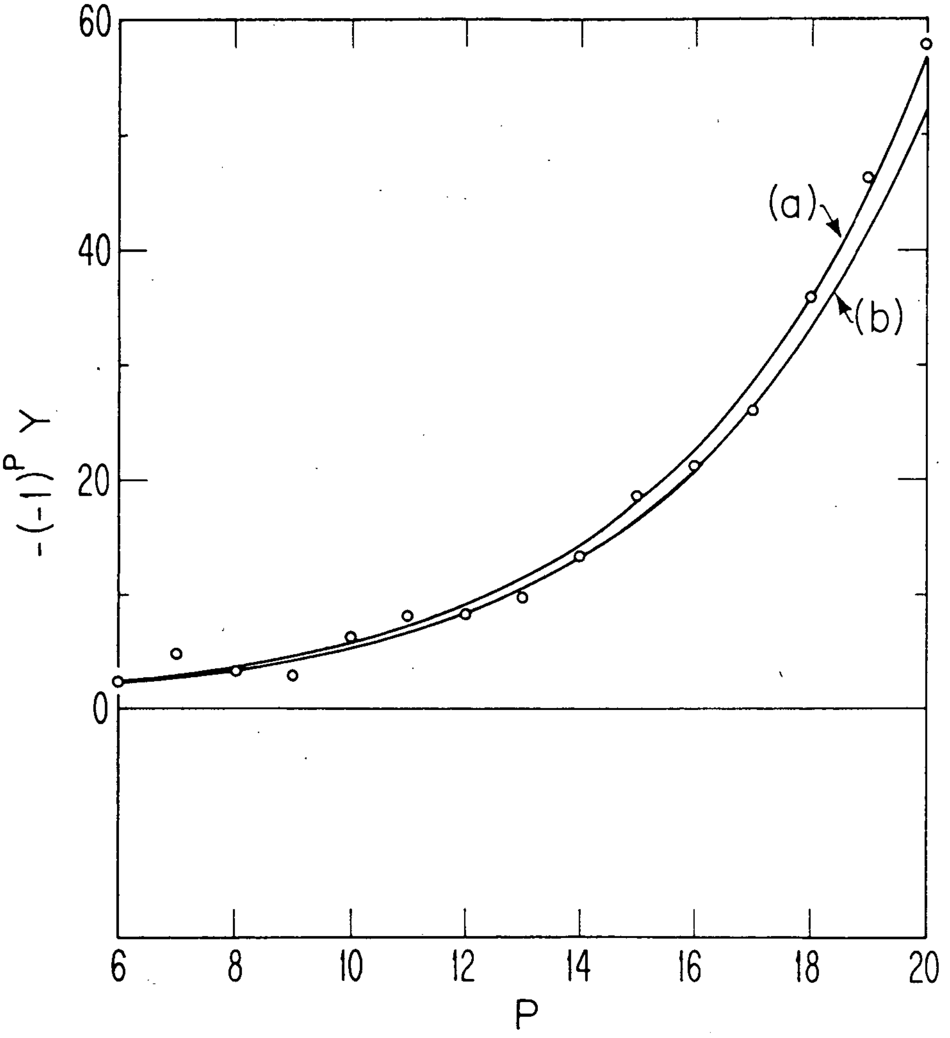

FIGURE 14. Growth of the moment $Y = \langle x^2 p_x \rangle_{av}$.

(b) Simulation of beams in long transport systems

The question of (nonlinear) saturation of an unstable mode is beyond the capabilities of a linearized theory and is most convincingly investigated by computer simulation. To this end, we present below characteristic examples which shed light on the continuous solenoid K-V instabilities and the "structure" resonances found in periodic focusing.

(i) Solenoid Focusing

The findings of Section III (a) have been checked by simulating an initial K-V distribution beam matched to a continuous solenoid focusing system. The intensity is

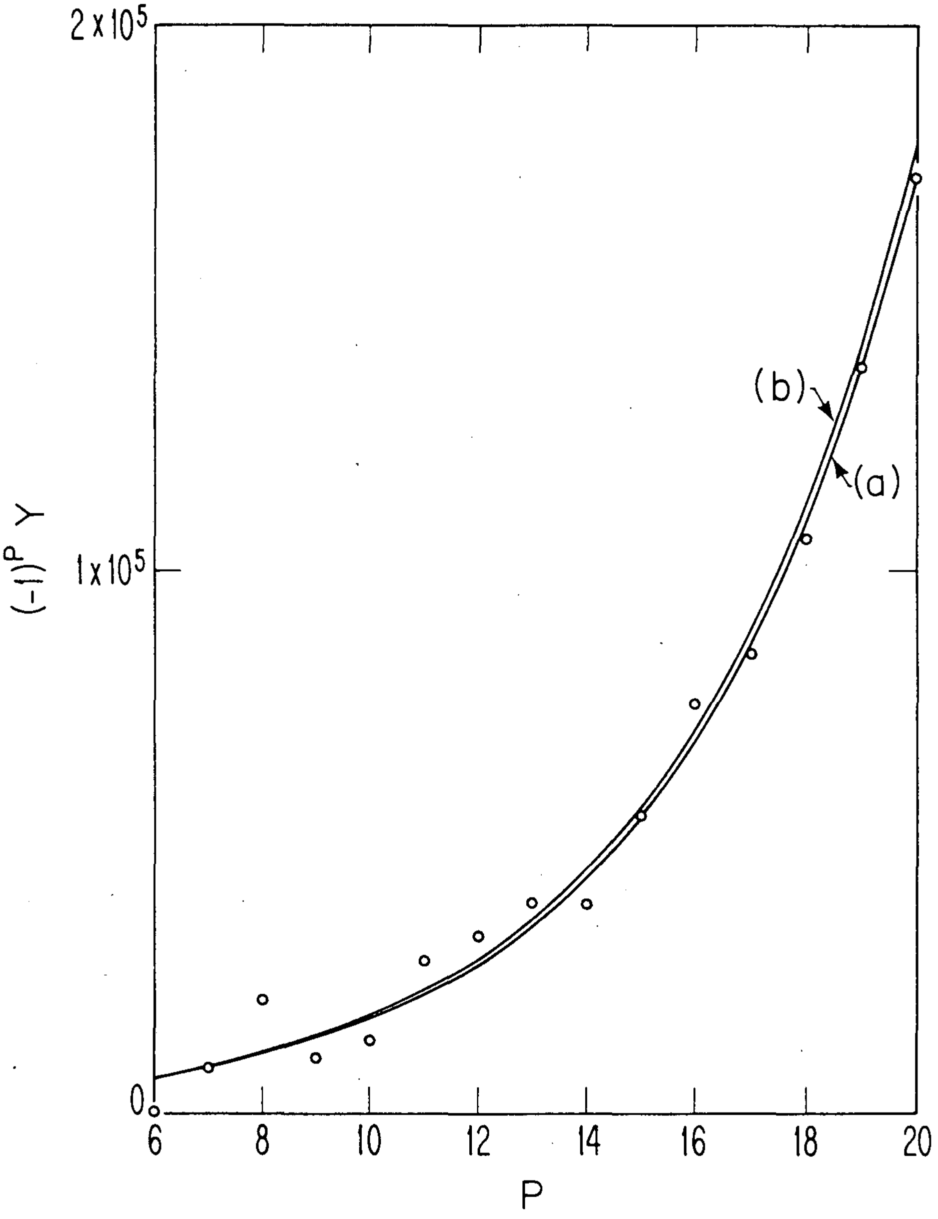

FIGURE 15. Growth of the moment $Y = \langle x^5 \rangle_{av}$.

described by the factor v/v_0, which is assumed to be 0.16 for the example shown in Fig. 20. Azimuthal symmetry has been imposed on the beam and hence all modes evaluated in the first column of Table I ($m = 0$) are expected to be unstable. There is evidence for rapid growth of instabilities of rather low order ($j = 2, 3$). The saturation of these instabilities leads to a different phase-space distribution, but evidently to no

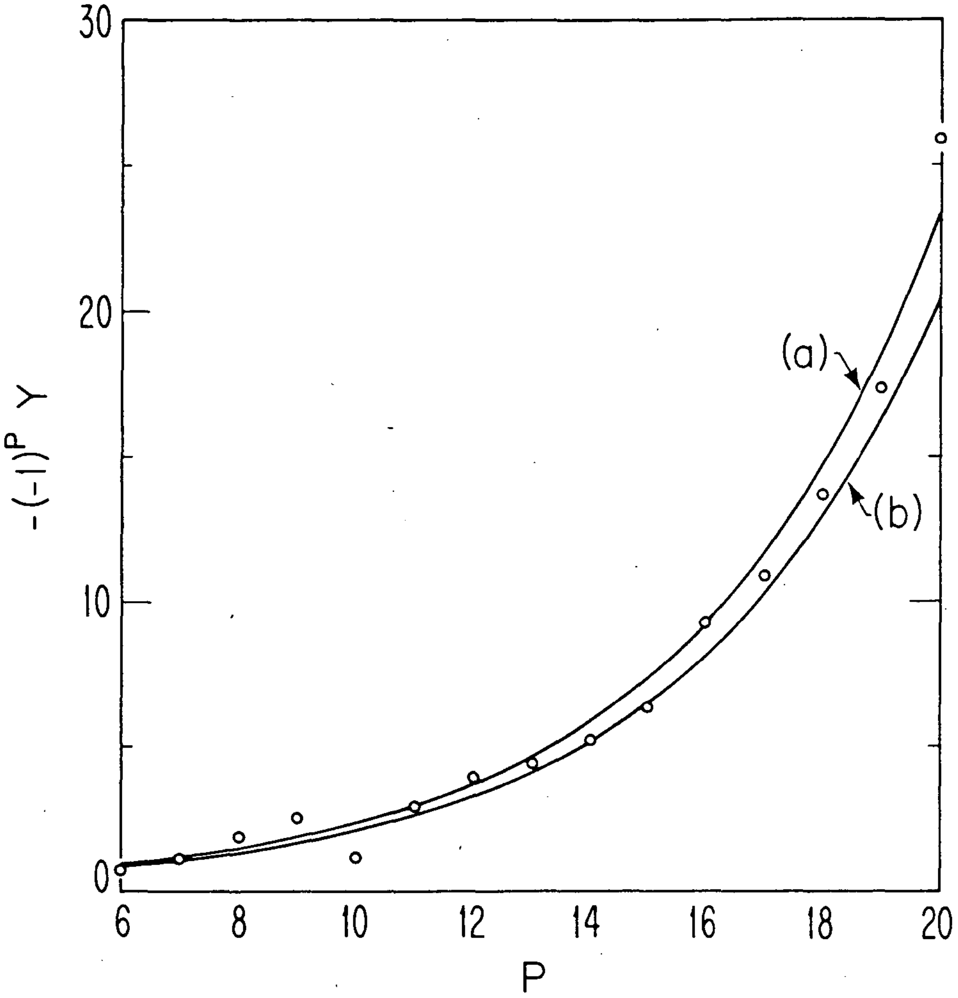

FIGURE 16. Growth of the moment $Y = \langle y p_y^2 \rangle_{av}$.

noticeable increase of phase-space volume. The r.m.s. emittance even remains constant within < 1%. This supports the conclusion that the K-V instabilities found for $\nu/\nu_0 < 0.39$ (similar in periodic focusing to $\sigma/\sigma_0 < 0.39$) have no effect on beam quality, but only emerge as a result of a non-monotonic distribution function.

(ii) FODO quadrupole focusing

In Fig. 21 we show an initial K-V distribution in a FODO channel with $\sigma_0 = 90°$ and $\sigma = 45.7°$. According to Section IV (b), this case is in the center of a third-order "structure" resonance, and projections onto the $x - p_x$ and $y - p_y$ planes clearly show the dominant character of this particular mode. The r.m.s. emittances have grown by a factor of 2.0 in $x - p_x$ and 2.5 in $y - p_y$ after 50 cells (with no further growth).

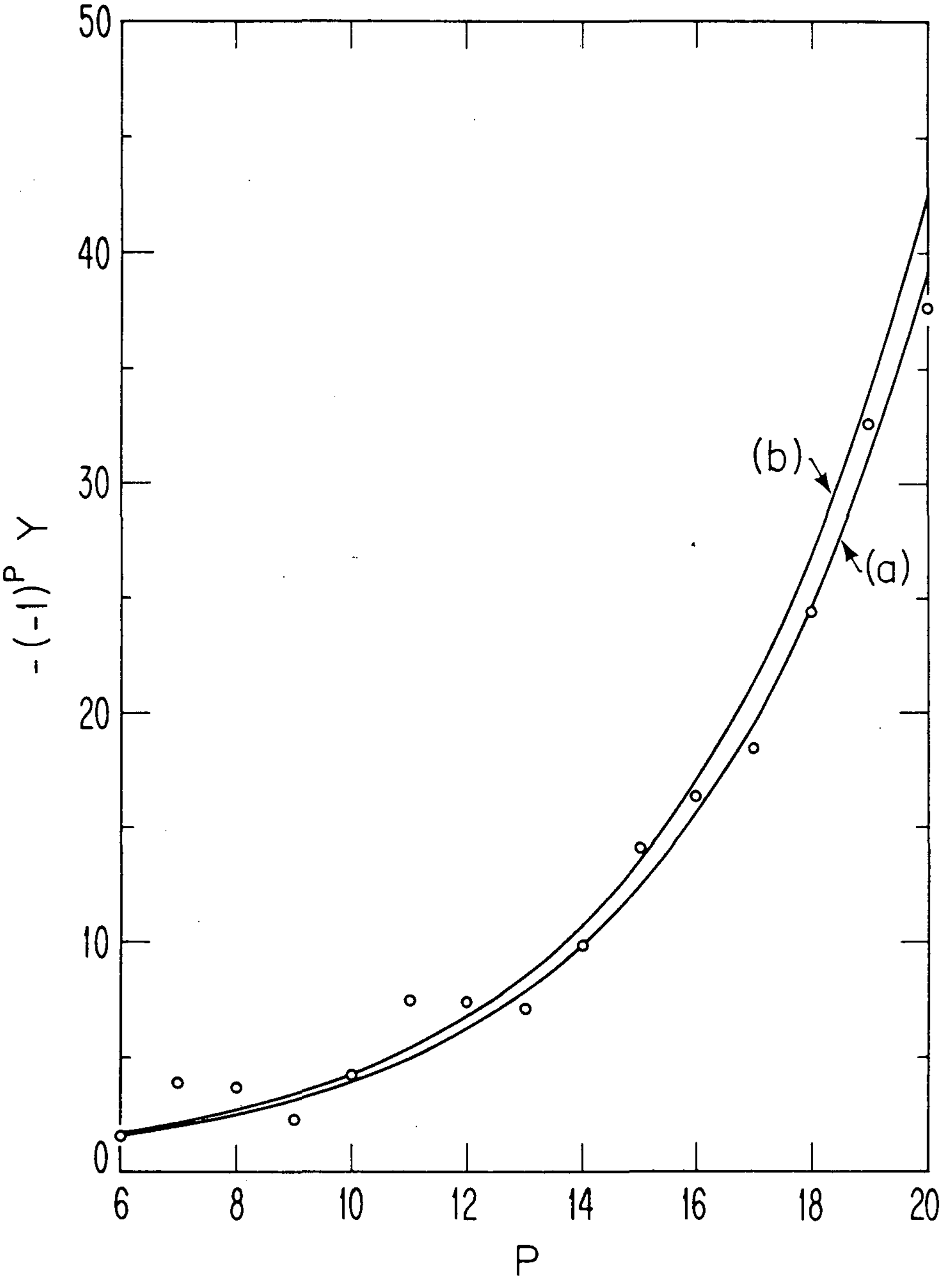

FIGURE 17. Growth of the moment $Y = \langle y^2 p_y \rangle_{av}$.

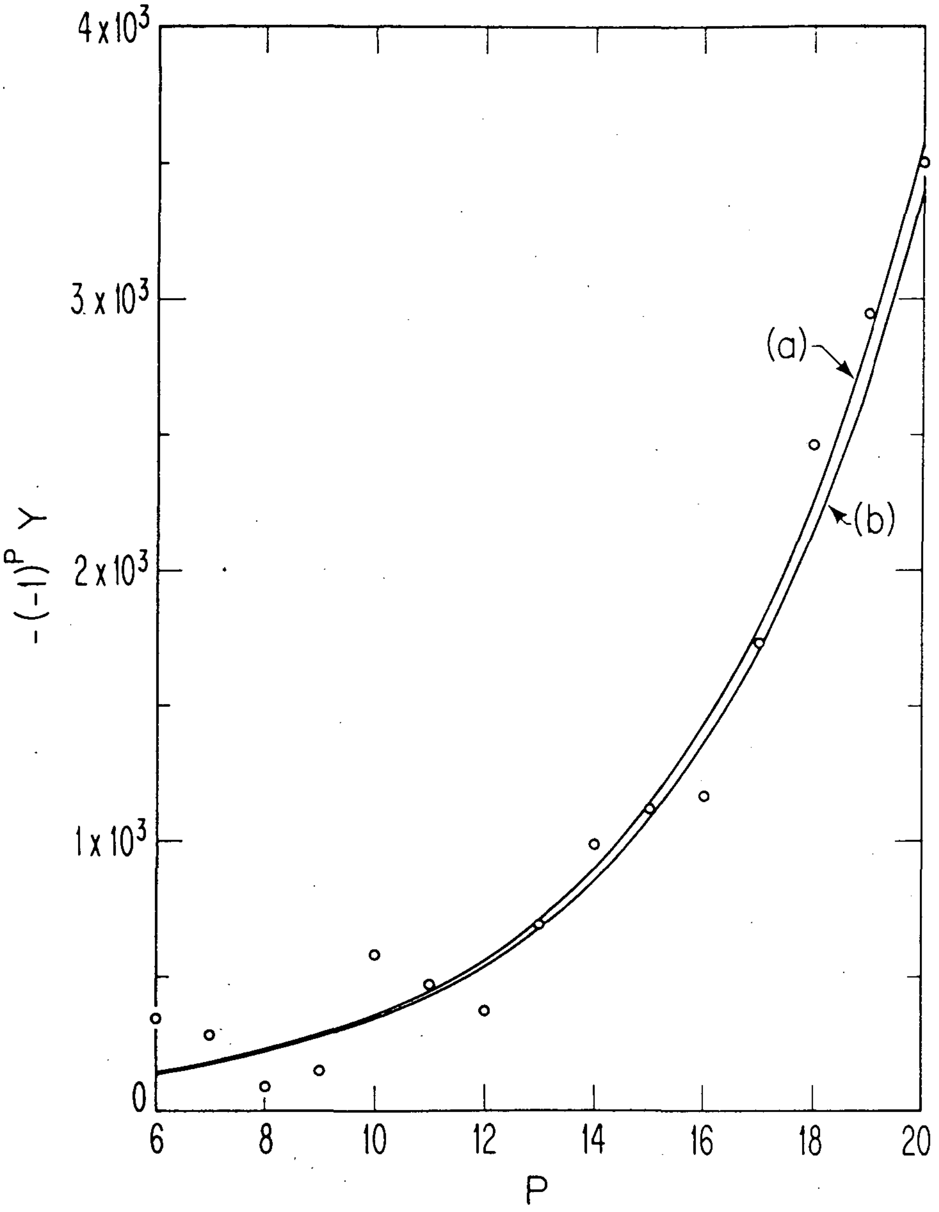

FIGURE 18. Growth of the moment $Y = \langle y^5 \rangle_{av}$.

The third-order "structure" resonance is evidently suppressed in a FODO channel with $\sigma_0 = 60°$. Furthermore simulations of such a 60° system exhibit a qualitative behavior resembling that of a continuous solenoid. Thus even for systems with strongly depressed tune (cases with σ as low as 6° have been simulated) the instabilities result in a rearranged phase-space distribution but saturate before any growth in the

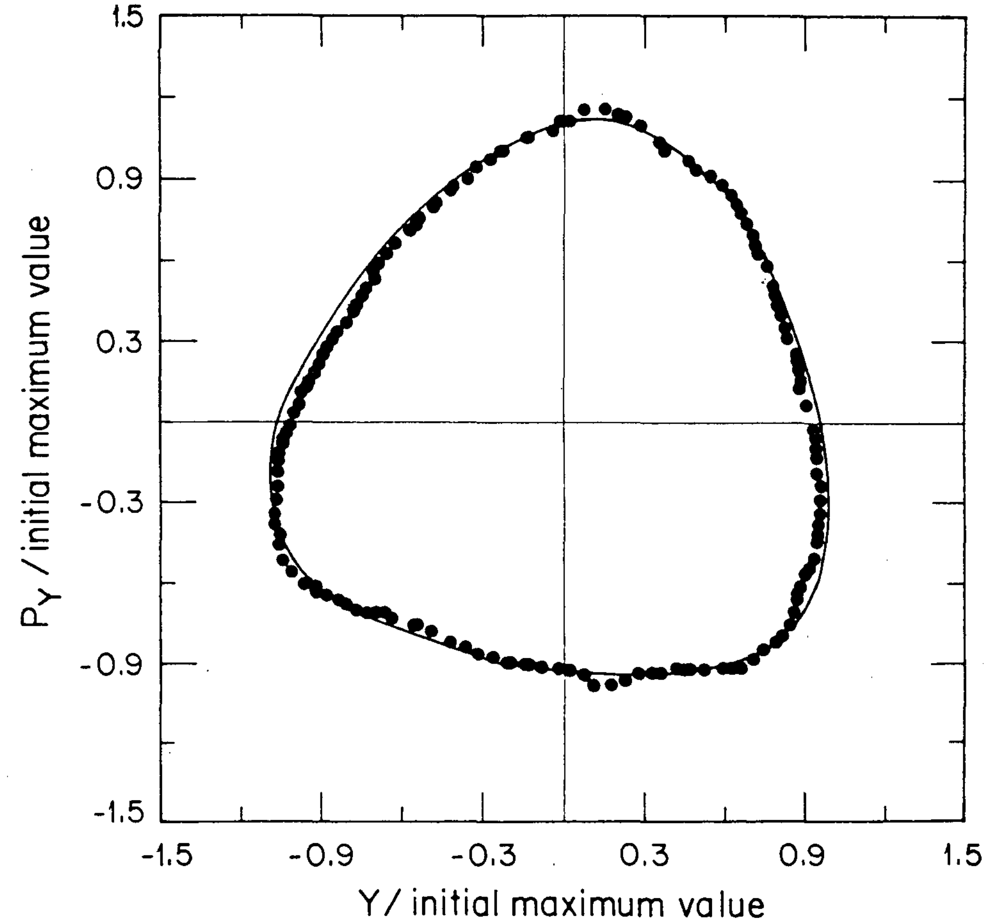

FIGURE 19. Boundary of p_y vs. y projection, at period number 16. The dots denote simulation results and the curve represents the theoretically expected boundary.

r.m.s. emittance is observed. These results suggest that although the system is unstable, in agreement with the analytic predictions, no restriction on allowable tune depression is imposed if r.m.s. emittance is a proper measure of beam quality.[19,20] This conclusion is illustrated in Fig. 22 with $\sigma = 12.7°$ and an initial "waterbag" distribution (in contrast to the K-V distribution it is assumed that the *interior* of a hyper-ellipsoid in four-dimensional phase-space is uniformly filled, which produces a more realistic beam). Initial matching has been performed by assuming the same r.m.s. quantities as would apply for an exactly matched K-V distribution. This gave rise to 10% r.m.s. emittance growth, due to lack of detailed matching, but no further emittance growth over 100 focusing periods.

Figures 23 and 24 demonstrate the importance of σ_0 in a more direct way. Figure 23 gives the ratio of r.m.s. emittance to initial emittance for a K-V distribution initially depressed from $\sigma_0 = 90°$ to $\sigma = 7°$. The emittance is seen to grow rapidly at first and then more slowly for the duration of the run. In Fig. 24 the tune is initially depressed from $\sigma_0 = 60°$ to $\sigma = 6°$; there is no detectable change in r.m.s. emittance.

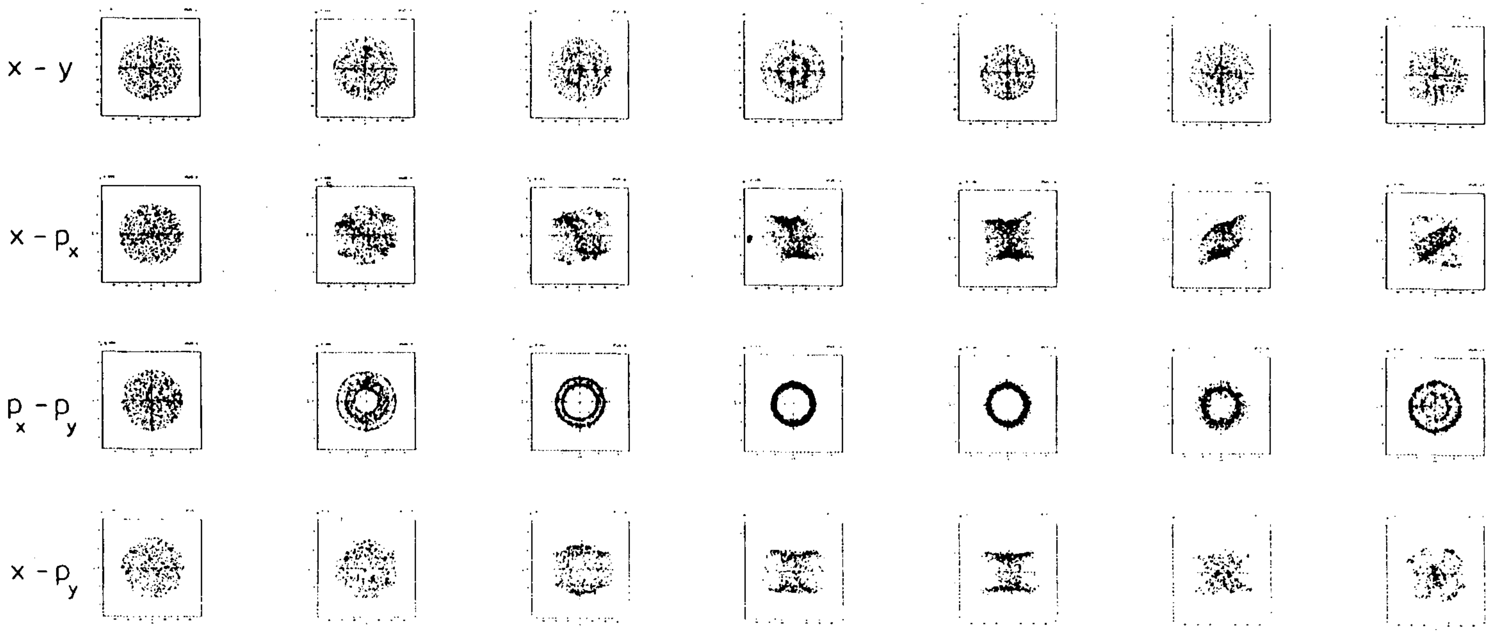

FIGURE 20. Phase space projections of initial K-V distribution in a continuous solenoid with $v/v_0 = 0.16$. The beam is assumed azimuthally symmetric with $1.3 \cdot 10^5$ simulation particles. Frames are in time steps of 1/10th of a betatron period.

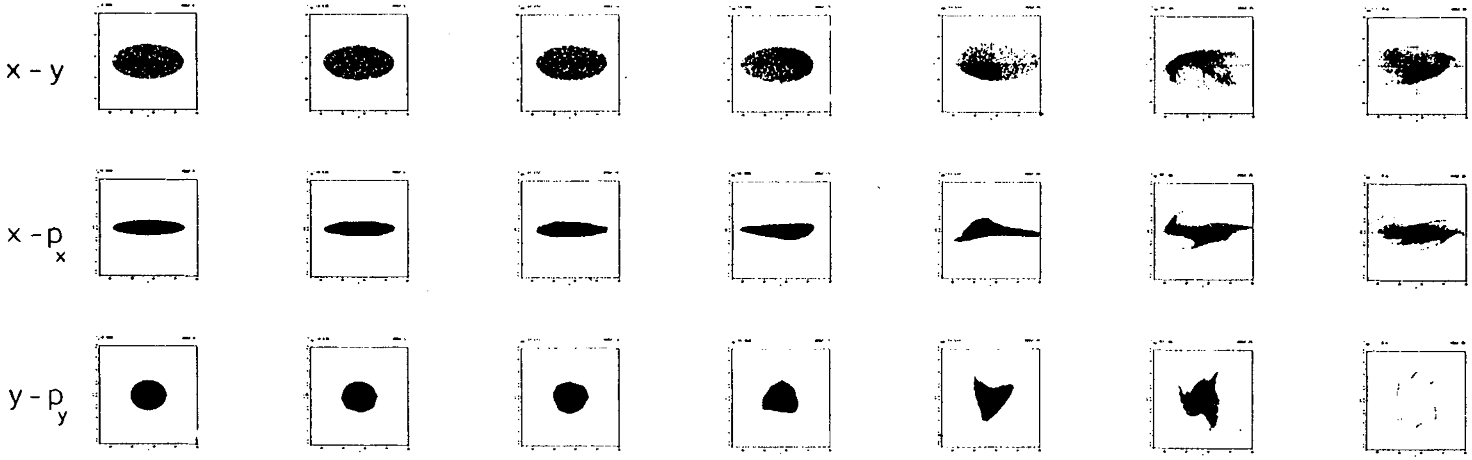

FIGURE 21. Intitial K-V distribution in a FODO channel with $\sigma_0 = 90°$, $\sigma = 45.7°$ and 8.10^3 simulation particles. Frames every 5th focusing period.

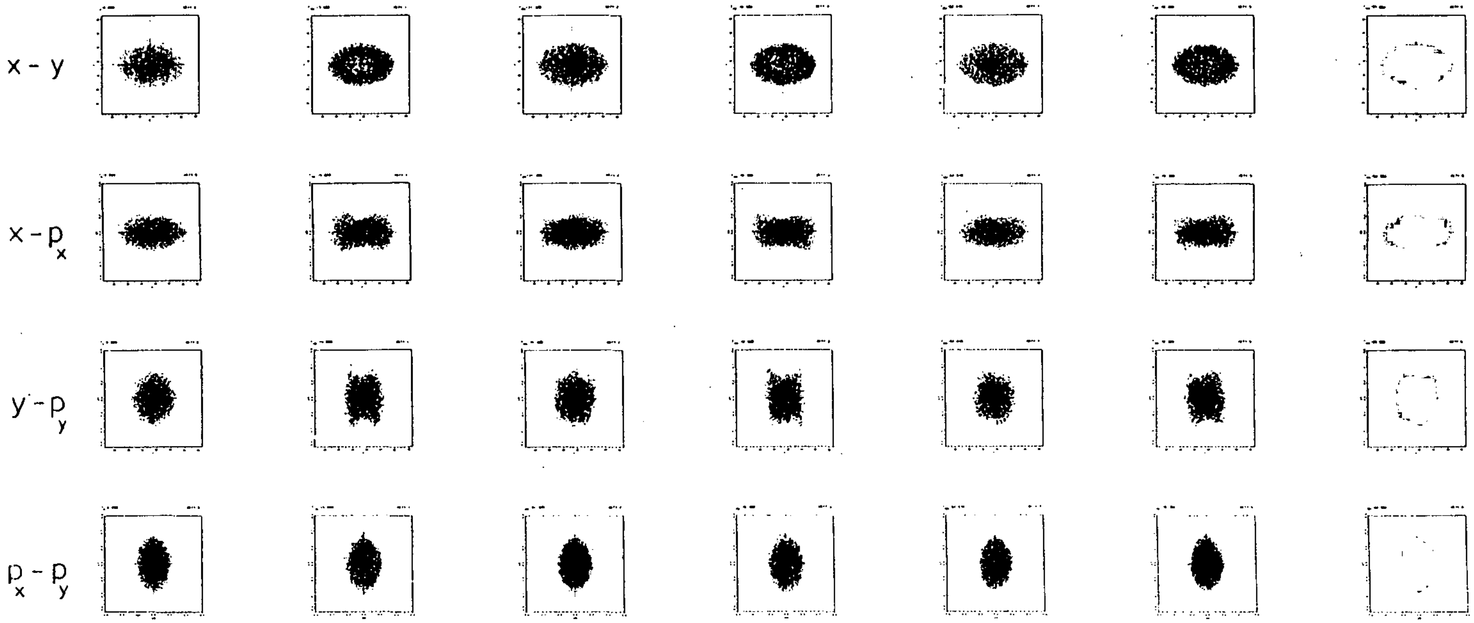

FIGURE 22. Initial "waterbag" distribution (r.m.s. matched) in a FODO channel with $\sigma_0 = 60°$, $\sigma = 12.7°$ and 8.10^3 simulation particles. Frames every 5th focusing period.

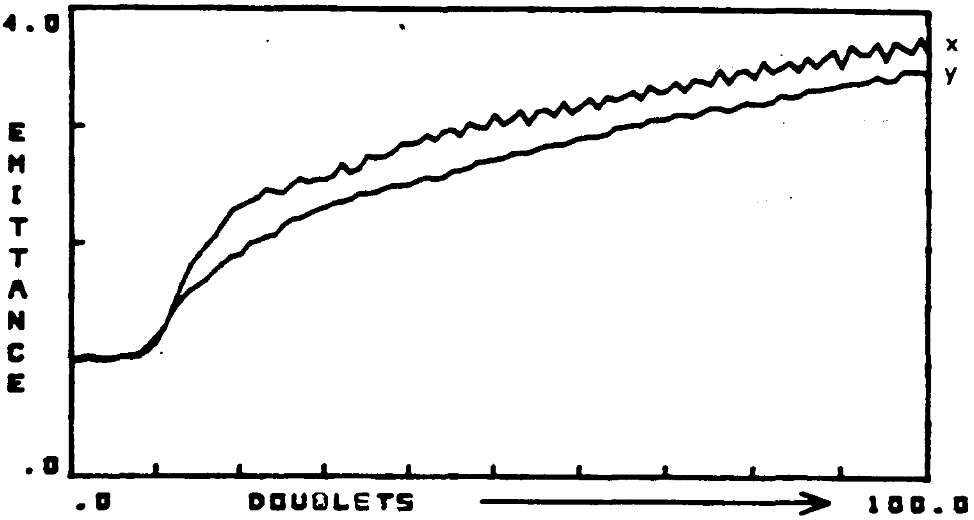

FIGURE 23. Ratio of r.m.s. emittance to its initial value for a K-V distribution with $\sigma_0 = 90°$ and $\sigma = 7°$.

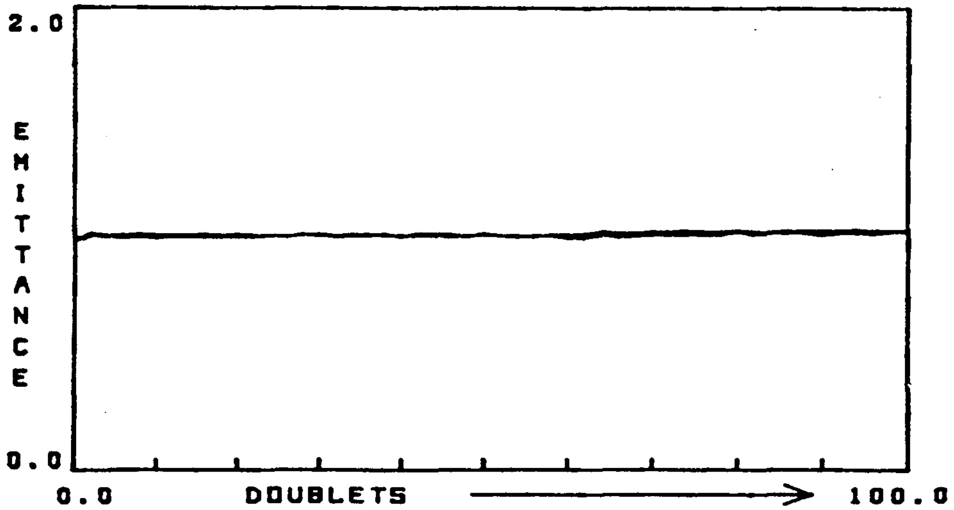

FIGURE 24. Ratio of r.m.s. emittance to its initial value for a K-V distribution with $\sigma_0 = 60°$ and $\sigma = 6°$.

VI. CONCLUSION

The special character of the microcanonical or K-V distribution assumed in the present work may lead to instabilities that would not arise with other, more realistic, distributions. Simulations[16] do, however, suggest that in regions where instability is strong (*i.e.*, lead to substantial growth in r.m.s. emittance) the behavior of non-KV systems does not differ substantially. Some insight into the physical mechanism causing instability for the K-V and other distributions can be obtained from a fluid model[13] and by invoking the concept of negative-energy waves. In particular, the extended regions of instability found for continuous solenoid focusing (which also occur for periodic focusing at the same threshold values in terms of tune depression) can be interpreted as coupling of positive and negative energy oscillations[14] and are a characteristic feature of a distribution function that is a non-monotonic function of the Hamiltonian. These instabilities cause a marked redistribution of density in phase space, but do not lead to a growth in r.m.s. emittance. For quadrupole transport, on the other hand, the strength of the focusing force seems to provide a mechanism which causes emittance growth for $\sigma_0 > 60°$; for smaller values of σ_0 the saturated state is very similar to that reached in the case of continuous focusing. If one disregards the minor patches of instability found analytically as peculiar to the K-V distribution, the results of the linear analysis seem to provide a valid guide for design of periodic transport systems for high intensity beams and are particularly significant for $\sigma_0 > 60°$.

In this spirit, it appears prudent not merely to require that $\sigma_0 < 90°$ (in order to avoid significant envelope instabilities), but to impose the restriction $\sigma_0 \leq 60°$ with the object of avoiding a pronounced instability of the third-order mode. If the restriction $\sigma_0 \leq 60°$ is adopted, one may expect that beam intensities will be limited only by potential instabilities of fourth or higher order and that significant instabilities of this nature will not occur for $\sigma/\sigma_0 \gtrless 0.4$ (see Sect. IV, b, iv, and Table I)—e.g., for $\sigma \gtrless 24°$ if $\sigma_0 = 60°$.

Simulation work indicates that, for $\sigma_0 \leq 60°$, the remaining instabilities saturate at low levels and the r.m.s. emittance is not affected by the rearrangement in phase space. If r.m.s. emittance is an adequate measure of beam quality there is then no limit on allowable tune depression. However, if the transported beam is to be delivered to a small focal spot, a practical limit then would be set ultimately by aberrations in the final focusing system.

The expected transportable intensities or beam power, based on a 60°–24° transport line and the associated maximum beam radii in symmetric FODO quadrupole transport systems are then given by the scaled-variable entries of Table III. The

TABLE III
Scaled-Variable Parameters
for a Tune Depression from $\sigma_0 = 60°$ to $\sigma = 24°$

Occupancy Factor	θ	Q'	u_0	[FM]
1	1.32	1.66	3.20	.764
2/3	1.42	1.54	3.34	.688
1/2	1.57	1.40	3.54	.601
1/3	1.84	1.19	3.87	.481
1/4	2.09	1.04	4.13	.405
1/5	2.32	.944	4.36	.354
1/6	2.52	.867	4.56	.315
1/8	2.89	.757	4.89	.263
1/10	3.22	.680	5.16	.228
1/20	4.51	.485	6.13	.145

quantities tabulated in Table III are

$$\theta = K^{1/2}\cdot L, \text{ where } L \text{ is the half-period of the lattice;}$$

$$Q' = \frac{4q^2}{A}\,\frac{Nr_p}{\beta^2\gamma^3\epsilon K^{1/2}}, \quad \text{where } \pi\epsilon \text{ is the (un-normalized) emittance in either plane (meter radians);}$$

$$u_0 = K^{1/4}\,\epsilon^{-1/2}\,a \text{ (maximum scaled beam radius); and}$$

$[\mathrm{FM}] \equiv Q'/u_0{}^{2/3}$ is a "figure of merit" that enters into a formula of the type proposed by Maschke[21] and analyzed by Reiser[22] for the maximum transportable beam current or power [Eq. (23)]. (The maximum beam radius becomes less if the intensity is reduced.)

$$\begin{aligned} P &= C_5\,(A/q)^{4/3}\,(\gamma - 1)\,(\beta\gamma)^{7/3}\,\epsilon^{2/3}\,B_Q{}^{2/3}.\,[\mathrm{FM}] \qquad (23)\\ &= C_5\,(A/q)^{4/3}\,(\gamma - 1)\,(\beta\gamma)^{5/3}\,\epsilon_N{}^{2/3}\,B_Q{}^{2/3}.\,[\mathrm{FM}], \end{aligned}$$

where

$$C_5 = (\pi/\mu_0)c^{-1/3}\,(M_{p,0}\,c^2/e)^{4/3} = 3.43 \times 10^{15} \text{ (MKSA units)},$$

$$\epsilon_N = \beta\gamma\epsilon \text{ (meter-radians)},$$

and B_Q is the quadrupole pole-tip field (Tesla).

The figure of merit [FM] in Table III increases as $\sigma^{-2/3}$ as σ is decreased from 24°, but the required aperture increases also and care must be taken in transporting very high currents that the aperture to length ratio of the quadrupoles does not become too large.[8,22]

ACKNOWLEDGMENTS

It is a pleasure to acknowledge our indebtedness to V.O. Brady, J. Bisognano, and S. Chattopadhyay for frequent helpful discussions and assistance during the course of this work.

REFERENCES AND NOTES

1. See, for example, R. L. Gluckstern, R. Chasman, and K. Crandall, *Proc. 1970 Natl. Accelerator Lab. Linear Accelerator Conf.* (M. R. Tracy, Ed), v. **2**, p. 823 (FNAL, Batavia, I11., 1970).
2. R. C. Davidson and N. A. Krall, *Phys. Fluids*, **13**, 1543 (1970).
3. I. M. Kapchinskij and V. V. Vladimirskij, *Proc. 1959 Internat. Conf. High Energy Accelerators*, p. 274 (CERN, Geneva, Switzerland, 1959).
4. E. D. Courant and H. S. Snyder, *Ann. Phys.* (NY), **3**, 1 (1958).
5. This boundary condition is consistent with that used to obtain the space-charge force constant commonly used in the envelope equations.[3] We have calculated the image forces produced by an elliptical beam co-axially situated within a circular tube, and find them to be remarkably linear and relatively small—even if the beam almost touches the wall of the tube. We accordingly conclude that the presence of a vacuum pipe may be neglected for the present purposes.
6. R. L. Gluckstern, *Proc. 1970 Nat. Accelerator Lab. Linear Accelerator Conf.* (M. R. Tracy, Ed.), v. **2**, p. 811 (FNAL, Batavia, I11, 1970).

7. Eq. (19) of Ref, 6, where $v^2/\omega_0{}^2 = (v/v_0)^2\,[1 - (v/v_0)^2]$. For any specified value of v/v_0 the beam intensity is given by[8] $Q = 2\epsilon K^{1/2}\,(v_0/v - v/v_0)$ and the envelope radius by $a^2 = \epsilon K^{-1/2}\, v/v_0$.
8. G. R. Lambertson, L. J. Laslett, and L. Smith, IEEE Trans. Nucl. Sci., *NS-24*, 933 (1977), wherein $\pi\epsilon$ denotes a **normalized** emittance (i.e., wherein ϵ is $\beta\gamma$ times our ϵ) and Q represents our $Q' \simeq Q/(\epsilon K^{1/2})$.
9. Computations pertaining to a periodic transport channel are conveniently performed in terms of "scaled variables"—such as introduced in Ref. 8.
10. The results summarized in this article have been described in somewhat greater detail in an internal report (HI-FAN-15, Lawrence Berkeley Laboratory; 12 October 1977). With few exceptions, the periodic transport channels we have examined have been **symmetrical**, in the manner indicated by Figs. 1a–b. In some instances this restriction may result in certain modes remaining stable under conditions such that instability would result if the symmetry were broken—thus only by such a breaking of the symmetry does the second-order odd mode (or "*xy* mode") with $\sigma_0 < 180°$ exhibit instability in a FODO quadrupole focusing channel.
11. Further discussion and analysis of the third-order instability in a periodic interrupted-solenoid transport system is given in an internal report by Bisognano, Laslett, and Smith (HI-FAN-44, Lawrence Berkeley Laboratory, September, 1978).
12. I. Hofmann, *IEEE Trans. Nucl. Sci.*, **NS-26**, 3083 (1979).
13. I, Hofmann, Particle Accelerators, **11**, 31 (1980).
14. P. Lapostolle, *IEEE Trans. Nucl. Sci.*, **NS-18**, 1101 (1971).
15. I. Haber, *Proc. Heavy Ion Fusion Workshop* (R. C. Arnold, Ed.), ANL-79-41, p. 317 (Argonne Natl. Lab., Argonne, Ill., 1978).
16. I. Haber, *IEEE Trans, Nucl. Sci.*, **NS-26**, 3090 (1979).
17. Samuel Penner and Annija Galejs, *IEEE Trans. Nucl. Sci.*, **NS-26**, 3068 (1979).
18. I. Haber and A. W. Maschke, *Proc. Heavy Ion Fusion Workshop* (L. W. Smith, Ed.), BNL 50769 (Brookhaven Natl. Lab., Upton, N.Y., 1977), p. 122.
19. I. Bozsik and I. Hofmann, Proc. Conf. Charged Particle Optics, Giessen, Germany, 1980; published in *Nucl. Instr. Meth.*, **187**, 305 (1981). I. Haber and A. W. Maschke, *Phys, Rev. Letters*, **42**, 1479 (1979).
20. I. Hofmann, Proc. Conf. Charged Particle Optics, Giessen, Germany, 1980; published in *Nucl. Instr. Meth.* **187**, 281 (1981).
21. A. W. Maschke, cited by E. D. Courant in *ERDA Summer Study of Heavy Ions for Inertial Fusion* (R. O. Bangerter, W. B. Herrmannsfeldt, D. L. Judd, and Lloyd Smith, Eds.), LBL-5543, Appendix 6–2, p. 72 (Lawrence Berkeley Laboratory, Berkeley, Calif. and Lawrence Livermore Laboratory, Livermore, Calif., 1976).
22. M. Reiser, *Particle Accelerators*, **8**, 167 (1978).

5

Impedances

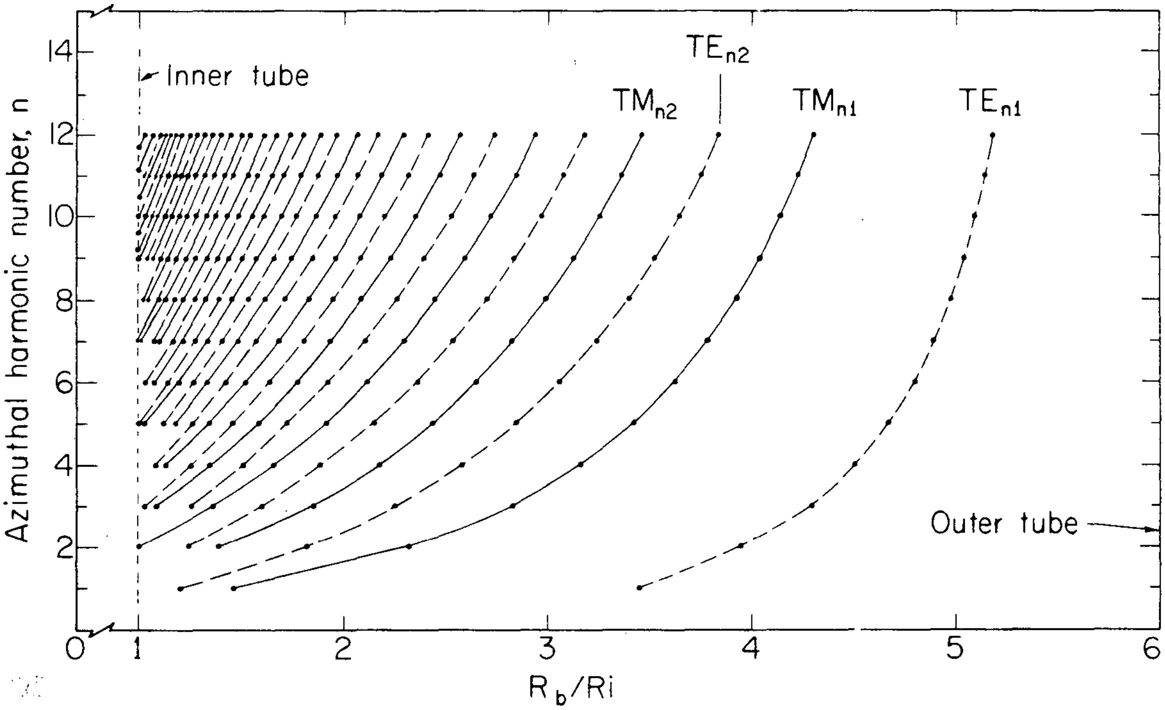
Azimuthal harmonic number, n
14
12
10
8
6
4
2
0
1
2
3
4
5
6
R_b/Ri
Inner tube
Outer tube
TM_{n2}
TE_{n2}
TM_{n1}
TE_{n1}

IOWA STATE COLLEGE JOURNAL OF SCIENCE
Vol. 33 No. 4 May 15, 1959 pp. 431-439

Reprinted by permission of the <u>Iowa State College Journal of Science</u>, 1987.

A METHOD OF APPLYING EXTREMAL METHODS TO PROBLEMS OF ELECTRICAL RESISTANCE*

L. Jackson Laslett

Department of Physics and Institute for Atomic Research
Iowa State College, Ames

INTRODUCTION

In a paper by Carlson and Hendrickson[1] use has been made of variational methods to secure upper and lower limits for electrical resistance. These methods, as presented, were based on techniques formulated by Schwinger and involved consideration of an integral equation for the current- or potential-distribution at a boundary surface. The presentation of Carlson and Hendrickson has the advantage of suggesting the applicability of similar techniques to problems in other fields of physics but, for this reason, may suffer from a lack of obvious physical motivation for the detailed mathematical steps. It is the purpose of the present note to indicate that the same technique may be introduced for resistance problems, in what may appear to be a more natural way, by use of well-known extremal theorems for resistance. It may be supposed that analogous extremal theorems exist in other fields of physics and that in some cases direct application of these theorems will lead to useful alternative methods of solution for specific problems.

B. UPPER LIMIT TO RESISTANCE

Use is made of the theorem[2] that an upper-limit, $R_{u.\ell.}$, is given by

$$R_{u.\ell.} = \frac{\iiint \rho J^2 \, d\tau}{\left[\iint \vec{J} \cdot \vec{ds} \right]^2} ,$$

where ρ is the resistivity of the material and $\vec{J}$ is an assumed current distribution (for which div $\vec{J} = 0$) such that $\rho \vec{J}$ is not necessarily derivable

from a potential or, if it is, the potential from which it may be derived is not necessarily constant over the electrodes.

In terms of any assumed emergent current distribution, J_n, at one of the electrodes (designated as electrode number two), it is appropriate to consider the current distribution throughout the resistive medium to be

$$\vec{J} = \frac{1}{\rho} \operatorname{grad} \iint_2 \mathcal{G}_1 \, J_n \, ds ,$$

where $\mathcal{G}_1$ is a Green's function, of $\vec{r}$ and $\vec{r}'$, such that

(i) $\operatorname{div}(\frac{1}{\rho} \operatorname{grad} \mathcal{G}_1) = - \delta(\vec{r}-\vec{r}'),$

(ii) $\mathcal{G}_1 = 0$ on electrode number 1, and

(iii) $\frac{\partial \mathcal{G}_1}{\partial n} = 0$ on the other boundaries of the resistive material.

$\mathcal{G}_1$ thus represents the potential arising from a point source of unit current when electrode number one serves as the sink.

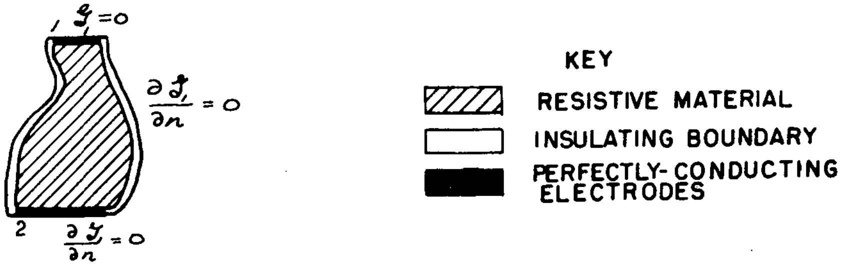

It will be noted that the expression considered for $\vec{J}$ is such that, if J_n were the true distribution of the emergent current, the expression $- \iint_2 \mathcal{G}_1 J_n \, ds$ would represent the true potential function for the problem, save for an arbitrary constant term. That this is so is seen from the use of Green's theorem (equivalent to a reciprocation theorem for currents):

$$V = - \iint \frac{V \partial \mathcal{G}_1 / \partial n}{\rho} \, ds + \iint \frac{\mathcal{G}_1 \partial V / \partial n}{\rho} \, ds$$

$$= V_1 - \iint_2 \mathcal{G}_1 J_n \, ds .$$

By the nature of $\mathcal{G}_1$ as a source-function, the expression considered for $\vec{J}$ will, of course, be consistent with the J_n assumed at the electrode.

---

* Contribution No. 668.

[1] J.F. Carlson and T.J. Hendrickson. 1953. Variational methods for problems in resistance. Ames Laboratory Manuscript LR-132: Jour. Appl. Physics <u>24</u>:1462-1465.

[2] Cf. W.R. Smythe. Static and Dynamic Electricity (McGraw-Hill Book Company, Inc., New York, 1950) second edition, sect. 6.11, p. 233; or see Appendix I. This theorem is analogous to Thomson's theorem in electrostatics.

Accordingly

$$R_{u.\ell.} = \frac{\iiint \left(\vec{J}\cdot \text{grad} \iint_2 \mathcal{G}_1 J_n \, ds\right) d\tau}{\left[\iint J_n \, ds\right]^2}$$

$$= \frac{\iiint \text{div} \left(\vec{J} \iint_2 \mathcal{G}_1 J_n \, ds\right) d\tau}{\left[\iint J_n \, ds\right]^2} \quad \text{(since div } \vec{J} = 0 \text{ throughout the volume)}$$

$$= \frac{\iint ds' \iint J_{n'} \, \mathcal{G}_1 (\vec{r}', \vec{r}) \, J_n \, ds}{\left[\iint J_n \, ds\right]^2}$$

the integration being only over the surface of electrode number 2, since either J_n or $\mathcal{G}_1$ will vanish on the other boundaries of the medium. To obtain an estimate for the resistance one assumes a functional form for the emergent current distribution, J_n, which is presumed not to depart violently from the correct distribution and which is sufficiently simple to permit performing the indicated integrations without undue difficulty. Since the expression for $R_{u.\ell.}$ is homogeneous of degree zero in J_n, no further normalization is required.

By way of comparison with the example of Carlson and Hendrickson[1], it is noted that

$$G_1 = \frac{1}{2\pi\rho} \int_2 \mathcal{G}_1 \, d\phi \,,$$

$$K_1 = \left[\frac{\pi b^2}{\ell} G_1 - 1\right] \text{ at } z = \ell \qquad \text{(i.e., at electrode number 2), and}$$

$$\chi(r) \propto J_n(r) \,.$$

Hence, for that case,

$$R_{u.\ell.} = \rho \, \frac{\iint \chi(r') \, r' \, G_1(r', r) \, r \, \chi(r) \, dr' \, dr}{\left[\int \chi(r) \, r \, dr\right]^2}$$

$$= \frac{\rho\ell}{\pi b^2} \; \frac{\iint r \, \chi(r) \, [K_1(r, r') + 1] \, r' \, \chi(r') \, dr \, dr'}{\left[\int \chi(r) \, r \, dr\right]^2}$$

$$= \frac{\rho\ell}{\pi b^2} [1 + \Gamma] \,, \text{ in agreement with eq. (22) of the paper cited (LR-132).}$$

C. LOWER LIMIT TO RESISTANCE

In analogy with the procedure of section B, use is made of the theorem[3] that a lower limit, $R_{\ell.\ell.}$, is given by

$$\frac{1}{R_{\ell.\ell.}} = \frac{\iiint \frac{1}{\rho} (\text{grad } V)^2 \, d\tau}{V_o^2} \,,$$

where V is a scalar function of position which assumes the specified values for the potential on the two electrodes and V_o represents the potential difference between the electrodes.

It is desirable to consider in this case, in addition to electrodes 1 and 2, a third surface, number 3, which physically forms a natural extension of electrode 2 but which constitutes an insulating boundary in the resistance problem of interest.

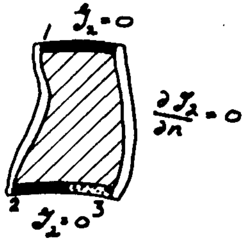

The potentials of electrodes 1 and 2 are then taken to be V_o and zero, respectively; the actual potential distribution over surface 3 is not known, but will be considered to be given by an assumed trial function, Φ .

Following again the procedure of Carlson and Hendrickson[1], use is made of a Green's function, $\mathcal{G}_2$, such that

(i) $\text{div} \left(\frac{1}{\rho} \text{ grad } \mathcal{G}_2\right) = - \delta(\vec{r} - \vec{r}')$;

(ii) $\mathcal{G}_2 = 0$ on surfaces 1, 2, and 3; and

(iii) $\partial \mathcal{G}_2 / \partial n = 0$ on the other boundaries of the resistive medium.

$\mathcal{G}_2$ thus represents the potential arising from a point source of unit current when surfaces 1, 2, and 3 serve as sinks at potential zero.

For use in the expression for $R_{\ell.\ell.}$ a potential distribution $V = V_1 + V_2$ is employed, where

---

[3] See Appendix II; an essentially similar result in electrostatics is presented by H. Bateman, "Partial Differential Equations of Mathematical Physics" (Dover Publications, New York, 1944), sect. 2.41, p. 152.

5-3

$$V_1 = -V_0 \iint_1 \frac{1}{\rho}\,\partial\mathcal{G}_2/\partial n\, ds$$

and
$$V_2 = -\iint_3 \frac{\Phi}{\rho}\frac{\partial\mathcal{G}_2}{\partial n}\,ds\ .$$

It is noted by use of Green's theorem or by the reciprocation theorem for currents, that V_1 represents the potential distribution which would be obtained if electrode 1 were at potential V_0, surfaces 2 and 3 at zero potential, and the remaining surfaces remained current barriers; similarly V_2 is the potential corresponding to a distribution Φ over surface 3, with electrodes 1 and 2 grounded and with the remaining surfaces impervious. The composite potential distribution V would be, in fact, the correct potential function for the problem at hand if the actual potential distribution over surface 3 were substituted for Φ .

By making use of the form adopted for V ,

$$\frac{1}{R_{l.l.}} = \frac{\displaystyle\iiint \frac{(\nabla V_1 + \nabla V_2)^2\, d\tau}{\rho}}{V_0^{\,2}}$$

$$= \frac{\displaystyle\iiint \frac{1}{\rho}\,(\nabla V_1)^2\, d\tau + 2\iiint \frac{1}{\rho}\,\nabla V_1\cdot\nabla V_2\, d\tau + \iiint \frac{1}{\rho}\,(\nabla V_2)^2\, d\tau}{V_0^{\,2}}$$

$$= \frac{1}{V_0}\iint_1 \frac{1}{\rho}\frac{\partial V_1}{\partial n}\,ds + \frac{1}{V_0^{\,2}}\iint_1 \frac{V_1}{\rho}\frac{\partial V_2}{\partial n}\,ds + \frac{1}{V_0^{\,2}}\iint_3 \frac{V_2}{\rho}\frac{\partial V_1}{\partial n}\,ds$$

$$+ \frac{1}{V_0^{\,2}}\iint_3 \frac{V_2}{\rho}\frac{\partial V_2}{\partial n}\,ds$$

$$= \frac{1}{R_0} - \frac{2}{V_0}\iint_3\iint_1 \frac{\Phi}{\rho\rho'}\frac{\partial^2 V_2}{\partial n\,\partial n'}\,ds\,ds'$$

$$- \frac{1}{V_0^{\,2}}\iint_3\iint_3 \frac{\Phi}{\rho}\frac{\partial^2\mathcal{G}_2}{\partial n\,\partial n'}\frac{\Phi'}{\rho'}\,ds\,ds'\ ,$$

where R_0 is the resistance obtained when electrode 1 is at the potential V_0 and both surfaces 2 and 3 are grounded.

It is convenient to introduce the relative distribution of potential on surface 3:

$$\Psi \equiv \Phi/V_0\ ,$$

whereupon

$$\frac{1}{R_{\ell.\ell.}} = \frac{1}{R_0} - 2\iint_3\iint_1 \frac{\Psi}{\rho\rho'}\frac{\partial^2\mathcal{G}_2}{\partial n\,\partial n'}\,ds\,ds' - \iint_3\iint_3 \frac{\Psi}{\rho}\frac{\partial^2\mathcal{G}_2}{\partial n\,\partial n'}\frac{\Psi'}{\rho'}\,ds\,ds'.$$

This last expression gives an upper limit to the conductance, and hence a lower limit to the resistance, in the problem of interest, through the use of various trial distributions for the potential on surface 3. In the form written it suffers, however, from the disadvantage that not only should a reasonable choice be made for the <u>form</u> of the trial potential, but also the scaling factor is of importance. For a given trial function, χ, a scaling factor f may be introduced such that $\Psi = f\chi$ and the last two terms in the expression for $\frac{1}{R_{\ell.\ell.}}$ become

$$-2f\iint_3\iint_1 \frac{\chi}{\rho\rho'}\frac{\partial^2\mathcal{G}_2}{\partial n\,\partial n'}\,ds\,ds' - f^2\iint_3\iint_3 \frac{\chi}{\rho}\frac{\partial^2\mathcal{G}_2}{\partial n\,\partial n'}\frac{\chi'}{\rho'}\,ds\,ds'\ .$$

The optimum choice of f, for a given χ , is

$$f = -\frac{\displaystyle\iint_3\iint_1 \frac{\chi}{\rho\rho'}\frac{\partial^2\mathcal{G}_2}{\partial n\,\partial n'}\,ds\,ds'}{\displaystyle\iint_3\iint_3 \frac{\chi}{\rho}\frac{\partial^2\mathcal{G}_2}{\partial n\,\partial n'}\frac{\chi'}{\rho'}\,ds\,ds'}$$

and the expression for $\frac{1}{R_{\ell.\ell.}}$ assumes the convenient homogeneous form:

$$\frac{1}{R_{\ell.\ell.}} = \frac{1}{R_0} + \frac{\left[\displaystyle\iint_3\iint_1 \frac{\chi}{\rho\rho'}\frac{\partial^2\mathcal{G}_2}{\partial n\,\partial n'}\,ds\,ds'\right]^2}{\displaystyle\iint_3\iint_3 \frac{\chi}{\rho}\frac{\partial^2\mathcal{G}_2}{\partial n\,\partial n'}\frac{\chi'}{\rho'}\,ds\,ds'}\ .$$

The physical significance of the choice of scale factor may be seen in the following manner: For the <u>correct</u> distribution of voltage over surface 3, the current density, $J_n = -(1/\rho)(\partial V/\partial n)$, will be zero at each point on surface 3; thus

$$\frac{1}{\rho}\iint_1 \frac{1}{\rho'}(\partial^2\mathcal{G}_2/\partial n\partial n')\,ds' + \frac{1}{\rho}\iint_3 \frac{\Psi'}{\rho'}(\partial^2\mathcal{G}_2/\partial n\partial n')\,ds'$$

will then be zero at each point of surface 3. In the present case the trial function χ has been scaled in such a way that the <u>integral</u> $\iint_3 \Psi J_n\, ds$ vanishes; i.e., so that

$$\iint_3\iint_1 \frac{\Psi}{\rho\rho'}\frac{\partial^2\mathcal{G}_2}{\partial n\,\partial n'}\,ds\,ds' + \iint_3\iint_3 \frac{\Psi}{\rho}\frac{\partial^2\mathcal{G}_2}{\partial n\,\partial n'}\frac{\Psi'}{\rho'}\,ds\,ds' = 0\ .$$

This condition imposed on Ψ then clearly includes the case in which Ψ assumes the true values of Φ/V_0.

5-4

A simplification results in the special case that $\frac{1}{V_o}\frac{\partial V_1}{\partial n}$ is independent of position on surface 3 and (say) equals $-1/L$. This situation arises, for example, in a problem in which V_1 represents the potential in a conductor of constant cross-section and of constant resistivity across the cross-section, as in the example of reference 1. In this case the double surface integral which appears in the numerator above, and which is identical with

$$-\frac{1}{V_o}\iint_3 \frac{\chi}{\rho}\frac{\partial V_1}{\partial n}\,ds, \text{ becomes } \frac{1}{L}\iint_3 \frac{\chi}{\rho}\,ds \text{ and we obtain}$$

$$\frac{1}{R_{\ell.\ell.}} = \frac{1}{R_o} + \frac{1}{L^2}\,\frac{\left[\iint_3 \frac{\chi}{\rho}\,ds\right]^2}{\iint_3\iint_3 \frac{\chi}{\rho}\,\frac{\partial^2 \mathcal{G}_2}{\partial n\partial n'}\,\frac{\chi'}{\rho'}\,ds\,ds'},$$

involving integrations only over the surface 3.

For comparison with the example of Carlson and Hendrickson[1], one notes that for that case

$$\rho = \text{const.},$$

$$\frac{1}{V_o}\frac{\partial V_1}{\partial n} = -1/\ell,$$

$$G_2 = \frac{1}{2\pi\rho}\int \mathcal{G}_2\,d\phi,$$

$$K_2 = \left[-1 - \pi b^2\ell\,\frac{\partial^2 \mathcal{G}_2}{\partial n\partial n'}\right] \text{ at } z = \ell \text{ (i.e., at electrode 3),}$$

and $\frac{\rho\ell}{\pi b^2} = R_o$.

Hence, for the example chosen,

$$\frac{1}{R_{\ell.\ell.}} = \frac{1}{R_o} - \frac{1}{R_o}\,\frac{\left[\int \chi(r)\,r\,dr\right]^2}{\iint r\chi(r)\,[K_2(r,r')+1]\,r'\chi(r')\,dr\,dr'}$$

$$= \frac{1}{R_o}\,\frac{\iint r\chi(r)\,K_2(r,r')\,r'\chi(r')\,dr\,dr'}{\iint r\chi(r)\,K_2(r,r')\,r'\chi(r')\,dr\,dr' + \left[\int \chi(r)\,r\,dr\right]^2}$$

$$= \frac{1}{R_o}\,\frac{\Lambda}{\Lambda+1},$$ in consistency with eq. (35) of the referenced paper (LR-132).

D. EXAMPLE

As an example consider the following "two dimensional" problem, which also may be solved rigorously by a simple Schwarz-Christoffel transformation when L is large:

A slab of homogeneous resistive material, of height h, extends from x = 0 to b and y = 0 to L. Current enters the specimen at y = L by an electrode extending from x = 0 to b and leaves at y = 0 by an electrode extending from x = 0 to a.

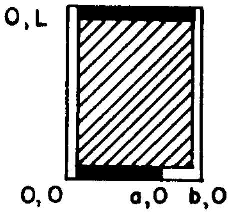

1. Upper limit:

In view of the two-dimensional character of this example, it suffices to use a Green's function, G_1, such that

(i) $\nabla^2_{x,y}G_1 = -\rho\,\delta(x,y;x',y'),$

(ii) $G_1 = 0$ at $y = L$, and

(iii) $\partial G_1/\partial n = 0$ on the other boundaries.

Then
$$R_{u.\ell.} = \frac{\iint J_n(x)\,G_1(x,x')\,J_n(x')\,dx\,dx'}{h\left[\int J_n(x)\,dx\right]^2}.$$

A suitable form for the Green's function will be

$$A_o(L-y') + \sum_1^\infty A_n \cos n\pi x/b \cosh n\pi y/b \sinh n\pi(L-y')/b, \text{ for } y < y';$$

$$A_o(L-y) + \sum_1^\infty A_n \cos n\pi x/n \sinh n\pi(L-y)/b \cosh n\pi y'/b, \text{ for } y > y';$$

with
$$\lim_{\varepsilon\to 0}\left[\left.\frac{\partial G_1}{\partial y}\right|_{y=y'-\varepsilon} - \left.\frac{\partial G_1}{\partial y}\right|_{y=y'+\varepsilon}\right] = \rho\,\delta(x-x').$$

Accordingly, $A_o = \rho/b$,

$$A_n = \frac{2\rho}{\pi} \frac{\cos n\pi x'/b}{n \cosh n\pi L/b} \qquad (n \geqslant 1)\text{ , and}$$

$$G_1(x,0;x',0) = \rho\left[\frac{L}{b} + \frac{2}{\pi}\sum_1^\infty \frac{1}{n}\cos n\pi x/b \cos n\pi x'/n \tanh n\pi L/b\right].^4$$

If one selects an assumed approximate distribution function J_n = const. $(0 < x < a)$ and performs the requisite integrations termwise,

$$R_{u.\ell.} = \frac{\rho\left[\frac{La^2}{b} + 2\frac{b^2}{\pi^3}\sum \frac{1}{n^3}\sin^2 n\pi a/b \tanh n\pi L/b\right]}{h\,a^2}$$

$$= \frac{\rho}{h}\left[\frac{L}{b} + \frac{2}{\pi^3}\frac{b^2}{a^2}\sum\frac{1}{n^3}\sin^2 n\pi a/b \tanh n\pi L/b\right], \quad \text{and}$$

for L large,

$$R_{u.\ell.} \simeq \frac{\rho}{h}\left[\frac{L}{b} + \frac{2}{\pi^3}\frac{b^2}{a^2}\sum\frac{1}{n^3}\sin^2 n\pi a/b\right] .$$

The term supplementing $\frac{\rho L}{hb}$ represents the estimated addition to the resistance of the sample as a result of limiting the area of electrode number 2.

2. Lower Limit:

One again makes use of a two-dimensional Green's function, G_2, which is now required to satisfy the conditions:

(i) $\nabla^2_{x,y} G_2 = -\rho\,\delta(x,y;x',y')$,

(ii) $G_2 = 0$ at $y = 0$, $y = L$, and

(iii) $\frac{\partial G_2}{\partial x} = 0$ at $x = 0$, $x = b$.

---

[4] It should be remarked that Professor Carlson has pointed out that in this case the series may be summed, when L is large, to

$$G_1(x,0:x',0) \simeq \rho\left[\frac{L}{b} - \frac{1}{\pi}\ell n(2\,|\cos\pi x/b - \cos\pi x'/b\,|\,)\right].$$

(Private communication.)

Then

$$\frac{1}{R_{\ell.\ell.}} = \frac{1}{R_o} + \frac{1}{L^2}\frac{h^2\left[\int \chi(x)\,dx\right]^2}{h\iint \chi(x)\left[\frac{\partial^2 G_2(x,y;x',y')}{\partial y\,\partial y'}\right]_{y,y'=0}\chi(x')\,dx\,dx'} .$$

or

$$R_{\ell.\ell.} = R_o - \frac{\rho^2}{hb^2}\frac{\left[\int \chi(x)\,dx\right]^2}{\iint \chi(x)\left[G_2'' + \frac{\rho}{Lb}\right]\chi(x')\,dx\,dx'} .$$

A formal expression for the Green's function may be written as

$$A_o\,y\,(L-y') + \sum_1^\infty A_n \cos n\pi x/b \sinh n\pi y/b \sinh n\pi(L-y')/b, \text{ for } y < y';$$

$$A_o\,y'\,(L-y) + \sum_1^\infty A_n \cos n\pi x/n \sinh n\pi(L-y)/b \sinh n\pi y'/b, \text{ for } y > y';$$

with $A_o = \frac{\rho}{Lb}$,

$$A_n = \frac{2\rho}{\pi}\frac{\cos n\pi x'/b}{n \sinh n\pi L/b} \qquad (n \geqslant 1) .$$

For a trial function, $\chi(x)$, one might prefer to employ a distribution which near the electrode is proportional to $\sqrt{x-a}$; for illustrative convenience, however, the function

$$\chi(x) = \frac{\pi}{2}\frac{x-a}{b-a}$$

is selected. By formal integration* in the case that L is large, one is led to the result

$$R_{\ell.\ell.} \simeq R_o + \frac{\rho}{2\pi h}\frac{1}{\sum_1^\infty n\frac{\cos^2 n\pi a/b}{\left[1 - (2n\frac{b-a}{b})^2\right]^2}}, \text{ for a non-integral value of } \frac{b}{2(b-a)},$$

---

* Despite the poor performance, with respect to convergence, of the series for G_2'' it is felt that the character of the series obtained after the double integration warrants confidence in the result of proceeding formally in this manner (with the particular trial function selected).

and

$$R_{\ell.\ell.} \simeq R_o + \frac{\rho}{2\pi h} \frac{1}{m\frac{\pi^2}{16} + \sum_{\substack{1\\ n\neq m}}^{\infty} n \frac{\cos^2 n\pi a/b}{\left[1 - (2n\frac{b-a}{b})^2\right]^2}} ,$$

when $\frac{b}{2(b-a)}$ equals an integer, m .

3. Exact Solution:

As was mentioned in the introductory paragraph of section D, the present problem admits of a simple exact solution for L large. A suitable Schwarz-Christoffel transformation is[5]

$$W = \sin^{-1}\left[\frac{\sin\frac{1}{2}\frac{\pi z}{b}}{\sin\frac{1}{2}\frac{\pi a}{b}}\right] .$$

At large distances above the x-axis, the potential function is

$$V \simeq \frac{\pi}{2}\frac{y}{b} - \ell n \sin\frac{\pi a}{2b}$$

and the change of the stream function in traversing the electrode is

$$\Delta U = \frac{\pi}{2} .$$

Accordingly, the exact resistance for L large is

$$R \simeq \frac{\rho}{h}\left[\frac{L}{b} - \frac{2}{\pi}\ell n \sin\frac{\pi a}{2b}\right] .$$

4. Numerical Results:

Values for the supplemental resistance, obtained from the approximate formulas by numerical summation, are given in Table I.

---

[5] W.R. Smythe, l.c., sect. 4.22, pp. 90-91.

TABLE I

Values of the Supplemental Resistance, $R-R_o$, in units $\rho/2\pi h$.

	$R_{u.\ell.}$	$R_{\ell.\ell.}$	R_{exact}
Trial Function	J_n = const.	$\chi = \sin\frac{\pi}{2}\frac{x-a}{b-a}$	- - -
a/b = 1/4	4.26	3.04	3.842
a/b = 1/2	1.70	1.15	1.386
a/b = 3/4	0.39_2	0.26_8	0.317

APPENDIX I

Proof of the theorem that the current distribution is such that the "heating," $\iiint \rho J^2 \, d\tau$, is a minimum for fixed total current:

Let $\vec{J}_o$ be the correct current distribution, and $\vec{J}$ any other solenoidal current distribution corresponding to the same total current, I, at the electrodes.

Then (i) $\operatorname{div} \vec{J}_o = 0 = \operatorname{div} \vec{J}$,

(ii) $\iint \vec{J}_o \cdot \vec{ds} = \pm I = \iint \vec{J} \cdot \vec{ds}$, and

(iii) $\rho \vec{J}_o$ is derivable from a potential:

$\rho \vec{J}_o = -\overrightarrow{\text{grad } V}$, with V constant on the electrodes.

It then follows that

$$\begin{aligned}
\iiint \rho (J^2 - J_o^2) \, d\tau &\equiv 2 \iiint \rho \vec{J}_o \cdot (\vec{J}-\vec{J}_o) \, d\tau + \iiint \rho (\vec{J}-\vec{J}_o)^2 \, d\tau \\
&\equiv -2 \iiint (\overrightarrow{\text{grad } V}) \cdot (\vec{J}-\vec{J}_o) \, d\tau + \iiint \rho (\vec{J}-\vec{J}_o)^2 \, d\tau \\
&\equiv -2 \iiint \operatorname{div} [V(\vec{J}-\vec{J}_o)] \, d\tau + 2 \iiint V \operatorname{div}(\vec{J}-\vec{J}_o) \, d\tau \\
&\qquad + \iiint \rho (\vec{J}-\vec{J}_o)^2 \, d\tau \\
&\equiv -2 \iint V(\vec{J}-\vec{J}_o) \cdot \vec{ds} + 2 \iiint V \operatorname{div}(\vec{J}-\vec{J}_o) \, d\tau \\
&\qquad + \iiint \rho (\vec{J}-\vec{J}_o)^2 \, d\tau \\
&= \iiint \rho (\vec{J}-\vec{J}_o)^2 \, d\tau \geqslant 0 \, ,
\end{aligned}$$

and the heating is least for the correct current distribution.

APPENDIX II

Proof of the theorem that the potential distribution is such that the heating, $\iiint (1/\rho)(\text{grad } V)^2 \, d\tau$, is a minimum for a fixed interelectrode potential difference:

Let V_o be the correct potential distribution, for which

(i) $\operatorname{div} (\frac{1}{\rho} \text{ grad } V_o) = 0$,

(ii) V_o assumes the prescribed potentials at the electrodes,

and (iii) $\partial V_o / \partial n = 0$ on the other boundaries.

V is taken to correspond to the same potential difference between the electrodes and, for convenience, might be considered to assume the same values as V_o on the electrodes. It then follows that

$$\begin{aligned}
\iiint \frac{(\nabla V)^2 - (\nabla V_o)^2}{\rho} \, d\tau &\equiv 2 \iiint \frac{\nabla V_o \cdot \nabla (V-V_o)}{\rho} \, d\tau + \iiint \frac{[\nabla (V-V_o)]^2}{\rho} \, d\tau \\
&\equiv 2 \iiint \operatorname{div} \left[(V-V_o) \frac{\text{grad } V_o}{\rho} \right] d\tau \\
&\qquad -2 \iiint (V-V_o) \operatorname{div} (\frac{1}{\rho} \text{ grad } V_o) \, d\tau \\
&\qquad + \iiint \frac{[\nabla (V-V_o)]^2}{\rho} \, d\tau \\
&\equiv 2 \iint \frac{V-V_o}{\rho} \frac{\partial V_o}{\partial n} \, ds - 2 \iiint (V-V_o) \operatorname{div}(\frac{\text{grad } V_o}{\rho}) \, d\tau \\
&\qquad + \iiint \frac{[\nabla (V-V_o)]^2}{\rho} \, d\tau \\
&= \iiint \frac{[\nabla (V-V_o)]^2}{\rho} \, d\tau \geq 0 \, ,
\end{aligned}$$

and the heating is least for the correct potential distribution.

UNCLASSIFIED

IS-189

Physics and Mathematics (UC-34)
TID 4500, August 1, 1959

UNITED STATES ATOMIC ENERGY COMMISSION
Research and Development Report

EVALUATION OF THE ZEROS OF CROSS-PRODUCT BESSEL FUNCTIONS

by

L. Jackson Laslett and William Lewish

September 1960

Ames Laboratory
at
Iowa State University of Science and Technology
F. H. Spedding, Director
Contract W-7405 eng-82

UNCLASSIFIED

CONTENTS

EVALUATION OF THE ZEROS OF CROSS-PRODUCT BESSEL FUNCTIONS

L. Jackson Laslett and William Lewish*

ABSTRACT

Computational results for the characteristic values and characteristic solutions of Bessel's equation are presented. Specifically, the results pertain to the first two solutions subject to the Neumann boundary condition at r = a, b and to the first solution subject to the Dirichlet condition, when (b-a)/(b+a) is small (0.1, 0.01, 0.001). Approximate analytic formulas are derived to complement the computational results. The possible application of the data to phenomena involving the interaction of an intense circulating beam and the electromagnetic fields within a particle accelerator is indicated, as is also the utility of the results for estimation of the loss-factor, Q, for resonant electromagnetic modes of possibly high order within a toroidal vacuum chamber of rectangular cross section.

I. INTRODUCTION

In a number of physical or engineering problems in which use of cylindrical coordinates is appropriate, separation of variables leads to Bessel's differential equation,

$$\frac{1}{r}\frac{d}{dr}\left[r\frac{dZ}{dr}\right]+\left[q^2-\frac{n^2}{r^2}\right]Z=0, \qquad (1)$$

---

* Associated with the Department of Statistics, Iowa State University, Ames, Iowa

A resume of the results reported here has been submitted to <u>Mathematics of Computation</u>.

for the radial dependence of the variable of interest. Solutions are typically sought which satisfy the Dirichlet boundary condition ($Z = 0$) or the Neumann boundary condition ($dZ/dr = 0$) at $r = a$ and $r = b$. If the solution to Eq. (1) is written as a linear combination of Bessel and Neumann functions, application of the Dirichlet or Neumann boundary conditions respectively leads to the following equations for determining the eigenvalues, q:

$$J_n(q\,a)\,Y_n(q\,b) - J_n(q\,b)\,Y_n(q\,a) = 0 \quad , \tag{2a}$$

or

$$J_n'(q\,a)\,Y_n'(q\,b) - J_n'(q\,b)\,Y_n'(q\,a) = 0. \tag{2b}$$

The zeros of the cross-product Bessel functions which appear on the left-hand side of Eqs. (2 a, b) are frequently sought for cases in which n is not large, because of the interest in the lower-order modes which are possible in the physical problem under consideration. Cases may also arise, however, in which attention should be directed to the higher-order modes in order to determine the circumstances in which such possibly-unwanted modes may become excited. An example of the latter situation is the interest which is currently attached to the resonant electromagnetic modes which may be excited[1] within a toroidal vacuum chamber of rectangular cross section by an azimuthally-modulated circulating beam such as that of a particle accelerator.

---

[1] V. Kelvin Neil, "A Study of Some Coherent Electromagnetic Effects in High Current Particle Accelerators", Ph. D. thesis (Physics, University of California and Lawrence Radiation Laboratory, Berkeley, California, 1960, UCRL-9124).

Solutions to Eqs. (2a) and (2b) have been discussed by a number of writers[2-7] and results presented in the form of approximate algebraic formulas, in tables or graphically. For application to problems in which $\frac{b-a}{b+a}$ is small and in which n may be large, however, it appeared appropriate to make an independent investigation of the initial roots of Eqs. (2a) and (2b) by study of characteristic solutions to Bessel's equation (1) in the interval $a \leq r \leq b$ without explicit reference to the usual Bessel and Neumann functions. Approximate analytic formulas have been obtained for the first characteristic value and function associated with the Dirichlet boundary condition and for the first two eigenvalues and functions associated with the Neumann boundary condition. An in-

---

[2] James McMahon, Ann. of Math. 9, 23-30 (1894).

[3] A. Kalähne, Zeits. für Math. u. Physik 54, 55-86 (1907).

[4] William Marshall, Ann. of Math. 11, 153-160 (1910).

[5] Rohn Truell, J. Appl. Phys. 14, 350-352 (1943).

[6] Don Kirkham, J. Math. and Phys. 36, 371-377 (1958).

[7] W. N. Wong, "Electromagnetic Fields in a Donut Space", Midwestern Universities Research Association internal report MURA-555, Madison, Wisconsin, 1960.

dependent systematic determination of these characteristic values and functions has also been made numerically with the CYCLONE digital electronic computer at Iowa State University for cases in which $\frac{b-a}{b+a}$ was assigned the values 0.001, 0.01, and 0.1 and for a special set of cases in which this quantity was given the value 0.0001. It is the purpose of this report to summarize the results of this analytic work and to present the results of the numerical investigation.

II. TRANSFORMATION OF BESSEL'S EQUATION

It may be noted that, due to the nature of the customary Bessel functions of high order, and in particular because the function J_n remains quite small until its argument is comparable to its order, the lowest characteristic values, q, will be in the neighborhood of n/b for n large. For this reason and to focus attention on the interval $a \leq r \leq b$, it is convenient to define

$$\eta \equiv \frac{b-a}{b+a} \quad , \tag{3a}$$

$$\delta \equiv \eta^2 \left[(q \frac{b+a}{2})^2 - n^2 \right] \quad , \tag{3b}$$

and

$$x \equiv 2 \frac{r - (b+a)/2}{b-a} \quad . \tag{3c}$$

In terms of these quantities[+]

[+] Physically, it is seen that the quantity η which is introduced here, represents the ratio of the width (b-a) to the diameter (b+a) of the annular region under consideration. For η only slightly less than unity, this region extends substantially from r = 0 to r = b, and the roots $q\frac{b+a}{2}$ of Eqs. (2a) or (2b) may then be expected to approach one-half the corresponding roots, μ, of the simpler equations $J_n(\mu) = 0$ or $J_n'(\mu) = 0$, respectively.

$$r = \frac{b + a}{2} (1 + \eta x), \text{ with } -1 \leq x \leq 1, \tag{4}$$

and Bessel's equation (1) assumes the form

$$\frac{d}{dx}\left[(1 + \eta x) \frac{dZ}{dx}\right] + \left[(1 + \eta x)\delta + \frac{2 + \eta x}{1 + \eta x} \cdot \eta^3 n^2 \cdot x\right] Z = 0. \tag{5}$$

The solutions to Eq. (5) which are of interest are those for which the Dirichlet boundary condition (Z = 0) or, alternatively, the Neumann boundary condition ($dZ/dx = 0$) applies at $x = \pm 1$. In the case that the Dirichlet boundary condition is to be applied, it is convenient for some purposes to make the transformation

$$S = (1 + \eta x)^{1/2} Z , \tag{6}$$

in terms of which Eq. (5) may be written

$$\frac{d^2S}{dx^2} + \left[\delta + \frac{(\eta^2/4) + \eta^3 n^2 (2 + \eta x) x}{(1 + \eta x)^2}\right] S = 0 \tag{7}$$

with $S(\pm 1) = 0$.

For $\eta \ll 1$, the terms in Eqs. (5) and (7) which contain η, save in some cases those which involve the combination $\eta^3 n^2$, may be treated as a perturbation or, in some approximations, ignored.

III. APPROXIMATE ANALYTIC FORMULAS

In a preliminary investigation of the present problem, estimates of the characteristic values and an indication of the nature of the characteristic functions were obtained by a variational solution of Eqs. (5) or (7). For the present purposes, however, it appears preferable to employ, where applicable, a standard perturbation procedure,[8] since a solution consistent to a certain order of smallness may thereby automatically be obtained. We assume throughout that $\eta \ll 1$ and commence by considering the case in which $\eta^3 n^2$ also is small.

(a) Application of Perturbation Method, with $\eta^3 n^2$ Small

The differential Eqs. (5) and (7) may be put into an appropriate form, to which the standard perturbation procedure[8] is directly applicable, by regarding n as the small parameter in terms of which the perturbation development is performed, but regarding n as possibly sufficiently large that quantities such as $\eta^2 n^2$ or $\eta^3 n^2$ are not necessarily negligible. Equations (5) and (7) accordingly are written

$$\frac{d^2Z}{dx^2} + \eta\left[\frac{d}{dx}\left(x\,\frac{dZ}{dx}\right) + (\delta + 2\,\eta^2 n^2)\cdot x\cdot Z - \eta^3 n^2 x^2 Z\right] = -\,\delta\cdot Z, \qquad (8)$$

and

$$\frac{d^2S}{dx^2} + \eta\left[2\eta^2\left(n^2 - \frac{1}{4}\right)\cdot x\cdot S - 3\,\eta^3\left(n^2 - \frac{1}{4}\right) x^2 S\right] = -\left(\delta + \frac{\eta^2}{4}\right) S, \qquad (9)$$

where the quantities contained within the square brackets are to be regarded as the perturbation Hamiltonian acting on the dependent variable--i.e., H'Z or H'S, respectively--and the quantities $-\delta$ and $-\left(\delta + \frac{\eta^2}{4}\right)$ which appear on the right-hand sides of Eqs. (8) and (9) play the role

---

[8] L. I. Schiff, Quantum Mechanics (McGraw-Hill Book Co., Inc., New York, 1955), Ed. 2, Chapt. VII, Sect. 25, pp. 151-154. We gratefully acknowledge the assistance provided by Dr. C. L. Hammer in discussing with us the use of the perturbation method for which results are described in Sect. III(a) of this report.

normally filled by the energy in quantum-mechanical applications of the perturbation technique.

The basic solutions to the unperturbed equation,

$$\frac{d^2u}{dx^2} = -\lambda u \quad , \tag{10}$$

adjusted to be orthonormal in the interval $-1 \leq x \leq 1$, are

$$u_m = \frac{1}{\sqrt{2}}, \ \sin\frac{\pi}{2}x \ , \ \cos\pi x, \ \sin\frac{3\pi}{2}x \ , \ \cos 2\pi x \quad , \ldots\ldots ,$$

with

$$\lambda_m = (m\pi)^2, \ m = 0, \frac{1}{2}, 1, \frac{3}{2}, 2, \ldots ,$$

for the case that the Neumann boundary condition applies, and

$$u_m = \cos\frac{\pi}{2}x \ , \ \sin\pi x \ , \ \cos\frac{3\pi}{2}x \ , \ \sin 2\pi x \quad , \ldots ,$$

with

$$\lambda_m = (m\pi)^2, \ m = \frac{1}{2}, 1, \frac{3}{2}, 2, \ldots ,$$

for use with the Dirichlet boundary condition. The results of a perturbation analysis of Eq. (8) are then to be obtained from the formulas[8]

$$-\delta_m = -\lambda_m + \eta H'_{m,m} + \eta^2 \sum_{k \neq m} \frac{H'_{m,k} H'_{k,m}}{\lambda_k - \lambda_m} \quad ,$$

or

$$\delta_m = (m\pi)^2 - \eta H'_{m,m} - \eta^2 \sum_{k \neq m} \frac{H'_{m,k} H'_{k,m}}{\pi^2 (k^2 - m^2)} \ , \tag{11a}$$

and

$$Z_m = u_m + \eta \sum_{k \neq m} \frac{H'_{k,m}}{\lambda_k - \lambda_m} u_k$$

$$= u_m + \eta \sum_{k \neq m} \frac{H'_{k,m}}{\pi^2(k^2 - m^2)} u_k \quad , \tag{11b}$$

with analogous expressions for use with Eq. (9). The matrix elements $H'_{k,m}$ in Eqs. (11a, b) represent the integral $\int_{-1}^{1} u_k H' u_m \, dx$.

(i) Results for the first Neumann solution:

With m = 0, the matrix elements for Eq. (8) are found, to the desired order, to be

$$H'_{o,o} = -\frac{\eta^3 n^2}{3} \text{ from the } x^2 \text{ term in } H', \tag{12a}$$

and

$$H'_{o,k} = H'_{k,o} = (-)^{\frac{\ell-1}{2}} \sqrt{2}\,\left(\frac{2}{\pi}\right)^2 \frac{\delta + 2\eta^2 n^2}{\ell^2}$$

$$= (-)^{\frac{\ell-1}{2}}\, 2\sqrt{2}\,\left(\frac{2}{\pi}\right)^2 \eta^2 n^2 \frac{1}{\ell^2} \quad , \tag{12b}$$

from the x term in H', where ℓ = 2k assumes odd values (1, 3, . . .) and in which the result has been simplified by anticipating the result that δ will be very small (v. i.).

By use of Eqs. (11a, b) it then follows that

$$\delta \doteq \frac{1}{3}\eta^4 n^2 - 8\left(\frac{2}{\pi}\right)^6 \eta^6 n^4 \sum_{\ell \text{ odd}} \frac{1}{\ell^6}$$

$$= \frac{1}{3}\eta^4 n^2 - \frac{8}{15}\eta^6 n^4 \;,^{9a} \tag{13a}$$

and

$$Z \doteq \frac{1}{\sqrt{2}} + 2\sqrt{2}\,\left(\frac{2}{\pi}\right)^4 \eta^3 n^2 \sum_{\ell \text{ odd}} (-)^{\frac{\ell-1}{2}} \frac{1}{\ell^4} \sin\frac{\ell}{2}\pi x$$

$$= \frac{1}{\sqrt{2}}\left[1 + \eta^3 n^2 \left(x - \frac{x^3}{3}\right)\right] .^{9b} \tag{13b}$$

[9a] The summation of $1/\ell^6$ for ℓ odd, may be determined in terms of the Riemann zeta function (Ref. 12, Sect. IX, p. 269):

$$\sum_{\ell \text{ odd}} \frac{1}{\ell^6} = \frac{63}{64}\zeta(6) = \frac{63}{64}\,\frac{\pi^6}{945} = \frac{\pi^6}{(64)(15)} \quad ;$$

(cont.)

For small values of $\eta^3 n^2$, the characteristic solution of concern here is, of course, nearly constant. From Eq. (13b), moreover, it is seen that in particular,

$$Z(-1) : Z(o) : Z(1) \doteq 1 - \frac{2}{3}\,\eta^3 n^2 : 1 : 1 + \frac{2}{3}\,\eta^3 n^2 \quad , \tag{13c}$$

for $\eta^3 n^2$ small, and the slope at $x = 0$ similarly is given by

$$Z'(o)/Z(o) \doteq \eta^3 n^2 \quad . \tag{13d}$$

The features of the solution indicated by Eqs. (13c, d) will be checked in Sect. IV(a) by comparison with computational results.

(ii) Results for the first Dirichlet solution:

With $m = \frac{1}{2}$ and by use of Eq. (9), results of the desired degree of approximation are obtained by application of the perturbation method through first order. The desired matrix elements for Eq. (9) are

$$H'_{\frac{1}{2},\,\frac{1}{2}} = -\left(1 - \frac{6}{\pi^2}\right) \eta^3 \left(n^2 - \frac{1}{4}\right) \tag{14a}$$

and

$$H'_{k,\,\frac{1}{2}} = -(-)^k\, 16 \left(\frac{2}{\pi}\right)^2 \eta^2 \left(n^2 - \frac{1}{4}\right) \frac{k}{(4k^2 - 1)^2} \quad , \tag{14b}$$

[9a] whereupon

$$8\left(\frac{2}{\pi}\right)^6 \sum_{\ell\,\mathrm{odd}} \frac{1}{\ell^6} = \frac{(8)\,(64)}{\pi^6} \quad \frac{\pi^6}{(64)\;(15)} = \frac{8}{15}$$

, as employed in Eq. (13a) of the text.

[9b] One may readily verify, for the interval $-1 \leq x \leq 1$, the Fourier development

$$\frac{1}{4}\left(\frac{\pi}{2}\right)^4 \left(x - \frac{x^3}{3}\right) = \sin\frac{\pi}{2}x - \frac{1}{3^4}\sin\frac{3\pi}{2}x + \frac{1}{5^4}\sin\frac{5\pi}{2}x - \frac{1}{7^4}\sin\frac{7\pi}{2}x + \ldots,$$

which is used in obtaining Eq. (13b) of the text.

with $k = 1, 2, 3, \ldots$. Accordingly, by formulas analogous to Eqs. (11a, b),

$$\delta + \frac{\eta^2}{4} \doteq \left(\frac{\pi}{2}\right)^2 + \left(1 - \frac{6}{\pi^2}\right) \eta^4 \left(n^2 - \frac{1}{4}\right)$$

$$\delta \doteq \left(\frac{\pi}{2}\right)^2 - \frac{\eta^2}{4} + \left(1 - \frac{6}{\pi^2}\right)\left(n^2 - \frac{1}{4}\right) \eta^4 \quad , \qquad (15a)$$

and

$$S \doteq \cos\frac{\pi}{2}\, x - 16\left(\frac{2}{\pi}\right)^4 \eta^3 \left(n^2 - \frac{1}{4}\right) \sum_{k=1}^{\infty} (-)^k \frac{k}{(4k^2-1)^3} \sin k\pi x$$

$$= \cos\frac{\pi}{2}\, x + \frac{1}{\pi}\left(n^2 - \frac{1}{4}\right) \eta^3 \left[(1 - x^2)\sin\frac{\pi}{2} x - \frac{2}{\pi} \cdot x \cdot \cos\frac{\pi}{2} x \right] .^{9c} \qquad (15b)$$

The corresponding form for Z is given by $S/\sqrt{1 + \eta x}$ Eq. (6) and when $\eta \ll 1$, will differ little from the form of S itself. To the order considered in the present analysis, the factors $(n^2 - \frac{1}{4})\, \eta^4$ and $(n^2 - \frac{1}{4})\, \eta^3$ which appear in Eqs. (15a, b) might well be replaced by $\eta^4 n^2$ and $\eta^3 n^2$, respectively; we leave the results in the present form, however, since these expressions are exact in the case $n = \frac{1}{2}$, for which

$$Z = \frac{\cos\frac{\pi}{2} x}{\sqrt{1 + \eta x}}$$

. With η small, the following simple characteristics of the derivative are suggested by Eq. (15b):

[9c] The Fourier development

$$\frac{\pi^3}{256}\,(1 - x^2)\sin\frac{\pi}{2} x - \frac{\pi^2}{128} \cdot x \cdot \cos\frac{\pi}{2} x = -\sum_{k=1}^{\infty} (-)^k \frac{k}{(4k^2-1)^3} \sin k\pi x \;,$$

for $-1 \leq x \leq 1$, is employed to obtain Eq. (15b) of the text.

$$Z'(1) : Z'(-1) \doteq -\frac{1 + (2/\pi^2)\,\eta^3 n^2}{1 - (2/\pi^2)\,\eta^3 n^2} \cdot \sqrt{\frac{1-\eta}{1+\eta}} \ , \tag{15c}$$

and

$$Z'(o) : Z(o) \doteq \frac{1}{2}\left(1 - \frac{4}{\pi^2}\right) \eta^3 n^2 - \frac{\eta}{2} \tag{15d}$$

$$\doteq 0.29736\ \eta^3 n^2 - \frac{1}{2}\eta \ . \tag{15d'}$$

(iii) Results for the second Neumann solution:

With $m = \frac{1}{2}$ the matrix elements for Eq. (8) are found, to the desired order, to be

$$H'_{\frac{1}{2},\frac{1}{2}} = -\frac{1}{3}\left(1 + \frac{6}{\pi^2}\right) \eta^3 n^2 \ , \tag{16a}$$

$$H'_{\frac{1}{2},o} = H'_{o,\frac{1}{2}} = \sqrt{2}\left(1 + \frac{8}{\pi^2}\ \eta^2 n^2\right) \tag{16b}$$

so that

$$H'_{\frac{1}{2},o} \cdot H'_{o,\frac{1}{2}} \cong 2 + 8\left(\frac{2}{\pi}\right)^2 \eta^2 n^2 \ , \tag{16c}$$

and

$$H'_{\frac{1}{2},k} = H'_{k,\frac{1}{2}} = 8(-)^k \left[\frac{\delta + 2\,\eta^2 n^2}{\pi^2}\ \frac{4k^2+1}{(4k^2-1)^2} - \frac{2k^2}{(4k^2-1)^2}\right]$$

$$\doteq -8(-)^k \left[\frac{1}{4(4k^2-1)} - \frac{2}{\pi^2}\,\eta^2 n^2\ \frac{4k^2+1}{(4k^2-1)^2}\right] \tag{16d}$$

so that

$$H_{\frac{1}{2},k} \cdot H_{k,\frac{1}{2}} \cong 64\left[\frac{1}{16}\ \frac{1}{(4k^2-1)^2} - \frac{1}{\pi^2}\ \eta^2 n^2\,\frac{4k^2+1}{(4k^2-1)^3}\right] , \tag{16e}$$

where k = 1, 2, 3, . . . and in which Eq. (16d) has been obtained through use of the fact that, for the present purpose, δ is substantially $(\pi/2)^2$.

It then follows, by application of the formulas (11a) and (11b), that

$$\delta \doteq \left(\frac{\pi}{2}\right)^2 + \frac{1}{3}\left(1 + \frac{6}{\pi^2}\right) \eta^4 n^2 + \left(\frac{2}{\pi}\right)^2 \eta^2 \left[2 + 8\left(\frac{2}{\pi}\right)^2 \eta^2 n^2\right]$$

$$-64\left(\frac{2}{\pi}\right)^2 \eta^2 \sum_{k=1}^{\infty}\left[\frac{1}{16}\frac{1}{(4k^2-1)^3} - \frac{1}{\pi^2}\eta^2 n^2 \frac{4k^2+1}{(4k^2-1)^4}\right]$$

$$= \left(\frac{\pi}{2}\right)^2 + 2\left(\frac{2}{\pi}\right)^2\left[1 - 2\sum_{k=1}^{\infty}\frac{1}{(4k^2-1)^3}\right]\eta^2$$

$$+\left\{\frac{1}{3}\left(1 + \frac{6}{\pi^2}\right) + 8\left(\frac{2}{\pi}\right)^4\left[1 + 2\sum_{k=1}^{\infty}\frac{4k^2+1}{(4k^2+1)^4}\right]\right\}\eta^4 n^2$$

$$= \left(\frac{\pi}{2}\right)^2 + \frac{3}{4}\eta^2 + \left(1 + \frac{10}{\pi^2}\right)\eta^4 n^2 \quad ,^{9d,e} \qquad (17a)$$

$$Z \doteq \sin\frac{\pi}{2}x \quad - \frac{4}{\pi^2}\eta\left(1 + \frac{8}{\pi^2}\eta^2 n^2\right)$$

$$-\frac{8}{\pi^2}\eta\sum_{k=1}^{\infty}(-)^k\left[\frac{1}{(4k^2-1)^2} - \frac{8}{\pi^2}\eta^2 n^2\frac{4k^2+1}{(4k^2-1)^3}\right]\cos k\pi x$$

$$= \sin\frac{\pi}{2}x \quad - \left(\frac{2}{\pi}\right)^2\left[1 + 2\sum_{k=1}^{\infty}(-)^k\frac{1}{(4k^2-1)^2}\cos k\pi x\right]\eta$$

[9d] Use may be made of the Fourier development

$$\frac{\pi^3}{128}x^2\cos\frac{\pi}{2}x - \frac{3\pi}{32}\left(1 + \frac{\pi^2}{12}\right)\cos\frac{\pi}{2}x - \frac{3\pi^2}{64}\cdot x\cdot\sin\frac{\pi}{2}x + \frac{1}{2}$$

$$= \sum_{k=1}^{\infty}(-)^k\frac{1}{(4k^2-1)^3}\cos k\pi x$$

to simplify the result leading to Eq. (17a) of the text: By setting $x = 1$ in this development it follows that

$$\sum_{k=1}^{\infty}\frac{1}{(4k^2-1)^3} = \frac{1}{2} - \frac{3\pi^2}{64}$$

and

$$2\left(\frac{2}{\pi}\right)^2\left[1 - 2\sum_{k=1}^{\infty}\frac{1}{(4k^2-1)^3}\right] = \frac{3}{4} \quad .$$

$$-2\left(\frac{2}{\pi}\right)^4\left[1-2\sum_{k=1}^{\infty}(-)^k\frac{4k^2+1}{(4k^2-1)^3}\cos k\pi x\right]\eta^3 n^2$$

$$=\sin\frac{\pi}{2}x-\frac{1}{2}\eta\left(x\sin\frac{\pi}{2}x+\frac{2}{\pi}\cos\frac{\pi}{2}x\right)$$

[9e] Use may also be made of the Fourier development

$$-\frac{1}{32}\left[\frac{\pi^4}{24}x^3\sin\frac{\pi}{2}x-\frac{\pi^4}{8}\left(1-\frac{4}{\pi^2}\right)\cdot x\cdot\sin\frac{\pi}{2}x+\pi\cos\frac{\pi}{2}x\right]$$

$$=8\sum_{k=1}^{\infty}(-)^k\frac{k^2}{(4k^2-1)^4}\cos k\pi x\,,$$

in which setting $x = 1$ leads to the result

$$8\sum_{k=1}^{\infty}\frac{k^2}{(4k^2-1)^4}=\frac{\pi^4}{384}-\frac{\pi^2}{64}\;.$$

By combining this result with the sum found in Ref. (9d) above it follows that

$$8\sum_{k=1}^{\infty}\frac{k^2}{(4k^2-1)^4}-\sum_{k=1}^{\infty}\frac{1}{(4k^2-1)^3}=\frac{\pi^4}{384}+\frac{\pi^2}{32}-\frac{1}{2}\;,$$

$$\sum_{k=1}^{\infty}\frac{4k^2+1}{(4k^2-1)^4}=\frac{\pi^4}{384}+\frac{\pi^2}{32}-\frac{1}{2}\;,$$

and

$$\frac{1}{3}\left(1+\frac{6}{\pi^2}\right)+8\left(\frac{2}{\pi}\right)^4\left[1+2\sum_{k=1}^{\infty}\frac{4k^2+1}{(4k^2-1)^4}\right]$$

$$=\frac{1}{3}+\frac{2}{\pi^2}+\frac{8}{\pi^2}+\frac{2}{3}$$

$$=1+\frac{10}{\pi^2}\;,$$

as was employed to obtain Eq. (17a) in the form cited in the text.

$$- \frac{1}{\pi} \eta^3 n^2 \left[\left(1 + \frac{4}{\pi^2} - x^2\right) \cos \frac{\pi}{2} x + \frac{2}{\pi} \cdot x \cdot \sin \frac{\pi}{2} x \right] .^{9f,g} \qquad (17b)$$

The form of the solution given by Eq. (17b) is such as to suggest

$$Z(1) : Z(-1) \doteq - \frac{1 - \frac{1}{2}\eta - \frac{2}{\pi^2} \eta^3 n^2}{1 + \frac{1}{2}\eta + \frac{2}{\pi^2} \eta^3 n^2} , \qquad (17c)$$

and

$$Z(o) : Z(-1) \doteq \frac{1}{\pi}\eta + \frac{1}{\pi}\left(1 + \frac{4}{\pi^2}\right) \eta^3 n^2 \qquad (17d)$$

$$\doteq 0.318310\, \eta + 0.447316\, \eta^3 n^2 \ . \qquad (17d')$$

[9f] The Fourier development

$$\frac{\pi^2}{8} \cdot x \cdot \sin \frac{\pi}{2} x + \frac{\pi}{4} \cos \frac{\pi}{2} x = 1 + 2 \sum_{k=1}^{\infty} (-)^k \frac{1}{(4k^2 - 1)^2} \cos k\pi x$$

is employed in obtaining the coefficient of η in Eq. (17b) of the text.

[9g] The Fourier development

$$- \frac{\pi^3}{32} x^2 \cos \frac{\pi}{2} x + \frac{\pi}{8} \left(1 + \frac{\pi^2}{4}\right) \cos \frac{\pi}{2} x + \frac{\pi^2}{16} \cdot x \cdot \sin \frac{\pi}{2} x$$

$$= 1 - 2 \sum_{k=1}^{\infty} (-)^k \frac{4k^2 + 1}{(4k^2 - 1)^3} \cos k\pi x$$

is likewise employed in obtaining the coefficient of $\eta^3 n^2$ in Eq. (17b) of the text.

The results described in the sub-section (Sect.III(a) may be considered applicable for $\eta^3 n^2 << 1$; of equal or greater interest, however, are the results discussed below for $\eta^3 n^2 > 1$.

(b) Character of Solution When $\eta^3 n^2$ is Large

In cases for which $\eta << 1$ but $\eta^3 n^2$ is not small, the main features of the solutions to Eq. (5) may be obtained conveniently by consideration of the simpler equation

$$\frac{d^2 Z}{dx^2} + \left[\delta + 2\,\eta^3 n^2 x\right] Z = 0 \quad . \tag{18}$$

Solutions of this approximate equation, (18), may be written explicitly in terms of Bessel and Neumann functions of order $\frac{1}{3}$ or equivalently, in terms of Bessel functions of order $\pm\frac{1}{3}$:

$$Z = \xi^{1/2} \left[A J_{1/3}\left(\frac{\xi^{3/2}}{3\eta^3 n^2}\right) + B J_{-1/3}\left(\frac{\xi^{3/2}}{3\eta^3 n^2}\right) \right] , \tag{19}$$

where

$$\xi \equiv \delta + 2\,\eta^3 n^2 x \; . \tag{20}$$

To the extent that Eq. (20) adequately represents the solution to the exact differential Eq. (5), the desired eigenvalues, δ , may be determined by solution of

$$J_{1/3}(y_+)\, J_{-1/3}(y_-) - J_{1/3}(y_-) J_{-1/3}(y_+) = 0, \tag{21a}$$

or

$$J_{2/3}(y_+)\, J_{-2/3}(y_-) - J_{2/3}(y_-)\, J_{-2/3}(y_+) = 0 \tag{21b}$$

for the Dirichlet or Neumann boundary conditions respectively, where

$$y_+ \equiv \frac{(\delta + 2\eta^3 n^2)^{3/2}}{3\eta^3 n^2} \quad , \qquad (22a)$$

$$y_- \equiv \frac{(\delta - 2\eta^3 n^2)^{3/2}}{3\eta^3 n^2} \quad , \qquad (22b)$$

and the solutions would be sought by trial, aided by published tables of $J_{\pm 1/3}$ and $J_{\pm 2/3}$.[10, 11] In the event that $\delta < 2\eta^3 n^2$, Eqs. (21a, b) may be expressed more conveniently in terms of the associated Bessel functions as

$$J_{1/3}(t_+)\, I_{-1/3}(t_-) + I_{1/3}(t_-)\, J_{-1/3}(t_+) = 0 \qquad (23a)$$

or

$$J_{2/3}(t_+)\, I_{-2/3}(t_-) - I_{2/3}(t_-)\, J_{-2/3}(t_+) = 0 \quad , \qquad (23b)$$

for the Bessel and Neumann conditions respectively, and with

$$t_+ \equiv \frac{(2\eta^3 n^2 + \delta)^{3/2}}{3\eta^3 n^2} \quad , \qquad (24a)$$

$$t_- \equiv \frac{(2\eta^3 n^2 - \delta)^{3/2}}{3\eta^3 n^2} \quad . \qquad (24b)$$

In any case, of course, characteristic values of δ for solutions to Eq. (18) must necessarily be somewhat less negative than $-2\eta^3 n^2$ in order that the coefficient of Z in Eq. (18) be positive for some values of x in the interval $-1 \leq x \leq 1$.

For the purpose of obtaining convenient approximate formulas for the characteristic values of δ, it is useful to note that for $\eta^3 n^2$ somewhat

---

[10] National Bureau of Standards Computation Laboratory, Tables of Bessel Functions of Fractional Order, (Columbia University Press, New York, 1948-49), vols. I and II.

[11] G. N. Watson, Theory of Bessel Functions, (Cambridge University Press and MacMillan Co., New York, 1948), Ed. 2. Note: $Y_{1/3} = \left[J_{1/3} - 2J_{-1/3}\right] / \sqrt{3}$.

greater than unity (f. ex., for $\eta^3 n^2 > 6$) the argument t_- which appears in Eqs. (23a, b) becomes sufficiently large that these equations effectively reduce to

$$J_{1/3}(t_+) + J_{-1/3}(t_+) = 0, \tag{25a}$$

or

$$J_{2/3}(t_+) - J_{-2/3}(t_+) = 0 \quad , \tag{25b}$$

respectively. This simplification, which very materially assists the estimation of δ, corresponds to setting A = B in Eq. (19) for the solution Z. Under these circumstances, then, the solution of interest is taken as substantially of the form

$$Z \dot{\propto} \begin{cases} \xi^{1/2}\left[J_{1/3}\left(\dfrac{\xi^{3/2}}{3\eta^3 n^2}\right) + J_{-1/3}\left(\dfrac{\xi^{3/2}}{3\eta^3 n^2}\right)\right] , \text{ for } \xi \geq 0, & (26a) \\ \dfrac{\sqrt{3}}{2}\, i^{4/3} |\xi|^{1/2} H_{1/3}^{(1)}\left(i\dfrac{|\xi|^{3/2}}{3\eta^3 n^2}\right) , \text{ for } \xi \leq 0 , & (26b) \end{cases}$$

in which the first Hankel function becomes sufficiently small at x = -1 as to satisfy adequately the boundary condition normally imposed at that point. The Eqs. (25a) or (25b) for the characteristic values δ may then be considered as arising simply by application of the desired boundary condition at x = +1. A reasonably good description of the solution Z(x) for $x < -\dfrac{\delta}{2\eta^3 n^2}$ --that is, for $\xi < 0$--is afforded by replacing Eq. (26b) by its asymptotic form,

$$Z \approx \frac{3}{\sqrt{2\pi}}\, \frac{\eta^{3/2} n}{|\xi|^{1/4}} \exp\left(-\frac{|\xi|^{3/2}}{3\eta^3 n^2}\right) \qquad (\xi < 0) , \tag{27a}$$

and, with less accuracy, the Eq. (26a) for $\xi > 0$ may likewise be written

$$Z \approx \frac{3\sqrt{2/\pi}\;\eta^{3/2}\,n}{\xi^{1/4}} \cos\left(\frac{\xi^{3/2}}{3\eta^{3}n^{2}} - \frac{\pi}{4}\right) \quad (\xi > 0)\,. \tag{27b}$$

These asymptotic forms, Eqs. (27a, b), may alternatively be obtained directly by use of the W-K-B procedure Ref. 8, Sect. 28, pp. 184 ff .[‡]

Solution of Eqs. (25a) and (25b) by aid of published tables[10, 11] leads to the following simple estimates for the characteristic values δ, applicable in cases for which $\eta^3 n^2$ is at least somewhat large in comparison to unity:

For the first Neumann root: $\delta \cong -2\,\eta^3 n^2 + 1.61724\,\eta^2 n^{4/3}$, (28a)

For the first Dirichlet root: $\delta \cong -2\,\eta^3 n^2 + 3.71151\,\eta^2 n^{4/3}$, (28b)

For the second Neumann root: $\delta \cong -2\,\eta^3 n^2 + 5.15619\,\eta^2 n^{4/3}$. (28c)

The numerical factors associated with $\eta^2 n^{4/3}$ in Eqs. (28a, b) are seen, as could be expected, to be twice the numerical coefficients given in series developments for the first maximum and first zero of J_n when n is large[12] [Ref. 11, Sect. 15.83, p. 521; Ref. 12, Sect. VIII. 3.6, p. 143]. The values of $\eta^3 n^2$, at which $\delta = 0$ for the first Dirichlet root and for the second Neumann root, also may be estimated directly from Eqs. (23a) and (23b), again by reference to published tables,[10, 11] as 6.412 and 17.133, respectively, which do not differ greatly from the values suggested by the approximate Eqs. (28b, c).

The nature of the characteristic solutions is such that, for large values

---

[‡] The authors are indebted to Dr. A. M. Sessler for calling attention to this point.

[12] E. Jahnke and F. Emde, Funktionentafeln, (Dover Publications, New York, 1945), Ed. 4.

of $\eta^3 n^2$, the magnitude of the solutions is large only for x near +1. A more quantitative statement concerning this feature can be made by reference to a universal curve which is constructed by plotting (Fig. 1) a solution of the form of Eqs. (26a, b),

$$Z \overset{\sim}{\propto} v^{1/2}\left[J_{1/3}(v^{3/2}) + J_{-1/3}(v^{3/2})\right] \ \underline{\text{vs}}.\ v \ , \tag{29}$$

with v regarded as linearly dependent upon x in accordance with the relation

$$v \equiv \frac{\delta + 2\eta^3 n^2 x}{3^{2/3}\eta^2 n^{4/3}} \ . \tag{30}$$

The various characteristic solutions of interest may then be considered as depicted by the curve of Fig. 1 with the $x = 1$ boundary located at A ($v = 0.7775$), B ($v = 1.7843$), or C ($v = 2.4788$), corresponding respectively to the three roots listed in Eqs. (28a, b, c). This representation will be substantially correct if $\eta^3 n^2$ is sufficiently large that the boundary $x = -1$ lies well to the left in Fig. 1 in a region where the function has become quite small in accord with the Hankel-function form of Eq. (29) appropriate for $v < 0$. The function plotted in Fig. 1 is seen to be less than $\frac{1}{e}$ of its maximum value for $v < -0.52$ and thus becomes small in this sense for displacements

$$\Delta v = 1.3,\ 2.3,\ 3.0$$

to the left of the points A, B, C, respectively. The corresponding annular regions, within which the solution Z assumes prominence, are then, delimited by

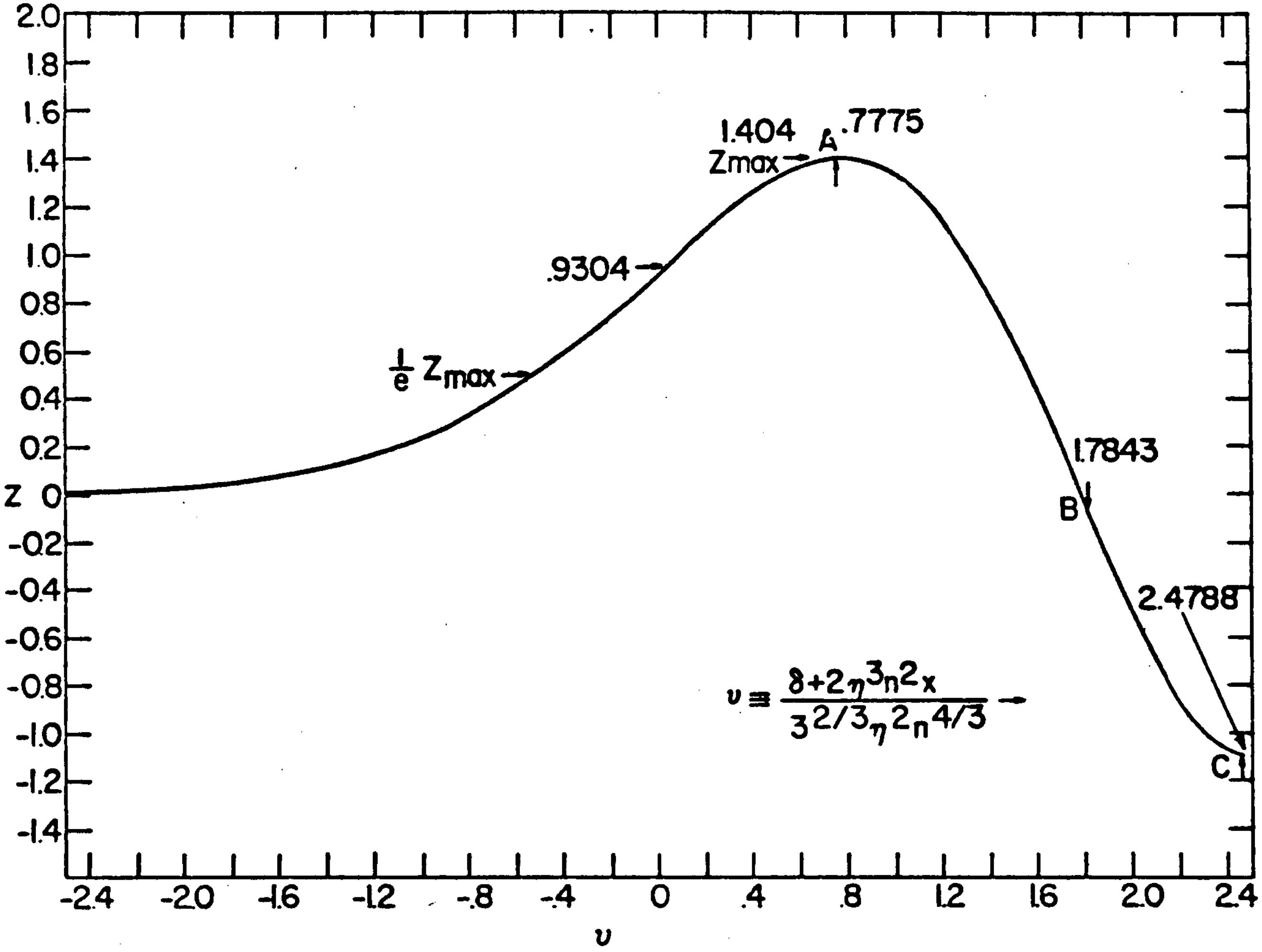

FIGURE 1. UNIVERSAL CURVE, PLOTTED FROM EQN. (29)

$$\left(1 - \frac{1.35}{\eta\, n^{2/3}}\right) \leq x \leq 1 \qquad \text{(for the first Neumann eigenfunction),} \qquad (31a)$$

$$\left(1 - \frac{2.39}{\eta\, n^{2/3}}\right) \leq x \leq 1 \qquad \text{(for the first Dirichlet eigenfunction),} \qquad (31b)$$

and

$$\left(1 - \frac{3.12}{\eta\, n^{2/3}}\right) \leq x \leq 1 \qquad \text{(for the second Neumann eigenfunction)} \quad . \qquad (31c)$$

IV. COMPUTATIONAL RESULTS

The differential Eq. (5), suitably scaled, was integrated with the CYCLONE digital computer at Iowa State University by use of the Runge-Kutta process.[13, 14] The primary purpose of the work was to determine characteristic values of δ and to tabulate the corresponding functions for solutions satisfying the Neumann or Dirichlet boundary conditions at $x = \pm 1$, for a number of representative values of n and for η given in turn the values 0.001, 0.01, and 0.1. In each case the value of δ (or in two instances the value of n) was adjusted by trial, to give solutions of the desired form, conforming to the prescribed boundary conditions.

In performing the integration a larger number of steps was employed to traverse the interval $-1 \leq x \leq 1$ in cases in which $\eta^3 n^2$ was large since more rapid changes of the function occur in certain portions of that interval in such cases. The effect of truncation error was found by tests

---

[13] S. Gill, Proc. Cambridge Phil. Soc. 47, 96-108 (1951).

[14] D. J. Wheeler, "Solution of a System of Ordinary Differential Equations", University of Illinois Computer Laboratory sub-routine F 1-114, (University of Illinois, Urbana, 1953).

in which the interval size was halved, to be sufficiently small that use of the finer interval only affected the final value of the function or its derivative (in the Dirichlet or Neumann cases, respectively) by less than 10^{-6} of the maximum value and the consequent errors in δ could thus be judged when tabulating the results of the computations.

In addition to the tabulation of results from the computations outlined above, an opportunity was taken to make a limited number of checks of the approximate analytic results described in Sect. III. For the purpose of obtaining tables of certain integrals of interest in physical application of the eigensolutions, a special series of runs was also made with η assigned the small value 0.0001 and $\eta^3 n^2$ given various values in the interesting range extending from 1/2 to 20.

We make below, first a brief comparison between some of the computational results and the analytic theory for the form of the eigenfunctions, following which the main body of numerical results is presented in tabular and graphical form.

(a) Computational Checks of Theoretical Results for the Eigenfunctions

To permit a comparison of the computational results with the theoretical expressions for the form of the characteristic solutions when $\eta^3 n^2$ is small, Table I lists $Z(+1)/Z(-1)$ and $Z'(o)/Z(o)$ for the first Neumann solutions, Table II gives $Z'(+1)/Z'(-1)$ and $Z'(o)/Z(o)$ for the first Dirichlet solution, and Table III contains $Z(+1)/Z(-1)$ and $Z(o)/Z(-1)$ for the second Dirichlet solution, for examples in which η assumes the values 0.1, 0.01,

Table I. Comparison of observed and theoretical eigenfunctions for first Neumann solution.

η	$\eta^3 n^2$	$Z(+1)/Z(-1)$		$Z'(o)/Z(o)$	
		Computer	Theory	Computer	Theory
0.1	0.1	1.14303	1.14286	0.0997	0.1000
0.01	0.04	1.054769	1.054795	0.03998	0.04000
0.001	0.1	1.14249	1.14286	0.09986	0.10000
0.0001	0.5	1.9205	2.0000	0.4841	0.5000

Table II. Comparison of observed and theoretical eigenfunctions for first Dirichlet solution.

η	$\eta^3 n^2$	$Z'(+1)/Z'(-1)$		$Z'(o)/Z(o)$	
		Computer	Theory	Computer	Theory
0.1	0.1	-0.94213	-0.94195	-0.02022	-0.02026
0.01	0.04	-1.0062312	-1.0062307	+0.00689435	+0.00689431
0.001	0.1	-1.040319	-1.040326	+0.0292346	+0.0292358
0.0001	0.5	-1.2244	-1.2254	+0.14851	+0.14863

Table III. Comparison of observed and theoretical eigenfunctions for second-Neumann solution.

η	$\eta^3 n^2$	Z(+1)/Z(-1)		Z(o)/Z(-1)	
		Computer	Theory	Computer	Theory
0.1	0.1	-0.8697	-0.8687	0.0717	0.0766
0.01	0.04	-0.974146	-0.974128	0.0208	0.0211
0.001	0.1	-0.95944	-0.95932	0.0441	0.0450
0.0001	0.5	-0.8281	-0.8159	0.199	0.224

0.001, and 0.0001. The theoretical results listed in Tables I-III are calculated from Eqs. (13c, d), (15c, d), and (17c, d) of Sect. III(a).

The most striking feature of the solutions for large values of $\eta^3 n^2$ is the localization of such solutions to a region close to $x = 1$. Table IV presents values of the coordinate x at which the solution equals $\frac{1}{e}$ of its maximum value as determined computationally and as calculated from Eqs. (31a, c) of Sect. III(b) for $\eta = 0.0001$ and $\eta^3 n^2 = 20$.

Table IV. Coordinate at which the characteristic solutions equal $\frac{1}{e}$ of their maximum value for $\eta = 0.0001$ and $\eta^3 n^2 = 20$.

Solution	x	
	Computer	Theory
1st Neumann	0.509	0.503
1st Dirichlet	0.123	0.120
2nd Neumann	-0.143	-0.149

(b) Tabulation of the Eigenvalues and Characteristic Solutions

The computational results for the eigenvalues for a series of values of n and with η given the values 0.001, 0.01, and 0.1, are listed in Table V. Included in Table V, for comparative purposes, are also characteristic values of δ for $\eta = 1$, obtained from published tables[15] of Bessel functions of the first kind. Entries are also given for $\eta = 0.001$, which indicate the values of n at which the values of δ for the first Dirichlet solution and for the second Neumann solution pass through zero (n = 80110 and 130953, respectively); from the discussion of Sect.III(b) it was to be expected that with η small, these roots would occur when $\eta^3 n^2 = 6.412$ and 17.133, or at $n \cong 8.007 \times 10^4$ and 1.309×10^5 in the case $\eta = 0.001$. The general dependence of the eigenvalues on n is depicted in Fig. 2, in which hyperbolic scales[16] are used for the ordinates and abscisae, in order to provide a substantially linear scale near the origin.

The character of the solutions associated with the computational results summarized in Table V, is described by the reproductions of the teleprinter output from the computer, which are included with this report, and in the accompanying graphs (Figs. 3-20) of selected eigenfunctions.

---

[15] Harvard University Computation Laboratory, <u>Tables of Bessel Functions of the First Kind</u>, (Harvard University Press, Cambridge, Massachusetts, 1948), vols. III, IV, V, VII, & IX.

[16] R. Legros, <u>Ann. phys.</u> (Sér. 12) <u>1</u>, 335-356 (1946).

Table V. Values of δ for the first Neumann eigenvalue, the first Dirichlet eigenvalue, and the second Neumann eigenvalue.

η :		η = 0.001			η = 0.01			η = 0.1			η = 1.0[a]	
Root :	N_1	D_1	N_2	N_1	D_1	N_2	N_1	D_1	N_2	N_1	D_1	N_2
n=0	0	2.4674011	2.46740209	0	2.467376	2.467476	0	2.4648915	2.4749309	(0)	1.445797	3.670493
1/2	0	"	"	"	"	"	.00000839	2.4649013	2.474989	0.089633	2.217401$_1$	5.049703
1	0	"	"	"	"	"	0.0000330	2.4649308	2.4751343	-0.152511	2.670493	6.106071
2	0	"	"	"	"	"	0.0001255	2.4650481	2.4757499	-1.667909	2.593654	7.243048
5	0	"	"	"	"	"	0.0005019	2.4658332	2.4802714	-14.709967	-5.765268	2.666867
10	0	"	"	"	2.467377	2.467478	-0.0019893	2.4681254	2.4994189	-65.361612	-47.614970	-32.367035
20	0	2.4674021	"	.0000012	2.467378	2.467484	-0.0680405	2.4693426	2.6189112	-276.5774	-238.492	-208.010
30							-0.335704	2.4435640	2.9276509			
40							-0.905569	2.3513268	3.4493650			
50	0	2.4674011	2.46740210	.0000050	2.467386	2.467529	-1.799205	2.143523	4.0878274			
75							-5.418144	0.8024951	5.142091			
100	0	2.4674011	2.46740211	-0.000020	2.467409	2.467720	-11.009312	-2.103247	4.361139			
150							-28.210824	-13.285380	-2.541564			
200	0.00000002	2.4674011	2.46740217	-0.000720	2.467421	2.468957	-53.56333	-31.956122	-16.514506			
500	0.00000004	2.4674015	2.4674026	-0.032070	2.463969	2.498479						
1000	-0.00000020	2.4674014	2.4674046	-0.456025	2.401502	2.835214						
1500				-1.717081	2.130264	3.657827						
2000	-0.00000720	2.4674015	2.4674169	-3.876713	1.441630	4.535002						
2500				-6.921675	0.145494	4.843058						
3000				-10.857817	-1.875544	4.303889						
4000				-21.440133	-8.287472	0.828077						
5000	-0.00032495	2.467367	2.4677163	-35.682279	-17.993822	-5.740178						
10000	-0.005290	2.466738	2.4718184									
20000	-0.082838	2.456331	2.533433									
50000	-2.030430	2.042788	3.787091									
75000	-6.127374	0.515508	4.811675									
80110		0										
100000	-12.476797	-2.763631	3.907135									
130953			0									
150000	-32.066830	-15.395587	-3.890509									
200000	-60.999918	-36.537911	-19.657327									

---

[a] From published tables.[15]

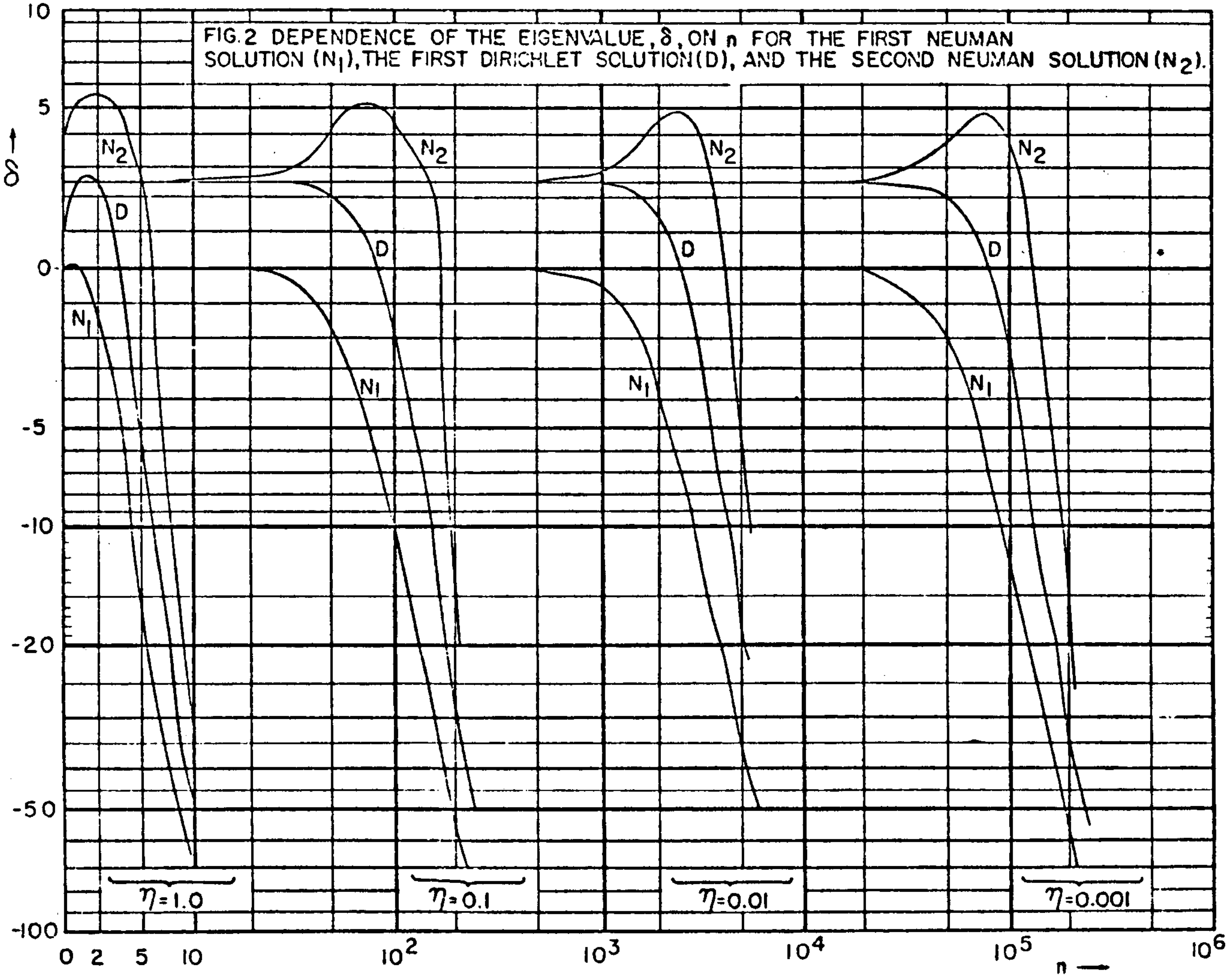

FIG. 2 DEPENDENCE OF THE EIGENVALUE, δ, ON n FOR THE FIRST NEUMAN SOLUTION (N_1), THE FIRST DIRICHLET SOLUTION (D), AND THE SECOND NEUMAN SOLUTION (N_2).

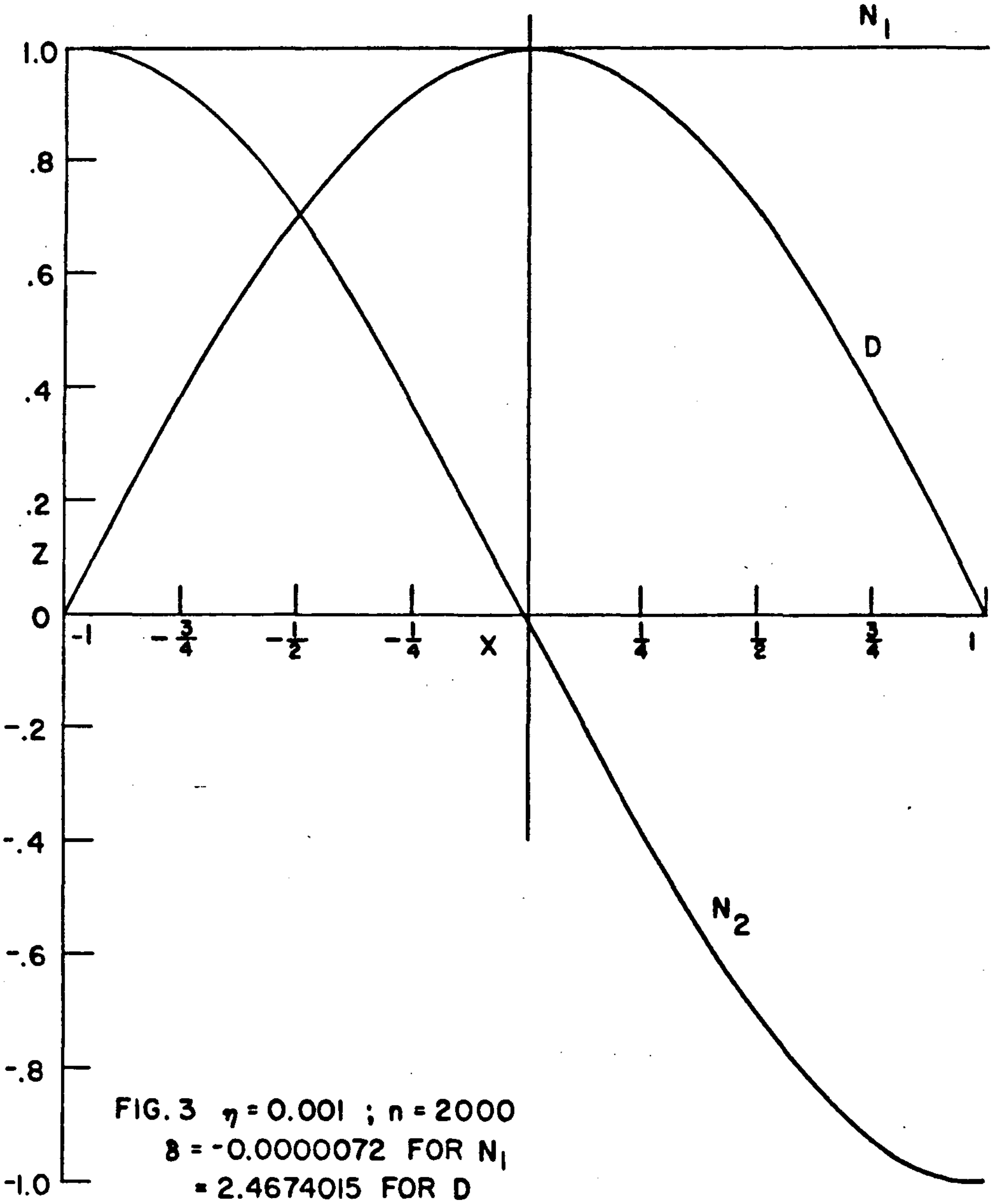

FIG. 3 $\eta = 0.001$; $n = 2000$
$\delta = -0.0000072$ FOR N_1
$= 2.4674015$ FOR D
$= 2.4674169$ FOR N_2

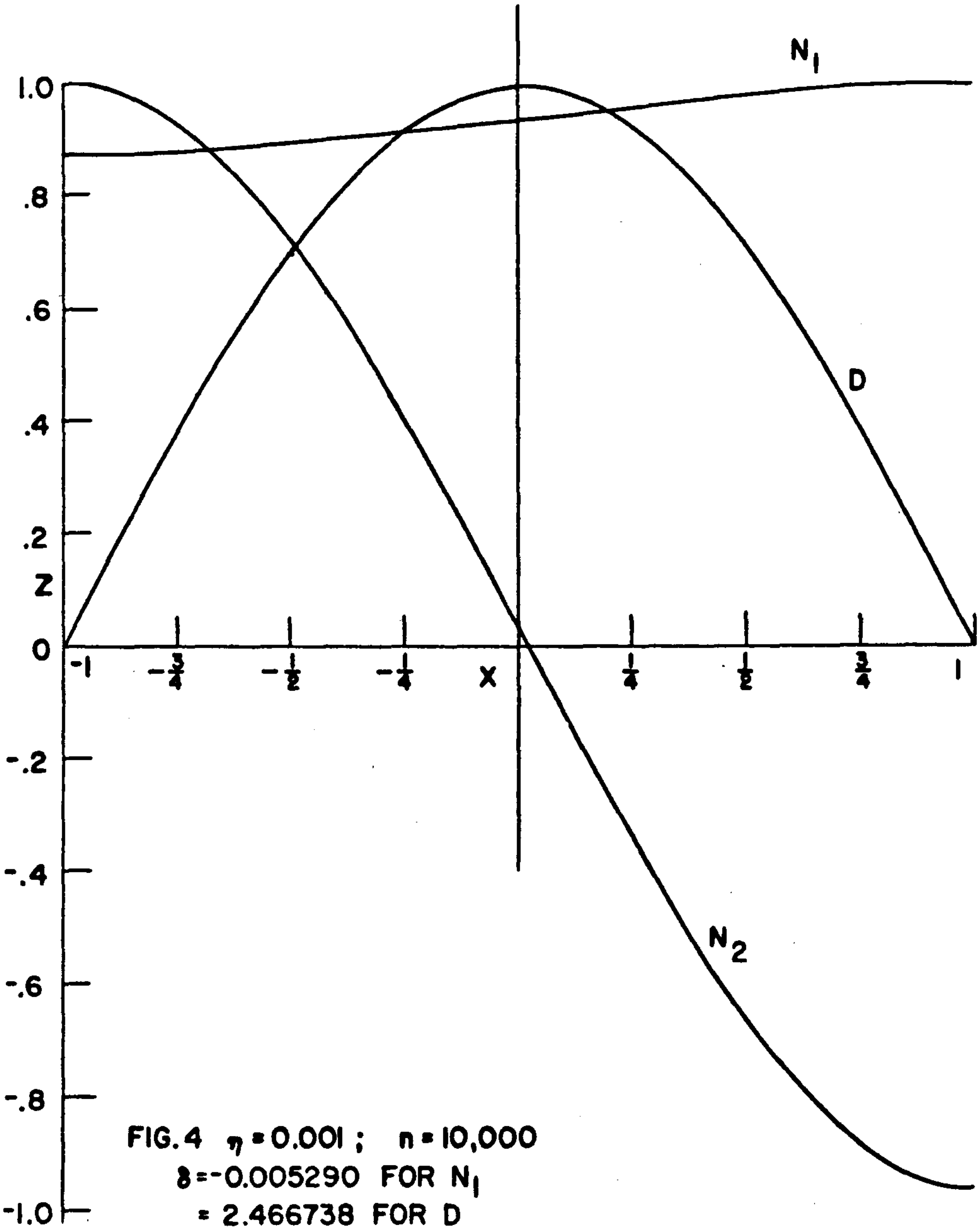

FIG. 4 $\eta = 0.001$; $n = 10{,}000$

$\delta = -0.005290$ FOR N_1

$= 2.466738$ FOR D

$= 2.4718184$ FOR N_2

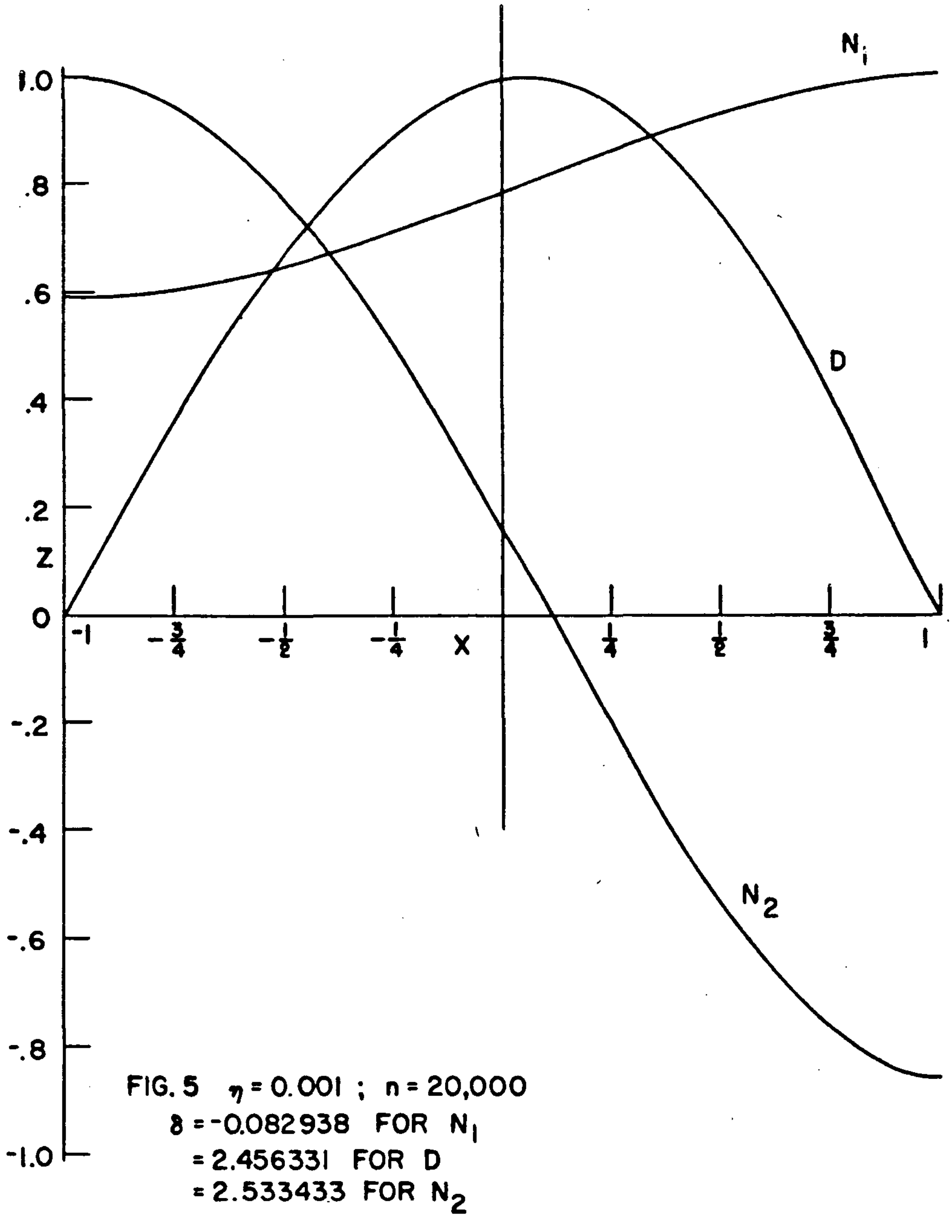

FIG. 5 $\eta = 0.001$; $n = 20{,}000$
$\delta = -0.082938$ FOR N_1
$= 2.456331$ FOR D
$= 2.533433$ FOR N_2

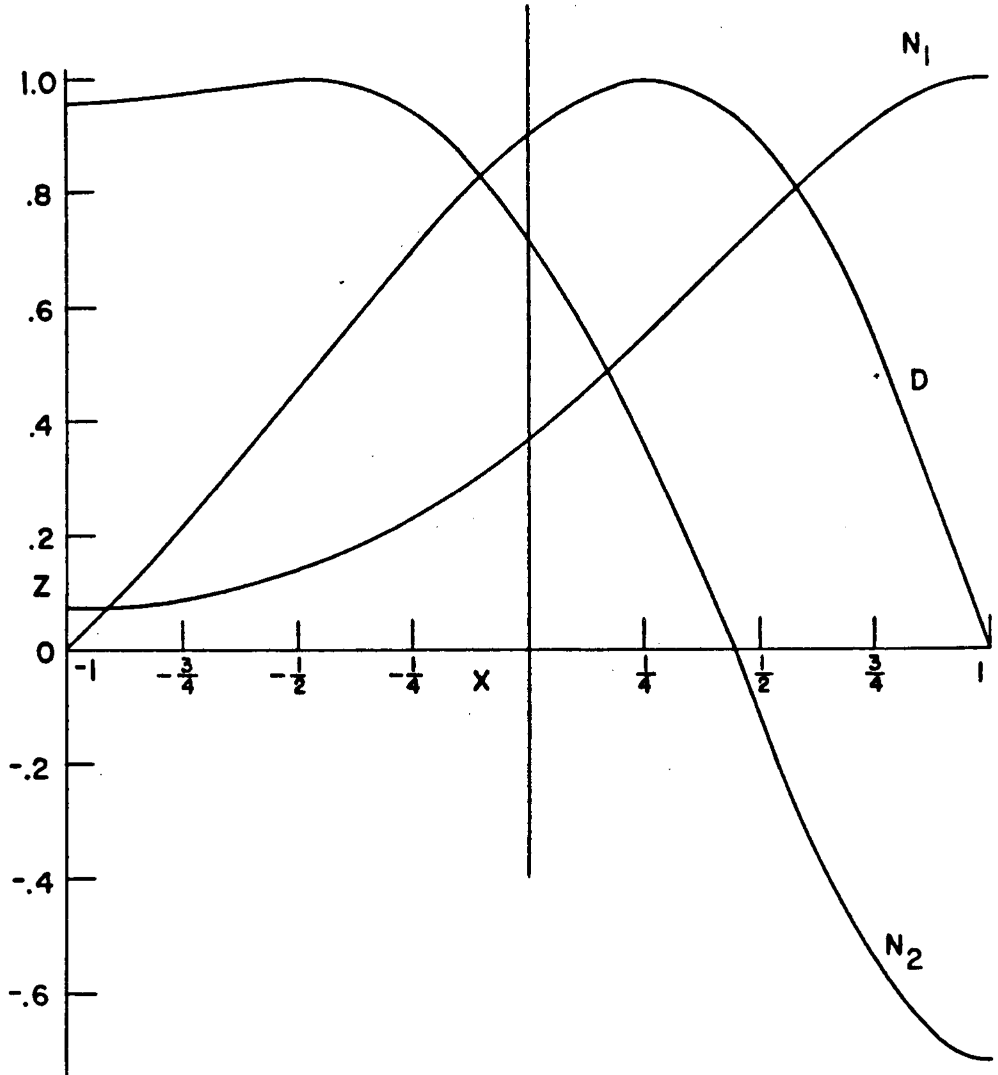

FIG. 6 $\eta = 0.001$; $n = 50{,}000$
$\delta = -2.030430$ FOR N_1
$= 2.042788$ FOR D
$= 3.787091$ FOR N_2

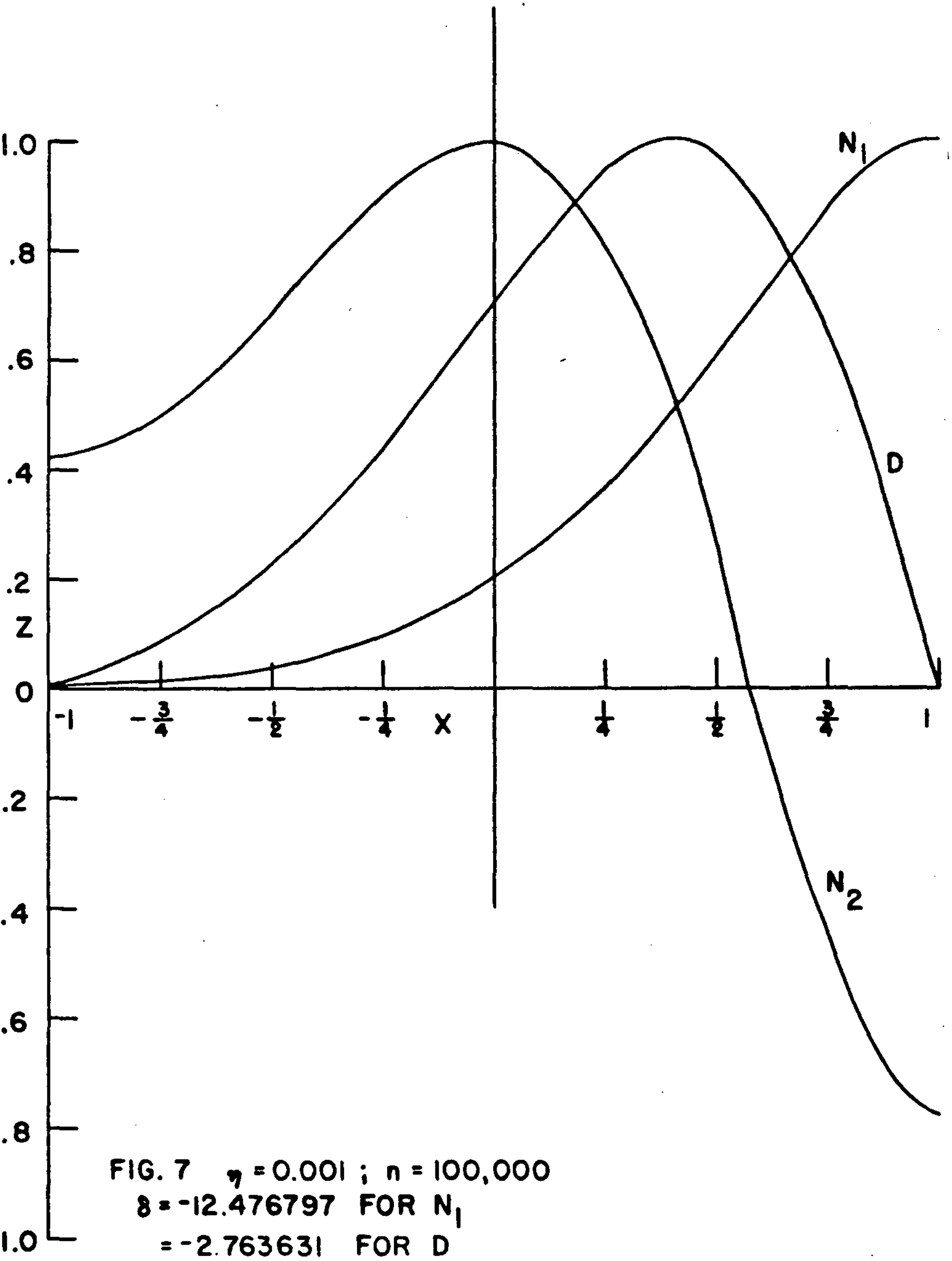

FIG. 7 $\eta = 0.001$; $n = 100{,}000$
$\delta = -12.476797$ FOR N_1
$= -2.763631$ FOR D
$= 3.907135$ FOR N_2

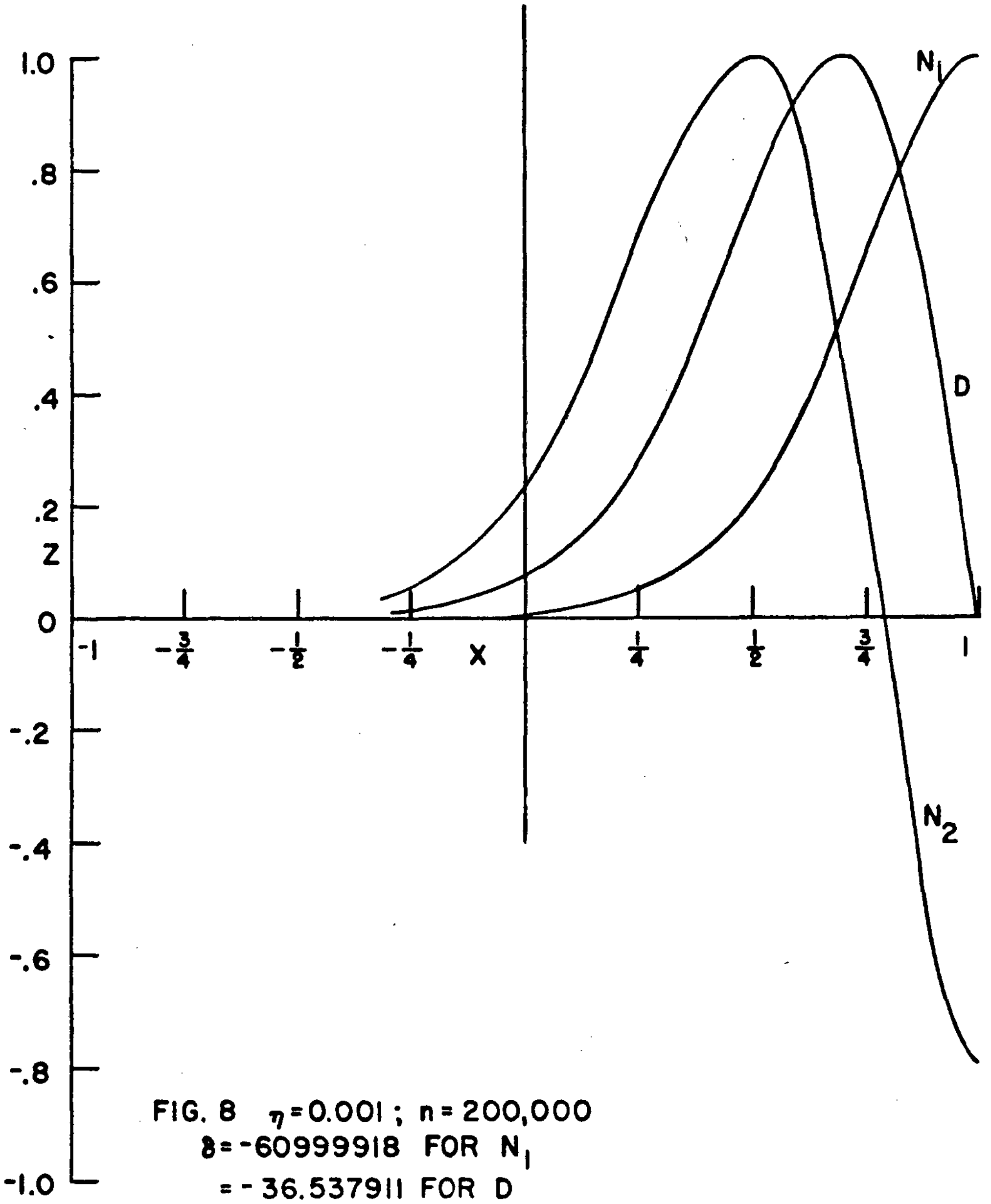

FIG. 8 $\eta = 0.001$; $n = 200{,}000$
$\delta = -60999918$ FOR N_1
$= -36.537911$ FOR D
$= 19.657327$ FOR N_2

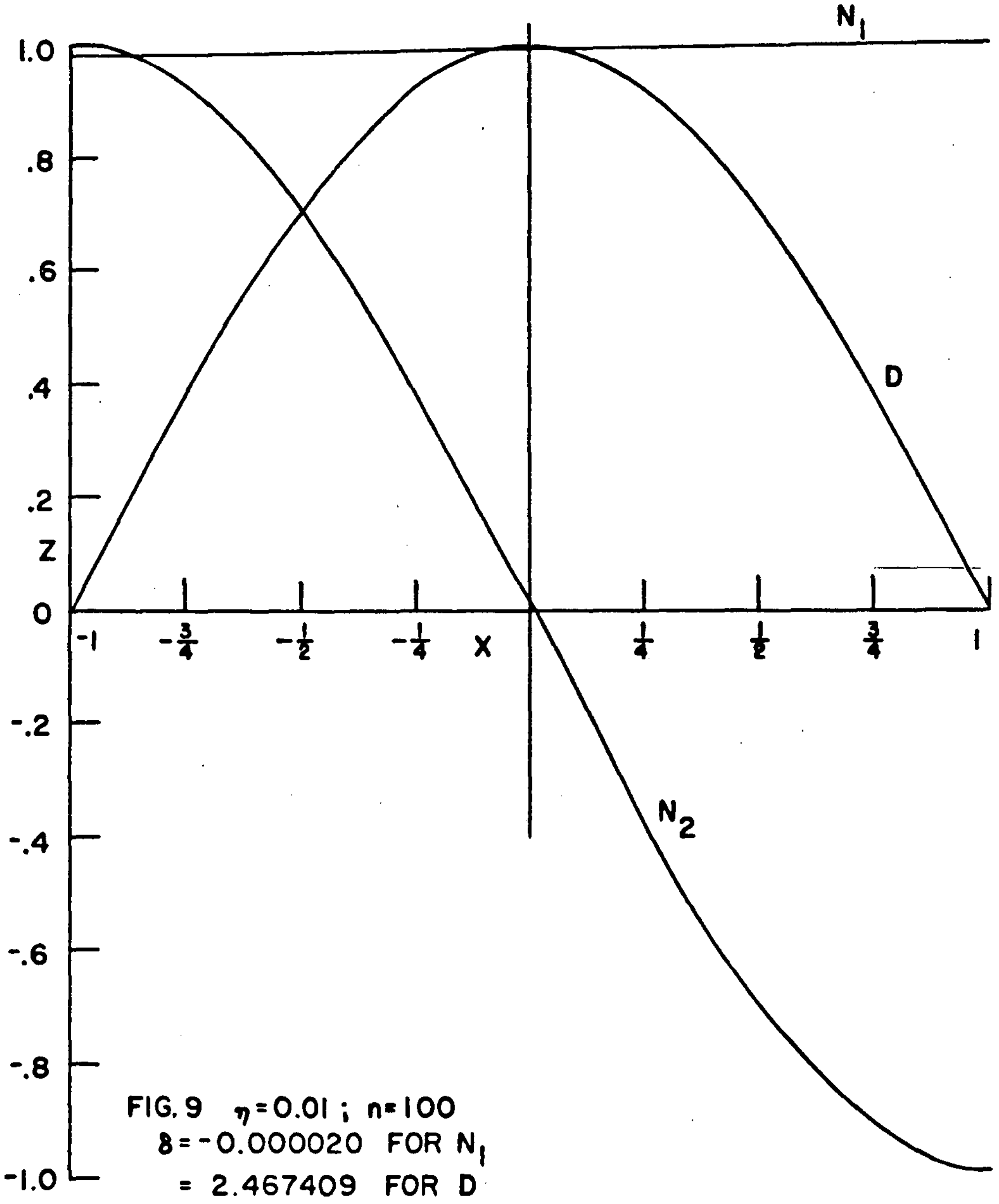

FIG. 9 $\eta = 0.01$; $n = 100$
$\delta = -0.000020$ FOR N_1
$= 2.467409$ FOR D
$= 2.467720$ FOR N_2

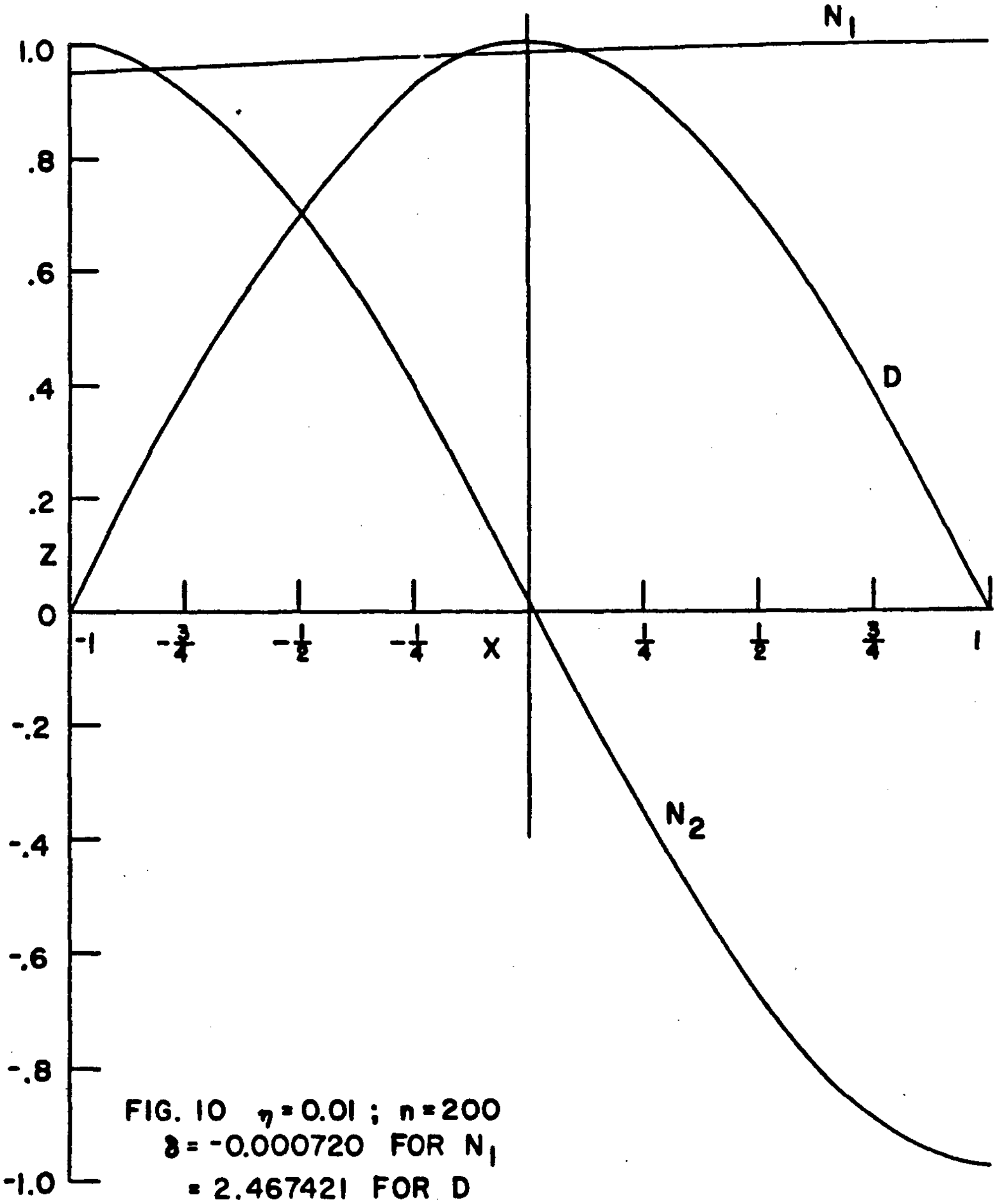

FIG. 10 $\eta = 0.01$; $n = 200$
$\delta = -0.000720$ FOR N_1
$= 2.467421$ FOR D
$= 2.468957$ FOR N_2

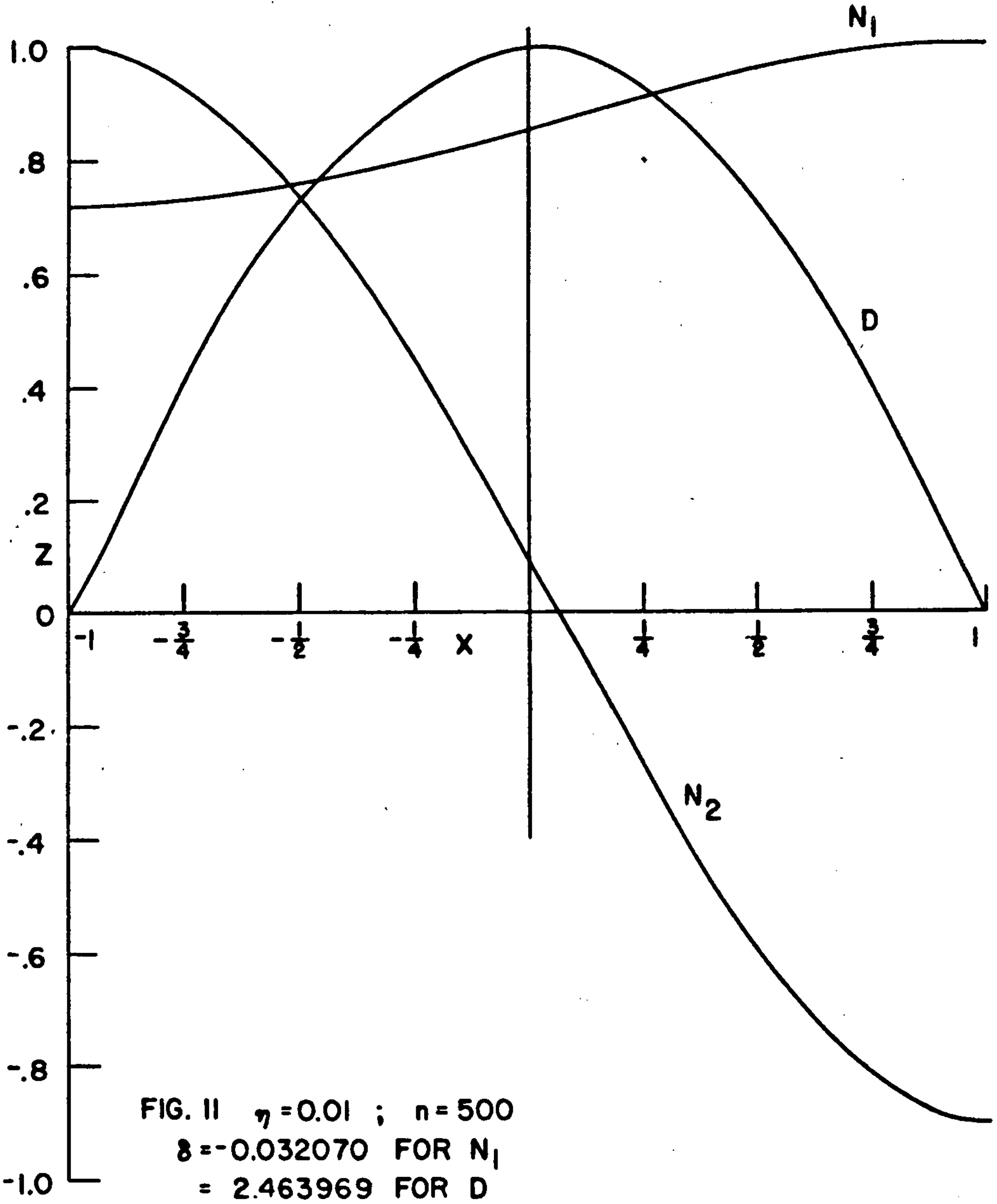

FIG. 11 $\eta = 0.01$; $n = 500$
$\delta = -0.032070$ FOR N_1
$= 2.463969$ FOR D
$= 2.498479$ FOR N_2

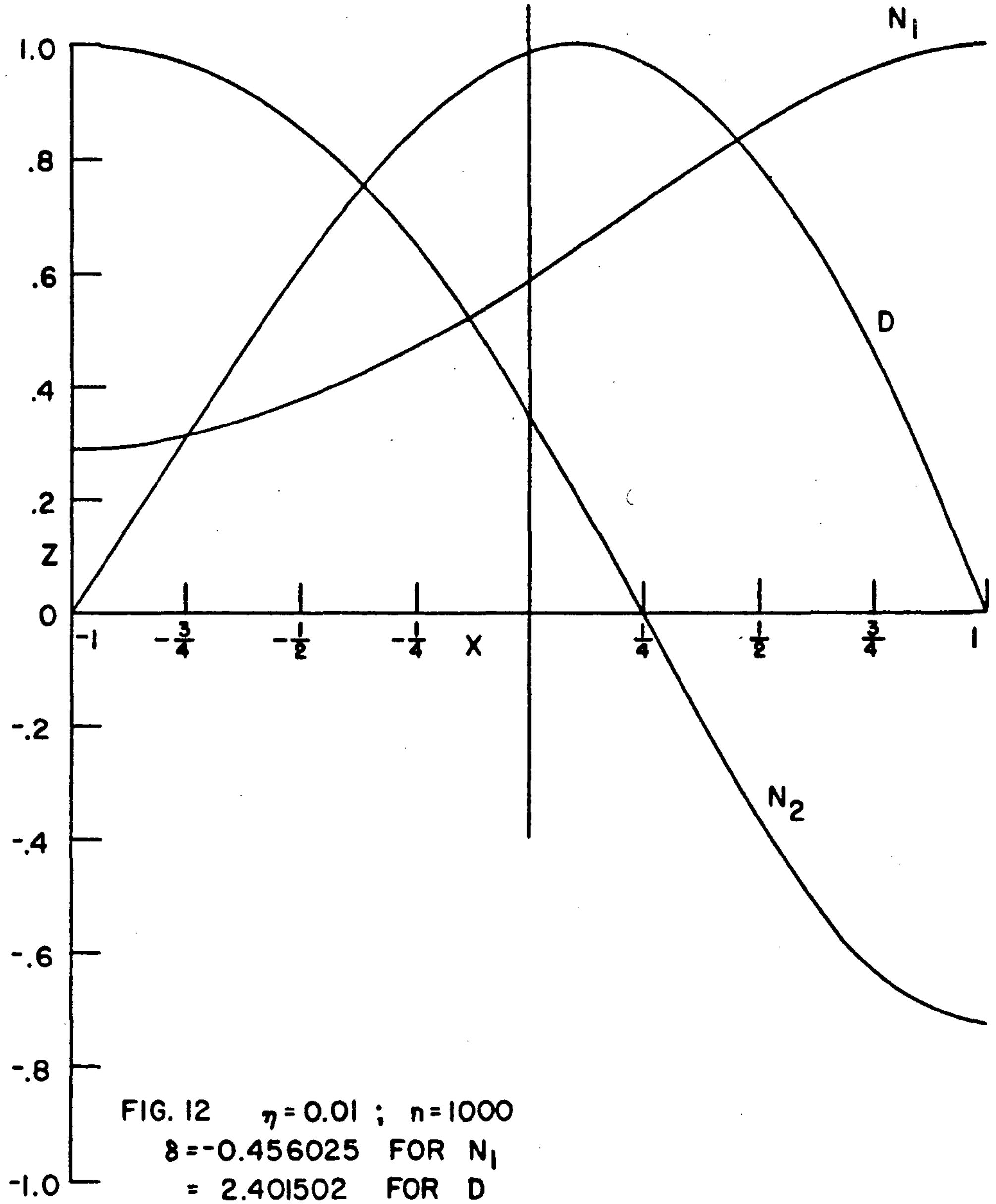

FIG. 12 $\eta = 0.01$; $n = 1000$
$\delta = -0.456025$ FOR N_1
$= 2.401502$ FOR D
$= 2.835214$ FOR N_2

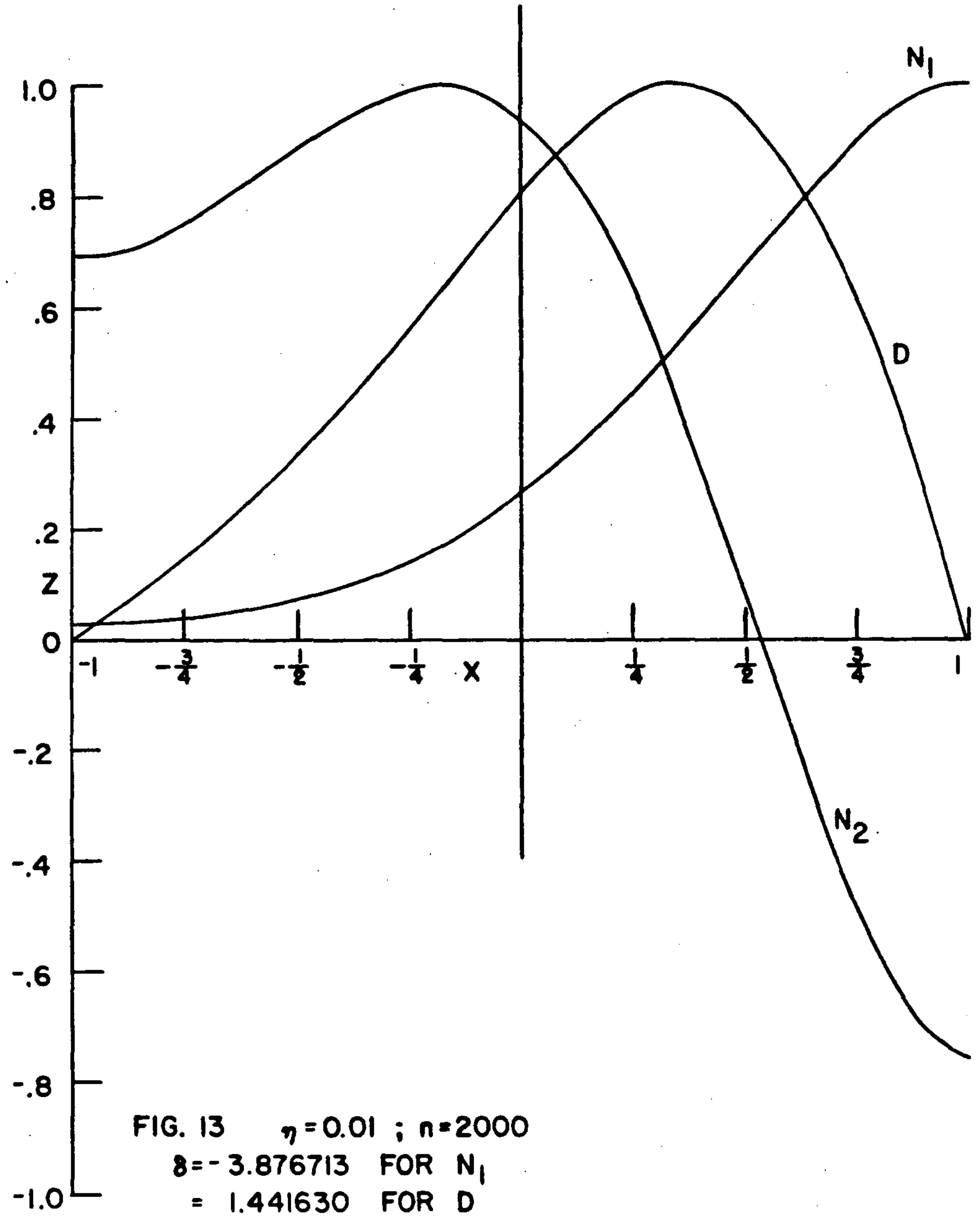

FIG. 13 $\eta = 0.01$; $n = 2000$
$\delta = -3.876713$ FOR N_1
$= 1.441630$ FOR D
$= 4.535002$ FOR N_2

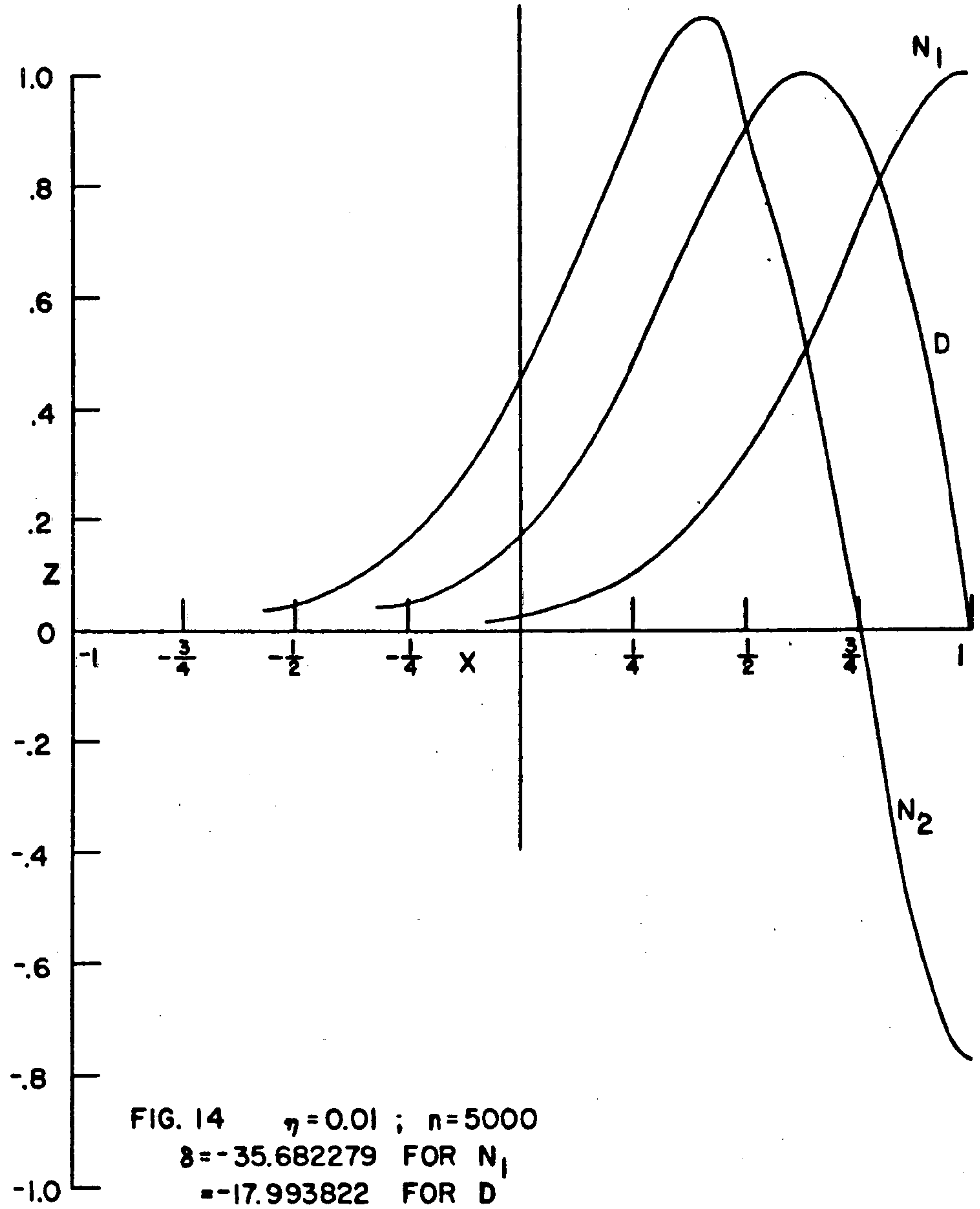

FIG. 14 $\eta = 0.01$; $n = 5000$
$\delta = -35.682279$ FOR N_1
$= -17.993822$ FOR D
$= -5.740178$ FOR N_2

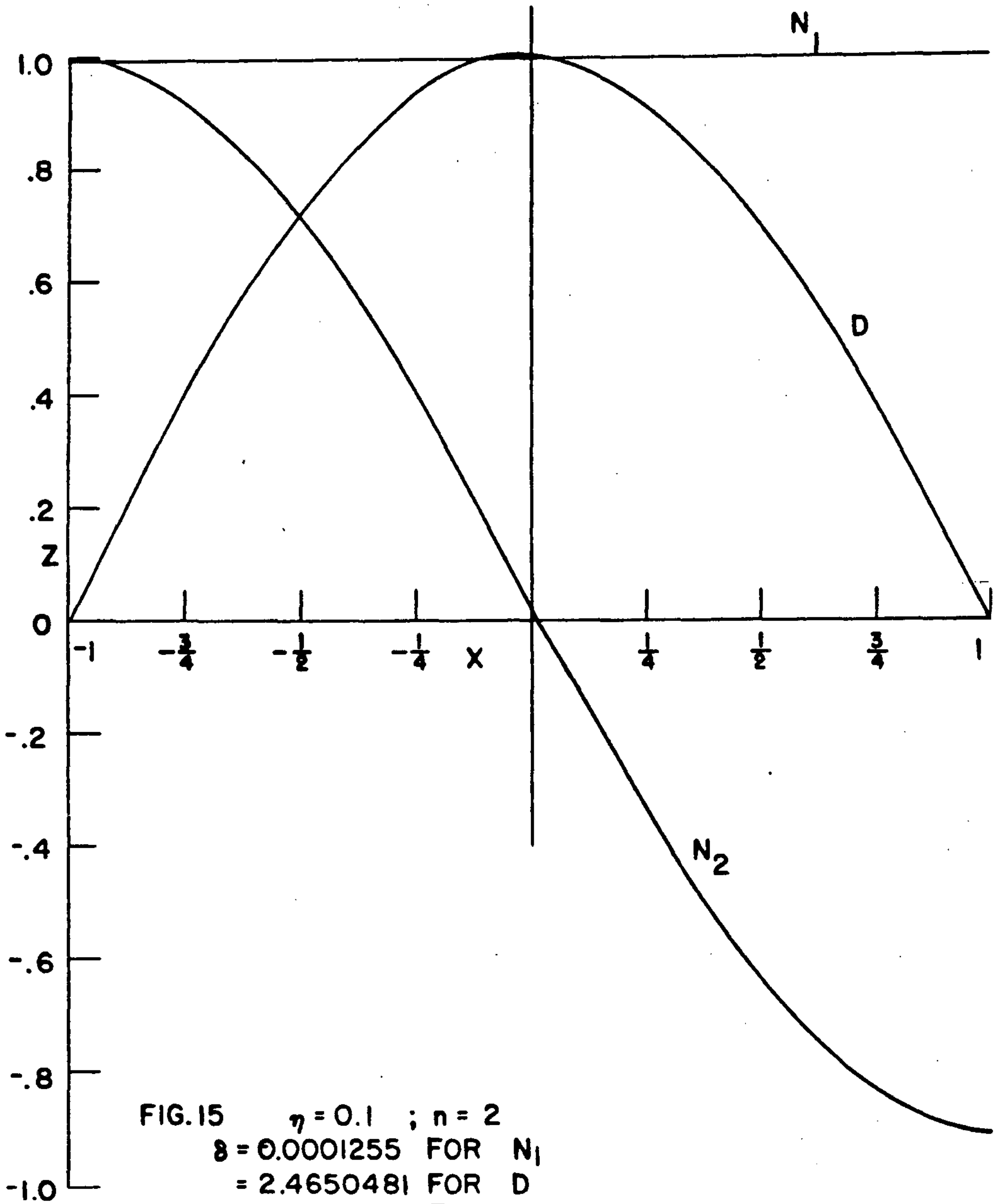

FIG. 15 $\eta = 0.1$; $n = 2$
$\delta = 0.0001255$ FOR N_1
$= 2.4650481$ FOR D
$= 2.4757499$ FOR N_2

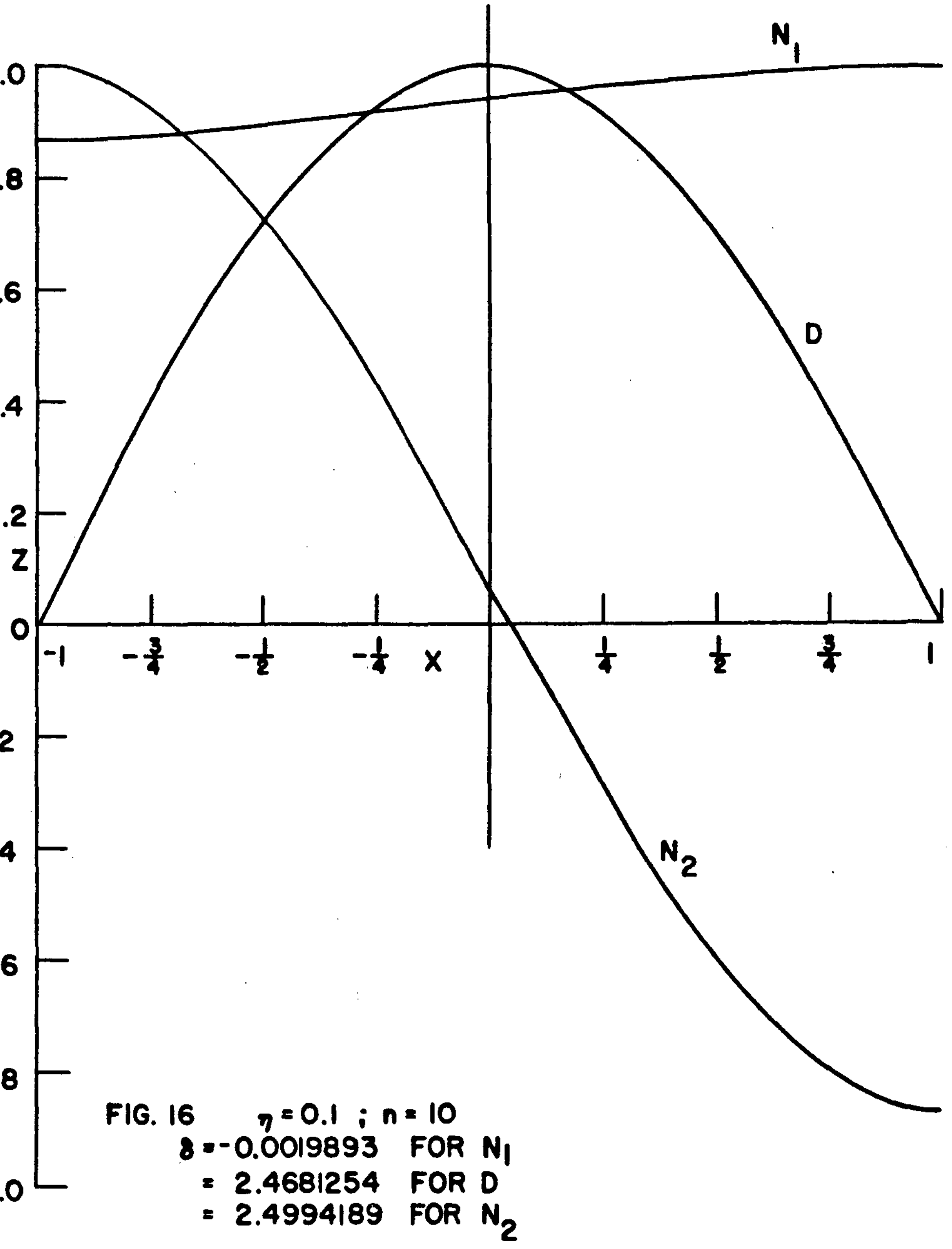

FIG. 16 $\eta = 0.1$; $n = 10$

$\delta = -0.0019893$ FOR N_1

$= 2.4681254$ FOR D

$= 2.4994189$ FOR N_2

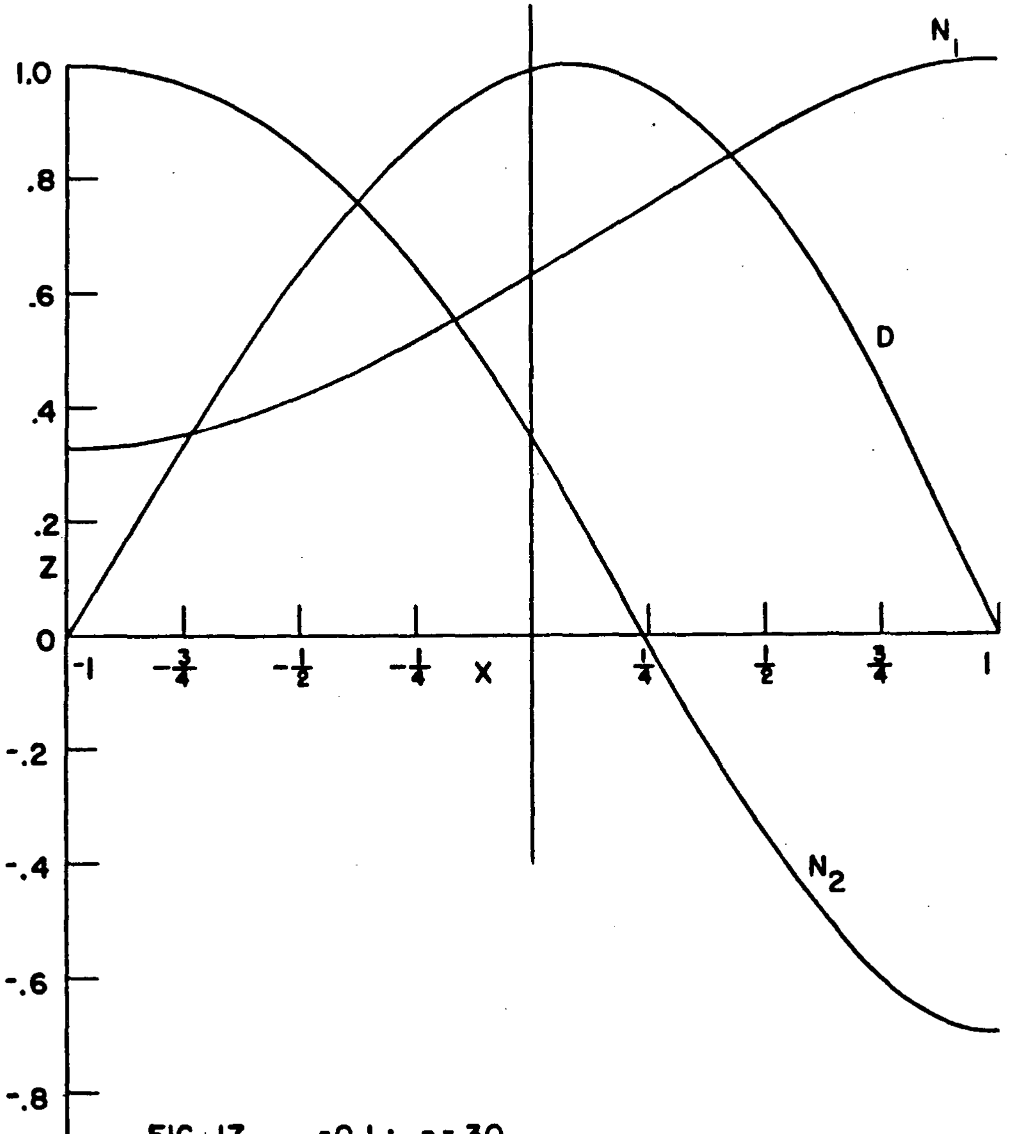

FIG. 17 $\eta=0.1$; $n=30$

$\delta=-0.335704$ FOR N$_1$

$=2.4435640$ FOR D

$=2.9276509$ FOR N$_2$

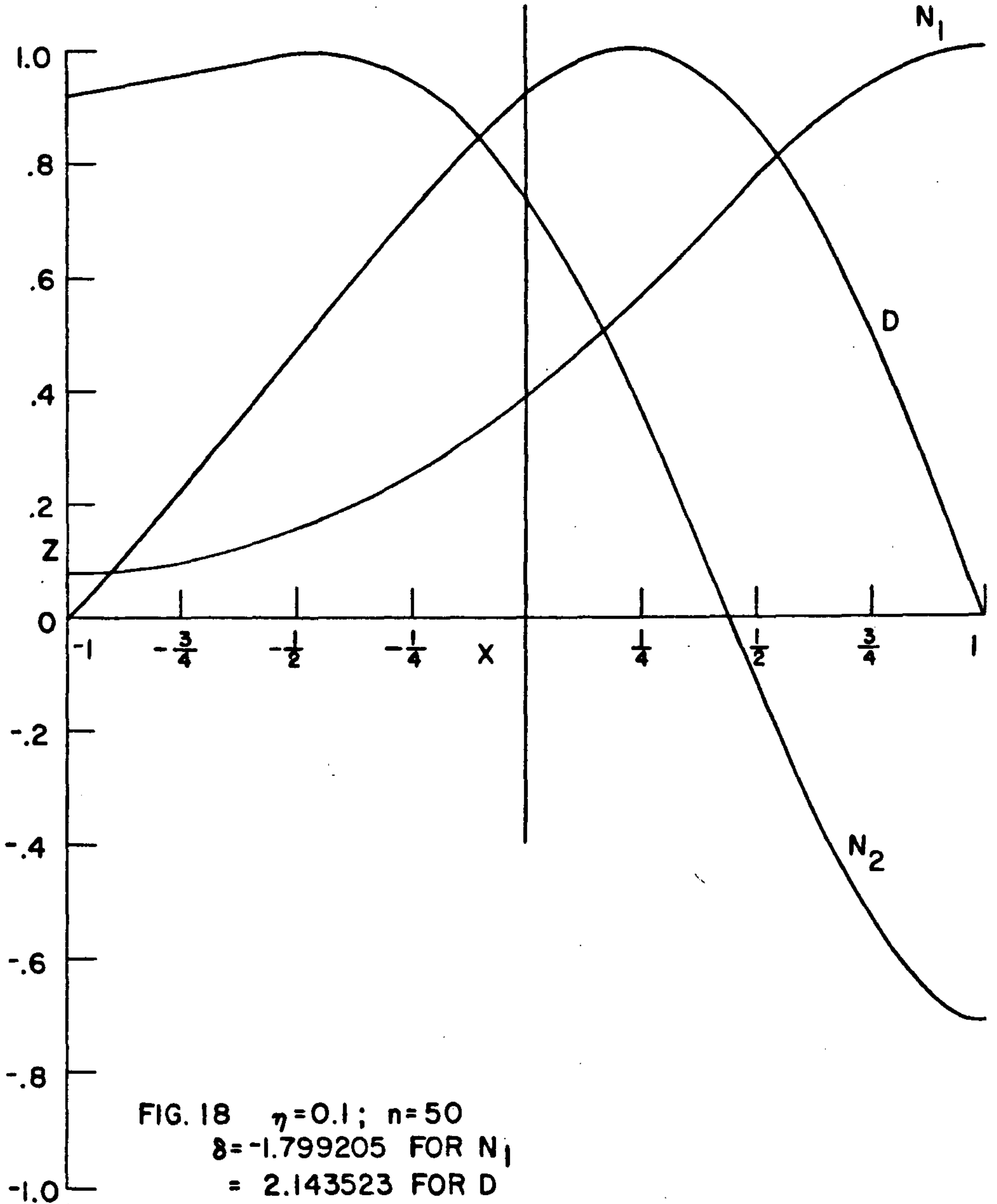

FIG. 18 $\eta = 0.1$; $n = 50$
$\delta = -1.799205$ FOR N_1
$= 2.143523$ FOR D
$= 4.087827$ FOR N_2

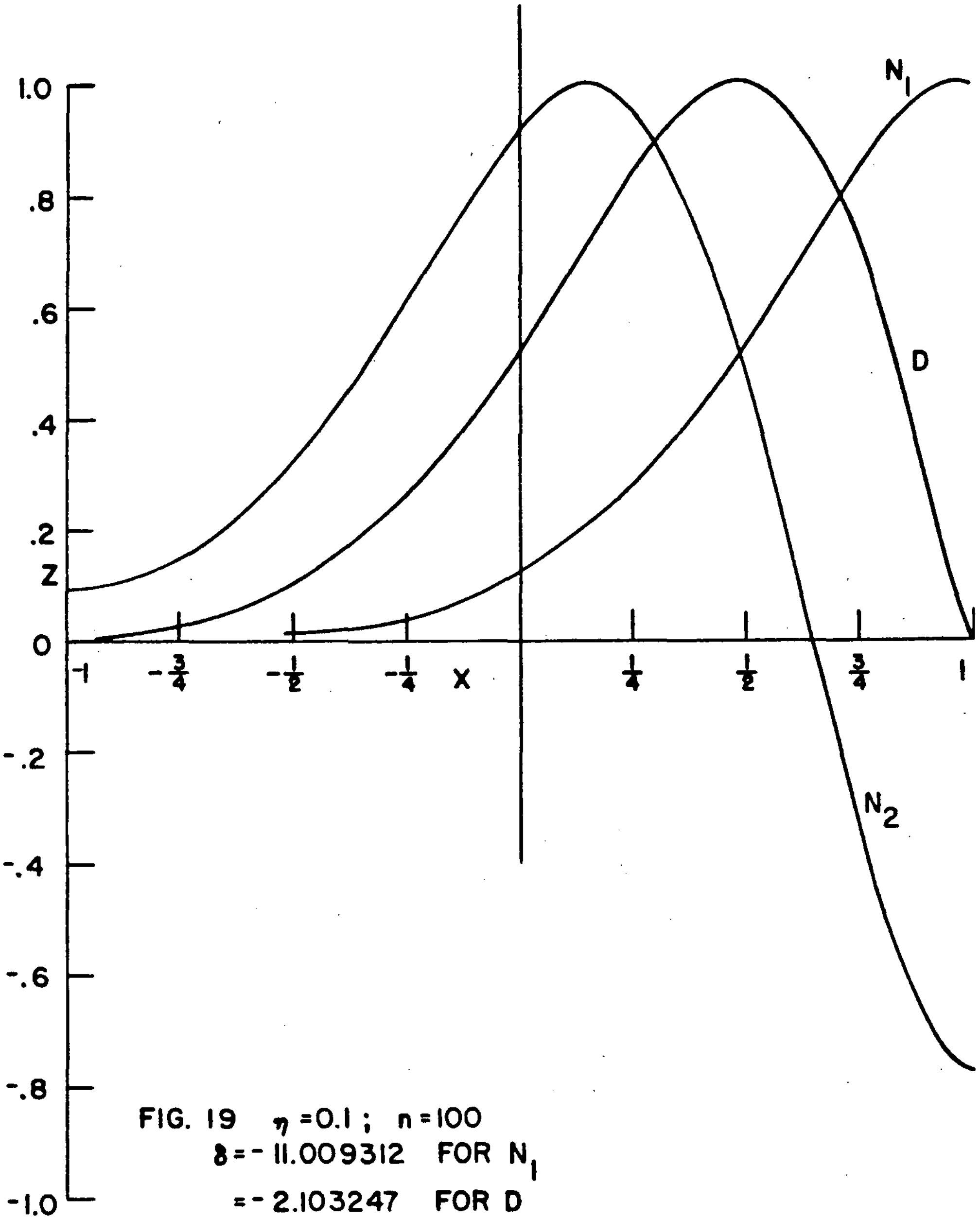

FIG. 19 $\eta = 0.1$; $n = 100$
$\delta = -11.009312$ FOR N_1
$= -2.103247$ FOR D
$= 4.361139$ FOR N_2

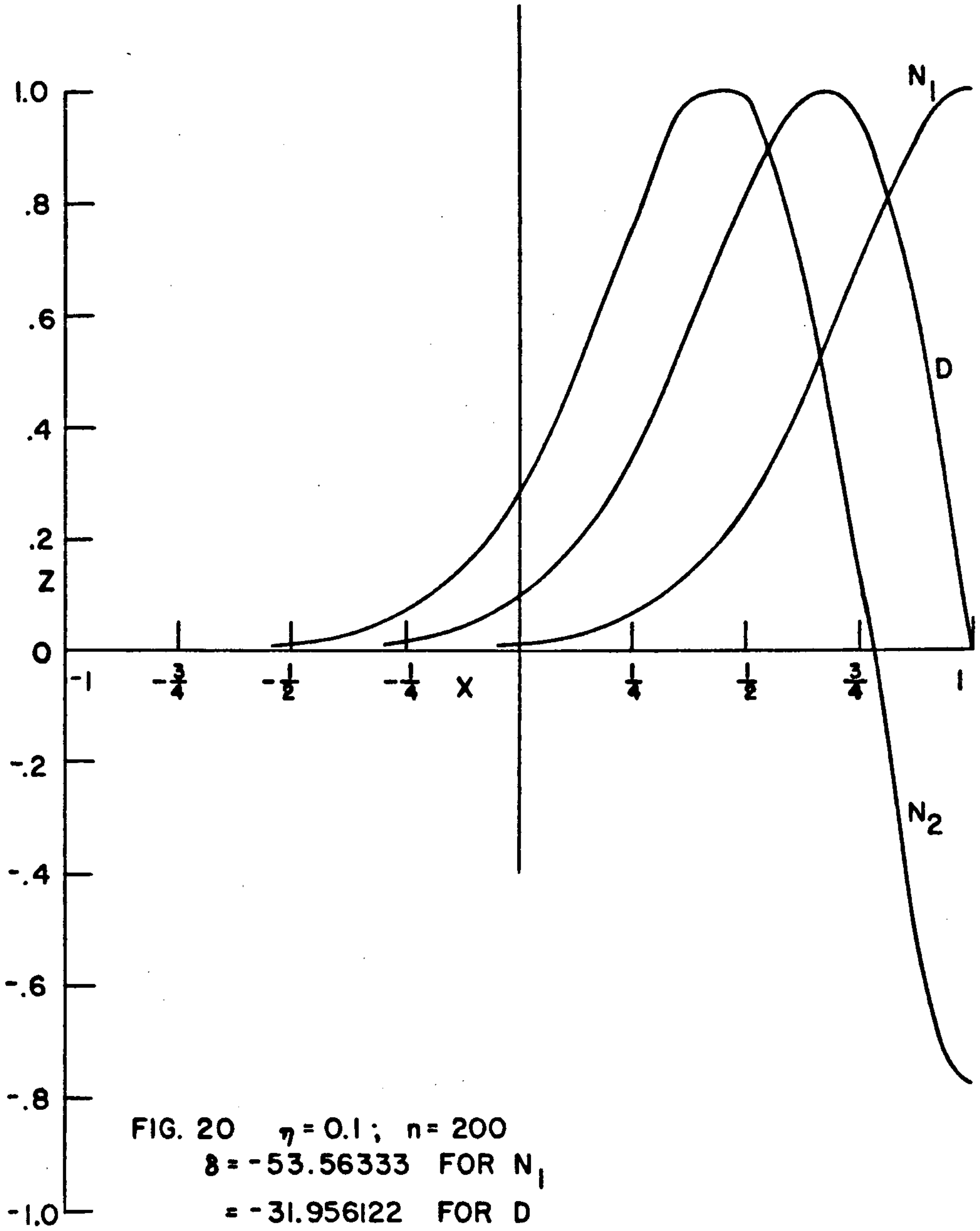

FIG. 20 $\eta = 0.1$; $n = 200$
$\delta = -53.56333$ FOR N_1
$= -31.956122$ FOR D
$= -16.514506$ FOR N_2

The output format for the Neumann solutions is to be interpreted as follows, where the subscripts 1 and 2 serve to distinguish two computations, for identical values of η and n, made in the course of a single run, and s is an integer employed in scaling the program:

Run No.	Total Steps	Steps between prints	2^{-s}(Total steps)	s
η	$\eta/2^{s-1}$	N	D_1	D_2
$2^{s-1}(x+1)$	Z_1	P_1	Z_2	P_2

$$N = \left(\frac{\eta n}{2^{s-1}\pi}\right)^2 , \quad D = \frac{\delta}{(2^{s-1}\pi)^2} , \quad P = \frac{1}{2^{s-1}\pi} \frac{dZ}{dx} .$$

For the Dirichlet solutions the same format is used except D_2, Z_2, and P_2 are omitted.

A comparison between the computationally-determined values of δ and the predictions of the approximate theoretical results of Sect. III is provided by Table VI. A similar comparison of the characteristic functions was presented previously, in connection with Tables I-IV.

Table VI. Characteristic values, δ , as determined computationally and as estimated by theoretical formulas.

η	n	First Neumann Eigenvalue			First Dirichlet Eigenvalue			Second Neumann Eigenvalue		
		Small-n Formula	Computer Result	Large-n Formula	Small-n Formula	Computer Result	Large-n Formula	Small-n Formula	Computer Result	Large-n Formula
0.001	0		0		2.467400850	2.4674011		2.467401850	2.46740209	
	20		0		2.467400850	2.4674021		2.467401851	2.46740209	
	50		0		2.467400851	2.4674011		2.467401855	2.46740210	
	75				2.467400852			2.46740186		
	100	0.000000003	0		2.467400854	2.4674011		2.46740187	2.46740211	
	200	0.000000012	0.00000002		2.467400866	2.4674011		2.46740193	2.46740217	
	500	0.000000050	0.00000004		2.467400948	2.4674015		2.46740235	2.4674026	
	1000	-0.0000002	-0.00000020		2.467401242	2.4674014		2.46740386	2.4674046	
	2000	-0.0000072	-0.00000720		2.467402419	2.4674015		2.46740990	2.4674169	
	5000	-0.000325	-0.00032495		2.467410652	2.467367		2.46745218	2.4677163	
	10000	-0.0053	-0.005290		2.467440058	2.466738		2.46760317	2.4718184	
	20000	-0.0852	-0.082838	+0.07797	2.467557679	2.456331	1.2149	2.46820714	2.533433	1.9992
	50000	-3.3325	-2.030430	-2.0210	2.468381033	2.042788	1.8367	2.47243490	3.787091	4.4978
	100000		-12.476797	-12.4934		-2.763631	-2.7727		3.907135	3.9329
	200000		-60.999918	-61.0846		-36.537911	-36.5899		-19.657327	-19.6928
0.01	0	0	0		2.4673761	2.467376		2.4674761	2.467476	
	1/2				2.4673761	2.467376		2.4674761		
	1				2.4673761	2.467376		2.4674761	2.467476	
	2				2.4673761			2.4674762	2.467476	
	5		0		2.4673762	2.467376		2.4674766	2.467476	
	10		0		2.4673765	2.467377		2.4674781	2.467478	
	20		0.0000012		2.4673777	2.467378		2.4674842	2.467484	
	50	+0.000005	0.0000050		2.4673859	2.467386		2.4675264	2.467529	
	100	-0.00002	-0.000020		2.4674153	2.467409		2.4676774	2.467720	
	200	-0.00072	-0.000720		2.4675329	2.467421		2.4682814	2.468957	
	500	-0.0325	-0.032070		2.4683563	2.463969		2.4725091	2.498479	
	1000	-0.530	-0.456025	-0.38278	2.4712968	2.401502	1.7115	2.4876083	2.835214	3.1562
	1500	-2.6925	-1.717081	-1.7231	2.4761977	2.130264	1.8729	2.5127735	3.657827	4.3535
	2000		-3.876713	-3.9248	2.4830590	1.441630	1.3524	(2.5480048)	4.535002	4.9928
	2500		-6.921675	-7.0127		0.145494	0.0932		4.843058	4.9951
	3000		-10.857817	-11.0026		-1.875544	-1.9412		4.303889	4.3095
	4000		-21.440133	-21.7312		-8.287472	-8.4334		0.828077	0.7398
	5000		-35.682279	-36.1728		-17.993822	-18.2670		-5.740178	-5.9152
0.1	0	0	0		2.4648913	2.4648915		2.4749011	2.4749309	
	1/2	0.0000083	0.00000839		2.4649011	2.4649013		2.4749514	2.474989	
	1	0.0000328	0.0000330		2.4649305	2.4649308		2.4751024	2.4751343	
	2	0.0001248	0.0001255		2.4650481	2.4650481		2.4757064	2.4757499	
	5	0.0005	0.0005019		2.4658715	2.4658332		2.4799341	2.4802714	
	10	-0.002	-0.0019893		2.4688120	2.4681254		2.4950333	2.4994189	
	20	-0.072	-0.0680405	+0.07797	2.4805742	2.4693426	1.2149	2.5554298	2.6189112	1.9992
	30	-0.402	-0.335704	-0.2925	2.5001779	2.4435640	1.6598	2.6560908	2.9276509	3.0064
	40	-1.312	-0.905569	-0.9876	2.5276230	2.3513268	1.8773	2.7970160	3.4493650	3.8536
	50	-3.25	-1.799205	-2.0210	2.5629095	2.143523	1.8367	(2.9782057)	4.0878274	4.4978
	75		-5.418144	-6.1349	(2.6854323)	0.8024951	0.4890		5.142091	5.0584
	100		-11.009312	-12.4934		-2.103247	-2.7727		4.361139	3.9329
	150		-28.210824	-32.1107		-13.285380	-15.4195		-2.541564	-3.9055
	200		-53.563133	-61.0846		-31.956122	-36.5899		-16.514506	-19.6928

(c) Integrals of the Eigenfunctions

In particular physical applications such as occur in determining the feedback between a centrally-located beam and the electromagnetic fields within a toroidal vacuum chamber or in estimating the loss figure (Q) for a resonant mode, certain integrals of the characteristic solutions will be found useful and in a sense may be regarded as providing a normalization factor for solutions of otherwise arbitrary magnitude. To obtain such integrals as would be generally useful, in an approximate sense, when η is small, three special series of computer runs were made, with $\eta = 0.0001$ and with $\eta^3 n^2$ assigned values generally in the range $\frac{1}{2}$ to 20, from the results of which the requisite integrals were evaluated by an approximate hand calculation. The character of some of the solutions obtained in these runs is illustrated by Figs. 21, 22, and 23. The salient features of the solutions and the values determined for the integrals are summarized in Tables VII, VIII, and IX. The particular quantities denoted

$$F_1 \equiv \left(\frac{2}{\pi}\right)^2 \frac{\left[dZ/dx\right]_o^2}{\int_{-1}^{1} Z^2\, dx} ,$$

$$G \equiv \frac{\left[Z(o)\right]^2}{\int_{-1}^{1} Z^2\, dx} , \text{ and } F_2 \equiv \left(\frac{2}{\pi}\right)^2 \frac{\left[dZ/dx\right]_o^2}{\int_{-1}^{1} Z^2\, dx} ,^{**} \text{ also}$$

are plotted in Figs. 24, 25, and 26, for the first Neumann solution, the

---

** The quantities F and G are seen to be so defined that if Z were a simple circular function, $\sin\frac{\pi}{2}x$ or $\cos\frac{\pi}{2}x$, respectively, these quantities would become equal to unity.

first Dirichlet solution, and the second Neumann solution, respectively.

Table VII. Salient features and integrated square of first characteristic solution subject to the Neumann boundary condition. $\eta = 0.0001$.

$\eta^3 n^2$	δ	$\frac{Z_i}{Z_f}$[a]	$\frac{[dZ/dx]_o}{Z_f}$	$\frac{\int_{-1}^{1} Z^2 dx}{Z_f^2}$	$(\frac{2}{\pi})^2 \frac{[dZ/dx]_o^2}{\int_{-1}^{1} Z^2 dx}$
1/2	-0.127783	0.52069	0.3576	1.1780	0.0440
1	-0.46206	0.28920	0.5228	0.8719	0.1270
2	-1.4544	0.11072	0.6245	0.6531	0.2420
3	-2.6424	0.05144	0.6273	0.5634	0.2831
4	-3.927	0.02681	0.6015	0.5102	0.2874
5	-5.2714	0.01506	0.5665_5	0.4732	0.2749
6	-6.659_5	0.00893	0.5293	0.4451	0.2551
8	-9.5299	0.00352	0.4575	0.4044	0.2098
10	-12.492	0.00154	0.3942	0.3754	0.1678
15	-20.161	0.00026	0.2738	0.3279	0.0926
20	-28.081	0.00006	0.1941	0.2979	0.0512

---

[a] The subscripts i and f refer to the initial and final values, at x = -1 and x = +1, respectively; the subscript o refers to the midpoint of the interval, at x = 0.

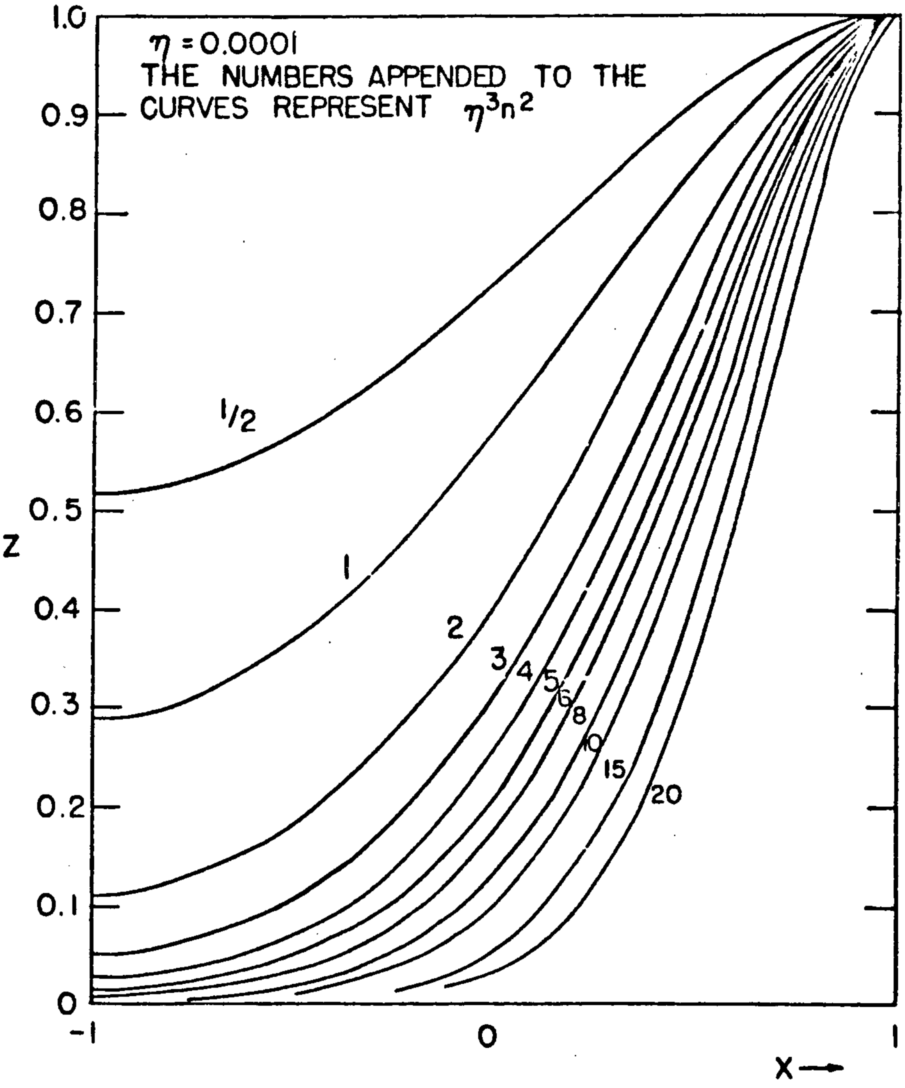

FIGURE 21

CHARACTERISTIC SOLUTIONS SUBJECT TO THE NEUMANN BOUNDARY CONDITION

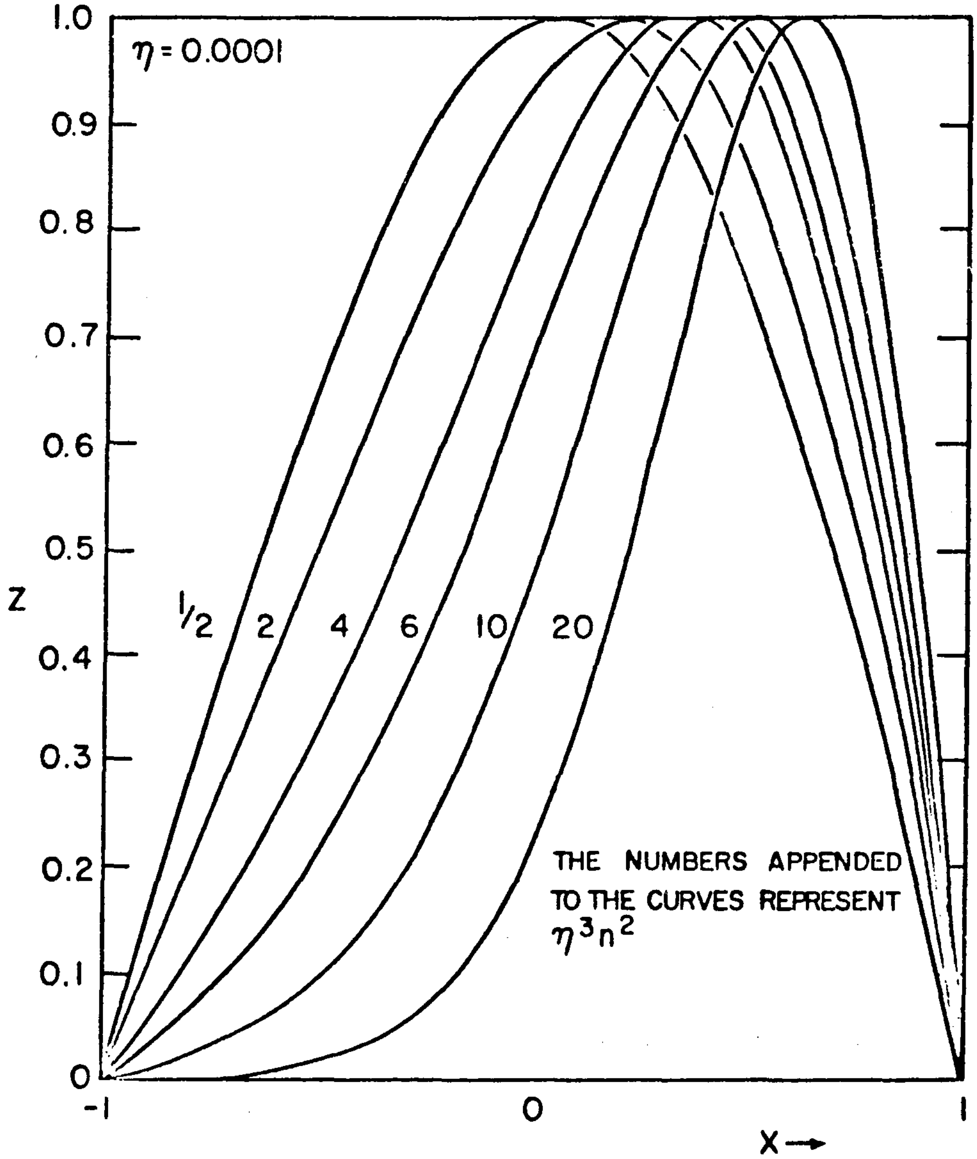

FIGURE 22

CHARACTERISTIC SOLUTIONS SUBJECT TO THE DIRCHLET BOUNDARY CONDITION

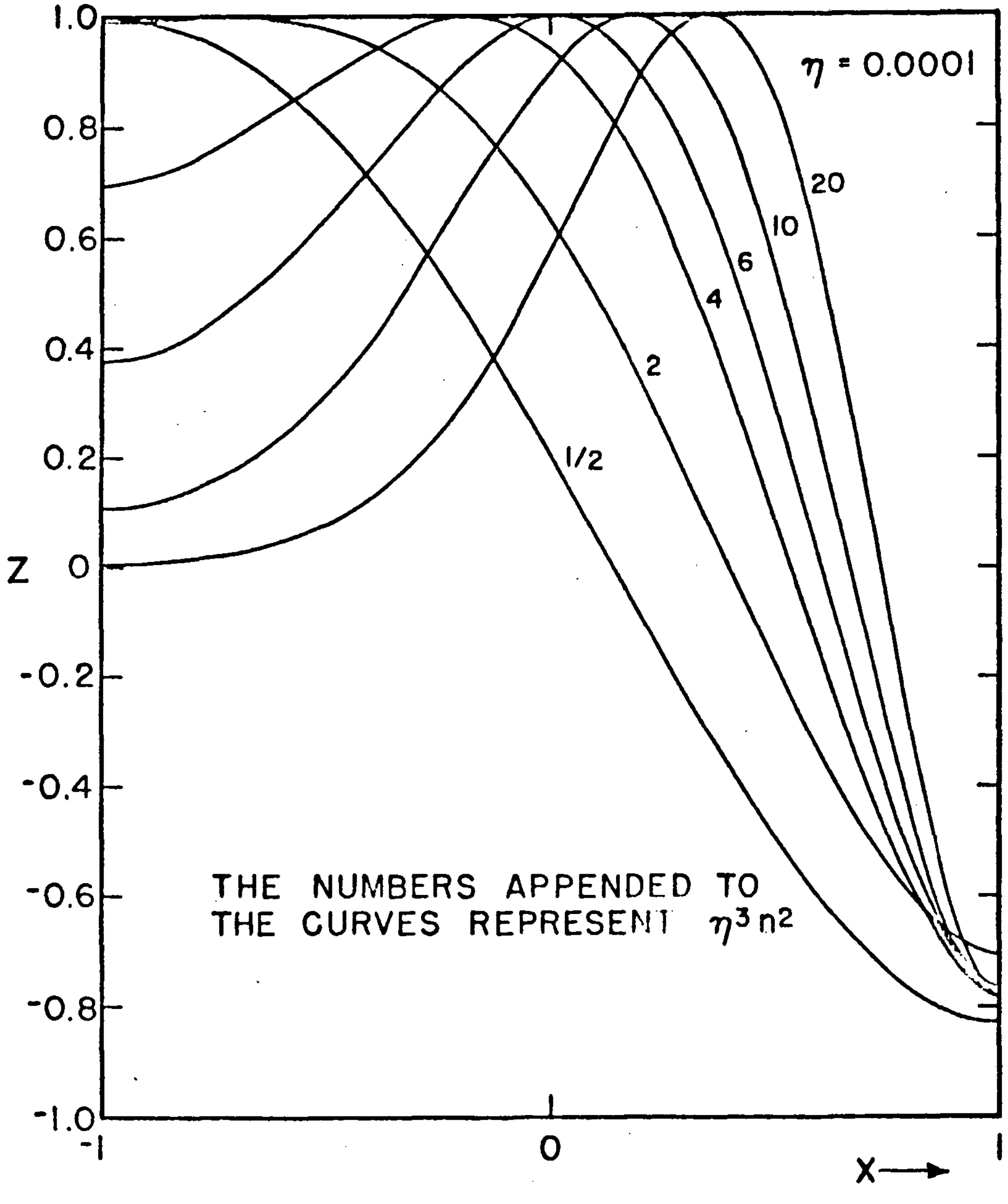

FIGURE 23

CHARACTERISTIC SOLUTIONS SUBJECT TO THE NEUMANN BOUNDARY CONDITION.

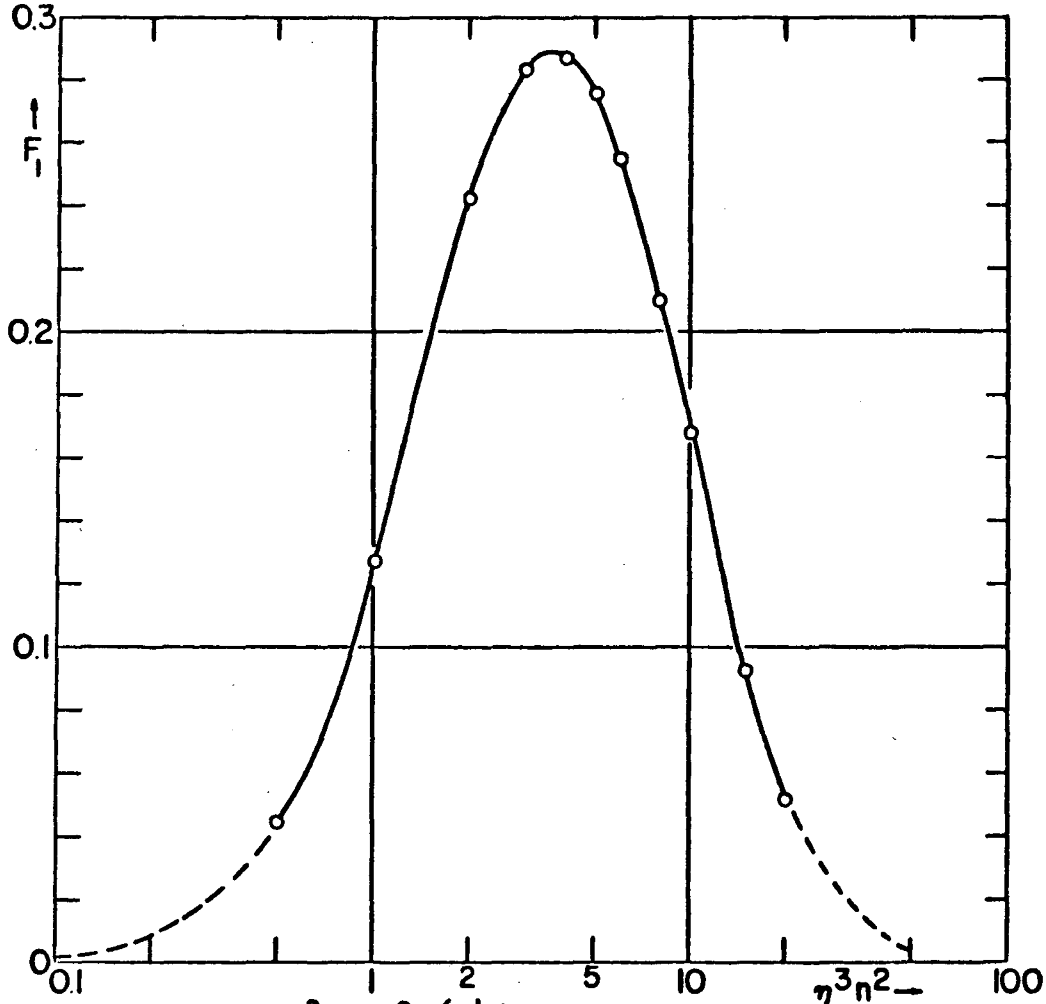

FIGURE 24 $F_1 = (\frac{2}{\pi})^2 [Z(0)]^2 / \int_{-1}^{1} Z^2 \, dx$ FOR FIRST SOLUTION SUBJECT TO NEUMANN BOUNDARY CONDITION

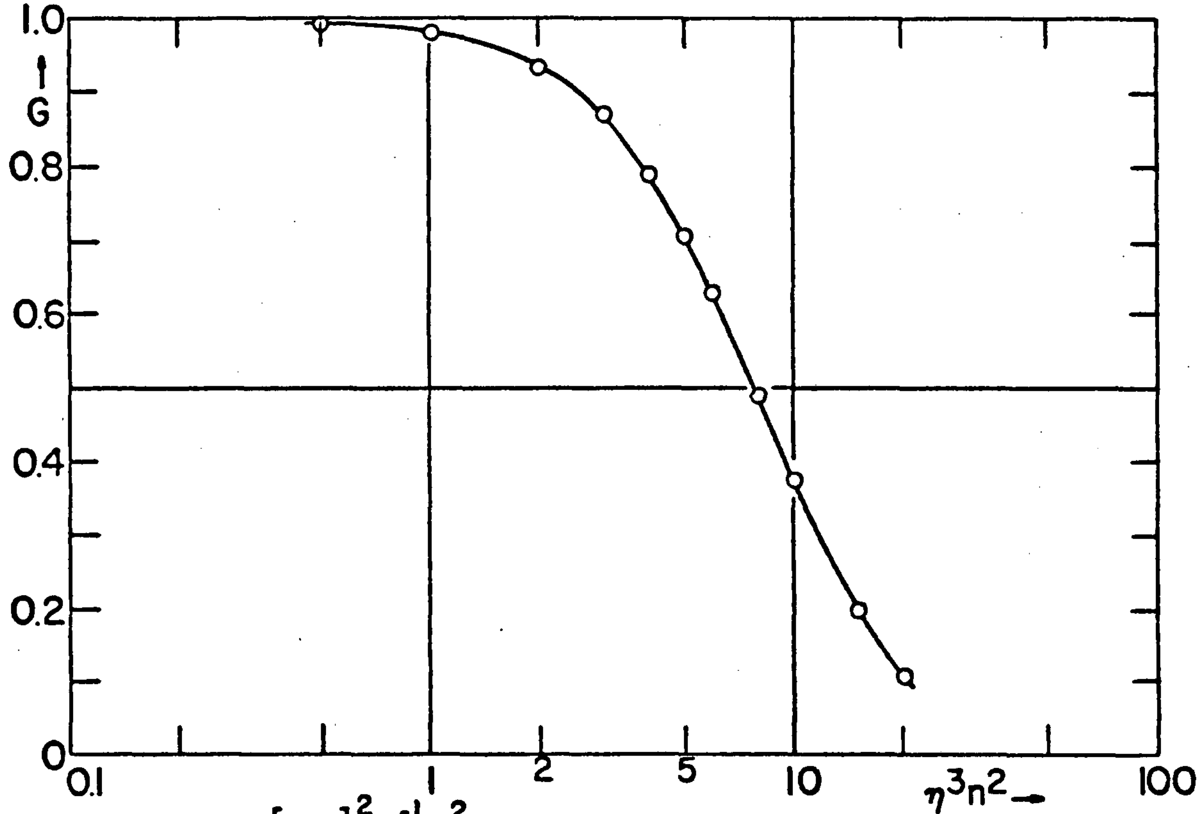

FIGURE 25 $G = [Z(0)]^2 / \int_{-1}^{1} Z^2\,dx$ FOR FIRST SOLUTION SUBJECT TO DIRICHLET BOUNDARY CONDITION

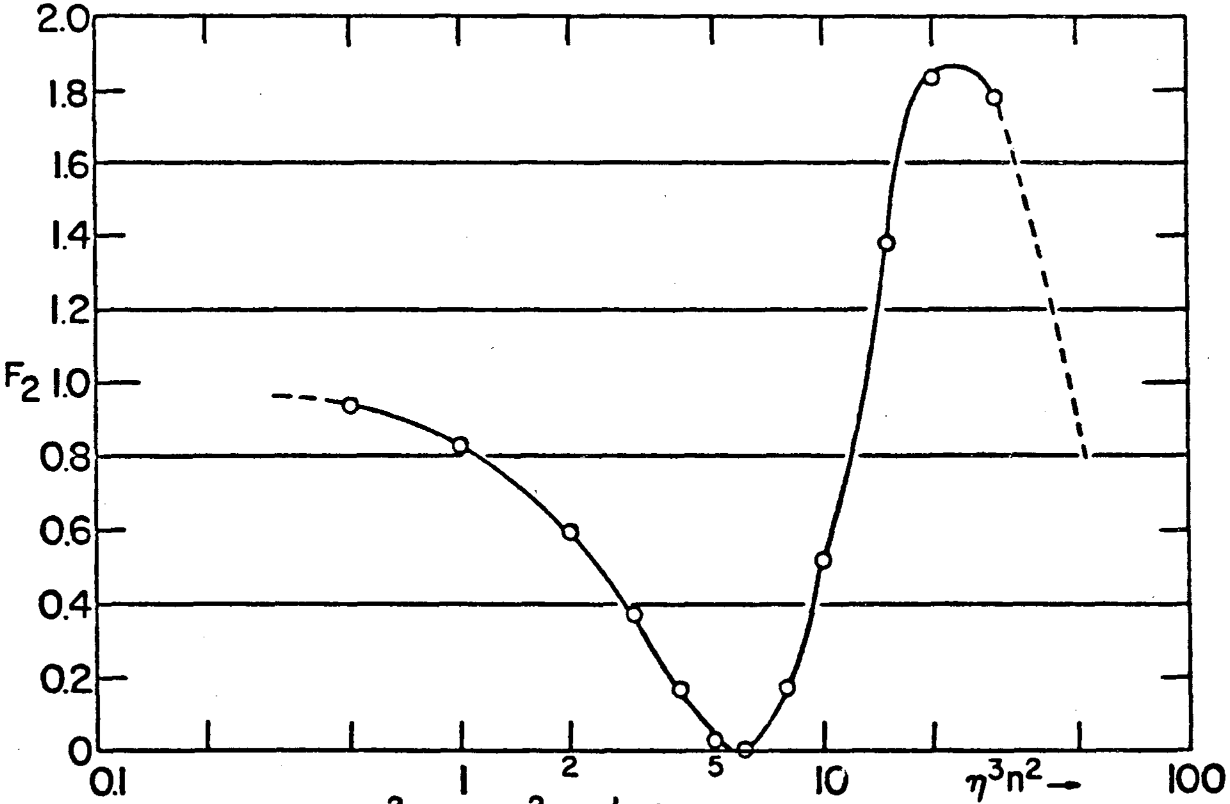

FIGURE 26 $F_2 = (\frac{2}{\pi})^2 \left[dZ/dx\right]_0^2 / \int_{-1}^{1} Z^2\,dx$ FOR SECOND SOLUTION SUBJECT TO NEUMANN BOUNDARY CONDITIONS

Table VIII. Salient features and integrated square of first characteristic solution subject to the Dirichlet boundary condition. $\eta = 0.0001$.

$\eta^3 n^2$	δ	$\frac{[dZ/dx]_i^a}{[dZ/dx]_f}$	$\frac{Z(o)}{[dZ/dx]_f}$	$\frac{\int_{-1}^{1} Z^2\,dx}{(dZ/dx)_f^2}$	$\frac{[Z(o)]^2}{\int_{-1}^{1} Z^2\,dx}$
1/2	2.44989	-0 81674	-0.57593	0.3330_7	0.9959
1	2.39757	-0.66744	-0.52222	0.2773_4	0.9833
2	2.19214	-0.44766	-0.43275	0.1999_3	0.9367
3	1.86207	-0.30299	-0.36266	0.1513_9	0.8688
4	1.42218	-0.20749	-0.30734	0.1196_4	0.7895
5	0.88798	-0.14394	-0.26319	0.0979_4	0.7073
6	0.27375	-0.10118	-0.22752	0.0824_9	0.6275
8	-1.14815	-0.05192	-0.17412	0.0623_4	0.4863
10	-2.77031	-0.02786	-0.13669	0.0499_7	0.3739
15	-7.42438	-0.00686	-0.08063	0.0328_7	0.1978
20	-12.6550	-0.00199	-0.05119	0.0250_0	0.1048

[a] The subscripts i and f refer to the initial and final values, at x = -1 and x = +1, respectively.

Table IX. Salient features and integrated square of second characteristic solution subject to the Neumann boundary condition. $\eta = 0.0001$.

$\eta^3 n^2$	δ	$\frac{Z_i{}^a}{Z_f}$	$\frac{[dZ/dx]_o}{Z_f}$	$\frac{\int_{-1}^{1} Z^2 \, dx}{Z_f{}^2}$	$(\frac{2}{\pi})^2 \frac{(dZ/dx)_o{}^2}{\int_{-1}^{1} Z^2 \, dx}$
1/2	2.5405	-1.2076	1.7294	1.282_2	0.9454
1	2.8182	-1.3666	1.8363	1.645_4	0.8306
2	3.4688	-1.4092	1.7648	2.131_1	0.5923
3	4.0673	-1.2001	1.3936	2.141_9	0.3675
4	4.5023	-0.9222	0.8964	1.934_7	0.1683
5	4.7470	-0.6744	0.3950	1.686_4	0.0375
6	4.8154	-0.4846	-0.0546	1.542_0	0.0008
8	4.5447	-0.2525	-0.7599	1.329_7	0.1760
10	3.9027	-0.1371	-1.2495	1.210_3	0.5288
15	1.3587	-0.0352	-1.8894	1.046_6	1.382_5
20	-2.0086	-0.0107	-2.0731	0.950_0	1.833_4
30	-10.2162	-0.0013_6	-1.9083	0.829_8	1.779

---

[a] The subscripts i and f refer to the initial and final values, at x = -1 and x = +1, respectively; the subscript o refers to the midpoint of the interval, at x = 0.

V. CONCLUSION

The analytic and computational work presented in this report provides information concerning the characteristic values of δ, and for the shape of the first characteristic functions when the parameter η is small. Since the contribution from δ makes a relatively small change in the characteristic value for the original Bessel equation when n is large, use of Eq. (3b) in connection with the values of δ found here should afford accurate characteristic values for q in such cases.

In application of these results to the excitation of electromagnetic modes by an azimuthally-modulated beam circulating within the vacuum chamber of a particle accelerator, however, the quantity δ enters essentially <u>directly</u> in determining whether or not a resonant electromagnetic mode is excited by the beam. With a modulated coasting beam moving at a radius R_o with an angular speed $\omega_o = \beta c/R_B$, the ϕ, t dependence of the charge-current density and hence of the electromagnetic fields, may be expressed in terms of circular functions of argument $n(\phi - \omega_o t)$. For the radial dependence of the fields one employs, of course, Bessel functions (or their derivatives), $Z_n(qr)$. The axial variation, finally, may be expressed in terms of circular functions, whose argument we may denote by κz. Maxwell's equations for the electromagnetic field then require the relation

$$\kappa^2 = \frac{n^2 \omega_o^2}{c^2} - q^2$$

$$= \frac{n^2 \beta^2}{R_B^2} - q^2 \quad .$$

By introducing the average radius of the chamber, $R_{Av} \equiv \frac{b + a}{2}$, this relation may be put in the convenient form

$$(qR_{Av})^2 = n^2 \left(\frac{\beta \; R_{Av}}{R_B}\right)^2 - (\kappa \, R_{Av})^2 \quad .$$

Resonant excitation of the chamber will occur if κ times the chamber height, h, is an odd multiple of π:

$$\kappa = (2m + 1)\pi/h \quad .$$

The resonant values of q are thus such that

$$(qR_{Av})^2 = n^2\left(\frac{\beta \; R_{Av}}{R_B}\right)^2 - \left[(2m + 1)\pi \; \frac{R_{Av}}{h}\right]^2 \quad ,$$

or, in terms of δ, η $\left(\equiv \frac{b - a}{b + a}\right)$, and the chamber width w (= b - a),

$$\delta = (\eta \, n)^2 \left[\left(\frac{\beta \, R_{Av}}{R_B}\right)^2 - 1 \right] - \left[(m + \tfrac{1}{2})\pi \; \frac{w}{h}\right]^2 \quad .$$

Typically $\beta \; R_{Av}/R_B$ will be close to unity (for a relativistic beam moving close to the center of the aperture) and w/h, although normally greater than unity, will not be large. For resonance to occur then, it usually may be expected that δ would have to be somewhat negative, and hence, for the lower-order resonant modes, $\eta^3 n^2$ would be roughly of order unity.

As one example of resonance associated with the first Neumann root corresponding to a transverse -electric (TE) mode of oscillation, one may note that $\eta = 0.01$ and $n = 2000$ leads to an eigenvalue $\delta = -3.88$. If $\beta \; R_{Av}/R_B = 1$, resonance would occur in this case with $m = 0$ for $w \simeq \frac{5}{4} h$. For this example $\eta \, n = 20$ and $\eta^3 n^2 = 4$. If $\eta^3 n^2$ becomes quite large, of course, the mutual coupling between the beam and the electromagnetic fields (involving the factors F or G shown in Figs. 24-26 and listed in Tables VII-IX) may be greatly reduced, due to the localization of the characteristic functions close to the outer wall of the vacuum chamber. In any case, with η quite small as is typical of modern high-energy accelerators, the values of the harmonic number, n, which could lead to resonance will necessarily be quite large. The possibility of a self-generated instability resulting from the mutual interaction between an intense coasting beam and the associated electromagnetic fields, however, lends interest to a study of these high-order modes.

The loss-factor, Q, associated with the resonant electromagnetic modes of a toroidal vacuum chamber, can also be estimated, when η is small and (in particular) with n large, from the results given in this report. The evaluation of

$$\frac{1}{Q} \equiv \frac{\langle \text{Power Loss} \rangle_{Av}}{\omega\,(\text{Energy Stored})} \tag{32}$$

for a transverse electric (TE) mode leads to[17]

$$\frac{1}{Q} = 4\,\frac{R_{surf.}}{Z\ \text{space}}\,\frac{k^2}{K^3}\left\{\frac{1}{h} + \frac{1}{4q^2}\left[\frac{n^2}{b}\left(1 + \frac{b}{a}\frac{[Z(a)]^2}{[Z(b)]^2}\right) + \frac{q^4 b}{k^2}\left(1 + \frac{a}{b}\frac{[Z(a)]^2}{[Z(b)]^2}\right)\right]\frac{[Z(b)]^2}{\int_a^b Z^2 r\,dr}\right\}, \tag{33a}$$

where $K \equiv \frac{\omega}{c}$, $R_{surf.} = \frac{\text{resistivity}}{\text{skin depth}} = \frac{\mu_o \omega}{2} \cdot (\text{skin depth})$,

$Z_{space} = \sqrt{\mu_o/\epsilon_o} = \mu_o c = 4\pi \times 10^{-7} \times 3 \times 10^8 = 120\pi = 377$ ohms, and $Z(r)$ satisfies the Neumann boundary condition at $r = a, b$. When a and b are nearly equal ($\eta << 1$), the result given by Eq. (33a) can be simplified

---

[17] The loss-factor, Q, of a toroidal cavity can be obtained for the TE modes

(Cont. on pg. 67)

(Ref. 17 cont.)

by use of the field components (rationalized MKS units)

$$B_\phi = -n \frac{Z}{r} \sin \kappa z \sin n\phi \cos \omega t$$
$$B_r = \frac{dZ}{dr} \sin \kappa z \cos n\phi \cos \omega t$$
$$B_z = -\frac{q^2}{\kappa} Z \cos \kappa z \cos n\phi \cos \omega t$$
$$E_\phi = \frac{\omega}{\kappa} \frac{dZ}{dr} \cos \kappa z \cos n\phi \sin \omega t$$
$$E_r = n \frac{\omega}{\kappa} \frac{Z}{r} \cos \kappa z \sin n\phi \sin \omega t$$
$$E_z = 0, \text{ with } q^2 + \kappa^2 = (\omega/c)^2 = K^2 ,$$

representing standing waves of a resonant TE mode. Application of Eq. (32) then leads to Eq. (33a) of the text. In the special case of a pill box $[a = 0$ and $Z(r) = J_n(qr)]$, Eq. (33a) simplifies to

$$\frac{1}{Q} = 4 \frac{R_{surf.}}{Z_{space}} \frac{1}{K^3} \left[\frac{\kappa^2}{h} + \frac{1}{2b} \frac{q^4 b^2 + n^2 \kappa^2}{q^2 b^2 - n^2} \right] ,$$

which may be seen to agree with a result given by Smythe[18] (Sect. 15.17, Eq. (8), p. 535) in which his a becomes our b, d becomes h, m becomes n, p becomes $\kappa h/\pi$, β_{mn} becomes q, β_{mnp} becomes K, and his $\nu\mu\gamma\delta$ may be identified as R_{surf}/Z_{space}. Similarly with a circular-function distribution for Z, as could be the case for η and $\eta^3 n^2$ both small, Eq. (33b) of the text may be expressed as

$$\frac{1}{Q} \doteq 4 \frac{R_{surf.}}{Z_{space}} \frac{1}{K^3} \left[\frac{\kappa^2}{h} + \frac{\kappa^2 k^2_\phi + (k^2_r + k^2_\phi)^2}{(k^2_r + k^2_\phi)\, w} \right] ,$$

in which k_ϕ has been employed to denote n/R, and we note $q^2 \cong k^2_r + k^2_\phi$. This result too, may be seen to agree with a formula given by Smythe[18] (Sect. 15.16, Eq. (9), p. 534) for a rectangular resonator, in which his

(Ref. 17 cont.)

a becomes our w , d becomes h, m becomes $k_r w/\pi$, n becomes $k_\phi b/\pi$, p becomes $\varkappa h/\pi$, and we let his b → ∞ to eliminate inclusion of losses from the end walls of Smythe's cavity.

[18] William R. Smythe, Static and Dynamic Electricity (McGraw-Hill Book Co., Inc., New York, 1950), Ed. 2.

cont. from p. 64.

to

$$\frac{1}{Q} \cong 4 \frac{R_{\text{surf.}}}{Z_{\text{space}}} \frac{\varkappa^2}{K^3} \left\{ \frac{1}{h} + \frac{1}{2q^2 w} \left(\frac{n^2}{R^2} + \frac{q^4}{\varkappa^2}\right)\left(1 + \frac{[Z(-1)]^2}{[Z(1)]^2}\right) \frac{[Z(1)]^2}{\int_{-1}^{1} Z^2 \, dx} \right\}, \qquad (33b)$$

where R denotes the average radius, $\frac{b + a}{2}$, w represents the width, b - a, and Z is now regarded as a function of x. Values of $Z(-1)/Z(+1)$ and of $[Z(1)]^2 / \int_{-1}^{1} Z^2 \, dx$ for representative values of $\eta^3 n^2$, are obtainable from Tables VIII and IX for the first two solutions conforming to the Neumann boundary condition.

Similarly, the result for a transverse magnetic (TM) mode is[19]

$$\frac{1}{Q} = 4 \frac{R_{\text{surf.}}}{Z_{\text{space}}} \frac{1}{K} \left\{ \frac{1}{h} + \frac{b}{4q^2} \left[1 + \frac{a}{b} \frac{(dZ/dr)_a{}^2}{(dZ/dr)_b{}^2} \right] \frac{(dZ/dr)_b{}^2}{\int_a^b Z^2 r \, dr} \right\}, \qquad (34a)$$

where Z(r) satisfies the Dirichlet boundary condition at r = a, b. Again, when a and b are nearly equal, Eq. (34a) may conveniently be simplified to

$$\frac{1}{Q} \cong 4 \frac{R_{\text{surf.}}}{Z_{\text{space}}} \frac{1}{K} \left\{ \frac{1}{h} + \frac{2}{q^2 w^3} \left[1 + \frac{a}{b} \frac{(dZ/dx)_i{}^2}{(dZ/dx)_f{}^2} \right] \frac{(dZ/dx)_f{}^2}{\int_{-1}^{1} Z^2 dx} . \right\} \qquad (34b)$$

Values of $\frac{(dZ/dx)_i}{(dZ/dx)_f}$ and of $\frac{(dZ/dx)_f{}^2}{\int_{-1}^{1} Z^2 dx}$, for representative values of $\eta^3 n^2$, are obtainable from Table VIII for the first Dirichlet solution.

---

[19] The loss-factor for a TM mode can be obtained by use of the field components

$$B_\phi = \frac{\omega}{c^2 \kappa} \frac{dZ}{dr} \sin \kappa z \cos n\phi \sin \omega t$$

$$B_r = n \frac{\omega}{c^2 \kappa} \frac{Z}{r} \sin \kappa z \sin n\phi \sin \omega t$$

$$B_z = 0$$

(Ref. 19 cont.)

$$E_\phi = - n \frac{Z}{r} \cos \varkappa z \sin n\phi \cos \omega t$$

$$E_r = \frac{dZ}{dr} \cos \varkappa z \cos n\phi \cos \omega t$$

$$E_z = \frac{q^2}{\varkappa} Z \sin \varkappa z \cos n\phi \cos \omega t,$$

with $q^2 + \varkappa^2 = (\omega/c)^2 = K^2$. Application of Eq. (32) then leads to Eq. (34a) of the text. In the special case of a pill box $\left(a = o \text{ and } Z(r) = J_n(qr)\right)$, Eq. (34a) simplifies to

$$\frac{1}{Q} = 4 \frac{R_{surf.}}{Z_{space}} \frac{1}{K} \left(\frac{1}{h} + \frac{1}{2b}\right) ,$$

in agreement with a result given by Smythe,[18] for p (or $\varkappa$) $\neq 0$ (Sect. 15.17, Eq. (9), p. 535). Similarly for Z represented by a simple circular function, Eq. (34b) may be written

$$\frac{1}{Q} \doteq 4 \frac{R_{surf.}}{Z_{space}} \frac{1}{K} \left[\frac{1}{h} + \frac{k_r^2}{(k_r^2 + k_\phi^2)w}\right] ,$$

with k_ϕ denoting n/R and use of $q^2 \cong k_r^2 + k_\phi^2$. This result is consistent with an expression given by Smythe[18] (Sect. 15.16, Eq. (10), p. 534) when his b is permitted to approach infinity after his n is replaced by $k_\phi b/\pi$ and other appropriate identifications are made in the notation.

Particle Accelerators, 1973, Vol. 4, pp. 151-157 © Gordon and Breach, Science Publishers Ltd. Printed in Glasgow, Scotland

Reprinted by permission of Gordon & Breach.

LONGITUDINAL COUPLING IMPEDANCE OF A STATIONARY ELECTRON RING IN A CYLINDRICAL GEOMETRY†

ANDRIS FALTENS AND L. JACKSON LASLETT

Lawrence Berkeley Laboratory, University of California, Berkeley, California, USA

The longitudinal (azimuthal) coupling impedance is investigated for a stationary electron-ring beam circulating between a co-axial pair of conducting tubes. Proximity of the beam to the inner tube is found to be advantageous for reducing $(|Z_n|/n)_{\max}$. Similar results are shown to be attainable with operation near the the outer tube, provided the quality factors Q for higher-order resonant modes are deliberately made small. Illustrative computational results are presented graphically and a convenient approximate formula is suggested that may serve to guide the selection of desirable parameters for a typical fully-compressed electron ring.

1. INTRODUCTION

In evaluating the effectiveness of electron rings for the useful acceleration of ions, the requirement of longitudinal (azimuthal) stability appears to constitute a severe constraint. Another paper[1] appearing in this issue is concerned with the selection of parameters for an electron-ring accelerator, and considers explicitly the stability requirements for a fully-compressed loaded ring at the time of release from the magnetic well. That paper reiterates the necessity of strongly limiting the self-generated azimuthal electric fields, that could excite an unstable azimuthal modulation of the electron ring beam, if rings of useful holding power are to be obtained. Such electric fields may be expected to be reduced by the presence of nearby conducting material, that in a magnetic acceleration column might conveniently take the form of conducting tubes co-axial with the electron ring. It may be of interest, therefore, to report in the present paper results from an analysis of the longitudinal coupling impedance of a toroidal electron beam situated co-axially between a pair of infinitely long conducting tubes. The analysis for a pair of tubes constitutes an extension of previous work[2-5] concerned with an electron ring situated interior to a single tube, a ring inside a compressor chamber,[6,7] and of similar work[8] relating to a cylindrical layer of electrons situated between two walls. A two-tube configuration may represent a better approximation to arrangements for magnetic acceleration that would be attractive on other grounds and, in addition, may aid in suppression of the longitudinal instability.

2. COMPUTATIONAL PROCEDURE

The present analysis is restricted to rings that are essentially stationary with respect to the tube structure, and (when losses are present) would require revision for application to rings with an axial speed comparable to that of light. No dielectric material is considered to be present, and no special frequency-sensitive elements are introduced (save for such as may aid in controlling the 'quality factor', Q).

The longitudinal coupling impedance, associated with an electron-ring beam of major radius R and with a postulated current modulation $I_n = I_0 \exp[j(\omega t - n\phi)]$, is defined in terms of the corresponding longitudinal (azimuthal) electric field E_ϕ as $Z_n = -2\pi R E_\phi / I_n$. Perturbation analyses[9] have suggested the relation between $|Z_n|/n$ and the amount of Landau damping that must be present (*e.g.*, from energy spread) if longitudinal stability is to be assured.

We commence the analysis, for determination of Z_n, by making a formal series development for the steady-state electromagnetic fields associated with a current distribution $I_0\,\delta(r-R)\,\delta(z)\exp[j(\omega t - n\phi)]$, subject to boundary conditions that correspond to outgoing (or damped) waves for $|z|$ large and to conducting surfaces at $r = R_{\mathrm{IN}}, R_{\mathrm{OUT}}$. Radial coordinates can be expressed conveniently in terms of the radius of the inner tube, so that, in these units,

---

† Work supported by the U.S. Atomic Energy Commission. *Editor's Note:* A résumé of this paper was presented at the Symposium on Collective Methods of Acceleration, Dubna, USSR, September 1972.

the radial interval of interest extends from unity to $f = R_{OUT}/R_{IN}$ and the ring beam is situated at $R = \rho R_{IN}$ $(1 < \rho < f)$. The angular frequency is $\omega = n\beta c/R = n\beta c/(\rho R_{IN})$. The series development of the electromagnetic field then employs characteristic functions, R_m, and characteristic values, g_m, of the Bessel equation

$$x\frac{\mathrm{d}}{\mathrm{d}x}\left(x\frac{\mathrm{d}R_m}{\mathrm{d}x}\right)+(g_m{}^2x^2-n^2)R_m=0$$

with $R_m|_{x=1} = R_m|_{x=f} = 0$ for the transverse-magnetic (TM) modes—and correspondingly the functions S_m and values h_m, with $S'_m|_{x=1} = S'_m|_{x=f} = 0$ for the transverse-electric (TE) modes.[10] The z-dependence of the fields is contained in factors that, for the TM modes, are circular functions of $\omega t - k_m|z| - n\phi$ with

$$k_m = [(\omega/c)^2-(g_m/R_{IN})^2]^{1/2}$$

and $\omega = n\omega_{\odot} = n\beta c/R$ for frequencies above cut-off, and are of the form $\exp(-\alpha_m|z|)$ times a circular function of $\omega t - n\phi$ with $\alpha_m = [(g_m/R_{IN})^2-(\omega/c)^2]^{1/2}$ for frequencies below cut-off—and similarly for the TE modes.

The azimuthal electric field is found in these terms to be such that

$$\frac{1}{n}Z_n = 2\pi Z_0\rho\left\{\sum_m[(n/\rho)^2-(g_m/\beta)^2]^{1/2}F_{TM} + \sum_m[(n/\rho)^2-(h_m/\beta)^2]^{-1/2}F_{TE}\right\},$$

where $Z_0=\sqrt{\mu_0/\varepsilon_0}=120\pi$ ohms, the 'coupling factors' F_{TM}, F_{TE} are

$$F_{TM}=\frac{[R_m(\rho)]^2}{[fR'_m(f)]^2-[R'_m(1)]^2},$$

and

$$F_{TE}=\frac{[S'_m(\rho)]^2}{(f^2h_m{}^2-n^2)[S_m(f)]^2-(h_m{}^2-n^2)[S_m(1)]^2},$$

and the coefficients before these factors have the character $-j$ and $+j$ respectively when the characteristic values g_m or h_m exceed $n\beta/\rho$. The formal expression written above for Z_n/n clearly requires modification to take account of a non-vanishing transverse extent of the beam and to make allowance for losses that will prevent the factors $[(n/\rho)^2-(g_m/\beta)^2]^{1/2}$ and $[(n/\rho)^2-(h_m/\beta)^2]^{-1/2}$ from becoming exactly zero or infinite under 'resonant' conditions.

With respect to the first of the modifications just mentioned, we may note that for a large m, a combination of two of the terms just written will make a contribution that can be estimated as $-j(Z_0/\beta\gamma^2)(1/m)$, a capacitive impedance by virtue of the factor $-j$. Such terms, summed over large m to a limiting value that will depend on the minor dimensions of the ring, will provide a contribution to Z_n/n of the form $-j(Z_0/\beta\gamma^2)$ times a logarithmic factor in which the minor dimensions of the ring appear in the argument. This result is concordant with the expected low-frequency inductive impedance whose dominant (logarithmic) term is given approximately by $2\pi\beta cj[(Z_0/2\pi c)\ln(8R/a)]$ for a circular ring of round wire (major and minor radii: R, a), combined with the corresponding capacitive contribution (larger, by a factor $1/\beta^2$) of opposite sign—or (more generally) with a contribution to Z_n/n of the form $-j(Z_0/\beta\gamma^2)\ln(D/a)$, where D is related to a major dimension of dominant importance[7] (such as R, λ, or the spacing to the wall). In practice, terms of high m value were diminished by a 'convergence factor' that served to suppress terms for which $m\pi \gg$ outer tube radius/minor radius, and the details of this procedure did not appear to affect the results materially for parameter values of interest in the present work.

With respect to the potentially resonant factors $[(n/\rho)^2-(g_m/\beta)^2]^{1/2}$ and $[(n/\rho)^2-(h_m/\beta)^2]^{-1/2}$, for the TM and TE modes respectively, these were replaced by

$$\{(n/\rho)^2-[(1+j/2Q_{TM})g_m/\beta]^2\}^{1/2}$$

and

$$\{(n/\rho)^2-[(1+j/2Q_{TE})h_m/\beta]^2\}^{-1/2}.$$

Such a replacement, although leading to a typical resonant-factor behavior, perhaps can be justified rigorously only if (i) the boundary condition at a resistive wall can be correctly written in terms of a surface resistance $\mathscr{R}_s$ as $E_\phi/H_z = (1+j)\mathscr{R}_s$ *and* (ii) the corresponding complex characteristic value (g_m or h_m) is given with sufficient accuracy by a first-order development from the case in which $\mathscr{R}_s = 0$. With the exception of cases in which the quality factors are very low (*e.g.*, < 10), however, the resonant factors written above are believed to be suitable in applications of the present work. In performing the computations, one has the option of either (i) computing for each n the Q_{TM} and Q_{TE} values for the m-value lying closest to resonance in each case, using a specified specific volume resistivity ρ_v for the tube material ($\mathcal{R}_s = \sqrt{\mu_0 \omega \rho_v / 2}$), or (ii) simply specifying a single value of Q to be used throughout (thereby permitting the user to represent loss mechanisms deliberately introduced into the structure).

3. EXPECTED CHARACTER OF THE COUPLING IMPEDANCE

The selection of geometrical configurations for which the longitudinal coupling impedance can be expected to be favorable or unfavorable for electron-ring stability may be guided by some general considerations. A ring beam enclosed within a structure with highly-conducting walls potentially can excite resonances that will lead to unacceptably high values of the coupling impedance. Reflections may be expected to be suppressed for certain (high-n) modes, however, if the boundary is poorly reflecting and is situated in the radiation-field zone for such modes—with the result that the corresponding impedance then should be close to that cited for a beam in free space ($Z_n/n \cong 354 i^{1/3} n^{-2/3}$ ohms,[7,12,13] for n well below a critical harmonic number that is of the order of γ^3).[13-15] For lower n, where the free-space coupling impedance would be unacceptably high, a surface of high conductivity close to the beam should serve to lower E_ϕ at the beam and so act to reduce the coupling impedance substantially if resonant responses are avoided for such n-values.

In a computational investigation of coupling impedance for a ring beam in the presence of one or two co-axial tubes, it is of interest, therefore, to include an examination of cases in which the beam is situated only a small distance *outside* an inner conducting tube, in an effort to provide coupling impedances that for low n will be well below the free-space values. If, with such geometry, mechanical considerations require the presence of an additional tube exterior to the beam, one may anticipate that the selection of a suitably large radius for this outer tube will preclude the excitation of dangerous low-order resonances. Under such conditions, the provision of only moderate losses, by any one of several means at the outer radius, may suffice to suppress adequately the contributions of high-order (possibly resonant) TE_{nm} modes (high m)—for which the $m-1$ sign reversals of $E_\phi(r)$ ultimately must serve to reduce the coupling between the electromagnetic field and a beam of appreciable radial extent.

For purposes of comparison, there also is interest in cases in which the beam is located just *inside* an outer tube, with an inner tube either absent or assigned a considerably smaller radius. Under these latter circumstances the surface conductivity of the wall should be high for the low-frequency (low-n) modes, but the resonances that can occur for larger values of n should be suppressed by a deliberate reduction of the quality factor ('de$Q$-ing') for high-frequency fields.

4. COMPUTATIONAL RESULTS

The possibility of attaining undesirably large values of coupling impedance as a result of resonances is illustrated in Fig. 1 for a two-tube structure

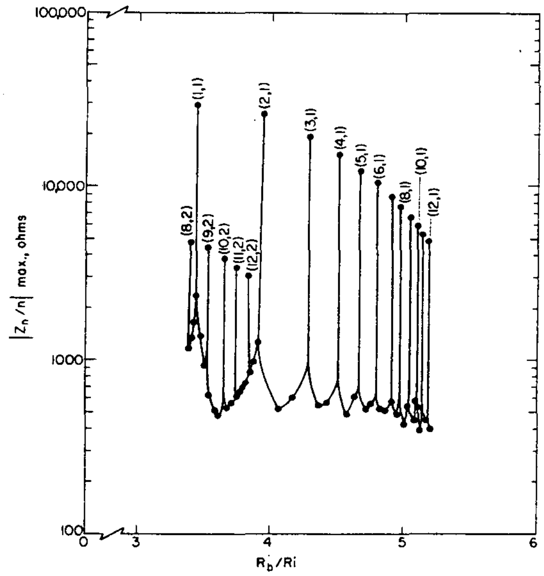

FIG. 1. Maximum longitudinal coupling impedance, divided by n, for the first 12 azimuthal modes for coaxial copper tubes of radius ratio 6. For wall resistivity $\rho_v = 1.8 \times 10^{-6}\ \Omega$-cm the Q's are in the range of 10^4-10^5. Beam locations were chosen to excite the $\mathrm{TE}_{n,1}$ and $\mathrm{TE}_{n,2}$ resonances and to exhibit resonant behavior.

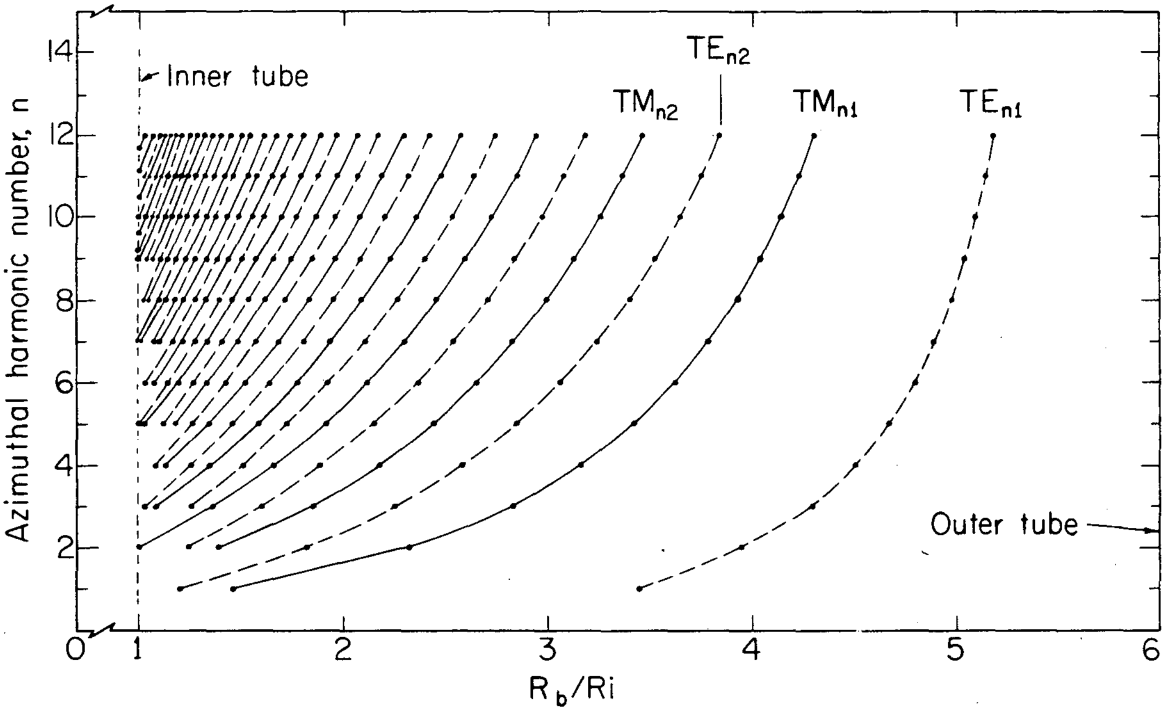

FIG. 2. Resonant beam radii for coaxial tubes with radius ratio 6. For a given n the TE$_{nm}$ and TM$_{nm}$ resonances alternate, with m increasing to the left.

with a radius ratio 1 : 6 and high values of Q which would be appropriate for tubes constructed of a good conductor such as copper. By reference to a mode chart (Fig. 2) that shows the beam radii for resonant excitation of the wave-guide modes in such a geometry (with $\beta = v/c = 0{\cdot}999703$), it is evident that the largest value of $|Z_n|/n$ occurs when the beam is located so as to excite the TE$_{1,1}$ resonance, the second highest value corresponds to excitation of the TE$_{2,1}$ mode, *etc.*, with the low-n TE$_{n,1}$ modes dominating the coupling impedance in the region where the TE$_{n,1}$ modes are excited—that is, from approximately midgap to the outer wall. The TE$_{n,1}$ modes are distinctive[15]—and can be particularly troublesome—because the associated $E_\phi(r)$-field experiences no sign reversal. The TE$_{1,1}$ resonant beam radius for the case of a *single* tube is $R_B \cong \beta R_{\mathrm{OUT}}/1.8412$ and the corresponding resonant radius for a *pair* of tubes whose radius ratio does not greatly exceed unity is close to $R_B \cong \beta(R_{\mathrm{IN}}+R_{\mathrm{OUT}})/2$, while the resonant radii for other TE$_{n,1}$ modes will be progressively larger. The existence of these potentially-resonant modes thus deserves recognition when considering operation with the ring beam fairly close to an outer cylindrical wall.

The curves of Fig. 3 again indicate the behavior of Z_1 *vs.* R_B for $R_{\mathrm{OUT}}/R_{\mathrm{IN}} = 6$, and illustrate the influence of the quality factor Q. One notes that, as expected, for Q sufficiently large,

(i) For $\omega < \omega_{\mathrm{resonant}}$ [$\rho > n\beta/$(characteristic value, h)]

$Z_{n,\mathrm{Real}}$ is relatively small (in comparison to $Z_{n,\mathrm{Imag.}}$) and is approximately proportional to $1/Q$ (as may be interpreted as due to wall resistance acting on image currents), while $Z_{n,\mathrm{Imag.}}$ is rather insensitive to Q;

(ii) For $\omega = \omega_{\mathrm{resonant}}$

$Z_{n,\mathrm{Real}} \cong |Z_{n,\mathrm{Imag.}}|$, each assuming large values $\propto \sqrt{Q}$;

(iii) For $\omega > \omega_{\mathrm{resonant}}$

$Z_{n,\mathrm{Real}}$ is large (in comparison to $Z_{n,\mathrm{Imag.}}$) and is rather insensitive to Q—corresponding to power

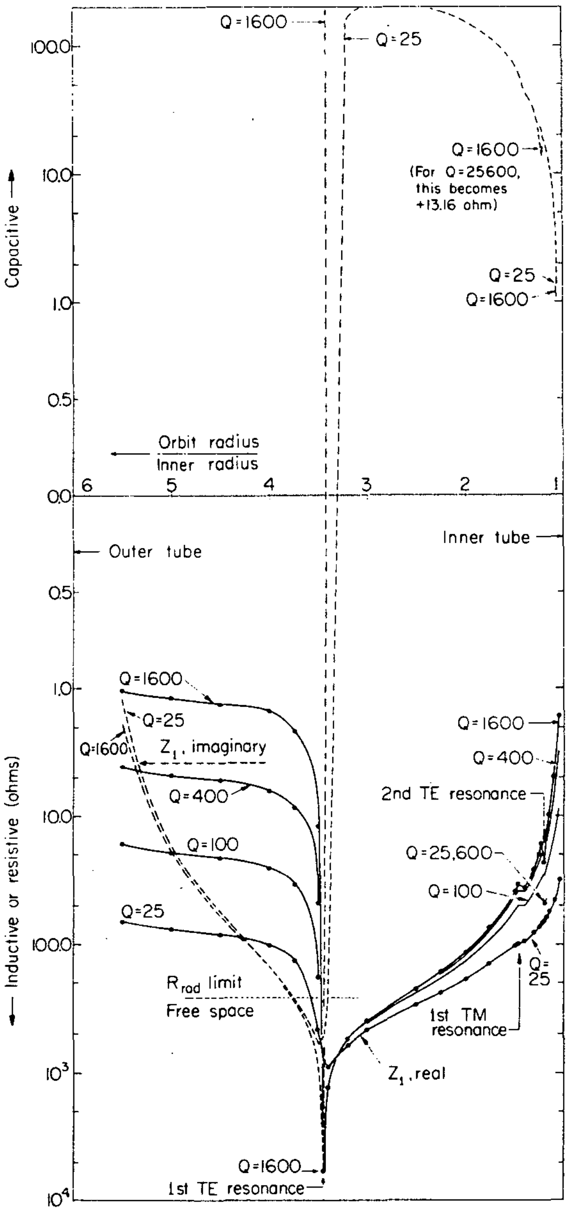

FIG. 3. Longitudinal coupling impedance for $n = 1$, for coaxial tubes with a radius ratio of 6. For this case, $\gamma = 41$, and the minor dimensions a and b are 0.02 R_{inner}.

radiated down the tubes (and ultimately absorbed, remotely, in the tube walls or emerging from the ends).

The curves of Fig. 4 depict the results of computations intended to indicate how $(|Z_n|/n)_{\max}$ can be held to reasonably low values either (i) by operating with a moderate value of Q and situating the beam close to an inner tube (so that excitation of low-order resonances is precluded), or (ii) by operating with the beam close to an outer tube, with Q deliberately caused to decrease at the higher frequencies in order to reduce the extent to which the higher-order resonances can be excited. In performing computations pertaining to this latter type of operation, the computations (with selected Q values) were extended to sufficiently large values of n that $|Z_n|/n$ appeared to have become distinctly a monotonically decreasing function of n that essentially merged into the free-space curve for this quantity. Two illustrative examples of the computational results for the two cases described are shown in Figs. 5 and 6.

It will be recognized that, in the selection of parameters for an electron-ring device, a decision to operate with a ring situated close to a conducting tube necessarily restricts the amount of energy spread (and attendant radial spread) that can be present and that also could act to suppress the

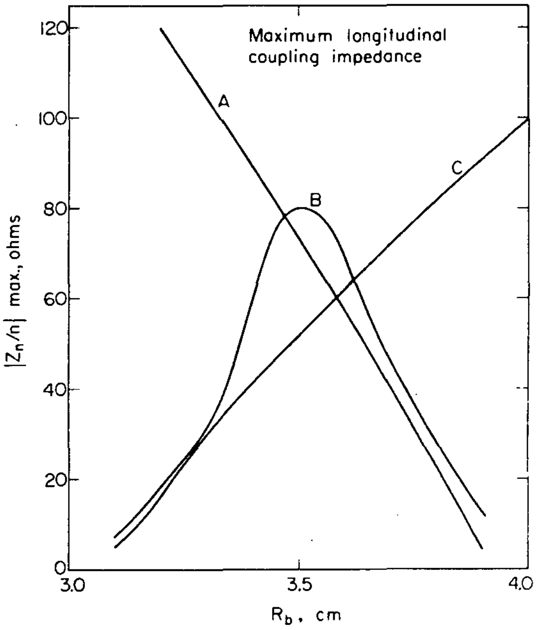

FIG. 4. Maximum longitudinal coupling impedance divided by n. A—Beam located close to an outer wall at 4 cm and $Q(n)$ adjusted to minimize $|Z_n/n|$. B—Beam located between two walls at 3 cm and 4 cm and $Q(n)$ adjusted to minimize $|Z_n/n|$. C—Beam located close to an inner wall at 3 cm and Q made high for all n.

longitudinal instability. As a guide for finding suitable parameters, therefore, it is convenient to have at hand a simple relationship that relates $(|Z_n|/n)_{\max}$ to the 'clearance' throughout the range of possible practical interest for these parameters. The results shown in Fig. 4 for a beam situated at a small distance outside an inner conducting tube suggest that with reasonable accuracy one may write $(|Z_n|/n)_{\max} \cong 300\,(R_B - R_{\mathrm{IN}})/R_{\mathrm{IN}}$ ohms, for $R_{\mathrm{IN}}/30 \leqq R_B - R_{\mathrm{IN}} \leqq R_{\mathrm{IN}}/3$, under these circumstances. Thus, with $(R_B - R_{\mathrm{IN}})/R_{\mathrm{IN}} = 0.2$—that should provide sufficient clearance for a beam with a radial spread arising from $\Delta E/E \gtrsim 10$ per cent (full width at half maximum)—we should expect to achieve a longitudinal coupling impedance such that $|Z_n|/n \cong 60$ ohms. The results shown in Fig. 4 are quite insensitive to γ, decreasing typically by about 2 per cent when γ is increased from 20 to 82. The minor dimensions of the beam have a larger effect on Z_n/n than the γ dependence, because the self field term and the term due to excitation of high m modes decrease as the beam minor dimensions are increased. The curve C in Fig. 4 is moved approximately 0.05 cm to the left as the minor dimensions are decreased from 0.1 cm to 0.05 cm, and approximately 0.15 cm to the right as the minor dimensions are increased to 0.2 cm, for a < 10 per cent change of $|Z_n|/n$ in the region around 60 Ω. At much greater spacings from the inner tube the dependence of $|Z_n|/n$ on the minor dimensions becomes negligible because of the dominance of the low n and m modes.

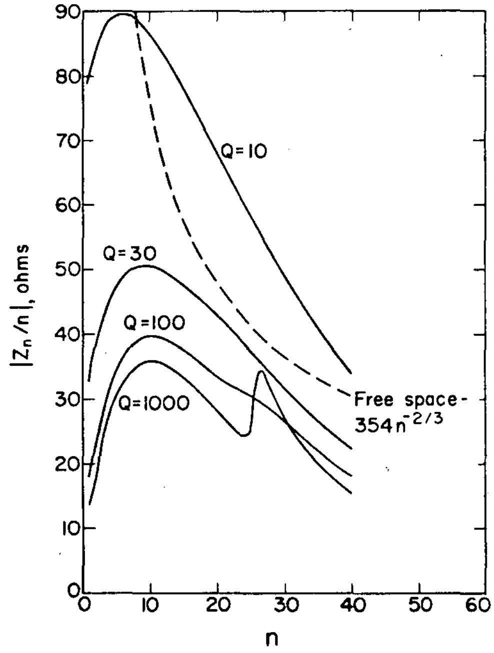

FIG. 5. Typical curves of $|Z_n/n|$ versus n for a beam radius $R_b = 3.4$ cm near an inner tube at 3 cm and an outer tube at 27 cm, with Q as a parameter. $\gamma = 41$ and the minor dimensions a and b are 1 mm. At this radius, resonant behavior (due to the presence of the outer tube) is seen to be developing at $n \simeq 27$, whereas the $|Z_n/n|_{\max}$ of the first peak is at $n \simeq 10$. For min $|Z_n/n|$ for all n at this radius, Q should decrease from ~ 1000 at $n \simeq 10$ to ~ 30 at $n \simeq 27$. $|Z_n/n|_{\max}$ for this case was taken as 40 Ω in the construction of curve C in Fig. 4.

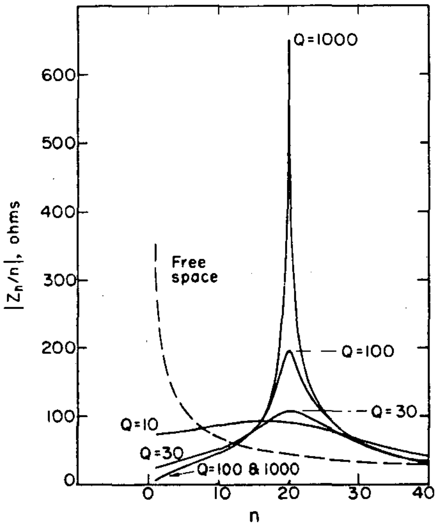

FIG. 6. Typical curves of $|Z_n/n|$ versus n for a beam radius $R_b = 3.6$ cm near an outer tube at 4 cm, and an inner tube at 0.444 cm, with Q as a parameter. The clearance to the wall, 4 mm, is the same as in Fig. 5, $\gamma = 41$, and the minor dimensions a and b are 1 mm. At this radius, resonant behavior is seen at $n = 20$, therefore minimum $|Z_n/n|$ for all n would be obtained by switching from high Q to low Q at $n \simeq 13$. $|Z_n/n|_{\max}$ for this case was taken as 60 Ω in the construction of curve A in Fig. 4.

5. CONCLUSIONS

An examination of the longitudinal coupling impedance that can be attained for a ring beam between a pair of co-axial conducting tubes has indicated that low values of $|Z_n|/n$ may be conveniently attained by situating the beam a small distance outside an inner conducting tube. If, alternatively, the beam is close to an outer tube, similar results may be obtained if the quality factors for higher multiples of the circulating frequency are reduced so as to suppress potentially resonant fields. For an electron beam with $\gamma = 41$ and a 3.5-cm orbit radius surrounding a tube of radius 2.9 or 3.2 cm, it should be possible in this way to achieve values of $(|Z_n|/n)_{\max}$ that are approximately 62 or 28 ohms, respectively.

ACKNOWLEDGEMENTS

It is a pleasure to express indebtedness to Dr. J. M. Peterson for emphasizing the desirability of examining the influence of an inner tube on longitudinal coupling impedance, to Drs. A. Garren, D. Möhl, and A. Sessler for many helpful discussions during the course of this work, and our thanks to Mrs. Barbara (Harold) Levine for assistance with much of the computational work.

REFERENCES

1. D. Möhl, L. J. Laslett, and A. M. Sessler, 'On the Performance Characteristics of Electron Ring Accelerators', LBL Report 1062, Sept. 1972; Particle Accelerators, this issue.
2. R. J. Briggs, 'Coherent "Radiative" Instabilities of the Compressed Electron Ring', WC/ERA-11, *in Proc. 1968 Symposium on Electron Ring Accelerators*, UCRL-18103, p. 434-441 (Lawrence Berkeley Laboratory, 1968).
3. I. N. Ivanov, 'Influence of Shielding on the Negative-Mass Effect', P9-3476-2 (Joint Institute for Nuclear Research, Dubna, Aug., 1967); A. G. Bonch-Osmolovsky and E. A. Perel'shteyn, 'Longitudinal Instabilities in Circular Charged Beams', Part I, P9-4424 and Part II, P9-4425 (Joint Institute for Nuclear Research, Dubna, 1969).
4. A. Garren and D. Möhl, 'Longitudinal Coupling Impedance of an Electron Ring in a Long Metal Tube', ERAN-176 (Lawrence Berkeley Laboratory, 1971; unpublished).
5. I. L. Korenev and L. A. Yudin, 'Instabilities of the Electron Ring in the Waveguide', Radiotechnical Institute of the Academy of Sciences of the USSR (April, 1971).
6. A. Garren, 'The Longitudinial Coupling Impedance of a Circular Beam Between Infinite Plane-Parallel Laminated Plates of Arbitrary Electrical Properties', ERAN-150 (Lawrence Berkeley Laboratory, 1971; unpublished); A. C. Entis, A. A. Garren, D. Möhl, 'Shielding of Coherent Radiation to Suppress Longitudinal Instability in Electron-Ring Compressors: Laminated Sidewalls', ERAN-174 (Lawrence Berkeley Laboratory, 1972; unpublished).
7. A. G. Bonch-Osmolovsky, 'Influence of Metallic Surfaces on the Stability and Focusing of Relativistic Electron Rings', P9-6318 (Joint Institute for Nuclear Research, Dubna, 1972).
8. R. J. Briggs and V. K. Neil, *Plasma Physics*, **9**, p. 209 (1967).
9. V. K. Neil and A. M. Sessler, *Rev. Sci. Instr*, **36**, 429 (1965).
10. The characteristic functions introduced here can be expressed in terms of the customary Bessel and Neumann functions as

    $$R_m(x) \propto J_n(g_m)\,Y_n(g_m x) - J_n(g_m x)\,Y_n(g_m),$$

    with

    $$J_n(g_m)\,Y_n(g_m f) - J_n(g_m f)\,Y_n(g_m) = 0,$$

    and

    $$S_m(x) \propto J_n'(h_m)\,Y_n(h_m x) - J_n(h_m x)\,Y_n'(h_m),$$

    with

    $$J_n'(h_m)\,Y_n'(h_m f) - J_n'(h_m f)\,Y_n'(h_m) = 0.$$
11. C. Pellegrini and A. M. Sessler, 'Effect of Coherent Radiation During Ring Compression', WC/ERA-22, *in Proc. 1968 Symposium on Electron Ring Accelerators*, UCRL-18103, pp. 442-445 (Lawrence Berkeley Laboratory, 1968).
12. *Cf.* A. G. Bonch-Osmolovsky, *et al.*, P9-5622 (Joint Institute for Nuclear Research, Dubna, 1971); D. Keeley and P. Goldreich, 'Coherent Synchrotron Radiation' (Lick Observatory, University of California at Santa Cruz, private communication, 1970).
13. D. Möhl, 'Longitudinal Instability in an ERA Acceleration Column', ERAN-178 (Lawrence Berkeley Laboratory, 1971; unpublished).
14. G. A. Schott, *Electromagnetic Radiation* (Cambridge, 1912).
15. J. Schwinger, *Phys. Rev.*, **75**, 1912 (1949).
16. L. Jackson Laslett and William Lewish, 'Evaluation of the Zeros of Cross-Product Bessel Functions', IS-189 (Ames Laboratory, Iowa State University, Ames, Iowa, 1960; unpublished).

Received 15 November 1972

AN ESTIMATE OF LIMITS TO THE LONGITUDINAL COUPLING IMPEDANCE

A. Faltens and L.J. Laslett
Lawrence Berkeley Laboratory

Various simple models of structures in a storage ring and their contributions to the longitudinal coupling impedance are considered in an attempt to focus attention on possible problem areas and their solutions. In all cases emphasis is placed on the physical mechanism which is the source of the undesirable impedance. None of the mechanisms or structures considered prevent the attainment of a low $|Z_n/n|$, of the order of 1Ω, if sufficient care is taken over the frequency range from 0.1 MHz to about 10 GHz.

The various results and views in this note evolved mainly during the time of the Berkeley Electron Ring Accelerator project, in which a substantial effort was devoted to calculating, estimating, and measuring the properties of various beam-surrounding geometries which would simultaneously satisfy longitudinal and transverse stability requirements, and allow penetration of slowly increasing magnetic guide fields and fast inflection fields. Initially, interest centered on the low harmonic "inductive wall" effects, and later shifted to the microwave frequency region. It was shown that there are practical limits to attainable impedances, with the longitudinal impedance being the limiting one, with the limits manifesting themselves in the frequency region where free space wavelength and chamber dimensions are comparable. A value of $|Z_n/n|$ of about 30Ω was the lowest which might be attained in the geometries considered for electron ring accelerators.[1,2] The

corresponding limits for ISABELLE are less than 1Ω. Also, as in recent results from CERN, it was found that stability was determined by the instantaneous local energy spread in a beam filament. Multiturn injection of a beam with an instantaneous energy spread plus an energy ramp in time gave the same high-frequency thresholds as injection without the ramp, thereby imposing more stringent limits on allowable coupling impedances.

Before considering the effects of boxes and bends in the vacuum chamber, it may be appropriate to ask why a metallic vacuum chamber is necessary. The coupling impedance of a completely unshielded beam in free space may be obtained from synchrotron radiation results. The power radiated by an electron in a circular orbit, as derived by J. Schwinger,[3] is:

$$P\,(\omega,t) = \frac{3^{1/6}\Gamma\left(\frac{2}{3}\right)e^2}{\pi R}\left(\frac{\omega}{\omega_o}\right)^{1/3}\left[1 - \frac{\Gamma\left(\frac{2}{3}\right)}{2}\left(\frac{\omega}{2\omega_{crit}}\right)^{1/3} + \ldots\right]$$

for $\omega << \omega_{crit}$, independently of particle energy and therefore presumably the type of particle, and,

$$P\,(\omega,t) = \frac{3}{4}\left(\frac{3}{2\pi}\right)^{1/2}\frac{e^2}{R}\left(\frac{E}{mc^2}\right)^4\left(\frac{\omega_o}{\omega_{crit}}\right) \times$$

$$\left(\frac{\omega}{\omega_{crit}}\right)^{1/2} e^{-\omega/\omega_{crit}} \times \left[1 + \frac{55\omega_{crit}}{72\omega} + \ldots\right]$$

for $\omega >> \omega_o$ (2π times the revolution frequency), and $\omega_{crit} = (3/2)\,\omega_o\,(E/mc^2)^3$, or in our notation the harmonic number of the critical frequency is $n_{crit} \simeq (3/2)\,\gamma^3$.

---

1. A. Faltens, G.R. Lambertson, J.M. Peterson, J.B. Rechen <u>Proc. IXth Int. Conf. on High Energy Accelerators</u>, 1974, p. 226.
2. A. Faltens and L.J. Laslett, Particle Accelerators 4, 151, 1973.
3. J. Schwinger, Phys. Rev. 75, 1912 (1949).

The power raditated at any harmonic, n, may be related to the real part of the coupling impedance, R_n, and the n^{th} harmonic current Fourier amplitude, I_n, of a δ-function charge traveling in a circle as $p_n = I_n^2 R_n/2$. Inclusion of the reactive terms leads to the result:[4]

$$\frac{Z_n}{n} = 354\ n^{-2/3}\left(\frac{\sqrt{3}}{2} + j\ \frac{1}{2}\right).$$

At very low harmonics, the more precise result is about 10% smaller, about 320Ω for n = 1, but very much larger than the "long wavelength limit",

$$\frac{Z_n}{n} \simeq -\left(jZ_o/\beta\gamma^2\right)\ \ln\frac{R}{na} \leq -\ j4\Omega$$

obtained by using the static inductance and capacity of a beam, and also greater than the tolerable impedance for ISABELLE.[5] The beam must, therefore, be shielded to suppress the low-harmonic radiation.

One shielding geometry of interest is a metallic pipe surrounding the beam. Such a pipe is an effective shield for wavelengths longer than its waveguide-cutoff wavelength, which for a circular pipe is given by

$$\lambda_{co} = \frac{2\pi a}{2.405} \quad \text{for TM or E-type waves.}$$

The harmonic number at which propagation begins for a 4 cm radius pipe of 2960 meter circumference is $n_{co} \simeq 2960/\lambda_{co} \simeq 28\ 325$, at which harmonic the $|Z_n/n|$ of free space has dropped to about 0.38Ω. Right at cutoff the impedance of the idealized smooth pipe is much less than this, but eventually, with increasing frequency many modes will propagate and the impedance should approach the free space values. The question regarding the beam pipe is: "At what frequency will it give behavior similar to free space, that is, for which wavelengths will the changes in pipe direction, wall losses, imperfections, clearing electrodes, etc. destroy the coherence of the radiated waves and scatter them randomly into the chamber until their energy is dissipated?" A reasonable estimate for this wavelength is about a centimeter, for which $|Z_n/n| \simeq 0.1\ \Omega$. Taking into account the local curvature of the particles only in the magnets, $n_{crit} \simeq 10^5$ at injection and $\simeq 3 \times 10^7$ at final energy, so we are interested in wavelengths down to centimeters and microns respectively.

In the nonphysical model of a perfectly smooth pipe bent into a circle, there will be resonances which for an aluminum wall could have high Q values, leading to higher coupling impedances than the free space values if the beam is able to excite them. Analogous problems using the eigenfunctions of a pill box cavity, coaxial cylinders, or a single cylinder showed that resonance that could be excited by a beam would occur at harmonic numbers n where

$$\frac{r_{beam}}{\beta R_{outer\ wall}} \simeq \frac{1}{1 + 0.80862n^{-2/3}},$$

where the required slowing of the phase velocity of the wave may be thought of as arising from the wave traveling at a slightly larger radius than the beam. In a straight, smooth pipe this synchronism does not occur because the phase velocity of any

---

[4] A.G. Bonch-Osmolovsky, P9-6318, J.I.N.R., Dubna, 1972.

[5] W. Schnell, "Stacking & Acceleration", Summary Report of Working Group, Vol. I, p. 126.

mode is always greater than c, and the beam in vacuum will always travel at less than the velocity of light. The waves of course can be slowed down by loading of various types, and in ISABELLE this will undoubtedly be more important than the curvature effects, but the point is that even with smooth walls resonant effects may occur for $n \simeq 10^6$ at high γ.

One such "smooth wall" resonance is illustrated in the Appendix, where the properties of an 8 cm × 8 cm square cross sectioned aluminum chamber of 2960 meter circumference have been computed. The results of this computation are that a beam of $\gamma = 200$ will resonate at harmonic numbers of about 2.5×10^6 with modes having a $Q \sim 3 \times 10^5$. Fortunately, the $|Z_n/n|$ of these modes is only $\sim 0.2\Omega$, or about a factor of 10 above what radiation into space would give at that frequency, and no resonances at all are excited at the injection energy.

Returning to the real geometry of a beam pipe with bends, discontinuities, etc., resonances may be expected at the cutoff harmonic, n_{co} and even lower if resonant structures are introduced into the chamber. A rule of thumb for attainable cavity impedances is: $R \simeq \sqrt{f\ (\mathrm{MHz})}\ \mathrm{M}\,\Omega/\mathrm{meter}$. The maximum useful length for a cavity is $\ell \simeq \lambda/2$ before transit time effects start to decrease R; if the cavity length is much longer than $\lambda/2$, the net interaction with a beam is due to a length of $\lambda/2$ or less, with the remainder of the length acting as a load on the cavity. Combining the above yields an estimate for single, simple cavities of:

$$\frac{R_n}{n} \leq 4.7 \times 10^8 \left(\frac{\lambda}{2\ell}\right) n^{-3/2}$$

As an example of the sort of structure which should be avoided or modified, we consider a 30 cm long section of 12 cm diameter pipe inserted in the standard 8 cm pipe in order to join beam pipes and provide a space for clearing electrodes and monitors (Fig. 1). The R_n/n for such an empty cavity could be as high as 50Ω. If this structure is complicated by insertion of clearing electrodes suspended at their midpoints, then this object is expected to resonate in a lower Q, half-wave TEM mode, coupling to the beam with the longitudinal fringing fields at its ends. Capacitive bypassing of such a clearing electrode is unattractive because a very large capacity, $C \sim 400\ \mu\mathrm{F}$, is required for the $L \approx 12\mathrm{nH}$ inductances which are to be bypassed. A well conducting clearing electrode at a 4 cm radius and ~ 30 cm long will resonate near $n = 4500$ with a Q of ~ 3000, and also produce an R_n/n of a few tens of ohms. By contrast, the contribution to Z_n/n from inductive wall effects is almost negligible. At low frequencies, the "inductance" of the empty box is due to the capacity of the fringing fields at the corners, which is effective over a distance comparable to the step size, $\Delta \simeq b - a$. The "inductance" of the box with clearing electrodes is approximately the inductance of the electrostatically shielded volume between the clearing electrode and the chamber outer wall. The impedances may be estimated as:

$$\frac{Z_n}{n} \simeq \frac{j\mu_o\omega_o}{2\pi} \left(\ell n\frac{b}{a}\right)\left(b-a\right) \simeq j\ 0.001\Omega, \text{and}\ \frac{j\omega_o\mu_o}{2\pi}\left(\ell n\frac{b}{a}\right)\left(\ell\right) \simeq j\ 0.0153\Omega$$

respectively. The impedance due to the use of bellows for the outer wall certainly is small compared to the latter value, but could be reduced by bridging the bellow convolutions with longitudinally conducting strips of metal. The precise value of the low-n (Z_n/n) may be measured.[6]

---

[6] A. Faltens, E.C. Hartwig, D. Mohl, and A.M. Sessler, 8th Int. Conf. on High Energy Accelerators, 1971, p. 338

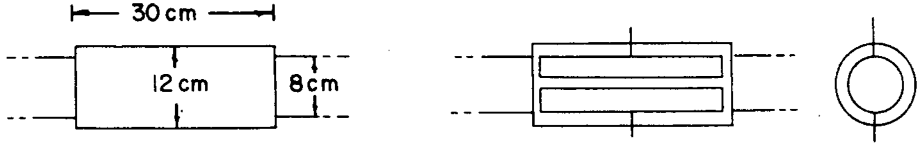

(a) JUNCTION BOX

(b) JUNCTION BOX WITH CLEARING ELECTRODES

Fig. 1

After the obvious resonant structures are eliminated or otherwise made harmless, the beam pipe is still left with bends and other discontinuities. If no lossy materials are introduced at the discontinuities, then each junction simply transmits and reflects the incident waves, making each section of beam pipe no worse than an approximately 5 meter long cavity, for which a resonance at $n \approx n_{co}$ is expected with an $R_n/n \leq 1\Omega$. A long structure such as this poses questions which can only be answered statistically: will one of the cavity resonances fall exactly on some beam harmonic; what will be the transit time factor; and how many cavities will be resonant at the same frequency? Taking the worst case limit for each would make $Z_n/n \simeq 500$ for an estimated total of 500 beam pipe sections. The Z of an n = 28 000 resonance can be expected to be less than 30 000, so the probability of some harmonic hitting it is essentially 1. The transit time factor as used here oscillates as $\sin^2(\pi\ell/\lambda)$ with increasing cavity length, giving an expected value of 1/2. Simultaneous resonance of many sections is more likely at the cutoff frequency than at higher frequencies, therefore the potential problem is serious. However, the problem is easily overcome as only a small amount of loss, attainable by numerous means, will lower the Q's sufficiently to make the impedance very low. If the de-Qing is very successful, then the coupling impedance will approach the free space limits again, as any radiated energy from the beam would be absorbed. As the problem area is right around the cutoff frequency region, the $|Z_n/n|$ thus would tend towards 0.38Ω, perhaps enhanced by a small factor due to weak resonances remaining after de-Qing.

In the frequency region far above cutoff, that is, where modes are simultaneously propagating, the quality factors of individual resonances will be smaller than perhaps expected because any discontinuity, unless it is specially designed to counteract the effect, will scatter energy into other propagating modes. Likewise, the Q's of single resonators may be expected to be high only for frequencies below the cutoff frequency of the beam pipe. At these very high frequencies and at high γ the beam fields travel essentially as plane waves, parallel to the beam, with nearly identical fields to the fields of a TEM wave in a coaxial transmission line, and their scattering at obstacles may be estimated geometrically. Given a beam incident upon a number of obstacles, the reflection of the fields at the first obstacle will be higher than at subsequent ones because of the time required to re-establish the fields. In the rest frame of the particle the fields would be re-established with a transverse speed of c or less, which in the laboratory frame would be $v_t \leq c/\gamma$. The impedance of an isolated obstacle in the shape of a concentric disc with inner and outer radii a and b, respectively, based on the above considerations is:

$$Z = \frac{Z_o}{2\pi} \ell n \frac{b}{a} .$$

As an example, for a = 3 cm, b = 4 cm.

$$Z \cong 17\Omega ,$$

and only one such obstacle would be effective per beam pipe junction. The total impedance for wavelengths of 1 cm or less, for which the above mechanism might apply is ~ 8.5 kΩ, and

$Z_n/n \le 0.028\Omega$, and therefore no suprises or high impedances are expected for very high frequencies ($n > 10^5$).

The ordinary skin resistance contributes a term $Z_n/n = (1+j)\sqrt{\omega_0\mu\rho/2n}\ (\ell/2\pi a)$, which is important only at low harmonics, with a peak magnitude of 1.7Ω, and decreasing as $n^{-1/2}$. A small amount of wall impedance, of the order of $j1\Omega$, is desirable to offset the space charge term $Z_n/n \simeq jZ_0/\beta\gamma^2\ (\ell n\ b/a) \simeq -j1\Omega$ at the injection energy.

The preceding limits and the harmonic range over which they are important may be all combined on one graph (Fig. 2). Some specific items such as rf cavities and kicker magnets have been excluded here because they are treated separately elsewhere and because their impedances can be made small. The expected $|Z_n/n|$ curve, after elimination of low frequency resonances and diminution of wall inductances due to discontinuities, should follow the heavy line, and stay below 1Ω for all frequencies except the first two harmonics. On the other hand, any resonant object in a wide frequency band is potentially very harmful and should be avoided. The graph was constructed to show the large possible variation of coupling impedance. The single cavity approximation assumes only one cavity in the ring at any harmonic, and the presence of harmful low-harmonic resonances is unlikely in any event. The value of Z_n/n for vacuum chamber resonances is an estimate for the worst case of ~ 500 sections acting similarly.

The general recipe for obtaining low $|Z_n/n|$ for all n is therefore to shield the beam with a nearby good conductor to decrease the low harmonic free space impedance. The shielding geometry will in most practical cases introduce resonances at higher frequencies, and at that point it is beneficial to provide attenuation, which, in the limit of sufficient attenuation at high frequencies will make the impedance approach the free space values (see Ref. 2 for some computed examples). There is a trade-off between low-n and high-n $|Z_n/n|$'s, as measures taken to move the

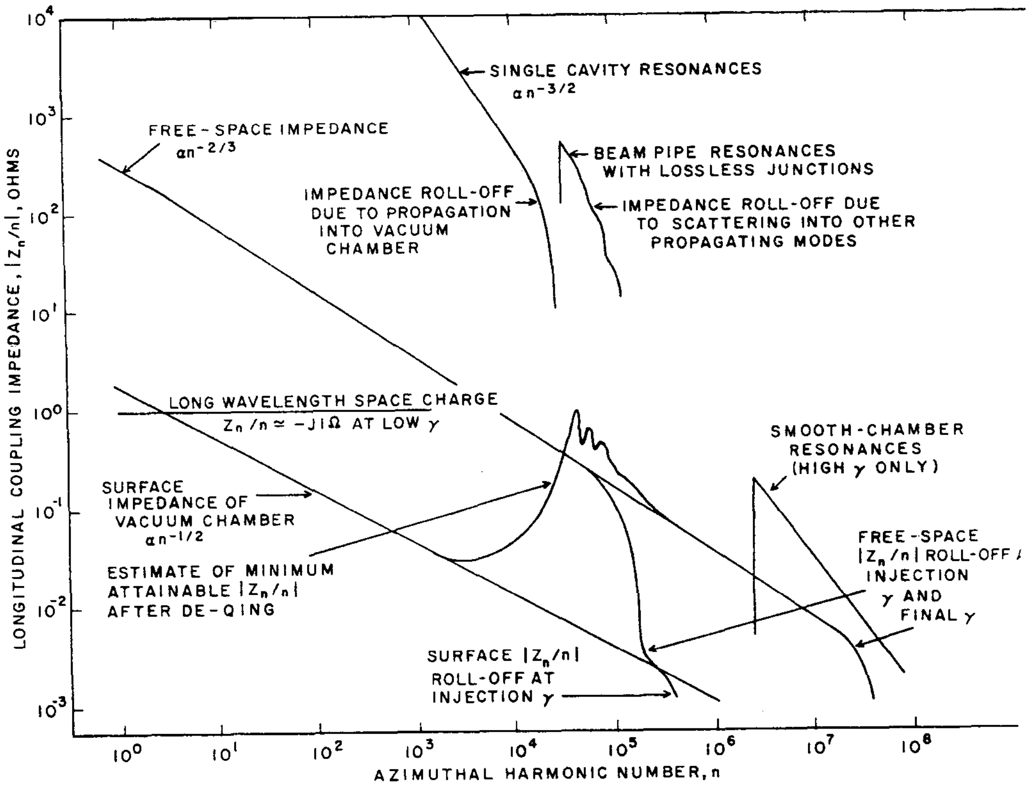

Fig. 2. Estimate of Coupling Impedance Limits

resonant behavior to higher frequencies by decreasing the shielding pipe diameter tend to increase the very low harmonic surface impedance. For the parameters of interest to ISABELLE, a maximum $|Z_n/n|$ of the order of 1Ω is estimated to be possible for all n.

APPENDIX

Coupling Impedance Contribution From the Electromagnetic Modes of a Toroidal Vacuum Chamber

The electromagnetic modes of a number of structures such as cylinders, pillbox cavities, and toroidal vacuum chambers may couple resonantly with an azimuthal current and produce a contribution to the longitudinal coupling impedance. The effect of such modes is computed for a toroidal aluminum vacuum chamber of square cross section of 8 cm × 8 cm and major radius of 471 meters such as might approximate the ISABELLE vacuum chamber if it were smoothly bent in a circle. Resonant behavior is exhibited only for $\gamma > \gamma_{inj}$, and a contribution to Z_n/n of 0.2Ω is computed for $\gamma = 200$.

The solution of the electromagnetic modes for the geometry:

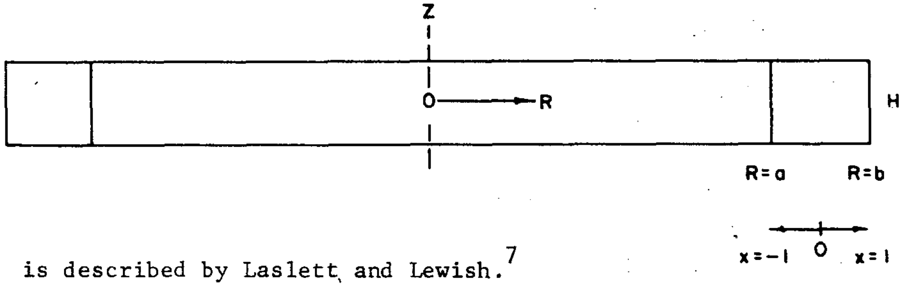

is described by Laslett and Lewish.[7]

The solution for the TE fields at high azimuthal harmonic numbers is depicted in Fig. A-1, where the functions Z and Z′, which are proportional to the B and E fields, are plotted across the normalized chamber radius, x. A beam located in the chamber midplane has a peak normalized coupling impedance on resonance of

---

[7] L.J. Laslett and W. Lewish, Iowa State Report IS-189, 1960.

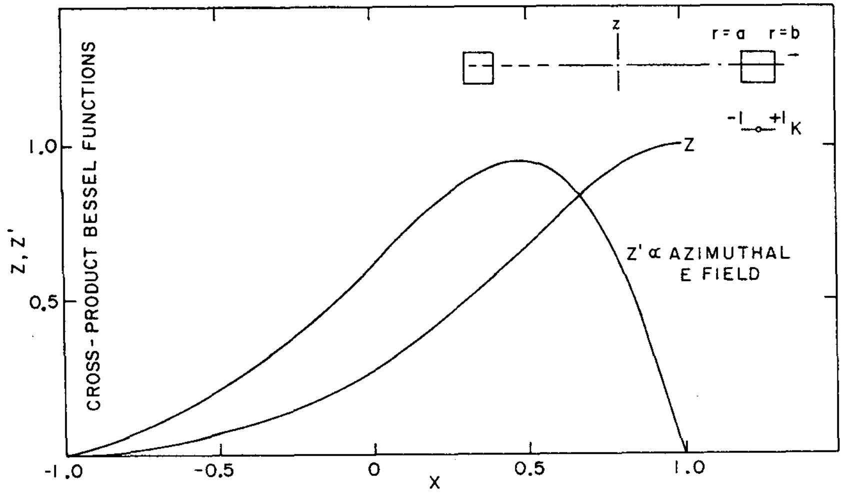

Fig. A1. Z & Z′ functions vs normalized chamber radius for $n = 2.47 \times 10^6$, $\eta = 8.49 \times 10^{-5}$, $\eta = (b-a)/(b+a)$, and square chamber cross section.

$$\frac{R_n}{n} = \frac{\pi Z_o^{\ 2}}{\rho ƛ^2 K^2 n^2} \quad \frac{\frac{1}{\eta^2}\left(\frac{dZ}{dx}\right)^2_{\text{beam}}}{\langle R\rangle^2 q^2 \eta \int (1+\eta x) Z^2 dx + \frac{H}{4}\left\{\frac{n^2}{\langle R\rangle}\left(\frac{Z^2{}_{\text{outer}}}{1+\eta x_o} + \frac{Z^2{}_{\text{inner}}}{1+\eta x_i}\right)\right.}$$

$$\left. + \frac{q^4}{K^2}\langle R\rangle \left((1+\eta x_o) Z^2{}_{\text{outer}} + (1+\eta x_i) Z^2{}_{\text{inner}}\right)\right\}$$

where $q^2 + K^2 = \left(\frac{\omega}{c}\right)$, $\langle R\rangle = \frac{b+a}{2}$, $K = \frac{\pi}{H}$, and $\eta = \frac{b-a}{b+a}$

A handier version of this formula, in terms of the chamber Q is:

$$\frac{R}{n} = \frac{4\pi Z_o Q}{n q^2} \quad \frac{ƛ}{H < R >^2 \eta^3} \quad \frac{\left(\frac{dZ}{dx}\right)^2_{\text{beam}}}{\int_{-1}^{1} (1+\eta x) Z^2 dx}$$

Either formula, evaluated at the first resonance, which occurs for $n \cong 2.5 \times 10^6$ for a beam at the center with $\gamma \cong 200$, results in a value of $(R_n/n) \simeq 0.2\Omega$. The resonant radii for successive azimuthal resonances in this region are spaced by only 16 nanometers, which in combination with the high Q's of these resonances ($> 10^5$) may warrant reexamination of the usual relations between the peak value $|Z_n/n|$ and longitudinal stability.

6

Beam Transport for Heavy Ion Fusion

APPENDIX A

$$I = qe\,\beta c\,N = \frac{1}{4}\,\frac{A}{q}\,\frac{ec}{r_p}\,\beta^3\gamma^3\,\epsilon\,K^{1/2}\,Q'$$

$$= \frac{1}{4}\,\frac{Aec}{q\,r_p}\,\beta^3\gamma^3\,K\,a^2\,\frac{Q'}{U_o^2}$$

$$= \frac{1}{4}\,\frac{e^2}{m_p r_p}\,\beta^2\gamma^2\,B'\,a^2\,\frac{Q'}{U_o^2}$$

$$= \pi\epsilon_o c^2\,\beta^2\gamma^2\,B'\,a^2\,\frac{Q'}{U_o^2}$$

$$= \frac{\pi}{\mu_o}\,(\beta\gamma)^2\,B'\,a^2\,\frac{Q'}{U_o^2}$$

$$= \frac{\pi}{\mu_o}\,(\beta\gamma)^2\,B\,a\,\frac{Q'}{U_o^2}$$

$$= \frac{10^7}{4}\,(\beta\gamma)^2\,B\,a\,\frac{Q'}{U_o^2} \qquad \text{(MKS—A units).}$$

TRANSPORT OF INTENSE ION BEAMS*

G. Lambertson, L.J. Laslett, L. Smith

Lawrence Berkeley Laboratory
University of California
Berkeley, Calfornia 94720

Summary

The possibility of using intense bursts of heavy ions to initiate an inertially confined fusion reaction has stimulated interest in the transport of intense unneutralized heavy ion beams by quadrupole or solenoid systems. We have examined this problem in some detail, using numerical integration of the coupled envelope equations for the quadrupole case. The general relations which emerge are used to develop examples of high energy transport systems and as a basis for discussing the limitations imposed by a transport system on achievable intensities for initial acceleration.

Solution of the Envelope Equations

The envelope equations of Kapchinskij and Vladimirskij (KV) are1).

$$\frac{d^2a_x}{ds^2} = -K_x(s)a_x + \frac{\varepsilon^2}{\beta^2\gamma^2a_x^3} + \frac{4q^2}{A}\frac{Nr_p}{\beta^2\gamma^3}\frac{1}{a_x+a_y}$$

$$\frac{d^2a_y}{ds^2} = -K_y(s)a_y + \frac{\varepsilon^2}{\beta^2\gamma^2a_y^3} + \frac{4q^2}{A}\frac{Nr_p}{\beta^2\gamma^3}\frac{1}{a_x+a_y}\,, \qquad (1)$$

where $a_{x,y}$ = beam half-width, height; $\pi\varepsilon$ = normalized emittance in either plane, q and A are the ion charge state and atomic weight, N is the number of particles per unit length, r_p is the classical proton radius and

$$K_{x,y} = \pm\frac{B'(s)}{[B\rho]} \quad \text{for quadrupoles}$$

$$= \frac{1}{4}\left[\frac{B_s(s)}{[B\rho]}\right]^2 \quad \text{for solenoids (in a frame rotating at the Larmor frequency).}$$

If K(s) is a step-wise function of s, of constant magnitude or zero, Eqns. (1) can be put into dimensionless form by setting

$$s = K^{-1/2}\theta \quad \text{and} \quad a = K^{-1/4}\varepsilon^{1/2}(\beta\gamma)^{-1/2}u:$$

$$\frac{d^2u_x}{d\theta^2} = -S_x(\theta)u_x + \frac{1}{u_x^3} + \frac{Q}{u_x+u_y}$$

$$\frac{d^2u_y}{d\theta^2} = -S_y(\theta)u_y + \frac{1}{u_y^3} + \frac{Q}{u_x+u_y}\,, \qquad (2)$$

where $Q = \frac{4q^2}{A}\,\frac{Nr_p}{\beta\gamma^2\varepsilon K^{1/2}}$ and $S(\theta)$ is a step function of unit amplitude. If $S(\theta)$ is periodic, the necessary aperture and the current for a matched beam can be expressed as functions of Q. For quadrupoles,

$$a = C_1\left(\frac{A}{q}\right)^{1/3} B_Q^{-1/3}(\beta\gamma)^{-1/3}\varepsilon^{2/3}u_m^{4/3},$$

$$I = C_2\left(\frac{A}{q}\right)^{1/3} B_Q^{2/3}(\beta\gamma)^{5/3}(\varepsilon)^{2/3}u_m^{4/3}\,\frac{Q}{u_m^2} \qquad (3)$$

$$= \frac{C_2}{C_1}(\beta\gamma)^2B_Qa\,\frac{Q}{u_m^2}\,,$$

where $C_1 = \left(\frac{m_pc}{e}\right)^{1/3} = 1.46$ [MKSA units]

$$C_2 = \frac{1}{4}\left(\frac{4\pi}{\mu_o}\right)^{5/6}\left(\frac{m_pc^2}{r_p}\right)^{1/6} = 3.66 \times 10^6$$

B_Q and a are defined by $K = \frac{B_Q}{[B\rho]a}$, and u_m is the maximun value of $u_{x,y}$ for the periodic solution of Eqns. (2). B_Q is in Teslas, a and ε in meters and I in electrical amperes.

For a continuous solenoid, let $u_x = u_y = u$, a constant for a matched beam. Equations (2) yield the relation $Q = 2(u^2 - 1/u^2)$, from which one obtains:

$$a = C_3\left(\frac{A}{q}\right)^{1/2} B_s^{-1/2}\varepsilon^{1/2}u \qquad (4)$$

$$I = C_4B_s(\beta\gamma)\varepsilon\left(u^2 - \frac{1}{u^2}\right) = \frac{C_4}{C_3^2}\left(\frac{q}{A}\right)(\beta\gamma)B_s^2a^2\left(1 - \frac{1}{u^4}\right)$$

where $C_3 = \left(\frac{2m_pc}{e}\right)^{1/2} = 2.50188$

$$C_4 = \frac{1}{4}\left(\frac{4\pi}{\mu_o}\right) = 2.5 \times 10^6\,.$$

Q, or the corresponding u_m or u, can be regarded as a free parameter measuring the influence of the space-charge force on particle motion. In the quadrupole case the relation between Q and u_m depends on the lattice structure. It is convenient to use the phase advance per period, $\mu = \int\frac{ds}{\beta} = \int\frac{d\theta}{u_x^2} = \int\frac{d\theta}{u_y^2}$, as the space charge parameter, since it has a more immediate physical significance than Q or u_m. In Fig. 1 is plotted Q/u_m^2 and $u_m^{4/3}$ for a FODO lattice with equal drift and magnet lengths and a phase advance per period of 120° at zero intensity. It is evident from the figure and from the form of Eqns. (4) for the solenoid case that, on the basis of these simple considerations, there is no limit to the current which can be transported, provided that the aperture can be made large enough and the variation in individual particle motion with intensity is tolerable.

---

* Work supported by the U.S. Energy Research and Development Administration.

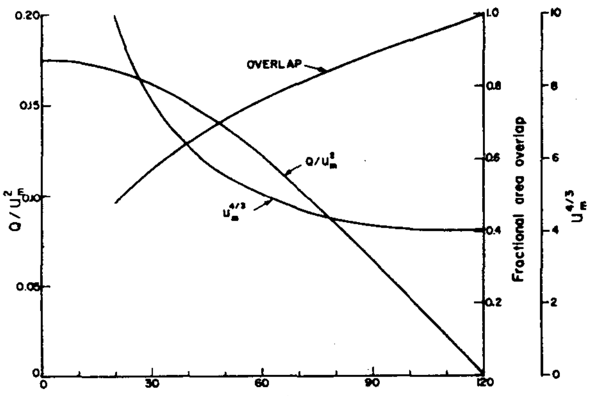

XBL 773-7861

Transport at High Energy

As an application of these equations, we consider a situation in which a beam is extracted from an accelerator, passed through a buncher and allowed to drift some distance to shorten the pulse and increase the current to meet the targeting requirements. It is assumed that the rate of increase of current with distance is sufficiently slow that the transverse motion will adjust itself adiabatically to the matched conditions if it is matched at the entrance to the channel, where the current is low. We further assume that the elements at the end which focus the beam onto the pellet are adjusted to accept the phase-space configuration of the peak of the current pulse, which requires that there be a substantial overlap of the phase space ellipses for peak and lower intensities. The quantity, η, also shown in Figure 1, is the fraction of the zero intensity phase-space area lying inside the higher intensity ellipse, assuming an emittance independent of intensity. It can be seen that requiring η to be larger than, say, 50% sets a definite limit on peak current for a given quadrupole field. Table I gives four examples: energy, peak current and emittance are target requirements[2], B_Q was chosen arbitrarily for U_{238}^{+1} and as high as seemed realistic for I_{127}^{+1} because of the constraint on η.

TABLE I

Examples of High Energy Transport

Ion Type	U_{238}^{+1}		I_{127}^{+1}	
Energy (GeV)	100	40	40	10
I_{peak}(kA)	3.0	1.25	7.5	5
ε(10^{-5} m-radians)	4.0	1.8	3.0	1.6
B_Q(T)	1	1	3	3
a(cm)	4.2	3.0	2.1	2.6
μ(deg)	107	100	92	44
η	.95	.92	.89	.67

Solenoid focusing does not look favorable for the cases considered. It is not difficult to show that $\eta = 1 - \frac{4}{\pi} \tan^{-1} \frac{u-1}{u+1}$, whence $u < 2.5$ for $\eta > .50$.

Eqns. (4) then demand very high fields and large apertures.

Transport at Low Energy

Equations (3) and (4) indicate that particle current must be much reduced at lower energy. Hence, to provide a final high current, the accelerator system is required to build up the current by orders of magnitude by some combination of stacking in transverse space and longitudinal compression.

Additional considerations will affect the application of Eqns. (3) and (4). We assume that there is no need to transport a reduced current as well as the highest current through the same system, or equivalently, that the lower current portion may have a lower emittance. This would then permit the zero-intensity phase shift μ_0 to approach the pass-band limit of 180° and μ to be made as small as allowed by the aperture or other considerations. However, a strong field B_Q may result in quadrupole lengths and drift lengths that are too short, relative to the aperture, to permit fields that are reasonably linear and defined in length (as was assumed in the analysis). For the strong quadrupole case, then, we introduce the additional requirement that the ratio of aperture radius to quadrupole length not exceed a limiting value R and this results in the following limit on particle current in the FODO lattice with equal drift and quadrupole lengths:

$$I = C_5\left(\frac{A}{q}\right)(\beta\gamma)^3 R^2 \,\frac{\Theta^2 Q}{u_m^2}\,,$$

where $C_5 = \frac{1}{16}\left(\frac{4\pi}{\mu_0}\right)^{1/2}\left(\frac{m_p c^2}{r_p}\right)^{1/2} = 1.9 \times 10^6$

and 2Θ is the cell length in the scaled variable, θ.

The quantity $\Theta^2 \frac{Q}{u_m^2}$ will depend on the phase advances, but has a maximum value close to unity.

Two other limitations should be kept in mind. First, the electrostatic potential in the beam can become comparable to the kinetic energy and, second, if B_S or B_Q approaches $\frac{2[B\rho]}{a}$, ions entering a lens at radius a, will be turned back at low intensity for a quadrupole and at any intensity for a solenoid. Both potential/kinetic energy and $Ba/2[B\rho]$ must be much less than unity for the paraxial ray approximation used in this paper to be valid.

For a numerical example, we consider a beam of U_{238}^{+1} at a kinetic energy of 1.0 MeV and the same normalized emittance as the 100-GeV example of Table I. With a strong B_Q and no restriction on R, the first column of Table II shows that a current of 4.65 amperes can be transported by the FODO system. Restricting R to about 0.5 reduces the current to 1.0 ampere (column 2); with reduced B_Q, a better compromise is found at 2.42 ampere in column 3 but with somewhat larger aperture roughly proportional to the ratio I/B_Q in consistency with Eqns. (3) and the approximate constancy of Q/u_m^2.

TABLE II

Ion Type		U^{+1}_{238}	
Energy (MeV)		1.0	
$\varepsilon(10^{-5}$ m-radian)		4.0	
B_Q(tesla)	3.0	3.0	1.5
R	0.68	0.52	0.50
I(Ampere)	4.65	1.0	2.42
a(cm)	41.4	21.5	45.0
μ_0(deg)	160.0	120.0	160.0
μ(deg)	35.3	87.7	44.7

At this energy, the solenoid becomes comparable in effectiveness with quadrupoles. A choice between the two will depend on special features of the transport problem to be solved.

Critique of the Envelope Equation Approach

Although the phase-space distribution underlying the KV envelope equations is not very realistic, the results are known to provide a useful guide for moderate intensities. However, since we are interested in understanding beam behavior under extreme space charge conditions, we have investigated a number of effects not described by Eqns. (1).

a) Incoherent image forces should be taken into account in any case other than that of a round beam in a round pipe, since both economic and focusing field strength limitations demand that these beams substantially fill the vacuum channel. A simple, if somewhat academic, test can be made by assuming an elliptical chamber, confocal with an elliptical beam; in this situation the image forces are linear,3) but change the functional form of the space charge terms in Eqns. (1). It was found that even if the chamber coincides everywhere with the beam edge, the relations described by Fig. (1) change very little. In the more realistic case of an elliptical beam in a round pipe, we have found by numerical computation that the non-linear part of the image fields is small compared to non-linear fields due to a degree of non-uniformity one might reasonably expect in the charge distribution.

Coherent image forces, which attract the beam to the enclosing pipe, come into play if the beam is steered improperly or is deflected by a lens placement error. We find that a coherent motion of the beam is stable, but with a reduction in phase advance comparable to the reduction in the incoherent motion.

b) For a round beam, born in a field free region but transported by a continuous solenoid, there exists an infinity of stationary self-consistent phase space distributions in addition to the KV distribution. We have examined a broader class of these distributions than in previous work4) and find that in all cases the spatial distribution tends toward uniformity with increasing current, although the individual particle motion becomes highly non-linear except for the KV distribution. Moreover, the dependence of current and aperture on A/q, B_S, $\beta\gamma$ and ε is as given in Eqns. (4), independent of the form of the distribution function in the high-intensity limit. It is not clear to us, however, whether any of the distributions examined offers a better description of a real beam than the KV distribution. It is known that a large sub-class of these distributions is stable for small perturbation of initial conditions,5) but we found that the KV distribution is unstable, with a threshold in current, for a large number of modes (see also Ref. 4). The lowest threshold occurs at u = 1.6, which would imply that Eqns. (4) have a very limited range of validity. On the other hand, the KV distribution has special mathematical properties and we prefer to believe that Eqns. (4) are probably qualitatively correct for more realistic distributions which are probably stable.

c) Since the Hamiltonian is not a constant of the motion for a quadrupole transport line, it is not possible to construct stationary (i.e., periodic) solutions by the technique outlined in the previous paragraph. As a partial step away from the KV distribution we examined a "self-inconsistent" problem by tracing individual particle trajectories in a field with a linear part generated by the periodic solution of the envelope equation, plus cubic terms appropriate to a parabolic density profile of the same outer dimensions. For intensities such that μ is less than ~20°, we find a large growth in amplitude of some particles and the development of an island structure in their phase space, indicative of resonant behavior in the periodic non-linear field. We are thereby led to suspect that a quadrupole transport system may be subject to unstable behavior at high intensity.

References

1) I.M. Kapchinskij and V.V. Vladimirskij, Proc. Internat. Conf. on High Energy Accelerators, CERN 1959, p. 274.

2) Final Report of ERDA Summer Study of Heavy Ions For Inertial Fusion, LBL-5543, p. 14-15 (Dec. 1976).

3) E. Regenstreif, CERN/PS/DL 76-4, June 1976.

4) Proc. 1970 Proton Linac Conference (NAL); R.L. Gluckstern, p. 811 and R.L. Gluckstern, R. Chasman, K. Crandall, p. 823.

5) R.C. Davidson and N.A. Krall, Phys. Fluids 13, 1543 (1970).

VALUES OF Q'/u_0^2 IN THE ASYMPTOTIC LIMIT

We present here tabular values of Q'/u_0^2 pertaining to matched solutions of the scaled K-V envelope equations, for a symmetric periodic A-G lattice of hard-edge quadrupole lenses. The quantities Q' and u_0 are respectively scaled measures (corresponding to envelope equations with $K=1$ and $\epsilon=1$) of an intensity parameter and of the <u>maximum</u> envelope radius (analogous to the unscaled envelope radius a_{max}) -- see Hofmann, Laslett, Smith, and Haber, Particle Accelerators, <u>13</u>, 145-178 (1983), esp. p. 177.

The quantity Q'/u_0^2 may be of particular interest in describing the transportable current (in a single channel) in terms of the maximum matched envelope radius (a_{max}) and the focusing magnetic field at that location (B_{Edge}) as

$$I = \frac{\pi}{\mu_0}(\beta\gamma)^2 B'^2 a^2 \frac{Q'}{u_0^2} = \frac{10^7}{4}(\beta\gamma)^2 B'^2 a^2 \frac{Q'}{u_0^2} \qquad \text{(MKS-A units)}$$

$$= \frac{10^7}{4}(\beta\gamma)^2 B\, a\, \frac{Q'}{u_0^2}$$

-- see Appendix A, and examples in Appendix B. The quantity Q'/u_0^2 in general is a function of σ_0, σ, and η, but for numerical values we here shall direct attention to the asymptotically limiting value (maximum value) attained in the limit of space-charge dominance ($\sigma \to 0$). Of interest also may be values of scaled half period (<u>vs.</u> σ_0 and η) and some measure of matched-envelope flutter (<u>e.g.</u>, $\frac{a_{max}}{a_{mid.}} = \frac{u_0}{u_{mid.}}$).

η	σ_0 (Deg.)	Θ	$\frac{Q'}{u_0^2}$	$\frac{a_{max}}{a_{mid}} = \frac{u_0}{u_{mid}}$	$\frac{a_{max.}}{a_{min.}} = \frac{u_0}{v}$
2/3	30.	1.0209 4577	0.10313	1.1195	1.2618
	40.	1.1738 823	0.12746	1.1597	1.3611
	50.	1.30523654	0.14785	1.1997	1.4659^{+}
	60.	1.42015371	0.16485	1.2391	1.5758^{-}
	70.	1.5215 8494	0.17896	1.2776	1.6896
	80.	1.61136905	0.19060	1.3148	1.8062

η	σ_0 (Deg.)	Θ	$\frac{Q'}{u_0^2}$	$\frac{a_{max}}{a_{mid}} = \frac{u_0}{u_{mid}}$	$\frac{a_{max.}}{a_{min.}} = \frac{u_0}{v}$
3/5	30.	1.0556 1165	0.096217	1.1212^{-}	1.2648
	40.	1.2136 9643	0.11882	1.1622^{-}	1.3654
	50.	1.3494 4425	0.13771	1.2030	1.4717
	60.	1.4681 7563	0.15343^{-}	1.2434^{-}	1.5831
	70.	1.5729 4365	0.16642^{+}	1.2829	1.6987
	80.	1.6656 5250	0.17711	1.3211^{+}	1.8172^{-}

η	σ_0 (Deg.)	Θ	$\frac{Q'}{u_0^2}$	$\frac{a_{max}}{a_{mid}} = \frac{u_0}{u_{mid}}$	$\frac{a_{max}}{a_{min}} = \frac{u_0}{v}$
1/2	30.	1.12622633	0.08418_3	1.1238	1.2697
	40.	1.29481965	0.10382	1.1661	1.3724^+
	50.	1.43954938	0.12017	1.2083	1.4811^+
	60.	1.56609292	0.13370	1.2502	1.5952
	70.	1.67771031	0.14484	1.2914	1.7136
	80.	1.77643753	0.15395	1.3315	1.8352

η	σ_0 (Deg.)	Θ	$\frac{Q'}{u_0^2}$	$\frac{a_{max}}{a_{mid}} = \frac{u_0}{u_{mid}}$	$\frac{a_{max}}{a_{min}} = \frac{u_0}{v}$
1/3	30.	$1.3270\,7134_5$	0.06019_3	1.1286^+	1.2785
	40.	$1.5256\,2466_2$	0.07405_5	1.1731	1.3851
	50.	1.6960 0722	0.08551_2	1.2180^-	1.4982
	60.	$1.8449\,1063_6$	0.09492^-	1.2628^-	1.6172
	70.	$1.9761\,8092_5$	0.10258	1.3071	1.7412
	80.	$2.0922\,2431_5$	0.10878	1.3506	1.8688

η	σ_0 (Deg.)	Θ	$\frac{Q'}{u_0^2}$	$\frac{a_{max}}{a_{mid}} = \frac{u_0}{u_{mid}}$	$\frac{a_{max.}}{a_{min.}} = \frac{u_0}{V}$
$\frac{1}{10}$	30.	2.3147 6612	0.019580	1.1358	1.2915
	40.	2.6609 5317	0.024004	1.1837	1.4041
	50.	2.9579 3391	0.027618	1.2325	1.5242
	60.	3.2173 8288^{+}	0.030545^{+}	1.2819	1.6512
	70.	3.4460 1504	0.032893	1.3313	1.7843
	80.	3.6480 3747	0.034755^{+}	1.3803^{+}	1.9222

APPENDIX A

$$I = qe\beta c N = \frac{1}{4}\frac{A}{q}\frac{ec}{r_p}\beta^3\gamma^3 \epsilon K^{1/2} Q'$$

$$= \frac{1}{4}\frac{Aec}{q r_p}\beta^3\gamma^3 K a^2 \frac{Q'}{u_0^2}$$

$$= \frac{1}{4}\frac{e^2}{m_p r_p}\beta^2\gamma^2 B' a^2 \frac{Q'}{u_0^2}$$

$$= \pi \epsilon_0 c^2 \beta^2\gamma^2 B' a^2 \frac{Q'}{u_0^2}$$

$$= \frac{\pi}{\mu_0}(\beta\gamma)^2 B' a^2 \frac{Q'}{u_0^2}$$

$$= \frac{\pi}{\mu_0}(\beta\gamma)^2 B a \frac{Q'}{u_0^2}$$

$$= \frac{10^7}{4}(\beta\gamma)^2 B a \frac{Q'}{u_0^2} \qquad \text{(MKS-A units).}$$

APPENDIX B

--Examples--

We here illustrate application of the equation

$$I = \frac{10^7}{4} (\beta\gamma)^2 \cdot Ba \frac{Q'}{u_0^2}$$

[Appendix A] for transport of ions with $\beta\gamma = 0.36331$ (as from an ion with $A \cong 200$ and K.E. = 12.0 GeV, such as would result from acceleration from rest of a charge $q=3$ ion through a potential difference of 4.0 GV). For numerical use of the formula, we shall adopt

$$a_{max} = 0.024 \text{ m.} \quad \text{and} \quad B_{Edge} = 2.0 \text{ Tesla.}$$

We shall presume the lattice shall be constructed with an occupancy $\eta = 1/3$ and the half-period so adjusted that the value of σ_0 becomes substantially 75 degrees.

Under conditions of pronounced tune depression, as would result from use of a sufficiently small value of emittance that operation is well into the regime of space-charge dominance, we then may employ the value

$$\frac{Q'}{u_0^2} \cong 0.10585 \qquad \text{[see HI-FAN-303].}$$

Substitution of the appropriate values into the formula cited above then leads to the expectation

$$I = \frac{10^7}{4} (0.36331)^2 \; 2.0 \; (0.024) \; (0.10585)$$

$$= 1676.6 \text{ Amp.}$$

Computations (e.g., with Program AGNKJ) to check such a result can be undertaken through use of a value of ϵ sufficiently small as to insure pronounced space-charg dominance. The appropriate value of $K = \frac{B'}{[B\rho]} = \frac{B/a}{[B\rho]}$ for the ions in such a case becomes definite and the corresponding value for the half period becomes given in terms of the scaled half period (Θ) by $L = \Theta/\sqrt{K}$. [For $\sigma_0 = 75$ deg and $\eta = 1/3$, we have $\Theta = 2.0359922$ (see HI-FAN-303).] In the numerical computations (Program AGNKJ) for which results are summarized below, we have taken $L = 1.9418235$ m and $K = 1.09934173$ m^{-2}. It is seen that when ϵ is small, so that σ is quite small, the values of transportable current (I) for $B = 2.0\,T$ and $a_{max} = 0.024$ m are quite insensitive to the value of ϵ (as expected) and close to the predicted value calculated above.

$p = 4$ $(\eta = 1/3)$ $A = 200.$, $q = 3.$

$K = 1.09934173$ m^{-2} K.E. = 12.0 GeV $L = 1.9418235$ m.

$[V = 4.0$ GV$]$

$\underline{\epsilon = 1.36 \times 10^{-6}}$:

Q	I (Amp.)	a_{max} (m)	B_{Edge} (Tesla)	σ (Deg.)
0.	- - -	0.00289268	0.2410568	75.0000
6.7013889×10^{-5}	1676.202	0.024	2.000000	0.994355

$\underline{\epsilon = 1.0 \times 10^{-7}}$:

Q	I (Amp.)	a_{max} (m)	B_{Edge} (Tesla)	σ (Deg.)
6.7026394×10^{-5}	1676.515	0.024	2.000000	0.074205

VALUES OF Q'/u_0^2 vs. σ/σ_0

L. Jackson Laslett

The quantity $k = \frac{Q'}{u_0^2}$, regarded as a scaled-variable expression that is a function of σ_0, η, and σ (or of σ/σ_0), is a useful indicator of the electrical current transportable by a periodic symmetrical hard-edge A-G quadrupole focussing channel. This applicability arises from the relation

$$I = \frac{\pi}{\mu_0} (\beta\gamma)^2 B a k$$

$$= 2.5 \times 10^6 (\beta\gamma)^2 B a k \qquad \text{(MKS-A units)}$$

for magnetic lenses, wherein "a" denotes the maximum matched envelope radius (mete and B the strength of the quadrupole focusing field at that radius (in Tesla). [An analogous expression for electric focussing arises through the substitution $B = \frac{E}{\beta c}$, with which it may be useful to introduce the relation $V = \pm\frac{1}{2} E a^2$ for the electrostatic potential at the beam edge ($r=a$).]

For a lattice of given σ_0 and η, the quantity k increases with intensity, or with increasingly pronounced tune depression (decreasing σ), approaching a definite upper limit as $\sigma \to 0$ in the region of space-charge dominance. There then may be little advantage in pressing the tune depression beyond such a value that k is close to its asymptotically limiting value.

For any value of σ/σ_0, in any event, the corresponding value of k introduced into the formula cited initially then gives the transportable electrical current by a beam whose maximum matched envelope radius and "edge" value of quadrupole focussing field are respectively limited by "a" (meter) and B (Tesla).

It is noted that the "emittance" (ϵ) does not appear explicitly in the formula cited. It will be recognized that for strongly pronounced tune depressions, the value of ϵ will not significantly affect the transportable current (although it will influence the value σ of the strongly depressed tune, with σ approximately proportional to ϵ). In such a case $k = Q'/u_0^2$ has however virtually attained its asymptotic limit and thus is substantially constant -- and the substantially constant value of I (independence with respect to the value of ϵ) under such circumstances thus presents no contradiction.

The relationship presented by the formula cited initially for the transportable current (I) is derived in Appendix A, and some computational checks (through use of Program AGNKJ) presented in Appendix B. It is of interest to present, for some specific value of the occupancy η (such as $\eta = 1/2$), curves (each of constant σ) depicting values of $k = Q'/u_0^2$ vs. σ/σ_0. It is found that for very pronounced tune depressions ($\sigma \to 0$), the factor k increases monotonically with increasing σ (even as $\sigma \to 180$ deg), but with only a slow increase for values of σ much greater than 90 deg. (say for values of σ greater than 120 deg

Under more moderate operating conditions, however (i.e., such that σ/σ_0 is somewhat greater than, or significantly greater than, zero), the advantage of a large value for σ_0 may be diminished or even overturned—so that (entirely aside from additional issues concerning possible instabilities of collective modes) there may be virtually no advantage to use of values of σ_0 in excess of 90 deg.*

---

* Data for construction of curves whose nature is such as to address and illustrate such characteristics may be obtained through use of the Program SQUAD.

APPENDIX A

To derive the equation for transportable current initially cited in the text, we first recall the definitions of ~~certain~~ scaled variables [see Hofmann et al., Particle Accelerators, 13, 145–178 (1983)]:

$$Q' = \frac{4q^2}{A}\frac{N r_p}{\beta^2\gamma^3\epsilon K^{1/2}}$$

and

$$u_0 = K^{1/4}\epsilon^{-1/2} a\,, \; *$$

wherein (in terms of magnetic focusing) $K = \frac{B'}{[B\rho]}$.

With substitution of such values one finds

$$\frac{Q'}{u_0^2} = \frac{4q^2}{A}\frac{r_p}{\beta^2\gamma^3 K}\frac{N}{a^2}$$

$$= \frac{4q^2}{A}\frac{r_p}{\beta^2\gamma^3}\frac{[B\rho]}{B}\frac{N}{a}.$$

Substitution of the expression $[B\rho] = \frac{\beta\gamma A m_0 c}{qe}$ and that for the classical radius of an ion of unit atomic weigh then leads to

$$k = \frac{Q'}{u_0^2} = \frac{qe}{\pi\epsilon c\beta\gamma^2}\frac{1}{B}\frac{N}{a}$$

$$= \frac{\sqrt{\mu_0/\epsilon_0}}{\pi}\frac{qe}{\beta\gamma^2}\frac{1}{B}\frac{N}{a}$$

$$= \frac{qe Z_0}{\pi\beta\gamma^2}\frac{1}{B}\frac{N}{a} \cong \frac{120\, qe}{\beta\gamma^2}\frac{1}{B}\frac{N}{a}$$ (MKS-A uni

---

* Thus, for an ion beam of specific characteristics within a specific lattice, u_0 and the physical envelope radius (a) are directly proportional and Q' serves as an intensity parameter (shown here in terms of N, the number of ions per meter).

The equation just written thus leads explicitly and directly to the expression for transportable linear ion density (N, ions/meter):

$$N = \frac{\pi}{\sqrt{\mu_0/\epsilon_0}}\ \beta\gamma^2\ \frac{Ba}{qe}\ k$$

$$\cong \frac{\beta\gamma^2}{120.}\ \frac{Ba}{qe}\ k.$$

It then follows that

$$\lambda = qeN = \frac{\pi}{\sqrt{\mu_0/\epsilon_0}}\ \beta\gamma^2\ Ba\ k$$

$$\cong \frac{\beta\gamma^2}{120.}\ Ba\ k \qquad \text{electrical (Coulomb/m)}$$

and

$$I = \beta c\lambda = \frac{\pi}{\sqrt{\mu_0\epsilon_0}\sqrt{\mu_0/\epsilon_0}}\ \beta^2\gamma^2\ Ba\ k$$

$$= \frac{\pi}{\mu_0}\ (\beta\gamma)^2\ Ba\ k$$

$$= 2.5\times10^{+6}\ (\beta\gamma)^2\ B\cdot a\ k \qquad \text{(MKS-A units)},$$

as cited in the text for the transportable electrical current.

Comment: In application one should note that, if "B" and "a" are each given, $B' = B/a$ and, (for an ion beam of specific characteristics) $K = \frac{B'}{[B\rho]}$ is then also given. For an intended occupancy (η) and zero-intensity tune (σ_0) the scaled half period (Θ) is fixed and the half period to employ then is given by $L = \frac{\Theta}{\sqrt{K}}$.

APPENDIX B

The relation

$$I = \frac{\pi}{\mu_0}(\beta\gamma)^2 B a k$$

$$= 2.5\times 10^6 (\beta\gamma)^2 B\cdot a \quad k \qquad \text{(MKS-A units)}$$

cited originally in the text has been checked by independent AGNKJ computations for a beam formed of ions with

$A \cong 209.$, $q \cong 2.$

$\epsilon = 2.0\times 10^{-6}$ (un-normalized)

K.E. $= 10.0$ GeV $[V_{ion} \cong 5.0 \text{ GeV}]$

$\beta\gamma = 0.323414$

$(\beta \cong 0.307721)$.

In a lattice with $\eta = \frac{1}{2}$ and K so selected $(K \doteq 0.6131617585\ \bar{\text{m}}$ that $\sigma_0 = 60.$ degrees

we have performed the following checks:

1) With $Q = 1.56609292\times 10^{-6}$

$[$corresponding to $Q' = Q/(\epsilon K^{1/2}) = 1.00$ $]$,

AGNKJ leads to $\sigma/\sigma_0 = 0.4992826$

and also to $a = 0.00506729_2$ m.

$B_{(Edge)} = 0.3286463$ T.

$I = 43.315$ Amp.

For σ/σ_0 as recorded immediately above,

we expect (Program SQUAD) $k = {Q'}^{1/2}/u_0 = 0.099469_{66}$;

for such values of a and of B as shown above,

we accordingly expect

$$I = 2.5\times 10^{+6} * (0.323414)^2 \times (0.3286463)(0.00506729_2) \times 0.099469_{66}$$

$= 43.31_6$ Amp. -- essentially as found in direct AGNKJ computations

2) With $Q = 4.69827876 \times 10^{-6}$

[corresponding to $Q' = Q/(\epsilon K^{1/2}) = 3.00$],

AGNKJ leads to $\sigma/\sigma_0 = 0.211511\dot{3}$

and also to $a = 0.00775172_4$ m.

$B_{(\text{Edge})} = 0.5027489$ T.

$I = 129.945$ Amp.

For σ/σ_0 as recorded immediately above, we expect (Program SQUAD) $k = Q'/u_0^2 = 0.1275_{1672}$; for such values of a and of B as shown above, we accordingly expect

$$I = 2.5 \times 10^{+6} \times (0.323414)^2 \times (0.5027489) \times (0.00775172_4) \times 0.127516_{72}$$

$= 129.94_9$ Amp. -- essentially as found in the direct AGNKJ computati cited immediately above.

APPENDIX C

[Remark concerning a_{max}/a_{min}]

One normally expects the matched envelope dimensions, or their scaled equivalents u_0, V, & u_{mid}, to increase as the intensity parameter (Q') is increased. For *large values of σ_0*, however, one finds that as Q' is increased from zero the maximum radius (u_0) at first decreases and then only later begins to increase. [The relation between u_0 and the physical radius (a_{max}) of course remains most simple if the emittance is held constant -- see p. A-1.]

It may be of interest to illustrate the relative magnitudes of u_0, v, & u_{mid} (or of a_{max}, b, & a_{mid}) -- particularly since the ratio a/b can become quite great for the larger values of σ_0 when Q' is small. Such behavior is illustrated in the tabulations given (p. C-2) for $\eta = 1/2$, $Q' = 0.$ or $100.$, and various values of σ_0. The variations of the ratio u/v are apparent. The values for u_{mid} are quite roughly the arithmetic mean of the corresponding values for u_0 and v.

$$\boxed{\eta = \tfrac{1}{2}}$$

For $Q' = 0$.

σ_0 (eg.)	u_0	v	$u_{mid.}$	u_0/v	σ (Deg)
170.	6.81745	0.32306	3.81650	21.1029	170.
160.	4.83264	0.45844	2.73465	10.5415	160.
150.	3.96230	0.56472	2.28143	7.0163	150.
120.	2.86797	0.82503	1.79493	3.4762	120.
90.	2.44476	1.07296	1.70956	2.2785	90.
60.	2.27945	1.37087	1.79627	1.6628	60.
30.	2.35564	1.84607	2.09159	1.2760	30.

For $Q' = 100$.

σ_0 (Deg.)	u_0	v	$u_{Mid.}$	u_0/v	σ (Deg.)
170.	23.30472	8.72659	14.93213	2.6705	1.4808
160.	23.34428	8.85528	15.03598	2.6362	1.4422
150.	23.41315	9.07268	15.21146	2.5806	1.3802
120.	23.85330	10.31610	16.21693	2.3122	1.0903
90.	24.89689	12.71414	18.17297	1.9582	0.7324
60.	27.34894	17.14462	21.87507	1.5952	0.3984
30.	34.46615	27.14494	30.66828	1.2697	0.1392

ILLUSTRATIONS OF SOME SCALING LAWS FOR TRANSVERSE FOCUSING BY ELECTROSTATIC QUADRUPOLE LENSES

L. Jackson Laslett
U.C. Lawrence Berkeley Laboratory
October 10, 1986

HIFAR Note-107

Refs., for "Handy Formulas":

1) For electrostatic focusing: Appendix to HI-FAN-307
2) " magnetic " : HI-FAN-303
3) Q/u^2 in the asymptotic limit: HIFAR-Note 62
4) Q/u^2 vs. σ/σ_0 : HIFAR-Note 63

A discussion 7-8 October 1986 with J. Hovingh concerning an informal memo to D. Keefe introduced the issue of presuming (á la T. Fessenden) the tune depression to be extreme ($\sigma/\sigma_0 \to 0$) when estimating transportable beam currents.

We here discuss this issue with particular reference to the equations presented in ① and ② of Ref. 1 for electrostatic focusing and present some numerical results (Program AGNKJ) by way of illustration.

We presume that we do not have a great amount of freedom with respect to σ_0 or η (occupancy) -- thus, as in the following examples, we may wish to examine provisional use of the values

$$\sigma_0 = 70.000 \text{ degrees} \quad \& \quad \eta \doteq 2/3 .$$

We also presume that, for electrostatic focusing, the technological constraint on electric quadrupole potentials and/or fields can be represented reasonably well by imposing a limit on $(\pm)V_e/R_e$ for suitably-proportioned electrodes in conjunction with aperture dimensions of possible interest in practice -- for example, $(\pm)V_e/R_e$ not to exceed 2.33×10^6 V/m and perhaps set to 2.0×10^6 V/m.

With this point of view one may wish to examine the transportable current, per beam, on the assumption of various matched-envelope radii (a, and an associated value of R_e) -- while not attaching major importance to the value (σ) of the depressed tune.

If this viewpoint is adopted, the handy formulas of dominant interest for electrostatic focusing are[1]:

$$N = \frac{2\pi}{\mu_0 c^2} \frac{\gamma^2 k}{q e} \left[\frac{V_e}{R_e}\right] \frac{a^2}{R_e} \quad \text{ions/meter} \qquad (1)$$

and (non-relativistically)

$$L = \sqrt{\frac{[\text{Kinetic Energy}]/(qe)}{[V_e/R_e]}}\, R\, \Theta \text{ for the lattice half-period}, \qquad (2)$$

where Θ is the "scaled" half-period (a function of σ_0 & η) and k is a quotient Q'/u^2 that (for given σ_0 & η) approaches a definite limit as $N \to \infty$ and $\sigma \to 0$. [In practice, the value of k may be found[4] to be within 90% of its limiting value once $\sigma \leq 0.3\,\sigma_0$. The use of the limiting value, or of a value only slightly discounted therefrom, accordingly may be appropriately convenient for an initial design survey.]

A third formula, that addresses the value of σ, introduces a third coefficient g (again dependent upon σ_0 and η) whose value may be of interest under conditions of pronounced tune depression and serves to relate σ to the emittance ϵ:

$$\sigma = \epsilon \frac{g L}{k \Theta a^2} \quad \text{degrees (per full period).} \qquad (3)$$

To illustrate these concepts, we consider a beam of ions with $A = 209$, $q = 1$, and $KE = 0.003$ GeV ($\beta \cong 0.00553$). We examine now the utilization of a symmetric electrostatic quadrupole lattice with

$$\sigma_0 = 70.0000 \text{ deg.} \ \& \ \eta = 2/3 \ \ (\text{or } p = 2(1-\eta)/\eta = 1).$$

For such a lattice, $\Theta = 1.52158494$

and $k \to 0.1790$ in the high-intensity limit (<u>not</u> discounted).

We then shall proceed to examine the transportable beam intensity for a succession of matched-envelope radii (a) and presumed associated radii to the electrodes ($R_e = a + .009$) while imposing (and employing) the technological constraint

$$(\pm) V_e / R_e = 2.0 \times 10^6 \text{ volt/meter.}$$

At this stage of the work we shall devote no concern to the values attained by the depressed tune, and hence shall have no concern for the coefficient g (that, for a given transport situation, relates σ to ϵ); for the AGNKJ computations to be specific, however, we assign the value $\epsilon = 7.5 \times 10^{-5}$ meter·radian (unnormalized, without factor π) for the reference case.

Such calculations of transportable beam intensity (per beam) of course will influence the number of parallel beam channels one may elect to recommend.

The reference cases treated in this sequence of examples are those for which "a" and R_e are taken to be as shown in the following Table. We have included in this Table, (i) the value of electrode potential for each case as computed from $(\pm) V_e / R_e = 2.0 \times 10^6$ v./m., (ii) an estimate of the transportable ions/meter for highly depressed tune, and (iii) the half-period L as given by Eqn. (2). The focusing constant K then of course is taken to be $K = (\Theta / L)^2$.

EXAMPLE CASES

a (m)	R_e (m)	V_e (kV)	Ions/m, N (approx.)*	L (m) ($\eta = 2/3$)	K (m^{-2})
0.015	0.024	±48.	1.16×10^{12}	0.2887004	27.777778
0.020	0.029	±58.	1.71×10^{12}	0.3173517	22.988506
0.025	0.034	±68.	2.28×10^{12}	0.3436223	19.607843
0.030	0.039	±78.	2.86×10^{12}	0.3680223	17.094017
0.035	0.044	±88.	3.46×10^{12}	0.3909022	15.151515
0.040	0.049	±98.	4.05×10^{12}	0.4125151	13.605442

* Undiscounted.

With these parameters, computations confirm that $\sigma_0 = 70.0000$ deg. When the beam intensity is adjusted so that (with $\epsilon = 7.5 \times 10^{-5}$) the indended matched-envelope radius is indeed attained, one finds the results tabulated below for these respective cases. The values tabulated for k are those which would have to be inserted into Eqs. (1) to provide such adjusted values of N.

a (m)	b (m)	N (ions/m)	I (amp)	σ (Deg.)	k (from tabulated N)
0.0150	0.0088	$1.068_{393} \times 10^{12}$	0.284	19.707	0.1641
0.0200	0.0118	$1.660_{026} \times 10^{12}$	0.441	12.148	0.1733
0.0250	0.0148	$2.250_{00} \times 10^{12}$	0.598	8.410	0.1762
0.0300	0.0177^{+}	$2.844_{187} \times 10^{12}$	0.756^{-}	6.252	0.1775^{-}
0.0350	0.0207	$3.442_{734} \times 10^{12}$	0.915^{-}	4.878	0.1781^{-}
0.0400	$0.023\dot{7}$	$4.045_{019} \times 10^{12}$	1.075^{-}	3.941^{-}	0.1784

All for cases such that $\pm V_e/R_e = 2.0 \times 10^{6}$ V/m.

Comments:

One notes from this tabulation that, even in the case for which the tune depression is least pronounced ($\sigma \cong 19.7$ deg.), the value of k is within 90% of its asymptotic maximum (or, equivalently, the transportable N is within 90% of the value that would be suggested through use of k_∞).

If one is not troubled by the somewhat small values of σ that are shown in the last few lines of the Table, these examples illustrate the increase of current per beam that can result from use of larger beam channels (roughly proportional to a^2/R_e -- *i.e.*, to the extent that k may be regarded as constant).

Of course if, on the other hand, one feels that the examples in one or more of the cases with L large lead to distressingly small values of σ, one then may be impelled to reduce the current planned for such lattices—or, alternatively, risk operating with a larger (degraded) emittance. [At the *upper* end of the tabulations, where one might suppose it quite permissible to employ smaller values of σ, an increase of current unacceptably would increase the matched envelope radii in such lattices and lead to unacceptably large electrical focusing fields, but use of *smaller* values of ϵ (if achievable) of course would be permissible.]

The effects of such changed conditions of operation are indicated for some cases in the following Tables.

<u>Case I</u>: $L = 0.2887004$ m.; $K = 27.777\,778\ m^{-2}$

Comment	N	ϵ	a	σ, deg.
Ref. Case:	$1.068\,393 \times 10^{12}$	7.5×10^{-5}	0.0150	19.707
$N \times 3$:	$3.205\,178 \times 10^{12}$	7.5×10^{-5}	0.0250	7.057
$\epsilon \times \frac{1}{3}$:	$1.154\,526 \times 10^{12}$	2.5×10^{-5}	0.0150	6.540

<u>Note:</u> With N multiplied by 3, a^2 is changed by a factor 2.78 or a increases by a factor approximately $\sqrt{3}$. Correspondingly σ becomes multiplied by $0.358 = 1/2.79$, or approximately by a factor $1/3$. The increase of beam size presumably would be unacceptable for reasons of electrical difficulty associated with the quads.

<u>Note:</u>

With ϵ reduced to a value $1/3$ as great, the intensity leading to $a = 0.0150$ m is <u>not</u> changed markedly (only an increase of circa 8%) from that found for the reference case, but σ is changed by a factor 3.32 (or approximately by a factor 3).

Case II: $L = 0.4125151$ m.; $K = 13.605442$ m^{-2}

Comment	N	ϵ	a	σ, deg.
Ref. Case:	4.045019×10^{12}	7.5×10^{-5}	0.0400	3.941
$N \times \frac{1}{2}$:	2.022510×10^{12}	7.5×10^{-5}	0.0284	7.809
$\epsilon \times 2$:	4.045019×10^{12}	1.5×10^{-4}	0.0402	7.809

Note:

When N is multiplied by $\frac{1}{2}$, a^2 becomes multiplied by 0.505 or "a" mult. approx. by $1/\sqrt{2}$. Concurrently, σ becomes multiplied by 1.98, or approximately by 2.

Note: Under these conditions of pronounced tune depression, a change of ϵ scarcely affects the relation between N and "a", so that the reference N still leads to virtually the same reference value of a. The value of σ, however, is changed from the reference case by a factor 1.98, or approximately by a factor 2, as a result of a factor 2 increase in the value of ϵ.

A-G BEAM TRANSPORT WITH MAGNETIC FOCUSING IN TERMS OF A LIMITING MAGNETIC FIELD AND WITH PRONOUNCED TUNE DEPRESSION

December 1985

INTRODUCTION

Evidence has suggested the suitability of A-G beam transport under conditions of very pronounced tune depression -- e.g., to $\sigma \cong 6$ degrees or below, provided $\sigma_0 < 90$ degrees. Under such circumstances one can design a transport system with fair accuracy (say when $\sigma < 20$ deg.) by reference to the asymptotic beam behavior exhibited under conditions of extreme space-charge dominence.

For a given ion species and kinetic energy (or β), and for a provisional choice of σ_0 and occupancy η, specification of intensity as N ions/meter and of magnetic field strength (B) at the maximum matched-envelope radius then permits one to estimate the magnitude of this matched-envelope radius (substantially independent of emittance under conditions of space-charge dominance) and the corresponding associated half-period of the A-G magnetic transport lattice. Such estimates could prove useful, for example, in considering the design of a "H.-I.-F. Driver."

With the further specification of the emittance ($\pi\epsilon$), moreover, one can estimate also the depressed individual particle tune σ. Such an estimate could prove desirable in order to conform that the assumed conditions indeed are such as to carry the operation into the domain of space-charge dominance and also, possibly, to afford any warning of particularly extreme tune depression.

NOTATION

We are concerned with a hard-edge periodic sequence of magnetic quadrupole lenses, with occupancy η $(=\frac{2}{p+2})$ and focusing constant $K = \frac{qeB'}{\text{momentum}}$.

We introduce a scaled half period $\Theta = \sqrt{K}\,L$, wherein L represents the half-period of the A-G lattice. For a given value of η there is a one-to-one correspondence between Θ and σ_0.

We introduce a scaled matched-envelope radius (usually cited numerically, unless otherwise indicated, for the point of maximum radius)

$$u = a\,K^{1/4}/\epsilon^{1/2},$$

where "a" represents the matched-envelope radius and $\pi\epsilon$ the emittance (un-normalized).

Finally we introduce a scaled intensity parameter

$$Q' = \frac{Q}{\epsilon K^{1/2}} \qquad \text{with} \qquad Q = \frac{4q^2 r_p N}{\gamma^3\beta^2 A},$$

wherein r_p is the classical radius of a particle of unit atomic weight and N the linear particle density (e.g., ions/meter).

The use of such scaled variables permits the envelope equations to be written in such a form that the focusing constant becomes ±1 (and zero), the half period becomes Θ, and the emittance term becomes simply $\frac{1}{u^3}$ (or $\frac{1}{v^3}$ for other transverse direction). The space-charge term in such equations then is simply $\frac{Q'}{u+v}$. The character of envelope behavior in the extreme space-charge dominated regime may be examined by ignoring (omitting) the respective terms $\frac{1}{u^3}$ or $\frac{1}{v^3}$ in such equations.

Reference has been made to such scaling on p. 177 of Hofmann, Laslett, Smith, and Haber, Part. Acc. 13, 145-178 (1983) and in earlier work cited in Ref. 8 of that paper. It should be noted that a definition for a quantity Q given as Eq. (2) of E.P. Lee et al. [LBL-19560, prepared for presentation at the 1985 Part. Acc. Conf. (Vancouver, Canada)] differs (by a factor $\frac{1}{2}$) from that given here, and care may be required with respect to the manner in which λ_o is to be interpreted and evaluated $(\lambda_o = eN)$.*

The quantities to be employed in the equations to be presented below are

(i) The scaled half-period, Θ,

and. (ii) The asymptotic limiting value $k = Q'/u^2$

approached under conditions of pronounced tune depression.

Also, for estimation of σ when ϵ is specified, one likewise can make use of the asymptotically limiting value

(iii) $g = Q'\sigma$,

in which σ will be considered to be expressed in <u>degrees</u> (per full period). In use of this coefficient for estimation of σ, ϵ will enter as a factor.

* Note misprint: M_o^2 evidently should read Mc^2.

TABULATIONS

The quantities Θ, k, and (if desired) g can be evaluated numerically and tabulated as functions of σ_0 and η. As is to be expected, one finds that k varies approximately in direct proportion to η when η is small, so that a useful supplemental tabulation might well present k/η vs. σ_0 and η.

EQUATIONS

With N and B considered as given, and a provisional value of k taken from the tabular material, it is convenient to employ an equation that gives directly the value of the (maximum) matched envelope radius (a). With a value available also for Θ, additional formulas then also give the associated half-period (L) -- either in terms of the envelope radius ("a") just found and the assumed value of B or directly in terms of N and B.

Finally, with a value assumed for the emittance and a value available for g, one can employ formulas suitable for estimation of σ — most simply as a simple scaling relation in terms of a and L (and the quantities k, Θ, & g).

Such formulas are presented below. In forms in which numerical values have been entered for basic constants, use of the MKS-A system has been assumed ($\mu_0 = 4\pi \times 10^{-7}$ H/m). We then employ B (Tesla), N (ints/meter), and "a" (maximum matched envelope radius, meter); if one wishes to restrict the value of B at the pole tip, it may be desirable to discount B somewhat in order to provide for some clearance.

5

i)
$$a = \frac{4}{k}\,\frac{m_p c\, r_p}{e}\,\frac{1}{\gamma^2\beta}\,\frac{qN}{B}$$
$$= \frac{4}{k}\,\frac{\mu_0}{4\pi}\,ec\,\frac{1}{\gamma^2\beta}\,\frac{qN}{B}$$
$$\doteq \frac{1.921\times10^{-17}}{k}\,\frac{1}{\gamma^2\beta}\,\frac{qN}{B} = \frac{1.921\times10^{-17}}{(k/\eta)\,\eta}\,\frac{1}{\gamma^2\beta}\,\frac{qN}{B}\,.$$

ii)
$$L = \sqrt{A\,\frac{m_p c}{e}\,\gamma\beta\,\frac{a}{2B}}\;\Theta$$
$$\doteq \sqrt{3.11\,A\,\gamma\beta\,\frac{a}{qB}}\;\Theta$$
$$= \sqrt{\frac{5.97\times10^{-17}}{k}\,A\,\frac{N}{\gamma B^2}}\;\Theta\,.$$

iii)
$$\sigma_{Deg.} = \epsilon\,\frac{gL}{a^2 k\,\Theta}$$
$$\doteq 2.09\times10^{25}\,\gamma^{7/2}\,\beta^{2}\,\frac{A^{1/2}B}{q^2 N^{3/2}}\,\epsilon\sqrt{k}\,g\,.$$

It is recalled that these relations are intended for estimation of beam characteristics under conditions of A-G magnetic-quadrupole focusing with very pronounced tune depression (strong space-charge dominance).

VALUES OF $\Theta = \sqrt{K}\,L$

p	η	$\sigma_0 = 60°$	$\sigma_0 = 75°$	$\sigma_0 = 90°$
0	1	1.31844943	1.4560805	1.57079633
1	2/3	1.42015371	1.56784617	1.69071429
2	1/2	1.56609292	1.72858897	1.86361748
4	1/3	1.844910636	2.0359922	2.19463275
6	1/4	2.09362342	2.3103220	2.49017270
8	1/5	2.317763834	2.5575876	2.75660121
10	1/6	2.522880046	2.783884	3.00045499
14	1/8	2.89075137	3.189762	3.43784945
18	1/10	3.217382885	3.550153	3.82623986
38	1/20	4.510231286	4.976670	5.36363620

cf HI-FAN-47

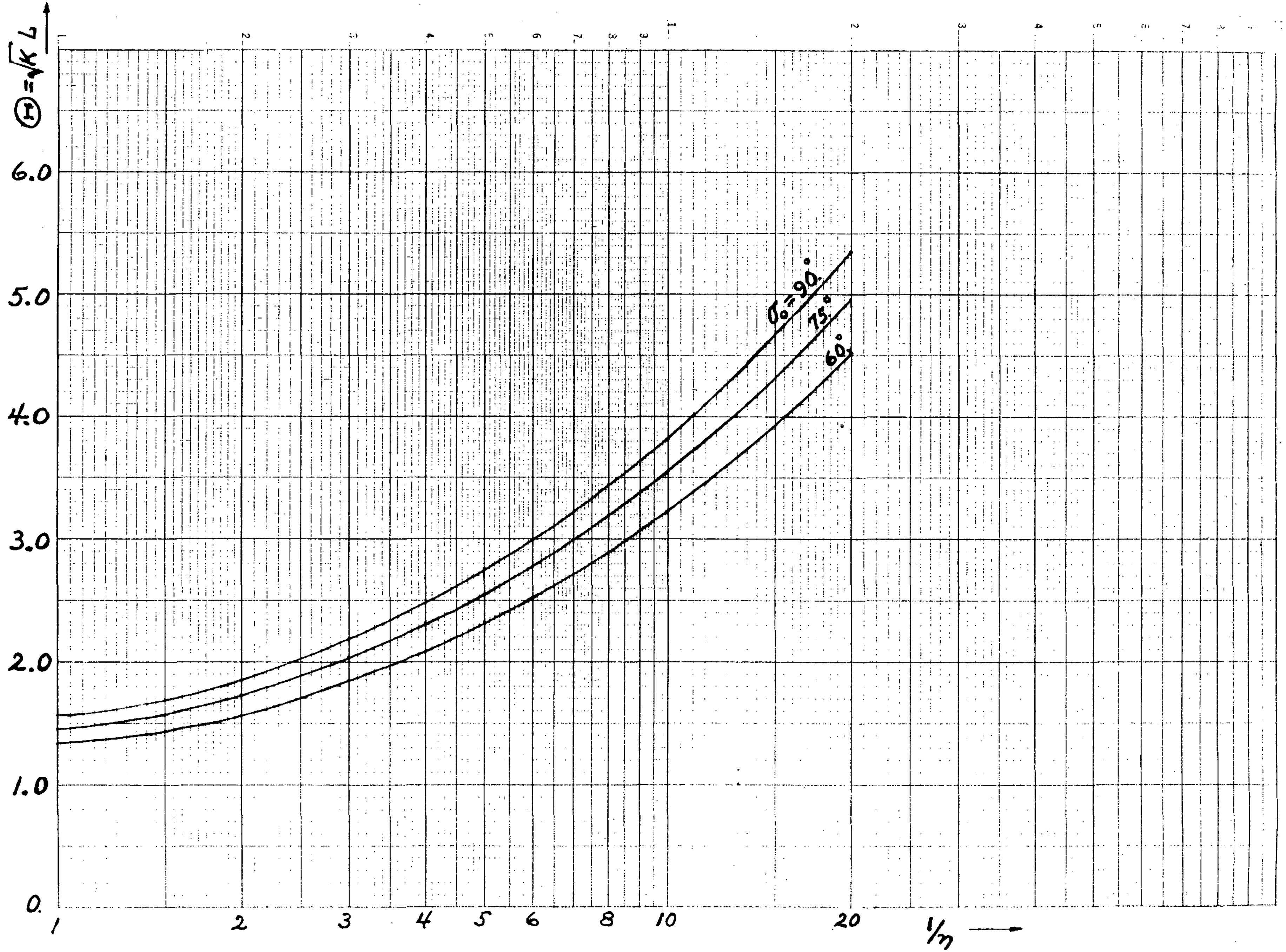

Θ = √K L
6.0
5.0
4.0
3.0
2.0
1.0
0.
1
2
3
4
5
6
8
10
20
1/η
σ₀ = 90°
75°
60°

VALUES OF $k = \frac{Q'}{u^2}$

p	η	$\sigma_0 = 60°$	$\sigma_0 = 75°$	$\sigma_0 = 90°$
0	1	0.19446	0.21907	0.23768
1	2/3	0.16485	0.18506	0.20014$^-$
2	1/2	0.13370	0.14963$^-$	0.16134
4	1/3	0.094917	0.10585	0.11375
6	1/4	0.073144	0.081416	0.087335
8	1/5	0.05940$\dot{7}$	0.066048	0.070770
10	1/6	0.049985	0.055530	0.059453
14	1/8	0.037926	0.042091	0.045021$^-$
18	1/10	0.030545	0.033879	0.036216
38	1/20	0.015472	0.017139$^+$	0.018299

VALUES OF k/η

p	η	$\sigma_0 = 60°$	$\sigma_0 = 75°$	$\sigma_0 = 90°$
0	1	0.19446	0.21907	0.23768
1	2/3	0.24728	0.27760	0.30020$^+$
2	1/2	0.26740	0.29925	0.32268
4	1/3	0.28475	0.31755	0.34126$^-$
6	1/4	0.2925$\dot{8}$	0.32566$^+$	0.34934
8	1/5	0.29703	0.33024	0.35385
10	1/6	0.29991	0.33318	0.35672
14	1/8	0.30341	0.33673	0.36016
18	1/10	0.30545	0.33879	0.36216
38	1/20	0.30944	0.34279	0.36598

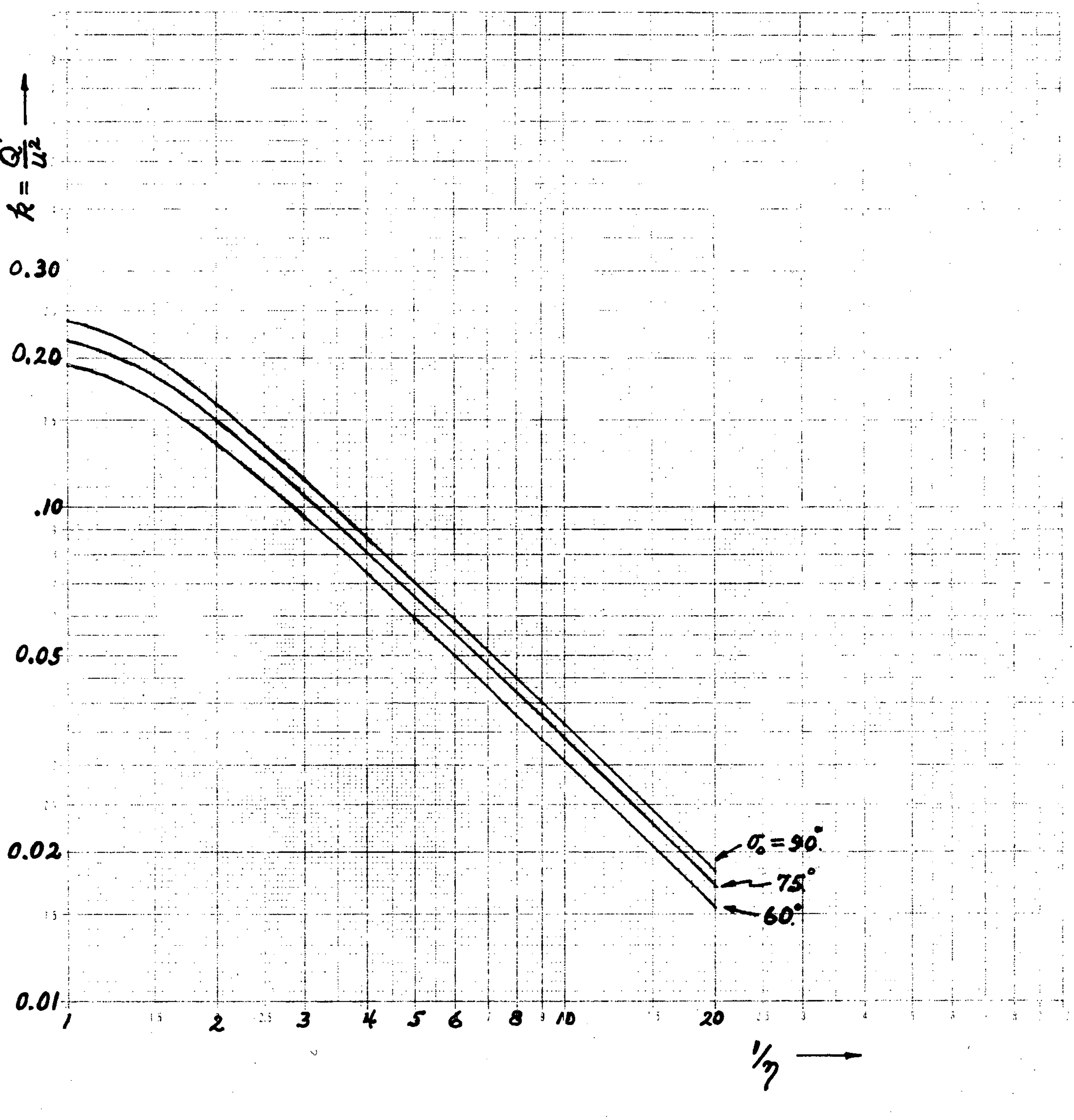
$k = \frac{Q'}{U^2}$
0.30
0.20
.10
0.05
0.02
0.01
1
2
3
4
5
6
8
10
20
$1/\eta$
$\sigma_0 = 90°$
75°
60°

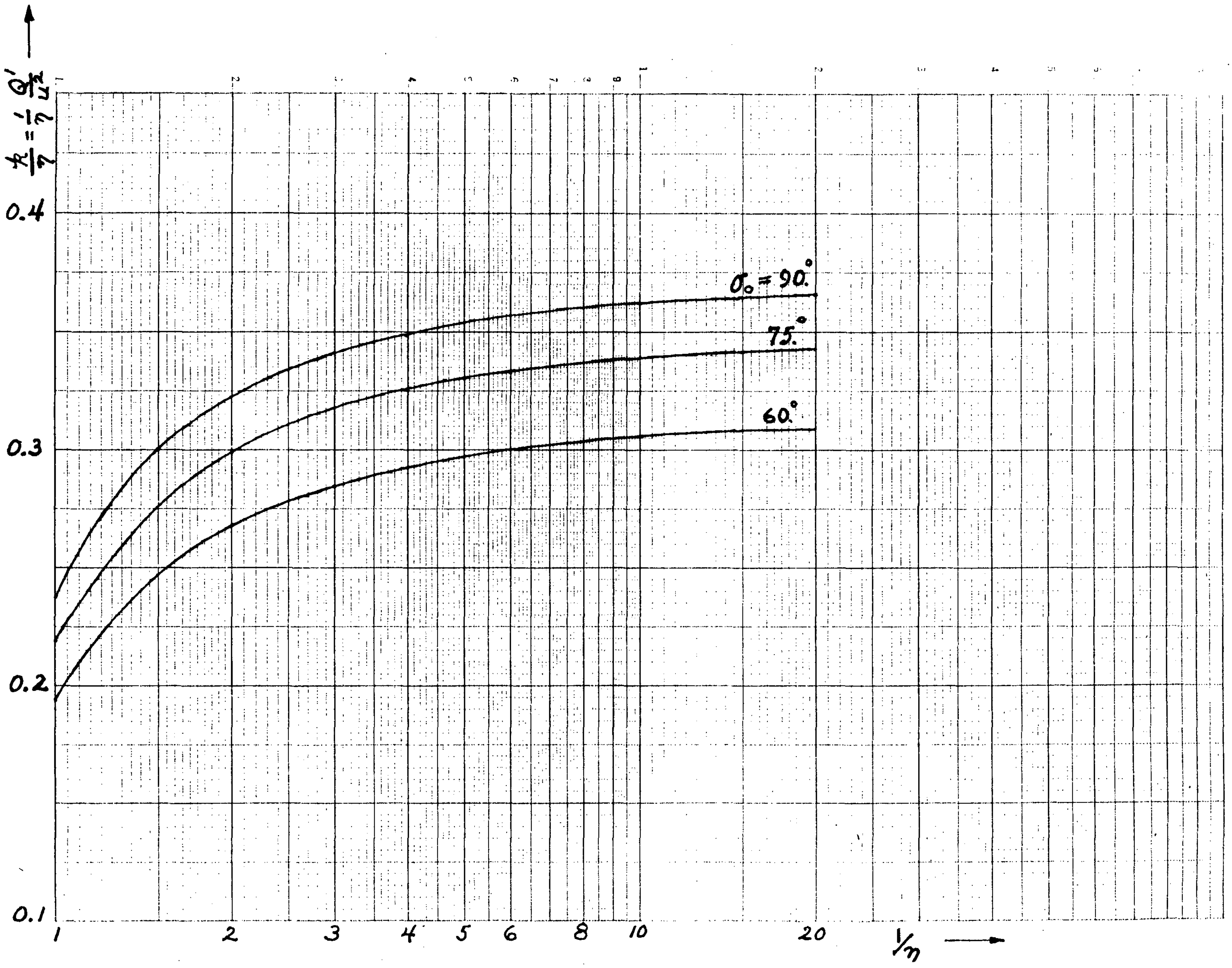
$\frac{x}{l} = \frac{1}{\eta} Q_{L}^{\prime 2}$
0.4
0.3
0.2
0.1
$\sigma_0 = 90°$
75°
60°
1
2
3
4
5
6
8
10
20
$1/\eta$

VALUES OF $g = Q' \cdot \sigma$ (Deg.)

p	η	$\sigma_0 = 60°$	$\sigma_0 = 75°$	$\sigma_0 = 90°$
0	1	47.3_3	66.30	86.9_0
1	2/3	43.9_3	61.5_6	80.7_1
2	1/2	39.8_4	55.8_5	73.2_5
4	1/3	33.8_3	47.4_4	62.2_6
6	1/4	29.8_2	41.8_2	54.9_1
8	1/5	26.9_4	37.7_9	49.6_2
10	1/6	24.7_5	34.7_2	45.6_1
14	1/8	21.6_0	30.3_1	39.8_2
18	1/10	19.4_1	27.2_4	35.7_9
38	1/20	13.8_5	19.4_4	25.5_5

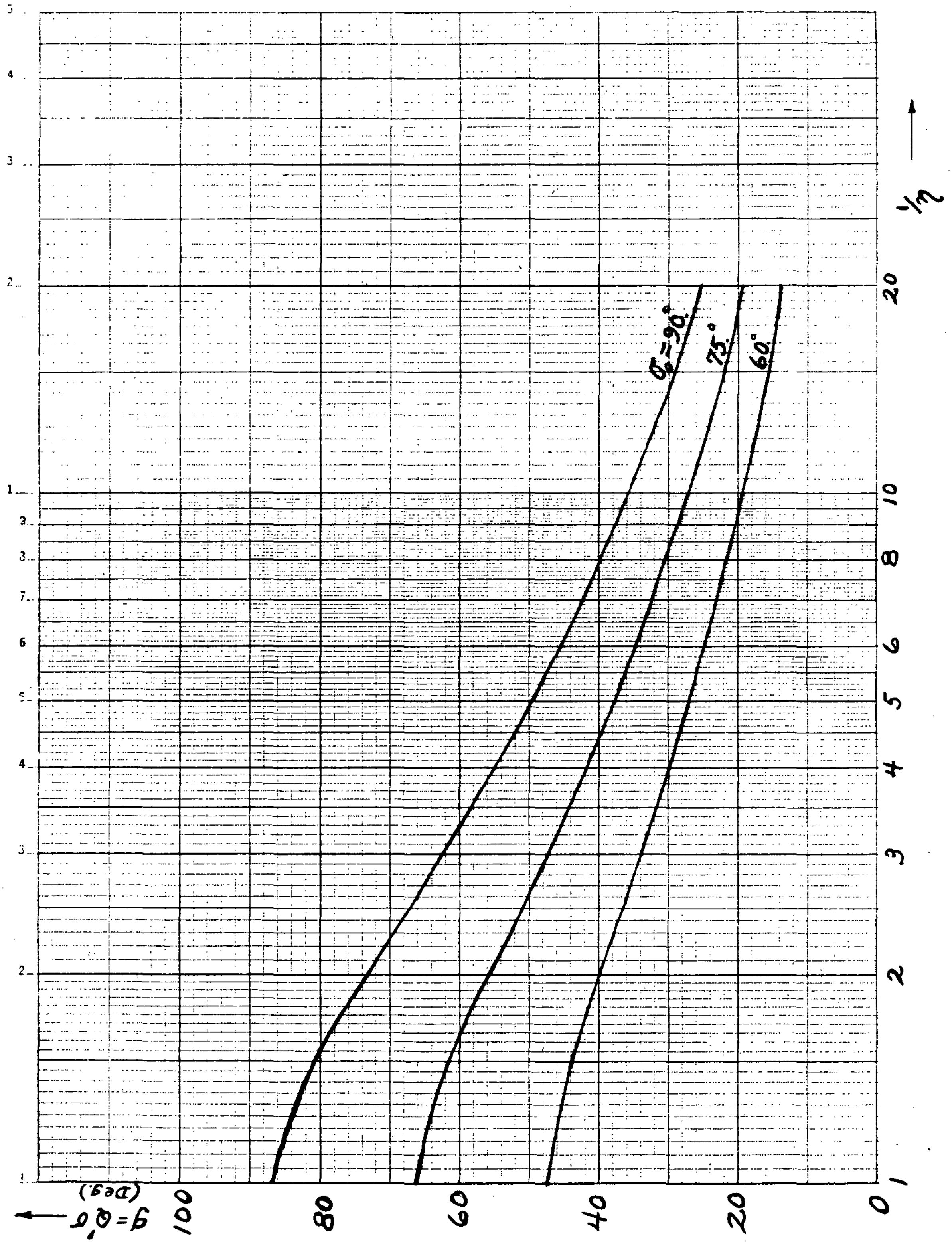
φ = φ'f (Deg.)
100
80
60
40
20
0
1/η
1
2
3
4
5
6
8
10
20
σc = 90°
75°
60°

⑥

EXAMPLES AND CHECK

We now illustrate the behavior that the equations we have presented above are intended to describe. We consider for this purpose a lattice with occupancy 1/3 and visualize operation with $\sigma_0 = 75$ degrees, so that we may make use of

$$\Theta = 2.0359922,$$
$$k = 0.10585, \quad \text{and}$$
$$g = 47.44 \quad .$$

in the domain of strong time depression. We then consider first the transport of a singly-charged ion ($q=1$) with $A \cong 137$ and kinetic energy 2.0 GeV

$$(\gamma \cong 1.01556,$$
$$\beta \cong 0.17438$$
$$\beta\gamma \cong 0.17709)$$

and $\epsilon = 3.0 \times 10^{-6}$. [Later we shall consider the transport of a similar ion of charge state 2, to illustrate (guided by the cited formulas) the various ways in which the operating conditions may be modified in response to the change of charge state.]

$$\boxed{q=1}$$

We presume (for purposes of illustration) that we wish to operate with a field $B = 2.0$ tesla at the <u>edge</u> of a beam of matched envelope radius $a = 0.012$ meter. The first of the cited equations then provides, when solved for the linear density of ions,

$$N = \frac{k\,\gamma^2\beta\,a\,B}{1.921 \times 10^{-17}\,q} = \frac{0.10585 \times 0.17985 \times 0.012 \times 2.0}{(1.921 \times 10^{-17})\,(1)}$$

$$= 2.36 \times 10^{13} \text{ ions/meter.}$$

The associated half-period for the lattice similarly becomes

$$L = \sqrt{3.11\,A\,\gamma/\beta\,\frac{a}{qB}}\;\Theta = \sqrt{3.11 \times 137 \times 0.17709\,\frac{0.012}{(1)(2.0)}}\;2.0359922$$

$$= 1.37 \text{ meter.}$$

[The corresponding value of the focusing constant then of course is

$$K = (\Theta/L)^2 \cong 2.2 \ m^{-2}.]$$

Finally, with the value $\epsilon = 3.0 \times 10^{-6}$, one may estimate the value of the depressed tune most simply by

$$\sigma = \epsilon\,\frac{gL}{a^2 k\Theta} = 3.0 \times 10^{-6}\;\frac{47.44 \times 1.37}{(0.012)^2\,(0.10585)(2.0359922)}$$

$$= 6.3 \text{ degrees.}$$

[Similar values have been obtained, by way of a check, by the computer program AGNKJ.]

* * *

$$\boxed{q = 2}$$

Upon changing to consideration of operation with $q=2$, several optional alternative responses may be seen (from inspection of the equations) to be available -- thus:

(a) Keep B and N as before, then one expects the envelope radius "a" to double and σ to be reduced to one-quarter its value for $q=1$;

(b) Keep B and "a" as before, then one expects N to become one-half as great and σ to be reduced by the factor $1/\sqrt{2}$;

(c) Keep N the same as before, but permit "a" to become greater by just the factor $\sqrt{2}$, then one expects the required B to be greater by the factor $\sqrt{2}$ and σ to be reduced by the factor $\frac{1}{2\sqrt{2}}$.

With option (a), moreover, L will be unchanged from the value used for $q=1$; with options (b) and (c) L will be less than in the case $q=1$ by the factor $1/\sqrt{2}$.

8

(a) $B = 2.0$ tesla and $N = 2.36\ldots \times 10^{13}$, one expects

$$a = \frac{1.921\times 10^{-17}\ qN}{k\ \gamma^2\beta\ B} = \frac{(1.921\times 10^{-17})(2)(2.36\times 10^{13})}{0.10585 \times 0.17985 \times 2.0}$$

$$= 0.024 \text{ meter}$$

$$L = \sqrt{3.11\ A\ \gamma\beta\ \frac{a}{qB}}\ \Theta = \sqrt{3.11 \times 137 \times 0.17709\ \frac{0.024}{(2)(2.0)}}\ 2.0359922$$

$$= 1.37 \text{ meter (as before).}$$

$$\sigma = \epsilon\ \frac{gL}{a^2 k \Theta} = 3.0\times 10^{-6}\ \frac{47.44 \times 1.37}{(0.024)^2\,(0.10585)(2.0359922)}$$

$$= 1.6 \text{ degrees.}$$

(b) $B = 2.0$ tesla and $a = 0.012$ meter:

$$N = \frac{k\ \gamma^2\beta\ a\ B}{1.921\times 10^{-17}\ q} = \frac{0.10585 \times 0.17985 \times 0.012 \times 2.0}{(1.921\times 10^{-17})\ (2)}$$

$$= 1.18 \times 10^{13} \text{ ions/meter}$$

$$L = \sqrt{3.11\ A\ \gamma\beta\ \frac{a}{qB}}\ \Theta = \sqrt{3.11 \times 137 \times 0.17709\ \frac{0.012}{(2)(2.0)}}\ 2.0359922$$

$$= 0.97 \text{ meter.}$$

$$\sigma = \epsilon\ \frac{gL}{a^2 k\ \Theta} = 3.0\times 10^{-6}\ \frac{47.44 \times 0.97}{(0.012)^2\ (0.10585)\ (2.0359922)}$$

$$= 4.4^{+} \text{ degrees.}$$

(c) $N = 2.36\times10^{13}$ and $a = \sqrt{2}\ 0.012 \cong 0.017$ meter:

$$B = \frac{1.921\times10^{-17}\ qN}{k\ \gamma^2\beta\ a} = \frac{(1.921\times10^{-17})\ (2)\ (2.36\times10^{13})}{0.10585\ \ 0.17985\ \ 0.017}$$

$$= 2.8 \text{ tesla.}$$

$$L = \sqrt{3.11\ A\ \gamma\beta\ \frac{a}{qB}}\ \Theta = \sqrt{3.11\times137\times0.17709\ \frac{0.017}{(2)(2.8)}}\ 2.0359922$$

$$= 0.97 \quad \text{(as in option (b) above).}$$

$$\sigma = \epsilon\ \frac{gL}{a^2 k\,\Theta} = 3.0\times10^{-6}\ \frac{47.44\times0.97}{(0.017)^2(0.10585)(2.0359922)}$$

$$= 2.2 \text{ degrees.}$$

These results are summarized below:

q		B (tesla)	N (ions/meter)	a (meter)	L (meter)	σ (deg.)
1		2.0	2.36×10^{13}	0.012	1.37	6.3
2	(a)	2.0	2.36×10^{13}	0.024	1.37	1.6
	(b)	2.0	1.18×10^{13}	0.012	0.97	4.4^{+}
	(c)	2.8	2.36×10^{13}	0.017	0.97	2.2

The potential advantage of the use of the higher charge state presumably resides in a reduction of the electric field required per unit acceleration.

APPENDIX

~ Work Sheets ~

i)
$$k \equiv \frac{Q'}{u^2} = \frac{Q/(\epsilon K^{1/2})}{(aK^{1/4}/\epsilon^{1/2})^2} = \frac{Q}{Ka^2} = \frac{\dfrac{4q^2 r_p N}{\gamma^3\beta^2 A}}{\dfrac{qeB'}{\gamma\beta A m_p c}\, a^2} = 4\,\frac{m_p c}{e}\, r_p\, \frac{qN}{\gamma^2\beta}\, \frac{1}{B' a^2}$$

$$= 4\,\frac{m_p c}{e}\, r_p\, \frac{qN}{\gamma^2\beta}\, \frac{1}{Ba}$$

or

$$a = \frac{4}{k}\,\frac{m_p c}{e}\, r_p\, \frac{qN}{\gamma^2\beta}\, \frac{1}{B}$$

$$= \frac{4}{k}\,\frac{\mu_0}{4\pi}\, ec\, \frac{1}{\gamma^2\beta}\, \frac{qN}{B} \qquad \text{where } \mu_0 = 4\pi\times 10^{-7}$$

$$\doteq \frac{1.921\times 10^{-17}}{k}\, \frac{1}{\gamma^2\beta}\, \frac{qN}{B}\,.$$

ii)
$$L = \frac{\Theta}{\sqrt{K}} = \sqrt{\frac{\gamma\beta A\, m_p c}{qe\, B'}}\,\Theta = \sqrt{\frac{\gamma\beta A\, m_p c}{qe\, B}\, a}\;\Theta$$

$$= \sqrt{\frac{\gamma\beta A\, m_p c}{qe B}\;\frac{4}{k}\,\frac{m_p c}{e}\, r_p\, \frac{qN}{\gamma^2\beta}\,\frac{1}{B}}\;\Theta$$

$$= \sqrt{\frac{4}{k}\left(\frac{m_p c}{e}\right)^2 r_p\, \frac{A}{\gamma}\, \frac{N}{B^2}}\;\Theta$$

$$= \sqrt{\frac{4}{k}\,(m_p c^2 \times 10^{-7})\, \frac{A}{\gamma}\, \frac{N}{B^2}}\;\Theta\,.$$

Numerically,

$$L \doteq \sqrt{\frac{\gamma\beta A\, m_p c}{qe\, B}\, a}\;\Theta = \sqrt{3.11\;A\;\gamma\beta\;\frac{a}{qB}}\;\Theta$$

and

$$L \doteq \sqrt{\frac{4}{k}\,(m_p c^2 \times 10^{-7})\,\frac{A}{\gamma}\,\frac{N}{B^2}}\;\Theta = \sqrt{\frac{5.97\times 10^{-17}}{k}\, A\, \frac{N}{\gamma B^2}}\;\Theta\,.$$

iii) $$\sigma = \frac{g}{Q'} = \frac{g}{k u^2} = \frac{g \epsilon}{k a^2 K^{1/2}} = \epsilon \frac{g L}{k a^2 \Theta} .$$

Numerically,

$$\sigma \doteq 2.09 \times 10^{25} \gamma^{7/2} \beta^2 \frac{A^{1/2} B}{z^2 N^{3/2}} \epsilon k^{1/2} g .$$

MULTI-BEAM INJECTION INTO A HEAVY-ION INDUCTION-LINAC DRIVER WITH ELECTROSTATIC FOCUSING EMPLOYED INITIALLY

L. Jackson Laslett

U.C. Lawrence Berkeley Laboratory, Berkeley, California

January, 1986

I. INTRODUCTION AND SUMMARY

At realistic injection energies, the velocity of ions injected into a heavy-ion "driver" (for inertial fusion) is sufficiently low that A-G electrostatic focusing may be used advantageously. The permissible linear ion density (N, ions/meter) of an individual beam then is limited (as we show) by the focusing field gradients or potentials that are technologically achievable in such a system. For the transport of a sufficiently great total charge (or particle number) such a restriction then requires either the use of individual beams of inconveniently great length, the acceleration of a large number of individual beams, or some combination of these features.

Formulas that serve to illustrate these characteristics are derived in an Appendix and are discussed below, with some numerical illustrations in a later Section. The formulas presented are to be understood in the same spirit as those given in an earlier report [HI FAN-303] for magnetic focusing, in that operation is considered to be well into the asymptotic region where space-charge effects dominate and the individual-particle tune in consequence is strongly depressed ($\lambda_D \ll a$, or $\sigma \ll \sigma_0$). The basic formulas for electric focusing of course are equivalent to those for magnetic focusing if one simply makes the replacements $\beta c B \rightleftharpoons E$, $\beta c B' \rightleftharpoons E'$, or *etc.*; differences in the character of the technological restrictions (and the treatment of "clearances") in these respective cases can, however, significantly re-direct the conclusions to be drawn from the analysis.

To the extent that the analysis to be presented below suggests that a practical design for the low-energy initial portion of a heavy-ion driver unavoidably would require the use of a large number of individual beams (say $n_b \gg 32$), the design may differ significantly from that appropriate in later (higher-β) regions where magnetic focusing would be used. Most particularly, the use of electromagnets (most probably involving a thermally-insulated superconductivity design) with their more pronounced clearance requirements, could lead to designs that incorporate a smaller number of comparitively large diameter beams. To the extent that a change in the number of beams appears to be desirable, an increased importance should be attached to the investigation (analytically and experimentally) of means whereby it may prove to be technologically feasible to combine beams without unacceptable degradation of transverse emittance.

We now proceed to discuss and illustrate in some detail the issues associated with electrostatic focusing. It may be hoped that an analogous treatment of magnetic focusing can later be presented separately.

II. BASES OF ANALYSIS

Relevant design formulas for operation under conditions of extreme tune depression are expressed it terms of the following basic coefficients, that each are functions of the zero-intensity "tune" (σ_0) and occupancy (η):

$$\Theta = \sqrt{K}\,L \quad \text{(scaled half period)},$$

$$k = Q'/u^2, \quad \text{and}$$

$$g = Q'\cdot\sigma \quad \text{(degrees)}.$$

For the quantities k and g interest will be associated with their values in the limit of extreme tune depression, or with values within a few percent of such asymptotic limits. To the extent that k is roughly proportional to occupancy, it may be desirable to tabulate and plot values of k/η. [The coefficient g will be of interest for computing the value of σ for a particular design once a value of ϵ is assigned (see Appendix §③), in order to verify that a suitable (strongly-depressed) tune is in fact attained and that the value assumed for the coefficient k is indeed applicable.] Values of these coefficients (Θ, k, k/η, and g) have been tabulated and plotted in HI-FAN-303 for $\sigma_0 = 60°$, $75°$ & $90°$ and various values of η. Values alternatively might be derived, of course, from handy formulas of the type derived by E. P. Lee and presented in LBL-19560/HI-FAN-275.

VALUES FOR PRONOUNCED TUNE DEPRESSION
FROM $\sigma_0 = 75°$

η	Θ	k	k/η	g
1	1.4560805^{-}	0.21907	0.21907	66.30
$2/3$	1.56784617	0.18506	0.27760	61.56
$1/2$	1.72858897	0.14963^{-}	0.29925	55.85
$1/3$	2.0359922	0.10585	0.31755	47.44
$1/4$	2.3103220	0.081416	0.32566^{+}	41.82
$1/5$	2.5575876	0.066048	0.33024	37.79
$1/6$	2.783884	0.055530	0.33318	34.72
$1/8$	3.189762	0.042091	0.33673	30.31
$1/10$	3.550153	0.033879	0.33879	27.24
$1/20$	4.976670	0.017139^{+}	0.34279	19.44

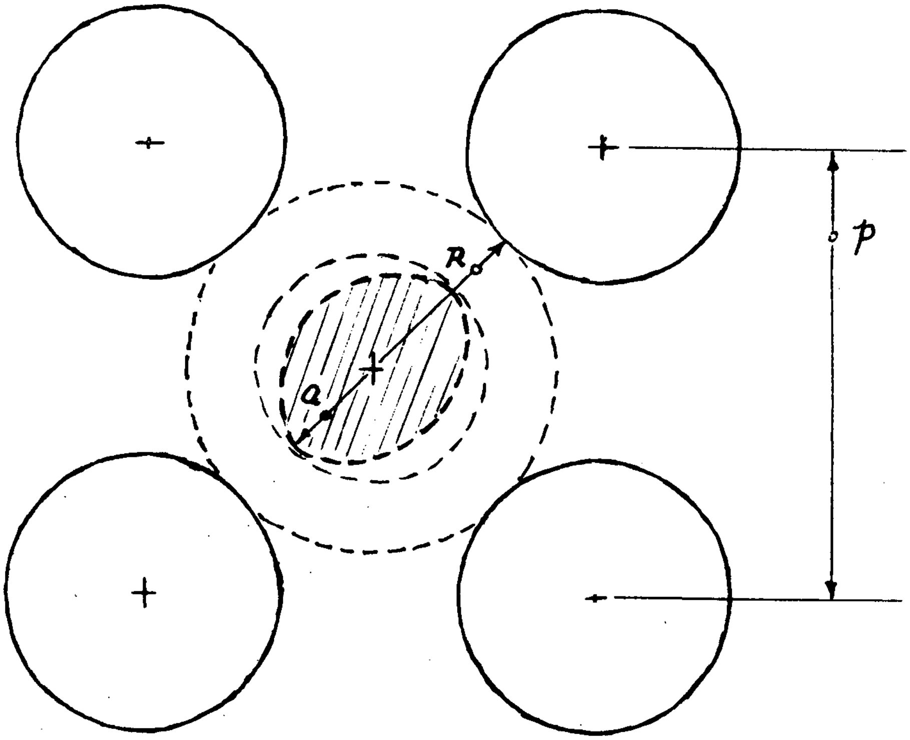
R
a
p

MBE-4 Lattice
"80% situation"

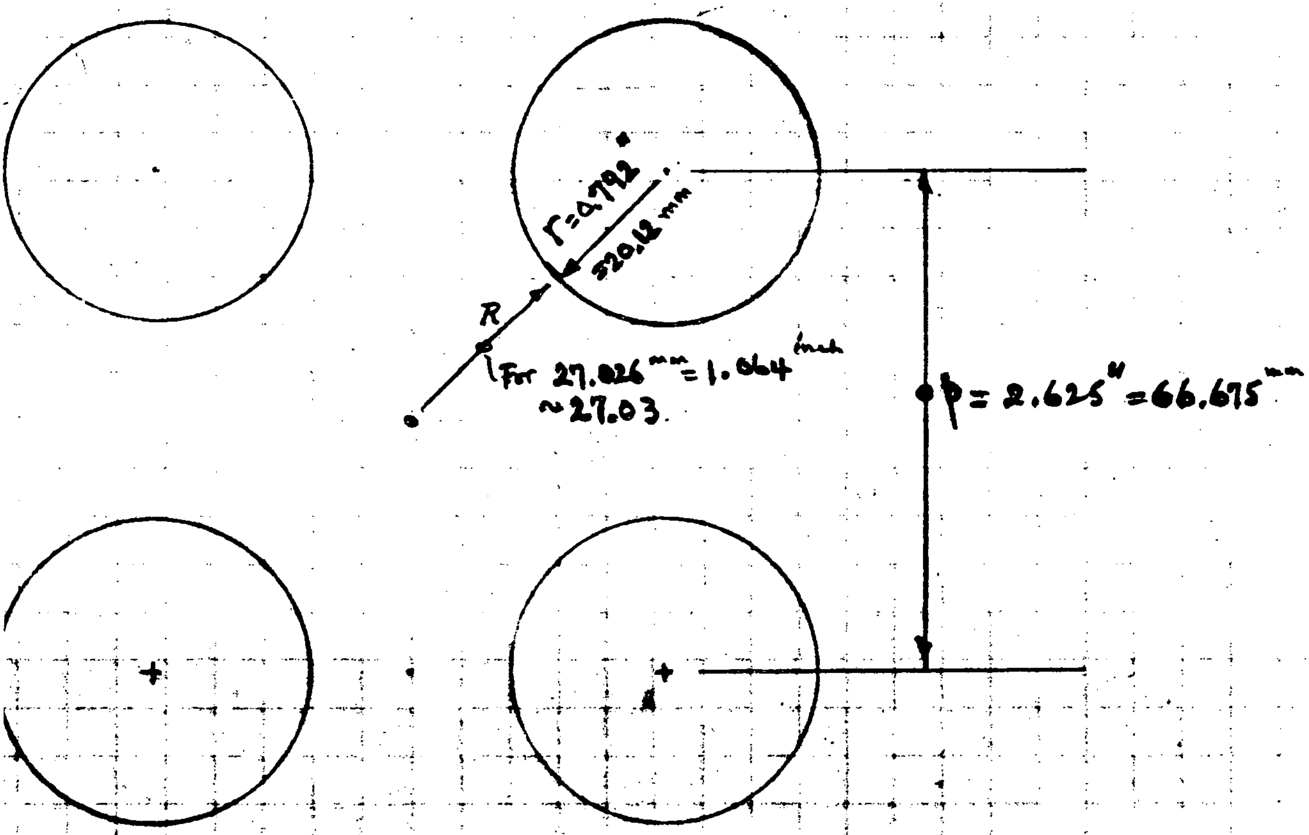

Some additional quantities, possibly of a less fundamental nature, also will be influential in limiting the design. One such quantity relates to the strength of the electrostatic field that is technologically realizable. A simple but attractive design for a quadrupole lattice may be formed from rods of circular cross-section (at potentials $\pm V_{Electrode}$) arranged in an array of full transverse period (or "pitch") p and with the surfaces closest to the beam surrounding a circular locus of radius R (see sketch). The ratio p/R should be such as to provide a quadrupole field of good quality, in the sense that the dodecapole component of potential is either zero or small, and in the design adopted for the MBE-4 experiment this ratio (in our present notation) is essentially 2.467, (the so-called "80% case" -- see C.M. Celata, *et al.*, LBL-19527/HIFAN-283). With a particular value adopted for this ratio, the peak electric fields within such an array will scale in direct proportion to $V_{Electrode}/R$, and experience suggests (A. Faltens) the restriction $V_{Electrode}/R = 2.333 \times 10^6$ V/m for an array similar to that adopted for the MBE-4 device. To the extent that the electric field so produced is substantially of a quadrupole character, moreover, the applied potential at other radii less than R may be written as proportional to r^2 so that at the beam edge ($r=a$)

$$V_{Edge} = \frac{1}{2} E' a^2 = (a/R)^2 \cdot V_{Electrode} .$$

The adoption of a value for the ratio p/R can furthermore be useful in forming an estimate of the size of the "bore" required to accommodate an array of n_b individual beams (linear cross-sectional dimension approximately proportional to $p\sqrt{n_b}$).

5

The need to remain within a suitable limit to the "aspect ratio", a/L, is sometimes cited as an additional constraint to be met in order to avoid difficulties from the transverse non-linearities that necessarily must be associated with an A-G modulation in the z-direction. This ratio is closely related, however, to the quadrupole potential V_{Edge} at the edge of the beam $(r=a)$

$$\frac{a}{L} = \sqrt{\frac{qeV_{Edge}}{\text{Kinetic Energy}}}\ \frac{1}{\Theta} \qquad \text{(non-relativistically)}$$

and in most applications the quadrupole potential is sufficiently low (relative to the kinetic energy) that the aspect ratio will lie well below any reasonably specified limit.

An additional quantity of interest is the limit one may wish to assign to the head-tail velocity tilt, $(\Delta\beta/\beta)_{Full}$, since the value of the velocity tilt is directly related to the spatial average of the longitudinal acceleration field (in the absence of bunching) and to the length of the beam pulse. Longitudinal space-charge fields, evaluated as proportional to $d\lambda/dz$, may also merit attention since it is desirable that they remain small -- perhaps in relation to the average applied acceleration field.

III. DESIGN CONSIDERATIONS

In approaching the design of the early portion of a heavy-ion induction linac (with electrostatic focusing) one may wish to consider various alternative sizes for the individual beams (and their associated focusing structure) and the use of various numbers (n_b) of beams. Thus a possible set of alternative beam and focusing-structure dimensions might include values such as those shown below and the possible associated focusing potentials then might be as shown included in the tabulation.

Case (Example)	a (cm)	R−a (cm)	R (cm)	$V_{electrode}$ (at R) (kV)	V_{Edge} (at a) (kV)
A	0.75	0.85	1.6	±37.	±8.2
B	1.0	0.85	1.85	±43.	±12.6
C	1.5	0.9	2.4	±56.	±21.87
D	2.0	1.0	3.0	±70.	±31.11
E	2.5	1.0	3.5	±82.	±41.7
F	3.0	1.0	4.0	±93.3	±52.5
G	4.0	1.0	5.0	±116.7	±74.67

[The electrode voltages listed here have been computed so that $V_{Electrode}/R = 2.333 \times 10^6$ V/m, and the voltages at the edge of the beam then are given by $V_{Edge} = (a/R)^2 V_{Electrode}$.] We note that some clearance (R−a) has been provided that is as large as 1 cm for all but the smaller beams shown in the Table.

7

For any assumed values of σ_0 and of occupancy (η) -- i.e., for any assumed value of Θ -- the appropriate value of the half-period (L) then will follow (Appendix, Sect. ②) and may be found to be significantly shorter for those cases characterized by the smaller dimensions (R). With the values selected for σ_0 <u>fixed</u> (say at 75°), it thus might be reasoned that the cases with the larger values of R (and of L) might permit use of a somewhat greater value of the occupancy (η) -- as would be advantageous with respect to the value that then would be assumed by the coefficient $k = Q'/u^2$ for such cases. It also is found, however, that (for any specified n_b) the cases with greater values of a^2/R permit larger acceleration rates (for a specified $\Delta\beta/\beta$ limit -- See Appendix, Sect. ④) so such cases may be less able to afford the extra space required to achieve an increased occupancy. One thus may wish to examine the consequences and possible advantages of adopting lattices of greater occupancy for the larger-radius beams, but one may wish also to consider proceeding more cautiously with use of (say) a constant value of η. In either case, having made a choice with respect to this issue, one then has available specific values for the coefficients Θ, k, and g wherewith to proceed further to examine the design.

For each type of individual beam (such as one of the types A - G indicated above) the transportable number of ions per meter (N) then follows immediately (Appendix, Sect. ①), and indeed N is seen to be greater in those cases for which the ratio a^2/R is large. The transport of a desired total amount of charge then may be accomplished by means of n_b beams whose individual lengths vary in *inverse proportion* to n_b (Appendix, p. A2).

For each such combination of beam dimensions (as for cases A - G) and number of beams (n_b), the length (l) or duration ($\tau = \frac{l}{\beta c}$) thus is determined and therefrom (for an assumed limit to the permissible head-tail velocity tilt) the permissible average acceleration field $\langle E \rangle$ follows (Appendix, Sect. ④). This permissible value of $\langle E \rangle$ is inversely proportional to l and hence directly proportional to n_b. Small values of l and correspondingly large permissible values of $\langle E \rangle$ thus appear to be realized through the use of beams of the larger dimensions and/or through the use of a large number of such beams.

A design trend in either of the directions just mentioned, in the interest of permitting rapid acceleration, of course would act strongly to increase the requisite bore of the acceleration cores through which the beams must pass. One might not be surprised, on the other hand, if it were found that for the various cases leading to the *same* permissible value of $\langle E \rangle$ the quantity $p\sqrt{n_b}$ (proportional to $\frac{R^{3/2}}{a\,k^{1/2}}$ --see Appendix, Sect. ⑤) shows *no very pronounced* variation.

Further impressions concerning the relative merits of such alternative designs accordingly may require some careful economic analysis, in which the size of the acceleration cores would play an important part, although intercomparisons on other grounds may also be quite informative however. In any case it is noteworthy that among all the various design combinations of the types we have outlined the requisite core flux per unit length ($\langle\Phi\rangle$, as in $V\cdot s/m$) will have the *same value* (save for possible allowances for end extensions of imperfectly formed pulses) -- see Append. Sect. ⑥, p. A6).

IV. EXAMPLES

With Tabulations

We proceed now to illustrate, by way of example, possible designs for a heavy-ion induction linear accelerator in the early stages -- specifically to accommodate Bi^{+1}_{209} ions of $\beta \cong 0.00553$ (Kinetic Energy $\cong 3.0 \times 10^{6}$ eV). The total charge to be accelerated will be taken to be 300 μC (3.0×10^{-4} coulomb). The supposition will be that the design can proceed on the assumption that the space-charge depression of individual-particle tune is pronounced (space-charge dominance) and to this end one may assume a quite small value for the emittance (e.g., $\epsilon \sim 3.0 \times 10^{-5}$ rad.·m.).

In the first sequence of examples we shall adhere to constant values for σ_0 and η throughout, deferring until a second sequence of examples the possibility of increasing the occupancy factor for focusing structures present in lattices of greater half period.

$A = 209.$ $q = 1.$ $K.E. = 3.0 \times 10^6$ eV $(\beta \doteq 0.00553)$ 300 μCoulomb

$\boxed{A}$

$\sigma_0 = 75$ Deg. & $\eta = 1/2$

We adopt the coefficients (see HIFAN-303):

$$Ⓗ = 1.728589$$
$$k \equiv Q'/u^2 = 0.142$$ (discounted by a few percent from the asymptotic limit)
$$g \cong 55.85$$

Auxiliary quantities (some of a technological character) are:

$$V_{Electrode}/R = 2.33_3 \times 10^6 \text{ V/m.},$$
$$p/R = 2.467,$$ ("80% design"),

and, for calculation of $\langle E \rangle$ (and $\langle \Phi \rangle$), the limiting value

$$\left(\frac{\Delta\beta}{\beta}\right)_{Full} = 0.20$$

We now consider the following cases:

Case	a (cm)	R (cm)	p (cm)	$V_{Electrode}$ (kV)	V_{Edge} (kV)	L (m)	N (ions/m)	λ (Coul/m)	I (Amp)
A	0.75	1.6	3.95	±37.	±8.2	0.248 ~9 3/4"	$4.04^+ \times 10^{11}$	6.48×10^{-8}	0.107_4
B	1.0	1.85	4.56	±43.	±12.6	0.267 10 1/2 "	6.22×10^{11}	9.96×10^{-8}	0.165
C	1.5	2.4	5.92	±56.	$\pm 21.8_7$	0.304^- ~12"	1.079×10^{12}	1.728×10^{-7}	0.286^+
D	2.0	3.0	7.40	±70.	±31.11	0.339^+ ~13.4"	1.534×10^{12}	2.46×10^{-7}	0.407^+
E	2.5	3.5	8.63^+	±82.	±41.7	0.367^- ~14.4"	2.055×10^{12}	3.29×10^{-7}	0.546
F	3.0	4.0	9.87	±93.3	±52.5	0.392 ~15.4"	2.59×10^{12}	4.15×10^{-7}	0.688^-
G	4.0	5.0	12.34^-	$\pm 116.7^-$	±74.67	0.438 ~17 1/4"	3.68×10^{12}	5.90×10^{-7}	0.978

It is seen that even in Case "G" (for which $V_{Electrode}$ has become rather large) the ratio a/L has remained less than $\frac{1}{10}$. The tune σ will not be very pronouncedly depressed from $\sigma_0 = \pi/5$ in the first couple of cases unless the emittance is notably less than 3.0×10^{-5} at this energy, but with such an ϵ, the depressed tune drops rapidly as one passes to subsequent cases in the tabulatio (see Appendix, Sect. ⑤).

We now pass to exhibiting a tabulation for these cases, with various numbers (n_b) of individual beams employed to transport a total of 300 microcoulombs, to show (i) the required beam length (l_0), (ii) the corresponding beam duration (τ_0), and (iii) the permissible spatial average acceleration field ($\langle E \rangle$) for $(\Delta\beta/\beta)_{Full} = 0.20$ Such values are entered in the format:

l_0 (m) τ_0 (μsec)
$\langle E \rangle$ (MV/m)

It should be recalled that for *all* *such* *cases* we expect the *same* value of $\langle \Phi \rangle$, namely $\langle \Phi \rangle = 0.724$ V·s/m [see Appendix, Sect. ⑥].

Case	n_b: 256	128	64	32	16
A	18.1 m 10.9 μs 0.0664 MV/m	36.2 21.8 0.0332	72.3 43.6 0.0166	145. 87.3 0.00829	289. 175. 0.00415
B	11.8 7.09 0.102	23.5 14.2 0.0510	47.0 28.4 0.0255	94.1 56.8 0.0128	188. 114 0.00638
C	6.78 4.09 0.177	13.6 8.18 0.0885	27.1 16.4 0.0442	54.3 32.7 0.0221	109. 65.4 0.0111
D	4.77 2.88 0.252	9.54 5.75 0.126	19.1 11.5 0.0629	38.1 23.0 0.0315	76.3 46.0 0.0157
E	3.56 2.15 0.337	7.12 4.30 0.169	14.2 8.59 0.0843	28.5 17.2 0.0421	57.0 34.4 0.0211
F	2.83 1.70 0.425	5.65 3.41 0.212	11.3 6.82 0.106	22.6 13.6 0.0531	45.2 27.3 0.0265
G	1.99 1.20 0.604	3.97 2.40 0.302	7.95 4.79 0.151	15.9 9.59 0.0755	31.8 19.2 0.03775

The results summarized for cases A-G in the previous tabulation contain estimates of permissible acceleration field $\langle E \rangle$, based on the assignment of a limiting $\left(\frac{\Delta p}{p}\right)_{full}$ but without any explicit consideration of "longitudinal space-charge factors." From this tabulation one can infer (by the equivalent of linear interpolation) the number n_b of beams to be used if $\langle E \rangle$ is to have some desired value (as 0.03, 0.05, ··· 0.30 MV/m). From the value of n_b so obtained, one then can compute the corresponding value of $\sqrt{n_b}\, p$ (in meters), as would be indicative of the linear dimensions of the required bore for an induction-core assembly surrounding such an array. We present such results in the following tabulation, in the format

n_b [no. of beams]
$\sqrt{n_b}\, p$ (meters).

Case	$\langle E \rangle = 0.03\ \frac{MV}{m}$	0.05	0.10	0.20	0.30
A	116. 0.425 m.	193. 0.548	386. 0.775	772. 1.096	1157. 1.343
B	75. 0.396	125. 0.511	251. 0.723	502. 1.022	753. 1.252
C	43. 0.390	72. 0.504	145. 0.712	289. 1.007	434. 1.234
D	31. 0.409	51. 0.528	102. 0.746	203. 1.056	305. 1.293
E	23. 0.412	38. 0.532	76. 0.753	152. 1.064	228. 1.303
F	18. 0.420	30. 0.542	60. 0.766	121. 1.084	181. 1.327
G	13. 0.440	21. 0.568	42. 0.803	85. 1.136	127. 1.391

It is noteworthy that, with the possible exception of the first and last cases (Case A & Case G), the values of $\sqrt{n_b}\, p$ for any particular value of $\langle E \rangle$ are virtually identical from case to case.

APPENDIX

Convenient Formulas

We employ $\Theta = \sqrt{K}\, L$ (scaled half period)

$k = Q'/u^2$ (as in the asymptotic limit)

$g = Q' \cdot \sigma$ (degrees, as in the asymptotic limit).

①
$$k = \frac{Q'}{u^2} = \frac{Q/(\epsilon K^{1/2})}{(aK^{1/4}/\epsilon^{1/2})^2} = \frac{Q}{Ka^2} = \frac{\dfrac{4q^2 r_p N}{\gamma^3\beta^2 A}}{\dfrac{qeE'}{\gamma\beta^2 A m_p c^2}\, a^2} = \frac{4q\, r_p m_p c^2 N}{\gamma^2 e E' a^2}$$
$$= \frac{qeN}{\pi\epsilon_0 \gamma^2 E' a^2}$$
$$= \frac{qeN}{2\pi\epsilon_0\gamma^2 V_{Edge}},$$

so

$$N = 2\pi\epsilon_0\gamma^2 \frac{V_{Edge}}{qe} k = \frac{2\pi}{\mu_0 c^2}\gamma^2 \frac{V_{Edge}}{qe} k$$
$$= \frac{2\pi}{\mu_0 c^2} \frac{\gamma^2 k}{qe} \left[\frac{V_{Electrode}}{R}\right] \frac{a^2}{R}$$

or

$$\lambda = qeN = 2\pi\epsilon_0\gamma^2 k \left[\frac{V_{Electrode}}{R}\right]\frac{a^2}{R}$$
$$= \frac{2\pi}{\mu_0 c^2}\gamma^2 k \left[\frac{V_{Electrode}}{R}\right]\frac{a^2}{R}$$ Coulomb/meter
(in a single beam).

Note: $\mu_0 = 4\pi \times 10^{-7}$.

$$l_0 = \frac{\text{Total Charge}}{n_b \lambda}$$ (where n_b denotes the number of individual beams)

$$= \frac{\mu_0 e^2}{2\pi} \frac{\text{Total Charge}}{\left[\frac{V_{Electrode}}{R}\right] \gamma^2 \frac{a^2}{R} k \, n_b} .$$

② $$L = \frac{\Theta}{\sqrt{K}} = \sqrt{\frac{\gamma \beta^2 A \, m_p c^2}{q e E'}} \; \Theta$$

$$= \sqrt{\frac{\gamma \beta^2 \frac{A}{q} \frac{m_p c^2}{e}}{2 V_{Edge}}} \; \Theta a$$

$$= \sqrt{\frac{\gamma \beta^2 \frac{A}{q} \frac{m_p c^2}{e}}{2 \left[\frac{V_{Electrode}}{R}\right]} R} \; \Theta$$

and, in the non-relativistic limit,

$$L \cong \sqrt{\frac{[\text{Kinetic Energy}]/(qe)}{\left[\frac{V_{Electrode}}{R}\right]} R} \; \Theta .$$

③ $$\sigma = \frac{g}{Q'} = \frac{g}{k u^2} = \frac{g}{k a^2 K^{1/2}/\epsilon} = \epsilon \frac{g L}{k \Theta a^2}$$ degrees.

④ With respect to velocity tilt,

$$\left(\frac{\Delta\beta}{\beta}\right)_{Full} = l_0 \, \frac{dv/dt}{v^2} = l_0 \, \frac{\text{acceleration}}{\beta^2 c^2}$$

and non-relativistically

$$\left(\frac{\Delta\beta}{\beta}\right)_{Full} \cong \frac{l_0}{2} \, \frac{qe\langle E\rangle}{\text{Kinetic Energy}} \, .$$

Thus

$$\langle E\rangle \doteq \frac{2\left(\frac{K.E.}{qe}\right)}{l_0}\left(\frac{\Delta\beta}{\beta}\right)_{Full} \qquad \text{spatial average of longitudinal field}$$

$$= \frac{4\pi}{\mu_0 c^2} \, \frac{\left(\frac{\text{Kinetic Energy}}{qe}\right)\left[\frac{V_{Electrode}}{R}\right]\gamma^2 \frac{a^2}{R} \, k \, n_b}{\text{Total Charge}} \left(\frac{\Delta\beta}{\beta}\right)_{Full}$$

or

$$n_b \doteq \frac{\mu_0}{4\pi} c^2 \, \frac{\langle E\rangle \cdot (\text{Total Charge}) \cdot \frac{R}{a^2}}{\left(\frac{\text{Kinetic Energy}}{qe}\right)\left[\frac{V_{Electrode}}{R}\right]\gamma^2 \, k \left(\frac{\Delta\beta}{\beta}\right)_{Full}} \, .$$

⑤ Thus

$$p\sqrt{n_b} = \left[\frac{p}{R}\right] R \sqrt{n_b}$$

$$\doteq \left[\frac{p}{R}\right] \frac{R^{3/2}}{a} \sqrt{\frac{\mu_0}{4\pi} c^2 \, \frac{\langle E\rangle \cdot (\text{Total Charge})}{\left(\frac{\text{Kinetic Energy}}{qe}\right) \frac{V_{Electrode}}{R} \gamma^2 k \left(\frac{\Delta\beta}{\beta}\right)_{Full}}}$$

where p denotes the "pitch" of the transverse lattice.
(In MBE-4, $p/R = 66.675^{mm}/27.026^{mm} \cong 2.467$.)

Note: $\frac{\mu_0}{4\pi} c^2 = \frac{1}{4\pi\epsilon_0} = 10^{-7} c^2 \cong 8.988 \times 10^9$,

and $\sqrt{\frac{\mu_0}{4\pi} c^2} \cong 9.480 \times 10^4$.

⑥ Also, with respect to acceleration cores,

$$\langle \Phi \rangle = \langle E \rangle \tau_0 = \langle E \rangle \frac{l_0}{\beta_0 c}$$

$$= 2 \, \frac{\left(\frac{K.E.}{qe}\right)}{\beta_0 c} \left(\frac{\Delta\beta}{\beta}\right)_{Full} \qquad \text{volt·sec/meter.}$$

<u>Check:</u> For pronounced tune depression (with $\sigma_0 = 75.$ deg. & $\eta = 2/3$):

$\Theta = 1.56784617$

$k = 0.18506$

$g = 61.56$ deg.

1/ With $\frac{V_{Electrode}}{R} = 2.333 \times 10^6$ v/m,

$a = 0.04$ m, $R = 0.05$ m, and $\gamma \cong 1.0$:

$$\lambda = \frac{1}{1.7975 \times 10^{10}} \; 0.18506 \; (2.33_3 \times 10^6) \; \frac{(0.04)^2}{0.05}$$

$$= (5.563 \times 10^{-11}) \; 0.18506 \; (2.33_3 \times 10^6) \; \frac{(0.04)^2}{0.05} = 7.68_6 \times 10^{-7}$$

coulomb/meter
(in a single beam).

For a total charge of 3.0×10^{-4} coulomb in $n_b = 64$ beams,

$$l_0 = (1.7975 \times 10^{10}) \frac{3.0 \times 10^{-4}}{2.33_3 \times 10^6 \; \frac{(0.04)^2}{0.05} \; 0.18506 \times 64} = 6.10 \text{ m.}$$

2/ With $\frac{K.E.}{qe} = 3.0 \times 10^6$ v. (K.E. = 3.0 MeV & $\beta \cong 0.00553$ for Bi^{+1}_{209}),

$$L \cong \sqrt{\frac{3.0 \times 10^6}{2.33_3 \times 10^6} \; 0.05 \; 1.5678\cdots} = 0.3975 \text{ m} \quad (\cong 15.65 \text{ inch}).$$

3/ Using the above, and with $\epsilon = 3.0 \times 10^{-5}$ (a rather small value),

$$\sigma = 3.0 \times 10^{-5} \; \frac{61.56 \cdot 0.3975}{0.18506 \times 1.5678\cdots \times (0.04)^2} = 1.58_1 \text{ degrees}$$

(indicating, for the assumed value of ϵ, a very pronounced tune depression).

4/ For $\left.\begin{array}{l}\frac{K.E.}{qe} = 3.0\times10^{6}\ v., \\ l_o = 6.10\ m.,\end{array}\right\}$ as above

and $(\Delta\beta/\beta)_{Full} = 0.2$:

$$\langle E\rangle = \frac{2\ (3.0\times10^{6})}{6.10}\ 0.2 = 0.197\times10^{6}\ v./m.$$

With again Total Charge $= 3.0\times10^{-4}$ coulomb, etc.,
we again find (from the final equation of §④)

$$n_b = (8.988\times10^{9})\ \frac{(0.197\times10^{6})(3.0\times10^{-4})\ \frac{0.05}{(0.04)^2}}{(3.0\times10^{6})\ (2.333\times10^{6})\ 0.18506\ \times\ 0.2} = 64.\ \text{beams.}$$

5/ With $p/R = 2.467$, and based on the above result, we find

$$p\sqrt{n_b} = 2.467\ (0.05)\sqrt{64} = 0.99\ \text{m.}\quad (\sim 39.\ \text{inch})$$

or, computed from earlier input assumptions,

$$p\sqrt{n_b} = \underbrace{(9.486\times10^{4})}_{\sqrt{\frac{\mu_0}{4\pi}c^2}}(2.467)\ \frac{(0.05)^{3/2}}{0.04}\sqrt{\frac{(0.197\times10^{6})\ (3.0\times10^{-4})}{(3.0\times10^{6})(2.333\times10^{6})0.18506\ \times 0.2}}$$

$= 0.99$ m.

6/ $$\langle\Phi\rangle = 2\ \frac{\frac{K.E.}{qe}}{\beta_o c}\left(\frac{\Delta\beta}{\beta}\right)_{Full} \cong 2\ \frac{3.0\times10^{6}}{0.00553\ (3.0\times10^{8})}\ 0.2 = 0.723\ \ v.s/m\ ;$$

or with $\tau_o = \frac{l_o}{\beta_o c} = \frac{6.10}{0.00553\ (3.0\times10^{8})} \cong 3.7\times10^{-6}$ sec.,

$\langle\Phi\rangle = \langle E\rangle\ \tau_o = 0.72\ \ V{\cdot}s/m.$

$\boxed{B}$

$\sigma_0 \cong 75$ DEG & η VARIOUS

We continue with a second sequence of examples in which we intend that again $\sigma_0 = 75$ degrees but the occupancy increases somewhat as one progresses from Case A to Case G (see remark on p. 7), with approximate estimates for the coefficients Θ and k as indicated below.

Case	a (cm)	$R-a$ (cm)	R (cm)	$V_{Electrode}$ (at R) (kV)	V_{Edge} (at a) (kV)	η	Estimated Values	
							Θ	k *
A	0.75	0.85	1.6	±37.	±8.2	~0.47	1.78	0.134
B	1.0	0.85	1.85	±43.	±12.6	1/2	1.72859	0.142
C	1.5	0.9	2.4	±56.	±21.87	~0.53	1.69	0.152
D	2.0	1.0	3.0	±70.	±31.11	~0.57	1.64	0.1625
E	2.5	1.0	3.5	±82.	±41.7	~0.60	1.62	0.169
F	3.0	1.0	4.0	±93.3	±52.5	~0.63	1.60	0.174
G	4.0	1.0	5.0	±116.7	±74.67	2/3	1.56785	0.180

* The values tabulated for k have been discounted by a few percent from their respective estimated asymptotic limits.

For these cases we then, as before, again calculate the transportable linear beam densities or current (N, λ, & I)--using, as before,

$$V_{Electrode} / R = 2.333 \times 10^6 \text{ v/m.}$$

We include in this tabulation the quantity p, calculated, as before, by $p/R = 2.467$, ("80 % design").

Case	a (cm)	R (cm)	p (cm)	$V_{Electrode}$ (kV)	V_{Edge} (kV)	L (m)	N (ions/m)	λ (Cou/m)	I (Amp.)
A	0.75	1.6	3.95	±37.	±8.2	0.255 ~10."	3.82×10^{11}	6.12×10^{-8}	0.101
B	1.0	1.85	4.56	±43.	±12.6	0.267 ~10.5"	6.22×10^{11}	9.96×10^{-8}	0.165
C	1.5	2.4	5.92	±56.	±21.87	0.297 ~11.7"	$1.15^{+}\times 10^{12}$	1.85×10^{-7}	0.307
D	2.0	3.0	7.40	±70.	±31.11	0.322 ~12.7"	$1.76^{-}\times 10^{12}$	2.81×10^{-7}	0.466
E	2.5	3.5	8.63^{+}	±82.	±41.7	0.344 ~13.5"	$2.45^{-}\times 10^{12}$	3.92×10^{-7}	0.649^{+}
F	3.0	4.0	9.87	±93.3	±52.5	0.363 ~14.3"	3.17×10^{12}	5.08×10^{-7}	0.843^{-}
G	4.0	5.0	12.34^{-}	$\pm 116.7^{-}$	±74.67	0.3975 ~15.65"	4.67×10^{12}	7.48×10^{-7}	1.24

This tabulation is again followed by one giving, vs. the number of beams (n_b), the beam length (l_0), beam durations (τ_0), and possible spatial average acceleration field ($\langle E\rangle$) for transport of a total charge of 300 μCoulomb, subject to the restriction $\Delta\beta/\beta)_{Full} = 0.20$
The format, as before, is as follows:

l_0 (m)	τ_0 (μsec)
$\langle E\rangle$ (MV/m)	

As with the examples presented earlier in Sub-section **A**, all the cases considered here again have the value $\langle \Phi\rangle = 0.724$ V.S/m.

Case	n_b: 256	128	64	32	16
A	19.16 m 11.56 μs 0.0626 MV/m	38.33 23.12 0.0313	76.65 46.24 0.0157^{-}	153. 92.5 0.00783	$307.^{-}$ 185. 0.00391
B	11.8 7.09 0.102	23.5 14.2 0.0510	47.0 28.4 0.0255	94.1 56.8^{-} 0.0128^{-}	188. 114^{-} 0.00638
C	6.34^{-} 3.82 0.189^{+}	12.67 7.64 0.0947	25.3 15.3 0.0474^{-}	50.7 30.6 0.0237	101. 61.1^{+} 0.0118
D	4.17 2.51 0.288	8.33 5.03 0.144	16.7 10.05 0.0720	33.3 20.1 0.0360	66.7 40.2 0.0180
E	2.99 1.80^{+} 0.401	5.98 3.61 0.201^{-}	12.0^{-} 7.22 0.100	23.9 14.4 0.0500	47.9 28.9 0.0250
F	2.31^{-} 1.39 0.520	4.61 2.78 0.260	9.22 5.56 0.130	18.4^{+} 11.1 0.0650	36.9 22.3^{-} 0.0325
G	1.57 0.945 0.766	3.13^{+} 1.89 0.383	6.27 3.78 0.191	12.5 7.56 0.0957	25.1 15.1 0.0479^{-}

From the results just tabulated one now presents the number of beams n_b one infers must be used if $\langle E \rangle$ is to have some desired value (as 0.03, 0.05, ... 0.30 MV/m) and from such n_b also show the values of $\sqrt{n_b}\,p$. [The values tabulated for n_b are given after rounding to the nearest integer, but the associated values of $\sqrt{n_b}$ are evaluated prior to such rounding.] The format, as before, is as follows:

n_b [no. of beams]
$\sqrt{n_b}\,p$ (meters)

Case	$\langle E \rangle = 0.03$ MV/m	0.05	0.10	0.20	0.30
A	123. 0.437 m	204. 0.564	409. 0.798	818. 1.129	1226 1.382
B	75. 0.396	125. 0.511	251. 0.723	502. 1.022	753. 1.252
C	41. 0.377	68. 0.487	135. 0.688	270. 0.973	405. 1.192
D	27. 0.382	44. 0.493	89. 0.698	178. 0.987	267. 1.209
E	19. 0.378	32. 0.488	64. 0.690	128. 0.975	191. 1.195
F	15. 0.379	25. 0.489	49. 0.692	98. 0.979	148. 1.199
G	10. 0.391	17. 0.504	33. 0.713	67. 1.009	100. 1.235

As was noted with the earlier sequence of cases (see p. 14), the values of $\sqrt{n_b}\,p$ as found here for any particular value of $\langle E \rangle$ are seen to be virtually equal from case to case. One thus can write, roughly, $\sqrt{n}\,p \cong 2.2\sqrt{\langle E \rangle_{MV/m}}$ meters in all the cases considered in the present tabulation -- esp. for cases C through F shown on this sheet.

APPENDIX

Convenient Formulas

We employ $\Theta = \sqrt{K}\, L$ (scaled half period)

$k = Q'/u^2$ (as in the asymptotic limit)

$\mathcal{J} = Q' \cdot \sigma$ (degrees, as in the asymptotic limit).

①

$$k = \frac{Q'}{u^2} = \frac{Q/(\epsilon K^{1/2})}{(aK^{1/4}/\epsilon^{1/2})^2} = \frac{Q}{Ka^2} = \frac{\frac{4q^2 r_p N}{\gamma^3\beta^2 A}}{\frac{qeE'}{\gamma\beta^2 A m_p c^2}\, a^2} = \frac{4q\, r_p m_p c^2 N}{\gamma^2 e E' a^2}$$

$$= \frac{qeN}{\pi \epsilon_0 \gamma^2 E' a^2}$$

$$= \frac{qeN}{2\pi \epsilon_0 \gamma^2 V_{Edge}},$$

so

$$N = 2\pi\epsilon_0 \gamma^2 \frac{V_{Edge}}{qe} k = \frac{2\pi}{\mu_0 c^2} \gamma^2 \frac{V_{Edge}}{qe} k$$

$$= \frac{2\pi}{\mu_0 c^2} \frac{\gamma^2 k}{qe} \left[\frac{V_{Electrode}}{R}\right] \frac{a^2}{R}$$

or

$$\lambda = qeN = 2\pi\epsilon_0 \gamma^2 k \left[\frac{V_{Electrode}}{R}\right] \frac{a^2}{R}$$

$$= \frac{2\pi}{\mu_0 c^2} \gamma^2 k \left[\frac{V_{Electrode}}{R}\right] \frac{a^2}{R}$$ Coulomb/meter (in a single beam).

Note: $\mu_0 = 4\pi \times 10^{-7}$.

$$l_0 = \frac{\text{Total Charge}}{n_b \lambda}$$ (where n_b denotes the number of individual beams)

$$= \frac{\mu_0 e^2}{2\pi} \frac{\text{Total Charge}}{\left[\frac{V_{Electrode}}{R}\right] \gamma^2 \frac{a^2}{R} k\, n_b} .$$

② $$L = \frac{\Theta}{\sqrt{K}} = \sqrt{\frac{\gamma \beta^2 A\, m_p c^2}{q e E'}}\ \Theta$$

$$= \sqrt{\frac{\gamma \beta^2 \frac{A}{q} \frac{m_p c^2}{e}}{2 V_{Edge}}}\ \Theta a$$

$$= \sqrt{\frac{\gamma \beta^2 \frac{A}{q} \frac{m_p c^2}{e}}{2\left[\frac{V_{Electrode}}{R}\right]} R}\ \Theta$$

and, in the non-relativistic limit,

$$L \cong \sqrt{\frac{[\text{Kinetic Energy}]/(qe)}{\left[\frac{V_{Electrode}}{R}\right]} R}\ \Theta .$$

③ $$\sigma = \frac{g}{Q'} = \frac{g}{k u^2} = \frac{g}{k a^2 K^{1/2}/\epsilon} = \epsilon \frac{g L}{k \Theta a^2}$$ degrees.

④ With respect to velocity tilt,

$$\left(\frac{\Delta\beta}{\beta}\right)_{Full} = l_0 \frac{dv/dt}{v^2} = l_0 \frac{\text{acceleration}}{\beta^2 c^2}$$

and non-relativistically

$$\left(\frac{\Delta\beta}{\beta}\right)_{Full} \cong \frac{l_0}{2} \frac{qe\langle E\rangle}{\text{Kinetic Energy}} .$$

Thus

$$\langle E\rangle \doteq \frac{2\left(\frac{K.E.}{qe}\right)}{l_0}\left(\frac{\Delta\beta}{\beta}\right)_{Full}$$

spatial average of longitudinal field

$$= \frac{4\pi}{\mu_0 c^2} \frac{\left(\frac{\text{Kinetic Energy}}{qe}\right)\left[\frac{V_{Electrode}}{R}\right]\gamma^2 \frac{a^2}{R}\, k\, n_b}{\text{Total Charge}}\left(\frac{\Delta\beta}{\beta}\right)_{Full}$$

or

$$n_b \doteq \frac{\mu_0}{4\pi}c^2 \frac{\langle E\rangle \cdot (\text{Total Charge}) \cdot \frac{R}{a^2}}{\left(\frac{\text{Kinetic Energy}}{qe}\right)\left[\frac{V_{Electrode}}{R}\right]\gamma^2\, k \left(\frac{\Delta\beta}{\beta}\right)_{Full}} .$$

⑤ Thus

$$p\sqrt{n_b} = \left[\frac{p}{R}\right] R\sqrt{n_b}$$

$$\doteq \left[\frac{p}{R}\right]\frac{R^{3/2}}{a}\sqrt{\frac{\mu_0}{4\pi}c^2 \frac{\langle E\rangle \cdot (\text{Total Charge})}{\left(\frac{\text{Kinetic Energy}}{qe}\right)\frac{V_{Electrode}}{R}\gamma^2 k\left(\frac{\Delta\beta}{\beta}\right)_{Full}}}$$

where p denotes the "pitch" of the transverse lattice.
(In MBE-4, $p/R = 66.675^{mm}/27.026^{mm} \cong 2.467$)

Note: $\frac{\mu_0}{4\pi}c^2 = \frac{1}{4\pi\epsilon_0} = 10^{-7}c^2 \cong 8.988 \times 10^9$,

and $\sqrt{\frac{\mu_0}{4\pi}c^2} \cong 9.480 \times 10^4$.

⑥ Also, with respect to acceleration cores,

$$\langle \Phi \rangle = \langle E \rangle \tau_0 = \langle E \rangle \frac{l_0}{\beta_0 c}$$

$$= 2\,\frac{\left(\frac{K.E.}{qe}\right)}{\beta_0 c}\left(\frac{\Delta\beta}{\beta}\right)_{Full} \qquad \text{volt}\cdot\text{sec/meter.}$$

Check: For pronounced tune depression (with $\sigma_0 = 75.$ deg. & $\eta = 2/3$):

$\Theta = 1.56784617$

$k = 0.18506$

$\mathcal{J} = 61.56$ deg.

1/ With $\frac{V_{Electrode}}{R} = 2.333 \times 10^{6}$ v/m,

$a = 0.04$ m, $R = 0.05$ m, and $\gamma \cong 1.0$:

$$\lambda = \frac{1}{1.7975 \times 10^{10}}\ 0.18506\ (2.333 \times 10^{6})\ \frac{(0.04)^2}{0.05}$$

$$= (5.563 \times 10^{-11})\ 0.18506\ (2.33_3 \times 10^{6})\ \frac{(0.04)^2}{0.05} = 7.68_6 \times 10^{-7}$$

coulomb/meter
(in a single beam).

For a total charge of 3.0×10^{-4} coulomb in $n_b = 64$ beams,

$$l_0 = (1.7975 \times 10^{10}) \frac{3.0 \times 10^{-4}}{2.33_3 \times 10^{6}\ \frac{(0.04)^2}{0.05}\ 0.18506 \times 64} = 6.10 \text{ m.}$$

2/ With $\frac{K.E.}{qe} = 3.0 \times 10^{6}$ v. (K.E. = 3.0 MeV & $\beta \cong 0.00553$ for Bi^{+1}_{209}),

$$L \cong \sqrt{\frac{3.0 \times 10^{6}}{2.33_3 \times 10^{6}}\ 0.05}\quad 1.5678\cdots = 0.3975 \text{ m} \quad (\cong 15.65 \text{ inch}).$$

3/ Using the above, and with $\epsilon = 3.0 \times 10^{-5}$ (a rather small value),

$$\sigma = 3.0 \times 10^{-5}\ \frac{61.56 \cdot 0.3975}{0.18506 \times 1.5678\cdots \times (0.04)^2} = 1.58_1 \text{ degrees}$$

(indicating, for the assumed value of ϵ, a very pronounced tune depression).

4/ For $\left.\begin{array}{l} \frac{K.E.}{qe} = 3.0\times10^{6}\ \text{V.}, \\ \ell_0 = 6.10\ \text{m.}, \end{array}\right\}$ as above

and $(\Delta\beta/\beta)_{Full} = 0.2$:

$$\langle E\rangle = \frac{2\ (3.0\times10^{6})}{6.10}\ 0.2 = 0.197\times10^{6}\ \text{V./m.}$$

With again Total Charge $= 3.0\times10^{-4}$ coulomb, etc.,
we again find (from the final equation of §④)

$$n_b = (8.988\times10^{9})\ \frac{(0.197\times10^{6})(3.0\times10^{-4})\ \frac{0.05}{(0.04)^2}}{(3.0\times10^{6})(2.33_3\times10^{6})\ 0.18506\ \times\ 0.2} = 64.\ \text{beams.}$$

5/ With $p/R = 2.467_1$, and based on the above result, we find

$$p\sqrt{n_b} = 2.467_1\ (0.05)\sqrt{64} = 0.99\ \text{m.}\quad (\sim 39.\ \text{inch})$$

or, computed from earlier input assumptions,

$$p\sqrt{n_b} = (\underbrace{9.486\times10^{4}}_{\sqrt{\frac{\mu_0}{4\pi}c^2}})(2.467_1)\ \frac{(0.05)^{3/2}}{0.04}\sqrt{\frac{(0.197\times10^{6})(3.0\times10^{-4})}{(3.0\times10^{6})(2.33_3\times10^{6})0.18506\times0.2}}$$

$= 0.99$ m.

6/ $$\langle\Phi\rangle = 2\ \frac{\frac{K.E.}{qe}}{\beta_0 c}\left(\frac{\Delta\beta}{\beta}\right)_{Full} \doteq 2\ \frac{3.0\times10^{6}}{0.00553\,(3.0\times10^{8})}\ 0.2 = 0.723\ \text{V}\cdot\text{s/m}\ ;$$

or with $\tau_0 = \frac{\ell_0}{\beta_0 c} = \frac{6.10}{0.00553\,(3.0\times10^{8})} \cong 3.7\times10^{-6}$ sec.,

$$\langle\Phi\rangle = \langle E\rangle\,\tau_0 = 0.72\ \text{V}\cdot\text{s/m.}$$

7

Nonlinear Dynamics, Stochasticity, Stochastic Diffusion and All That

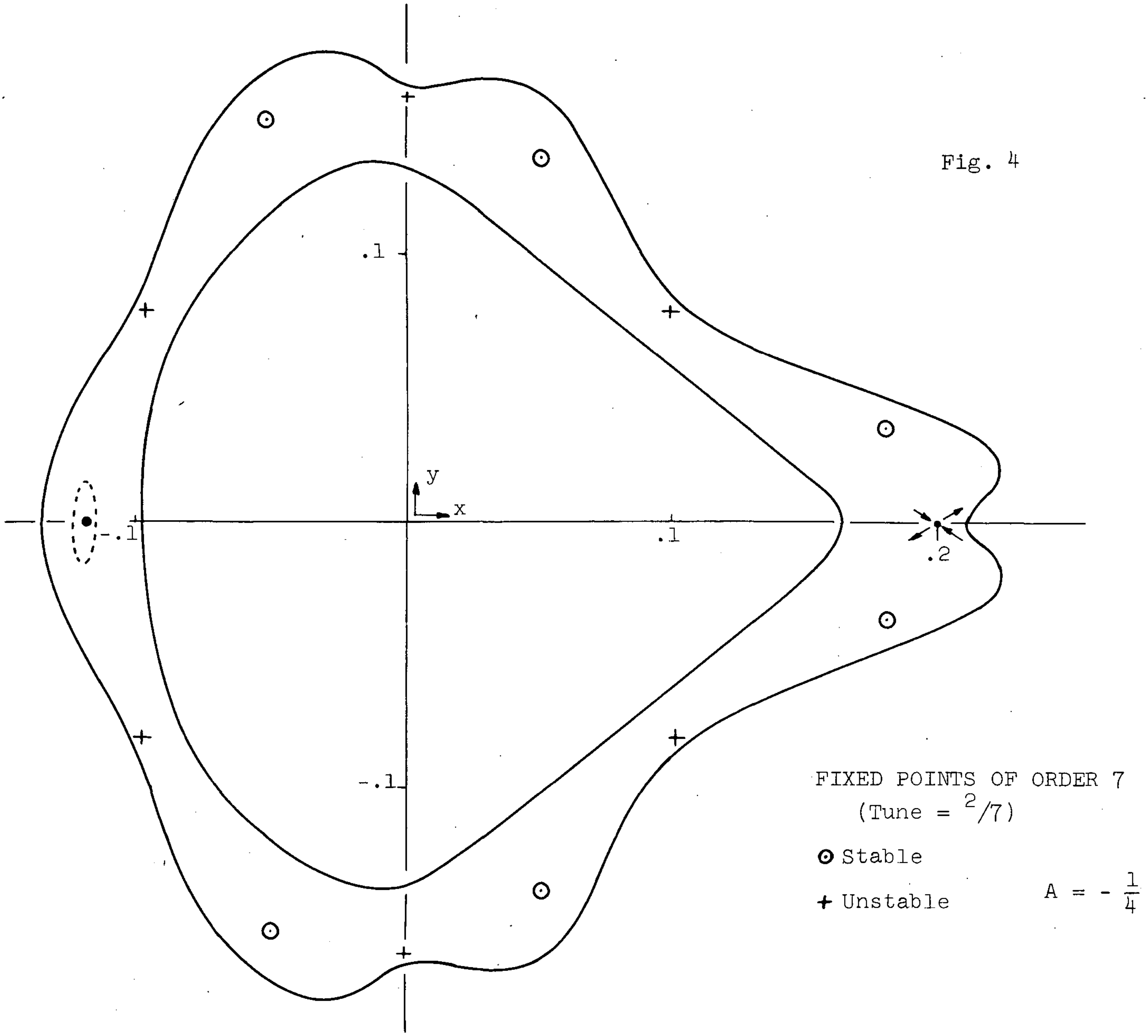

Fig. 4

UNCLASSIFIED

AEC Computing and Applied Mathematics Center
Courant Institute of Mathematical Sciences
New York University

Mathematics NYO-1480-101

LONG-TERM STABILITY FOR PARTICLE ORBITS

L. Jackson Laslett
Edwin M. McMillan
Jürgen Moser

Contract No. AT(30-1)-1480

UNCLASSIFIED

LONG-TERM STABILITY FOR PARTICLE ORBITS

This report contains the lecture delivered by Dr. L. J. Laslett at a one-day conference on The Mathematical and Computational Aspects of Accelerator Design, and a discussion by Dr. J. Moser of some of the points raised by Dr. Laslett. Two appendices contain some further comments by Dr. Laslett and Dr. E. McMillan. In addition to the talks reported here, the Conference also heard a report by Dr. G. Parzen on the iterative techniques used to calculate the eigenfrequencies in recent cavities in connection with linear accelerator design. He reported on the difficulties caused by shapes that consist of two nearly disconnected domains of unequal size, and of methods for overcoming these difficulties. Dr. Symon reported[1] on non-linear resonance phenomena due to the coupling of two particles, and Dr. E. Courant reported[2] on the effect of coupling in many particles. Dr. A. Garren described some sophisticated features of automation in codes used in accelerator design.

We thank all participants of the Conference for their contribution, and hope that this report will stimulate mathematicians to concern themselves with aspects of long-range stability.

---

[1] See H. Meier and K. R. Symon, "Analytical and Computational Studies on the Interaction of a Sum and a Difference Resonance," Proc. of the Intern. Conf. on High-Energy Accelerators and Instrumentation - CERN 1959

[2] See E. D. Courant and A. M. Sessler, "Transverse Coherent Resistive Instabilities of Azimuthally Bunched Beams in Particle Accelerators," The Review of Scientific Instruments, Vol. 37, No. 11, 1579-1588, Nov., 1966.

LONG-TERM STABILITY FOR PARTICLE ORBITS

L. Jackson Laslett*

The three accelerator papers on the program for this afternoon will be concerned with types of dynamical problems that arise in the study of particle accelerators, although the same mathematical problems may well arise also in other contexts. The accelerators with which we are concerned presumably will be of the "alternating-gradient" type, in which -- for very good reasons -- the functional character of the focusing force experienced by an individual displaced particle changes periodically as the particle proceeds on its way. Dr. Symon will review some of the quite striking effects that can develop from "coupling resonances," when the equations of motion are non-linear, and Dr. Courant will summarize the complications that develop with beam intensities sufficiently great that inter-particle forces must be considered.

My own paper is intended to report results on some computer experiments that I had hoped might cast light on the question of long-term stability -- specifically, in my work, for motion with only one spatial degree of freedom. For most accelerator projects this question may not be one of as immediate importance as the questions to be discussed by my colleagues this afternoon, but the answers could be vital for the proton storage-ring devices now being considered

---

* Lawrence Radiation Laboratory, University of California, Berkeley, California

or under construction. The general problem appears to be a very interesting and quite difficult one, and I would look forward to comments from our mathematician friends concerning what one can say at this time in simple terms with respect to this problem.

Thus, for my own part, I would like this afternoon to call to your attention this question of long-term stability and report on a few elementary computational experiments that I performed last summer for my own orientation and amusement. As for motivation, the first Figure indicates some of the numbers that may be relevant for characterizing modern accelerators with respect to the interval over which one would wish them to exhibit stability of the particle motion. We note in particular that a representative particle may be called upon to traverse some 10^7 periods of the alternating-gradient (A-G) focusing structure. These parameters are indeed essentially the same as the number of oscillations or periods successfully experienced by the beams of existing high-energy synchrotrons, and so we have the opportunity of concluding from experience that treacherous long-term instabilities need not be troublesome in a conventional A-G design.

PRESENT AND FUTURE A-G SYNCHROTRONS

Oscillation Wavelength: One to Several Hundred Meters

Period of Structure: 10 to 100 m.

Time Interval: $\sim$ 1 sec.

No. of Periods Traversed:

$$\frac{(3 \times 10^8 \text{ m/sec})(1 \text{ sec})}{(10 \text{ to } 100 \text{ m})} \sim 10^7$$

Fig. 1

It would not be out of the question, moreover, to think of computational experiments that would subject particles with a limited number of selected initial conditions to algebraic transformations that could simulate passage through some 10^7 periods of the A-G structure, although one would have to be attentive to the possibility of obtaining misleading results as a consequence of round-off or truncation errors -- especially if the structure of the problem is such that the distinction between the initial conditions for stable *vs.* unstable motion is very fine grained.

A storage ring, on the other hand, might be of comparable dimensions -- or at least involve a similar number of oscillations per second and number of periods traversed per second -- but would be intended to retain particles for hours. Thus, as we see on Fig. 2, one's interest in long-range stability becomes extended to intervals some 10^4 times as great -- i.e., possibly to 10^{11} periods, or even to 5×10^{11} periods of the structure.

PRESENT AND FUTURE A-G SYNCHROTRONS

Oscillation Wavelength: One to Several Hundred Meters

Period of Structure: 10 to 100 m.

Time Interval: $\sim$ 1 sec.

No. of Periods Traversed:

$$\frac{(3 \times 10^8 \text{m/sec})(1 \text{ sec})}{(10 \text{ to } 100 \text{ m})} \sim 10^7$$

STORAGE RINGS

Time Interval: $\sim$ 3 hrs. or $\sim 10^4$ sec.

No. of Periods Traversed: $\sim 10^{11}$

Fig. 2

Here past experience is not particularly helpful, since the storage rings that have been operated to date have been electron rings (or electron-positron rings) in which radiation damping can helpfully play a dominant role that is effectively absent (by a relative factor of ten orders-of-magnitude or more) for protons.

Cosmologically, the universe is supposed to be only some 5×10^9 years old, corresponding to no more than that many planetary periods at the present rate, so astronomical evidence may provide little assurance to the storage-ring designer unless we are prepared to be relatively restrained in our non-linearities, and unless we have some theoretical scaling laws that then could be applied to relate the long-term stability of our proposed device to that of another system that observationally has appeared to be stable.

I could illustrate the mathematical form in which one might pose this problem in our application by considering explicitly the case of a single spatial degree of freedom -- such as the transverse particle displacement, in the median plane of the accelerator, measured from the equilibrium orbit (Fig. 3).

In the ideal case of an A-G accelerator that is perfectly constructed and aligned, the linearized equations of motion would be a simple equation of the form of Hill's equation (to which the Floquet theory would apply) -- as shown at the top of the Figure, where $F(\theta)$ is periodic in θ and in practice might be represented simply by one of the two forms indicated.

LINEARIZED EQUATIONS

$$\frac{d^2u}{d\theta^2} + F(\theta)u = 0$$

$$\text{where} \quad F(\theta) = \begin{cases} \text{Periodic Square Wave} \\ \text{or} \\ a + b \cos N\theta \end{cases}$$

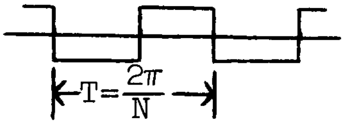

TYPICAL NON-LINEAR EQUATIONS

<u>One degree of Freedom</u>

$$\frac{d^2u}{d\theta^2} + (a+b \cos N\theta)u + \alpha(\sin N\theta)u^2 - \beta(\cos N\theta)u^3 = 0$$

<u>Two coupled degrees of Freedom</u>

$$\frac{d^2u}{d\theta^2} + (a+b \cos N\theta)u + \alpha(\sin N\theta)(u^2-v^2)-\beta(\cos N\theta)(u^3-3uv^2)=0$$

$$\frac{d^2v}{d\theta^2} + (a'-b \cos N\theta)v - 2\alpha(\sin N\theta)uv + 3\beta(\cos N\theta)u^2v = 0$$

Fig. 3

In actuality, some non-linearity of the restoring (focusing) force will be present, either deliberately or inadvertently introduced. My own interest in the effect of non-linearities arose in connection with designs for fixed-field alternating-gradient (FFAG) accelerators, as proposed by Symon and others of the Midwestern Universities Research Association (M.U.R.A.), in which non-linearities necessarily would be prominent at the amplitudes of interest. Representative terms that could be added to account for quadratic and cubic components to the force would, in that application, be of the form shown in the middle of the Figure, and below it one sees the Hamiltonian pair of equations that one could take to describe the corresponding motion in two spatial degrees of freedom.

The inclusion of a periodic θ-dependent coefficient for the linear terms in these equations is not significant, since that feature can be transformed away by an explicit, well-behaved transformation. What is important is that we do not have linear equations, to which the well-behaved properties of the Floquet solutions apply, nor do we have a θ-independent Hamiltonian that could be taken as a constant of the motion. (As is of course known, Dr. Moser has investigated the possibility of systematically introducing a series of transformations for the working variables such that the θ-dependence of the Hamiltonian function becomes displaced to higher and higher order -- this is done with the expectation, as I understand it, that the new Hamiltonian functions will progressively become better approximations to a constant of the motion, as in fact certainly seems to be the case in limited applications of this technique to the study of solutions over moderately long intervals.)

One has the impression that the essential features of solutions to equations of this form can be exhibited by suitably constructed non-linear algebraic transformations whose short-term phase-plane characteristics would be qualitatively similar to those implied by the differential equations, and for which computational studies would be both faster and less affected by numerical error. Such transformations can, in fact, be regarded as special cases of the differential equations, with the periodic coefficients becoming periodic delta functions of the independent variable (discrete, localized lenses). What is required of the transformation is simply that the iterated values of the coordinate and conjugate-momentum variables, as functions of the previous values of these variables, satisfy the Poisson-bracket conditions -- or any other of the several alternative forms in which one can express the necessary and sufficient conditions for a system to be Hamiltonian. In one spatial degree of freedom, this condition can be simply stated as requiring that the transformation be area preserving in the two-dimensional q,p phase plane.

A simple transformation in which I became interested some ten years ago at M.U.R.A. pertained to motion in one spatial degree of freedom and was believed to simulate the solution to the radial motion in the median plane of a spirally-ridged FFAG accelerator if the coordinate and momentum for this case are plotted at one-period intervals of the structure. This transformation is shown in Fig. 4, in which A is a constant and I regard x and y respectively as a coordinate and its canonically-conjugate momentum.

$$T: \quad \begin{aligned} x' &= Ax \pm (1-A^2)y + (1-A)[x \pm (1-A)y]^2 \\ y' &= \mp x + Ay \pm [x \pm (1-A)y]^2 \end{aligned}$$

If $T(x_1,y_1) = (x_2,y_2)$, then $T^{-1}(x_1,-y_1) = (x_2,-y_2)$

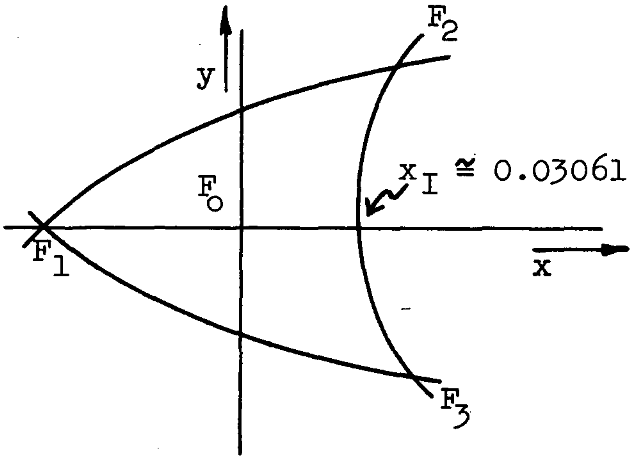

Sketch for $A = -{}^5/8$

$\cos^{-1}A \cong (0.35745)(2\pi)$

Area ≅ 5.5×10^{-3}
(would shrink to zero
if $A \to -{}^1/2$)

$$F_1: \left(-\frac{\sqrt{41}-5}{26}, 0\right) = (-0.053966\cdots, 0)$$

$$F_{2,3}: \left(\frac{1}{26}, \pm\frac{4\sqrt{41}-16}{169}\right) = (0.03846\cdots, \pm 0.05688\cdots)$$

Fig. 4

The upper and lower signs can be taken as referring to the forward or inverse transformation, respectively. The constant A can be interpreted as the cosine of the phase advance per iteration that would be exhibited by solutions to the linearized transformation, and A normally would be taken to have an absolute value less than unity. It also turns out that to avoid being exactly at a one-third resonance when the quadratic terms are present, one likewise should avoid the value $A = -1/2$ (for which $\cos^{-1}A = 2\pi/3$).

This transformation, as written, was intended to simulate the solutions in a spirally-ridged FFAG accelerator when viewed at a suitable point of symmetry in the structure (and at homologous points, spaced at intervals, $2\pi/N$, equal to one period of the structure). In this form the transformation (T) has the great convenience of exhibiting a symmetry about the x-axis, as has been noted on the Figure and as is evident from inspection of the transformation equations. The phase diagram, as revealed by short-term computations -- or roughly by application of Moser's methods or in some respects by more simple analytic considerations -- looks somewhat as sketched on the Figure [for $A = -5/8$, $\cos^{-1}A \cong 0.35745(2\pi) \cong 128.7$ deg.], and in this respect the proposed transformation appears consistent with trajectories computed for some typical FFAG structures in which one would plan to employ the greater part of the apparently stable region that is situated within the roughly triangular boundary shown.

What appears to be a stable area is bounded by the curves that I have drawn through the three unstable fixed points of order 3 (F_1, F_2, F_3), that are rigorous fixed points whose coordinates can be explicitly obtained from the roots of a quadratic equation. In calling your attention to transformations of this form (and to the analogous non-linear differential equations). I do not mean to imply that present accelerator or storage-ring projects visualize such pronounced excursions toward the boundaries of regions so obviously influenced by non-linear resonant effects, but smaller non-linearities may well be present in practice and future accelerator concepts may again involve strongly non-linear restoring forces. I also would not wish to imply that the most important problems to pursue in this connection are those that involve only <u>one</u> spatial degree of freedom. It may well be that results of some computational experiments -- and theoretical work by Kolmogorov and others that I hope Dr. Moser will review for us -- can set the designer's mind at rest with respect to possible long-range instability in one degree of freedom and that emphasis should be given in this context to the much more difficult problems that arise with systems having two (or more) spatial degrees of freedom.

In any event, I thought last spring that for me it would prove instructive to examine the performance of the transformation just shown, using the CDC-6600 computer in double precision, since my previous look at this problem had been with the earlier IBM-704. This work was undertaken at Berkeley with the programming assistance of Mrs. Levine and with helpful advice from Eric Beals and Loren Meissner. By using double precision, we had available some 96 bits -- although truncation rather than true rounding was used in the arithmetic operations -- and it was possible to investigate spurious fluctuations and drifts both by computational experiments and/or by a rough analysis.

In investigating the behavior of an algebraic transformation such as the one just proposed, one of course has a wide choice of working variables. Thus, if desired, new variables could be introduced that would result in a transformation having symmetry about the $+45^{\circ}$ diagonal, or one could select variables that would reduce the number of computational steps (and hence improve the speed and accuracy of the work) required to perform each iteration. One may merely regard the introduction of such new variables as a mathematical operation, but, in some instances, use of the new variables rather easily can be interpreted as viewing the dynamics at some other reference point within the lattice of the physical structure.

For my own computational experiments, it was convenient to introduce new ("working") variables defined in Fig. 5 for the direct or inverse transformations, respectively. In terms of these variables the transformation assumed the form shown at the bottom of the Figure.

By introduction of the working variables

$$q = x \mp (1-A)y$$
$$p = \pm y$$

for the direct transformation T or its inverse,

$$q' = Cp + q$$
$$p' = (q'-1)q' + p$$

with

$$C = 2(1-A)$$

Fig. 5

This transformation seemed particularly suitable for repeated iteration, but phase diagrams plotted in terms of these working variables (q,p) do not show any apparent symmetry and it therefore was convenient to express results in terms of the original x,y variables whenever output data were printed. The parameter A $(= -5/8$, a binary fraction) and derived parameters [such as $(1-A) = 13/8$ and $C = 2(1-A) = 13/4$] were stored exactly in the computer memory, and double-precision octal I-O was available if required for resumption of any particular run.

An initial attempt to reveal erratic or stochastic behavior gave negative results, in that for runs of as many as 10^7 forward iterations,[†] starting with $x = +0.026 = 0.85\ x_I$, there appeared to be no computationally significant anomolous

---

[†] 941.169 sec of CP time were required for a run consisting of 10^7 forward iterations followed by 10^7 reverse iterations.

drift -- e.g., after correction for computational drift and allowance for computational fluctuations, the +x intercept of the apparent invariant phase curves could be said to remain constant to an absolute accuracy of about 10^{-27}, or a relative accuracy of about 4×10^{-26} in this example.

A positive, and hence more dramatic, effect can be obtained, however, by examining in some detail the character of the apparent separatrix. For this purpose we note that the transformation T^3 will return a phase point to any one of the unstable third-order fixed points (F_1, F_2, F_3), and that the "separatrices" drawn through the fixed points can represent at these points the directions of outgoing and ingoing eigenvectors for the transformation T^3 when the latter is linearized about the fixed points. If a true separatrix F_2F_3 exists, a line segment formed of points situated very near to F_2 and that lie on a curve whose slope is that of the appropriate (outgoing) eigenvector through that point should iterate under T^3 so as to approach F_3 along a similar eigenvector direction and, in the process, should generate a single smooth curve (F_2F_3). The symmetry of the present transformation (with respect to the x-axis) would imply, therefore, that the curve so generated cross the x-axis with a vertical slope.

Numerically, forward iteration of a line segment from the neighborhood of F_2 down toward the x-axis should be favorable with respect to unavoidable computational errors, and detection of a non-vertical crossing would imply the non-existence of a firm separatrix between F_2 and F_3 (and, by application of T and T^2 or T^{-1}, correspondingly also would imply the absence of firm separatrices F_3F_1 and F_1F_2.)

Our work with double-precision arithmetic made it unambigously clear that extension of the eigenvector direction at F_2 led to non-vertical crossing of the x-axis (at crossing, slope $\cong +10^6$), although if single-precision arithmetic had been employed the results might have been ambiguous in this case. /Checks of the computational process could be made by use of different compiler systems, writing the algebraic statements in a different order or form, influencing the truncation errors (as by introducing intermediate steps such as "times 3" followed by "divide by 3" into one or more equations for each iteration), and by use of varied starting conditions. Although some of these steps affected noticeably the location of individual iterates (x,y) near the x-axis, they had no significant effect on the curve that was generated in this process./

As is indicated in Fig. 6, the situation thus is such that a line segment QRS originating at F_2 with the eigenvector slope will transform, after repeated iterations of T^3, to generate the S-curve shown just below the x-axis (initially with an eigenvalue, for T^3, $\lambda_I \cong 2.102$).

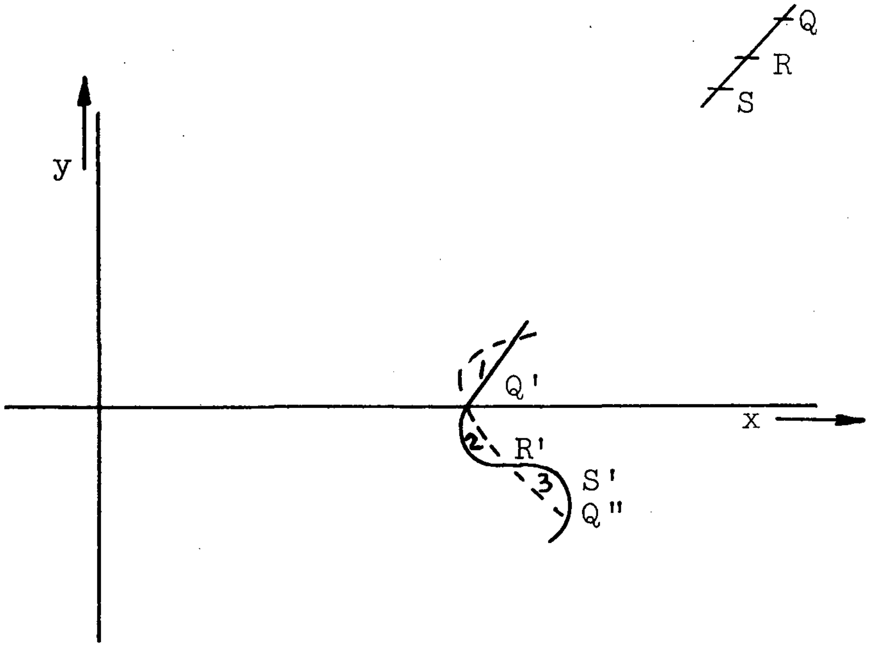

Fig. 6

A similar sequence of inverse iterations from F_3 will generate the dashed curve, and forward iteration would cause points on the dashed curve to approach F_3 in the absence of computational errors. Thus only particular points (e.g.: Q, R, and their iterates) that lie on both curves can originate arbitrarily close to F_2 and ultimately approach F_3.. The area 1 transforms to the equal area 3 (unit Jacobian) and areas 1 and 2 are equal by virtue of the symmetry of the transformation, so all the loops shown -- and their iterates under the transformation T -- are equal in this example.

It will be recognized that points, such as Q' and R', that approach F_3 ultimately do so in smaller and smaller steps $(\lambda_{II}^{-1} = \lambda_I = 0.48)$. Conservation of the areas mentioned thus requires that the curve bounding the transforms of the areas 2 and 3 correspondingly must become increasingly elongated laterally, and (as suggested by Fig. 7) the solid curve Q'R'S'Q" will become increasingly sinuous.

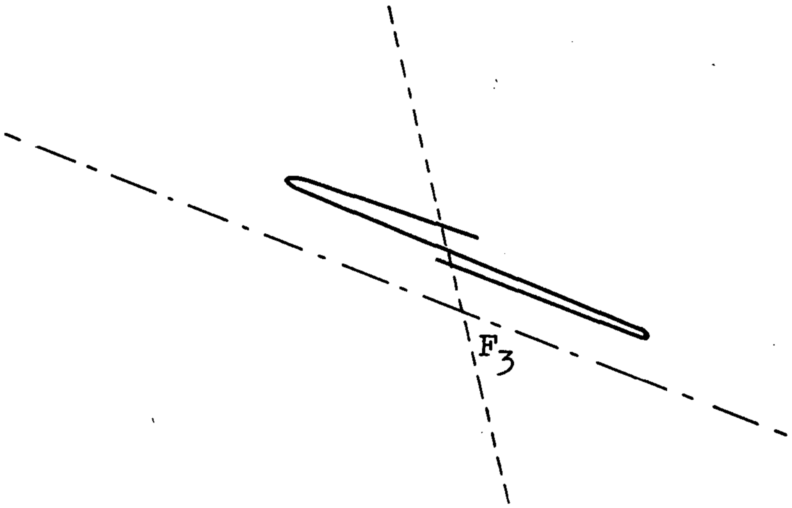

Fig. 7

The areas shown (transforms of regions 2 and 3) each have the approximate magnitude 4.8×10^{-11}, or roughly $1/10^8$ times the area of the entire superficially-stable region $F_1F_2F_3$. The uniqueness of the transformation precludes that a finger such as that shown extending to the left will be intersected by one of its iterates, although such an iterate could well cross the dashed line. If the transformation continues to be applied, these fingers thus cannot remain at all times within the finite area that at first might have been supposed to be a stable region, and an observed means of escape is that in which an iterate of this finger does cross the dashed line to enter a loop extending to the right.

It will be appreciated that the evolution of these fingers necessarily will become quite complex, and certainly they will make inroads into the ostensible "interior" region, but at this point it is by no means clear that the entire "interior" region need be consumed in this way. What is clear is that the non-smooth joining of the forward and backward eigenvector directions from F_2 and F_3, respectively -- either by a disparity of slope (as in the present example) or by a disparity of some higher derivative -- will imply that these curves do not generate a true separatrix and the truly stable area (if one exists) consequently is somewhat smaller.

In the "interior," closer to the "stable" fixed point at the origin, other (higher-order) fixed-point systems may be found. It can become increasingly difficult in such cases, however, to examine whether smooth or non-smooth intersection of their extended eigenvectors occurs, and a computational investigation would offer little hope of establishing absolute smooth joining.

It is interesting and somewhat informative to examine other area-preserving transformations in these respects. Professor deVogelaere, who is now at Berkeley and has been very generous in discussion of these points, has for some time been directing attention to a very simple transformation that requires little calculational precision to exhibit the failure of eigenvectors, when extended, to join smoothly. In its original form this transformation was of the form shown at the top of Fig. 8,

De Vogelaere's Transformation

$$x' = y + x^2$$

$$y' = -x + x'^2$$

$$\frac{1}{2}\,\mathrm{Tr.} = 0.$$

Modified De Vogelaere Transformation

$$x' = y + Tx + (1-T)x^2$$

$$y' = -x + Tx' + (1-T)x'^2$$

$$\frac{1}{2}\,\mathrm{Tr.} = T.$$

Fig. 8

and can be shown to possess the same symmetry property with respect to the x-axis that was noted for the transformation I mentioned originally. This particular form may be somewhat distressing to a physicist, since the trace of the matrix for the linearized transformation vanishes (phase advance = $\pi/2$), and one would be situated at a "quarter-integral resonance." A simple generalization of this transformation can be made, however, without affecting the interesting features by adopting the form shown at the bottom of the Figure. For either transformation, an unstable fixed point, of order 1, occurs at the point (1,0), and the eigenvector directions extended from this point show a gross failure to join smoothly on crossing the negative x axis. This behavior is indicated on Fig. 9.

Although this transformation may not be representative in any evident way of accelerator-orbit behavior, its study can be informative concerning features that can arise in non-linear problems. One can find, for example with T = -1/8, systems of unstable fixed points for which the eigenvalues are *negative* and that do not appear to have associated with them a corresponding system of stable fixed points.

[E.g., for T = -1/8: Order 4/1, with eigenvalues -3.197
and -0.3128 at x = 0.5615983, y = 0;

Order 8/2, with eigenvalues -8.369
and -0.1195 at x = 0.4562733, y = 0.]

Also, with T > 0 (e.g., +1/8), one finds for example a system of unstable and stable fixed points of order 19/4 in the "interior" that roughly exhibits the classical "island structure" but for which the extended eigenvectors very easily can be shown *not* to intersect smoothly (both on the inner and on the outer island boundaries). [One member of the stable and of the unstable fixed-point systems of this family will be found respectively at x = -0.38429776, y = 0 and x = +0.50736937, y = 0. The eigenvalues for the latter are $\lambda_I = 1/\lambda_{II} \cong 3.221$]

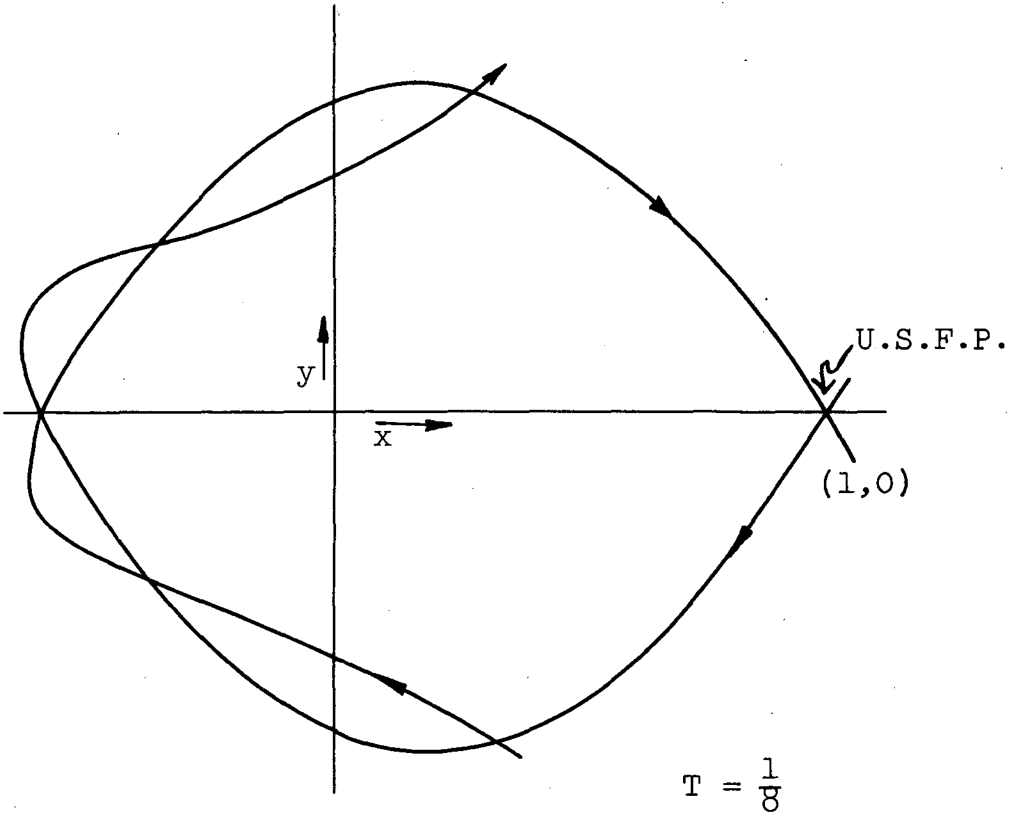

Fig. 9

Somewhat closer to the origin, however, one finds a similar system of order 9/2 (indicated on Fig. 10), for which the intersections appeared completely smooth to the limit of my computational accuracy /̲fixed-points at $x = -0.29000009$, $y = 0$ and at $x = +0.32176070$, $y = 0$ (with $\lambda_I = 1/\lambda_{II} \cong 1.179$)_̲7.

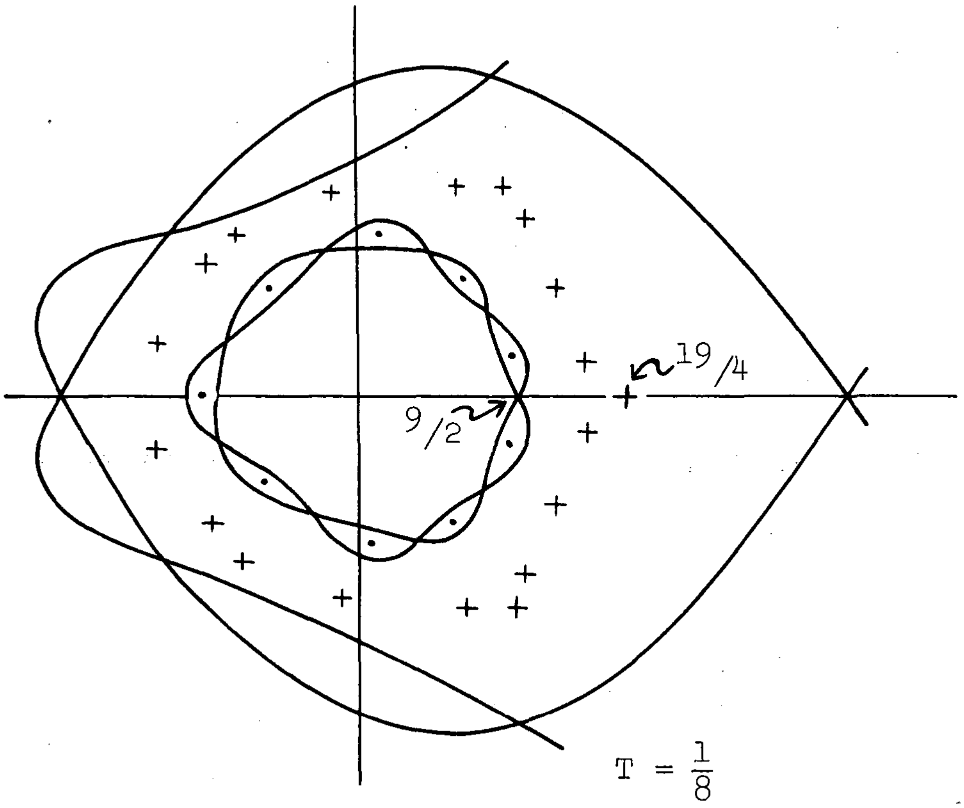

Fig. 10

Experience with each of the transformations mentioned could be said to be not inconsistent with the view that some of the curves commonly regarded as stability boundaries are not firm and imply a sort of stochastic behavior of phase points in their neighborhood, but, so far as we can tell, others may be perfect barriers and indeed may have true invarient phase curves nearby (ignoring, of course, the fluctuations of the parameters that in practice would be present as a result of "noise" in a physical system). The designer of particle accelerators -- or, more particularly, of storage rings --

of course would like to know whether any regularity of behavior can be anticipated in this regard, and whether quantitative or reasonably-accurate semi-quantitative estimates can be made of diffusion rate in a region that possibly is characterized by stochastic behavior. It may be, of course, that such detailed and subtle features of behavior are highly sensitive to the exact values of the physical parameters that determine the transformation, and as such would be beyond the precise physical control of the experimenter.

(I might add that the systems of unstable fixed points that have been found for both my transformation and for that of Professor deVogelaere appear to show what to me is a quite surprising regularity: I believe that deVogelaere noticed empirically that for his transformation, linearized about the fixed points of a certain class, the quantity $\frac{1}{2}$ Trace - 1 showed an exponential dependence on the fixed-point order. It may be that other interesting features of such transformations can also be found to exhibit regularities -- such as that suggested by Mel'nikov in regard to the dimensions of the areas that are developed by the failure of separatrices to join smoothly -- and that some of these regularities might permit one to draw inferences that would have practical application.)

An interesting class of transformations has been proposed by Dr. McMillan, for which it is possible to establish that the eigenvectors through the fixed point or fixed points <u>do</u> form a true impenetrable separatrix. He finds it convenient in this connection to consider the transformations to be written in a form showing symmetry about the +45° axis (rather than about the x-axis) -- a form in which each of the transformations previously mentioned can be written by a suitable change of variables. This form is taken to be, for the forward transformation, that which will be seen on Fig. 11 in the upper left-hand corner. Such a transformation has a simple physical

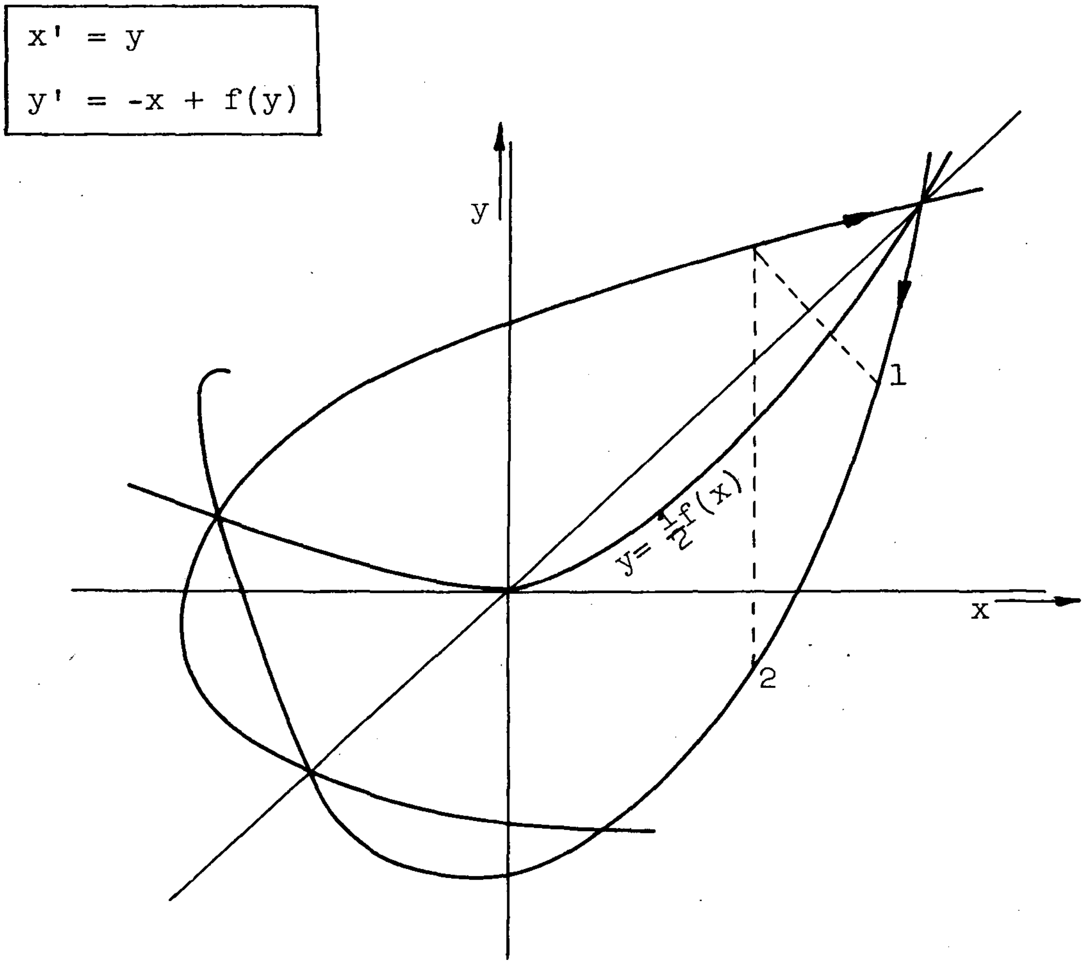

$$\boxed{\begin{aligned} x' &= y \\ y' &= -x + f(y) \end{aligned}}$$

Fig. 11

interpretation in terms of a structure formed simply from a periodic sequence of identical non-linear lenses [$\Delta y = -x + f(x)$] placed with unit separation just before the measurement planes and with linear lenses [$\Delta y = -x$] situated just after each of these planes. For a fixed point of order one, the trace of the matrix for the transformation linearized about that point is just the derivative of f at that point, and stability of the linearized system requires $\left|\frac{1}{2} f'\right| < 1$.

The transformation in the form shown can be executed by a simple graphical construction, in which one first mirrors the initial point about the diagonal and then vertically reflects the resulting y-value about the curve $y = \frac{1}{2} f(x)$. A fixed point of order 1 is synonymous with the intersection of the diagonal with this latter curve. Referring to Fig. 12, McMillan has pointed out [UCRL-17795] that if the function $f(y)$ can be expressed as $\phi(y) + \phi^{-1}(y)$, where ϕ^{-1} is the inverse of ϕ, then $x = \phi(y)$ will be an invariant curve. The phase diagram shown in the Figure is for an example in which

$$x = \phi(y) = a - \frac{1}{y + a} \quad \text{and} \quad f(y) = \frac{2y}{a^2 - y^2} ,$$

with fixed points at $x = y = \pm \sqrt{a^2 - 1}$ $(|a| > 1)$.

Example in which

$f(y) = \phi(y) + \phi^{-1}(y)$

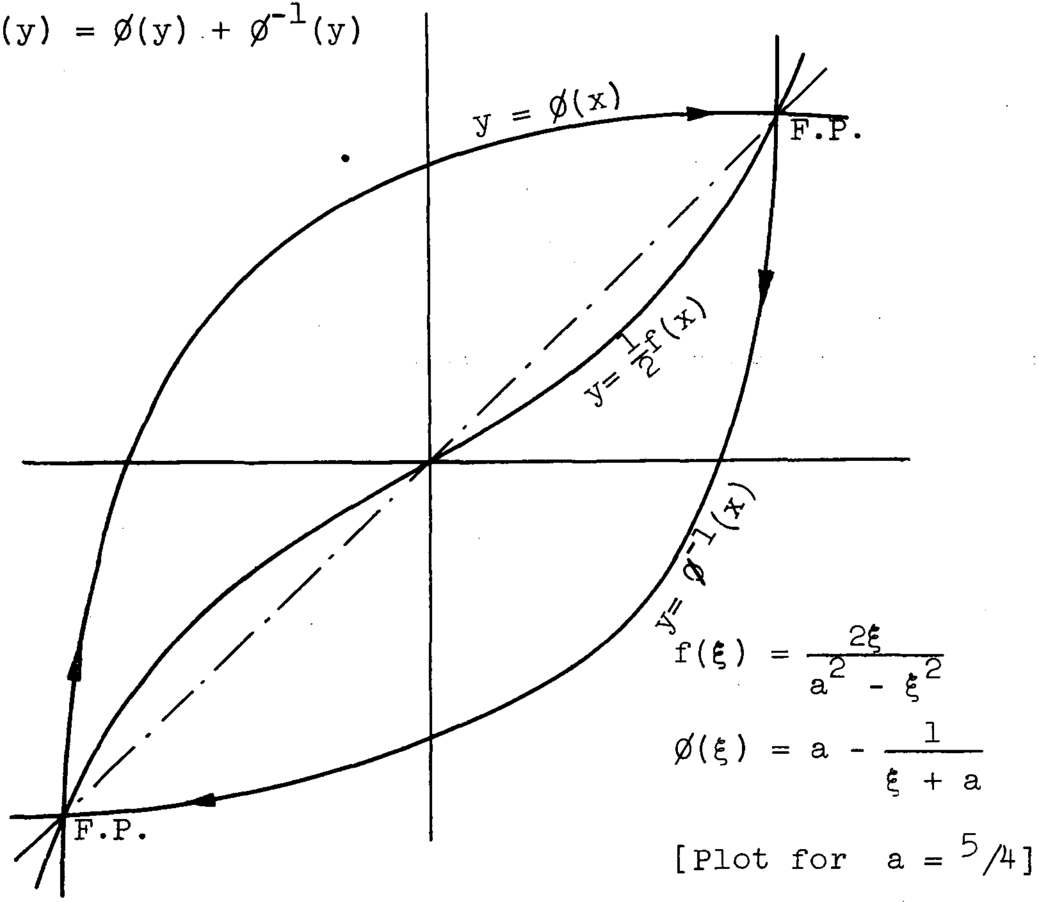

Fig. 12

An interesting and simple, although perhaps artificial, example of this class is one suggested by Dr. Judd, for which, as indicated on Fig. 13, one employs a step-wise linear f(x).

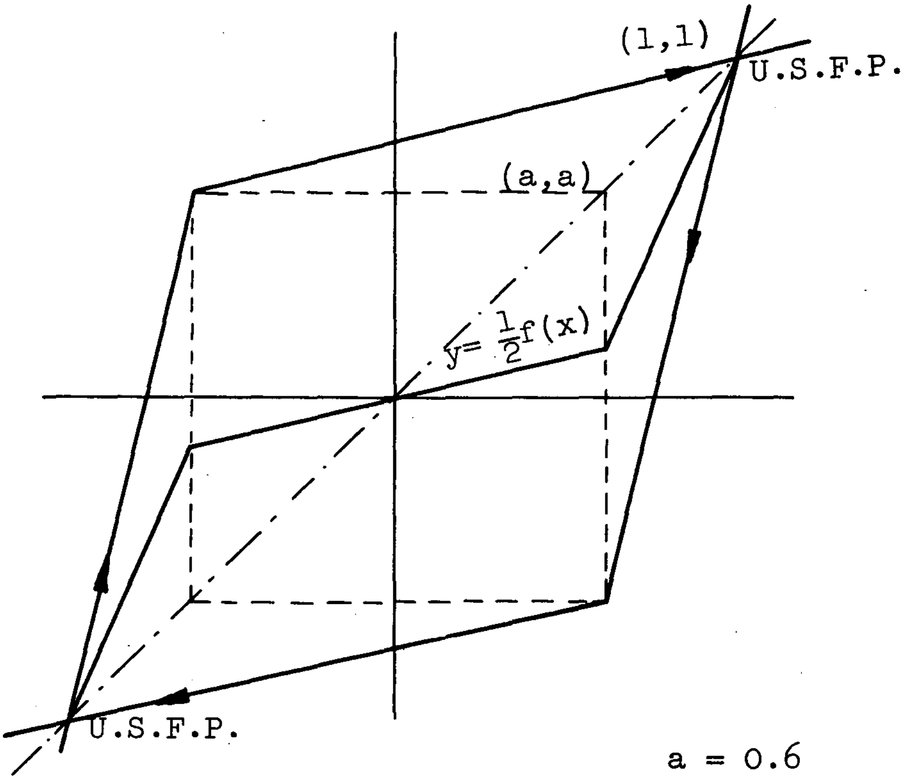

Fig. 13

Here the broken-line separatrix shown is a rigorous barrier. Also, of course, motion of sufficiently small amplitude to remain within the dotted square will trace the perfect elliptical invariant phase trajectories that are characteristic of truly linear motion. Outside of this dotted square, moreover, stable fixed points can be found /for example, with a = 0.6:

an order-6 FP at $x = y = 9/13$ and an order-7 FP at $-x = y = 378/6837$ that are surrounded by an elliptical boundary within which the motion is again truly linear (and truly stable "in the small"). In Fig. 14 one such region is shown as the hatched area in the upper right-hand portion of the diagram -- the motion being controlled in such a case in a periodic way by *definite values* of f' at successive

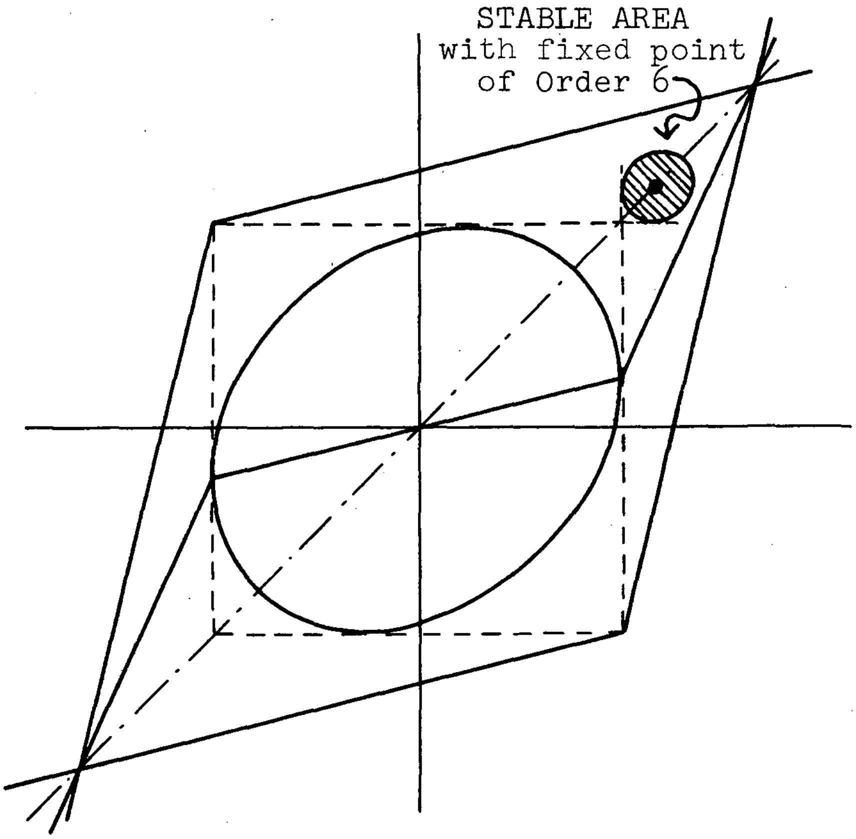

Fig. 14

iterations. Other points, including those neighboring unstable fixed points of the same family, however, show the failure of extended eigenvector directions to intersect smoothly and evidently are characterized by a sort of stochastic behavior that is confined to a finite region.‡ Nonetheless, the motion within the diamond is not completely ergotic, since, as we have seen, there exist in this area regions of limited extent within which the motion follows true simple invariant phase trajectories.

In presenting this material I do not mean to imply that it contains much information that is new to the mathematicians who have been following recent developments of the theory. I am afraid that some of the computational results fail, as might be expected, to give definitive experimental answers to some of the significant questions, and my own work has neglected entirely the more important (and more difficult) problems that arise with motion in more than one spatial degree of freedom. I also would not wish to claim that the questions of long-range stability are of quite as immediate importance to the accelerator designer as those, for example,

---

‡ In this transformation (and also in a similar transformation with f(y) analytic), some cases were found in which the eigenvectors, when extended, generated a double-S (or double-Z), rather than a single S (or Z) between successive iterates.

that concern collective motion. I would like to suggest, however, that the properties of such transformations as the one I mentioned at the beginning suggest questions that inherently are quite fascinating, and that it would be quite helpful for future design work if our mathematical colleagues could assist us in obtaining a better -- and hopefully somewhat quantitative -- understanding of these properties.

Selected References

Arnol'd, V. I., Ivest. Akad. Nauk USSR 25, 21-86 (1961).
Doklady " " " 137, 255-257 (1961);
" " " 138, 13-15 (1961).
(Eng. Trans. 2, 247-249; 501-503; also 562-564.)
Russian Math. Surveys, 18, No. 5 (A.N.Kolmogorov issue), 9-36 (Sept.-Oct., 1963); No. 6, 85-191 (Nov.-Dec. 1963).

Chirikov, B. and Keil, E., Draft Report ISR-TH-BC/EEK, "Stochasticity in many-dimensional systems" (CERN, Geneva, 29 May 1967).

DeVogelaere, R., Contributions to the Theory of Nonlinear Oscillations, v. IV; also U.S. Office of Naval Research Technical Report 62-1 (Contract Nonr-222(80)), (September, 1962).

McMillan, E. M., UCRL-17795 (Sept. 5, 1967).

Mel'nikov, V. K., Soviet Mathematics 4, 266-270 (1963).

Moser, J., Nachr. Akad. Wiss., Göttingen, Math.-Phys. Klasse (Sect. A), 1-20 (1962-63). Proc. Nat. Acad. Sci. U.S.A. 47, 1824-1831 (November, 1961).

Appendix A

I would like to call specifically to your attention a situation we encountered in which an area-preserving algebraic transformation, when linearized about certain high-order fixed points, exhibited negative eigenvalues. This phenomenon arose in connection with some runs that I made using a modification of Professor deVogelaere's transformation, namely

$$T: \begin{cases} x' = y + Tx + Cx^2 \\ y' = -x + Tx' + Cx'^2 \end{cases}$$

with $C = 1 - T$ and $T = -1/8$.

This transformation, whose phase plots are symmetrical about the x-axis, has an unstable fixed point of order 1 at the point (1,0) and the eigenvector-directions extended from this point develop loops in the familiar way (as qualitatively sketched in Fig. 1). In seeking higher-order fixed points in the "interior" of this diagram, the following families of unstable fixed points appeared for which the eigenvalues are negative:

Family 1 ("Tune" = 1/4):

x	y
0.5615983	0
0.2846170	-0.5060428
-0.4504872	0
0.2846170	0.5060428

Eigenvalues: $\lambda = -3.197, -0.3128$

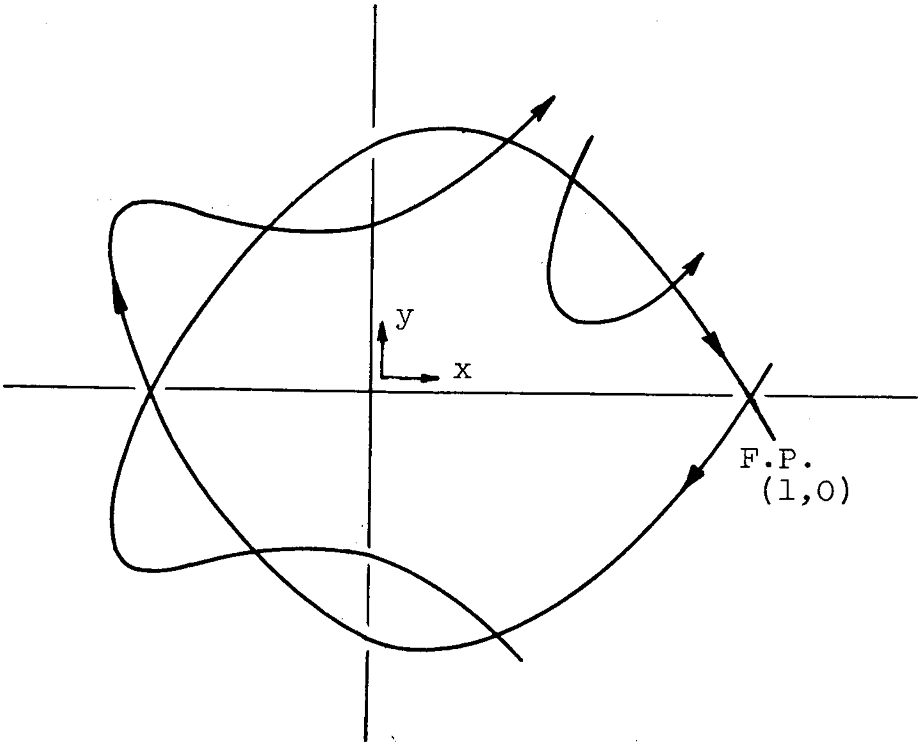

Fig. 1

Family 2 ("Tune" = 2/8):

x	y
0.4562733	0
0.1771744	-0.4431055
-0.4299377	0.0845201
0.3462146	0.5215085
0.6130793	0
0.3462146	-0.5215085
-0.4299377	-0.0845201
0.1771744	0.4431055

Eigenvalues: $\lambda = -8.369, -0.1195$

Phase trajectories formed by extending the eigenvector directions for the system described as Family 2 are shown in Fig. 2 in the region near the points

$$(0.6130793, 0) \quad \text{and} \quad (0.4562733, 0).$$

It does not appear necessary to have an associated family of stable fixed points in such a negative-λ case, and none was found.

With reference to Fig. 2, we may consider a point such as A_n, that lies at the intersection of a phase trajectory that approaches the right-hand one of the two fixed points shown and a trajectory that is directed away from the left-hand point in the figure. After 8 applications of the transformation, this point moves so as to lie closer to the right-hand fixed point (but on the extended eigenvector segment that lies on the opposite side of this fixed point, since

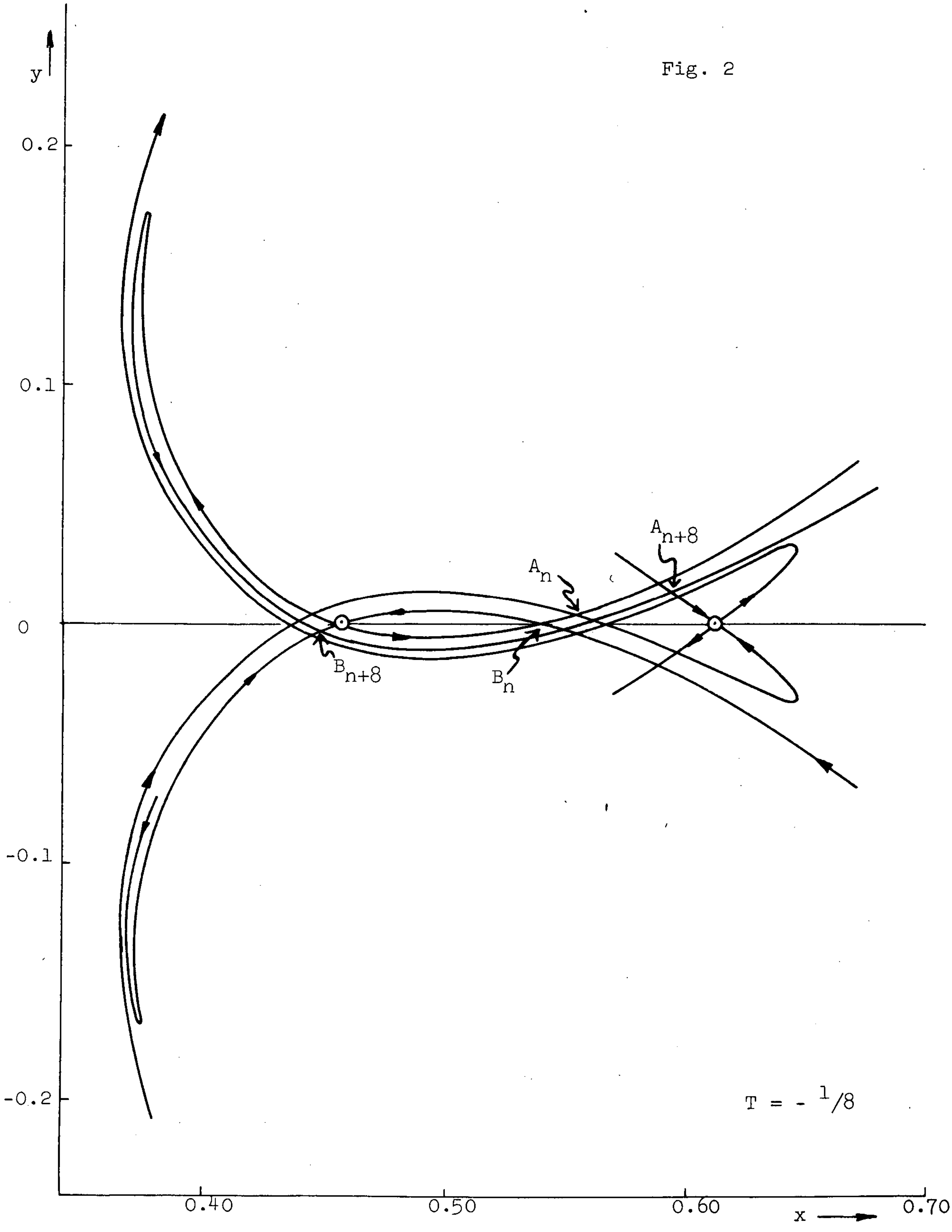
y
0.2
0.1
0
-0.1
-0.2
Fig. 2
A_{n+8}
A_n
B_{n+8}
B_n
$T = -\,^1/8$
0.40
0.50
0.60
0.70
x

$\lambda \cong -0.1195 < 0$), while it also comes to lie more remotely from the left-hand fixed point (and on the extension of the eigenvector segment on the opposite side of this fixed point, since $\lambda \cong -8.369 < 0$). This new point is designated A_{n+8} on the drawing.

The point B_n lies on the intersection of outward- and inward-directed eigenvectors from the left-hand fixed point. Its T^8 iterate is seen to lie on another such intersection -- closer in on the eigenvector for which $|\lambda| < 1$ and more remotely on the extension of the vector for which $|\lambda| > 1$. This performance may suggest that it is <u>not</u> necessary for a loop such as that shown between B_n and the left-hand fixed point to enclose another (e.g., stable) fixed point of this rotation number. I thus wonder whether the behavior of such fixed points (with λ real and <u>negative</u>) may be <u>qualitatively distinct</u> from that expected in cases for which $\lambda > 0$ (and for which one expects to find a "string of islands" such that one then inquires concerning the smoothness or lack of smoothness with which eigenvector directions, when extended, intersect). The type of phase trajectories indicated in Fig. 2 may be most readily adaptable to fit in with the rather gross loops that develop in this region of the phase plot from the eigenvectors extended from the order-1 fixed point at (1,0). [To avoid confusion on the drawing of Fig. 2, I have not shown there the order-4 unstable fixed point (0.5615983, 0), of Family 1, that falls in this region of the diagram. This point does not lie on the intersection of any of the Family-2 trajectories shown in the Figure -- it lies on the x-axis some three-and-one-half or four millimeters to the right of the point A_n. The features illustrated in this diagram can be exhibited without any exceptional computational accuracy, and I have found it convenient to ad lib runs by sitting at a readily-programmed Olivetti-Underwood "101 Programma".]

As a second point, I neglected to mention on Tuesday, during the discussion concerning "my" transformation, that this transformation also has an order-1 fixed point at (1,0). The transformation in question had the form

$$\begin{cases} x' = Ax + (1 - A^2)y + (1 - A)[x + (1 - A)y]^2 \\ y' = -x + Ay + [x + (1 - A)y]^2. \end{cases}$$

The extensions of the eigenvectors from this order-1 fixed point also develop gross loops, as might be expected. This behavior is sketched in Fig. 3, where the hatched area is the triangular area (with order-3 fixed points at its vertices) to which I directed attention in my talk. As before, the constant A has been given the value $-5/8$.

This same transformation, but with $A = -1/4$, shows a quite striking approximate constancy of the "tune" with respect to amplitude. With this value of A ($A = -1/4$) the small-amplitude tune corresponds to about 0.2902 (2π) radians phase advance per iteration, and a system of 7 stable and 7 unstable fixed points (tune = $2/7 \doteq 0.2857$) develops at a

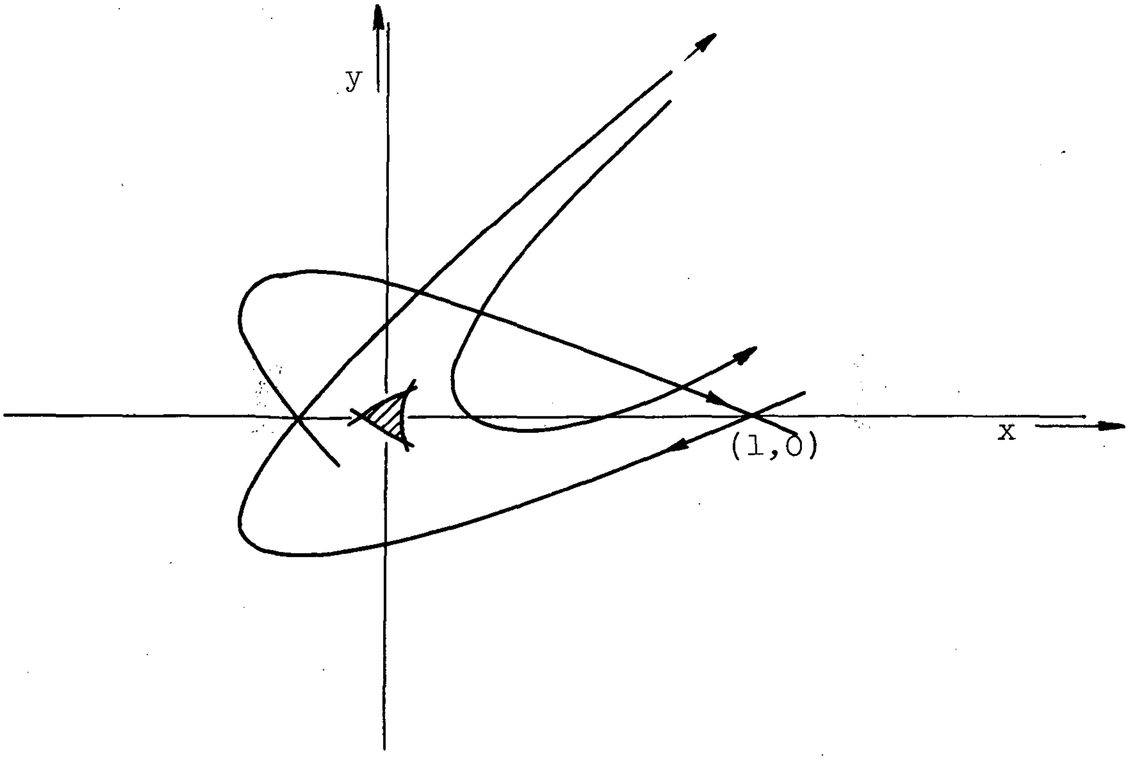

A = - 5/8

Fig. 3

rather large amplitude. [The x-coordinates of the fixed points that lie on the x-axis are given below:

Stable F.P.: -0.123211 58766 12485 36429 040273;

U.S. F.P.: +0.2 (exact), (half trace + 1.05078125).

Reasonably-appearing phase curves can be drawn inside and outside this system (Fig. 4).]

As a final point, you may recall that during my talk I mentioned in passing that certain regularities appeared to be present in the eigenvalues (or, more simply, in the matrix trace) for the successive families of fixed points of a particular class. You might be interested in the results for fixed points of tune $\frac{m}{4m+1}$ for Professor deVogelaere's transformation (the transformation T, with the parameter T set equal to zero). These results, from the CDC-6600, are given in the attached Table, titled "TRACE", and apply to this transformation after linearization about the fixed points in question.

It will be noted that the amount by which $\frac{1}{2}$ Trace differs from unity is closely the same in absolute value for the stable and unstable fixed-point families of the same order, particularly for those with a tune having a large denominator. As Professor deVogelaere has pointed out, a plot of $\log|1 - \frac{1}{2}\text{Trace}|$ <u>vs</u> this denominator is highly linear through many decades. Somewhat similar regularities also appeared with my transformation (taking $A = -5/8$).

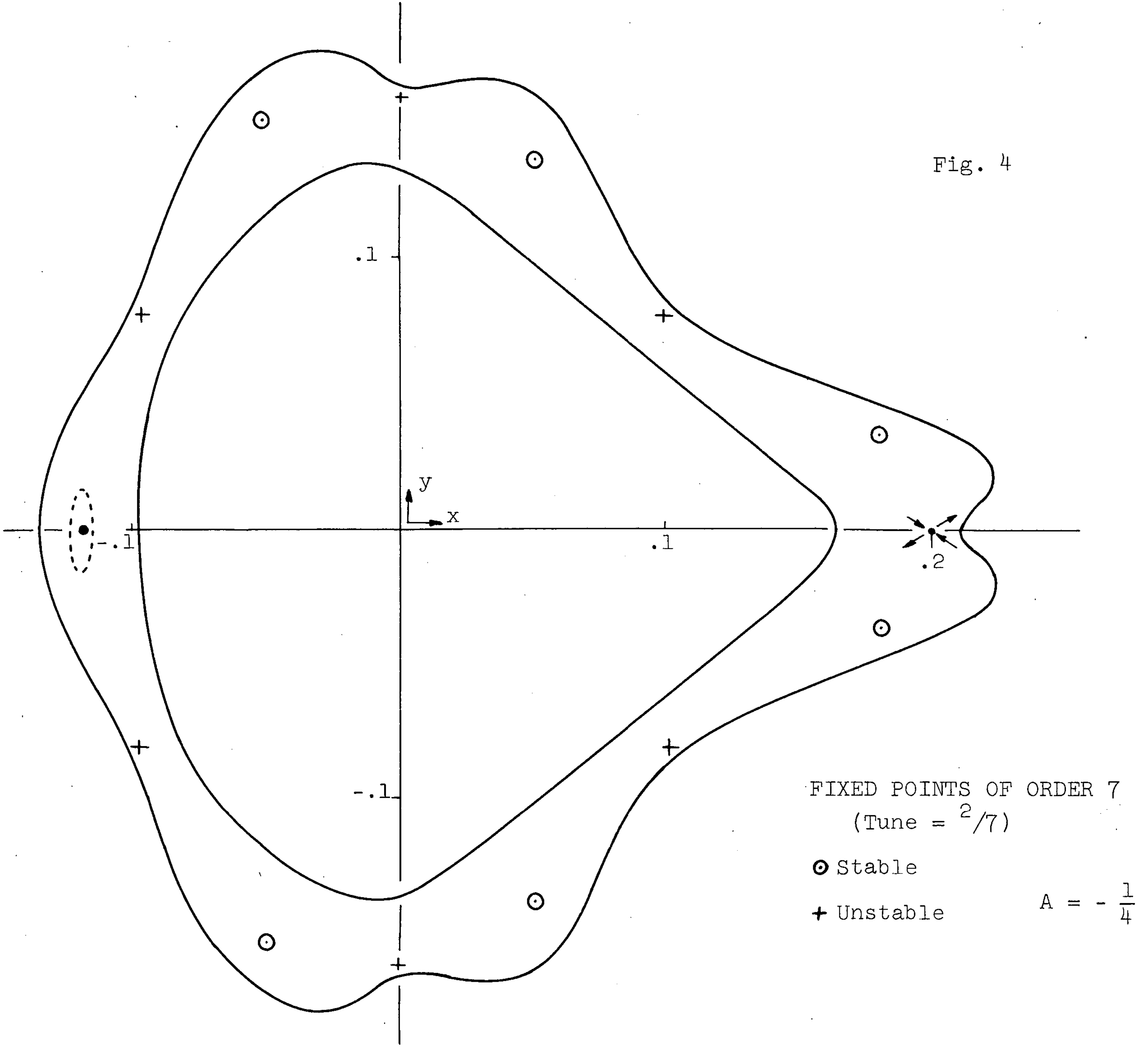

Fig. 4

FIXED POINTS OF ORDER 7
(Tune = $^2/7$)

TRACE -- with Characteristic Exponent or Eigenvalue

Rotation		$\left\lvert 1 - \frac{1}{2}\text{ Trace}\right\rvert$	μ (radians and degrees) or λ_I
4/17	Stable	1.4425105233511725112475209	2.0291926112 rad. = 116.26417 deg.
	Unstable	1.4396912169066324693644279 3	3.6650211326385369731925414 6
5/21	Stable	$5.7813842878779832846897813 \times 10^{-1}$	1.1352987670 65.04783
	Unstable	$5.8036264715679285844257943 \times 10^{-1}$	1.8041053065948079401047563 5
6/25	Stable	$2.1759794076036170323557400 \times 10^{-1}$	0.6722827659 38.51897
	Unstable	$2.1788566763236692069200659 \times 10^{-1}$	$9.1304428221204405827208083 \times 10^{-1}$
7/29	Stable	$7.829060692954532623645218 \times 10^{-2}$	0.3983316626 22.82272
	Unstable	$7.831797137551201910136569 \times 10^{-2}$	$4.8176517658506550100501700 \times 10^{-1}$
8/33	Stable	$2.728644682248974445483034 \times 10^{-2}$	0.2341429028 13.41540
	Unstable	$2.728895164746296854366273 \times 10^{-2}$	$2.62496498671242605069895_2 \times 10^{-1}$
9/37	Stable	$9.297924278312693516295 99 \times 10^{-3}$	0.1364724784 7.81930
	Unstable	$9.298155267586262957338 78 \times 10^{-3}$	$1.4598307113818504968531 79 \times 10^{-1}$
10/41	Stable	$3.117336279665538493898 97 \times 10^{-3}$	0.0789804692 4.52525
	Unstable	$3.117357765700242329110 98 \times 10^{-3}$	$8.213908547928453767087 80 \times 10^{-2}$
11/45	Stable	$1.032892976982646266855 82 \times 10^{-3}$	0.0454548311 2.60437
	Unstable	$1.032894986652856473364 35 \times 10^{-3}$	$4.649559228189882993717 76 \times 10^{-2}$
12/49	Stable	$3.392839381958650237025 7 \times 10^{-4}$	0.0260500720 1.49256
	Unstable	$3.392841268928288862724 6 \times 10^{-4}$	$2.639083624004760732239 8 \times 10^{-2}$
13/53	Stable	$1.107387458876112719151 7 \times 10^{-4}$	0.0148822572 0.85269
	Unstable	$1.107387636632479404429 \times 10^{-4}$	$1.499327182763705338994 5 \times 10^{-2}$

<u>TRACE</u> -- Continued

14/57	Stable	3.597507701874426428512	x 10^{-5}	0.0084823691	0.48600	
	Unstable	3.597507869862235287326	x 10^{-5}	8.518395228840448345675		x 10^{-3}
15/61	Stable	1.164736575122263454806	x 10^{-5}	0.0048264663	0.27654	
	Unstable	1.164736591051033262679	x 10^{-5}	4.838123045135810082937		x 10^{-3}
16/65	Stable	3.76188982802960206947	x 10^{-6}	0.0027429518	0.15716	
	Unstable	3.76188984318697930160	x 10^{-6}	2.74671537799954849551		x 10^{-3}
17/69	Stable	1.21302583785923977869	x 10^{-6}	0.0015575789	0.08924	
	Unstable	1.21302583930697271578	x 10^{-6}	1.55879228547447310154		x 10^{-3}
18/73	Stable	3.9073431514620690060	x 10^{-7}	0.0008840072	0.05065	
	Unstable	3.9073431528502623898	x 10^{-7}	8.843979646269819787		x 10^{-4}
19/77	Stable	1.2579061979687540848	x 10^{-7}	0.0005015788	0.02874	
	Unstable	1.2579061981024041544	x 10^{-7}	5.017045535711146920		x 10^{-4}
20/81	Stable	4.048890866188331620	x 10^{-8}	0.0002845660	0.01630	
	Unstable	4.048890866317540574	x 10^{-8}	2.846065075505638042		x 10^{-4}
21/85	Stable	1.303401892994049370	x 10^{-8}	0.0001614560	0.00925	
	Unstable	1.303401893006593882	x 10^{-8}	1.614690281164473223		x 10^{-4}
22/89	Stable	4.19742353638860984	x 10^{-9}	0.0000916234	0.00525	
	Unstable	4.1974235364008412	x 10^{-9}	9.1627595583722791		x 10^{-5}
23/93	Stable	1.35249829376673101	x 10^{-9}	0.0000520096	0.00298	
	Unstable	1.3524982937679288	x 10^{-9}	5.2010934205562950		x 10^{-5}
24/97	Stable	4.3612513115999777	x 10^{-10}	0.0000295340	0.00169	
	Unstable	4.3612513116011556	x 10^{-10}	2.9534319420601064		x 10^{-5}

STABLE FIXED POINTS -- Coordinates of Fixed Points on x-axis

Rotation	x_o
4/17	-0.405787495533527606179670330
5/21	-0.3898327790576272411210745517
6/25	-0.376256564258982703826351991
7/29	-0.364375876292784753973866988
8/33	-0.353849991897727178101212375
9/37	-0.344454467825082214779278635
10/41	-0.3360136625106348627695919205
11/45	-0.328382766046255557958214443
12/49	-0.321441972573218211407301229
13/53	-0.315092612636619870929695716
14/57	-0.309253536442459300884027290
15/61	-0.303857827005765909029891050
16/65	-0.298850010528990438538647972
17/69	-0.294183791444198337338681611
18/73	-0.289820254666633978578222174
19/77	-0.285726451504977016300760846
20/81	-0.281874288628402645655758688
21/85	-0.27823965234541592668327308
22/89	-0.274801714559297280796278695
23/93	-0.271542379067610302194439393
24/97	-0.268445836701300885933631152

UNSTABLE FIXED POINTS -- Coordinates and Eigenvector-Slopes of Fixed Points on x-axis

Rotation	x_0	Eigenvector Slope
4/17	0.4965060846376725718580 47332	± 1.19087319776336072103372725
5/21	0.46245681852215980741716 6287	± 1.98025640724266507001182499
6/25	0.43491989920263406876327 6322	± 3.64483037151381605548980 96
7/29	0.41297125434110467779820 53091	± 6.71149665458175416010959
8/33	0.39514318120128392356210 3066	± 12.13194932674224587711334
9/37	0.38028378479061446738668 478	± 21.65256874244943270658525
10/41	0.36761569339894578922505 2500	± 38.39742281882535095763 53
11/45	0.35661850151189326255921 4861	± 67.89919574521975384403 8
12/49	0.34693329389747516415728 7819	± 119.93094467021028541293 0
13/53	0.33830354092672216903757 6515	± 211.74390558804250663261
14/57	0.33053985402552183331053 5365	± 373.77790810525522489253
15/61	0.32349853536198397292009 3128	± 659.72253985475741663301
16/65	0.31706804409355469021833 772	± 1164.23127759143813146135
17/69	0.31116013250997198908335 5634	± 2054.08906983771121440622
18/73	0.30570384083580695724148 746	± 3623.01421605602480677 46
19/77	0.30064130789936682191514 8229	± 6387.95045856901804089 7
20/81	0.29592477453311364779836 1329	± 11258.14336841298826259
21/85	0.29151439360049880578482 880	± 19831.80650990849558229
22/89	0.28737659944598143465490 3827	± 34916.28816384722538324
23/93	0.28348287388331658004295 3742	± 61439.46161324262454 1
24/97	0.27980879867711957042906 8096	±108045.42855652189560 2

UNSTABLE FIXED POINTS -- Coordinates and Eigenvector-Slopes of Fixed Points near Negative x-axis

Rotation	x_o	y_o	Eigenvector Slopes, from upper F.P., for $\lambda \gtrsim 1$
4/17	-0.374963547975391591167940018	±0.1059206297719378880335235985	0.915486568783131693553300896 2.643243716380710957237796760
5/21	-0.370979222273613582347268599$_5$	±0.076240725638902658433412233	1.296582025464099543923400036 2.697943670311007182181211146
6/25	-0.363360430000666384442227247	±0.057124516632160203007080502	1.62198974578660483326242039 2.59545656091817951642492881
7/29	-0.354799885030699916627188833	±0.044662298494267490408919155	1.8831866989852810751563540 2.5294029554032894752569088
8/33	-0.346384947641954153109214825	±0.036155601696951380707060071	2.0958394793051152906058737 2.5203670128578479810549472
9/37	-0.338456350459898304615153470	±0.030063055808040875997004950	2.2735196256654867498100389 2.5501109094473573751463494
10/41	-0.331089352530756057848620544	±0.02552113867392451901906386	2.425483218694276943146054 2.603884480416832690781204
11/45	-0.324270647171535629173200926	±0.022025303003541669253251617	2.5584286643518998960738116 2.6722903765866525976589024
12/49	-0.317958929780800613936981251	±0.019264829387199782429528874	2.6774112341632897363909809 2.7493648481699475750699039
13/53	-0.312106262884832988816311803	±0.017038966471621903572171853	2.786211224111726315951442 2.831281990313632622526412

UNSTABLE FIXED POINTS -- near negative x-axis -- Continued

14/57	-0.306665846880174961760996189	±0.015212653456478366785589701	2.8875759592867647514946485 2.9155921632160939962612297
15/61	-0.301594745181758972978848546	±0.013691912060098667750220235	2.98344770709623458485973 3.00074835801797030168621
16/65	-0.29685461990371039921986437	±0.012409479227135966967667072	3.075172816638866086836259 3.085796178029668174989598
17/69	-0.292411664472703019119058302	±0.011316046543926678118726977	3.163674983099432211082672 3.170166636821707266037392
18/73	-0.288236227231789099079304058	±0.010374715612948833543028581	3.2495872938313320205429 3.2535376525569821477697
19/77	-0.284302340581867119271190549	±0.009557375155113915940587013	3.33334713195506387450208 3.33574239886664091863436
20/81	-0.280587249052701960844405559	±0.008842267851511150343049067	3.4152617043102799591962 3.4167095355863915233517
21/85	-0.27707097468107878695467275	±0.00821231666554353688336967	3.4955520696750023864899 3.4964248555929535977352
22/89	-0.27373593262040534223520233	±0.007653949101572963481466505	3.574382187359892100404 3.575907087079015179917
23/93	-0.27056659828187875545358686	±0.00715625567931681763591264	3.6518778642681330455689 3.6521928967283763252765
24/97	-0.267549222310577829183807391	±0.006710377458137833432946976	3.728139039631599455481 3.728327777110349067290

DISCUSSION FOLLOWING LASLETT'S PAPER

Jürgen Moser*

I should like to add some comments about some recent theoretical work on the problems of the type discussed by Laslett as well as mention some numerical experiments conducted by other people.

It is hard to believe that these questions have their origin in the theory of accelerator design. In fact, originally the basic principle for the orbit stability of the Alternating Gradient Synchrotron depends to a large extent on the linear theory. However, in the course of deeper studies of the particle orbits in an accelerator, the nonlinear effects became more and more important and a source of concern. It was crucial to have some guarantee that the nonlinear terms would not destroy the stability which was so carefully provided for by the linear theory. This led to very delicate and difficult theoretical problems which also were approached with numerical experiments conducted on simplified model equations as we have just learned from Dr. Laslett's presentation.

First, to mention some numerical studies of quadratic measure preserving mappings, I want to refer to the interesting work of Hénon, "Numerical Study of Quadratic Area-Preserving Mappings", 1967, to be published. He studied simple quadratic mappings of the same nature as Laslett mentioned toward the end of his talk (transformation by Dr. McMillan). The main

---

* Courant Institute of Mathematical Sciences, New York University

results are the following:

In the neighborhood of an elliptic fixed point, one finds well organized curve patterns which disintegrate at larger distances. Immediately the problem arises to determine the size of this "stability region" as well as determine this curve pattern possibly by analytic procedure. Henon restricted himself to the description of the computations and comparison of his results with asymptotic series obtained by G. D. Birkhoff. The remarkable fact is that the agreement between the numerical results and these asymptotic series is tremendously close. However, no clear indication for the size of this stability region is in sight.

It would require more space to refer to various theoretical studies which have been made in this direction. First of all, it is to be mentioned that the curve pattern observed in most of these problems in general does not exist in the mathematically rigorous sense as a continuous family of invariant curves. This fact was known to Poincare and is closely related to his nonexistence proof of integrals. Of course, one can easily construct examples for which such family of closed curves does exist; however, this is an exceptional situation. For a rigorous proof of this last statement we refer to Rüssmann[1]. The situation is actually

---

[1] H. Rüssmann, "Über die Existenz einer Normalform inhaltstreuer elliptischer Transformationen," Math. Ann. 137, 1967, pp. 64-67.

very delicate insofar as arbitrarily small changes of the mapping lead to a distribution of the curve pattern. On the other hand, by changes of sufficiently high order terms, one can force the existence of a family of smooth closed curves. The situation is somewhat reminiscent of the distribution of rational numbers on the real line. Both the rational numbers on the real line. Both the rationals as well as the irrationals are dense yet the irrationals form the majority.

To continue this analogy: it is rather easy to establish the existence of irrational numbers and, similarly, it is not too hard to establish the existence of mappings which do not possess such a continuous curve pattern. It is usually a more difficult problem to decide whether a preassigned number, say π is irrational. Therefore, one would expect it should be difficult to decide whether a given mapping of this sort belongs to one class or the other. In this connection, I want to refer to a paper of mine[2] in which it is shown rigorously that even the simple polynomial mappings do not possess a family of closed curves. This includes, in particular, the example by McMillan.

---

[2] J. Moser, "On the Integrability of Area-preserving Cremona Mappings near an Elliptic Fixed Point," Bol. Soc. Mat. Mexicana, 1961, pp. 176-180.

At this point, it seems confusing that the numerical evidence does not match the theoretical prediction of non-existence of such a curve pattern. It turns out that this paradox can be resolved: even though there is no continuous family of closed invariant curves there does exist a large set of closed curves which, however, do not join together into a continuous family. They are interrupted by infinitely many gaps so that one obtains a "Cantor set" of closed curves. This was proven in my paper[3] as well as in Arnold's paper[4]. It is to be emphasized that the closed curves so obtained are by no means pathological, they are differentiable, and, in fact, analytic curves. However, their distribution is pathological. The crucial point of these investigations is that they insure stability of the elliptic fixed point since points starting in the interior of such curves are forced to remain there.

What happens in the gaps left by the invariant curves mentioned above is only partially understood. These regions contain, in general, infinitely many fixed points of the

---

[3] J. Moser, "On Invariant Curves of Area-preserving Mappings of an Annulus," Nachr. Akad. Wiss., Göttingen, Math. Phys. Kl. IIa, Nr. 1, 1962, pp. 1-20.

[4] V. I. Arnold, "Proof of A. N. Kolmogorov's Theorem on the Preservation of Quasi-periodic Motions under Small Perturbations of the Hamiltonian", Uspekhi Mat. Nauk U.S.S.R. 18, Ser. 5 (113), 1963, pp. 13-40.

mapping or one of its higher iterates. However, the behavior of the consecutive iterates in these regions is quite irratic and irregular, in particular near unstable fixed points. These domains are often referred to as "regions of instability". For an instructive schematic picture we refer to the paper by Arnold[5]. There are conjectures, more or less informal, that these regions of instability contain open invariant sets in which the mappings are ergodic. Nothing of this sort has been proven and there is some numerical evidence, especially in the work of John M. Greene, Forrestal Research Center, Princeton,[6] for extremely ergodic behavior in these domains. In fact, he expressed the opinion that there are invariant domains in which the unstable fixed points are dense. Since this situation is typical for ergodicity, one may take this as an indication for the existence of ergodic domains.

Comparing the numerical and theoretical results, one has to be very careful: the theoretical results are strictly applicable only in extremely small neighborhoods of elliptic fixed points (in some paper, Henon estimates a radius of validity of the proof as about 10^{-300}!). This is due to the

---

[5] V. I. Arnold, "Small Divisor and Stability Problems in Classical and Celestial Mechanics,"Uspekhi Mat. Nauk, 18, No. 6 (114), 1963, pp. 81-192.

[6] Private communication.

shortcoming of proofs which are very crude in the details of the estimate. One would have to resort to numerical experiments, such as Laslett presented here, to obtain the feeling for the actual size of the stability region. In all these numerical studies one finds, in fact, a sizeable neighborhood covered to a large extent by invariant curves. On which parameters or properties the size of this stability region depends seems still to be quite in the dark. For this reason, I consider the closer study of numerical experiments extremely worthwhile and instructive.

ADDENDUM TO UCRL 17795, "SOME THOUGHTS ON STABILITY IN NONLINEAR PERIODIC FOCUSING SYSTEMS", Sept. 5, 1967.

Edwin M. McMillan*

March 29, 1968

1.) Introduction

In UCRL 17795, it was shown that curves in the x,y plane having reflection symmetry about the positive diagonal are invariant under the transformation:

$$\begin{aligned} x' &= y \\ y' &= -x+f(y), \end{aligned} \qquad (1).$$

where $f(y)$ is the sum of the two values of x corresponding to the given y. It is required that there be just two values, but the two branches on which they occur are not required to have a common analytic form. An example given was the pair of rectangular hyperbolas $y = 1 - a/(x+1)$ and $y = -1 + a/(1-x)$, with $f(y) = 2ay/(1-y^2)$, mentioned in paragraph 3 and illustrated in Fig. 1. The question whether there are other invariant curves belonging to the same $f(y)$ was left open.

This question was answered by John M. Greene in a letter to L. Jackson Laslett (March 8, 1968). He pointed out that all curves of the form $(1-x^2)(1-y^2) + 2axy = \text{const.}$ are such invariants. If the constant has the value $2a-a^2$, the equation factors into two equations representing the rectangular hyperbolas, which are now seen to be simply the separatrices

---

* Lawrence Radiation Laboratory, University of California, Berkeley, California

of a family of invariant curves. In the course of checking the invariance of "Green's function" by the methods of UCRL 17795, I found that it is a special case of a broader class, which can be called "double quadratic" curves.

2.) "Double quadratic" curves

Any equation which is quadratic in x can be solved explicitly for x. If x and y occur in it symmetrically, it represents a curve with the required symmetry about the positive diagonal. The most general equation with these properties is:

$$Ax^2y^2 + B(x^2y+xy^2) + C(x^2+y^2) + Dxy + E(x+y) + F = 0, \qquad (2)$$

whose solution is:

$$x = \frac{1}{2(Ay^2 + By + C)} \left[- (By^2+Dy+E) \pm \sqrt{(By^2+Dy+E)^2-4(Ay^2+By+C)(Cy^2+Ey+F)} \right] \qquad (3).$$

The sum of the two values of x gives $f(y)$:

$$f(y) = - \frac{By^2 + Dy + E}{Ay^2 + By + C} \qquad (4).$$

Since $f(y)$ does not depend on F, all members of the family generated by giving different values to F are invariant under the transformation (1), with $f(y)$ given by (4).

We thus have the remarkable result that an $f(y)$ which is the ratio of any two quadratic functions of y leads to a family of invariant curves, with the single restriction that the coefficients of y^2 in the numerator and of y in the denominator must be of equal magnitude and opposite in sign.

The first order fixed points, if they exist, are at $f(y) = 2y$, and are therefore the solutions of:

$$2Ay^3 + 3By^2 + (2C+D)y + E = 0 \tag{5}$$

The number of parameters in (4) is easily reduced; E can be eliminated by a coordinate displacement along the positive diagonal, either A or B can be made equal to D or E by a change of scale, and any one of the remaining parameters can be set equal to unity. Thus we have a two-parameter system. Some interesting cases are:

(1) $A = 1,\ B = 0,\ C = -1,\ D = 2a,\ E = 0,\ F = c.$

$$x^2y^2 - x^2 - y^2 + 2a\,x\,y + c = 0. \qquad \text{("Green's function")}$$

$$f(y) = \frac{2\,a\,y}{1 - y^2}$$

The first order fixed points are at $y = 0, \pm\sqrt{1-a}$. The separatrices are displaced rectangular hyperbolas, as pointed out above.

(2) $A = 1,\ B = 0,\ C = 1,\ D = -2a,\ E = 0,\ F = c.$

$$x^2y^2 + x^2+y^2 + 2a\,x\,y + c = 0.$$

$$f(y) = \frac{2\,a\,y}{1 + y^2}$$

The first order fixed points are at $y = 0, \pm\sqrt{a-1}$.
The separatrix is the curve given by setting $c = 0$.
In cases (1) and (2), if a is negative, the curve is rotated by 90°, and the first order fixed points (except the one at $x = 0$) become second order fixed points. (See paragraph 6 and Fig. 3b of UCRL 17795)

(3) $A = 0,\ B = 1,\ C = -1,\ D = 0,\ E = 0,\ F = c.$

$$x^2y + xy^2 - x^2 - y^2 + c = 0.$$

$$f(y) = \frac{y^2}{1 - y}$$

The first order fixed points are at $y = 0, \frac{2}{3}$.
The separatrices are the curve given by setting $c = \frac{8}{27}$, the line $x+y+2 = 0$, and the curve $xy -x-y + 2 = 0$.
(I thank Dr. Laslett for finding the last two of these.)

(4) $A = 1,\ B = -2,\ C = 1,\ D = 0,\ E = 0,\ F = c.$

$$x^2y^2 -2\,(x^2y+xy^2) + x^2+y^2 + c = 0.$$

$$f(y) = \frac{2y^2}{(1-y)^2}$$

The first order fixed points are at $y = 0, \frac{1}{2}(3 \pm \sqrt{5})$.

STRUCTURE IN R.F. PHASE PLOTS *

L. Jackson Laslett

10 February 1970

I. Introduction

Phase plots that depict the results of repeated applications of various non-linear area-preserving transformations have been found to develop a remarkable complexity of structure.[1] This behavior, and the associated question concerning the existence of invariant phase curves, have posed challenging problems to the mathematicians. Contributions to the theory have come from H. Poincaré,[2] J. Moser,[3] R. deVogelaere,[4] H. Russmann,[5] A.N. Kolmogorov,[6] V.I. Arnol'd,[7] V.K. Mel'nikov,[8] and B.V. Chirikov,[9] to mention the names of a few who have worked on these problems.

The subject just described holds a certain fascination for the accelerator designer who is interested in the long-term stability of betatron oscillations in a cyclic accelerator or storage ring. In this application the use of a (periodic) alternating-gradient structure precludes the Hamiltonian function serving as a constant of the motion, and the possible presence of non-linearities prevents use of a quadratic invariant form[10,11] such as can be obtained from the Floquet theory for Hill's equation. In such a situation it may be convenient, particularly for computational work, to replace the non-linear differential equations of the system by a <u>transformation</u> whose successive iterations may typify passage through successive periods of the alternating-gradient structure. Such transformations frequently can be interpreted, if desired, as describing the passage of a particle through a sequence of linear focussing elements and localized non-linear lenses. Transformations that are <u>algebraic</u> frequently are chosen as examples for specific study -- again partly for reasons of convenience, and in the expectation that the algebraic nature of these transformations should

---

* Work supported by the U.S. Atomic Energy Commission.

not in itself give to the results any particularly distinctive character. The possible connection of non-linear transformations with accelerator performance, in fact, motivated the studies of the present writer that are described in reference 12.

The theory of energy oscillations, or "synchrotron oscillations," in a synchrotron[13] should describe the energy and phase oscillations that occur when a charged particle passes repetitively through one or more "accelerating cavities" situated at localized points around the accelerator ring. Since these oscillations normally are of a relatively low frequency, it often is legitimate as well as convenient to analyze them theoretically on the basis of differential equations derived on the supposition that the accelerating field is uniformly distributed around the orbit.[10,14,15] Strictly, however, the energy changes experienced by a particle are essentially <u>impulsive</u>, and depend on the sine of the electrical phase angle ϕ at which the particle traverses the cavity, so that the motion in this degree of freedom (assumed uncoupled to the betatron motion) is basically described by the repeated application of a <u>non-linear</u> (and non-algebraic) <u>transformation</u> connecting the energy variation and phase to values pertaining to the previous transit.

The differential-equation approach to the theory of synchrotron oscillations leads to a Hamiltonian that constitutes a constant of the motion for an individual particle and to a critical value for this function that defines a stability boundary enclosing a region ("bucket") that is truly stable under the assumptions introduced. The fact that the particle motion in this degree of freedom is more properly described by a sequence of transformations (due to localized forces, virtually of a delta-function character) suggests, however, that it would be of interest to examine the extent to which the complex phenomena arising from repeated application of non-linear transformations may make their appearance in this situation. This question has been examined computationally, for a specific example, in the work described in this report. The complex character of what appears superficially to be a separatrix between stable and unstable regions has been seen to be present, although not to a degree that would provide grounds for concern for the customary use of radio-frequency acceleration systems in present accelerator technology.

II. Derivation of the Transformation

We consider here the case of a stationary bucket with no acceleration (stable phase angle, $\phi_s = \pi$). To obtain the working transformation, we consider a single cavity operating at a harmonic number **h**. The quantities denoted E_n and ϕ_n are respectively the energy with which a particle enters the cavity and the electrical phase angle present at the time of transit. With γ_τ denoting the transition energy in rest-energy units, we have

$$\frac{dt}{t} = \frac{1}{\beta^2}\left(\frac{1}{\gamma_\tau^2} - \frac{1}{\gamma^2}\right)\frac{dE}{E} .$$

and the transformations may be written

$$\Delta E_{n+1} = \Delta E_n + eV_o \sin(\phi_s + \Delta\phi_n)$$

$$\Delta\phi_{n+1} = \Delta\phi_n + \omega_{RF} h t_{RF}\left[1 + \frac{1}{\beta_s^2}\left(\frac{1}{\gamma_\tau^2} - \frac{1}{\gamma_s^2}\right)\frac{\Delta E_{n+1}}{E_s}\right]$$

$$= \Delta\phi_n + 2\pi h\left[1 + \frac{1}{\beta_s^2}\left(\frac{1}{\gamma_\tau^2} - \frac{1}{\gamma_s^2}\right)\frac{\Delta E_{n+1}}{E_s}\right] .$$

The latter equation equivalently can be written

$$\Delta\phi_{n+1} = \Delta\phi_n + \frac{2\pi h}{\beta_s^2}\left(\frac{1}{\gamma_\tau^2} - \frac{1}{\gamma_s^2}\right)\frac{\Delta E_{n+1}}{E_s} .$$

If one now sets $\phi_s = \pi$ and defines

$$x = \frac{\Delta\phi}{\pi}, \qquad y = \frac{\Delta E}{E_s} ,$$

the transformation becomes

$$y_{n+1} = y_n - \frac{eV_o}{E_s}\sin(\pi x_n)$$

$$x_{n+1} = x_n + \frac{2h}{\beta_s^2}\left(\frac{1}{\gamma_\tau^2} - \frac{1}{\gamma_s^2}\right) y_{n+1} .$$

With $K = \frac{eV_o}{E_s}$, $\lambda = \frac{2\pi h}{\beta_s^2}\left(\frac{1}{\gamma_\tau^2} - \frac{1}{\gamma_s^2}\right)$, and $\lambda' = \frac{\lambda}{\pi}$, the transformation finally assumes the form

$$y_{n+1} = y_n - K \sin(\pi x_n)$$

$$x_{n+1} = x_n + \lambda' y_{n+1} \ .$$

This transformation is area-preserving (unit Jacobian) and phase trajectories are expected to be symmetrical with respect to reflection in the origin ($x \longrightarrow -x$ and $y \longrightarrow -y$). No attempt has been made to effect a change of variables that would result in further symmetries.

In x,y-space, the stable fixed point is at the origin, unstable fixed points at $x = \mp 1$, $y = 0$, and the phase advance per transit of small-amplitude oscillations is

$$\delta = \cos^{-1}\left(1 - \frac{\lambda K}{2}\right) = 2 \sin^{-1} \frac{\sqrt{\lambda K}}{2} \cong \sqrt{\lambda K}$$

with the synchrotron oscillation frequency becoming

$$\Omega = \omega_o \frac{\delta}{2\pi} \cong \omega_o \frac{\sqrt{\lambda K}}{2\pi}$$

in terms of the going-around-frequency ω_o.

If one linearizes the transformation about the unstable fixed points, one finds the eigenvalue factors

$$E = 1 + \frac{1}{2}\lambda K \pm \sqrt{\left(1 + \frac{1}{2}\lambda K\right)^2 - 1}$$

and the corresponding eigenvector slopes

$$\frac{dy}{dx} = \frac{K\pi}{E-1} = \frac{E-1}{E\lambda'} \ .$$

In the limiting case that the transformation may be replaced by a pair of differential equations,

$$\frac{dy}{dn} = -K \sin \pi x$$

$$\frac{dx}{dn} = \lambda' y \ ,$$

the motion is described by the Hamiltonian function

$$H = \lambda' \frac{y^2}{2} - \frac{K}{\pi} \cos \pi x,$$

which is a constant of the motion and has the value $H = K/\pi$ at the stability boundary. In this latter case, the complete bucket area is easily found to be $J = \frac{16}{\pi}\sqrt{\frac{K}{\lambda}}$ in x,y units.

For numerical work we have taken

$$K = \frac{\pi}{10} \quad \text{and} \quad \lambda = \frac{\pi}{10}, \quad \text{so} \quad \lambda' = \frac{1}{10}.$$

One then expects $\delta = 2 \sin^{-1}\frac{\sqrt{\lambda K}}{2} \cong 0.3155^{\text{rad}}$, or about 20 transits per oscillation when the oscillation-amplitude is small. In addition, by reference to the differential-equation formulation, one estimates the maximum permissible value of y for "stable" oscillations (half bucket height) to be approximately 2, and the full bucket area to be close to $\frac{16}{\pi} \doteq 5.092958$. Similarly, the eigenvalues for this specific transformation, when it is linearized about the unstable fixed points, are found to be

$$E \doteq 1.36736, \quad 0.731336,$$

with the corresponding eigenvector slopes

$$\frac{dy}{dx} \doteq 2.68663, \quad -3.67357\ ,$$

respectively. A sketch is shown in Fig. 1.

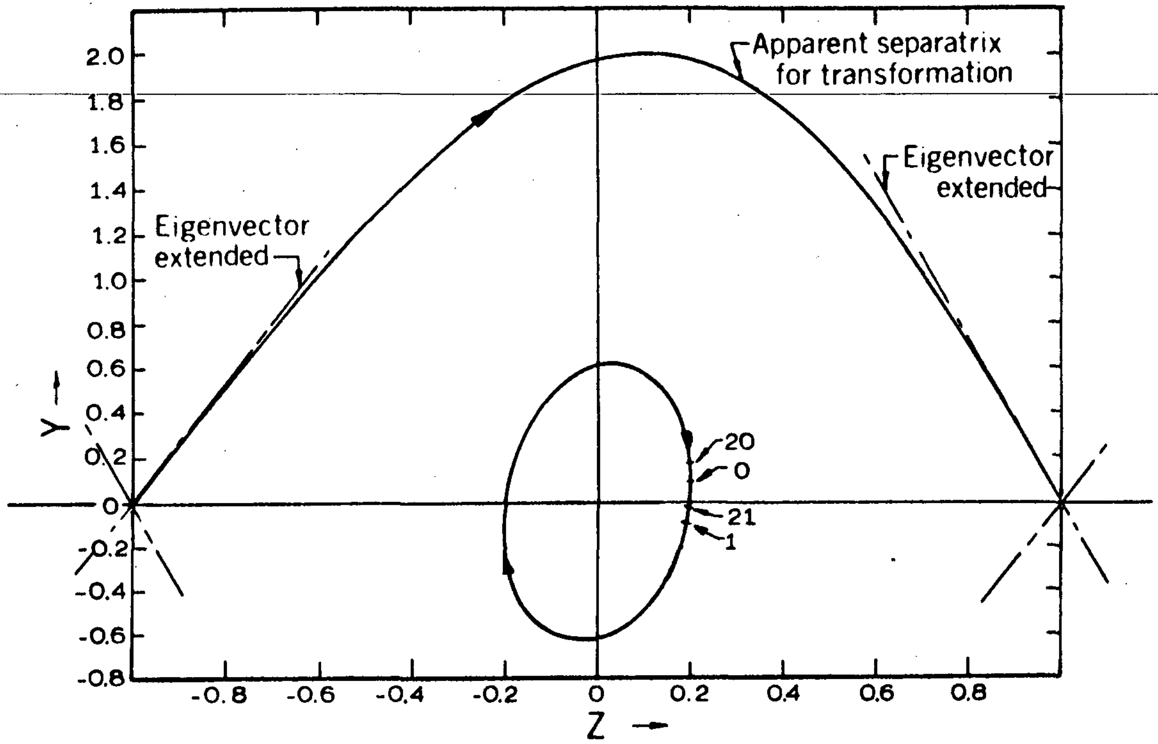

XBL 702 6142

Figure 1

III. Computational Results

The transformation was programed for execution on the C.D.C.-6600 computer, in single-precision, using the LRL BRF teletype system. To demonstrate the presence of structure in an ostensibly smooth separatrix, one can begin with a line segment that is situated very close to the left-hand unstable fixed point and coincides in direction with the outward eigenvector for that point. A segment whose extremities differ in their distance from the unstable fixed point by a factor E is suitable, and the evolution of points along this line segment can be followed, by repeated applications of the transformation, as the iterates approach the right-hand unstable fixed point. The development of loops in the iterated line segment, that are cut by extensions from the right-hand fixed point of the growing eigenvector direction for the inverse transformation, constitutes evidence for the existence of the type of structure in question.

Loops of this character were found to develop with the transformation described here, as is illustrated in Fig. 2. To expedite the plotting that lack of symmetry otherwise would make inconvenient, the plotted quantities were derived from **x,y** by an area-preserving coördinate transformation

$$x_P = A(x - 1) + By$$

$$y_P = C(x - 1) + Dy$$

with

$$A = 1.3470514468 \qquad B = 0.3666848450$$

$$C = -1.1519744152 \qquad D = 0.4287797927$$

[This transformation has the effect of transforming the eigenvectors through the point (1,0) so that they coincide with the new coördinate axes.]

The points Q, Q' indicated at the intersections shown on Fig. 2 are "Queen points", with Q' the iterate of Q.* The invariant area of each of the half loops shown can be estimated from the graph as about 10^{-11} in **x,y** units, which may be contrasted with an area of approximately 5 within the entire apparent bucket of Fig. 1.

---

* The approximate **x,y** coördinates of these points are $(0.999994602, 1.983053 \times 10^{-5})$ for Q and $(0.999996052, 1.450287 \times 10^{-5})$ for Q'.

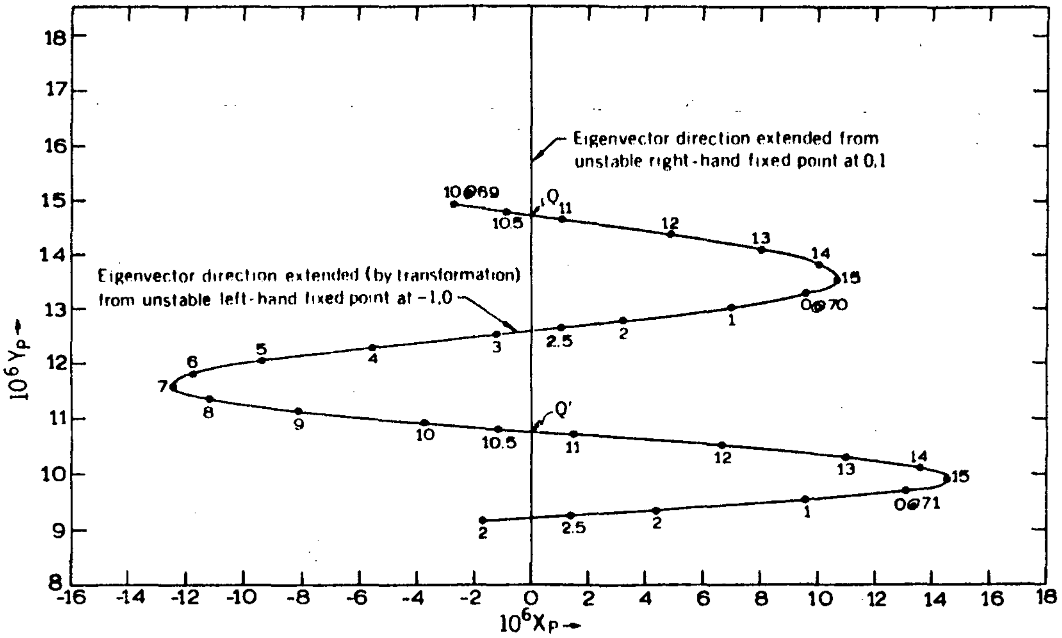

XBL 702 6143

Figure 2

Some computational check of the work can be obtained by repeating the iterations with a line segment that initially is situated closer to the left-hand unstable fixed point by some orders of magnitude (e.g., by a factor $E^{-8} \cong 0.081835$ or $E^{-16} \cong 0.0066969$). This check was made in the work reported here and did not affect the results shown on Fig. 2.

Confirmatory work should be able to demonstrate the existence of loop structure by showing a non-smooth intersection of the extended eigenvector directions in a region near the top of the bucket (where $x \cong 0$ and $y \cong 2$). Numerical accuracy of the computations made from the neighborhood of the points ($\mp 1,0$), with the forward and inverse transformations respectively, should be good in this region near $x = 0$, but the effects to be sought are quantitatively more subtle. Details of the intersection at a Queen point for which $\mathbf{x} \cong 0.1004234$, $\mathbf{y} \cong 2.008464315$ are shown in Fig. 3.* To construct this plot it again was necessary to employ a coördinate transformation designed to eliminate most of the curvature and slope from the line segments iterated to the neighborhood of this point.** The scale of the plot shown as Fig. 3 is sufficiently expanded that some truncation noise from single-precision computations is noticeable, but the failure of the two phase-trajectories to intersect smoothly is evident. Double-precision computations were also made on the C.D.C.-6600 computer to check this point, with results shown on Fig. 4 that fully confirm this inference concerning the non-smooth intersection.

From Fig. 3 or Fig. 4 one can estimate that the angle of intersection of the two curves shown is roughly characterized by a difference of slope

---

* The points designated by Q and Q′ on Fig. 2 occur respectively 39 and 40 iterations following attainment of the point Q on Fig. 3.

** The (area-preserving) coördinate transformation employed for this purpose in the present work was

$$x_{DP} = x - x_Q$$

$$y_{DP} = y - y_Q + (2.564861730 \times x_{DP} + 0.000038665) \times x_{DP} ,$$

with

$$x_Q = 0.10043075210$$

$$y_Q = 2.00846431485 .$$

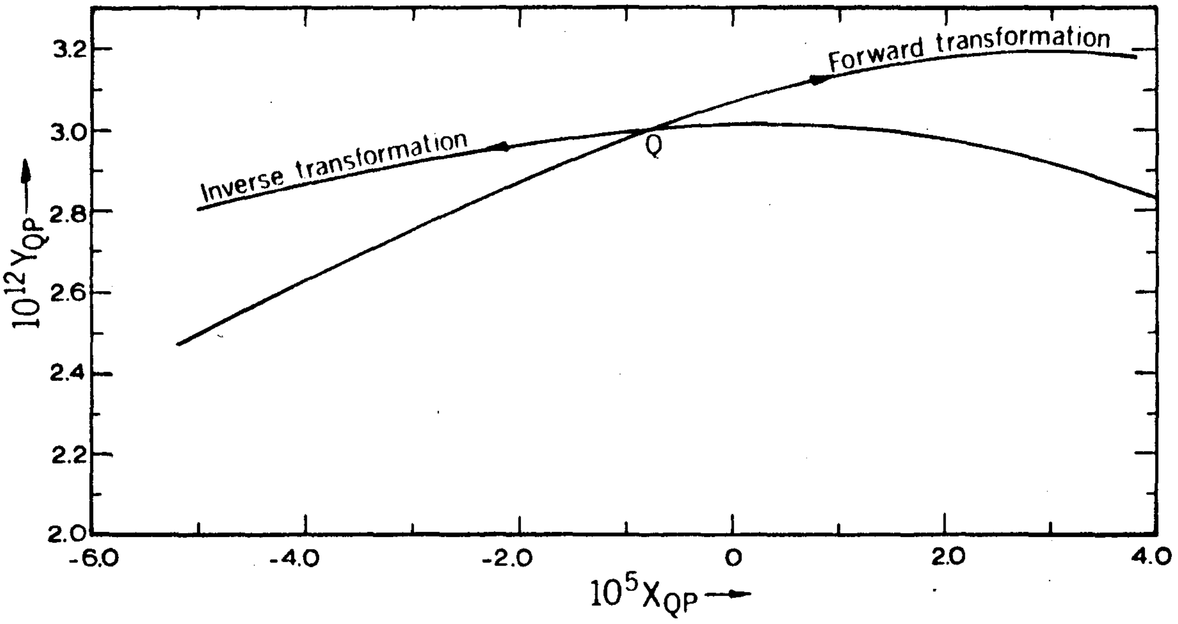

XBL 702 6144

Figure 3

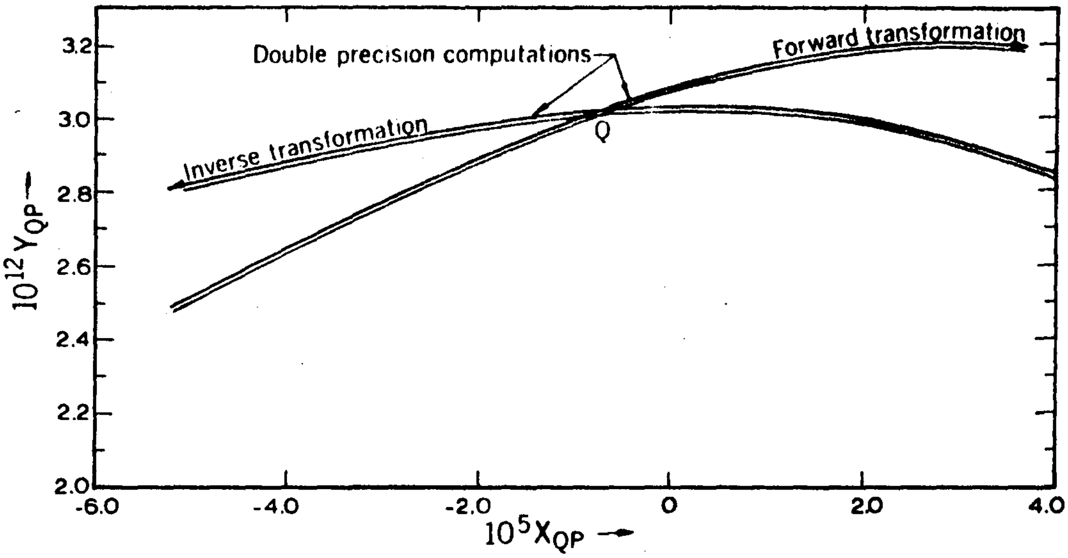

XBL 702 6145

Figure 4

$\Delta(\frac{dy}{dx}) \cong 7.2 \times 10^{-9}$. With a postulated parabolic or sinusoidal trend for the difference between the curves and a separation $h \cong 0.099$ between their successive intersections in this region, the area of a half loop could be estimated as roughly

$$0.18\ h^2\ \Delta(\frac{dy}{dx}) = 0.18(0.099)^2(7.2 \times 10^{-9})$$
$$\cong 1.3 \times 10^{-11},$$

in adequate agreement with the estimate ($\cong 10^{-11}$) obtained from inspection of Fig. 2.

It is of some interest to observe the evolution, for a short time, of a (curved) line segment that starts near the left-hand unstable fixed point, but just inside (i.e., to the right of) the eigenvector of positive slope that passes through the point $(-1,0)$. As such an example, we have taken a line segment of which one end is situated at $(-1+\epsilon, 0)$ and the other at or near the transform of this last-mentioned point.* The evolution of such a line segment with $\epsilon = 2.5 \times 10^{-6}$ is indicated by the dashed lines on Figs. 5 and 6.

IV. Acknowledgements

It is a pleasure to acknowledge the discussions with Messrs. H. Lancaster and E. Hartwig that stimulated initiation of the present study, and to thank Mrs. Barbara Levine for programming the C.D.C.-6600 computer to perform the confirmatory double-precision computations mentioned in Sect. III.

---

* The transform of $(-1+\epsilon, 0)$ is at $y_o = \frac{\pi}{10} \sin \pi\epsilon \cong \frac{\pi^2\epsilon}{10}$, $x_o = \epsilon + \frac{1}{10} y_o - 1 \cong (1+\frac{\pi^2}{100})\epsilon - 1$. We have taken intermediate points with coördinates

$$y = f \cdot y_o\ ,\ x = \frac{y}{20} + \sqrt{\epsilon^2 + (\frac{1}{\pi^2} + \frac{1}{400})y^2} - 1\ ,$$

with $0 \leq f \leq 1$.

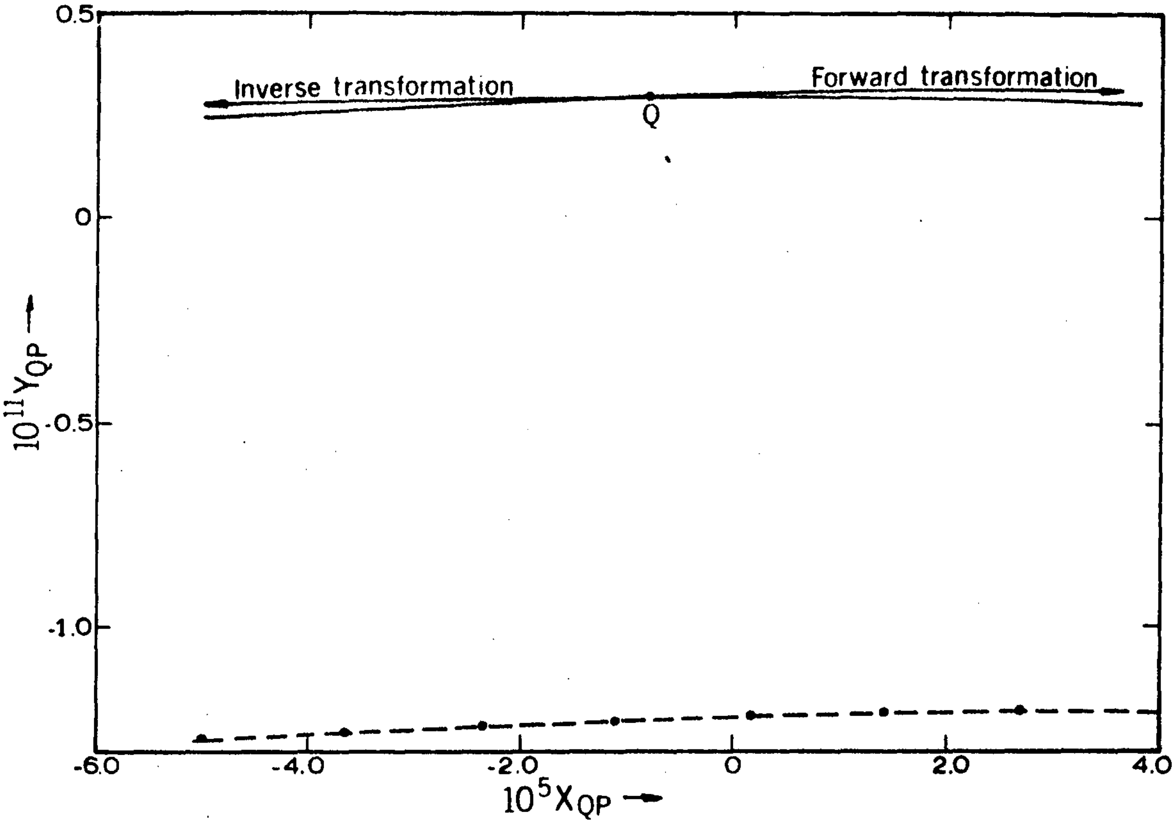

XBL 702 6146

Figure 5

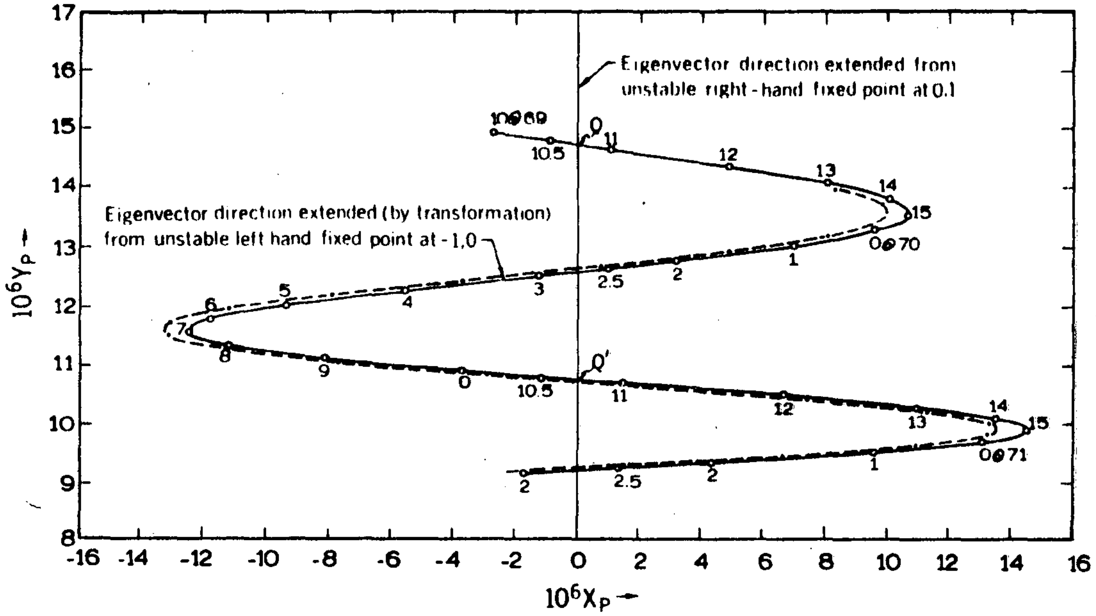

XBL 702 6147

Figure 6

V. References and Notes

1. See, for example, sketches and diagrams in Refs. 7, 8, and 12 cited below.

2. H. Poincaré, Les Méthodes nouvelles de la Mécanique Céleste (Gauthier-Villars, Paris, 1892-99).

3. J. Moser, J. Nach. Akad. Wiss. Göttingen, Math.-Phys. Klasse (Sect. A), 1-20 (1962-63); Proc. Nat. Akad. Sci. U.S.A. 47, 1824-1831 (November 1961); "On the Integrability of Area-Preserving Cremona Mappings near an Elliptic Fixed Point," Bol. Soc. Mat. Mexicana, 176-180 (1961). See also Ref. 12 cited below.

4. R. deVogelaere, "Contributions to the Theory of Nonlinear Oscillations," v. IV.

5. H. Russmann, Math. Ann. 137, 64-67 (1967).

6. See the papers of Arnol'd (Ref. 7) and work cited therein.

7. V.I. Arnol'd, Russian Math. Surveys 18, (No. 5), 9-36 (September-October 1963); ibid., (No. 6), 85-191 (November-December 1963).

8. V.K. Mel'nikov, Soviet Mathematics 4, 266-270 (1963).

9. For an interesting application of Chirikov's work, see his paper on "Some Estimates of a Single Particle Lifetime in a Geomagnetic Trap due to a weak Nonadiabaticity," Communication at the Internat. Geophysical Congress, Madrid, 1969 (Preprint, Novosibirsk, 1969).

10. E.D. Courant and H.S. Snyder, Ann. Phys (N.Y.) 3, 1-48 (1958).

11. L. Jackson Laslett, in "Focussing of Charged Particles" (A. Septier, ed.), v. 2, Chapt. 5.3, 355-420 (Academic Press, Inc., New York, 1967).

12. L. Jackson Laslett, Edwin M. McMillan, and Jürgen Moser, "Long-Term Stability for Particle Orbits," Report NYO-1480-101 (Courant Institute of Mathematical Sciences, New York University, New York, 1968). See also the published computational work of M. Hénon and C. Heiles, "The Applicability of the Third Integral of Motion: Some Numerical Experiments," Astron. J. (USA) 69 (No. 1), 73-79 (February 1964). Professor Hénon has pointed out (private communication) that his transformation can be made identical, by means of a coördinate transformation, to that presented in Fig. 4 of NYO-1480-101.

13. E.M. McMillan, Phys. Rev. 68, 143-144 (1945).

14. J.J. Livingood, "Principles of Cyclic Particle Accelerators" (Van Nostrand, Princeton, New Jersey, 1961).

15. H. Bruck, "Accélérateurs Circulaires des Particles" (Presses Universitaires de France, Paris, 1966).

Example of the Evolution of Tangential-Mapping Parameters for A Non-Linear, Algebraic, Area-Preserving Transformation[*]

L. Jackson Laslett

January 1974

---

[*] Work supported by the U.S. Atomic Energy Commission.

McMillan's form of an area-preserving transformation,

$$\left.\begin{aligned} x_{N+1} &= y_N \\ y_{N+1} &= -\, x_N + f(y_N) \end{aligned}\right\}$$

has the tangential-mapping transformation characterized by the matrix

$$\begin{pmatrix} 0 & 1 \\ -1 & f'(y_N) \end{pmatrix}$$

of which cumulative products are to be formed (starting with the identity matrix) as the transformation proceeds. If the cumulative matrix is denoted

$$\begin{pmatrix} A & B \\ C & D \end{pmatrix}$$

(with AD-BC = 1), one will have real eigenvalues (a reciprocal pair) if $\frac{1}{2}$ Trace $\equiv \frac{1}{2}$ (A+D) is such that $\left|\frac{1}{2} \text{ Trace}\right| \geqslant 1$. The magnitude of the eigenvalue of larger magnitude then will be

$$|\lambda_1| = \left|\tfrac{1}{2} \text{ Trace}\right| + \sqrt{(\tfrac{1}{2} \text{ Trace})^2 - 1} \; ,$$

with $\psi_1 \equiv \log_{10}|\lambda_1|$, and the sign of λ_1 will be the same as the sign of $\frac{1}{2}$ Trace.

This transformation -- for the dynamical variables x, y and for the matrix elements A, B, C, D of the corresponding tangential transformation -- has been programmed as a double-precision interactive (TTY) program ("FIG8D") for the L.B.L. CDC-6600 computer for the specific particular case in which*

$$f(\xi) = \tfrac{1}{2}(3\xi-1) - \tfrac{1}{2}\,\frac{k^2}{\xi+1} + \sqrt{\xi^2+k^2} \quad ,$$

although data are entered (and printed) in single precision.

The program normally prints x, y; the matrix elements A, B, C, D of the tangential transformation; ψ_1; and a flag (LF) whose sign indicates the sign of λ_1 when $|\lambda_1| > 0$ (specifically the sign of $\frac{1}{2}$ Trace). If the value of AD-BC departs from unity by as much as TEST (= 1.0×10^{-9}) -- presumably because of these matrix elements becoming large -- printing occurs (with asterisk flags) and the elements are then restored to provide the unit matrix $\begin{pmatrix} 1 & 0 \\ 0 & 1 \end{pmatrix}$ for continuation of execution of the transformation of x, y. If desired, "noise" can also be introduced into the program (by use of the external Library function RANF) as a random-number addition to x and to y immediately after each application of the transformation. Also, if desired, a quantity "OSC" can be printed that provides at least a rough measure (for $k \cong 0.1$)* of the amount of oscillation and that becomes unity for points lying on the separatrix in this case ($k = 0.1$).

It will be recalled that, for the particular transformation cited, McMillan has demonstrated the existance of a firm separatrix,

$$\left.\begin{aligned} y &= x - 1 + \sqrt{x^2 + k^2} \\ \& \qquad x &= y - 1 + \sqrt{y^2 + k^2} \end{aligned}\right\} ,$$

---

* See Fig. 8 of McMillan's paper in "Topics in Modern Physics -- A Tribute to Edward U. Condon", p. 234.

but that within the region so enclosed a computational run launched with $x_0 = y_0 = 0.25$ (for $k = 0.1$) led to a highly scattered distribution of phase points (confined to that region). We have found, within the region enclosed by the separatrix just mentioned, a number of families of fixed point -- notably families of order 5, 6, & 7 -- in addition to the order-1 fixed point at

$$x = y = -0.32837\ 02811\ 6359$$

A run, performed with the program FIG8D, launched at $x_0 = y_0 = 0.25$ again showed a striking scatter of phase points, and in addition it was noted that the sign of λ (for the cumulative tangential transformation) continued to alternate during the course of the run. The results of this run indicated (in no general disagreement with the results previously reported) a general outward drift of the phase points as the number of iterations (N) approached 1000, and this appeared to be followed by an inward movement as $N \rightarrow 2000$; further iterations led to large amplitudes near $N = 3000$, 6000, 10000 and smaller amplitudes near (for example) $N = 5000$ and 20000.

TRANSFORMATION OF McMILLAN'S FIG. 8. $k = 0.1$

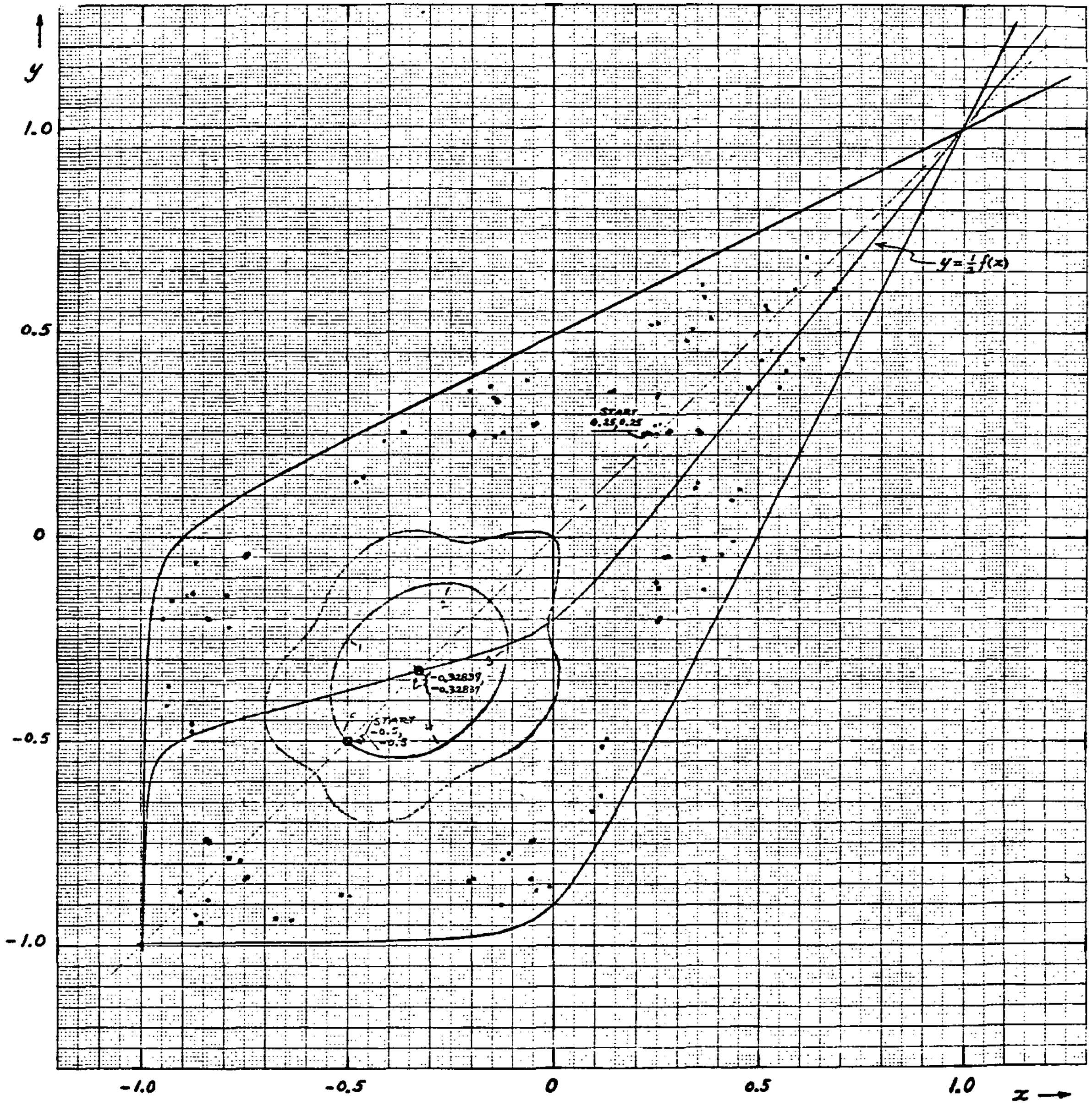

For iterations commenced at 0.25, 0.25;
Points 0 through 50 and 301 through 350.

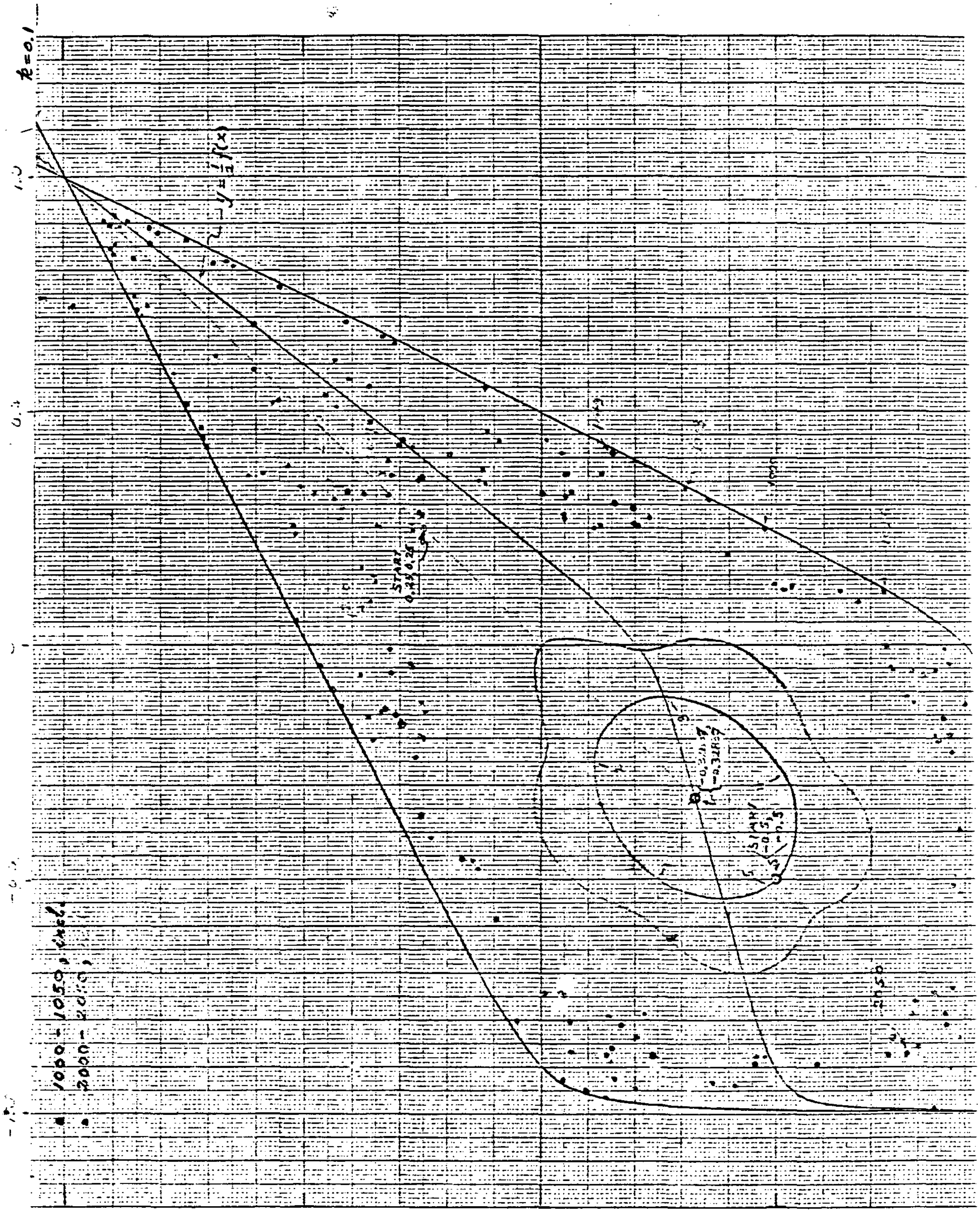
k=0.1
y = ½ f(x)
1.0
0.5
0
-0.5
-1.0
■ 1000 - 1050, excl.
● 2000 - 2050
START 0.25, 0.25
START -0.5, -0.5
2050
1.0
0.5
0
-0.5

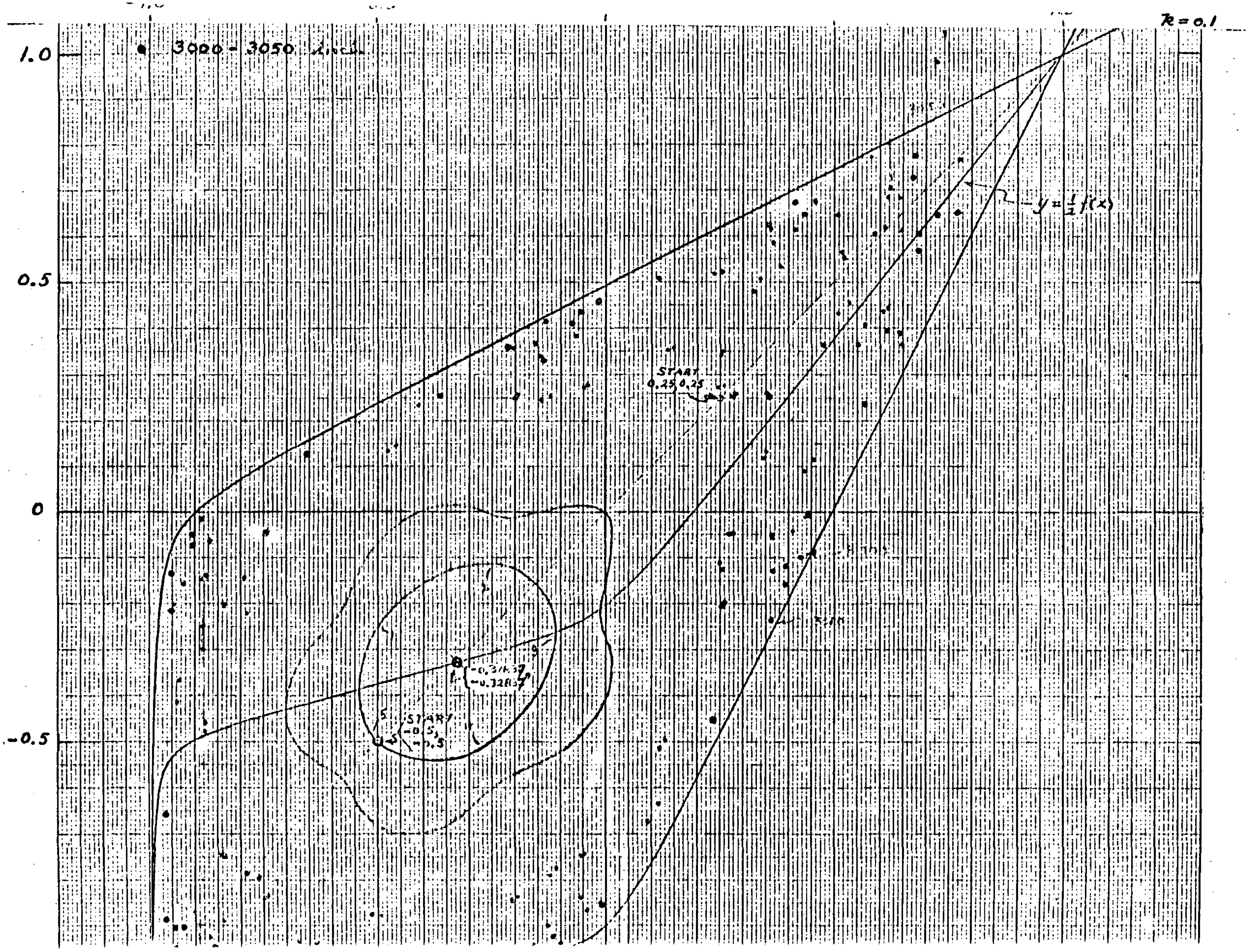
k = 0.1
● 3000 - 3050
$y = \frac{1}{2} f(x)$
1.0
0.5
0
-0.5
START 0.25, 0.25
START -0.5, -0.5
5
-0.31637
-0.32857
9

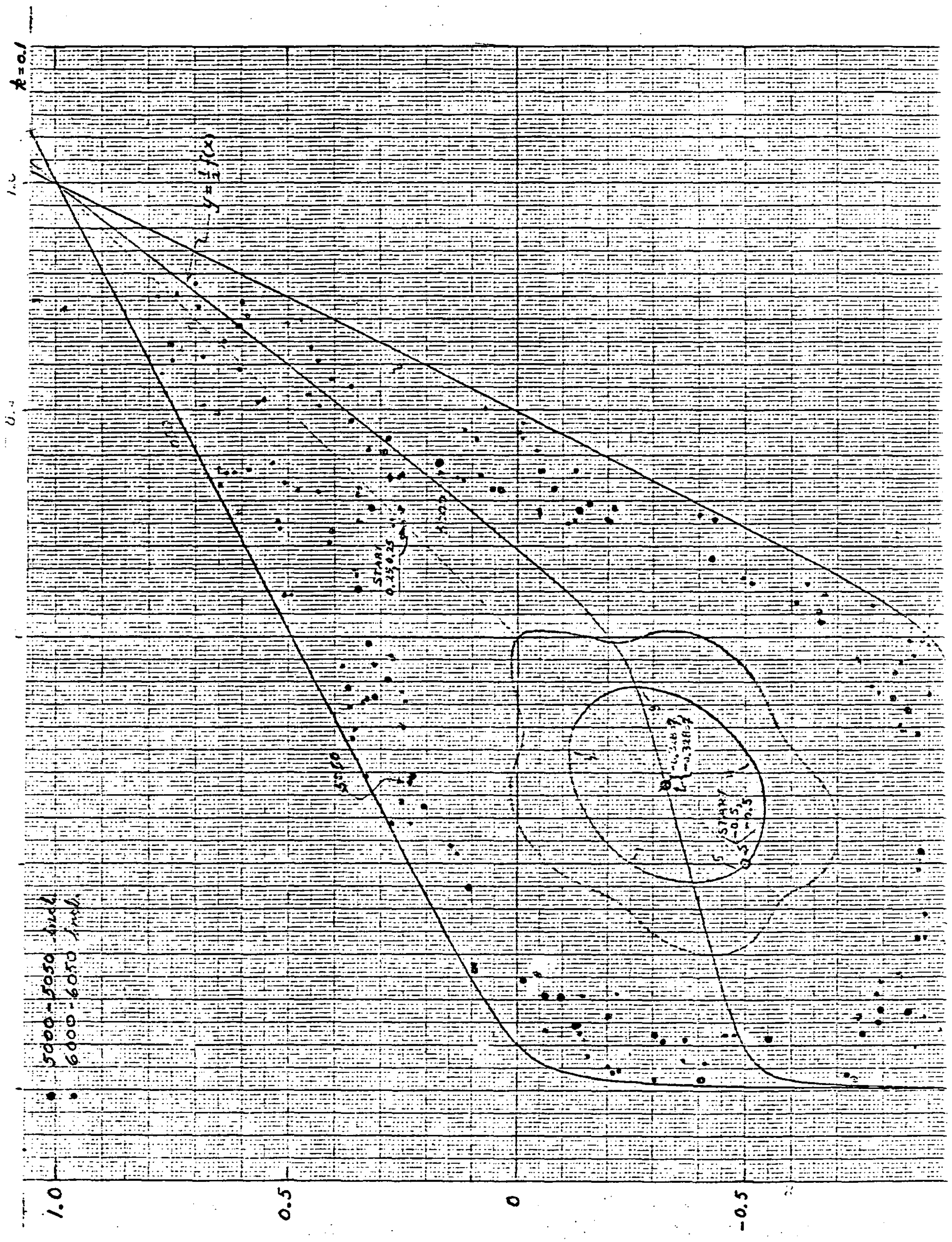
k=0.1
y = ½ f(x)
5000-5050 incl.
6000-6050 incl.
START 0.25 0.25
START -0.5, -0.5
5000
6000
1.0
0.5
0
-0.5

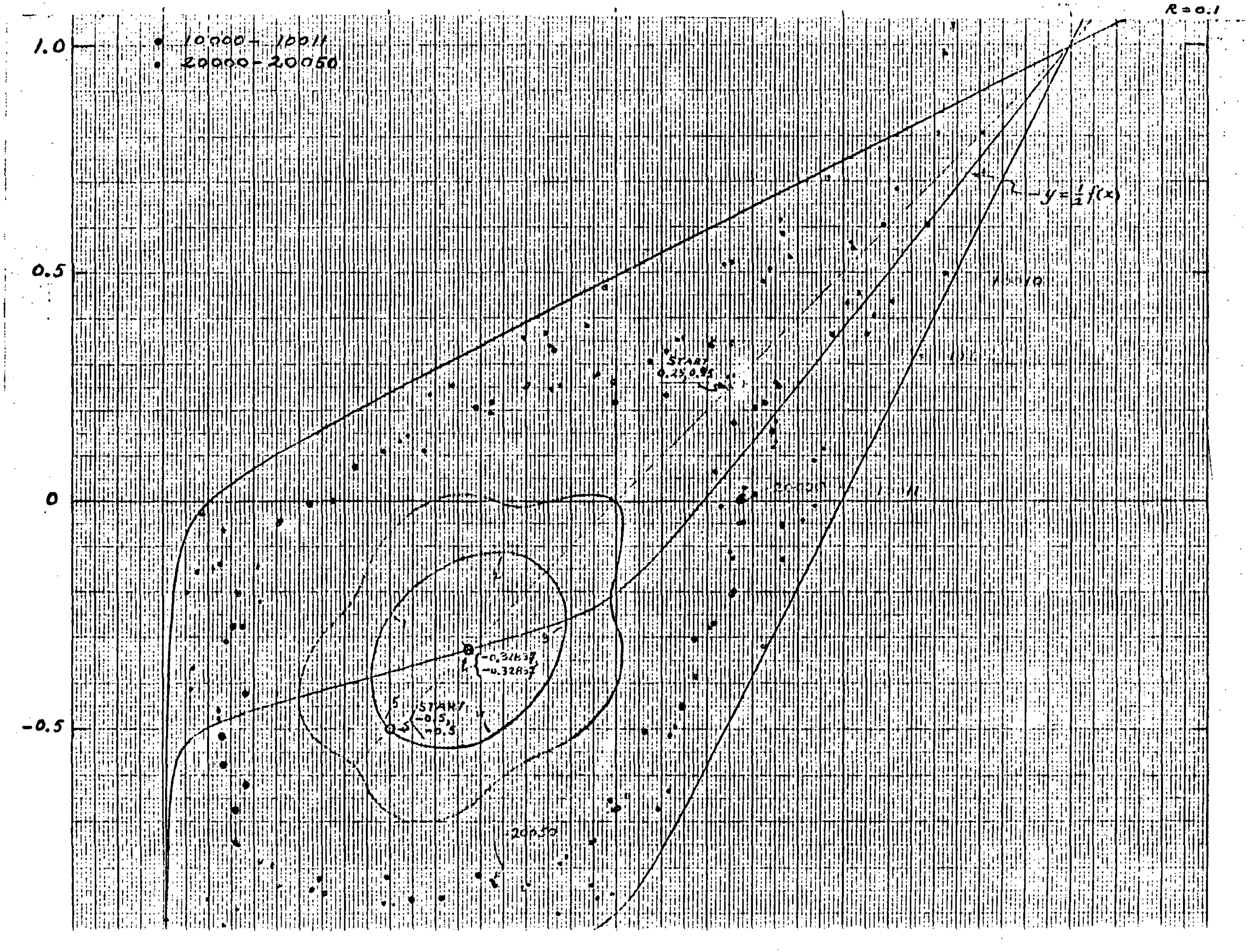
R = 0.1
● 10000 - 10011
• 20000 - 20050
1.0
0.5
0
-0.5
$y = \frac{1}{2} f(x)$
10
11
START
0.25, 0.95
START
-0.5,
-0.5
-0.31637,
-0.32857
9
5
20050

```
 TYPE INITIAL X,Y (SINGLE PRECISION)
-0.32837028116359,-0.32837028116359!

  K =  1.0000E-01

  N =        0,    X = -3.28370281164E-01  Y = -3.28370281164E-01

 TO CONTINUE WITH THESE DATA, TYPE 1 -- OTHERWISE 0
1!

 TO ADD NOISE, TYPE 1 -- OTHERWISE 0
0!
 TO PRINT OSC. MAGNITUDE, TYPE 1 -- OTHERWISE 0
0!
 TYPE NUMBER OF PRINT STEPS
1!
 TYPE ITERATIONS PER PRINT (.LE. 131070)
1!

    N          X            Y          A OR C      B OR D   LOG 10 LAM  LF

     0 -3.2837E-01 -3.2837E-01  1.0000E+00  0.          0.            1
                               0.          1.0000E+00

     1 -3.2837E-01 -3.2837E-01


 TYPE ADDITIONAL NUMBER OF PRINT STEPS
0!

  N =        1,    X = -3.28370281164E-01  Y = -3.28370281164E-01
                   A =  0.                 B =  1.00000000000E+00
                   C = -1.00000000000E+00  D =  5.54460160127E-01
                DET =  1.00000000000E+00
        LOG 10 LAM =  0.                 LF =  1
```

```
TYPE INITIAL X,Y (SINGLE PRECISION)
0.9949874371066l,0.9949874371066l!

  K =  1.0000E-01

  N =         0,    X =   9.94987437107E-01  Y =   9.94987437107E-01

TO CONTINUE WITH THESE DATA, TYPE 1 -- OTHERWISE 0
1!

 TO ADD NOISE, TYPE 1 -- OTHERWISE 0
0!
 TO PRINT OSC. MAGNITUDE, TYPE 1 -- OTHERWISE 0
0!
 TYPE NUMBER OF PRINT STEPS
1!
 TYPE ITERATIONS PER PRINT (.LE. 131070)
1!

   N         X           Y           A OR C      B OR D   LOG 10 LAM  LF

     0  9.9499E-01  9.9499E-01  1.0000E+00  0.          0.             1
                                0.          1.0000E+00

      1  9.9499E-01  9.9499E-01


 TYPE ADDITIONAL NUMBER OF PRINT STEPS
0!

  N =         1,    X =   9.94987437107E-01  Y =   9.94987437107E-01
                    A =   0.                 B =   1.00000000000E+00
                    C =  -1.00000000000E+00  D =   2.49624372644E+00
                  DET =   1.00000000000E+00
       LOG 10 LAM =   2.99940165179E-01 LF =   1
```

```
 TYPE INITIAL X,Y (SINGLE PRECISION)
-0.99498743710661,-0.99498743710661!

  K =  1.0000E-01

  N =      0,   X = -9.94987437107E-01  Y = -9.94987437107E-01

TO CONTINUE WITH THESE DATA, TYPE 1 -- OTHERWISE 0
1!

TO ADD NOISE, TYPE 1 -- OTHERWISE 0
0!
 TO PRINT OSC. MAGNITUDE, TYPE 1 -- OTHERWISE 0
0!
 TYPE NUMBER OF PRINT STEPS
1!
 TYPE ITERATIONS PER PRINT (.LE. 131070)
1!

    N        X           Y          A OR C      B OR D    LOG 10 LAM  LF

      0 -9.9499E-01 -9.9499E-01   1.0000E+00 0.         0.            1
                                  0.         1.0000E+00

      1 -9.9499E-01 -9.9499E-01


TYPE ADDITIONAL NUMBER OF PRINT STEPS
0!

  N =      1,   X = -9.94987437107E-01  Y = -9.94987437104E-01
                A =  0.                 B =  1.00000000000E+00
                C = -1.00000000000E+00  D =  1.99503756273E+02
              DET =  1.00000000000E+00
       LOG 10 LAM =  2.29994016518E+00 LF =  1
```

It is probably not surprising that during any epoch (of, say, 100 iterations) the phase points follow a motion that does not depart markedly from a curve similar to a reduced replica of the separatrix. Diffusion -- if that is the proper term -- outward or inward from such a curve might be expected to occur gradually. It is, however, important to be aware of the extent to which limited computational accuracy (even with double-precision computations) can distort these results. This question of computational accuracy perhaps can be judged by a computational experiment in which uniformly distributed "noise" between the limits $\pm \frac{1}{2} 10^{-28}$ was introduced into x and into y after each iteration. The results agreed substantially with those for a noise-free run for $N \lesssim 700$ (through 5 decimal figures), but thereafter departed markedly from the results obtained without the deliberate introduction of this small amount of noise. The occurrence of scattering in the points thus appears to be valid, but the slow throb of amplitude observed in the first run of this series may be influenced by computational errors.

Because of the effects just mentioned, it may be particularly useful to examine the characteristics of the higher-order fixed points that have been identified. The locations of fixed points of orders 5, 6, and 7 are tabulated below, with the coordinates of one member of each family given to approximately 12-decimal precision

Order 5 -- Stable

$x_o = y_o = -\ 0.0471\ 1132\ 9376_1$

x	y
-0.047 111	-0.047 111
-0.047 111	-0.41826
-0.41826	-0.65883
-0.65883	-0.41826
-0.41826	-0.047111

Order 5 -- Unstable

$x_o = y_o = -\ 0.5724\ 7793\ 9150$

x	y
-0.57248	-0.57248
-0.57248	-0.21679
-0.21679	-0.020348
-0.020348	-0.21679
-0.21679	-0.57248

Order 6 -- Stable

$x_o = 0.2820\ 4836\ 6504,$ $y_o = 0.1092\ 1187\ 0733$

x	y
0.28205	0.10921
0.10921	-0.47466
-0.47466	-0.84564
-0.84564	-0.47466
-0.47466	0.10921
0.10921	0.28205

Order 6 -- Unstable

$x_o = y_o = 0.2363\ 2698\ 7529$

x	y
0.23633	0.23633
0.23633	-0.12927
-0.12927	-0.77254
-0.77254	-0.77254
-0.77254	-0.12927
-0.12927	0.23633

Order 7 -- Stable

$x_o = y_o = 0.4365\ 2169\ 5083_4$

x	y
0.43652	0.43652
0.43652	0.16261
0.16261	-0.50601
-0.50601	-0.91595
-0.91595	-0.50601
-0.50601	0.16261
0.16261	0.43652

Order 7 -- Unstable

$x_o = y_o = -\ 0.8592\ 6979\ 4727_3$

x	y
-0.85927	-0.85927
-0.85927	-0.10009
-0.10009	0.34506
0.34506	0.47323
0.47323	0.34506
0.34506	-0.10009
-0.10009	-0.85927

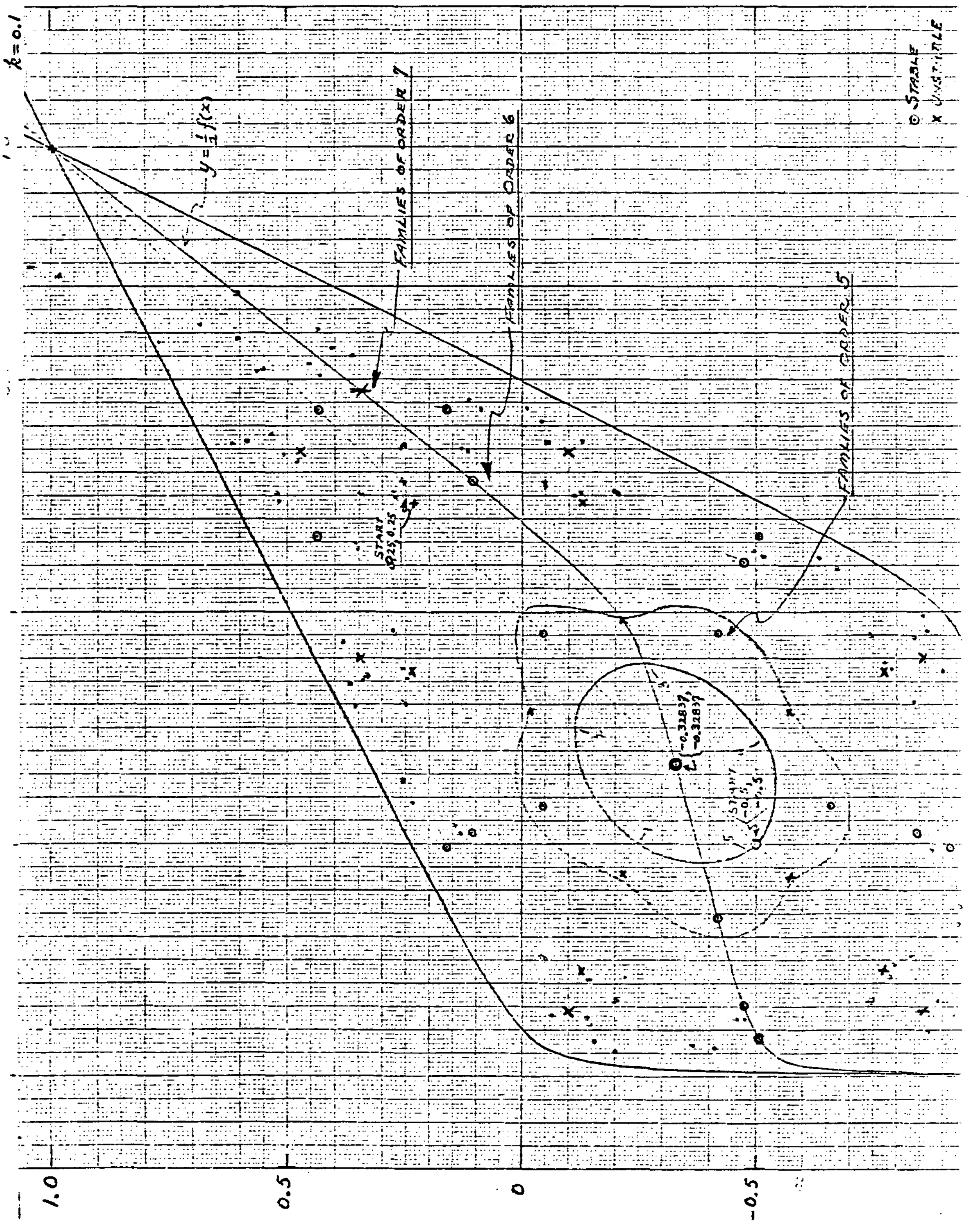
k = 0.1
$y = \frac{1}{2} f(x)$
FAMILIES OF ORDER 7
FAMILIES OF ORDER 6
FAMILIES OF ORDER 5
START 0.25, 0.25
-0.32837, -0.32837
START -0.5, -0.5
⊙ STABLE
× UNSTABLE
1.0
0.5
0
-0.5

The matrix elements A, B, C, D, printed for runs starting at the values of x_0, y_0 just recorded and returning (after 5, 6, or 7 applications of the transformation, were found to be the following:

	A	B	C	D
Order 5				
Stable	$0.9214\ 3239\ 726_0$	$-0.2950\ 4352\ 205_8$	$0.2950\ 4352\ 205_9$	$0.9907\ 9359\ 788_7$
Unstable	$0.7299\ 4894\ 221_8$	$-0.1794\ 5685\ 005_2$	$0.1794\ 5685\ 005_2$	1.3258 3963 480
Order 6				
Stable	1.3380 6309 073	$-0.9080\ 0152\ 953_3$	2.4018 1063 234	$-0.8825\ 0526\ 899_3$
Unstable	$0.1905\ 3887\ 125_8$	$0.5967\ 7888\ 782_5$	$-0.5967\ 7888\ 782_3$	3.3791 2655 195
Order 7				
Stable	1.1863 9656 723	-1.5747 2725 767	1.5747 2725 767	-1.2472 7766 156
Unstable	$-0.7764\ 3655\ 568_6$	$-2.3874\ 1029\ 30_6$	$2.3874\ 1029\ 30_7$	6.0529 4518 014

Certain expected symmetries will be evident in many of these results.

From these results the characteristics of the fixed-point families listed below follow.

	Half Trace	$\mu = \cos^{-1}$(Half Trace)	λ_1	ψ_1
Order 5				
Stable	$0.956\ 112\ 997\ 574^{-}$	17.0375 deg. = 0.0473265 rev.		
Unstable	1. 027 894 288 51		1.265 731 772	0.102 341 682
Order 6				
Stable	0.227 778 910 87	76.8337 deg. = 0.213427 rev.		
Unstable	$1.784\ 832\ 711\ 60_4$		3.263 219 606	0.513 646 3016
Order 7				
Stable	-0.030 440 5472	91.7444 deg. = 0.254846^{-} rev.		
Unstable	$2.638\ 254\ 3122_3$		$5.079\ 644\ 45_2$	0.705 833 3151

Other fixed points, of higher order, of course exist. Thus, in the region that may be of particular interest we have the following systems:

2/11 Systems:

Order 11 -- Stable

$x_o = y_o = -0.7049\ 2510\ 9783_3$

Order-11 -- Unstable

$x_o = y_o = 0.1315\ 4928\ 9881_9$

$\psi_1 = 0.44335008, \quad \lambda_1 \cong +\ 2.775_6$

2/13 Systems:

Order 13 -- Stable

$x_o = y_o = -\ 0.8224\ 4803\ 1800_7$

Order 13 -- Unstable

$x_o = y_o = 0.3136\ 4321\ 5938_4$

$\psi_1 = 0.7955\ 5975, \quad \lambda_1 \cong +\ 6.245_4$

```
 TYPE INITIAL X,Y (SINGLE PRECISION)
-0.7049251097833,-0.7049251097833!

  K =  1.0000E-01

  N =       0,   X = -7.04925109783E-01  Y = -7.04925109783E-01

 TO CONTINUE WITH THESE DATA, TYPE 1 -- OTHERWISE 0
1!

 TO ADD NOISE, TYPE 1 -- OTHERWISE 0
0!
 TO PRINT OSC. MAGNITUDE, TYPE 1 -- OTHERWISE 0
0!
 TYPE NUMBER OF PRINT STEPS
11!
 TYPE ITERATIONS PER PRINT (.LE. 131070)
1!

    N         X           Y           A OR C      B OR D    LOG 10 LAM  LF

      0 -7.0493E-01 -7.0493E-01  1.0000E+00  0.          0.          1
                                 0.          1.0000E+00

      1 -7.0493E-01 -1.5742E-01

      2 -1.5742E-01  1.4935E-01

      3  1.4935E-01  5.6847E-02

      4  5.6847E-02 -4.5379E-01

      5 -4.5379E-01 -7.8201E-01

      6 -7.8201E-01 -4.5379E-01

      7 -4.5379E-01  5.6847E-02

      8  5.6847E-02  1.4935E-01

      9  1.4935E-01 -1.5742E-01

     10 -1.5742E-01 -7.0493E-01

     11 -7.0493E-01 -7.0493E-01

 TYPE ADDITIONAL NUMBER OF PRINT STEPS
0!

  N =      11,   X = -7.04925109783E-01  Y = -7.04925109783E-01
                 A = -3.32314195875E-01  B = -1.18574894794E+00
                 C =  1.18574894794E+00  D =  1.22173705659E+00
               DET =  1.00000000000E+00
       LOG 10 LAM =  0.                 LF =  1
```

```
 TYPE INITIAL X,Y (SINGLE PRECISION)
0.1315492898819,0.1315492898819!

   K =  1.0000E-01

   N =        0,    X =  1.31549289882E-01   Y =  1.31549289882E-01

 TO CONTINUE WITH THESE DATA, TYPE 1 -- OTHERWISE 0
1!

 TO ADD NOISE, TYPE 1 -- OTHERWISE 0
0!
 TO PRINT OSC. MAGNITUDE, TYPE 1 -- OTHERWISE 0
0!
 TYPE NUMBER OF PRINT STEPS
11!
 TYPE ITERATIONS PER PRINT (.LE. 131070)
1!

     N         X            Y           A OR C       B OR D   LOG 10 LAM   LF

       0  1.3155E-01  1.3155E-01  1.0000E+00  0.          0.              1
                                  0.          1.0000E+00

       1  1.3155E-01 -2.7340E-01

       2 -2.7340E-01 -7.5742E-01

       3 -7.5742E-01 -6.1935E-01

       4 -6.1935E-01 -5.7370E-02

       5 -5.7370E-02  1.4327E-01

       6  1.4327E-01 -5.7370E-02

       7 -5.7370E-02 -6.1935E-01

       8 -6.1935E-01 -7.5742E-01

       9 -7.5742E-01 -2.7340E-01

      10 -2.7340E-01  1.3155E-01

      11  1.3155E-01  1.3155E-01


 TYPE ADDITIONAL NUMBER OF PRINT STEPS
0!

   N =      11,    X =  1.31549289882E-01  Y =  1.31549289882E-01
                   A =  3.38972357076E-01  B = -2.27898226816E-01
                   C =  2.27898226815E-01  D =  2.79687230662E+00
                 DET =  1.00000000000E+00
         LOG 10 LAM =  4.43350082393E-01 LF =  1
```

```
 TYPE INITIAL X,Y (SINGLE PRECISION)
-0.8224480318007,-0.8224480318007!

  K =  1.0000E-01

  N =       0,    X = -8.22448031801E-01  Y = -8.22448031801E-01

 TO CONTINUE WITH THESE DATA, TYPE 1 -- OTHERWISE 0
1!

 TO ADD NOISE, TYPE 1 -- OTHERWISE 0
0!
 TO PRINT OSC. MAGNITUDE, TYPE 1 -- OTHERWISE 0
0!
 TYPE NUMBER OF PRINT STEPS
13!
 TYPE ITERATIONS PER PRINT (.LE. 131070)
1!

    N          X           Y            A OR C       B OR D    LOG 10 LAM  LF

      0 -8.2245E-01 -8.2245E-01  1.0000E+00  0.          0.             1
                                 0.          1.0000E+00

      1 -8.2245E-01 -1.1088E-01

      2 -1.1088E-01  2.9982E-01

      3  2.9982E-01  3.7281E-01

      4  3.7281E-01  1.4175E-01

      5  1.4175E-01 -4.9108E-01

      6 -4.9108E-01 -8.8704E-01

      7 -8.8704E-01 -4.9108E-01

      8 -4.9108E-01  1.4175E-01

      9  1.4175E-01  3.7281E-01

     10  3.7281E-01  2.9982E-01

     11  2.9982E-01 -1.1088E-01

     12 -1.1088E-01 -8.2245E-01

     13 -8.2245E-01 -8.2245E-01


 TYPE ADDITIONAL NUMBER OF PRINT STEPS
0!

  N =      13,    X = -8.22448031801E-01  Y = -8.22448031801E-01
                  A = -5.79649985966E-01  B = -8.52506469794E-01
                  C =  8.52506469794E-01  D = -4.71375356811E-01
                DET =  1.00000000000E+00
       LOG 10 LAM =  0.                 LF = -1
```

```
 TYPE INITIAL X,Y (SINGLE PRECISION)
0.3136432159384,0.3136432159384!

  K =  1.0000E-01

  N =       0,    X =  3.13643215938E-01  Y =  3.13643215938E-01

 TO CONTINUE WITH THESE DATA, TYPE 1 -- OTHERWISE 0
1!

 TO ADD NOISE, TYPE 1 -- OTHERWISE 0
0!
 TO PRINT OSC. MAGNITUDE, TYPE 1 -M OTHERWISE 0
0!
 TYPE NUMBER OF PRINT STEPS
13!
 TYPE ITERATIONS PER PRINT (.LE. 131070)
1!

    N         X            Y           A OR C       B OR D    LOG 10 LAM  LF

      0  3.1364E-01  3.1364E-01  1.0000E+00  0.          0.             1
                                 0.          1.0000E+00

      1  3.1364E-01 -1.7785E-02

      2 -1.7785E-02 -7.4384E-01

      3 -7.4384E-01 -8.6696E-01

      4 -8.6696E-01 -2.2147E-01

      5 -2.2147E-01  2.7133E-01

      6  2.7133E-01  4.1372E-01

      7  4.1372E-01  2.7133E-01

      8  2.7133E-01 -2.2147E-01

      9 -2.2147E-01 -8.6696E-01

     10 -8.6696E-01 -7.4384E-01

     11 -7.4384E-01 -1.7785E-02

     12 -1.7785E-02  3.1364E-01

     13  3.1364E-01  3.1364E-01


 TYPE ADDITIONAL NUMBER OF PRINT STEPS
0!

  N =      13,    X =  3.13643215938E-01  Y =  3.13643215938E-01
                  A =  1.45205244129E-01  B =  3.01613679064E-01
                  C = -3.01613679070E-01  D =  6.26030550105E+00
                DET =  1.00000000000E+00
         LOG 10 LAM =  7.95559752095E-01 LF =  1
```

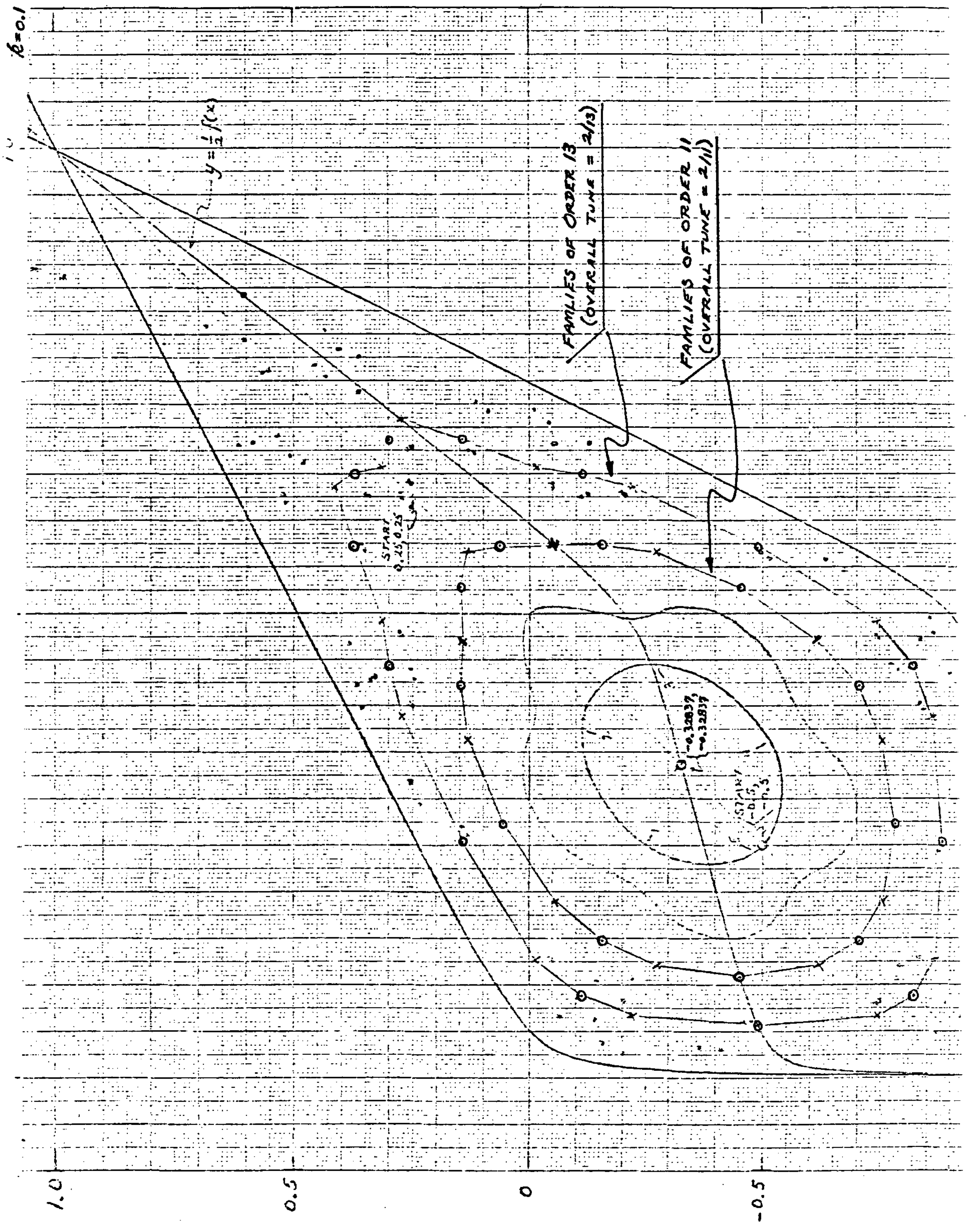k=0.1
1.0
$y = \frac{1}{2}f(x)$
FAMILIES OF ORDER 13 (OVERALL TUNE = 2/13)
FAMILIES OF ORDER 11 (OVERALL TUNE = 2/11)
START 0.25, 0.25
−0.32837, −0.32837
START −0.5, −0.5
1.0
0.5
0
−0.5

Expanding eigenvector directions, extended from such unstable fixed points as (for example) those of orders 6 and 7 may fail to form simple curves that would generate simple island structures surrounding the stable fixed points of the same order. The extended eigenvector segments then develop into increasingly thin and increasingly long curved fingers that cover an extensive region of phase space. Phase points near these fingers also would be expected to move in an apparently erratic manner, and small changes in coordinate values (*e.g.* from "noise" or from truncation errors) could lead to pronounced changes after a few additional iterations.*

There nevertheless may be apparently firm smooth invariant curves in certain regions of limited extent surrounding stable fixed points such as those of order 7, and points executing what appears to be erratic motion may avoid intruding into these "protected" regions.

---

* For example in some trials with noise $\pm \frac{1}{2} (1.0 \times 10^{-21})$ or $\pm \frac{1}{2} (1.0 \times 10^{-14})$ added to x and to y after each execution of the transformation, valid runs (say ~ 5-decimal accuracy) could not extend beyond some 300-400 or circa 200 iterations, respectively.

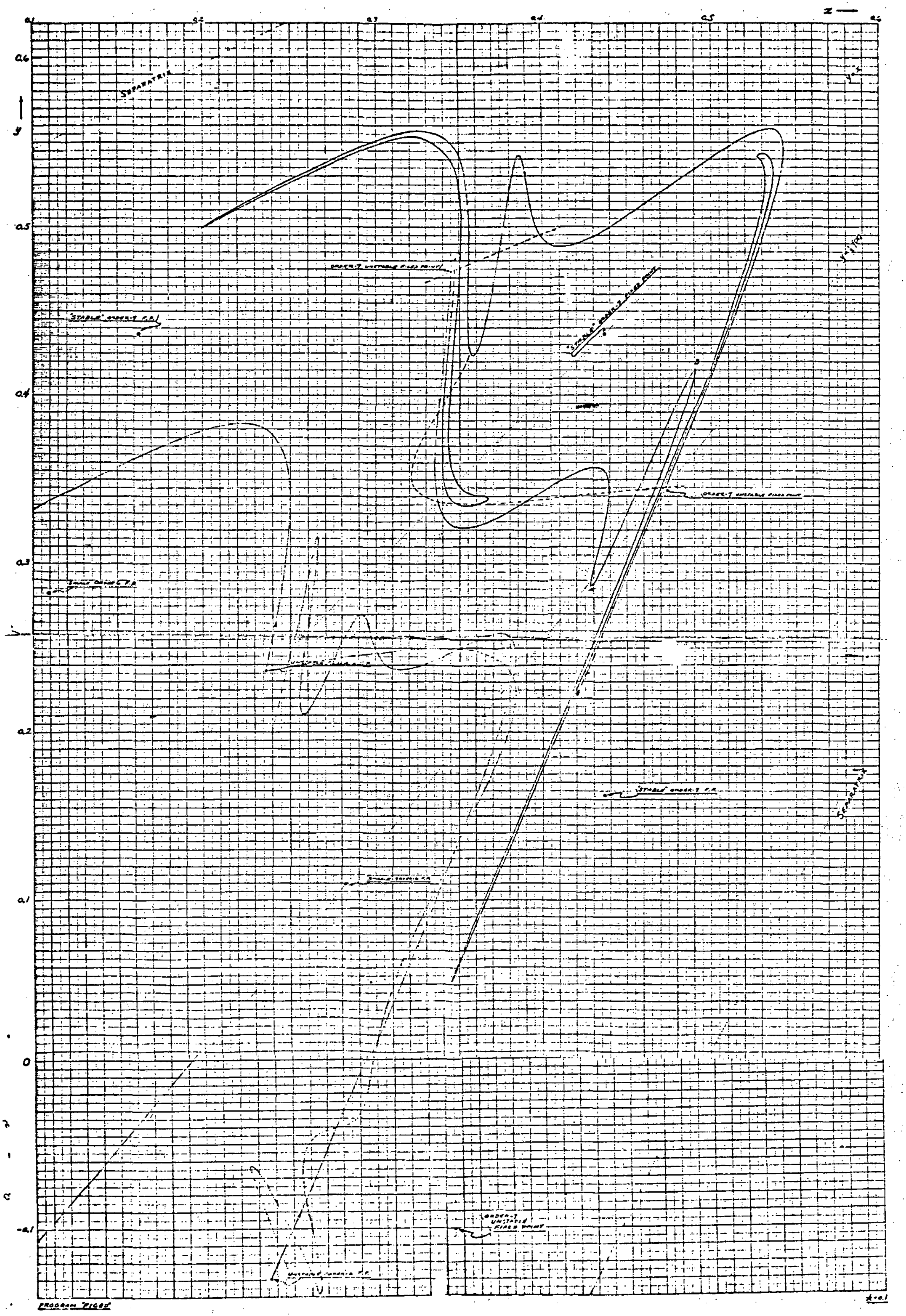
x
y
0.1
0.2
0.3
0.4
0.5
0.6
0
-0.1
SEPARATRIX
SEPARATRIX
y = x
y = 1/10
ORDER-7 UNSTABLE FIXED POINT
"STABLE" ORDER-7 FIXED POINT
"STABLE" ORDER-9 F.P.
ORDER-7 UNSTABLE FIXED POINT
STABLE ORDER 6 F.P.
"STABLE" ORDER-7 F.P.
ORDER-7 UNSTABLE FIXED POINT
PROGRAM "PIGEO"
k = 0.1

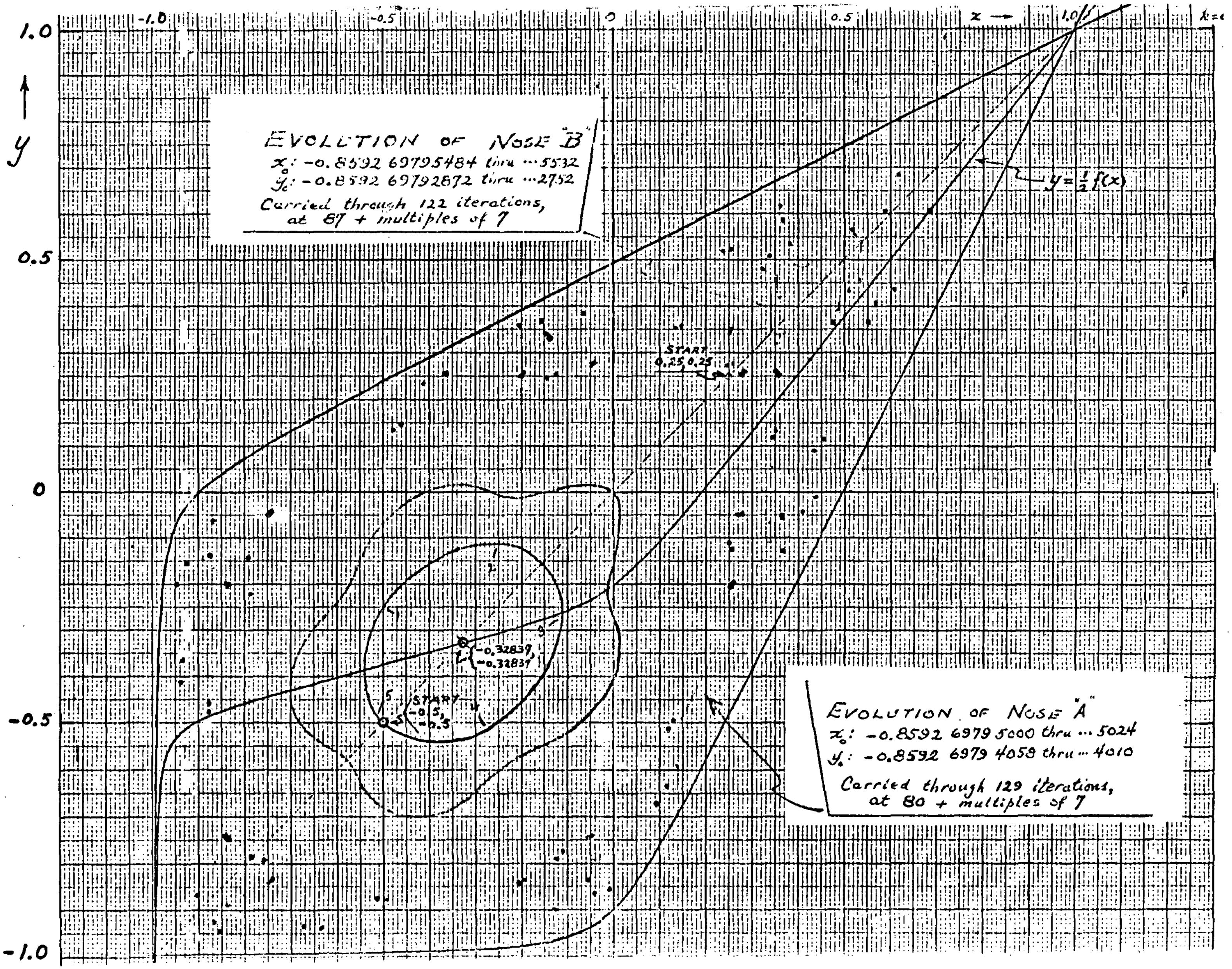

EVOLUTION OF NOSE "B"
x_0: -0.8592 69795484 thru ···5532
y_0: -0.8592 69792872 thru ···2752
Carried through 122 iterations,
at 87 + multiples of 7

EVOLUTION OF NOSE "A"
x_0: -0.8592 6979 5000 thru ··· 5024
y_0: -0.8592 6979 4058 thru ··· 4010
Carried through 129 iterations,
at 80 + multiples of 7

A further examination of the regions "enclosed" by the loops associated with the order-7 unstable fixed points revealed the presence of two curious fixed-point families of order 28 ("tune" = 4/28). There thus are four numbers of the "stable" order-28 family and four members of the associated unstable fixed-point family within each of the seven regions. The stable family of order 28 can be generated by launching a computation at the point

$$x_o = y_o = 0.4763\ 7231\ 3613_9$$

on the positive principal diagonal, or, alternatively, by launching the computations at a point (14 iterations removed) at

$$x_o = y_o = 0.3978\ 1128\ 9467$$

(also on the positive principal diagonal). For this family,

$$\tfrac{1}{2}\ \text{Trace} = 0.9674\ 4823\ 621$$

The unstable family can be generated by computations launched at

$$x_o = -\ 0.9101\ 2951\ 4108$$

$$y_o = -\ 0.5026\ 1156\ 6232$$

on the curve $y = \frac{1}{2} f(x)$, or, alternatively, at the point (14 iterations removed)

$$x_o = -\ 0.9215\ 6710\ 6809_6$$

$$y_o = -\ 0.5095\ 6132\ 7058_0$$

[also on the curve $y = \frac{1}{2} f(x)$]. For this family

$$\psi_1 = 0.07663\ 9137$$

and

$$\lambda_1 = +\ 1.1929\ 9641$$

(for the 28-iteration period).

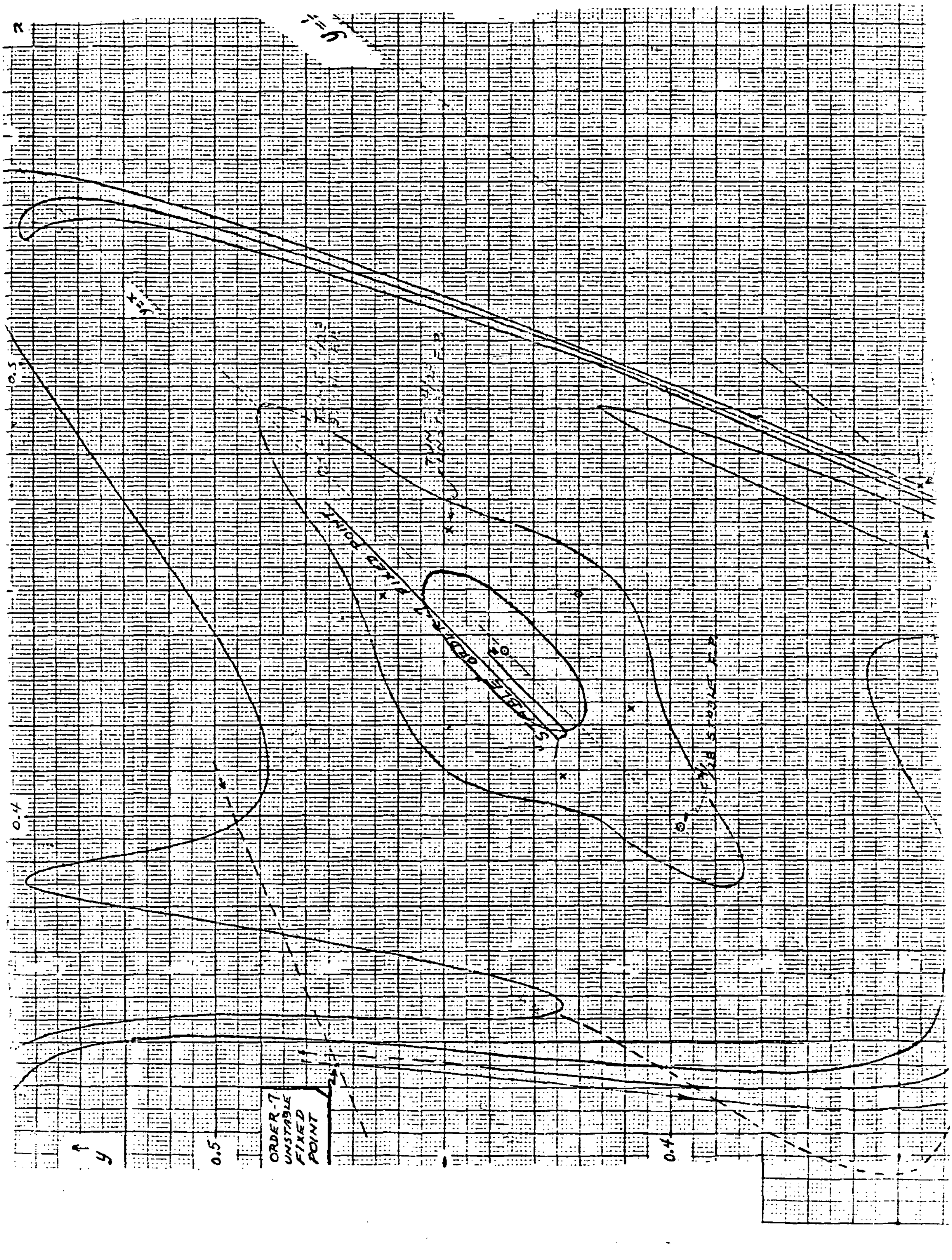
ORDER-7 UNSTABLE FIXED POINT
STABLE ORDER-7 FIXED POINT
y
0.5
0.4
0.5
0.4
y=x

```
TYPE INITIAL X,Y (SINGLE PRECISION)
0.4763723136139,0.4763723136139!

 K =  1.0000E-01

 N =       0,    X =  4.76372313614E-01  Y =  4.76372313614E-01

TO CONTINUE WITH THESE DATA, TYPE 1 -- OTHERWISE 0
1!

TO ADD NOISE, TYPE 1 -- OTHERWISE 0
0!
TO PRINT OSC. MAGNITUDE, TYPE 1 -- OTHERWISE 0
0!
TYPE NUMBER OF PRINT STEPS
28!
TYPE ITERATIONS PER PRINT (.LE. 131070)
1!
FOR SHORT PRINT, SHORT WITH DIAGNOSTIC, OR FULL -- TYPE 1, 2, OR 3



2!
```

```
 N         X             Y           A OR C       B OR D      LOG 10 LAM   LF

   0  4.7637E-01  4.7637E-01  1.0000E+00  0.           0.            1
                              0.          1.0000E+00

   1  4.7637E-01  2.2155E-01

   2  2.2155E-01 -4.0506E-01

   3 -4.0506E-01 -9.2033E-01

   4 -9.2033E-01 -6.1244E-01

   5 -6.1244E-01  1.0931E-01

   6  1.0931E-01  4.2006E-01

   7  4.2006E-01  4.4905E-01

   8  4.4905E-01  2.1012E-01

   9  2.1012E-01 -4.0530E-01

  10 -4.0530E-01 -9.0902E-01

  11 -9.0902E-01 -5.9869E-01

  12 -5.9869E-01  1.0552E-01

  13  1.0552E-01  3.9781E-01

  14  3.9781E-01  3.9781E-01

  15  3.9781E-01  1.0552E-01

  16  1.0552E-01 -5.9869E-01

  17 -5.9869E-01 -9.0902E-01

  18 -9.0902E-01 -4.0530E-01

  19 -4.0530E-01  2.1012E-01

  20  2.1012E-01  4.4905E-01

  21  4.4905E-01  4.2006E-01

  22  4.2006E-01  1.0931E-01

  23  1.0931E-01 -6.1244E-01

  24 -6.1244E-01 -9.2033E-01

  25 -9.2033E-01 -4.0506E-01

  26 -4.0506E-01  2.2155E-01
                                X =   4.76372313614E-01   Y =   4.76372313614E-
  27  2.2155E-01  4.7637E-01    A =   6.82562748217E-01   B =   3.81055969019E-
                                C =  -3.81055969019E-01   D =   1.25233372420E+
  28  4.7637E-01  4.7637E-01  DET =   1.00000000000E+00
                       LOG 10 LAM =   0.                  LF =   1

TYPE ADDITIONAL NUMBER OF PRINT STEPS
```

```
 TYPE INITIAL X,Y (SINGLE PRECISION)
-0.910129514108,-0.502611566232!

  K =  1.0000E-01

  N =        0,   X = -9.10129514108E-01  Y = -5.02611566232E-01

 TO CONTINUE WITH THESE DATA, TYPE 1 -- OTHERWISE 0
1!

 TO ADD NOISE, TYPE 1 -- OTHERWISE 0
0!
 TO PRINT OSC. MAGNITUDE, TYPE 1 -- OTHERWISE 0
0!
 TYPE NUMBER OF PRINT STEPS
28!
 TYPE ITERATIONS PER PRINT (.LE. 131070)
1!
 FOR SHORT PRINT, SHORT WITH DIAGNOSTIC, OR FULL -- TYPE 1, 2, OR 3



2!
```

```
N        X            Y            A OR C       B OR D     LOG 10 LAM  LF

  0 -9.1013E-01 -5.0261E-01   1.0000E+00  0.          0.              1
                              0.          1.0000E+00

  1 -5.0261E-01  1.5862E-01

  2  1.5862E-01  4.2374E-01

  3  4.2374E-01  4.0886E-01

  4  4.0886E-01  1.0692E-01

  5  1.0692E-01 -6.0661E-01

  6 -6.0661E-01 -9.1475E-01

  7 -9.1475E-01 -4.0396E-01

  8 -4.0396E-01  2.1657E-01

  9  2.1657E-01  4.6325E-01

 10  4.6325E-01  4.4880E-01

 11  4.4880E-01  1.6631E-01

 12  1.6631E-01 -5.0956E-01

 13 -5.0956E-01 -9.2157E-01

 14 -9.2157E-01 -5.0956E-01

 15 -5.0956E-01  1.6631E-01

 16  1.6631E-01  4.4880E-01

 17  4.4880E-01  4.6325E-01

 18  4.6325E-01  2.1657E-01

 19  2.1657E-01 -4.0396E-01

 20 -4.0396E-01 -9.1475E-01

 21 -9.1475E-01 -6.0661E-01

 22 -6.0661E-01  1.0692E-01

 23  1.0692E-01  4.0886E-01

 24  4.0886E-01  4.2374E-01

 25  4.2374E-01  1.5862E-01

 26  1.5862E-01 -5.0261E-01
                               X = -9.10129514108E-01  Y = -5.02611566232E
 27 -5.0261E-01 -9.1013E-01    A =  1.01965564575E+00  B = -7.19027277337E
                               C = -4.37385946307E+00  D =  1.01156625466E
 28 -9.1013E-01 -5.0261E-01  DET =  1.00000000000E+00
                   LOG 10 LAM =  7.66391376290E-02 LF =  1

TYPE ADDITIONAL NUMBER OF PRINT STEPS
```

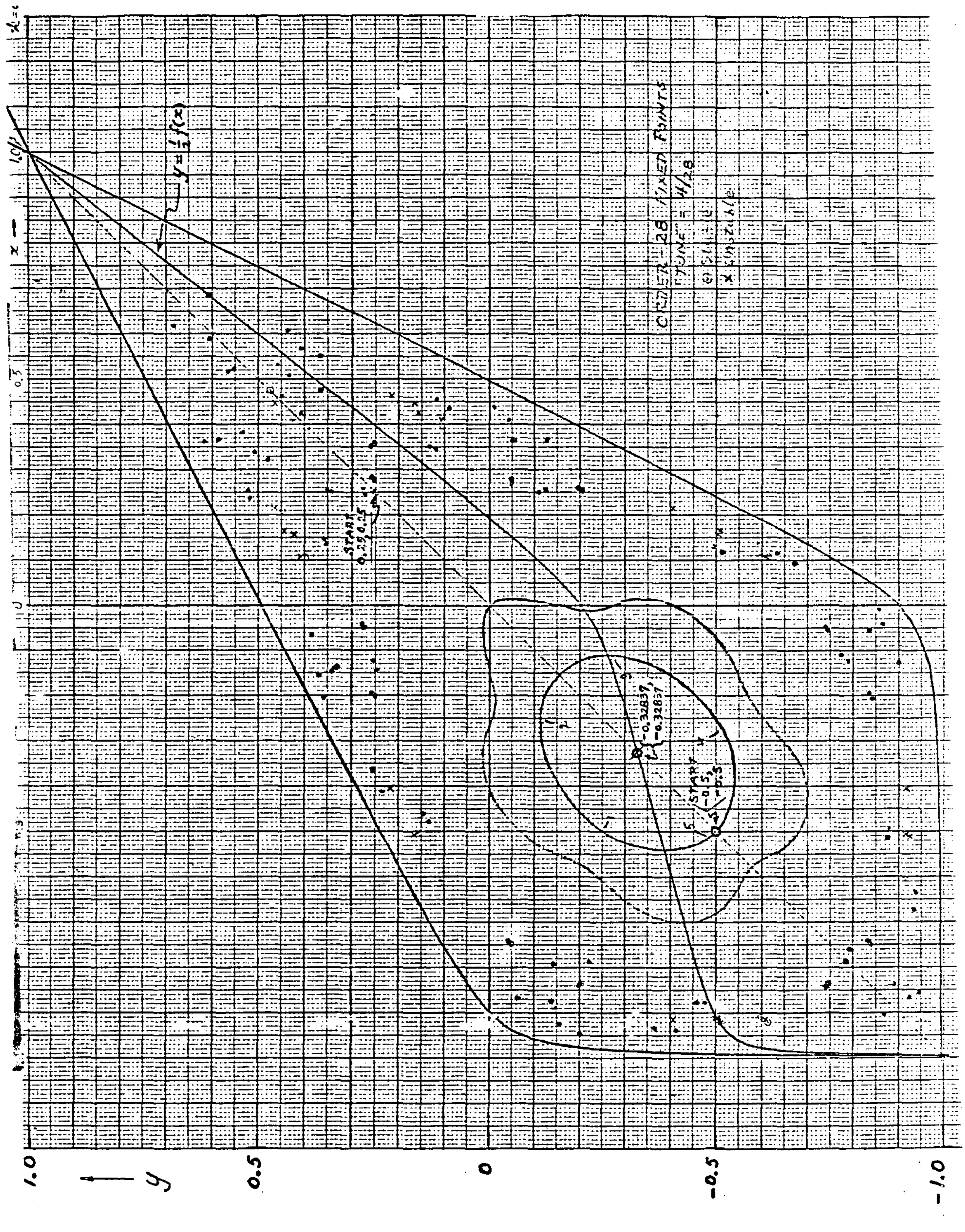
ORDER 28 FIXED POINTS
"TUNE" = 4/28
○ STABLE
x UNSTABLE
$y = \frac{1}{2} f(x)$
x →
1.0
0.5
0
START 0.25, 0.25
-0.32837, -0.32837
START -0.5, -0.5
1.0
0.5
0
-0.5
-1.0
← y

These fixed points are seen to group in tight clusters and might merge for a somewhat different value of the parameter k (here we have retained the value $k = 0.1$).

Additional fixed-point systems of course can be found. Thus, there exists an unstable system of order 8 that can be computed by commencing at

$$x_o = y_o = 0.5939\ 6695\ 4780$$

on the positive principal diagonal or, alternatively, at the point (4 iterations removed)

$$x_o = y_o = -\ 0.90601\ 32316\ 60_{86}$$

on the negative principal diagonal. For this family

$$\psi_1 = 0.8391\ 5092\ 27^{-}$$

and

$$\lambda_1 = +\ 6.904\ 7971$$

(for the 8-iteration period). An associated (stable) order-8 family (1/2 trace = 0.297 627 29025) has also been found. The fixed points of this latter family can be obtained computationally by launching a solution at

$$x_o = 0.608\ 997\ 372\ 735_6, \qquad y_o = \tfrac{1}{2} f(x_o) = 0.513\ 770\ 756\ 622$$

or at a point (4 iterations removed) with coordinates

$$x_o = -\ 0.952\ 316\ 214\ 059_{17}$$

$$y_o = \tfrac{1}{2} f(x_o) = -\ 0.537\ 889\ 794\ 977$$

```
 TYPE INITIAL X,Y (SINGLE PRECISION)
0.593966954780,0.593966954780!

  K =  1.0000E-01

  N =        0,   X =  5.93966954780E-01  Y =  5.93966954780E-01

 TO CONTINUE WITH THESE DATA, TYPE 1 -- OTHERWISE 0
1!

 TO ADD NOISE, TYPE 1 -- OTHERWISE 0
0!
 TO PRINT OSC. MAGNITUDE, TYPE 1 -- OTHERWISE 0
0!
 TYPE NUMBER OF PRINT STEPS
8!
 TYPE ITERATIONS PER PRINT (.LE. 131070)
1!
 FOR SHORT PRINT, SHORT WITH DIAGNOSTIC, OR FULL -- TYPE 1, 2, OR 3
3!

     N         X            Y           A OR C      B OR D   LOG 10 LAM  LF

     0  5.9397E-01  5.9397E-01  1.0000E+00  0.          0.           1
                                0.          1.0000E+00

     1  5.9397E-01  3.9617E-01  0.          1.0000E+00 2.9756E-01   1
                               -1.0000E+00  2.4881E+00

     2  3.9617E-01 -9.4690E-02 -1.0000E+00  2.4881E+00 5.9041E-01   1
                               -2.4722E+00  5.1509E+00

     3 -9.4690E-02 -9.0601E-01 -2.4722E+00  5.1509E+00 0.          -1
                               -1.0235E+00  1.7281E+00

     4 -9.0601E-01 -9.0601E-01 -1.0235E+00  1.7281E+00 6.1029E-01  -1
                                1.3749E+00 -3.2983E+00

     5 -9.0601E-01 -9.4690E-02  1.3749E+00 -3.2983E+00 5.5780E-01  -1
                                2.4975E+00 -5.2641E+00

     6 -9.4690E-02  3.9617E-01  2.4975E+00 -5.2641E+00 0.           1
                                6.6941E-01 -1.0106E+00

     7  3.9617E-01  5.9397E-01  6.6941E-01 -1.0106E+00 4.9334E-01   1
                               -8.4259E-01  2.7658E+00

     8  5.9397E-01  5.9397E-01 -8.4259E-01  2.7658E+00 8.3915E-01   1
                               -2.7658E+00  7.8922E+00

 TYPE ADDITIONAL NUMBER OF PRINT STEPS
0!

  N =        8,   X =  5.93966954780E-01  Y =  5.93966954780E-01
                  A = -8.42585004407E-01  B =  2.76583747427E+00
                  C = -2.76583747427E+00  D =  7.89220897514E+00
                DET =  1.00000000000E+00
       LOG 10 LAM =  8.39150922660E-01 LF =  1

      1921.500  COMPUTING UNITS REMAIN*

 FOR  NEW K, COORDS., OR TERMINATE,  TYPE 1, 2, OR 9
```

```
 FOR Y=0.5*F, TYPE 1 -- OTHERWISE 0
1!
 TYPE INITIAL X (SINGLE PRECISION)
0.6089973727356!

  K =  1.0000E-01

  N =       0,    X =  6.08997372736E-01  Y =  5.13770756622E-01

 TO CONTINUE WITH THESE DATA, TYPE 1 -- OTHERWISE 0
1!

 TO ADD NOISE, TYPE 1 -- OTHERWISE 0
0!
 TO PRINT OSC. MAGNITUDE, TYPE 1 -- OTHERWISE 0
0!
TYPE NUMBER OF PRINT STEPS
8!
 TYPE ITERATIONS PER PRINT (.LE. 131070)
1!
 FOR SHORT PRINT, SHORT WITH DIAGNOSTIC, OR FULL -- TYPE 1, 2, OR 3
3!

    N         X            Y           A OR C       B OR D   LOG 10 LAM  LF

      0  6.0900E-01  5.1377E-01  1.0000E+00  0.          0.              1
                                 0.          1.0000E+00

      1  5.1377E-01  1.8177E-01  0.          1.0000E+00 2.9629E-01      1
                                -1.0000E+00  2.4838E+00

      2  1.8177E-01 -5.3789E-01 -1.0000E+00  2.4838E+00 5.6058E-01      1
                                -2.3797E+00  4.9107E+00

      3 -5.3789E-01 -9.5232E-01 -2.3797E+00  4.9107E+00 1.9752E-01     -1
                                -2.8568E-01  1.6930E-01

      4 -9.5232E-01 -5.3789E-01 -2.8568E-01  1.6930E-01 6.5486E-01     -1
                                 1.6071E+00 -4.4528E+00

      5 -5.3789E-01  1.8177E-01  1.6071E+00 -4.4528E+00 0.             -1
                                 1.1539E+00 -2.5750E+00

      6  1.8177E-01  5.1377E-01  1.1539E+00 -2.5750E+00 0.             -1
                                 1.1390E+00 -1.6750E+00

      7  5.1377E-01  6.0900E-01  1.1390E+00 -1.6750E+00 0.             -1
                                 1.6750E+00 -1.5852E+00

      8  6.0900E-01  5.1377E-01  1.6750E+00 -1.5852E+00 0.             -1
                                 3.0296E+00 -2.2702E+00


 TYPE ADDITIONAL NUMBER OF PRINT STEPS
0!

  N =       8,    X =  6.08997372736E-01  Y =  5.13770756622E-01
                  A =  1.67496915691E+00  B = -1.58523197160E+00
                  C =  3.02955960102E+00  D = -2.27022373740E+00
                DET =  1.00000000000E+00
      LOG 10 LAM =  0.                   LF = -1

      1977.160  COMPUTING UNITS REMAIN*
```

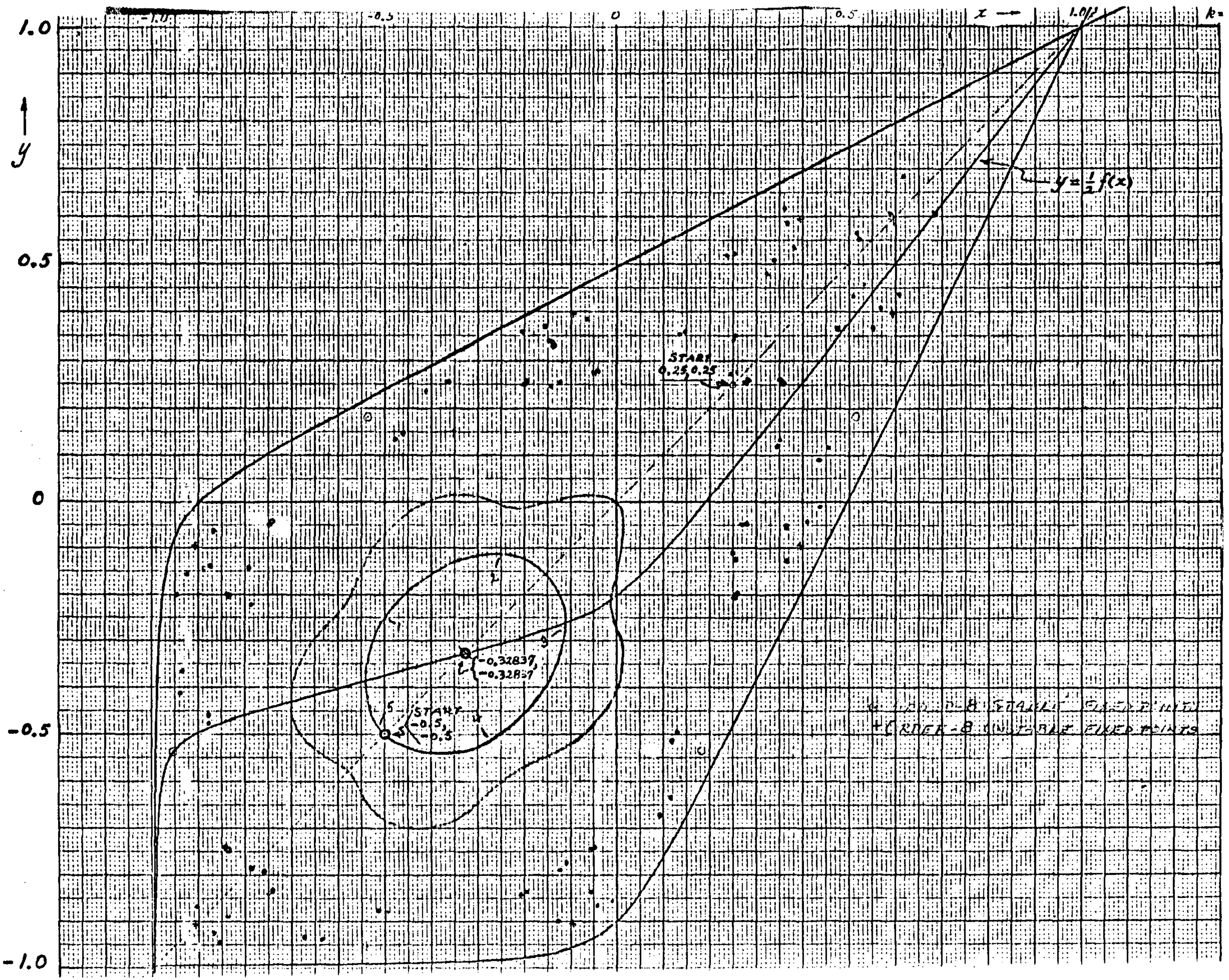1.0
0.5
0
-0.5
-1.0
y
-1.0
-0.5
0
0.5
x
1.0/β
k=
y = ½ f(x)
START 0.25, 0.25
START -0.5, -0.5
-0.32837, -0.32837
1
2
3
4
5
○ ORDER-8 STABLE FIXED POINTS
+ ORDER-8 UNSTABLE FIXED POINTS

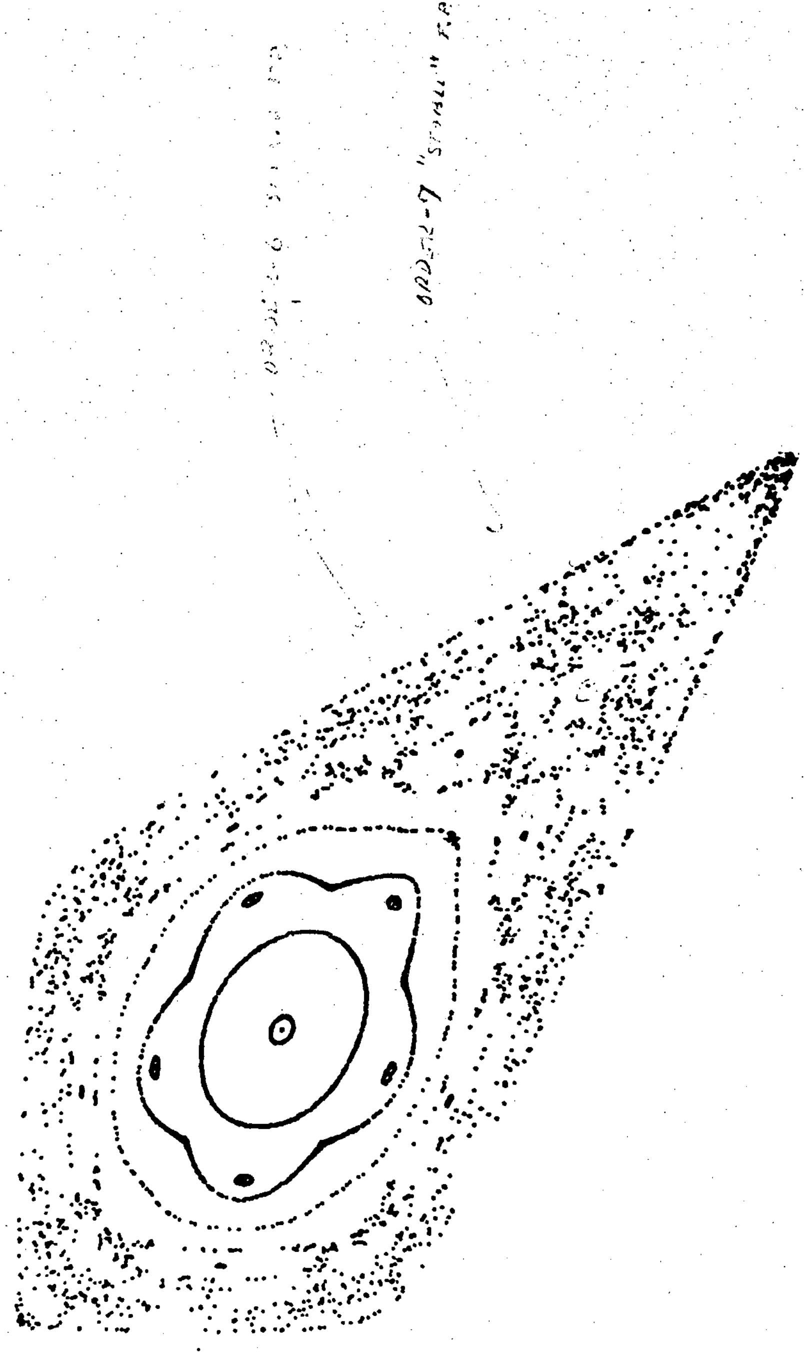
ORDER-6 STABLE FP
ORDER-7 "STABLE" F.P

PROGRAM FIG8D

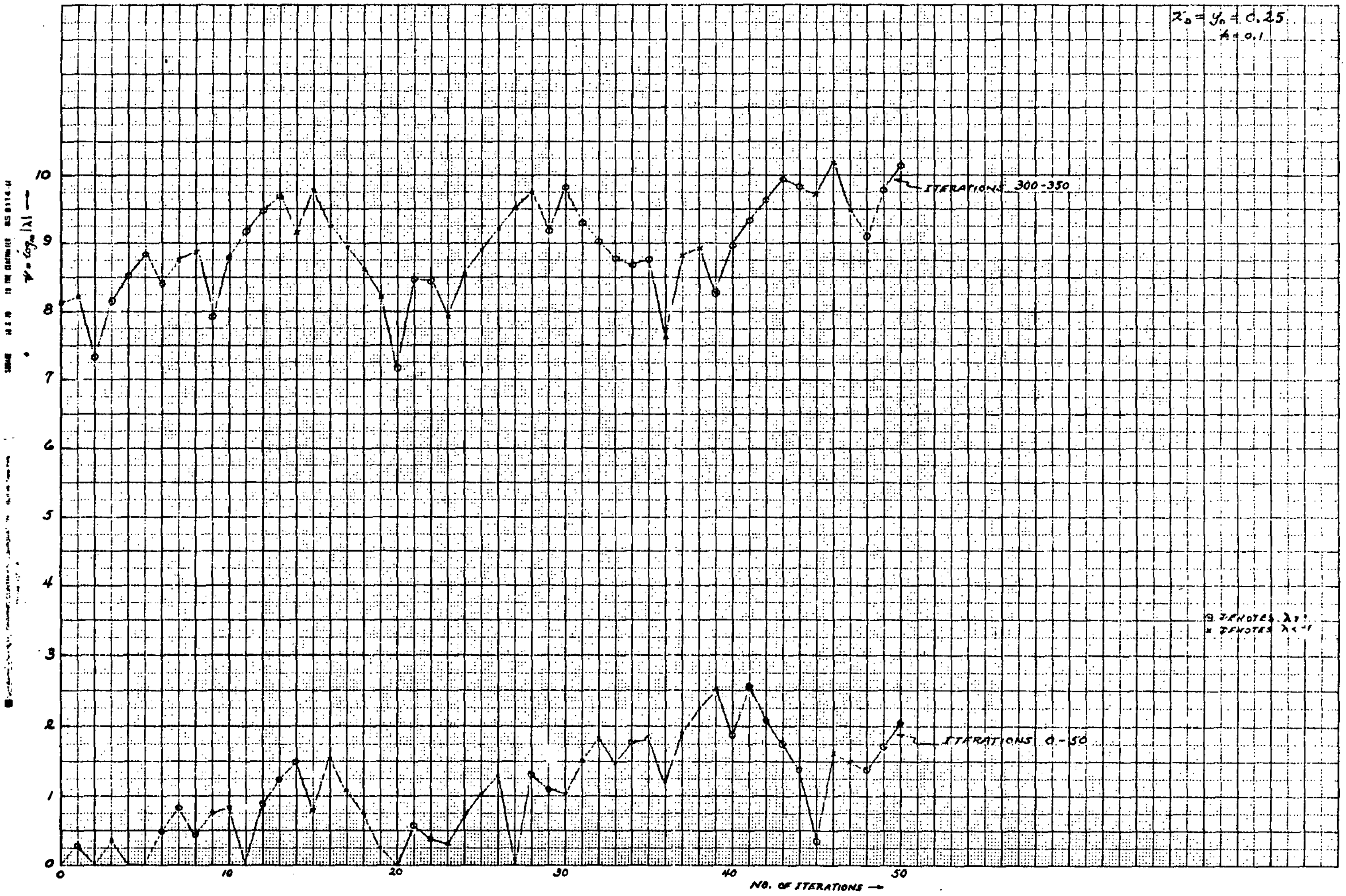

PROGRAM F168D

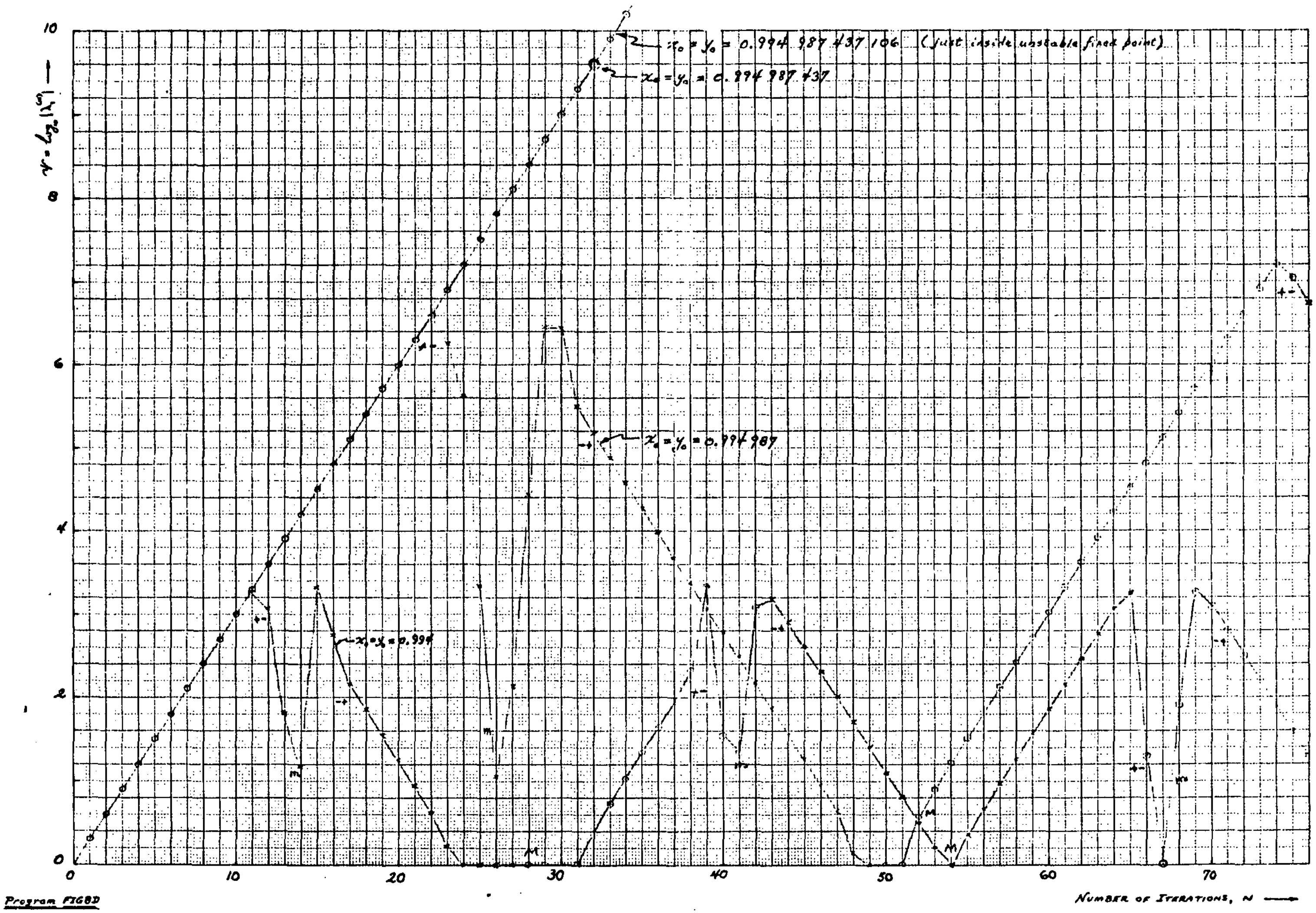

Program FIG8D

A Remark Concerning a Transformation Examined by Froeschlé*

L. Jackson Laslett

Lawrence Berkeley Laboratory
University of California
Berkeley, California

March 6, 1974

Froeschlé(1-3) has examined certain area-preserving mappings with the object of gaining insight into the stochastic, or apparently stochastic, behavior of such mappings in certain regions. He directs attention in this connection to the behavior of $\psi_n = \log_{10} \lambda_n$ and of quantities related to ψ_n, where $|\lambda_n|$ is an eigenvalue (of magnitude greater than unity) of the cumulative matrix for the tangential mapping. In attempting to relate the behavior of a transformation to that of a C-system, however, it is also of interest to inquire into the sign of λ_n -- i.e., into the sign of the trace of the cumulative tangential-mapping transformation -- and this matter we pursue in the present note with respect to the transformation denoted by Froeschlé as T_1 in our Ref. 1.

The transformation T_1 of Froeschlé(1) is cited by him as associated with the earlier work of Hénon (cited here as our Ref. 4) and is written

---

* Work supported by the U.S. Atomic Energy Commission.

$$x_{n+1} = x_n \cos\alpha - (y_n - x_n^2) \sin\alpha$$

$$y_{n+1} = x_n \sin\alpha + (y_n - x_n^2) \cos\alpha,$$

where α is a constant (taken to be such that $\cos\alpha = 0.22$ in the work of Ref. 1 and throughout the numerical work reported in the present Note). We consider it convenient to express the transformation T_1 in terms of other variables, so that the transformation assumes the form advocated by McMillan.(5) To this end we write

$$\left.\begin{aligned} x &= \sqrt{\sin\alpha}\quad Y \\ y &= \frac{X - Y\cos\alpha}{\sqrt{\sin\alpha}} \end{aligned}\right\} \quad \underline{\Omega} \quad \left\{\begin{aligned} X &= \frac{x}{\sqrt{\sin\alpha}} \cos x + y\sqrt{\sin\alpha} \\ Y &= \frac{x}{\sqrt{\sin\alpha}} \end{aligned}\right. ,$$

for which the functional determinant (Jacobian) is -1. The transformation T_1 applied to x,y is then found to be equivalent to the following transformation for X,Y:

$$X_{n+1} = Y_n$$

$$Y_{n+1} = -X_n + 2Y_n \cos\alpha + Y_n^2 \sin^{3/2}\alpha,$$

which will be recognized as being of McMillan's (area-preserving) form(5)

$$X_{n+1} = Y_n$$

$$Y_{n+1} = -X_n + f(Y_n)$$

where

$$f(Y) = 2Y \cos \alpha + Y^2 \sin^{3/2} \alpha$$

in this instance.

The matrix of the tangential-mapping associated with this transformation -- *i.e.*, the matrix taking dX_n, dY_n into dX_{n+1}, dY_{n+1} -- is

$$\begin{pmatrix} a & b \\ c & d \end{pmatrix} = \begin{pmatrix} 0 & 1 \\ -1 & f'(Y_n) \end{pmatrix}$$

with

$$f'(Y) = 2(\cos \alpha + Y \sin^{3/2} \alpha)$$

and the half-trace is

$$\begin{aligned} htr &= \tfrac{1}{2}(a+d) \\ &= \tfrac{1}{2} f'(Y) \\ &= \cos \alpha + Y \sin^{3/2} \alpha. \end{aligned}$$

From a cumulative-product matrix, formed by the repeated multiplication of such tangential-mapping matrices -- *i.e.*, from

$$\begin{pmatrix} A & B \\ C & D \end{pmatrix}_n = \begin{pmatrix} 0 & 1 \\ -1 & f'(Y_{n-1}) \end{pmatrix} \cdots \begin{pmatrix} 0 & 1 \\ -1 & f'(Y_o) \end{pmatrix} \begin{pmatrix} 1 & 0 \\ 0 & 1 \end{pmatrix}$$

-- we form $HTR = \frac{1}{2}(A+D)$ and then, when $|HTR| \geqslant 1$, the eigenvalues are$^{(6)}$ $HTR \pm \sqrt{(HTR)^2-1}$ and

$$|\lambda_1| = |HTR| + \sqrt{(HTR-1)(HTR+1)}$$

with the sign of λ_n identical to the sign of HTR. Related quantities of interest to Froeschle,[(1)] in addition to

$$\psi_n = \log_{10}|\lambda_n|,$$

are

$$\theta_n = \frac{1}{n} \log_{10} |\lambda_n|$$

and the "Cesaro mean"

$$\mu_n = \frac{1}{n} \sum_{m=1}^{n} \theta_m.$$

The transformation specified above has a first-order stable fixed point at the origin, with $HTR = \cos\alpha$. There also is an order-1 fixed point on the principal diagonal at

$$X = Y = \frac{2(1-\cos\alpha)}{\sin^{3/2}\alpha}$$

that (for $\cos\alpha = 0.22$) is unstable and lies at

$$X = Y \doteq 1.619137656439$$

(with the larger eigenvalue $\lambda \doteq 3.252548810736$). In addition, for $\cos\alpha = 0.22$, there is a family of five stable and five unstable order-5 fixed points -- with the approximate co-ordinates listed below:

Order-5 Fixed Points

$(\cos \alpha = 0.22)$

Stable Family		Unstable Family[a]	
X	Y	X	Y
0.669716	0.669716	-0.382322	-0.382322
0.669716	0.057097	-0.382322	0.354932
0.057097	-0.641453	0.354932	0.659868
-0.641453	0.057097	0.659868	0.354932
0.057097	0.669716	0.354932	-0.382322

a) $\lambda \cong 1.77_4$ for the total of 5 iterations.

Half Trace ≅ 0.7528856 Half Trace ≅ 1.1689567

In executing the transformation (which we have done computationally in double precision on the LBL C.D.C.-6600 computer)* we find, as noted by Froeschle´,(1) certain regions of apparent smooth stable behavior (in the neighborhood of the stable fixed points mentioned) that are surrounded by regions of irregular (stochastic?) and in some cases evidently unstable behavior. Froeschle´ has chosen(1) to identify these regions by means of starting values $y_o = 0$, $x_o = 0, 0.01, 0.02,$ etc. and notes(1) erratic behavior for

$$0.53 \leqslant x_o \leqslant 0.57 \quad \text{and for} \quad 0.81 \leqslant x_o.$$

Corresponding starting values

---

* See Fig. 1. For starting values of the type x_o, o in Froeschle´'s notation, the corresponding values X,Y were entered to single-precision accuracy (and the succeeding computations executed in double precision).

```
 FOR Y=0.5*F, TYPE 1 -- OTHERWISE 0
0!
 TYPE INITIAL X & Y (F-FORMAT ONLY, 2 LINES)
0.6697163826!
0.6697163826!

                 COS =  2.2000E-01        SIN =  9.7550E-01

  N =        0,     X =  6.69716382600E-01    Y =  6.69716382600E-01

 TO CONTINUE WITH THESE DATA, TYPE 1 -- OTHERWISE 0
1!

 TO ADD NOISE, TYPE 1 -- OTHERWISE 0
0!
 TYPE NUMBER OF PRINT STEPS
5!
 TYPE ITERATIONS PER PRINT (.LE. 131070)
1!
 FOR TTY OUTPUT, TYPE 1 -- FOR PLOT, TYPE 2
1!
 FOR SHORT PRINT, SHORT WITH DIAGNOSTIC, OR FULL -- TYPE 1, 2, OR 3
2!

     N           X              Y             PSI          PSI/N      CESARO     LF

       0  6.69716E-01  6.69716E-01  0.

       1  6.69716E-01  5.70970E-02

       2  5.70970E-02 -6.41453E-01

       3 -6.41453E-01  5.70970E-02

       4  5.70970E-02  6.69716E-01

       5  6.69716E-01  6.69716E-01


 TYPE ADDITIONAL NUMBER OF PRINT STEPS
0!

  N =        5,     X =  6.6971638268574699754286388814D-01
                    Y =  6.697163825924890839544517585D-01

  N =        5,     X =  6.69716382686E-01    Y =  6.69716382592E-01
                    A =  1.34087142372E+00    B = -8.82547809256E-01
                    C =  8.82547809716E-01    D =  1.64899751058E-01
                  DET =  1.00000000000E+00
        LOG 10 LAM =  0.                    LF =  1
```

```
 FOR Y=0.5*F, TYPE 1 -- OTHERWISE 0
0!
 TYPE INITIAL X & Y (F-FORMAT ONLY, 2 LINES)
-0.38232231729!
-0.38232231729!

                 COS =  2.2000E-01         SIN =  9.7550E-01

  N =         0,     X = -3.82322317290E-01   Y = -3.82322317290E-01

 TO CONTINUE WITH THESE DATA, TYPE 1 -- OTHERWISE 0
1!

 TO ADD NOISE, TYPE 1 -- OTHERWISE 0
0!
 TYPE NUMBER OF PRINT STEPS
5!
 TYPE ITERATIONS PER PRINT (.LE. 131070)
1!
 FOR TTY OUTPUT, TYPE 1 -- FOR PLOT, TYPE 2
1!
 FOR SHORT PRINT, SHORT WITH DIAGNOSTIC, OR FULL -- TYPE 1, 2, OR 3
2!

    N          X             Y           PSI         PSI/N      CESARO    LF

       0 -3.82322E-01 -3.82322E-01  0.

       1 -3.82322E-01  3.54932E-01

       2  3.54932E-01  6.59868E-01

       3  6.59868E-01  3.54932E-01

       4  3.54932E-01 -3.82322E-01

       5 -3.82322E-01 -3.82322E-01


 TYPE ADDITIONAL NUMBER OF PRINT STEPS
0!

  N =         5,     X = -3.823223172974069564583717612D-01
                     Y = -3.823223172812120446023461381D-01

  N =         5,     X = -3.82322317297E-01   Y = -3.82322317281E-01
                     A =  8.53056324152E-02   B = -8.98196232846E-01
                     C =  8.98196232866E-01   D =  2.25210772113E+00
                   DET =  1.00000000000E+00
            LOG 10 LAM =  2.49030928820E-01  LF =  1
```

GRAPHIC CONTROLS CORPORATION Buffalo, New York Printed in U.S.A. SQUARE 10 X 10 TO THE CENTIMETER AS 8014 GT

FIG. 1.

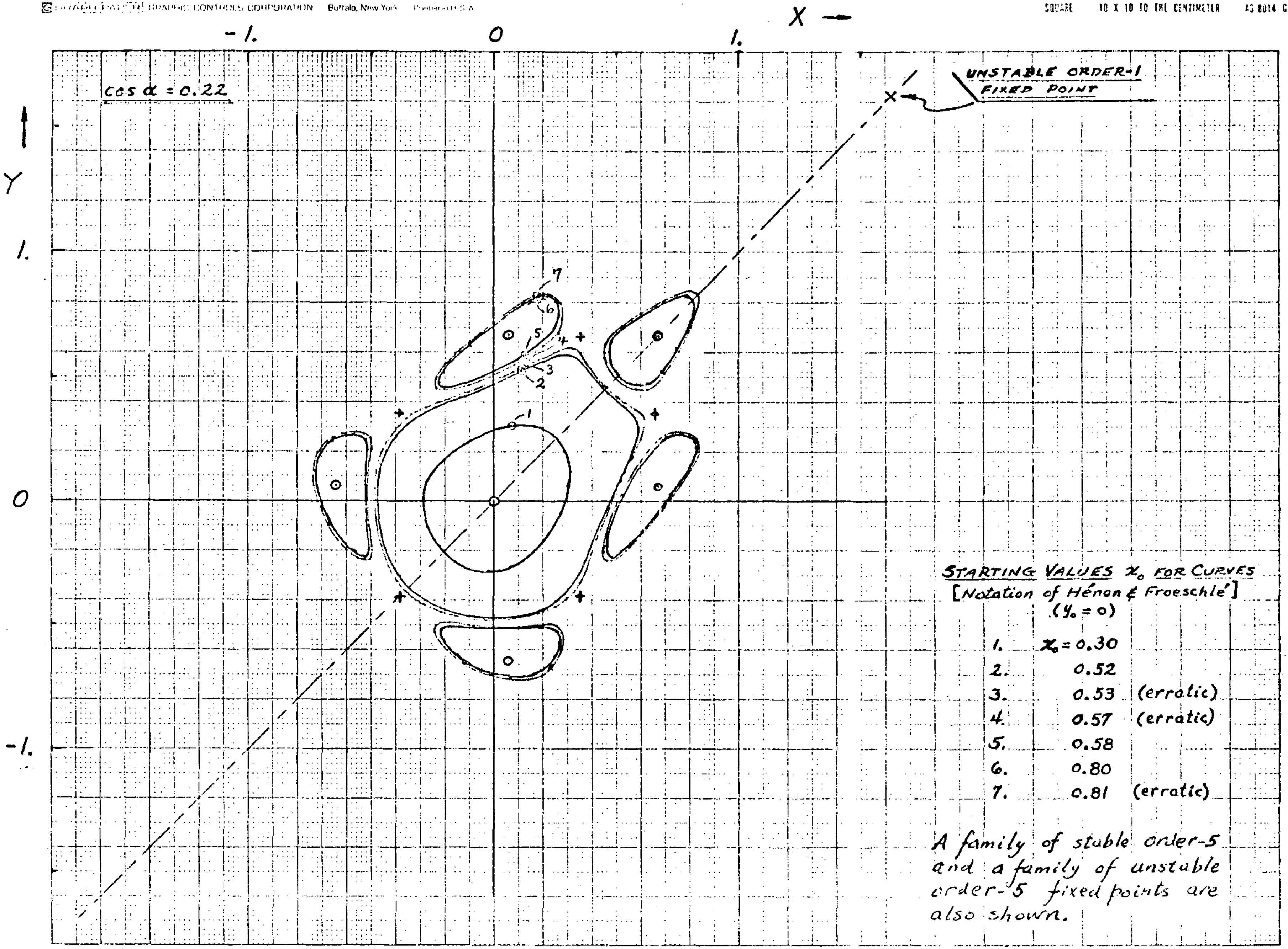

STARTING VALUES x_0 FOR CURVES
[Notation of Hénon & Froeschlé]
($y_0 = 0$)

1.	$x_0 = 0.30$	
2.	0.52	
3.	0.53	(erratic)
4.	0.57	(erratic)
5.	0.58	
6.	0.80	
7.	0.81	(erratic)

A family of stable order-5 and a family of unstable order-5 fixed points are also shown.

SQUARE 10 X 10 TO THE CENTIMETER AS-8014-G7
GRAPHIC CONTROLS CORPORATION Buffalo, New York Printed in U.S.A.

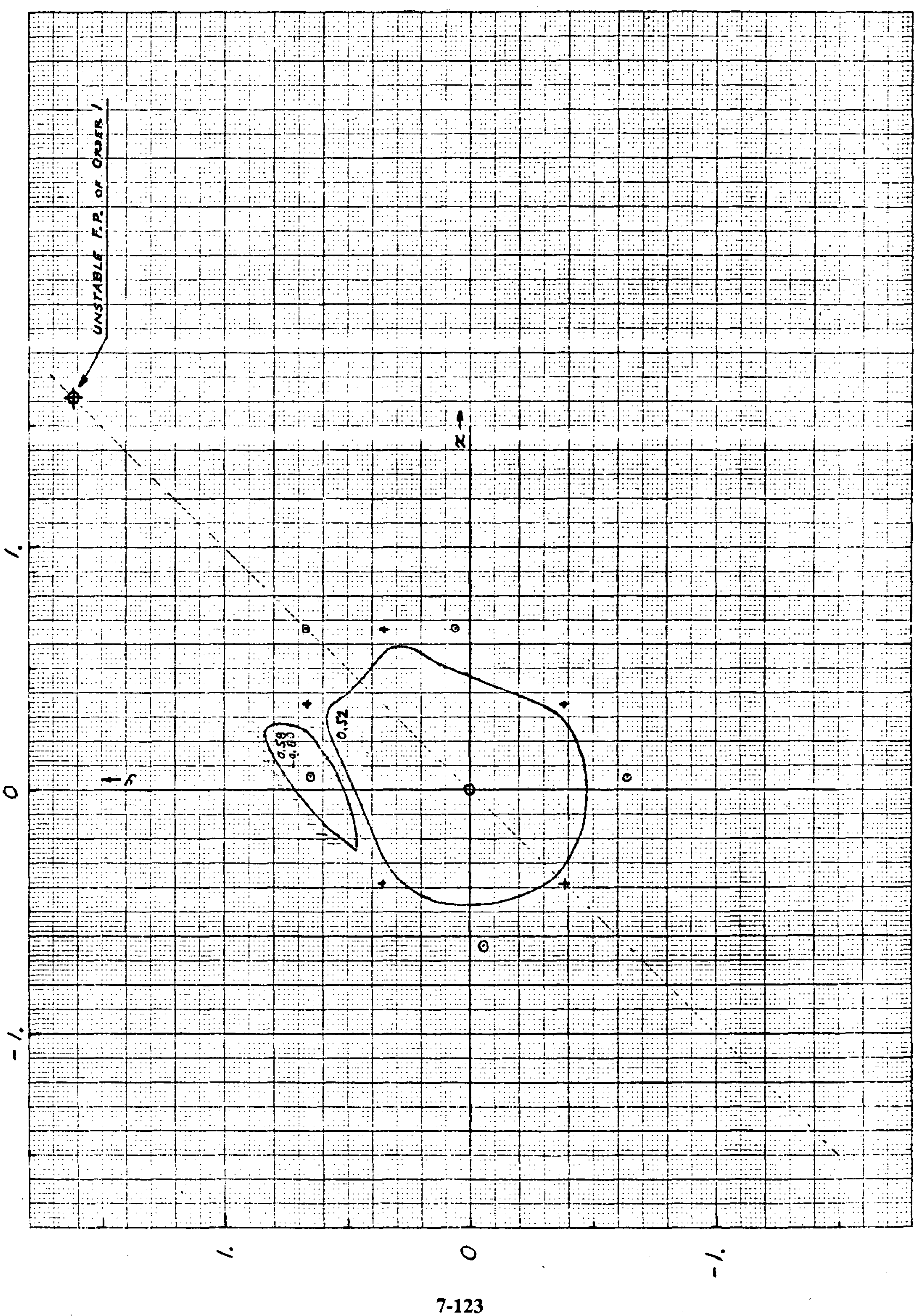

$$Y_o = \frac{x_o}{\sqrt{\sin\alpha}}\ , \quad X_o = \frac{\cos\alpha}{\sqrt{\sin\alpha}} \quad x_o = Y_o \cos\alpha$$

of course show the same behavior when introduced into the McMillan form of the transformation under consideration.

$$\begin{pmatrix} 0.118055 \\ 0.536614 \end{pmatrix} \lessapprox \begin{pmatrix} X \\ Y \end{pmatrix} \lessapprox \begin{pmatrix} 0.126965 \\ 0.577114 \end{pmatrix} \quad \text{and} \quad \begin{pmatrix} 0.180424 \\ 0.820109 \end{pmatrix} \lessapprox \begin{pmatrix} X \\ Y \end{pmatrix}.$$

The starting point $x_o = 0.30$, $y_o = 0$, for which some specific detailed results are given by Froeschlé in Ref. 1, corresponds essentially to

$$X \doteq 0.06682367053919, \qquad Y \doteq 0.30374395699631$$

and exhibits very smooth behavior.

We have made computational runs -- usually of 2000 iterations duration, unless terminated (in a case corresponding to $x_o = 0.55$, $y_o = 0$) by $|Y|$ becoming very large $(|Y| > 10^{160})$ -- for starting values similar to those mentioned above, namely for X_o, Y_o corresponding to $y_o = 0$ and

$$x_o = 0.30;\ 0.52,\ 0.53,\ \ldots\ 0.57,\ 0.58;\ 0.80,\ 0.81$$

The quantity $\psi_n = \log_{10}|\lambda|$ (when $|\mathrm{HTR}| \geqslant 1$) and the <u>sign</u> of λ (LF = sign of HTR) were printed, but with a diagnostic warning and a re-initialization of the cumulative matrix $\begin{pmatrix} A & B \\ C & D \end{pmatrix}$ to the unit matrix $\begin{pmatrix} 1 & 0 \\ 0 & 1 \end{pmatrix}$ whenever the determinant $\begin{vmatrix} A & B \\ C & D \end{vmatrix}$ came to differ from unity (as a result of the matrix elements themselves becoming very large) by as much as 10^{-9}. There also was exercised an option to print growth factors for cumulative differential distance growth:

$$[(\partial X_n/\partial X_o)^2 + (\partial Y_n/\partial X_o)^2]^{\frac{1}{2}} = \sqrt{A^2+C^2} \quad ,$$

$$[(\partial X_n/\partial Y_o)^2 + (\partial Y_n/\partial Y_o)^2]^{\frac{1}{2}} = \sqrt{D^2+B^2} \quad ,$$

(and their common logarithms), although these quantities are not invariant to a canonical change of variables (as, for example, a simple scaling of X by a constant factor and of Y by the reciprocal of that factor) and also, in fact, their logarithms do not differ markedly (understandably) from $\psi = \log|\lambda|$ when ψ is large.

We tabulate below an account of these various runs (in which, of course, printing was not requested at each iteration). Tests of program accuracy with respect to co-ordinate values (X,Y) were made by repeating a run and introducing noise (uniform, in the range $\pm 0.5 \times 10^{-28}$) into each of the co-ordinates after each iteration and examining the resultant difference in the co-ordinate values at the end of the two runs. Throughout all these runs (including those in which phase plots were definitely erratic and suggested a stochastic behavior) the sign of λ_n [LF = Sign (HTR)] continued to flip, so that the true stochastic behavior required for a C-system (a lower positive bound to λ_n)(7) does not appear to be established.

x_o (with $y_o=0$)	Length of Run (Iterations)	Did $\lvert DET-1 \rvert$ exceed 10^{-9}?(a)	Co-ordinate Error at End of Run(b)	$\psi_n = \log_{10} \lvert \lambda_n \rvert$ near End of Run(c)
0.30	10000	No	6×10^{-24}	> 2, (2.6)
0.52	2000	No	6×10^{-25}	2, (2.7)
0.53	2000	No	1×10^{-24}	2 to 3, (2.9)
0.54	2000	Yes, @ N=998	1×10^{-8}	- - -
0.55	970	Yes, @ N=484(us)	- - -	Co-ordinates became large
0.56	2000	Yes, @ N=763	6×10^{-5}	- - -
0.57	2000	No	6×10^{-24}	3, (3.8)
0.58	2000	No (us)	7×10^{-22}	6, (6.8)
0.80	2000	No	8×10^{-27}	≃ 1, (1.4)
0.81	2000	No	1×10^{-19}	8, (8.6)

(a) If Yes, the cumulative tangential-mapping matrix $\begin{vmatrix} A & B \\ C & D \end{vmatrix}$ was re-initialized.

(b) The *larger* of the errors in X and in Y, resulting from noise.

(c) Estimated typical value, for runs in which matrix not re-initialized.

As a partial check of the work, graphs similar to those published by Froeschlé (Ref. 1, Figs. 2 and 4a) were constructed, and appeared to depict results in complete agreement with those curves. Specifically, the graph of our Fig. 2 shows the evolution of the Cesaro mean μ, through 10000 iterations, for $x_o = 0.3$, $y_o = 0$ (and $\cos \alpha = 0.22$), and is to be compared with Froeschlé's Fig. 2. Likewise, our Figs. 3 & 4 show μ *vs.* x_o, as evaluated after 200, 300, 500, 900, 1000, 2000, 5000, and 10000 iterations -- of which the results for $n = 2000$ (on our Fig. 4) may be compared with the corresponding curve of Froeschlé's Fig. 4a.

It has seemed of interest also to construct curves showing the evolution of μ, vs. n, for a sequence of starting values x_o (with $y_o = 0$), namely $x_o = 0.20$, 0.30, 0.40, 0.50, 0.52, 0.53, 0.54, 0.55, 0.56, 0.57, 0.58, 0.60, 0.70, 0.80, and 0.81 -- see Figs. 5-8. Computation of results required for such plots was terminated if $|HTR - 1| \geqslant$ TEST, with TEST normally taken to be 10^{-9} although some dotted-line extentions of the results were obtained (for Fig. 7) by setting TEST = 5.0×10^{-5}.

As noted by Froeschle′,(1) the use of the Cesaro mean, μ, for constructing such plots (or, perhaps preferably, use of the similar quantity μ^* introduced in Sect. IV, p. 20, of Ref. 1) certainly removes the distressing fluctuations that would be seen on plots of Ψ or of θ vs. n. It may be noteworthy, however, that the plot of μ vs. n for $x_o = 0.53$ -- a case for which erratic phase plots have been obtained(1) -- appears to show a monotonic decrease of μ with increasing n, extending from $n \cong 60$ through to the end of the run (n = 10000). This behavior seems somewhat at variance with that seen by Froeschle′ for his transformation T_2, in which a run leading to "ergotic" coverage of the phase plane appeared to give values of μ^* (and of θ) that did not tend to zero (see upper curves on Fig. 1 of Ref. 1). Returning to the transformation under consideration in the present Note (equivalent to Froeschle′'s transformation T_1), we also notice from Fig. 7 that the curve of μ vs. n for the starting condition $x_o = 0.57$ -- that also exhibits erratic phase-plane behavior -- shows a slow rise (at a very modest rate) only after the computations have progressed to fairly large n values. μ vs. n plots of other cases leading to erratic behavior (e.g., with $x_o = 0.54$, 0.56, and 0.81), moreover, fail to provide any clear evidence of "leveling off" before it was judged advisable to terminate computation of μ in the interest of computational accuracy (as judged by $|HTR - 1|$).

In view of the remarks of the preceding paragraph, it may be suspected that the Cesaro mean, as introduced by Froeschle´,(1)

$$\mu_n = \frac{1}{n} \sum_{m=1}^{n} \theta_m ,$$

is a bit sluggish in its response to changes (e.g., to growth) of θ_m or of ψ_m. A possible alternative indicator, namely

$$\nu_n = \frac{\sum_{m=1}^{n} e^{-\frac{n-m}{\tau}} \theta_m}{\sum_{m=1}^{n} e^{-\frac{n-m}{\tau}}} ,$$

$$= \frac{\sum_{m=1}^{n} e^{-\frac{n-m}{\tau}} \frac{\log_{10}|\lambda|_m}{m}}{\sum_{m=1}^{n} e^{-\frac{n-m}{\tau}}} ,$$

might serve desirably to give relatively greater emphasis to recent values of θ -- taking, for example, $\tau = 50$ (iterations). For comparison with some of the results obtained for μ, we have made evaluations of υ_n (as defined above) for $x_o = 0.52, 0.53, \ldots 0.58, 0.80$, and 0.81 -- taking $1/\tau = 0.02$ (and $\cos \alpha = 0.22$, as before).

The results, in the form of plots of ν vs. n -- Figs. 9-11 -- may be compared with those given previously for μ vs. n on similar scales (Figs. 6-8). Plotting typically was at intervals of 50, 100, or 200 iterations as the runs progressed, and the fluctuations do not generally appear to be particularly troublesome in the plots of ν vs. n. The greater responsiveness of the ν vs. n graphs is apparent and may be helfpul -- thus the runs begun with $x_o = 0.52$ and with $x_o = 0.53$ are seen to drop to lower values during the course of 10000-iteration runs and, indeed, show less distinction between them (despite the erratic character assigned to the phase plots of the $x_o = 0.53$ run). The succeeding runs -- with x_o = .54, 0.55, 0.56, and 0.57 -- also are more responsive, so that their eventual up-turns may be more evident. Similarly, in the final two runs of this sequence, that commenced with $x_o = 0.80$ clearly drops further on the ν vs. n plots and the run with $x_o = 0.81$ gives some indication of a developing upward trend before evaluations of $\log_{10} |\lambda|$ were terminated. It is of interest to note [see Ref. 9, Sect. 4 (which refers in that Section to a pair of non-linear differential equations derived from a time-independent Hamiltonian function) -- esp. the two paragraphs beginning near the bottom of p. 8 and continuing through p. 10] that an approach of an eigenvalue pair (λ_1 & $\lambda_2 = 1/\lambda_1$) to a common value of magnitude unity can be associated with a confluence of eigenvector directions, since the eigenvector slopes are given(9,6) by $\frac{\lambda - A}{B}$. The general circulation of points within or around the quite simple phase diagram shown as Fig. 1 in Ref. 9 appears to be sufficient reason to cause, in that case, such confluences to occur (more frequently when the circulation about the phase plane is more rapid) and in $\ln |\lambda_1|$ having no positive lower bound.

In conclusion, we may say that the evolution of the Cesaro mean μ, employed by Froeschle´, or (perhaps preferably) the evolution of the similar quantity ν suggested here, provides a helpful indication of the development of the magnitude of the (greater) eigenvalue of the cumulative tangential-mapping matrix. From the examples rpeorted in the present note, however, graphs of such quantities evidently do not always provide a completely clear early means of distinguishing runs leading to apparently stochastic phase plots from those that do not -- see, for example, our graphs pertaining to a run commenced with $x_o = 0.53$ and $y_o = 0$.

Of particular significance, moreover, may be observation that in all the cases examined there continued to be reversals in the sign of the eigenvalue, so that the motion under examination can be said to be not strictly that of a C-system. Such sign reversals have been seen also to occur in previous studies -- both with non-linear area-preserving algebraic transformations (with or without the region of interest enclosed by a firm separatrix)(8) and also for a non-linear pair of first-order Hamiltonian differential equations (with or without explict time dependence in the equations).(9)

References

1. C. Froeschlé, Astron. & Astrophys. 9, 15 (1970).
2. C. Froeschlé & J.-P. Scheidecker, J. Comput. Phys. 11, 3 (1973).
3. C. Froeschlé & J.-P. Scheidecker, Paper IV-1 (Session IV, 15 Sept. 1973) of the International Conference on Point Transformations and their Applications (Laboratory of Automation and of System Analysis, Toulouse, France; 10-14 Sept. 1973).
4. M. Hénon, Q. Appl. Math. 27, No. 3 (1969).
5. E. M. McMillan, in "Topics in Modern Physics -- A Tribute to Edward U. Condon." (Colorado Assoc.University Press, Boulder, Colo.; 1971).
6. The eigen-vector slopes are given by

$$\frac{dy}{dx} = \frac{\lambda - A}{B} = \frac{C}{\lambda - D}$$

[and when $A = 0$ and $B = 1$ are simply given by $\frac{dy}{dx} = \lambda$ (with the two values of λ of course constituting a reciprocal pair)].
7. The writer is indebted to Mr. Paul J. Channell (LBL) for advice on this point concerning C-system properties.
8. See ERAN-224 (U.C. Lawrence Berkeley Laboratory, Berkeley California; January 1974) and a related similar report now in preparation.
9. ERAN-223 (U.C. Lawrence Berkeley Laboratory, Berkeley, California; 26 November 1973).

Fig. 2.

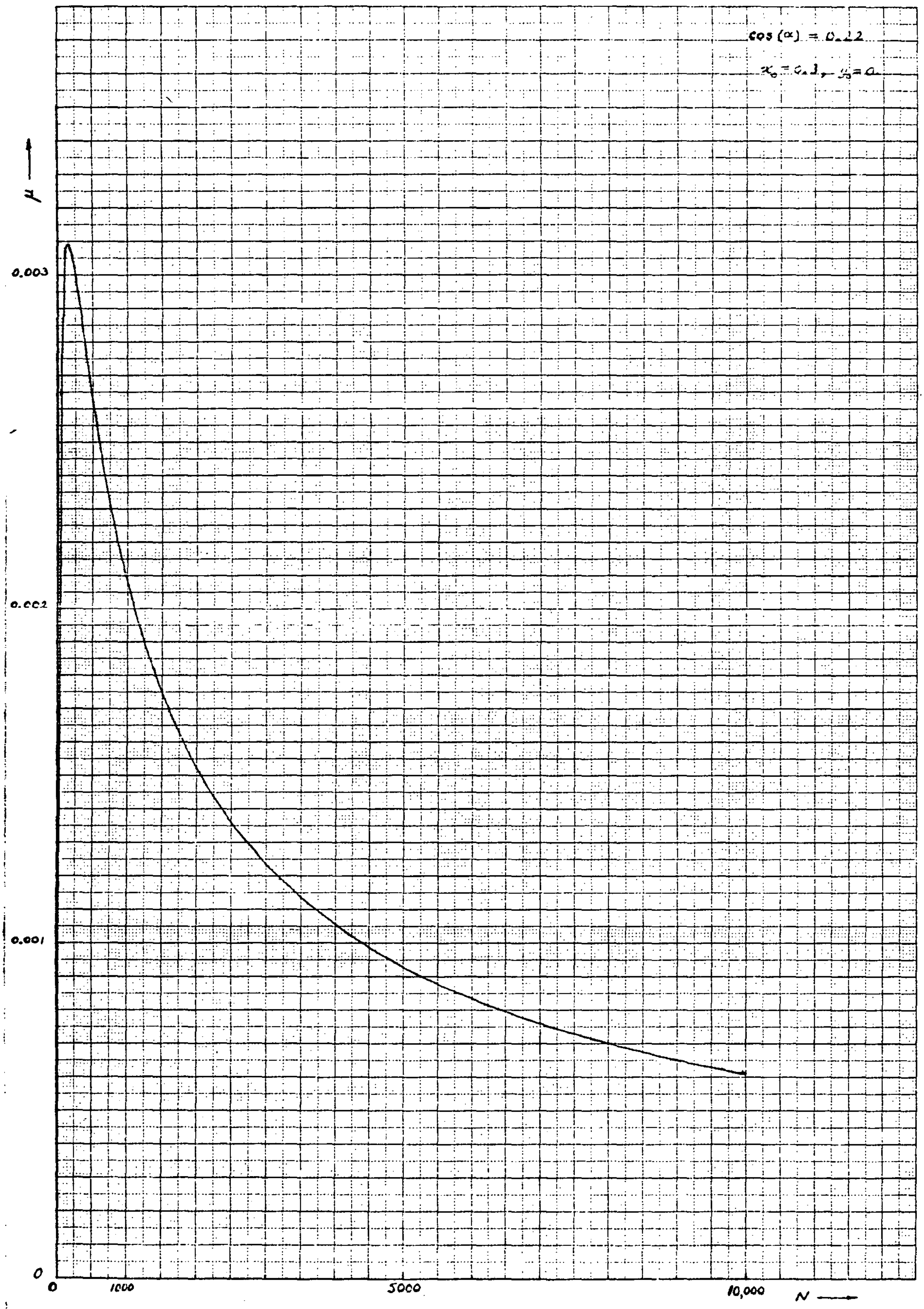

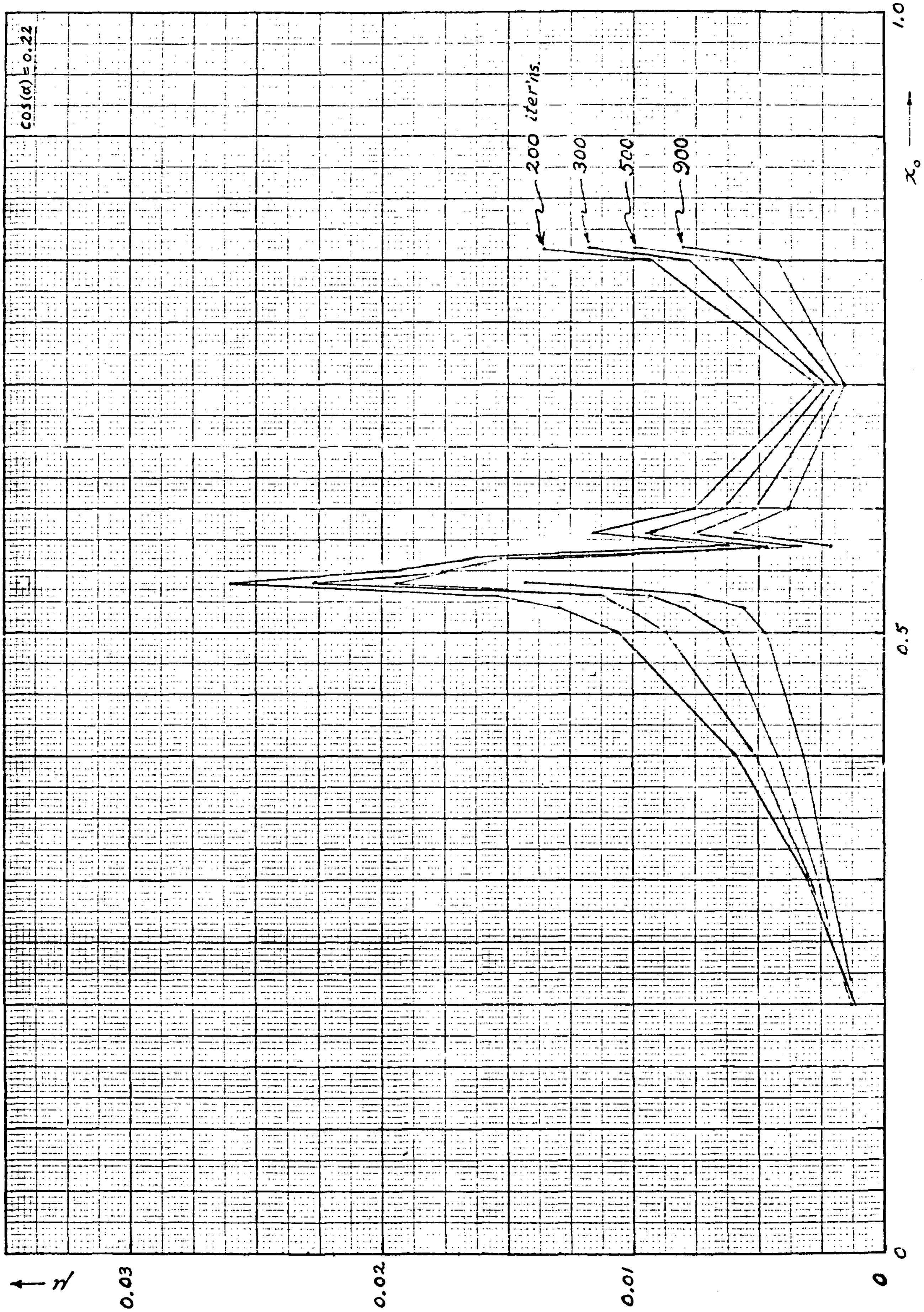

FIG. 3.

K&E 20 X 20 TO THE INCH 46 1240
7 X 10 INCHES MADE IN U.S.A.
KEUFFEL & ESSER CO.

K+E 20 X 20 TO THE INCH 46 1240
7 X 10 INCHES MADE IN U.S.A.
KEUFFEL & ESSER CO.

FIG. 4.

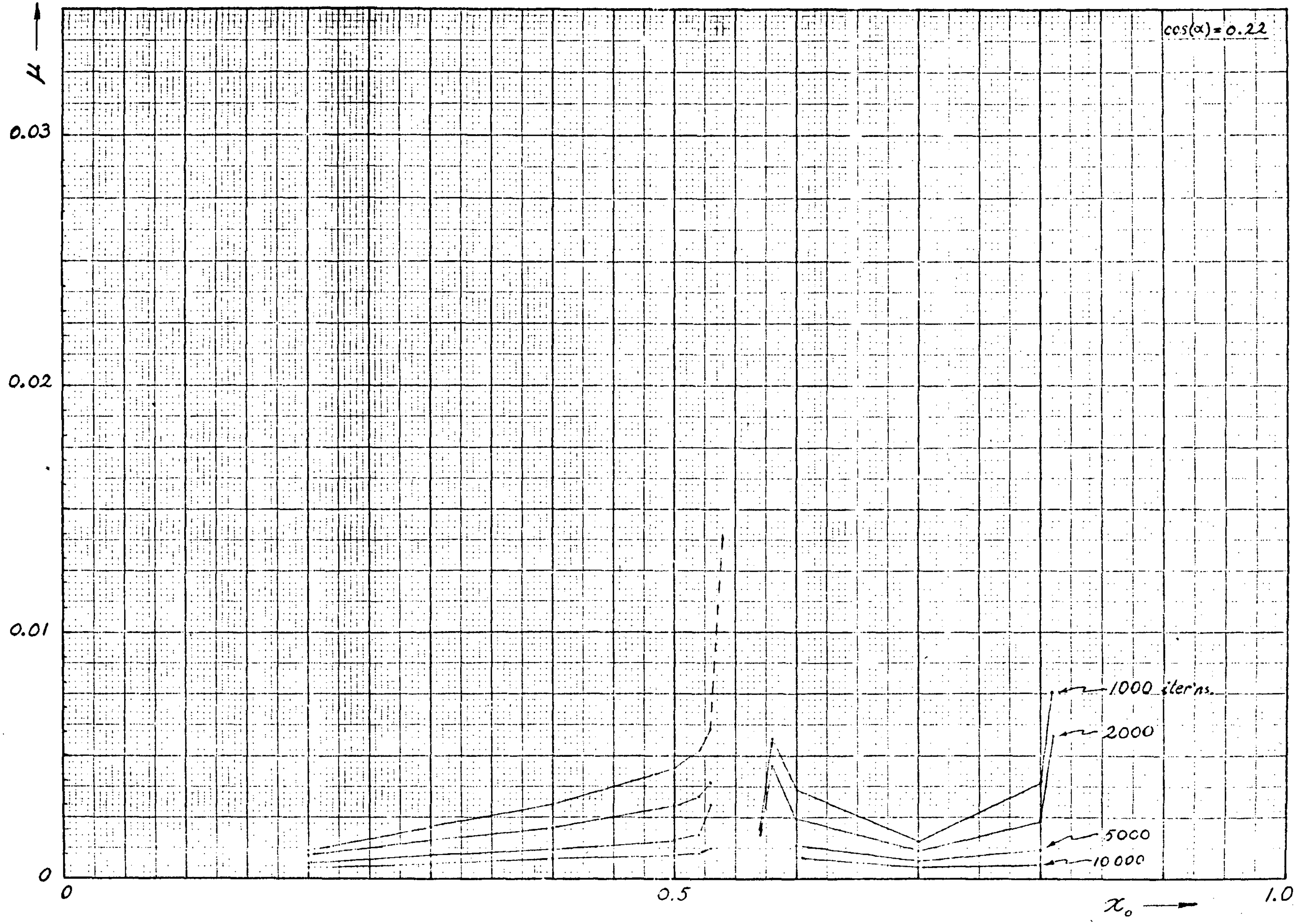

Fig. 5.

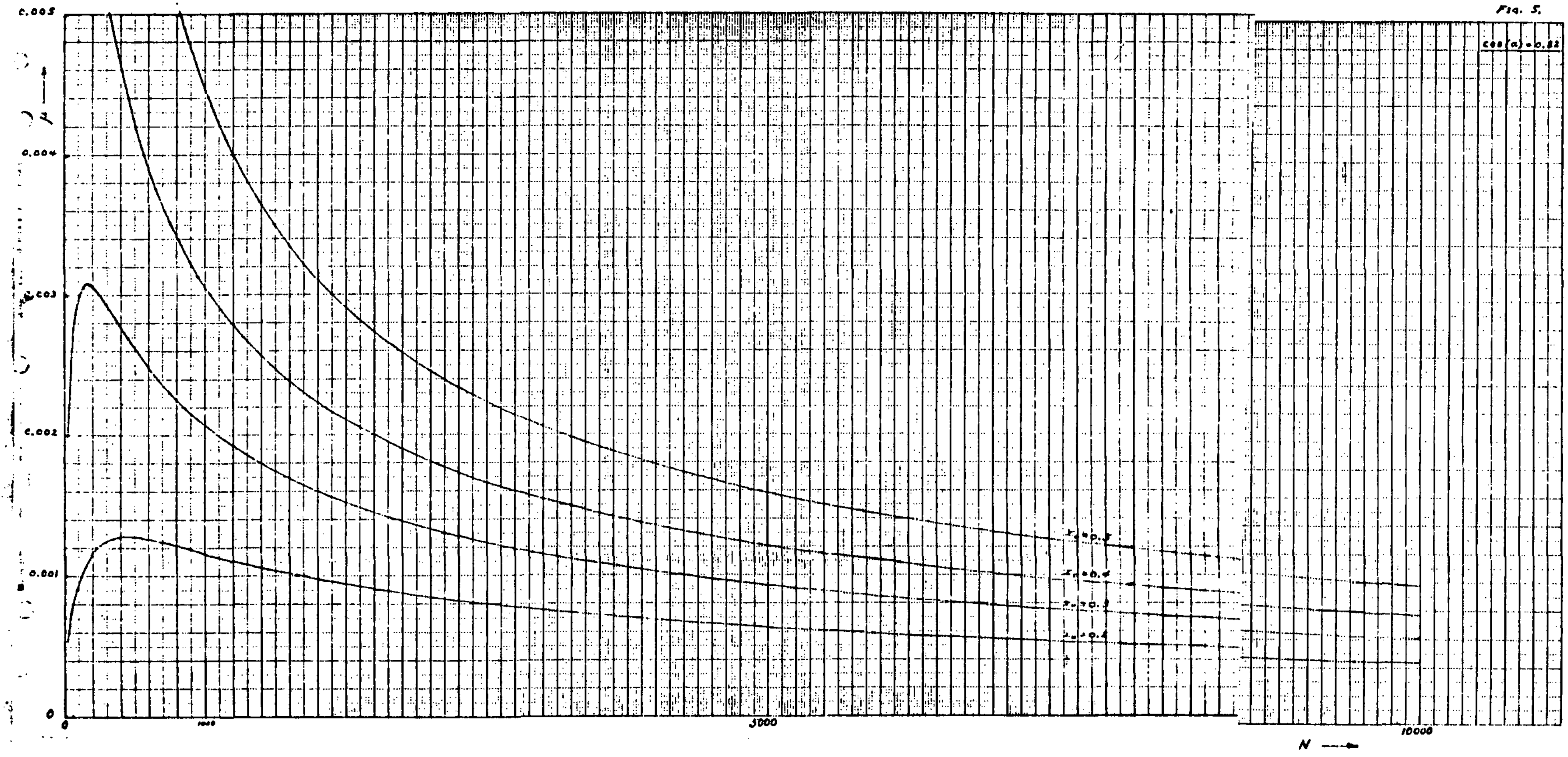
cos (α) = 0.82
$x_r = 0.5$
$x_r = 0.6$
$x_r = 0.7$
$x_r = 0.8$
λ
0.005
0.004
0.003
0.002
0.001
0
1000
5000
10000
N

Fig. 6.

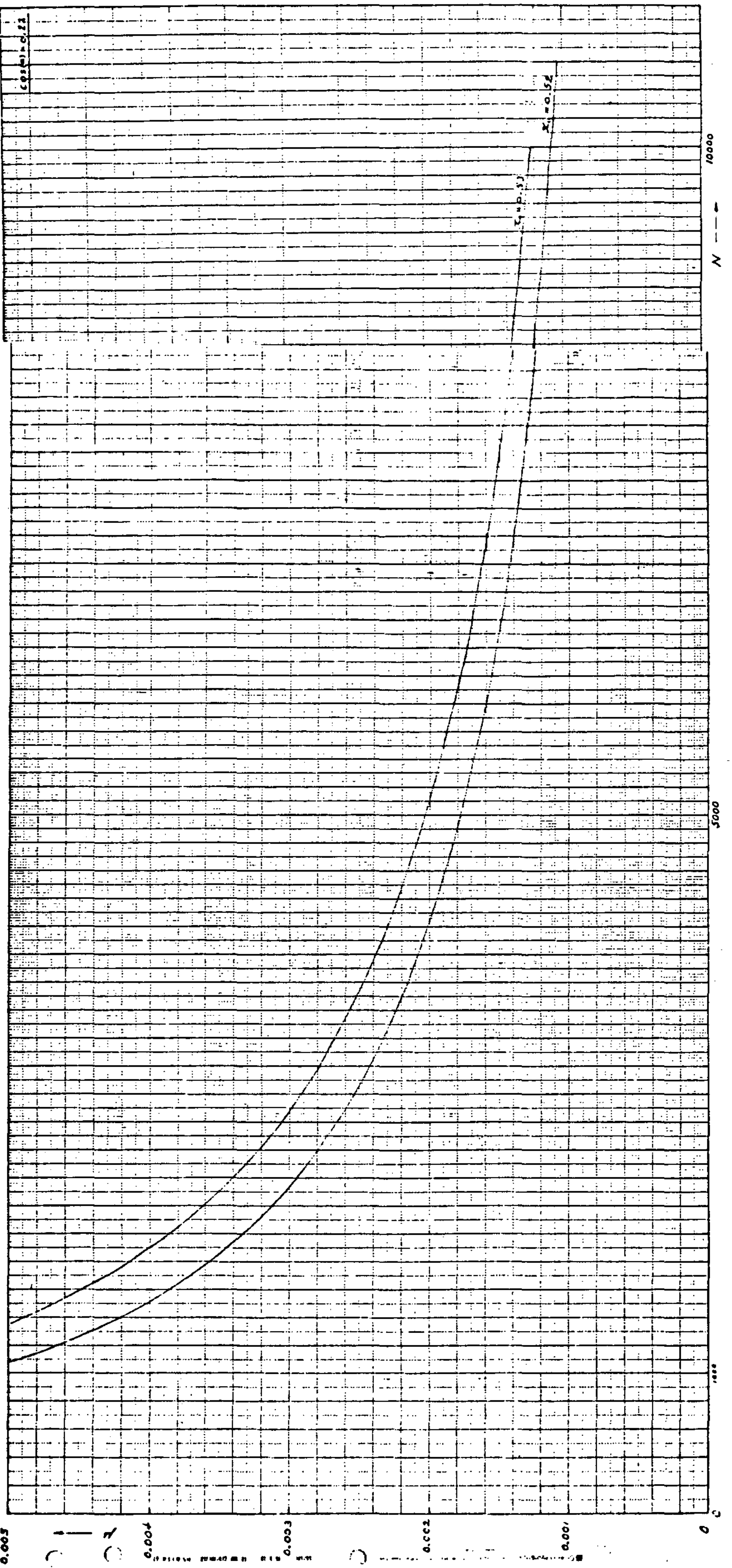
$C_{DS}(m) = 0.22$
$x_1 = 0.53$
$x_1 = 0.52$
10000
5000
1000
0
N ⟶
0.005
0.004
0.003
0.002
0.001
0
⟵ γ

FIG. 7.

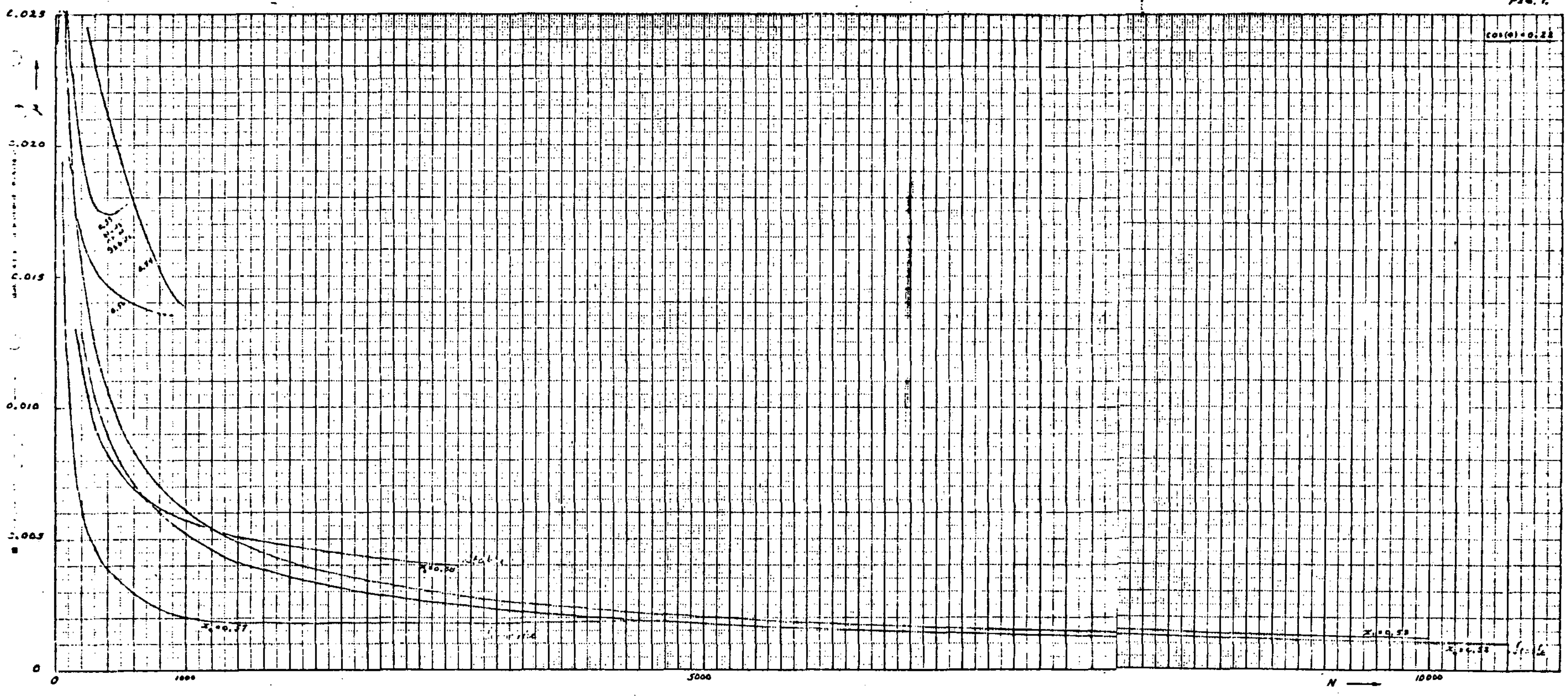
cos(φ) = 0.28
0.025
λ
0.020
0.015
0.010
0.005
0
0
1000
5000
N
10000
0.44
0.33
0.40
x₁ = 0.50
x₁ = 0.37
x₁ = 0.53
x₁ = 0.28

FIG. 8.


cos(α) = 0.22
0.025
0.020
0.015
0.010
0.005
0
μ
0
1000
5000
10000
N
$x_0 = 0.81$
blows up at 3019 lbs.
$x_0 = 0.60$
$x_0 = 0.60$
$x_0 = 0.70$

FIG. 9.

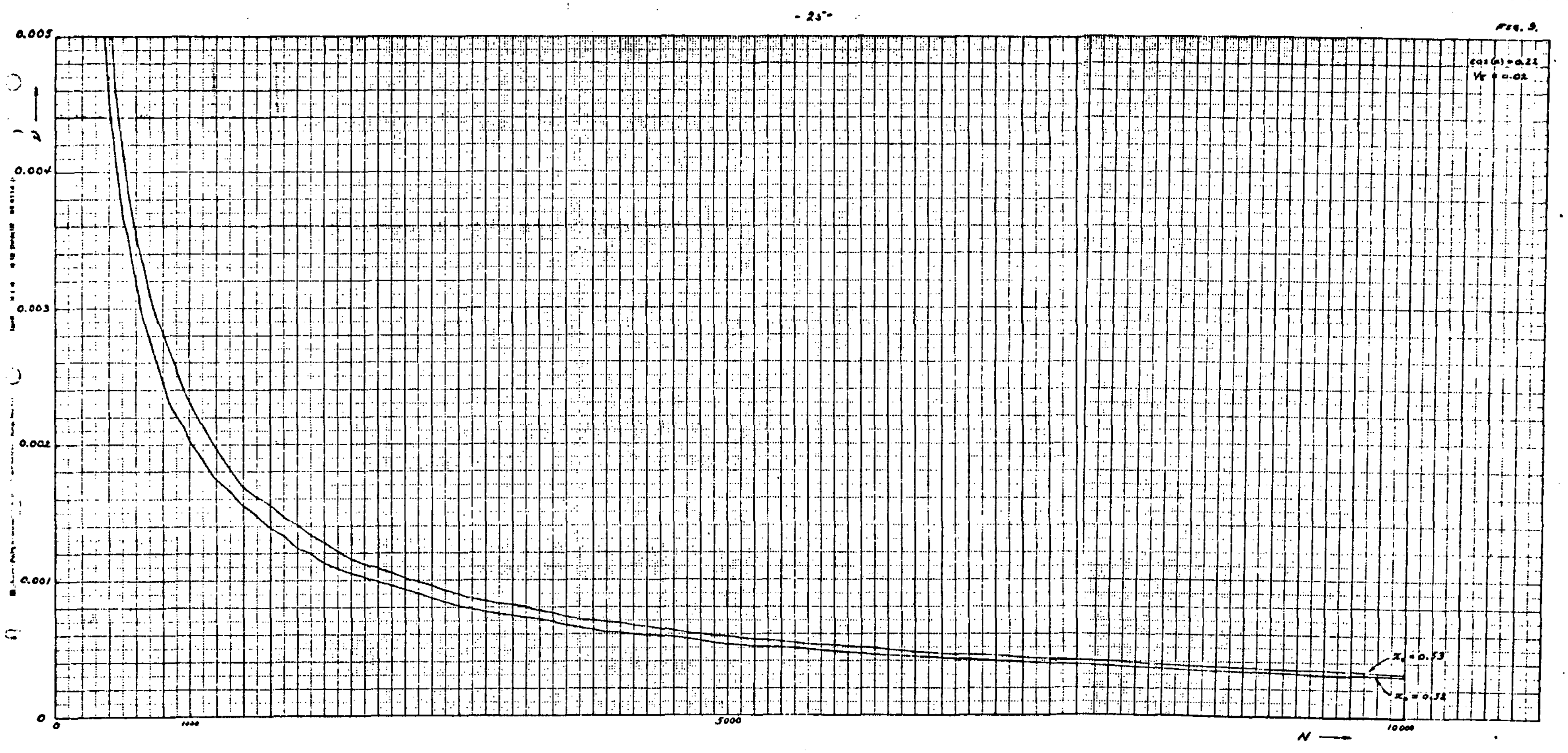
- 25" -
cos(α) = 0.22
V/s = 0.02
λ →
0.005
0.004
0.003
0.002
0.001
0
0
1000
5000
10000
N →
$x_0 = 0.53$
$x_0 = 0.52$

Fig. 10.


cos(μ) = 0.22
Y_f = 0.02
λ
0.025
0.020
0.015
0.010
0.005
0
0
1000
5000
10000
N
X_0 = 0.53
X_0 = 0.56
X_0 = 0.54
X_0 = 0.58
X_0 = 0.57

FIG. 11.

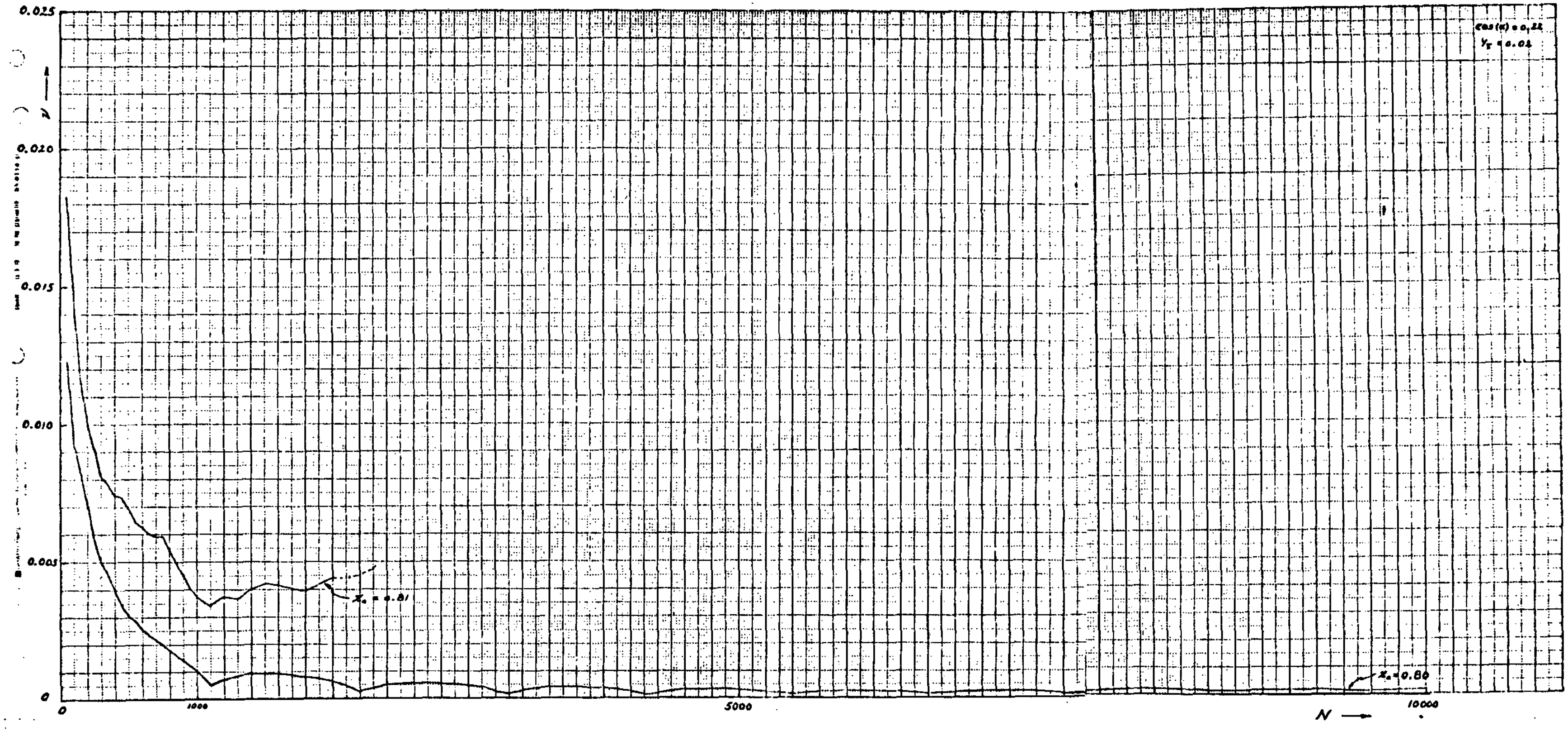
$\cos(\alpha) = 0.22$
$y_T = 0.02$
λ →
0.025
0.020
0.015
0.010
0.005
0
0
1000
5000
10000
N →
$x_0 = 0.81$
$x_0 = 0.80$

On A Form of McMillan's Transformation Suggested by P. Channell*

L. Jackson Laslett

Lawrence Berkeley Laboratory
University of California
Berkeley, California

April 19, 1974

Paul Channell has indicated an interest in the McMillan transformation

$$\left.\begin{aligned} x' &= y \\ y' &= -x + f(y) \end{aligned}\right\}$$

in which, in particular, he proposes taking the function f to be such that

$$f(\xi) = \xi^2 + \sqrt{\xi} .$$

Since $f(\xi)$ can be written in this case as

---

* Work supported by the U.S. Atomic Energy Commission.

$$f(\xi) = \phi(\xi) + \phi^{-1}(\xi),$$

where $\phi(\xi) = \xi^2$, the condition expressed by Eqn. (11) of McMillan's Chapter in the Condon Festschrift is fulfilled and we have the assured firm invariant curves (parabolas)

$$y = x^2$$

and

$$x = y^2$$

connecting the order-1 fixed points at 1,1 and at 0,0 (as is readily confirmed).

Within these boundaries we have the order-1 fixed points on the principal diagonal:

$$x,y:\ (3 - \sqrt{5})/2 \cong 0.381966$$
$$0.$$
$$1.$$

and outside,

$$(3 + \sqrt{5})/2 \cong 2.618034$$

The differential transformation is characterized by the matrix

$$\begin{pmatrix} 0 & 1 \\ -1 & f'(y) \end{pmatrix} = \begin{pmatrix} 0 & 1 \\ -1 & 2y + \dfrac{1}{2\sqrt{y}} \end{pmatrix},$$

with a half-trace

$$\text{htr} = y + \frac{1}{4\sqrt{y}} \, .$$

The values of htr at the three interior order-1 fixed points listed are

$$\frac{13 - 3\sqrt{5}}{8} \cong 0.78647451$$

$$\infty$$

$$5/4.$$

For the first of these, we have cos $\mu = 0.78647451 \cdots$ and

$$\mu \cong 0.106 \; (2\pi) = 0.106 \text{ osc.};$$

For the fixed points at 0,0 & 1,1 there are the respective (growing) eigenvalues and eigenvector slopes

$$dy/dx = \lambda = [\text{htr}] + \sqrt{[\text{htr}]^2 - 1} = \begin{array}{c} \infty \\ 2 \end{array} .$$

Within the area bounded by the curves

$$y = x^2$$

and

$$x = y^2$$

many apparantly smooth invariant curves appear to exist [Interactive TTY Program FIRMB]. Some complexity has appeared to arise, however, as a result of some order-22 fixed-point systems that have been found to occur. Approximate co-ordinates for the fixed points of the stable and unstable order-22 fixed-point systems are appended. To determine whether phase-plane trajectories launched in the neighborhood of one of these unstable order-22 fixed points exhibit erratic behaviour may require careful attention to the accuracy of (double-precision) computations performed in this region of the phase plane, since it has been found (Program FIRMB) that significant vlaues for phase-plane coördinates are obtained (with double precision) in this region only for computational runs that do not exceed some 6000 iterations.

STABLE ORDER-22 FIXED POINTS

```
0.990838351
0.990838351

 N        X             Y             A OR C        B OR D      LOG 10 LAM   LF

    0  9.9084E-01    9.9084E-01    1.0000E+00    0.            0.             1
                                   0.            1.0000E+00

    1  9.9084E-01    9.8633E-01

    2  9.8633E-01    9.7515E-01

    3  9.7515E-01    9.5209E-01

    4  9.5209E-01    9.0707E-01

    5  9.0707E-01    8.2309E-01

    6  8.2309E-01    6.7766E-01

    7  6.7766E-01    4.5932E-01

    8  4.5932E-01    2.1105E-01

    9  2.1105E-01    4.4629E-02

   10  4.4629E-02    2.1917E-03

   11  2.1917E-03    2.1917E-03

   12  2.1917E-03    4.4629E-02

   13  4.4629E-02    2.1105E-01

   14  2.1105E-01    4.5932E-01

   15  4.5932E-01    6.7766E-01

   16  6.7766E-01    8.2309E-01

   17  8.2309E-01    9.0707E-01

   18  9.0707E-01    9.5209E-01

   19  9.5209E-01    9.7515E-01

   20  9.7515E-01    9.8633E-01

   21  9.8633E-01    9.9084E-01

   22  9.9084E-01    9.9084E-01
```

```
N =      0,    X = 9.90838351000E-01   Y = 9.90838351000E-01

N =     22,    X = 9.908383513509446439264231372D-01
               Y = 9.908383509714732546699412460D-01

N =     22,    X = 9.90838351351E-01   Y = 9.90838350971E-01

               A = 8.62923092694E-01   B = -9.29856723477E-01
               C = 9.29856836676E-01   D = 1.56869562891E-01
             DET = 1.00000000000E+00
      LOG 10 LAM = 0.                 LF = 1
```

UNSTABLE ORDER-22 FIXED POINTS

```
 FOR Y=0.5*F, TYPE 1 -- OTHERWISE 0
1!

 TYPE INITIAL X (F-FORMAT ONLY)
0.00065558151!

     N        X            Y           A OR C      B OR D     LOG 10 LAM  LF

     0  6.5582E-04  1.2805E-02  1.0000E+00  0.           0.           1
                                0.          1.0000E+00

     1  1.2805E-02  1.1267E-01

     2  1.1267E-01  3.3555E-01

     3  3.3555E-01  5.7919E-01

     4  5.7919E-01  7.6096E-01

     5  7.6096E-01  8.7220E-01

     6  8.7220E-01  9.3369E-01

     7  9.3369E-01  9.6585E-01

     8  9.6585E-01  9.8195E-01

     9  9.8195E-01  9.8931E-01

    10  9.8931E-01  9.9142E-01

    11  9.9142E-01  9.8931E-01

    12  9.8931E-01  9.8195E-01

    13  9.8195E-01  9.6585E-01

    14  9.6585E-01  9.3369E-01

    15  9.3369E-01  8.7220E-01

    16  8.7220E-01  7.6096E-01

    17  7.6096E-01  5.7919E-01

    18  5.7919E-01  3.3555E-01

    19  3.3555E-01  1.1267E-01

    20  1.1267E-01  1.2805E-02

    21  1.2805E-02  6.5582E-04

    22  6.5582E-04  1.2805E-02
```

```
N =       0,    X =  6.5581510000E-04  Y =  1.2804658614E-02


N =      22,    X =  6.5581507766499782283032908804D-04
                Y =  1.2804652902684695825924719991D-02

N =      22,    X =  6.5581507766 5E-04  Y =  1.28046529027E-02
                A =  1.47108266745E+00  B =  1.04677056105E-02
                C =  1.39931852731E+02  D =  1.67547718049E+00

              DET =  1.00000000000E+00
       LOG 10 LAM =  4.45271278648E-01 LF =  1
```

UNSTABLE ORDER-22 FIXED POINTS (with different starting point)

```
 TYPE INITIAL X (F-FORMAT ONLY)
0.9914196378!

     N         X             Y           A OR C         B OR D       LOG 10 LAM   LF

      0  9.9142E-01   9.8931E-01    1.0000E+00    0.              0.             1
                                    0.            1.0000E+00

      1  9.8931E-01   9.8195E-01

      2  9.8195E-01   9.6585E-01

      3  9.6585E-01   9.3369E-01

      4  9.3369E-01   8.7220E-01

      5  8.7220E-01   7.6096E-01

      6  7.6096E-01   5.7919E-01

      7  5.7919E-01   3.3555E-01

      8  3.3555E-01   1.1267E-01

      9  1.1267E-01   1.2805E-02

     10  1.2805E-02   6.5582E-04

     11  6.5582E-04   1.2805E-02

     12  1.2805E-02   1.1267E-01

     13  1.1267E-01   3.3555E-01

     14  3.3555E-01   5.7919E-01

     15  5.7919E-01   7.6096E-01

     16  7.6096E-01   8.7220E-01

     17  8.7220E-01   9.3369E-01

     18  9.3369E-01   9.6585E-01

     19  9.6585E-01   9.8195E-01

     20  9.8195E-01   9.8931E-01

     21  9.8931E-01   9.9142E-01

     22  9.9142E-01   9.8931E-01
```

```
N =  0,         X = 9.91419637800E-01  Y = 9.89306737297E-01

N = 22,         X = 9.914196378113597401189282078D-01
                Y = 9.893067373544913026507419436D-01

N = 22,         X = 9.91419637811E-01  Y = 9.89306737354E-01
                A = 7.38424527951E-01  B = 6.71918003791E-01
                C = 1.15822073528E+00  D = 2.40813962306E+00

              DET = 1.00000000000E+00
       LOG 10 LAM = 4.45272047966E-01 LF = 1
```

```
008. SCALE -- 0.985 TO 0.995
008. 0.99
008. 0.991
008. 0.9908
008. 0.9393,0.9914
008. ORDER 22?
008  STABLE ORDER-22 FP AT CIRCA X=Y=0.990838351
 *ROLLO* DH 02
 ROLLIN COMPLETE M
 KILLED BY REQUEST
JOB ENDED - DISCONNECTED
```

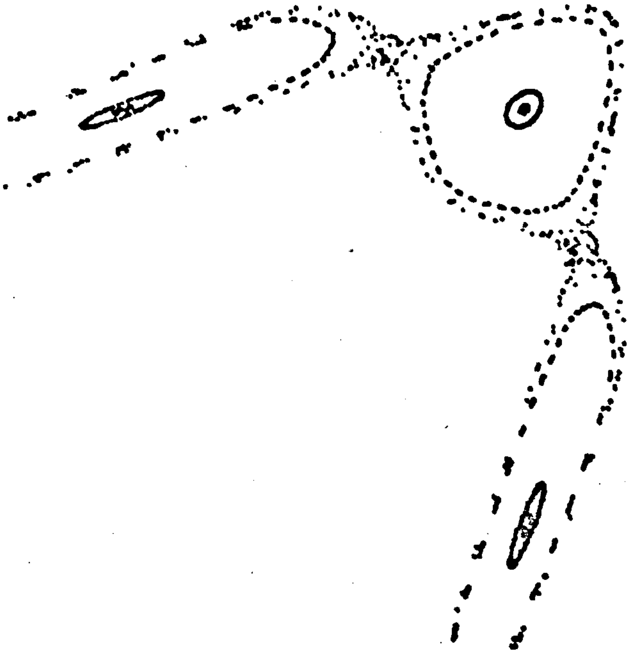

Computations extending the approximate (circa 10D accuracy) outgoing eigenvector direction from the unstable order-22 fixed point at 0.9914196379, 0.9893067373 (approximately) toward the positive principal diagonal (by double-precision computations, as in Program FIRMB)* did suggest, however, that such an extension does not intersect the principal diagonal at right angles (and hence would lead to the development of loops). The results of such computations are conveniently examined through use of the variables

$$SM = \frac{x + y}{\sqrt{2}} \quad \text{and} \quad DF = \frac{x - y}{\sqrt{2}} ,$$

For which one can examine whether or not the extension of the eigenvector direction traverses the line DF = 0 <u>vertically</u>.

The skeptical reader may wish a more thorough examination of this question -- as certainly could be undertaken in an entirely straightforward manner -- but it appears quite likely that loops of increasing elongation will develop as the eigenvector-directions extended approach the mirror point at 0.9893 ···, 0.9914. In the case that has been tentatively examined here, the crossing of the principal diagonal occurs in the neighborhood of x = y = 0.9918 -- <u>i.e.</u>, further from the origin than the stable order-22 fixed point at 0.9908 ···, 0.9908 ··· .

---

[*] The starting values in these computations lay in the range

$0.99141963895 < \chi < 0.9914196407$

$0.9893067405 < \chi < 0.9893067458$

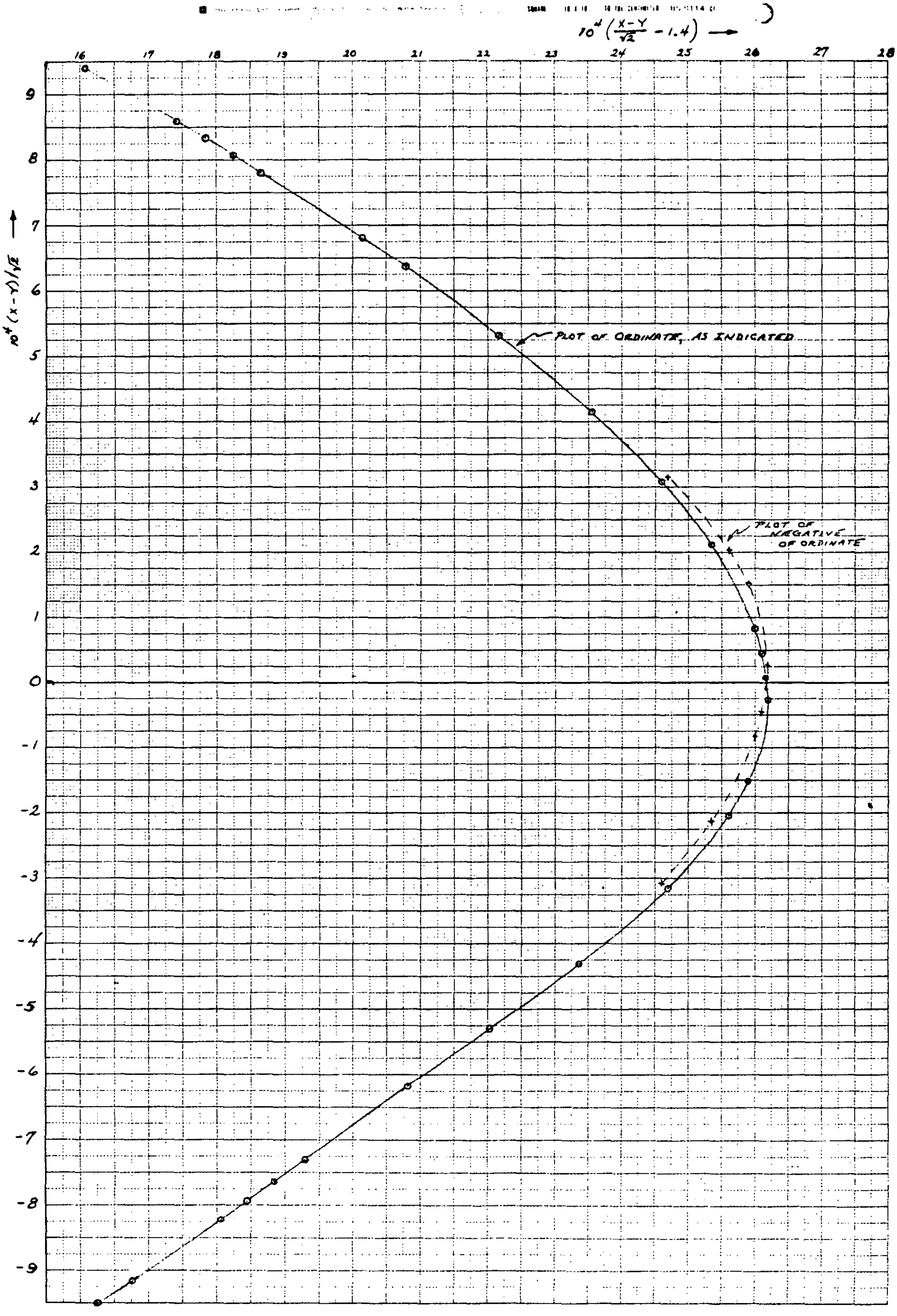

Program FIRMB

Structure in R.F. Phase Plots[*]

ERAN-57 Continued

L. Jackson Laslett

Lawrence Berkeley Laboratory
University of California
Berkeley, California

May 20, 1974

In ERAN-57 we gave some examples of the structure that can develop in R.F. phase plots if the synchrotron oscillations are described (for a coasting beam) not by differential equations of the form

$$\frac{dY}{dn} = - K \sin(\pi X)$$

$$\frac{dX}{dn} = \lambda' Y$$

but by a discrete transformation

$$Y_{n+1} = Y_n - K \sin(\pi X_n)$$

$$X_{n+1} = X_n + \lambda' Y_{n+1}.$$

---

[*] Work supported by the U.S. Atomic Energy Commission

[Here $K = eV_o/E_s$, for $\phi_s = \pi$, and $\lambda' = \lambda/\pi = 2h(dt/t)/(dE/E)$ if we identify X as the electrical-phase error $(\Delta\phi)$ divided by π and Y as $\Delta E/E_s$.] The transformation is seen to be area-preserving, and we accordingly may regard X,Y as a canonically-conjugate pair of variables. The computational results reported in ERAN-57 were confined to examples in which $K/\pi = 0.1$ and $\lambda' = \lambda/\pi = 0.1$

We recently have returned to examine this problem somewhat further, aided by the availability of a TEKTRONICS memory 'scope available for interactive use with the LBL CDC-6600 computer (double-precision program RFBUK). For mathematical or computational reasons it has proven convenient to employ the new variables

$$x = X$$
$$y = Y - \frac{1}{2} K \sin(\pi X)$$

in this recent work, so that, in terms of these new variables, the transformation assumes the form

$$x_{n+1} = x_n + \lambda'[y_n - \frac{1}{2} K \sin(\pi x_n)]$$

$$y_{n+1} = y_n - \frac{1}{2} K [\sin(\pi x_{n+1}) + \sin(\pi x_n)].$$

The change of variables, from X,Y to x,y is characterized by a functional determinant of unity and the transformation written in terms of the new variables again is area preserving. It will be seen that in terms of these new variables possible phase-point trajectories will be symmetrical about both the x- and the y-axes. In execution of the program RFBUK, the generalized coordinate x is moduloed so as always to remain between -1 and +1.

For fixed-points of order-1, such as occur at $\pm 1,0$ (and at $\pm 1, m\frac{2}{\lambda'}$), the eigenvalues are given by

$$\mathrm{EIG}_{1,2} = 1 - Q \pm SQ$$

and the associated eigenvector slopes by

$$(dy/dx)_{1,2} = \pm SQ/\lambda',$$

where

$$Q = \frac{\pi}{2} K\lambda' \cos(\pi x_{FP}) \quad \text{and} \quad SQ = \sqrt{Q(Q-2)}$$

The transformation employed here of course permits harmonic passage through the (thin)cavity, with homologous phase trajectories occurring at intervals $\Delta y = 2/\lambda'$. With $\lambda' = 0.1$ and $K/\pi - 0.1$ (as in ERAN-57), buckets with fairly clean sepatrices (and apparent half-height $\delta y \cong 1.98331$) make their appearance. The eigenvalues and eigenvector slopes associated with the unstable fixed point at -1,0 are, in this case,

$$\mathrm{EIG} = 1.36735945464072 \text{ (and its reciprocal)}$$

and

$$dy/dx = \pm 3.18011432635279,$$

respectively. Additional structures are present in the phase diagram, however, as is illustrated by the order-2 fixed-point systems that develop at $y = 10$. These order-2 systems become more clearly evident on plots made to a larger scale -- the stable fixed points are

$$0,10 \quad \text{and} \quad \pm 1,10,$$

while the unstable fixed points are close to

$$\pm\, 0.507851592430673,\ 10.$$

The apparent separatrix formed by extension of the outgoing eigenvector direction from the fixed point at -1,0 (with $K/\pi = 0.1$ and $\lambda' = 0.1$) is found, on close examination, to be <u>not</u> a simple smooth curve traversing the vertical axis at right angles -- and hence does <u>not</u> join smoothly with the reverse extension of the ingoing eigenvector direction that approaches 1,0. This failure to intersect smoothly is made evident by a large-scale graph showing the extended eigenvector-directions in the immediate neighborhood of the y-axis. [To achieve a reasonable graph, some of the curvature has been removed by plotting

$$y_c = 10^{11}\,(y-1.98330928669 + 2.34117x^2)\ \underline{\text{vs.}}\ 10^5x.]$$

By virtue of the symmetry of the transformation, the reverse extension of the incoming eigenvector direction to 1,0 can be constructed by reversing the sign of x, and it is apparent that the two curves cross at $x = 0$ with an angle $2(dy/dx) \cong 7 \times 10^{-9}$. Such a failure of these curves to join smoothly of course necessarily will require that their further extensions (forward or backward, respectively) will lead to the development of loops that become increasingly slender and elongated -- see ERAN-57, esp. Figs. 2 or 6. This irregularity, for the parameters mentioned, seems, however, to be rather minor -- the area of one of the half-loops just mentioned has been estimated in ERAN-57 as roughly 10^{-11} x,y-units in this case.

If we now increase considerably the value of the parameter K in the transformation, the dimension of the main buckets will become a larger fraction of the distance between such buckets, and the smoothness (or lack of smoothness)

$K/\pi = 0.1$

$\lambda' = 0.1$

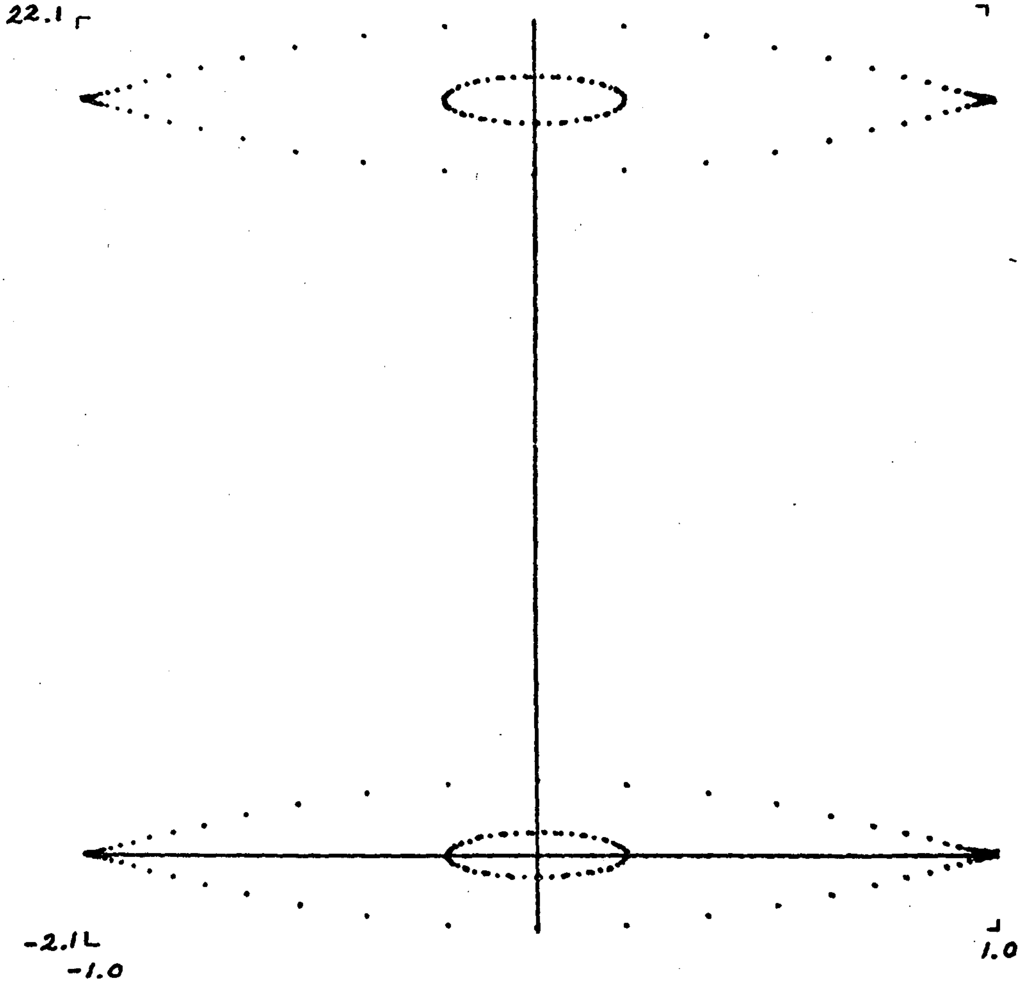

$K/\pi = 0.1$

$\lambda' = 0.1$

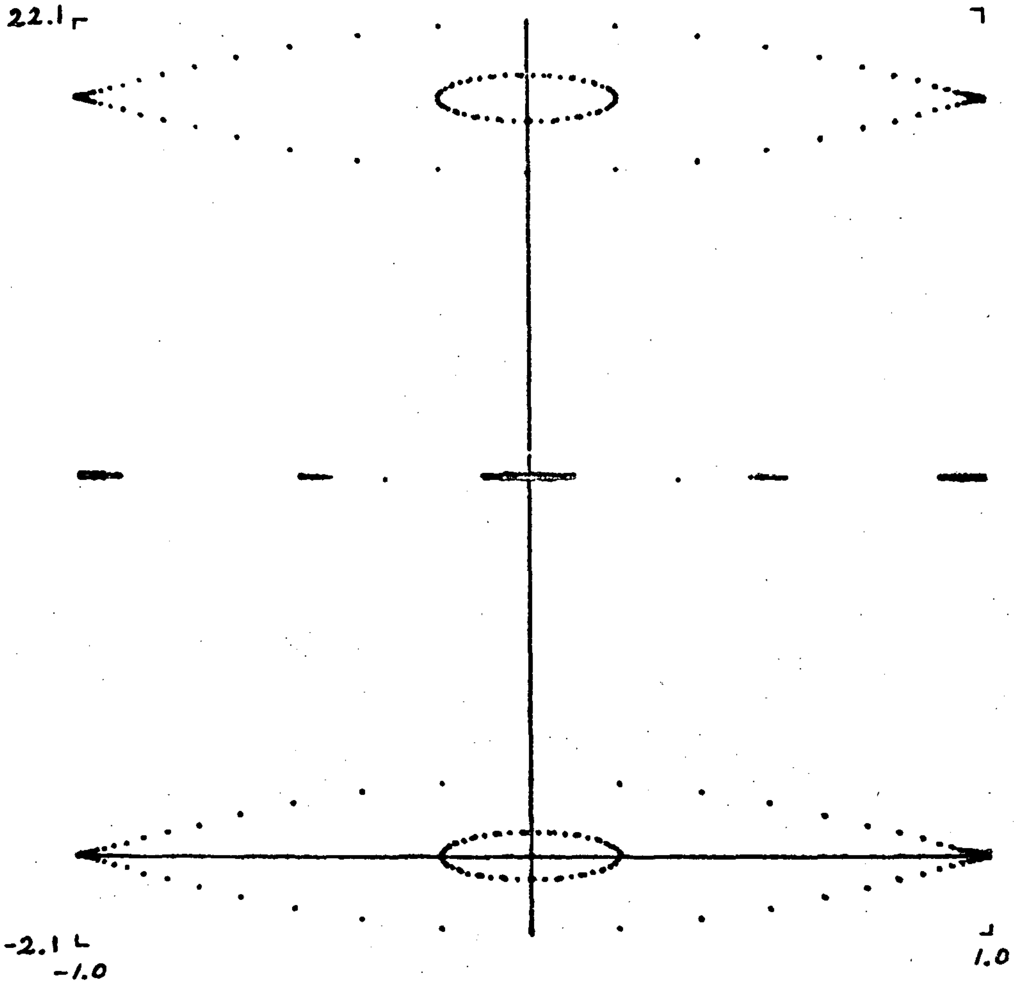

$K/\pi = 0.1$

$\lambda' = 0.1$

SCALE
X: 0.4 TO 0.6
Y: 9.8 TO 10.2

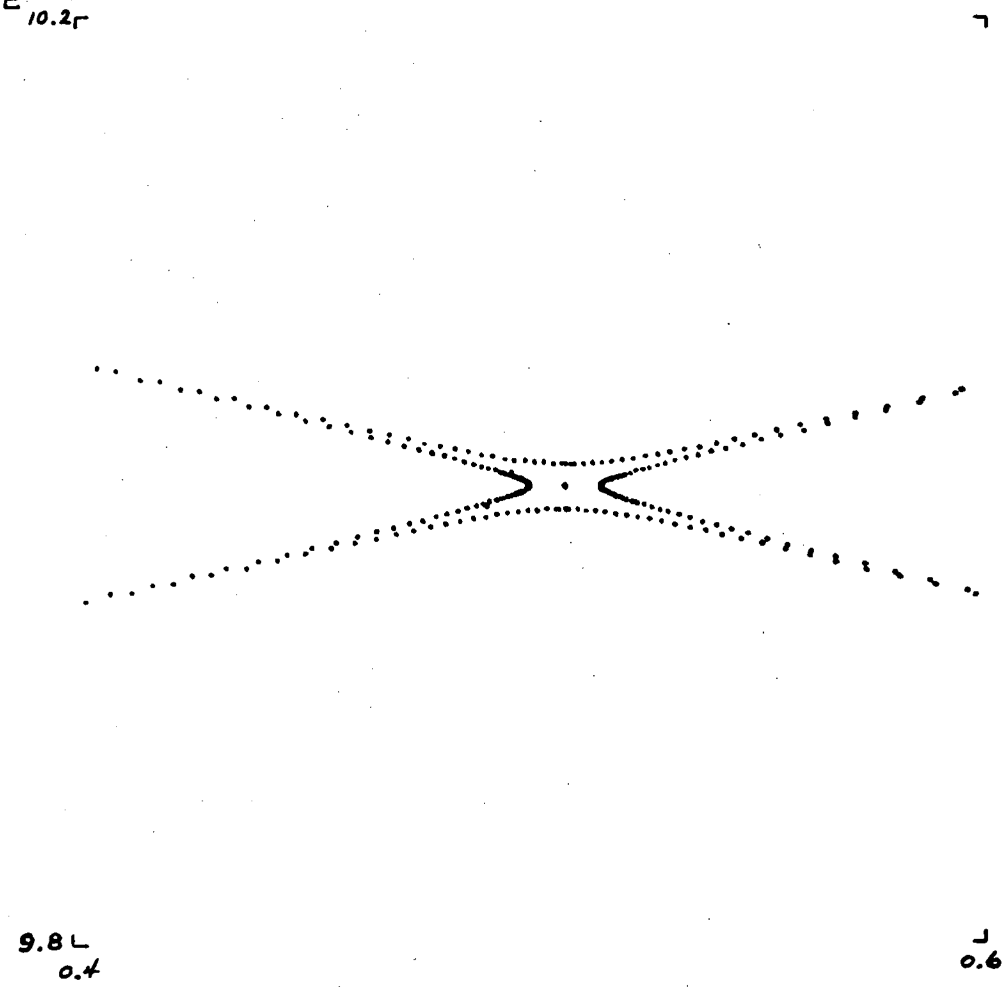

$K/\pi = 0.1$

$\lambda' = 0.1$

SCALE:
X: -1.0 TO 1.0
Y: 9.8 TO 10.2

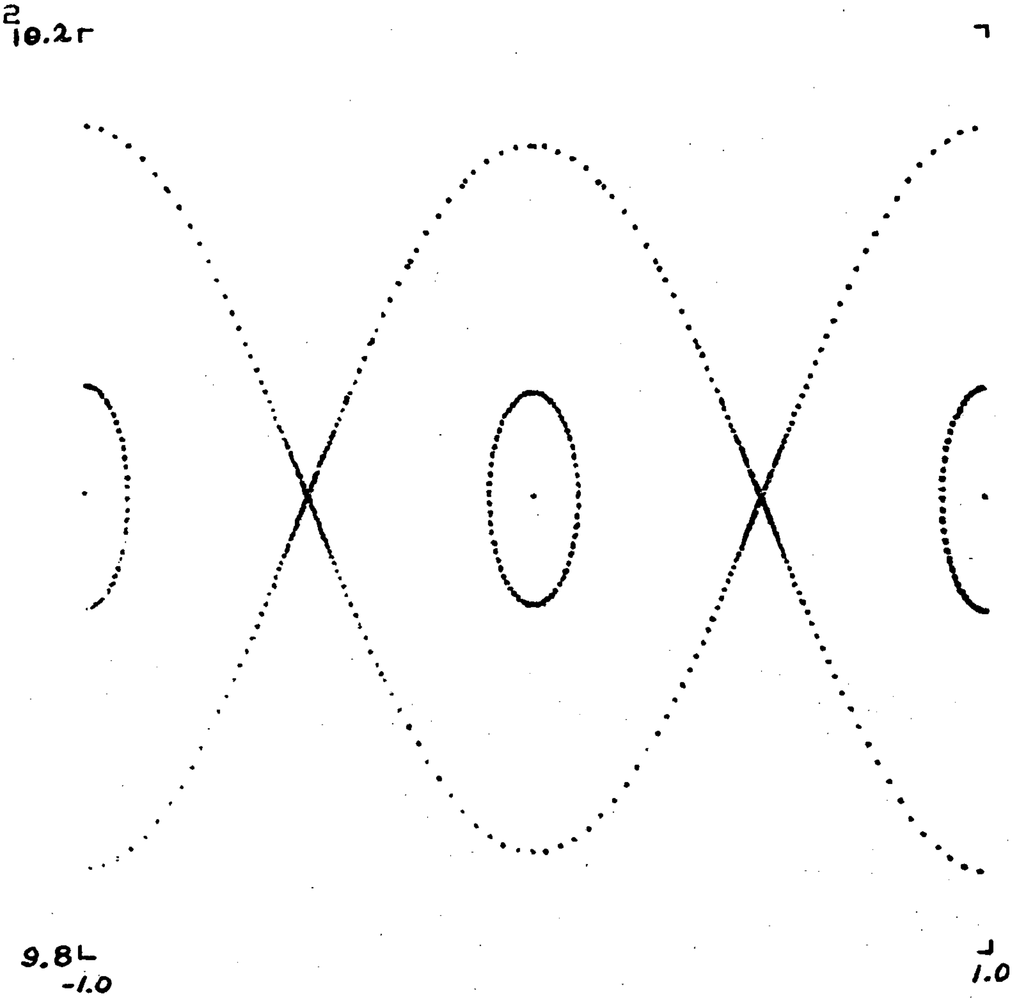

$K/\pi = 0.1$

$\lambda' = 0.1$

SCALE:
X: -1.0 TO 1.0
Y: -2.1 TO 2.1

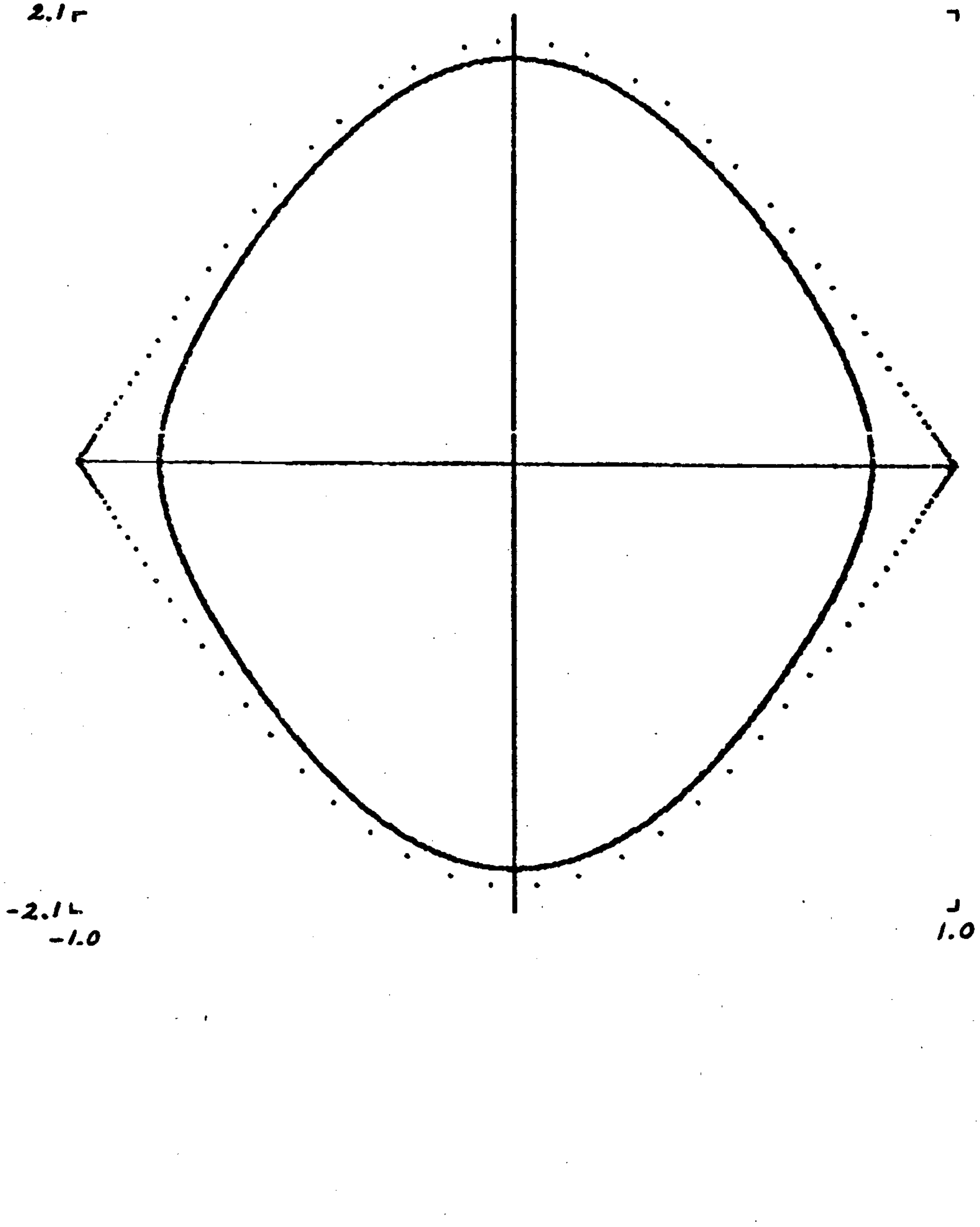

GRAPH PAPER GRAPHIC CONTROLS CORPORATION Buffalo, New York Printed in U S A SQUARE 10 X 10 TO THE CENTIMETER AS-8014-60

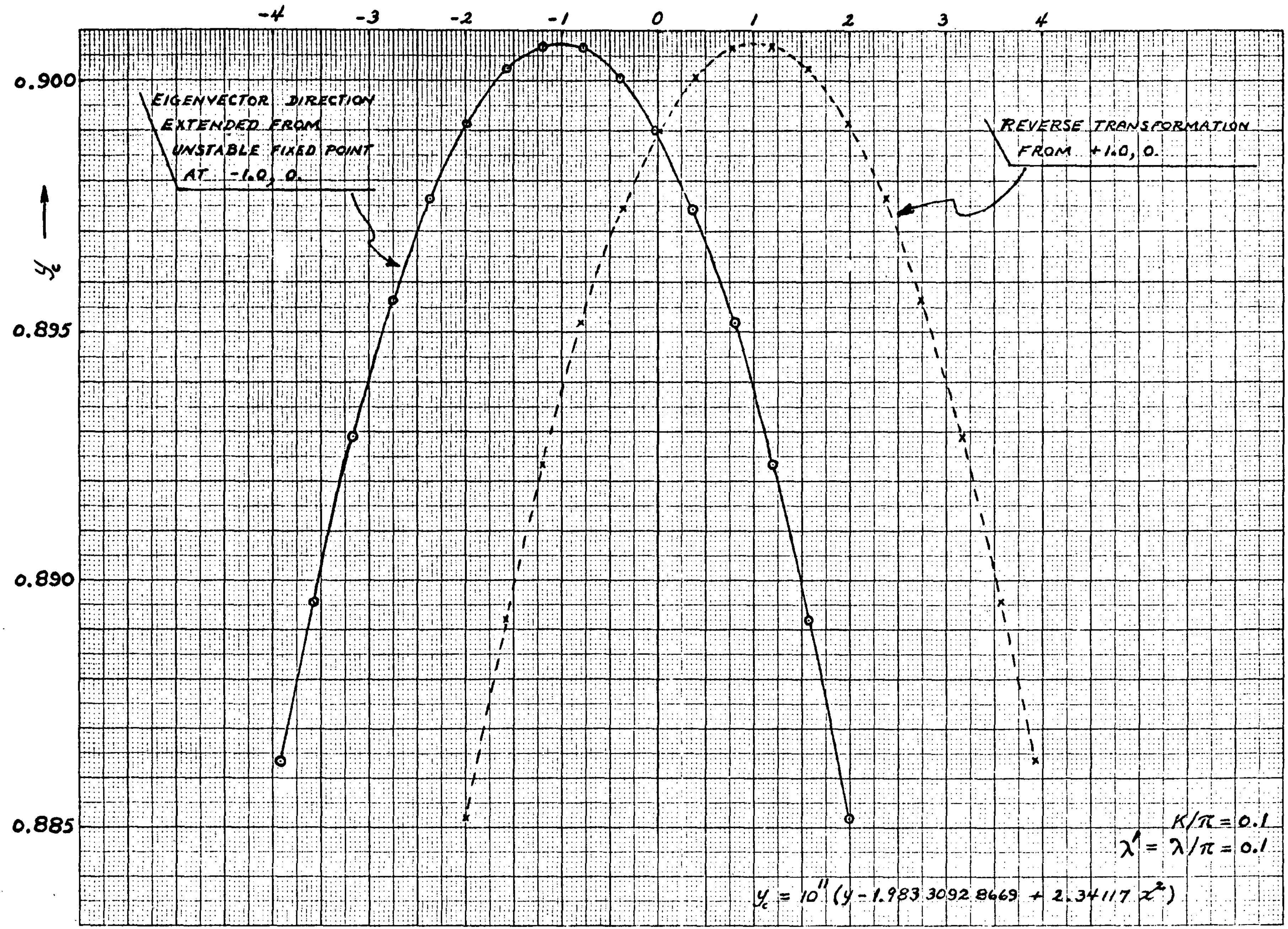

of the apparent separatrices can become significantly modified.* This is illustrated by computations in which K/π was increased eight-fold** to the value 0.8 (while λ' remained equal to 0.1).

In computational work with these parameters ($K/\pi = 0.8$, $\lambda' = 0.1$ -- again with Program RFBUK) we immediately find that phase trajectories launched near the unstable fixed points of the main bucket system (e.g., near -1,0 or -1, 20) are distinctly ragged (although this raggedness does not appear to extend much into the interior of the bucket region). The fixed-point system of order-2 (e.g., near $y = 10$), moreover, opens up so that its general structure appears evident on a phase diagram that extends from $y = -6$ to $y = + 26$. The unstable fixed points of this system at $y = 10$ appear to lie approximately at $x = \pm 0.5616567$ and evidence for higher-order systems is readily found (e.g., with stable fixed point near 0,6.61).

In summary, we have confirmed the existance of the somewhat subtle structure of the R.F. phase plots described in ERAN-57 and have indicated, by an example, that this structure and the complexity of the phase diagram become more obvious as the heights of the major buckets become an increasingly large fraction of the spacing between these buckets.†

---

* A situation of this nature has been discussed by G.M. Zaslavskij and B.V. Chirikov, Soviet Physics Uspekhi 14 (No. 5), 549-672 (March-April 1972); Usp. Fix. Nauk 105, 3-39 (September 1971).

** The result, quite roughly, should be an increase of the height of the "bucket" by the square root of this factor.

† Reference was made to synchrotron-oscillation modes that might arise in a rather more complicated R.F. acceleration system in L. Jackson Laslett, "Problems and Advances in High-Energy Accelerator Design", Physics Today (Nov. 1964), pp. 42-48, esp. p. 44 and Fig. 5.

$K/\pi = 0.8$

$\lambda' = 0.1$

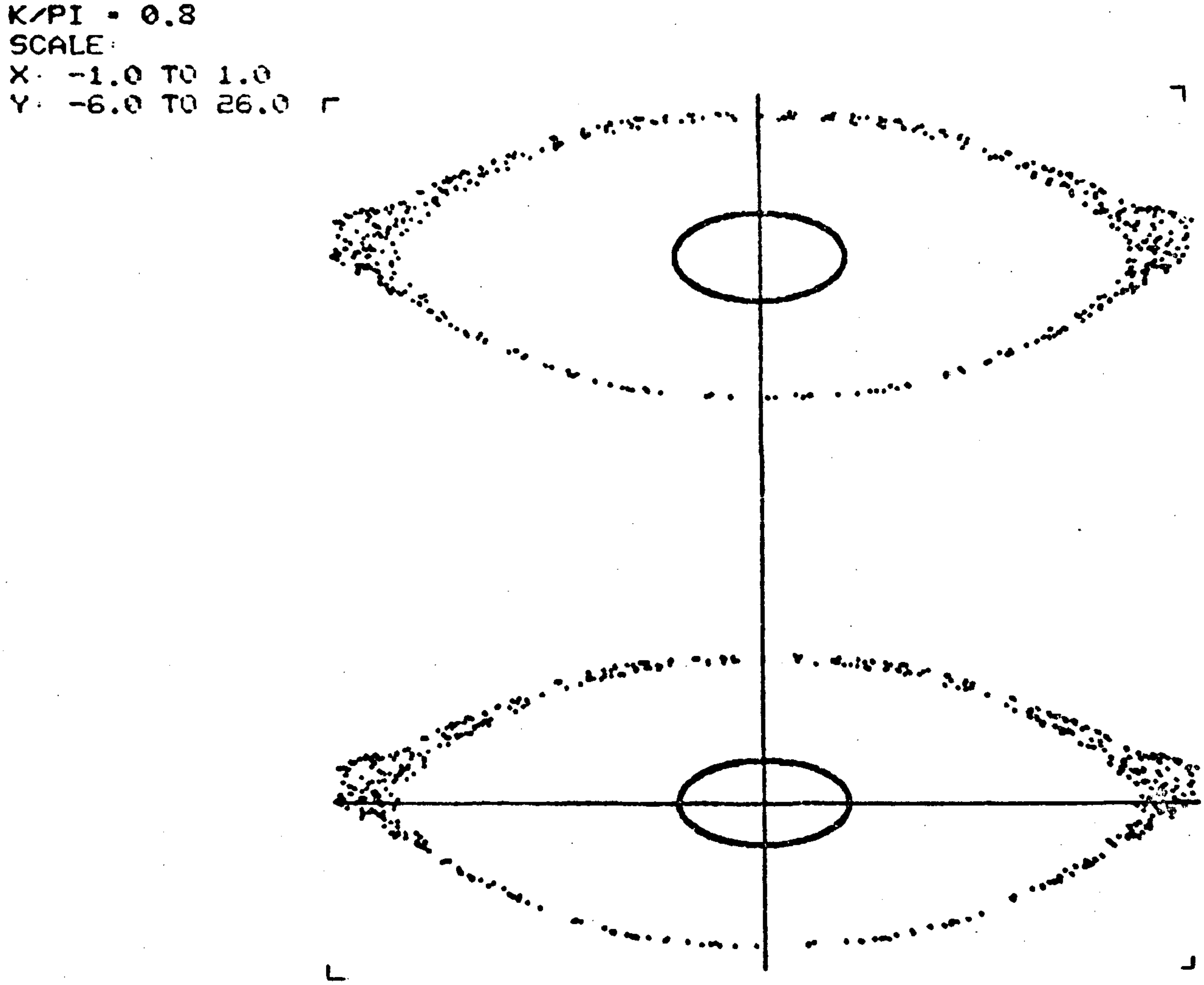

$K/\pi = 0.1$

$\lambda' = 0.1$

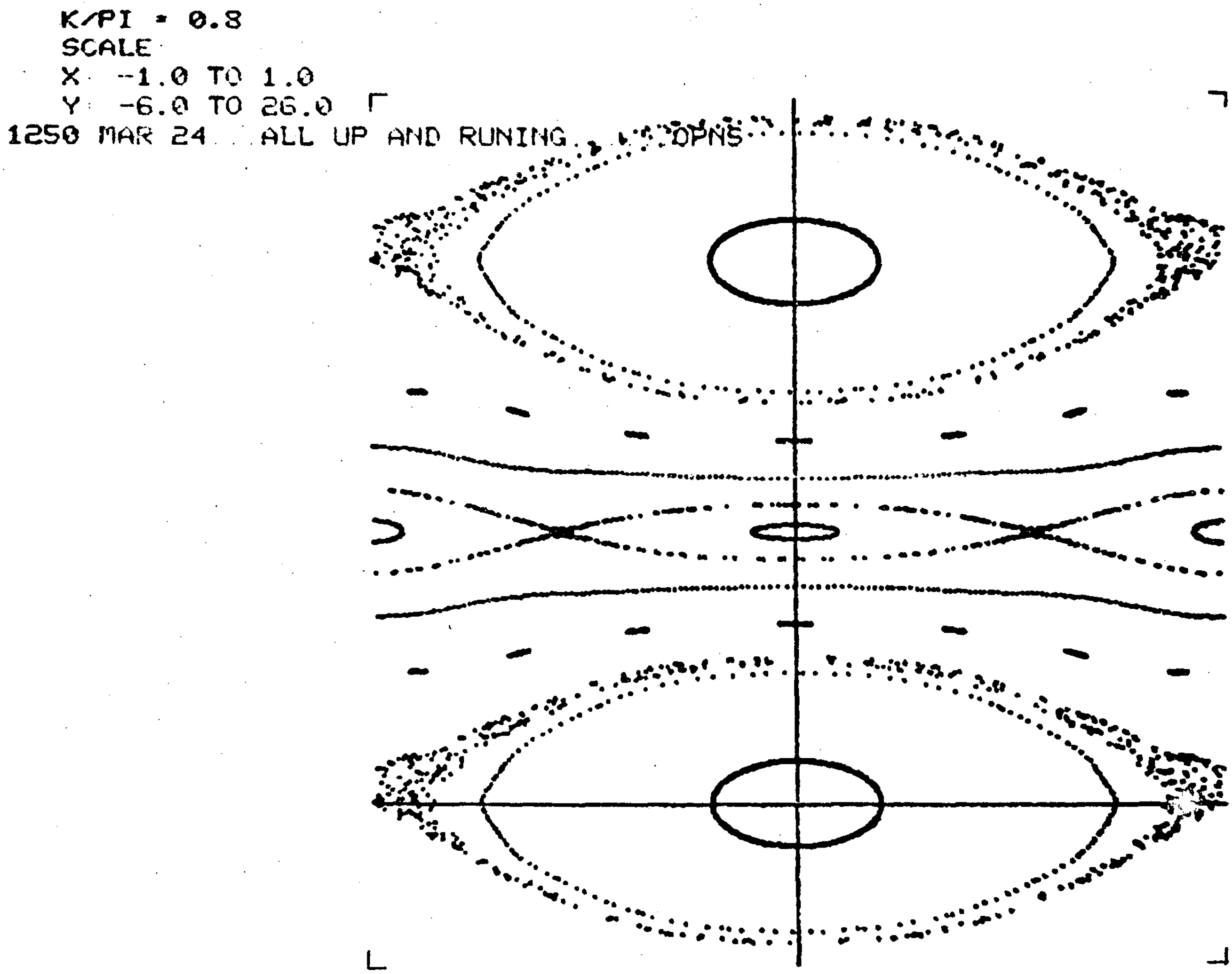

```
K/PI = 0.8
SCALE
X  -1.0 TO 1.0
Y  -6.0 TO 26.0
1250 MAR 24   ALL UP AND RUNING [illegible]OPNS
```

$K/\pi = 0.1$

$\lambda' = 0.1$

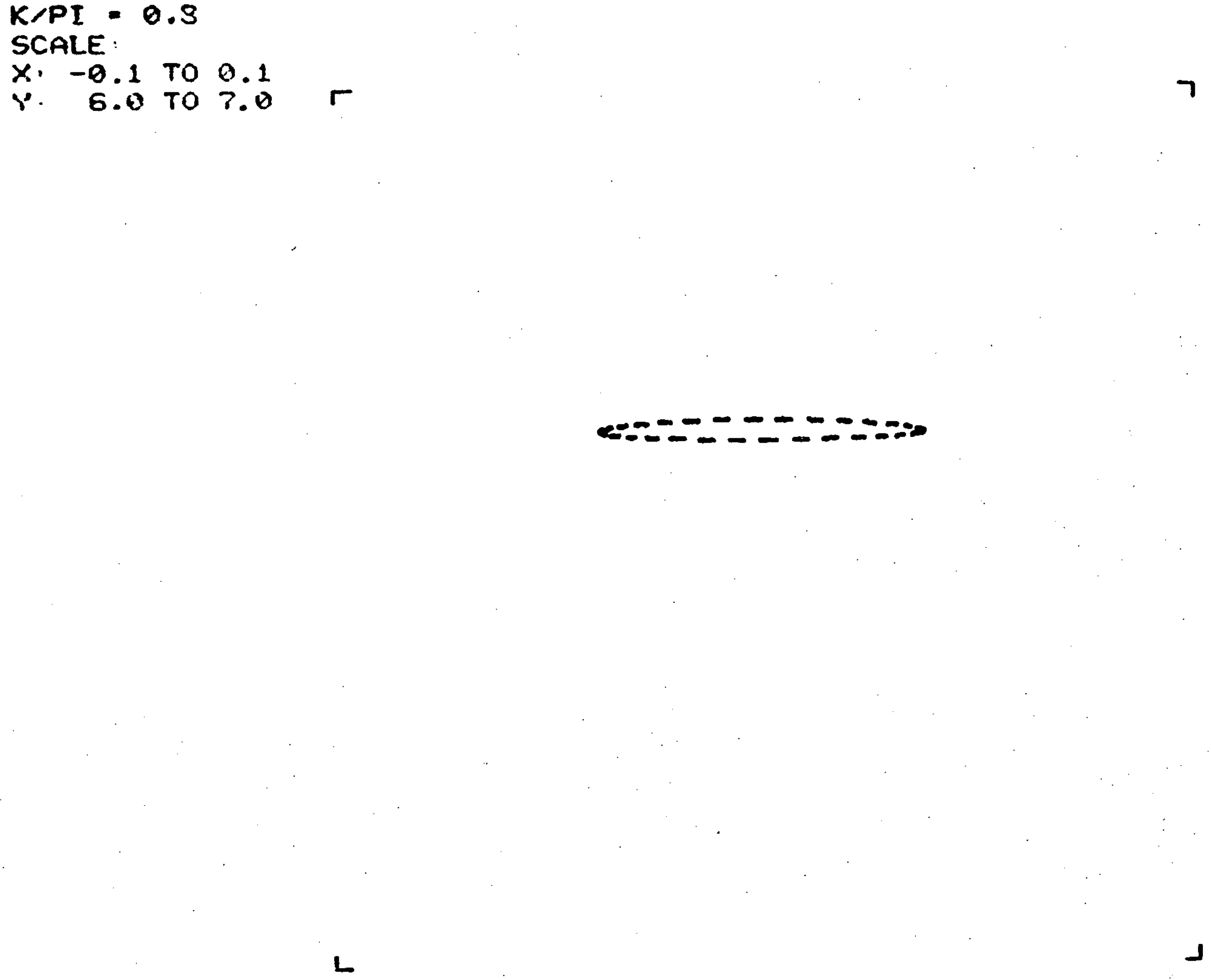

Presented at IXth International
Conference on High Energy
Accelerators, SLAC, Stanford,
CA, May 2-7, 1974

LBL-3016

"STOCHASTICITY"[*]

L. Jackson Laslett

Lawrence Berkeley Laboratory
University of California
Berkeley, California

Detailed examination of computed particle trajectories has revealed a complexity and disorder that is of increasing interest to accelerator specialists. To introduce this topic, I would like you to consider for a moment the analysis of synchrotron oscillations for a particle in a coasting beam, regarded as a problem in one degree of freedom. A simple analysis replaces the electric field of the RF-cavity system by a traveling wave, having the speed of a synchronous reference particle, and leads to a pair of differential equations of the form

$$dy/dn = -K\sin\pi x, \tag{1a}$$

where y measures the fractional departure of energy from the reference value, πx measures the electrical phase angle at which the particle traverses the cavity, and K is proportional to the cavity voltage; and

$$dx/dn = \lambda' y, \tag{1b}$$

in which λ' is proportional to the change of revolution period with respect to particle energy. It will be recognized that these equations can be derived from a Hamiltonian function

$$H = (1/2)\lambda' y^2 - (K/\pi)\cos\pi x . \tag{2}$$

Because this Hamiltonian function does not contain the independent variable explicitly, it will constitute a constant of the motion and possible trajectories in the x,y phase space will be just the curves defined by H = Constant, namely the familiar simple curves in phase space that are characteristic of a physical (non-linear) pendulum.

If we note, however, that a localized cavity can affect the energy of a particle only when the particle encounters the cavity, it is natural to replace the differential equations by difference equations. Thus, measuring energy y_n at the n^{th} entry to the cavity, we write the transformation

$$\left.\begin{aligned} y_{n+1} &= y_n - K\sin\pi x_n \\ x_{n+1} &= x_n + \lambda' y_{n+1} \end{aligned}\right\} \quad (3a,b)$$

(which can readily be shown to be area-preserving). Although alternatively the motion in this case could again be expressed by differential equations derivable from a Hamiltonian function, the Hamiltonian now would contain a periodic δ-function of the independent variable as a factor multiplying the term $-(K/\pi)\cos\pi x$ and hence could not be taken as a constant of the motion. (The differential equations, moreover, would be non-linear, so that Floquet theory could not be applied.) The use of such a Hamiltonian formulation nonetheless can be helpful in analytic work, but difference equations of course are attractive for computational investigations.

It is of interest to take a quick look at some computational results obtained through use of a transformation equivalent to (3a,b) but written in terms of working variables $Y = y - (K/2)\sin\pi x$, $X = x$, so that the transformation assumes the form

$$\left.\begin{aligned} X_{n+1} &= X_n + \lambda'[Y_n - (K/2)\sin\pi X_n] \\ Y_{n+1} &= Y_n - (K/2)[\sin\pi X_n + \sin\pi X_{n+1}] \end{aligned}\right\}, \quad (3a',b')$$

with the result that the resulting phase diagrams will necessarily have a desirable symmetry about both the X- and Y-axes. With $K/\pi = 0.1$ and $\lambda' = 0.1$ we find what appear to be conventional bucket diagrams with buckets separated in Y by $2/\lambda'$ for successive harmonic modes, although we may wish to return to the question of whether the bucket boundaries are as simple and definite as appears on Fig. 1.

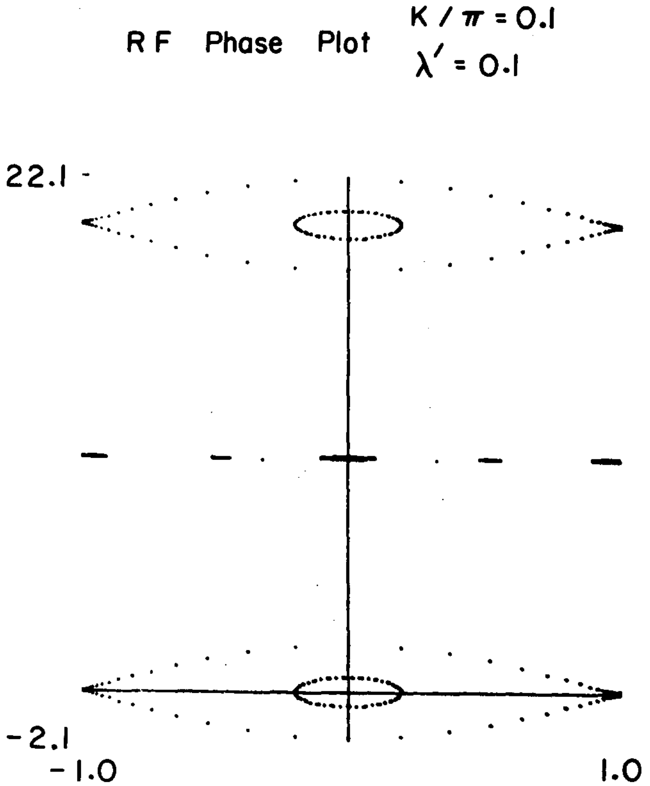

Fig. 1. - X,Y phase plot for a coasting beam under the influence of an R.F. cavity with $K/\pi = 0.1$, $\lambda' = 0.1$ - as computed by Eqns. (3a',b'). X is plotted mod. 2.

We also find evidence of some "sub-harmonic" structure (with higher order fixed points) that, if enlarged some 60X, has the appearance shown in Fig. 2.[3]

---

[*] Work supported by the U.S. Atomic Energy Commission.

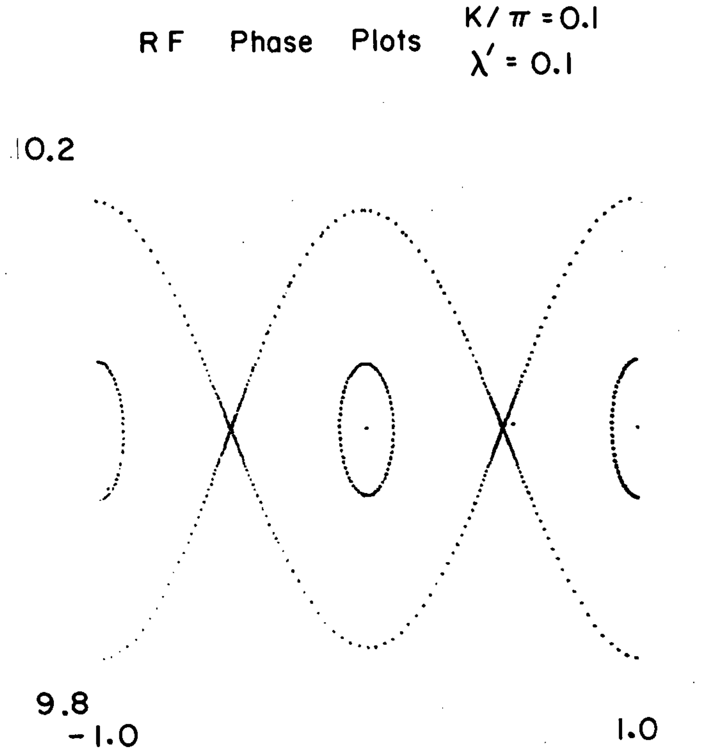

Fig. 2. - Circa 60-fold vertical enlargement of central portion of Fig. 1, near Y = 10.0, showing sub-harmonic structure.

If the cavity voltage is increased eight-fold (so K/π = 0.8), the bucket areas are expected to become larger, and we indeed find this to be the case (Fig. 3), with an accompanying very marked increase of complexity that is immediately apparent in the phase plot. Of particular interest is the evident diffuse character of phase trajectories generated by points launched close to the first-order unstable fixed points situated at X = ±1, since the bucket boundary in consequence no longer appears clearly defined.

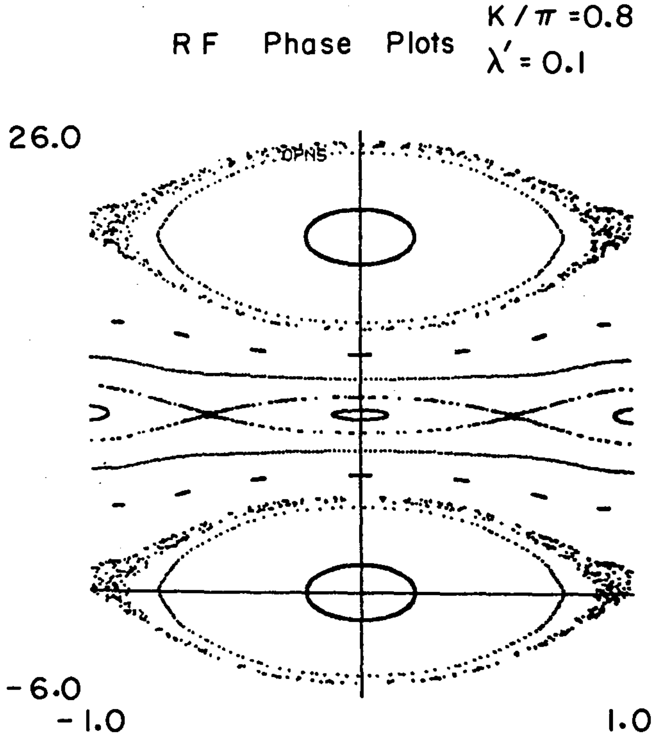

Fig. 3. - Phase plot similar to Fig. 1, but for operation with K/π = 0.8, showing the obvious development of complex structure.

In the first example (K/π = 0.1), on the other hand, where the bucket width is some two and one-half times smaller in relation to the bucket separation, the presence of structure in the separatrix can be revealed computationally only with considerable care.[4] To do this, one can extend from the unstable fixed points the eigenvector directions of the transformation linearized about these fixed points, and examine whether such curves intersect smoothly. One finds in fact that they do not quite do so, but generate loops (of a nature to be illustrated later) that in this instance (K/π = 0.1) have a very small area that amounts to only about $1/(5 \times 10^{11})$ of the area of the bucket itself.

Similar questions concerning the character of phase trajectories and the possible erratic or stochastic behavior of canonical mappings can arise in problems with more than one degree of freedom. As an example, Hénon and Hiles[5] and subsequently Walker and Ford[6] studied a model of an astronomical system, for which the Hamiltonian function was taken to be

$$H = \frac{1}{2}(p_1^2 + p_2^2 + q_1^2 + q_2^2) + q_1^2 q_2 - \frac{1}{3} q_2^3 . \qquad (4)$$

The cubic terms appearing here as coupling terms become increasingly significant for increasingly large values of H -- which is itself a constant of the motion. With the coupling terms present, however, and in the absence of any simple constant of the motion other than H, a given phase trajectory might be expected to wander (ergodically) over virtually all of a three-dimensional surface specified by H = Constant (and that will be a closed surface for values of H below the dissociation energy). If, on the other hand, some additional integral of the motion were in fact also acting, the phase points of a given trajectory then would be constrained to lie on a two-dimensional surface, and graphs of the intersection of such surfaces with some selected plane or other surface (a "surface-of-section") would lead to simple curves in this plane rather than to a scattering of points. Computations of this nature indicated that for sufficiently small values of energy (*e.g.*, $H \leqslant 1/12$) only curves that to computer accuracy were smooth (and relatively simple) were formed by intersection with the plane $q_1 = 0$ (and $p_1 \geqslant 0$). Examples in which the energy of the particles was successively raised, however, resulted in the development of ragged island structures or of apparent stochastic behavior over increasingly large portions of this surface-of-section (Fig. 4).

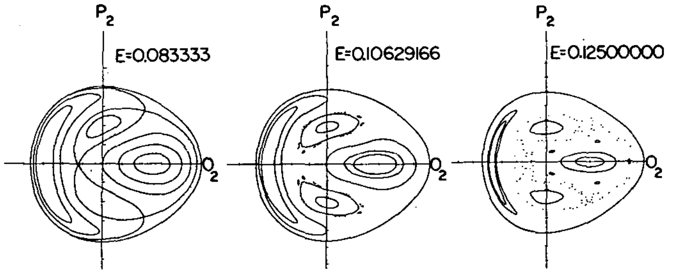

Fig. 4. - Phase plots, in the surface of section $q_1 = 0$, resulting from the equations implied by the Hamiltonian function (4) -- for increasing values of the energy. [After Walker and Ford.[6]]

Such behavior appears concordant with the "KAM" (Kolmogorov-Arnol'd-Moser) theory (see Refs. 58, 59, & 60 of our Ref. 1c), which suggests that many of the invariant curves or surfaces present in the absence of the perturbation will persist, with only minor distortion, in the presence of a sufficiently small perturbation (see, however, Note 7). It is of interest, of course, to determine or to estimate the circumstances (e.g., perturbation strength) at which the KAM theory becomes inapplicable and extended regions of erratic (or stochastic) behavior develop. As was suggested by our first examples, and has been expounded more extensevely by Zaslavskij and Chirikov,[1c, 8] one means for obtaining such estimates may be by determining the ratio of resonance width [$\delta\omega = (d\omega/dI)_r \delta I$] to the distance ($\Delta\omega$) to the nearest neighboring resonance.

Additional tests (to be mentioned below) may be required to determine the degree of disorder associated with the movement of phase points in such stochastic regions. We may first note, however, that the existence of nested closed invariant curves in a plane -- as suggested by the KAM theorem for a problem in one degree of freedom -- prevents phase points from moving outward or inward to regions of substantially different "amplitude" (in the absence of noise). With more than one degree of freedom, however, stochastic layers may intersect, to form an intricate system of channels along which a phase point can slowly diffuse and result in instability. The possibility of such "Arnol'd diffusion" has been demonstrated by Arnol'd [Ref. 35 of our Ref. 1c; stated simply the example considered by Arnol'd is comprised of a physical pendulum and a simple-harmonic oscillator, with a time-dependent coupling (that also depends on the phases, or angle variables, of these oscillations)].

It should be pointed out that some non-linear transformations -- say for a system with one degree of freedom -- will not lead to the disappearance of some or all of the invariant phase curves at substantial amplitudes. Thus for transformations of the form

$$x_{n+1} = y_n; \quad y_{n+1} = -x_n + f(y_n), \qquad (5a,b)$$

McMillan[9] has shown that if $f(y)$ can be written as $\Phi(y) + \Phi^{-1}(y)$ (where Φ^{-1} denotes the function inverse to Φ), then the curves $y = \Phi(x)$ and $x = \Phi(y)$ will constitute invariant curves. Such curves will pass through the first-order fixed point(s) situated at the intersection(s) of $y = (1/2)f(x)$ with the principal diagonal. An enclosed area can thereby be formed from which phase points cannot escape even if the behavior in portions of the interior becomes highly stochastic. This is illustrated by an example (Fig. 5) in which

$$f(y) = \frac{1}{2}(3y-1) - \frac{1}{2}\frac{k^2}{y+1} + \sqrt{y^2+k^2} \qquad (6a)$$

and

$$\Phi(x) = x - 1 + \sqrt{x^2+k^2}\ . \qquad (6b)$$

Such a situation also can develop when $f(y)$ is a stepwise linear function of y with discontinuities of slope, as has been noted by Dr. Judd [see, for example, Figs. 13 and 14 (pp. 27-28) of Ref. 10]. If $f(y)$ is of the form

$$f(y) = -(By^2 + Dy)/(Ay^2 + By + C), \qquad (7)$$

moreover, the entire phase plane will be covered by a family of simple invariant curves -- see, for example, the cases[9] $f(y) = 2ky/(1+y^2)$, with the invariants $x^2y^2 + x^2 + y^2 - 2kxy = \text{Constant}$, and $f(y) = 2ky/(1-y^2)$, with the invariants $x^2y^2 - x^2 - y^2 + 2kxy = \text{Constant}$, illustrated by Figs. 6-8.

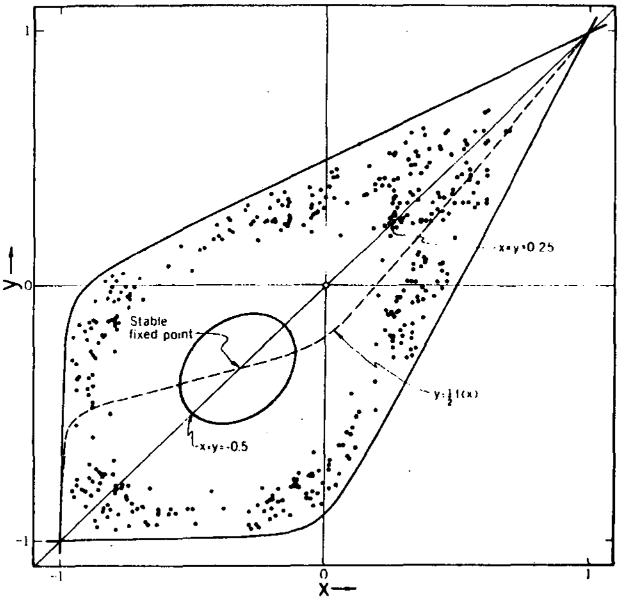

Fig. 5. - Phase diagram for the transformation (5a,b), with f(y) given by Eqn. (6a). The scattered points result from computations initiated with $x_0 = y_0 = 0.25$, but must remain within the separatrix defined by the function Φ [Eqn. (6b)].

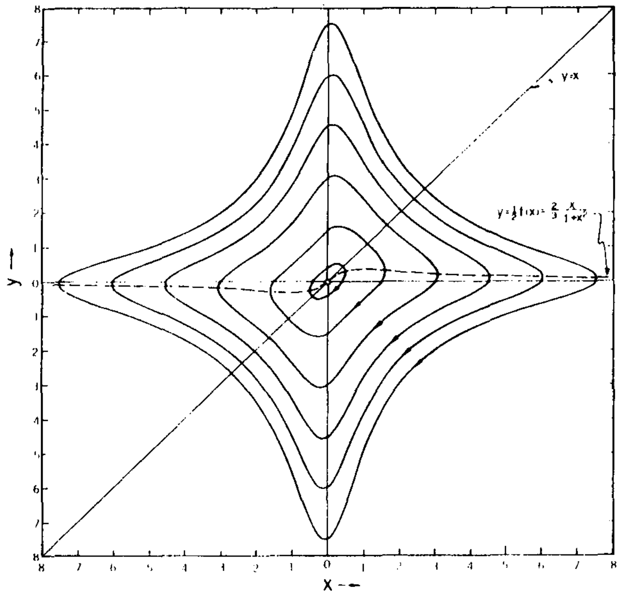

Fig. 6. - Invariant curves for the transformation (5a,b) with $f(y) = 2ky/(1+y^2)$ and $k = 2/3$. [Figs. 6-10 after McMillan.[9]]

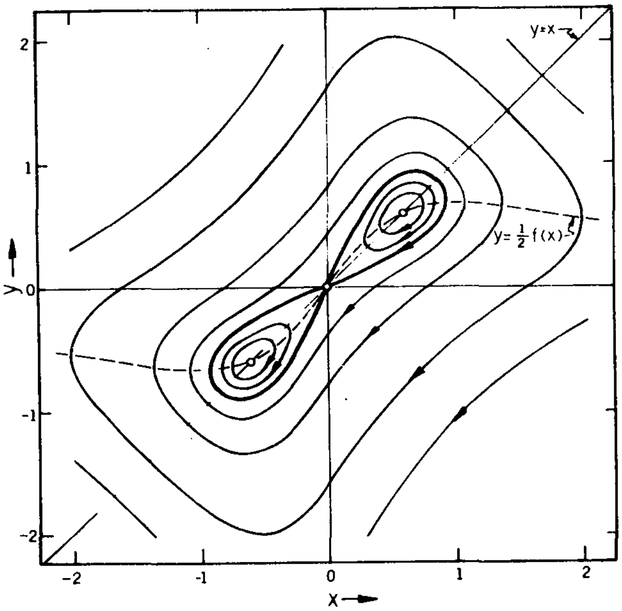

Fig. 7. - Invariant curves for the same transformation as in Fig. 6, but with k = 1.36.

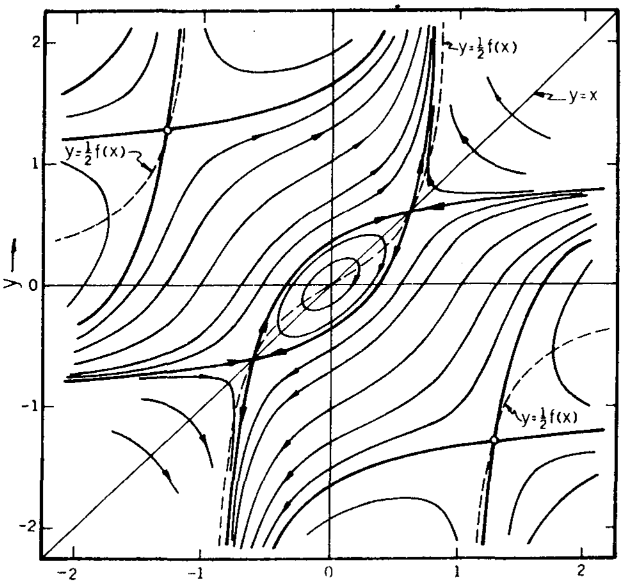

Fig. 8. - Invariant curves for the transformation (5a,b) with $f(y) = 2ky/(1-y^2)$ and k = 0.64.

It is of interest to examine the mechanism whereby irregular behavior can develop in the neighborhood of unstable fixed points, taking as an illustration an example suggested by Progessor deVogelaere that [when generalized and rewritten in variables leading to the form (5a,b) advocated by McMillan] employs

$$f(y) = 2[Ty + (1 - T)y^2]. \qquad (8)$$

First-order fixed points appear at (0,0) and at (1,1). For T = 0, this transformation, when linearized about the unstable fixed point at (1,1), can be represented by the matrix $\begin{pmatrix} 0 & 0 \\ -1 & 4 \end{pmatrix}$, with eigenvalues and eigenvector slopes

$$\lambda = 2 \pm \sqrt{3}, \quad dy/dx = \lambda. \qquad (9)$$

A line segment extending downward from the fixed point (1,1) with the slope $2 + \sqrt{3}$, if subjected to repeated applications of the transformation, generates the loops shown in Fig. 9; similarly a line segment of slope $2 - \sqrt{3}$, if extended by the inverse transformation, generates the mirror-image curve (mirrored about the principal diagonal). Points such as A, B, C ··· progress toward the fixed point in smaller and smaller steps and, since the transformation is area-preserving, the associated loops clearly must become increasingly elongated as they become increasingly narrow from repeated applications of the forward transformation. The evolution of such loops clearly will become quite intricate (Fig. 10),

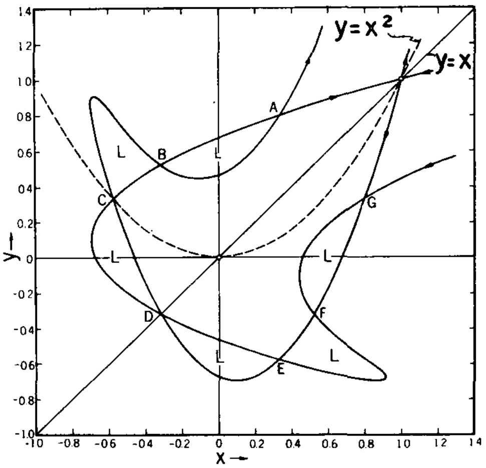

Fig. 9. - Plot of the extensions of the eigenvector directions from the unstable fixed point at (1,1), for the deVogelaere transformation expressed in McMillan's variables [Eqns. (5a,b) and (8), with T = 0]. The areas of the loops marked L are all equal, by virtue of the area-preserving character of the transformation and the inherent symmetry about the principal diagonal.

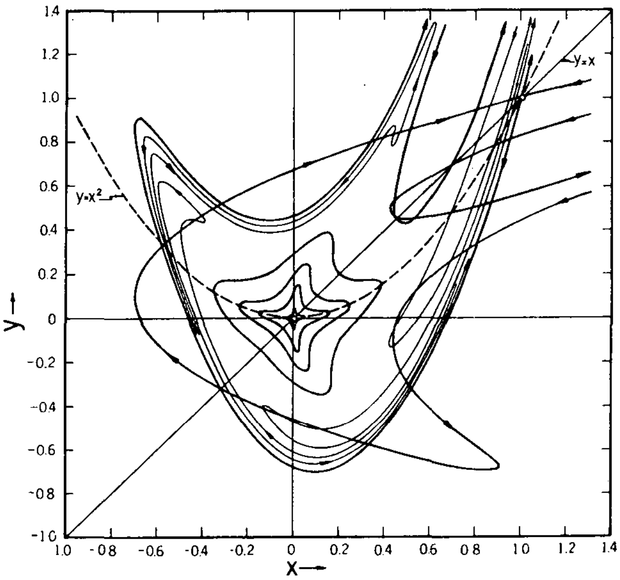

Fig. 10. - A partial extension of the curves shown on Fig. 9.

but the loops apparently need not permeate the entire "interior" -- portions of an inward loop can, in fact, enter, on a later iteration, into the interior of an outward-lying loop (as indicated on Fig. 10).[11] It is clear, however, that the development of such a loop system can readily give rise to an apparent stochastic motion of phase points in portions of the phase diagram - - most particularly near an unstable fixed point such as that mentioned here.

The existence of a firm separatrix, or of an extensive family of invariant curves generally, can be extremely sensitive to the exact form of the transformation.[12] A case of some physical interest arises in computational studies relating to the Toda Lattice.[13] This one-dimensional lattice consists of particles interacting through exponential pair potentials and can propagate certain non-linear wave forms ("solitons") without change of shape. One computational investigation[14] of stability for a three-particle lattice (with periodic boundary conditions) has commenced with a Hamiltonian function

$$H = \frac{1}{2}(P_1{}^2+P_2{}^2+P_3{}^2)+e^{-(Q_1-Q_3)}+e^{-(Q_2-Q_1)}+e^{-(Q_3-Q_2)}. \quad (10)$$

By a canonical transformation of variables, in recognition of the invariance of this system to translation -- so that $I_1 = P_1 + P_2 + P_3$ constitutes a constant of the motion -- the Hamiltonian (10) becomes expressible as a function of two pair of conjugate variables in the form

$$H = \frac{1}{2}(p_1{}^2+P_2{}^2)+ \frac{1}{24}[e^{(2q_2+2\sqrt{3}q_1)}+e^{(2q_2-2\sqrt{3}q_1)}+e^{-4q_2}], \quad (11)$$

which is identical to the Hénon-Heiles Hamiltonian function (4) through terms of third order. It is of interest to examine whether in the present case constants of the motion other than H act to restrict the motion. Computationally it was found -- again using the surface-of-section $q_1 = 0(p_1 > 0)$ -- that in this case simple invariant curves apparently continued to exist in the q_2p_2, plane, even for very large values of H. Stimulated by this result, Hénon[15] has directed attention to an additional integral of the motion that is valid in this case; the constants of the motion for the three-particle lattice then can be written in a form that we may express as[16]

$$H = \text{Constant} \quad (12a)$$

$$P_1 + P_2 + P_3 = \text{Constant, and} \quad (12b)$$

$$P_1P_2P_3 - P_1e^{-(Q_3-Q_2)} - P_2e^{-(Q_1-Q_3)} - P_3e^{-(Q_2-Q_1)} = \\ = \text{Constant}. \quad (12c)$$

[Evidently[15] further analytic work in fact has now established that the n-particle Toda lattice with periodic boundary conditions (or with fixed ends) is a "completely integrable" system.]

It is of some interest to seek means for anticipating whether stochastic behavior will occur in various portions of a phase diagram and to examine the character of such stochastic behavior as does occur. What we here have loosely termed stochastic behavior can be catalogued with respect to a hierachy of properties (ergodicity, mixing, ···), indicative of increasing disorder, that are fundamentally significant for statistical mechanics.[1a,e] Of particular interest to the accelerator designer, of course, is the determination of a threshold beyond which stochastic behavior will set in and may act to carry a phase point to unacceptably large amplitudes. As noted earlier, stochastic behavior appears to be associated with overlapping resonances,[1c] and this concept has served as the basis for some analytic estimates of stochasticity limits.[1c,17] It has been noted by René deVogelaere and confirmed in subsequent computations[18] that for a particular class of fixed-point families -- say those with rotation of the form m/(4m+1) -- there is a closely linear relationship between the order of the resonance (4m+1) and $\ln|1 - \frac{1}{2}\,\text{Trace}|$ through many decades ("Trace" denoting the trace of the tangential-mapping or differential matrix associated with the 4m+1 iterations required to map a given fixed point onto itself). Such regularities, and others relating to the apparent size of the stable areas about high-order fixed points (e.g., as estimated from the intersection angle of eigenvectors), have been considered useful indicators of the change in character of a mapping at certain amplitudes.[19,8,20]

A computational procedure of considerable interest for recognizing stochasticity is that in which one follows the evolution of the distance between two initially very close points in phase space. In practice it can prove desirable to reduce the separation from time to time by a recorded factor whenever the separation becomes excessive during the computations, or, perhaps preferably, to evaluate the growth of an infinitesimal vector through use of the cumulative tangential-mapping matrix. A high degree of stochasticity can be ascribed to the behavior of the transformation if there are such vectors whose length generally grows beyond the first iteration by a factor greater than unity (while others may similarly contract). (Ref. 1a, p. 55; for examples, see Ref. 21.) An analogous procedure -- that can be more attractive, although possibly of a less direct basic significance -- is an investigation of the growth of the eigenvalue(s) of the cumulative tangential mapping. Such eigenvalues can change sign repeatedly during the course of many iterations, and hence will be seen to decrease from time to time, but an exponentially increasing trend in eigenvalue magnitude is likely to be associated with a similar type of increase for the lengths of the vectors mentioned previously. The nature of eigenvalue growth has been illustrated by Froeschlé[22] for the transformation[23]

$$\left.\begin{aligned} x_{n+1} &= x_n \cos\alpha - (y_n-x_n{}^2)\sin\alpha \\ y_{n+1} &= x_n \sin\alpha + (y_n-x_n{}^2)\cos\alpha \end{aligned}\right\}. \quad (13a,b)$$

The general characteristics of this transformation, expressed in variables such that the transformation has the symmetry of McMillan's form, is seen on Fig. 11. On an expanded scale (X10), we see (Fig. 12) the sudden onset of erratic behavior as the starting values for the transformation are successively increased (in steps $\Delta x_o = 0.0025$, for $y_o = 0$), and on a scale expanded by a further factor 100/6 we see (Fig. 13) the presence of a great deal of additional structure within a portion of this "stochastic" region. Associated with the transition to the stochastic region there appears to be a marked change in the manner of growth of $\psi_n = \log|\lambda_n|$ (linear, vs. n, in the stochastic case -- indicative of an exponential trend for $|\lambda_n|$) or of the "Cesaro mean" $\mu_n = \frac{1}{n}\sum_{m=1}^{n}\frac{1}{m}\psi_m$ (constancy in the stochastic case, monotonically decreasing otherwise -- Fig. 14).[24] Such methods indeed may prove useful in investigating computationally the possible development of stochastic motion in storage-ring devices. Extended computations of this nature can present challenging problems with respect to computer accuracy.[25]

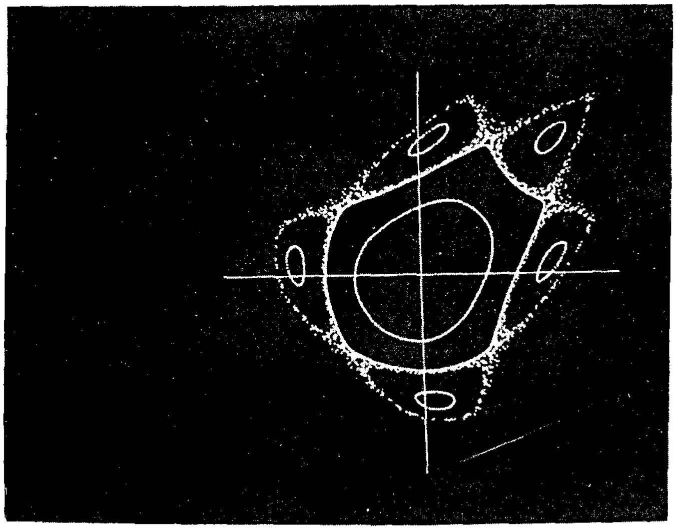

Fig. 11. - Apparently-smooth phase curves and a scattering of points resulting from iteration of the transformation (11a,b), with $\cos\alpha = 0.22$ and coordinates X,Y appropriate to expressing the transformation in the form (5a,b).[23] Five islands of stability (containing stable fixed points of order 5) are seen surrounding the area associated with the order-1 fixed point at the origin. The outermost smooth curve, shown as bounding this inner area, resulted from the starting values $x_0 = 0.5350$, $y_0 = 0$ (Froschlé notation), and the scattered points result from $x_0 = 0.5375$, $y_0 = 0$. Scale (as indicated by the coordinate axes): -1.0 to 1.0

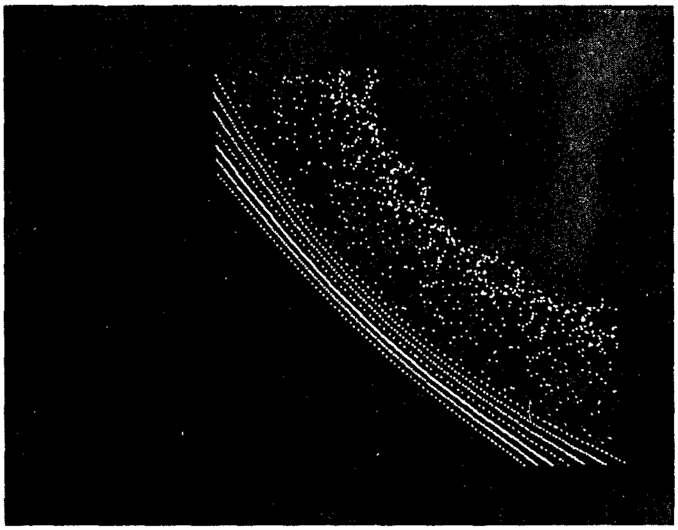

Fig. 12. - Enlarged portion (10X) of Fig. 11, showing seven smooth phase trajectories resulting from starting values $x_0 = 0.5200, 0.5225, \cdots 0.5350$ (and $y_0 = 0$) and a scattering of points resulting from $x_0 = 0.5375$, $y_0 = 0$. Note the occurrence of open areas within the region covered by the scattered points -- for example the area surrounding an (unplotted) stable fixed point of order 65 at $X \cong 0.476$, $Y \cong 0.521$
Scale: 0.38 to 0.58

Fig. 13. - Detailed multiple-island structure in the immediate neighborhood of an order-65 stable fixed point (shown here just below the center of the diagram) of which mention has been made in the caption to Fig. 12. Scales: 0.470 to 0.482 for X, 0.516 to 0.528 for Y.

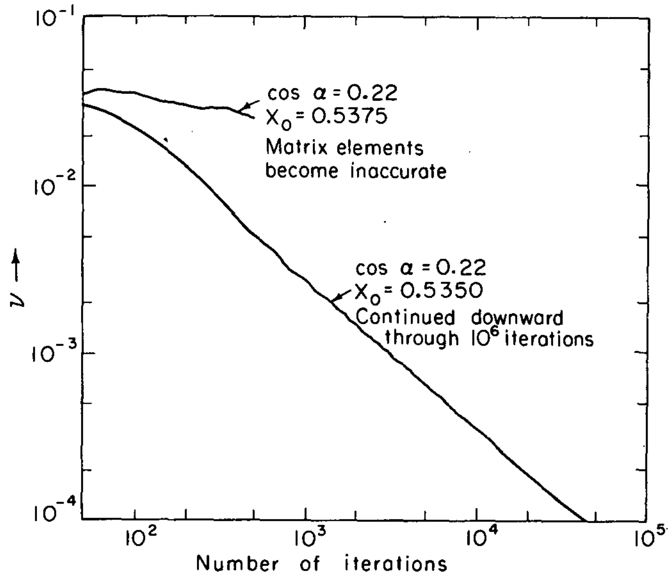

Fig. 14. - Plots of the "sliding mean", ν_n (Note 24), vs. n, obtained from computations begun (i) with initial conditions leading to the last smooth curve of Fig. 12 ($x_0 = 0.5350$) and (ii) with initial conditions leading to the scattered points on that Figure ($x_0 = 0.5375$), of which only the results for the latter case indicate a general exponential upward trend of $|\lambda_n|$.

References and Notes

1. (a) An authorative treatment of the mathematical aspects of the problems discussed here is given by V.I. Arnol'd and A. Avez, "Ergotic Problems of Statistical Mechanics" (Benjamin, New York, N.Y.; 1968) and (b) by Jürgen Moser, "Stable and Random Motions in Dynamical Systems" (Princeton Univ. Press, Princeton, N.J.; 1973); (c) an extended discussion of which portions relate more immediately to those of interest to an accelerator designer is presented, with many references, by G.M. Zaslavskij and B.V. Chirikov, Uspekhi Fizicheskikh Nauk 105 and Engl. Transl. Sov. Phys. Usp. 14, 549-568 (1972), with further discussion and examples (d) by B.V. Chirikov in Nucl. Phys. Inst. Report 267 (Novosibirsk, USSR) with Engl. Transl. by A.T. Sanders, CERN Trans. 71-40 (CERN, Geneva, Switzerland; October 1971); and (e) related questions of ergotic theory in statistical mechanics are summarized by J.L. Lebowitz and O. Penrose, Physics Today, pp. 23-29 (February 1973).

2. CNRS Internat. Conf. on Point Transformations and their Applications, Laboratoire d'Automatique et d'Analyse des Systèmes, Toulouse, France (10-14 September 1973).

3. K.R. Symon and A.M. Sessler, Proc. CERN Symposium on High Energy Accelerators and Pion Physics 1, 44-58 (CERN, Geneva, Switzerland; 1956).

4. L. Jackson Laslett, ERAN-57 (Lawrence Berkeley Laboratory; 1970).

5. M. Henón and C. Heiles, Astron. J. 69, 73-79 (1964).

6. G.H. Walker and J. Ford, Phys. Rev. 188, 416-432 (1969).

7. The present example in fact is exceptional in that the unperturbed frequencies, being equal, are "rationally connected" and the analysis requires special treatment -- see F.G. Gustavson, Astron. J. 71, 670-686 (1966); J. Moser, "Lectures on Hamiltonian Systems", Memoirs Amer. Math. Soc., No. 81, 1-60 (1968).

8. See also V.K. Mel'nikov, Soviet Math. 4, 266-270 (1963).

9. Edwin M. McMillan, "A Problem in the Stability of Periodic Systems", *in* "Topics in Modern Physics -- A Tribute to Edward U. Condon", pp. 219-244 (Colorado Asso. University Press, Boulder, Colorado; 1971). A transformation written in the form (5a,b) is convenient for the study of area-preserving transformations in the plane because of the "double symmetry" pointed out by McMillan (p. 225). The transformation can be interpreted as describing the effect of a simple linear focusing system supplemented by a periodic sequence of thin non-linear lenses that introduce at such points a Δy specified by $f(x)$.

10. Laslett, McMillan, and Moser, Courant-Institute Report NYO-1480-101 (New York University, N.Y.; 1 July 1968).

11. A wealth of island structure of course can develop throughout the area of such phase diagrams. In some instances a family of unstable fixed points for which the eigenvalues are *negative* may arise (in place of a stable family, for which λ is purely imaginary), and the appearance of phase trajectories can thereby be drastically affected -- see Ref. 10, esp. Fig. 2 (p. 35) of the Appendix, drawn for $T = -1/8$. For discussion of the occurrence and consequences of loop systems, see S. Smale, "Diffeomorphisms with Many Periodic Points ...", (Princeton Univ. Press, Princeton, N.J.; 1965); E. Zehnder, Comm. Pure Appl. Math. 26, 131-182 (1973); Ref. 1c, Sect. 6.1; and Ref. 1d, Sect. 2.6.

12. The loss of a firm separatrix can be illustrated computationally for the transformation (5a,b) by modifying the function $f(y)$ of (6a) so as to introduce the quantity $1 - b$ as a factor multiplying the second term on the right and setting $b \neq 0$ (for example, $b = 0.05$) -- L. Jackson Laslett, ERAN-239 (in preparation; 1974).

13. See, for example, M. Toda, Prog. Theoret. Phys. (Kyoto) Suppl. 45, 174-200 (1970); references cited therein; and related papers in this issue of the Supplement.

14. J. Ford, S.D. Stoddard, and J.S. Turner, Prog. Theoret. Phys. (Kyoto) 50, 1547-1560 (1973).

15. Cited in Ref. 13, p. 1558.

16. The validity of these (time-independent) expressions as constants of the motion of course can be confirmed directly by forming their Poisson-bracket expressions with the Hamiltonian function (10).

17. B.V. Chirikov, E. Keil, and A.M. Sessler, CERN Report ISR-TH/69-59 (CERN, Geneva, Switzerland; 15 October 1969).

18. *E.g.*, Ref. 10, pp. 42-43, where is also listed a quantity $\lambda_I = \lambda - 1$ for fixed-point families that have rotation $\frac{m}{4m+1}$.

19. John M. Greene, J. Math. Phys. 9, 760-768 (1968).

20. James H. Bartlett, "Stability of Area-Preserving Mappings", Paper III-3 of Ref. 2.

21. J. Ford and G.H. Lunsford, Phys. Rev. A1, 59-70 (1970).

22. C. Froeschlé, Astron. and Astrophys. 9, 15-23 (1970); C. Froeschlé and J.-P. Scheidecker, *ibid.* 22, 431-436 (1973); and other references cited therein.

23. This transformation can be put into McMillan's form[9] by the change of variables $x = \sqrt{\sin\alpha}\, Y$, $y = (X - Y\cos\alpha)/\sqrt{\sin\alpha}$, with $f(Y)$ then becoming $2Y\cos\alpha + Y^2 \sin^{3/2}\alpha$.

24. The curves of Fig. 14 are plots of

$$\nu_n \equiv \sum_{m=1}^{n} \frac{1}{m} \psi_m \exp\left(-\frac{n-m}{\tau}\right) \Big/ \sum_{m=1}^{n} \exp\left(-\frac{n-m}{\tau}\right) \text{ with}$$

$1/\tau = 0.015$, the sliding exponential factor being designed to provide some smoothing of the results (L. Jackson Laslett, unpublished LBL Report). Extended computations of this nature can present challenging problems with respect to computer accuracy. (Refs. 24 & 25).

25. C. Froeschlé and J.-P. Scheidecker, J. Comp. Phys. 11, 423-439 (1973); ____, Astrophys. & Space Sci. 25, 373-386 (1973).

26. I am deeply indebted to Paul J. Channell (LBL) for many stimulating and helpful conversations concerning topics discussed here. Responsibility for the views expressed in this paper, however, remains exclusively my own.

BECON-2
LBL-6459

EVOLUTION OF THE AMPLITUDE DISTRIBUTION FUNCTION FOR A BEAM SUBJECTED TO STOCHASTIC COOLING

L. Jackson Laslett

U.C. Lawrence Berkeley Laboratory*

Berkeley, California, U.S.A.

I. INTRODUCTION. The suggestion of S. van der Meer(1) for stochastic cooling or feedback damping of a circulating charged particle beam offers promise of increasing the luminosity of a storage ring and may be a particularly attractive technique if antiprotons are to be employed as one of the beams in such a device. Encouraging initial tests of such a system have been reported from CERN by P. Bramham et al.,(2) and further tests are in progress in that Laboratory.(3)

The original report of van der Meer(1) considered the repeated use of a kicker to suppress the transverse phase-space displacement of the centroid of a group of particles detected at a pick-up station situated up-stream (e.g., by $5\lambda_\beta/4$),(2) and the report estimated the expected rate of damping of the mean-square oscillation amplitude. In the present report we extend this analysis so as to provide information on the manner in which the character of the amplitude distribution function may be affected by the damping procedure mentioned above. It is believed that information concerning the evolution of the form of the distribution function may be of particular interest in cases in which a "halo" is imposed on the distribution by injection of a group of particles to supplement those in a beam that has already been subjected to appreciable feedback damping. Results of the analytic work will be illustrated, and compared with the results of simulation computations.

For consistency with the approach of van der Meer, we continue to assume that the kicker truly results in a zero transverse phase-space displacement for the centroid of the group of particles to which it is applied--although with a single pick-up device, capable of detecting spatial displacements only, the time scale of the damping process in fact may be doubled. We further ignore such potentially significant complications as imperfect amplifier performance, extraneous noise, or loss of particles to the chamber walls, and we restrict the analysis to the case in which complete "mixing" (or phase decoherence) is assumed to occur between successive applications of the correction procedure.

II. ANALYSIS. A single application of the full van der Meer correction leads to new particle amplitudes A_i' given, for N particles, by

$$A_i'^2 = A_i^2 - (2/N)A_i\Sigma_j A_j \cos(\phi_i-\phi_j) + (1/N^2)\Sigma_j\Sigma_k A_j A_k \cos(\phi_j-\phi_k). \tag{1}$$

Thus, for random relative phases and $N \gg 1$, the average change of the A_i^2 is expected to be

$$<\Delta(A^2)> = -(2/N) <A^2> + (1/N) <A^2> = -(1/N) <A^2>, \tag{2}$$

as given by van der Meer.(1) Accordingly, with $u = A^2$, $\tau = t/N$, and time (t) measured in units of the time between successive corrections,

$$d<u>/d\tau = -<u> \tag{3}$$

with the solution $<u> = C\exp(-\tau)$ [where $C = <u>|_{t=0}$] (4)

--regardless of the form of the initial distribution, provided only that complete phase mixing occurs between successive corrections. A similar analysis [Appendix A] can be performed for a beam considered to be composed of (say) two groups for which the evolution of their individual mean square amplitudes is of interest.

A binominal development of Eq.(1) to obtain $\Delta(u_i^p)$ suggests the relations

To be presented at International Accelerator Conference, Institute for High Energy Physics, Serpukhov, Moscow Region, July 11-17, 1977

$$d\langle u^p\rangle/d\tau = -2p\ \langle u^p\rangle + p^2\ \langle u\rangle\ \langle u^{p-1}\rangle, \tag{5}$$

at least for integer $p \geqslant 0$, thus providing a soluble sequence of ordinary differential equations for the (even) amplitude moments [with $\langle u\rangle$, corresponding to $p=1$, given by Eq.(4)]. A distribution function $f(u;\tau)$, of squared amplitude that satisfies the partial differential equation

$$\partial f/\partial\tau = 2\,\partial(uf)/\partial u + C\exp(-\tau)\,\partial(u\,\partial f/\partial u)/\partial u \tag{6}$$

will be found (by integration over the distribution and the assumption of reasonable characteristics for f and for $\partial f/\partial u$ at the limits) to be consistent with the moment equation (5).(4) Numerical or analytic solution of Eq.(6) thus may provide a useful means for predicting the evolution of the form of a prescribed initial distribution and indeed (Sect.III) has been found in test examples to provide results consistent with simulation computations.

A formal analytic solution to Eq.(6) can be written in terms of Laguerre polynominals in the form(6,7)

$$f(u;\tau) = \langle u\rangle^{-1}\ \exp(-v)\sum_{m=0}\alpha_m\ \exp(-m\tau)\ L_m(v) \tag{7a}$$

(as can be readily confirmed, term-by-term, by reference only to the Laguerre differential equation), where we have written

$$v = u/\langle u\rangle \text{ and } \langle u\rangle \text{ is as given by Eq.(4).} \tag{7b}$$

With the adoption of this solution, the coefficients α_m are to be evaluated in terms of the initial distribution function (making use of the weighted orthonormality of the Laguerre polynominals) as(8)

$$\alpha_m = \int_0^\infty f(u;0)\ L_m(u/C)\,du. \tag{7c}$$

The formal solution, Eq.(7a), is attractive, and informative, in that it immediately suggests that as time increases (and the higher order factors $\exp(-m\tau)$ become increasingly small), the <u>form</u> of the distribution $f(u;\tau)$ will approach a pure exponential function, of width characterized by $\langle A^2\rangle = \langle u\rangle = C\exp(-\tau)$ -- as was found in initial simulation computations. We note, however, the alternative closed form solution given in(7).

III. EXAMPLE. As an example we consider the evolution of the two-group distribution function

$$f(u;0) = n_1\ \exp(-u/C_1) + n_2\ \exp(-u/C_2), \tag{8a}$$

with $n_1 + n_2 = 1$ and the initial mean square amplitude then given by

$$C = \langle u\rangle\big|_{\tau=0} = n_1C_1 + n_2C_2. \tag{8b}$$

Such an initial distribution may typify a beam composed of a core and a halo component, of which mention has been made in the Introduction. Simulation computations performed with the initial distribution specified by Eq.(8a) indicate the expected melding of the groups to form ultimately a composite group of simple exponential form whose mean square amplitude continues to damp in the expected manner ($\langle u\rangle = C\exp(-\tau)$). Figures 1a-d illustrate this behavior, with results for the individual groups indicated by dashed lines and results for the total distribution shown by a solid line. [Note that, because of the shrinkage of amplitude as the damping progresses, we have plotted $\langle u\rangle f(u;\tau)$ <u>vs.</u> $u/\langle u\rangle$.]

Results in agreement with those depicted on Figs.1a-d are obtained through use of the formula given in(7) for $f(u;\tau)$. With the initial distribution considered here, this formula gives(9) (with $\langle u\rangle = C\exp(-\tau)$)

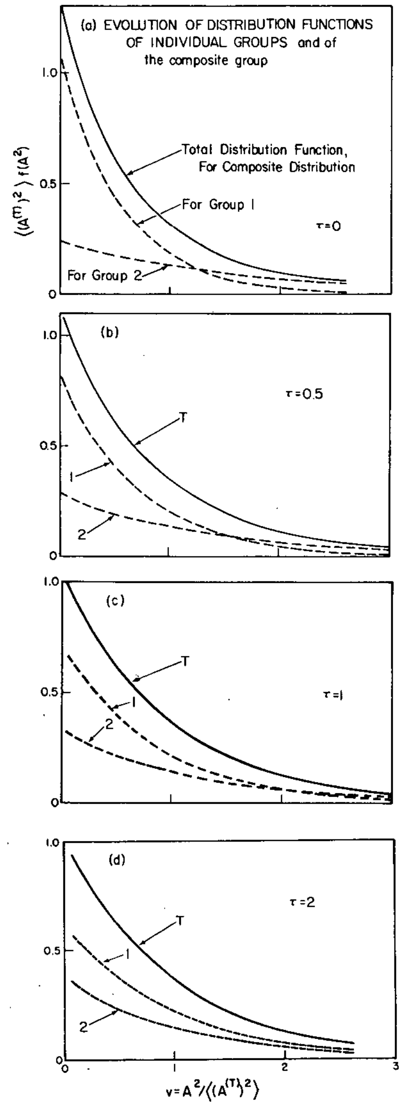

Fig.1. $n_1 = 0.6$, $n_2 = 0.4$

$C_1 = 5.0$, $C_2 = 15.0$ (C=9.0).

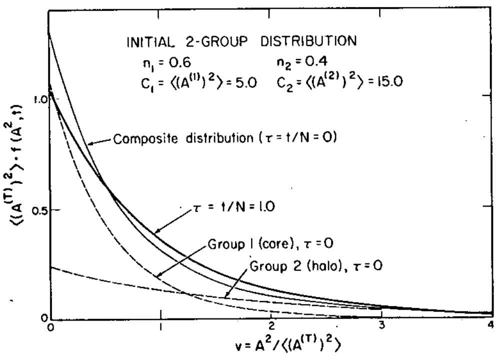

Fig.2. Composite A^2 distribution for $\tau = 0$ and $\tau = 1$.

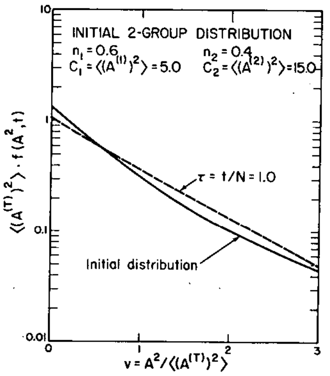

Fig.3. Approach of A^2 distribution to an exponential form.

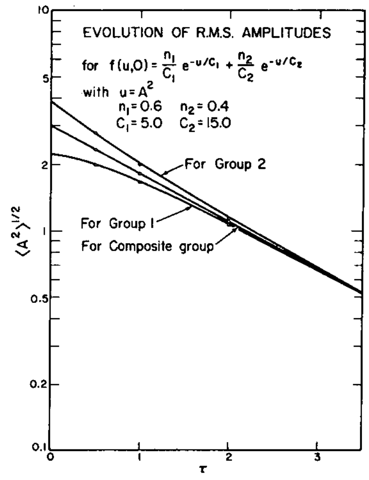

Fig.4. Convergence of the root-mean-square amplitudes to a common value.

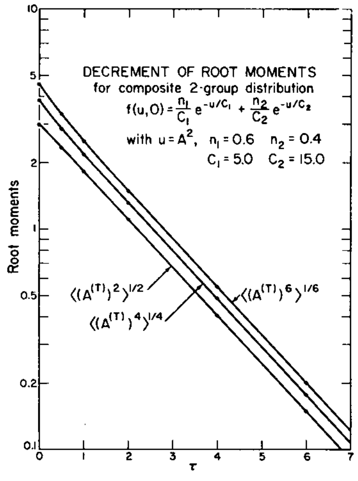

Fig.5. Evolution of root moments of composite distribution, to approach constant ratios.

$$f(u;\tau) = \frac{e^{-u/<u>}}{<u>} \left[n_1 \frac{C}{(1-e^{-\tau})C + e^{-\tau}C_1} \exp\left(- \frac{C-C_1}{C} \frac{u}{(1-e^{-\tau})C + e^{-\tau}C_1} \right) + n_2 \frac{C}{(1-e^{-\tau})C + e^{-\tau}C_2} \exp\left(- \frac{C-C_2}{C} \frac{u}{(1-e^{-\tau})C + e^{-\tau}C_2} \right) \right] \tag{9}$$

The distribution $f(u;\tau)$ can also be computed, with identical results, from Eqs.(7) in cases for which the convergence of Eq.(7a) permits numerical evaluation.(10) The change of form of the distribution function for the composite beam is directly shown, by a comparison of results for $\tau = 0$ and for $\tau = 1.0$, on Fig.2. The approach of this distribution function to an exponential form is most clearly apparent from the semi-logarithmic plot of Fig.3.

The behavior of the mean square amplitudes of the individual groups is most readily computed from the results presented in Appendix A. The convergence of the associated root-mean-square amplitudes, for the individual groups and for the composite group, to a common value is illustrated graphically in Fig.4. Similarly, $< (A^{(T)})^2 >^{\frac{1}{2}}$ and higher root-moments approach constant ratios, characteristic of an exponential distribution function $f(u;t)$ as illustrated in Fig.5.

IV. ACKNOWLEDGEMENTS. It is a pleasure to acknowledge the encouragement and help received, through many discussions, from P. Channell, A. Faltens, Glen Lambertson, H. Levine, and Lloyd Smith. We also are indebted to Dr. Smith for suggesting the form of the two-group distribution adopted in Eq.(8a) for purposes of illustration.

APPENDIX A

Evolution of the Mean Square Amplitudes of the Individual Groups of a Two-Group Distribution

For a distribution regarded as comprised of two groups,

$$\Delta[(A_{i_1}^{(1)})^2] = -(2/N)A_{i_1}^{(1)} \quad \Sigma_{j_1} A_{j_1}^{(1)} \cos(\phi_{i_1}^{(1)} - \phi_{j_1}^{(1)}) + \Sigma_{j_2} A_{j_2}^{(2)} \cos(\phi_{i_1}^{(1)} - \phi_{j_2}^{(2)})$$

$$+ (1/N^2)\Sigma_j \Sigma_k A_j A_k \cos(\phi_j - \phi_k)$$

for the $i_1^{\underline{th}}$ particle of Group 1. The random phase assumption then leads to

$$\frac{d}{dt} < (A^{(1)})^2 > = -(2/N) < (A^{(1)})^2 > + (1/N^2)[N^{(1)} < (A^{(1)})^2 > + N^{(2)} < (A^{(2)})^2 >]$$

or

$$\frac{d}{d\tau} < (A^{(1)})^2 > = -2 < (A^{(1)})^2 > + [n_1 < (A^{(1)})^2 > + n_2 < (A^{(2)})^2 >]$$

(where, as in the text, $N^{(1)} = n_1 N$ and $N^{(2)} = n_2 N$), and similarly for $d < (A^{(2)})^2 > /d\tau$. Accordingly, with C_1, C_2 denoting the initial respective mean square amplitudes of groups 1 and 2, we may write the solution of these equations as

$$< (A^{(1)})^2 > = [C_1 + n_2(C_2 - C_1)(1 - e^{-\tau})]e^{-\tau}, \quad < (A^{(2)})^2 > = [C_2 + n_1(C_1 - C_2)(1 - e^{-\tau})]e^{-\tau}.$$

APPENDIX B

Equation (6) as a Fokker-Planck Equation

With $f(u;\tau)$ denoting the distribution function for $u = A^2$ and $\psi(u,\delta u)$ denoting the probability of an increment δu to the quantity u in a time interval δt,

$$f(u;t \;+\delta t) = \int_{-u}^{\infty} f(u-\delta u;t)\;\psi(u-\delta u,\delta u)\;d(\delta u),$$

as is characteristic of a Markoff process. A Taylor development of this relation then leads to

$$\frac{\partial f}{\partial t} = -\frac{\partial}{\partial u}\left[f \cdot <\delta u>\right] + \frac{1}{2}\frac{\partial^2}{\partial u^2}\left[f \cdot <(\delta u)^2>\right],$$

where the quantities $<\delta u>$ and $<(\delta u)^2>$ are functions of u that represent averages (over the permissible range of δu) of changes or squared changes of u expected per unit interval δt.

In the present application, with δu for an i$\underline{\text{th}}$ particle given by

$$\delta u = \delta(A^2) = -(2/N)A_i\Sigma_j A_j \;\cos(\phi_i - \phi_j) + (1/N^2)\Sigma_m\Sigma_n A_m A_n \cos(\phi_m - \phi_n),$$

the presumption of random phase leads to

$$<\delta u> = -2A^2/N + <A^2>/N = -(2/N)u + <u>/N.$$

Similarly,

$$<\delta(u^2)> = -(4/N)u^2 + (4/N)u <u>.$$

Accordingly,

$$<(\delta u)^2> \equiv <\delta(u^2)> -2u <\delta u> = (2/N)u <u>.$$

[It may be worth noting that we have found $<(\delta u)^p>$ to be zero through order 1/N for all integer p > 2.] The partial differential equation then becomes

$$\frac{\partial f}{\partial t} = \frac{\partial}{\partial u}\left[-2\,\frac{uf}{N} + \frac{<u>f}{N}\right] + \frac{1}{2}\,\frac{\partial^2}{\partial u^2}\;(2\,\frac{u<u>f}{N})\;.$$

or

$$\frac{\partial f}{\partial \tau} = 2\,\frac{\partial}{\partial u}\,(uf) \;+\; <u>\,\frac{\partial}{\partial u}\,(u\,\frac{\partial f}{\partial u}),$$

wherein (as given originally by van der Meer$^{(1)}$) $<u>$ may be taken [consistently with Eq.(6)] to be given by Eq.(4) of the text.

REFERENCES AND NOTES

1. S. van der Meer, CERN Internal Report CERN/ISR-PO/72-31 (CERN, Geneva, Switzerland; 1972)--cited in Ref.2.
2. P. Bramham, G. Carron, H. G. Hereward, K. Hübner, W. Schnell, and L. Thorndahl Nuclear Instr.and Meth., 125, 201-202 (1975).
3. G. Carron, L. Faltin, W. Schnell, and L.Thorndahl, Bull. Am. Phys. Soc. 22 (No.2), 148 (Feb. 1977)--Abstract G6, 1977 Particle Acc. Conf.
4. An alternative derivation of the partial differential equation for $f(u;\tau)$ [Eq.(6)] can be obtained through use of the Fokker-Planck equation$^{(5)}$-- see Appendix B.

5. See S. Chandrasekhar, Rev. Mod. Phys, 15, 1-89 (1943); reprint in N. Wax (Ed.), Selected Papers on Noise and Stochastic Processes (Dover Publications, Inc., New York; 1954), pp. 3-91.

6. In finding the solution shown by Eq. (7a) we originally commenced with the moment equations (5) and introduced an amplitude distribution function $g(A;\tau)$ $[=2A\, f(A^2;\tau)]$ that should satisfy the partial differential equation

$$\partial g/\partial\tau = \partial(Ag)/\partial A + (C/4)\exp(-\tau)\,\partial[A\partial(g/A)/\partial A]/\partial A.$$

We then wrote $z = (A^2/C)\exp(\tau)$ and regarded $g(A;\tau)$ as a function $G(z;\tau)$ to obtain a partial differential equation in which none of the coefficients was explicitly τ-dependent. We next replaced G by the dependent variable $S = [(1/\sqrt{z})\exp(z-\tau/2)]G$ to obtain a partial differential equation that, by separation of variables, led to a solution in terms of Laguerre polynominals. Transcription of this solution into the original variables led to a result equivalent to Eq. (7a). For numerical solution of the partial differential equation, it may be convenient to introduce the independent variable $w = A\exp(\tau/2)$ and to employ as the dependent variable a function $H(w;\tau) = [\exp(-\tau/2)]g$. The partial differential equation for H is

$$\partial H/\partial\tau = (1/2)\,\partial(wH)/\partial w + (C/4)\,\partial[w\partial(H/w)/\partial w]/\partial w$$

--again an equation in which none of the coefficients is τ-dependent--and it is expedient to seek solutions that have the formal character of being odd with respect to w.

7. An alternative, closed-form solution may be written

$$f(u;\tau) = \langle u\rangle^{-1}\exp(-u/\langle u\rangle)\,\frac{\exp[-(1-e^{-\tau})^{-1}u/C]}{1-e^{-\tau}}\times$$
$$\int_0^\infty \exp[-(e^{\tau}-1)^{-1}x/C]\, I_0(2(1-e^{-\tau})^{-1}\sqrt{ux}/C)\, f(x;0)\,dx,$$

where I_0 is the zero-order modified Bessel function of the first kind--see I. S. Gradshteyn and I. M. Ryzhik, Table of Integrals. . . (Academic Press, New York; 1965), Sec. 8.976 (1), p.1038 (with $\alpha = 0$) to relate this solution to that proposed by Eq. (7) in the text.

8. Since f(u) is normalized to unity and $L_0(u/C) = 1$, $\alpha_0 = 1$. Also, since the initial value of $\langle u\rangle$ is C and $L_0(u/C) - L_1(u/C) = u/C$, we find $\alpha_0 - \alpha_1 = 1$ and, hence, $\alpha_1 = 0$.

9. Note that $\int_0^\infty e^{-\beta x} I_0(\gamma\sqrt{x})\,dx = (1/\beta)\exp(\tfrac{1}{4}\gamma^2/\beta)$.

10. For the example of Sec. III, evaluation of Eq. (7c) leads to $\alpha_m = n_1(1-C_1/C)^m + n_2(1-C_2/C)^m$--see Gradshteyn and Ryzhik (cited in (7)), Sec. 7.414 (6), p. 844. The resultant Eq. (7a) may not have suitable convergence characteristics for small τ under certain circumstances however--thus consider, for example, an initial distribution (8a) with $n_1 = 0.75$, $n_2 = 0.25$, $C_1 = 4.0$, and $C_2 = 16.0$ ($C = 7.0$), for which the factor $1 - C_2/C = -9/7$ and the coefficients α_m ultimately increase essentially in geometrical progression (with alternating sign).

*Work supported by the U.S. Energy Research and Development Administration.

Presented at the Workshop on
Non-Linear Dynamics, La Jolla, CA,
December 27-30, 1977

LBL-7247

SOME ILLUSTRATIONS OF STOCHASTICITY

L. Jackson Laslett
University of California Lawrence Berkeley Laboratory
Berkeley, California*

A complex, and apparently stochastic, character frequently can be seen to occur in the solutions to simple Hamiltonian problems. Such behavior is of interest, and potentially of importance, to designers of particle accelerators -- as well as to workers in other fields of physics and related disciplines. Even a slow development of disorder in the motion of particles in a circular accelerator or storage ring could be troublesome, because a practical design requires the beam particles to remain confined in an orderly manner within a narrow beam tube for literally tens of billions of revolutions. The material I shall present is primarily the result of computer calculations I and others have made to investigate the occurrence of "stochasticity," and is organized in a manner similar to that adopted for presentation at a 1974 accelerator conference.[1]

As an introductory example, one can consider the longitudinal motion of a particle subjected to the radio-frequency electric fields employed to bunch, and sometimes accelerate, a beam within a synchrotron type of accelerator. If the electric field is regarded as equivalent to a simple travelling wave, having the speed of a reference particle in a "coasting beam," the motion is characterized by the pair of differential equations.

$$\frac{dy}{dn} = -K \sin\pi x \tag{1a}$$

$$\frac{dx}{dn} = \lambda' y \tag{1b}$$

wherein y - fractional departure of energy from the reference value,

πx = electrical phase angle of field vs. particle,

$K \propto$ applied voltage, and

$\lambda' \propto$ derivative of revolution period with respect to energy.

---

* Work supported by the U.S. Dept. of Energy, Office of Energy Research.

K and λ' will be regarded as specified constants. The differential equations will be recognized as derivable from a Hamiltonian function

$$H = \frac{1}{2} \lambda' y^2 - \frac{K}{\pi} \cos \pi x, \tag{2}$$

in which the independent variable (n) is the revolution number and does not appear explicitly in the Hamiltonian. Because n does not appear explicitly, the Hamiltonian of course is a constant of the motion. One accordingly obtains simple phase trajectories (in x,y space) -- of the familiar type characteristic of a physical (non-linear) pendulum (as was recognized by McMillan in connection with discovery of the principle of phase stability[4]).

In practice, however, the radio-frequency fields in fact are provided by localized cavities, so that the travelling-wave description constitutes an idealization and the motion is more appropriately represented by difference equations:

$$y_{n+1} = y_n - K \sin \pi x_n \tag{3a}$$

$$x_{n+1} = x_n + \lambda' y_{n+1}, \tag{3b}$$

with y_n measuring energy at the entrance to the n^{th} cavity. These transformation equations are readily shown to be area preserving $[\partial(x_{n+1},y_{n+1})/\partial(x_n,y_n) = 1]$ -- the motion in fact could be described through use of a Hamiltonian function, but one that would contain a periodic δ-function of the independent variable as a factor multiplying the term $-\frac{K}{\pi} \cos \pi x$. There thus is no evident simple constant of the motion, and the non-linearity of the equations precludes application of Floquet theory to this problem. (The use of a Hamiltonian formulation nonetheless can be helpful in analytic work, but difference equations of course are convenient for computational investigations.)

It is of interest to take a quick look at some computational results obtained through use of a transformation equivalent to (3a,b) but written in terms of working variables $Y = y - (K/2) \sin\pi x$, $X = x$, so that the transformation assumes the form

$$\left.\begin{aligned} X_{n+1} &= X_n + \lambda'[Y_n - (K/2) \sin\pi X_n] \qquad &(3a') \\ Y_{n+1} &= Y_n - (K/2)[\sin\pi X_n + \sin\pi X_{n+1}] \qquad &(3b') \end{aligned}\right\},$$

with the result that the resulting phase diagrams will necessarily have a desirable symmetry about both the X- and Y-axes. With $K/\pi = 0.1$ and $\lambda' = 0.1$ we find what appear to be conventional bucket diagrams with buckets separated in Y by $2/\lambda'$ for successive harmonic modes, although we may wish to return to the question of whether the bucket boundaries are as simple and definite as appears on Fig. 1.

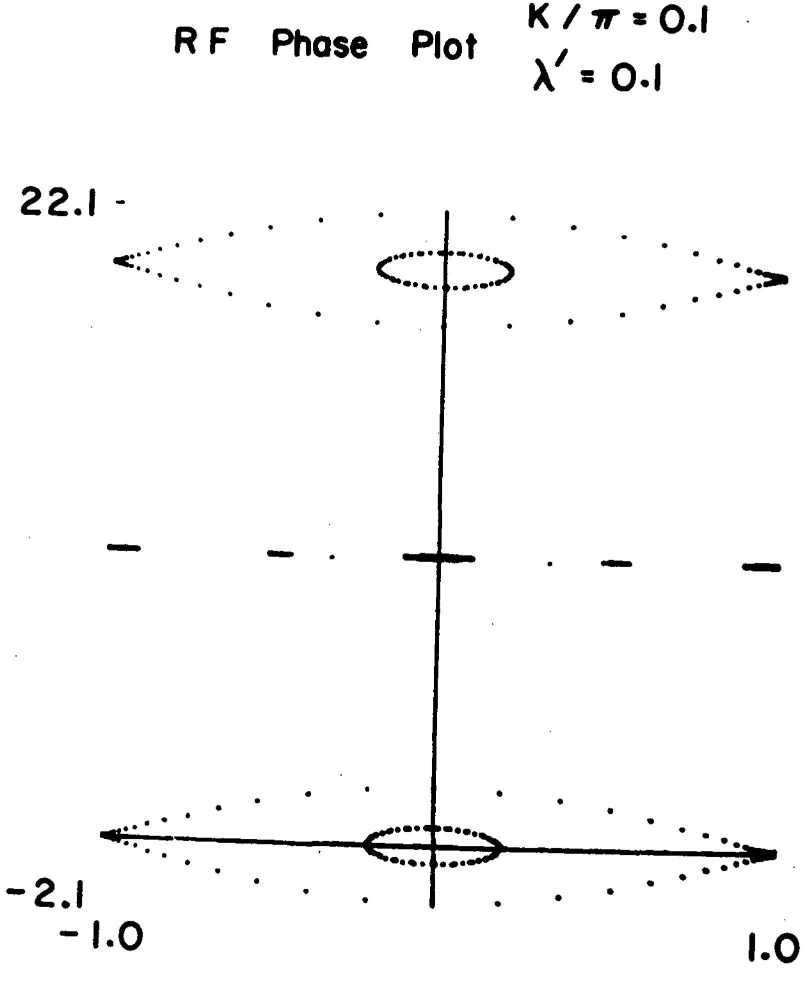

XBL 744-741

Fig. 1 -- X, Y phase plot for a coasting beam under the influence of an R.F. cavity with $K/\pi = 0.1$, $\lambda' = 0.1$ -- as computed by Eqns. (3a',b'). X is plotted mod. 2.

We also find evidence of some "sub-harmonic" structure (with higher order fixed points) that, if enlarged some 60X, has the appearance shown in Fig. 2.

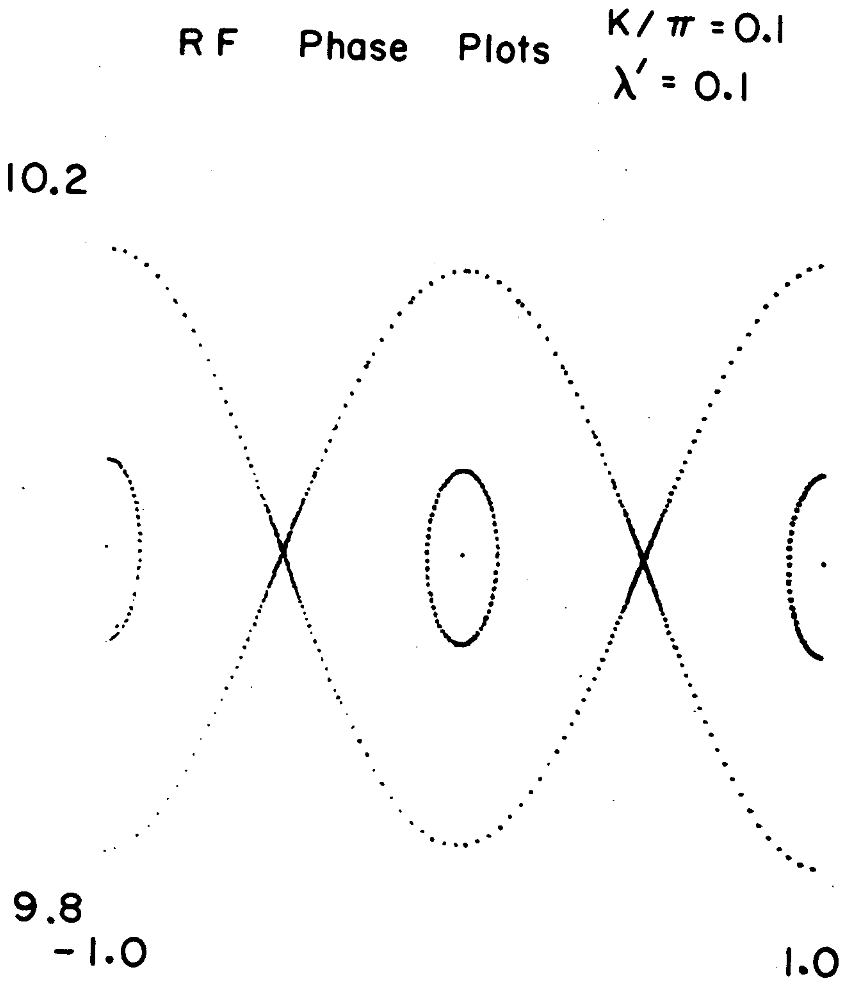

XBL 744-737

Fig. 2 -- Circa 60-fold vertical enlargement of central portion of Fig. 1, near Y = 10.0, showing sub-harmonic structure.

If the cavity voltage is increased eight-fold (so $K/\pi = 0.8$), the bucket areas are expected to become larger, and we indeed find this to be the case (Fig. 3), with an accompanying very marked increase of complexity

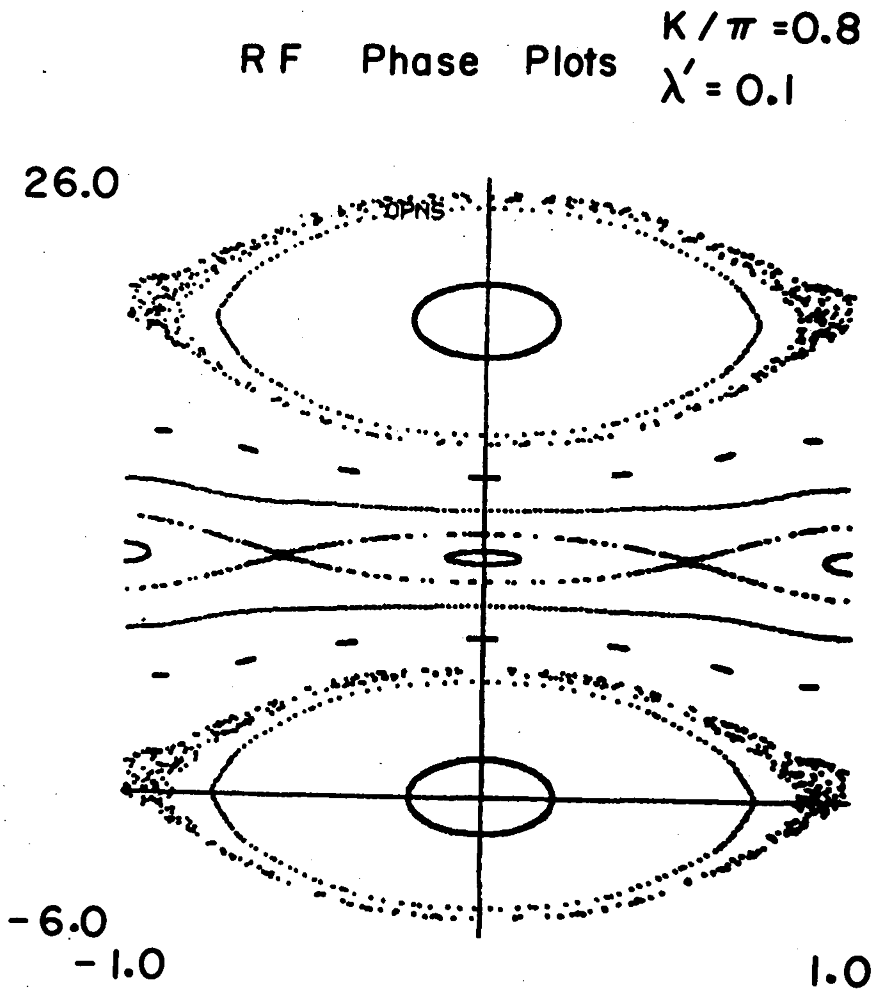

XBL 744-739

Fig. 3. - Phase plot similar to Fig. 1, but for operation with K/π = 0.8, showing the obvious development of complex structure.

that is immediately apparent in the phase plot. Of particular interest is the evident diffuse character of phase trajectories generated by points launched close to the first-order unstable fixed points situated at $X = \pm 1$, since the bucket boundary in consequence no longer appears clearly defined.

In the first example (K/π = 0.1), on the other hand, where the bucket width is some two and one-half times smaller in relation to the bucket separation, the presence of structure in the separatrix can be revealed computationally only with considerable care.[6] To do this, one can extend from the unstable fixed points the eigenvector directions of the transformation linearized about these fixed points, and examine whether such curves intersect smoothly. One finds in fact that they do not quite do so, but generate loops (of a nature to be illustrated later) that in this instance ($K/\pi = 0.1$) have a very small area that amounts to only about $1/(5 \times 10^{11})$ of the area of the bucket itself.

Another example of a "time-dependent" non-linear problem in the phase plane arose in connection with the development of spiral-sector fixed-field accelerators (as have now evolved into very effective cyclotrons for physical research). The equations for particle motion in these devices again required a time-dependent Hamiltonian and were distinctly non-linear. The limitations of computer performance at that time (1956) understandably motivated us to study the behavior of simple algebraic transformations that at least would duplicate approximately the short-term particle motion. Such an area-preserving transformation is

$$x_{n+1} = Ax_n \pm (1 - A^2)y_n + (1 - A)\,[x_n \pm (1-A)y_n]^2 \tag{4a}$$

$$y_{n+1} = \mp x_n + Ay_n \pm [x_n \pm (1-A)y_n]^2, \tag{4b}$$

where the ± signs refer to the forward or inverse transformation, respectively, and A represents the cosine of the phase advance per iteration for solutions to the linearized (small-amplitude) transformations. The constant A normally would be taken to have an absolute value less than unity and, to avoid a one-third resonance when the quadratic terms are present, one also should avoid the value $A = -1/2$ (for which $\cos^{-1}A = 2\pi/3$).

The region of interest to the accelerator designer at that time is that contained within the roughly triangular area indicated on Fig. 4, sketched for $A = -5/8$ [$\cos^{-1} A \cong (0.35745)(2\pi)$], wherein the apparent separatrices through the fixed points F_1, F_2, F_3 are associated with the 2/3 resonance and also illustrate the symmetry of the transformation (4a,b) with respect to the x-axis. It was only by rather careful computations [aided by Mrs. H. (Barbara) Levine -- see Ref. 12] that I could establish that the trajectories extending from the fixed points F_1, F_2, F_3 do not intersect smoothly and hence give rise to (rather modest) regions of erratic behavior similar to those seen in phase diagrams for the earlier example. Outside the area F_1, F_2, F_3 indicated in Fig. 4, however,

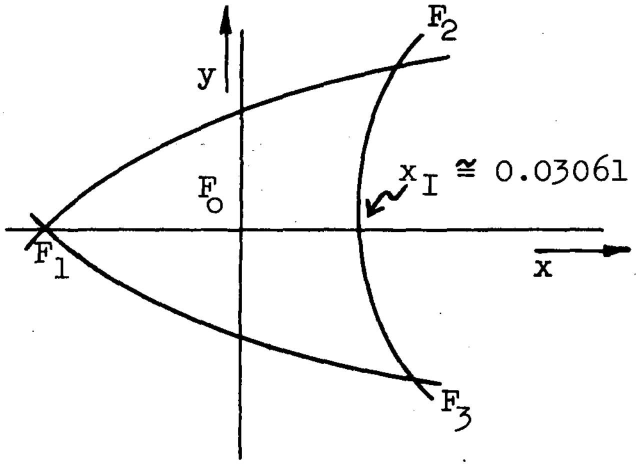

Sketch for $A = -{}^5/8$

$\cos^{-1}A \cong (0.35745)(2\pi)$

Area $\cong 5.5 \times 10^{-3}$
(would shrink to zero
if $A \to -{}^1/2$)

$$F_1\colon \left(-\frac{\sqrt{41}-5}{26},\ 0\right) = (-0.053966\cdots,\ 0)$$

$$F_{2,3}\colon \left(\frac{1}{26},\ \pm\frac{4\sqrt{41}-16}{169}\right) = (0.03846\cdots,\ \pm\,0.05688\cdots)$$

XBL 7712-11142

Fig. 4 - Apparent separatrices through the third-order unstable fixed points of the transformation (4a,b), with A = -5/8.

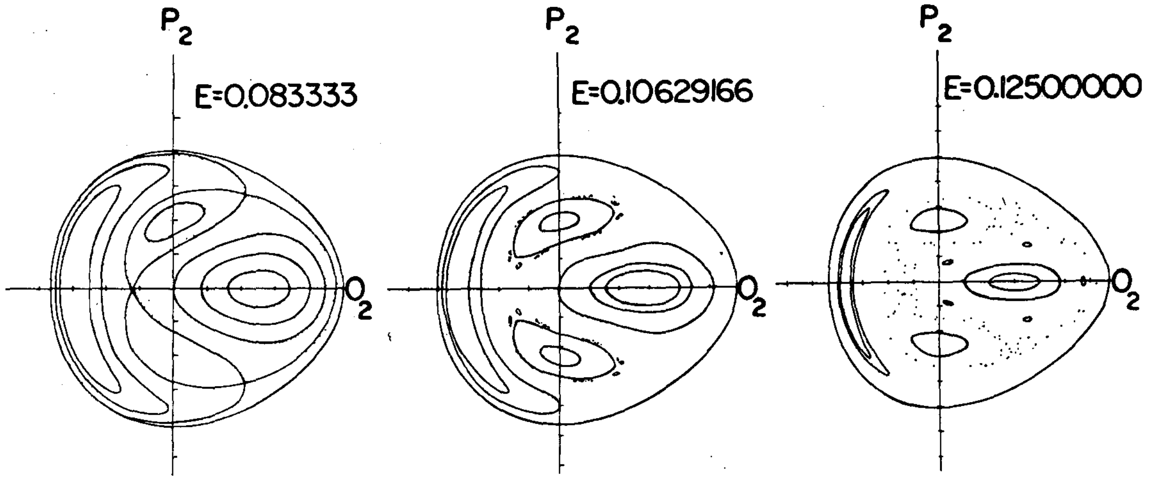

XBL 744-740

Fig. 5 - Phase plots, in the surface of section $q_1 = 0$, resulting from the equation implied by the Hamiltonian function (5) -- for increasing values of the energy. [After Walker and Ford.[8]]

the transformation (4a,b) develops gross loops in phase trajectories extending from an order-1 fixed point at (1,0), and in this respect exhibits a behavior similar to that shown by a transformation of deVogelaere which will be mentioned later.

Similar questions concerning the character of phase trajectories and the possible erratic or stochastic behavior of canonical mappings can arise in problems with more than one degree of freedom. As an example, Hénon and Hiles[7] and subsequently Walker and Ford[8] studied a model of an astronomical system, for which the Hamiltonian function was taken to be

$$H = \frac{1}{2}(p_1{}^2 + p_2{}^2 + q_1{}^2 + q_2{}^2) + q_1{}^2 q_2 - \frac{1}{3} q_2{}^3. \qquad (5)$$

The cubic terms appearing here as coupling terms become increasingly significant for increasingly large values of H -- which is itself a constant of the motion. With the coupling terms present, however, and in the absence of any simple constant of the motion other than H, a given phase trajectory might be expected to wander (ergodically) over virtually all of a three-dimensional surface specified by H = Constant (and that will be a closed surface for values of H below the dissociation energy). If, on the other hand, some additional integral of the motion were in fact also acting, the phase points of a given trajectory then would be constrained to lie on a two-dimensional surface, and graphs of the intersection of such surfaces with some selected plane or other surface (a "surface-of-section") would lead to simple curves in this plane rather than to a scattering of points. Computations of this nature indicated that for sufficiently small values of energy (e.g., $H < 1/12$) only curves that to computer accuracy were smooth (and relatively simple) were formed by intersection with the plane $q_1 = 0$ (and $p_1 > 0$). Examples in which the energy of the particles was successively raised, however, resulted in the development of ragged island structures or of apparent stochastic behavior over increasingly large portions of this surface-of-section (Fig. 5).

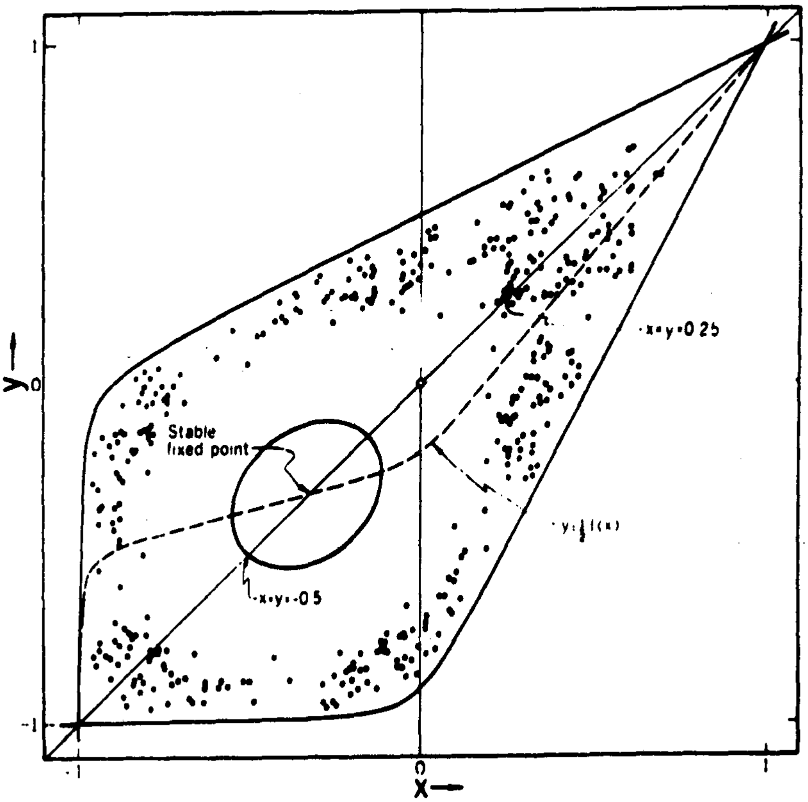

XBL 744-684

Fig. 6 - Phase diagram for the transformation (6a, b), with f(y) given by Eqn. (7a). The scattered points result from computations initiated with $x_0 = y_0 = 0.25$, but must remain within the separatrix defined by the function Φ [Eqn. (7b)]. k = 0.1.

Such behavior appears concordant with the "KAM" (Kolmogorov-Arnol'd-Moser) theory (see Ref. 58, 59 & 60 of our Ref. 2c), which suggests that many of the invariant curves or surfaces present in the absence of the perturbation will persist, with only minor distortion, in the presence of a sufficiently small perturbation (see, however, Note 9). It is of interest, of course, to determine or to estimate the circumstances (e.g., perturbation strength) at which the KAM theory becomes inapplicable and extended regions of erratic (or stochastic) behavior develop. As we suggested by our first examples, and has been expounded more extensively by Zaslavskij and Chirikov,[2c,10] one means for obtaining such estimates may be by determining the ratio of resonance width $[\delta\omega = (d\omega/dI)_r \delta I]$ to the distance ($\Delta\omega$) to the nearest neighboring resonance.

Additional tests (to be mentioned below) may be required to determine the degree of disorder associated with the movement of phase points in such stochastic regions. We may first note, however, that the existence of nested closed invariant curves in a plane -- as suggested by the KAM theorem for a problem in one degree of freedom -- prevents phase points from moving outward or inward to regions of substantially different "amplitude" (in the absence of noise). With more than one degree of freedom, however, stochastic layers may intersect, to form an intricate system of channels along which a phase point can slowly diffuse and result in instability. The possibility of such "Arnol'd diffusion" has been demonstrated by Arnol'd [Ref. 35 of our Ref. 2c; stated simply the example considered by Arnol'd is comprised of a physical pendulum and a simple-harmonic oscillator, with a time-dependent coupling (that also depends on the phases, or angle variables, of these oscillations)].

It should be pointed out that some non-linear transformations -- say for a system with one degree of freedom -- will not lead to the disappearance of some or all of the invariant phase curves at substantial amplitudes. Thus for transformations of the form

$$x_{n+1} = y_n; \; y_{n+1} = -x_n + f(y_n), \tag{6a,b}$$

McMillan[11] has shown that if $f(y)$ can be written as $\Phi(y) + \Phi^{-1}(y)$ (where Φ^{-1} denotes the function inverse to Φ), then the curves $y = \Phi(x)$ and $x = \Phi(y)$ will constitute invariant curves. Such curves will pass through the first-order fixed point(s) situated at the intersections(s) of $y = (1/2)f(x)$ with the principal diagonal. An enclosed area can thereby be formed from which phase points cannot escape even if the behavior in portions of the interior becomes highly stochastic. This is illustrated by an example (Fig. 6) in which

$$f(y) = \frac{1}{2}(3y-1) - \frac{1}{2}\frac{k^2}{y+1} + \sqrt{y^2 + k^2} \tag{7a}$$

and

$$\Phi(x) = x - 1 + \sqrt{x^2 + k^2} \quad . \tag{7b}$$

Such a situation also can develop when $f(y)$ is a stepwise linear function of y with discontinuities of slope, as has been noted by Drs. Judd and

McMillian [see, for example, Figs. 13 and 14 (pp. 27-28) of Ref. 12]. If $f(y)$ is of the form

$$f(y) = -(By^2 + Dy)/(Ay^2 + By + C), \tag{8}$$

moreover, the <u>entire</u> phase plane will be covered by a family of simple invariant curves -- see, for example, the cases[11] $f(y) = 2ky/(1+y^2)$, with the invariants $x^2y^2 + x^2 + y^2 - 2kxy$ = Constant, and $f(y) = 2ky/(1-y2)$, with the invariants $x^2y^2 - x^2 - y^2 + 2kxy$ = Constant, illustrated by Figs. 7-8.

It is of interest to examine the mechanism whereby irregular behavior can develop in the neighborhood of unstable fixed points, taking as an illustration an example suggested by Professor deVogelaere that [when generalized and rewritten in variables leading to the form (6a,b) advocated by McMillan] employs

$$f(y) = 2[Ty + (1 - T)y^2]. \tag{9}$$

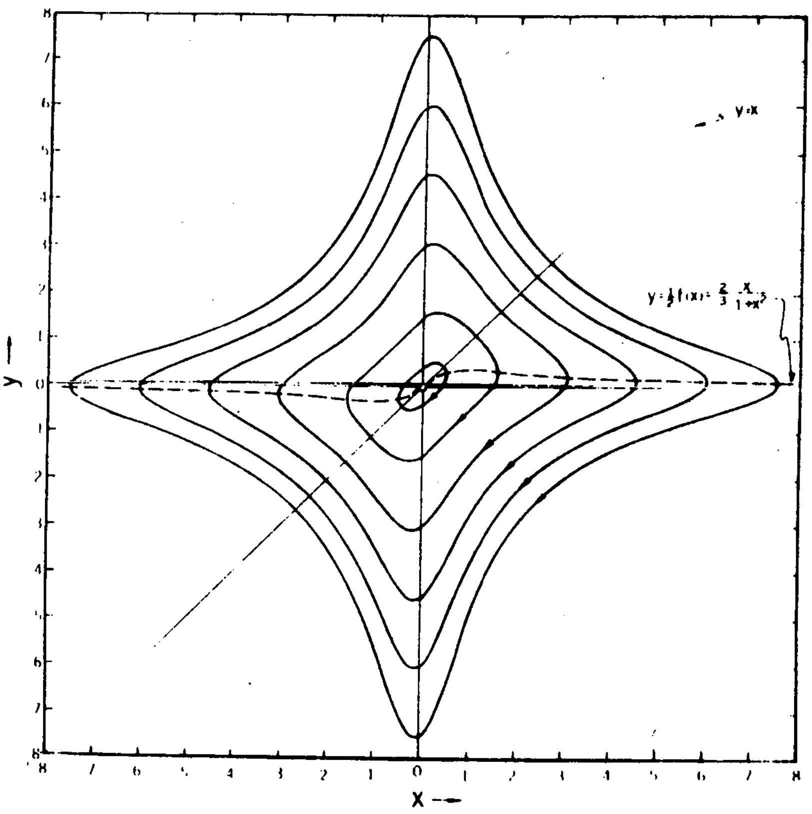

XBL 744-680

Fig. 7 - Invariant curves for the transformation (6a, b) with $f(y) = 2ky/(1+y^2)$ and $k = 2/3$. [Figs. 7 - 11 after McMillan.[11]]

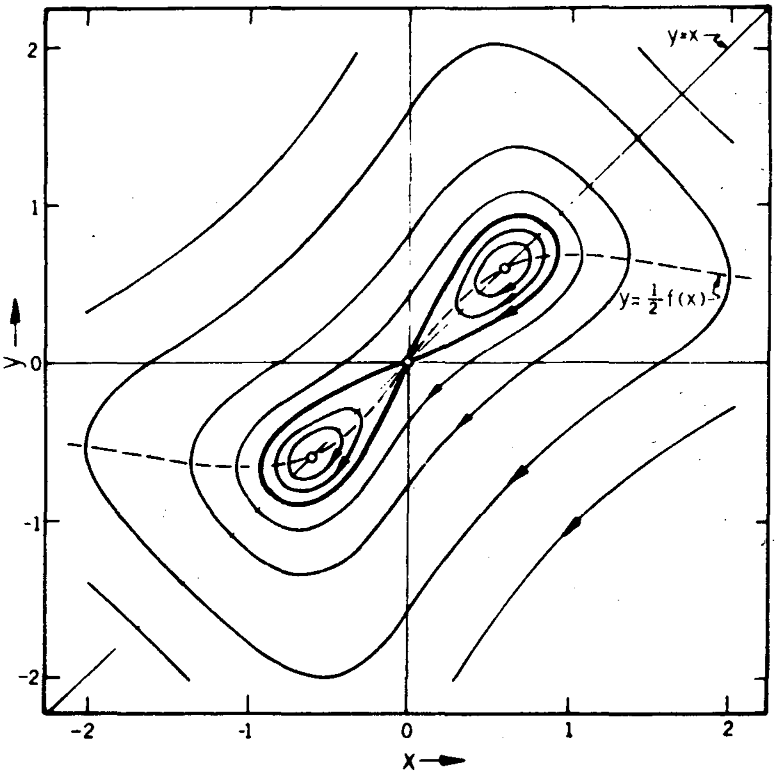

XBL 744-681

Fig. 8 - Invariant curves for the same transformation as in Fig. 7, but with k = 1.36.

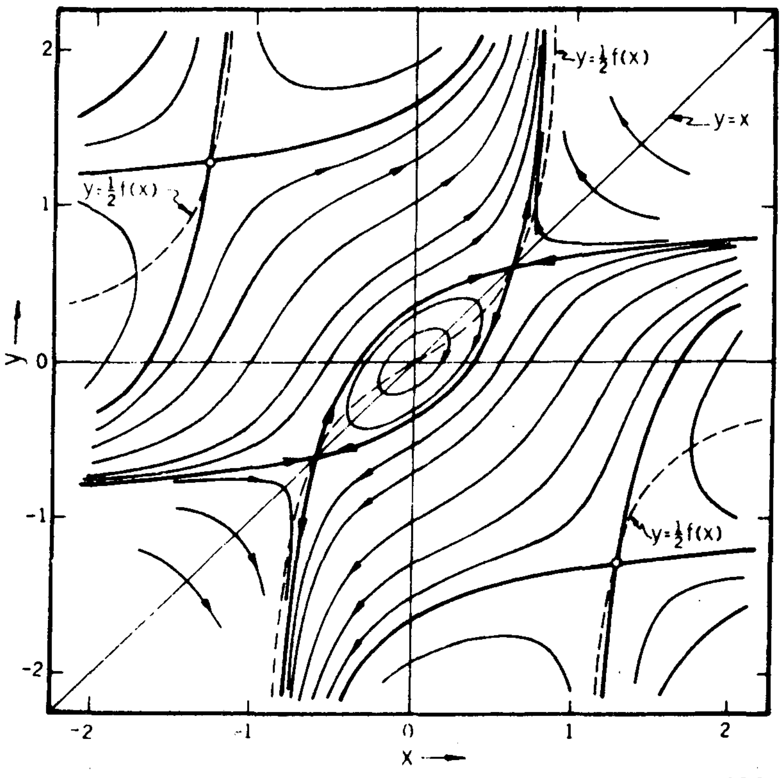

XBL 744-682

Fig. 9 - Invariant curves for the transformation (6a, b) with $f(y) = 2ky/(1-y^2)$ and k = 0.64.

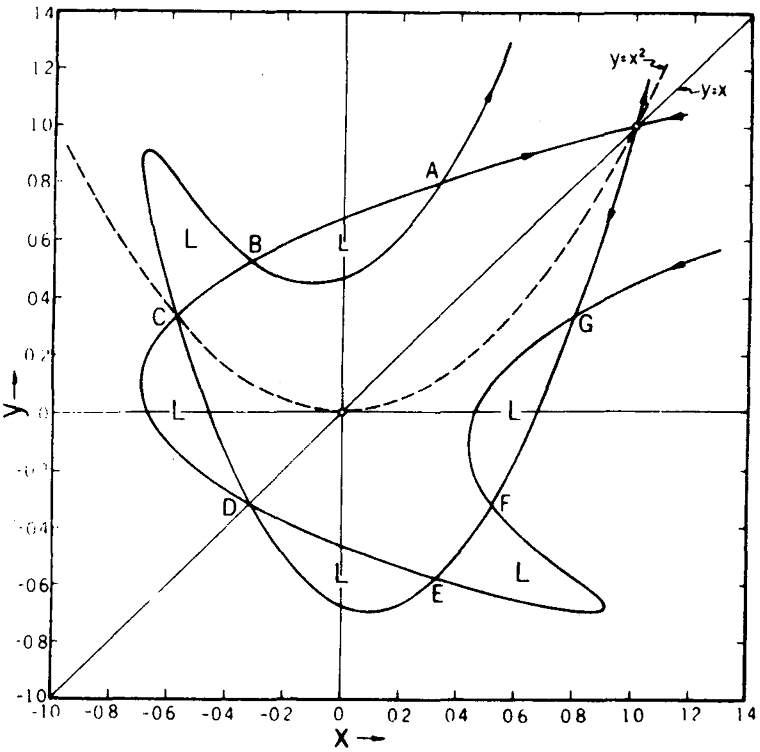

Fig. 10 - Plot of the extensions of the eigenvector directions from the unstable fixed point at (1,1), for the deVogelaere transformation expressed in McMillan's variables [Eqns. (6a, b) and (9), with T = 0]. The areas of the loops marked L are all equal, by virtue of the area-preserving character of the transformation and the inherent symmetry about the principal diagonal.

First-order fixed points appear at (0,0) and at (1,1). For T = 0, this transformation, when linearized about the unstable fixed point at (1,1), can be represented by the matrix $\begin{bmatrix} 0 & 0 \\ -1 & 4 \end{bmatrix}$, with eigenvalues and eigenvector slopes

$$\lambda = 2 \pm \sqrt{3}, \quad dy/dx = \lambda.$$

A line segment extending downward from the fixed point (1,1) with the slope $2 + \sqrt{3}$, if subjected to repeated applications of the transformation, generates the loops shown in Fig. 10; similarly a line segment of slope $2 - \sqrt{3}$, if extended by the inverse transformation, generates the mirror-image curve (mirrored about the principal diagonal). Points such as A, B, C ... progress toward the fixed point in smaller and smaller steps and, since the transformation is area-preserving, the associated loops clearly must become increasingly elongated as they become increasingly narrow from repeated applications of the forward transformation. The evolution of such loops clearly will become quite intricate (Fig. 11), but the loops apparently need not permeate the entire "interior". Portions of an inward loop can, in fact, enter, on a later iteration, into the interior of an outward-lying loop, as indicated on Fig. 11. A wealth of island structure, of course, can develop throughout the area of such phase diagrams.

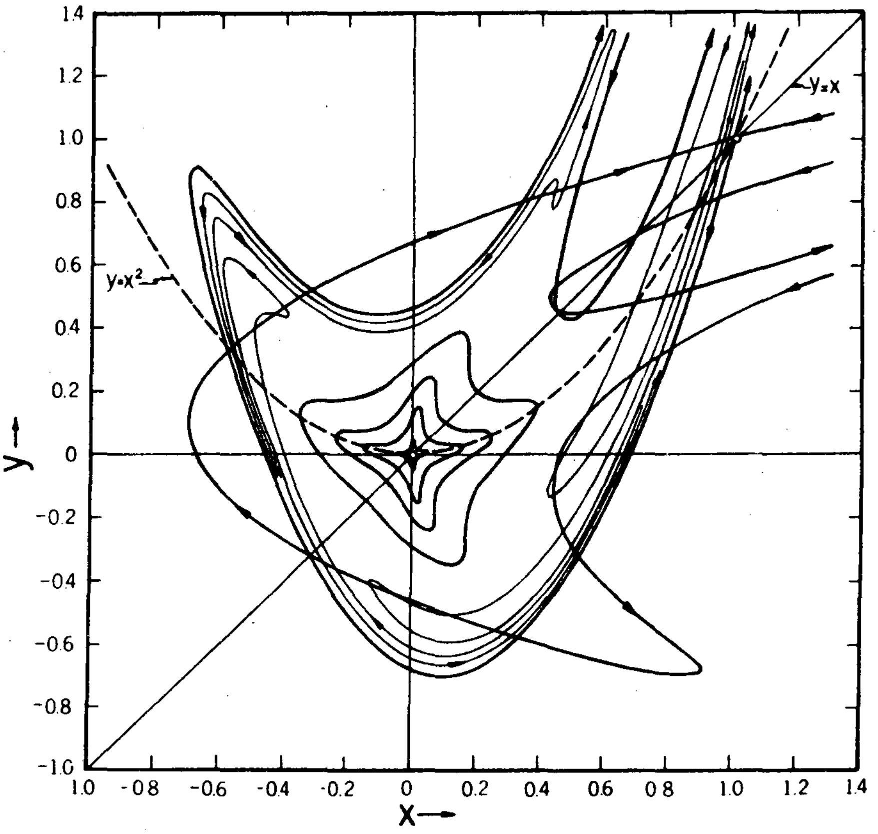

XBL 744-679

Fig. 11 - A partial extension of the curves shown on Fig. 10.

In some instances a family of unstable fixed points for which the eigenvalues are negative may arise (in place of a stable family, for which λ is purely imaginary), and the appearance of phase trajectories can thereby be drastically affected. Phase trajectories in the neighborhood of two such eighth-order ("tune" = 2/8) fixed points are shown on Fig. 12 for the transformation of deVogelaere written to exhibit symmetry about the x-axis

$$x_{n+1} = y_n + Tx_n + (1 - T)x_n^2 \tag{10a}$$

$$y_{n+1} = -x_n + Tx_{n+1} + (1-T)x_{n+1}^2, \tag{10b}$$

with $T = -1/8$. In any case it is clear, however, that the development of a loop system such as that shown on Fig. 11, can readily give rise to an apparent stochastic motion of phase points in portions of the phase diagram -- most particularly near an unstable fixed point.

The existence of a firm separatrix, or of an extensive family of invariant curves generally, can be extremely sensitive to the exact form of the transformation.[14] A case of some physical interest arises in computational studies relating to the Toda Lattice.[15] This one-dimensional lattice consists of particles interacting through exponential pair potentials and can propagate certain nonlinear wave forms ("solitons") without change of shape. One computational investigation[16] of stability for a three-particle lattice (with periodic boundary conditions) has commenced with a Hamiltonian function

$$H = \tfrac{1}{2}(P_1^2 + P_2^2 + P_3^2) + e^{-(Q_1-Q_3)} + e^{-(Q_2-Q_1)} + e^{-(Q_3-Q_2)}. \tag{11}$$

By a canonical transformation of variables, in recognition of the invariance of this system to translation -- so that $I_1 = P_1 + P_2 + P_3$ constitutes a constant of the motion -- the Hamiltonian (11) becomes expressible as a function of two pair of conjugate variables in the form

$$H = \frac{1}{2}(p_1{}^2 + p_2{}^2) + \frac{1}{24}[e^{(2q_2+2\sqrt{3}q_1)} + e^{(2q_2-2\sqrt{3}q_1)} + e^{-4q_2}], \qquad (12)$$

which is identical to the Hénon-Heiles Hamiltonian function (5) through terms of third order. It is of interest to examine whether in the present case constants of the motion other than H act to restrict the motion. Computationally it was found -- again using the surface-of-section $q_1 = 0 (p_1 > 0)$ -- that in this case simple invariant curves apparently continue to exist in the q_2p_2, plane, even for very large values of H. Stimulated by this result, Hénon[17] has directed attention to an additional integral of the motion that is valid in this case; the constants of the motion for the three-particle lattice then can be written in a form ~~that~~ we may express as[18]

$$H = \text{Constant} \qquad (13a)$$

$$P_1 + P_2 + P_3 = \text{Constant, and} \qquad (13b)$$

$$P_1P_2P_3 - P_1e^{-(Q_3-Q_2)} - P_2e^{-(Q_1-Q_3)} - P_3e^{-(Q_2-Q_1)} = \text{Constant.} \qquad (13c)$$

Evidently[17] further analytic work in fact has now established that the n-particle Toda lattice with periodic boundary conditions (or with fixed ends) is a "completely integrable" system.

It is of some interest to seek means for anticipating whether stochastic behavior will occur in various portions of a phase diagram and to examine the character of such stochastic behavior as does occur. What we here have loosely termed stochastic behavior can be catalogued with respect to a hierarchy of properties (ergodicity, mixing, $\cdots$), indicative of increasing disorder, that are fundamentally significant for statistical mechanics.[2a,e] Of particular interest to the accelerator designer, of course, is the determination of a threshold beyond

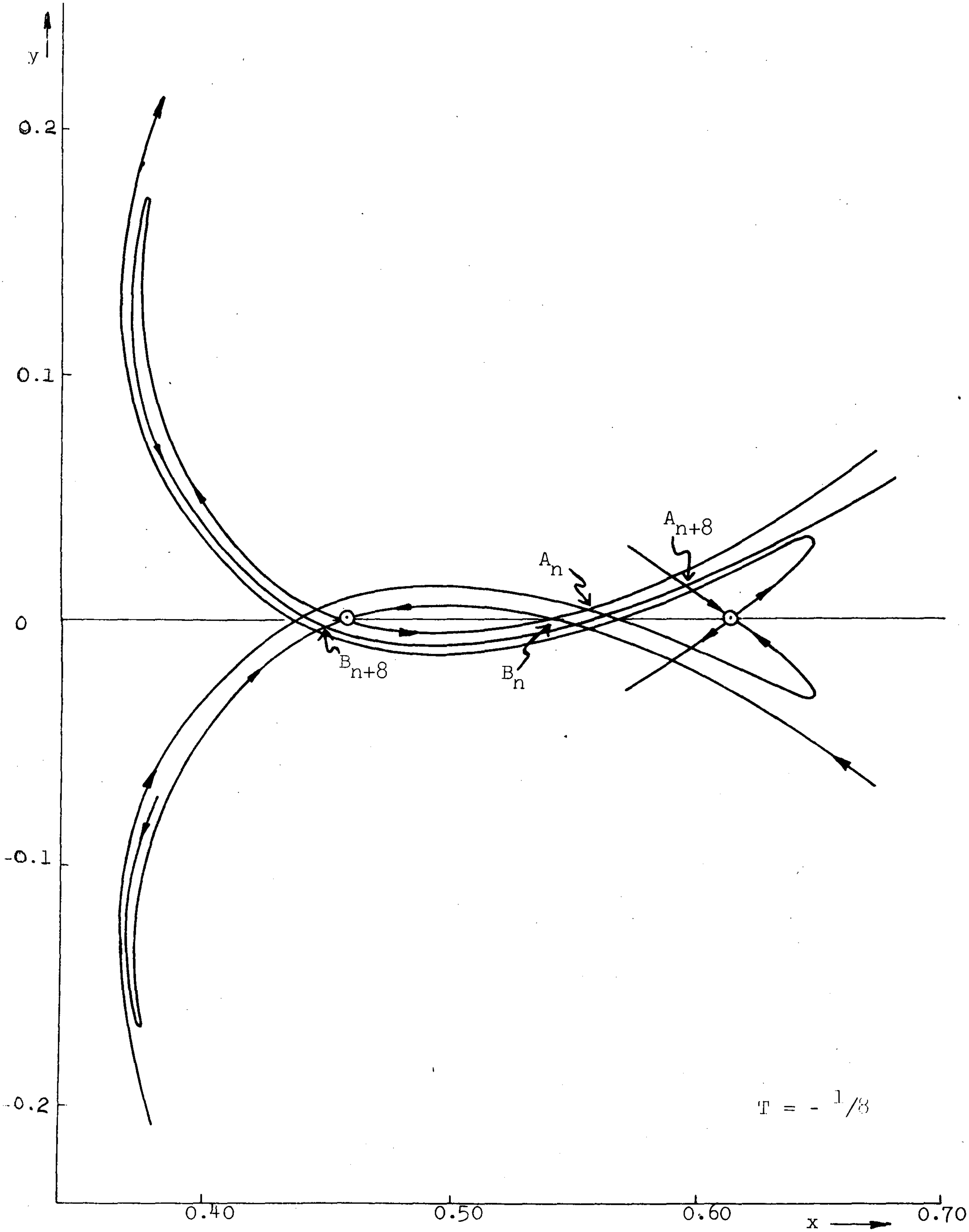

Fig. 12 - Phase trajectories for the transformation (10a,b) with T = -1/8, in the neighborhood of two fixed points for which the eigenvalue is <u>negative.</u>

which stochastic behavior will set in and may act to carry a phase point to unacceptably large amplitudes. As noted earlier, stochastic behavior appears to be associated with overlapping resonances,[2c] and this concept has served as the basis for some analytic estimates of stochasticity limits.[2c,19] It has been noted by René deVogelaere and confirmed in subsequent computations[20] that for a particular class of fixed-point families -- say those with rotation of the form m/(4m+1) -- there is a closely linear relationship between the order of the resonance (4m+1) and $\ell n|1 - \frac{1}{2}\,\text{Trace}|$ through many decades ("Trace" denoting the trace of the tangential-mapping or differential matrix associated with the 4m+1 iterations required to map a given fixed point onto itself). Such regularities, and others relating to the apparent size of the stable areas about high-order fixed points (e.g., as estimated from the intersection angle of eigenvectors), have been considered useful indicators of the change in character of a mapping at certain amplitudes.[21,10,22]

A computational procedure of considerable interest for recognizing stochasticity is that in which one follows the evolution of the distance between two initially very close points in phase space. In practice it can prove desirable to reduce the separation from time to time by a recorded factor whenever the separation becomes excessive during the computations, or, perhaps preferably, to evaluate the growth of an infinitesimal vector through use of the cumulative tangetial-mapping matrix. A high degree of stochasticity can be ascribed to the behavior of the transformation if there are such vectors whose length generally grows beyond the first iteration by a factor greater than unity (while others may similarly contract). (Ref. 2a, p. 55; for examples, see Ref. 23.) An analogous procedure -- that can be more attractive, although possibly of a less direct basic significance -- is an investigation of the growth of the eigenvalue(s) of the cumulative tangential mapping. Such eigenvalues can change sign repeatedly during the course of many interations, and hence will be seen to decrease from time to time, but an exponentially increasing trend in eigenvalue magnitude is likely to be associated with a similar type of increase for the lengths of the vectors mentioned previously. The nature of eigenvalue growth has been illustrated by Froeschlé[24] for the transformation[25]

$$x_{n+1} = x_n \cos\alpha - (y_n - x_n^2) \sin\alpha \qquad (14a)$$

$$y_{n+1} = x_n \sin\alpha + (y_n - x_n^2) \cos\alpha \qquad (14b)$$

The general characteristics of this transformation, expressed in variables such that the transformation has the symmetry of McMillan's form, is seen on Fig. 13. On an expanded scale (X10), we see (Fig. 14) the sudden onset of erratic behavior as the starting values for the transformation are successively increased (in steps $\Delta x_0 = 0.0025$, for $y_0 = 0$), and on a scale expanded by a further factor 100/6 we see (Fig. 15) the presence of a great deal of additional structure within a portion of this "stochastic" region. Associated with the transition to the stochastic region there appears to be a marked change in the manner of growth of $\psi_n = \log|\lambda_n|$ (linear, vs. n, in the stochastic case -- indicative of an exponential trend for $|\lambda_n|$) or of the "Cesaro mean" $\mu_n = \frac{1}{n} \sum_{m=1}^{n} \frac{1}{m} \psi_m$ (constancy in the stochastic case, monotonically decreasing otherwise -- Fig. 16).[26] Such methods indeed may prove useful in investigating computationally the possible development of stochastic motion in storage-ring devices. Extended computations of this nature can present challenging problems with respect to computer accuracy.[27]

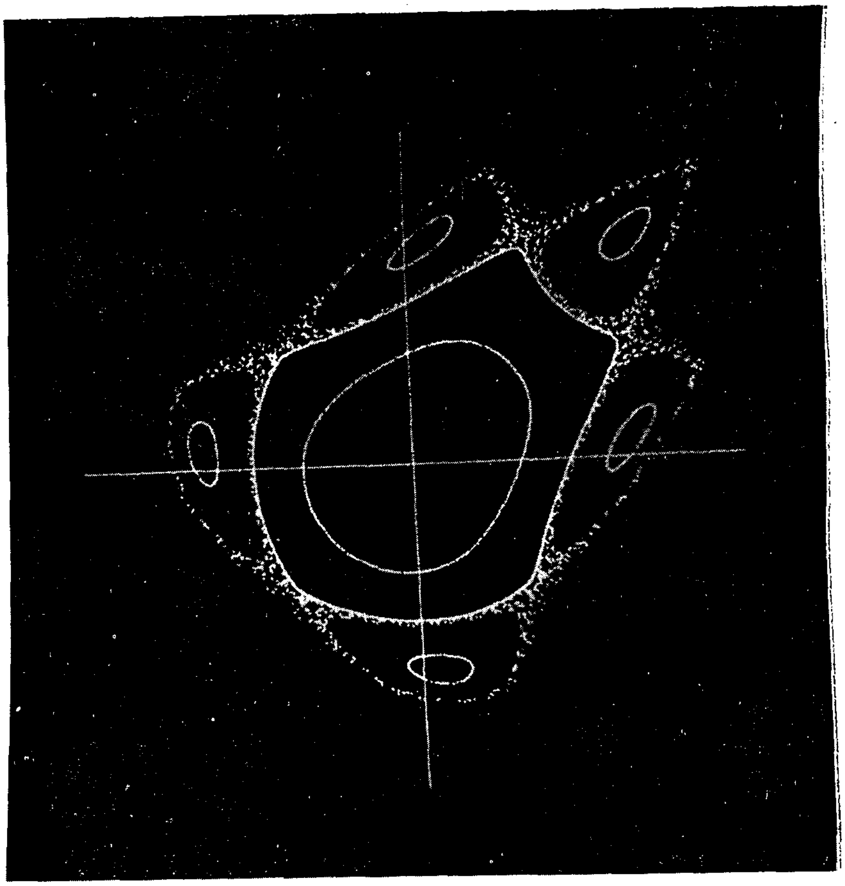

XBB 744-2448

Fig. 13 - Apparently smooth phase curves and a scattering of points resulting from iteration of the transformation (14a,b), with cos α = 0.22 and coordinates X,Y appropriate to expressing the transformation in the form (6a,b).[25] Five islands of stability (containing stable fixed points of order 5) are seen surrounding the area associated with the order-1 fixed point at the origin. The outermost smooth curve, shown as bounding this inner area, resulted from the starting values x_0 = 0.5350, y_0 = 0 (Froschlé notation), and the scattered points result from x_0 = 0.5375, y_0 = 0. <u>Scale</u> (as indicated by the coordinate axes): -1.0 to 1.0

XBB 744-2446

Fig. 14 - Enlarged portion (10X) of Fig. 13, showing seven smooth phase trajectories resulting from starting values x_0 = 0.5200, 0.5225, ... 0.5350 (and y_0 = 0) and a scattering of points resulting from x_0 = 0.5375, y_0 = 0. Note the occurrence of open areas within the region covered by the scattered points -- for example the area surrounding an (unplotted) stable fixed point of order 65 at X ≅ 0.476, Y ≅ 0.521
<u>Scale</u>: 0.38 to 0.58

XBB 744-2447

Fig. 15 - Detailed multiple-island structure in the immediate neighborhood of an order-65 stable fixed point (shown here just below the center of the diagram) of which mention has been made in the caption to Fig. 14.
<u>Scales</u>: 0.470 to 0.482 for X, 0.516 to 0.528 for Y.

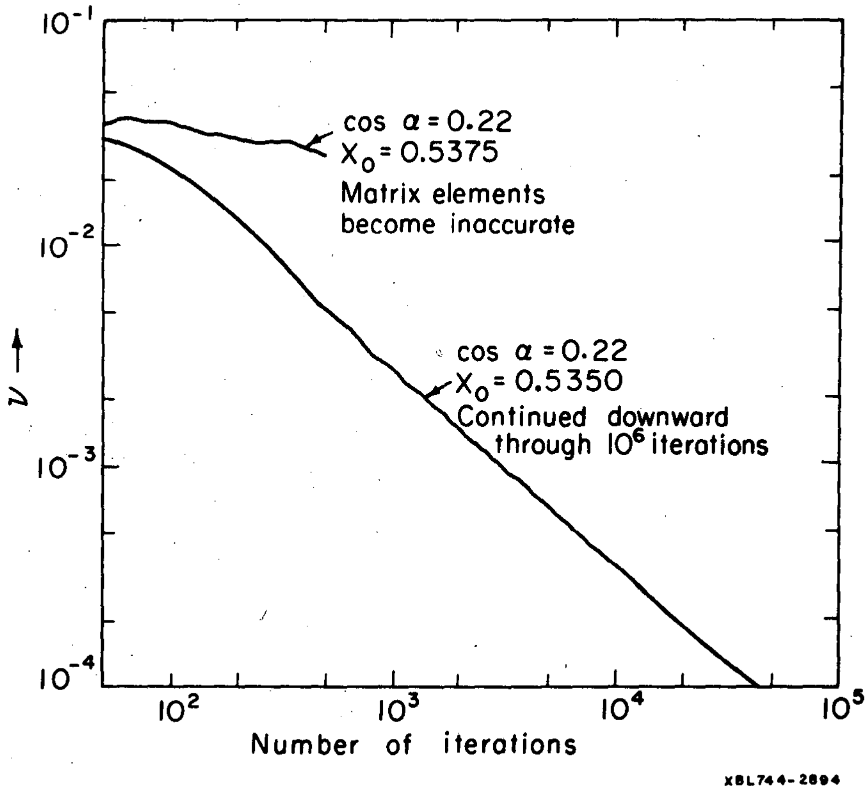

Fig. 16 - Plots of the "sliding mean", ν_n (Note 26), vs. n, obtained from computations begun (i) with initial conditions leading to the last smooth curve of Fig. 14 (x_0 = 0.5350) and (ii) with initial conditions leading to the scattered points on that Figure (x_0 = 0.5357), of which only the results for the latter case indicate a general exponential upward trend of $|\lambda_n|$.

REFERENCES AND NOTES

1. L. Jackson Laslett, "Stochasticity", Proc. IX International Conf. on High Energy Accelerators, Stanford Linear Accelerator Center, CONF 740522 (S.L.A.C., Stanford, Calif.; 1974), pp. 394 - 400.

2. (a) An authoritative treatment of the mathematical aspects of the problems discussed here is given by V.I. Arnol'd and A. Avez, "Ergodic Problems of Statistical Mechanics" (Benjamin, New York, N.Y.; 1968) and (b) by Jürgen Moser, "Stable and Random Motions in Dynamical Systems" (Princeton Univ. Press, Princeton, N.J.; 1973); (c) an extended discussion of which portions relate more immediately to those of interest to an accelerator designer is presented, with many references, by G.M. Zaslavskij and B.V. Chirikov, Uspekhi Fizicheskikh Nauk 105 and Engl. Transl. Sov. Phys. Usp. 14, 549-568 (1972), with further discussion and examples (d) by B.V. Chirikov in Nucl. Phys. Inst. Report 267 (Novosibirsk, USSR) with Engl. Transl. by A.T. Sanders, CERN Trans. 71-40 (CERN, Geneva, Switzerland; October 1971); and (e) related questions of ergodic theory in statistical mechanics are summarized by J.L. Lebowitz and O. Penrose, Physics Today, pp. 23 - 29 (February 1973).

3. CNRS Internat. Conf. on Point Transformations and their Applications, Laboratoire d'Automatique et d'Analyse des Systèmes Toulouse, France (10-14 September 1973). This conference was concerned with both Hamiltonian and non-Hamiltonian systems.

4. E.M. McMillan, Phys. Rev. 68, 143-144 (1945).

5. K.R. Symon and A.M. Sessler, Proc. CERN Symposium on High Energy Accelerators and Pion Physics 1, 44-58 (CERN, Geneva, Switzerland; 1956).

6. L. Jackson Laslett, ERAN-57 (Lawrence Berkeley Laboratory; 1970).

7. M. Henón and C. Heiles, Astron. J. 69, 73-79 (1964).

8. G.H. Walker and J. Ford, Phys. Rev. 188, 416-432 (1969).

9. The present example in fact is exceptional in that the unperturbed frequencies, being equal, are "rationally connected" and the analysis requires special treatment -- see F.G. Gustavson, Astron. J. 71, 670-686 (1966); J. Moser, "Lectures on Hamiltonian Systems", Memoirs Amer. Math. Soc., No. 81, 1-60 (1968).

10. See also V.K. Mel'nikov, Soviet Math. 4, 266-270 (1963).

11. Edwin M. McMillan, "A Problem in the Stability of Periodic Systems", *in* "Topics in Modern Physics -- A Tribute to Edward U. Condon", pp. 219-244 (Colorado Asso. University Press, Boulder, Colorado; 1971). A transformation written in the form (6a,b) is convenient for the study of area-preserving transformations in the plane because of the "double symmetry" pointed out by McMillan (p. 225). The transformation can be interpreted as describing the effect of a simple linear focusing system supplemented by a periodic sequence of thin non-linear lenses that introduce at such points a Δy specified by $f(x)$.

12. Laslett, McMillan, and Moser, Courant-Institute Report NYO-1480-101 (New York University, N.Y.; 1 July 1968).

13. Fig. 12 is taken from Fig. 2 (p. 35) of the Appendix to Ref. 12. The fixed points shown are situated on the x-axis at $x \cong 0.4562733$ and 0.6130793, with the negative eigenvalue $\lambda \cong -8.369$ (in addition to its reciprocal, $\lambda \cong -0.1195$) for this family, and the point A_{n+8} is the eighth iterate of point A_n. For discussion of the occurrence and consequences of loop systems, see S. Smale, "Diffeomorphisms with Many Periodic Points ...", (Princeton University Press, Princeton, N.J.; 1965); E. Zehnder, Comm. Pure Appl. Math. 26, 131-182 (1973); Ref. 2c, Sect. 6.1; and Ref. 2d, Sect. 2.6.

14. The loss of a firm separatrix can be illustrated computationally for the transformation (6a, b) by modifying the function f(y) of (7a) so as to introduce the quantity $1 - b$ as a factor multiplying the second term on the right and setting $b \neq 0$ (for example, $b = 0.05$) -- L. Jackson Laslett, ERAN-239 (1974).

15. See, for example, M. Toda, Prog. Theoret. Phys. (Kyoto) Suppl. 45, 174-200 (1970); references cited therein; and related papers in this issue of the Supplement.

16. J. Ford, S.D. Stoddard, and J.S. Turner, Prog. Theoret. Phys. (Kyoto) 50, 1547-1560 (1973).

17. Cited in Ref. 16, p. 1558.

18. The validity of these (time-independent) expressions as constants of the motion of course can be confirmed directly by forming their Poisson-bracket expressions with the Hamiltonian function (11).

19. B.V. Chirikov, E. Keil, and A.M. Sessler, CERN Report ISR-TH/69-59 (CERN, Geneva, Switzerland; 15 October 1969).

20. E.g., Ref. 12, pp. 42-43, where is also listed a quantity $\lambda_I = \lambda - 1$ for fixed-point families that have rotation $\frac{m}{4m+1}$.

21. John M. Greene, J. Math. Phys. 9, 760-768 (1968).

22. James H. Bartlett, "Stability of Area-Preserving Mappings", Paper III-3 of Ref. 3.

23. J. Ford and G.H. Lunsford, Phys. Rev. A1, 59-70 (1970).

24. C. Froeschlé, Astron. and Astrophys. 9, 15-23 (1970); C. Froeschlé and J.P. Scheidecker, Ibid. 22, 431-436 (1973); and other references cited therein.

25. This transformation, (14a,b), can be put into McMillan's form[11] by the change of variables $x = \sqrt{\sin\alpha}\,Y$, $y = (X - Y\cos\alpha)/\sqrt{\sin\alpha}$, with $f(Y)$ then becoming $2Y\cos\alpha + Y^2 \sin^3/2\alpha$.

26. The curves of Fig. 16 are plots of

$$\nu_n \equiv \sum_{m=1}^{n} \frac{1}{m} \Psi_m \exp(-\frac{n-m}{\tau}) / \sum_{m=1}^{n} \exp(-\frac{n-m}{\tau}) \quad \text{with} \quad 1/\tau = 0.015, \text{ the}$$

sliding exponential factor being designed to provide some smoothing of the results (L. Jackson Laslett, unpublished LBL Report). Extended computations of this nature can present challenging problems with respect to computer accuracy.[27]

27. C. Froeschlé and J.-P. Scheidecker, J. Comp. Phys. 11, 423-439 (1973); Astrophys. & Space Sci. 25, 373-386 (1973).

28. I am deeply indebted to Paul J. Channell for many stimulating and helpful conversations concerning topics discussed here. Responsibility for the views expressed in this paper, however, remains exclusively my own.

Presented at the Joint US/CERN School on
Particle Accelerators, Sardinia, Italy,
January 31-February 5, 1985

LBL-18987

NONLINEAR DYNAMICS
A PERSONAL PERSPECTIVE*

L. Jackson Laslett

Lawrence Berkeley Laboratory
University of California
Berkeley, California 94720

December 1984

---

* This work was supported by the Office of Energy Research, Office of Basic Energy Sciences, Department of Energy under Contract No. DE-AC03-76SF00098.

NONLINEAR DYNAMICS
A PERSONAL PERSPECTIVE*

L. Jackson Laslett
Lawrence Berkeley Laboratory
University of California
Berkeley, California 94720

INTRODUCTION AND OUTLINE

The earlier talks in this Conference have given us a welcome insight into the phenomena that I shall call collectively by the term stochasticity. It is good to see the attention that this field now is receiving, since I have had the feeling that for many years it was rather unfashionable in the West. The increasing availability of digital computers during the last few decades certainly has assisted in providing illustrative examples that serve to spread an awareness of the characteristics of these phenomena, but we should not overlook that many of the basic features and concepts were appreciated by early workers such as Poincaré, Maxwell,(1)† and the elder Birkhoff.

I was asked to present a "Personal Perspective" relating to work in this field, which might be interpreted as an invitation to mention historical instances in which, of my personal knowledge, the evolution of accelerator technology led to accelerator designers developing certain specific issues related to possible stochastic behavior. The phenomena encountered in studying such issues have a very captivating intrinsic interest; with the increasing availability of personal computers and interactive terminals, some may wish to review such issues or to pursue related issues partly for enlightenment but also partly for fun.

In this connection, a few comments or caviats may be in order:

(1) For execution of some problems, a high-precision capability may be essential, but

(2) There are some issues that (as we shall see) can be illustrated quite usefully with the aid of no more than a simple desk calculator;

(3) An interactive graphic capability can be exceedingly convenient, and revealing ("serendipity");

(4) Algebraic transformations can be more convenient to study than the evolution of solutions to differential equations, and yet provide

---

*This work was supported by the Office of Energy Research, Office of Basic Energy Sciences, Department of Energy under Contract No. DE-AC03-76SF00098.

†References are given at the end of the this Introduction (p. 3).

equally valid illustrations of significant phenomena, but

(5) If one wishes to examine solutions to differential equations, adoption of a "Hamiltonian" or "canonical" integration algorithm would be reassuring. Such an algorithm has been presented, as a 3^{rd}-order algorithm, by R. Ruth,$^{(2)}$ and it is understood that Dr. Ruth has since developed a similar 4^{th}-order integration algorithm -- at least for equations derivable from a Hamiltonian function of the form

$$H = f(\vec{p}) + V(\vec{q}, t) .$$

With integration procedures of more conventional type (e.g., for Runge-Kutta algorithms), features such as conservation of phase-space area are not precisely maintained for Hamiltonian systems, and one must guard against the development of significant consistent spurious damping of phase-space area in extended runs. One may reasonably presume that physical systems of interest to us may differ, perhaps inadvertently, from those postulated for our computations but that, nonetheless, the physical systems in fact will be canonical.

The phenomena we have heard discussed in these recent sessions of our Conference of course have their implications in fields that extend far beyond the dynamics of particles in accelerators and storage rings. The field of astronomy certainly presents situations of obvious interest in this regard. To move outside of fields of physical science, it is noteworthy that quite simple and reasonable models for the annual change of populations of prey and predator can lead to astonishing oscillatory or erratic variations of the representative populations.$^{(3)}$ I suspect that similar effects might be seen in economic models. The sensitivity of behavior with respect to details of even quite simple models, as we have begun to recognize in some of our own work, surely should lead model makers to view their results with less than complete assurance.

Issues I hope to discuss are:$^{(4)}$

Development of Stochasticity
from Area-Preserving Transformations;

Limiting (Resonant) Frequencies
for Particle Motion in the Median Plane
of a Strong-Focusing Ring -- Examples;

Bifurcation.

REFERENCES AND NOTES:

1. See quotation from Maxwell, given on p. 111 of M. V. Berry's very informative article in the A.I.P. Conference Proceedings, No. 46 (1978).

2. Proc. 1983 Particle Accelerator Conf., IEEE Trans. Nucl. Sci. NS-30 (No. 4), pp. 2669-2671.

3. See, for example, Review Articles by Robert M. May, Nature (London) 261, 459-467 (10 June 1976); 269, 471-477 (6 October 1977).

4. Similar discussions of some of these issues have been given earlier in Proc. 1974 Internat. Conf. High Energy Accelerators, pp. 394-401 (Stanford, California; 1974) and A.I.P. Conference Proceedings, No. 46 (Siebe Jorna, Ed.), pp. 221-247 (Amer. Inst. Physics, N.Y.; 1978).

I. CANONICAL TRANSFORMATIONS

The direct use of canonical transformations can be convenient for the investigation and illustration of trajectory behavior in particle accelerators or storage rings ("tracking studies"). McMillan has proposed$^{(1)}$ a convenient form for a transformation, that we shall generalize to several degrees of freedom, and is such that

(1) it is canonical,

(2) it is readily obtained from a transformation for which there is a simple particle-optics interpretation, and

(3) it exhibits interesting (and useful) symmetries.

One may start by considering a linear homogeneous transformation followed by a thin-lens abrupt non-linear change of slope (or "momentum"):

$$\left.\begin{aligned} Q_i' &= a_iQ_i + b_iP_i \\ P_i' &= c_iQ_i + d_iP_i + F_i(Q_1', Q_2', \ldots) \end{aligned}\right\} , \qquad (1)$$

wherein primes denote iterates. We require that

$$\begin{vmatrix} a_i & b_i \\ c_i & d_i \end{vmatrix} = 1 \qquad (1a)$$

and

$$\frac{\partial F_i}{\partial Q_j'} = \frac{\partial F_j}{\partial Q_i'} \qquad (1b)$$

(so that, if one wishes, one may write $F_i = -\frac{\partial}{\partial Q_i'} V(Q_1', Q_2', \ldots)$)

in order that the transformation be canonical.

[In numerical work with transformations such as (1) it is desirable that the coefficients a_1, b_1, etc., and coefficients entering into the functions F_i in multi-dimensional cases, be so selected and employed that the above conditions for canonical behavior are satisfied exactly. Small errors in the specification of such constants can result in a troublesome progressive and consistent failure of solutions to satisfy conservation theorems (such as those that pertain to phase-space areas or volume).]

One may now rewrite the transformation (1) in terms of other variables, introducing

$$\left.\begin{aligned} x_i &= b_i^{-1/2}\, Q_i \\ y_i &= a_i b_i^{-1/2}\, Q_i + b_i^{1/2}\, P_i \end{aligned}\right\} \tag{2}$$

to obtain

$$\left.\begin{aligned} x_i' &= y_i \\ y_i' &= -x_i + f_i\,(y_1, y_2, \ldots) \end{aligned}\right\}, \tag{3}$$

where $f_i(y_1,y_2,\ldots) = (a_i + d_i)y_i + b_i^{1/2}\, F_i(b_1^{1/2}\, y_1,\, b_2^{1/2}\, y_2,\, \ldots)$ (3a)

and wherein we require (in multi-dimensional cases, in correspondence to Eqn. (1b)) that

$$\frac{\partial f_i}{\partial y_j} = \frac{\partial f_j}{\partial y_i}\ . \tag{3b}$$

The transformation (3) is in the McMillan form, generalized to permit its application in cases that involve more than a single conjugate pair of variables.(2)

As an area-preserving transformation for a single pair of canonical variables, the McMillan transformation (3) has several interesting and potentially helpful simple characteristics:(1)

(1) Geometrically, an application of the transformation can be represented on the x,y diagram by a reflection about the principal diagonal followed by a vertical reflection (parallel to the y axis) about the curve $y = 1/2\ f(x)$.

(2) If two points are iteratively related, by one application of the transformation, such points mirrored about the principal diagonal also are iteratively related (in the inverse order).

(3) If two points are iteratively related, by one application of the transformation, such points mirrored vertically about the curve $y = 1/2\ f(x)$ also are iteratively related (in the inverse order).

(4) Order-1 fixed point(s) lie on the intersection of the curve $y = 1/2\ f(x)$ with the principal diagonal $y = x$.

(5) If the function $f(\eta) = \Phi(\eta) + \Phi^{-1}(\eta)$, where Φ^{-1} denotes the <u>inverse</u> function, then curves $y = \Phi(x)$ and $x = \Phi(y)$ each constitute invariant curves (intersecting at order-1 fixed points). When such curves completely enclose an area of the phase plane, phase points of course then are unable to move into or out from such an area as a result of applications of the transformation (although erratic motion nonetheless may develop within the area) -- see Fig. I.1.(4)

It is interesting that several area-preserving transformations of which use has been made in the past can be put into McMillan's form (3) by means of some simple (sometimes linear) change of variables. We list some examples of this equivalence in Note 5 at the end of this Chapter.

It can be informative to employ a simple algebraic transformation to illustrate a mechanism for the development of stochasticity. It is convenient for this purpose to consider a quadratically nonlinear transformation proposed by deVogelaere and rewritten in McMillan's form (with $f(y) = 2y^2$):

$$\left.\begin{aligned} x' &= y \\ y' &= -x + 2y^2 \end{aligned}\right\} . \qquad (4)$$

This transformation possesses a stable order-1 fixed point at the origin and an unstable (hyberbolic) order-1 fixed point at 1, 1 -- as illustrated in Fig. I.2 by intersections of the curve $y = 1/2\ f(x) = x^2$ with the principal diagonal. The motion of points in the immediate neighborhood of the unstable fixed point is governed by the tangential-mapping transformation evaluated at that point. This local linearization leads to eigenvector directions $dy/dx = 2 \pm \sqrt{3}$ along which points will move directly away from or directly toward the fixed point, with distances from the fixed point then changing by the respective factors $\lambda = 2 \pm \sqrt{3}$ per iteration.

It is now instructive to depict, as on Fig. I.2, the evolutionary track followed by line segments originating with these slopes close to the unstable fixed point and extended by repeated applications of the transformation or its inverse. A line segment such as GFE thus transforms to a segment EDC as a result of one application of the forward transformation, and the points CDE likewise lead to points EFG under the application of the inverse transformation. The line segments that in this way are extended from the fixed point, by repeated application of this transformation and of its inverse, do <u>not</u>, however, intersect smoothly (e.g., at points such as D on Fig. I.2) and thus result in the formation of the "loops" designated by L on Fig. I.2. Such loops are all of equal area, as a result of the area-preservation and diagonal symmetry of the transformation. Accordingly, as a line segment such as GFE is advanced by repeated applications of the forward transformation, it will develop loops that become increasingly elongated as their intersection points (such as points C, B, and A) approach the

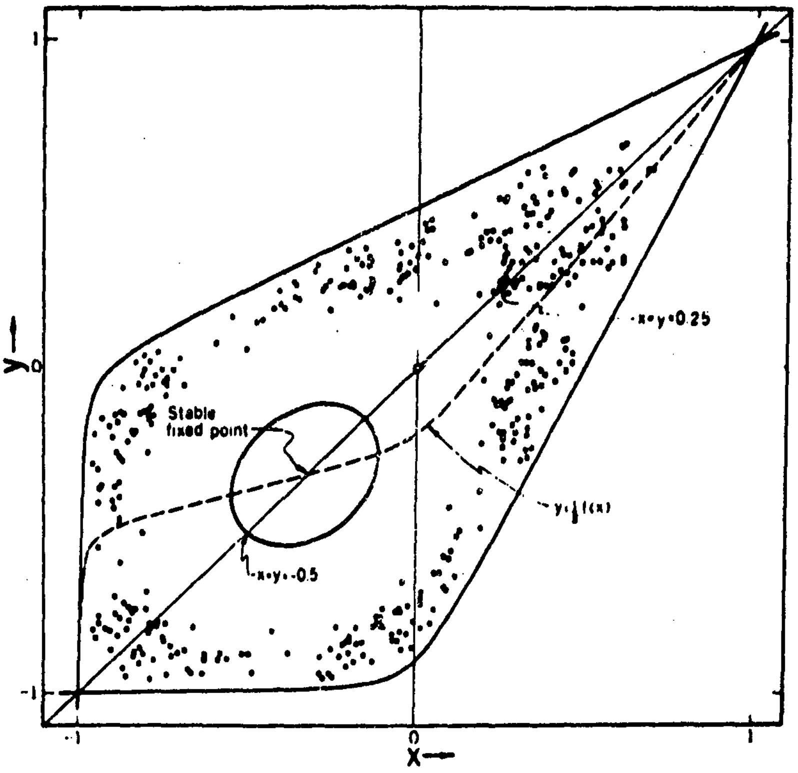

XBL 8410-4188

Fig. I.1. The case $f(x) = (3x - 1)/2 - k^2/2(x + 1) + \sqrt{x^2 + k^2}$, with 0.1 as the value of k. The invariant boundary consists of two hyperbolas. The results of two computer runs are shown. A run starting at $x = y = -0.5$ generates the apparently smooth curve surrounding the stable fixed point at $x = y \approx -0.328$, and a run starting at $x = y = 0.25$ gives, for the first 400 iterations, the scattered points indicated as dots.

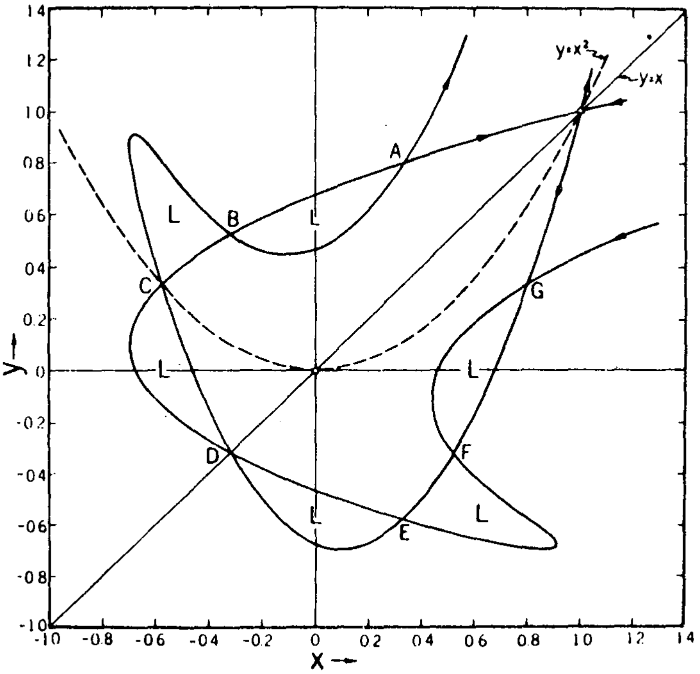

XBL 8410-4189

Fig. I.2 Initial portion of trajectories under the transformation $x' = y$, $y' = -x + 2y^2$, leading away from (or toward) the unstable fixed point at $x = 1$, $y = 1$. The arrows indicate the directions in which points are moved by the transformation. The point pairs AG, BF, CE illustrate the first symmetry, the point pairs AE, BD the second symmetry. The areas of the loops marked L are all equal.

fixed point with a closer and closer spacing.

As a result of these loops developing into "worms" that are progressively narrower and more elongated, the phase-plane diagram can rapidly develop a great complexity (Fig. I.3) and repeated applications of the transformation to a phase point situated in this region will lead to a "stochastic" or apparently irregular scatter of its iterates. The region affected by such stochastic behavior need not, however, extend fully into the "interior" of the diagram. Thus, smooth closed phase trajectories may exist in this example at small amplitudes, as is suggested by some simple curves drawn near the origin on Fig. I.3. [These latter curves are characterized by a distinctive four-pointed shape as a result of the phase advance per iteration for this transformation approaching $2\pi/4$ as the amplitude approaches zero.]

Similar stochastic behavior of course can originate in association with unstable fixed points of higher order. Fig. I.4 illustrates such features of the Hénon-Froeschlé mapping(5b,7) (with $\cos\alpha = 0.22$), re-expressed in the McMillan form. Additional details of this example have been shown in Refs.(10) (Figures on p. 399) and(11) (Figures on pp.342 and 343).

Synchrotron motion, although frequently described by means of simple nonlinear differential equations, is most appropriately described by means of a transformation that recognizes the impulsive character of the forces applied at discrete cavity locations. The construction of a Hamiltonian function for such a problem thus strictly requires the inclusion of δ-functions or similar location-dependent functions to specify the localization of these forces and the Hamiltonian will not constitute a constant of the motion.

A transformation to describe synchrotron motion for a coasting beam may be written, in the form of the "standard mapping",(5c,8) as

$$\left.\begin{aligned} y' &= y - K\sin\pi x \\ x' &= x + ky' \end{aligned}\right\}, \qquad (5)$$

wherein

y = Fractional departure of energy from the reference value at the entrance to the cavity,

πx = electrical phase angle of field relative to the particle,

$K \propto$ applied voltage, and

$k \propto$ derivative of revolution period with respect to energy.

To obtain a convenient symmetry in the phase plots, it is useful to introduce the variables $X = x$ and $Y = y - (K/2)\sin\pi x$, thereby measuring energy departures at mid-passage through the cavities. One accordingly then employs the transformation

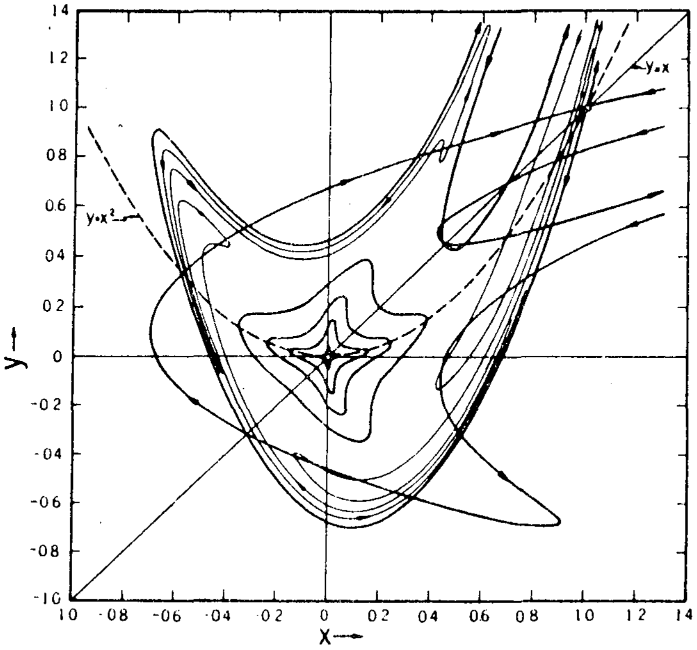

XBL 8410-4190

Fig. I.3 A partial extension of the curves of Fig. I.2, showing "tentacles" reaching off the figure and "worms" in the interior. Since the entrance channel for the "worms" becomes very narrow, the figure becomes difficult to draw completely as the iteration progresses. Some apparently closed curves around the stable fixed point at x = 0, y = 0 are also shown. The peculiar behavior near the orgin seems less mysterious if one recalls that the function y = 1/2f(x) approaches the limit of zero slope, where the curve degenerates to four points, and where the slightest perturbation can cause a slow migration about the center and a concomitant slow change in radius.

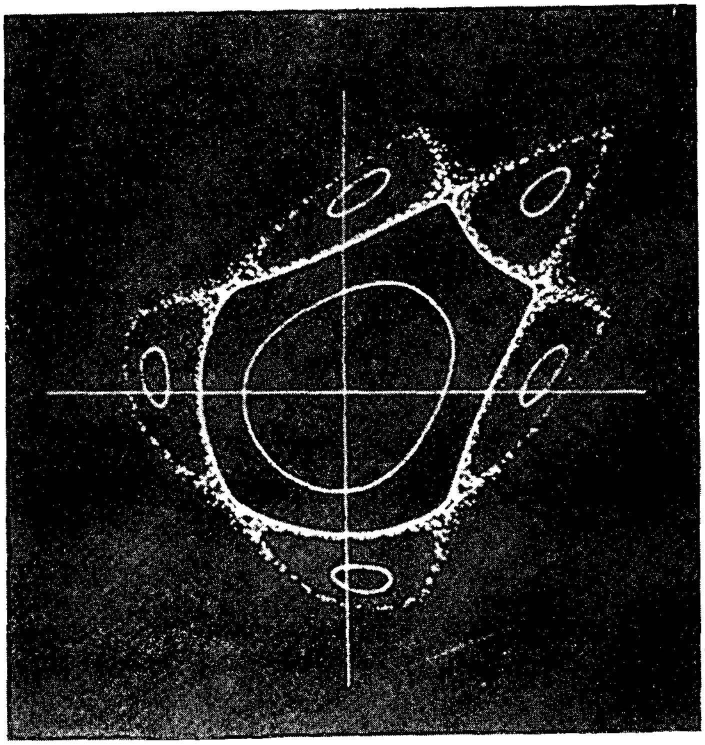

XBB 840-7763

Fig. I.4. Apparently smooth phase curves and a scattering of points resulting from iteration of the Hénon-Froeschlé transformation, with cos α = 0.22 and coordinates x,y appropriate to expressing the transformation in the McMillan form. Five islands of stability (containing stable fixed points of order 5) are seen surrounding the area associated with the order-1 fixed point at the orgin. The outermost smooth curve, shown as bounding this inner area, resulted from the starting values X_0 = 0.5350, Y_0 = 0 (Froeschlé notation), and the scattered points result from X_0 = 0.5373, Y_0 = 0. Scale (as indicated by the coordinate axes): -1.0 to 1.0.

$$\left.\begin{aligned} X' &= X + k\,[\,Y - (K/2)\sin \pi X\,] \\ Y' &= Y - (K/2)\,[\,\sin \pi X + \sin \pi X'\,] \end{aligned}\right\} \qquad (6)$$

and plots Y vs. X modulo 2. A stable first-order fixed point occurs at $X = 0$, $Y = 0$; other similar fixed points, that correspond to harmonic operation, occur at $X = 0$ and Y equal to any integer multiple of $2/k$.

For K and k small, the phase advance of small-amplitude synchrotron oscillations from one cavity transit to the next is approximately $\sigma_s = \sqrt{\pi Kk}$ radian and substantially-smooth separatrices appear to extend between unstable fixed points at $X = \pm 1$ to enclose stable "bucket areas" of half height $\delta Y \cong 2\sqrt{K/\pi k}$ -- see Fig. I.5, plotted for $K = 0.1\pi$ and $k = 0.1$, wherein one also sees depicted indications of sub-harmonic trajectories in the region between the major buckets shown at $Y = 0$ and at $Y = 20$. The ratio of bucket height to the separation of major buckets thus may be measured by $\frac{2}{\pi}\sigma_s$ and will be small when the phase advance σ_s is small.

For substantially larger values of K (or of k), corresponding to values of σ_s very much greater than normally employed in accelerator operation, bucket heights may become comparable with the separation between major buckets. The development of stochasticity, especially in the neighborhood of the unstable fixed points at $X = \pm 1$, then becomes very pronounced -- see Fig. I.6, plotted for $K = 0.8\pi$ and with $k = 0.1$ (as before). In the case to which Fig. I.5 applies ($K = 0.1\pi$, $k = 0.1$), however, the development of stochasticity is so subtle that it can be demonstrated computationally only with considerable care and it results in the formation of loops whose estimated individual areas are a fraction only $\sim 1/(5 \times 10^{11})$ of the full area of a major bucket [result reported in unpublished 1960 Lawrence Berkeley Laboratory Report ERAN-57 and cited in A.I.P. Proceedings No. 46, p. 226 (1978)(11)].

An algebraic transformation may be employed as a means of obtaining an approximate representation of solutions to differential equations. As an example, we may note a transformation cited earlier (5d,9).

$$\left.\begin{aligned} X' &= AX + (1-A^2)Y + (1-A)[\,X + (1-A)Y\,]^2 \\ Y' &= -X + AY + [\,X + (1-A)Y\,]^2 \end{aligned}\right\} , \qquad (7)$$

that was originally introduced in the expectation that it would depict approximately the median-plane motion of charged particles in a spiral-sector accelerator. First-order fixed points occur at the origin (0,0) and at (1,0). With the parameter A assigned the value $A = -5/8$, the fixed point at the origin is stable (small-amplitude tune, $\sigma_0 = \cos^{-1} A \cong 128.68$ deg., or approximately 0.35745 times 2π radian), while the point at (1,0) is unstable. The region

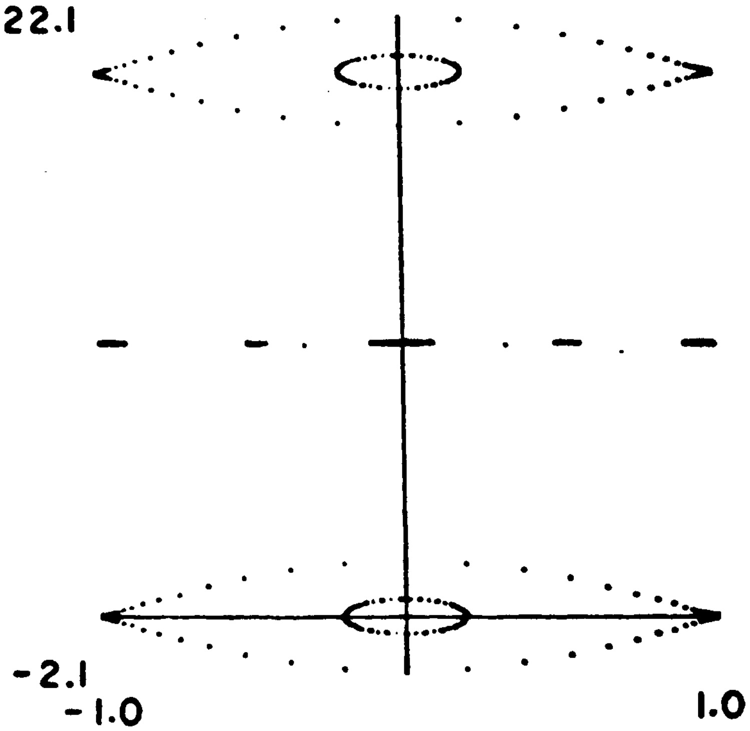

XBL 851-826

Fig. I.5 X,Y phase plot for a coasting beam under the influence of an R.F. cavity with $K/\pi = 0.1$, $k = 0.1$ -- as computed by Eqs. (6). X is plotted mod. 2.

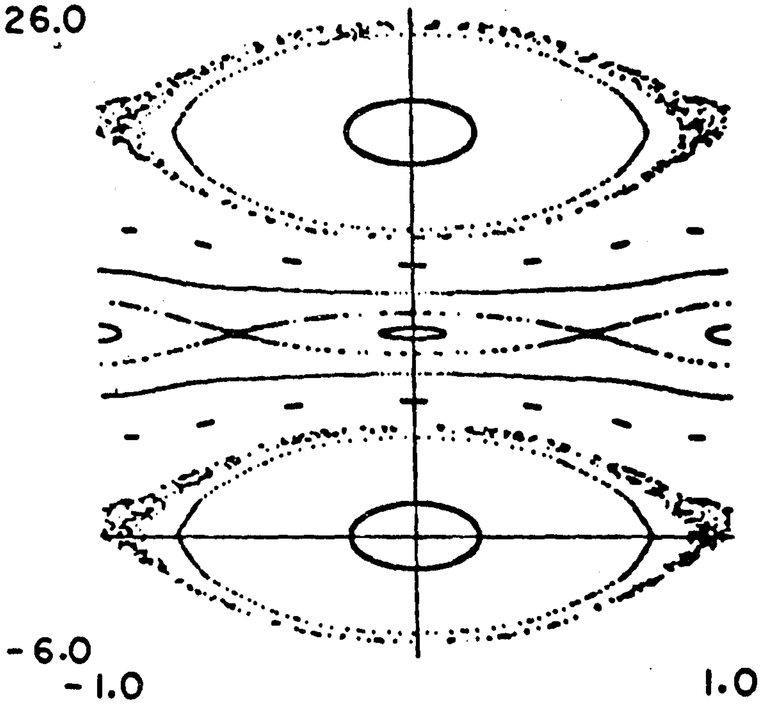

XBL 851-825

Fig. I.6 Phase plot similar to Fig. I.5, but for operation with $K/\pi = 0.8$, showing the obvious development of complex structure.

considered to be of interest for accelerator operation was the roughly triangular region enclosed by the apparent separatrices that connect the third-order unstable fixed points F_1, F_2, F_3 shown on Figs. I.7 and I.8 (and for which the area approaches zero if the small-amplitude tune approaches $2\pi/3$).

It then was of interest to inquire whether these curves can be demonstrated to be imperfect separatrices and, if so, to investigate the extent to which the resulting stochasticity permeates into the interior. Eigenvector directions extended toward the x-axis from the fixed points F_2, F_3, were found,(6) upon careful examination, not to intersect smoothly. The areas of the loops so generated constituted, however, only a very small fraction (circa $1/10^8$) of the area F_1 F_2 F_3 and no evidence was found to indicate stochasticity within any significant portion of the region of interest.

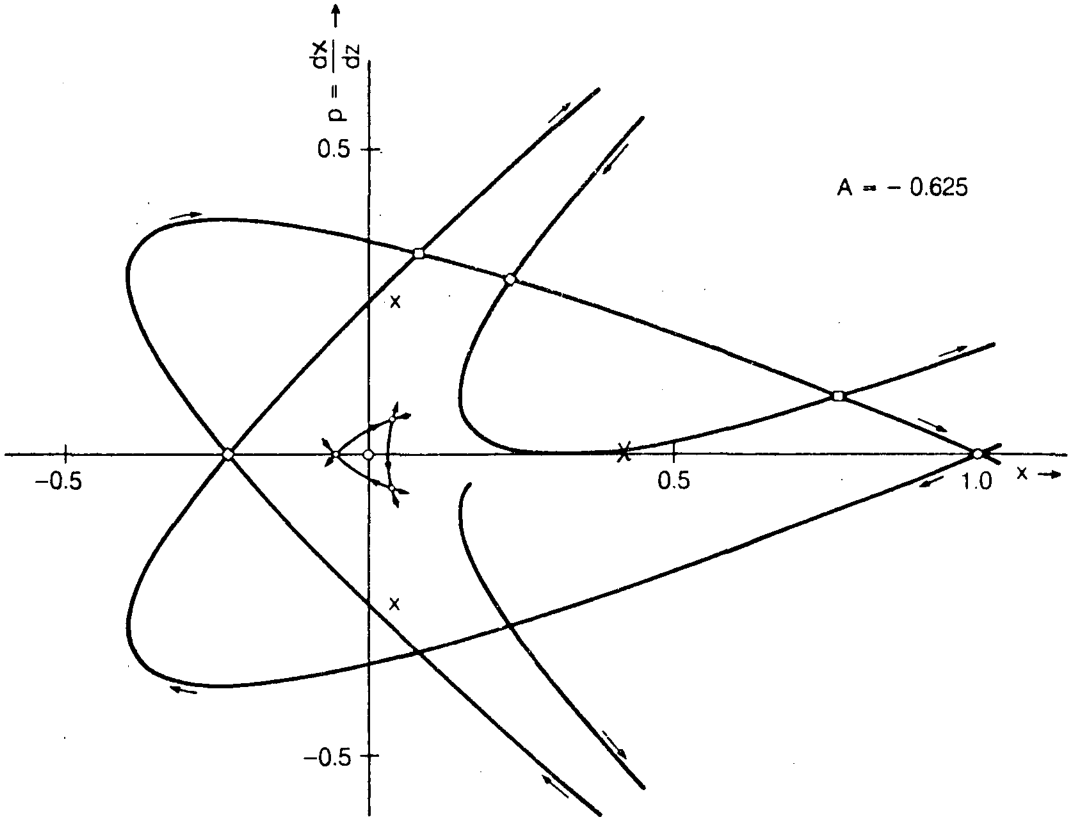

Fig. I.7 Phase diagram for the area-preserving transformation (7) with A = −5/8. Large loops are seen to develop from eigenvector directions extended from the first-order unstable fixed point situated at (1,0). Points denoted by squares (⊡) are related by the transformation, as are also points denoted by diamonds (◈). Our interest will be confined primarily, however, to the roughly triangular area sketched near the third-order unstable fixed points F_1, F_2, F_3 shown by small circles near the center of the diagram. Points denoted by crosses (X) are third-order fixed points that are strongly unstable with reflection.

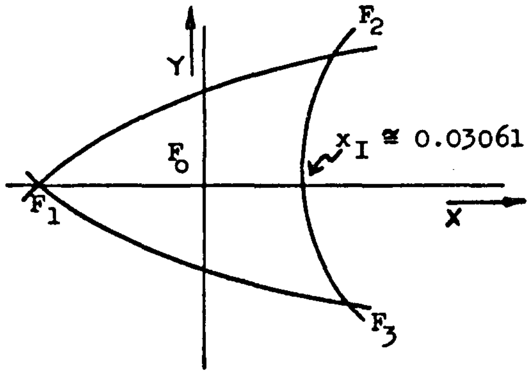

Sketch for $A = -{}^5/8$

$\cos^{-1}A \cong (0.35745)(2\pi)$

Area $\cong 5.5 \times 10^{-3}$
(would shrink to zero
if $A \rightarrow -{}^1/2$)

$$F_1: \left(-\frac{\sqrt{41}-5}{26}, 0\right) = (-0.053966\cdots, 0)$$

$$F_{2,3}: \left(\frac{1}{26}, \pm\frac{4\sqrt{41}-16}{169}\right) = (0.03846\cdots, \pm 0.05688\cdots)$$

XBL 851-824

Fig. I.8. Detail of Fig. 7, showing the apparently stable area bounded by the third-order fixed points F_1, F_2, F_3. [Transformation (7), with $A = -5/8$.]

REFERENCES AND NOTES

1. Edwin M. McMillan, "A Problem in the Stability of Periodic Systems," in "Topics in Modern Physics--A Tribute to Edward V. Condon," pp. 219-244 (Colorado Assoc. University Press, Boulder, Colorado; 1971).

2. McMillian's original work,$^{(1)}$ pertaining to a single pair of working variables, introduced the change of variables

$$\left.\begin{array}{l} x = Q \\ y = aQ + bP \end{array}\right\}$$

(a "scaling" transformation, for which the Jacobian although constant is not necessarily equal to unity) to obtain his form

$$\left.\begin{array}{l} x' = y \\ y' = -x + f(y) \end{array}\right\},$$

with $f(y) = (a + d)y + bF(y)$. The phase advance σ per iteration of y vs. x oscillatory motion is given, for small amplitude motion by $\cos\sigma = 1/2 \left.\frac{df(y)}{dy}\right|_{y=0}$ and, if $F(y)$ is restricted to terms of order higher than the first, $\cos\sigma = (a + d)/2$. The canonical character of the transformation (3) given in the text can be verified through evaluation of the fundamental Poisson bracket expressions or, alternatively, by rewriting the equations (3) in the form

$$\left.\begin{array}{l} x_i = -y_i' + f_i(y_1,y_2,\ldots) \\ \quad = -y_i' - \partial V(y_1,y_2,\ldots)/\partial y_i \\ x_i' = y_i \end{array}\right\}$$

and noting that such equations are derivable from a generating function

$$G(y_1,y_2,\ldots;\, y_1',y_2',\ldots) = V(y_1,y_2,\ldots) + \sum_i y_i\, y_i'$$

by application of the relations

$$\left.\begin{array}{l} x_i = -\,\partial G/\partial y_i \\ x_i' = +\,\partial G/\partial y_i' \end{array}\right\} .$$

As a multi-dimensional illustration of a transformation of the form (1) introduced in the text, we may refer to a form that (with a change of notation, including interchange of "old" with "new" variables) was employed by Meier and Symon$^{(3)}$ in a study of coupling resonances:

$$\left.\begin{aligned} Q_1' &= (\cos \sigma_1)Q_1 + (\sin \sigma_1)P_1 \\ P_1' &= (-\sin \sigma_1)Q_1 + (\cos \sigma_1)P_1 - \frac{k}{2}(Q_2')^2 \\ Q_2' &= (\cos \sigma_2)Q_2 + (\sin \sigma_2)P_2 \\ P_2' &= (-\sin \sigma_2)Q_2 + (\cos \sigma_2)P_2 - kQ_1'Q_2' \end{aligned}\right\} .$$

This transformation is seen to be of the form (1) with $V(Q_1', Q_2') = (k/2)Q_1'(Q_2')^2$.

3. H. Meier and K. R. Symon, Proc. 1959 Internat. Conf. on High-Energy Accelerators, p. 253-262 (C.E.R.N., Geneva; 1959).

4. Figure I.1 has been presented by McMillan as Fig. 8 of Ref. (1). The transformation illustrated is for $f(x) = (1/2)\ (3x - 1) - (1/2)k^2/(x + 1) + \sqrt{x^2 + k^2}$ with 0.1 as the value of k. This function is expressible as $f(x) = \Phi(x) + \Phi^{-1}(x)$, with $\Phi(x) = x - 1 + \sqrt{x^2 + k^2}$ and $\Phi^{-1}(x) = (1/2)\ (x + 1) - (1/2)k^2/(x + 1)$. The curves $y = \Phi(x)$ and $y = \Phi^{-1}(x)$ are shown as boundary curves passing through the two order-1 unstable fixed points. The erratic distribution of points that fall within a portion of the region interior to this boundary originated from $x_0 = y_0 = 0.25$. McMillan has also shown, and illustrated by Figs. 4-7 of Ref.(1), that a function of the form $f(x) = -(Bx^2 + Dx)/(Ax^2 + Bx + C)$ employed in his area-preserving transformation will lead to the phase plane being covered by nested invariant curves of the form

$$Ax^2y^2 + B(x^2y + xy^2) + C(x^2 + y^2) + D\ xy = \text{const.}$$

5. We list here several area-preserving transformations that can be put into McMillan's form by means of a suitable change of variables.

   a.) <u>The DeVogelaere Transformation</u> (generalized, cf Refs. 1 and 6):

$$\begin{aligned} X' &= Y + F(X) \\ Y' &= -X + F(X') \quad . \end{aligned}$$

With introduction of variables such that

$$\begin{aligned} X &= x \\ Y &= y - F(x) \quad , \end{aligned}$$

the transformation assumes the area-preserving McMillan form with $f(y) = 2\ F(y)$.

b.) A Transformation of Hénon and Froeschlé:(7)

$$\left.\begin{aligned} X' &= X\cos\alpha - (Y - X^2)\sin\alpha \\ Y' &= X\sin\alpha + (Y - X^2)\cos\alpha \end{aligned}\right\}$$

With introduction of variables x,y such that

$$\left.\begin{aligned} X &= (\sin\alpha)^{1/2}\, y \\ Y &= (\sin\alpha)^{-1/2}\,(x - y\cos\alpha) \end{aligned}\right\} \text{(a linear transformation)},$$

the transformation assumes the area-preserving McMillan form with $f(y) = 2\,(\cos\alpha)y + (\sin\alpha)^{3/2}\, y^2$.

c.) A "Generalized Standard Mapping":(8)

$$\left.\begin{aligned} I' &= I + g(\theta) \\ \theta' &= \theta + I' \end{aligned}\right\} .$$

With the linear change of variables given by

$$\left.\begin{aligned} \theta &= y \\ I &= y - x \end{aligned}\right\} ,$$

we obtain the area-preserving McMillan transformation with $F(y) = 2y + g(y)$.

d.) A transformation cited in Note 9:

$$\left.\begin{aligned} X' &= AX + (1 - A^2)Y + (1 - A)\,[\,X + (1 - A)Y\,]^2 \\ Y' &= -X + AY + [\,X + (1 - A)Y\,]^2 \end{aligned}\right\} .$$

We introduce variables x,y by a linear "scaling transformation" such that

$$X = \frac{1}{4}\,\frac{(1 + A)^{3/4}}{(1 - A)^{1/4}}\,(x + y)$$

$$Y = \frac{1}{4}\,\frac{(1 + A)^{3/4}}{(1 - A)^{5/4}}\,(-x + y) \qquad ,$$

For which the Jacobian has the value $\frac{1}{8}\left(\frac{1+A}{1-A}\right)^{3/2}$, to obtain the area-preserving McMillan transformation with

$$f(y) = 2Ay + (1 - A^2)^{3/4}\, y^2 .$$

6. L. Jackson Laslett, Edwin M. McMillan, and Jurgen Moser, "Long-Term Stability for Particle Orbits," Courant Institute Report NYO-1480-101 (New York University, N.Y.; 1968).

7. M. Hénon, Q. Appl. Math. XXVII, 291-312 (1969). See also C. Froeschle, Astron. and Astrophys. 9, 15-23 (1970).

8. A. Lichtenberg and M. A. Lieberman, "Regular and Stochastic Motion," p. 156 (Springer; 1983).

9. This transformation was employed in the expectation that it would depict the median-plane motion of charged particles in a spiral-sector FFAG accelerator operated near a third-integral resonance. Some properties of this transformation have been described and discussed in Ref. 6.

10. L. Jackson Laslett, Proc. 1974 Internat. Conf. High Energy Accelerators, pp. 394-401 (Stanford, California; 1974).

11. L. Jackson Laslett, A.I.P. Conference Proceedings, No. 46 (Siebe Jorna, Ed.), pp. 221-247 (Amer. Inst. Physics, N.Y.; 1978).

II. LIMITING (RESONANT) FREQUENCIES FOR PARTICLE MOTION IN THE MEDIAN PLANE

Erratic dynamical behavior can impose definite limits to the permissible amplitudes of individual-particle oscillations in alternating-gradient focusing systems when nonlinearities are present. Thus, the limiting amplitude for motion in the median plane of a strong focusing ring typically occurs in association with a system of fixed points in the phase plane, with a detectable stochasticity first making its appearance in the neighborhood of the unstable fixed points of the system.

Stochasticity in the phase plane for motion with a single spatial degree of freedom of course may be contained by the occurrence of a surrounding KAM (Kolmogorov-Arnol'd-Moser) closed curve, but regions of sufficient amplitude can be found wherein stochastic behavior will carry a phase point to markedly greater, and totally unacceptable, amplitudes. [An associated phenomenon is that of period-doubling bifurcation (to be illustrated in Chapter III), wherein a change of a parameter of a focusing system leads to a previously stable fixed-point system becoming unstable with reflection and to a new fixed-point system of double period becoming created. A sequence of such period-doubling bifurcations, occurring for smaller and smaller increments of the governing parameter, results in a bifurcation lattice or "tree" that may be claimed to terminate in "chaos".]

Informative illustrations of amplitude limitations for stable motion accordingly may be obtained by the examination of solutions to simple differential equations representative of median-plane motion in an idealized alternating-gradient ring. Examples of such equations, for which results are presented below, are

$$\frac{d^2x}{dZ^2} = - A \left(x + 1/8 \, x^2\right) \cos Z \tag{1}$$

and

$$\frac{d^2x}{dZ^2} = - A \left(x + 1/12 \, x \;\; + 1/384 \, x \; \right) \cos Z, \tag{2}$$

wherein the factor cos Z results in a alternating gradient focusing action with a period scaled to 2π. With appropriate scaling of the dependent variable, Eqn. (1) is intended to represent the effect of alternating sextupole fields (to supplement the quadrupole focusing), while Eqn. (2) represents x motion (suitably scaled) in a Maxwellian magnetic field for which the y component in the median plane is taken to be proportional to $I_2(x)/x$ prior to truncation.(1) It will be recognized that, for simplicity in constructing these equations, the obliquity of the trajectories has been neglected to the extent that the longitudinal component of velocity is treated as constant. Trajectories computed from such equations should be strictly area-preserving when plotted on a x, x' = dx/dZ plane. Use of a canonical integration algorithm thus in principle would be preferable for such computations, but application of a fourth-order Runge-Kutta-Gill algorithm with a suitably small step size has appeared also to be satisfactory for the present illustrative purposes.

The coefficient A that appears in Eqns. (1) and (2) serves to determine the "tune" (or the phase advance, σ_0, per period) for small-amplitude oscillations. For a fixed value of A that results in reasonable stable motion about the origin, the solutions to Eqn.(1) are found to exhibit tunes that decrease with increasing amplitude, while the tunes for solutions to Eqn. (2) become greater for large amplitude solutions. In either case, it is of interest to examine, for various values of σ_0, the extent to which the tune assumes a different value at the limit of stable motion and to attempt to identify the fixed-point system that appears to be associated with the onset of instability in such cases.$^{(2)}$ Such investigations are conveniently conducted by means of phase plots wherein values of x, x' for solutions to the equation of interest are plotted at one-period intervals -- e.g., for the present equations, at Z = 0 mod. 2π.

With Eqn. (1), the symmetry is such that plots made at Z=0 mod. 2π (or, alternatively , at Z = π mod. 2π) will exhibit a symmetry in x' about the x axis, and solutions to Eqn. (2) when so plotted will exhibit also a symmetry in x about the x' axis. In directing attention here to instabilities associated with motion confined to the x, Z plane, one, of course, must recognize that motion occurring in two transverse directions will be subject to additional limitations, perhaps of a different character (Arnol'd diffusion?), that well may merit investigation.

A.

$$\boxed{\frac{d^2x}{dZ^2} = -A(x + 1/8\ x^2)\ \cos Z}$$

Median-plane motion of the type of interest here is illustrated by Fig. II.1 for solutions to Eqn. (1) with A = 0.2736, for which the small-amplitude tune is such that $\sigma_0 \cong 74.59$ deg. One notes the appearance of a pronounced order 5/1 fixed-point system (σ = 72 deg.) at an intermediate amplitude. Some stochasticity indeed may be present in association with this system -- and, if so, might be demonstrable computationally with sufficient care -- but one sees that in any case this system is surrounded by an apparently smooth closed phase trajectory (launched at $x_0 = 1.55$, $x'_0 = 0$). At a somewhat larger amplitude, however, an order 16/3 system (σ = 67.5 deg.) becomes evident, for which some small loops may be seen on the Figure near the stable fixed points of this system, but for which

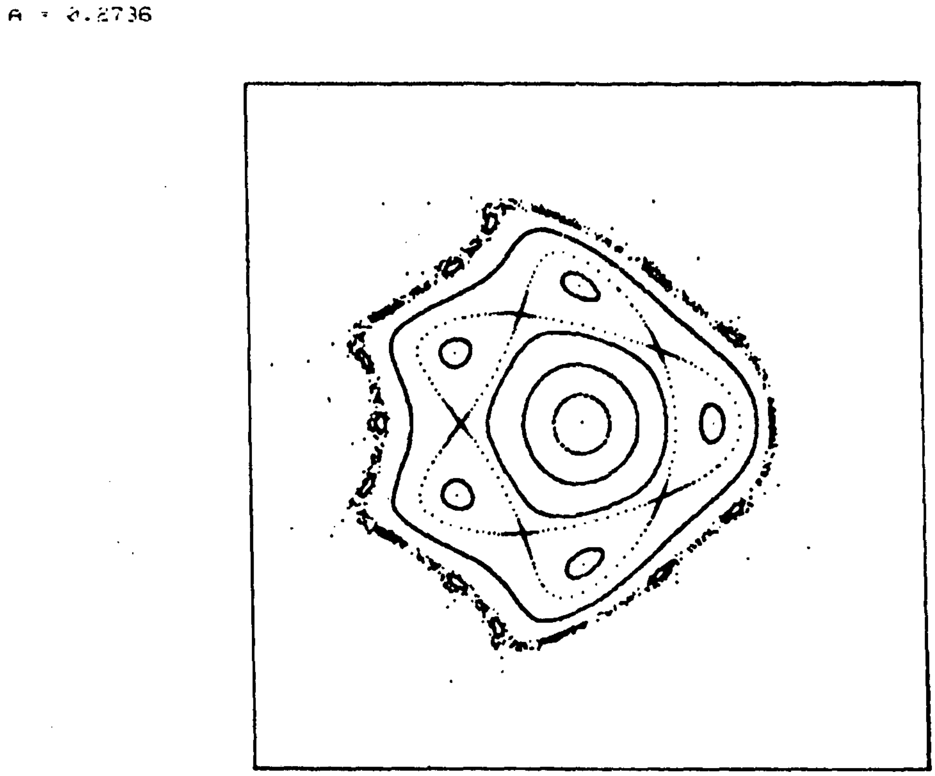

XBL 851-827

Fig. II.1 x' vs. x phase plot, at Z=0 mod.2π, for solutions to Eqn. (1) with A = 0.2736 ($\sigma_0 \cong 74.59$ deg.) to the scales:
Horizontal: -3.0 to 3.0, for x;
Vertical: -0.3 to 0.3, for x'.
Instability is seen to arise from stochasticity associated with a fixed-point system of order 16/3 (σ = 3 X 360/16 = 67.5 deg.). The apparently smooth phase trajectory situated somewhat inside this fixed-point system resulted from a computation launched at x_0 = 1.55, x_0' = 0.

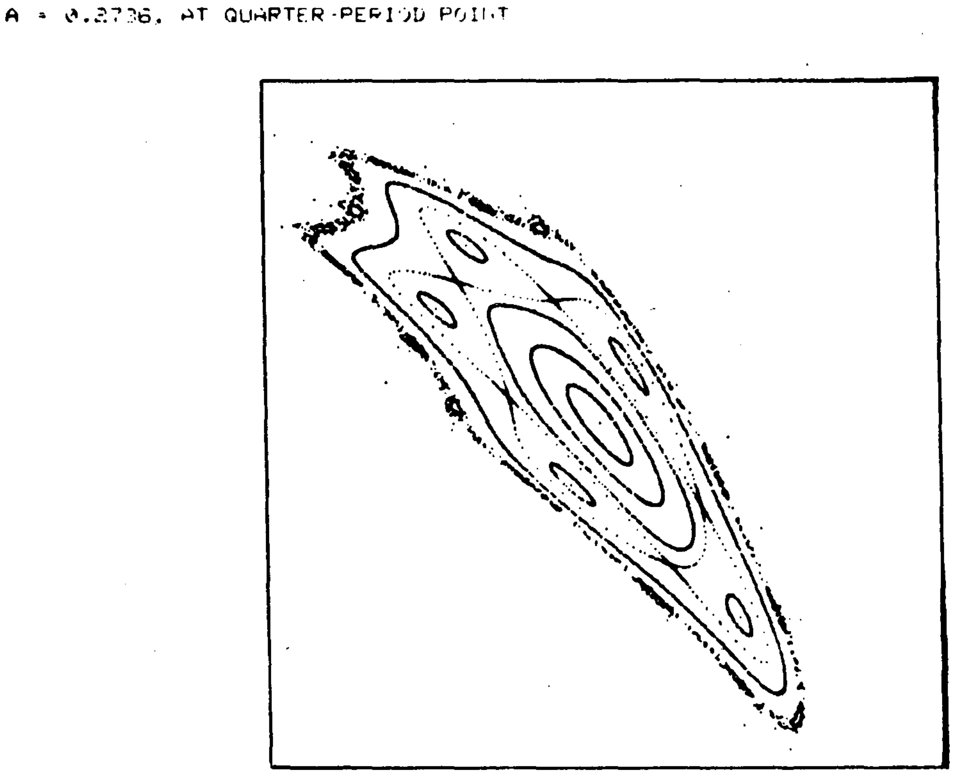

XBL 851-828

Fig. II.2 Phase plot for the runs of Fig. 1, plotted at $Z = \pi/2$ <u>mod.</u> 2π. Scales:
Horizontal: -2.0 to 2.0, for x;
Vertical: -0.6 to 0.6, for x'.

it is more notable that stochasticity associated with the unstable fixed points develops to reveal a gross instability.

Figure II.2 illustrates the manner in which the computational runs portrayed in Fig. II.1 appear if plotted at the quarter-period points $Z = \pi/2$ mod 2π. One expects maximum spatial excursions to occur near the centers of focusing regions, and phase plots constructed for $Z = 0$ mod. 2π accordingly seem most appropriate for the present work.

It is of interest to examine in a similar manner the character of solutions to Eqn. (1) for various values of the parameter A. Results are shown by a sequence of phase plots (Figs. II.3-II.8a) and are summarized in the following Table. In some instances the fixed-point system associated with the first onset of gross stochastic instability appears to be of a rather high order (and indeed in such cases may become more difficult to specify). It may be particularly notable that with variations of A covering a fairly small range in this sequence of cases, many distinctly different fixed-point systems appear to be associated in turn with the stability limit.

Parameter A	Small-Amplitude Tune, σ_0 (deg)	Estimated Range of x at Z=0 mod. 2π & Associated Tune (deg)	Nearby Fixed-Point System Order, & Tune(deg)
0.23	61.303277	-2.4 to 1.69 (~52.6 deg)	7/1, 1 X 360/7=51.4286
0.24	64.265071	-2.3 to 1.72 (~56.0 deg)	13/2, 2 X 360/13=55.3846
0.25	67.273942	-1.7 to 1.43 (~61.6 deg)	6/1, 1 X 360/6=60.
0.26	70.334408	-1.89 or ~ 1.9 to 1.61 (~62.8 deg)	23/4, 4 X 360/23=62.6087
0.26525	71.963493	-1.86 to 1.65 (~64.7 deg)	39/7, 7 X 360/39=64.6154 28/5, 5 X 360/28=64.2857
0.26670	72.416288	-1.82 to 1.57 (~65.9 deg)	11/2, 2 X 360/11=65.4545

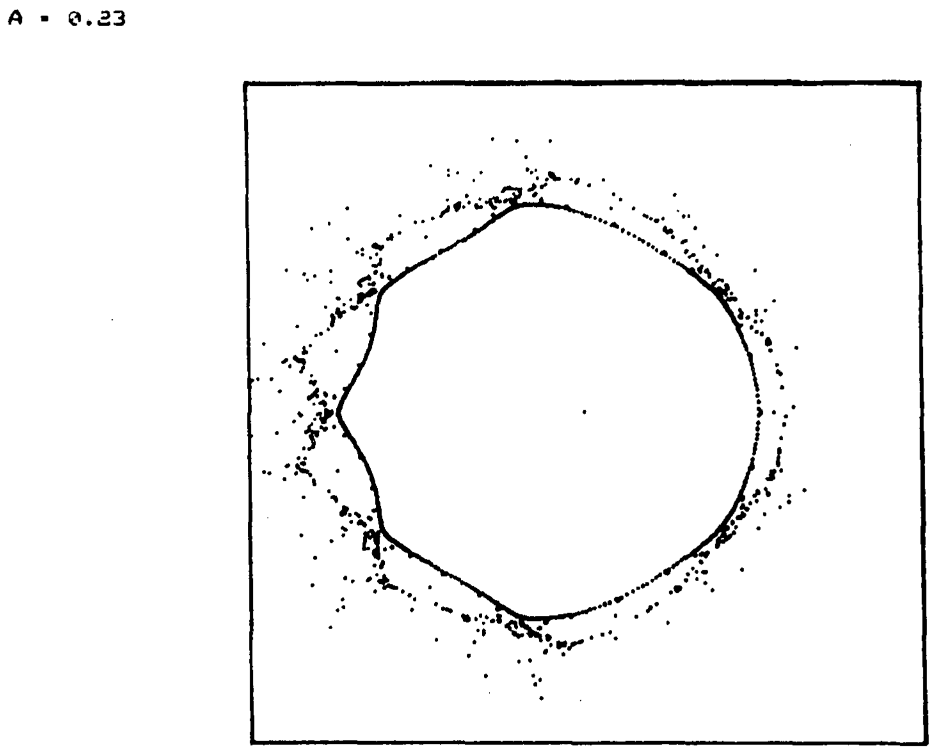

XBL 851-829

Fig. II.3 Phase plot for A = 0.23; Scales:
Horizontal: −3.25 to 3.25 for x;
Vertical: −0.30 to 0.30, for x'.
Shown are an apparently limiting phase trajectory (launched with $x_0 = -2.4$, $x_0' = 0$), a sequence of order 7/1 stable fixed points, and an erratic run resulting from a launch substantially at an order 7/1 unstable fixed point (taken to be at approximately $x_0 = -2.465$, $x_0' = 0$).

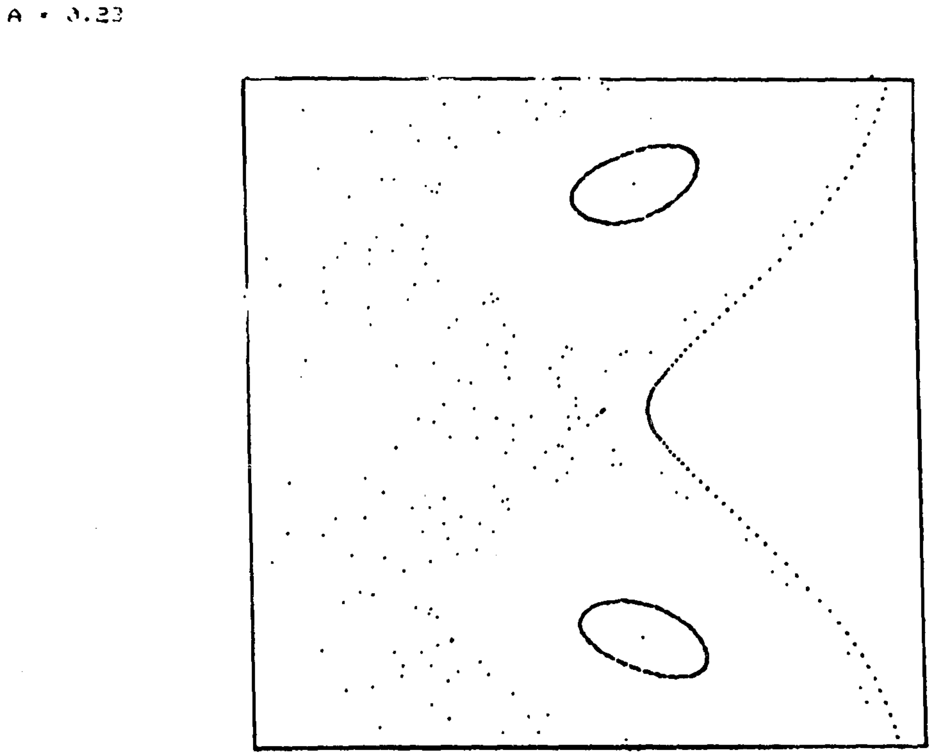

XBL 851-830

Fig. II.3a Detail related to Fig. II.3 (A=0.23); <u>Scales</u>:
Horizontal: -3.0 to -2.0, for x;
Vertical: -0.08 to 0.08, for x'.
Shown are a portion of the apparently limiting trajectory launched with $x_0 = -2.4$, two members of the stable order 7/1 fixed-point system (with surrounding loops), and an unstable sequence of points resulting from a launch substantially at an unstable order 7/1 fixed point.

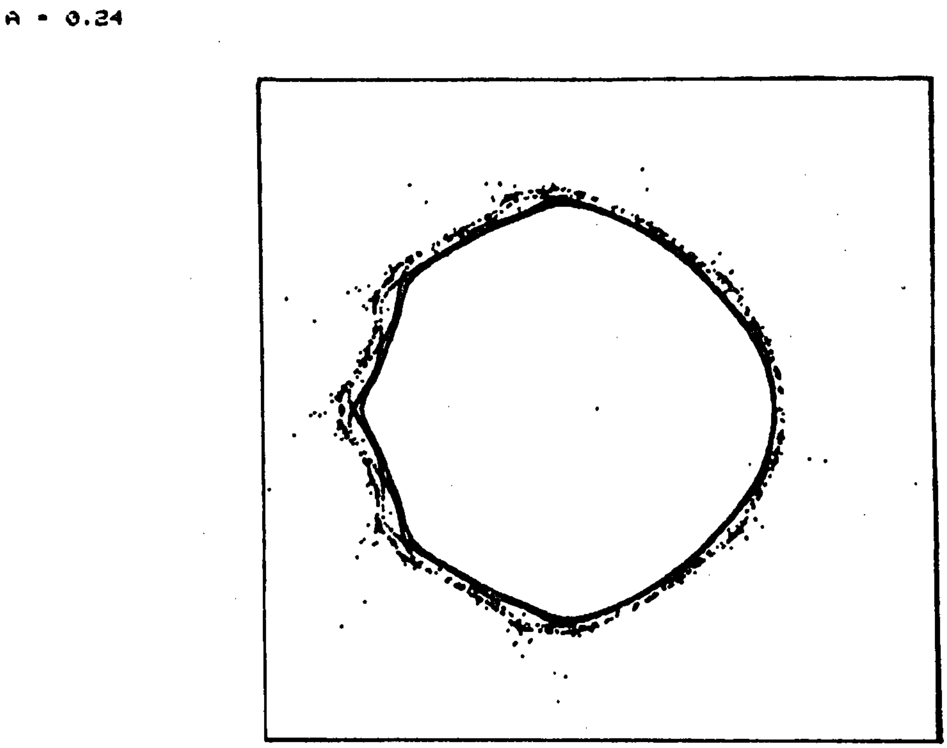

XBL 851-831

Fig. II.4 Phase Plot for A = 0.24; <u>Scales</u>:
Horizontal −3.25 to 3.25, for x;
Vertical: −0.30 to 0.30, for x'.
An apparently stable limiting trajectory is shown that results from a launch with $x_0 = -2.3$, $x_0' = 0$. Features of stable and unstable order 13/2 fixed-point systems also are shown. A run launched substantially at an unstable fixed point of this system ($x_0 = -2.384407_{0663}$, $x_0' = 0$) shows evident stochasticity and a run launched on the x-axis at $x_0 = -2.5$ shows a pronounced blow up in the course of traversing some 714 periods of the structure (see Detail, Fig. II.4a).

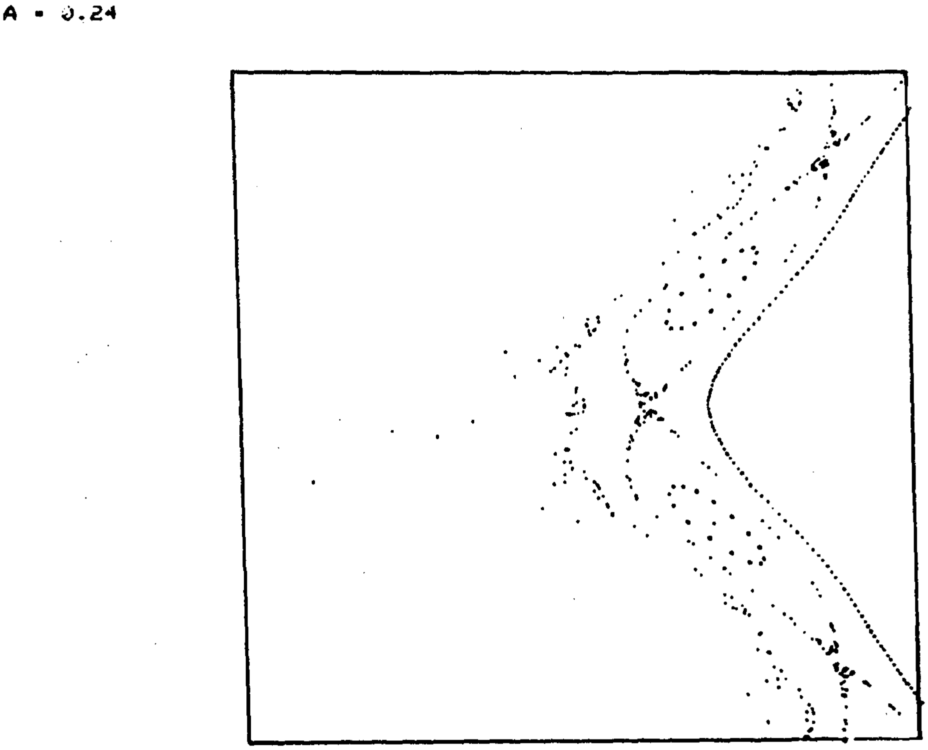

XBL 851-832

Fig. II.4a Detail related to Fig. II.4 (A = 0.24); Scales:
Horizontal -3.0 to -2.0, for x;
Vertical -0.08 to 0.08, for x'.
Shown are a portion of the apparently stable trajectory launched with $x_0 = -2.3$, two members of the stable order 13/2 fixed-point system (with surrounding loops), an evidently stochastic trajectory originating near an unstable order 13/2 fixed point, and the pronounced instability of a run launched on the x-axis at $x_0 = -2.5$ (a small distance beyond the order 13/2 system).

A = 0.25

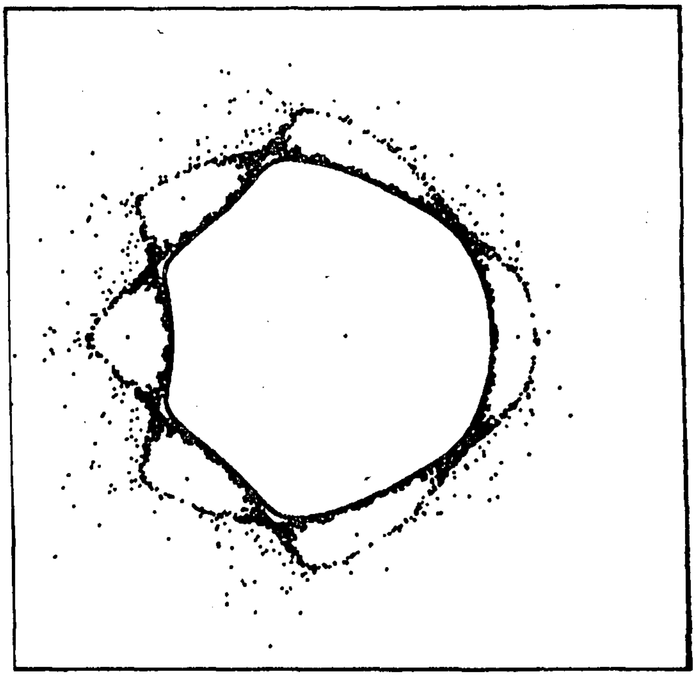

XBL 851-833

Fig. II.5 Phase plot for A = 0.25; Scales:
Horizontal: -3.25 to 3.25, for x;
Vertical: -0.30 to 0.30, for x'.
A limiting apparently stable phase trajectory is shown, as a result of a launch at x_0 = -1.7, x_0' = 0. Stable order 6/1 fixed points also are shown, together with the results of a clearly stochastic run originating in the immediate neighborhood of an unstable fixed point of the order 6/1 system.

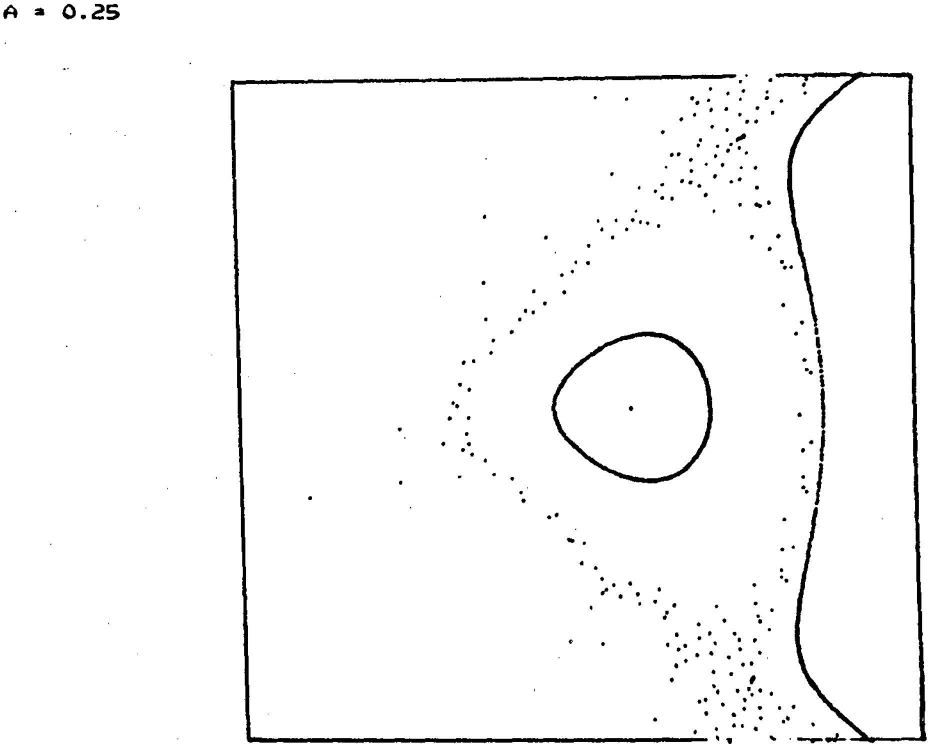

XBL 851-834

Fig. II.5a Detail related to Fig. II.5 (A = 0.25); Scales:
Horizontal: -3.0 to -1.5, for x;
Vertical: -0.08 to 0.08, for x'.
Shown are a portion of the limiting stable trajectory launched with $x_0 = -1.7$, a member of the stable order 6/1 fixed-point system, (with a surrounding small loop), and the stochastic instability resulting from a launch at an unstable fixed point of order 6/1.

A = 0.26

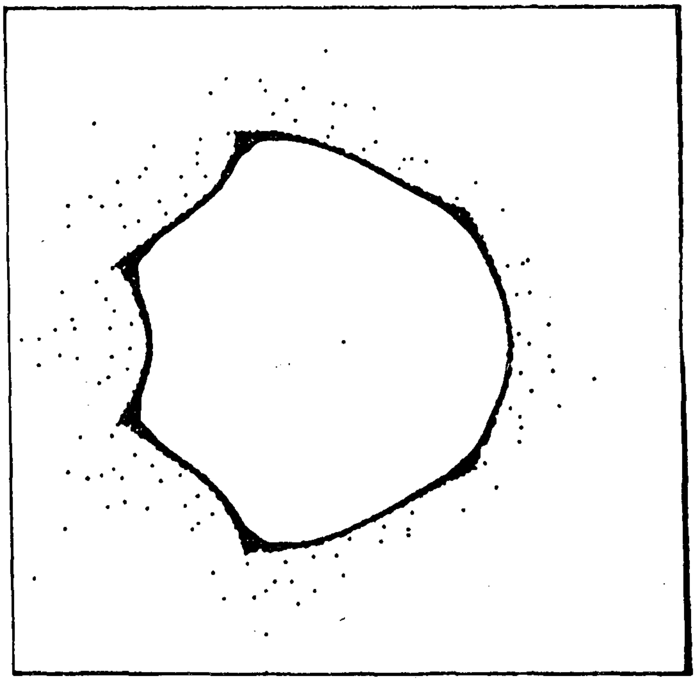

XBL 851-835

Fig. II.6 Phase plot for A = 0.26; Scales:
Horizontal: -3.25 to 3.25, for x;
Vertical: -0.30 to 0.30, for x'.
A limiting apparently stable phase trajectory is shown, as a result of a launch at x_0 = -1.9 and x_0' = 0. Also shown is a surrounding order 23/4 fixed-point system from which stochastic instability is seen to develop.

A = 0.26, USING 4096 FULL R-K-G STEPS PER PERIOD.

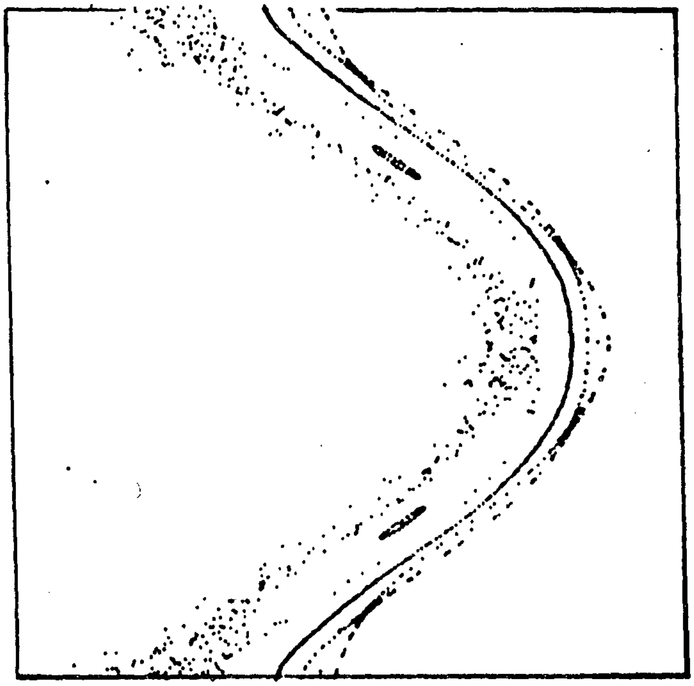

XBL 851-836

Fig. II.6a Detail related to Fig. II.6 (A = 0.26); <u>Scales</u>:
Horizontal: -2.10 to -1.85, for x;
Vertical: -0.05 to 0.05, for x'.
An apparently smooth phase trajectory, originating on the x-axis at x_0 = -1.89, is shown and evidently indicates substantially the limit of stability. Portions of an order 40/7 system have been added, at smaller amplitude, to the right of this trajectory segment. At larger amplitude a distinctly stochastic motion, ultimately leading to blow-up, is seen to result from a launch at x_0 = -1.903935420 and x_0' = 0 from an unstable fixed point of the order 23/4 system.

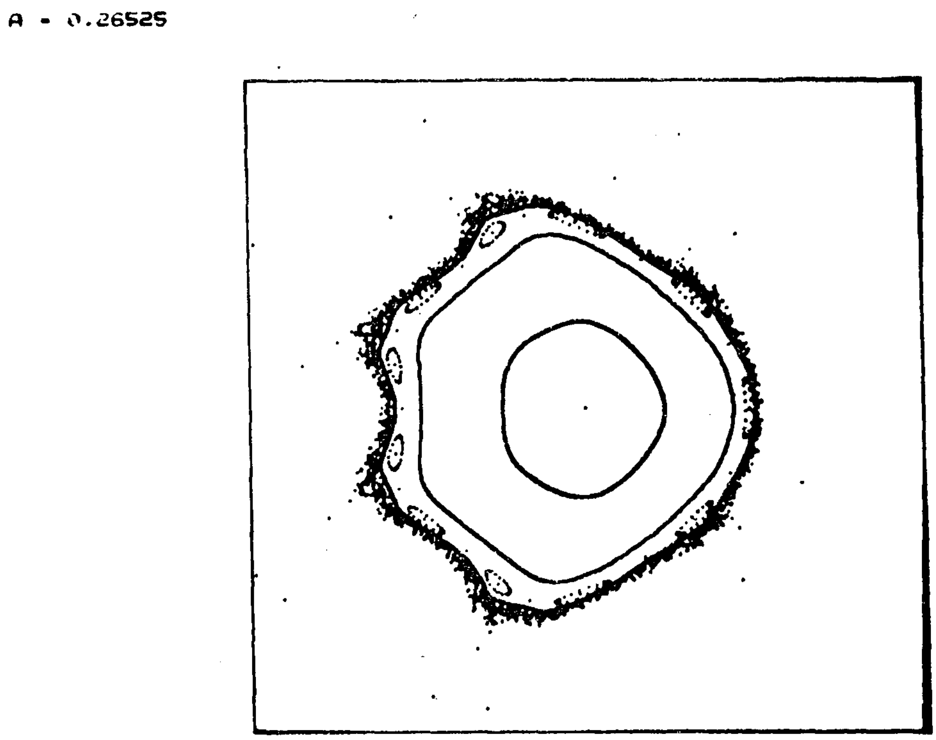

XBL 851-837

Fig. II.7 Phase plot for A = 0.26525; <u>Scales</u>:
Horizontal: -3.25 to 3.25, for x;
Vertical: -0.30 to 0.30, for x'.

For this value of A, the small-amplitude tune is such that σ = 71.963493 deg. When examined on an enlarged scale (see Figs. II.7a-d), several fixed-point systems become evident at amplitudes near to the stability boundary -- e.g., systems of order 11/2, 50/9, 39/7, and 28/5, for which the respective tunes become $\sigma \cong$ 65.4545, 64.80, 64.6154, and 64.2857 degrees. A limiting boundary curve appears to result from a launch with $x_0 = -1.86$, $x_0' = 0$, just outside the system of order 50/9, and is shown as the outermost closed curve on this figure (together with two additional closed curves, of considerably smaller amplitudes, that are also shown encircling the origin). The presence of stable fixed points of an order 11/2 system (together with small surrounding loops) and of unstable order 11/2 fixed points also is indicated; some stochasticity may be associated with these unstable order -11/2 fixed points (see Fig. II.7d), but the order 11/2 system is contained within the apparently smooth limiting boundary curve mentioned above. The features of the order 50/9 fixed-point system are not readily depicted on the present rather coarse scale, but one sees an evident instability that results from a run originating near an unstable fixed point of the order 28/5 system (here taken to be at x_0 = -2.05607625, x_0' = 0.0520677).

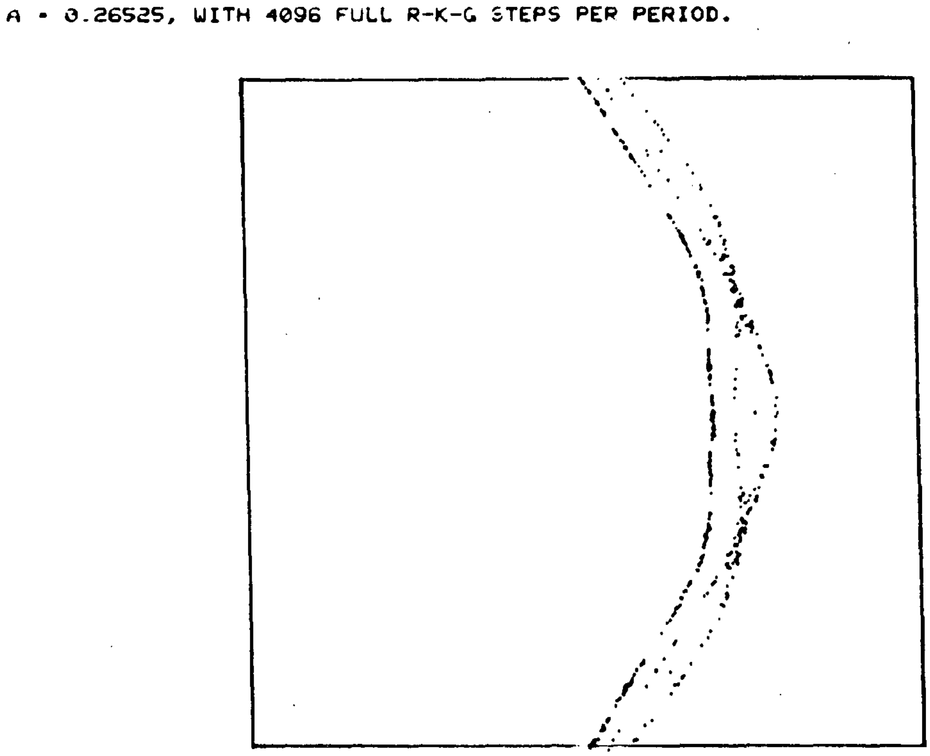

XBL 851-838

Fig. II.7a Detail related to Fig. II.7 (A = 0.26525); Scales:
Horizontal: -2.00 to -1.80, for x;
Vertical: -0.02 to 0.02, for x'.
This figure shows a portion of the presumed smooth "limiting boundary curve" that results from a launch at $x_0 = -1.86$, $x_0' = 0$, and to which reference was made in the caption to Fig. II.7. At smaller amplitudes, to the right of this trajectory segment, one sees portions of order 50/9 fixed-point systems, with some evident stochasticity noticeable in the neighborhood of the unstable fixed points of this system. It of course is a matter of judgement whether the so-called boundary curve, as computed here, is truly sufficiently smooth that phase points are precluded from crossing into regions of larger amplitude.

A = 0.26525, WITH 4096 FULL R-K-G STEPS PER PERIOD.

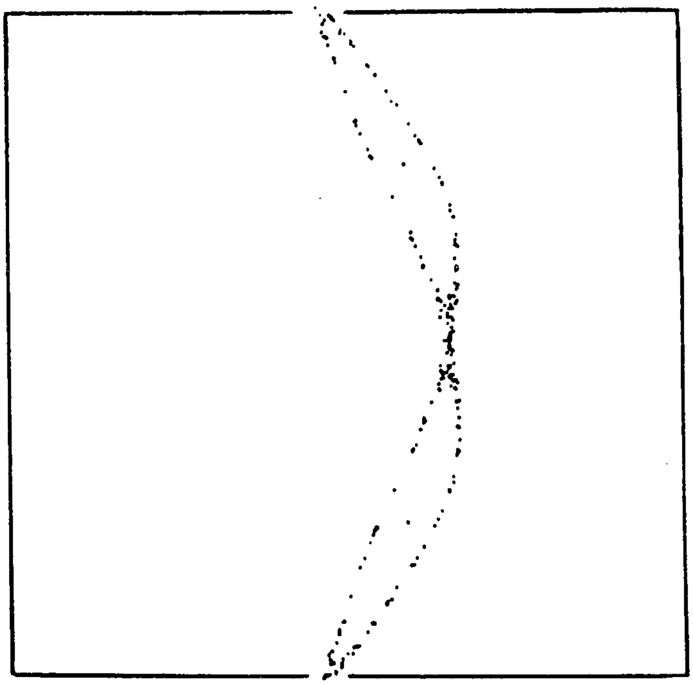

XBL 851-839

Fig. II.7b Detail related to Fig. II.7 (A = 0.26525); Scales:
Horizontal: -2.00 to -1.80, for x;
Vertical: -0.02 to 0.02, for x'.
Portions of order 39/7 fixed-point systems, with evidence of some stochastic behavior in the neighborhood of the unstable fixed point shown for this system.

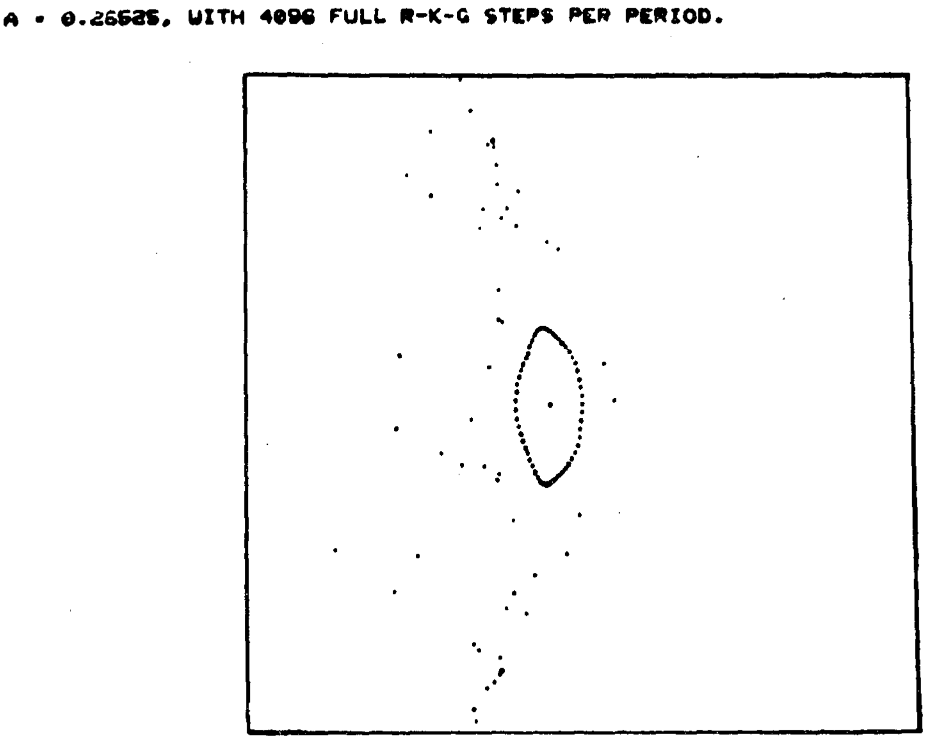

Fig. II.7c Detail related to Fig. II.7 (A = 0.26525); <u>Scales</u>:
Horizontal: -2.00 to -1.80, for x;
Vertical: -0.02 to 0.02, for x'.
Highly stochastic instability associated with unstable fixed points of an order 28/5 system, shown together with a stable fixed point (and surrounding loop) of this same order.

A = 0.26525

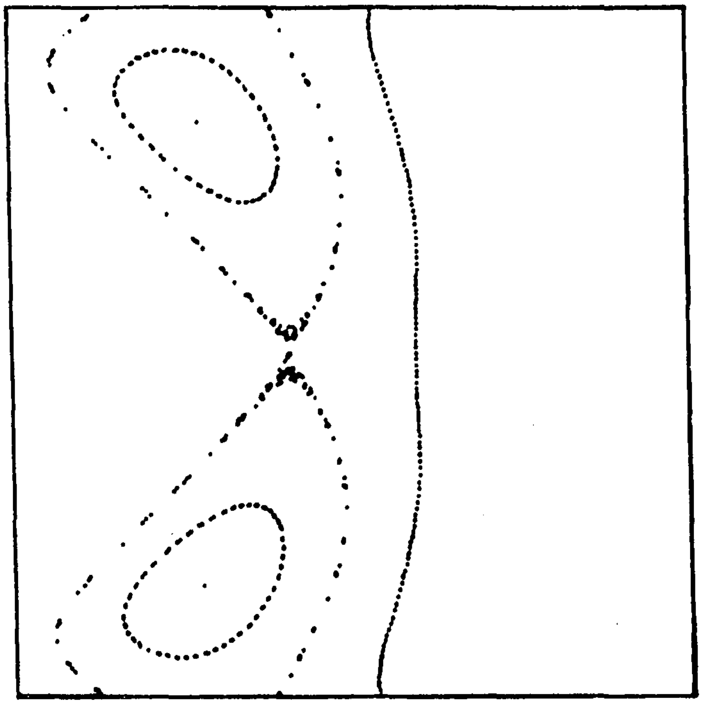

XBL 851-841

Fig. II.7d Detail related to Fig. II.7 (A = 0.26525); Scales:
Horizontal: -2.00 to -1.50, for x;
Vertical: -0.06 to 0.06, for x'.
Detail of fixed points of order 11/2 systems, indicating possible stochasticity near the unstable order 11/2 fixed point. Also shown is a portion of an apparently smooth phase trajectory of somewhat smaller amplitude that results from a launch with $x_0 = -1.7$, $x_0' = 0$.

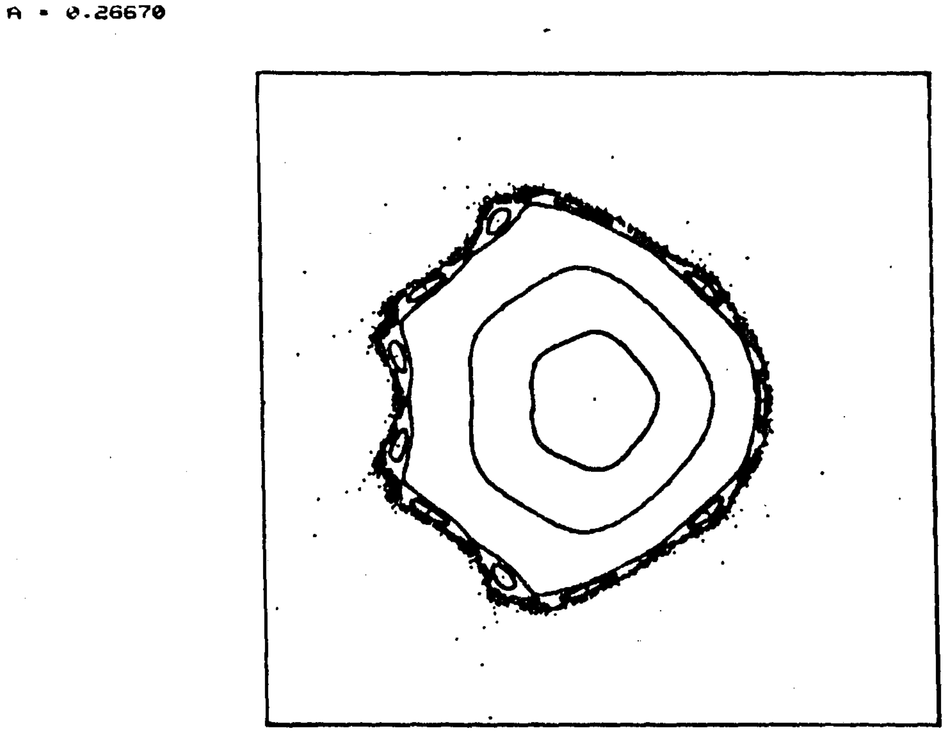

XBL 851-842

Fig. II.8 Phase plot for A = 0.26670; Scales:
Horizontal: -3.25 to 3.25, for x;
Vertical: -0.30 to 0.30, for x'.
Shown is the erratic and clearly unstable phase motion that results from a launch with x_0 = -1.8377526, x_0' = 0, just beyond an unstable fixed point of order 11/2. Also shown are stable fixed points (and encircling loops) of order 11/2. The limiting closed phase trajectory appears to be that which results from a launch with x_0 = -1.82, x_0' = 0 -- shown here together with additional curves that encircle the origin with a smaller amplitude.

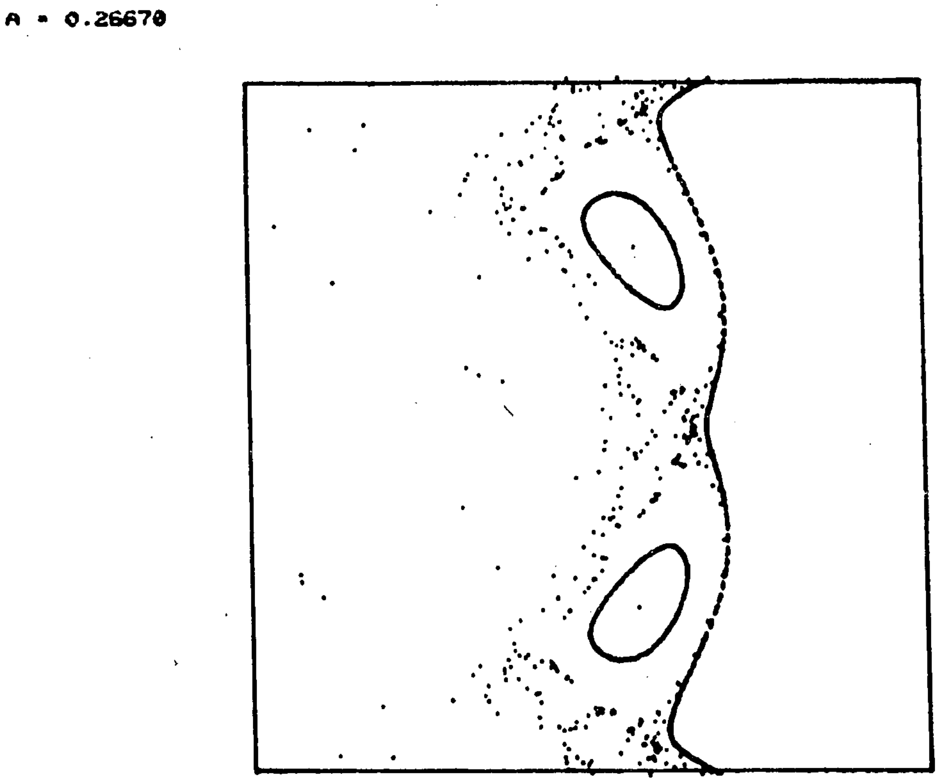

XBL 851-843

Fig. II.8a Detail related to Fig. II.8 (A = 0.26670); Scales:
Horizontal: -2.50 to -1.50, for x;
Vertical: -0.08 to 0.08, for x'.
This detail shows a portion of the apparently smooth curve, resulting from a launch at $x_0 = -1.82$, $x_0' = 0$, that may be regarded as situated at the edge of the region of stability [plotted for 2500 periods]. At only slightly greater amplitude clearly unstable stochastic motion is seen to develop from a launch at an unstable order 11/2 fixed point ($x_0 = -1.83775252$, $x_0' = 0$). Two of the stable order 11/2 fixed points also are shown, together with small surrounding loops.

B.

$$\boxed{\frac{d^2x}{dZ^2} = -A\,(\,x + 1/12\;x^3 + 1/384\;x^5\,)\cos Z}$$

The character of solutions to Eqn.(2) also could be examined in the manner in which solutions to Eqn. (1) were examined in the preceding sub-section. An overall indication of the nature of solutions to Eqn. (2) is shown, for $A = 0.2088$, in Fig. II.9. With this value of the parameter A, the tune for small-amplitude motion is such that $\sigma_0 = 55.1621$ degrees and σ increases with increasing amplitude with the result that a pronounced order 6/1 fixed-point system ($\sigma = 60$ deg.) is seen to occur at intermediate amplitudes.

The largest simple, apparently smooth, closed phase trajectory shown on Fig. II.9 resulted from a launch with $x_0 = 1.6$ and $x_0' = 0$ ($\sigma \cong 68.87$ deg.), and shortly beyond this curve systems of order 5/1 fixed points make their appearance. It is of interest to note that there are, in fact, <u>two</u> systems of stable order 5/1 fixed points (and similarly <u>two</u> systems of unstable order 5/1 fixed points). Thus, one system of stable order 5/1 fixed points has one member of this family situated on the positive x-axis ($x \cong 1.782071$) and the remaining four members situated symmetrically above and below the x-axis, while the second family has its members similarly situated save for a reversal of sign for the x-coordinate of each member. With respect to the unstable order 5/1 fixed points, one member of one family is situated on the positive x'-axis ($x' \cong 0.19289322$) with other members of that family symmetrically situated to the right and left of that axis, while the second unstable family is similar save for a reversal of sign of x' for each member. The mapping of phase points in the neighborhood of the unstable order 5/1 fixed points presents, moreover, a distinctly stochastic character, and a run launched on the x-axis with $x_0 = 1.89$ is found to lead to a gross instability ("blow-up", not shown).

At still larger amplitudes on Fig. II.9 one finally sees the locations of stable and unstable fixed points of order 14/3 ($\sigma \cong 77.1429$ deg.), with two members of the stable system lying on the x'-axis at $x' \cong \pm\, 0.22460743$ and two members of the unstable system on the x-axis at $x \cong \pm\, 1.99832577$. The unstable order 14/3 system is locally very strongly unstable (half trace of tangential-mapping transformation $\cong$ 16.2579), while the stable family (HTR $\cong$ 0.91026484) can be of interest in giving rise to a bifurcation (<u>without</u> period doubling) when the parameter A is slightly reduced (Chapter III).

Figure II.9a shows some detail of the phase plane in the near neighborhood of the stable order 5/1 fixed point situated (as on Fig. II.9) on the x-axis at $x \cong 1.782071$. The outermost trajectories indicate the presence of 11 stable and 11 unstable order 55/11 fixed points, arranged to surround the order 5/1 fixed

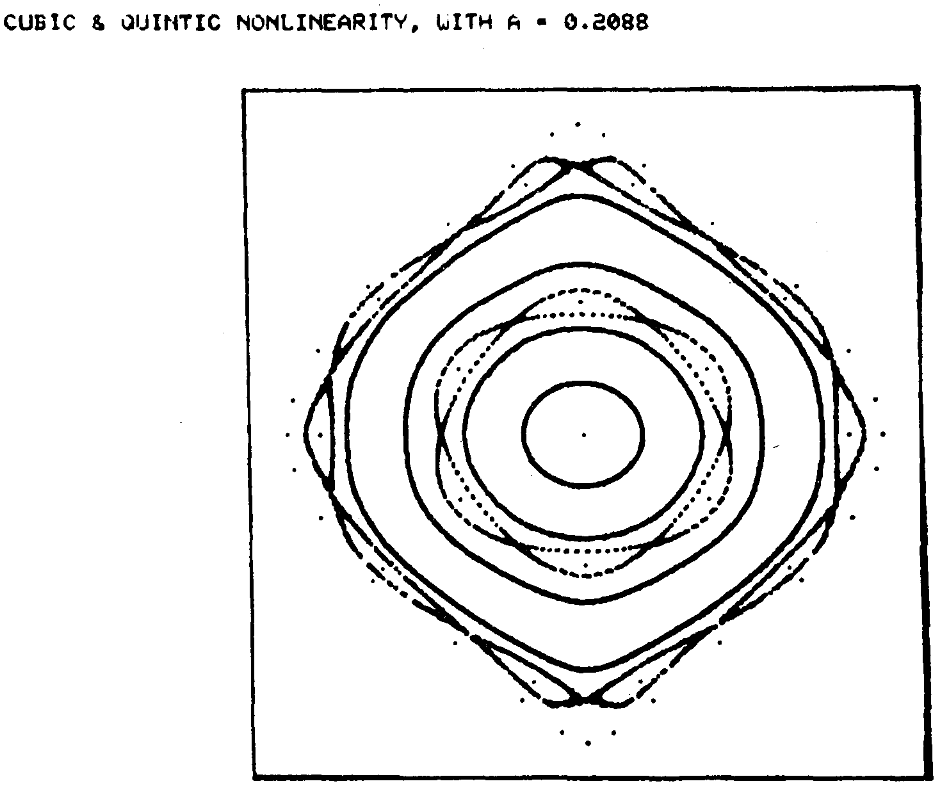

XBL 851-844

Fig. II.9 Phase plot, at $Z = 0$ mod. 2π, for solutions to Eqn. (2) with $A = 0.2088$ ($\sigma_0 = 55.1621$ deg.). Scales:

Horizontal: -2.25 to 2.25, for x;
Vertical: -0.25 to 0.25, for x'.

Distinctive features include systems of stable and unstable order 6/1 fixed points, two stable and two unstable order 5/1 systems, and the locations of stable and unstable order 14/3 fixed points. The largest simple, apparently smooth, closed phase trajectory originated from a launch with $x_0 = 1.6$ and $x_0' = 0$.

point situated near the center of this diagram. The stochastic evolution of phase points for a run launched near an unstable order 5/1 fixed point (e.g., near $x_0 = 1.68129339$, $x_0' = 0.04744928$) would carry such points to regions further removed from the stable order 5/1 fixed point shown here.

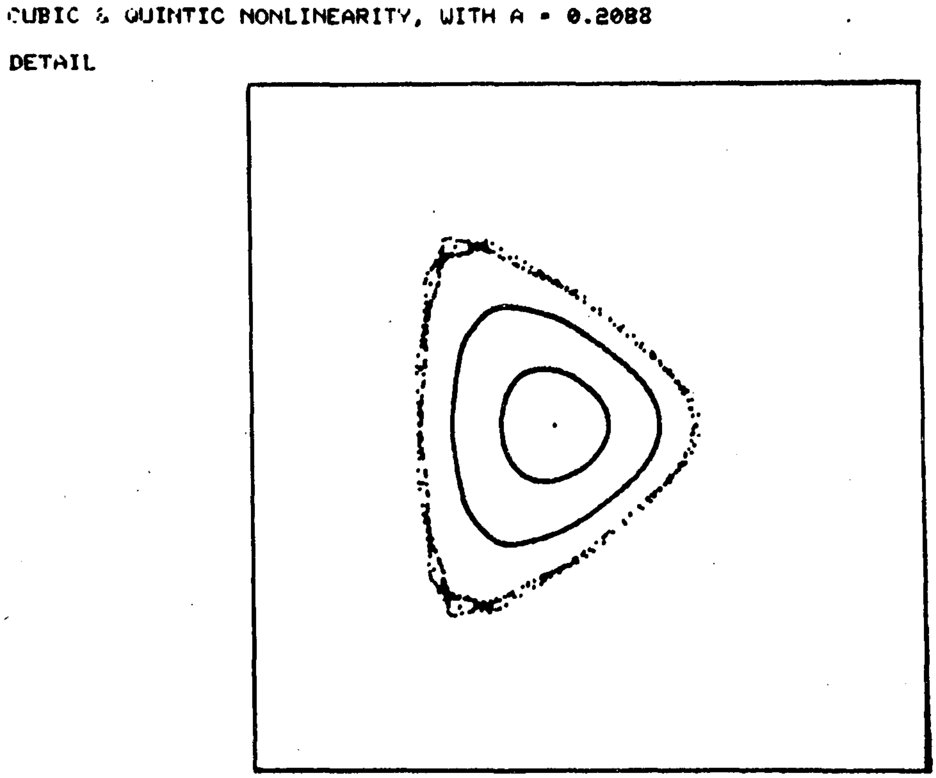

XBL 851-845

Fig. II.9a Detail related to Fig. II.9, for Eqn.(2) with
A = 0.2088, Scales:
Horizontal: 1.60 to 2.00, for x;
Vertical: -0.06 to 0.06, for x'.
Phase trajectories surrounding a stable order 5/1 fixed point are shown, together with indications of stable and unstable fixed points of order 55/11 in this vicinity.

REFERENCES OR NOTES

1. A curl-free, divergence-free magnetic field that is longitudinally periodic with period P and is of a quadrupole character with respect to its dependence on ϕ can be constructed from terms of the form

$$B_r = k\, I_2'(kr) \cos kZ \sin 2\phi$$

$$B\phi = (2/r)\, I_2(kr) \cos kZ \cos 2\phi$$

$$B_Z = -k\, I_2(kr) \sin kZ \sin 2\phi \quad ,$$

with k any integer multiple of $2\pi/P$. The nonlinearities necessarily introduced thereby into median-plane motion ($\phi = 0$) accordingly are such as arise from terms of the form $I_2(kr)/r$.

2. Convergence to a numerical evaluation of phase-plane coordinates for fixed points of interest, and the evaluation of the local tune or stability characteristics for small-amplitude oscillations about the periodic orbit corresponding to any such fixed point, can make use conveniently of the "tangential-mapping transformation" that tracks an infinitesimal displacement (δx, $\delta x'$) through the appropriate interval in Z. For other phase trajectories, estimates of tune are obtainable by the technique of counting axis crossings in the x, x' phase plane.

III. BIFURCATION -- ILLUSTRATIONS

For Area-Preserving Transformations and Solutions to Differential Equations

A distinct change can occur in the nature of the fixed-point systems characterizing area-preserving transformations, or solutions to canonical differential equations, as a parameter of the transformation is changed. One finds such changes to occur when a fixed-point system that previously was locally stable becomes unstable as a result of a parameter change and new (stable) fixed points split off to make their appearance. In cases such that the previously stable system becomes unstable with reflection, the new system is found to have a period twice that of its predecessor. A sequence of such period-doubling bifurcations, occurring for smaller and smaller changes of the governing parameter, results in a bifurcation lattice or "tree" that may be claimed to terminate in "chaos".

Illustrations of bifurcation are conveniently obtained by examination of simple area-preserving algebraic mappings,(1) and also can be found in phase-plane mappings that represent solutions to canonical differential equations characteristic of median-plane motion in alternating-gradient particle accelerators or storage rings.

A. An Area-Preserving Quadratic Mapping

The area-preserving quadratic mapping (M)

$$\left.\begin{aligned} x_{n+1} &= y_n + F(x_n) \\ y_{n+1} &= -x_n + F(x_{n+1}) \end{aligned}\right\} \quad , \tag{1}$$

with $F(x) = Tx + (1-T)x^2$ [a generalized deVogelaere form, with parameter T], serves conveniently to illustrate the development of a sequence of period-doubling bifurcations as the parameter T is varied. The transformation (1) results in phase diagrams that exhibit a convenient symmetry about the x-axis. For $|T| < 1$ the origin constitutes a stable first-order fixed point and the point (1, 0) is an unstable first-order fixed point.

For T somewhat negative, phase points representing small-amplitude motion encircle the origin somewhat more rapidly than once per four iterations ($\cos^{-1} T > 90$ deg.), but at larger amplitudes one can find solutions that are locked into order -4/1 fixed-point systems. Such order - 4/1 fixed-point systems are illustrated on Fig. 1 for T = -0.1030. The half-trace (HTR) for the tangential-mapping transformations, for M^4 linearized about a stable fixed point of the system,(2) then may be computed to be circa -0.9883_{57} -- so that while this fixed-point system is stable, it is close to being unstable with reflection. It accordingly becomes of interest to examine the structure of the phase-space diagram, in the vicinity of such a stable fixed point as that seen in Fig. III.1 to lie on the positive x-axis, as the parameter T is varied (to become somewhat more negative).

For T = -0.1030 (as in Fig. III.1) the character of the phase trajectories in the neighborhood of the stable order - 4/1 fixed point on the positive x-axis is shown to an enlarged scale on Fig. III.2. One notes close to this stable fixed point the occurrence of apparently smooth surrounding phase trajectories that indicate the general nature of flow under action of M^4 in this region of phase space.

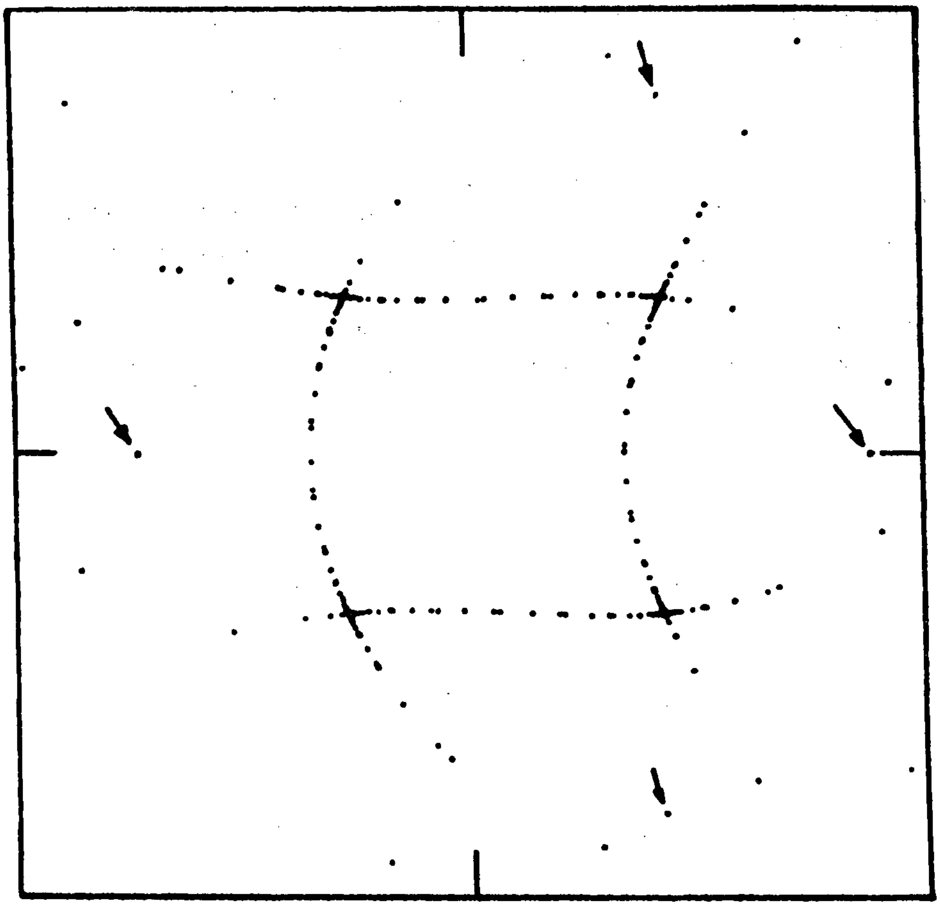

XBL 851-846

Fig. III.1 T = -0.1030 De-Vogelaere Variables
Scales: -0.60 to +0.60
Locations of 4-th Order unstable and stable fixed points.
The 4 stable fixed points are indicated by arrows. We shall follow the behavior in the neighborhood of the fixed point on the positive x-axis (x = 0.532268206310) as T becomes more negative.

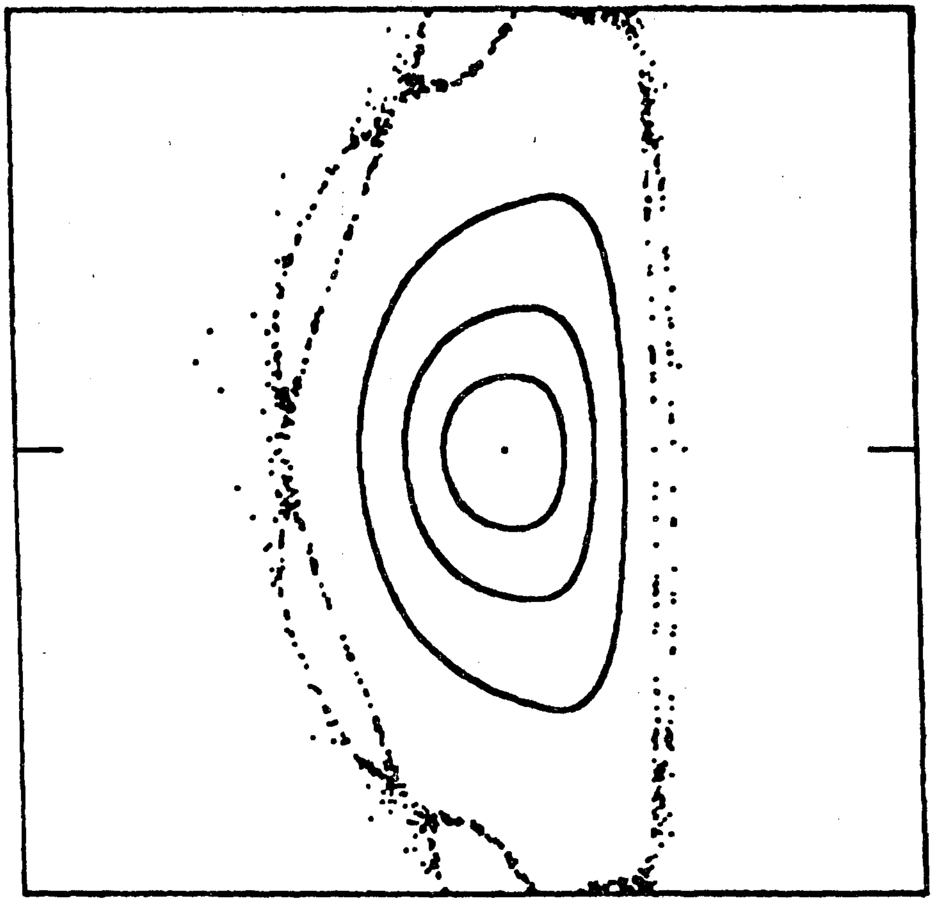

XBL 851-847

Fig. III.2. T = -0.1030 De-Vogelaere Variables
Enlarged plot of neighborhood about stable fixed point on the positive x-axis (x-scale: 0.45 to 0.60).

For T assigned the slightly more negative value $T = -0.1034$, the order - 4/1 fixed point on the positive real axis not only shifts its location slightly but, more significantly, becomes locally unstable, with reflection ($HTR < -1$). Because of this local instability, phase points tend to move away from (or toward) the fixed point, along eigenvector directions, while jumping from one side of the fixed point to the other in the manner characteristic of motion in the neighborhood of a hyperbolic fixed point with reflection (negative eigenvalues). The general circulatory character that was noted earlier for flow in this region evidently remains, however, to take effect at an appreciable distance from the fixed point and results in the diagrams shown (for $T = -0.1034$) on Fig. III.3 and (to a further enlarged scale) on Fig. III.4.

New (stable) fixed points are seen to occur within the loops of the "lazy-8" features that Figs. III.3 and III.4 show developing from the unstable fixed point. Because the unstable fixed point is unstable <u>with reflection</u> (under action of M^4), the phase-space coordinates will jump from one of these new stable fixed points to the other under action of M^4. The new fixed-point system (of which two members are seen on each of Figs. III.3 and III.4) thus constitutes a system of order - 8/1 (period = 8) and illustrates the occurrence of a period-doubling bifurcation.

It is of some interest to note the qualitative change in character of a diagram such as Fig. III.4 when further reductions are made in the parameter T. Such a change is illustrated by Figs. III.5 - III.14, with $T = -0.11125$ for the final Figure of this sequence. One notices, in progressing through this sequence, the development of an increasingly pronounced stochasticity about the unstable order - 4/1 fixed points and an enlargement of the area of the lazy-8 loops that surround the stable order - 8/2 fixed points.

When the existence of the order - 8/2 fixed-point system first became apparent (<u>e.g.</u>, for $T = -0.1034$), the half-trace of the tangential-mapping transformation for the order - 4/1 system was just slightly more negative than -1 (for M^4) and the half trace for the new order - 8/2 system was just slightly less than +1 (for M^8). With selection of increasingly negative values of the parameter T, the half-trace for the order - 4/1 system becomes driven to increasingly negative values and the half-trace of the order - 8/1 system is driven from values near +1 downward toward the critical value $HTR = -1$.

For $T = -0.11126$, the order - 8/2 fixed points have themselves become unstable ($HTR < -1$ for M^8) and generate loops within which new fixed points of an order - 16/4 system can be found. Such loops are illustrated in Figs. III.15 and III.16 for fixed points situated on the positive x-axis near $x = 0.581$ and $x = 0.486$.

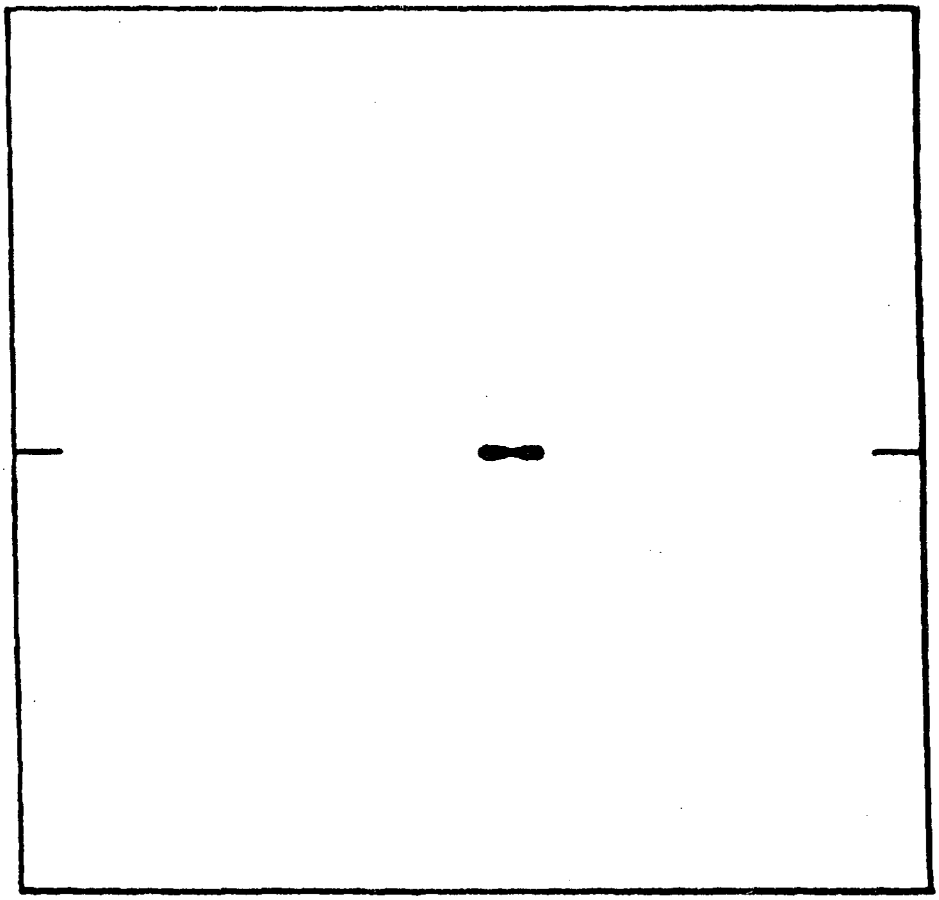

XBL 851-848

Fig. III.3 T = -0.1034 De-Vogelaere Variables
Scales: 0.45 to 0.60
±0.003

Development of bifurcation
1/4: Unstable
2/8: Stable

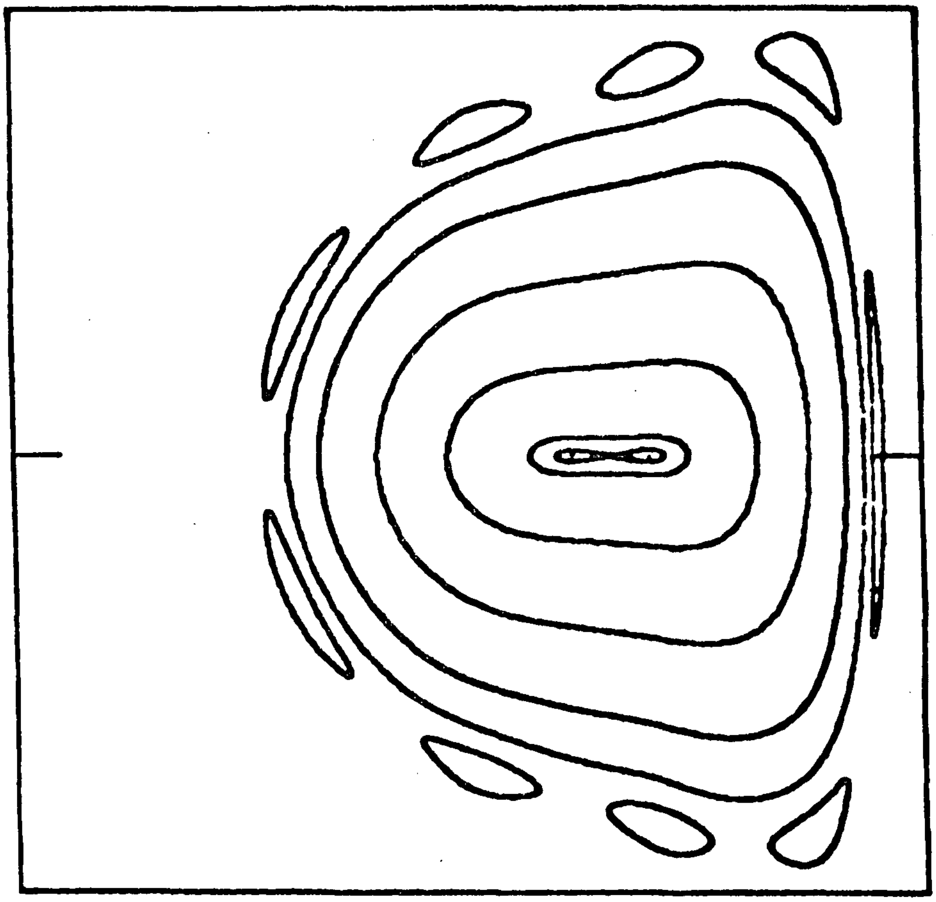

XBL 851-849

Fig. III.4 T = -0.1034 De-Vogelaere Variables
Scales: 0.48 to 0.56
±0.0025
Enlarged view of bifurcation.

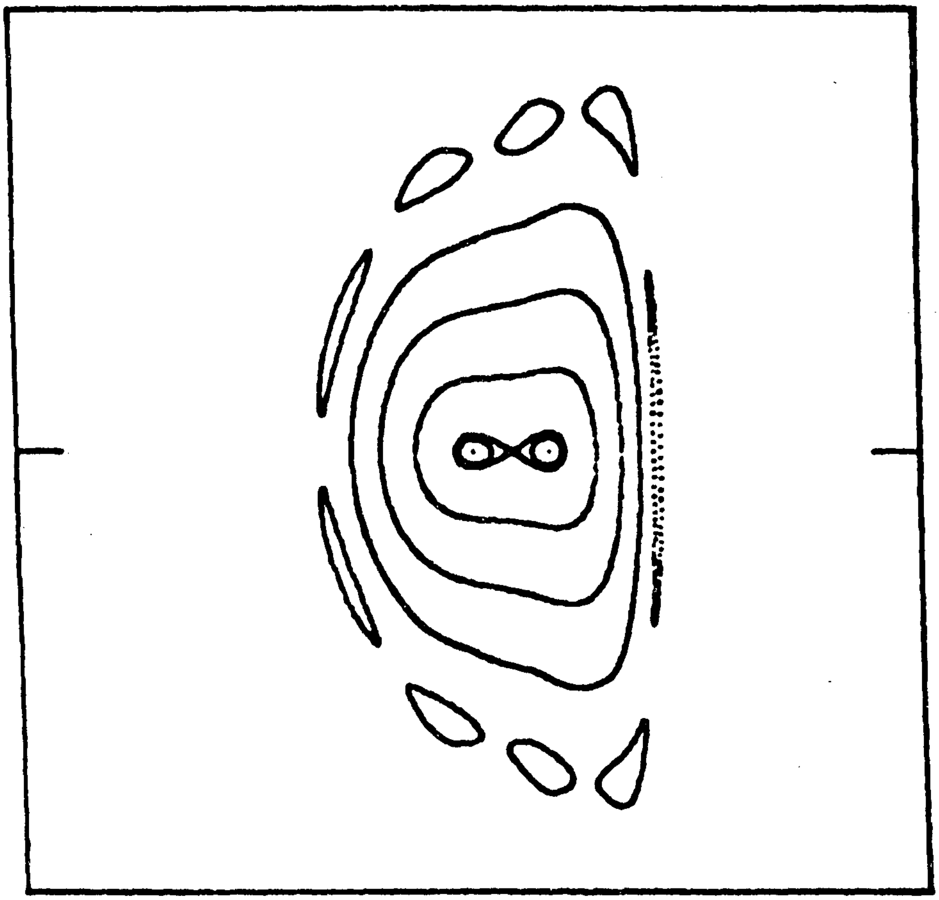

XBL 851-850

Fig. III.5 T = -0.1035 De-Vogelaere Variables
<u>Scales</u>: 0.45 to 0.60
±0.003

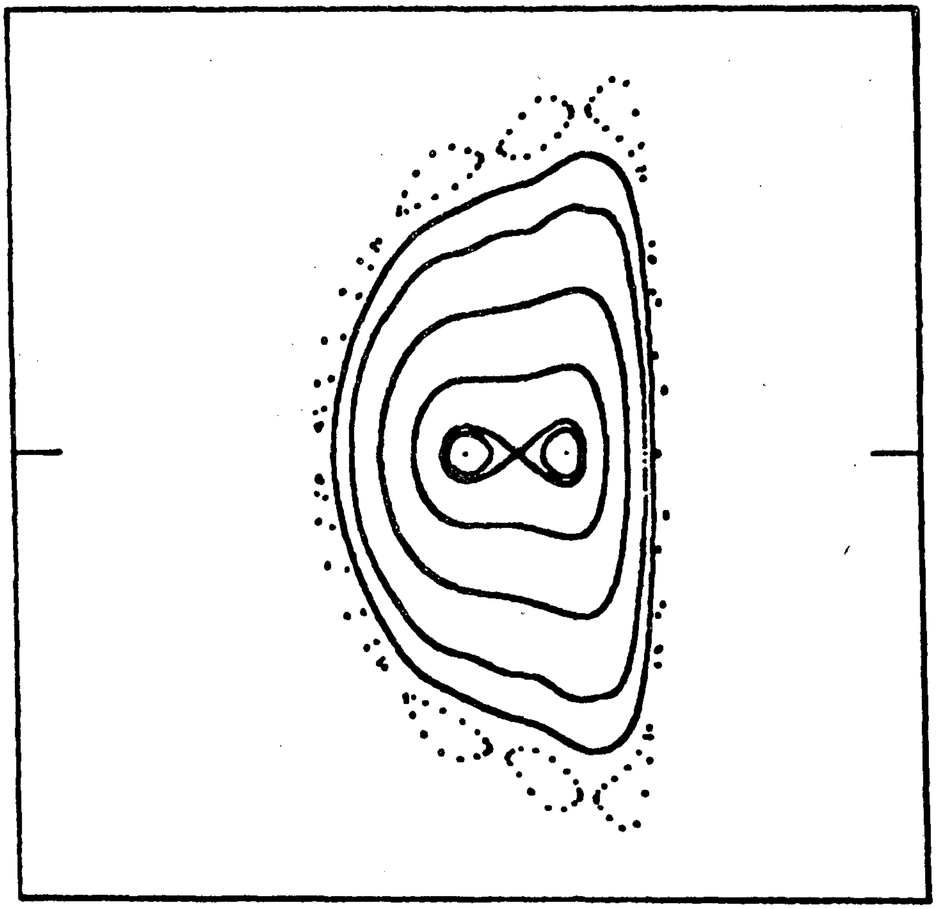

XBL 851-851

Fig. III.6 T = -0.0136 De-Vogelaere Variables
Scales: 0.45 to 0.60
±0.003

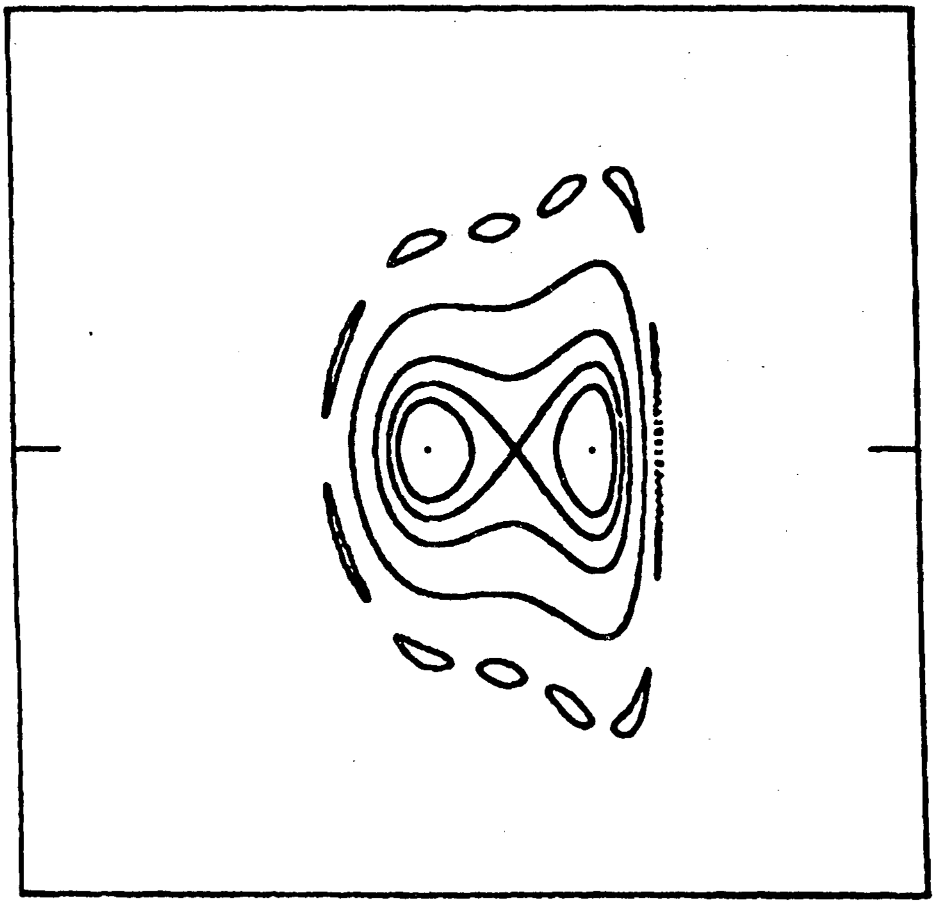

XBL 851-852

Fig. III.7 T = -0.1040 De-Vogelaere Variables
<u>Scales</u>: 0.45 to 0.60
±0.003

Note extensions of eigenvector directions from the unstable fixed point appear to form smooth closed curves.

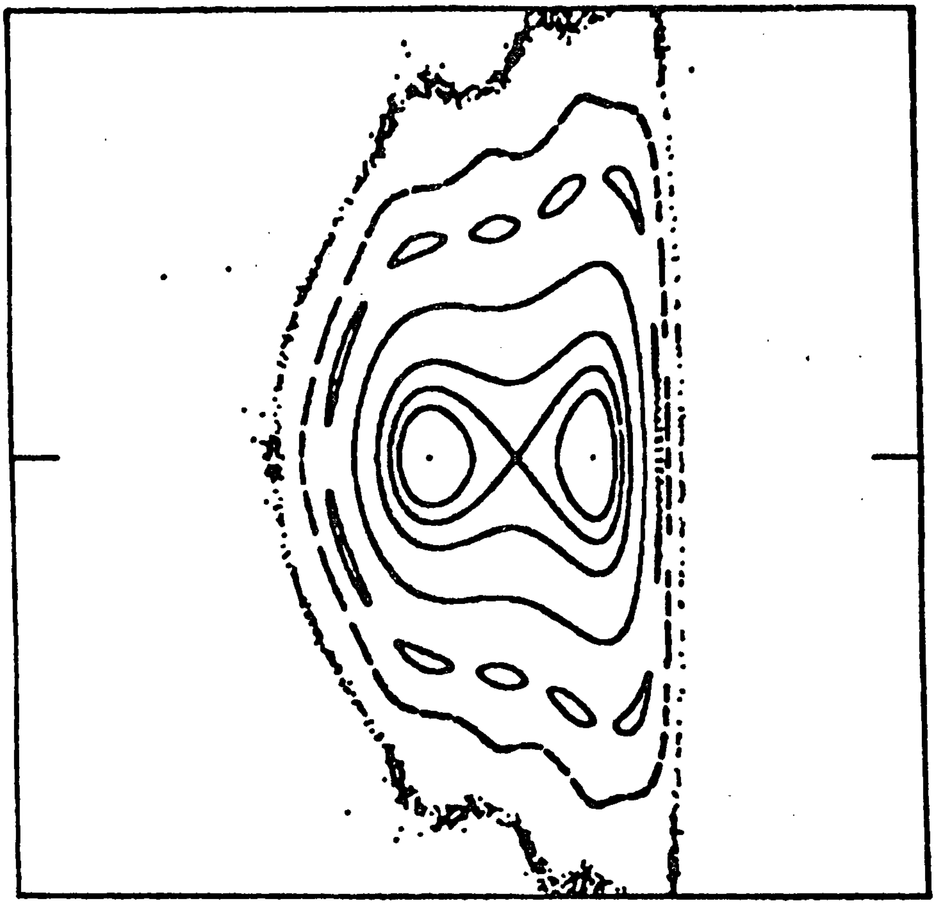

XBL 851-853

Fig. III.8. T = -0.1040 De-Vogelaere Variables

<u>Scales</u>: 0.45 to 0.60

±0.003

Plot with inclusion of stochastic boundary.

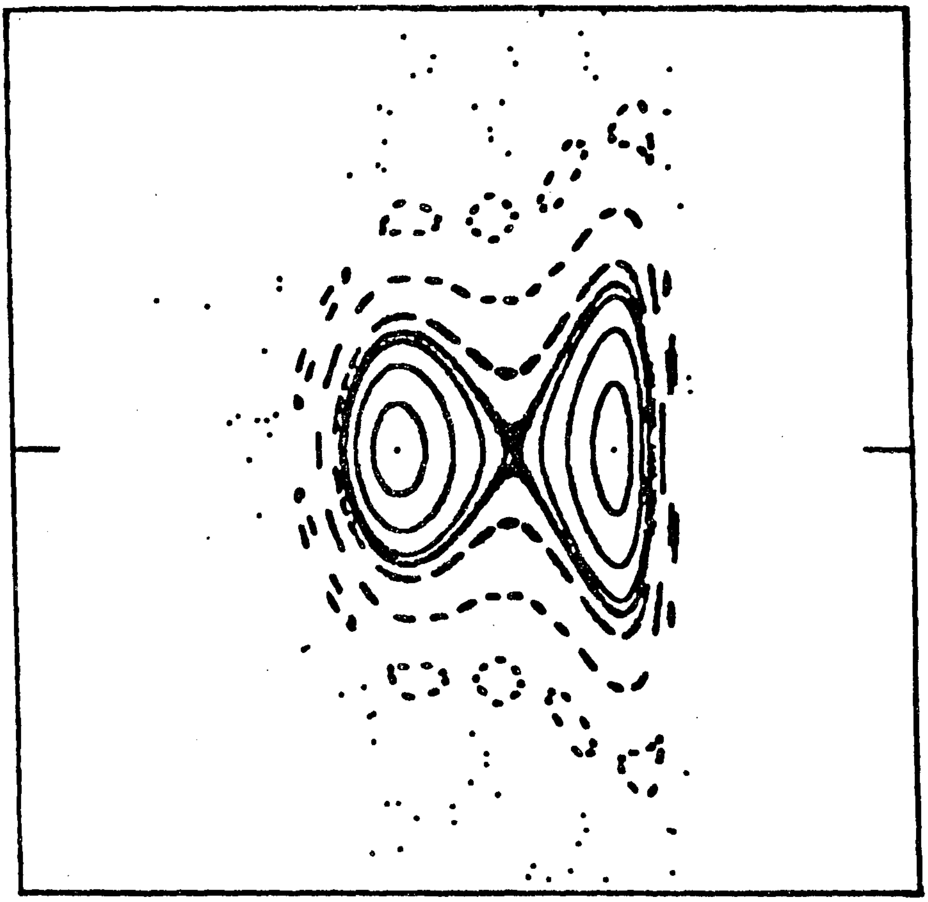

XBL 851-854

Fig. III.9. T = -0.1045 De-Vogelaere Variables

Scales: 0.45 to 0.60
±0.003

Note development of evident stochasticity about the unstable fixed point at x = 0.534416773867

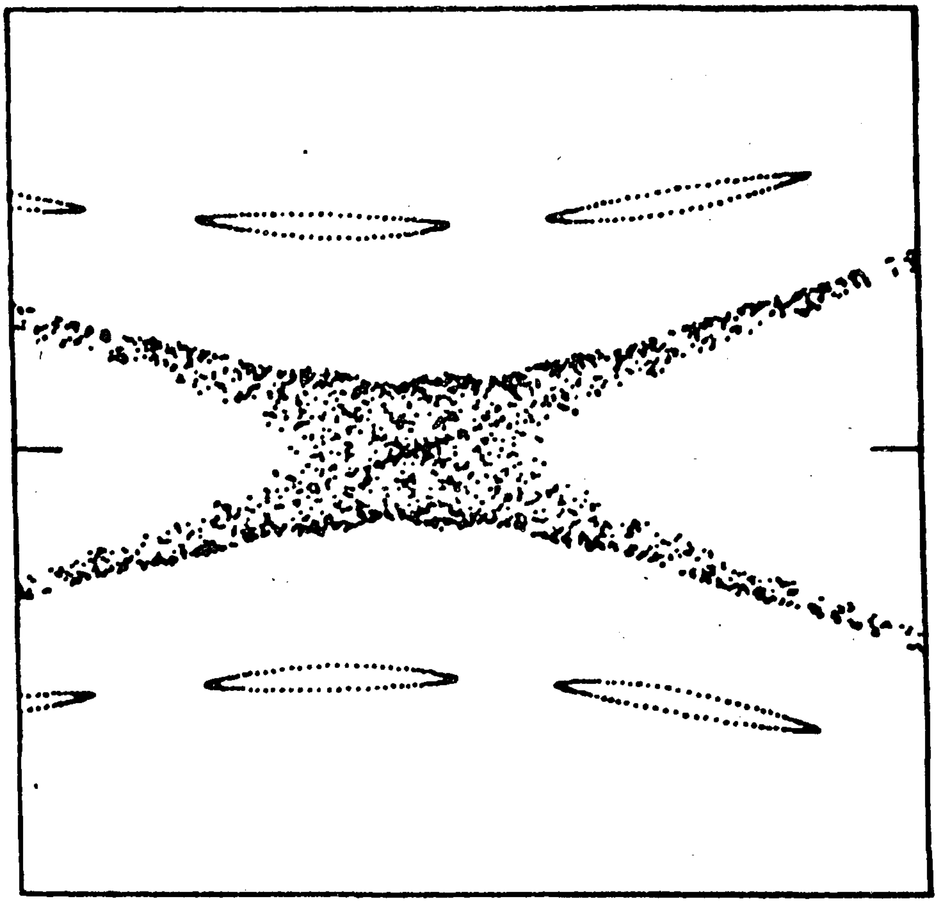

XBL 851-855

Fig. III.10 T = -0.1045 De-Vogelaere Variables
Scales: 0.53 to 0.54
±0.001

Detail -- to emphasize stochastic region about the unstable fixed point at x = .534416773867

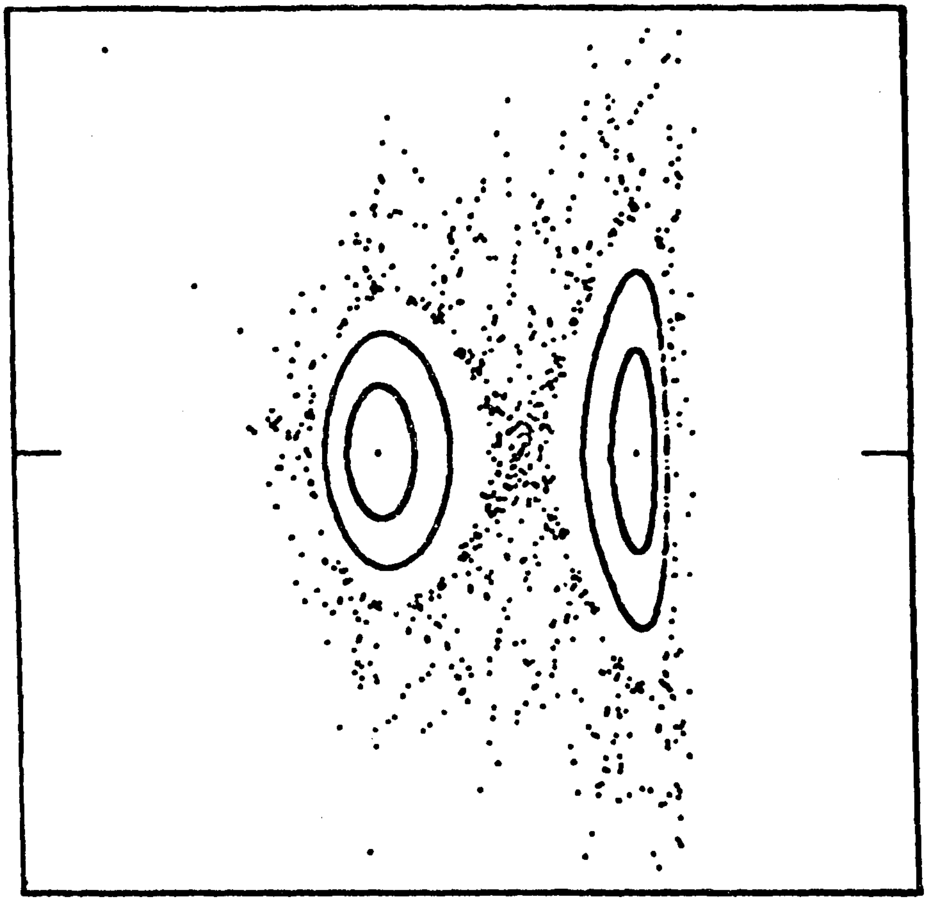

XBL 851-856

Fig. III.11. T = -0.1050 De-Vogelaere Variables
<u>Scales</u>: 0.45 to 0.60
±0.003

Note the violent instability at the fixed point (x = 0.535127642205).

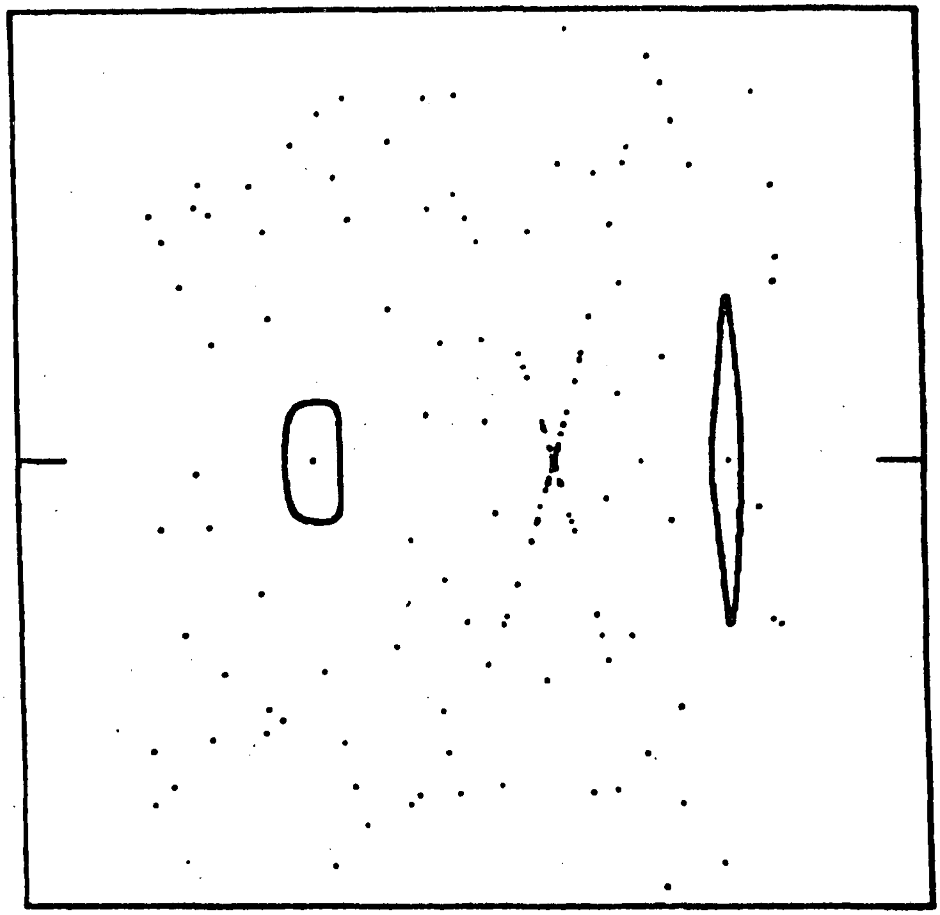

XBL 851-857

Fig. III.12. T = -0.1075 De-Vogelaere Variables
Scales: 0.45 to 0.60
±0.003

Some stochastic points, associated with the unstable fixed point, are shown (x = 0.538642977693 for this fixed point). Also shown are two of the stable 8-th order fixed points, together with a surrounding phase trajectory.

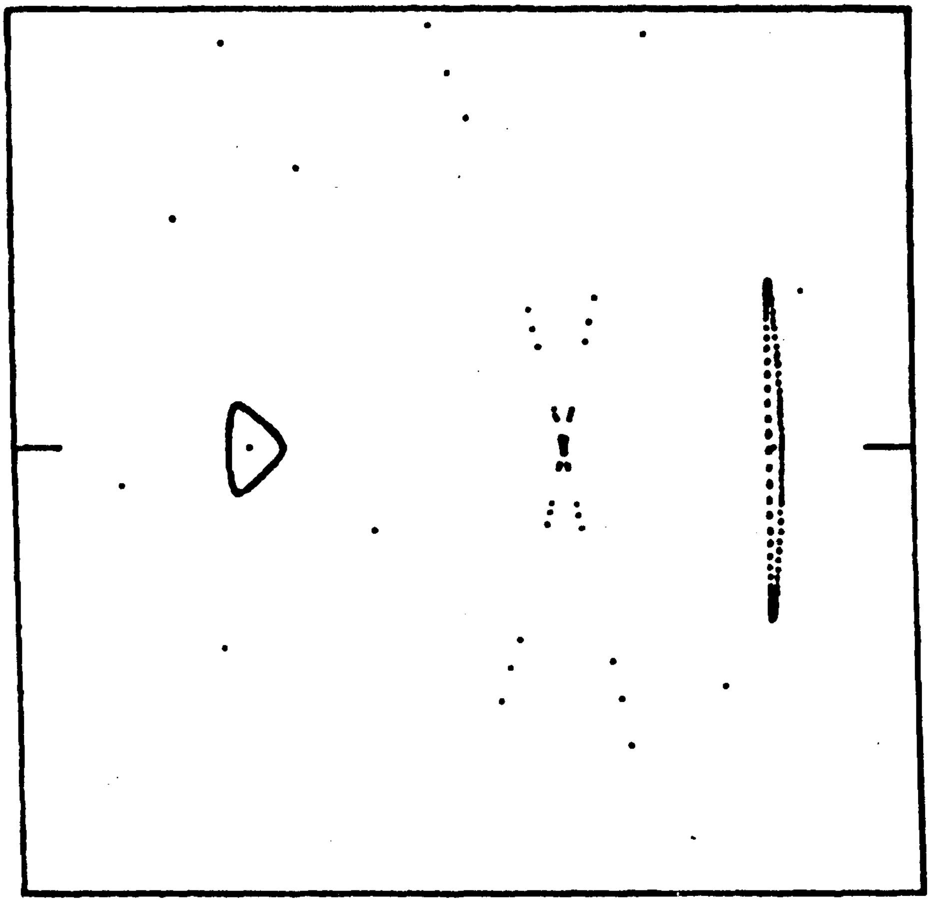

XBL 851-858

Fig. III.13. T = -0.1100 De-Vogelaere Variables
<u>Scales</u>: 0.45 to 0.60
±0.003

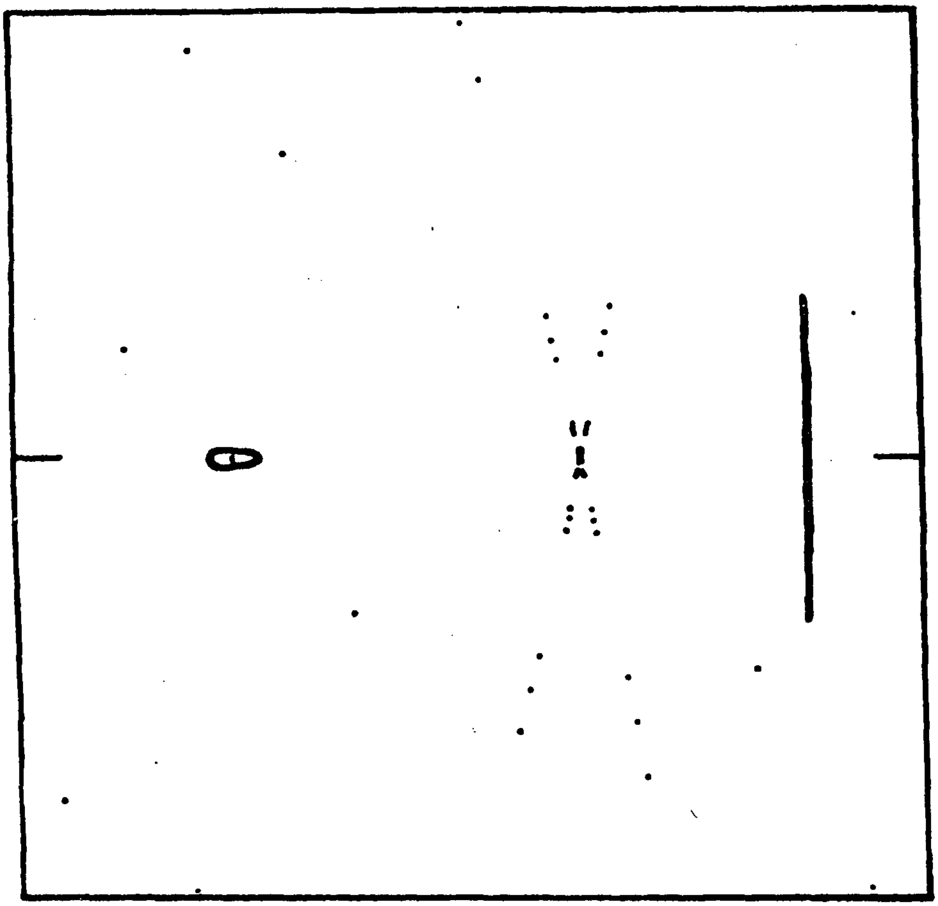

XBL 851-859

Fig. III.14. T = -0.11125 De-Vogelaere Variables
Scales: 0.45 to 0.60
±0.003
Neighborhood of 4th order (unstable) and 8-th order (stable) fixed points just prior to additional bifurcation.

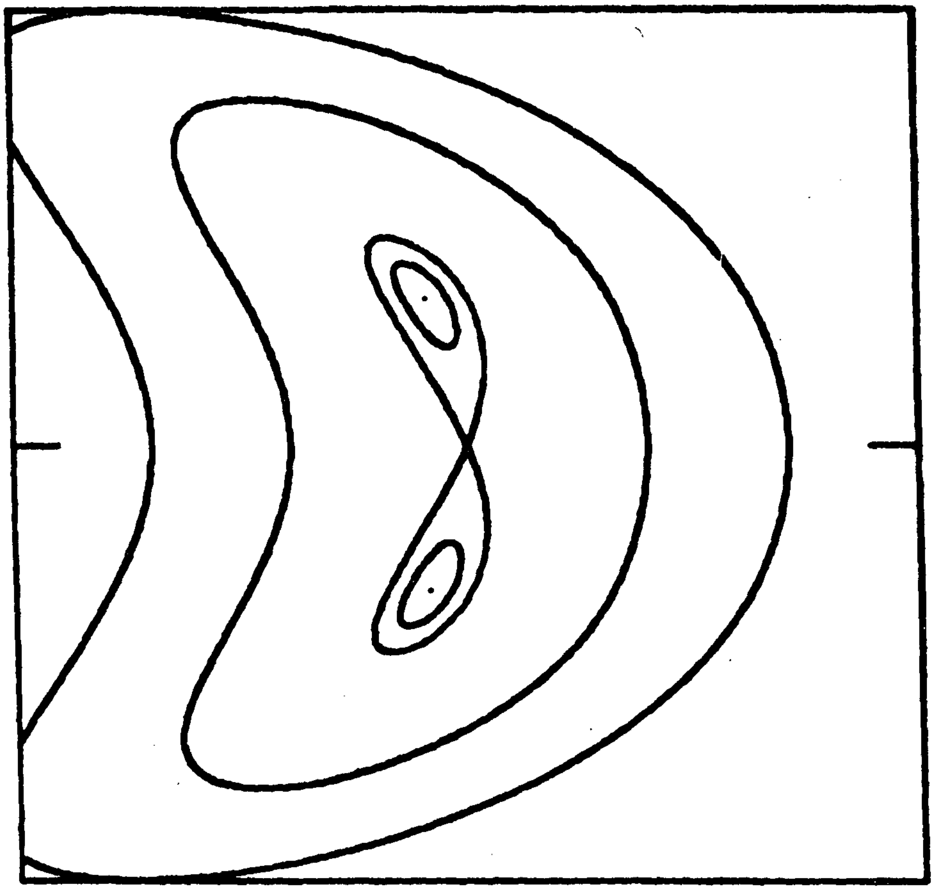

XBL 851-860

Fig. III.15. T = -0.11126 De-Vogelaere Variables
Scales: 0.581340 to 0.581355
±0.0002
After the second bifurcation (leading to Order-16 fixed points), one of the (now unstable) Order-8 fixed points develops vertical loops, that contain stable Order-16 fixed points.

The fixed points shown are
2/8: 0.581347619364, 0.
4/16: 0.581346959845, ±0.000068014914

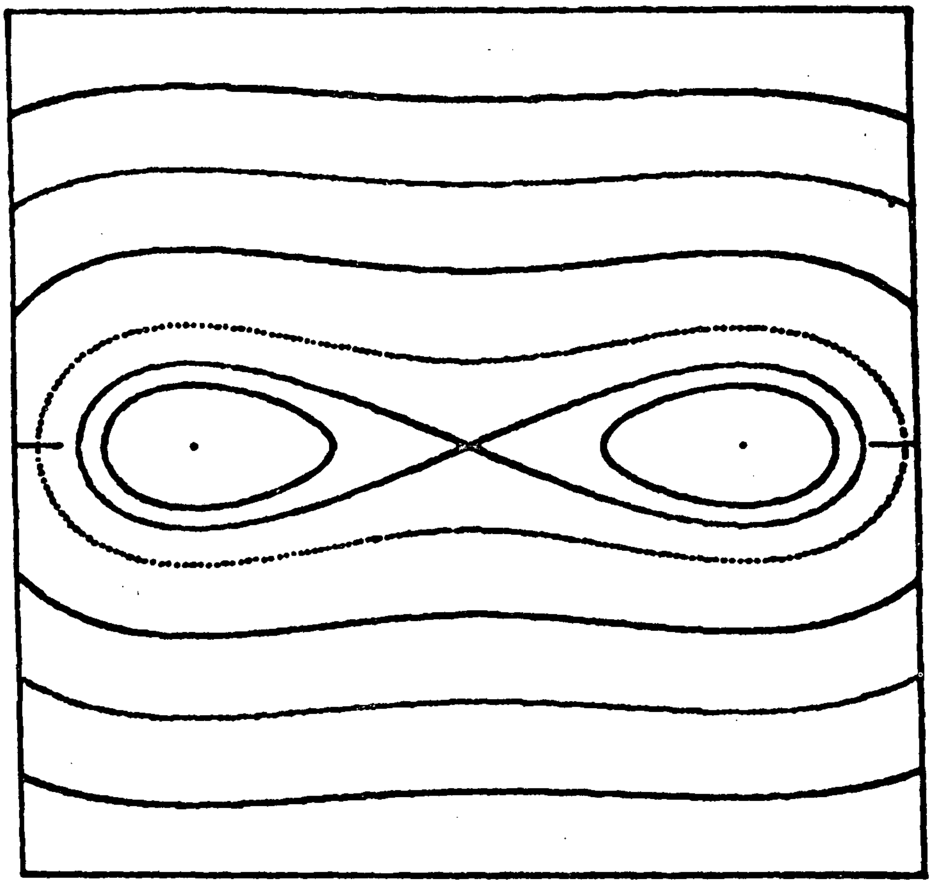

XBL 851-861

Fig. III.16 T = -0.11126 De-Vogelaere Variables
Scales: 0.4852 to 0.4860
± 0.000001
After the second bifurcation (leading to Order-16 fixed points), one of the (now unstable) Order-8 fixed points develops horizontal loops, that contain stable Order-16 fixed points.

The fixed points shown are
2/8: 0.485601872680, 0.
4/16: 0.485356977954, 0.
0.485849305665, 0.

Following this second bifurcation, a further reduction of T leads to a third period-doubling bifurcation, generating a fixed-point system of order - 32/8, that is illustrated for T = -0.11223 by Figs. III.17 and III.18.

As new stable fixed-point systems become created and then are driven toward instability (with reflection) by continued change of the parameter T, a regular convergent sequence of successive period doublings appears to become established -- as is suggested schematically by the sketch of Fig. III.19. Some sequential regularity in the locations or separations of the fixed points also may develop, as is indicated for the present example by the bifurcation tree shown in Fig. III.20 to depict the locations of such fixed points as are situated on the positive x-axis. Under circumstances such that a sequence of this nature has been carried to completion, one may expect the phase-plane motion in such a region to appear particularly "chaotic".

B. A Differential Equation with Quadratic Nonlinearity

The differential equation

$$\frac{d^2x}{dZ^2} = -A\,(x + 1/8\,x^2)\ \cos Z, \qquad (2)$$

that has been used to show the effect of a quadratic nonlinearity, can be used to provide solutions that illustrate the occurrence of bifurcations. Such examples include, for the parameter A in the range $0.265 < A < 0.275$, fixed-point systems that develop from fixed points of order 6/1 (tune: $\sigma = 1 \times 360/6 = 60$ deg.) and of order 11/2 (tune: $2 \times 360/11 = 65.45...$deg.).

It must be stated, with respect to each of the systems mentioned, that the bifurcation process occurs somewhat outside of the normal region of stability in the x, x' phase plane. Thus, with A = 0.2651, for which the small-amplitude tune is $\sigma_0 \cong 71.9167$, the range of stable motion may be judged to be given by $-1.93 < x < 1.67$ (measured for x' = 0, at Z = 0 mod. 2π) and the tune has dropped to $\sigma \cong 64$ deg. at such amplitudes. With this value of A, two members of the stable order - 6/1 fixed-point system that is close to becoming unstable and generating a period-doubling bifurcation, are found to lie on the x-axis at x= -2.6916782 and at x = 2.0097530. Similarly, with A = 0.2735 ($\sigma_0 \cong 74.5570$) the range of stability may be estimated as lying within the limits $-1.72 < x < 1.64$ and the tune has dropped to $\sigma \cong 68.1$ deg. at such amplitudes. With this value of A one member of the stable order - 11/2 fixed-point system that is close to giving rise to a period-doubling bifurcation is found to lie on the positive x-axis at x = 1.80151231.

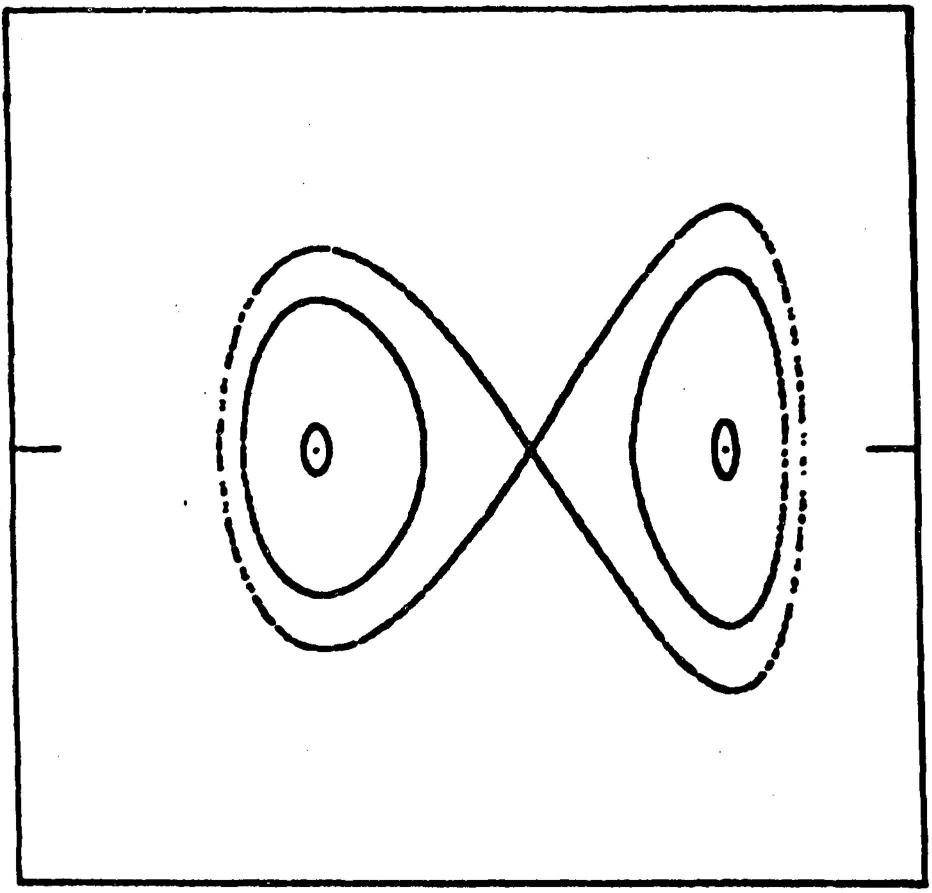

XBL 851-862

Fig. III.17. T = -0.11223 De-Vogelaere Variables
Scales: 0.4965 to 0.4990
±0.000002
After the third bifurcation (leading to Order-32 fixed points), one of the (now unstable) Order-16 fixed points develops horizontal loops, that contain stable Order-32 fixed points.

The fixed points shown are
4/16: 0.497936225267, 0.
8/32: 0.497335279454, 0.
0.498484243334, 0.

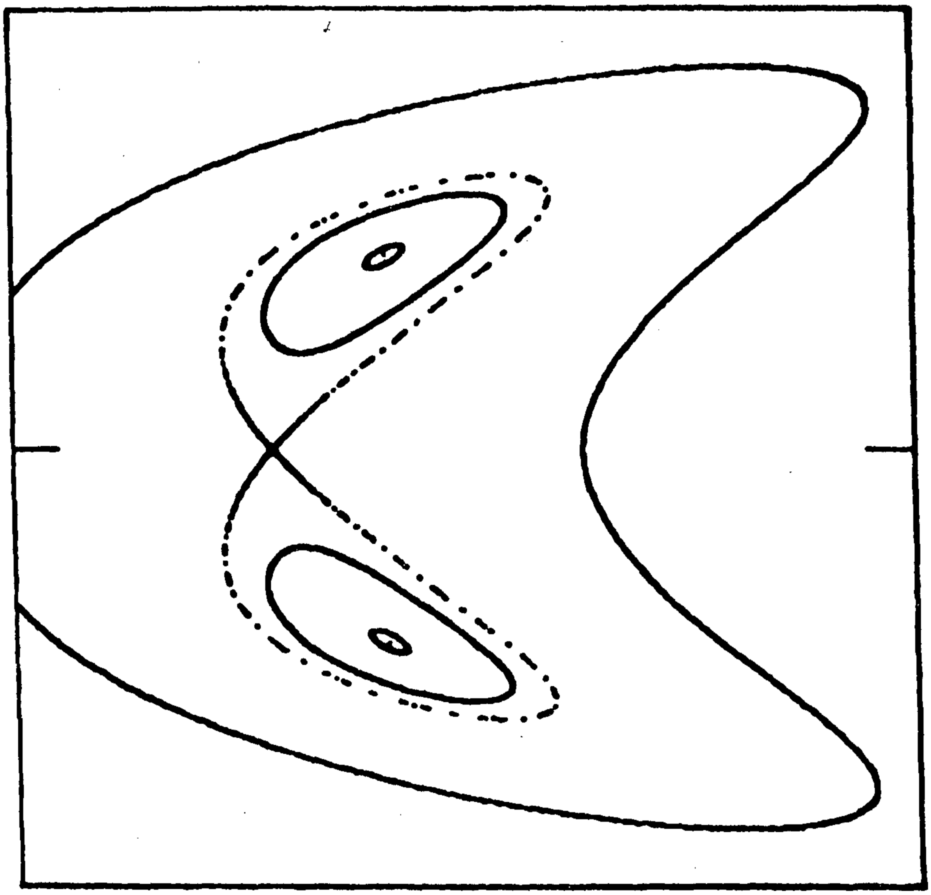

XBL 851-863

Fig. III.18. T = -0.11223 De-Vogelaere Variables
Scales: 0.4737 to 0.4738
±0.0001
After the third bifurcation (leading to Order-32 fixed points), one of the (now unstable) Order-16 fixed points develops vertical loops, that contain stable Order-32 fixed points.

The fixed points shown are
4/16: 0.473728930908, 0.
8/32: 0.473741772757, ±0.000044371638

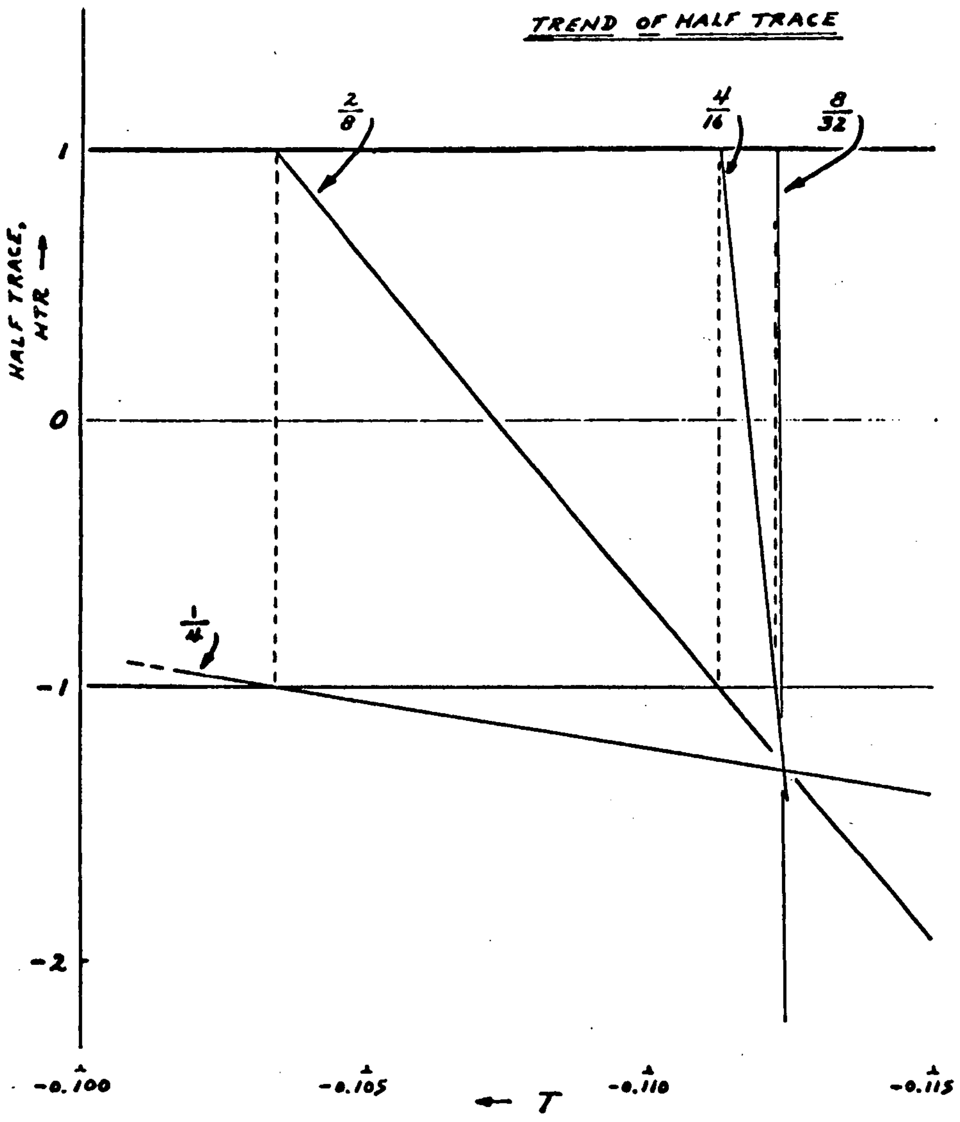

XBL 851-867

Fig. III.19.

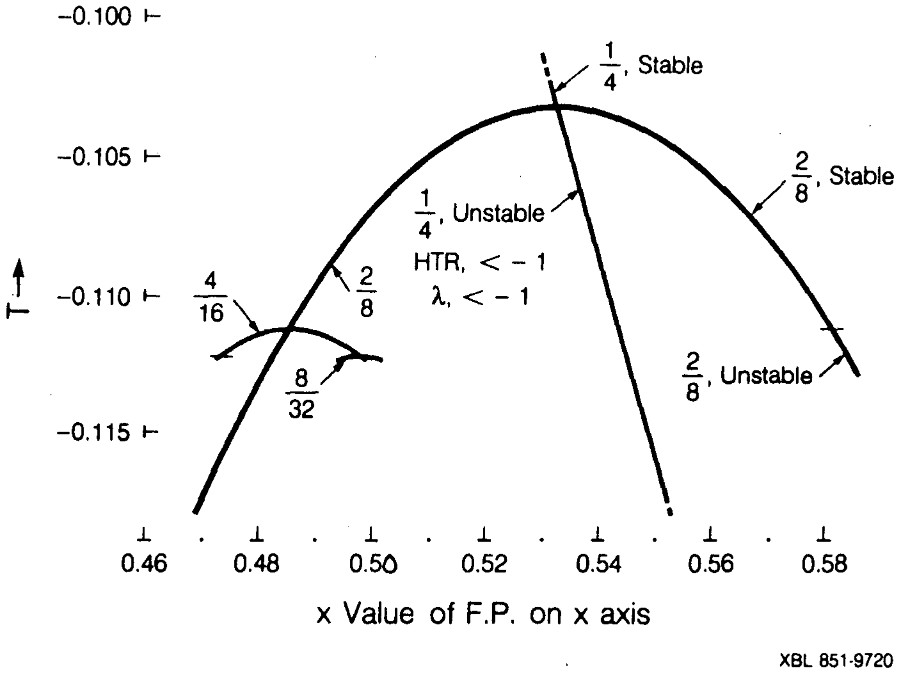
-0.100
-0.105
-0.110
-0.115
T
1/4, Stable
2/8, Stable
1/4, Unstable
HTR, < - 1
λ, < - 1
4/16
2/8
8/32
2/8, Unstable
0.46
0.48
0.50
0.52
0.54
0.56
0.58
x Value of F.P. on x axis
XBL 851-9720

Fig. III.20

Characteristics of fixed-point systems of order-6/1 are listed in Table I for $0.2650 \leq A \leq 0.2670$, together with the values of small-amplitude tune (σ_0) associated with these values of A. The values given for HTR refer to the half trace of the tangential-mapping transformation (for 6 periods, $\Delta Z = 6(2\pi)$). For the unstable systems with HTR > +1, phase-plane coordinates are given as x_0, $\pm x_0'$ for such order-6/1 fixed-points lying close to the negative x-axis. For the systems with HTR < +1, x coordinates are given for the members of such systems that lie on the negative x-axis and for the members that lie on the positive x-axis. It is this latter type of fixed-point system for which, when HTR becomes less than -1, the order-6/1 system becomes unstable with reflection and an additional (originally stable) system of order 12/2 becomes created. x-values for fixed points of such a fixed-point system, and that lie on the negative x-axis, are tabulated in Table II (together with the half trace of the 12-period tangential-mapping transformation). Such an order 12/2 system will in turn become unstable, with reflection, for A sufficiently great -- leading to a fixed point system of order 24/4. Fixed points situated on the negative x-axis are given in Table III for a few values of the parameter A, and it is seen that one may expect a further period-doubling bifurcation to develop from this order - 24/4 system for values of A slightly greater than 0.266847.

TABLE I

Order-6/1 Systems

A	Small-Amp'l. Tune, σ_0 (Deg.)	HTR > +1			HTR < +1		
		x_0	$\pm x_0'$	HTR	x_{left}	x_{right}	HTR
0.2650	71.8856	-2.343555	0.072379	2.409455	-2.688509	2.008182	-0.980123
0.2651	71.9167	-2.346288	0.072410	2.421250	-2.691678	2.009753	-0.998529
0.2652	71.9479	-2.349017	0.072441	2.433116	-2.694840	2.011317	-1.017065
0.2653	71.9791	-2.351741	0.072472	2.445054	-2.697996	2.012874	-1.035730
0.2654	72.0103	-2.354459	0.072502	2.457065	-2.701145	2.014424	-1.054527
0.2655	72.0415	-2.357173	0.072533	2.469148	-2.704288	2.015968	-1.073454
0.2657	72.1039	-2.362587	0.072593	2.493531	-2.710553	2.019035	-1.111705
0.2660	72.1975	-2.370672	0.072682	2.530658	-2.719902	2.023585	-1.170082
0.2665	72.3538	-2.384051	0.072827	2.594021	-2.735355	2.031037	-1.270082
0.2666	72.3850	-2.386713	0.072856	2.606920	-2.738426	2.032508	-1.290493
0.2667	72.4163	-2.389371	0.072884	2.619894	-2.741491	2.033972	-1.311043
0.2670	72.5101	-2.397315	0.072969	2.659276	-2.750648	2.038326	-1.373531

TABLE II

Order - 12/2 System, incl. FP$^{'s}$ on negative x-axis

A	x_1	x_2	HTR
0.2652	-2.738676	-2.646999	0.864839
0.2653	-2.759982	-2.627668	0.720072
0.2654	-2.776328	-2.613297	0.577487
0.2655	-2.790168	-2.601434	0.437093
0.2657	-2.813553	-2.582010	0.162918
0.2660	-2.842510	-2.559010	-0.231660
0.2665	-2.882070	-2.529416	-0.844114
0.2666	-2.889138	-2.524347	-0.959735
0.26662	-2.890526	-2.523360	-0.982582
0.26663	-2.891216	-2.522870	-0.993971
0.26664	-2.891904	-2.522381	-1.005336
0.26665	-2.892591	-2.521895	-1.016678
0.2667	-2.895992	-2.519495	-1.073042
0.2670	-2.915447	-2.506055	-1.398966

Table III

Order 24/4 System, incl. FP's on negative x-axis

A	X_1	x_2	HTR
0.26664	-2.529700	-2.515630	0.95723
0.26665	-2.535224	-2.510339	0.86600
0.26670	-2.549481	-2.497244	0.40488
0.26675	-2.558737	-2.489151	-0.06446
0.26680	-2.566240	-2.482813	-0.54199
0.26684	-2.571515	-2.478471	-0.92988
0.266843	-2.571891	-2.478165	-0.95918
0.266844	-2.572015	-2.478064	-0.96896
0.266846	-2.572264	-2.477862	-0.98851
0.266847	-2.572388	-2.477761	-0.99830
0.266848	-2.572512	-2.477661	-1.0081
0.26685	-2.572759	-2.477461	-1.028

Figure III.21, sketched for $A = 0.2667$, indicates the locations of such associated fixed points as lie in the neighborhood of the order - 6/1 fixed point situated on the negative x-axis at $x = -2.741491$. This plot is to the scales:

Horizontal: -3.0 to -2.4, for x;

Vertical: -0.002 to 0.002, for x'.

The fixed points shown on the negative x-axis are explicitly:

For order - 6/1 system: $x \doteq -2.741491$

For order - 12/2 system: $x \doteq -2.895992$ & $x \doteq -2.519495$

For order - 24/4 system: $x \doteq -2.549481$ & $x \doteq -2.497244$.

The development of the order - 12/2 system is illustrated by Figs. III.22 - III.24, each plotted to the scales:

Horizontal: -3.0 to -2.5, for x;

Vertical: -0.005 to 0.005, for x'.

Fig. III.22, for $A = 0.2651$, shows the order - 6/1 fixed point (stable for this value of A) at $x_0 = -2.691678...$, $x_0' = 0$, together with two surrounding phase trajectories.

Fig. III.23, for $A = 0.2652$, shows the order - 6/1 fixed point (now unstable, for this value of A) and two of the order - 12/2 fixed points that result from the period-doubling bifurcation. Also evident is the presence of nine small order - 54/9 islands surrounding the fixed points in this region of the phase plane.

Fig. III.24, for $A = 0.2653$, presents a diagram similar to that shown (for $A = 0.2652$) in Fig. III.23, wherein the unstable order - 6/1 fixed point and two order - 12/2 stable fixed points are again seen and for which some stochasticity appears evident in the neighborhood of the unstable fixed points of the order - 54/9 system.

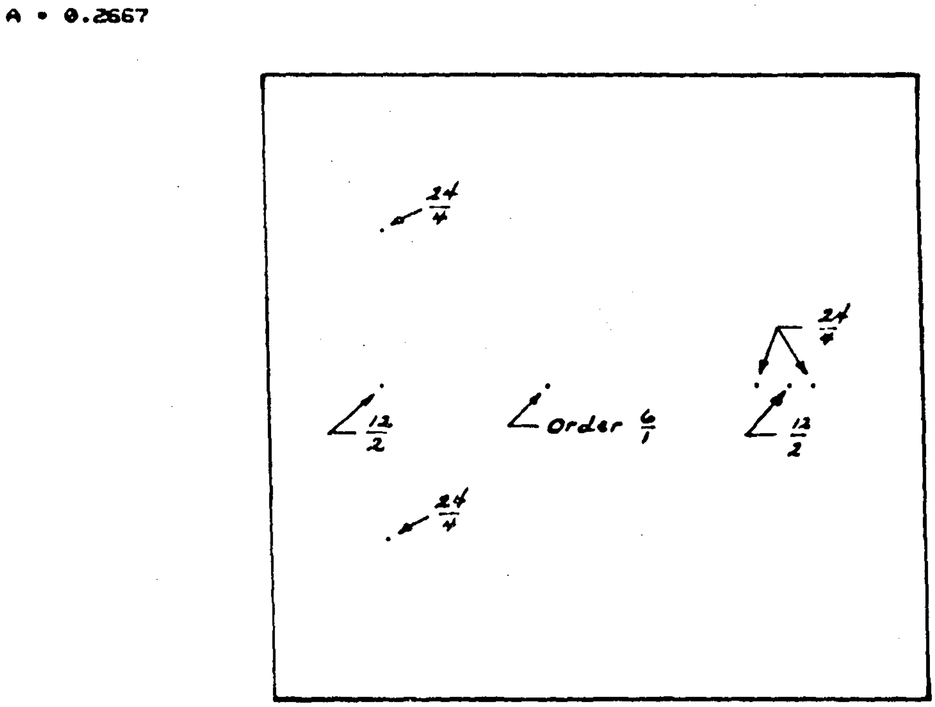

XBL 851-866

Fig. III.21 A = 0.2667

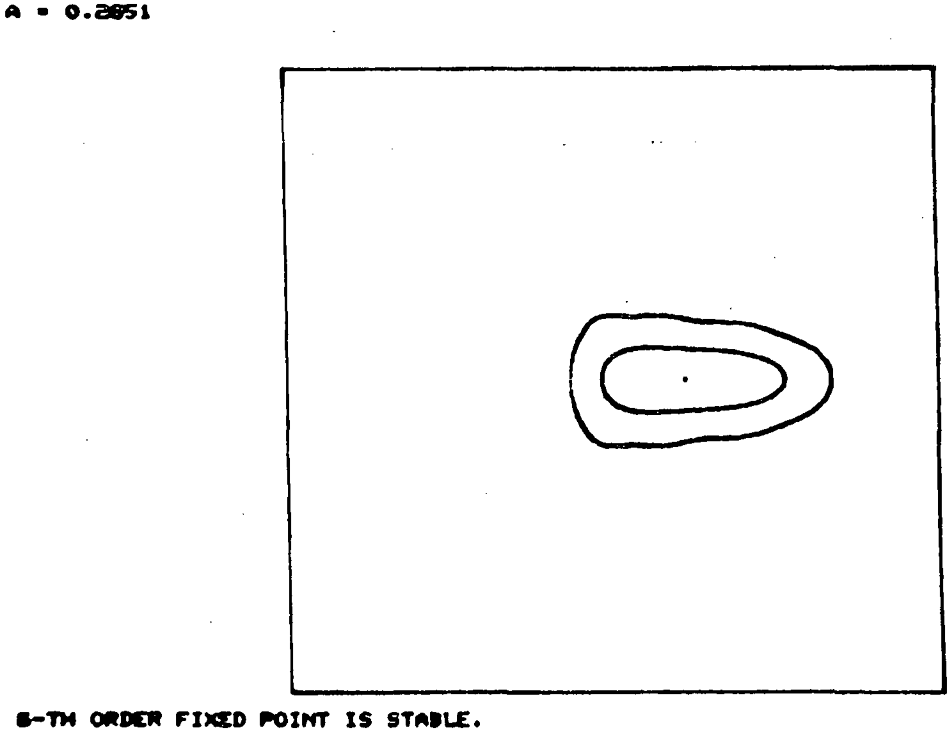

XBL 851-865

Fig. III.22 A = 0.2651
6th order fixed point is stable.

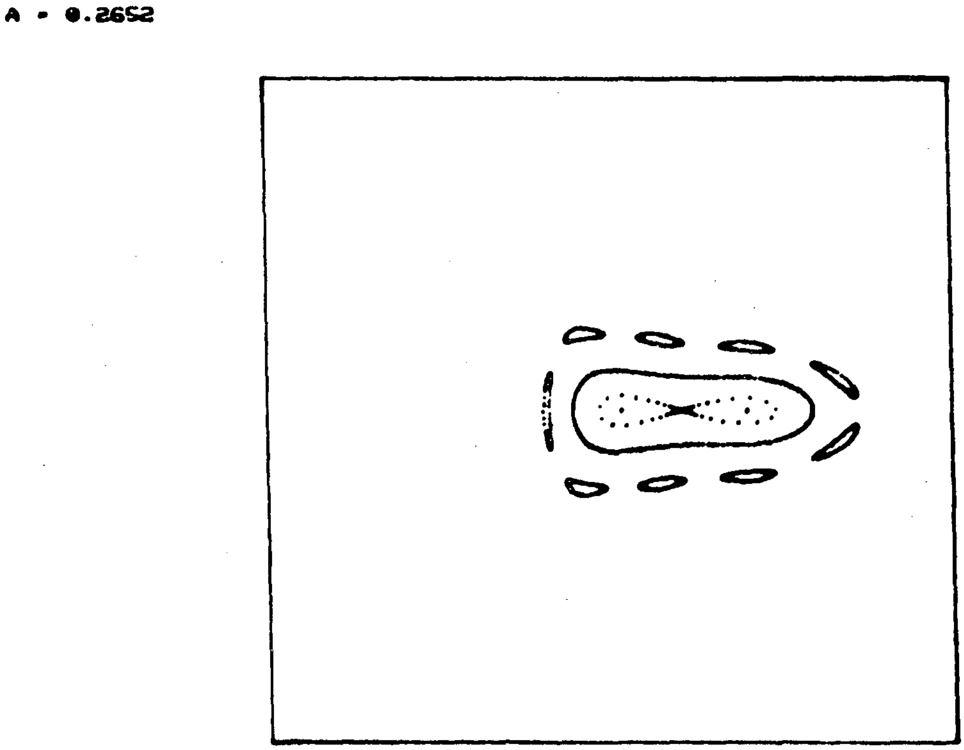

XBL 851-864

Fig. III.23 A = 0.2652

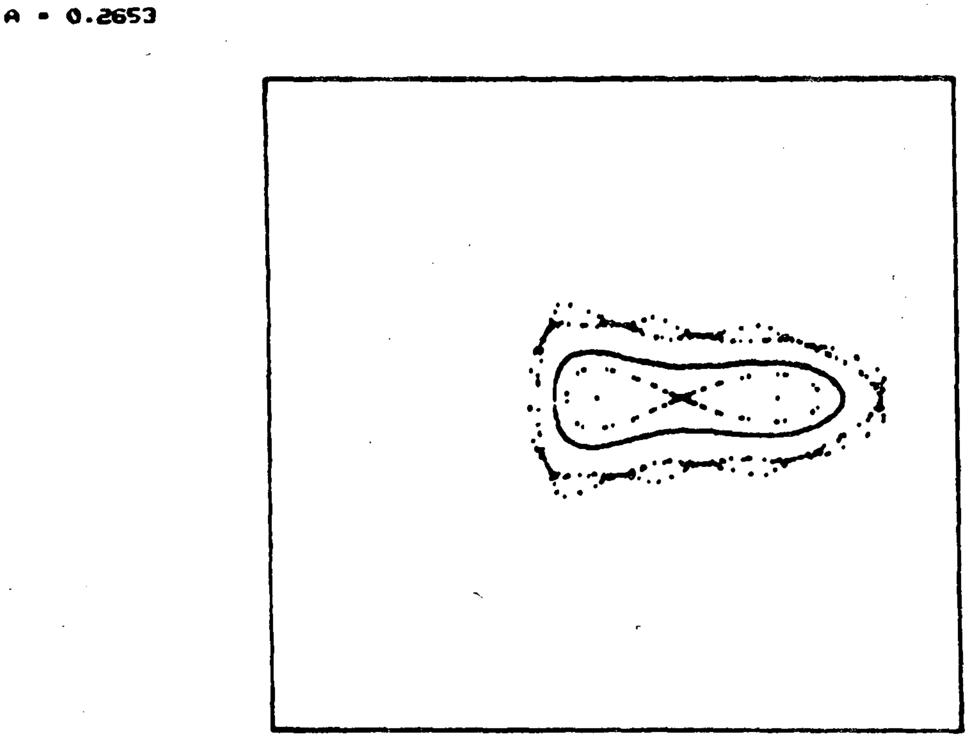

XBL 851-886

Fig. III.24 A = 0.2653

Somewhat more detail may be seen on Figs. III.25 and III.26, with the scales:

Horizontal: -2.9 to -2.5, for x;

Vertical: -0.003 to 0.003, for x'.

Fig. III.25, for A = 0.26520, is similar to Fig. III.23 (to a somewhat enlarged scale), but also suggests the presence of members of an order - 96/16 fixed-point system at the outer edge of the plot.

Fig. III.26 for A = 0.26525, illustrates in somewhat greater detail features such as were evident (for A = 0.26520) on Fig. III.25. The strong scatter of points seen on the present figure results from a run launched substantially at one of the fixed points of the unstable order - 96/16 fixed-point system.

The bifurcation leading to an order - 24/4 system is illustrated by Figs. III.27 and III.28, to the scales:

Horizontal: -2.60 to -2.45, for x;

Vertical: -0.0002 to 0.0002, for x'.

Fig. III.27 for A = 0.26663, shows an order - 12/2 fixed point (stable for this value of A) situated on the negative x' axis (at x ≅ -2.522870) and two surrounding phase trajectories.

Fig. III.28, for A = 0.26665, shows the order - 12/2 fixed point (now unstable, and situated at x_o ≅ -2.521895) and the associated development through bifurcation of an order - 24/4 system of which two fixed points are shown.

Figure III.29 shows the trend, vs. A, of the tangential-mapping half trace for the fixed-point systems just discussed. On sees, as the half trace of one system passes to values more negative than -1, the genesis of a new system of double period.

Figure III.30 indicates the development of a bifurcation tree that depicts, for fixed points situated on the negative x-axis, the locations (and hence the spacings) of the fixed points for the systems just discussed.

One also finds a fixed-point system of order 11/2 (σ = 2x360/11 = 65.4545...) from which, as the parameter A is increased, period-doubling bifurcations develop -- see Tables IV and V. The transition leading to the birth of an order - 22/4 system is illustrated by Figs. III.31 and III.32, to the scales:

Horizontal: 1.795 to 1.805, for x;

Vertical: -0.01 to 0.01, for x'.

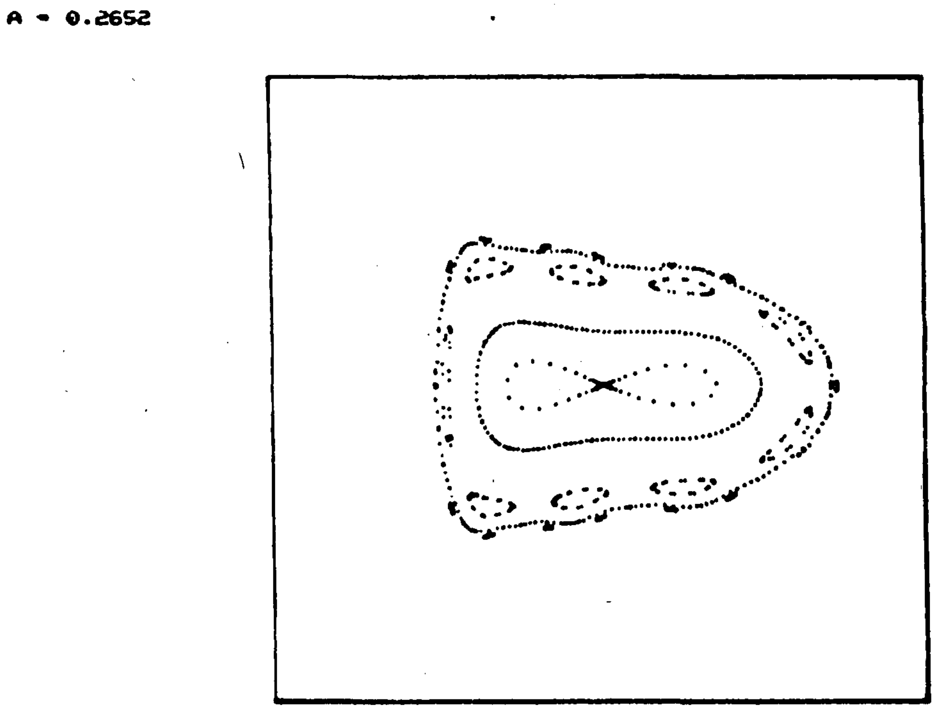

XBL 851-885

Fig. III.25 A = 0.2652

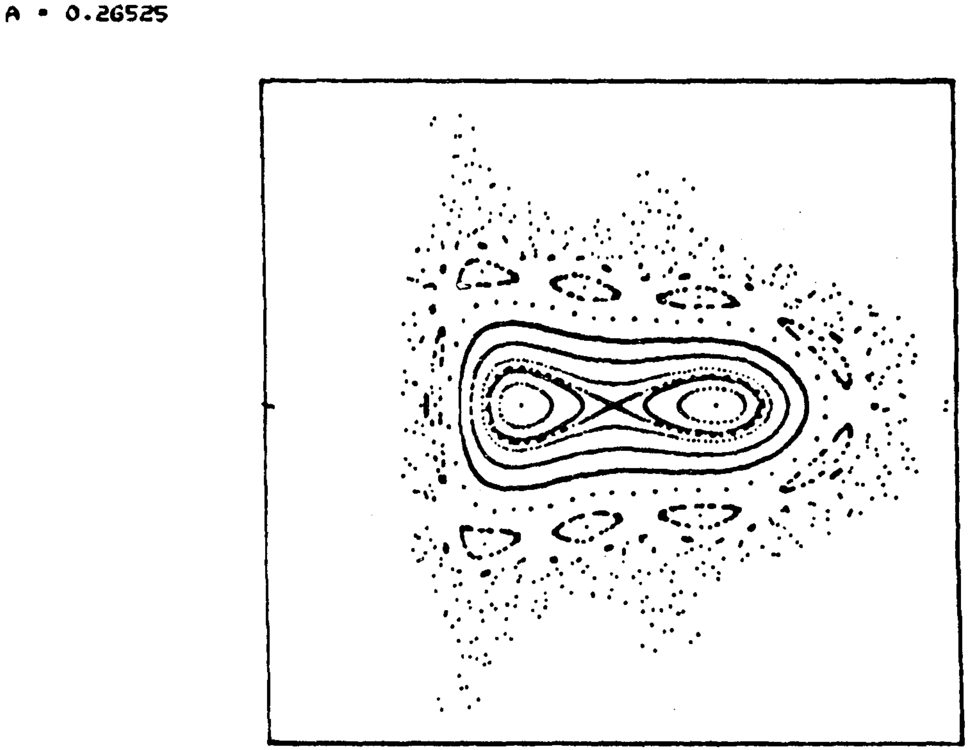

XBL 851-884

Fig. III.26 A = 0.26525

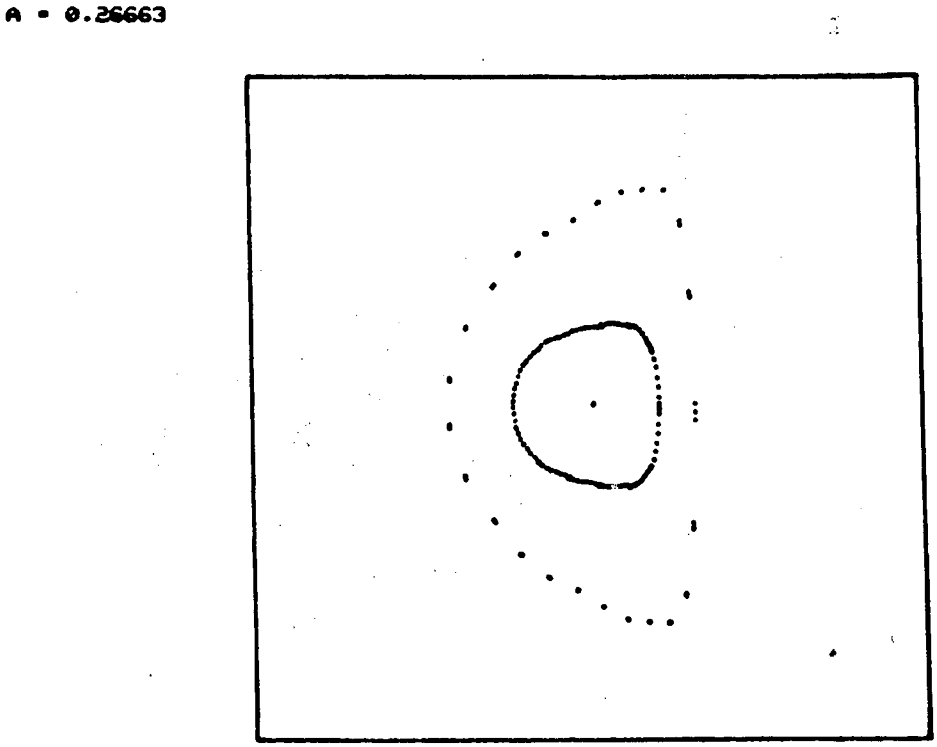

XBL 851-883

Fig. III.27 A = 0.26663

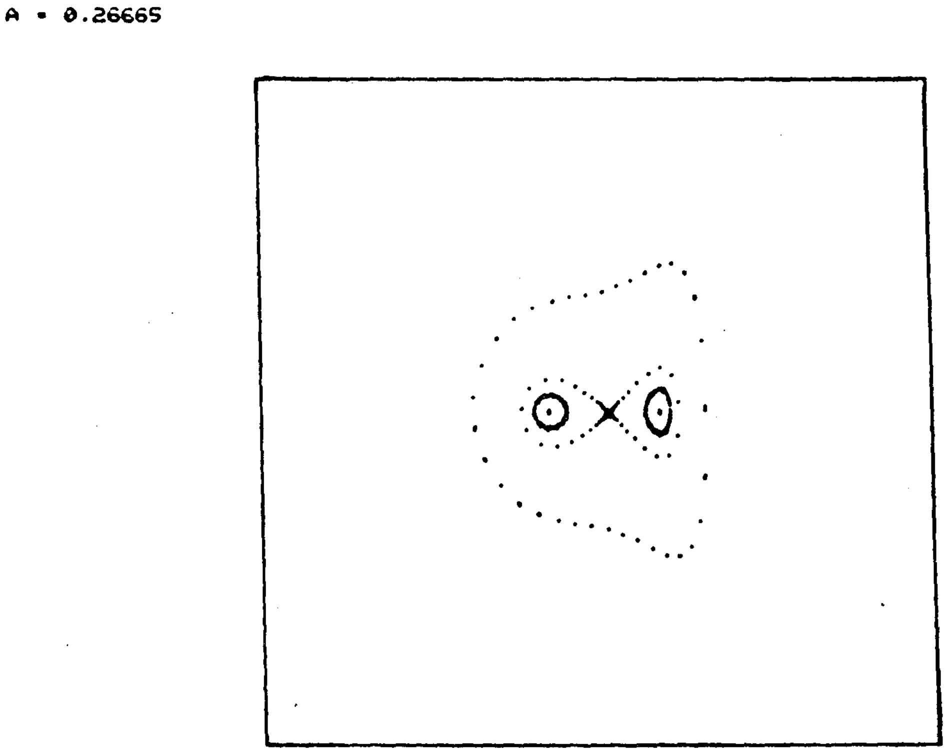

XBL 851-882

Fig. III.28 A = 0.26665

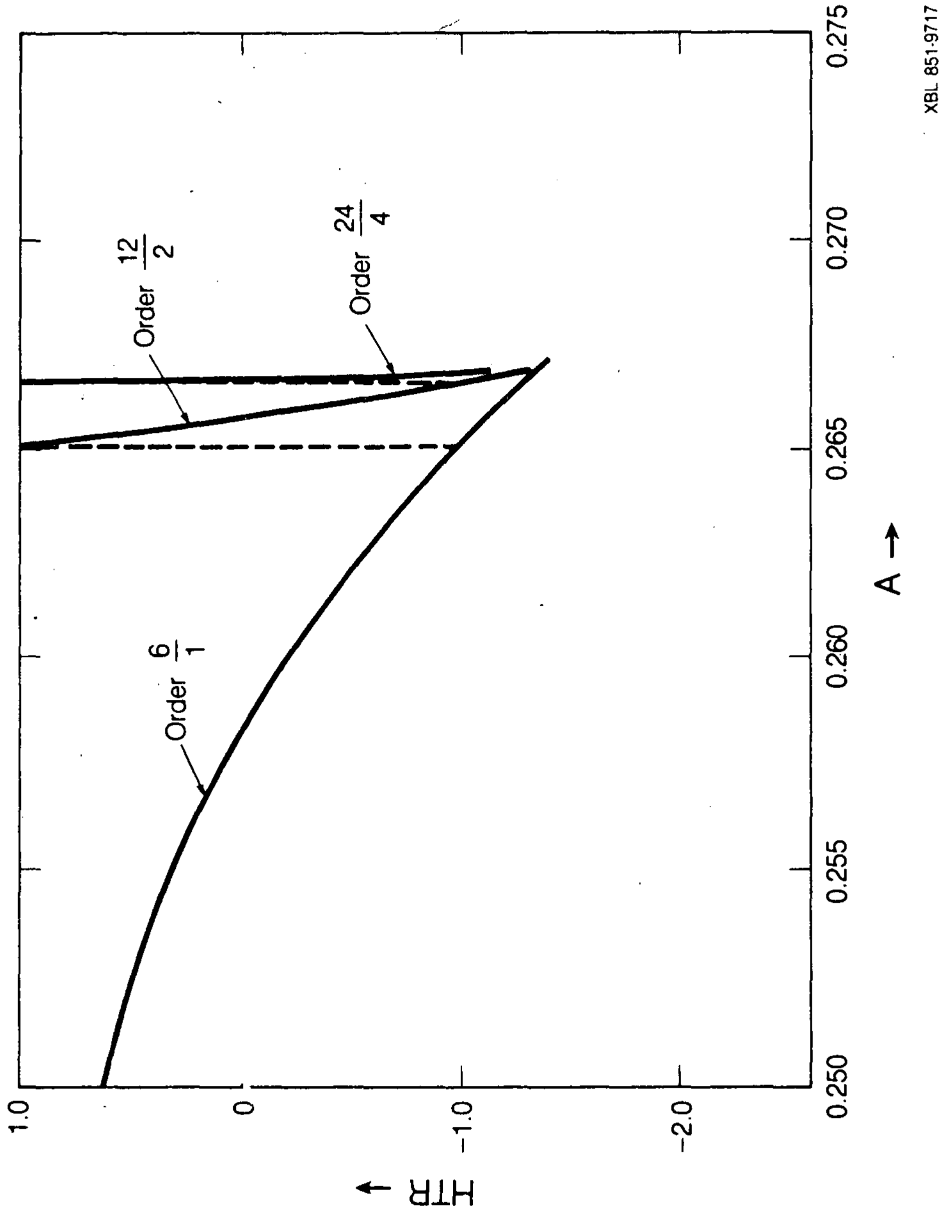
HTR →
1.0
0
−1.0
−2.0
A →
0.250
0.255
0.260
0.265
0.270
0.275
Order $\frac{6}{1}$
Order $\frac{12}{2}$
Order $\frac{24}{4}$
XBL 851-9717

Fig. III.29

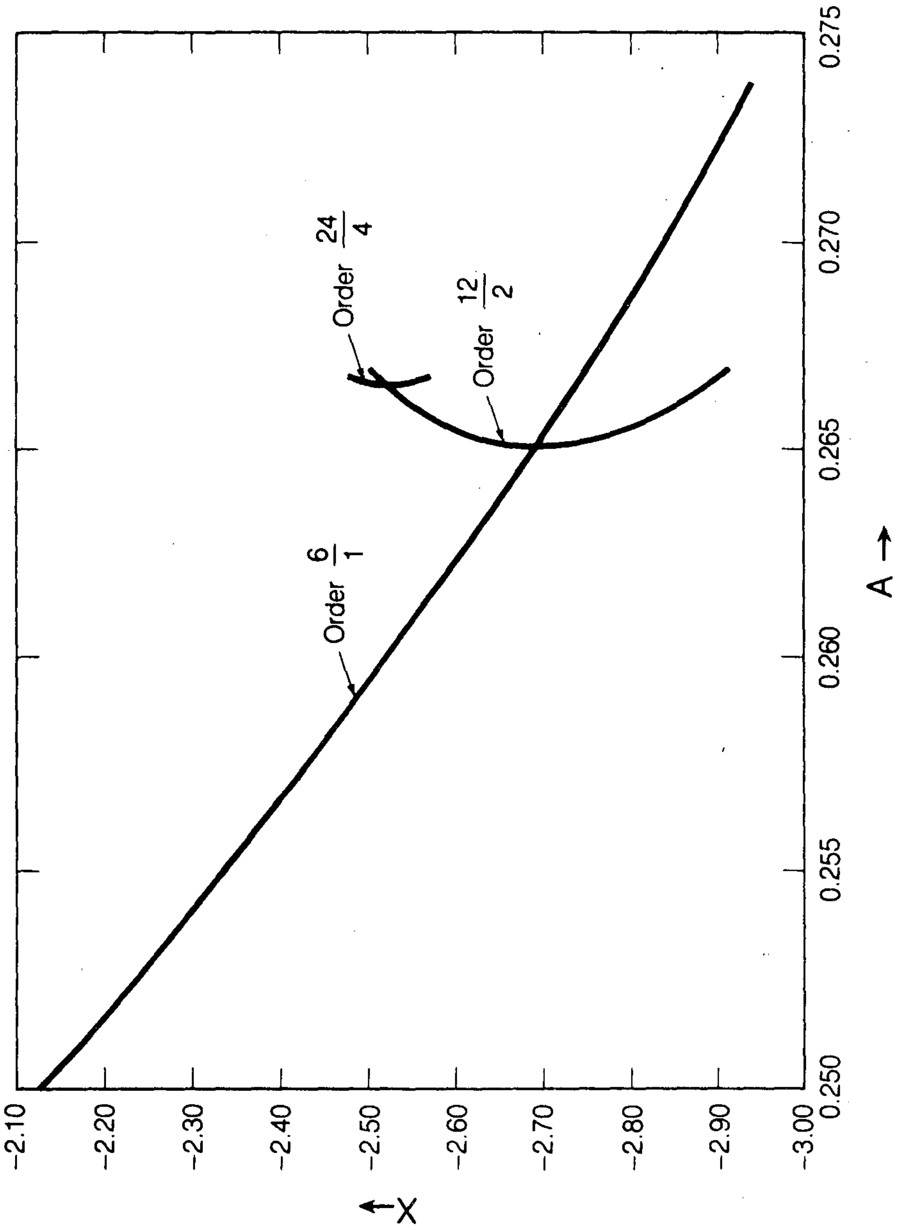

XBL 851-9719

Fig. III.30

Table IV

Coordinates on x-axis of Order -- 11/2 Fixed-Point Systems

A	Small-Amp'l Tune, σ_0 (Deg.)	HTR > +1		HTR < +1	
		x	HTR	x	HTR
0.2500	67.27394	-0.999353	1.000189	0.903246	0.999810
0.2550	68.79742	-1.347417	1.005812	1.193517	0.994174
0.2600	70.33441	-1.600037	1.050365	1.409902	0.949182
0.2650	71.88555	-1.786583	1.247550	1.581892	0.746606
0.2667	72.41629	-1.837753	1.391772	1.632457	0.595998
0.2668	72.44756	-1.840593	1.402071	1.635320	0.585177
0.2670	72.51013	-1.846219	1.423348	1.641007	0.562794
0.2675	72.66665	-1.859973	1.480681	1.655016	0.502310
0.2680	72.82332	-1.873297	1.544336	1.668729	0.434871
0.2700	73.45155	-1.922605	1.873355	1.720731	0.081897
0.2725	74.24035	-1.976496	2.500251	1.779691	-0.608400
0.2734	74.52529	-1.994150	2.800794	1.799374	-0.946613
0.2735	74.55698	-1.996062	2.837019	1.801512	-0.987672
0.27355	74.57283	-1.997014	2.855352	1.802578	-1.008476
0.2736	74.58868	-1.997964	2.873835	1.803641	-1.029466
0.2737	74.62039	-1.999857	2.911251	1.805761	-1.072004
0.2738	74.65210	-2.001741	2.949273	1.807871	-1.115298
0.2739	74.68382	-2.003615	2.987909	1.809971	-1.159359
0.2740	74.71554	-2.005481	3.027166	1.812062	-1.204199
0.27425	74.79488	-2.010106	3.128075	1.817249	-1.319776
0.2745	74.87426	-2.014678	3.233031	1.822377	-1.440468
0.2750	75.03314	-2.023668	3.455560	1.832462	-1.697941

TABLE V

Some Coordinates of Order - 22/4 Systems

A	Small Amp'l Tune, σ_0 (Deg.)	x	±x'	HTR
0.27355	74.57283	1.801872	0.003584	0.932590
0.2736	74.58868	1.801200	0.006667	0.769102
0.2737	74.62039	1.799858	0.010374	0.452546
0.2738	74.65210	1.798516	0.013068	0.150275
0.2739	74.68382	1.797176	0.015292	-0.137238
0.2740	74.71554	1.795837	0.017231	-0.409504
0.2742	74.77901	1.793162	0.020564	-0.906304
0.27424	74.79171	1.792627	0.021167	-0.997749
0.27425	74.79488	1.792494	0.021315	-1.020187
0.2745	74.87426	1.789158	0.024729	-1.524411

Fig. III.31, for A = 0.27350, shows a stable order - 11/2 fixed point situated on the positive x-axis and surrounded by a small closed phase trajectory.

Fig. III.32, for A = 0.27360, shows the evolution of eigenvector directions extended from the order - 11/2 fixed point (now unstable, with reflection) situated on the positive x-axis. Small loops are seen to be generated in this way, within which one sees two fixed points (and surrounding curves) of a stable order - 22/4 system that has come into existence for this value of A.

Fig. III.33, again for A = 0.27360, presents information related to that of Fig. III.32, but to the somewhat more extended scale:

Horizontal: 1.1 to 1.9, for x;

Vertical: -0.15 to 0.15, for x'.

One sees now <u>three</u> small loops of the type for which one was shown on Fig. III.32, save that now the width of the loops is scarcely noticeable on the present scale. Also shown are two order - 11/2 fixed points for which HTR > +1 (indicated by

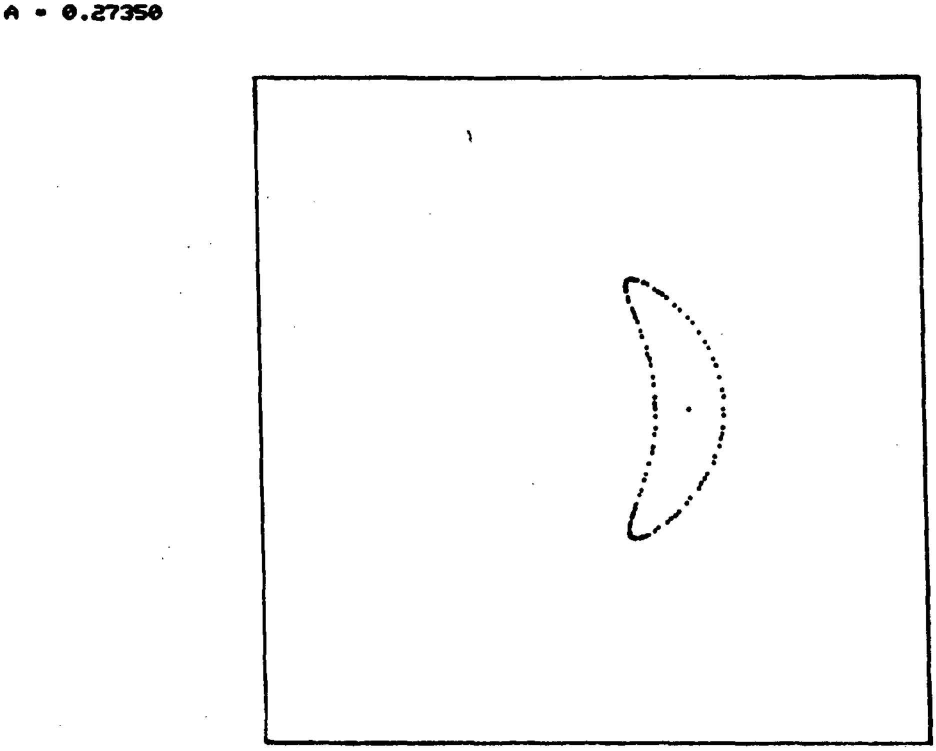

XBL 851-881

Fig. III.31 A = 0.27350

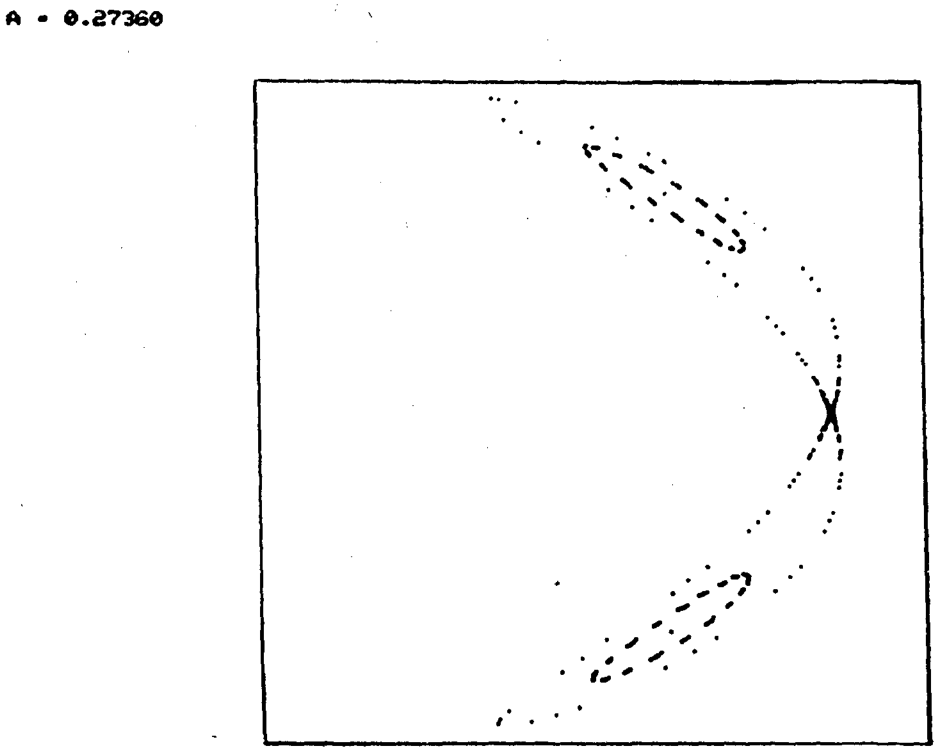

XBL 851-880

Fig. III.32 A = 0.27360

A = 0.27360

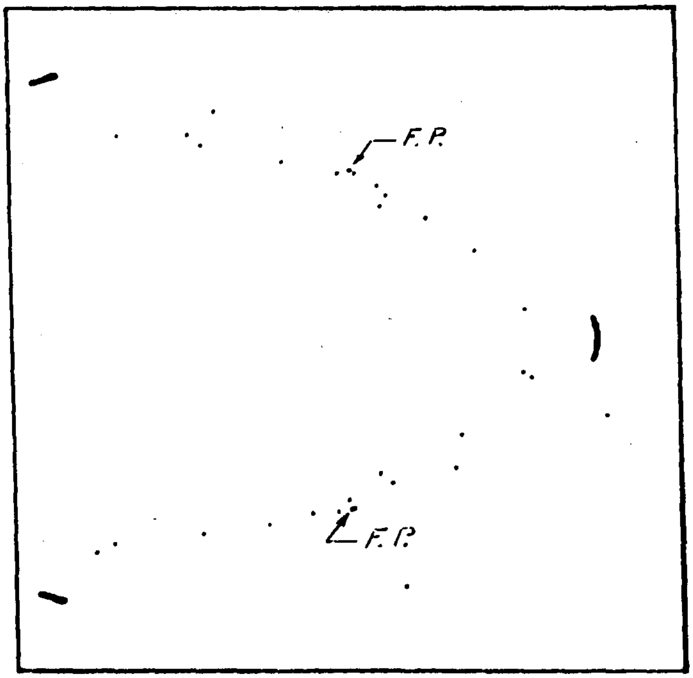

XBL 851-879

Fig. III.33 A = 0.27360

arrows) and an indication of the stochastic behavior that rapidly develops from a launch in such a region of the phase plane.

The fixed-point system of order 22/4 itself becomes unstable, with reflection, when the parameter A becomes as large as 0.27425 (as may be seen from Table V). The resulting additional bifurcation is illustrated on Fig. III.34 to the scales:

Horizontal: 1.785 to 1.800, for x;

Vertical: 0.015 to 0.025, for x'.

Fig. III.34, for A = 0.27425, shows a narrow loop that develops from an extension of the eigenvector directions associated with the unstable order - 22/4 fixed point (unstable with reflection) situated near the center of the diagram. Such loops encircle stable fixed points of an order - 44/8 system, of which two are seen on the diagram (as indicated by arrows at, approximately,

$$x = 1.789457,\ x' = 0.022340$$

and

$$x = 1.795888,\ x' = 0.020075$$

The trend, <u>vs</u>. A, of HTR (the tangential-mapping half trace) for the order - 11/2 and order - 22/4 systems mentioned above is illustrated by the graph of Fig. III.35.

Additional fixed-point systems that lead to period-doubling bifurcation of course also can be found. We cite here, without further illustration, an order - 23/4 system that becomes unstable with reflection for A as great as 0.2628:

A	Small Amp'l Tune, σ_0 (Deg.)	Coordinate on Positive x axis	HTR
0.2627	71.17022	1.673937	-0.970413
0.2628	71.20126	1.675894	-1.057670

For A = 0.2628 an order - 46/8 stable system is formed (with HTR = 0.56173), for which one fixed point is found to be situated at

$$x \simeq 1.674\,107,\ x' \simeq 0.006399$$

A = 0.27425

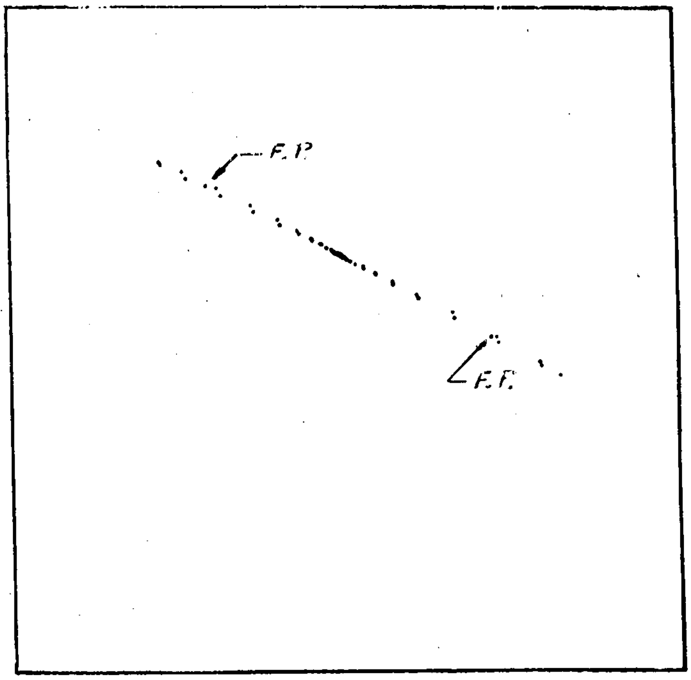

XBL 851-878

Fig. III.34 A = 0.27425

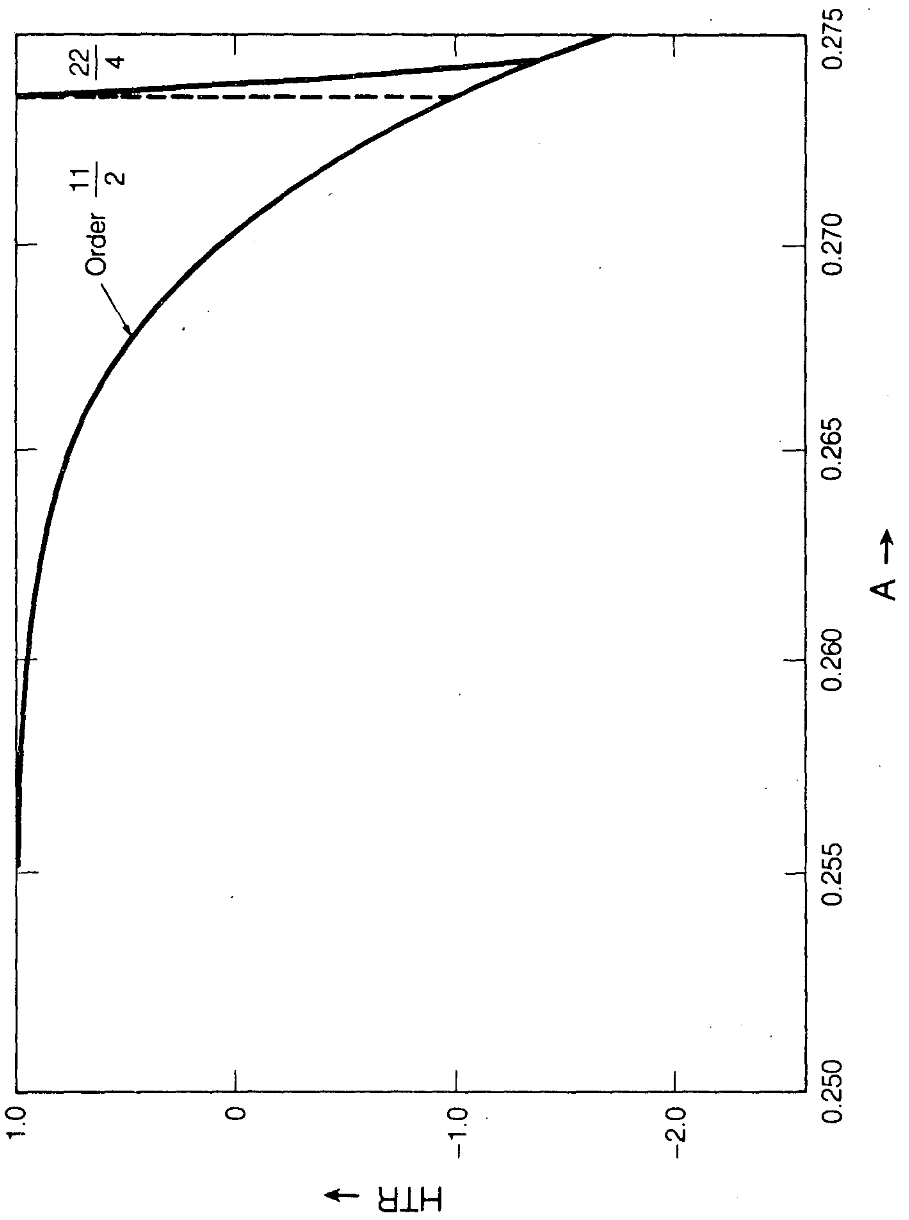

XBL 851-9718

Fig. III.35

C. A Differential Equation with Cubic and Quintic Nonlinearity

The differential equation

$$\frac{d^2x}{dZ^2} = -A\,(\,x + 1/12\,x^3 + 1/384\,x^5\,)\,\cos Z$$

also can be used to provide solutions that illustrate the occurrence of bifurcations. One sequence of examples can be introduced conveniently by considering two systems of order - 14/3 fixed-points for a range of values of the parameter A such that $0.200 \leq A \leq 0.2088$. One of these fixed-point systems will be strongly unstable for any value of A within the range mentioned, and for such a system two of the 14 fixed-points can be found to lie on the x-axis (at equal values of $|x|$). The other of these fixed-point systems is such that two members of any such system lie on the x'-axis (at equal values of $|x'|$) and will be locally stable for the larger values of A (such as A = 0.2087 and A = 0.2088). For values of A equal to 0.2086 or less, however , this second system also becomes locally unstable (HTR > +1) and one finds, as shall be illustrated, that additional fixed-point systems (at first, once again, only of order 14/3) then occur. Characteristics of the two order - 14/3 fixed-point systems mentioned earlier are listed in Table VI, wherein the columns headed HTR provide the half trace of the tangential-mapping transformation (for $\Delta Z = 14(2\pi)$). [For the second type of fixed-point system cited in Table VI, it is of interest to note that further increases of the parameter A carry the value of HTR to -1.0 (at $A \simeq 0.21619$) but not beyond, since further increases of A then lead to HTR becoming less negative!]

Table VI

Order -- 14/3 Systems

at x=0 A	Small-Amp'l Tune, σ_0 (Deg.)	Fixed point at x_0=0		Fixed point	
		±x	HTR	±x'	HTR
0.200	52.6619	2.132726	48.025758	0.242921	17.885314
0.201	52.9447	2.117613	42.423693	0.240836	14.320294
0.202	53.2278	2.102467	37.475516	0.238752	11.318874
0.203	53.5113	2.087283	33.107939	0.236670	8.806001
0.204	53.7951	2.072057	29.255340	0.234589	6.715351
0.205	54.0792	2.056788	25.859036	0.232509	4.988429
0.206	54.3637	2.041473	22.866618	0.230429	3.573762
0.2068	54.5915	2.029186	20.731897	0.228766	2.636284
0.2069	54.6200	2.027648	20.480026	0.228558	2.530064
0.207	54.6485	2.026109	20.231347	0.228350	2.426151
0.2075	54.7911	2.018409	19.034446	0.227310	1.939918
0.208	54.9337	2.010695	17.911591	0.226271	1.506006
0.2081	54.9623	2.009151	17.695506	0.226063	1.425130
0.2082	54.9908	2.007606	17.482168	0.225855	1.346147
0.2083	55.0194	2.006061	17.271542	0.225647	1.269025
0.2084	55.0479	2.004515	17.063595	0.225439	1.193734
0.2085	55.0765	2.002968	16.858294	0.225231	1.120243
0.2086	55.1050	2.001421	16.665604	0.225023	1.048520
0.2087	55.1336	1.999874	16.455495	0.224815	0.978538
0.2088	55.1621	1.998326	16.257932	0.224607	0.910265
0.209	55.2193	1.995228	15.870323	0.224192	0.778733
0.210	55.5052	1.979704	14.074649	0.222112	0.214188

A change in the character of phase-plane motion in the neighborhood of an order - 14/3 fixed-point is indicated on Figs. III.36-III.39 as a consequence of the system becoming unstable (HTR > +1) when the parameter A is reduced from A = 0.2087 to A = 0.2086. These plots are to the scales:

Horizontal: -0.001 to 0.001, for x;

Vertical: 0.223 to 0.227, for x'.

Fig. III.36, for A = 0.2087, shows three small smooth phase trajectories encircling the stable order - 14/3 fixed point situated on the positive x' axis.

Fig. III.37, for A = 0.2086, shows a single loop that develops from a launch quite close to the now unstable order - 14/3 fixed-point situated on the x' axis at x' ≅ 0.225023. Because this fixed point has become unstable <u>without reflection</u>, it is possible for a single loop to be formed in this way.

Fig. III.38, again for A = 0.2086, shows the addition of an additional loop that arises from a separate run launched from the neighborhood of the unstable order - 14/3 fixed point. Each of these two loops encircles a fixed point of a new fixed-point system, but such fixed points constitute <u>separate</u> periodic orbits--and hence are members of separate new fixed-point systems, each of order 14/3 (no period doubling).

Fig. III.39, again for A = 0.2086, shows further detail in the motion of phase points close to the unstable order - 14/3 fixed point and to the two new (stable) order - 14/3 fixed points present on this diagram.

The result of the change from A = 0.2087 to A = 0.2086 thus has been seen to involve the change of one order - 14/3 system from stable to unstable (HTR > +1) and the creation of two new stable systems of the same order. It is of interest now to follow the locations and stability characteristics of these new systems as the parameter A is further reduced. The fixed points of one of the new systems have phase-plane coordinates identical to coordinates of the other system, save for a reversal of sign for x'. Thus, for one of the stable fixed points shown on Fig. III.38 (for A = 0.2086) the coordinates are approximately

x = 0, x' = 0.226004

with a second member of this family at

x = 0, x' = -0.223995,

while for the other stable family fixed points occur at

x = 0, x' = 0.223995

and, for a second member of this family at

x = 0, x' = -0.226004

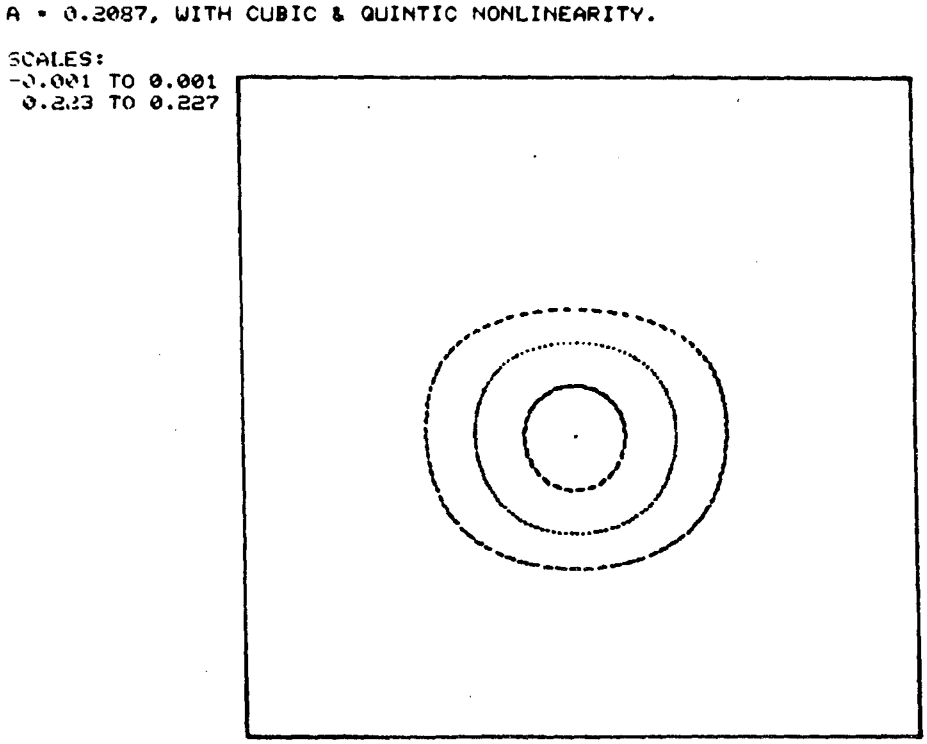

XBL 851-877

Fig. III.36 A = 0.2087, with cubic and quintic nonlinearity.

Scales:

-0.001 to 0.001

0.223 to 0.227

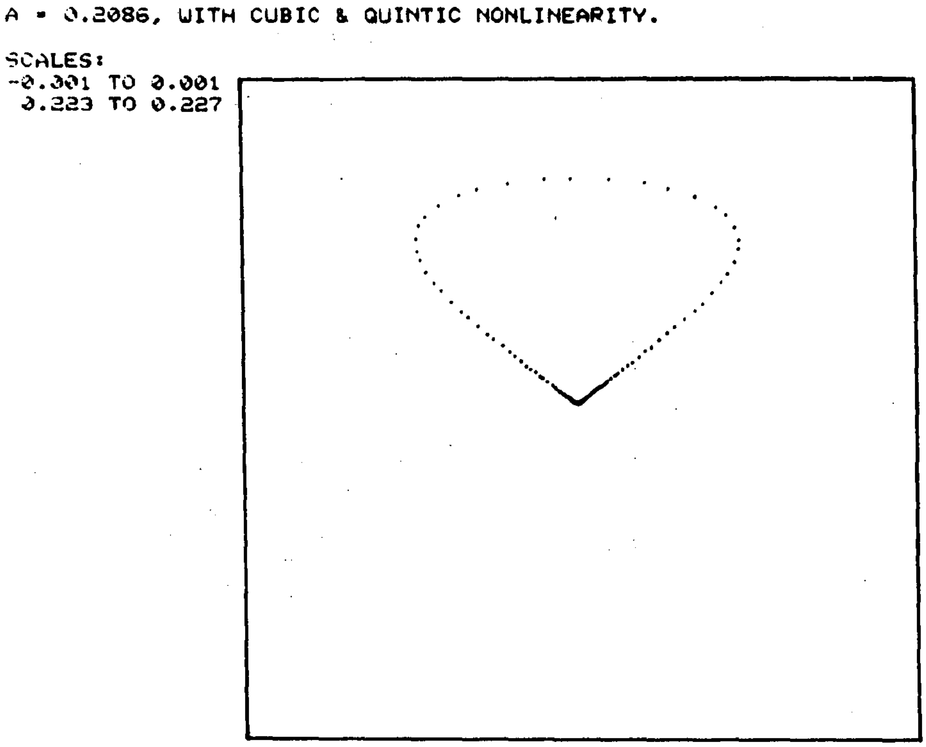

XBL 851-876

Fig. III.37 A = 0.2086, with cubic and quintic nonlinearity.
Scales:
-0.001 to 0.001
0.223 to 0.227

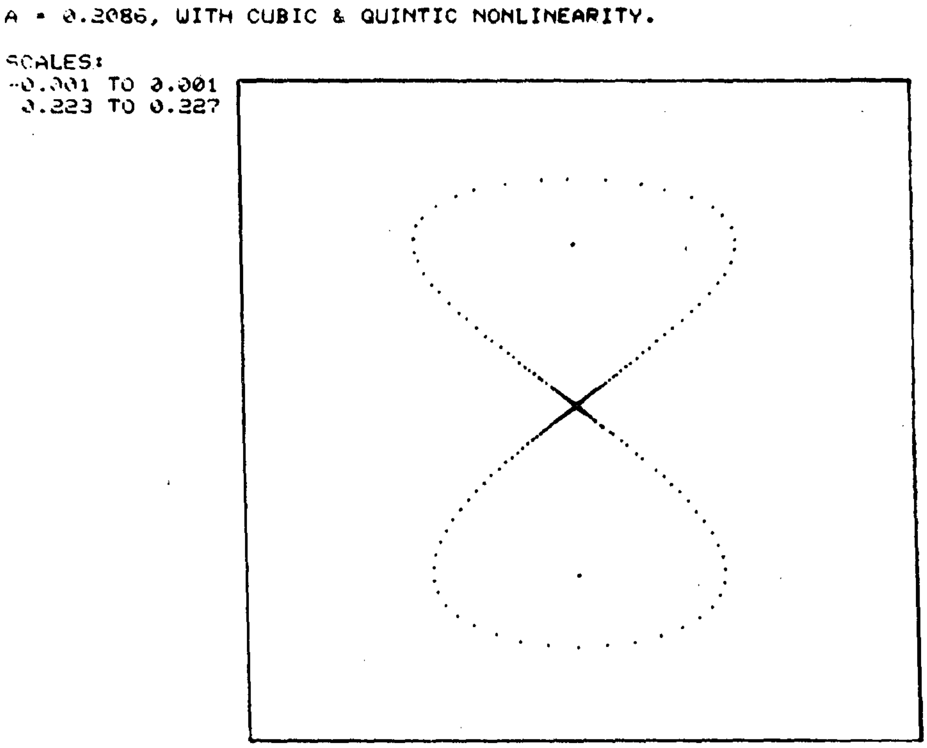

XBL 851-875

Fig. III.38 A = 0.2086, with cubic and quintic nonlinearity.
Scales:
-0.001 to 0.001
0.223 to 0.227

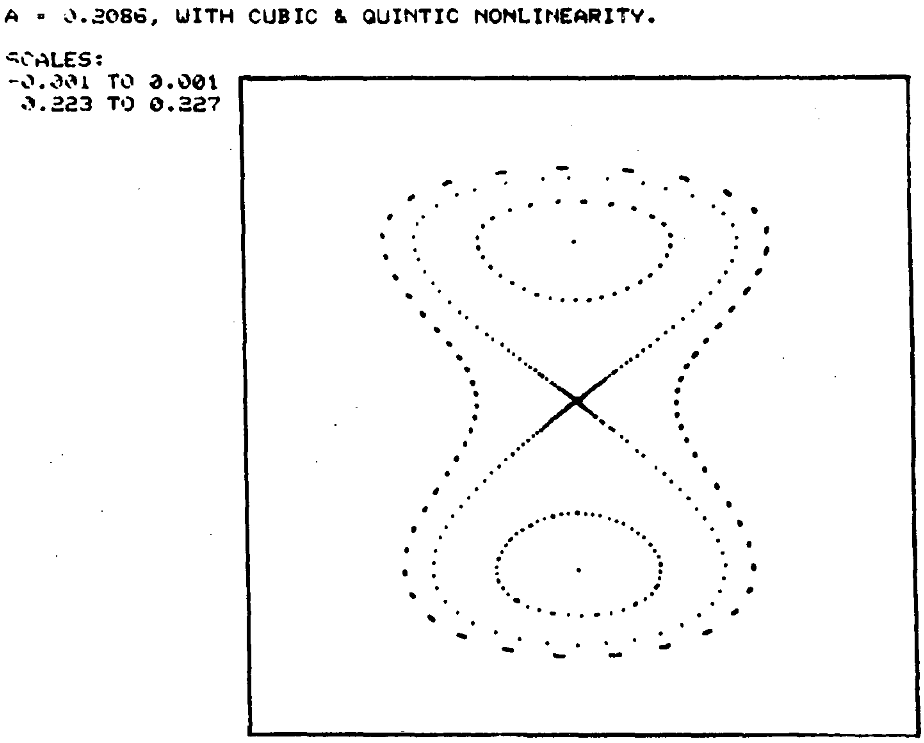

XBL 851-874

Fig. III.39 A = 0.2086, with cubic and quintic nonlinearity.

Scales:

-0.001 to 0.001

0.223 to 0.227

The locations of such fixed points on the positive x' axis are plotted, vs. A, on Fig. III.40 (together with similar information for one of the systems presented in Table VI). Table VII lists these x' values for the new order - 14/3 system, together with the associated value of the half trace (HTR) for the tangential-mapping transformation. It is seen from this tabulation that with reductions of the parameter A to 0.2069, and beyond, the value of HTR for these systems becomes less than -1. Associated with this transition into instability with reflection one may now expect to find (as will be illustrated) the occurrence of period-doubling bifurcation.

TABLE VII

Additional Order - 14/3 Fixed Points on x'-Axis

A	Small Amp'l Tune, σ_0 (Deg.)	±x'	∓x'	HTR
0.2068	54.5915	0.233266	0.222992	-1.090469
0.2069	54.6200	0.232957	0.222952	-1.007070
0.2070	54.6485	0.232643	0.222916	-0.920183
0.2075	54.7911	0.230997	0.222818	-0.435180
0.2080	54.9337	0.229147	0.222930	0.129613
0.2085	55.0765	0.226742	0.223602	0.768309
0.2086	55.1050	0.226004	0.223995	0.904419

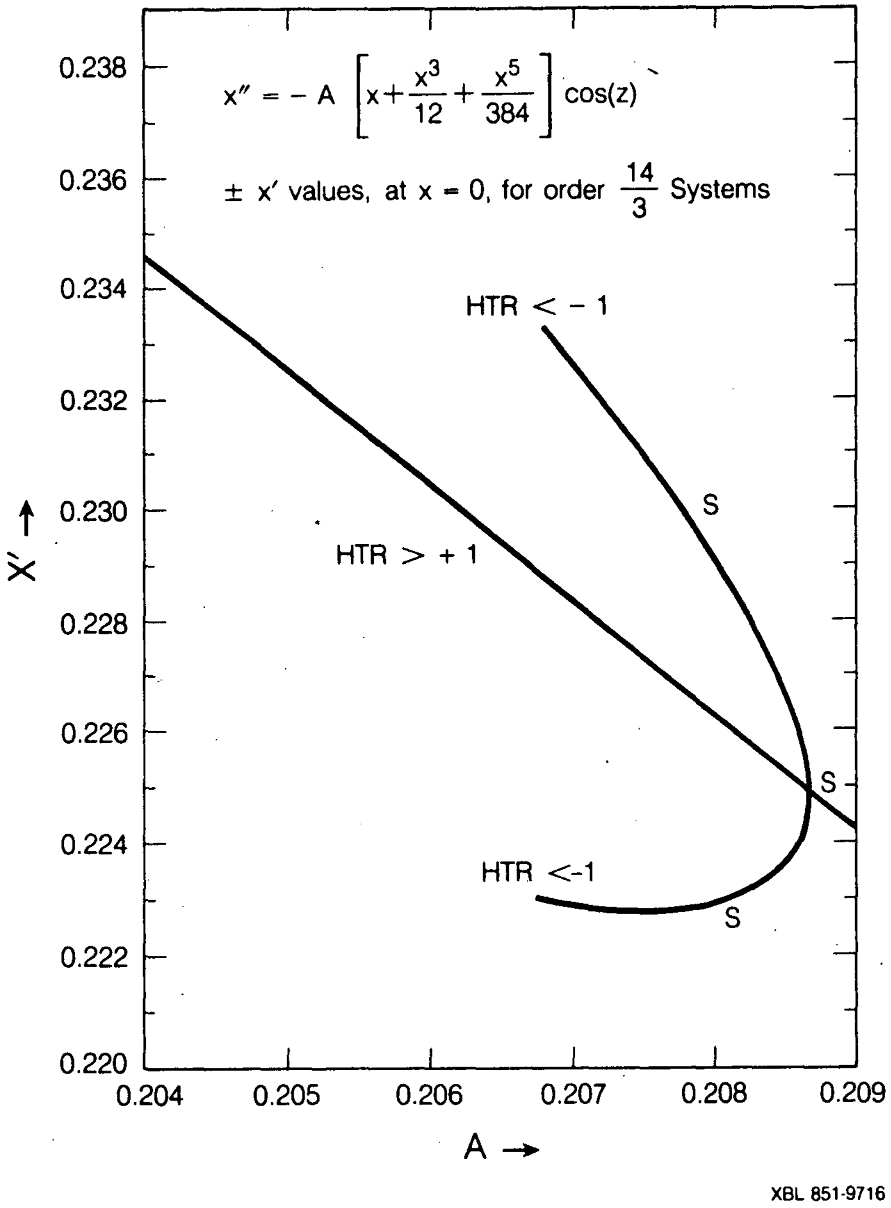
$x'' = -A\left[x+\frac{x^3}{12}+\frac{x^5}{384}\right]\cos(z)$
± x′ values, at x = 0, for order $\frac{14}{3}$ Systems
HTR < − 1
HTR > + 1
HTR <−1
S
S
S
X′ →
A →
0.238
0.236
0.234
0.232
0.230
0.228
0.226
0.224
0.222
0.220
0.204
0.205
0.206
0.207
0.208
0.209
XBL 851-9716

Fig. III.40

Figures III.41 and III.42, for A = 0.2070, respectively indicate the phase motion about the fixed points that Table VII shows to be situated on the x' axis at x' ≅ 0.232643 and at x' ≅ 0.222916 -- plotted to the scales:

<u>For Fig. III.41</u> Horizontal: -0.004 to 0.004, for x;
Vertical: 0.2326 to 0.2327, for x'.

<u>For Fig. III.42</u> Horizontal: -0.0005 to 0.0005, for x;
Vertical: 0.22235 to 0.22345, for x'.

For A = 0.2069, the fixed points shown on Figs. III.41 and III.42 have become unstable with reflection, and are situated on the x' axis at the respective locations x' ≅ 0.232957 and x' ≅ 0.222952. The extension of eigenvector directions from such fixed points then indicates that each has given rise to an order - 28/6 fixed-point system (period-doubling bifurcation). The stable order - 28/6 fixed points close to x = 0, x' = 0.232957, are found to lie at x ≅ ± 0.001123, x' ≅ 0.232949, as indicated on Figs. III.43 and III.44 to the scales:

Horizontal: -0.004 to 0.004, for x;
Vertical: 0.2329 to 0.2330, for x'.

The stable order - 28/6 fixed points close to x= 0, x' ≅ 0.222952 are found to lie on the x'-axis at x' ≅ 0.223175 and x' ≅ 0.222750 (constituting a second stable system of order 28/6), as can be seen on Figs. III.45 and III.46 to the scales:

Horizontal: -0.0001 to 0.0001, for x;
Vertical: 0.2224 to 0.2235, for x'.

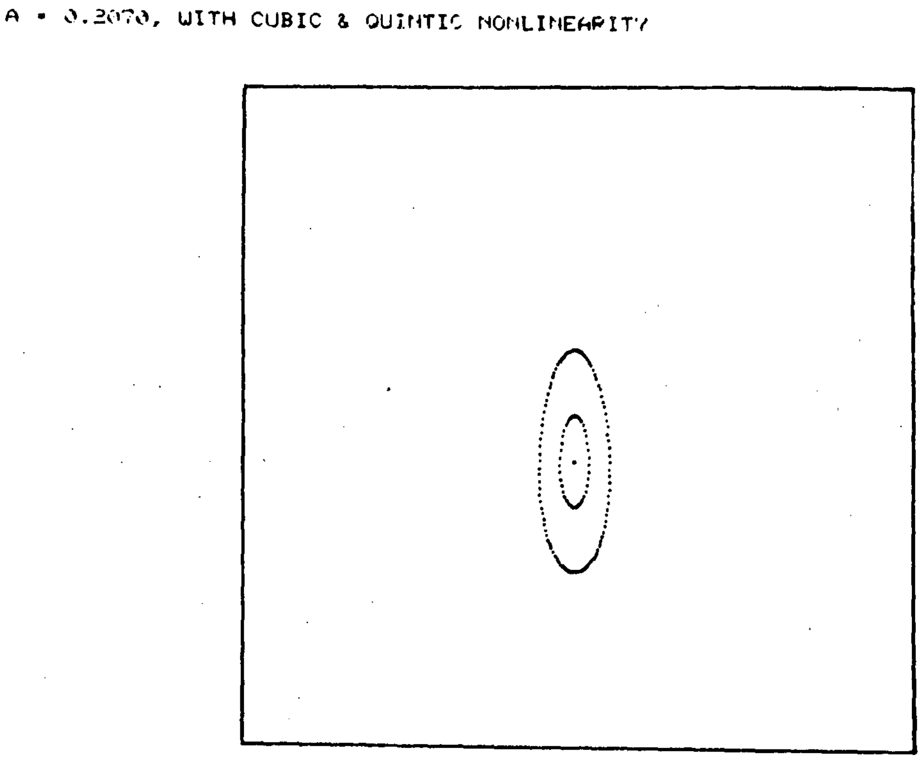

XBL 851-873

Fig. III.41 A = 0.2070, with cubic and quintic nonlinearity.

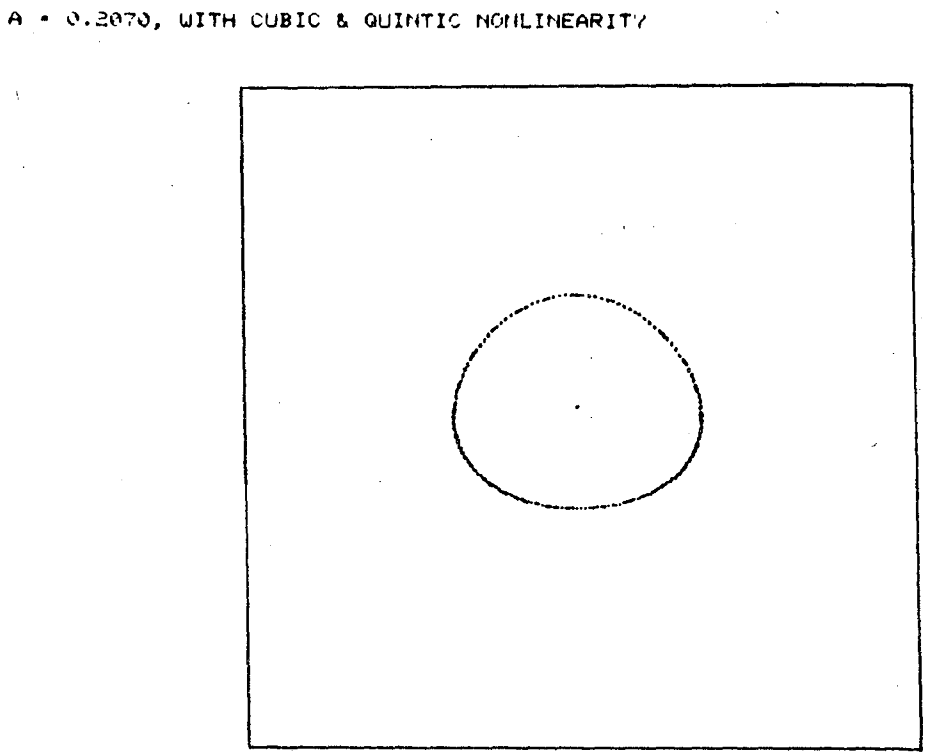

XBL 851-872

Fig. III.42 A = 0.2070, with cubic and quintic nonlinearity.

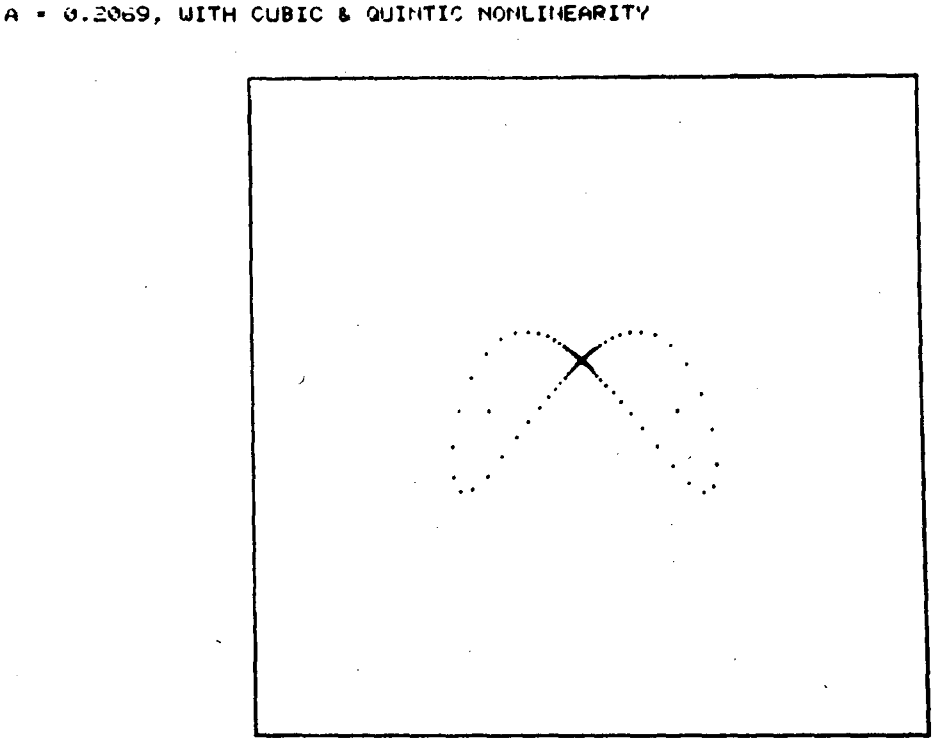

XBL 851-871

Fig. III.43 A = 0.2069, with cubic and quintic nonlinearity.

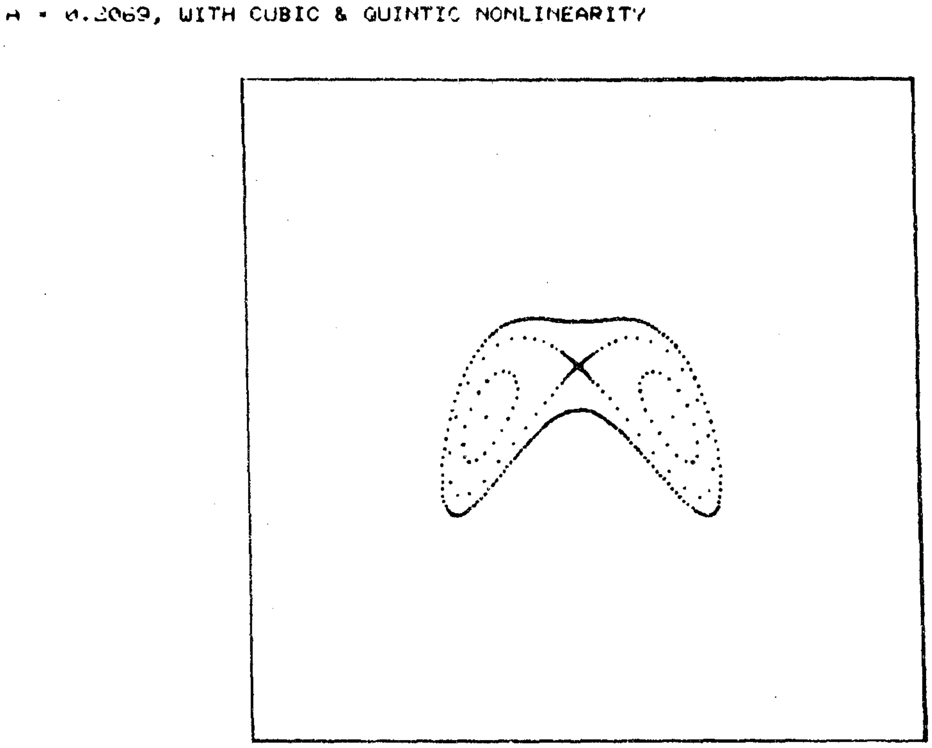

XBL 851-870

Fig. III.44 A = 0.2069, with cubic and quintic nonlinearity.

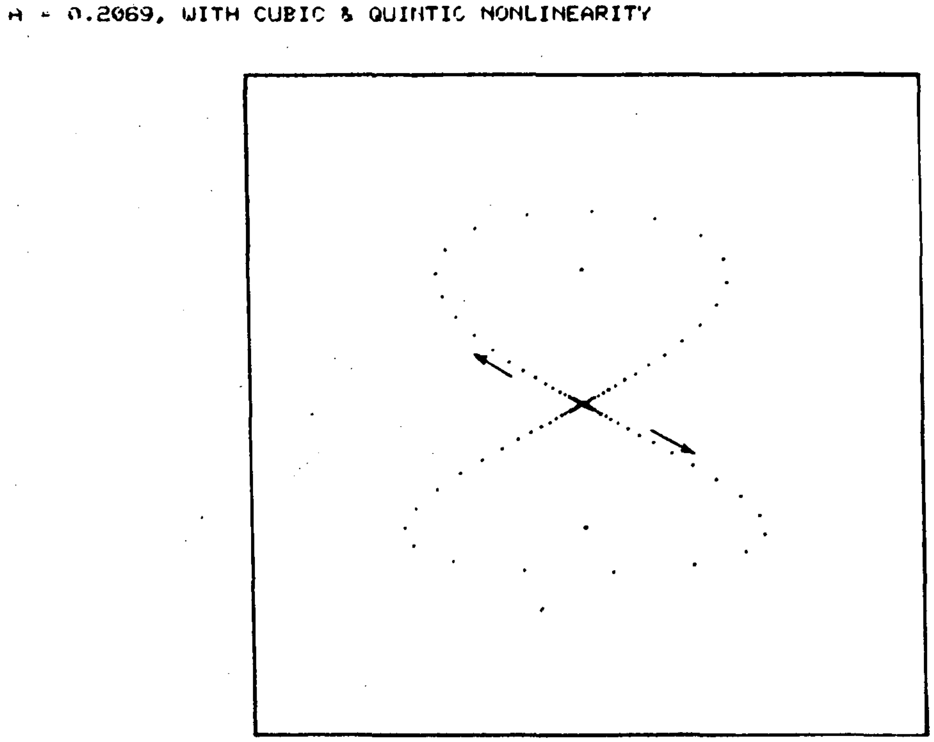

XBL 851-869

Fig. III.45 A = 0.2069, with cubic and quintic nonlinearity.

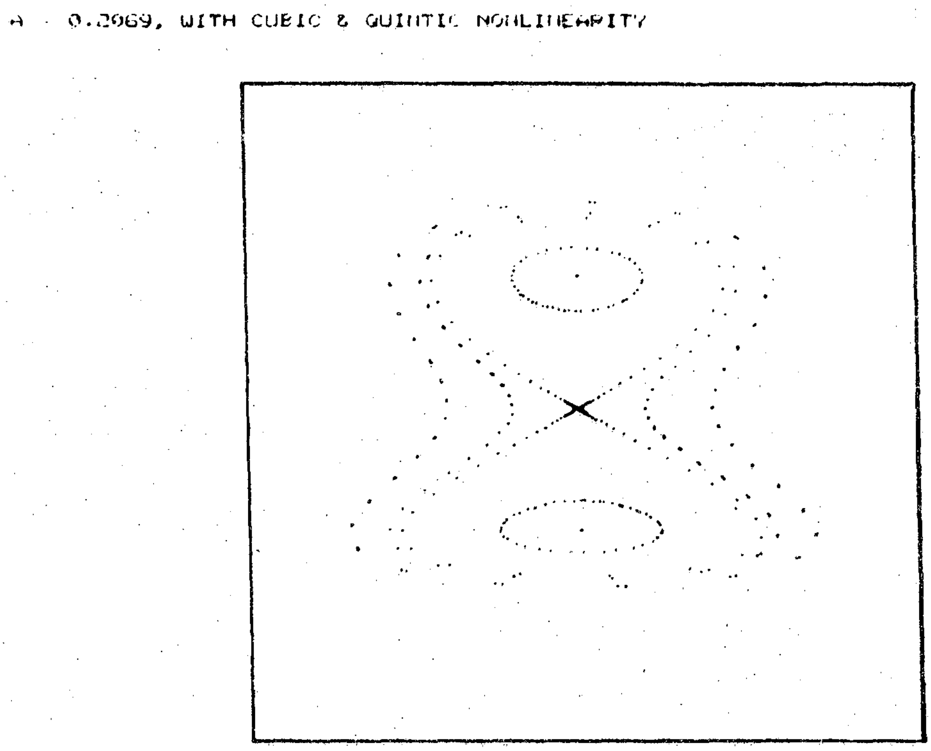

XBL 851-868

Fig. III.46 A = 0.2069, with cubic and quintic nonlinearity.

REFERENCES OR NOTES

1. Computational illustrations of period-doubling bifurcations have been given in a paper by T. C. Bountis, "Period Doubling Bifurcations and Universality in Conservative Systems," Physica D, 3D, No. 3, 577-589 (August, 1981).

2. The tangential-mapping transformation about the fixed points (x_n, y_n) of M^N is represented by the matrix product

$$\prod_{n=1}^{N} \begin{pmatrix} F'(x_n) & 1 \\ -1 + F'(x_n)\, F'(x_{n+1}) & F'(x_{n+1}) \end{pmatrix} .$$

8

Other Research Fields

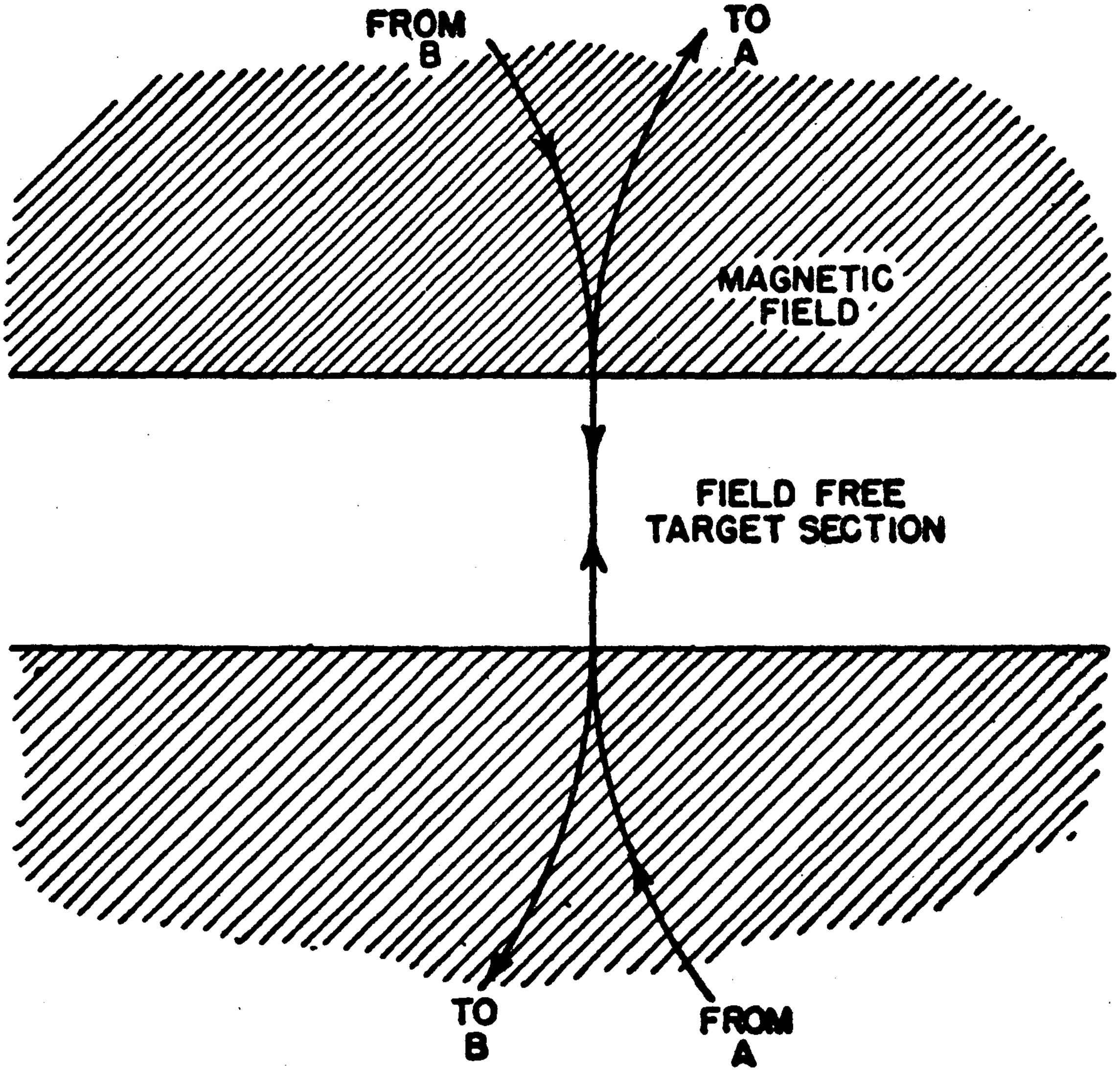
FROM
B
TO
A
MAGNETIC
FIELD
FIELD FREE
TARGET SECTION
TO
B
FROM
A

Reprinted from THE PHYSICAL REVIEW, Vol. 75, No. 3, 458–465, February 1, 1949
Printed in U. S. A

The Application of a Magnetic Lens Spectrometer to the Measurement of Gamma-Radiation from Zn^{65} and Co^{60}

ERLING N. JENSEN, L. JACKSON LASLETT, AND WILLIAM W. PRATT
*Institute for Atomic Research and Department of Physics, Iowa State College, Ames, Iowa**

(Received September 29, 1948)

A thin magnetic lens spectrometer for the investigation of gamma-ray spectra is described. The effect of the thickness of the radiator used for the production of photoelectrons and the influence of the earth's magnetic field are reported. Based on a calibration of the instrument by means of annihilation radiation and the F line of ThB, energy values of 1.10_6 Mev for the gamma-ray of Zn^{65}, and 1.15_6 and 1.31_7 Mev for the two lines of Co^{60} are obtained. The probable error is estimated as 0.5 percent.

I. INTRODUCTION

THE use of a thin magnetic lens spectrometer for the study of beta- and gamma-radiations has been reported by several investigators.[1–4] The flexibility of such an instrument and, if iron-free, the convenience of its linearity have been previously indicated.[1] It is the purpose of this paper to describe briefly a magnetic lens spectrometer which we have constructed, to present the results of studies to determine the corrections which should be made to data obtained with it, and to give the energies found for the gamma-radiations from Zn^{65} and Co^{60}.

II. DESCRIPTION OF SPECTROMETER

The spectrometer is shown in Figs. 1 and 2. The design is similar to that employed by previous workers,[1–3] save that the instrument is mounted with its axis parallel to the magnetic field of the earth and, to minimize scattering, the chamber proper has been constructed of aluminum tubing. To preserve linearity, nonferromagnetic materials have been used throughout.

The spectrometer chamber is 7 inches in diameter and 40 inches long, evacuated by means of a two-stage oil diffusion pump backed by a mechanical pump. The baffles, shown in Fig. 2, are of micarta, ½-inch thick, except for the gamma-ray shields, which are of lead sheathed with aluminum. Baffle *C*, which is adjustable by means of a brass rod passing out of the chamber through a Wilson seal, serves to delimit the electrons analyzed and so, for a given diameter of source and counter window, determines the intensity and resolution obtained. The lead shield surrounding the counter is primarily for the purpose of absorbing scattered gamma-radiation and was designed to lie within the shadow of the lead shield in the center of the spectrometer. An indication of the small extent of electron scattering obtained with the arrangement described is seen from the fact that, with no current in the coil, the counting rates obtained with and without a 10 microcurie beta-ray source in the instrument were, respectively, 21.1 ± 0.4 and 20.7 ± 0.2 cts/min.

Radioactive sources are mounted on Lucite holders at the end of a brass tube which enters the upper end of the spectrometer through a Wilson seal and through a 2½-inch gate valve modified to be suitable for vacuum service. The counter is mounted within a similar brass tube at the lower end of the instrument, where Wilson seals are again used to facilitate assembly and adjustment. The counter was originally used with a mica window of 4 mg/cm² surface density; for the ThB measurements a 1.1 mg/cm² window was used and for the most recent work a thin Formvar-polystyrene film ($\cong$0.3 mg/cm²) was employed.

The coil for producing the magnetic field consists of 2799 turns of No. 12 single cotton-covered enameled copper wire, wound on a form consisting of a brass hub and two aluminum

---

* Paper No. 42 from the Institute for Atomic Research. Work performed at the Ames Laboratory of the Atomic Energy Commission.

[1] M. Deutsch, L. G. Elliott, and R. D. Evans, Rev. Sci. Inst. **15**, 178 (1944).

[2] W. Rall and R. G. Wilkinson, Phys. Rev. **71**, 321 (1947).

[3] L. C. Miller and L. F. Curtiss, J. Research Nat. Bur. of Standards **38**, 359 (1947).

[4] E. A. Quade and D. Halliday, (*a*) Phys. Rev. **72**, 181(A) (1947); (*b*) Rev. Sci. Inst. **19**, 234 (1948).

Reprinted by permission of the American Institute of Physics.

castings. Every fourth layer of wire is followed by a copper sheet, 0.030-inch thick, provided with 12 tabs which are soldered to water-cooled brass blocks mounted on the exterior surface of the castings. The completed coil has an inside radius of 9.9 cm, an outside radius of 28.3 cm, and an axial length of 10 cm. When the full number of turns is used with 220 volts across the coil, a focal length of 25 cm is obtained for electrons of approximately 3.4 Mev energy.

The focusing current for the coil is provided by a 2 kw motor-generator set. To stabilize the current, a portion of it is passed through a bridge circuit which has as one of its elements a 60-watt tungsten lamp bulb to serve as a nonlinear resistance. Changes in the coil current affect the balance of the bridge and the resulting error-signal, when amplified, is used to correct the generator field. The magnetic field is thereby maintained constant within a probable error of 0.1 percent. The coil current is measured by means of a series resistance and a potentiometer.

III. DETERMINATION OF GAMMA-RAY ENERGIES

A. General Method. In the work described in this paper, the gamma-ray energies were determined by a study of the spectra of photoelectrons produced in radiator foils. For calibration, use was made of photoelectrons produced by the annihilation radiation from Zn^{65} and of conversion electrons from ThB (F line). Each gamma-ray source *S* (Fig. 2), a few mm thick, was mounted in a Lucite holder *H* and covered by an aluminum cap *G*, which carried the radiator *R*.

The spectra obtained from Zn^{65} and Co^{60} sources are shown in Figs. 3 and 4. In addition to the photoelectric conversion lines generated in the lead by gamma- and annihilation radiation, a broad distribution of Compton electrons is also obtained.

To permit an accurate determination of the energies of the photoelectrons ejected from the radiator, attention must be given to the effect of radiator thickness and to the influence of the earth's magnetic field, which is in the direction of the spectrometer axis.

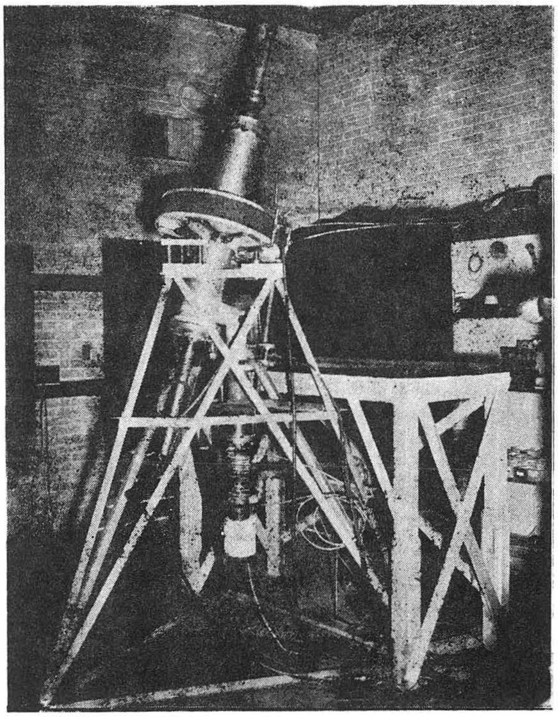

FIG. 1. The magnetic lens spectrometer, aligned with its axis parallel to the magnetic field of the earth.

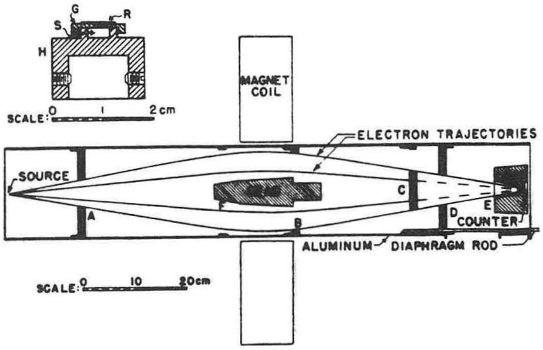

FIG. 2. Diagram of spectrometer chamber. *Insert:* Source holder.

B. Effect of the Magnetic Field of the Earth. For a focusing field of a *given shape* the momentum of the focused electrons will quite generally be proportional to the strength of the field and, if the field in question is proportional to the coil current, we may write for this momentum

$$P = I \cdot F, \qquad (1)$$

where I is the current in the coil and F is dependent upon the shape of the field. In the presence of an additional magnetic field H, superposed upon that produced by the coil current, F may be regarded as a function of the ratio H/I, since the shape of the field would remain un-

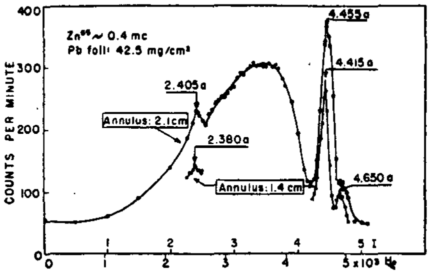

FIG. 3. Spectrum of Zn^{65}, showing the photoelectric-conversion peaks produced in a lead radiator by annihilation radiation and the 1.11 Mev gamma-ray, in addition to the broad distribution of Compton electrons. The sharper peaks shown separately were obtained with an adjustment which permitted the K and L lines to be resolved. The annulus is the width of the electron beam at the center of the spectrometer.

changed if H and I were to vary in a mutually proportional manner. The relation between the current I_1 required to focus electrons of a given energy in the presence of the field H, and the current I_0 required in its absence may therefore be written,

$$I_1F(H/I_1) = I_0F(0). \tag{2}$$

One then finds, to a first approximation, that

$$I_1 - I_0 = -HF'(0)/F(0), \tag{3}$$

indicating that this difference is independent of the energy of the electrons. This is in agreement with the conclusions of Quade and Halliday,[4b] who have shown experimentally that for their spectrometer very little error is made by applying Eq. (3) to electron energies as low as 10 kev.

In the use of the spectrometer, it is the current necessary to focus electrons in the *absence* of an external field which is to be taken as proportional to the momentum, so the difference $I_1 - I_0$ must be determined and applied as a correction. This correction is most readily found by observing the change in the focusing current required when the current in the coil is reversed. It is, however, of interest to note that an approximate calculation, described in the Appendix, leads to a value for the correction which is independent of the energy and is in good numerical agreement with that found empirically. When all the turns on the focusing coil are employed, the current required to focus a particular conversion line is found to change by 0.012 amp when the current is reversed, so the correction then to be applied because of the presence of the magnetic field of the earth has been taken as ±0.006 amp.

C. Effect of Radiator Thickness. The photoelectrons ejected from a radiator will, for a particular gamma-ray energy, have energies which depend upon the depth of the point from which they originate. The momentum distribution of the emergent electrons will, to a first approximation, be rectangular, with a width equal to the momentum loss associated with a full traversal of the radiator foil.** Figure 5(A) shows a momentum distribution of this type, which extends from a momentum P_a to the maximum momentum P_m. The result of the combination of this distribution function with the transmission curve of the spectrometer must be considered and will indicate the manner by which the experimental data may be corrected in cases for which the effect of radiator thickness is not completely negligible. The result of an analysis of this character will be applicable with equal validity to internal conversion lines which arise from a source of non-vanishing thickness.

The transmission curve of a magnetic lens spectrometer has been investigated by Deutsch

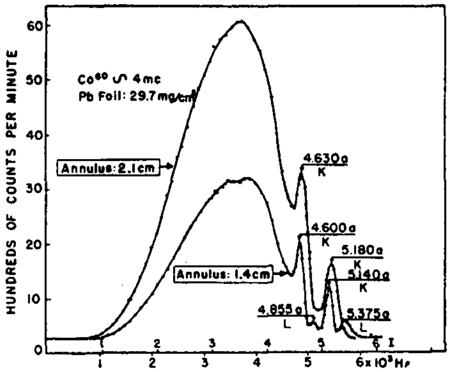

FIG. 4. Spectrum of Co^{60}, showing the photoelectric-conversion peaks produced in a lead radiator by the two gamma-rays present.

** To a higher order of approximation it might be supposed that, because of the change of the rate of momentum loss as the electrons lose energy in the foil, a *trapezoidal* distribution should be considered. In addition, the *scattering* of electrons in their passage through the foil would cause the distribution to drop and tail off on the low momentum side. An approximate analysis of these phenomena, as well as the experimental results reported here, indicates, however, that these effects are not of importance in the energy range with which we are concerned in the present paper. At lower energies scattering will certainly play a prominent role [cf. Bethe, Rose, and Smith, Proc. Am. Phil. Soc. **78**, 573 (1938)].

et al.[1] and has approximately the shape of an isosceles triangle for the case in which the image and counter windows have the same size. As the current is changed in the coil of the spectrometer, the width of the transmission curve will vary in direct proportion to the momentum of the electrons which it passes. For a triangular transmission curve, we therefore take the half-width b as equal to a constant K multiplied by the momentum P_0 corresponding to the point of maximum transmission. This is illustrated by Fig. 5(B). The constant K evidently serves as a measure of the resolution of the instrument. When, in order to obtain the expected line shape, we pass such a transmission curve across the momentum distribution for the electrons, there are two cases to consider. The first of these is that for which the momentum spread of the electrons is less than the full width of the transmission curve, as illustrated by Fig. 5(C); the other is that for which the momentum spread is greater than the width of the transmission curve and is shown in Fig. 5(D).

In the case of a **thin** radiator, specifically one for which the momentum spread $P_m - P_a$ is less than $2b$, the maximum transmission is found to occur when

$$P_0 \cong (P_a + P_m)/2, \tag{4}$$

neglecting terms small compared to $P_m - P_a$. Thus

$$P_m \cong P_0 + a/2, \tag{5}$$

where

$$a \equiv P_m - P_a. \tag{6}$$

The effect of radiator thickness is, therefore, to give maximum transmission at a momentum which is less than the maximum momentum of the electrons by an amount which is equal in a first approximation to one-half the momentum loss experienced by electrons which traverse the full thickness of the radiator.

For a thick radiator, for which $P_m - P_a > 2b$, maximum transmission is to be expected when the transmission curve lies just inside the momentum distribution, if terms in K^2 are neglected. Thus

$$P_m \cong P_0(1 + K), \tag{7}$$

where

$$K = b/P_0. \tag{8}$$

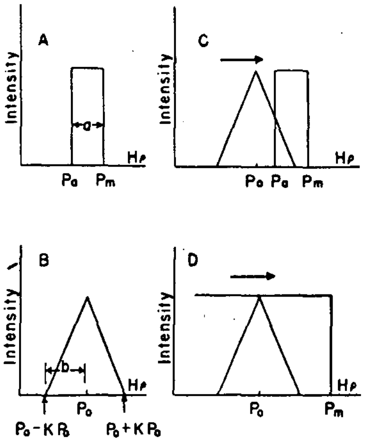

FIG. 5. Momentum distribution and transmission curve of spectrometer, as assumed for the purposes of the analysis given in the text.

In determining, from the current corresponding to maximum transmission, the upper limit of the momentum distribution of electrons generated by an unknown gamma-ray, the factor $(1+K)$ may be absorbed into the calibration constant of the spectrometer *provided* the radiator thickness is such that Eq. (7) is applicable. It should be noted that, owing to the variation of the rate of momentum loss, a radiator which can be correctly regarded as a thin foil for high energies may, on the other hand, be effectively a thick foil at lower energies. We shall, therefore, apply the correction indicated by Eq. (7) in an *explicit* fashion in those cases to which it applies. In analyzing the data reported in this paper, we have based the energy determinations on the positions of the *maxima* of the curves obtained, subject to the corrections indicated above, since the maximum appears to be the point most accurately located for every line.

The complete line shape which results from a combination of a rectangular momentum distribution and a triangular transmission curve has been calculated for the case that a/P_m, the relative momentum spread from the radiator, is 0.03 and the resolution of the spectrometer is such that $K = 0.021$. The calculated curve is represented by the broken line in Fig. 6 and may be compared with the solid line, which gives the results experimentally obtained under these conditions with photoelectrons produced in lead by Zn^{65} radiation ($P_m \cong 4800$ gauss-cm). The

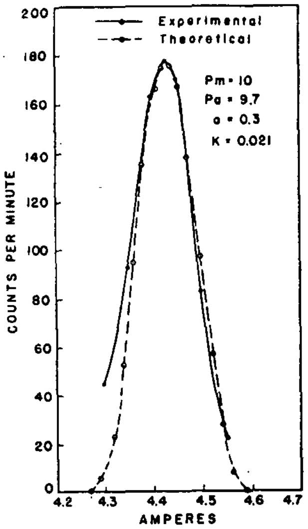

FIG. 6. Resultant line shape obtained with electrons for which $P_m \simeq 4800$ gauss-cm. The dotted curve represents the line shape calculated for $a/P_m = 0.03$ and $K = 0.021$; the solid curve represents the shape obtained experimentally under comparable conditions.

two curves were made to fit at their peaks and it is felt that their shapes are in satisfactory agreement. The somewhat larger counting rate obtained experimentally on the low momentum side of the line may be ascribable to straggling and scattering phenomena, the importance of which is indicated, for example, by the work of White and Millington.[5]

An experimental study was made of the positions of the points of maximum intensity when various radiator thickness are used. For this purpose the 1.1 Mev gamma-ray of Zn^{65} was again used, with the results shown in Figs. 7 and 8. It is seen that, in agreement with our previous discussion, the shift of the peaks obtained with thin foils is proportional to the thickness of the radiator, but becomes constant when the foil thickness exceeds a value of approximately 65 mg/cm². The slope of the initial part of the curve in Fig. 8 corresponds to 1.7_5 gauss-cm/mg-cm^{-2}. The theoretical rate of energy loss in lead, as obtained from a formula given by Heitler,[6] is 1.0 Mev/gm-cm^{-2} for electrons of the energy with which we are concerned here. This theoretical energy loss corresponds to a momentum loss of 3.5 gauss-cm/mg-cm^{-2} and, when compared with the slope of the experimental curve, affords confirmation of the statement that the peaks should be shifted by an amount which is half the momentum loss associated with a full traversal of the radiator foil.

The horizontal portion of the curve of Fig. 8 occurs at a current value which is 2.3 percent below the extrapolated value for zero foil thickness. This implies that $K = 0.023$, which is consistent with the expected resolution for the spectrometer at the time the data were obtained. The break in the curve of Fig. 8 occurs, as expected, at a radiator thickness for which $a = 2b$. Similar data obtained with a lower energy gamma-ray, for which the photoelectrons have an energy of 0.177 Mev, indicate that the break occurs for a foil thickness between 6.6 and 11.3 mg/cm². In this case the condition $a = 2b$ would imply a thickness of 10 mg/cm².

IV. RESULTS

The photoelectric conversion lines obtained with lead radiators were measured for the Zn^{65} and Co^{60} radiations at each of two settings of the adjustable baffle. For these baffle positions, the radial width of the effective aperture at the center of the spectrometer assumed the values 2.1 and 1.4 cm. The resolution of the spectrometer was characterized by $K = 0.023$ and $K = 0.021$ in these two cases. As may be seen from Figs. 3 and 4, lines were obtained from both the K and L shells of the lead in the second series of measurements.

For calibration, the F line of ThB and the photoelectric line produced by the Zn^{65} annihilation radiation were measured at each of the two adjustments of the instrument. For the two adjustments the calibrations from the annihilation radiation and the F line of ThB agree to 0.1 percent and 0.3 percent, respectively. The ThB sample was deposited on an aluminum foil 0.00025 inch thick and mounted on the Lucite source holder by means of a thin Formvar-polystyrene film. The line obtained with this source is shown in Fig. 9.

The results of the measurements are summarized in Table I. Lines which are similar in character and for which the intensity measurements are made with equal precision can, presumably,

---

[5] B. A. White and B. A. Millington, Proc. Roy. Soc. (London) **A120**, 701 (1928).

[6] W. Heitler, *The Quantum Theory of Radiation* (Oxford University Press, London, 1936), p. 219.

be located with the same *relative* accuracy, although the lines are of different momenta and occur at different current values. In the work reported here, however, the data obtained were such that the location of the various lines could not be determined in all cases with the same relative accuracy; accordingly, the estimated weighting factors indicated in Table I were applied to the current/momentum ratios.

In calculating, from the data of Table I, the momenta of the photoelectrons generated in the lead radiator by the Zn^{65} gamma-ray, a correction of 74 gauss-cm was taken as appropriate to the foil thickness employed. For the Co^{60} determinations the correction was assigned the values 51 and 64 gauss-cm for the thinner and thicker Pb radiators, respectively. The correction made for the Th radiator was 48 gauss-cm and that for the U foil was 70 gauss-cm. Upon converting from the resulting momenta to the corresponding energy values and adding the binding energy appropriate to the photoelectric process involved, the gamma-ray energies shown in the final column of Table I resulted. Averaging for each line the energy values so found, taking into account the weights assigned to the individual determinations and to the calibration measurements, the following gamma-ray energies are obtained:

$$\mathrm{Zn}^{65}, \qquad 1.10_6\ \mathrm{Mev};$$
$$\mathrm{Co}^{60},\ \mathrm{I}, \quad 1.15_5\ \mathrm{Mev};$$

and

$$\mathrm{Co}^{60},\ \mathrm{II}, \quad 1.31_7\ \mathrm{Mev}.$$

A conservative estimate of the probable error for the values of the gamma-ray energies is ±0.5 percent. The constant of the spectrometer has the values 1063 and 1074 gauss-cm/amp. for the two adjustments used.

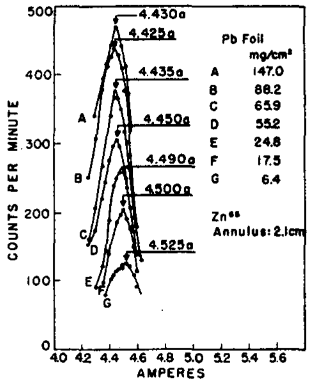

FIG. 7. Photoelectric lines obtained from the 1.11 Mev gamma-ray of Zn^{66} with various thicknesses of the lead radiator.

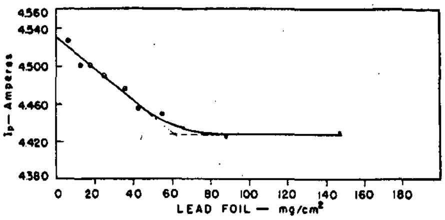

FIG. 8. Current values corresponding to the peaks of the lines of Fig. 7, as a function of radiator thickness. The results of additional data, not shown in Fig. 7, are included. In determining the slope of the line, the points designated by the heavy solid circles were given half the weight of those marked by open circles.

It is that seen the value found for the energy of the Zn^{65} radiation is below the energy for either of the Co^{60} gamma-rays. Because of the possible interest[7] in the use of these radiations as standards, a direct comparison of the energies was felt to be desirable. To this end a source with *both* activities was put into the spectrometer. As reported[8] previously, the individual peaks in the composite spectrum were readily identified and indicated that the gamma-ray from Zn^{65} is of lower energy than either of the Co^{60} lines.

The energies found for the Co^{60} gamma-rays are in good agreement with those given by Miller and Curtiss,[3] although somewhat higher than the values of Deutsch *et al.*[7] The energy found for the Zn^{65} gamma-ray is lower than the value given in an early report by Deutsch,

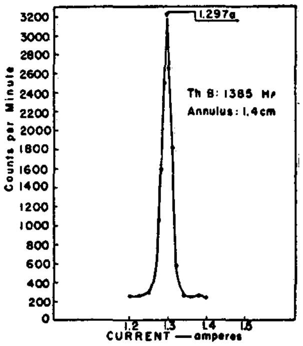

FIG. 9. The *F* line of ThB.

---

[7] M. Deutsch, L. G. Elliott, and A. Roberts, Phys. Rev. 68, 193 (1945).

[8] E. N. Jensen, L. J. Laslett, and W. W. Pratt, Phys. Rev. 73, 529 (1948).

TABLE I. Positions of conversion lines measured in magnetic-lens spectrometer.

Line	Momentum (gauss-cm)	Aperture width (cm)	Radiator thickness (mg/cm²)	Coil current (amp.)*	Relative weight (of curr./momentum ratio)	Gamma-ray energy (Mev)
Annih.	2608/1.023**	2.1	42.5 Pb	2.401 (av.)	5	
ThB	1385†		Negligible	1.303	10	
Zn^{65} (K)			42.5 Pb	4.454††	20	1.10_6
Co^{60}, I (K)			29.7 Pb	4.624	10	1.15_0
Co^{60}, II (K)			29.7 Pb	5.174	10	1.31_7
Annih.	2608/1.021**	1.4	42.5 Pb	2.374	3	
ThB	1385†		Negligible	1.291	10	
Zn^{65} (K)			42.5 Pb	4.409	10	1.10_6
(L)			42.5 Pb	4.644	5	1.10_6
Co^{60}, I (K)			42.0 U	4.501	10	1.16_0
(K)			28.5 Th	4.524	10	1.15_5
(K)			37.0 Pb	4.583	10	1.15_6
(K)			29.7 Pb	4.594	10	1.15_6
(L)			29.7 Pb	4.849	5	1.16_2
Co^{60}, II (K)			42.0 U	5.011	10	1.31_6
(K)			28.5 Th	5.045	10	1.31_4
(K)			37.0 Pb	5.104	10	1.31_5
(K)			29.7 Pb	5.134	10	1.32_1
(L)			29.7 Pb	5.369	5	1.32_1

* 0.006 amp. has been subtracted from the observed current values to correct for the magnetic field of the earth.

** Since the radiator is *thick*, in the sense $a>2b$, for electrons of the energy with which we are concerned here, the momentum value of 2608 gauss-cm corresponding to 0.5108 Mev must be divided by $1+K$ to correct for radiator thickness.

† C. D. Ellis, Proc. Roy. Soc. (London) **A138**, 318 (1932).

†† Obtained from the sloping portion of the curve of Fig. 8, so that data obtained with several foil thicknesses are, in effect, included.

Roberts, and Elliott[9] and that obtained by Mandeville and Fulbright[10] through a study of Compton electrons.

V. ACKNOWLEDGMENTS

We should like to indicate our gratitude to Dr. J. M. Keller for helpful discussions on the theory of the spectrometer and to Dr. A. F. Voigt for his invaluable contribution in the preparation of the radioactive sources. Acknowledgment should also be made to Messrs. R. B. Leachman and R. C. Skar for constructing the Geiger-Müller counters, to the staff of the College Instrument Shop for their cooperation during the construction of the spectrometer, and to Mr. E. R. Rathbun for assistance with the operation of the instrument.

We are particularly indebted to Dr. F. N. D. Kurie and Capt. W. H. Ferguson (U. S. N., Ret.) of the Department of Physics, Washington University, for their kindness in furnishing us with a sample of ThB. By the cooperation of Mrs. G. W. Fox and Dr. P. H. Carr, it was possible to transport this sample by air to Ames in a few hours.

APPENDIX: APPROXIMATE CALCULATION OF THE CORRECTION FOR THE MAGNETIC FIELD OF THE EARTH

The solution of the differential equations for the trajectories of paraxial electrons in an axial magnetic field $H_z=H_0/[1+(z/a)^2]$ has been given by Glaser.[11] When the object distance and image distance are equal ($u=v=2f$), the focal length f may be written

$$f=\Lambda[H\rho]^2\Big/\int_{-\infty}^{\infty}H_z^2dz, \qquad \text{(i)}$$

where Λ is a numerical coefficient, calculable in terms of f/a, which takes on values extending from $\Lambda=4$ for f/a large (thin lens) to π^2 for f/a small (solenoid). Here $[H\rho]$ serves as a measure of the momenta of the electrons in question in terms of their radius of curvature in a uniform magnetic field.

Assuming that to a field of the shape mentioned above, there is added a small constant axial field H, one can attempt to fit the resultant field in an approximate way to an equation of the original form and so obtain new values, H_0' and a' for the parameters. In this way we find that $H_0'-H_0\cong 8H/7$ and $a'-a\cong(12a/7)(H/H_0)$.

Introducing a constant A which connects the current in the coil with the magnetic field produced, so that

$$\int_{-u}^{u}H^2_{\text{coil}}dz=AI^2, \qquad \text{(ii)}$$

we then write the approximate relation for the *total* field as

$$\int_{-u}^{u}H_z^2dz\cong AI^2+2H\int_{-u}^{u}H_{\text{coil}}dz. \qquad \text{(iii)}$$

The currents I_1 and I_0, which are respectively required to focus electrons of a given momentum in the presence and absence of the external field, are then, by Eq. (i), connected by the relation

$$\frac{AI_0^2}{\Lambda(f/a)}=\left[AI_1^2+2H\int_{-u}^{u}H_{\text{coil}}dz\right]\frac{1}{\Lambda(f/a')}. \qquad \text{(iv)}$$

From this it follows that the difference I_0-I_1 is

---

[9] M. Deutsch, A. Roberts, and L. G. Elliott, Phys. Rev. **71**, 389(A) (1942).

[10] C. E. Mandeville and H. W. Fulbright, Phys. Rev. **64**, 265 (1943).

[11] W. Glaser, Zeits. f. Physik **117**, 285 (1941).

approximately

$$I_0-I_1=H\left[\left(\frac{1}{A}\right)\int_{-u}^{u}(H_{\text{coil}}/I)dz + (6/7)(I/H_0)\frac{d\ln\Lambda}{d\ln(f/a)}\right]. \qquad \text{(v)}$$

Through the use of Eqs. (i) and (ii) an approximate value of A is readily estimated experimentally by fucusing electrons of known energy, while H_0/I and $\int_{-u}^{u}(H_{\text{coil}}/I)dz$ may be calculated from the geometry of the coil, the latter quantity being given closely by $4\pi/10$ times the number of turns on the coil.

For the spectrometer described in the present paper, the following values apply when all the turns on the coil are employed:

$$f=25\text{ cm},\quad a\cong 13.6\text{ cm},\quad f/a=1.84,$$

$$\Lambda=5.1,\quad d\Lambda/d(f/a)=-0.65,\quad \frac{d\ln\Lambda}{d\ln(f/a)}=-0.23,$$

$$A=2.27\times 10^5\text{ gauss}^2\text{-cm/amp.}^2,$$

$$H_0/I=93.5\text{ gauss/amp.},$$

$$\int_{-u}^{u}(H_{\text{coil}}/I)dz=3230\text{ gauss-cm/amp.},$$

$$\text{and } H=0.56\text{ gauss.}$$

With the substitution of these values in Eq. (v) we find $I_0-I_1=0.007$ amp., in close agreement with the correction found experimentally.

Reprinted from THE PHYSICAL REVIEW, Vol. 76, No. 6, 858, September 15, 1949
Printed in U. S. A.

Reprinted by permission of the American Institute of Physics.

On the Half-Life of Na^{22}

L. JACKSON LASLETT
*Institute for Atomic Research and Department of Physics, Iowa State College, Ames, Iowa**

August 8, 1949

THE radioactivity of Na^{22}, first discovered by Frisch,[1] has been described by the present writer[2,3] as producible by the deuteron bombardment of magnesium and the half-life estimated as 3.0 years.[3] More recently, Saha[4] has given a value of 2.8 years for the half-life of this activity. During the past three years the decay of a Na^{22} sample has been followed in this laboratory and it is the purpose of the present note to report the value obtained for the half-life.

The Na^{22} sample used was produced in 1937 by the bombardment of magnesium metal with deuterons produced by the cyclotron in Professor Lawrence's laboratory at Berkeley. The magnesium target was subsequently mounted in the recess of a brass plate, covered with a mica sheet hermetically sealed to the brass, and, by means of a Lauritsen electroscope,[5] its activity was compared at intervals with that from a standard uranium oxide source

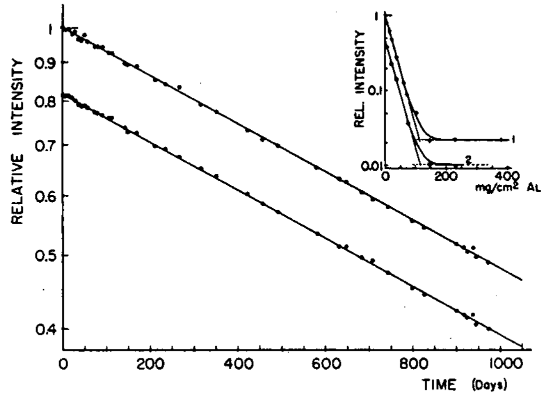

FIG. 1. Logarithmic decay curves of Na^{22} activity, measured with respect to that of an uranium oxide standard, for two source positions. *Insert*: Aluminum absorption curves (logarithmic scale of ordinates) taken (1) at the beginning and (2) after completion of the decay measurements.

The resultant decay curves, for two different source positions, are shown in Fig. 1 and indicate a half-life of 94^8 days or 2.6^0 years.[6] It should be mentioned that diffusion of the active material from the surface into the magnesium metal would, if appreciable, result in an underestimation of the half-life, since the greater portion of the activity measured was readily absorbable (positrons). Some confirmation of the belief that diffusion and similar processes played no significant role in the present work is afforded, however, by the observation that absorption curves taken at the beginning and end of the measurements (curves 1 and 2 of the insert, Fig. 1) appeared entirely similar and were in agreement with one obtained[3] shortly after the sample was first prepared.

It is a pleasure for the writer to indicate once again his gratitude to Professor Lawrence for the privilege of using the cyclotron in connection with the preparation of the sample used in the work reported here.

---

* Contribution No. 80 from the Institute for Atomic Research. Work performed at the Ames Laboratory of the AEC.

[1] O. R. Frisch, Nature **136**, 220 (1935).

[2] L. J. Laslett, Phys. Rev. **50**, 388(A) (1936).

[3] L. J. Laslett, Phys. Rev. **52**, 529 (1937).

[4] N. K. Saha, Trans. Bose Res. Inst. (Calcutta) **14**, **57** (1939–41); cited in Chem. Abstracts **42**, 450i (1948).

[5] The electroscope, manufactured by the F. C. Henson Company (Pasadena), was used to measure the ionization in a chamber approximately 2¼ inches in diameter and 3 inches long, into which the radiation passed through an aluminum window of 1.2 mg/cm² surface density. The surface density of the mica covering the source was 5.2 mg/cm². We are indebted to Dr. A. F. Voigt for making available to us this electroscope in its modified form.

[6] A value of 2.6 years was provisionally communicated to Dr. G. T. Seaborg during the course of this work and has subsequently appeared in the review article of Seaborg and Perlman (Rev. Mod. Phys. **20**, 585 (1948)).

Reprinted from THE PHYSICAL REVIEW, Vol. 86, No. 6, 1047–1048, June 15, 1952
Printed in U. S. A.

Reprinted by permission of the American Institute of Physics.

Secondary Electron Spectrum of Pr^{142}†

ERLING N. JENSEN, L. JACKSON LASLETT, AND D. J. ZAFFARANO
Institute for Atomic Research and Department of Physics, Iowa State College, Ames, Iowa

(Received April 21, 1952)

IN a previous publication concerning the radiations of Pr^{142}, the authors[1] reported the presence of one gamma-ray, having an energy of 1.57_6 Mev, and two beta-groups, with maximum energies of 2.15_4 Mev and 0.63_6 Mev. Other investigators[2] have reported a number of low energy gamma-rays for Pr^{142}. In the original work of the present authors[1] a search was made for low energy gamma-rays, but none was found. If these gamma-rays existed, however, they would have been observed as photoelectric lines superposed on a broad distribution of electrons which was ascribed to secondary electrons produced by bremsstrahlung.

Dr. Alburger[3] of Brookhaven National Laboratory has suggested that the broad distribution of electrons ascribed to secondary electrons produced by bremsstrahlung, as reported in our original paper,[1] might be due to beta-rays that have passed through part of the Lucite holder and then scattered from another part of the source holder. On repeating the experiment with $Sr^{90}-Y^{90}$ it was found that a substantial fraction, but not all, of the electron distribution attributed to bremsstrahlung was, in fact, due to scattered beta-particles, as suggested.

It seemed worthwhile, therefore, to re-examine the secondary electron spectrum of Pr^{142} in order to make a search for low energy gamma-rays under more favorable circumstances and also to determine the existence or nonexistence of an appreciable number of secondary electrons produced by bremsstrahlung. A sample of spectrographically pure (contaminants of Nd, La, and Ce less than 0.1 percent) Pr_6O_{11} made available through the courtesy of Dr. F. H. Spedding and Mr. T. A. Butler of this laboratory was irradiated in the Argonne pile and then examined with a thin-lens spectrometer[4] modified to incorporate ring focusing.[5]

The irradiated praseodymium was placed in a brass holder and covered with a copper cap, of surface density 2.92 g/cm², on which was fastened a uranium foil of surface density 42 mg/cm². The secondary electron spectrum obtained with this source is shown by the solid line in Fig. 1. The insert in Fig. 1 shows a scale drawing of the arrangement of the Pr^{142}, brass holder, copper cap, and uranium foil. Spectra were obtained with and without the solder ring on the shoulder of the brass holder and no change in the shape of the spectrum was observed. Only one gamma-ray was observed, having an energy of 1.57_6 Mev as reported previously.[1]

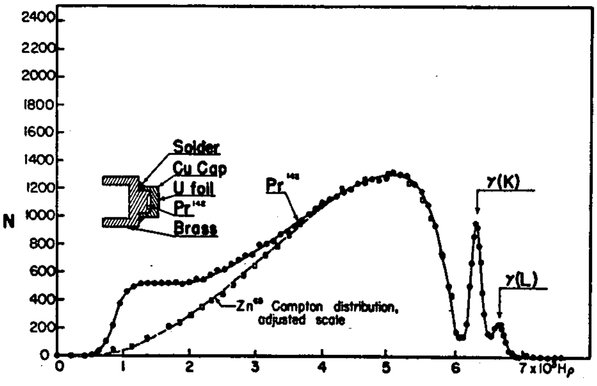

FIG. 1. The solid line, given by the circles, is the secondary electron spectrum of Pr^{142} as obtained with the arrangement shown in the insert. The broken line, given by squares, was obtained from the Compton distribution produced by the Zn^{65} gamma-ray (1.12 Mev) normalized to the Compton distribution from Pr^{142}. N is the number of counts per minute.

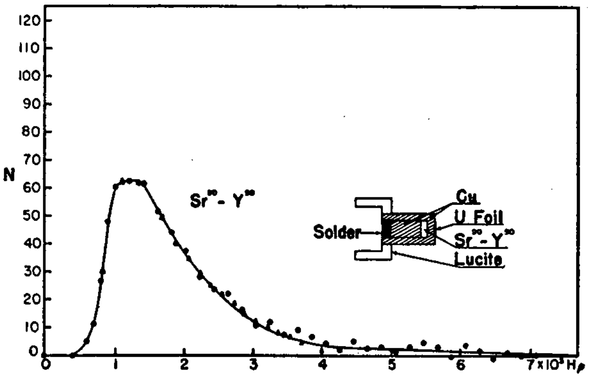

FIG. 2. The curve given by the solid circles is the secondary electron spectrum from the copper capsule and uranium foil, as produced by bremsstrahlung arising in the copper capsule due to the absorption the of beta-particles from Sr^{90}-Y^{90}. The arrangement of source, copper capsule, and uranium foil is shown in the insert. N is the number of counts per minute for this distribution. The triangles were obtained by subtracting the two curves shown in Fig. 1 and multiplying by an appropriate normalizing factor.

Since no low energy gamma-rays were observed and the material surrounding the source was sufficient to absorb completely electrons with an energy greater than 5 Mev, it was concluded that the broad distribution of electrons observed at the low energy end of the spectrum, in addition to the expected Compton distribution, is due to secondary electrons that are produced in the copper cap and uranium foil by the bremsstrahlung arising in the copper cap as a result of the absorption of the beta-particles.

As a check of the foregoing interpretation for the broad distribution of electrons at the low energy end of the spectrum shown in Fig. 1, a source of $Sr^{90}-Y^{90}$ was placed in a copper capsule to which was fastened the same uranium foil as that used with the Pr^{142} source. This copper capsule had the same diameter as the copper cap used with the praseodymium source. The $Sr^{90}-Y^{90}$ source, which is gamma-free and emits beta-particles with a maximum energy[6] (2.23 Mev) close to that for Pr^{142}, was found to give a secondary electron spectrum as shown by the circles and solid line in Fig. 2. The insert in Fig. 2 shows a scale drawing of the arrangement of source, copper capsule, and uranium foil. The end of the capsule on which the uranium foil was fastened had a surface density of 2.43 g/cm² while the sides of the capsule had a surface density of 2.12 g/cm². This was sufficient to absorb completely electrons with an energy of about 4 Mev.

The broken line shown in Fig. 1 was obtained from the Compton distribution produced by the Zn^{65} gamma-ray (1.12 Mev).[7] This was obtained under conditions similar to those for the Compton distribution for Pr^{142}. The scale of the Zn^{65} curve has been adjusted to match the Pr^{142} Compton distribution at the maximum ordinate and at the Compton high energy "edge." The triangles shown in Fig. 2 were obtained by substracting the two curves shown in Fig. 1 and normalizing the ordinates. It may be seen that the two secondary electron distributions produced by bremmstrahlung are in good agreement. It appears, then, that the broad distribution of electrons at the low energy end of the Pr^{142} spectrum shown in Fig. 1 is due to bremsstrahlung.

The secondary electron spectrum of Pr^{142}, shown in Fig. 1, is therefore regarded as a composite of the photoelectrons and Compton electrons arising from a single gamma-ray, plus the electrons produced by bremsstrahlung. This conclusion, accordingly, in no way alters the final results and conclusions regarding the radiations from Pr^{142} nor the decay scheme reported in the previous publication.[1]

The authors wish to express their appreciation to Messrs. Earl W. McMurry and James T. Jones, Jr. for their assistance in obtaining part of the data.

---

† Contribution No. 183 from the Institute for Atomic Research and Department of Physics, Iowa State College, Ames, Iowa. Work was performed in the Ames Laboratory of the AEC.

[1] Jensen, Laslett, and Zaffarano, Phys. Rev. **80**, 862 (1950).

[2] C. E. Mandeville, Phys. Rev. **75**, 1287 (1949); Cork, Schreffler, and Fowler, Phys. Rev. **74**, 1657 (1948); E. R. Rae, Proc. Phys. Soc. (London) 63A, 292 (1950).

[3] D. E. Alburger (private communication).

[4] Jensen, Laslett, and Pratt, Phys. Rev. **75**, 458 (1949).

[5] Pratt, Boley, and Nichols, Rev. Sci. Instr. **22**, 92 (1951); Keller, Koenigsberg, and Paskin, Rev. Sci. Instr. **21**, 713 (1950).

[6] E. N. Jensen and L. J. Laslett, Phys. Rev. **75**, 1949 (1949).

[7] Jensen, Laslett, and Pratt, Phys. Rev. **76**, 430 (1949).

Reprinted from THE JOURNAL OF THE ACOUSTICAL SOCIETY OF AMERICA, Vol. 28, No. 4, 724, July, 1956
Copyright, 1956 by the Acoustical Society of America.
Printed in U. S. A.

Reprinted by permission of the American Institute of Physics.

On the Electromagnetic Analogy to Sound Propagation

L. JACKSON LASLETT*
Department of Physics and Institute for Atomic Research,
Iowa State College, Ames, Iowa
(Received April 8, 1956)

KRAICHNAN[1] has developed an interesting correspondence between the paths of sound rays in fluids undergoing shear flow and the trajectories of charged particles in magnetic fields. To establish this analogy one assumes (i) the eddy size to be large compared to the sound wavelength and (ii) the velocity (w) of the fluid flow to be small in comparison to the speed of sound (c). Kraichnan's development then makes use of the wave equation for sound propagation and the Hamilton-Jacobi theory of particle dynamics, while referring in the discussion to the associated principles of Fermat and of least action. It is felt that the following brief derivation, which proceeds directly from these two variational principles, may be of interest.

For the ray description of sound propagation, one may employ Fermat's principle

$$\delta\int\frac{ds}{c+w\cos(\mathbf{w},d\mathbf{s})}=0; \tag{1}$$

for $w \ll c$, this becomes

$$\delta\int(ds-d\mathbf{s}\cdot\mathbf{w}/c)=0. \tag{2}$$

Similarly, for the *trajectory* of a particle of charge q (emu or mks units) in a magnetic field $\mathbf{B}=\nabla\times\mathbf{A}$, the principle of least action may be applied in the form

$$\delta\int(\mathbf{p}+q\mathbf{A})\cdot d\mathbf{s}=0, \tag{3}$$

where $\mathbf{p}$, denoting the *mechanical* momentum, is parallel to $d\mathbf{s}$ and is constant in magnitude (since no work is done on the particle). This last equation may then be written

$$\delta\int(ds+q\,d\mathbf{s}\cdot\mathbf{A}/p)=0. \tag{4}$$

There is an evident correspondence between Eqs. (2) and (4) if

$$\mathbf{w}/c=-q\mathbf{A}/p. \tag{5}$$

Sound rays are accordingly seen to be influenced by the fluid motion if $\nabla\times\mathbf{w}\neq0$; the relation between the vorticity ($\mathbf{\Psi}$) of the fluid motion and the magnetic field governing the analogous particle trajectory is obtained by forming the curl of Eq. (5). We thus find

$$\mathbf{\Psi}/c=-q\mathbf{B}/p \tag{6}$$

or

$$\begin{aligned}\mathbf{B}&=-(p/q)(\mathbf{\Psi}/c)\\&=-[B\rho](\mathbf{\Psi}/c),\end{aligned} \tag{7}$$

where $[B\rho]$ denotes the magnetic rigidity of the charged particle whose trajectory is under consideration. This result is identical with that of Kraichnan, who considers a charge $e=c_0q$.

The writer would like to express his appreciation to Dr. K. U. Ingard and Mr. W. W. Lang for their interest in the development presented here.

---

* Presently at the University of Illinois, on leave from Iowa State College, to work with the Midwestern Universities Research Association.

[1] R. H. Kraichnan, J. Acoust. Soc. Am. 27, 527 (1955).

Reprinted from THE PHYSICAL REVIEW, Vol. 102, No. 2, 590–591, April 15, 1956
Printed in U. S. A.

Reprinted by permission of the American Institute of Physics.

Attainment of Very High Energy by Means of Intersecting Beams of Particles

D. W. KERST,[*] F. T. COLE,[†] H. R. CRANE,[‡] L. W. JONES,[‡] L. J. LASLETT,[§] T. OHKAWA,[||] A. M. SESSLER,[¶] K. R. SYMON,[**] K. M. TERWILLIGER,[‡] AND NILS VOGT NILSEN[††]
Midwestern Universities Research Association,[‡‡] *University of Illinois, Champaign, Illinois*

(Received January 23, 1956)

IN planning accelerators of higher and higher energy, it is well appreciated that the energy which will be available for interactions in the center-of-mass coordinate system will increase only as the square root of the energy of the accelerator. The possibility of producing interactions in stationary coordinates by directing beams against each other has often been considered, but the intensities of beams so far available have made the idea impractical. Fixed-field alternating-gradient accelerators[1] offer the possibility of obtaining sufficiently intense beams so that it may now be reasonable to reconsider directing two beams of approximately equal energy at each other. In this circumstance, two 21.6-Bev accelerators are equivalent to one machine of 1000 Bev.

The two fixed-field alternating-gradient accelerators could be arranged so that their high-energy beams circulate in opposite directions over a common path in a straight section which is common to the two accelerators, as shown in Fig. 1. The reaction yield is proportional to the product of the number of particles which can be accumulated in each machine. As an example, suppose we want 10^7 interactions per second from 10-Bev beams passing through a target volume 100 cm long and 1 cm^2 in cross section. Using 5×10^{-26} cm^2 for the nucleon interaction cross section, we find that we need 5×10^{14} particles circulating in machines of radius 10^4 cm.

There is a background from the residual gas proportional to the number of particles accelerated. With 10^{-6} mm nitrogen gas, we would have 15 times as many encounters with nitrogen nucleons in the target volume as we would have with beam protons. Since the products of the collisions with gas nuclei will be in a moving coordinate system, they will be largely confined to the orbital plane. Many of the desired *p-p* interaction products would come out at large angles to the orbital plane since their center of mass need not have high speed in the beam direction, thus helping to avoid background effects.

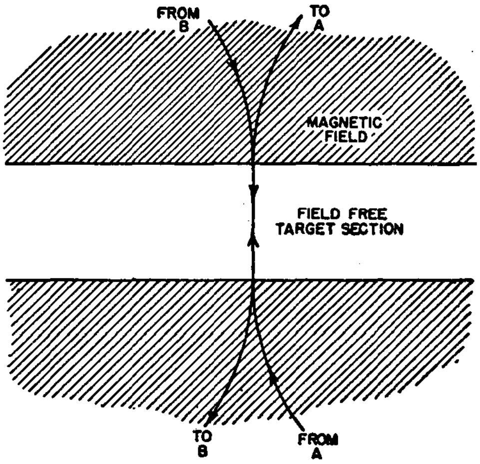

FIG. 1. The target straight section. *B* and *A* can be adjacent or concentric fixed-field alternating-gradient accelerators.

Multiple scattering at 10^{-6} mm pressure is not troublesome above one Bev; but beam life is limited by nuclear interaction with residual gas to ~1300 seconds. Consequently, in about 1000 seconds the high-energy beam of 5×10^{14} particles must be established in each accelerator. The fixed-field nature of the accelerator allows it to contain beams of different energy simultaneously. It may be possible to obtain this high beam current in this time by using $\sim10^3$ successive frequency modulation cycles of radio-frequency acceleration, each cycle bringing up 5×10^{11} particles. It is encouraging to learn that Alvarez and Crawford[2] succeeded in building up a ring of protons by successively bringing up several groups of particles to the same final energy by frequency modulation in the 184-in. Berkeley cyclotron.

The number of particle groups which may be successively accelerated without leading to excessive beam spread can be estimated by means of Liouville's theorem.[3] One can readily convince himself that there is adequate phase space at high energy to accommodate the necessary number, N, of particle groups. Assume for simplicity that synchrotron and betatron phase space are separately conserved, so that for the former

$$(\Delta p)_f(\Delta S)_f = N(\Delta p)_i(\Delta S)_i,$$

where ΔS and Δp are the arc length and momentum spread at injection and final energy. Then, employing the fact that $P\sim R^{k+1}$, where R is the radius and k is the field index, one obtains

$$N=2(k+1)(\Delta R/R)(p_f/p_i)(\Delta S_f/\Delta S_i)(E_i/\Delta E_i).$$

Using typical numbers such as

$$(p_f/p_i)\sim 100,\quad k\sim 100,\quad R\sim 0.5\text{ cm},$$
$$R\sim 10^4\text{ cm},\quad (\Delta E_i/E_i)\sim 10^{-3},$$

one finds that there is room for $N\sim 10^3$ frequency-modulation cycles.

The betatron phase space available is so large that it cannot be filled in one turn by the type of injectors used in the past which can inject 10^{11} particles. Thus there is the possibility of attaining and exceeding the yield used for this example by improving injection.

The more difficult problem of whether one can, in fact, use all of the synchrotron and betatron phase space depends in detail upon the dynamics of the proposed scheme and this is presently under study.

---

[*] University of Illinois, Urbana, Illinois.

[†] State University of Iowa, Iowa City, Iowa.

[‡] University of Michigan, Ann Arbor, Michigan.

[§] Iowa State College, Ames, Iowa.

[‖] University of Tokyo, Tokyo, Japan.

[¶] The Ohio State University, Columbus, Ohio.

[**] University of Wisconsin, Madison, Wisconsin.

[††] Norwegian Institute of Technology, Trondheim, Norway.

[‡‡] Supported by the National Science Foundation.

[1] Keith R. Symon, Phys. Rev. 98, 1152(A) (1955); L. W. Jones *et al.*, Phys. Rev. 98, 1153(A) (1955); K. M. Terwilliger *et al.*, Phys. Rev. 98, 1153(A) (1955); D. W. Kerst *et al.*, Phys. Rev. 98, 1153(A) (1955).

[2] L. Alvarez and F. S. Crawford, private communication.

[3] We are indebted to Professor E. Wigner who pointed out to us the importance of this consideration.

Reprinted from Science, March 18, 1966, Vol. 151, No. 3716, pages 1384-1385

Reprinted by permission
from SCIENCE.

Rotation of Mercury: Theoretical Analysis of the Dynamics of a Rigid Ellipsoidal Planet

Abstract. *The second-order nonlinear differential equation for the rotation of Mercury implies locked-in motion when the period is within the range*

$$\frac{2\mathrm{T}}{3}\left[1-\lambda\cos\frac{2\pi\mathrm{t}}{\mathrm{T}}\pm\frac{2}{3}\ (21\lambda\mathrm{e}/2)^{\frac{1}{2}}\right]$$

where e *is the eccentricity and* T *is the period of Mercury's orbit, the time* t *is measured from perihelion, and* λ *is a measure of the planet's distortion. For values near* 2T/3, *the instantaneous period oscillates about* 2T/3 *with period* $(21\lambda\mathrm{e}/2)^{-\frac{1}{2}}\mathrm{T}$.

Radar (*1*) and visual (*2*) observations of the planet Mercury indicate a rotation period T_r = 58.4 ± 0.4 days, close to ⅔ of the orbit period T = 87.97 days. Colombo (*3*) and Liu and O'Keefe (*4*) have surmised that a stable "locked-in" motion of this type can occur as a result of the inverse-cube term in the planetary potential (*5, 6*) that arises for a body with unequal moments of inertia in the orbital plane. The existence of such a solution to the equations that govern the rotation of a rigid distorted planet has been demonstrated by Liu and O'Keefe by means of digital computations. In this report we present approximate analytic formulas that may afford further physical insight into the character of locked-in motion, that could facilitate the interpretation of observational data, and that indicate the dependence of the results upon the various parameters of the model. For simplicity, and for clarity in exposition, the analysis is carried to no higher order than is required to exhibit the salient features of the phenomenon.

The differential equation for the orientation, θ, of the planet is given by equation 4 of the report by Liu and O'Keefe (*4*). In terms of the variable $\tau = 2\pi t/T$ it becomes, after insertion of the equation for the Keplerian orbit (*7*) of eccentricity e,

$$\frac{d^2\theta}{d\tau^2}+\frac{3}{2}\lambda\left[\frac{1+e\cos f(\tau)}{1-e^2}\right]^3\times$$
$$\sin 2[\theta-f(\tau)]=0 \qquad (1)$$

with the largest of the principal moments of inertia (C) taken perpendicular to the orbital plane, $\lambda \equiv (B-A)/C$ measuring the difference between the two smaller moments of inertia (B and A), and f denoting the true anomaly. (Since damping effects have been ignored in this analysis, Eq. 1 is derivable from a simple Hamiltonian function, with periodic coefficients, in which $p = d\theta/d\tau$ is the canonical momentum conjugate to θ, and Liouville's theorem concerning the conservation of phase-space area applies to the variables θ and p.)

Substitution of the explicit variation of the true anomaly with time, as given by

$$f(\tau)=\tau+2e\sin\tau \qquad (2)$$

through the first-order term in e, converts Eq. 1 to the approximate form

$$\frac{d^2\theta}{d\tau^2}+\frac{3}{2}\lambda\Big[(1+3e\cos\tau)\sin 2(\theta-\tau)-$$
$$4e\sin\tau\cos 2(\theta-\tau)\Big]=0 \qquad (3)$$

which forms the basis of the remainder of our analysis. [It is noted, from Eq. 2, that τ is to be regarded as measured from the time of perihelion passage, and θ is the angle made by the smallest of the moments of inertia (A) with the major axis of the orbit.] One expects that there may be periodic (locked-in) solutions to Eqs. 1 or 3 that are stable, in the sense that neighboring solutions describe oscillatory motion about these periodic solutions.

We consider, specifically, solutions for which

$$d\theta/dt \approx (3/2)(2\pi/T)$$

and write

$$\theta=\frac{3}{2}\tau+\eta, \qquad (4)$$

so that Eq. 3 becomes

$$\frac{d^2\eta}{d\tau^2}+\frac{3}{2}\lambda\Big[(\cos\tau+\frac{7}{2}e-$$
$$\frac{1}{2}e\cos 2\tau)\sin 2\eta+$$
$$(\sin\tau-\frac{1}{2}\ e\sin 2\tau)\cos 2\eta\Big]=0 \qquad (5)$$

When η is small, Eq. 5 may be linearized, to assume the form

$$\frac{d^2\eta}{d\tau^2}+\frac{3}{2}\lambda\ (2\cos\tau+7e-e\cos 2\tau)\eta$$
$$=-\frac{3}{2}\lambda(\sin\tau-\frac{1}{2}e\sin 2\tau) \qquad (6)$$

For $\lambda^2 \ll 1$, an approximate particular integral to the inhomogeneous Eq. 6 is readily obtained, and the solution to the corresponding linear homogeneous equation may be derived (*8*) by ignoring terms of average value zero in the coefficient of η. The solution thus includes a periodic motion, of period T, and a long-period oscillation of amplitude α_0:

$$\eta=\frac{3}{2}\lambda(\sin\tau-\frac{1}{8}e\sin 2\tau)+$$
$$\alpha_0\sin\left[(\frac{21}{2}\lambda e)^{\frac{1}{2}}\tau+\alpha_1\right] \qquad (7a)$$

or, for $\alpha_0 \ll \pi$,

$$\theta=\frac{3\pi t}{T}+\frac{3}{2}\lambda(\sin\frac{2\pi t}{T}-\frac{1}{8}e\sin\frac{4\pi t}{T})+$$
$$\alpha_0\sin\left[(\frac{21}{2}\lambda e)^{\frac{1}{2}}\frac{2\pi t}{T}+\alpha_1\right] \qquad (7b)$$

where α_0 and α_1 are arbitrary constants.

If α_0 is not small, so that the slow excursions of η preclude linearization, a similar averaging of the coefficient of $\sin 2\eta$ in Eq. 5 suggests that these oscillations are essentially described by an equation of the form applicable to the motion of a physical pendulum:

$$\frac{d^2\eta}{d\tau^2}+\frac{21}{4}\lambda e\sin 2\eta=0 \qquad (8)$$

for which one may write the first integral

$$\frac{1}{2}(\frac{d\eta}{dt})^2-\frac{21}{8}\lambda e\cos 2\eta=c \qquad (9)$$

where c is a constant. With the excursions of η limited to $\pm\pi/2$ for oscillatory motion, the *maximum* value that

$d\eta/d\tau$ can assume for locked-in motion (*9*) occurs when $\eta = 0$, and is

$$|d\eta/d\tau|_{\max} = (\tfrac{21}{2}\lambda e)^{\frac{1}{2}}$$

With inclusion of the contributions from the first terms on the right-hand side of Eq. 7b, therefore, the values of $d\theta/dt$ for locked-in motion are expected to lie between the limits

$$\left[\frac{d\theta}{dt}\right]_{\max,\min} = \frac{3\pi}{T}\left[1 + \lambda\cos\frac{2\pi t}{T} \pm \frac{2}{3}(\frac{21}{2}\lambda e)^{\frac{1}{2}}\right] \quad (10)$$

where we have neglected the term proportional to λe.

The foregoing analysis serves to confirm that locked-in rotational motion with a period approximately 2/3 the period of revolution is dynamically possible. The form of the solution shown in Eq. 7b suggests, however, that observations of the rotation will indicate rates that vary during the course of a planetary year and that, in addition, slower variations of the rotational rate may occur with a period given by

$$T_{\mathrm{lib}} = (\tfrac{21}{2}\lambda e)^{-\frac{1}{2}}\,T \qquad (11)$$

when the amplitude (α_0) of this libration is not large. An expression of the form given by Eq. 7b may be useful for interpretation of data obtained by the sequential observation of surface features on the planet. More simply, the *instantaneous* periods—as could be inferred from radar observations—would be (by differentiation of Eq. 7b when the term proportional to λe is neglected)

$$T_{\mathrm{i}} = \frac{2\pi}{d\theta/dt}$$

$$= \frac{2}{3}\left\{1 - \lambda\cos\frac{2\pi t}{T} - \frac{2}{3}\alpha_0(\tfrac{21}{2}\lambda e)^{\frac{1}{2}} \times \cos\left[(\tfrac{21}{2}\lambda e)^{\frac{1}{2}}\frac{2\pi t}{T} + \alpha_1\right]\right\}T \qquad (12)$$

for α_0 small, and, for any α_0 compatible with locked-in motion, would lie between the limits obtained from Eq. 10:

$$\left[T_{\mathrm{i}}\right]_{\max,\min} = \frac{2}{3}\left[1 - \lambda\cos\frac{2\pi t}{T} \mp \frac{2}{3}(\tfrac{21}{2}\lambda e)^{\frac{1}{2}}\right]T \quad (13)$$

For favorable values of α_0 a determination of λ may be feasible through observation of the slow libratory motion, with a period close to that expressed by Eq. 11, that is represented by the last term of Eq. 12. If, however, α_0 is very small—as could well result from the action of damping mechanisms—the term

$$-\frac{2}{3}\lambda\cos\frac{2\pi t}{T}$$

in Eq. 12 will represent the larger contribution to the variation of the instantaneous period.

Substitution of the values $T = 87.97/365$ yr, $e = 0.2$, and $\lambda = 5 \times 10^{-5}$, as suggested by Liu and O'Keefe (*4*), into Eq. 11 leads to a libration period $T_{\mathrm{lib}} = 23.5$ yr for small-amplitude variations, in substantial agreement with their computational results. Correspondingly, from the last term of Eq. 13, the maximum variation of the instantaneous period of rotation that could arise from this libratory motion would be approximately ± 0.40 day, in good agreement with recent computational results of Liu and O'Keefe (*10*). It is highly unlikely, of course, that such large variations are now actually occurring, because of the damping that would have resulted from tidal effects.

Although the detailed results presented in this report have been with reference to motion for which the rotation period is close to 2/3 the period of revolution, the existence of other stable modes of locked-in motion should not be overlooked. The possible range of variation for the rotational speed in general will be substantially smaller for the higher-order modes, for reasonable values of the parameter λ, and this feature will have significant implications concerning the magnitude of the damping present at times when the speed of planetary rotation may have been considerably greater than that now observed. Lower limits, which depend on λ, can be set to the rate of decrease of the rotational energy through the agency of damping if the rotational motion has passed through the higher-order modes during the past history of the planet. Similarly, an upper limit can be set on the amount of damping that will permit the rotation to remain locked in to the mode analyzed in this report. Other work (*11*) indicates, moreover, that damping torques acting at present would shift the phase of the periodic solutions presented here, and this result suggests that information concerning the current magnitude of such torques may be inferred from more detailed observation of the rotational motion.

L. JACKSON LASLETT
ANDREW M. SESSLER
Lawrence Radiation Laboratory,
University of California, Berkeley

References and Notes

1. G. H. Pettengill and R. B. Dyce, *Nature* **206**, 1240 (1965).
2. W. E. McGovern, S. H. Gross, S. I. Rasool, *ibid.* **208**, 375 (1965).
3. G. Colombo, *ibid.* **208**, 575 (1965).
4. H. Liu and J. A. O'Keefe, *Science* **150**, 1717 (1965).
5. S. F. Peale and T. Gold, *Nature* **206**, 1240 (1965).
6. P. Goldreich, *ibid.* **208**, 375 (1965).
7. This ignores the (small) effect of the nonuniform rotation (as computed in this paper) upon the orbital motion. Interestingly enough, it leads, most dramatically, to a perihelion motion which contains both a secular term and a term with period $(21\lambda e/2)^{-\frac{1}{2}}T$. These terms are small—of the same order as the perihelion advance present when $A = B \neq C$ —even when compared with the general relativistic perihelion advance of 43.8 seconds of arc per century.
8. K. R. Symon *et al.*, *Phys. Rev.* **103**, 1837, 1858 (1956).
9. This result is $2/\pi$ times as great as the corresponding value that would have been inferred from use of $\alpha_0 = \pi/2$ in the solution given by Eq. 7 for the linearized problem. The period of these slow oscillations, moreover, will not be that suggested by the last term in Eqs. 7a and 7b but will approach infinity as the amplitude approaches $\pi/2$.
10. We are grateful for the opportunity to discuss Liu and O'Keefe's work with them, and we appreciate their courtesy in making some of their recent computational results available to us.
11. L. J. Laslett and A. M. Sessler, in preparation.
12. Work supported by the AEC. We thank Penelope A. Collom for assistance with numerical checks.

21 January 1966

Reprinted from AMERICAN JOURNAL OF PHYSICS, Vol. 34, No. 8, 702–703, August 1966
Printed in U. S. A.

Reprinted by permission from the American Journal of Physics, Copyright 1966 by American Association of Physics Teachers.

Trajectory for Minimum Transit Time Through the Earth

L. JACKSON LASLETT
Lawrence Radiation Laboratory and Department of Physics,*
University of California, Berkeley, California,

THE tantalizing theoretical possibility of very rapid transit between points on the Earth's surface by gravitational fall through frictionless tunnels[1-3] has recently been discussed by Cooper.[4] The differential equation for the plane curve leading to a minimum transit time between two given points on the surface is given in Cooper's note, and the results a of computer solution are presented graphically. The differential equation may be written conveniently in a form that expresses the dependence of θ as a function of r, and in these terms it becomes

$$(d/dr)\{r^2[R^2-r^2]^{-\frac{1}{2}}[1+r^2(d\theta/dr)^2]^{-\frac{1}{2}}(d\theta/dr)\}=0. \quad (1)$$

A solution to Eq. (1), symmetric about $\theta=0$, may then be obtained as

$$\theta=\pm\frac{r_0}{R}\int_{r_0}^{r}\frac{1}{r}\left(\frac{R^2-r^2}{r^2-r_0^2}\right)^{\frac{1}{2}}dr \quad (2a)$$

$$=\pm\left\{\sin^{-1}\left[\frac{R}{r}\left(\frac{r^2-r_0^2}{R^2-r_0^2}\right)^{\frac{1}{2}}\right]-\frac{r_0}{R}\sin^{-1}\left(\frac{r^2-r_0^2}{R^2-r_0^2}\right)^{\frac{1}{2}}\right\}, \quad (2b)$$

in which the constant of integration r_0 may be identified with the radius of closest approach to the Earth's center.

For class presentation, Eq. (1) is most directly obtained from the variational statement

$$\delta\int_A^B ds/v=\delta\int_A^B [(g/R)(R^2-r^2)]^{-\frac{1}{2}}[(dr)^2+(rd\theta)^2]^{\frac{1}{2}}=0 \quad (3)$$

[in which we neglect the rotation of the earth and employ the speed acquired from the potential-energy change $\Delta V=-\frac{1}{2}mg(R^2-r^2)/R$] by writing the Euler–Lagrange equation that results from regarding r as the *independent* variable. The first integral

$$r^2[R^2-r^2]^{-\frac{1}{2}}[r^2+(dr/d\theta)^2]^{-\frac{1}{2}}=r_0[R^2-r_0^2]^{-\frac{1}{2}} \quad (4)$$

then follows immediately, and the resulting explicit expression for $d\theta/dr$ may be integrated as shown by Eqs. (2a,b). The solution given by Eq. (2b) corresponds to a diametrical trajectory ($\theta=\pm\pi/2$) in the limiting case for which r_0 vanishes.

For journeys between points separated by more than a few kilometers, very high maximum speeds will be attained on a path of the form given by Eq. (2b). An interesting problem for the student is an evaluation of the "number of g's" experienced by a passenger (or the force with which he presses on the seat of the train) at the lowest point of the trajectory. In addition, an elementary evaluation of the integral in Eq. (3) provides the transit time as a function of r_0.

---

* Work assisted by the U. S. Atomic Energy Commission.

[1] L. K. Edwards, Sci. American **213**, 30 (Aug. 1965).

[2] M. Gardner, Sci. American **213**, 10 (Sept. 1965).

[3] See, L. Lessing, Fortune **71**, 124 (Apr. 1965).

[4] P. W. Cooper, Am. J. Phys. **34**, 68 (1966).

LAWRENCE BERKELEY LABORATORY
TECHNICAL INFORMATION DEPARTMENT
UNIVERSITY OF CALIFORNIA
BERKELEY, CALIFORNIA 94720